Научном већу Института за физику у Београду

Предмет: Молба за покретање поступка за избор др Илије Симоновића у звање научни сарадник

У складу са критеријумима прописаним од стране Министарства за просвету, науку и технолошки развој за стицање научног звања научни сарадник, као и са критеријумима прописаним од стране Правилника о поступку и начину вредновања, и квантитативном исказивању научно-истраживачких резултата истраживача, молим Научно веће Института за физику у Београду да покрене поступак за мој избор у звање научни сарадник.

У прилогу достављам:

1. Мишљење руководиоца лабораторије

2. Стручну биографију

3. Преглед научне активности кандидата

4. Елементе за квалитативну оцену научног доприноса са доказима

5. Елементе за квантитативну оцену научног доприноса

6. Списак објављених радова и других публикација

7. Податке о цитираности

8. Уверење о стеченом високом образовању трећег степена докторских студија

9. Копије објављених радова и других публикација

15. октобар 2020.

Београд,

С поштовањем,

др Илија Симоновић

Научном већу Института за физику у Београду

Предмет: Мишљење руководиоца Центра о избору др Илије Симоновића у звање научни сарадник

Др Илија Симоновић је запослен у Лабораторији за неравнотежне процесе и примену плазме Института за физику у Београду. У истраживачком раду бави се теоријом ројева наелектрисаних честица у гасовима и течностима као и флуидним моделима стримера у овим срединама. С обзиром да испуњава све предвиђене услове у складу са Правилником о поступку, начину вредновања и квантитативном исказивању научноистраживачких резултата истраживача МПНТР, сагласан сам са покретањем поступка за избор др Илије Симоновића у звање научни сарадник.

За састав комисије за избор др Илије Симоновића у звање научни сарадник предлажем:

(1) др Саша Дујко, научни саветник, Институт за физику у Београду,

(2) др Данко Бошњаковић, научни сарадник, Институт за физику у Београду,

(3) проф. др Ђорђе Спасојевић, редовни професор Физичког факултета Универзитета у Београду.

др Гордана Маловић

научни саветник

руководилац Лабораторије за неравнотежне процесе и примену плазме

Биографија

Образовање:

Илија Симоновић рођен је 31. јула 1989. године у Крагујевцу, где је завршио основну и средњу школу. Школске 2008/2009. године је уписао основне студије на Физичком факултету Универзитета у Београду, смер Теоријска и експериментална физика. Завршио је основне студије школске 2011/2012. године са просечном оценом 9.85. Студентски пројекат под називом Градијентне теорије на некомутативном простору урадио је на Физичком факултету под менторством проф. др Марије Димитријевић. Мастер студије је уписао школске 2012/2013. и завршио их је са просечном оценом 10.0. Мастер рад под насловом Некомутативна гравитација на Мојаловом простору одбранио је 1. октобра 2013. године, под менторством проф. др Воје Радовановића. Докторске студије на Физичком факултету Универзитета у Београду уписао је школске 2013/2014. године на смеру Физика јонизованог гаса, плазме и технологија плазме.

Радно искуство:

Школске 2012/2013. године држао је рачунске вежбе, као сарадник у настави на предмету Електродинамика 1 и Електродинамика 2 код проф. др Воје Радовановића на Физичком факултету, Универзитета у Београду.

Од октобра 2013. године запослен је као истраживач-приправник у Лабораторији за гасну електронику Института за физику у Београду. У звање истраживач-сарадник изабран је 2016. године. Под менторством др Саше Дујка, био је ангажован на пројекту Фундаментални процеси и примене транспорта честица у неравнотежним плазмама, траповима и наноструктурама Министарства науке, просвете и технолошког развоја (бр. ОИ171037). Руководилац овог пројекта је био академик др Зоран Љ. Петровић. Научна активност кандидата везана је за проучавање транспортних коефицијената трећег реда за ројеве наелектрисаних честица, као и за изучавање транспорта електрона и динамике стримера у хомогеној флуидној средини. Докторску дисертацију под насловом Кинетички и флуидни модели неравнотежног транспорта електрона у гасовима и течностима одбранио је 30. септембра 2020. године на Физичком факултету у Београду.

Преглед научне активности

Научна активност и допринос Илије Симоновића везани су за изучавање транспорта наелектрисаних честица у неутралним гасовима и течностима у оквиру транспортне теорије ројева, као и испитивање динамике формирања и простирања стримера у овим срединама применом флуидних модела. Његово истраживање је у току израде докторске дисертације било фокусирано на три главне тематске целине. Прва тематска целина односи се на транспортне коефицијенте трећег реда за електроне у гасовима. Другу тематску целину чини транспорт електрона у течном аргону, течном криптону и течном ксенону. Трећа тематска целина односи се на транзицију електронске лавине у негативан стример и простирање стримера у овим течностима.

У оквиру прве тематске целине је одређена структура транспортног тензора трећег реда у свим конфигурацијама електричног и магнетског поља применом методе групних пројектора. При томе се структура у одсуству магнетског поља слаже са резултатима који су познати у литератури, док је структура транспортног тензора трећег реда у присуству магнетског поља први пут одређена у оквиру рада кандидата. Одређена структура је проверена на основу симетријских особина момената функције расподеле у методу више чланова за решавање Болцманове једначине.

Физичка интерпретација транспортног тензора трећег реда је пажљиво анализирана на основу флукс градијентне релације и приближног решења генералисане дифузионе једначине у којој је присутан овај тензор. Посебан акценат стављен је на утицај спољашњег електричног поља и колизионе фреквенце наелектрисаних честица роја на знак појединачних компоненти транспортног тензора трећег реда.

Вредности компоненти транспорног тензора трећег реда су одређене за електроне у пет моделних гасова и више атомских и молекуларних гасова, као и за позитроне у три молекуларна гаса, применом Монте Карло симулација и метода више чланова за нумеричко решавање Болцманове једначине. Резултати ове две методе се одлично слажу, што потврђује валидност коришћених техника. На основу ових резултата је испитан утицај еластичних, нееластичних и неконзервативних судара на транспортни тензор трећег реда. Профили зависности компоненти транспортног тензора трећег реда од спољашњег електричног поља су испитани на основу средње енергије честица роја и пресека за њихове сударе са честицама позадинског гаса, као и на основу примећене корелације између лонгитудиналне компоненте овог тензора и лонгитудиналне дифузије.

У другој тематској целини је проучаван транспорт електрона у течном аргону, течном криптону и течном ксенону применом Монте Карло симулација. Кохерентно еластично расејање на ниским енергијама је репрезентовано уз помоћ три ефективна сударна процеса, који добро репрезентују средњи трансфер енергије и импулса при кохерентном расејању. Пресек за ексцитовање електрона из валентне у проводну зону је апроксимиран одговарајућим пресеком за јонизацију изолованог атома, чији праг је снижен на вредност одговарајућег зонског процепа. Разматрано је

више различитих случајева за репрезентовање нееластичних судара у течној фази, како би се испитао утицај ових судара на транспорт електрона и динамику стримера.

Средња енергија, брзина дрифта, дифузиони тензор и коефицијент јонизације су одређени за електроне у течном аргону, течном криптону и течном ксенону у широком опсегу редукованог електричног поља. Ови транспортни подаци су упоређени са постојећим подацима из литературе, као и са одговарајућим вредностима у гасној фази. Посебан акценат је стављен на структурно индиковану негативну диференцијалну проводност у профилу зависности брзине дрифта електрона од резултујућег електричног поља у три разматране течности. Овај транспортни феномен је последица слабљења утицаја ефеката кохерентог расејања, који смањују трансфер импулса у еластичним сударима, са порастом спољашњег електричног поља. Анализа овог феномена, која је већ присутна у литератури, је проширена разматрањем енергијске расподеле електрона и просторно разложеног профила брзинских коефицијената за трансфер енергије и импулса у опсегу редукованог електричног поља у коме се јавља негативна диференцијална проводност. Значајна пажња посвећена је утицају броја ексцитација које су укључене у модел на брзински коефицијент за јонизацију, као и поређењу вредности овог коефицијената у течној и гасној фази.

Трећа тематска целина се односи на проучавање динамике формирања и простирања стримера у атомским течностима применом флуидних модела. Транспортни подаци за електроне у течном аргону, течном криптону и течном ксенону, који су одређени применом Монте Карло симулација, су коришћени као улазни подаци у једноиподимензионој нумеричкој имплементацији флуидног модела првог реда. У овом моделу се претпоставља да се наелектрисане честице налазе унутар цилиндра, чији се радијус не мења у времену. Такође се претпоставља да концентрација наелектрисаних честица не зависи од угаоне ни од радијалне координате, већ само од аксијалне координате. Еволуција концентрације наелектрисаних честица описана је дрифт дифузионом једначином, док је еволуција концентрације позитивних шупљина описана једначином баланса броја честица. Рекомбинација електрона и позитивних шупљина је описана скалираном Дебајевом формулом. Применом овог модела је испитана динамика формирања и простирања негативних стримера у три разматране течности. Посебан акценат стављен је на утицај броја ексцитација које су укључене у модел на брзину настанка и пропагације стримера. Такође је разматрано одступање резултата, који су добијени применом транспортних података из гасне фазе који су скалирани концентрацијом атома у течности, од одговарајућих резултата који су добијени на основу транспортних података из течне фазе. Уочено је да је ово одступање јако изражено у целом разматраном опсегу спољашњег електричног поља, при чему је оно најинтензивније на најнижим пољима. Примећено је да је просторни профил стримера у три разматране течности на квалитативном нивоу врло сличан одговарајућем профилу у гасној фази, при чему су просторне и временске скале формирања и простирања стримера ниже за три реда величине од одговарајућих скала у гасној фази, због знатно веће концентрације позадинских атома у течности.

Елементи за квалитативну оцену научног доприноса др Илије Симоновића

1 Квалитет научних резултата

1.1 Значај научних резултата

Најзначајнији радови др Илије Симоновића су:

I. Simonović, D. Bošnjaković, Z.Lj. Petrović, P. Stokes, R.D. White and S. Dujko
"Third-order transport coefficient tensor of charged-particle swarms in electric and magnetic fields"
Phys. Rev. E **101** (2020) 023203
M21, DOI: https://doi.org/10.1103/PhysRevE.101.023203; IF(2019) = 2.296

I. Simonović, D. Bošnjaković, Z.Lj. Petrović, R.D. White and S. Dujko
"Third-order transport coefficient tensor of electron swarms in noble gases"
Eur. Phys. J. D **74** (2020) 63
M23, DOI: https://doi.org/10.1140/epjd/e2020-100574-y; IF(2019) = 1.366

I. Simonović, N.A. Garland, D. Bošnjaković, Z.Lj. Petrović, R.D. White and S. Dujko
"Electron transport and negative streamers in liquid xenon"
Plasma Sources Sci. Technol. **28** (2019) 015006
M21a, DOI: https://doi.org/10.1088/1361-6595/aaf968; IF(2019) = 3.193

У првом раду кандидат је одредио структуру транспортног тензора трећег реда у свим конфигурацијама електричног и магнетског поља применом методе групних пројектора. Одређена структура у одсуству магнетског поља се слаже са резултатима ранијих аутора, док је структура овог тензора у присуству магнетског поља први пут одређена у оквиру рада кандидата. Ова структура је додатно проверена на основу анализе симетријских особина момената у развоју функције расподеле у фазном простору у оквиру методе више чланова за нумеричко решавање Болцманове једначине.

Физичка интерпретација појединачних компоненти транспортног тензора трећег реда је пажљиво анализирана на основу флукс градијентне релације и приближног решења генералисане дифузионе једначине. Разматран је утицај електричног поља, градијента средње енергије и колизионе фреквенце на знак ових компоненти.

У оквиру овог рада су израчунате вредности транспортног тензора трећег реда за наелектрисане честице у Максвеловом моделу, Ридовом моделу и моделу крутих сфера, као и за електроне у неону применом Монте Карло симулација и метода више чланова за нумеричко решавање Болцманове једначине. Резултати ове две методе се одлично слажу што потврђује валидност примене кинетичке теорије и исправност коришћених компјутерских кодова. На основу ових резултата испитан је утицај еластичних судара, нееластичних судара, јачине електричног и

магнетског поља, као и односа маса наелектрисаних честица роја и неутралних честица позадинске средине на транспортне коефицијенте трећег реда.

У другом раду проучен је транспортни тензор трећег реда за електроне у племенитим гасовима применом методе више чланова за нумеричко решавање Болцманове једначине. Профили зависности компоненти овог тензора од спољашњег електричног поља су анализирани на основу одговарајућих профила средње енергије и коришћених пресека за расејање електрона у овим гасовима. Посебан акценат је стављен на изучавање утицаја Рамзауер-Таунзендовог минимума у пресеку за еластичне сударе на транспортне коефицијенте трећег реда. У овом раду је анализирана корелација између профила зависности лонгитудиналних компоненти транспортног тензора трећег реда и дифузионог тензора од спољашњег електричног поља. Ова корелација је дискутована на основу физичких аргумената.

У трећем раду је изучаван транспорт електрона у течном ксенону применом Монте Карло симулација. Кохерентно еластично расејање је описано применом три ефективна сударна процеса који добро репрезентују средњи трансфер енергије и импулса у течној фази. Пресек за ефективну јонизацију је апроксимиран одговарајућим пресеком за јонизацију изолованог атома ксенона коме је праг снижен на вредност зонског процепа у течном ксенону. Разматрана су четири различита случаја за репрезентовање нееластичних судара у овој течности. Ови случајеви су дискутовани на основу експерименталних радова везаних за фотопроводност и екситонске спектре у течном ксенону.

Анализирани су профили зависности средње енергије, брзине дрифта, лонгитудиналне и трансверзалне карактеристичне енергије, као и брзинског коефицијента за јонизацију од спољашњег електричног поља. Ови резултати су упоређени са теоријским и експерименталним резултатима ранијих аутора који су присутни у литератури, као и са одговарајућим вредностима из гасне фазе. Посебан акценат је стављен на анализу структурно индуковане негативне диференцијалне проводности у профилу брзине дрифта на основу енергијских расподела електрона и просторно разложених брзинских коефицијената за ефективне сударне процесе који репрезентују кохерентно расејање. Такође је разматран утицај броја ексцитација, које су укључене у модел, на брзински коефицијент за ефективну јонизацију у течној фази. Поред тога је дискутована разлика између брзинских коефицијената за јонизацију у течном и гасном ксенону.

Транспортни подаци за електроне у течном ксенону, који су одређени применом Монте Карло симулација, су коришћени као улазни подаци у једноиподимензионој нумеричкој имплементацији флуидног модела првог реда. Овај модел је коришћен за испитивање динамике формирања и простирања негативних стримера у течном ксенону. Посебан акценат је стављен на испитивање утицаја броја ексцитација, које су укључене у модел, на брзину настанка и пропагације негативног стримера. Такође је разматрано одступање предвиђених брзина формирања и простирања стримера у моделу у коме су коришћени подаци из гасне фазе, који су скалирани на густину течности, од одговарајућих брзина у моделу у коме су коришћени подаци из течног ксенона.

1.2 Параметри квалитета часописа

Кандидат др Илија Симоновић је објавио укупно 8 радова у међународним часописима и то:

*3 рада у међународном часопису изузетних вредности Plasma Sources Science and Technology, следећих импакт фактора IF(2016)= 3.302, IF(2018) =4.128 , IF(2019) = 3.193;SNIP(2016) = 1.344, SNIP(2018)=1.857, SNIP(2019) = 1.632.

3 рада у врхунским међународним часописима Plasma Physics and Controlled Fusion, Scientific Reports и Physical Review E, следећих импакт фактора IF(2017)= 3.032, IF(2018)= 4.011, IF(2019)= 2.296, редом;SNIP(2017)= 1.353, SNIP(2018) = 1.274,SNIP(2019) = 0.85, редом.

2 рада у међународном часопису European Physical Journal D, следећих импакт фактора IF(2017)= 1.393, IF(2019)= 1.366; SNIP(2017) = 0.684, SNIP(2019) = 0.725.

Библиографски показатељи сумирани су у следећој табели.

	IF	M	SNIP
Укупно	22.721	60	9.719
Усредњено по чланку	2.8401	7.5	1.2148
Усредњено по аутору	3.9164	10.3428	1.6792

* Часопис Plasma Sources Science and Technology је био рангиран као М21а у 2016., 2017. и 2018. години а као М21 у 2019. години. Овде је М категорија датог часописа за сва три рада одређена у складу са Прилогом 2 Правилника о поступку, начину вредновања и квантитативном исказивању научноистраживачких резултата истраживача("Сл. гласник РС", бр. 24/2016 и 21/2017). При томе је за категорију часописа изабрана најбоља категорија у периоду од три године, укључујући годину публиковања рада и две године пре публиковања. Импакт фактори (IF) и (SNIP) библиографски подаци су увек наведени или за саму годину публиковања рада, или за претходну годину уколико је рад публикован у 2020. години, па подаци за ту годину још увек нису доступни у тренутку достављања документације.

1.3 Позитивна цитираност научних радова

Према подацима из базе Web of Science, радови Илије Симоновића цитирани су укупно 33 пута, од чега 17 пута изузимајући аутоцитате. Хиршов индекс је 2 ако се изузму аутоцитати, а 3 ако се сви цитати узму у обзир.

1.4 Међународна сарадња

Кандидат има међународну сарадњу. Активно сарађује са групом др Роналда Вајта са Џејмс Кук Универзитета у Таунсвилу (Аустралија).

2 Нормирање броја коауторских радова, патената и техничких решења

Сви радови кандидата су засновани на примени нумеричких прорачуна или компјутерских симулација. Радови кандидата категорије М21а имају 5 или 6 аутора, па ови радови не мењају значајно нормирани у односу на укупни број бодова. Радови категорије М21 имају 6 или 7 аутора, што мало значајније доприноси смањењу нормираног у односу на укупни број бодова. Радови категорије М23 имају 5 аутора, па се рачунају са пуном тежином.Укупан број остварених М поена у радовима у међународним часописима је 60, док је нормирани број остварених М поена у овим радовима 51.5.

3 Учешће у пројектима, потпројектима и пројектним задацима

Кандидат је учествовао на пројекту Фундаментални процеси и примене транспорта честица у неравнотежним плазмама, траповима и наноструктурама Министарства науке, просвете и технолошког развоја (бр. ОИ171037).

4 Активност у научним и научно-стручним друштвима

4.1 Рецензије научних радова

Др Илија Симоновић је био рецензент једног рада у часопису European Physical Journal D.

4.2 Организација научних скупова

Др Илија Симоновић је био члан ликалног организационог комитета две међународне конференције:

1. International Conference on Gas Discharges and Their Applications, која је одржана у Новом Саду од 2. до 7. септембра 2018. године.

2. POSMOL2019 која је одржана у Београду од 18 до 20 јула 2019. године.

4.3 Предавања по позиву на међународним конференцијама

Др Илија Симоновић је одржао предавање по позиву на међународном скупу POSMOL 2019, XX International Workshop on Low-Energy Positron and Positronium Physics and XXI International Symposium on Electron-Molecule Collisions and Swarms, 18 - 20 July 2019. Belgrade, Serbia

Кандидат је такође одржао Progress report на међународном скупу 30th Summer School and International Symposium on the Physics of Ionized Gases, 24-28 August 2020, Šabac, Serbia.

5 Утицај научних резултата

Значај научних резултата кандидата је описан у тачки 1, док се њихов утицај огледа у броју цитата који су наведени у тачки 1.3.

6 Конкретан допринос кандидата у реализацији радова у научним центрима у земљи и иностранству

Кандидат је своје истраживање реализовао у Институту за физику у Београду. Кандидат је дао кључан допринос у свим радовима у којима је коаутор. Његов допринос се огледа у извођењу математичких израза који су коришћени у компјутерским кодовима, добијању и интерпретацији резултата компјутерских симулација и нумеричких прорачуна, писању радова и комуникацији са рецензентима часописа.

Елементи за квантитативну оцену научног доприноса др Илије Симоновића

1 Остварени М-бодови по категоријама публикација

Категорија	М-подова по публикацији	Број публикација	Укупно М-бодова (нормирано)
М21а	10.0	3	30.0 (26.6)
М21	8.0	3	24.0 (18.9)
М23	3.0	2	6.0 (6.0)
М32	1.5	2	3.0 (3.0)
М33	1.0	9	9.0 (8.55)
М34	0.5	18	9.0 (7.65)
М70	6.0	1	6.0 (6.0)

2 Поређење оствареног броја М-бодова са минималним условима потребним за избор у научног сарадника

	Потребно	Остварено (нормирано)
Укупно	16	87 (76.7)
М10+М20+М31+М32+М33+М41+М42	10	72 (63.05)
М11+М12+М21+М22+М23	6	60 (51.5)

Списак публикација

Радови у међународном часопису изузетних вредности (категорија М21а)

1. J.Mirić, D. Bošnjaković, **I. Simonović**, Z.Lj. Petrović and S. Dujko
"Electron swarm properties under the influence of a very strong attachment in SF6 and CF3I obtained by Monte Carlo rescaling procedures"
Plasma Sources Sci. Technol. 25 (2016) 065010

2.N.A. Garland, **I. Simonović**, G.J. Boyle, D.G. Cocks, S. Dujko and R.D. White
"Electron swarm and streamer transport across the gas–liquid interface: a comparative fluid model study"
Plasma Sources Sci. Technol. 27 (2018) 105004

3.**I. Simonović**, N.A. Garland, D. Bošnjaković, Z.Lj. Petrović, R.D. White and S. Dujko
"Electron transport and negative streamers in liquid xenon"
Plasma Sources Sci. Technol. 28 (2019) 015006

Радови у врхунском међународном часопису (категорија М21)

1.Z.Lj. Petrović, **I. Simonović**, S. Marjanović, D. Bošnjaković, D. Marić, G. Malović and S. Dujko"Non-equilibrium of charged particles in swarms and plasmas- from binary collisions to plasma effects"
Plasma Phys. Control. Fusion 59 (2017) 014026

2.P.W. Stokes, **I. Simonović**, B. Philippa, D. Cocks, S. Dujko and R.D. White
"Third-order transport coefficients for localised and delocalised charged-particle transport"
Scientific Reports 8 (2018) 2226

3.**I. Simonović**, D. Bošnjaković, Z.Lj. Petrović, P. Stokes, R.D. White and S. Dujko
"Third-order transport coefficient tensor of charged-particle swarms in electric and magnetic fields"
Phys. Rev. E 101 (2020) 023203

Радови у међународном часопису (категорија М23)

1.J. Mirić, **I. Simonović**, Z.Lj. Petrović, R.D. White and S. Dujko
"Electron transport in mercury vapor: cross sections, pressure and temperature dependence of transport coefficients and NDC effects"
Eur. Phys. J. D 71 (2017) 289

2.**I. Simonović**, D. Bošnjaković, Z.Lj. Petrović, R.D. White and S. Dujko
"Third-order transport coefficient tensor of electron swarms in noble gases"
Eur. Phys. J. D 74 (2020) 63

Предавањепопозивусамеђународногскупаштампаноуизводу (М32)

1.**I. Simonović**, D. Bošnjaković, R.D. White, Z.Lj. Petrović and S. Dujko, "Transport Coefficients of Higher-Order for Electrons and Positrons in Neutral Gases and Nonpolar Liquids"
Book of Abstracts, POSMOL 2019, Belgrade, Serbia, 18-21 July 2019, (Edited by D. Cassidy, M.J. Brunger, Z.Lj. Petrović, S. Dujko, B.P. Marinković, D. Marić and S. Tošić), p. 30

2.**I. Simonović**, D. Bošnjaković, R. D. White, Z. LJ. Petrović and S. Dujko, "Kinetic and fluid modelling of non-equilibrium transport of charged-particle swarms in neutral gases and nonpolar liquids", 30th Summer School and International Symposium on the Physics of Ionized Gases, 24-28 August 2020, Šabac, Serbia

Саопштењесамеђународногскупаштампаноуцелини (М33)

*1. S. Dujko, D. Bošnjaković, J. Mirić, **I. Simonović**, Z.M. Raspopović, R.D. White, A.H. Markosyan, U. Ebert and Z.Lj. Petrović, "Recent results from studies of non-equilibrium electron transport in modeling of low-temperature plasmas and particle detectors", in Proceedings of the 9th EU-Japan Joint Symposium on Plasma Processing (JSPP2014) and EU COST MP1101 Workshop on Atmospheric Plasma Processes and Sources, 19-23 January 2014, BohinjskaBistrica, Slovenia

2.**I. Simonović**, ZoranLj. Petrović, SašaDujko,"Third-order transport coefficients for electrons I. Structure of skewness tensor", Proc. 27th Symposium on Physics of Ionized Gases - SPIG 2014, Belgrade, Serbia, (26 - 29 August 2014), Contributed Papers and Abstracts of Invited Lectures, Topical Invited Lectures and Progress Reports (Eds. D. Marić, A.R. Milosavljević and Z. Mijatović), pp. 130-133. ISBN: 978-86-7762-600-6

3.**I. Simonović**, ZoranLj. Petrović, SašaDujko, "Third-order transport coefficients for electrons II. Molecular gases", Proc. 27th Symposium on Physics of Ionized Gases - SPIG 2014, Belgrade, Serbia, (26 - 29 August 2014), Contributed Papers and Abstracts of Invited Lectures, Topical Invited Lectures and Progress Reports (Eds. D. Marić, A.R. Milosavljević and Z. Mijatović), pp. 134-137. ISBN: 978-86-7762-600-6

4. J. Mirić, D. Bošnjaković, **I. Simonović**, Z.Lj. Petrović and S. Dujko, "Monte Carlo Simulations of Electron Transport in CF3I and SF6 Gases",Proc. 28th Summer School and International Symposium on the Physics of Ionized Gases - SPIG 2016, Belgrade, Serbia, (Aug. 29 – Sep. 2), Contributed Papers and

Abstracts of Invited Lectures, Topical Invited Lectures, Progress Reports and Workshop Lectures (Eds. D. Marić, A. Milosavljević, B. Obradović and G. Poparić), pp. 104-107. ISBN: 978-86-84539-14-6

5. J. Mirić, **I. Simonović**, D. Bošnjaković, Z.Lj. Petrović and S. Dujko, "Electron Transport in Mercury Vapor: Dimer Induced NDC and Analysis of Transport Phenomena in Electric and Magnetic Fields",Proc. 28th Summer School and International Symposium on the Physics of Ionized Gases - SPIG 2016, Belgrade, Serbia, (Aug. 29 – Sep. 2), Contributed Papers and Abstracts of Invited Lectures, Topical Invited Lectures, Progress Reports and Workshop Lectures (Eds. D. Marić, A. Milosavljević, B. Obradović and G. Poparić), pp. 108-111. ISBN: 978-86-84539-14-6

6.**I. Simonović**, Z. LJ. Petrović, R.D. White and S. Dujko, "Transport coefficients for electron swarms in liquid argon and liquid xenon", Proc. 28th Summer School and International Symposium on the Physics of Ionized Gases - SPIG 2016, Belgrade, Serbia, (Aug. 29 – Sep. 2), Contributed Papers and Abstracts of Invited Lectures, Topical Invited Lectures, Progress Reports and Workshop Lectures (Eds. D. Marić, A. Milosavljević, B. Obradović and G. Poparić), pp. 120-123. ISBN: 978-86-84539-14-6

7.**I. Simonović**, Z. LJ. Petrović, R.D. White and S. Dujko, "Transition of an electron avalanche into a streamer in liquid argon and liquid xenon", Proc. 28th Summer School and International Symposium on the Physics of Ionized Gases - SPIG 2016, Belgrade, Serbia, (Aug. 29 – Sep. 2), Contributed Papers and Abstracts of Invited Lectures, Topical Invited Lectures, Progress Reports and Workshop Lectures (Eds. D. Marić, A. Milosavljević, B. Obradović and G. Poparić),pp. 124-127. ISBN: 978-86-84539-14-6

*8. S. Dujko, D. Bošnjaković, **I. Simonović**, Z.Lj. Petrović and R.D. White,"Non-equilibrium transport of electrons in gases and liquids and its application in modeling of particle detectors",Book of contributed papers, SAPP XXII, 22nd Symposium on Application of Plasma Processes and 11th EU-Japan Joint Symposium on Plasma Processing, ŠtrbskePleso, Slovakia, 18-24 January, 2019, (Edited by V. Medvecka, J. Orszagh, P. Papp and Š. Matejčik), p.57.

9. S. Dujko, **I. Simonović**, D. Bošnjaković, Z.Lj. Petrović and R.D. White, "Electron transport and propagation of negative streamers in liquid-phase xenon", 2019 IEEE 20th International Conference on Dielectric Liquids (ICDL), Roma, Italy, June 23-27, 2019

*Radovi sa zvezdicom predstavljaju koautorstvo na predavanju po pozivu štampanom u celini (M31), koje je bodovano kao saopštenje sa međunarodnog skupa štampano u celini (M33)

Саопштењесамеђународногскупаштампаноуизводу (M34)

1. Z.Lj. Petrović, S. Dujko, D. Marić, D. Bošnjaković, S. Marjanović, J. Mirić, O. Šašić, S. Dupljanin, **I. Simonović and R.D. White,"Swarms as an exact representation of weakly ionized gases",XIX International Symposium on Electron-Molecule Collisions and Swarms & XVIII International Workshop on Low-Energy Positron and Positronium Physics, POSMOL 2015, 17-20 July 2015, Lisboa, Portugal, Book of Abstracts, p. 4

2. S. Dujko, Z.Lj. Petrović, R.D. White, G. Boyle, A. Banković, **I. Simonović, D. Bošnjaković, J. Mirić, A.H. Markosyan and S. Marjanović,"Transport processes for electrons and positrons in gases and soft-condensed matter: Basic phenomenology and applications",XXIX International Conference on Photonic, Electronic and Atomic Collisions, 22-28 July 2015, Toledo, Spain

3.**I. Simonović**, Z.Lj. Petrović, and S. Dujko, "Third order transport coefficients for electrons and positrons in gases", XXIX International Conference on Photonic, Electronic and Atomic Collisions, 22-28 July 2015, Toledo, Spain

4.**I. Simonović**, Z.Lj. Petrović, R.D. White and S. Dujko,"Higher order transport coefficients for electrons and positrons in gases",XIX International Symposium on Electron-Molecule Collisions and Swarms & XVIII International Workshop on Low-Energy Positron and Positronium Physics, POSMOL 2015, 17-20 July 2015, Lisbon, Portugal, Book of Abstracts, p.69

5.**I. Simonović**, Z.Lj. Petrović, S. Dujko, "Third-order transport properties of electrons and positrons in electric and magnetic fields", Gaseous Electronics Meeting GEM2016 Geelong, Australia, February 14-17, 2016od 14. 02. 2016 do 17. 02. 2016Deakin University, Geelong, Victoria, Australia

6. Zoran Petrović, Jasmina Mirić, **Ilija Simonović**, Danko Bošnjaković, Saša Dujko,
Monte Carlo simulations of electron transport in strongly attaching gases,
Bulletin of the American Physical Society, 69th Annual Gaseous Electronics Conference (GEC2016),
Bochum, Germany, p. 71

7. Zoran Petrović, Jasmina Mirić, **Ilija Simonović**, Saša Dujko,"Electron transport in mercury vapor: magnetic field effects, dimer induced NDC and multi-term analysis",Bulletin of the American Physical Society, 69th Annual Gaseous Electronics Conference (GEC2016),
Bochum, Germany, p. 71

8. SašaDujko, **IlijaSimonović**, G. Boyle, R. White, Danko Bošnjaković, ZoranPetrović,"Transport properties of electrons and transition of an electron avalanche into a streamer in atomic liquids",
Bulletin of the American Physical Society, 69th Annual Gaseous Electronics Conference (GEC2016),
Bochum, Germany, p. 71

9. SašaDujko, **IlijaSimonović**, R. White, ZoranPetrović,"Third order transport coefficients for electrons and positrons in gases",Bulletin of the American Physical Society, 69th Annual Gaseous Electronics Conference (GEC2016), Bochum, Germany, p. 71

10. S. Dujko, D. Bošnjaković, I. Simonović**, Z.Lj. Petrović,R.D. WhiteandC. Kohn "Elementary physical processes of electrons and positrons in planetary atmospheric discharges",XIX International Workshop

on Low-Energy Positron and Positronium Physics and XX International Symposium on Electron-Molecule Collisions and Swarms, POSMOL2017, 22-24 July 2017, Amaroo on Mondalay Resort, Magnetic Island, Queensland, Australia, Book of Abstracts, p.57

11.**I. Simonović**, D. Bošnjaković, Z.Lj. Petrović, R.D. White and S. Dujko,"Skewness tensor for electrons and positrons in gases",XIX International Workshop on Low-Energy Positron and Positronium Physics and XX International Symposium on Electron-Molecule Collisions and Swarms, POSMOL2017, 22-24 July 2017, Amaroo on Mondalay Resort, Magnetic Island, Queensland, Australia, Book of Abstracts, p.78

12.**I. Simonović**, Z.Lj. Petrović, R.D. White, D. Bošnjaković and S. Dujko, "Transport properties of electrons and development of streamers in atomic liquids", XIX International Workshop on Low-Energy Positron and Positronium Physics and XX International Symposium on Electron-Molecule Collisions and Swarms, POSMOL2017, 22-24 July 2017, Amaroo on Mondalay Resort, Magnetic Island, Queensland, Australia, Book of Abstracts, p.79

13. J. Mirić, **I. Simonović**, D. Bošnjaković, Z.Lj. Petrović, R.D. White, and S. Dujko, "Hydrodynamic and non-hydrodynamic studies of electron transport in mercury vapor",XIX International Workshop on Low-Energy Positron and Positronium Physics and XX International Symposium on Electron-Molecule Collisions and Swarms, POSMOL2017, 22-24 July 2017, Amaroo on Mondalay Resort, Magnetic Island, Queensland, Australia, Book of Abstracts, p.80

14. P. Stokes, **I. Simonović**, B. Philippa, D. Cocks, S. Dujko and R.D. White, "Combined localised and delocalised transport phenomena", XIX International Workshop on Low-Energy Positron and Positronium Physics and XX International Symposium on Electron-Molecule Collisions and Swarms, POSMOL2017, 22-24, July 2017, Amaroo on Mondalay Resort, Magnetic Island, Queensland, Australia, Book of Abstracts, p.96

15. N. Garland, D. Muccignat, G. Boyle, D. Cocks, **I. Simonović, D. Bošnjaković, M. J. Brunger, S. Dujko, Z. Lj. Petrović, and R. D. White, "The Gas-Liquid Interface: Kinetic and Fluid Modelling of Charged Particle Transport",Book of Abstracts, POSMOL 2019, Belgrade, Serbia, 18-21 July 2019, (Edited by D. Cassidy, M.J. Brunger, Z.Lj. Petrović, S. Dujko, B.P. Marinković, D. Marić and S. Tošić), p. 33

16. S. Dujko, **I. Simonović**, R.D. White and Z.Lj. Petrović,"Positron Transport in H2 in Electric and Magnetic Fields Crossed at Arbitrary Angles", Book of Abstracts, POSMOL 2019, Belgrade, Serbia, 18-21 July 2019, (Edited by D. Cassidy, M.J. Brunger, Z.Lj. Petrović, S. Dujko, B.P. Marinković, D. Marić and S. Tošić), p. 80

17. S. Dujko, D. Bošnjaković, **I. Simonović** and C. Köhn, "Electron Transport and Streamers in the Atmosphere of Titan", Book of Abstracts, POSMOL 2019, Belgrade, Serbia, 18-21 July 2019, (Edited by D. Cassidy, M.J. Brunger, Z.Lj. Petrović, S. Dujko, B.P. Marinković, D. Marić and S. Tošić), p. 143

18. M. Casey, P. Stokes, **I. Simonović, D. Bošnjaković, M. J. Brunger, J. de Urquijo, S.Dujko, Z. Lj. Petrović, R. E. Robson, and R.D. White,"Foundations and Interpretations of the Pulsed-TownsendSwarm Experiment and the use of Machine Learningfor Self-Consistent Cross-Section Sets",Book of Abstracts, POSMOL 2019, Belgrade, Serbia, 18-21 July 2019, (Edited by D. Cassidy, M.J. Brunger, Z.Lj. Petrović, S. Dujko, B.P. Marinković, D. Marić and S. Tošić), p. 150

**Radovi sa dve zvezdice predstavljaju koautorstvo na predavanju po pozivu štampanom u izvodu (M32), koje je bodovano kao saopštenje sa međunarodnog skupa štampano u izvodu (M34)

Mr Ilija Simonović
Institute of Physics Belgrade
Pregrevica 118
11080 Belgrade
Email: isimonovic@ipb.ac.rs

Belgrade, June 15, 2019.

Dear Mr Simonović,

On behalf of the Local Organizing Committee, it is my pleasure to invite you to give an invited talk at the XX International Workshop on Low-Energy Positron and Positronium Physics and XXI International Symposium on Electron-Molecule Collisions and Swarms (POSMOL2019). Each invited talk is 30 minutes long, including 5 minutes for discussion. This invitation is for you personally.

The conference is organized by the Institute of Physics Belgrade and it will be held at the Serbian Academy of Sciences and Arts, Belgrade, Serbia, on July 18-20 2019. I would like also to inform you that in honor of the retirement of Professor Zoran Lj. Petrović, one day workshop will be held on the 21st of July, 2019, at the Serbian Academy of Sciences and Arts.

The one-page abstract should be emailed to posmol2019@ipb.ac.rs. The abstract submission is due the 1st of June, 2019. Information about the meeting is being posted at
http://www.posmol2019.ipb.ac.rs. Registration and housing information is also posted on this site.

Should you or the agency requesting this letter require any further information, please do not hesitate to contact us.

Best wishes,

Saša Dujko
Co-chair of POSMOL2019
Research Professor at the Institute of Physics Belgrade
Email: sasa.dujko@ipb.ac.rs
Phone: +381 11 3713 001 Fax: +381 11 3162 190

POSMOL 2019
Email: posmol2019@ipb.ac.rs
Web: posmol2019.ipb.ac.rs
Phone: +381 11 3713 056 Fax: +381 11 3162 190

Dr Ilija Simonović

Belgrade, 10 December, 2019

Dear **Dr Ilija Simonović,**

On behalf of the Scientific and Organizing Committees, we have a pleasure to invite you to attend the *30th Summer School and International Symposium on the Physics of Ionized Gases* (SPIG 2020) and present a **Progress invited talk**.

The SPIG 2020 will be held from August 24th to 28th, 2020 in Šabac, Serbia. The details of the conference are available at official website: http://www.spig2020.ipb.ac.rs/
Please note that due to the limited conference budget, the SPIG2020 organizers will try to provide partial support to students and early stage researchers, as well as colleagues from economically less privileged countries. Thank you for your understanding and support.

We look forward to welcoming you to Šabac.

Yours sincerely,

Luka Č. Popović
(Co-Chair of the Scientific Committee)

Dragana Ilić
(Co-Chair of the Loc. Org. Committee)

Duško Borka
(Co-Chair of the Scientific Committee)

Vladimir Srećković
(Co-Chair of the Loc. Org. Committee)

SPIG 2020 Organizer:
University of Belgrade, Faculty of Mathematics, Department of Astronomy

SPIG 2020 Co-organizers:
University of Belgrade, Institute of Physics
Astronomical Observatory of Belgrade

This is an overview of citations for this author.

Author *h*-index : 2   View *h*-graph ⊙

10 Cited Documents from "Simonović, Ilija" ✛ Add to list

Date range: 2016 ▾ to 2020 ▾   ☐ Exclude self citations of selected author   ▣ Exclude self citations of all authors   ☐ Exclude citations from books   **Update**
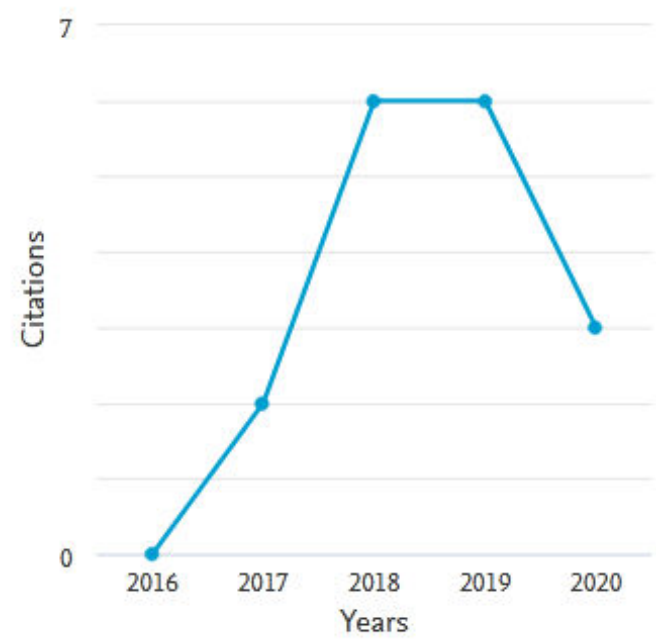
Sort on: Date (newest) ▾

☐ Page   🗑 Remove

Documents	Citations	<2016	2016	2017	2018	2019	2020	Subtotal	>2020	Total
	Total	0	0	**2**	**6**	**6**	**3**	**17**	0	**17**

На основу члана 29 Закона о општем управном поступку («Службени гласник РС» број 18/2016 и 95/2018), и члана 149 Статута Универзитета у Београду - Физичког факултета, по захтеву ИЛИЈЕ СИМОНОВИЋА, мастер физичара, издаје се следеће

У В Е Р Е Њ Е

ИЛИЈА СИМОНОВИЋ, мастер физичар, дана 30. септембра 2020. године, одбранио је докторску дисертацију под називом

"КИНЕТИЧКИ И ФЛУИДНИ МОДЕЛИ НЕРАВНОТЕЖНОГ ТРАНСПОРТА ЕЛЕКТРОНА У ГАСОВИМА И ТЕЧНОСТИМА"

пред Комисијом Универзитета у Београду - Физичког факултета и тиме испунио све услове за промоцију у ДОКТОРА НАУКА – ФИЗИЧКЕ НАУКЕ.

Уверење се издаје на лични захтев, а служи ради регулисања права из радног односа и важи до промоције, односно добијања докторске дипломе.

Уверење је ослобођено плаћања таксе.

ДЕКАН ФИЗИЧКОГ ФАКУЛТЕТА

Проф. др Иван Белча

Electron swarm properties under the influence of a very strong attachment in SF_6 and CF_3I obtained by Monte Carlo rescaling procedures

You may also be interested in:

Boltzmann equation and Monte Carlo studies of electron transport in resistive plate chambers
D Bošnjakovi, Z Lj Petrovi, R D White et al.

Non-conservative electron transport in CF4
S Dujko, R D White, K F Ness et al.

Positron transport in water vapour
A Bankovi, S Dujko, R D White et al.

High-order fluid model for streamer discharges: I. Derivation of model and transport data
S Dujko, A H Markosyan, R D White et al.

A multi-term solution of the nonconservative Boltzmann equation
S Dujko, R D White, Z Lj Petrovi et al.

Monte Carlo studies of electron transport in CF4
S Dujko, Z M Raspopovi and Z Lj Petrovi

Fluid modeling of resistive plate chambers: impact of transport data on development of streamers and induced signals
D Bošnjakovi, Z Lj Petrovi and S Dujko

Electron swarm properties under the influence of a very strong attachment in SF$_6$ and CF$_3$I obtained by Monte Carlo rescaling procedures

J Mirić[1], D Bošnjaković[1], I Simonović[1], Z Lj Petrović[1,2] and S Dujko[1]

[1] Institute of Physics, University of Belgrade, PO Box 68, 11080 Belgrade, Serbia
[2] Serbian Academy of Sciences and Arts, Knez Mihailova 35, 11001 Belgrade, Serbia

E-mail: sasa.dujko@ipb.ac.rs

Abstract

Electron attachment often imposes practical difficulties in Monte Carlo simulations, particularly under conditions of extensive losses of seed electrons. In this paper, we discuss two rescaling procedures for Monte Carlo simulations of electron transport in strongly attaching gases: (1) discrete rescaling, and (2) continuous rescaling. The two procedures are implemented in our Monte Carlo code with an aim of analyzing electron transport processes and attachment induced phenomena in sulfur-hexafluoride (SF$_6$) and trifluoroiodomethane (CF$_3$I). Though calculations have been performed over the entire range of reduced electric fields E/n_0 (where n_0 is the gas number density) where experimental data are available, the emphasis is placed on the analysis below critical (electric gas breakdown) fields and under conditions when transport properties are greatly affected by electron attachment. The present calculations of electron transport data for SF$_6$ and CF$_3$I at low E/n_0 take into account the full extent of the influence of electron attachment and spatially selective electron losses along the profile of electron swarm and attempts to produce data that may be used to model this range of conditions. The results of Monte Carlo simulations are compared to those predicted by the publicly available two term Boltzmann solver BOLSIG+. A multitude of kinetic phenomena in electron transport has been observed and discussed using physical arguments. In particular, we discuss two important phenomena: (1) the reduction of the mean energy with increasing E/n_0 for electrons in SF$_6$ and (2) the occurrence of negative differential conductivity (NDC) in the bulk drift velocity only for electrons in both SF$_6$ and CF$_3$I. The electron energy distribution function, spatial variations of the rate coefficient for electron attachment and average energy as well as spatial profile of the swarm are calculated and used to understand these phenomena.

Keywords: Monte Carlo, electron transport, electron attachment, SF$_6$, CF$_3$I

(Some figures may appear in colour only in the online journal)

1. Introduction

Electron transport in strongly attaching gases has long been of interest, with applications in many areas of fundamental physics and technology. Electron attaching gases support key processes for plasma etching and cleaning in semiconductor fabrication [1, 2], high-voltage gas insulation [3] and particle detectors in high energy physics [4–6]. The importance of studies of electron attachment has also been recognized in other fields, including planetary atmospheres, excimer lasers, plasma medicine and lighting applications, as well as in life science for understanding radiation damage in biological matter.

The fundamental importance of electron attachment processes has led to many experimental and theoretical swarm studies. For some gases the cross sections for attachment may be very large resulting in a rapid disappearance of free electrons that greatly complicates the measurements of transport coefficients [1, 7–9]. The pioneering studies date back to the 1970s, and the well-known swarm method of deriving cross section for electron attachment developed by Christophorou and his co-workers [10]. According to this method, trace amounts of an electron attaching gas are mixed into the buffer gases, typically nitrogen to scan the lower mean energies and argon to scan the higher mean energies. This technique results in the removal of electrons without disturbing the electron energy distribution function. In such mixtures the losses depend only on the very small amount of the added gas and we may measure the density reduced electron attachment rate coefficient. Electron attachment cross sections can be determined by deconvoluting the mixture data, since the electron energy distribution function is a known function of E/n_0 as calculated for the pure buffer gas. Examples of this procedure are cross sections for electron attachment in SF_6 and SF_6-related molecules [11–15] as well as cross sections and rate coefficients for a range of fluorocarbons [1, 12, 16–18] and other relevant gases for applications [1, 19–22]. In addition to non-equilibrium data, there is a separate category of experiments, including flowing afterglow, the Cavalleri diffusion experiment [9, 23, 24], and others that provide attachment rates for thermal equilibrium (i.e. without an applied electric field). These may be taken at different temperatures, but the range of energies covered by this technique is very narrow. These two techniques have been used to evaluate the cross sections for SF_6 and CF_3I, always under the assumption that the effect of attachment is merely on the number of particles and not on any other swarm properties.

A thorough understanding of the influence of attachment on the drift and diffusion of the electrons provides information which could be used in analysis of kinetic phenomena in complex electronegative gases and related plasmas. The attachment cooling and heating [25, 26], negative absolute electron flux mobility [27, 60] and anomalous phase shifts of drift velocity in AC electric fields [28] are some examples of these phenomena in strongly attaching gases, which may not be trivially predicted on the basis of individual collision events and external fields. Negative differential conductivity (NDC) induced by 3-body attachment for lower E/n_0 and higher pressures in molecular oxygen and its mixture with other gases is another example of phenomena induced by strong electron attachment [29]. The duality in transport coefficients, e.g. the existence of two fundamentally different families of transport coefficients, the bulk and flux, is caused by the explicit effects of electron impact ionization and electron attachment [7, 30–32]. The differences between two sets of data vary from a few percents to a few orders of magnitude and hence a special care is needed in the implementation of data in fluid models of plasma discharges [7, 31, 33–35]. On one hand, most plasma modeling is based on flux quantities while experiments aimed at yielding cross section data provide mostly but not uniquely the bulk transport data. This differentiation between flux and bulk transport properties is not merely a whimsy of theorists, but it is essential in obtaining and applying the basic swarm data. In addition, the production of negative ions has a large effect on the transport and spatial distribution of other charged particle species as well as on the structure of the sheath and occurrence of relaxation oscillations in charged particle densities [36–41].

There are three main approaches to the theoretical description of electron transport in gases: the kinetic Boltzmann equation, the stochastic particle simulation by the Monte Carlo method and semi-quantitative momentum transfer theory. Restrictions on the accuracy of momentum transfer theory for studies of electron transport in attaching gases, particularly under non-hydrodynamic conditions, have already been discussed and illustrated [31, 42, 43]. Boltzmann equation analyses for SF_6 and its mixtures with other gases (see for example [11, 44–50]) have been performed several times in the past. Two important studies devoted to the calculation of electron swarm parameters based on a Boltzmann equation have also been performed for CF_3I [51, 52]. Theories for solving the Boltzmann equation were usually restricted to low-order truncations in the Legendre expansions of the velocity dependence assuming quasi-isotropy in velocity space. The explicit effects of electron attachment were also neglected and electron transport was studied usually in terms of the flux data only. These theories had also restricted domains of validity on the applied E/n_0 in spite of their coverage of a considerably broader range. One thing that strikes the reader surveying the literature on electron transport in SF_6 is the systematic lack of reliable data for electron transport coefficients for E/n_0 less than 50 Td. Contemporary moment methods for solving Boltzmann's equation [31, 53] are also faced with a lot of systematic difficulties, particularly under conditions of the predominant removal of the lower energy electrons which results in an increase in the mean energy, i.e. attachment heating. Under these conditions the bulk of the distribution function is shifted towards a higher energy which in turn results in the high energy tail falling off much slower than a Maxwellian. This is exactly what may happen in the analysis of electron transport in strongly attaching gases such as SF_6 or CF_3I for lower E/n_0. The moment method for solving Boltzmann's equation under these circumstances usually requires the prohibitive number of basis functions for resolving the speed/energy dependency of the distribution function and/or unrealistically large computation time. As a consequence, the standard numerical schemes employed within the framework of moment methods usually fail.

The present investigation is thus mainly concerned with the Monte Carlo simulations of electron transport in strongly attaching gases. Monte Carlo simulations have also been employed for the analysis of electron transport in the mixtures of SF_6 [46, 54–57] and CF_3I [58] with other gases usually with an aim of evaluating the insulation strength and critical electric fields. However, electron attachment in strongly electronegative gases often imposes practical difficulties in Monte Carlo simulations. This is especially noticeable at lower E/n_0, where electron attachment is one of the dominant processes which may lead to the extensive vanishing of the seed electrons and

consequently to the decrease of the statistical accuracy of the output results. In extreme cases, the entire electron swarm might be consumed by attachment way before the equilibrated (steady-state regime) is achieved. An obvious solution would be to use a very large number of initial electrons, but this often leads to a dramatic increase of computation time and/ or required memory/computing resources which are beyond practical limits. Given the computation restrictions of the time, the workers were forced to develop methods to combat the computational difficulties induced by the extensive vanishing of the seed electrons. Two general methods were developed: (1) addition of new electrons by uniform scaling of the electron swarm at certain time instants under hydrodynamic conditions [26, 59] or at certain positions under steady-state Townsend conditions [60], when number of electrons reaches a pre-defined threshold, and (2) implementation of an additional fictitious ionization channel/process with a constant collision frequency (providing that the corresponding ionization rate is chosen to be approximately equal to the attachment rate) [54]. On the other hand, similar rescaling may be applied for the increasing number of electrons as has been tested at the larger E/n_0 by Li *et al* [61]. Further distinction and specification between methods developed by Nolan *et al* [26] and Dyatko *et al* [60] on one hand and Raspopović *et al* [59] on the other, will be discussed in later sections. These methods have not been compared to each other in a comprehensive and rigorous manner. This raises a number of questions. How accurate, these methods are? Which is the more efficient? Which is easier for implementation? What is their relationship to each other? Which one is more flexible? In this paper, we will try to address some of these issues. In particular, the present paper serves to summarize the salient features of these methods in a way which we hope will be of benefit to all present and future developers of Monte Carlo codes. Finally, it is also important to note that in the present paper we extend the method initially developed by Yousfi *et al* [54], by introducing time-dependent collision frequency for the fictitious ionization process.

This paper is organized as follows: in section 2, we briefly review the basic elements of our Monte Carlo code, before detailing the rescaling procedures employed to combat the computational difficulties initiated by the rapid disappearance of electrons. In the same section, we illustrate the issue of electron losses by considering the evolution of the number of electrons for a range of E/n_0 in SF_6 and CF_3I. In section 3, we evaluate the performance of rescaling procedures by simulating electron transport in SF_6 and CF_3I over a wide range of E/n_0. We will also highlight the substantial difference between the bulk and flux transport coefficients in SF_6 and CF_3I. Special attention will be paid to the occurrence of negative differential conductivity (NDC) in the profile of the bulk drift velocity. For electrons in SF_6 another phenomenon arises: for certain reduced electric fields we find regions where the swarm mean energy decreases with increasing E/n_0. In the last segment of the section 3, we discuss two important issues: (1) how to use the rescaling procedures in Monte Carlo codes, and (2) rescaling procedures as a tool in the modeling of non-hydrodynamic effects in swarm experiments. In section 4, we present our conclusions and recommendations.
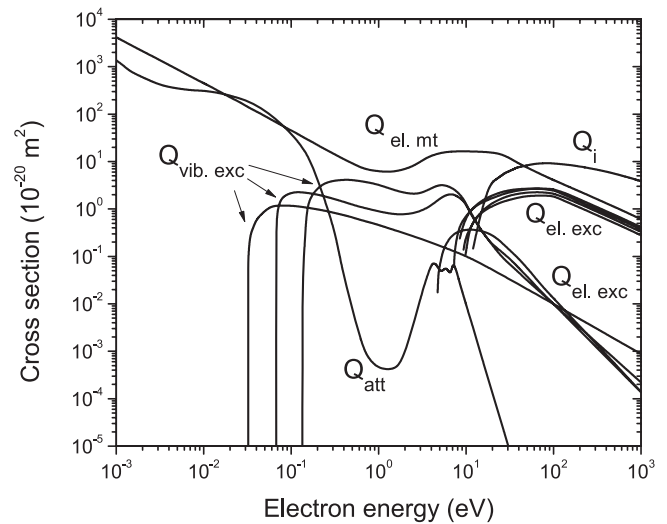

Figure 1. Electron impact cross-sections for CF_3I used in this study [62]: $Q_{el. mt}$ momentum transfer in elastic collisions, $Q_{vib. exc}$ vibrational excitation, $Q_{el. exc}$ electronic excitation, Q_{att} dissociative attachment and Q_i electron-impact ionization.

2. Input data and computational methods

2.1. Cross sections for electron scattering and simulation conditions

We begin this section with a brief description of cross sections for electron scattering in SF_6 and CF_3I. For the SF_6 cross sections we use the set developed by Itoh *et al* [47]. This set was initially based on published measurements of cross sections for individual collision processes. Using the standard swarm procedure, the initial set was modified to improve agreement between the calculated swarm parameters and the experimental values. The set includes one vibrational channel, one electronic excitation channel, as well as elastic, ionization and five different attachment channels.

This study considers electron transport in CF_3I using the cross section set developed in our laboratory [62]. This set of cross sections is shown in figure 1. It should be noted that this set is similar but not identical to that developed by Kimura and Nakamura [63]. We have used the measured data under pulsed Townsend conditions for pure CF_3I and its mixtures with Ar and CO_2 in a standard swarm procedure with the aim of improving the accuracy and completeness of a set of cross sections. It consists of the elastic momentum transfer cross section, three cross sections for vibrational and five cross sections for electronic excitations as well as one cross section for electron-impact ionization with a threshold of 10.4 eV and one cross section for dissociative attachment. For more details the reader is referred to our future paper [64].

For both SF_6 and CF_3I all electron scattering are assumed isotropic and hence the elastic cross section is the same as the elastic momentum transfer cross section. Simulations have been performed for E/n_0 ranging from 1 to 1000 Td. The pressure and temperature of the background gas are 1 Torr and 300 K, respectively. It should be mentioned that special care in our Monte Carlo code has been paid to proper treatment of the thermal motion of the host gas molecules and their influence
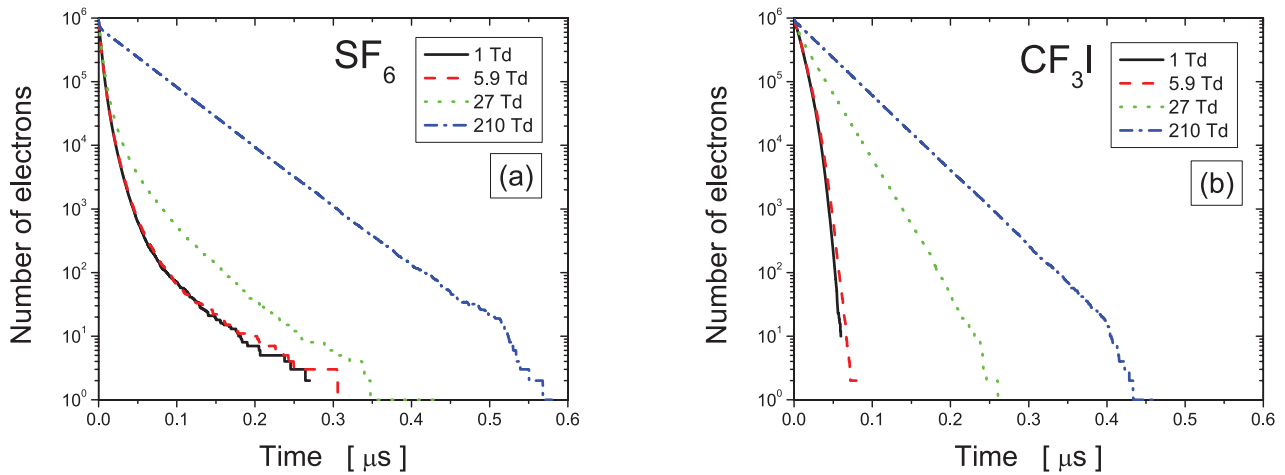
Figure 2. Electron number density decay for four different reduced electric fields as indicated on the graph. Calculations are performed for SF$_6$ (a) and CF$_3$I (b).

on electrons, which is very important at low electric fields, when the mean electron energy is comparable to the thermal energy of the host gas [65]. After ionization, the available energy is partitioned between two electrons in such a way that all fractions of the distribution are equally probable.

2.2. Monte Carlo method

The Monte Carlo simulation technique used in the present work is described at length in our previous publications [32, 53, 59, 66, 67]. In brief, we follow the spatiotemporal evolution of each electron through time steps which are fractions of the mean collision time. In association with random numbers, these finite time steps are used to solve the integral equation for the collision probability in order to determine the time of the next collision. The number of time steps is determined in such a way as to optimize the performance of the Monte Carlo code without reducing the accuracy of the final results. When the moment of the next collision is established, the additional sequences of random numbers are used, first to determine the nature of a collision, taking into account the relative probabilities of the various collision types, and second to determine the change in the direction of the electron velocity. All dynamic properties of each electron such as position, velocity, and energy are updated between and after the collisions. Sampling of electron dynamic properties is not correlated to the time of the next collision and is performed in a way that ensemble averages can be taken in both the velocity and configuration space. Explicit formulas for the bulk and flux transport properties have been given in our previous publications [59, 66]. To evaluate the accuracy of the Monte Carlo code, Boltzmann analyses were performed in parallel with the Monte Carlo calculations using the multi term method described in detail by Dujko *et al* [53]. In addition, we use the BOLSIG+, a publicly available Boltzmann solver based on a two term theory [68]. The most recent version of this code might be used to study the electron transport in terms of both the flux and bulk data which is very useful for some aspects of plasma modeling [7]. At the same time, the comparison between our results and those computed by BOLSIG+ which is presented in this paper, should

be viewed as the first benchmark for the bulk BOLSIG+ data. Our Monte Carlo code and multi term codes for solving the Boltzmann equation have been subject of a detailed testing for a wide range of model and real gases [31, 53, 59, 67].

In figure 2 we illustrate the losses of electrons during the evolution of the swarm towards the steady-state. The initial number of electrons is set to 1×10^6 and calculations are performed for a range of reduced electric fields E/n_0 as indicated on the graphs. For both SF$_6$ and CF$_3$I, we observe that at small E/n_0, i.e. at low mean energies, the number of electrons decreases much faster. This is a clear sign that collision frequency for electron attachment increases with decreasing E/n_0. Electrons in CF$_3$I are lost continuously and consequently the number of electrons in the swarm decreases exponentially with time. The same trend may be observed for electrons in SF$_6$ at 210 Td. For the remaining E/n_0 the number of electrons is reduced with time even faster. Comparing SF$_6$ and CF$_3$I, it is evident that the electrons are more efficiently consumed by electron attachment in SF$_6$ in the early stage of the simulation. Conversely, in the last stage of simulation the electrons are more consumed by electron attachment in CF$_3$I than in SF$_6$. In any case, the electron swarms in both cases are entirely consumed by attachment way before the steady-state regime and hence the simulations are stopped. In other words, the number density drops down by six orders of magnitude over the course of several hundred nanoseconds in both gases. To facilitate the numerical simulation, it is clear that some kind of rescaling of the number density is necessary to compensate for the electrons consumed by electron attachment. This procedure should not in any way disrupt the spatial gradients in the distribution function. On the other hand, releasing electrons with some fixed arbitrary initial condition would require that they equilibrate with the electric field during which time again majority of such additional electrons would be lost.

2.3. Rescaling procedures

To counteract the effect of attachment in an optimal fashion while keeping the statistical accuracy, the following rescaling procedures were proposed and applied so far:

(1) Uniform generation of new electrons with initial properties taken from the remaining electrons thus taking advantage of the equilibration that has been achieved so far [59]. To make this procedure effective i.e. to avoid losing population in some smaller pockets of the ensemble the population should be allowed to oscillate between N_1 and N_0, where $N_1 > N_0$ but their difference is relatively small. Here N_0 is minimum allowed number of electrons while N_1 is maximum number of electrons in the simulation after rescaling.

(2) Uniform scaling of an electron swarm by a factor of 2 or 3 at certain instants of time [26] or distance [60] depending on the simulation conditions where the probability of scaling for each electron is set to unity.

(3) Introduction of an additional fictitious ionization process with a constant ionization frequency (that is close to the rate for attachment), which artificially increases the number of simulated electrons [54, 61]. Uniform rescaling of the swarm is done by randomly choosing the electrons which are to be 'duplicated'. The newborn electron has the same initial dynamic properties, coordinates, velocity, and energy as the original. Following the creation of a new electron their further histories diverge according to the independently selected random numbers.

Comparing the procedures (1) and (2), it is clear that there are no essential differences between them. The only difference lies in the fact that in the procedure (2) duplicating is performed for all the electrons in the simulation while according the procedure (1), the probability of duplication is determined by the current ratio of the number of electrons to the desired number of electrons in the simulation, which is specified in advance. On the other hand, fictitious ionization collision generates a new electron which is given the same position, velocity and energy as the primary electron that is not necessarily the electron lost in attachment. In this paper, we shall refer to the procedure (1) as *discrete rescaling*, since the procedure is applied at discrete time instants. The procedure (2) shall be termed as *swarm duplication* and finally we shall refer to the procedure (3) as the *continuous rescaling* since the rescaling is done during the entire simulation. An important requirement is that the rescaling must not perturb/change/disturb the normalized electron distribution function and its evolution. Li *et al* [61] showed that the continuous rescaling procedure meets this requirement. In case of discrete rescaling as applied to the symmetrical yet different problem of excessive ionization, it was argued that one cannot be absolutely confident that the rescaled distribution is a good representation of the original [69], except when steady state is achieved [70].

In what follows, we discuss the continuous rescaling. Following the previous works [54, 61], the Boltzmann equation for the distribution function $f(\mathbf{r}, \mathbf{c}, t)$ without rescaling and $f^\star(\mathbf{r}, \mathbf{c}, t)$ with rescaling are given by:

$$(\partial_t + \mathbf{c} \cdot \nabla_{\mathbf{r}} + \mathbf{a} \cdot \nabla_{\mathbf{c}}) f(\mathbf{r}, \mathbf{c}, t) = -J(f), \tag{1}$$

and

$$(\partial_t + \mathbf{c} \cdot \nabla_{\mathbf{r}} + \mathbf{a} \cdot \nabla_{\mathbf{c}}) f^\star(\mathbf{r}, \mathbf{c}, t) = -J(f^\star) + \nu_{\mathrm{fi}}(t) f^\star, \tag{2}$$

where $\mathbf{a}$ is the acceleration due to the external fields, $J(f)$ is the collision operator for electron-neutral collisions and ν_{fi} is time-dependent fictitious ionization rate. If the collision operator is linear (i.e. if electron–electron collisions are negligible) and if the initial distributions (at time $t = 0$) are the same, it can be easily shown that the following relationship holds

$$f^\star(\mathbf{r}, \mathbf{c}, t) = f(\mathbf{r}, \mathbf{c}, t) \exp\left(\int_0^t \nu_{\mathrm{fi}}(\tau) \mathrm{d}\tau \right). \tag{3}$$

Substituting equation (3) into equation (2) and using the linearity of the collision operator yields the following equation

$$J(f^\star) = \exp\left(\int_0^t \nu_{\mathrm{fi}}(\tau) \mathrm{d}\tau \right) J(f). \tag{4}$$

Note that in contrast to Li *et al* [61] the collision frequency for the fictitious ionization is now a time-dependent function. In terms of numerical implementation, the only difference between our continuous rescaling procedure and the one described in [54, 61] is that we do not need to provide the fictitious ionization rate which is estimated by trial and error, in advance (*a priori*). Instead, our fictitious ionization rate is initially chosen to be equal to the calculated attachment rate at the beginning of the simulation. Afterwards, it is recalculated at fixed time instants in order to match the newly developed attachment rates. As a result, the number of electrons during the simulation usually does not differ from the initial one by more than 10%. It should be noted that the fictitious ionization process must not in any way be linked to the process of real ionization. It was introduced only as a way to scale the distribution function, or in other words, as a way of duplicating the electrons.

3. Results and discussion

In this section the rescaling procedures and associated Monte Carlo code outlined in the previous section are applied to investigate transport properties and attachment induced phenomena for electrons in SF_6 and CF_3I. Electron transport in these two strongly attaching gases provides a good test of different rescaling procedures, particularly for lower E/n_0 where electron attachment is the dominant non-conservative process. In addition to comparisons between different rescaling procedures, the emphasis of this section is the observation and physical interpretation of the attachment induced phenomena in the E/n_0-profiles of mean energy, drift velocity and diffusion coefficients. In particular, we investigate the differences between the bulk and flux transport coefficients. We do not compare our results with experimentally measured data as it would distract the reader's attention to the problems associated with the quality of the sets of the cross sections for electron scattering. There are no new experimental measurements of transport coefficients for electrons in SF_6, particularly for E/n_0 less than 50 Td and thus we have deliberately chosen not to display the comparison. On the other hand, one cannot expect the multi term results to be useful here as the conditions with excessive attachment would make convergence difficult in the low E/n_0 region, where comparison would be of
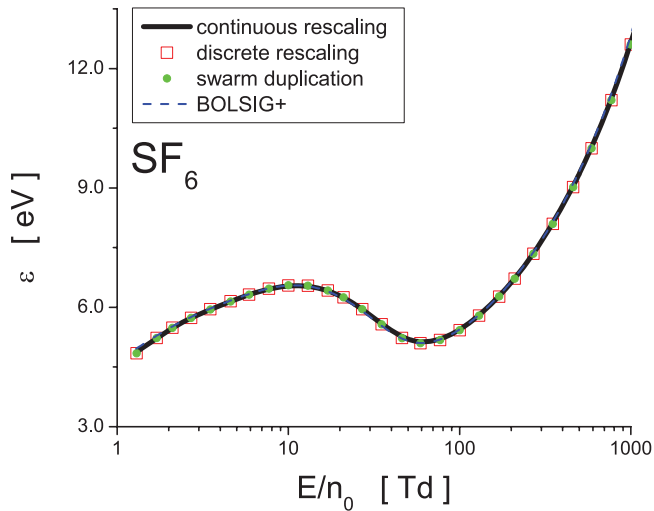
Figure 3. Variation of the mean energy with E/n_0 for electrons in SF_6. Monte Carlo results using three different techniques for electron number density compensation (rescaling) are compared with the BOLSIG+ results.

Figure 4. Electron energy distribution functions for E/n_0 of 10, 27, 59 and 210 Td. Cross sections for elastic momentum transfer (Qmt), electronic excitation (Qexc) and ionization (Qion) as well as for attachments that lead to the formation of SF_6^- (Qatt1) and SF_5^- (Qatt2) ions, are also included.

interest. Thus, for clarity the multi term results are omitted. Both experimental and theoretical work on electron swarms in SF_6 prior to 1990 is summarized in the papers of Phelps and van Brunt [11], Gallagher *et al* [71] and Morrow [72]. Recent results can be found in the book by Raju [22] and the review article of Christophorou and Olthoff [12]. The swarm analysis and further improvements of the cross sections for electron scattering in CF_3I is a subject of our future work [64].

3.1. Transport properties for electrons in SF_6 and CF_3I

3.1.1. Mean energy. In figure 3 we show the variation of the mean energy with E/n_0 for electrons in SF_6. The agreement between different rescaling procedures is excellent. This suggests that all rescaling procedures are equally valid for calculation of the mean energy (provided that rescaling is performed carefully). In addition, the BOLSIG+ results agree very well with those calculated by a Monte Carlo simulation technique. For lower E/n_0, the mean energy initially increases with E/n_0, reaching a peak at about 10 Td, and then surprisingly it starts to decrease with E/n_0. The minimum of mean energy occurs at approximately 60 Td. For higher E/n_0 the mean energy monotonically increases with E/n_0. The reduction in the mean energy with increasing E/n_0 has been reported for electrons in Ar [73] and O_2 [74] but in the presence of very strong magnetic fields. In the present work, however, the mean energy is reduced in absence of magnetic field which certainly represents one of the most striking and anomalous effects observed in this study. Moreover, this behavior is contrary to previous experiences in swarm physics as one would expect the mean swarm energy to increase with increasing E/n_0. This is discussed in detail below.

In order to understand the anomalous behavior of the mean energy of electrons in SF_6, in figure 4 we display the electron energy distribution functions for E/n_0 at 10, 27, 59 and 210 Td. Cross sections for some of the more relevant collision processes are also included, as indicated in the graph.
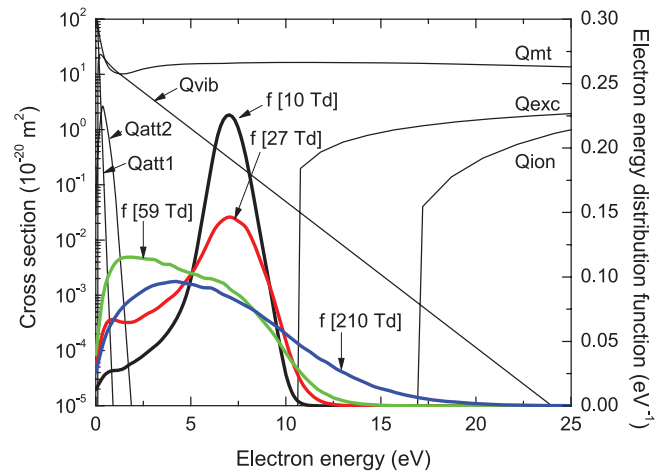
For clarity, the attachment cross sections for the formation of SF_4^-, F_2^- and F^- are omitted in the figure. For E/n_0 of 10 and 27 Td we observe the clear signs of 'hole burning' in the electron energy distribution function (EEDF). This phenomenon has been extensively discussed for electrons in O_2 [75, 76], O_2 mixtures [29, 77] and under conditions leading to the phenomenon of absolute negative electron mobility [27, 60] as well as for electrons in the gas mixtures of $C_2H_2F_4$, iso-C_4H_{10} and SF_6 used in resistive plate chambers in various high energy physics experiments at CERN [6]. For electrons in SF_6, the collision frequency for electron attachment decreases with energy and hence the slower electrons at the trailing edge of the swarm are preferentially attached. As a consequence, the electrons are 'bunched' in the high-energy part of the distribution function which in turn moves the bulk of the distribution function to higher energies. This is the well-known phenomenon of attachment heating which has already been discussed in the literature for model [25, 26] and real gases [6, 29]. In the limit of the lowest E/n_0 we see that due to attachment heating the mean energy attains the unusually high value of almost 5 eV. For a majority of molecular gases, however, the mean energy is significantly reduced for lower E/n_0 due to presence of rotational, vibrational and electronic excitations which have threshold energies over a wide range. As E/n_0 further increases the mean energy is also increased as electrons are accelerated through a larger potential. However, in case of SF_6, for E/n_0 increasing beyond 10 Td the mean energy is reduced. This atypical situation follows from the combined effects of attachment heating and inelastic cooling. From figure 4 we see that for E/n_0 of 27 and 59 Td the electrons from the tail of the corresponding distribution functions have enough energy to undergo the electronic excitation. Whenever an electron undergoes electronic excitations (or ionization) it loses the threshold energy of 9.8 eV (or 15.8 eV in case of ionization) and emerges from the collision with a reduced energy. This in turn diminishes the phenomenon of 'hole burning' in the distribution function by repopulating
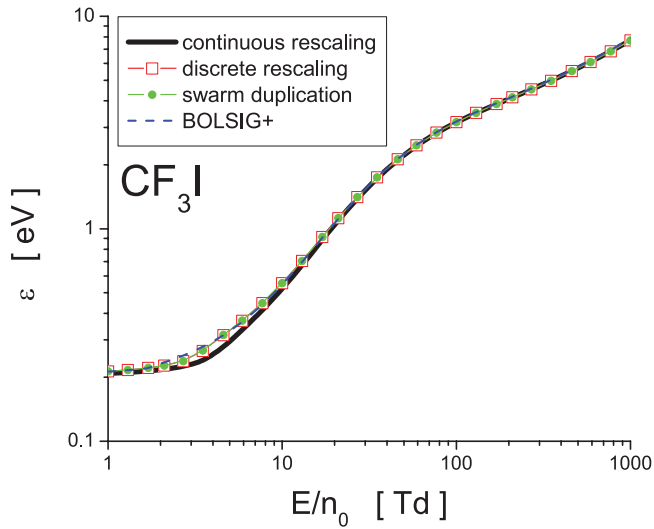
Figure 5. Variation of the mean energy with E/n_0 for electrons in CF_3I. Monte Carlo results using three different techniques for electron compensation are compared with the BOLSIG+ results.

Figure 6. Variation of the drift velocity with E/n_0 for electrons in SF_6. Monte Carlo results using three different techniques for electron number density compensation are compared with the BOLSIG+ results.

the distribution function at the lower energy. The combined effects of attachment heating and inelastic cooling and subsequent redistribution of low-energy electrons are more significant for the energy balance than the energy gain from electric field and losses in other collisions. The vibrational excitation with the threshold of 0.098 eV is of less importance having in mind the actual values of the mean energy. For E/n_0 higher than 60 Td, the dominant part in the energy balance is the energy gain from the electric field while attachment heating and induced phenomena are significantly suppressed. Thus, for E/n_0 higher than 60 Td the mean energy monotonically increases with increasing E/n_0.

The variation of the mean energy with E/n_0 for electrons in CF_3I is shown in figure 5. The agreement between different rescaling procedures is very good. Small deviations between discrete rescaling and swarm duplication from one side and continuous rescaling from the other side are present between approximately 3 and 20 Td. BOLSIG+ slightly overestimates the mean energy only in the limit of the lowest E/n_0. In contrast to mean energy of the electrons in SF_6, the mean energy of the electrons in CF_3I monotonically increases with E/n_0 without signs of anomalous behavior. If we take a careful look, then we can isolate three distinct regions of electron transport in CF_3I as E/n_0 increases. First, there is an initial region where the mean energy raises relatively slowly due to large energy loss of the electrons in low-threshold vibrational excitations. In this region the mean energy of the electrons is well above the thermal energy due to extensive attachment heating. The mean energy is raised much sharper between approximately 5 and 50 Td, indicating that electrons become able to overcome low-threshold vibrational excitations. The following region of slower rise follows from the explicit cooling of other inelastic processes, including electronic excitations and ionization, as these processes are now turned on. In conclusion, the nature of cross sections for electron scattering in CF_3I and their energy dependence as well as their mutual relations do not favor the development of the anomalous behavior of the swarm mean energy.
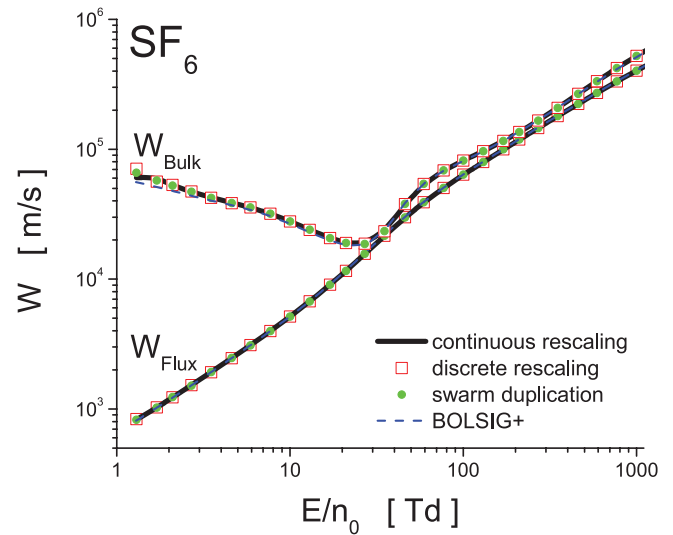

Figure 7. Variation of the drift velocity with E/n_0 for electrons in CF_3I. Monte Carlo results using three different techniques for electron number density compensation are compared with the BOLSIG+ results.
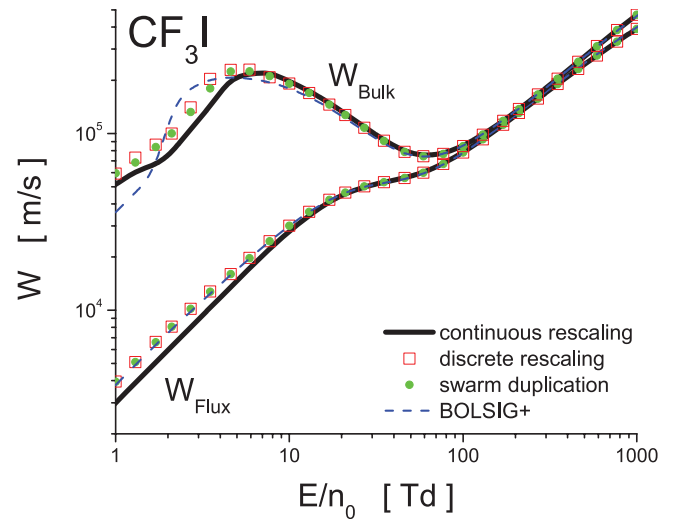
3.1.2. Drift velocity. In figures 6 and 7 we show variation of the bulk and flux drift velocity with E/n_0 for electrons in SF_6 and CF_3I, respectively. For electrons in SF_6 the agreement between different rescaling procedures for electron compensation is excellent for both the bulk and flux drift velocity over the entire E/n_0 range considered in this work. The BOLSIG+ bulk results slightly underestimate the corresponding bulk Monte Carlo results in the limit of the lowest E/n_0. For electrons in CF_3I, the agreement among different rescaling procedures for electron compensation is also good except for lower E/n_0 where the continuous rescaling gives somewhat lower results than other techniques.

For both SF_6 and CF_3I, we see that the bulk dominates the flux drift velocity over the entire E/n_0 range considered in this work. For lower E/n_0 this is a consequence of a very intense
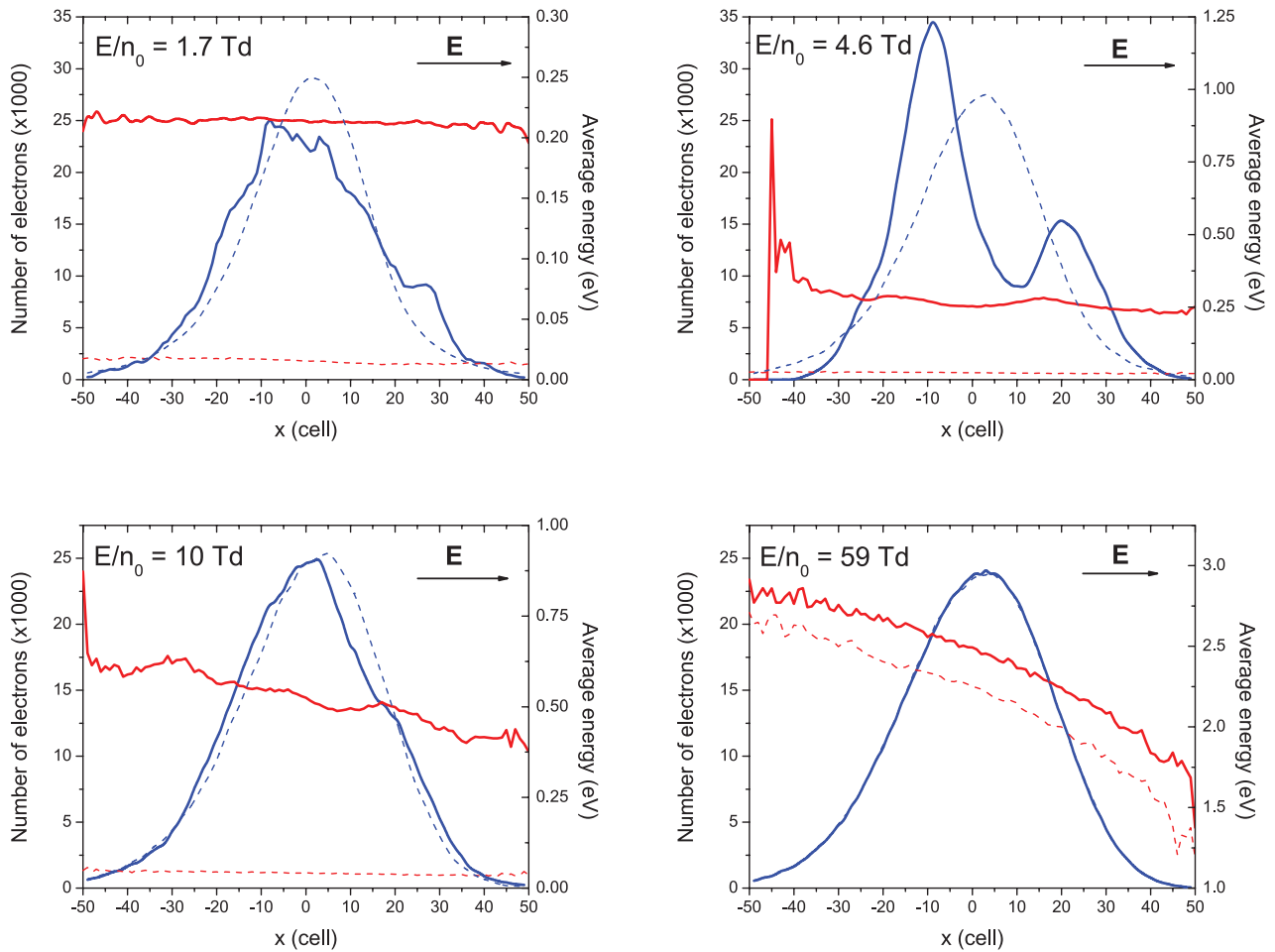
Figure 8. Spatial profile of electrons (blue curves) and spatially resolved averaged energy (red curves) at four different E/n_0 in CF$_3$I. Full lines denote the results when electron attachment is treated as a non-conservative process, while the dashed lines represent our results when electron attachment is treated as a conservative inelastic process with zero energy loss.

attachment heating while for higher E/n_0 this follows from the explicit effects of ionization. As mentioned above, when transport processes are greatly affected by attachment heating the slower electrons at the back of the swarm are consumed at a faster rate than those at the front of the swarm. Thus, in the case of drift, the electron attachment acts to push the centre of mass forward, increasing the bulk drift velocity above its flux component. For higher E/n_0 when ionization takes place, the ionization rate is higher for faster electrons at the front of the swarm than for slower electrons at the back of the swarm. As a result, electrons are preferentially created at the front of the swarm which results in a shift in the centre of mass. Of course, this physical picture is valid if collision frequency for ionization is an increasing function of electron energy. This is true for electrons in both SF$_6$ and CF$_3$I. The explicit effects of electron attachment are much stronger than those induced by ionization. When ionization is dominant non-conservative process, the differences between two sets of data are within 30% for both gases. When attachment dominates ionization, however, then the discrepancy between two sets of data might be almost two orders of magnitude, as for electrons in SF$_6$ in the limit of the lowest E/n_0.

The flux drift velocity is a monotonically increasing function of E/n_0 while the bulk component behaves in a qualitatively

different fashion. A prominent feature of electron drift in SF$_6$ and CF$_3$I is the presence of a very strong NDC in the profile of the bulk drift velocity. On the other hand, a decrease in the flux drift velocity with increasing E/n_0 has not been observed. Such behavior is similar of the recently observed NDC effect for positrons in molecular gases [78, 79] where Positronium (Ps) formation plays the role of electron attachment.

In order to provide physical arguments for an explanation of NDC in the bulk drift velocity, in figure 8 we show the spatial profile and spatially resolved average energy of electrons in CF$_3$I. Calculations are performed for four different values of E/n_0 as indicated in the graph. The direction of the applied electric field is also shown. Two fundamentally different scenarios are discussed: (1) the electron attachment is treated as a conservative inelastic process with zero energy loss, and (2) the electron attachment is treated regularly, as a true nonconservative process. The first scenario is made with the aim of illustrating that NDC is not primarily caused by the shape of cross section for attachment but rather by the synergism of explicit and the implicit effects of the number changing nature of the process on electron transport. Sampling of spatially resolved data in our Monte Carlo simulations is performed using the continuous rescaling. The continuous rescaling produces smoother curves and in most cases it is more reliable

as compared to the discrete rescaling and swarm duplication. The results of the first scenario are presented by dashed lines while the second scenario where electron attachment is treated as a true non-conservative process, is represented by full lines.

When electron attachment is treated as a conservative inelastic process, the spatial profile of electrons has a well defined Gaussian profile with a small bias induced by the effect of electric field. The non-symmetrical feature of spatial profile is further enhanced with increasing E/n_0. While for lower E/n_0 the spatial variation of the average energy is relatively low, for higher E/n_0, e.g. for E/n_0 of 59 Td the slope of the average energy is quite high, indicating that the electron swarm energy distribution is normally spatially anisotropic. It is important to note that there are no imprinted oscillations in the spatial profile of the electrons or in the profile of the average energy which is a clear sign that the collisional energy loss is governed essentially by 'continuous' energy loss processes [32].

When electron attachment is treated as a true non-conservative process, the spatial profile and the average energy of electrons are drastically changed. For all considered reduced electric fields spatially resolved average energy is greater as compared to the case when electron attachment is treated as a conservative inelastic process. For E/n_0 of 1.7 and 4.6 Td the spatial profiles of electrons depart from a typical Gaussian shape. For 1.7 Td there is very little spatial variation in the average energy along the swarm. When $E/n_0 = 4.6$ Td, however, the spatial profile is skewed, asymmetric and shifted to the left. This shift corresponds approximately to the difference between bulk drift velocities in the two scenarios. We observe that the trailing edge of the swarm is dramatically cut off while the average energy remains essentially unaltered. At the leading edge of the swarm, however, we observe a sharp jump in the average energy which is followed by a sharp drop-off. In addition, the height of spatial profile is significantly increased in comparison to the Gaussian profile of the swarm when electron attachment is treated as a conservative inelastic process. For higher E/n_0 the signs of explicit effects of electron attachment are still present but are significantly reduced. For $E/n_0 = 10$ Td the spatial dependence of the average energy is almost linear with a small jump at the leading edge of the swarm. Comparing trailing edges of the swarms at 4.6 and 10 Td we see that for higher electric field the spatial profile of electrons is by far less cut off. This suggests that for increasing E/n_0 there are fewer and fewer electrons that are consumed by electron attachment. Finally, for $E/n_0 = 59$ Td the spatial profile of electrons is exactly the same as the profile obtained under conditions when electron attachment is treated as a conservative inelastic process.

The spatially resolved attachment rates are displayed in figure 9 and are calculated under the same conditions as for the spatial profile of the electrons and spatially averaged energy. We see that the attachment rate peaks at the trailing edge of the swarm where the average energy of the electrons is lower. Attachment loss of these lower energy electrons causes a forward shift to the swarm centre of mass, with a corresponding increase in the bulk drift velocity. For increasing E/n_0, the spatially resolved attachment rate coefficients are reduced and linearly decrease from the trailing edge towards the leading
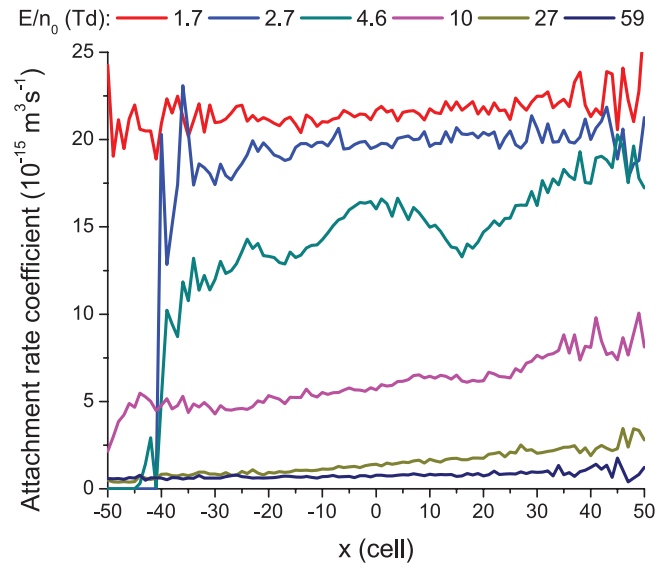

Figure 9. Spatially resolved attachment rate coefficient for a range of E/n_0 as indicated on the graph. Calculations are performed for electrons in CF_3I.

part of the swarm. At the same time the electrons at the leading edge of the swarm have enough energy to undergo ionization. This suggests much less explicit influence of electron attachment on the electron swarm behavior. As a consequence, NDC is removed from the profile of the bulk drift velocity.

In addition to the explicit effects of electron attachment there are implicit effects due to energy specific loss of electrons, which changes the swarm energy distribution as a whole, and thus indirectly changes the swarm flux. Generally speaking, it is not possible to separate the explicit from implicit effects, except by analysis with and without the electron attachment. Using these facts as motivational factors, in figure 10 we show the electron energy distribution functions for the same four values of E/n_0 considered above. The electron energy distribution functions are calculated when electron attachment is treated as a true non-conservative process (full line) and under conditions when electron attachment is assumed to be a conservative inelastic process (dashed line). As for electrons in SF_6, we observe a 'hole burning' effect in the energy distribution function which is certainly one of the most illustrative examples of the implicit effects. Likewise, we see that the high energy tail of the distribution function falls off very slowly even slower than for Maxwellian. Under these circumstances, when the actual distribution function significantly deviates from a Maxwellian, the numerical schemes for solving the Boltzmann equation in the framework of moment methods usually fail. Indeed, for E/n_0 less than approximately 20 Td we have found a sudden deterioration in the convergence of the transport coefficients which was most pronounced for the bulk properties. Furthermore, we see that the 'hole burning' effect is not present when electron attachment is treated as a conservative inelastic process. The lower energy part of the distribution function is well populated while high energy part falls off rapidly. For increasing E/n_0 and when electron attachment is treated as a true non-conservative process, the effect of hole burning is reduced markedly while
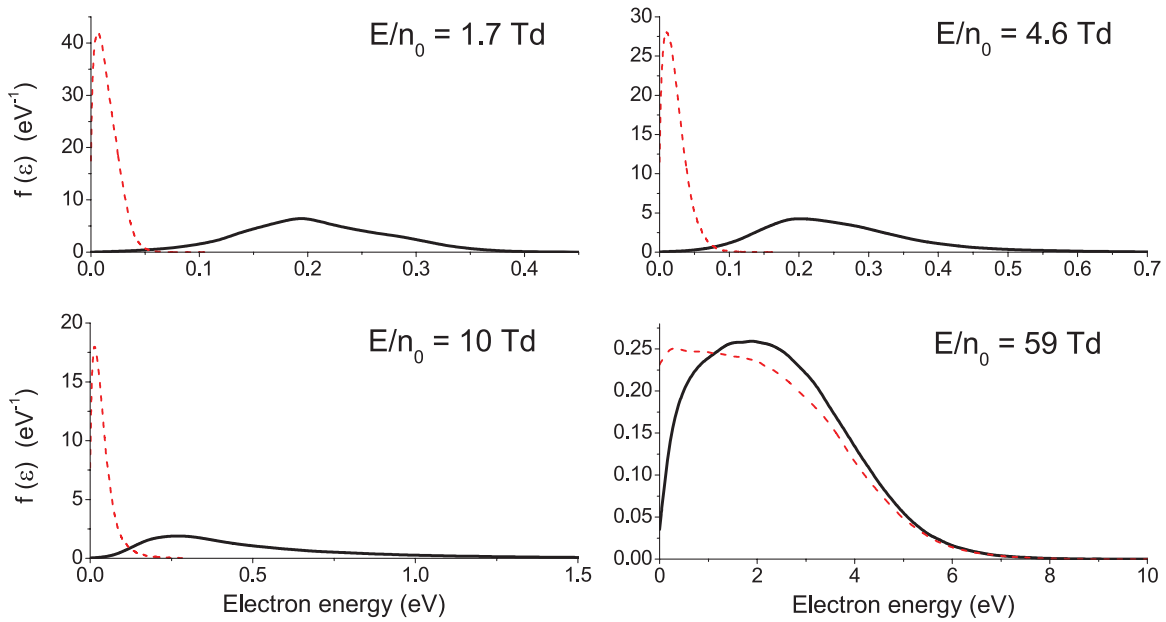
Figure 10. Energy distribution functions for four different E/n_0 for electrons in CF_3I. Black lines denote the results when electron attachment is treated as non-conservative process while dashed red lines represent our results when electron attachment is treated as a conservative inelastic process.

the high energy part of the distribution function coincides with the corresponding one when electron attachment is treated as a conservative inelastic process.

Before embarking on a discussion of our results for diffusion coefficients, one particular point deserves more mention. NDC phenomenon in the bulk drift velocity has not been experimentally verified, neither for SF_6 nor for CF_3I. On the other hand, as we have already seen, the two entirely different theoretical techniques for calculating the drift velocity predict the existence of the phenomenon. Thus, it would be very useful to extend the recent measurements of the drift velocity in both SF_6 and CF_3I to lower E/n_0 with the aim of confirming the existence of NDC. On the other hand, such measurements are most likely very difficult, even impossible due to rapid losses of electron density in experiment.

3.1.3. Diffusion coefficients. Variations of the longitudinal and transverse diffusion coefficients with E/n_0 for electrons in SF_6 are displayed in figures 11 and 12, respectively. From the E/n_0-profiles of the longitudinal and transverse flux diffusion coefficients, we observe that different rescaling procedures for Monte Carlo simulations agree very well. For the bulk components, the agreement is also very good for intermediate and higher E/n_0 and only in the limit of the lowest E/n_0 the agreement is deteriorated. Over the range of E/n_0 considered we see that there is an excellent agreement between continuous and discrete rescaling.

Comparing Monte Carlo and BOLSIG+ results, the deviations are clearly evident. They might be attributed to the inaccuracy of the two term approximation of the Boltzmann equation which is always considerably higher for diffusion than for the drift velocity. For higher E/n_0, inelastic collisions are significant and the distribution function deviates substantially from isotropy in velocity space. In these circumstances,
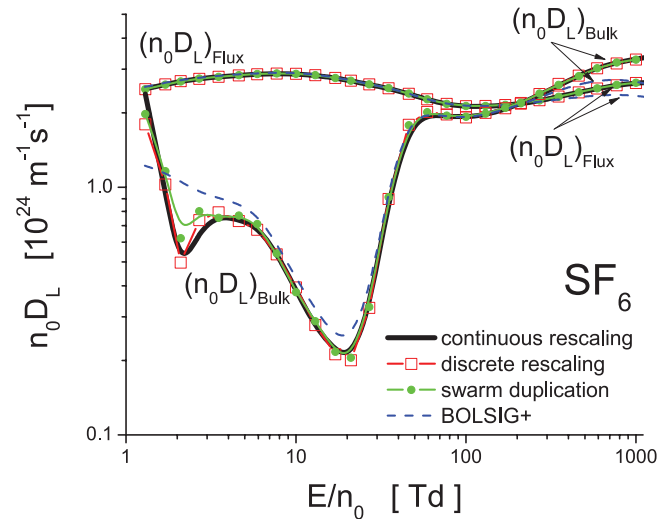

Figure 11. Variation of the longitudinal diffusion coefficient with E/n_0 for electrons in SF_6. Monte Carlo results using three different techniques for electron number density compensation are compared with the BOLSIG+ results.

the two term approximation of the Boltzmann equation fails and multi-term Boltzmann equation analysis is required. For lower E/n_0, however, the role of inelastic collisions is of less significance, but still discrepancies between the BOLSIG+ and Monte Carlo results are clearly evident, particularly for the longitudinal diffusion coefficient. This suggests that further analyses of the impact of electron attachment on the distribution function in velocity space of electrons in SF_6 would be very useful.

From the profiles of the longitudinal diffusion coefficient at lower and intermediate values of E/n_0 we observe the following interesting points. In contrast to drift velocity (and transverse diffusion coefficient shown in figure 12) we see
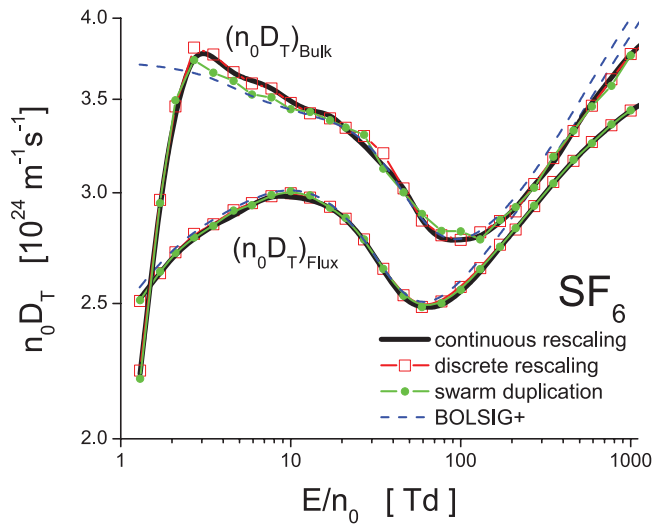
Figure 12. Variation of the transverse diffusion coefficient with E/n_0 for electrons in SF_6. Monte Carlo results using three different techniques for electron number density compensation are compared with the BOLSIG+ results.

Figure 13. Variation of the longitudinal diffusion coefficient with E/n_0 for electrons in CF_3I. Monte Carlo results using three different techniques for electron number density compensation are compared with the BOLSIG+ results.

that the bulk diffusion coefficient is smaller than the corresponding flux component. This indicates that the decrease in electron numbers due to attachment weakens diffusion along the field direction. As already discussed, attachment loss of electrons from the trailing edge of the swarm causes a forward shift to the swarm centre of mass, with the corresponding increases in the bulk drift velocity and mean energy. The same effects result in an enhancement of the flux longitudinal diffusion. It should be noted that when attachment heating takes place, the opposite situation (bulk is higher than flux) has also been reported [25]. This is a clear sign that the energy dependence of the cross sections for electron attachment is of primary importance for the analysis of these phenomena. For higher E/n_0, however, where the contribution of ionization becomes important, we observe that the diffusion is enhanced along the field direction, e.g. the bulk dominates the flux. This is always the case if the collision frequency for ionization is an increasing function of the electron energy, independently of the gaseous medium considered.

From the profiles of the transverse diffusion coefficient the bulk values are greater than the corresponding flux values over the range of E/n_0 considered in this work. Only in the limit of the lowest E/n_0 the opposite situation holds: the flux is greater than the bulk. In contrast to the longitudinal diffusion, spreading along the transverse directions is entirely determined by the thermal motion of the electrons. The flux of the Brownian motion through a transverse plane is proportional to the speed of the electrons passing through the same plane. Therefore, the higher energy electrons contribute the most to the transversal expansion, so attachment heating enhances transverse bulk diffusion coefficient.

Figures 13 and 14 show the variations of the longitudinal and transverse diffusion coefficients with E/n_0 for electrons in CF_3I, respectively. From the E/n_0-profiles of the bulk diffusion coefficients we observe an excellent agreement between different rescaling procedures for $E/n_0 > 10$ Td. The same applies for the flux component of the longitudinal diffusion.
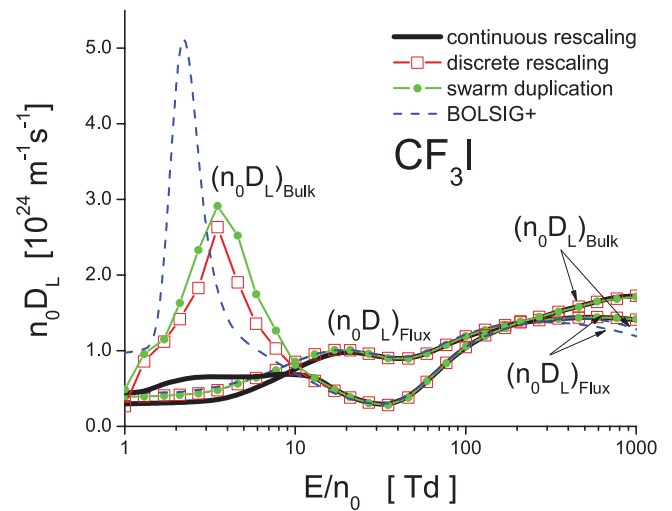

Figure 14. Variation of the transverse diffusion coefficient with E/n_0 for electrons in CF_3I. Monte Carlo results using three different techniques for electron number density compensation are compared with the BOLSIG+ results.
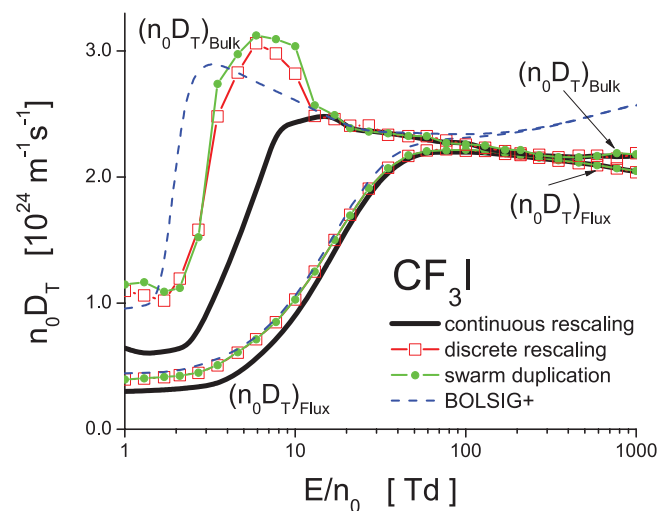
For $E/n_0 < 10$ Td the agreement is poor for bulk components, particularly between the continuous rescaling from one side and discrete rescaling and/or swarm duplication from the other side. The agreement is better for the flux components.

Comparing Monte Carlo and BOLSIG + results, we see that the maximum error in the two term approximation, for both diffusion coefficients occurs at lower and higher E/n_0. In contrast to SF_6, CF_3I has rapidly increasing cross sections for vibrational excitations in the same energy region where the cross section of momentum transfer in elastic collisions decreases with the electron energy. Under these conditions, the energy transfer is increased and collisions no longer have the effect of randomizing the direction of electron motion. As a consequence, the distribution function deviates significantly from isotropy in velocity space and two term approximation of the Boltzmann equation fails.

When considering the differences between the bulk and flux values of diffusion coefficients the situation is much more complex comparing to SF_6. From the E/n_0-profiles of the longitudinal diffusion coefficient one can immediately see that for lower and higher E/n_0, the bulk is greater than the corresponding flux values while at intermediate E/n_0 the opposite situation holds: the flux is greater than the bulk. The behavior of the transverse diffusion coefficient is less complex, as over the entire of E/n_0 the bulk is greater that the corresponding flux values.

As we have demonstrated, in contrast to drift velocity the behavior and differences between the bulk and flux diffusion coefficients is somewhat harder to interpret. This follows from the complexity of factors which contribute to or influence the diffusion coefficients. The two most important factors are the following: (a) the thermal anisotropy effect resulting from different random electron motion in different directions; and (b) the anisotropy induced by the electric field resulting from the spatial variation of the average energy and local average velocities throughout the swarm which act so as to either inhibit or enhance diffusion. Additional factors include the effects of collisions, energy-dependent total collision frequency, and presence of non-conservative collisions. Couplings of these individual factors are always present and hence sometimes it is hard to elucidate even the basic trends in the behavior of diffusion coefficients. In particular, to understand the effects of electron attachment on diffusion coefficients and associated differences between bulk and flux components, the variation in the diffusive energy tensor associated with the second-order spatial variation in the average energy with E/n_0 should be studied. This remains the program of our future work.

3.1.4. Rate coefficients. In figure 15 we show the variation of steady-state Townsend ionization and attachment coefficients with E/n_0 for electrons in SF_6. The agreement between different rescaling procedures and BOLSIG+ code is very good. It is important to note that the agreement is very good, even in the limit of the lowest E/n_0 considered in this work where the electron energy distribution function is greatly affected by electron attachment. The curves show expected increase in α/n_0 and expected decrease in η/n_0, with increasing E/n_0. The value obtained for critical electric field is 361 Td which is in excellent agreement with experimental measurements of Aschwanden [80].

In figure 16 we show variation of the steady-state Townsend ionization and attachment coefficients with E/n_0 for electrons in CF_3I. The agreement between different rescaling procedure and BOLSIG+ code is excellent for ionization coefficient. From the E/n_0-profile of attachment coefficient, we see that the continuous rescaling slightly overestimates the remaining scenarios of computation. The critical electric field for CF_3I is higher than for SF_6. This fact has been recently used as a motivational factor for a new wave of studies related to the insulation characteristics of pure CF_3I and its mixture with other gases, in the light of the present search for suitable alternatives to SF_6. The value obtained for critical electric field in our calculations is 440 Td which is in close agreement with experimental measurements under steady-state [63, 81]
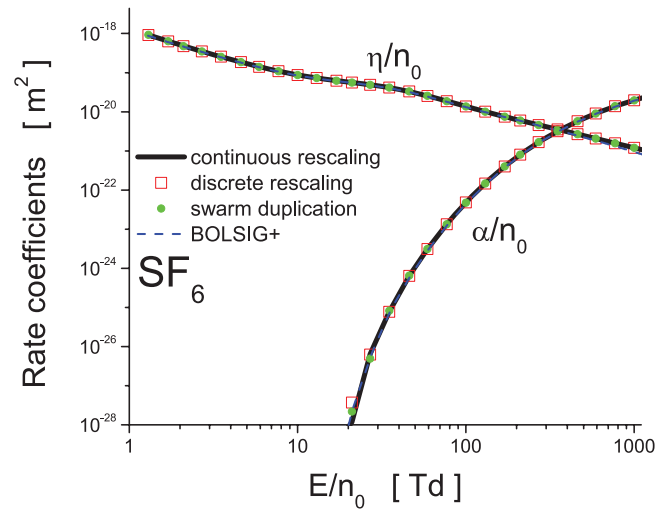

Figure 15. Variation of the rate coefficients with E/n_0 for electrons in SF_6. Monte Carlo results using three different techniques for electron number density compensation are compared with the BOLSIG+ results.
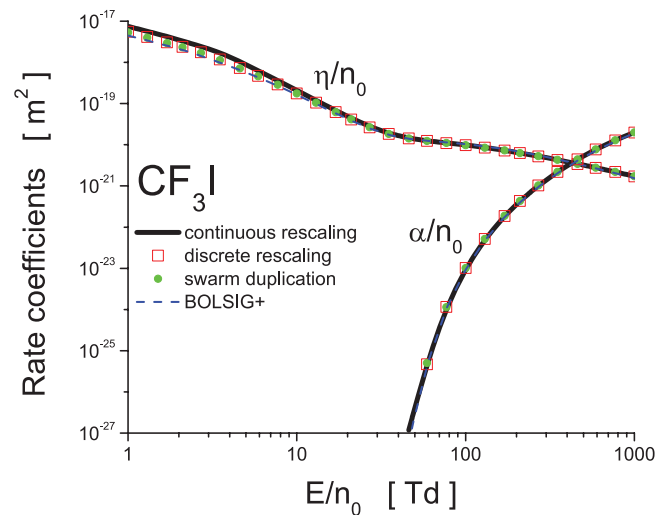

Figure 16. Variation of the rate coefficients with E/n_0 for electrons in CF_3I. Monte Carlo results using three different techniques for electron number density compensation are compared with the BOLSIG+ results.

and pulsed-Townsend [82] conditions, as well as with recent calculations performed by Kawaguchi *et al* [58] and Deng and Xiao [52].

3.2. Recommendations for implementation

In this section, we discuss the main features of the rescaling procedures and we give recommendations on how to use them in future Monte Carlo codes. Based on our experience achieved by simulating the electron transport in SF_6, CF_3I and other attaching gases, we have observed that if correctly implemented the procedures generally agree very well. The agreement between different rescaling procedures is always better for the flux than for the bulk properties. We found a poor agreement for the bulk diffusion coefficients, particularly for the lower E/n_0 while for mean energy, drift velocity and

rate coefficients the agreement is reasonably good. For lower E/n_0 when the distribution function is extremely affected by electron attachment, the agreement between swarm duplication and discrete rescaling is also good. This is not surprising as these two techniques are essentially the same.

In terms of implementation, the Monte Carlo codes can be relatively easily upgraded with the procedures for swarm duplication and/or discrete rescaling. Special attention during the implementation of these procedures should be given to the choice of the length of time steps after which the cloning of the electrons is done. If the length of this time step appears to be too long as compared to the time constant which corresponds to the attachment collision frequency, then the distribution function could be disturbed due to a low statistical accuracy. In other words, depleting certain pockets of the EEDF means that those cannot be recovered at all. On the other hand, if the length of the time steps is too small, the speed of simulation could be significantly reduced. The implementation of the continuous rescaling procedure is somewhat more complicated.

Which procedure is, the most flexible? It is difficult to answer this question because the answer depends on the criteria of flexibility. If the criterion for flexibility is associated with the need for *a priori* estimates which are necessary for setting the simulation, then the technique of continuous rescaling is certainly the most flexible. Once implemented, and thoroughly tested this procedure allows the analysis of electron transport in strongly attaching gases regardless of the energy dependence of the cross section for electron attachment. On the other hand, for the analysis of electron transport in weakly attaching gases, the discrete rescaling is very convenient because it is easier for implementation into the codes and less demanding in terms of the CPU time.

In terms of reliability and accuracy, the comparison of the results obtained for various transport properties using the rescaling procedures for Monte Carlo simulations and the Boltzmann equation codes shows that the rescaling procedures described herein are highly reliable. It should be noted that only the multi term codes for solving the Boltzmann equation may offer the final answer. Restrictions of the TTA for solving the Boltzmann equation were demonstrated many times in the past [7, 31], especially when it comes to the calculations of diffusion coefficients. Testing and benchmarking against other Boltzmann solvers are currently ongoing.

3.3. Experiments in strongly attaching gases: difficulties induced by non-hydrodynamic effects

It must be noted at this point that most processes scale with pressure, so the independence on pressure would be maintained and so would be the equilibration of EEDFs affected by excessive attachment. Most of the processes fall into that category. These processes are best visualized in an infinite uniform environment. Standard swarm experiments are built in such a way that boundaries are not felt over appreciable volume and thus, they mimic hydrodynamic conditions very well. However, going to high E/n_0 requires operating at lower pressures and there the boundaries may be felt over a larger

portion of the volume. In general, whenever boundaries of any kind are introduced selective losses resulting in very different mean free paths of different groups of particles may lead to selective losses. The resulting holes in the distribution may be filled in by collisions, so when considerable selective losses are introduced results may become the pressure dependent (even when the cross section is not dependent on the pressure). The same is true for temporal limitations. For example, if the frequency of collisions is small, so that the mean free time is comparable to the time required to accelerate to energies where cross sections decrease with the electron energy, the runaway effects may be developed. Similar effects may be created due to temporal variations of the field that do not allow full equilibration. The pressure dependence of the results will develop under such conditions (and so would the dependence on the size of the vessel). The development of a non-hydrodynamic theory for solving the Boiltzmann equation is difficult and the best solution is a Monte Carlo simulation technique. For that reason, rescaling procedures are essential in modeling of the non-hydrodynamic (non-local) development of charged particle ensembles.

Experiments in gases with a very large attachment (typically at low energies) may be difficult to carry out due to a large loss of electrons. The fact that experiments in diluted gas mixtures of such gases may be feasible, means that cross sections may be obtained. Yet, one should be aware of two main problems. Even in such mixtures and depending on the size of the experiment, attachment may be high enough to induce depletion of the distribution function thus making results pressure dependent or abundance dependent. If one wants to extend the calculations to pure attaching gas for smaller vessels and pressures, one needs to be aware that only techniques that take full non-hydrodynamic description of the swarm development, are required. Similar effects have been observed in gases always associated with strong attachment such as oxygen [76] and water vapor [83]. In any case, the critical effects that include NDC for bulk drift velocity as a result of excessive loss of electrons in attachment can be observed in gases like SF_6 and CF_3I based on hydrodynamic expansion and even based on the two term theory provided that theory takes into account the explicit and implicit non-conservative effects of the attachment.

4. Conclusion

In this paper, we have presented the development, implementation and benchmarking of the rescaling procedures for Monte Carlo simulations of electron transport in strongly attaching gases. The capabilities of the rescaling procedures have been described by systematic investigation of the influence of electron attachment on transport coefficients of electrons in SF_6 and CF_3I. Among many important points, the key results arising from this paper are:

(1) We have presented two distinctively different methods for compensation of electrons in Monte Carlo simulations of electron transport in strongly attaching gases, e.g. the discrete and the continuous procedures. In order to avoid the

somewhat arbitrary choice of the fictitious ionization rate, we have extended the continuous rescaling procedure, initially developed by Li *et al* [61], by introducing a time-dependent collision frequency for the fictitious ionization process.

(2) One of the initial motivating factors for this work was to provide accurate data for transport properties of electrons in SF_6 and CF_3I which are required as input in fluid models of plasma discharges. In this work, for the first time, we have calculated the mean energy, drift velocity and diffusion coefficients as well as rate coefficients for lower E/n_0 for electrons in SF_6 and CF_3I.

(3) We have demonstrated the differences which can exist between the bulk and flux transport coefficients and the origin of these differences. Our study has shown that the flux and bulk transport properties can vary substantially from one another, particularly in the presence of intensive attachment heating. Thus, one of the key messages of this work is that theories which approximate the bulk transport coefficients by the flux are problematic and generally wrong.

(4) We have demonstrated and interpreted physically the phenomenon of the anomalous behavior of the mean energy of electrons in SF_6, in which the mean energy is reduced for increasing E/n_0. The phenomenon was associated with the interplay between attachment heating an inelastic cooling. The same phenomenon has not been observed for electrons in CF_3I indicating that the role of the cross sections is vital.

(5) We have explained and identified a region of NDC in the bulk drift velocity, originating from the explicit influence of electron attachment. The phenomenon has been explained using the concept of spatially-resolved transport properties along the swarm.

(6) The publicly available two term Boltzmann solver, BOLSIG+, has been shown to be accurate for calculations of mean energy, drift velocity and rate coefficients for electrons in SF_6 and CF_3I. On the other hand, significant differences between our Monte Carlo and BOLSIG+ results for diffusion coefficients have been observed, particularly for electrons in CF_3I in the limit of the lowest E/n_0 considered in this work.

Various rescaling procedures for Monte Carlo simulations described in this work have recently been applied to modeling of electron transport in strongly attaching gases under the influence of time-dependent electric and magnetic fields. It will be challenging to investigate the synergism of magnetic fields and electron attachment in radio-frequency plasmas. Likewise, the remaining step to be taken, is to apply the rescaling procedures presented in this work to investigate the influence of positronium formation on the positron transport properties. This remains the focus of our future investigation. Finally, we hope that this paper will stimulate further discussion on methods of correct representation of the effects induced by electron attachment on transport properties of electrons in strongly attaching gases.

Acknowledgments

References

[1] Christophorou L G and Olthoff J K 2004 *Fundamental Electron Interactions with Plasma Processing Gases* (New York: Springer)

[2] Makabe T and Petrović Z Lj 2014 *Plasma Electronics: Applications in Microelectronic Device Fabrication* (New York: CRC Press)

[3] Christophorou L G and Pinnaduwage L A 1990 *IEEE Trans. Electr. Insul.* **25** 55

[4] Rolandi L, Riegler W and Blum W 2008 *Particle Detection with Drift Chambers* (Berlin: Springer)

[5] Sauli F 2014 *Gaseous Radiation Detectors* (Cambridge: Cambridge University Press)

[6] Bošnjaković D, Petrović Z Lj, White R D and Dujko S 2014 *J. Phys. D: Appl. Phys.* **47** 435203

[7] Petrović Z Lj, Dujko S, Marić D, Malović G, Nikitović Ž, Šašić O, Jovanović J, Stojanović V and Radmilović-Radjenović M 2009 *J. Phys. D: Appl. Phys.* **42** 194002

[8] Petrović Z Lj, Šuvakov M, Nikitović Ž, Dujko S, Šašić O, Jovanović J, Malović G and Stojanović V 2007 *Plasma Sources Sci. Technol.* **16** S1

[9] Huxley L G H and Crompton R W 1974 *The Drift and Diffusion of Electrons in Gases* (New York: Wiley)

[10] Christophorou L G, McCorkle D L and Anderson V E 1971 *J. Phys. B: At. Mol. Phys.* **4** 1163

[11] Phelps A V and van Brunt R J 1988 *J. Appl. Phys.* **64** 4269

[12] Christophorou L G and Olthoff J K 2000 *J. Phys. Chem. Ref. Data* **29** 267

[13] Jarvis G K, Kennedy R A and Mayhew C A 2001 *Int. J. Mass Spectrom.* **205** 253

[14] Dahl D A and Franck C M 2013 *J. Phys. D: Appl. Phys.* **46** 445202

[15] Rabie M, Haefliger P, Chachereau A and Franck C M 2015 *J. Phys. D: Appl. Phys.* **48** 075201

[16] Hunter S R and Christophorou L G 1984 *J. Chem. Phys.* **80** 6150

[17] Novak J P and Frechette M F 1988 *J. Appl. Phys.* **63** 2570

[18] Hunter S R, Carter J G and Christophorou L G 1988 *Phys. Rev.* A **38** 58

[19] Petrović Z Lj, Wang W C and Lee L C 1988 *J. Appl. Phys.* **64** 1625

[20] Petrović Z Lj, Wang W C, Suto M, Han J C and Lee L C 1990 *J. Appl. Phys.* **67** 675

[21] Raju G G 2006 *Gaseous Electronics: Theory and Practice* (New York: CRC Press)

[22] Raju G G 2012 *Gaseous Electronics: Tables, Atoms, and Molecules* (New York: CRC Press)

[23] Cavalleri G 1969 *Phys. Rev.* **179** 186

[24] Petrović Z Lj and Crompton R W 1985 *J. Phys. B: At. Mol. Phys.* **17** 2777

[25] Ness K F and Robson R E 1986 *Phys. Rev.* A **34** 2185

[26] Nolan A M, Brennan M J, Ness K F and Wedding A B 1997 *J. Phys. D: Appl. Phys.* **30** 2865

[27] Dujko S, Raspopović Z M, Petrović Z Lj and Makabe T 2003 *IEEE Trans. Plasma Sci.* **31** 711

[28] White R D, Robson R E and Ness K F 1999 *Phys. Rev.* E **60** 7457

[29] Dujko S, Ebert U, White R D and Petrović Z Lj 2011 *Japan J. Appl. Phys.* **50** 08JC01

[30] Robson R E 1991 *Aust. J. Phys.* **44** 685

[31] White R D, Robson R E, Dujko S, Nicoletopoulos P and Li B
     2009 *J. Phys. D: Appl. Phys.* **42** 194001
[32] Dujko S, White R D, Raspopović Z M and Petrović Z Lj 2012
     Nucl. Instrum. Methods Phys. Res. B **279** 84
[33] Robson R E, White R D and Petrović Z Lj 2005 *Rev. Mod.
     Phys.* **77** 1303
[34] Dujko S, Markosyan A H, White R D and Ebert U 2013
     J. Phys. D: Appl. Phys. **46** 475202
[35] Markosyan A H, Dujko S and Ebert U 2013 *J. Phys. D: Appl.
     Phys.* **46** 475203
[36] Bletzinger P 1990 *J. Appl. Phys.* **67** 130
[37] Stoffels E, Stoffelsd W, Venderm D, Haverlaag M,
     Kroesen G M W and de Hoog F J 1995 *Contrib. Plasma
     Phys.* **35** 331
[38] Chabert P and Sheridan T E 2000 *J. Phys. D: Appl. Phys.*
     33 1854
[39] Kono A 2002 *Appl. Surf. Sci.* **192** 115
[40] Zhao S X, Gao F, Wang Y N and Bogaerts A 2012 *Plasma
     Sources Sci. Technol.* **21** 025008
[41] Chabert P, Lichtenberg A J, Lieberman M A and
     Marakhtanov A M 2003 *J. Appl. Phys.* **94** 831
[42] Robson R E 1986 *J. Chem. Phys.* **85** 4486
[43] Vrhovac S B and Petrović Z Lj 1996 *Phys. Rev.* E **53** 4012
[44] Yousfi M, Segur P and Vassiliadis T 1985 *J. Phys. D: Appl.
     Phys.* **18** 359
[45] Itoh H, Miurat Y, Ikuta N, Nakao Y and Tagashira H 1988
     J. Phys. D: Appl. Phys. **21** 922
[46] Itoh H, Kawaguchi M, Satoh K, Miura Y, Nakano Y and
     Tagashira H 1990 *J. Phys. D: Appl. Phys.* **23** 299
[47] Itoh H, Matsumura T, Satoh K, Date H, Nakano Y and
     Tagashira H 1993 *J. Phys. D: Appl. Phys.* **26** 1975
[48] Frechette M F and Novak J P 1987 *J. Phys. D: Appl. Phys.*
     20 438
[49] Pinheiro M J and Loureiro J 2002 *J. Phys. D: Appl. Phys.* **35** 3077
[50] Tezcan S S, Akcayol M A, Ozerdem O C and Dincer M S
     2010 *IEEE Trans. Plasma Sci.* **38** 2332
[51] Li X, Zhao H, Wu J and Jia S 2013 *J. Phys. D: Appl. Phys.*
     46 345203
[52] Deng Y and Xiao D 2014 *Japan J. Appl. Phys.* **53** 096201
[53] Dujko S, White R D, Petrović Z Lj and Robson R E 2010
     Phys. Rev. E **81** 046403
[54] Yousfi M, Hennad A and Alkaa A 1994 *Phys. Rev.* E **49** 3264
[55] Dincer M S and Gaju G R 1983 *J. Appl. Phys.* **54** 6311
[56] Dincer M S, Ozerdem O C and Bektas S 2007 *IEEE Trans.
     Plasma Sci.* **35** 1210
[57] Satoh K, Itoh H, Nakano Y and Tagashira H 1988 *J. Phys. D:
     Appl. Phys.* **21** 931
[58] Kawaguchi S, Satoh K and Itoh H 2014 *Eur. Phys. J.* D **68** 100
[59] Rapopović Z M, Sakadžić S, Bzenić S and Petrović Z Lj 1999
     IEEE Trans. Plasma Sci. **27** 1241
[60] Dyatko N A and Napartovich A P 1999 *J. Phys. D: Appl.
     Phys.* **32** 3169
[61] Li Y M, Pitchford L C and Moratz T J 1989 *Appl. Phys. Lett.*
     54 1403
[62] Mirić J, Šašić O, Dujko S and Petrović Z Lj 2014 *Proc. 27th
     Summer School and Int. Symp. on the Physics of Ionized
     Gases (Belgrade) (*Belgrade: Institute of Physics) p 122
[63] Kimura M and Nakamura Y 2010 *J. Phys. D: Appl. Phys.*
     43 145202
[64] Mirić J, de Urquijo J, Bošnjaković D, Petrović Z Lj and
     Dujko S 2016 *Plasma Sources Sci. Technol.* submitted
[65] Ristivojević Z and Petrović Z Lj 2012 *Plasma Sources Sci.
     Technol.* **21** 035001
[66] Dujko S, White R D and Petrović Z Lj 2008 *J. Phys. D: Appl.
     Phys.* **41** 245205
[67] Petrović Z Lj, Raspopović Z, Dujko S and Makabe T 2002
     Appl. Surf. Sci. **192** 1
[68] Hagelaar G J M and Pitchford L C 2005 *Plasma Sources Sci.
     Technol.* **14** 722
[69] Kline L and Siambis J 1972 *Phys. Rev.* A **5** 794
[70] Kunhardt E and Tzeng Y 1986 *J. Comput. Phys.* **67** 279
[71] Gallagher J W, Beaty E C, Dutton J and Pitchford L C 1983
     J. Phys. Chem. Ref. Data **12** 109
[72] Morrow R 1986 *IEEE Trans. Plasma Sci.* **PS-14** 234
[73] Ness K F and Makabe T 2000 *Phys. Rev.* E **62** 4083
[74] White R D, Robson R E, Ness K F and Makabe T 2005
     J. Phys. D: Appl. Phys. **38** 997
[75] Skullerud H R 1983 *Aust. J. Phys.* **36** 845
[76] McMahon D R A and Crompton R W 1983 *J. Chem. Phys.*
     78 603
[77] Hegerberg R and Crompton R W 1983 *Aust. J. Phys.*
     36 831
[78] Banković A, Dujko S, White R D, Marler J P, Buckman S J,
     Marjanović S, Malović G, Garcia G and Petrović Z Lj 2012
     New J. Phys. **14** 035003
[79] Banković A, Dujko S, White R D, Buckman S J and
     Petrović Z Lj 2012 *Nucl. Instrum. Methods* B **279** 92
[80] Aschwanden Th 1984 *Gaseous Dielectrics* IV ed
     L G Christophorou and M O Pace (New York: Pergamon) p
     24
[81] Hasegawa H, Date H, Shimozuma M and Itoh H 2009
     Appl. Phys. Lett. **95** 101504
[82] de Urquijo J, Juarez A M, Basurto E and Hernandez-Avila J L
     2007 *J. Phys. D: Appl. Phys.* **40** 2205
[83] Robson R E, White R D and Ness K F 2011 *J. Chem. Phys.*
     134 064319

PAPER

Electron swarm and streamer transport across the gas–liquid interface: a comparative fluid model study

View the article online for updates and enhancements.

IOP ebooks™

Bringing you innovative digital publishing with leading voices to create your essential collection of books in STEM research.

Start exploring the collection - download the first chapter of every title for free.

Electron swarm and streamer transport across the gas–liquid interface: a comparative fluid model study

N A Garland[1] , I Simonović[2], G J Boyle[1,3] , D G Cocks[4] , S Dujko[2] and R D White[1]

[1] College of Science and Engineering, James Cook University, Townsville, QLD 4811, Australia
[2] Institute of Physics, University of Belgrade, Pregrevica 118, 11080 Belgrade, Serbia
[3] Deutsches Elektronen-Synchrotron DESY, Hamburg, Germany
[4] Plasma Research Laboratories, Australian National University, Canberra, 2601, ACT, Australia

E-mail: nathan.garland@my.jcu.edu.au

Abstract

In this work we present a comparative study of fluid modeling methods in order to determine a recommended procedure to describe electron transport and streamer propagation across gas–liquid interfacial regions. A test case of a cryogenic argon gas–liquid interface is simulated in this work to demonstrate applicability of the recommended procedures. The recommended non-local four moment model takes into consideration the density variation across the interface, and its associated impact on the transport properties/collisional transfer rates, as well as the spatial variation of the dielectric permittivity and the conduction band through the liquid binding energy, V_0. The study examines the impacts of various assumptions involved in the modeling of electron transport across the plasma-liquid interface, by comparing a local field (drift-diffusion) approximation with the non-local (four moment) model, as well as a step function change in the density to actual spatially dependent density variations across the interface. We provide recommendations on necessary physical considerations needed to adequately model transport phenomena across gas–liquid interfaces.

Keywords: electron transport, gas liquid interface, fluid model, streamer, ionization front, low temperature plasma

1. Introduction

Over the last century, there has been much effort applied to furthering the understanding of plasma discharges in gases, and developing advanced predictive models for both industrial applications, including microelectronic circuit manufacture [1–3], and for understanding complex natural phenomena such as lightning [4–6]. In addition to gas discharges, there is increasing interest in modeling discharges in liquids [7, 8] to better understand processes such as underwater arc welding and plasma medicine [9–12]. At the nexus of these two extremes is the gas–liquid interface, which has been of particular interest to the plasma community due to emerging applications such as plasma medicine. While advanced models for gas discharges, and recently liquid

discharges, are available [13–15] we believe there is an opportunity to unify the two extremes in order to model electron transport as a continuous process between gas and liquid. In this study we present the framework, and application, of such a model to electron transport across an argon gas–liquid interface.

Argon was chosen as the background medium for this study primarily because much work has already been done to understand electron transport in both gaseous and, recently, liquid argon [16, 17] and so the input data required for fluid models was readily available. In addition to the availability of input data, the study of electron transport over argon gas–liquid interfaces is directly applicable to the field of dual-phase particle detectors used to detect dark matter or neutrino scattering events [18–22]. In these experiments a very small

reduced electric field $\approx 10^{-2}$–10^{-1} Td, where 1 Td $= 10^{-21}$ V m^2, is applied to a large volume of cryogenic liquid argon, or xenon, to assist in extracting electrons produced by ionization events in the liquid [22]. These electrons are extracted through the surface of the liquid, where they transport across an interface into a vapor region atop the liquid. Once in the gas phase, the current produced by the extracted electrons is amplified by multiplier grids providing stronger reduced electric fields ($\approx 10^2$ Td) to generate avalanche events. We identify this application as one that could benefit from a modeling framework that could provide a continuous simulation of electron transport out of the liquid, across the interface, and into the gas phase.

Conversely, in terms of plasma transport from gas phase to liquid, a major application is plasma medicine and plasma treatment of liquids. The importance of electron transfer and electron induced chemistry at these plasma-liquid interfaces has been well established in recent years [11, 12, 23]. Despite this importance, it has been noted that radicals, ions, and photons are primarily considered when studying plasma-liquid reactions with little attention given to electron interactions with the liquid phase [11]. We note that this present study focuses on electron transport in argon, a non-polar atomic fluid that is relatively simple when compared to complex biological tissue or even water. Despite this, we believe the methodology and framework presented in this study presents an important first step towards simulating more complicated plasma-liquid interactions.

In order to model charged particle transport between gas and liquid media, a range of methods have been used in the literature. Some studies have modeled charged particle transport in gases and liquids as two separate models, each including distinctly different physics, coupled by matching conditions at the boundary [9, 24–27]. Alternatively, liquid interface effects have been simply treated as a density and energy absorption or emission boundary condition applied to a single gas phase model [10, 24, 27]. Finally, we note that there is an obvious temptation to simply use existing gas phase transport models and input data, and 'scale-up' the input data to liquid neutral densities in order to simulate transport in liquids [24, 28]. The errors in this assumption have been addressed in previous studies [16, 17, 29, 30], and in this study we demonstrate how to better accommodate transport in liquids through accurate input data.

The aims of this comparative study were to extend a recently proposed and benchmarked higher order four moment fluid model [13], as well as drift diffusion fluid models [4, 14, 15, 31, 32], to simulate electron transport across gas–liquid interfaces and formulate a recommendation for best practice future interfacial modeling. Interfacial considerations will be addressed by comparing the types of fluid model used but also through comparison of functional form assumptions for neutral density, n_0, variation of the interface. Inclusion of gas–liquid interface effects, such as variation of delocalized electron energy level, V_0, and dielectric permittivity, ε, into the proposed modeling framework will also be addressed.

We begin this study by briefly reviewing fluid models used for electron transport in gases and liquids in section 2 where distinctions between gas and liquid phase electron transport are highlighted. In section 3 a continuous fluid model of electron transport between gas and liquid media is proposed, with modifications to include some interfacial effects discussed. The results of the proposed interfacial fluid models are detailed in section 4, with key advantages and disadvantages of each model highlighted, with details of the numerical solution method employed in this study available in appendix B. Finally, in section 5, key recommendations drawn from the results of this study are made, with a focus on how to best accommodate interfacial electron transport in future fluid models.

2. Fluid modeling in gases and liquids

2.1. Fluid models for electron transport

Fluid models have been used to describe plasma phenomena such as streamers [4, 15, 33], industrial plasmas used in fabricating microelectronics [2, 34], and more recently biomedical [23, 24] applications of discharges. Fluid models are essentially continuity equations of velocity-averaged, spatially varying macroscopic variables, such as particle density, momentum, and energy [4, 13–15, 31] derived via velocity moments of the Boltzmann equation [13, 35]. This gives a relatively straightforward macroscopic model that provides a good description of the discharge dynamics, without the computational overhead of comprehensive particle based methods. Error bounds of fluid models are considered to be within 10%–20% [36], and are suited to providing a 'line-of-best-fit' description of charged particle properties, especially when non-trivial electron velocity distributions are present [13].

Advanced solution techniques, like partice-in-cell, Monte Carlo (MC) [37–39], or solutions of the Boltzmann kinetic equation [2, 4, 32, 36, 40, 41], directly yield an electron velocity distribution function (EVDF) as a function of space, velocity, and time $f(\mathbf{r}, \mathbf{v}, t)$. If electron velocity space dynamics are of importance then a particle based method should be used, in lieu of a fluid model as demonstrated in previous studies [13].

In this study we have selected three approaches to fluid modeling, and examined the results and subsequent appropriateness of each model towards describing interfacial electron transport between gas and liquid densities of liquid argon. Here we present a brief overview of the selected fluid models, with the finer details of the origins and formulations of the models deferred to previous comprehensive studies on fluid modeling specifically [4, 13–15, 31, 32].

2.1.1. Drift diffusion models. The most popular approach to fluid modeling of electron transport in gaseous plasmas has traditionally been a hydrodynamic drift diffusion continuity equation (1) of the electron density, $n_e(z, t) = \int f(\mathbf{r}, \mathbf{v}, t)\mathrm{d}\mathbf{v}$. The electron flux is obtained by assuming a steady-state of the

momentum balance equation, and that the field-driven component of electron energy is much greater than the thermal contribution [15, 32, 36, 42]. The generalized one-dimensional continuity equation is

$$\frac{\partial n_e}{\partial t} - \frac{\partial}{\partial z}\left(n_e W + D\frac{\partial n_e}{\partial z}\right) = n_e(\nu_I - \nu_a - \nu_r), \quad (1)$$

where input data terms are the drift velocity, W, diffusion coefficient, D, and ionization/attachment/electron–ion recombination collision rates, ν_I, ν_a, and ν_r. All input data are assumed to be functions of the local instantaneous reduced electric field, $\frac{E}{n_0}$, where E is the instantaneous electric field and n_0 is the neutral atom density.

Interpolation of steady state transport coefficients and collision rates is used to provide values for these input parameters. The steady state values are obtained from the steady state EVDF which can be found via MC simulations [37, 43] or a multi-term kinetic solution of the Boltzmann equation [17, 30, 35, 44], given appropriate microscopic inputs of electron scattering cross sections for the target gas (see section 2.2).

In addition to the electron continuity equation (1), continuity equations for the creation of positive, n_+, (via ionization reactions) and negative, n_-, (via attachment reactions) ion densities are used

$$\frac{\partial n_+}{\partial t} = n_e(\nu_I - \nu_r), \text{ and } \frac{\partial n_-}{\partial t} = n_e\nu_a, \quad (2)$$

where ion transport has been neglected over the transient time scales considered in this study for ionization front propagation [4, 15] owing to the significantly reduced mobility and diffusion of molecular ions [45, 46].

Alongside the continuity equations for charged species densities (1), (2), the space charge effects on the electric field, E, must be computed to determine any screening effects due to the creation of electrons and ions. To accommodate a spatially varying dielectric permittivity in an inhomogeneous, isotropic material we self-consistently solve

$$\frac{\partial}{\partial z}(\varepsilon_r(z)\varepsilon_0 E) = e(n_e + n_- - n_+), \quad (3)$$

$$E = -\frac{\partial\varphi}{\partial z}, \quad (4)$$

where e is the elementary charge, $\varepsilon_r(z)$ and ε_0 are the fluid's relative and the vacuum dielectric permittivities respectively. Boundary conditions are supplied on the electric potential are $\varphi(0, t) = 0$ and $\varphi(L, t) = \varphi_{\text{applied}}$ where φ_{applied} is a fixed voltage to produce the desired applied electric field in the absence of space-charge contributions.

While the model described by (1)–(4) has been traditionally used to describe charged particle transport within gases, the functional form of the model has been demonstrated to be applicable to describe transport within liquid discharges assuming appropriate modifications to the input data are made [13]. As the neutral density increases the single-scattering assumption used for gas transport breaks down as the effects of elastic coherent scattering and electron

interaction potential screening and polarization become important [17, 29, 30]. These effects are significant when the electron de Broglie wavelength is comparable to the average background particle spacing, $\lambda \sim n_0^{-\frac{1}{3}}$, which corresponds to low-energy electron scattering or scattering in very dense liquids.

Comprehensive formulations are available on how to modify gas phase electron interaction cross sections of non-polar atomic targets, such as noble liquids, to account for coherent scattering [30], and later the interaction potential screening and polarization [16, 29]. These structure modifications were implemented through a density dependent momentum transfer cross section (MTCS)

$$\Sigma_m(v, n_0) = 2\pi\int_0^\pi \Sigma(v, \chi, n_0)[1 - \cos\chi]\sin\chi\mathrm{d}\chi, \quad (5)$$

where v is the incoming electron speed, χ is the electron scattering angle off the target atom, and $\Sigma(v, \chi, n_0)$ is an effective differential cross section including coherent scattering and interaction potential modifications via

$$\Sigma(v, \chi, n_0) = \tilde{\sigma}(v, \chi)S(\Delta k; n_0), \quad (6)$$

where $\tilde{\sigma}(v, \chi)$ is the liquid phase differential cross section containing any screening and polarization effects [16, 29], $S(\Delta k; n_0)$ is the static structure factor and $\Delta k = \frac{2m_e v}{\hbar}\sin\frac{\chi}{2}$ is the wave number proportional to the change in momentum [30], where m_e is the electron mass and $\hbar$ is reduced Planck's constant. The static structure factor is a nonlinear function of n_0 of the target material, and may be calculated from molecular simulations, measured via experiments [29, 30, 37], or derived analytically through solutions of pair-correlation functions as per the Verlet–Weis corrected Percus–Yevick structure factor [47]. For detailed discussion on the static structure factor, and its implementation in liquid scattering, readers are directed to previous studies [29, 30, 37].

These fundamental liquid transport studies demonstrated substantially different cross sections for liquid transport at low incoming electron energies compared to transport in gas phase, particularly in reduced momentum transfer from preferential forward scattering [16, 29]. It was shown that, while energy transfer was impacted by modifications of the cross section due to potential screening, energy transfer was not explicitly modified by including coherent elastic scattering effects [30, 31] and energy transfer due to inelastic excitation collisions is considered localized to the immediate target atom. In summary, the functional form of the balance equations used to model electron transport is the same whether transport is in gas or liquid. However, explicit modifications to include liquid phase physics must be performed [17, 30] to obtain the appropriate cross sections for computing electron transport data. If the correct cross sections are used to generate input data for either gas or liquid transport, then the drift diffusion model (1), (2) can then be applied directly.

2.1.2. Higher order models. In addition to drift diffusion fluid models, so called higher order fluid models have gained

popularity for modeling charged particle transport in plasmas [4, 13, 35, 48]. In these models, the hierarchy of velocity moments of Boltzmann's equation is not truncated at the electron flux, but often extends to include four continuity equations for electron density, n_e, electron particle flux, $\Gamma = n_e\langle\mathbf{v}\rangle = \int f(\mathbf{r}, \mathbf{v}, t)\mathbf{v}d\mathbf{v}$, electron mean energy density, $n_\epsilon = n_e\langle\epsilon\rangle = \int f(\mathbf{r}, \mathbf{v}, t)\frac{1}{2}mv^2d\mathbf{v}$, and electron energy flux, $\Gamma_\epsilon = n_e\langle\boldsymbol{\xi}\rangle = \int f(\mathbf{r}, \mathbf{v}, t)\frac{1}{2}mv^2\mathbf{v}d\mathbf{v}$, where $\langle\mathbf{v}\rangle$, $\langle\epsilon\rangle$, and $\langle\boldsymbol{\xi}\rangle$ denote the electron average velocity, average energy, and average energy flux. Following the formulation of a four moment higher order model benchmarked in gas and liquid transport [13], we employ the following generalized model equations, in addition to the ion continuity equations (2)

$$\frac{\partial n_e}{\partial t} + \frac{\partial \Gamma}{\partial z} = n_e(\nu_I(\langle\epsilon\rangle) - \nu_a(\langle\epsilon\rangle) - \nu_r(\langle\epsilon\rangle)), \qquad (7)$$

$$\frac{\partial \Gamma}{\partial t} + \frac{\partial}{\partial z}(n_e\theta_m(\langle\epsilon\rangle)) + n_e\frac{e}{m_e}E = -\Gamma\nu_m(\langle\epsilon\rangle), \qquad (8)$$

$$\frac{\partial n_\epsilon}{\partial t} + \frac{\partial \Gamma_\epsilon}{\partial z} + eE\Gamma = -nS_\epsilon(\langle\epsilon\rangle), \qquad (9)$$

$$\frac{\partial \Gamma_\epsilon}{\partial t} + \frac{\partial}{\partial z}(n\theta_\xi(\langle\epsilon\rangle)) + n\theta_m(\langle\epsilon\rangle)eE$$
$$+ n_\epsilon\frac{e}{m_e}E = -\Gamma_\epsilon\nu_\xi(\langle\epsilon\rangle), \qquad (10)$$

where input data is required via collision rates for ionization, ν_I, attachment, ν_a, electron–ion recombination, ν_r, momentum transfer, ν_m, energy transfer, S_ϵ, energy flux transfer, ν_ξ, and higher order tensor product closure approximations, θ_m, and θ_ξ.

In this model, the higher order moments, $\theta_m = \langle v_z v_z \rangle$ and $\theta_\xi = \left\langle \frac{1}{2}mv^2 v_z v_z \right\rangle$, are closed by evaluation over the equilibrium steady-state EVDF used to also evaluate collision input rates, similar to that of the input data described in section 2.1.1. While we choose to specify generic expectation value expressions for θ_m and θ_ξ, to facilitate computation via any particle based method, we note that under the formalism of a three-term decomposition of the EVDF these expressions yield the exact results presented by Becker and Loffhagen [35]. The virtues of this closure technique were demonstrated previously [13] to provide a parameter free, physically sound alternative to other closure assumptions, such as non-physical heat flux assumptions or parameterization in terms of $\langle\epsilon\rangle$, previously used in literature [4, 13, 48].

The same process for generating a look-up table of steady state input data via an equilibrium EVDF, described in section 2.1.1, is used for this higher order model also. Higher order models differ to drift-diffusion models because more information of electron dynamics is natively included, so that phenomena such as temporal and spatial non-locality can be resolved [15]. In lieu of using $\frac{E}{n_0}$ to determine input data as per the drift-diffusion model, here the electron mean energy, $\langle\epsilon\rangle$, is used as the interpolating variable to determine input data at each point in space during the simulation [49].

As discussed in section 2.1.1, for a local field dependent model, a higher order model can also be equally applicable in gas or liquid, assuming the correct modifications have been made to generate accurate input data to account for liquid effects. For further details on the higher order moment model used in this study we refer the reader to a recent formulation and benchmarking study [13].

2.2. Transport data in gaseous and liquid argon

Following the generalized fluid models presented in the previous section, we present the electron scattering cross sections for gaseous and liquid argon, in addition to the resulting argon transport and collision data that serves as input to the fluid models presented in section 2.1. It should be noted that this study assumes that ion transport is neglected over the timescales studied [45, 46], and that, for simplicity, singly ionized molecular argon ions are only considered in this study. Furthermore, electron–ion recombination and the formation of excited states are neglected in this study as it was found that at the applied reduced fields used in this study, for the electron and ion densities in liquid argon, the resulting recombination rates [50–54] were significant orders of magnitude less than the other collisional processes considered in this work.

2.2.1. Electron scattering cross sections. As this study involves both gas and liquid extremes of argon we require two sets of electron scattering cross sections in order to generate input data for fluid models. The gaseous argon electron scattering cross sections of Hayashi [55, 56] were used as input to a multi-term solution of the Boltzmann equation [16, 17, 31] to generate input data for this study. The set comprising of an elastic MTCS, twenty five inelastic excitation cross sections, and an ionization cross section were retrieved from the online database www.lxcat.net.

As recommended by recent studies of electron transport and negative planar streamer fronts in atomic liquids [57, 58], liquid argon cross sections were compiled from recent works on accurate low-energy liquid cross sections, combined with necessary modification of the gas phase Hayashi cross sections for inelastic processes. To form the basis of the MTCS scattering cross section, the low-energy ($\leqslant$10 eV) MTCS for liquid argon proposed by Boyle *et al* [16] was taken in order to include the effects of coherent scattering and atomic potential screening which are critical for low-energy electron scattering in dense liquids. At higher incoming electron energies, where the liquid cross section converges to the gas cross section, the gaseous argon MTCS of Hayashi [55] was once again used. These two elastic scattering cross sections were joined and smoothed at $\sim$10 eV to form a single elastic scattering cross section.

As precise measurements, or calculations, of liquid phase ionization cross sections do not exist for atomic argon, a liquid argon ionization cross section was constructed by modifying the gaseous argon ionization cross section as detailed in [59–62]. The liquid argon ionization threshold energy, I_{liq}, was computed by modifying the gaseous argon threshold energy, $I_{\text{gas}} = 15.68$ eV, to account for dense liquid effects. The known gaseous ionization cross section of
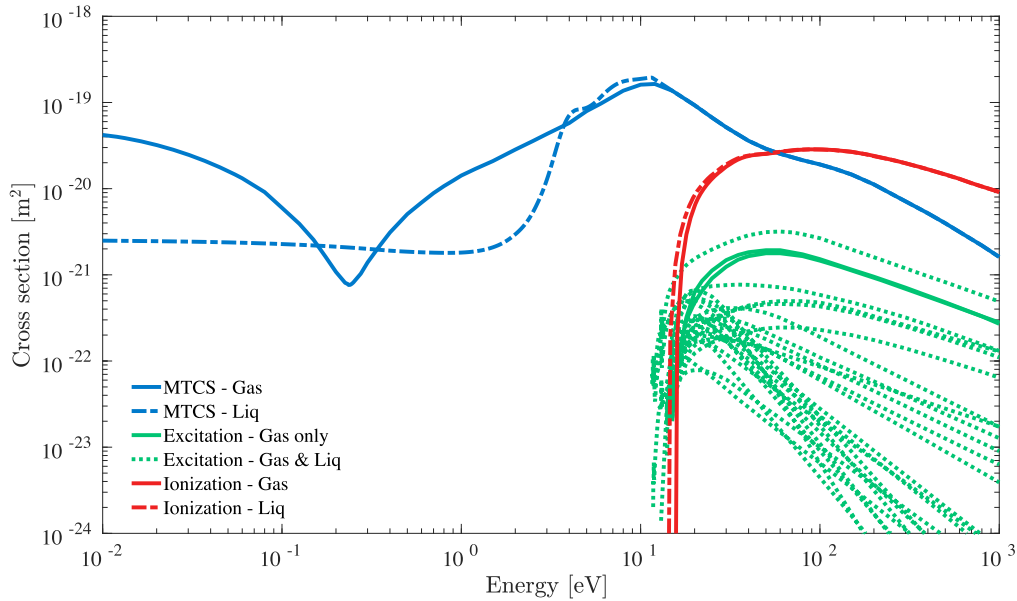
Figure 1. Gas and liquid argon electron scattering cross sections utilized in this study. Gas cross section data of Hayashi [55] via www.lxcat.net. Liquid cross section data of Boyle *et al* [16] and necessary modifications of Hayashi set detailed in section 2.2.1.

Hayashi [55] was then translated to the new threshold energy for liquid. The foundation and derivation of these modifications are detailed in [59], and the key result relevant to this present study can be summarized by the expression

$$I_{liq} = I_{gas} + P_+ + V_0 + E_{val}, \qquad (11)$$

where P_+ is the ion polarization energy of the positive ion ($P_+ = -1.08$ eV for argon [59]), V_0 is the energy of the delocalized electron level in the liquid i.e. the bottom of conduction band ($V_0 = -0.3$ eV for the liquid argon density used in this study [60]), and E_{val} is the change in energy of valence bands due to condensing the gas ($E_{val} = 0.1$ eV for argon [59]). This process yields the ionization threshold energy of $I_{liq} = 14.4$ eV.

In order to account for excitations in the liquid state, the set of inelastic atomic excitation cross sections of the Hayashi database was slightly modified to form a set of excitation cross sections for intermediate excitons in liquid argon [57, 58]. This is informed by the work of Laporte *et al* [63], which demonstrated that as dilute rare gases are compressed to high, liquid densities the presence of atomic excitations is replaced by excitations of intermediate excitons in the liquid phase [63]. As these intermediate excitons have a unique parentage, via the isolated atom's excited states [64, 65], we thus approximate the cross sections for intermediate exciton excitations by cross sections of the corresponding atomic excitations.

The threshold energies of the adopted excitation cross sections are unmodified from the atomic excitations out of necessity, because complete threshold energies for excitons in liquid argon are not available in the literature, especially for the optically forbidden transitions. This assumption is supported by the fact that thresholds for known intermediate excitons in liquid rare gases (argon, krypton and xenon) are

very close (within 5%) to the thresholds of atomic excitations [63, 65].

Finally, the reflectivity spectra of solid argon reported by Haensel *et al* [66] demonstrated that lines below 14.5 eV correspond to discrete excitonic states, while lines above 14.5 eV correspond to continuous interband transitions. We have therefore excluded the two atomic excitations which have thresholds above 14.5 eV (being 14.71 and 15.2 eV) as their energies are in the region of continuous band to band transitions. The final sets of electron scattering cross sections in both gaseous and liquid argon are shown in figure 1.

2.2.2. Fluid model input electron transport data. Using the electron scattering cross sections for both gas and liquid argon extremes (see figure 1) equilibrium electron transport data was calculated to serve as input data for the fluid models used in this study. A multi-term solution of the Boltzmann kinetic equation [16, 17, 31] was used to calculate EVDFs over a range of reduced electric field values at 85 K, a common cryogenic temperature, near the triple point, used in argon applications and experimental studies [51, 67–69]. These velocity distribution functions were then used to calculate the flux transport coefficients necessary for input to the drift-diffusion fluid model (1). Plots of electron drift velocity, longitudinal diffusion, and ionization collision rate, used as input for (1), (2), are shown in figure 2; though not used as a model input, a plot of the electron mean energy as a function of reduced field is included to demonstrate key differences between gas and liquid transport.

Reduced collision rates for input to the higher order fluid model are directly computed from spatially homogeneous steady-state EVDFs found via multi-term solution of the Boltzmann equation [17], these rates are presented in figure 3 demonstrating the variation of collision rates for momentum
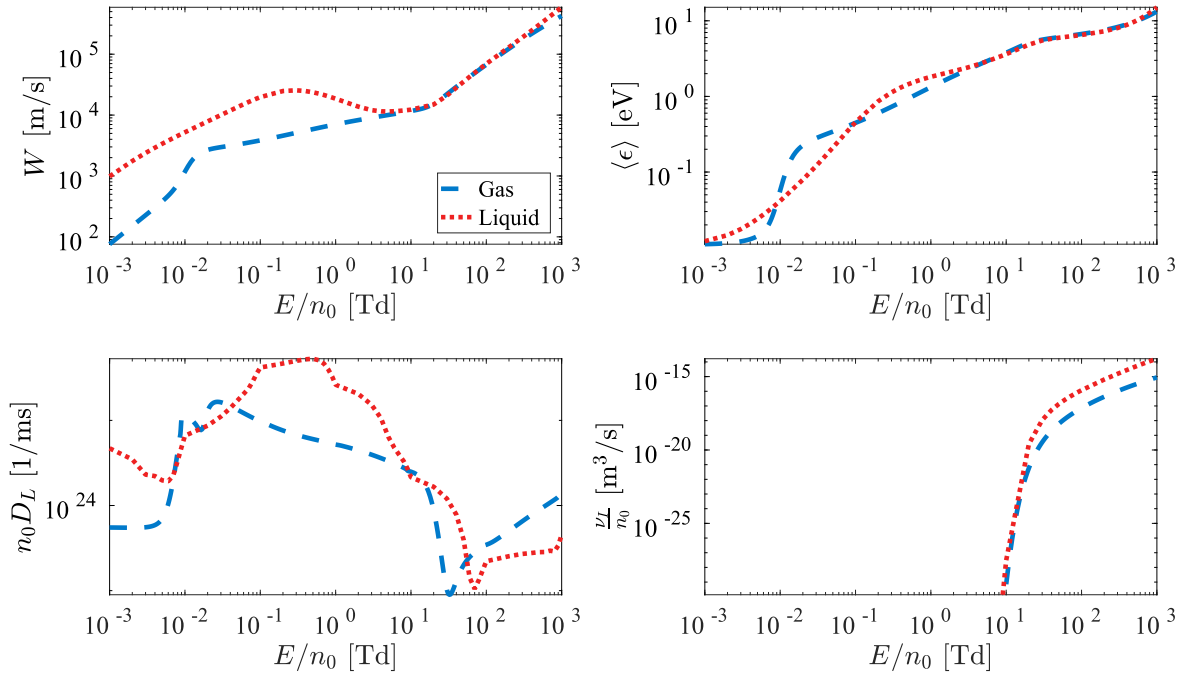
Figure 2. Input transport data of electrons in argon for local-field dependent electron fluid models. Dashed lines denote gas transport, dotted lines denote liquid transport. (Top-left) Drift velocity versus reduced field. (Top-right) Electron mean energy versus reduced field. (Bottom-left) Longitudinal reduced diffusion coefficient versus reduced field. (Bottom-right) Reduced ionization collision rate versus reduced field.
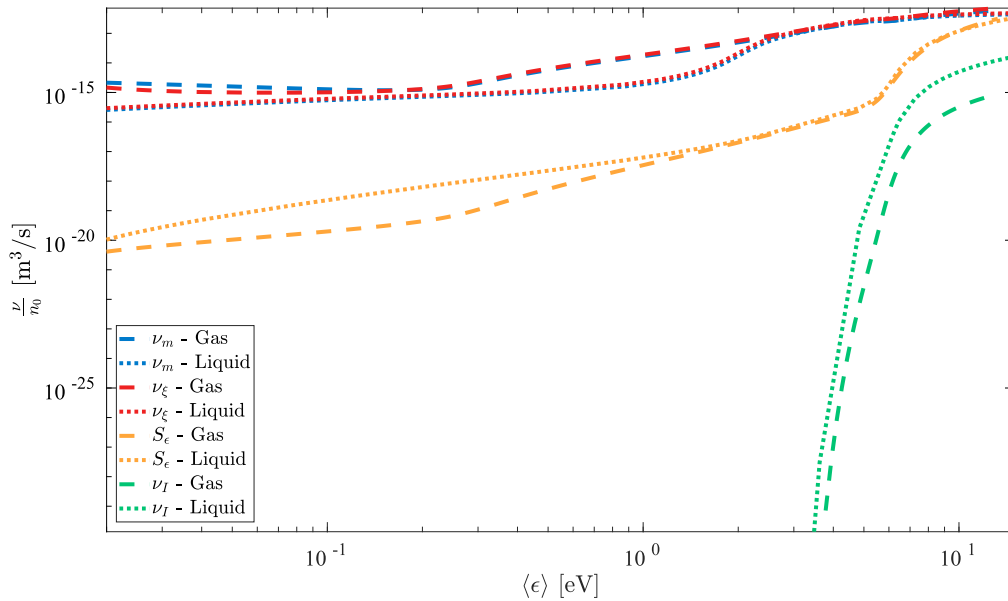

Figure 3. Input collision rates of electrons in argon for mean energy dependent higher order fluid model. Dashed lines denote gas transport, dotted lines denote liquid transport.

transfer ν_m/n_0, energy flux transfer ν_ξ/n_0, lumped energy loss S_ϵ/n_0, and ionization ν_I/n_0.

3. Modeling at the gas–liquid interface

Following the brief review of fluid modeling methods and associated input data for electrons in either gas or liquid presented in section 2, we now discuss necessary interfacial effects that should be considered when trying to model

electron transport between gas and liquid extrema as a continuous process. We consider four important factors of the gas–liquid interface model: (i) functional form of the variation in n_0, (ii) variation of input data for fluid models across the interface, (iii) variation of the delocalized electron energy level, V_0, across the interface, and (iv) variation of the relative dielectric permittivity, ε_r, across the interface. In this study we examine the effects of differing treatments of (i) the form of the interface, as well as (ii) the type of input data used in the models. The presence of spatially varying (iii) delocalized
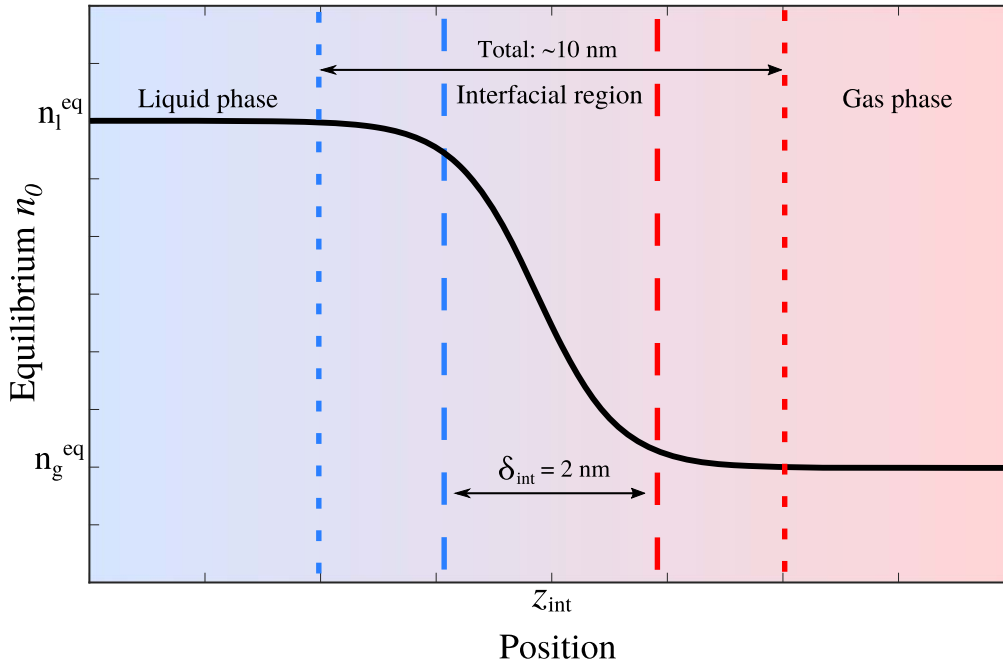
Figure 4. Equilibrium argon vapor–liquid interface as determined by molecular dynamics simulations [70, 71, 73]. The approximate length of the full interface transition region as well as the 90%–10% parameter length, δ_{int}, used in this study are marked explicitly.

electron energy level, V_0, and (iv) relative dielectric permittivity, ε_r, are assumed fixed properties in this study as they present essential physics, induced by large atomic densities, that cannot be ignored when simulating the gas–liquid interface.

3.1. Density profile variations

In order to accurately model electron transport between a gas phase plasma and a condensed liquid, the structure of the interfacial region must be known. For this study, we assume the existence of an equilibrium interfacial density profile formed between gas and liquid phases for atomic fluids, as outlined in figure 4. The existence of this interfacial profile in non-polar atoms, such as argon and xenon, has been probed in various molecular dynamics and MC studies [70–73]. These simulations employ Lennard-Jones (LJ) potentials as an approximation to the atomic interaction potentials between each atom of noble liquid [70–73]. Key measurables from these studies were equilibrium liquid and vapor densities, surface tension, and interface layer thickness.

Of particular use in this study, is a commonly proposed functional form describing the interfacial atomic density variation via a hyperbolic tangent function [73, 74]

$$n_0(z) = \frac{1}{2}(n_g^{\mathrm{eq}} + n_l^{\mathrm{eq}}) - \frac{1}{2}(n_g^{\mathrm{eq}} - n_l^{\mathrm{eq}})\tanh\left(\frac{2(z - z_{\mathrm{int}})}{\delta_{\mathrm{int}}}\right),$$
(12)

where n_g^{eq} and n_l^{eq} are the gas and liquid equilibrium densities, z_{int} is the center position of the interface, and δ_{int} is a measure of the thickness of the interface, defined as the distance between 90% and 10% of the liquid density. From previous studies conducted on the existence of noble liquid

interfaces, the value of δ_{int} is around $5\sigma_{\mathrm{LJ}}$, where $\sigma_{\mathrm{LJ}} = 0.34$ nm is the atomic diameter [68, 70, 71, 73, 74], while the liquid–vapor density ratios ($n_l^{\mathrm{eq}}:n_g^{\mathrm{eq}}$) were found to vary from 200:1 up to 500:1, depending on the cut-off distance employed in the LJ potentials [71, 73, 74].

3.2. Fluid model input data for continuum models between gas and liquid phases

With a well defined density configuration of the equilibrium interface between gas and liquid argon extremes, we now consider the effects of this density variation on the required fluid model input data. One question that we wish to probe in this study, is whether or not we must use n_0 dependent input data between gas and liquid density extremes, or if we can simply use pure gas and liquid data either side of a defined interface point, z_0, akin to a step-function profile. One factor to consider in answering this question is the electron-neutral collisional mean free path

$$\lambda_{\mathrm{mfp}} \approx \frac{1}{n_0\sigma},$$
(13)

where n_0 is some neutral background density and σ is an electron scattering cross section. For gas, liquid, or intermediate densities, a range of mean free paths can be calculated to determine if the collisional scattering dynamics and any non-equilibrium behavior will impact transport in the interfacial transition between gas and liquid. Typical liquid argon densities are $n_l^{\mathrm{eq}} \approx 10^{28}$ m^{-3} while the gas density at the equilibrium interface used in this study is roughly 300 times smaller than the liquid, resulting in mean free paths for electron scattering in liquid argon in the range 1–100 nm, while the corresponding mean free path range in gaseous argon is 0.3–30 μm. Since the equilibrium interfacial region

7

in argon is on the order of nanometers we must consider n_0 dependence in fluid model transport data in this interfacial region.

We now appropriately label fluid models introduced in section 2.1, and define explicitly whether n_0 dependent input data is used. Firstly, the simplest fluid model used in this study is a local-field dependent drift-diffusion model (1), (2), utilized with n_0 dependent input data to allow for both gaseous and liquid background media. This dependence is introduced by asserting the W, D_L and ν_I input parameters of (1), (2) are now functions of both the instantaneous reduced electric field and neutral density across the interface, $f\left(\frac{E}{n_0}\right) \to f\left(\frac{E}{n_0}, n_0\right)$. This model will henceforth be referred to as the *LFA* model.

Finally, taking the higher order model presented in (7)–(10) we recast the functional form of the input parameters such that any input parameter dependent on electron mean energy is now also a function of the neutral density $f(\langle\epsilon\rangle) \to f(\langle\epsilon\rangle, n_0)$. As this is a higher order four moment model this model will henceforth be referred to as the *4MM* model. Input data requirements accounting for the density variation for both the LFA and 4MM models are discussed and presented in appendix A using the results of a recently proposed and benchmarked study [75].

3.3. Space-charge field and spatially varying permittivity

Self-consistent solution of the electric field was performed via solution of (3) and (4) where the functional form of the spatially varying relative dielectric constant, $\varepsilon_r = \varepsilon_r(z)$, was specified using the same tanh function (12) used to modulate n_0, where liquid and gaseous argon constants were taken as $\varepsilon_r^l = 1.504$ and $\varepsilon_r^g = 1.0005$ respectively [76].

3.4. Accommodating spatial variation of V_0 across the interface

As gas densities increase to liquid values, we need to also consider the variation in the energy of the delocalized electron level in the liquid, V_0. This can be positive (neon, helium) or negative (argon, xenon) and is largely a function of the electron scattering length of the target atom [59, 60]. The dependence of V_0 on the neutral atomic density of argon, n_0, demonstrates an approximate linear roll-off from 0 eV in gas down to approximately -0.3 eV at the maximum liquid density used in this study [59, 60]. Given a known equilibrium $n_0(z)$ profile, and thus an equilibrium $V_0(z)$, an effective electric field is found by differentiating $V_0(z)$, and combined with the electric field, E, computed via (3) to yield the total electric field

$$E_{\text{total}} = E + E_{V_0}. \tag{14}$$

4. Results and discussion

Using the fluid models and input data presented in sections 2 and 3, we present results and discussion for two prototype

interfacial problems. Section 4.2 presents transient simulations of an electron swarm propagating from liquid argon into gaseous argon (left to right in this study's frame of reference). Brief results of an ionization front in gaseous argon penetrating into liquid argon (from right to left) are presented in section 4.3. We believe it is most instructive to start investigations with essentially swarm transport in the liquid phase transitioning to gas phase, where fields and ionization rates are low, before considering cases where space-charge field considerations are important due to ionization events. To examine the impacts of electron transport experiencing a gas–liquid interface transition in cryogenic argon, we present results from (i) large macroscopic length scales to examine the overall qualitative nature of the results, and (ii) small length scales at the immediate vicinity of the interfacial region in order to examine the impact of the interface transition. Liquid to gas results of section 4.2 are presented at early (2 ps), intermediate (15 ps), and late (50 ps) times to demonstrate the physics of electron transport over different time scales, while the gas to liquid results of section 4.3 are taken at 50 ps. Finally, following the results of the two prototype problems (liquid to gas and gas to liquid), section 4.4 demonstrates the distinctly different results produced by electron transport simulations that assume a simple step function interface, in lieu of the equilibrium tanh function transition proposed in this work.

4.1. Simulation conditions

An applied reduced field magnitude of $|E/n_0| = 300$ Td in gas phase, corresponding to 0.8 Td in the liquid, was applied to drive electrons into the gas–liquid interface; the appropriate sign was assigned in each simulation to drive electrons left to right or vice versa. In this study the neutral atom temperature was kept constant at $T_0 = 85$ K, a commonly used cryogenic temperature for liquid argon experiments [21, 69, 77]. The neutral density, n_0, was varied using the tanh function interfacial density ramp (12), where $n_l^{\text{eq}} = 1.8 \times 10^{28} \text{ m}^{-3}$ was obtained from the liquid argon coexistence curve at 85 K [77]. The van der Waals radius of argon $r_{\text{Ar}} = 188$ pm was used in computation of the Percus–Yevick structure factor [30, 37, 47]. Based on previous studies of equilibrium gas–liquid interface properties found in literature [70, 71, 73, 74], the ratio of equilibrium gas density to liquid density was assumed to be $n_g^{\text{eq}} = n_l^{\text{eq}}/300$, and the 10–90 interface width, δ_{int}, was assumed to be 2 nm. Using the specified reduced field strengths, and the density profile provided by a tanh function, the initial total effective reduced electric field (14) is shown in figure 5.

Naturally, the space-charge field effects will evolve over the course of simulations but by simply considering the initial total fields assists in understanding of the results presented in sections 4.2 and 4.3. From the liquid to gas plot of figure 5 it is clear that the effective field due to V_0 variation acts to impede electron transport from the liquid to the gas, while conversely it enhances electron transport into the liquid when the applied field is reversed on the right-hand plot.
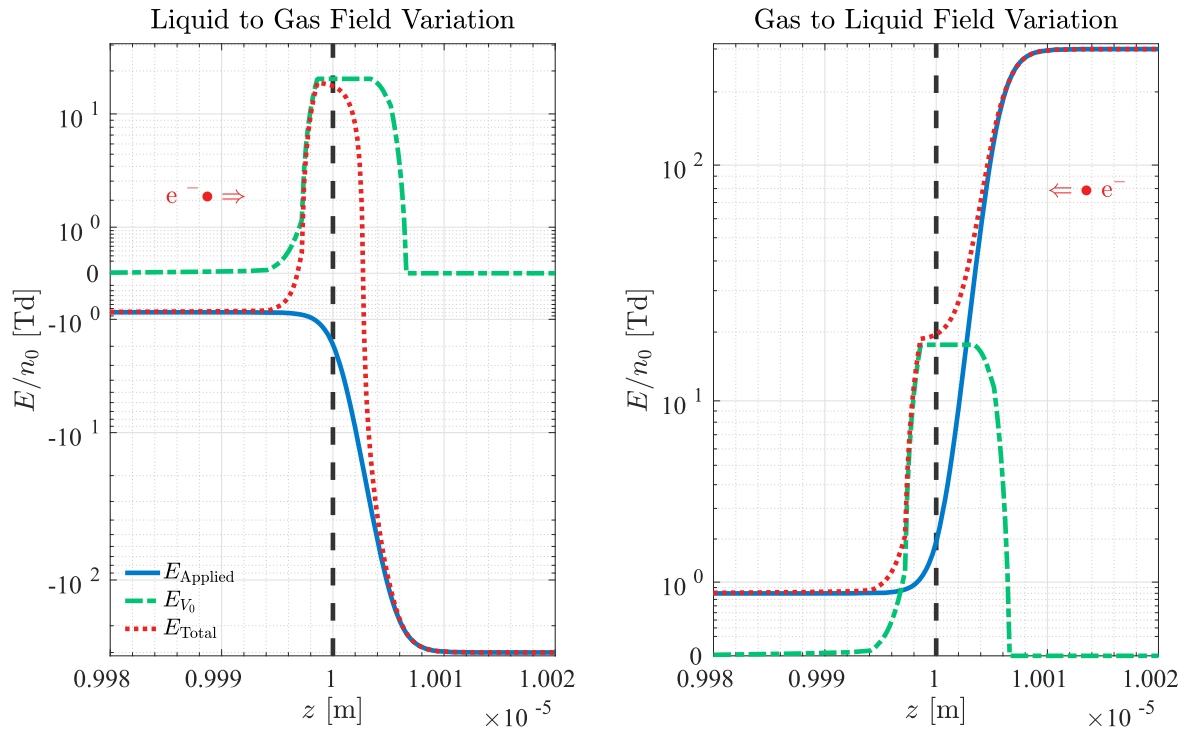
Figure 5. Reduced electric field profiles for applied and V_0 contributions for both simulation configurations presented. Note that symmetric logarithmic axes have been employed in this figure. The vertical dashed black line denotes the center point of the interface transition.

Initial conditions for simulation of streamer formation and propagation were assumed as a narrow Gaussian pulse of electron/ion densities created by an arbitrary ionization event prior to the simulation start. To ensure initial conditions did not experience immediate interfacial effects, initial charged particle densities for the liquid to gas simulation were set at $2\,\mu m$ from the interface and the ionization front propagating from gas to liquid was set at $100\,\mu m$ from the interface. Although there is no physical meaning to a mean energy in regions of zero density, the fluid model input parameters are interpolated from a mean energy value. Hence, to avoid numerical issues, we specify the initial values of mean energy, velocity and energy flux to be their steady-state values at the corresponding E/n_0 value, even in regions of zero density, as was done in previous fluid modeling studies [4, 13, 15]. At later times, when the density becomes non-zero, these fluid model parameters will then vary smoothly both spatially and temporally.

4.2. Electron transport from liquid argon into gaseous argon

Electron and ion density initial conditions of narrow Gaussian pulses were used in a simulation of electron transport across an interface, analogous to a single ionization event within a liquid argon detection chamber. Evolution of the electron density in figure 6 shows the initial pulse of electrons diffuses very quickly, leading to electron extraction from liquid into the gas phase as electrons impinge on the interface region. Qualitatively, both models predict similar results over all times however, it is clear the 4MM model demonstrates higher rates of electron extraction from the liquid. The LFA model predicts at least twice as much charge blocking on the

liquid side of the interface compared to the 4MM model. Examining the expanded interfacial region of figure 6, we see the charge build-up at a narrow scale, with the 4MM result demonstrating two distinct roll-off gradients across the interface. To interpret this structure it is beneficial to consider the average electron velocity.

Figure 7 demonstrates that far from the interfacial region, the average electron velocity has relaxed to an equilibrium value. However, near the interface we see that initially the 4MM result predicts a large positive velocity, due to the large initial diffusive flux, and never becomes negative. In contrast, at the immediate vicinity of the interface the LFA model predicts a negative average velocity due to the blocking field contribution of the V_0 potential in liquid argon. As time continues, the magnitude of these initially large velocities decreases but their sign differences remain. As the distance over which the blocking field is applied is very small, and the time for mean energy relaxation is quite long, the mean energy does not rapidly respond to the field variation. This is an example of non-local electron transport that the LFA model cannot predict, but the 4MM model can. These major differences in the average electron velocity at the interface are the drivers for deviations in electron density results observed in figure 6.

The top half of figure 7 also demonstrates a short, but persistent, relaxation length on the liquid side of the interface well before the interface is encountered. We believe this gradual decrease in electron average velocity prior to the interface is a further demonstration of spatial non-locality being predicted by the mean energy dependent model, which the LFA model simply cannot predict owing to its reliance on
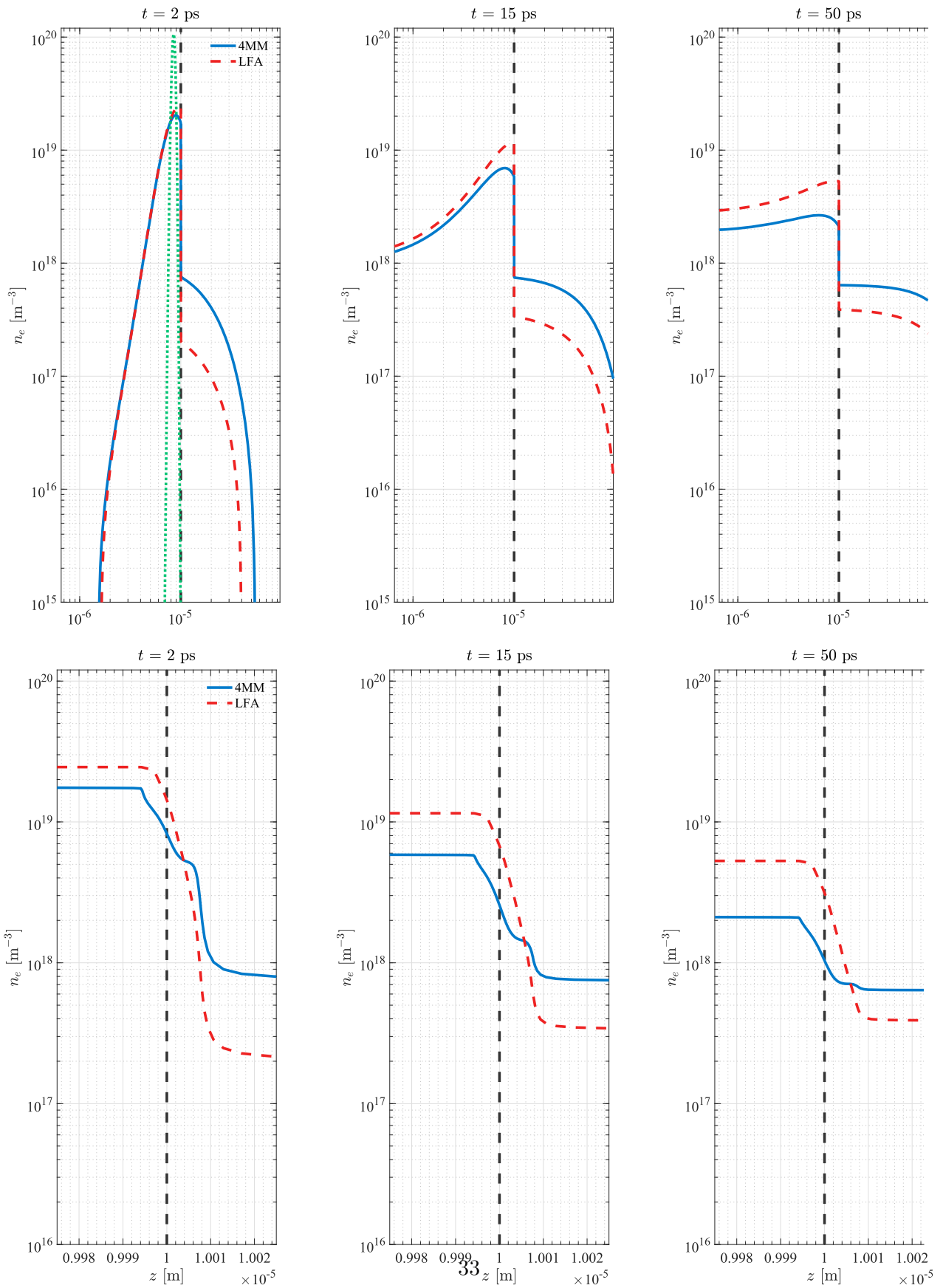
Figure 6. Electron density evolution for 4MM and LFA models at short, intermediate, and longer times as the electron swarm propagates from liquid to gaseous argon. Top view: macroscopic results. Bottom view: expanded view of interfacial results. Initial condition given by green dash–dot green line. Direction of field-driven propagation is from left to right.
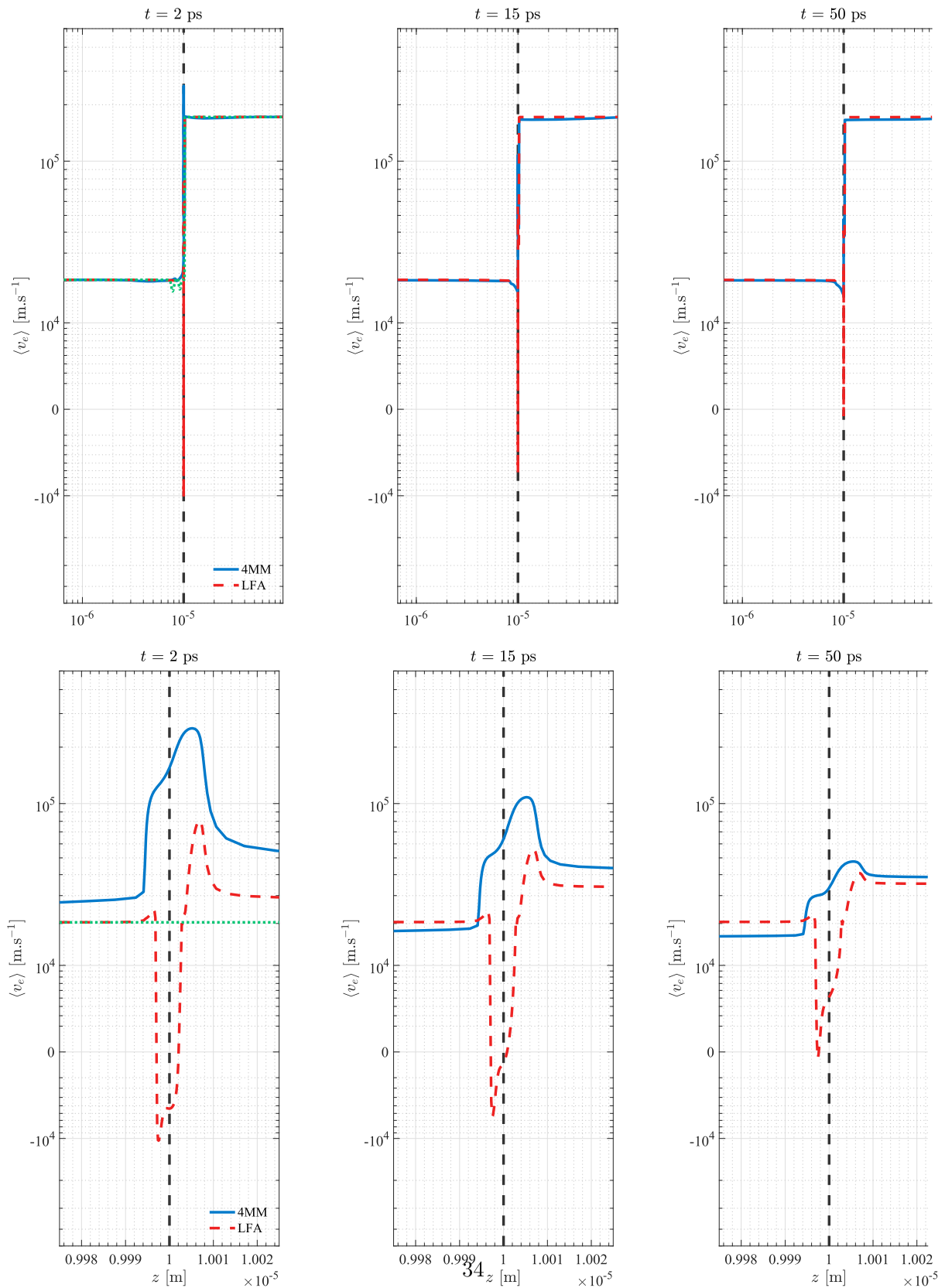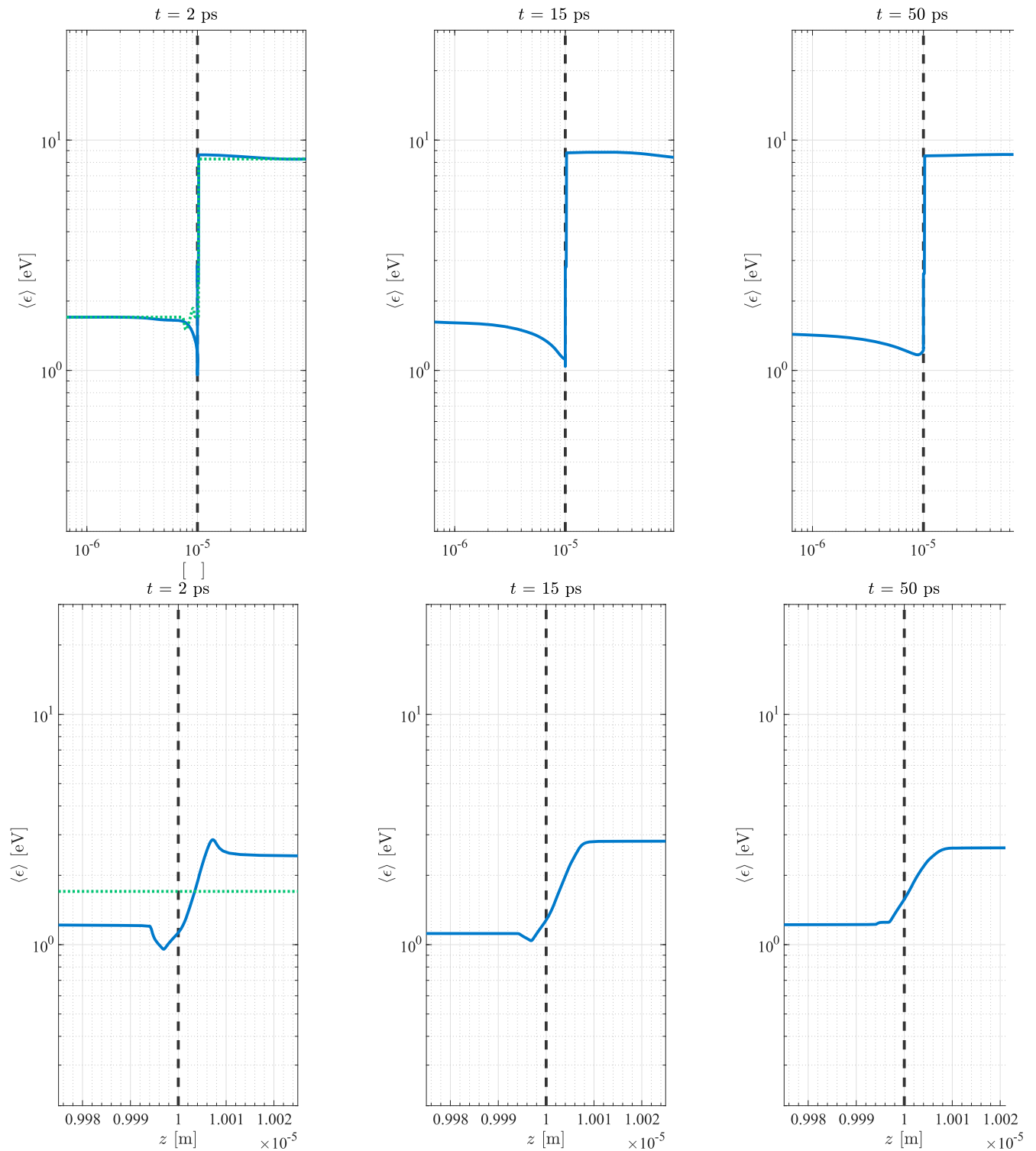
Figure 7. Average electron velocity for 4MM and LFA models at short, intermediate, and longer times as the electron swarm propagates from liquid to gaseous argon. Top view: macroscopic results. Bottom view: expanded view of interfacial results. Initial condition given by green dash–dot green line. Direction of field-driven propagation is from left to right. Note that symmetric logarithmic axes have been employed in this figure.
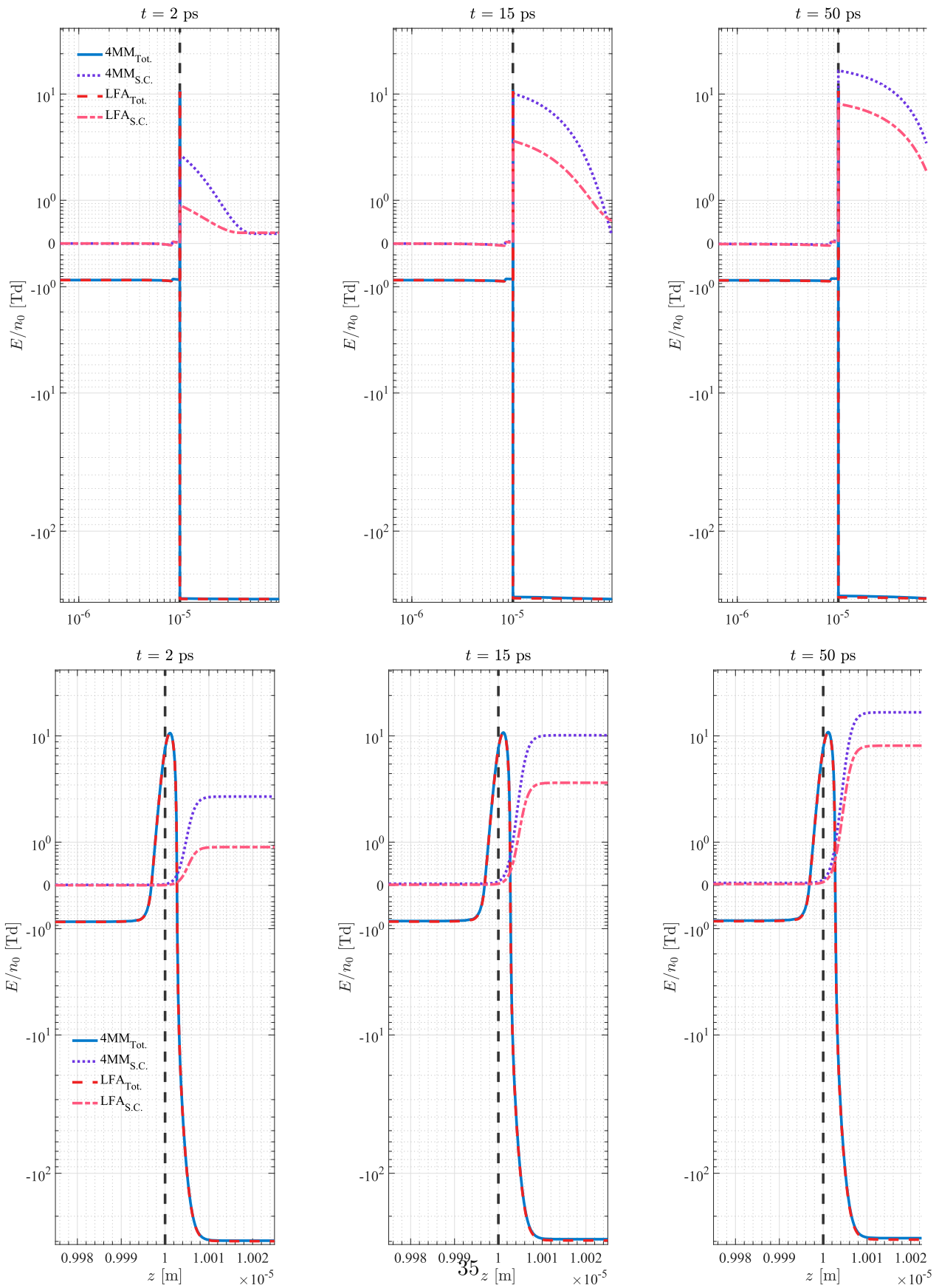
Figure 8. Total E/n_0 and space-charge contribution to E/n_0 for 4MM and LFA models at short, intermediate, and longer times as the electron swarm propagates from liquid to gaseous argon. Top view: macroscopic results. Bottom view: expanded view of interfacial results. Note that symmetric logarithmic axes have been employed in this figure.

Figure 9. Electron mean energy for 4 MM model at short, intermediate, and longer times as the electron swarm propagates from liquid to gaseous argon. Top view: macroscopic results. Bottom view: expanded view of interfacial results. Initial condition given by green dash–dot green line. Direction of field-driven propagation is from left to right.

the instantaneous electric field, shown in figure 8. From figure 8 we cannot see a significant variation in the total E/n_0 over the lifetime of this transient simulation; this is a result of the space charge effects being small compared to the applied field, as indicated in the figure where we have plotted the isolated contributions of space-charge effects.

Figure 9 demonstrates the electron mean energy of the 4MM model to assist in interpreting the results of the preceding figures. We can clearly see a gradual relaxation of $\langle \epsilon \rangle$ on the liquid side of the interface, consistent with the observed non-local effects on electron transport in figure 7. Far from the interface the mean energy relaxes to the

equilibrium value given by the value of E/n_0 in the gas or liquid. We note a clear minimum in mean energy is observed at short times in the expanded interface region of figure 9 due to the relatively high transient electron flux, combining with the sign change of the blocking electric field provided by the V_0 potential, as a result of the $\Gamma \cdot E$ term in the energy balance equation (9). This energy reduction immediately at the interface is only present at short times because of the large initial diffusive electron flux. As this large initial diffusive flux subsides over time, the energy loss via the $\Gamma \cdot E$ term becomes less significant, demonstrated at 15 and 50 ps.

4.3. Electron ionization front transport from gaseous argon into liquid argon

We now briefly present and discuss results of directing an electron streamer front in gaseous argon into liquid argon. This simulation was performed under the same conditions as the previous section, apart from simply reversing the sign of the applied electric field to yield a total reduced electric field configuration as shown in figure 5. The initial condition to this simulation was provided by allowing a streamer front to form in gaseous argon, before imposing a gas–liquid interface transition approximately 100 μm in front of the streamer front.

For brevity, we present electron transport profiles after 50 ps, instead of multiple time points, in figure 10. Examining the LFA and 4MM results produced by the tanh interface assumption, we see that the initial electron density of the streamer tip is transported across the interface with a notable attenuation of the electron density further into the liquid. Examining the expanded view of the interface, the LFA model predicts a larger charge-build up at the gas side of the interface compared to the 4MM model consistent with a noticeably lower speed immediately at the interface, arising from the combination of the increase in n_0 at the interface as well as space-charge screening effects on E/n_0.

When comparing the average electron velocity plot, the most distinguished point of difference between the two models is the clear spatial relaxation length of $\langle v_e \rangle$ following the interface transition. Results of the 4MM model indicate a decay to the equilibrium drift velocity value observed in liquid argon, which demonstrates the presence of spatial non-locality which is not replicated by the LFA model. Additionally, a discrepancy arises between the two models at the expanded interface scale, where a smaller average velocity is produced by the LFA model as a result of a weaker reduced field occurring at the gas–liquid interface. In this range, the mean energy dependent 4MM model does experience a reduction in average velocity, but to a lesser extent than that found in the LFA results.

Finally, to assist further in interpreting the 4MM results, the electron mean energy is presented in figure 10. Here we note that in the expanded interfacial region of figure 10 a reduction in mean energy occurs on the gas side, due to increasing collisional energy losses from an increasing n_0, however the electron mean energy experiences a slight increase over the interface due to the restorative effects of the

V_0 field via the $\Gamma \cdot E$ term in the energy balance equation (9). Once the effects of the interface transition have subsided, the mean energy decays to the equilibrium mean energy value for electrons in liquid argon with a clear relaxation length, indicating the presence of non-local electron transport.

4.4. Impact of step function input data

To determine if using a tanh function to modulate n_0 at the interface, which necessarily requires the density dependent fluid model input data, between gas and liquid extrema is actually required compared to simply using a standard step function variation in the density, we repeated the simulation of an ionization front propagating from gas to liquid. In this case we employed a step function transition between liquid on the left and gas on the right. For brevity, we present results at 50 ps in figure 10, demonstrating the vastly different qualitative results produced by assuming a step function transition.

From figure 10, we see that by assuming a step-function with the LFA model the electron densities are much higher over the macroscopic length scale. Approximately twice as many electrons are transported into the liquid as compared with any of the previous results. At the narrow length scale of the interface, we see the step-function LFA result actually decreases prior to the interface before experiencing a sharp build up of electrons on the liquid side; this is a starkly different qualitatively result compared to any of the previous results obtained using the smooth tanh function. On the other hand, while the step-function 4MM results are not equal to those achieved through the tanh assumption, they are very similar and produce no major deviations compared to the LFA results.

The step-function LFA electron density differences are consistent with a very high average velocity at the interface, demonstrated in figure 10, compared to any of the previous simulation results. This order of magnitude difference in the average velocity transports electrons into the liquid at a considerably higher rate compared to the results using the tanh interface assumption. This high average velocity occurs due to a large E/n_0, produced due to the small, gaseous argon value of n_0 assumed near the interface instead of a gradually increasing value. Once again, compared to the distinctly different observations of the LFA models we see no major deviation between 4MM results, with the only noticeable difference being the discontinuity immediately at the interface.

For completeness, figure 10 also shows the electron mean energy for the 4MM models using both tanh and step-function assumptions. We see no major differences in $\langle \epsilon \rangle$ for the two results, indicating why differences between 4MM results for the other variables were minimal. Since $\langle \epsilon \rangle$ is observably insensitive to the form of interface assumptions, and demonstrably a continuous variable, we believe that it is a much more reliable variable to use when determining input data compared to E/n_0 which suffers from being explicitly related to the assumptions we impose on n_0.
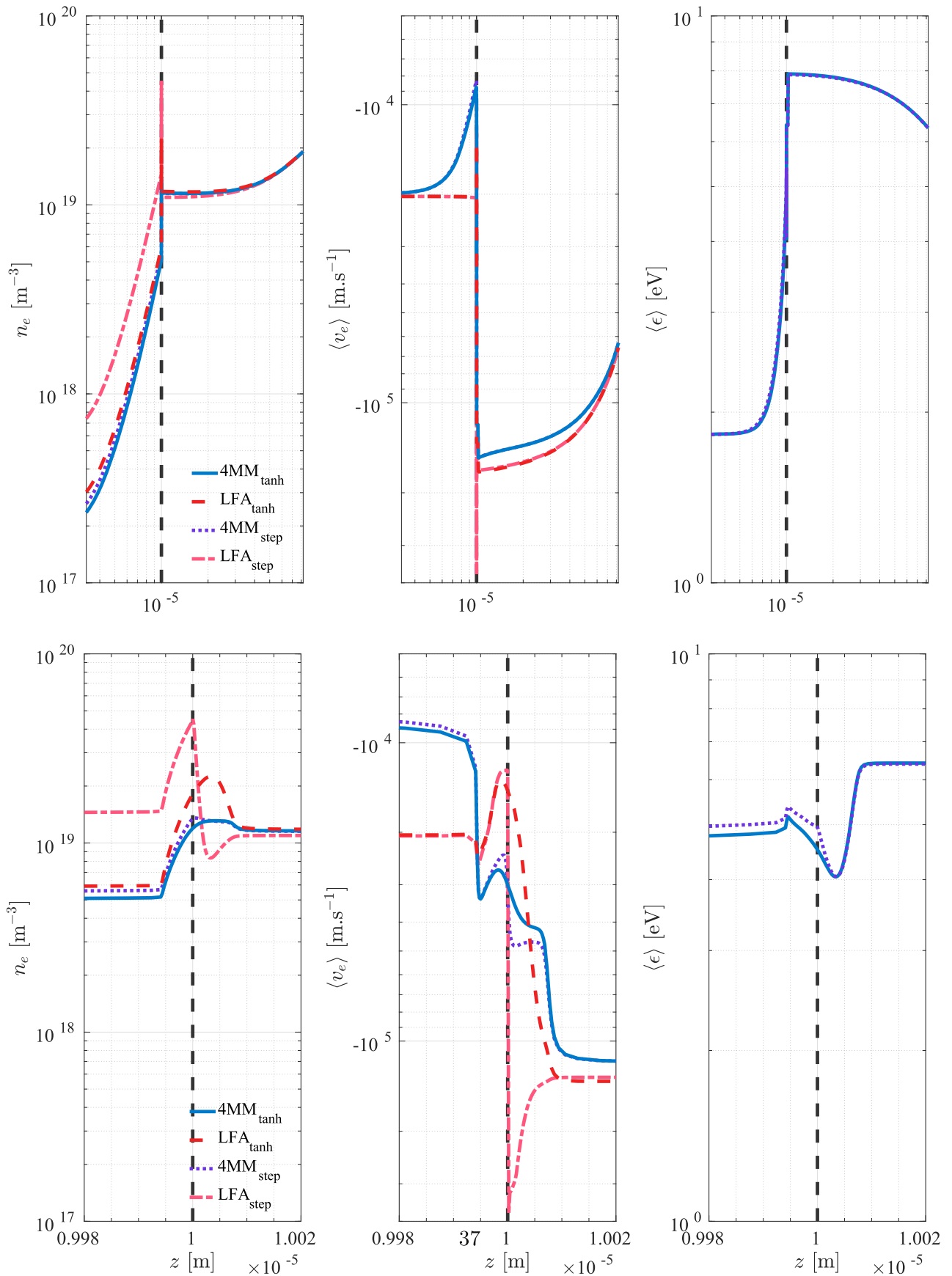
Figure 10. Electron density, average velocity and mean energy for 4 MM and LFA models after 50 ps of an electron streamer penetrating from gaseous to liquid argon. Results of assuming a tanh or step function interface on are shown for comparison. Top view: macroscopic results. Bottom view: expanded view of interfacial results. Direction of field-driven propagation is from right to left.

5. Conclusions

In this study we have presented results from multiple fluid models simulating (i) an electron swarm propagating from liquid argon into gaseous argon over an equilibrium interface density variation, and (ii) an electron streamer front being driven out of gaseous argon across the interface into liquid argon. We presented a method to account for large density variation from gas to liquid phase by assuming both a realistic density profile and step-function variation of n_0 in order to implement approximation rules for density dependent input transport data between gas and liquid extremes. Furthermore, we have accommodated interfacial effects of the spatial variation of both the dielectric constant, ε_r, through solution of Poisson's equation, and binding energy of an electron in liquid, V_0, through an effective applied electric field.

Using the proposed methods to compare local (LFA) and non-local transport (4MM) models and their sensitivities, our key recommendation to best describe electron transport between gas and liquid densities is to adopt a mean energy dependent higher order fluid model, such as the 4MM method used in this study. This model demonstrated greater flexibility and reliability in resolving non-local physics and interfacial electron transport compared to the local field drift-diffusion model. It was demonstrated that a drift-diffusion continuity equation (LFA) model required careful treatment of input data between gas and liquid extremes by way of approximating field dependent input data for intermediate densities using a tanh function, whereas the non-local 4MM model was relatively insensitive to the functional form of n_0 variation.

In summary, this work has presented the findings of a fundamental comparative modeling study of electron transport across cryogenic argon gas–liquid interfaces. We successfully demonstrated the importance of modifying gaseous electron transport models to account for interfacial and liquid effects when considering transport at the gas–liquid interface. A key message of this study is that vastly different electron transport is produced if gas phase input data is simply scaled to liquid densities, compared to using accurate liquid phase data. While this study has focused on a simple atomic liquid-gas system, we hope that this work will stimulate further modeling and experimental efforts to benchmark and refine the work presented. By expanding on the work of this study, extensions to complex interfacial systems, like those found in plasma medicine, can eventually be made to better understand important plasma applications. Further physical processes that should be considered in interfacial modeling may include electron solvation processes in polar liquids [11, 78], and condensed phase evaporation [74].

Acknowledgments

Appendix A. Input data at densities intermediate to the gas and liquid phases

In order accommodate $n_0(z)$ variation of input data, we have implemented an approximation method recently proposed, and benchmarked for simple atomic liquids, by Garland *et al* [75] that seeks to approximate input transport data and collision rates as weighted combinations of the gas and liquid extreme values. This process is analogous to Blanc's Law [79], or the energy-dependent approach proposed by Chiflikian [80], used for approximating transport data in gas mixtures, where instead we now seek to describe transport at intermediate densities between two density extremes of one substance instead of mixing two distinct gases. Where necessary to account for the differences in momentum transfer for gas and liquid systems, nonlinear weightings of gas and liquid extreme data are combined [75]. Using a zeroth order momentum transfer theory approximation [31, 75, 81], the nonlinear dependence is extracted via the angle-integrated structure factor evaluated at a given electron mean energy, $\langle \varepsilon \rangle$, and at a neutral atom density

$$s(\langle \varepsilon \rangle; n_0) = \frac{1}{2} \int_0^\pi S\left(\frac{2}{\hbar}\sqrt{2m_e \langle \varepsilon \rangle} \sin\frac{\chi}{2}; n_0\right)[1 - \cos\chi]\,\mathrm{d}\chi \tag{A.1}$$

where, for this work, the static structure factor, $S\left(\frac{2}{\hbar}\sqrt{2m_e \langle \varepsilon \rangle} \sin\frac{\chi}{2}; n_0\right)$, is assumed to be the analytic Verlet–Weis corrected Percus–Yevick structure factor [47] which has been demonstrated to be a good approximation of atomic liquid structure [16, 29, 37, 82]. The full analytic expression is included in a preceding study [75]. When considering largely localized energy transfer due to inelastic excitations, we use simpler linear combinations of gas and liquid extrema data as this was demonstrated to provide a sufficient first-order approximation to the intermediate density's transport data because explicit modifications to the energy balance equation (9) are not required [30, 75].

A.1. Local field dependent input data

For the LFA model the drift velocity at intermediate densities, W_{int}, is approximated as function of reduced field, $\frac{E}{n_0}$. A weighted sum of reciprocals of gas, W_g, and liquid, W_l, extreme values was used

$$\frac{1}{W_{\text{int}}\left(\frac{E}{n_0}\right)} = x_g s_{\text{int}}\left(\frac{E}{n_0}\right)\frac{1}{W_g\left(\frac{E}{n_0}\right)} + x_l \frac{s_{\text{int}}\left(\frac{E}{n_0}\right)}{s_l\left(\frac{E}{n_0}\right)}\frac{1}{W_l\left(\frac{E}{n_0}\right)}, \tag{A.2}$$
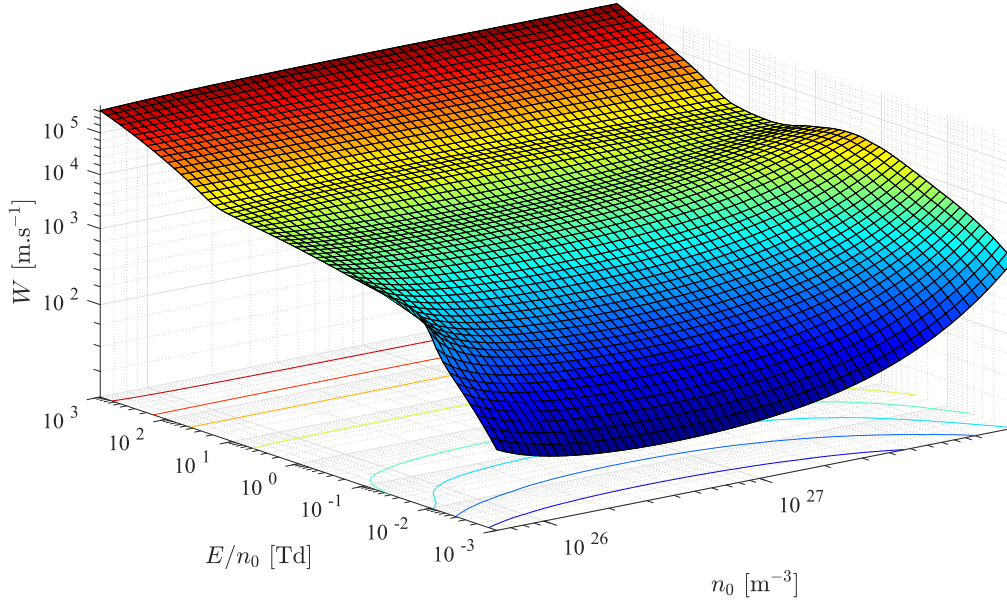
Figure A1. Drift velocity surface of electrons in argon as a function of $\frac{E}{n_0}$ and n_0 used to interpolate input data for LFA models.

where the density fractions, $x_{g,l}$, follow the relation

$$x_l = 1 - x_g. \tag{A.3}$$

These density fractions are determined by defining the intermediate density, n_{int}, as a sum of fractions of either density extrema

$$n_{\text{int}} = x_g n_g^{\text{eq}} + x_l n_l^{\text{eq}}, \tag{A.4}$$

and by combining (A.3) and (A.4) we find

$$x_g = \frac{n_l^{\text{eq}} - n_{\text{int}}}{n_l^{\text{eq}} - n_g^{\text{eq}}}. \tag{A.5}$$

The approximated angle-integrated structure factor at any intermediate points is given by

$$s_{\text{int}} \approx w s_g + (1 - w) s_l, \tag{A.6}$$

where s_g is defined as unity for the gas, s_l for the liquid extreme is evaluated via (A.1), and to ensure the approximation is physically grounded in both the high and low energy limits, the weighting factor, w, is fixed in the low energy limit by

$$w = \frac{S_{\text{int}}(0; n_{\text{int}}) - S_l(0; n_l)}{S_g(0; n_g) - S_l(0; n_l)}, \tag{A.7}$$

where $S(0; n)$ is the $\Delta k \to 0$ limit of the analytic structure factor [47], or otherwise proportional to the fluid compressibility which is a measurable input.

To demonstrate the output generated by this approximation method, we use (A.2) in conjunction with the accurate data of gas and liquid extremes described in section 2.2, to generate a drift velocity surface, shown in figure A1, which we interpolate onto as a function of the instantaneous $\frac{E}{n_0}$ and n_0 given at each point in space during the simulation.

We note that the reduced longitudinal diffusion coefficient $n_0 D_L$ was computed via a generalized Einstein relation

[83] once the drift velocity was known via (A.2)

$$\frac{D_L^{\text{int}}}{\mu_{\text{int}}} = \frac{k_B T_0}{q}\left(1 + (1 + \Delta_{\text{int}})\frac{\partial \ln \mu_{\text{int}}}{\partial \ln E}\right), \tag{A.8}$$

where $\mu_{\text{int}} = \frac{W_{\text{int}}}{E}$ is the electron mobility derived from the drift velocity (A.2), T_0 is the neutral atom temperature, and the correction factor [83]

$$\Delta_{\text{int}} = \frac{\check{\xi}_{\text{int}}}{2 k_B T_0 W_{\text{int}}}, \tag{A.9}$$

where ξ_{int} is the electron heat flux which can be approximated via a similar rule as used for W_{int} via nonlinear combinations of gas, ξ_g, and liquid, ξ_l, extreme values

$$\frac{1}{\check{\xi}_{\text{int}}\left(\frac{E}{n_0}\right)} = x_g s_{\text{int}}\left(\frac{E}{n_0}\right)\frac{1}{\xi_g\left(\frac{E}{n_0}\right)} + x_l \frac{s_{\text{int}}\left(\frac{E}{n_0}\right)}{s_l\left(\frac{E}{n_0}\right)}\frac{1}{\xi_l\left(\frac{E}{n_0}\right)}. \tag{A.10}$$

A.2. Higher order model input data

The 4MM model collision data was also approximated between gas and liquid densities with energy dependent approximation methods [75]. As an example, as was done for the drift velocity, nonlinear weights taken from the angle-integrated structure factor are used to generate a sum rule using gas, $\check{\nu}_m^g$, and liquid, $\check{\nu}_m^l$, data to yield a reduced momentum transfer collision frequency at intermediate densities, $\check{\nu}_m^{\text{int}}$, evaluated at a common mean energy, $\langle \varepsilon \rangle$,

$$\check{\nu}_m^{\text{int}}(\langle \varepsilon \rangle) = x_g s_{\text{int}}(\langle \varepsilon \rangle)\check{\nu}_m^g(\langle \varepsilon \rangle) + x_l \frac{s_{\text{int}}(\langle \varepsilon \rangle)}{s_l(\langle \varepsilon \rangle)}\check{\nu}_m^l(\langle \varepsilon \rangle), \tag{A.11}$$

where $\check{\nu}$ notation is used to denote a reduced collision rate
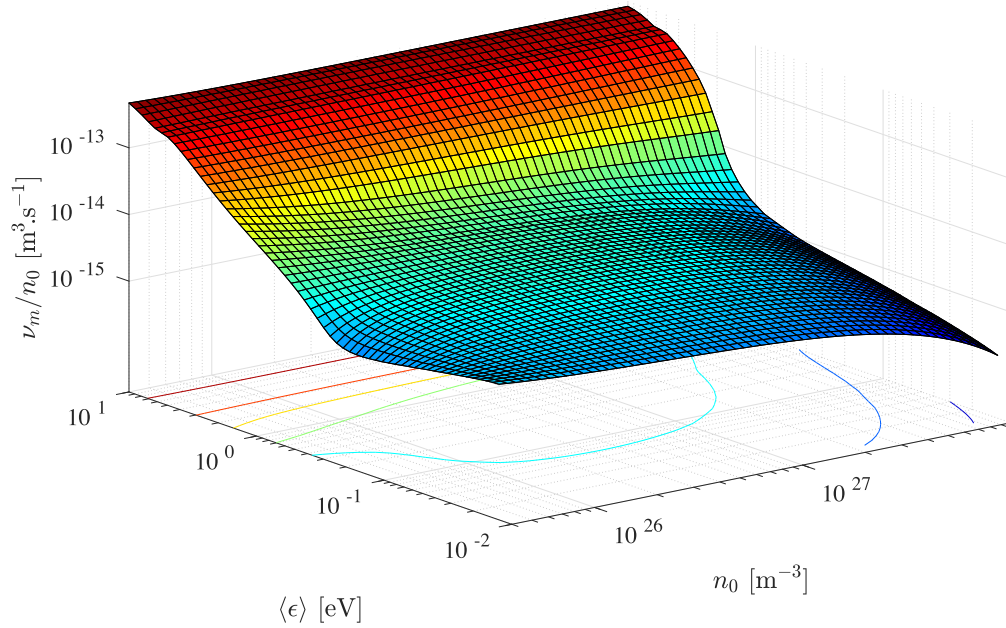
Figure A2. Reduced momentum transfer collision frequency, $\frac{\nu_m}{n_0}$, surface of electrons in argon computed via (A.11) as a function of $\langle \epsilon \rangle$ and n_0 used to interpolate input data for the 4MM model.
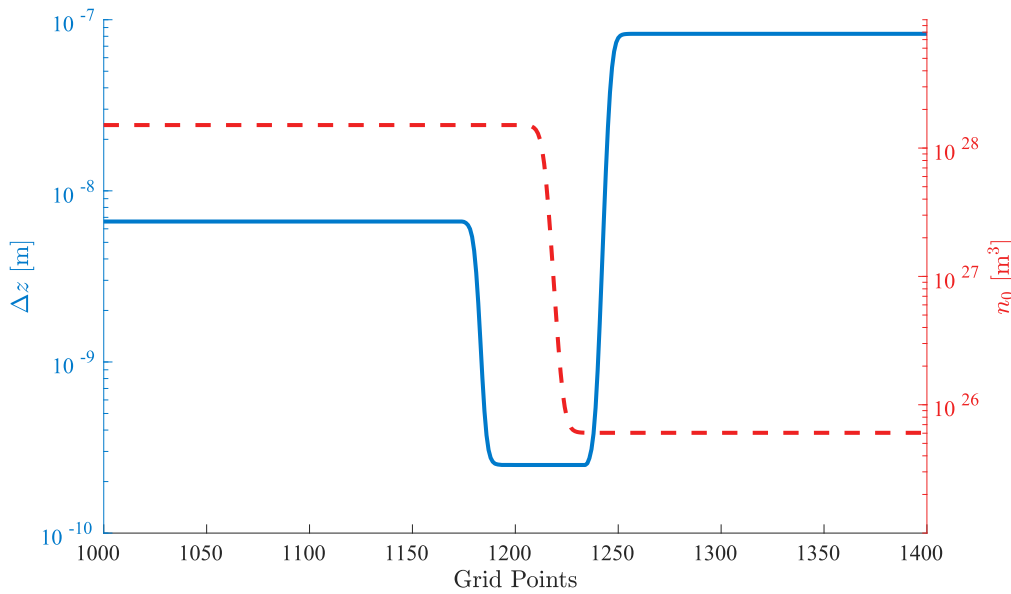

Figure B1. An example of the spatially varying numerical grid steps employed in discretization of the solution domain over the interface transition region.

scaled by n_0. To demonstrate the application of the nonlinear sum rule the reduced momentum transfer collision frequency surface generated via (A.11) is included in figure A2, demonstrating the reduction in momentum transfer collisions as the argon density increases.

Appendix B. Numerical solution of system of hyperbolic PDEs

Numerical solution of both the LFA and higher order fluid models for electron and ion properties was achieved by a custom flux-corrected transport (FCT) code [13], with explicit fourth order Runge–Kutta (RK4) time-integration used to advance forward in time [84–86]. Spatial discretization was performed via FCT by augmenting a monotonic first order upwinding scheme [87], with a second order conservative finite difference scheme. The FCT flux limiting algorithm of Boris and Book [85, 86] was used to enable resolution of sharp gradients found in ionization fronts. To account for the varying length scales present in the problems, we employed variably spaced grids, as shown in figure B1, to allow spatial steps appropriate to liquid, gas, and interfacial regions. Given the spatial grid sizes, time step size was chosen as the smallest

step computed via: (i) a Courant–Friedrichs–Lewy (CFL) condition of 0.05, or (ii) 1/20 of the fastest collisional relaxation time. Employing both the spatial discretization of FCT and RK4 time-integration assists in avoiding excessive numerical diffusion that may be introduced as a result of small time steps due to the small CFL number.

Solution of the coupled electric field evolution was obtained via second order finite difference discretization of (3) and (4), given fixed boundary conditions for electric potential at either end of the solution domain [13]. To ensure the accuracy of this scheme, systematic benchmarking was performed by comparing numerical solutions against known analytic solutions, and ensuring particle conservation was guaranteed at each time step. Typical systems used for benchmarking are square-wave advection, Gaussian pulse advection-diffusion, and the solution of Euler's equations for Sod's shock-tube [84–86].

Continuous boundary conditions were implemented to allow passage of information outside of the solution domain to avoid impacting the solution. To further assist in this aim, streamer formation and propagation was performed well inside the solution domain, away from the necessary boundaries, to minimize the impact of boundary conditions.

ORCID iDs

N A Garland ⬤ https://orcid.org/0000-0003-0343-0199
G J Boyle ⬤ https://orcid.org/0000-0002-8581-4307
D G Cocks ⬤ https://orcid.org/0000-0002-9943-7100
R D White ⬤ https://orcid.org/0000-0001-5353-7440

References

[1] Economou D J 2014 Pulsed plasma etching for semiconductor manufacturing *J. Phys. D: Appl. Phys.* **47** 303001
[2] Boeuf J P and Pitchford L C 1995 Two-dimensional model of a capacitively coupled rf discharge and comparisons with experiments in the Gaseous Electronics Conference reference reactor *Phys. Rev. E* **51** 1376–90
[3] Lymberopoulos D P and Economou D J 1995 Two-dimensional self-consistent radio-frequency plasma simulations relevant to the gaseous electronics conference rf reference cell *J. Res. Natl Inst. Stand. Technol.* **100** 473
[4] Dujko S, Markosyan A H, White R D and Ebert U 2013 High-order fluid model for streamer discharges: I. Derivation of model and transport data *J. Phys. D: Appl. Phys.* **46** 475202
[5] Morrow R and Lowke J J 1997 Streamer propagation in air *J. Phys. D: Appl. Phys.* **30** 614–27
[6] Qin J, Pasko V P, McHarg M G and Stenbaek-Nielsen H C 2014 Plasma irregularities in the d-region ionosphere in association with sprite streamer initiation *Nat. Commun.* **5** 1–6
[7] Marinov I, Starikovskaia S and Rousseau A 2014 Dynamics of plasma evolution in a nanosecond underwater discharge *J. Phys. D: Appl. Phys.* **47** 224017
[8] Akishev Y, Karalnik V, Medvedev M, Petryakov A, Shafikov A and Trushkin N 2017 Propagation of positive streamers on the surface of shallow as well as deep tap water in wide and narrow dielectric channels *Plasma Sources Sci. Technol.* **26** 025004

[9] Lindsay A D, Graves D B and Shannon S C 2016 Fully coupled simulation of the plasma liquid interface and interfacial coefficient effects *J. Phys. D: Appl. Phys.* **49** 235204
[10] Bruggeman P J *et al* 2016 Plasma-liquid interactions: a review and roadmap *Plasma Sources Sci. Technol.* **25** 053002
[11] Mariotti D, Patel J, Švrček V and Maguire P 2012 Plasma-liquid interactions at atmospheric pressure for nanomaterials synthesis and surface engineering *Plasma Process. Polym.* **9** 1074–85
[12] Richmonds C, Witzke M, Bartling B, Lee S W, Wainright J, Liu C C and Sankaran R M 2011 Electron-transfer reactions at the plasma-liquid interface *J. Am. Chem. Soc.* **133** 17582–5
[13] Garland N A, Cocks D G, Boyle G J, Dujko S and White R D 2017 Unified fluid model analysis and benchmark study for electron transport in gas and liquid analogs *Plasma Sources Sci. Technol.* **26** 075003
[14] Becker M M, Kählert H, Sun A, Bonitz M and Loffhagen D 2017 Advanced fluid modeling and PIC/MCC simulations of low-pressure ccrf discharges *Plasma Sources Sci. Technol.* **26** 044001
[15] Markosyan A H, Teunissen J, Dujko S and Ebert U 2015 Comparing plasma fluid models of different order for 1D streamer ionization fronts *Plasma Sources Sci. Technol.* **24** 065002
[16] Boyle G J, McEachran R P, Cocks D G and White R D 2015 Electron scattering and transport in liquid argon *J. Chem. Phys.* **142** 154507
[17] Boyle G J, Tattersall W J, Cocks D G, McEachran R P and White R D 2017 A multi-term solution of the space–time Boltzmann equation for electrons in gases and liquids *Plasma Sources Sci. Technol.* **26** 024007
[18] Akimov D, Bondar A, Burenkov A and Buzulutskov A 2009 Detection of reactor antineutrino coherent scattering off nuclei with a two-phase noble gas detector *J. Instrum.* **4** P06010
[19] Bondar A, Buzulutskov A, Grebenuk A, Pavlyuchenko D, Snopkov R and Tikhonov Y 2006 Two-phase argon and xenon avalanche detectors based on Gas Electron Multipliers *Nucl. Instrum. Methods Phys. Res.* A **556** 273–80
[20] Brunetti R *et al* 2005 WARP liquid argon detector for dark matter survey *New Astron. Rev.* **49** 265–9
[21] Sangiorgio S *et al* 2013 First demonstration of a sub-keV electron recoil energy threshold in a liquid argon ionization chamber *Nucl. Instrum. Methods Phys. Res.* A **728** 69–72
[22] Regenfus C 2010 The argon dark matter experiment (ArDM) *J. Phys.: Conf. Ser.* **203** 99–102
[23] Adamovich I *et al* 2017 The 2017 Plasma Roadmap: Low temperature plasma science and technology *J. Phys. D: Appl. Phys.* **50** 323001
[24] Babaeva N Y, Tian W and Kushner M J 2014 The interaction between plasma filaments in dielectric barrier discharges and liquid covered wounds: electric fields delivered to model platelets and cells *J. Phys. D: Appl. Phys.* **47** 235201
[25] Bruggeman P and Leys C 2009 Non-thermal plasmas in and in contact with liquids *J. Phys. D: Appl. Phys.* **42** 053001
[26] Gopalakrishnan R, Kawamura E, Lichtenberg A J, Lieberman M A and Graves D B 2016 Solvated electrons at the atmospheric pressure plasma-water anodic interface *J. Phys. D: Appl. Phys.* **49** 295205
[27] Lietz A M and Kushner M J 2016 Air plasma treatment of liquid covered tissue: long timescale chemistry *J. Phys. D: Appl. Phys.* **49** 425204
[28] Tian W and Kushner M J 2014 Atmospheric pressure dielectric barrier discharges interacting with liquid covered tissue *J. Phys. D: Appl. Phys.* **47** 165201

[29] Boyle G J, McEachran R P, Cocks D G, Brunger M J, Buckman S J, Dujko S and White R D 2016 *Ab initio* electron scattering cross-sections and transport in liquid xenon *J. Phys. D: Appl. Phys.* **49** 355201

[30] White R D and Robson R E 2011 Multiterm solution of a generalized Boltzmann kinetic equation for electron and positron transport in structured and soft condensed matter *Phys. Rev.* E **84** 031125

[31] Robson R, White R and Hildebrandt M 2017 *Fundamentals of Charged Particle Transport in Gases and Condensed Matter (Monograph Series in Physical Sciences)* (Boca Raton, FL: CRC Press)

[32] Hagelaar G J M and Kroesen G M W 2000 Speeding up fluid models for gas discharges by implicit treatment of the electron energy source term *J. Comput. Phys.* **159** 1–12

[33] Ebert U *et al* 2011 Multiple scales in streamer discharges, with an emphasis on moving boundary approximations *Nonlinearity* **24** C1–26

[34] Meunier J, Belenguer P and Boeuf J P 1995 Numerical-model of an Ac plasma display panel cell in neon-xenon mixtures *J. Appl. Phys.* **78** 731–45

[35] Becker M M and Loffhagen D 2013 Derivation of moment equations for the theoretical description of electrons in nonthermal plasmas *Adv. Pure Math.* **03** 343–52

[36] Robson R E, White R D and Petrović Z L 2005 Colloquium : Physically based fluid modeling of collisionally dominated low-temperature plasmas *Rev. Mod. Phys.* **77** 1303–20

[37] Tattersall W J, Cocks D G, Boyle G J, Buckman S J and White R D 2015 Monte Carlo study of coherent scattering effects of low-energy charged particle transport in Percus–Yevick liquids *Phys. Rev.* E **91** 043304

[38] Dujko S, White R D, Petrović Z L and Robson R E 2010 Benchmark calculations of nonconservative charged-particle swarms in dc electric and magnetic fields crossed at arbitrary angles *Phys. Rev.* E **81** 046403

[39] Birdsall C K 1991 Particle-in-cell charged-particle simulations, plus Monte Carlo collision with neutral atom, PIC-MCC *IEEE Trans. Plasma Sci.* **19** 65–85

[40] Robson R E, Nicoletopoulos P, Hildebrandt M and White R D 2012 Fundamental issues in fluid modeling: direct substitution and aliasing methods *J. Chem. Phys.* **137** 214112

[41] Turner M M, Derzsi A, Donkó Z, Eremin D, Kelly S J, Lafleur T and Mussenbrock T 2013 Simulation benchmarks for low-pressure plasmas: capacitive discharges *Phys. Plasmas* **20** 013507

[42] Becker M M and Loffhagen D 2013 Enhanced reliability of drift-diffusion approximation for electrons in fluid models for nonthermal plasmas *AIP Adv.* **3** 012108

[43] Dujko S, White R D and Petrović Z L 2008 Monte Carlo studies of non-conservative electron transport in the steady-state Townsend experiment *J. Phys. D: Appl. Phys.* **41** 245205

[44] White R D, Robson R E, Dujko S, Nicoletopoulos P and Li B 2009 Recent advances in the application of Boltzmann equation and fluid equation methods to charged particle transport in non-equilibrium plasmas *J. Phys. D: Appl. Phys.* **42** 194001

[45] Phelps A V 1991 Cross sections and swarm coefficients for nitrogen ions and neutrals in N_2 and argon ions and neutrals in Ar for energies from 0.1 eV to 10 keV *J. Phys. Chem. Ref. Data* **20** 557–73

[46] Viehland L A and Kirkpatrick C C 1995 Relating ion/neutral reaction rate coefficients and cross-sections by accessing a database for ion transport properties *Int. J. Mass Spectrom. Ion Process.* **149–150** 555–71

[47] Verlet L and Weis J-J 1972 Equilibrium theory of simple liquids *Phys. Rev.* A **5** 939–52

[48] Markosyan A H, Dujko S and Ebert U 2013 High-order fluid model for streamer discharges: II. Numerical solution and investigation of planar fronts *J. Phys. D: Appl. Phys.* **46** 475203

[49] Grubert G K, Becker M M and Loffhagen D 2009 Why the local-mean-energy approximation should be used in hydrodynamic plasma descriptions instead of the local-field approximation *Phys. Rev.* E **80** 036405

[50] Biondi M A and Brown S C 1949 Measurement of electron–ion recombination *Phys. Rev.* **76** 1697–700

[51] Foxe M, Hagmann C, Jovanovic I, Bernstein A, Kazkaz K, Mozin V, Pereverzev S V, Sangiorgio S and Sorensen P 2015 Low-energy (<10 keV) electron ionization and recombination model for a liquid argon detector *Nucl. Instrum. Methods Phys. Res.* A **771** 88–92

[52] Kubota S, Nakamoto A, Takahashi T, Hamada T, Shibamura E, Miyajima M, Masuda K and Doke T 1978 Recombination luminescence in liquid argon and in liquid xenon *Phys. Rev.* B **17** 2762–5

[53] Shinsaka K, Codama M, Srithanratana T, Yamamoto M and Hatano Y 1988 Electron–ion recombination rate constants in gaseous, liquid, and solid argon *J. Chem. Phys.* **88** 7529–36

[54] Thomas J and Imel D A 1987 Recombination of electron–ion pairs in liquid argon and liquid xenon *Phys. Rev.* A **36** 614–6

[55] Hayashi M 2003 *Bibliography of Electron and Photon Cross Sections With Atoms and Molecules Published in the 20th Century—Argon Report* NIFS-DATA-72 National Institute for Fusion Science of Japan

[56] Hayashi Database. www.lxcat.net, (Retrieved: 18 February 2018)

[57] Dujko S, Simonovic I, Boyle G, White R, Bosnjakovic D and Petrovic Z 2016 Transport properties of electrons and transition of an electron avalanche into a streamer in atomic liquids *APS Gaseous Electronics Conf. 2016 Abstracts* p MW6.036

[58] Simonović I, Petrović Z L and Dujko S 2017 Simulation of electron transport and negative planar streamer fronts in liquid argon anf liquid xenon *Proc. 21st Symp. on Application of Plasma Processes (SAPP XXI)* pp 226–30

[59] Schmidt W F and Illenberger E 2003 Low energy electrons in non-polar liquids *Nukleonika* **48** 75–82

[60] Evans C M and Findley G L 2010 Energy of the conduction band in near critical point fluids *Phys. Res. Int.* **2010** 1–6

[61] Asaf U and Steinberger I T 1974 Photoconductivity and electron transport parameters in liquid and solid xenon *Phys. Rev.* B **10** 4464–8

[62] Miyajima M, Takahashi T, Konno S, Hamada T, Kubota S, Shibamura H and Doke T 1974 Average energy expended per ion pair in liquid argon *Phys. Rev.* A **9** 1438–43

[63] Laporte P, Subtil J L, Reininger R, Saile V, Bernstorff S and Steinberger I T 1987 Evolution of intermediate excitons in fluid argon and krypton *Phys. Rev.* B **35** 6270–80

[64] Laporte P and Steinberger I T 1977 Evolution of excitonic bands in fluid xenon *Phys. Rev.* A **15** 2538–44

[65] Laporte P, Subtil J L, Asaf U, Steinberger I T and Wind S 1980 Intermediate and wannier excitons in fluid xenon *Phys. Rev. Lett.* **45** 2138–40

[66] Haensel R, Keitel G, Koch E E, Skibowski M and Schreiber P 1969 Reflection spectrum of solid argon in the vacuum ultraviolet *Phys. Rev. Lett.* **23** 1160–3

[67] Gushchin E M, Kruglov A A and Obodovskii I M 1982 Electron dynamics in condensed argon and xenon *Sov. Phys. —JETP* **55** 650–5

[68] Kalos M H, Percus J K and Rao M 1977 Structure of a liquid–vapor interface *J. Stat. Phys.* **17** 111–36

[69] Halpern B, Lekner J, Rice S and Gomer R 1967 Drift velocity and energy of electrons in liquid argon *Phys. Rev.* **156** 351–2

[70] Lee D J, Telo Da Gama M M and Gubbins K E 1984 The vapour–liquid interface for a Lennard-Jones model of argon-krypton mixtures *Mol. Phys.* **53** 1113–30

[71] Trokhymchuk A and Alejandre J 1999 Computer simulations of liquid/vapor interface in Lennard-Jones fluids: some questions and answers *J. Chem. Phys.* **111** 8510–23

[72] Yi P, Poulikakos D, Walther J and Yadigaroglu G 2002 Molecular dynamics simulation of vaporization of an ultra-thin liquid argon layer on a surface *Int. J. Heat Mass Transfer* **45** 2087–100

[73] Chapela G A, Saville G, Thompson S M and Rowlinson J S 1977 Computer simulation of a gsa–liquid surface: I *J. Chem. Soc. Faraday Trans.* II **73** 1133–44

[74] Ishiyama T, Yano T and Fujikawa S 2004 Molecular dynamics study of kinetic boundary condition at an interface between argon vapor and its condensed phase *Phys. Fluids* **16** 2899–906

[75] Garland N A, Boyle G J, Cocks D G and White R D 2018 Approximating the nonlinear density dependence of electron transport coefficients and scattering rates across the gas–liquid interface *Plasma Sources Sci. Technol.* **27** 024002

[76] Amey R L and Cole R H 1964 Dielectric constants of liquefied noble gases and methane *J. Chem. Phys.* **40** 146–8

[77] Lippold H 1969 Isothermal compressibility and density of liquid argon and neon up to pressures of 1000 kg/cm^2 *Cryogenics* **9** 112–4

[78] Abel B, Buck U, Sobolewski A L and Domcke W 2012 On the nature and signatures of the solvated electron in water *Phys. Chem. Chem. Phys.* **14** 22–34

[79] Blanc A 1908 Recherches sur les mobilités des ions dans les gaz *J. Phys. Théor. Appl.* **7** 825–39

[80] Chiflikian R V 1995 The analog of Blanc's law for drift velocities of electrons in gas mixtures in weakly ionized plasma *Phys. Plasmas* **2** 3902–9

[81] Boyle G J, White R D, Robson R E, Dujko S and Lj Petrović Z 2012 On the approximation of transport properties in structured materials using momentum-transfer theory *New J. Phys.* **14** 045011

[82] Lekner J 1967 Motion of electrons in liquid argon *Phys. Rev.* **158** 130–7

[83] Robson R E 1984 Generalized einstein relation and negative differential conductivity in gases *Aust. J. Phys.* **37** 35

[84] Zalesak S T 2012 The design of flux-corrected transport (FCT) algorithms for structured grids *Flux-Corrected Transport (Scientific Computation)* ed D Kuzmin *et al* 1 edn (Dordrecht: Springer) ch 2, pp 23–65

[85] Boris J P and Book D L 1973 Flux-corrected transport: I. SHASTA, a fluid transport algorithm that works *J. Comput. Phys.* **11** 38–69

[86] Zalesak S T 1979 Fully multidimensional flux-corrected transport algorithms for fluids *J. Comput. Phys.* **31** 335–62

[87] Swanson R C and Turkel E 1992 On central-difference and upwind schemes *J. Comput. Phys.* **101** 292–306

PAPER

Electron transport and negative streamers in liquid xenon

View the article online for updates and enhancements.

Electron transport and negative streamers in liquid xenon

I Simonović[1] ⬤, **N A Garland**[2] ⬤, **D Bošnjaković**[1] ⬤, **Z Lj Petrović**[1,3] ⬤,
R D White[2] ⬤ and **S Dujko**[1] ⬤

[1] Institute of Physics, University of Belgrade, Pregrevica 118, 11080 Belgrade, Serbia
[2] College of Science and Engineering, James Cook University, Townsville, QLD 4811, Australia
[3] Serbian Academy of Sciences and Arts, Knez Mihailova 35, 11000 Belgrade, Serbia

E-mail: sasa.dujko@ipb.ac.rs

CrossMark

Abstract

In this work we investigate electron transport, transition from an electron avalanche into a negative streamer, and propagation of negative streamers in liquid xenon. Our standard Monte Carlo code, initially developed for dilute neutral gases, is generalized and extended to consider the transport processes of electrons in liquids by accounting for the coherent and other liquid scattering effects. The code is validated through a series of benchmark calculations for the Percus–Yevick model, and the results of the simulations agree very well with those predicted by a multi term solution of Boltzmann's equation and other Monte Carlo simulations. Electron transport coefficients, including mean energy, drift velocity, diffusion tensor, and the first Townsend coefficient, are calculated for liquid xenon and compared to the available measurements. It is found that our Monte Carlo method reproduces both the experimental and theoretical drift velocities and characteristic energies very well. In particular, we discuss the occurrence of negative differential conductivity in the E/n_0 profile of the drift velocity by considering the spatially-resolved swarm data and energy distribution functions. Calculated transport coefficients are then used as an input in fluid simulations of negative streamers, which are realized in a 1.5 dimensional setup. Various scenarios of representing the inelastic energy losses in liquid xenon, ranging from the case where the energy losses to electronic excitations are neglected, to the case where some particular excitations are taken into account, and to the case where all electronic excitations are included, are discussed in light of the available spectroscopy and photoconductivity experiments. We focus on the way in which electron transport coefficients and streamer properties are influenced by representation of the inelastic energy losses, highlighting the need for the correct representation of the elementary scattering processes in the modeling of liquid discharges.

Keywords: liquid xenon, electron transport, Monte Carlo, inelastic collisions, negative streamers

1. Introduction

Transport of charged particles in liquids, plasma-liquid interactions and streamer discharges in the liquid phase constitute a growing field of research, which has many important applications [1, 2]. These applications include plasma medicine [3, 4], plasma water purification [5–9], transformer oils [10, 11] and particle detectors [12, 13]. In particular, there is a rich variety of liquid xenon particle detectors [14]. The wide range of existing and potential applications of these detectors includes gamma ray astrophysics [13], particle physics [15] and medical imaging [16], as well as direct dark matter detection [17, 18]. Liquid xenon is a very good detection medium, due to its physical properties [14]. Its high values of density and atomic number make liquid xenon very efficient in stopping penetrating radiation, while a significant abundance of many isotopes, with different values of nuclear spin, enables the study of both spin dependent and spin independent interactions [14]. Further optimization and understanding of such applications is dependent on an accurate knowledge

of the charged particle transport coefficients, streamer properties and the physical processes involved.

In addition to many useful applications, further theoretical and experimental investigation of transport phenomena in liquids would help in the development of insight into various effects, which are relevant for the interaction of charged particles with dense and disordered media [19]. These effects include multiple scattering effects and structure effects, trapping of charged particles in density fluctuations and the solvation of charged particles in polar liquids [19, 20]. As liquid rare gases are the simplest liquids, they are a good starting point for the development of theoretical models of transport and breakdown phenomena in the liquid phase [19].

1.1. A brief overview of electron transport in liquid rare gases

In recent years the modeling of charged particle transport processes in neutral gases has matured and a number of methods to treat this problem have been developed, e.g. various techniques for solving the Boltzmann equation [21], the Monte Carlo method [22] and semi-quantitative momentum transfer theory [21, 23]. For the more general case of the dense gases and liquids, there has been comparatively less investigation. Most investigations in liquid phase have been performed for electron transport in the sub-excitation energy region [19]. Lekner developed an *ab initio* method for determining the effective potential and the corresponding effective cross section for electron scattering on a focus atom in the liquid phase [24]. This effective potential is determined by using the potential of a single atom and the pair correlation function of the liquid. In addition, Cohen and Lekner have shown that the coherent elastic scattering can be represented in the Boltzmann equation by combining the effective cross section for the liquid phase and the static structure factor [25]. By simplifying the arguments of Lekner, Atrazhev and co-workers have shown that the effective cross section for elastic scattering in liquid argon, krypton and xenon are constant in the limit of lower electron energies [26, 27]. This work was extended by using the partial wave method for determining the effective cross sections for electron scattering in liquid argon and liquid xenon [28–31]. Based on these results, they have calculated mobility, mean energy, and characteristic energy of electrons in liquid argon and liquid xenon, in the framework of the Cohen–Lekner theory [30, 31]. The Cohen–Lekner theory was also used in the study of Sakai and co-workers, who have investigated the electron transport in liquid argon, krypton and xenon [32, 33]. In order to improve the agreement between the calculated and measured drift velocities, they have modified the cross section for elastic scattering empirically. In addition, they have demonstrated that the saturation of drift velocity at higher electric fields, which was previously observed in experiments, can be adequately described by including an effective inelastic cross section for vibrational modes. It was argued that these vibrational modes correspond to the change of the translational states of the clusters of atoms. More recently, Boyle *et al* [19, 34] have evaluated the differential cross sections for electron scattering in liquid argon and liquid xenon by solving

the Dirac–Fock scattering equations. In these works, Boyle *et al* [19, 34] extended Lekner's theory by considering multipole polarizabilities and non-local treatment of exchange [19, 34]. Transport coefficients have been calculated for electrons using these cross sections as an input into the multi term Boltzmann equation solution, for the lower values of the reduced electric field. It is also worth noting that in order to thermalize electrons to low energies in rare gases (especially those with Ramsauer–Townsend minimum) in the most efficient way and with a small experimental error, it was necessary to perform swarm experiments at higher pressures, where high density effects became observable [35–37]. One of the alternatives to avoid such effects and obtain low-energy cross sections and scattering lengths was to use molecular hydrogen in the mixture at low reduced electric fields, where the unique solution for the rotational energy loss cross sections for hydrogen exists [38].

Theoretical studies of electron transport processes in liquid rare gases, at higher electric fields, have been performed by several authors. In 1976, Atrazhev and co-workers studied the influence of density dependent scattering effects on the Townsend ionization coefficient [39]. The results of this work are two estimates of the first Townsend ionization coefficient, which have been made by considering the two distinctively different representations of energy losses in the electronic excitations. Jones and Kunhardt also studied electron transport in liquid xenon by using Monte Carlo simulations [40]. The semiclassical model used, was previously applied by Kunhardt for studying electron transport in liquid argon [41]. In this work, the interaction of electrons with the liquid is described in the framework of Van Hove's theory [42]. The group at Hokkaido University has also studied ionization in liquid xenon, as well as the electron attachment in the mixtures of liquid argon and electronegative impurities, including O_2, SF_6 and N_2O, using previously developed cross sections [32]. Considerable contributions in this field have been made by Boyle and co-workers who developed the fluid equation based model for electrons and positrons in liquids by utilizing dilute gas phase cross sections together with a structure factor for the medium [43–46].

1.2. Streamers in liquid rare gases

In comparison to gas phase modeling, there are only a few modeling studies of streamer propagation in liquids. Simulations of positive streamers in hydrocarbon liquids using 1.5D classical streamer model have been performed by Naidis and co-workers [10, 47]. Simulations are performed both without formation of expanding gaseous filaments and in conditions when such filaments due to vaporization are formed. Contemporary studies include both the experimental and numerical studies of propagating streamers inside bubbles elongated along the external electric field and compressed bubbles immersed in water [48, 49]. The salient feature of these studies is that transport coefficients of electrons in liquids required for streamer simulations are evaluated approximately, e.g. without taking into account more serious

perturbations to the transport due to the formation of bubbles and clusters.

Numerical modeling of streamer dynamics, in liquid argon and liquid xenon, has been performed by Babaeva and Naidis [50–52]. They have investigated the formation of a positive streamer in a strong non-uniform field and its subsequent propagation in a weak uniform field, by employing a two dimensional fluid model [50, 51]. Among many important points in these papers, it has been shown that the nature of the streamer propagation in the liquid phase is significantly influenced by the electron-ion recombination [50, 51]. In addition, they found that the calculated streamer velocities are of the same order of magnitude as the measured velocity of the breakdown wave in liquid argon [50, 51].

1.3. Motivational factors for this study

One of the most important conclusions from the previous studies of electron transport in atomic liquids is the fact that still there is no consensus on the importance of excitations in the liquid phase. For example, Atrazhev *et al* [39] have shown that if the portion of energy losses due to excitations is assumed to be just the same as in the gas phase, the first Townsend coefficient is underestimated. On the other hand, if the inelastic energy losses are completely neglected then the first Townsend coefficient is overestimated [39]. Along similar lines, Nakamura and co-workers also disregarded the explicit influence of energy losses associated with the electronic excitations in their calculations of transport properties of electrons in the liquid phase [20, 53]. Instead, they have represented the inelastic energy losses by using an effective inelastic cross section, which corresponds to vibrational modes [20, 32, 53]. In 1993, Jones and Kunhardt carried out Monte Carlo simulations in which the inelastic energy losses due to electronic excitations were included [40]. However, in this work it has not been specified which electronic excitations are included in the set of cross sections [40]. Atrazhev *et al* [39] have shown that a different representation of the inelastic energy losses leads to a significant difference in the calculated values of the ionization rate in liquid xenon. Thus, it is clear that a rigorous analysis of the inelastic energy losses in studies of electron transport in liquid rare gases is long overdue and the present study takes the first steps in this direction. We believe that this is of key importance for numerical studies of streamer propagation, since ionization controls the development of a discharge and occurs in both the streamer head and in the streamer channel.

In this work, we investigate how various representations of the inelastic energy losses affect transport properties of electrons and streamer dynamics in liquid xenon. Cross sections for electronic excitations are taken from the set for electron scattering in the gas phase compiled by Hayashi [54]. This set of cross sections yields swarm parameters in good agreement with the available measurements [55]. We identify and consider the following three global scenarios: (i) no electronic excitations, (ii) some electronic excitations are included and some of them are neglected, and (iii) all

electronic excitations are included in the modeling. Various representations of inelastic energy losses are first discussed in light of previous spectroscopy and photoconductivity experiments and then are used in Monte Carlo simulations. The calculated values of the first Townsend coefficient in these various cases are compared with respect to the experimental results of Derenzo *et al* [56]. These calculations are augmented by those in which gaseous xenon is scaled up to the liquid density. In addition to the study of transport processes, in this work we investigate the propagation of negative streamers in liquid xenon. The axial profiles of electric field and number density of electrons are calculated in the absence of vaporization and the occurrence of bubbles.

1.4. Organization of the paper

In section 2 we give the details of cross sections for elastic and inelastic scattering of electrons in liquid xenon. We identify and review the four different cases in three global scenarios for representing the inelastic energy losses. In section 3.1 we briefly outline the Monte Carlo method used in the present work and present the results of benchmark calculations for the Percus–Yevick model in section 3.2. In section 3.3 we present the basic elements of a fluid theory used to simulate negative streamers in liquid xenon. In section 4 we present the electron transport coefficients in liquid xenon with particular emphasis on the structure induced negative differential conductivity (NDC). In the same section, we discuss the transition from an avalanche into a streamer and propagation of negative streamers. In section 5 we present our conclusions and recommendations for future work.

2. Cross sections for electron scattering in liquid xenon

In the gas phase, the electron transport can be represented as a series of individual collisions, which are separated by free flights [19]. However, this picture is no longer valid in the liquid phase. Since no particular volume is owned by a single atom, due to small interparticle spacings in liquids, as compared to the range of interaction between electrons and the targets, the potential in which an excess electron is scattered is determined by many surrounding atoms [19, 24]. Namely, it has been shown that the polarization potential of a single atom is significantly screened by polarization potentials of neighboring atoms [19, 24]. Due to this effect, at low energies, the effective potential changes from an attractive long range potential, which corresponds to scattering on an isolated xenon atom, to a repulsive short range potential, which corresponds to scattering in the liquid phase [24, 28]. In addition, electron scattering on a focus atom will be influenced by electrostatic terms and non-local exchange terms of all neighboring atoms [19]. Moreover, the de Broglie wavelengths of excess electrons at thermal energies are larger than the interatomic spacing by several orders of magnitude [19].

This leads to significant coherent scattering effects, for low energy electrons, which make the electron scattering structure dependent and strongly anisotropic [19, 24]. The anisotropy of coherent scattering leads to a difference between the effective mean free paths for the transfer of energy and momentum [24, 57]. It has been shown that the effective mean free path for the transfer of energy is independent of the liquid structure, while the effective mean free path for the transfer of momentum is structure dependent [24, 57]. The coherent scattering effects and the modification of the scattering potential strongly influence the elastic scattering of the lower energy electrons. However, these effects are reduced with an increasing energy becoming negligible for electron energies higher than approximately 10 eV [39, 57]. This is demonstrated by the density independence of the measured drift velocity for swarms of electrons in compressed gases under high electric fields [58, 59].

Excitations in liquid xenon have been investigated in spectroscopy experiments [60–65]. It has been shown that the reflection spectrum of liquid xenon is very similar to the reflection spectrum of solid xenon [60, 61]. In this spectrum, intermediate $n = 1 \left[\Gamma\left(\frac{3}{2}\right) \right]$ and $n' = 1 \left[\Gamma\left(\frac{1}{2}\right) \right]$ excitons have been observed at 8.2 eV and 9.45 eV, respectively [61–63]. The former has parentage in the excited atomic $6s[3/2]_1$ state, while the latter has parentage in the $6s'[1/2]_1$ state [63]. In addition, a spectral line, which has developed from the two neighboring $5d[3/2]_1$ and $7s[3/2]_1$ states, has been observed at about 10.32 eV [63, 66]. Another spectral line has been observed at 9 eV [61–63]. This line belongs to the $n = 2$ $\left[\Gamma\left(\frac{3}{2}\right) \right]$ Wannier exciton, which does not originate from the states of an isolated atom [61–63]. Since excitons are closely related to the electron band structure, the presence of excitonic lines in the reflection spectrum indicates the existence of the valence band and the conduction band in liquid xenon [66]. In addition, the value of $\Gamma\left(\frac{3}{2}\right)$ band gap has been determined from the corresponding Wannier series [67]. The obtained value of the band gap is 9.22 eV, and it is in excellent agreement with the prediction on the change of the corresponding band gap in the solid phase [66, 67]. This value has been further verified by using the measured photoconductivity threshold in liquid xenon (9.202 eV) and the known difference between the photoconductivity threshold and the $\Gamma\left(\frac{3}{2}\right)$ band gap in the solid xenon (0.013 eV) [67].

Thus, a cross section set for electron scattering in liquid xenon has to include the cross sections for elastic scattering, inelastic energy losses and the interband transitions [40, 41]. We employ four different cases for representing the inelastic energy losses in order to study the influence of the inelastic collisions on the transport properties of electron swarms and the dynamics of negative streamers in liquid xenon. Each of these cases is discussed in light of previous spectroscopy and photoconductivity experiments. Elastic scattering and the interband transitions are represented in the same way in all cases considered.

2.1. Elastic scattering and interband transitions

The elastic scattering of low energy electrons is strongly influenced by the changes in the scattering potential and the coherent scattering effects [19, 24, 26, 34]. Moreover, the effective mean free paths for the transfer of momentum and energy in liquids are different due to a strong anisotropy of coherent scattering [24, 57]. These mean free paths are given by

$$
\begin{aligned}
\Lambda_0 &= (n_0 \sigma_m)^{-1} \\
&= \left(n_0 2\pi \int_0^\pi \mathrm{d}\chi \sin\chi (1 - \cos\chi) \sigma_{\mathrm{sp}}(\epsilon, \chi) \right)^{-1},
\end{aligned} \tag{1}
$$

$$
\begin{aligned}
\Lambda_1 &= (n_0 \tilde{\sigma}_m)^{-1} \\
&= \left(n_0 2\pi \int_0^\pi \mathrm{d}\chi \sin\chi (1 - \cos\chi) \sigma_{\mathrm{sp}}(\epsilon, \chi) S(\Delta k) \right)^{-1},
\end{aligned} \tag{2}
$$

where n_0 is the liquid number density, $\sigma_{\mathrm{sp}}(\epsilon, \chi)$ is the differential cross section for elastic scattering of an electron on a focus atom in the liquid phase, ϵ is the relative energy in the center of mass frame, χ is the angle through which the relative velocity is changed and $S(\Delta k)$ is the static structure factor, as a function of the transferred momentum. In these equations $\tilde{\sigma}_m$ and σ_m represent the momentum transfer cross sections with and without the structure modification, respectively [57].

As proposed by Tattersall and co-workers, the ratio $\gamma(\epsilon) = \frac{\Lambda_0}{\Lambda_1}$ represents the measure of the anisotropy of coherent scattering [57]. The coherent scattering is modeled as a combination of three distinct effective scattering processes, which give a good representation of the average transfer of momentum and energy [57]. In the first of these processes, represented by the σ_{both} cross section, both energy and momentum are transferred as in an ordinary binary collision [57]. In the second process, represented by the $\sigma_{\mathrm{momentum}}$ cross section, the electron is scattered in a random direction, but the speed of the electron remains unchanged. This leads to a transfer of momentum, without a concomitant transfer of energy [57]. In the third process represented by the σ_{energy} cross section the energy of the electron is reduced as in an ordinary binary collision, but the electron does not change the direction of its motion. This leads to a transfer of energy, which is accompanied by a minimal transfer of momentum [57]. It is important to emphasize that these effective scattering processes do not represent individual microscopic collisions, but rather provide a good representation of the average rates of momentum transfer and energy transfer in structured media [57].

The cross sections for the corresponding effective processes are determined from $\gamma(\epsilon)$ and the momentum transfer cross section, for electron scattering on a focus atom in the liquid phase, $\sigma_m(\epsilon)$ [57]. The values of $\sigma_m(\epsilon)$ and $\gamma(\epsilon)$, which are used in the present work, have been determined by Boyle *et al* [34].

For $\gamma(\epsilon) < 1$ these cross sections are calculated as [57]:

$$\sigma_{\text{both}}^{\gamma<1} = \gamma(\epsilon) \cdot \sigma_m(\epsilon)$$
$$\sigma_{\text{energy}}^{\gamma<1} = (1 - \gamma(\epsilon)) \cdot \sigma_m(\epsilon)$$
$$\sigma_{\text{momentum}}^{\gamma<1} = 0. \tag{3}$$

For $\gamma(\epsilon) > 1$, these cross sections are given by [57]

$$\sigma_{\text{both}}^{\gamma>1} = \sigma_m(\epsilon)$$
$$\sigma_{\text{energy}}^{\gamma>1} = 0$$
$$\sigma_{\text{momentum}}^{\gamma>1} = (\gamma(\epsilon) - 1) \cdot \sigma_m(\epsilon). \tag{4}$$

We model the elastic scattering by using these effective cross sections, for energies up to approximately 10 eV. At higher energies both σ_{momentum} and σ_{energy} are taken to be negligible, while σ_{both} is approximated by the elastic cross section for electron scattering in the gas phase [68]. This is a good approximation, since both modifications of the scattering potential and the coherent scattering effects are small for high energy electrons [39, 57].

The cross section for interband transitions is approximated by the cross section for the electron impact ionization, from the Hayashi's cross section set, which is shifted towards lower energies. Specifically, the cross section for ionization is shifted by 2.91 eV, so that its threshold is moved to 9.22 eV. This value corresponds to the $\Gamma\left(\frac{3}{2}\right)$ band gap in liquid xenon, which is the energy difference between the uppermost valence band and the bottom of the conduction band [67]. The use of this cross section gives a good energy balance for the interband transitions, since the energy levels of excess electrons in the conduction band can be represented by a continuous energy spectrum, due to a high density of states in the conduction band [41].

We should note that the energy of the bottom of the conduction band in liquid xenon $V_0 = -(0.66 \pm 0.05)$ eV [69, 70] is not explicitly included in our calculations. This is justified since the system is homogeneous and the inclusion of V_0 would be equivalent to introducing a constant electric potential of the entire system, which would not influence the electron dynamics due to the constant value of this potential. It should also be noted that V_0 is implicitly included in the formula for the difference between the value of the ionization potential of an isolated atom and the value of the band gap in the liquid phase [40]. The inclusion of V_0 in calculations is necessary in the case of the gas-liquid interface (and other situations in which the number density of the background atoms is inhomogeneous) since the change of V_0 across the interface produces an effective electric field as shown in the recent study of Garland and co-workers [71]. Thus, in our calculations we can effectively represent discrete energy levels of quasi free electrons in the conduction band which have a minimum of V_0 with a continuous energy spectrum of free electrons which have a minimum of 0 eV.

2.2. Case 1: No electronic excitations

In the first case, the inelastic energy losses are completely neglected. It was shown by Atrazhev *et al* that this approach overestimates the first Townsend coefficient in liquid xenon [39]. However, this case is considered in our study with the aim of establishing the influence of electronic excitations on the first Townsend coefficient. This case will be referred to as case 1.

2.3. Case 2: Only excitations $6s[3/2]_2$ and $6s[3/2]_1$ are included

In our remaining cases inelastic energy losses are taken into account, since it has been shown in experiments that both excitons and perturbed atomic excitations exits in liquid xenon [62, 63]. Moreover, it has been determined that the excitation of these electronic states is the main channel of energy loss of excess electrons in liquid argon, krypton and xenon under the moderate electric fields [72–74]. However, no cross sections for the excitation of these discrete states can be found in the literature. Since intermediate excitons have unique parentage in the excited states of the atom [62, 63, 75], we approximate the cross sections for both intermediate excitons and the perturbed atomic excitations by the cross sections for the corresponding excitations of an isolated atom. The cross sections for excitations, which are used in our work, are those from the Hayashi cross section set for electrons in gaseous xenon [54, 68].

We do not change the values of the thresholds for excitations, since only thresholds for optically allowed excitons are present in the literature [75], while the optically forbidden states have to be included in our model as well. Therefore, it would be somewhat inconsistent to modify the thresholds for the optically allowed transitions, while leaving the thresholds for the optically forbidden transitions unchanged. Moreover, it has been shown that in the reflection spectrum of liquid xenon, there exists an additional line, next to the $n = 1$ $\left[\Gamma\left(\frac{3}{2}\right)\right]$ exciton line [62, 63]. This line corresponds to the perturbed atomic $6s[3/2]_1$ state [62, 63]. It was determined by Laporte *et al* that about 10% of atomic clusters in liquid xenon, near the triple point, will give rise to the perturbed atomic line, instead of the corresponding exciton line [62]. This is caused by the fact that these clusters do not have a sufficient number of atoms for the formation of the exciton inside a volume which corresponds to the exciton radius [62, 63]. Therefore, if one was to construct a model which distinguishes intermediate excitons from the corresponding perturbed atomic states, one would have to know which percentage of atomic clusters give rise to the perturbed atomic lines, instead of the corresponding excitonic lines, for each atomic excitation. In addition, one would have to know the thresholds for all excitons and all perturbed atomic excitations, including the optically forbidden states. This is beyond the scope of our paper, and we model both the intermediate excitons and the perturbed atomic excitations with the corresponding excitations of an isolated atom. However, the difference between these thresholds is less than 5% for all observed excitons [62, 63, 75]. Thus, we anticipate a small error is made by using the thresholds from the gas phase.

We neglect the observed $n = 2\,\Gamma\left(\frac{3}{2}\right)$ Wannier exciton, in all of our cases, since it does not correspond to any individual atomic state. No other Wannier exciton, for $n > 1$, has been identified in the reflection spectra of liquid xenon [61–63, 75]. For simplicity, in the rest of this work the interband transition and the inelastic collisions will be sometimes referred to as ionization and excitations, respectively. Comparing to binary inelastic collisions, these processes are not the same, as every xenon atom is located in a cluster of the surrounding atoms. Thus, atomic excitations are replaced either by excitons or by perturbed atomic excitations, depending on the size of the atomic cluster [62, 63]. Likewise, binary ionization is replaced by the excitation of an electron from the valence band to a quasi free state in the conduction band [66, 67].

In the second case, only excitations with thresholds, which are lower than the threshold of the interband transition, are included in the cross section set. This includes $6s[3/2]_2$ and $6s[3/2]_1$ atomic states. These two excitations correspond to the first two inelastic collisions in the Hayashi's cross section set [54]. The former of this state is optically forbidden, while the latter is optically allowed. Both the $n = 1$ $\left[\Gamma\left(\frac{3}{2}\right)\right]$ exciton, and the corresponding perturbed atomic state, which have been observed in experiment [61–63], have parentage in the second of these excitations.

2.4. Case 3: The first four excitations from the Hayashi's set of cross sections are included

In the previous experimental investigation of photoconductivity in liquid xenon it has been shown that other discrete states should also be included in the set of cross sections. Specifically, a dip has been observed in the photoconductivity spectra of liquid xenon at 9.45 eV [67]. This dip is induced by the competition between continuous band to band transitions and the discrete $n' = 1\left[\Gamma\left(\frac{1}{2}\right)\right]$ exciton [67]. The observed dip in the photoconductivity spectra of liquid xenon indicates that the corresponding discrete state has decay channels alternative to dissociation like luminescence [66]. This indicates that the inelastic energy losses due to this discrete state should be included in the modeling of electron transport in liquid xenon. The $n' = 1\,\Gamma(\frac{1}{2})$ exciton has parentage in the $6s'[1/2]_1$ atomic state [62, 63]. Another atomic excitation exists between $6s[3/2]_1$ and $6s'[1/2]_1$ states [54]. This is the optically forbidden $6s'[1/2]_0$ state. In this case it is important to take into account both $6s'[1/2]_0$ and $6s'[1/2]_1$ states, in addition to the excitations which are included in the second case. The $6s'[1/2]_0$ state corresponds to the third electronic excitation in the set of cross sections developed by Hayashi [54]. The fourth electronic excitation in the Hayashi's cross section set corresponds to a combination of $6s'[1/2]_1$ and $6p[1/2]_1$ states [54]. Thus, we include the first four excitations from the Hayashi's cross section set in our third case. This case will be referred to as case 3.

2.5. Case 4: All electronic excitations from Hayashi's cross section set are included

In the experimental investigation of the photoconductivity spectra of liquid xenon near the triple point, no further structure could be ascertained above 9.45 eV [67], and the photoconductivity spectra has only been shown for energies lower than 10 eV [67]. However, in a latter experimental investigation of the density dependence of the photoconductivity spectra in fluid xenon by Reininger *et al*, two more dips have been observed for densities up to 77.86% of the triple point density [66]. This is the highest density for which results are reported in their study. The first of these dips is at 10.32 eV corresponding to the discrete transition, which is formed from the two neighboring $5d[3/2]_1$ and $7s[3/2]_1$ states [66]. The second dip is caused by the perturbed $5d'[3/2]_1$ atomic state and it is observed at 11.6 eV [66].

Thus, it is clear that the discrete states with energies above 10 eV exist in liquid xenon, since a line at 10.32 eV has been observed in the reflectivity spectra [60, 62, 63]. It is also clear that they cause dips in the photoconductivity in fluid xenon up to densities close to the triple point density [66]. This indicates that these states should be included in the calculation of inelastic energy losses of electrons in fluid xenon. However, we are not certain if these discrete states should be included in the representation of the inelastic energy losses in liquid xenon, or if they dissociate into a quasi-free electron in the conduction band and a quasi-free positive hole in the valence band. The presence of the line at 10.32 eV in the reflection spectrum of liquid xenon [60, 63] seems to indicate that these states have alternative decay channels to dissociation due to luminescence. This means that they also contribute to inelastic energy losses of excess electrons. We are not certain which percentage of these discrete states dissociates into a quasi-free electron and a quasi-free positive hole. This case for representing the inelastic energy losses in liquid xenon is based on the assumption that these discrete states always decay through luminescence, or some other non-dissociative process. Thus, the corresponding excitations fully contribute to the inelastic energy losses of excess electrons.

The atomic $5d[3/2]_1$ state corresponds to the 11th excitation of Hayashi's cross section set, while the $7s[3/2]_1$ state is included in the 12th Hayashi's excitation [54]. The $5d'[3/2]_1$ atomic excitation, which causes a dip in the photoconductivity at 11.6 eV, is not included in Hayashi's cross section set. However, the 14th Hayashi's excitation, which corresponds to $9s[3/2]_2$ state, has a threshold of 11.58 eV, and it gives the effective energy loss for all excitations in this energy range in the gas phase. All other effective excitations, from the Hayashi's set, include contributions from the optically forbidden states. Therefore, we should include these excitations in our model, since the absence of the optically forbidden states in the reflection spectrum does not mean that these states do not contribute to the energy losses of excess electrons. Thus, our fourth case for representing the inelastic
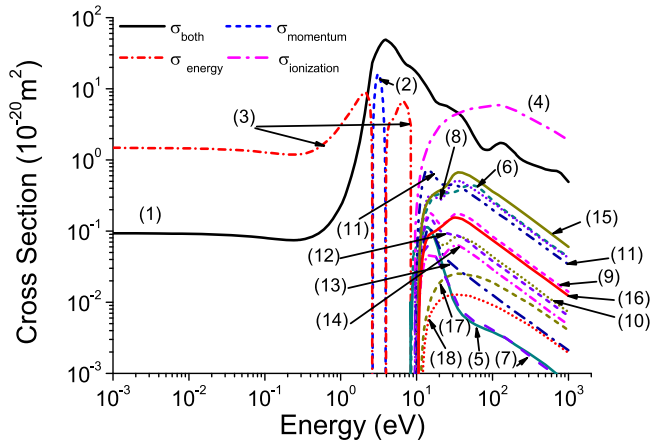
Figure 1. Cross sections for electron scattering in liquid xenon: (1) σ_{both}, (2) $\sigma_{momentum}$, (3) σ_{energy}, (4) ionization (the interband transition), effective electronic excitations: (5) $6s[3/2]_2$, (6) $6s[3/2]_1$, (7) $6s'[1/2]_0$, (8) $6s'[1/2]_1$ and $6p[1/2]_1$, (9) $6p[5/2]_2$ and $6p[5/2]_3$, (10) $6p[3/2]_1$ and $6p[3/2]_2$, (11) $5d[1/2]_0$, $5d[1/2]_1$, $6p[1/2]_0$, $5d[7/2]_4$ and $5d[3/2]_2$, (12) $5d[7/2]_3$, (13) $5d[5/2]_2$, (14) $5d[5/2]_3$, (15) $5d[3/2]_1$, (16) $7s[3/2]_2$, $7s[3/2]_1$, $7p[1/2]_1$, $7p[5/2]_2$, $6p'[3/2]_1$, $7p[5/2]_3$, $6d[1/2]_0$, $6d[1/2]_1$, $7p[3/2]_2$, $6d[3/2]_2$, $7p[3/2]_1$, $7p[1/2]_0$, $6d[7/2]_4$, $6d[7/2]_3$, $6p'[3/2]_2$, $6d[5/2]_2$, $6p[1/2]_1$, $6d[5/2]_3$, $6p'[1/2]_0$ and $6d[3/2]_1$, (17) $8s[3/2]_2$ and (18) $9s[3/2]_2$.

energy losses in liquid xenon includes all excitations from Hayashi's cross section set. This case will be referred to as case 4. The cross sections for electron scattering in liquid xenon included in all four cases considered in this work are shown in figure 1.

3. Methods of calculation

3.1. Monte Carlo method

In this work we use the Monte Carlo method to simulate a swarm of electrons in an infinite space, which is filled with a homogeneous background liquid, under the action of a static and uniform electric field. For this purpose, we have modified our existing Monte Carlo code, which has been developed for the study of electron transport in the gas phase [76–78]. Since the dispersion relation for electrons in liquid xenon can be taken to be parabolic and isotropic [40], the influence of the liquid on the electron motion is restricted to scattering events. Thus, the appropriate modification of the scattering dynamics is sufficient to make our Monte Carlo code applicable to the study of electron transport in liquid xenon. This modification has been done by including three effective scattering processes, which represent the coherent scattering of low energy electrons [57]. These scattering processes are described in section 2.1. Our study of the electron transport is performed under the assumption that the density of charged particles is very low (the swarm limit). Thus, we neglect the electron–electron interactions, the space charge effects and collisions with the results of previous collisions (holes and excited states). Therefore, the dynamics of each electron can be followed independently.

The dynamics of an individual electron is determined by the action of the electric field and by collisions between the electron and the atoms of the background liquid. The integral equation for the collisional probability is solved numerically by generating the random numbers from the uniform distribution on the interval (0,1) [76–78].

The type of the next collision is determined by using an additional random number, while taking into account the relative probabilities of all scattering processes for the corresponding value of the electron energy [76–78]. The change of direction of the electron motion after a collision is represented by a pair of angles, i.e. the scattering angle and the azimuthal angle. Isotropic scattering is assumed for all scattering processes, except for the effective scattering process which corresponds to the σ_{energy} cross section. In this process the direction of the electron motion is unchanged by the collision.

After the collision which is represented by the σ_{both} cross section the electron energy is reduced by the factor $\frac{2m\epsilon}{M}(1 - \cos\chi)$, where m is the electron mass, M is the mass of a background atom, ϵ is the initial energy of the electron and χ is the scattering angle. The same amount of energy is lost by a low energy electron in the effective scattering process, which is represented by σ_{energy} cross section. When an inelastic collision, or interband transition takes place, the energy of the incident electron is reduced by the energy loss (i.e. the threshold energy) of the corresponding process. After the interband transition, the remaining energy is redistributed between the primary electron and the secondary electron. The fraction of the postcollisional energy, which is obtained by each of these two electrons, is determined by using an additional random number.

In our Monte Carlo code, monomials of coordinates and velocity components of each individual electron are sampled and averaged, over the entire electron ensemble, at discrete sampling times [76–78]. These expressions are used to calculate both bulk and flux transport coefficients of the swarm, with explicit formulas given elsewhere [76–78].

As a large number of electrons must be followed, in order to reduce the statistical fluctuations of the output data, our Monte Carlo simulations are very time consuming. The computational time is particularly large for lower values of reduced electric field, where few inelastic collisions take place. Under these conditions due to a small rate of energy transfer in elastic collisions, the relaxation of energy is inefficient. In order to optimize the computational time and speed of our simulations in the limit of low reduced electric fields, the simulations are performed with a lower number of electrons until the swarm reaches the steady state. After relaxation the swarm is multiplied several times, by cloning each electron, until the desired number of electrons is obtained. When the multiplication is finished all transport properties are calculated from average monomials of both velocities and coordinates. For a more detailed description of our Monte Carlo code, we refer readers to our reviews [76–78].
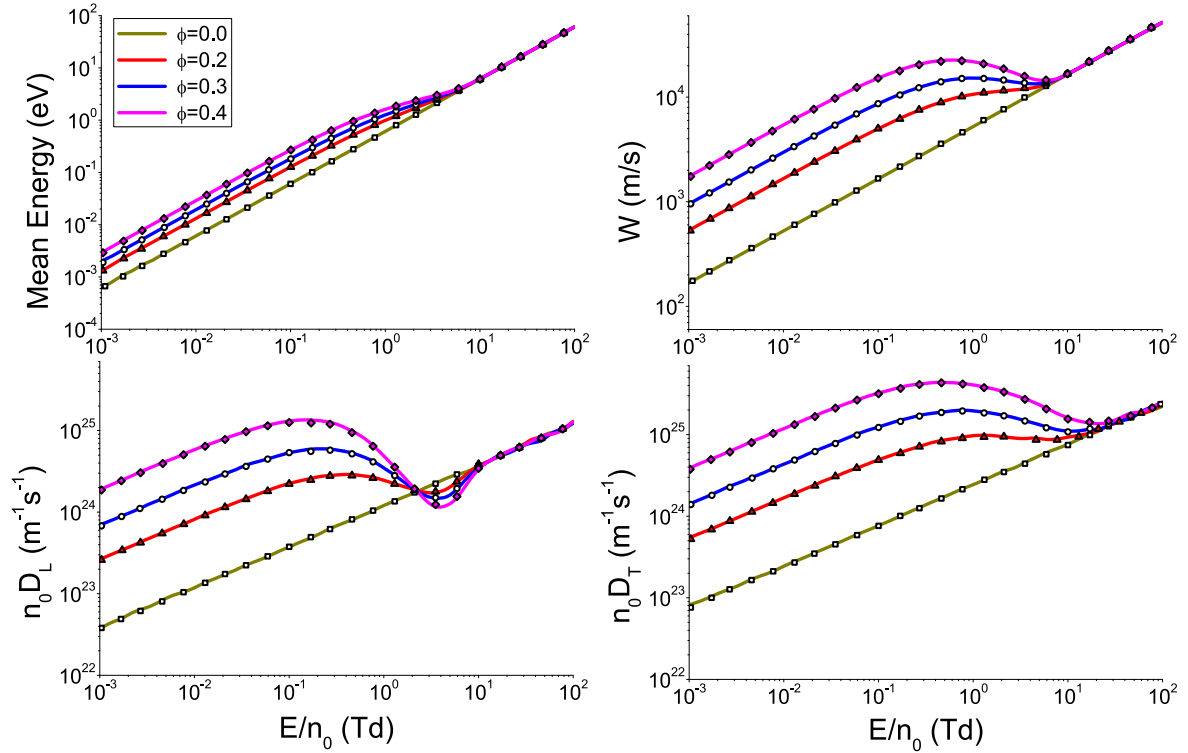
Figure 2. Comparison of our results for mean energy, drift velocity W, longitudinal diffusion coefficient $n_0 D_L$ and transverse diffusion coefficient $n_0 D_T$ of an electron swarm in the Percus–Yevick model liquid, with those of Tattersall *et al* [57]. Transport properties are presented as a function of the reduced electric field E/n_0 and the Percus–Yevick packing ratio ϕ. The present calculations are represented by lines, while the results of Tattersall *et al* [57] are represented by symbols.

3.2. Benchmark calculations

We present our benchmark calculations for the Percus Yevick model liquid, in order to test the implementation of the coherent scattering effects in our Monte Carlo code. The radial pair correlation function, which corresponds to this model, is obtained by applying the Percus Yevick approximation as a closure to the Ornstein–Zernike equation and by representing the interaction between the background molecules by the hard sphere potential [57, 79]. The corresponding static structure factor is obtained as a Fourier transform of this pair correlation function [57]. The modified Verlet and Weis structure factor for the Percus Yevick liquid [80] is used in this work, as in the study of Tattersall *et al* [57]. This structure factor is given by

$$
S(\Delta k) = \left(1 + \frac{24\eta}{\Delta k^2}\left[\frac{2}{\Delta k^2}\left(\frac{12\zeta}{\Delta k^2} - \beta\right)\right.\right.
$$
$$
+ \frac{\sin(\Delta k)}{\Delta k}\left(\psi + 2\beta + 4\zeta - \frac{24\zeta}{\Delta k^2}\right)
$$
$$
\left.\left.+ \cos(\Delta k)\left(\frac{2}{\Delta k^2}\left(\beta + 6\zeta - \frac{12}{\Delta k^2}\right) - \psi - \beta - \zeta\right)\right]\right)^{-1},
$$
$$(5)$$

where $\eta = \phi - \frac{\phi^2}{16}$, $\psi = \frac{(1+2\eta)^2}{(1-\eta)^4}$, $\beta = \frac{-6\eta\left(1+\frac{\eta}{2}\right)^2}{(1-\eta)^4}$, and $\zeta = \frac{\eta\psi}{2}$ [57]. The packing ratio ϕ determines the percentage of space which is occupied by the hard spheres. This ratio can be written as $\phi = \frac{4}{3}\pi r^3 n_0$, where r and n_0 are the hard sphere radius and the neutral number density respectively [57].

In figure 2 we show our benchmark results for mean energy, drift velocity and components of the diffusion tensor for electrons in the Percus Yevick liquid, for several values of the packing ratio ϕ. For comparison, the benchmark results of Tattersall *et al* [57] are included in the same figure. Our results are represented by lines, while the results of Tattersall and co-workers are represented by symbols. From a comparison between our results and those predicted by Tattersall *et al* [57], it is evident that the results are consistent for all E/n_0 and ϕ and for all transport coefficients. This suggests that the representation of the coherent scattering effects has been included properly in our Monte Carlo code [81].

In figure 2 we see that all transport properties are distinctively dependent on ϕ for the lower values of E/n_0. Due to coherent scattering effects, all transport properties increase with the increase of ϕ. At the higher values of E/n_0, however, the strong dependence of transport properties on ϕ is firstly reduced and then entirely removed as the influence of the coherent scattering is negligible for the high energy electrons. On the other hand, the behavior of the longitudinal diffusion coefficient D_L is more complex. We see that D_L increases with the increase of ϕ at low electric fields, but this dependence is inverted for E/n_0 between approximately 2 and 10 Td. The mean energy monotonically increases with the increase of E/n_0 for all values of ϕ. The drift velocity exhibits structure induced NDC, i.e. for E/n_0 approximately between

0.5 and 6 Td and for $\phi \geqslant 0.3$, values of drift velocity decrease as the driving field is increased. The quantitative criterion for the occurrence of the structure induced NDC has been discussed by White and Robson [82]. The decrease of the drift velocity with increasing field can be attributed to the reduction of the coherent scattering effects, which in turn enhance the directional motion of low energy electrons. The reduction of both D_L and D_T with an increasing E/n_0 is also clearly evident. In the limit of the highest E/n_0 considered, all profiles approach to that for $\phi = 0$. It is interesting to note that the values of E/n_0 for this transition decrease with increasing ϕ.

3.3. Fluid model of negative streamers

Our simulations of negative streamers in liquid xenon are performed by using a 1.5 dimensional fluid model [83, 84]. In this model, we assume that the space charge is contained inside a cylinder with radius R_0 and that the charge density varies along the axial direction only. The electron dynamics is described by the continuity equation for the electron number density

$$\frac{\partial n_e(x, t)}{\partial t} = \frac{\partial}{\partial x}\left(D_L \frac{\partial n_e(x, t)}{\partial x} + W n_e(x, t)\mathrm{sgn}(E)\right) + (\nu_i - \beta n_p(x, t))n_e(x, t), \quad (6)$$

where $n_e(x, t)$ and $n_p(x, t)$ are the number densities of electrons and positive holes, respectively, which are functions of the coordinate x and time t. In this equation D_L and W are the longitudinal diffusion and the drift velocity respectively, $\mathrm{sgn}(E)$ is the sign function of the electric field E which is oriented along the x-axis, while ν_i and β are the ionization rate and the recombination coefficient, respectively.

Since the hole mobility in liquid xenon is much smaller than the mobility of electrons [85, 86], the positive holes are assumed to be stationary, on the time scales relevant for this study. Thus, the time evolution of the number density of positive holes is described by the number balance equation

$$\frac{\partial n_p(x, t)}{\partial t} = (\nu_i - \beta n_p(x, t))n_e(x, t). \quad (7)$$

The total electric field in the system is represented as the sum of the uniform external field and the electric field due to space charge effects [83, 84]

$$E(x, t) = E_0 + \frac{e}{2\varepsilon_0\varepsilon_r}\int_0^l\left(\mathrm{sgn}(x - x')\right.$$
$$\left. - \frac{x - x'}{\sqrt{(x - x')^2 + R_0^2}}\right)(n_p(x', t) - n_e(x', t))\mathrm{d}x', \quad (8)$$

where E_0 is the external field, e is the elementary charge, ε_0 and ε_r are the vacuum permittivity and the relative permittivity, respectively, and l is the length of the system. The recombination coefficient is given by the scaled Debye formula [50–52]

$$\beta = \xi\beta_\mathrm{D} = \xi\frac{4\pi e\mu_e}{\varepsilon_0\varepsilon_r}, \quad (9)$$

where β_D is the Debye recombination coefficient, μ_e is the electron mobility, while ξ is the scaling factor which is taken to be 0.1 [10, 50, 51].

The above fluid equations are closed assuming the local field approximation—all transport properties of electrons at a given value of the coordinate x and time t are determined by the local instantaneous electric field, $E(x, t)$ and are evaluated from data computed in Monte Carlo simulations. In the numerical implementation of our fluid model, the spatial discretization is performed by using the second order central finite difference, while the fourth order Runge–Kutta method is used for the integration in time. In fluid simulations we follow the transition of an electron avalanche into a negative streamer and its subsequent propagation in liquid medium.

4. Results and discussion

4.1. Transport coefficients for electrons in liquid xenon

In our study of the transport properties of electrons in liquid xenon we cover a range of reduced electric fields between 1×10^{-3} and 2×10^3 Td. The number density of xenon atoms is 1.4×10^{28} m^{-3}, while the temperature of the background liquid is 163 K. For E/n_0 higher than 10 Td, we follow 10^6 electrons during the entire simulation. However, at lower fields our simulations begin with 10^4 electrons and after the relaxation to the steady state the electron swarm is gradually scaled up to 10^6 electrons by cloning each electron at fixed time intervals. The initial velocities of electrons are randomly selected from a Maxwell–Boltzmann velocity distribution which corresponds to a mean energy of 1 eV. All electrons start their trajectories from the same point in space. This point is chosen as the origin of our coordinate system. The cross sections for electron scattering employed in this work are shown in figure 1. The mean energy, drift velocity and diffusion coefficients are shown for cases 1 and 4, as differences between individual cases are too small to be clearly distinguished on logarithmic scale.

4.1.1. Mean swarm energy.
The comparison of the mean energies of electron swarms in liquid and gaseous xenon is shown in figure 3. For the lower values of electric fields up to approximately 0.6 Td, the mean energy is higher in liquid xenon than in gaseous xenon due to a significant reduction of the cross section for elastic scattering of the lower energy electrons in the liquid phase. Such behavior is different at higher fields as the mean energy of electrons approaches 1 eV, owing to the fact that the electron scattering in atomic liquids is similar to the scattering in dilute gases for the electron energies higher than 1 eV [19, 34]. The mean energy is lower in the liquid phase than in the gas phase for E/n_0 between approximately 0.6 and 350 Td. At the lower edge of this field region, the difference between the mean
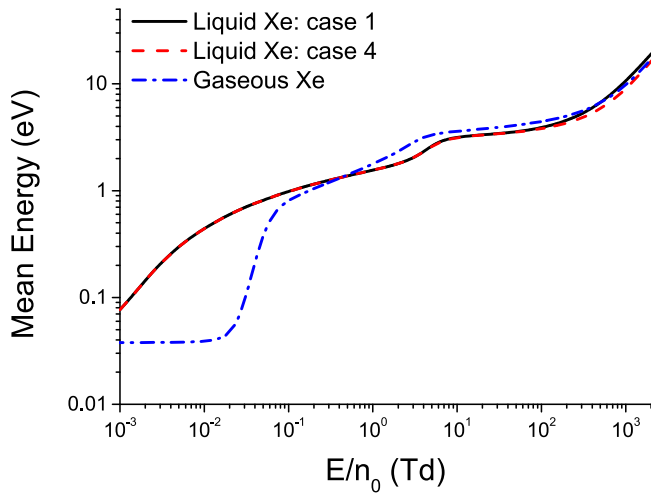
Figure 3. Comparison of the mean energies of electrons in gaseous and liquid xenon. The values of mean energy in liquid xenon, determined by employing two different methods for representing the inelastic energy losses, are shown. In the first case all excitations are neglected, while in the fourth case all excitations from Hayashi's cross section set for electron scattering in gaseous xenon [54, 68] are included.
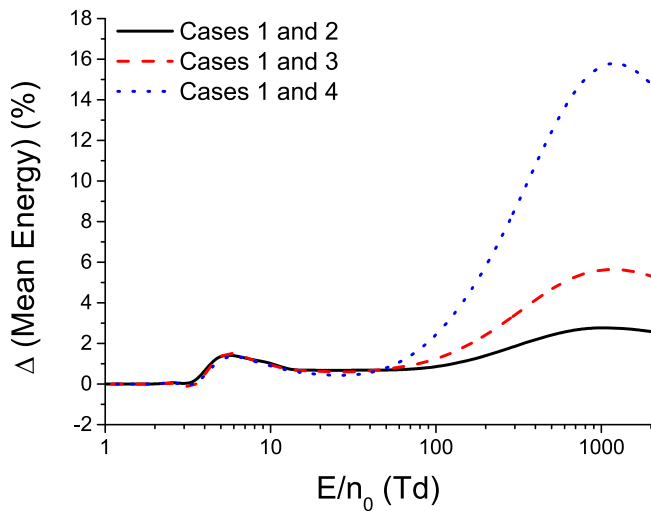

Figure 5. Comparison of the measured drift velocities in liquid xenon (Miller *et al* [88] and Huang and Freeman [89]) with the theoretical calculations. The theoretically determined drift velocities in liquid xenon include those of Boyle *et al* [34] as well as the bulk drift velocities calculated in this study by employing two different methods for representing the inelastic energy losses. The bulk drift velocity of electrons in gaseous xenon is also shown in this figure for comparison.

Figure 4. Percentage difference between the values of mean energy, for electrons in liquid xenon, which are determined by using different representations of the inelastic energy losses. All excitations are neglected in the first case. In the second and the third cases only the first two ($6s[3/2]_2$ and $6s[3/2]_1$) and the first four ($6s[3/2]_2$, $6s[3/2]_1$, $6s'[1/2]_0$ and an effective excitation which represents both $6s'[1/2]_1$ and $6p[1/2]_1$) excitations from the cross section set of Hayashi [54, 68] are included. All excitations from the cross section set of Hayashi are included in the fourth case.

energies in gaseous and liquid xenon can be attributed to the greater amount of energy losses in elastic collisions in the liquid phase in the energy region between approximately 0.4 and 10 eV [34]. This is represented by the combined effect of the scattering processes which correspond to σ_{both} and σ_{energy} cross sections. For E/n_0 between approximately 3 and 350 Td this energy difference is caused by the intensive ionization cooling in the liquid phase. Ionization

cooling of an electron swarm in gases has been discussed by Robson and Ness [87]. At higher fields the mean energy in the first case for representing excitations in liquid xenon is slightly higher, while the mean energy in the fourth case is slightly lower, than the mean energy in the gas phase.

In figure 4 we show the percentage difference between the calculated mean energy, assuming the first and the remaining three cases. This difference is negligible for E/n_0 less than 2 Td as electrons undergo elastic collisions only. For E/n_0 higher than 2 Td the mean energy reaches the highest value in the first case due to the absence of inelastic energy losses. The percentage differences between the values of mean energy in the first case and the remaining three cases reach two local maximums at about 5 and 1000 Td, and a local minimum around 27 Td. The first local maximum occurs due to the absence of inelastic energy losses, lower than the threshold energy for ionization, in the first case. The local minimum appears in the field region in which the energy losses due to ionization become comparable to the inelastic energy losses. For E/n_0 higher than 50 Td, the mean energy decreases with the increase of the number of excitations which are included in the model. This is a consequence of a significant competition between ionization and excitations with thresholds higher than 9.22 eV in this field region. The percentage difference between the mean energy in the first case and the remaining cases never exceeds 3%, 6% and 16% for the second, third and fourth cases respectively. Even though the percentage difference between the values of mean energy in various cases decreases for E/n_0 greater than 1000 Td, the absolute difference continues to rise monotonically in the entire field region covered in this study. For the values of E/n_0 lower than 50 Td, these differences are
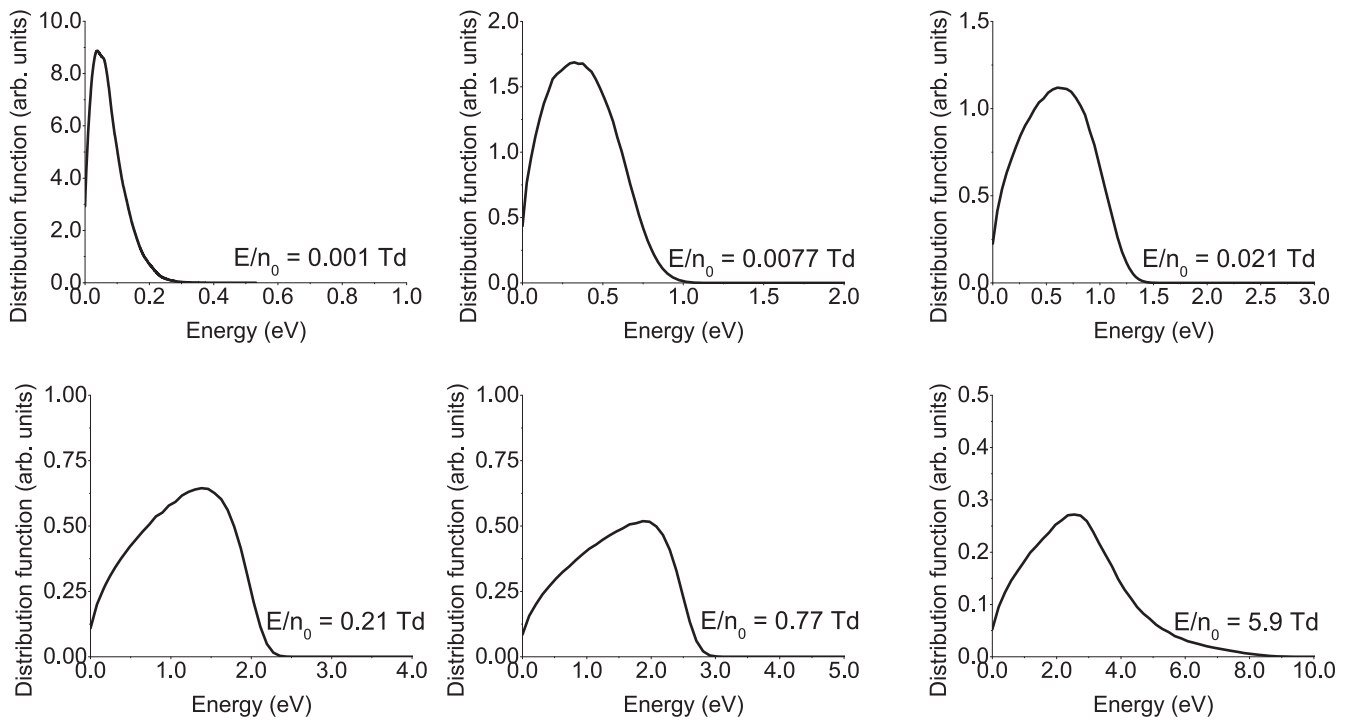
Figure 6. Energy distribution function of the electrons for various E/n_0 as indicated on the graph. Calculations are performed assuming the case 2 where excitations $6s[3/2]_2$ and $6s[3/2]_1$ from the set of cross sections developed by Hayashi are included.

very small and are close to the statistical uncertainty of the Monte Carlo simulations.

4.1.2. Drift velocity and NDC. In figure 5 we show bulk drift velocities assuming the first and the fourth cases for representing the inelastic energy losses as a function of E/n_0. For comparison, the theoretical [34] and experimental [88, 89] drift velocities in liquid xenon determined by previous authors are displayed in the same figure, along with the bulk velocity in gaseous xenon. For the values of E/n_0 lower than 1 Td, the drift velocity in the liquid phase exceeds the drift velocity in the gas phase. This is a consequence of the significant reduction of the rate for momentum transfer of the lower energy electrons in liquid xenon due to the modifications of the scattering potential and the coherent scattering effects. The lowering of the rate for momentum transfer enables the electric field to accelerate electrons more efficiently in liquid xenon than in the gas phase, which leads to a significant enhancement of the drift velocity compared to the gaseous xenon. However, this effect is reduced at higher fields as the scattering of a high energy electron on a xenon atom is weakly perturbed by the surrounding liquid. Thus, for the values of E/n_0 between approximately 0.02 and 2 Td the drift velocity in liquid xenon decreases with increasing field, until it reaches the values that are close to the drift velocity in gaseous xenon. The reduction of the drift velocity with increasing E/n_0 is a phenomenon that is well known as NDC [90–92]. While this phenomenon is caused by inelastic and non-conservative collisions in various gases [90, 92], the NDC observed in liquid argon and liquid xenon is entirely structure induced phenomenon [19, 34, 82]. The quantitative

criterion for the occurrence of the structure induced NDC has been discussed by White and Robson [82]. At the end of the field region, which corresponds to NDC, the drift velocity in gaseous xenon slightly exceeds the drift velocity in liquid xenon. For the values of E/n_0 higher than 10 Td the bulk drift velocity in the first case exceeds the bulk drift velocities in all other cases as well as the bulk drift velocity in the gas phase due to the strongest explicit effects of ionization in this case.

In order to understand the occurrence of NDC in liquid xenon at low electric fields, in figure 6 we show the energy distribution functions for a few values of E/n_0. Results are presented for the case two only, as the rate coefficients for those inelastic processes excluded in this case are negligible over the range of reduced electric fields considered. At low electric fields, up to approximately 0.008 Td, the majority of electrons have energies below approximately 0.7 eV. The cross section for momentum transfer is very small over the range of energies less than 0.7 eV and hence the drift velocity in liquid xenon is much greater than in the gas phase. However, for E/n_0 greater than approximately 0.02 Td (at this particular value of E/n_0 NDC begins to develop) a large fraction of electrons have energies between approximately 0.7 and 2 eV. There is a rapid rise in both σ_{both} and σ_{energy} with increasing energy in this region. As a consequence, these two cross sections quickly approach the cross section for elastic collisions in the gas phase. For E/n_0 between 0.2 and 1 Td the majority of the high energy electrons have energies between 1.5 and 3 eV where the cross sections σ_{both} and $\sigma_{momentum}$ increase rapidly and approach their maximal values. The rapid rise of both σ_{both} and $\sigma_{momentum}$ leads to a decrease of the drift velocity with increasing E/n_0. For E/n_0 higher than approximately 5 Td a large fraction of electrons have energies
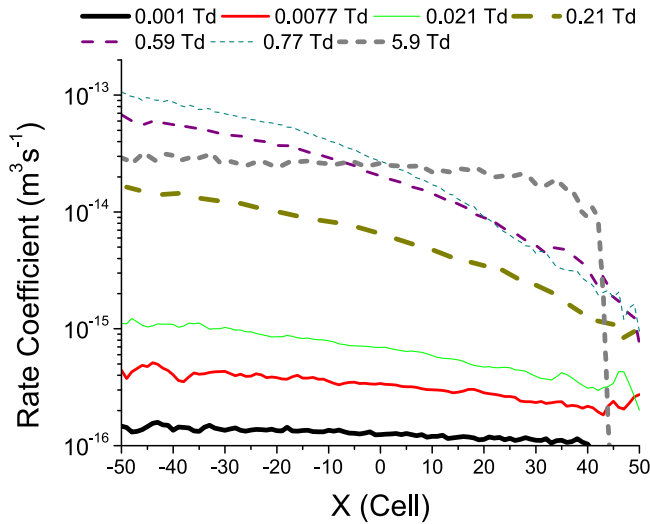
Figure 7. Spatially-resolved rate coefficient for the σ_{both}. Calculations are performed assuming the case 2 where excitations $6s[3/2]_2$ and $6s[3/2]_1$ from the set of cross sections developed by Hayashi are included.

Figure 8. Percentege difference between the values of drift velocities, for electrons in liquid xenon, which are determined by using different methods for representing the inelastic energy losses. These methods are described in the caption of figure 4. Flux and bulk results are represented by solid lines and dashed lines, respectively.

higher than approximately 4 eV, and at these energies the cross section for elastic scattering rapidly drops off with an increase of electron energy. In this range of fields, the drift velocity monotonically increases with E/n_0.

We may also observe that over the range of E/n_0, where the structure induced NDC occurs, the high-energy tail of the distribution function quickly drops off with increasing energy. This is caused due to rapid increase of energy transfer associated with the σ_{both} and σ_{energy}. For E/n_0 lower than approximately 0.008 Td and higher than approximately 4 Td, the high-energy tail of the distribution function drops off more slowly.

In figure 7 we show the spatially-resolved rate coefficient for the σ_{both}. In order to sample spatially-resolved rate coefficients we have divided the real space into cells. The space is divided uniformly into 100 cells in such a way that cells indexed by $(-50, +50)$ correspond to the real coordinates $(x_{cm} \pm 3\sigma)$, where x_{cm} is the coordinate of the center of mass of the swarm, and the σ is the standard deviation of the x-coordinate of the electrons [93]. Comparing the leading and trailing edges of the swarm, this property is higher at the leading edge where the average energy of the electrons is always greater than at the trailing edge. The slope of the spatially-resolved rate coefficient is the largest over the range of E/n_0 where NDC occurs. Moreover, we observe that the maximal values of this property at the leading edge of the swarm are higher for 0.59 and 0.77 Td than for a higher value of 5.9 Td. A similar behavior is observed for the spatially-resolved rate coefficient for the $\sigma_{momentum}$.

The drift velocity calculated in our study is in an excellent agreement with the theoretical results of Boyle *et al* [34]. Our values of the drift velocity are close to those predicted in the experiments of Miller *et al* and Huang and Freeman [88, 89]. However, while most theoretical calculations of the drift velocity predict a structure induced NDC, this effect has not been observed in the experiments. In the
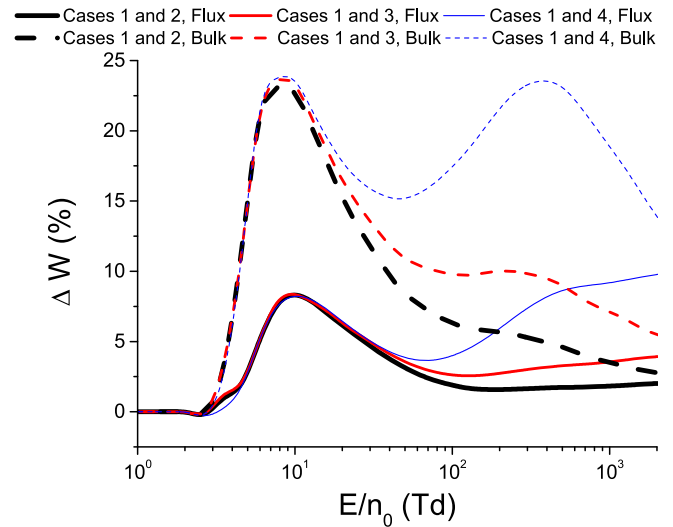
field region which corresponds to the onset of the structure induced NDC of the theoretically determined drift velocity, the experimental drift velocity saturates with increasing field. At higher fields, no experimental results are available.

This discrepancy between theoretical and experimental results has been attributed by Sakai *et al* [32] to the presence of additional channels of energy loss in liquids, which are not included in the existing theoretical models. These energy losses correspond to the changes in the translational states of pairs and triplets of xenon atoms upon the electron impact, and they occur for energies much lower than the first threshold for excitations [20, 32]. Sakai and co-workers have empirically derived the sets of cross sections for electron scattering in liquid argon, krypton and xenon [32] which include effective cross sections for representing these additional energy losses. However, an alternative explanation for this discrepancy between theory and experiment could be the presence of molecular impurities in the liquid rare gases used in the experiments. Indeed, it has been shown by Sakai *et al* [32] that even a small amount of molecular impurities in liquefied rare gases leads to a significant enhancement of the electron drift velocity. It might also be the case that the structure induced NDC would be observed in the profiles of the experimentally determined drift velocity at higher electric fields. Further experimental and theoretical investigations are required for the resolving this discrepancy. Thus, the measurement of the drift velocity of electrons in liquid xenon at higher electric fields is of a great importance. In any case, we do not include the effective cross section developed by Sakai *et al* [32] in our model, as it is not adjusted to our cross section for elastic scattering.

In figure 8 we show the percentage difference between the calculated drift velocity assuming the first and the remaining three cases. The flux drift velocity increases with the decrease of the number of excitations, which are
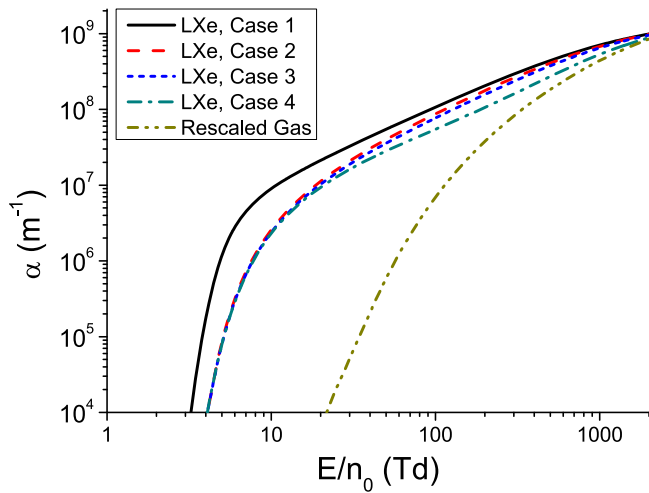
Figure 9. Variation of the first Townsend coefficient with E/n_0 for electrons in liquid xenon. Calculations are performed by assuming all four different methods for representing the inelastic energy losses. These methods are described in the caption of figure 4. The first Townsend coefficient for gaseous xenon, which is scaled up to liquid density is also shown, for comparison.

Figure 10. Comparison between the theoretical calculations of the first Townsend coefficient α determined in this study and the results of previous authors. These results include the measurements of Derenzo *et al* [56] and calculations of Atrazhev *et al* [39], Jones and Kunhardt [40] and Nakamura *et al* [53].

considered in the model. This is caused by the lowering of the chaotic component of the electron velocity due to the increase of the ionization cooling with the reduction of the inelastic energy losses [87]. In the case of the bulk drift velocity, this increase is even more pronounced due to the explicit effects of ionization. The percentage difference between drift velocities determined in the first case and the remaining three cases has a local maximum at about 8 Td, as the relative difference between rates for ionization has the highest values at low electric fields. This local maximum has a value of about 8% and 24% for flux and bulk drift velocity, respectively. For E/n_0 higher than 100 Td, the percentage difference between flux drift velocities in the first case and the last two cases rises due to increasing rates for inelastic collisions with thresholds higher than 9.22 eV in this field region. The percentage difference between the corresponding bulk drift velocities reaches another local maximum at about 200 Td and 400 Td for the third and the fourth cases respectively. Although the percentage difference between bulk drift velocities in different cases decreases after the last local maximum, the absolute difference monotonically increases in the entire field region below 2000 Td.

4.1.3. First Townsend coefficient. The first Townsend coefficient expresses the number of ion pairs generated by an electron per unit length. It is equal to the ionization collision frequency divided by the electron drift velocity. Our calculations of the first Townsend coefficient α determined by using different representations of the inelastic energy losses in liquid xenon are shown in figure 9. The first Townsend coefficient in gaseous xenon is scaled up to the liquid density and displayed in the same figure for comparison. It can be seen that α monotonically increases with increasing field in all four cases for representing the inelastic energy losses. We also observe that α is reduced with increasing number of
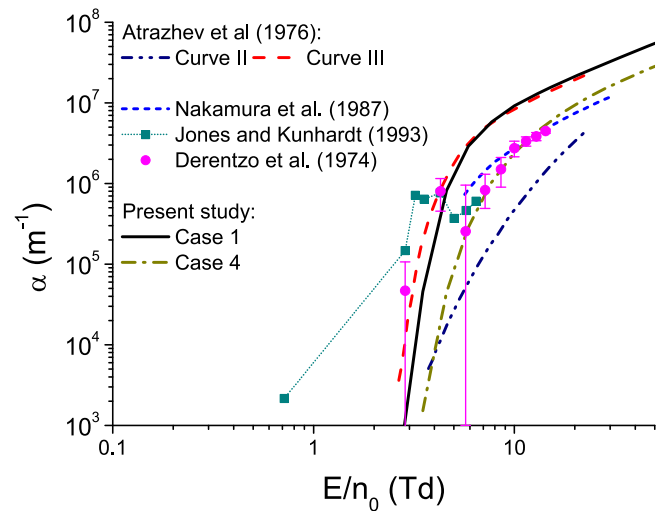
included excitations. In the first case, where all excitations are neglected, the coefficient α overestimates those calculated in the remaining three cases over the range of E/n_0 considered. While the absolute difference between the first Townsend coefficient in the first case and the remaining cases increases over the entire E/n_0 range covered in this study, the relative difference has the highest values at E/n_0 lower than approximately 20 Td. For E/n_0 greater than 20 Td the ionization rate coefficient in the fourth case, where all excitations are included, becomes significantly lower than the corresponding rate coefficients in the other three cases. This is a consequence of the increasing inelastic energy losses which have thresholds higher than 9.22 eV in this case.

The first Townsend coefficient in liquid xenon is much higher than the rescaled coefficient in gaseous xenon for E/n_0 lower than 100 Td. In the limit of the highest E/n_0 considered in the present work, however, we observe that the deviations between the ionization coefficients in liquid and rescaled gas are significantly reduced. One of the main reasons for the significant difference between the rate coefficients for ionization in the scaled gaseous xenon and liquid xenon is the reduction of the threshold for ionization in the liquid phase. An electron in gaseous xenon can undergo ionization only at energies higher than 12.13 eV. Moreover, it can lose a significant amount of energy in a wide range of inelastic scattering processes at energies lower than the threshold energy for ionization. However, in liquid xenon any electron with the energy higher than 9.22 eV can excite an electron from the valence band to the conduction band. Furthermore, there is a far lower number of inelastic scattering processes with thresholds which are lower than the threshold for ionization in the liquid phase compared to the gas phase.

In figure 10 we show the first Townsend coefficient measured by Derenzo *et al* [56] along with the theoretical results obtained by previous authors [39, 40, 53]. The values

of the first Townsend coefficient determined in this study by assuming the first and the fourth cases for representing the inelastic collisions are displayed in the same figure for comparison. The experimental results of Derenzo *et al* [56] are significantly higher than the values of α for electrons in gaseous xenon which are scaled to liquid density. An unusual feature of the first Townsend coefficient measured by Derenzo and co-workers is a non-monotonous behavior with the increase of the reduced electric field. However, this non-monotonicity is not outside the range of experimental uncertainty.

The two sets of results determined by Atrazhev *et al* [39] are calculated by assuming two different methods for representing the inelastic energy losses. The values of α represented by curve II are determined under the assumption that the percentage of inelastic energy losses in the liquid phase are just the same as in the gas phase [39]. This curve is significantly below all other curves presented in this figure. The underestimation of α in curve II demonstrates the significant reduction of the inelastic energy losses in liquid xenon compared to gaseous xenon as discussed by Atrazhev *et al* [39]. The values of α represented by curve III are determined by completely neglecting the inelastic energy losses in liquid xenon. This curve is in the best agreement with the first two experimental points of Derenzo *et al* [56] and with our case 1. The first Townsend coefficient determined by Jones and Kunhardt [40] is the only present theoretical result which predicts the non-monotonic behavior of α and it is in a good agreement with the first four experimental points of Derenzo *et al* [56]. However the values of α at higher fields are not shown in their work. The results of Nakamura *et al* [53] agree very well with the last segment of experimental points of Derenzo *et al* [56], while the values at lower fields are not displayed in their paper.

While our case 1 for representing the inelastic energy losses is in the best agreement with the first two experimental points of Derenzo *et al* [56], all other experimental points are in an excellent agreement with our remaining three cases. No experimental data are present in the field range in which there is a significant difference between our last three cases for representing the inelastic collisions in liquid xenon. However, the last two experimental points of Derenzo *et al* [56] are in a slightly better agreement with our fourth case than with the remaining cases.

A possible explanation for the high values of the first two experimental points determined by Derenzo *et al* [56] is the presence of another mechanism for populating the conduction band in liquid xenon, which is more significant than electron impact ionization at low electric fields. One example of such a mechanism is the dissociation of high order Wannier excitons ($n > 1$) due to scattering on the walls of the system, or under the influence of some other perturbation. Another possible explanation is the reduction of the inelastic energy losses at energies lower than 9.22 eV due to some other effects, which are not included in our model.
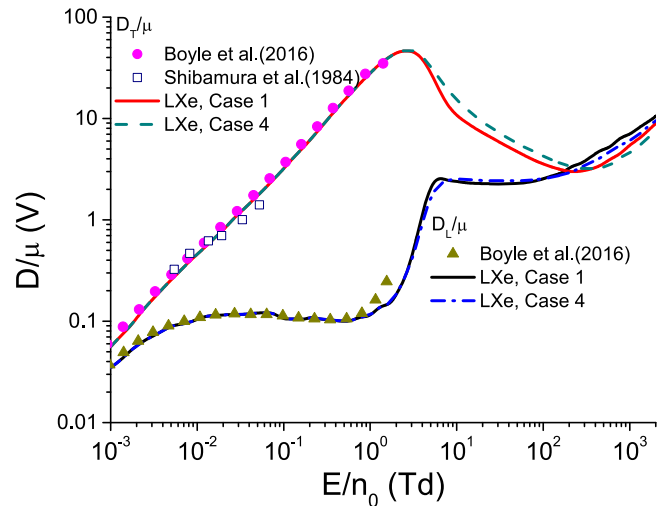

Figure 11. Comparison between the present calculations and those predicted by a multi term solution of the Boltzmann equation (Boyle *et al* [34]) and experimental measurements (Shibamura *et al* [94]) for the bulk values of D_L/μ and D_T/μ. Our results are evaluated by assuming the cases 1 and 4.

4.1.4. Longitudinal and transverse diffusion coefficients. In figure 11 we show the variation of D_L/μ and D_T/μ with E/n_0 assuming the first and the fourth cases for representing the inelastic collisions in liquid xenon. The calculated values of these quantities obtained by Boyle *et al* [34] are also displayed in the same figure for comparison, along with the characteristic energy measured by Shibamura *et al* [94]. Here D_L and D_T denote the longitudinal and the transverse components of the bulk diffusion tensor, while μ is the bulk mobility of electrons. The characteristic energy D_T/μ initially increases with increasing E/n_0, reaching a local peak around 2 Td, and then starts to decrease with E/n_0. For E/n_0 higher than approximately 300 Td, we see that D_T/μ again increases with E/n_0. The E/n_0 dependence of D_L/μ is more complicated. First, there is a region of slow rise of D_L/μ with increasing E/n_0 due to a reduction of the momentum transfer of the lower energy electrons in liquid xenon. Second, there is a region of slow decrease for E/n_0 between approximately 0.05 and 0.4 Td, and then for E/n_0 up to approximately 6 Td there is again a region of rapid rise. Between approximately 6 and 30 Td D_L/μ is reduced as the inelastic collisions start to exert their influence on the swarm. Finally, D_L/μ rises again as the electrons start to rapidly gain energy from the electric field. The complex behavior of D_L/μ in liquid xenon reflects the high sensitivity of this property with respect to the details of cross sections.

We also observe that D_L/μ agree very well with the results of Boyle *et al* [34] for E/n_0 lower than 0.7 Td. However, our results are lower than those of Boyle and co-workers at higher electric fields. The discrepancy can be attributed to the difference in the employed cross sections for the electron scattering, as Boyle and coworkers have neglected the inelastic collisions in their study. As the mean energy of electrons is around 1.8 eV at 1 Td, the most energetic electrons have enough energy to undergo inelastic collisions. The present calculations
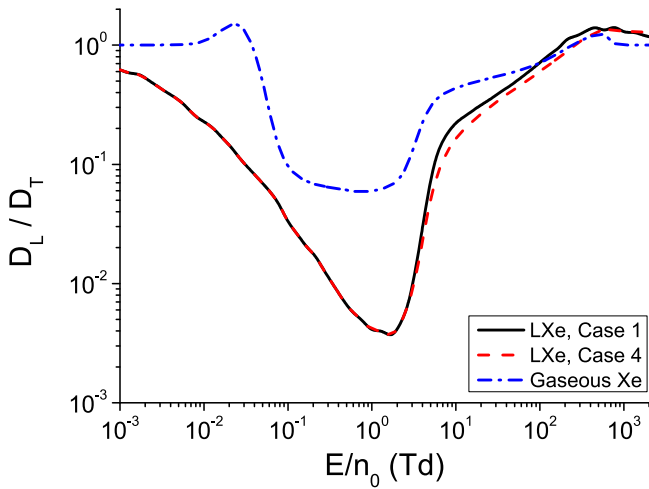
Figure 12. Comparison of the ratios between the bulk longitudinal diffusion and the bulk transversal diffusion in liquid xenon assuming cases 1 and 4 and the same ratio in gaseous xenon. These cases are described in the caption of figure 3.

of D_T/μ are in a good agreement with those predicted by Boyle *et al* [34] and Shibamura *et al* [94].

In figure 12 we show the ratio D_L/D_T for electrons in liquid xenon assuming the first and the fourth cases for representing the inelastic energy losses. The values of D_L/D_T for electrons in gaseous xenon are shown in the same figure for comparison. For electrons in liquid xenon this ratio is decreasing with increasing field up to approximately 1 Td, due to the rising rates for elastic scattering in this field region. However, this ratio is increasing at higher fields due to the reduction of the rate for elastic scattering of high energy electrons. The E/n_0 dependence of this ratio is different for electrons in gases at low electric fields. For the values of E/n_0 lower than 10^{-2} Td this ratio is constant in the gas phase as the mean energy of electrons is very close to the thermal values. There is a narrow range of the reduced electric field between approximately 10^{-2} and 2×10^{-2} Td in which this ratio is rising with increasing field, due to the influence of the Ramsauer–Townsend minimum. At higher fields the qualitative trend of behavior of D_L/D_T is the same for electrons in liquid and gaseous xenon though the minimum is more pronounced in the liquid phase.

4.2. Streamer calculations

In our fluid simulations, we follow the transition of an electron avalanche into a negative streamer as well as the subsequent propagation of this streamer. The initial condition for both electrons and positive holes is a Gaussian distribution which is given by

$$n_e(x, 0) = \frac{300}{0.05\pi R_0^2 \frac{l}{3}\sqrt{2\pi}} \exp\left(-\frac{(x - 0.95l)^2}{2\left(0.05\frac{l}{3}\right)^2}\right). \quad (10)$$

This Gaussian is positioned near the cathode. It should be noted that the initial number densities of electrons and positive holes are selected so that the space charge effects are

negligible. The values of l and R_0 are set to 5×10^{-5} m and 1×10^{-5} m respectively. The particular value of R_0 is chosen as an educated guess taking into account the initial distribution width and the spreading due to transverse diffusion. This value is in a good agreement with the values evaluated by the other authors [50, 51]. The length of the system l is determined by the requirement that the streamer velocity relaxes to a stationary value. The number of spatial cells used in our fluid simulations is 25000.

In figures 13 and 14 we show the formation and propagation of a negative streamer, assuming cases 1 and 4 for representing the inelastic energy losses, under the influence of the externally applied electric fields of 59 Td and 100 Td, respectively. For $E/n_0 = 59$ Td the difference between the ionization coefficients for liquid phase and rescaled gas is much higher than for $E/n_0 = 100$ Td. The simulations in the liquid phase are augmented by the simulation in which the transport data for electrons in the gas phase are for the gas phase scaled to the liquid density. The general features of the streamer profiles in the liquid xenon are the same as those of the streamers in gases [95, 96]. However, the space and time scales of the streamer formation are reduced by about three orders of magnitude due to a much greater number density of the background atoms in the liquid phase. The electron number density has a sharp peak in the streamer head where the electric field is significantly enhanced by the space charge effects. However, the number density is greatly reduced in the streamer channel where the external electric field is significantly screened. The further reduction of the number density of electrons in the streamer channel with increasing distance from the streamer head is clearly evident in the streamer profiles. This reduction can be attributed to the recombination of electrons and positive holes [50, 51]. A similar decrease of the electron number density in the streamer channel is observed for streamers in electronegative gases [50, 51].

We observe that the streamer formation as well as streamer propagation are greatly reduced with an increase of the number of excitations which are included in the model. The number density of electrons in both the streamer head and the streamer channel is also reduced. It can also be seen that the transition from an electron avalanche into a streamer is much slower in the case of the rescaled gas than in the first and the fourth cases of the liquid phase. Comparing figures 13 and 14, we see that this difference is much more pronounced at 59 Td than at 100 Td. To be specific, at 59 Td the distribution of electrons modeled in the case of the rescaled gas is still in the avalanche phase at the time instant when the streamer in the liquid phase, assuming the first case of representing inelastic energy losses, crosses the entire length l. On the other hand, at 100 Td the streamer modeled in the case of the rescaled gas is almost completely formed by the time when the streamer modeled in the first case reaches the boundary of the system. However, the streamer velocity and the number density of electrons calculated in the rescaled gas case are well below those in the liquid phase, assuming both cases 1 and 4, even at 100 Td. The observed streamer properties may be understood by considering the differences
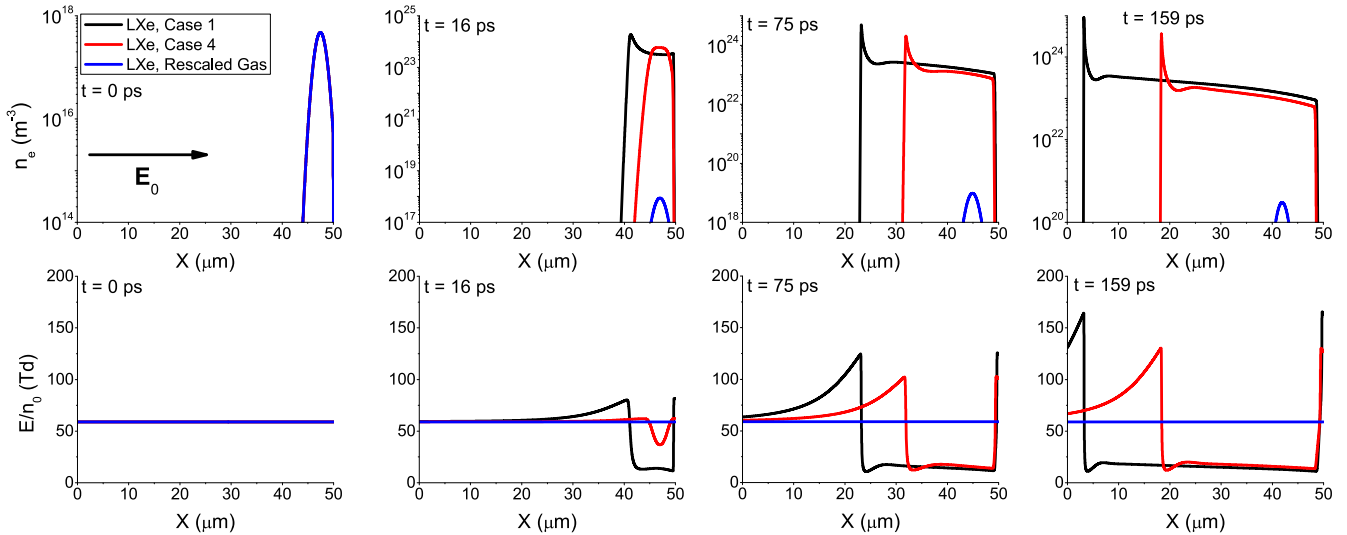
Figure 13. The formation and propagation of a negative streamer in liquid xenon for $E_0/n_0 = 59$ Td. The presented results are determined by assuming the first and the fourth cases for representing the inelastic energy losses. The results of streamer simulations obtained by using the gas phase transport properties which are scaled to liquid density are shown in the same figure for comparison. Here n_e refers to the electron number density, while E/n_0 refers to the reduced resultant electric field. The direction of the external electric field $\vec{E}_0$ is also shown in this figure.
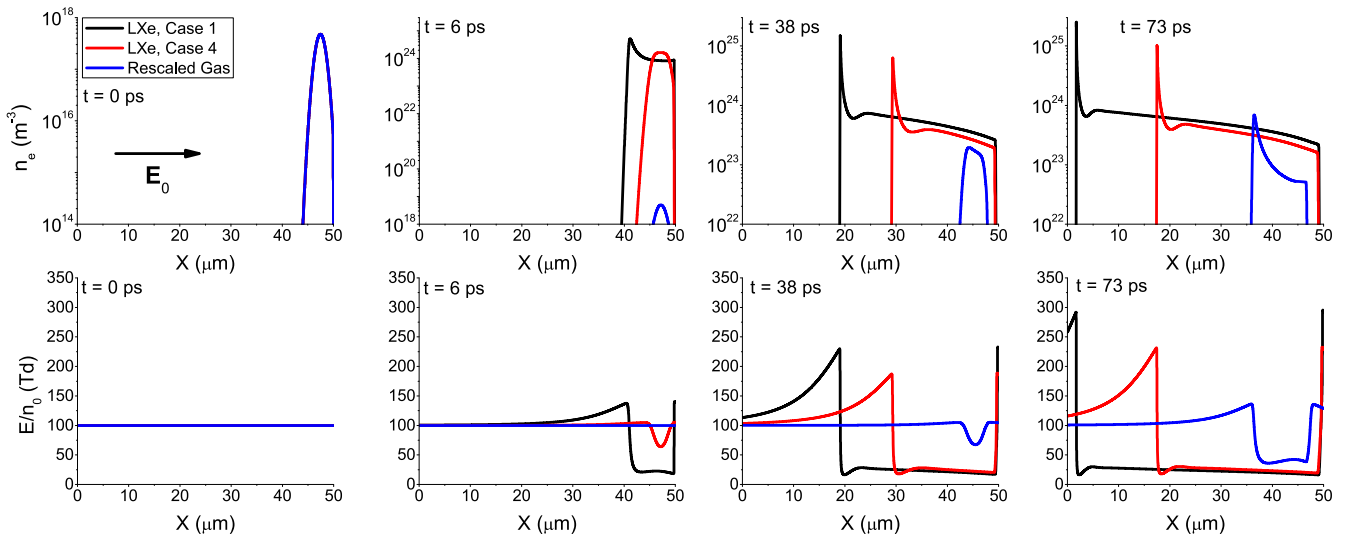
Figure 14. The formation and propagation of a negative streamer in liquid xenon for $E_0/n_0 = 100$ Td.

between the ionization coefficients in liquid and gaseous xenon. These differences are the most dominant at lower electric fields and gradually decrease with increasing field.

In figure 15 we show the profiles of negative streamers in liquid xenon for the applied reduced electric fields of 35 Td, 59 Td and 100 Td, respectively, at time 73 ps. The time instant of 73 ps has been carefully chosen since the fastest streamer in our simulations reaches the boundary of the system exactly at this time. The results are evaluated by considering all four cases for representing the inelastic energy losses. We observe that the number density of electrons in the streamer head and behind the ionization front in the streamer channel are decreased with the increase of the number of excitations in the model, independently of the applied electric

field. It can also be seen that the number density of electrons and the streamer velocity increase with increasing E_0/n_0.

The streamer velocities determined by employing all four cases for representing the inelastic energy losses, are shown in figure 16 along with the streamer velocity calculated by using the gas phase transport properties which are scaled to liquid density. For comparison, the bulk drift velocity obtained in the first case, is shown in the same figure. It can be seen that the streamer velocity greatly exceeds the bulk drift velocity. This is expected, as the velocity of a negative streamer is determined by the combination of the electron velocity and the rate of the electron impact ionization in the streamer head, where the electric field is significantly enhanced, as well as by the strong diffusive fluxes in the streamer front. It can also be
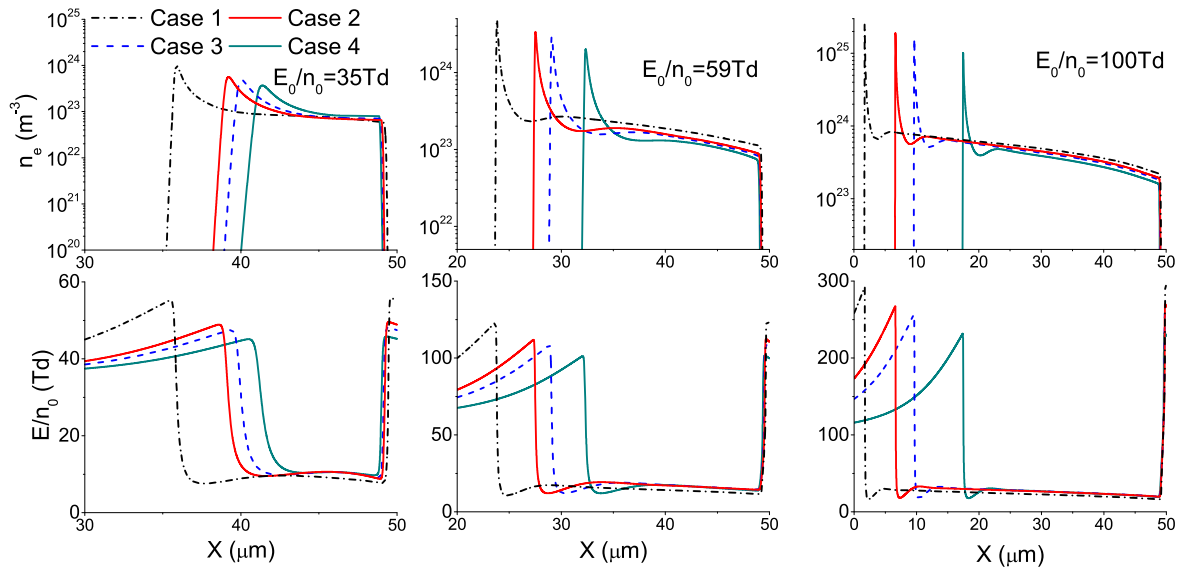
Figure 15. The spatial profiles of the electron number density n_e and the reduced electric field E/n_0 for three different values of the external electric field E_0. The displayed spatial profiles are determined by assuming all representations of the inelastic energy losses considered in the present work. All profiles are shown at 73 ps.
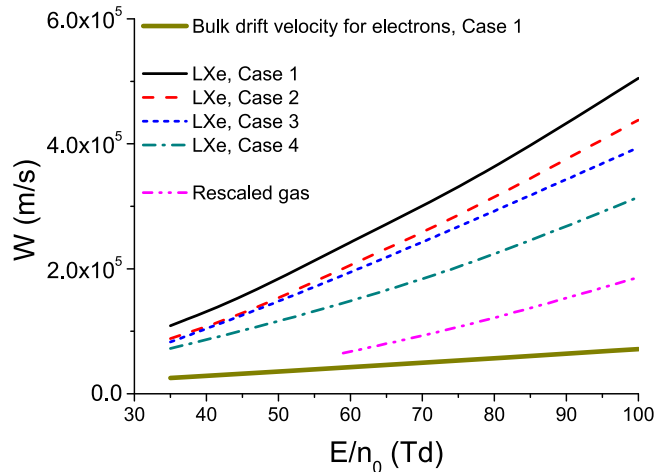

Figure 16. The streamer velocities calculated by assuming all representations of the inelastic energy losses considered in the present work. The streamer velocity obtained by using the gas phase transport data which is scaled to liquid density is displayed for comparison, as well as the bulk drift velocity of electrons, which is determined for the first case of representing the inelastic energy losses.

seen that the intensity of the streamer velocity determined in our fluid simulations strongly depends on the employed case for representing the inelastic energy losses in the liquid phase. The difference between the values of streamer velocities, which are obtained by assuming the first and the fourth cases, is about 40% at high electric fields. In addition, for the values of E_0/n_0 around 100 Td the streamer velocity determined by using the gas phase transport properties, which are scaled to liquid density, is about 2.5 times lower than the streamer velocity obtained in the first case for representing the inelastic energy losses. This difference is even more pronounced at lower electric fields. The differences between the calculated velocities of negative streamers are reflections of the

corresponding differences between the first Townsend coefficient (see figure 9).

5. Conclusion

We have investigated the influence of the inelastic energy losses in liquid xenon on the transport properties of electrons and the dynamics of negative streamers, by using Monte Carlo simulations and the 1.5 dimensional fluid model. Four cases for representing the inelastic energy losses in liquid xenon are discussed in light of previous spectroscopy and photoconductivity experiments. These cases are employed for determining the transport properties of electrons by using Monte Carlo simulations. Our Monte Carlo code has been modified by including three effective scattering processes, which give a good representation of the coherent scattering of low energy electrons in non-polar liquids. The validity of our Monte Carlo code has been tested by calculating the mean energy, the drift velocity and the components of the diffusion tensor for electrons in the Percus Yevick model liquid. Our benchmark results for the Percus Yevick model are in an excellent agreement with those calculated by Tattersall *et al* [57]. We have determined the values of mean energy, drift velocity, diffusion tensor and the first Townsend coefficient for electrons in liquid xenon. Our results are in a good agreement with those of Boyle *et al* [34], as well as with the available experiments [56, 88, 89, 94]. However, since our calculations of transport properties span a range of the reduced electric field much wider than that investigated in experiments, one should be cautious to trust the calculated data outside the range covered in the experiments. This should be noted since we have approximated the cross sections for inelastic scattering and interband transitions of electrons in liquid xenon by using the cross sections for

electron scattering on an isolated xenon atom. In addition, we have neglected the electron phonon scattering, and we did not take into account the structure of the conduction band since we have approximated each electron by a free particle moving between individual collisions. It has been shown that there is a significant difference between the values of the first Townsend coefficient determined by employing different representations of the inelastic energy losses. The transport properties of electrons obtained in our Monte Carlo simulations, are used as input data in our simulations of the streamer dynamics. These simulations are based on the first order fluid model, and they follow the transition of an electron avalanche into a negative streamer and the subsequent streamer propagation. The results of these simulations strongly depend on the number of excitations which are included in the model. The intensity of the streamer velocity in the case in which all excitations are neglected exceeds the corresponding intensity in the case in which all excitations are included by about 40%, at high electric fields. This difference is in agreement with the difference in rates for ionization in these cases. Moreover, the value of the streamer velocity determined by using the transport properties from the gas phase, which are scaled to liquid density, is over 2.5 times lower than the streamer velocity calculated in the case in which all excitations are neglected. Furthermore, the speed of transition of an electron avalanche into a streamer in the rescaled gas phase is significantly lower than in the other cases investigated in our study. This difference is especially pronounced for the reduced electric fields lower than 100 Td. These results indicate that the correct representation of the elementary scattering processes in liquids is of crucial importance for the modeling of the electron transport and the electrical discharges in the liquid phase.

Our work concerning the modeling of electron transport in liquid xenon can be extended by employing *ab initio* cross sections for inelastic scattering and interband transitions in the liquid phase after these cross sections are determined. Further improvement of the model would be achieved by taking into account electron phonon scattering and trapping of electrons in density fluctuations as well as by going beyond the free electron approximation by considering the structure of the conduction band.

The extension of our streamer calculations by investigating the propagation of positive and negative streamers in a point to plane geometry and by taking into account non-locality of the electron mean energy will be covered in future work. These calculations can be further generalized by considering the formation of gaseous filaments due to heating of the liquid, which is important on the nanosecond time scale.

Acknowledgments

ORCID iDs

I Simonović https://orcid.org/0000-0001-6704-9042
N A Garland https://orcid.org/0000-0003-0343-0199
D Bošnjaković https://orcid.org/0000-0002-2725-5287
Z Lj Petrović https://orcid.org/0000-0001-6569-9447
R D White https://orcid.org/0000-0001-5353-7440
S Dujko https://orcid.org/0000-0002-4544-9106

References

[1] Bruggeman P and Leys C 2009 *J. Phys. D: Appl. Phys.* **42** 053001
[2] Bruggeman P J *et al* 2016 *Plasma Sources Sci. Technol.* **25** 053002
[3] Fridman A and Friedman G 2012 *Plasma Medicine* (New York: Wiley)
[4] Kong M G, Kroesen G, Morfill G, Nosenko T, Shimizu T, van Djik J and Zimmermann J L 2009 *New J. Phys.* **11** 115012
[5] Jiang B, Zheng J, Qiu S, Wu M, Zhang Q, Yan Z and Xue Q 2014 *Chem. Eng. J.* **236** 348–68
[6] Malik M A, Ghaffar A and Malik S A 2001 *Plasma Sources Sci. Technol.* **10** 82
[7] Škoro N, Puač N, Živković S, Krstić-Milosević D, Cvelbar U, Malović G and Petrović Z L 2018 *Eur. Phys. J.* D **72** 2
[8] Puač N, Škoro N, Spasić K, Živković S, Milutinović M, Malović G and Petrović Z L 2017 *Plasma Process. Polym.* **15** e1700082
[9] Rond C, Desse J M, Fagnon J M, Aubert X, Er M, Vega A and Duten X 2018 *J. Phys. D: Appl. Phys.* **51** 335201
[10] Naidis G V 2015 *J. Phys. D: Appl. Phys.* **48** 195203
[11] Ushakov V Y, Klimkin V F and Korobeynikov S M 2007 *Impulse Breakdown of Liquids* (Berlin: Springer)
[12] Regenfus C and (The ArDM Collaboration) 2010 *J. Phys.: Conf. Ser.* **203** 012024
[13] Aprile E, Mukherjee R and Suzuki M 1990 *IEEE Trans. Nucl. Sci.* **37** 553
[14] Aprile E and Doke T 2010 *Rev. Mod. Phys.* **82** 2053
[15] Okada H, Doke T, Kashiwagi T, Kikuchi J, Kobayashi M, Masuda K, Shibamura E, Suzuki S, Takashima T and Terasawa K 2000 *Nucl. Instrum. Methods Phys. Res.* A **451** 427
[16] Egorov V V, Miroshnichenko V P, Rodionov B U, Bolozdinja A I, Kalashnikov S D and Krivoshein V L 1983 *Nucl. Instrum. Methods Phys. Res.* A **205** 373
[17] Aprile E and Baudis L 2008 *Proc. Sci.* **IDM2008** 018
[18] Gaitskell R 2008 *Proc. Sci.* **IDM2008** 018
[19] Boyle G J, McEachran R P, Cocks D G and White R D 2015 *J. Chem. Phys.* **142** 154507
[20] Sakai Y 2007 *J. Phys. D: Appl. Phys.* **40** R441
[21] White R D, Robson R E, Dujko S, Nicoletopoulos P and Li B 2009 *J. Phys. D: Appl. Phys.* **42** 194001
[22] Petrović Z L, Dujko S, Marić D, Malović G, Nikitović Ž, Šašić O, Jovanović J, Stojanović V and Radmilović-Radjenović M 2009 *J. Phys. D: Appl. Phys.* **42** 194002
[23] Robson R E, White R D and Petrović Z L 2005 *Rev. Mod. Phys.* **77** 1303
[24] Lekner J 1967 *Phys. Rev.* **158** 130

[25] Cohen M H and Lekner J 1967 *Phys. Rev.* **158** 305
[26] Atrazhev V M and Iakubov I T 1981 *J. Phys. C* **14** 5139
[27] Atrazhev V M and Dmitriev E G 1985 *J. Phys. C* **18** 1205
[28] Atrazhev V M, Iakubov I T and Pogosov V V 1995 *Phys. Lett. A* **204** 393
[29] Atrazhev V M and Timoshkin I V 1996 *Phys. Rev. B* **54** 252
[30] Atrazhev V M and Timoshkin I V 1998 *IEEE Trans. Dielectr. Electr. Insul.* **5** 450
[31] Atrazhev V M, Berezhnov A V, Dunikov D O, Chernysheva I V, Dmitrenko V V and Kapralova G 2005 *Proc. IEEE Int. Conf. on Dielectric Liquids (ICDL 2005)* p 329
[32] Sakai Y, Nakamura S and Tagashira H 1985 *IEEE Trans. Electr. Insul.* **EI-20** 133
[33] Nakamura S, Sakai Y and Tagashira H 1986 *Chem. Phys. Lett.* **130** 551
[34] Boyle G J, McEachran R P, Cocks D G, Brunger M J, Buckman S J, Dujko S and White R D 2016 *J. Phys. D: Appl. Phys.* **49** 355201
[35] Milloy H B and Crompton R W 1977 *Aust. J. Phys.* **30** 51
[36] Borghesani A F and Lamp P 2011 *Plasma Sources Sci. Technol.* **20** 034001
[37] Borghesani A F 2014 *Eur. Phys. J. D* **68** 62
[38] Petrović Z L, O'Malley T F and Crompton R W 1995 *J. Phys. B* **28** 3309
[39] Atrazhev V M, Iakubov I T and Roldughin V I 1976 *J. Phys. D: Appl. Phys.* **9** 1735
[40] Jones H M and Kunhardt E E 1993 *Phys. Rev. B* **48** 9382
[41] Kunhardt E E 1991 *Phys. Rev. B* **44** 4235
[42] Hove L V 1954 *Phys. Rev.* **95** 249
[43] Boyle G J, White R D, Robson R E, Dujko S and Petrović Z L 2012 *New. J. Phys.* **14** 045011
[44] Garland N A, Cocks D G, Boyle G J, Dujko S and White R D 2017 *Plasma Sources Sci. Technol.* **26** 075003
[45] White R D *et al* 2018 *Plasma Sources Sci. Technol.* **27** 053001
[46] Garland N A, Boyle G J, Cocks D G and White R D 2018 *Plasma Sources Sci. Technol.* **27** 024002
[47] Naidis G V 2016 *J. Phys. D: Appl. Phys.* **49** 235208
[48] Babaeva N Y, Naidis G V, Tereshonok D V and Smirnov B M 2017 *J. Phys. D: Appl. Phys.* **50** 364001
[49] Tereshonok D V, Babaeva N Y, Naidis G V, Panov V A, Smirnov B M and Son E E 2018 *Plasma Sources Sci. Technol.* **27** 045005
[50] Babaeva N Y and Naidis G V 1999 *Proc. 13th Int. Conf. on Dielectric Liquids (ICDL 1999) (Nara, Japan, July 20-25)* p 437
[51] Babaeva N Y and Naidis G V 1999 *Tech. Phys. Lett.* **25** 91
[52] Babaeva N Y and Naidis G V 2001 *J. Electrost.* **53** 123
[53] Nakamura S, Sakai Y and Tagashira H 1987 *JIEE Japan* **A107** 543
[54] Hayashi M 2003 *Bibliography of Electron and Photon Cross sections with Atoms and Molecules Published in the 20th Century—Xenon (NIFS-DATA-79)*
[55] Pitchford L C *et al* 2013 *J. Phys. D: Appl. Phys.* **46** 334001
[56] Derenzo S E, Mast T S and Zaklad B 1974 *Phys. Rev. A* **9** 2582
[57] Tattersall W J, Cocks D G, Boyle G J, Buckman S J and White R D 2015 *Phys. Rev. E* **91** 043304

[58] Bartels A 1973 *Phys. Lett.* **44A** 403
[59] Allen N L and Prew B A 1970 *J. Phys. B* **3** 1113
[60] Beaglehole D 1965 *Phys. Rev. Lett.* **15** 551
[61] Asaf U and Steinberger I T 1971 *Phys. Lett.* **34A** 207
[62] Laporte P and Steinberger I T 1977 *Phys. Rev. A* **15** 2538
[63] Laporte P, Subtil J L, Asaf U, Steinberger I T and Wind S 1980 *Phys. Rev. Lett.* **45** 2138
[64] Raz B and Jortner J 1968 *J. Chem. Phys.* **49** 3318
[65] Raz B and Jortner J 1970 *Proc. R. Soc. A* **317** 113
[66] Reininger R, Asaf U, Steinberger I T, Saile V and Laporte P 1983 *Phys. Rev. B* **28** 3193
[67] Asaf U and Steinberger I T 1974 *Phys. Rev. B* **10** 4464
[68] Hayashi M 2014 Hayashi Database www.lxcat.net
[69] von Zdrojewski W 1980 *Z. Naturforsch.* **35a** 672
[70] Reininger R, Asaf U and Steinberger I T 1982 *Chem. Phys. Lett.* **90** 287
[71] Garland N A, Simonović I, Boyle G J, Cocks D G, Dujko S and White R D 2018 *Plasma Sources Sci. Technol.* **27** 105004
[72] Gordon E B *et al* 1994 *Chem. Phys. Lett.* **217** 605
[73] Schüssler A S *et al* 2000 *Appl. Phys. Lett.* **77** 2786
[74] Gordon E B and Shestakov A F 2001 *Low Temp. Phys.* **27** 883
[75] Kunhardt E E, Christophorou L G and Luessen L H 1988 *The Liquid State and its Electrical Properties* (New York: Plenum) p 235
[76] Dujko S, Raspopović Z M and Petrović Z L 2005 *J. Phys. D: Appl. Phys.* **38** 2952
[77] Dujko S, White R D, Ness K F, Petrović Z L and Robson R E 2006 *J. Phys. D: Appl. Phys.* **39** 4788
[78] Dujko S, Raspopović Z M and Petrović Z L 2008 *J. Phys. D: Appl. Phys.* **41** 245205
[79] Perram J W 1975 *Mol. Phys.* **30** 1505
[80] Verlet L and Weis J J 1972 *Phys. Rev. A* **5** 939
[81] White R D and Robson R E 2011 *Phys. Rev. E* **84** 031125
[82] White R D and Robson R E 2009 *Phys. Rev. Lett.* **102** 230602
[83] Davies A J, Evans C J and Jones F L 1964 *Proc. R. Soc. A* **281** 164
[84] Bošnjaković D, Petrović Z L and Dujko S 2016 *J. Phys. D: Appl. Phys.* **49** 405201
[85] Hilt O and Schmidt W F 1994 *Chem. Phys.* **183** 147
[86] Hilt O and Schmidt W F 1994 *J. Phys. Condens. Matter* **6** L735
[87] Robson R E and Ness K F 1988 *J. Chem. Phys.* **89** 4815
[88] Miller L S, Howe S and Spear W E 1968 *Phys. Rev.* **166** 871
[89] Huang S S S and Freeman G R 1978 *J. Chem. Phys.* **47** 1355
[90] Petrović Z L, Crompton R W and Haddad G N 1984 *Aust. J. Phys.* **37** 23
[91] Robson R E 1984 *Aust. J. Phys.* **37** 35
[92] Vrhovac S B and Petrović Z L 1996 *Phys. Rev. E* **53** 4012
[93] Dujko S, White R D and Petrović Z L 2008 *J. Phys. D: Appl. Phys.* **41** 245205
[94] Shibamura E, Masuda K and Doke T 1984 *Proc. 8th Workshop on Electron Swarms*
[95] Li C, Brok W J M, Ebert U and Mullen J J A M 2007 *J. Appl. Phys.* **101** 123305
[96] Li C, Ebert U and Hundsdorfer W 2010 *J. Comput. Phys.* **229** 200

Non-equilibrium of charged particles in swarms and plasmas—from binary collisions to plasma effects

Non-equilibrium of charged particles in swarms and plasmas—from binary collisions to plasma effects

Z Lj Petrović[1,2], I Simonović, S Marjanović[1], D Bošnjaković[1], D Marić[1], G Malović[1] and S Dujko[1]

[1] Institute of Physics, University of Belgrade, POB 68, 11080 Zemun, Belgrade, Serbia
[2] Serbian Academy of Sciences and Arts, 11001 Belgrade, Serbia

E-mail: zoran@ipb.ac.rs

Abstract

In this article we show three quite different examples of low-temperature plasmas, where one can follow the connection of the elementary binary processes (occurring at the nanoscopic scale) to the macroscopic discharge behavior and to its application. The first example is on the nature of the higher-order transport coefficient (second-order diffusion or skewness); how it may be used to improve the modelling of plasmas and also on how it may be used to discern details of the relevant cross sections. A prerequisite for such modeling and use of transport data is that the hydrodynamic approximation is applicable. In the second example, we show the actual development of avalanches in a resistive plate chamber particle detector by conducting kinetic modelling (although it may also be achieved by using swarm data). The current and deposited charge waveforms may be predicted accurately showing temporal resolution, which allows us to optimize detectors by adjusting the gas mixture composition and external fields. Here kinetic modeling is necessary to establish high accuracy and the details of the physics that supports fluid models that allows us to follow the transition to streamers. Finally, we show an example of positron traps filled with gas that, for all practical purposes, are a weakly ionized gas akin to swarms, and may be modelled in that fashion. However, low pressures dictate the need to apply full kinetic modelling and use the energy distribution function to explain the kinetics of the system. In this way, it is possible to confirm a well established phenomenology, but in a manner that allows precise quantitative comparisons and description, and thus open doors to a possible optimization.

Keywords: charged particle swarms, non-equilibrium plasma, skewness, resistive plate chambers, positron traps, Monte Carlo simulations, Boltzmann equation

(Some figures may appear in colour only in the online journal)

1. Introduction

The idea of thermodynamic equilibrium (TE) is one of the most widely used ideas in the foundations of plasma physics. Not only is TE used as a background gas, but it is also used as the plasma itself, and, further, TE is implicitly incorporated in most theories through application of the Maxwell Boltzmann distribution function. On the other hand, the idea of local thermodynamic equilibrium (LTE) in principle means that TE is not maintained, and that energy converted into the effective temperature is being used as a fitting parameter, but also that all the principles of TE still apply for the adjusted (local) temperature. It is often overlooked that TE implies that each process is balanced by its inverse process. It is difficult to envisage just exactly how this condition could be met under circumstances where most of the energy that is fed into the non-equilibrium, low-temperature discharges comes from an external electric field. The notion

of non-equilibrium is implemented very well in a wide range of plasma models, starting from fluid models and hybrid models, all the way to fully kinetic codes such as particle-in-cell (PIC) modelling.

At end of a field of ionized gases, opposite to the fully developed plasma, at the lowest space charge densities, electrons are accelerated (gain energy) from the external electric field and dissipate in collisions with the background gas. This realm is known as a swarm (swarm physics), and is often described by simple swarm models. We shall try to illustrate how and where one may employ concepts developed in low-temperature plasmas for problems that are not traditional non-equilibrium plasmas such as positrons in gases and gas-filled traps, gas breakdown and particle detectors.

The three selected examples are: the use and properties of higher-order transport coefficients (skewness) and how they may be implemented to close the system of equations for modeling of atmospheric plasmas; modeling of resistive plate chamber (RPC) particle detectors with a focus on the development of avalanches, and prediction of the current and deposited charge; and, finally, modeling of a generic representation of the three stage gas-filled positron trap, where the same models as for electrons may be employed in a full kinetic description to calculate the temporal development of the energy distribution function, and, through that, to describe how and when individual elementary processes affect the performance of the trap.

This is a review article as it covers three different topics that will (or have been) be presented in detail elsewhere. Yet the majority of the results will be developed in this paper. Necessarily, as it is a broad review, some finer points will be omitted in pursuit of the bigger picture, however, all will be covered elsewhere and the relevant literature is cited.

2. Higher-order transport and plasma modeling

The fluid equations often employed in plasma modeling are a part of an infinite chain, and whenever the chain is broken one needs a higher-order equation and related quantities to close the system of equations (Dujko *et al* 2013). That is why a closing of the equations is forced, sometimes labeled as ansatz, although the closure is not quite arbitrary. It is often based on some principles or simplifying arguments (Robson *et al* 2005) involving higher-order equations and related transport coefficients. Robson *et al* (2005) claimed that some serious errors have been incorporated into fluid equations that are commonly used in plasma modeling, and suggested benchmarks to test plasma models.

Equations (1) and (2) shown below, are the flux gradient equation and generalized diffusion equation, respectively, truncated at the contribution of the third order transport coefficients (also known as skewness). The terms, including $\widehat{Q}^{(F)}$ and $\widehat{Q}^{(B)}$ are terms that represent the contribution of the skewness tensor:

$$\vec{\Gamma}(\vec{r},t) = \vec{W}^{(F)}n(\vec{r},t) - \widehat{D}^{(F)}\cdot\nabla\, n(\vec{r},t) + \widehat{Q}^{(F)}:(\nabla\otimes\nabla)n(\vec{r},t) + \ldots \tag{1}$$

$$\frac{\partial n(\vec{r},t)}{\partial t} + \vec{W}^{(B)}\cdot\nabla\, n(\vec{r},t) - \widehat{D}^{(B)}$$
$$: (\nabla\otimes\nabla)n(\vec{r},t) + \widehat{Q}^{(B)} \vdots (\nabla\otimes\nabla\otimes\nabla)n(\vec{r},t) + \ldots$$
$$= Rn(\vec{r},t) \tag{2}$$

where $\vec{\Gamma}(\vec{r},t)$, $n(\vec{r},t)$, $\vec{W}^{(F)}$, $\widehat{D}^{(F)}$, $\widehat{Q}^{(F)}$, $\vec{W}^{(B)}$, $\widehat{D}^{(B)}$, $\widehat{Q}^{(B)}$, R are the flux of charged particles, charged particle number density, flux drift velocity, flux diffusion tensor, flux skewness tensor, bulk drift velocity, bulk diffusion tensor, bulk skewness tensor and rate for reactions, respectively. If equations (1) and/or (2) are coupled to the Poisson equation for an electric field then the system of corresponding differential equations might be closed in the so-called local field approximation. This means that all transport properties are functions of the local electric field. The skewness tensor has been systematically ignored in previous fluid models of plasma discharges, although its contribution may be significant for discharges operating at high electric fields, and in particular for discharges in which the ion dynamics play an important role.

As for experimental determination of the higher-order diffusion of electrons, there have been some attempts, but those were mostly regarded as unsuccessful due to the end effects (Denman and Schlie 1990). In other words, those experiments may have failed to comply with both the requirements for negligible non-hydrodynamic regions and for lower pressures. An estimate was made that reliable skweness experiments would have to be up to 10 m long with pressures that are at least ten times smaller than those in standard swarm experiments. It seems that the only reliable yet very weak result was observed for H_2 in time of flight (TOF) emission experiments of Blevin *et al* (1976, 1978), as described in the PhD thesis by Hunter (1977). This is because the measurement was made away from the electrodes, thus providing a hydrodynamic environment.

At the same time some calculations were performed based on the available cross sections either by using a Monte Carlo simulation (MCS) and two term solutions of the Boltzmann equation (BE) (Penetrante and Bardsley 1990) or by using the momentum transfer theory (Vrhovac *et al* 1999). Whealton and Mason (1974) were the first to determine the correct structure of the skewness tensor in the magnetic field free case. For ions there have been more general studies and in particular theoretical studies. Koutselos gave a different prediction of the structure and symmetry of the tensor (Koutselos 1997) but those results were challenged (corrected) by Vrhovac *et al* (1999), who confirmed the structure of the skewness tensor previously determined by Whealton and Mason. Subsequently Koutselos confirmed the structure of the skewness tensor obtained by previous authors (Koutselos 2001).

Finally, having in mind the need for data in fluid modeling and the poor likelihood of experimental studies in the near future, a systematic study has been completed by Simonović *et al* (2016) dealing with the symmetry by using the group projector method (Barut and Raczka 1980, Tung 1984), multi-term Boltzmann equation solutions and MCS results in general terms. It should be noted that the third-order transport coefficients are often called skewness, but in principle it is the term that was to be applied only for the longitudinal diagonal
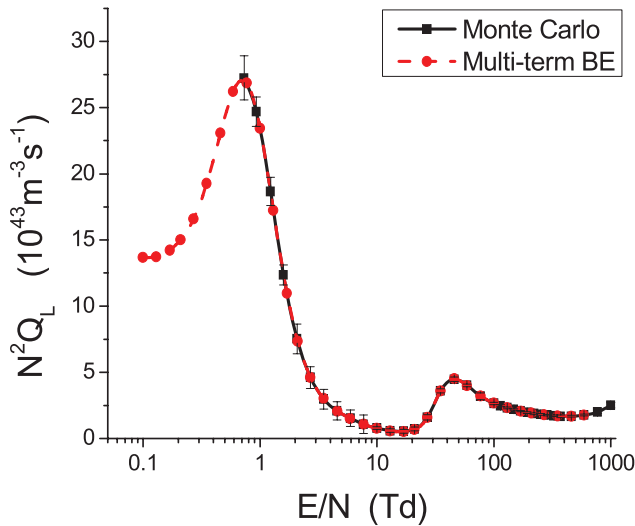
Figure 1. The longitudinal component of the skewness tensor calculated for electrons in methane.

Figure 2. The transverse component of the skewness tensor calculated for electrons in methane.

term, which defines most directly the (departure from the) shape of the moving Gaussian. We will, however, use the term skewness for the entire tensor and all its terms.

The structure of the skewness tensor is the following (Whealton and Mason [1974], Vrhovac *et al* [1999], Koutselos [2001], Simonović *et al* [2016]):

$$Q_{xab} = \begin{pmatrix} 0 & 0 & Q_{xxz} \\ 0 & 0 & 0 \\ Q_{xxz} & 0 & 0 \end{pmatrix}, \quad Q_{yab} = \begin{pmatrix} 0 & 0 & 0 \\ 0 & 0 & Q_{xxz} \\ 0 & Q_{xxz} & 0 \end{pmatrix}$$

$$Q_{zab} = \begin{pmatrix} Q_{zxx} & 0 & 0 \\ 0 & Q_{zxx} & 0 \\ 0 & 0 & Q_{zzz} \end{pmatrix},$$

where $a, b \in \{x, y, z\}$ and Q_{abc} are the independent, non-zero terms in the tensor (although some of them may be identical if they are established for different permutations of the same derivatives). The components of the tensor may be grouped as longitudinal $Q_L = Q_{zzz}$ and transverse $Q_T = \frac{1}{3}(Q_{zxx} + Q_{xxz} + Q_{xzx})$.

In this paper, we present results for skewness of electron swarms in methane. Methane is known for producing negative differential conductivity (NDC) and in this work we will demonstrate the unusual variation of the longitudinal and transverse components of the skewness tensor for *E/N* (electric field over the gas number density) regions in which NDC occurs. NDC is characterized by a decrease in the drift velocity despite an increase in the magnitude of the applied reduced electric field. Cross sections for electron scattering in methane are taken from Šašić *et al* ([2004]). For the purpose of this calculation we assumed a cold gas approximation: $T = 0$ K, which is justified as we covered mostly the *E/N* range where mean energies are considerably higher than the thermal energy. The initial number of electrons in the simulations was 10^7 and those were followed for sufficient time to achieve full equilibration with the applied field before sampling was applied. Sampling in an MCS is performed either
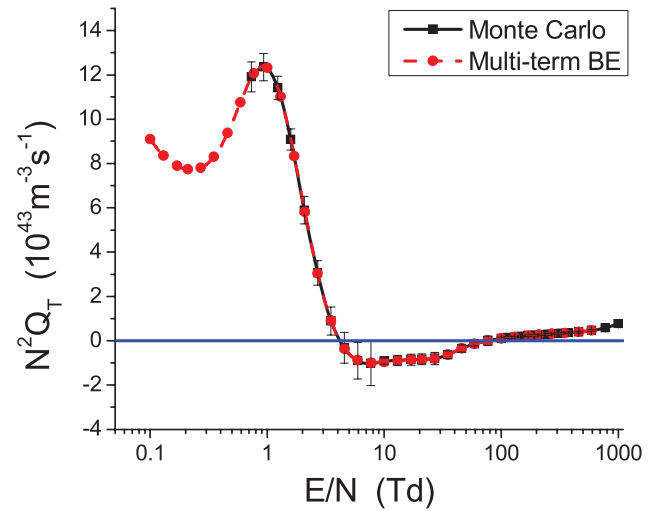
for the flux (velocity space) $Q_{abc}^{(f)} = \frac{1}{3!} \left\langle \frac{d}{dt} (r_a^* r_b^* r_c^*) \right\rangle$ or for the bulk (real space) $Q_{abc}^{(b)} = \frac{1}{3!} \frac{d}{dt} \langle r_a^* r_b^* r_c^* \rangle$ components (Simonović *et al* [2016]) where $r_a^* = r_a - \langle r_a \rangle$.

Uncertainties are established as the root mean square deviations. Statistical fluctuations in MCSs are more pronounced for skewness than for the lower-order transport coefficients. Thus, it is very important to present statistical uncertainties (errors) associated with the results. In addition to Monte Carlo results, the skewness tensor is calculated from the multi-term Boltzmann equation solution. The explicit formulas for skewness tensor elements in terms of moments of the distribution function will be given in a forthcoming paper (Simonović *et al* [2016]).

In figures [1] and [2] we show the variation of the longitudinal and transverse skewness tensor components with *E/N* for electrons in CH_4, respectively. In figure [3] we show the variation of independent components of the skewness tensor with *E/N*. The independent components of the skewness tensor have been calculated from a multi-term solution of the Boltzmann equation.

The first observation that is very important is that the multi-term Boltzmann equation results agree very well with those obtained in MCSs. This is an important cross check and it means that the techniques to calculate the skewness are internally consistent, although two very different approaches are implemented (having said that we assume that the solution to the Boltzmann equation and the MC are both well established and tested (Dujko *et al* [2010])).

We see that Q_T becomes negative in the same range of *E/N* where NDC occurs. At the same time Q_L remains positive. Q_{zxx} and the sum of Q_{xxz} and Q_{xzx} are negative in different regions of *E/N*.

Comparing the second- and third-order longitudinal transport coefficients we noticed that if diffusion decreases with increasing *E/N* then the skewness also decreases, but even faster (figures [4] and [5]). When it comes to the effect of the cross sections (or inversely to the ability to determine the cross sections from the transport data) it seems that skewness has a
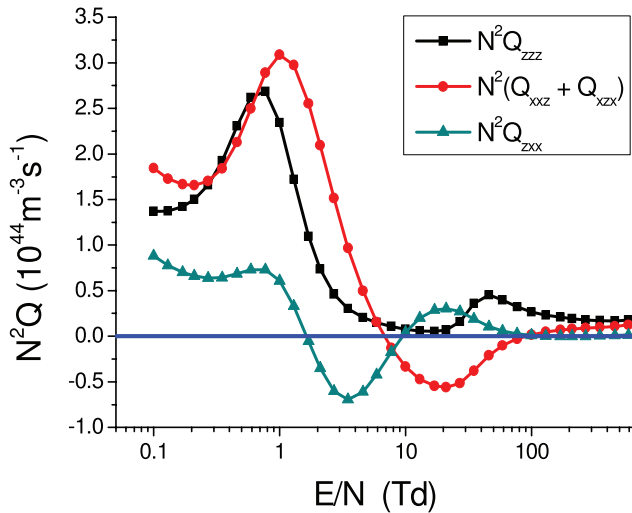
Figure 3. All independent components of the skewness tensor calculated for electrons in methane.
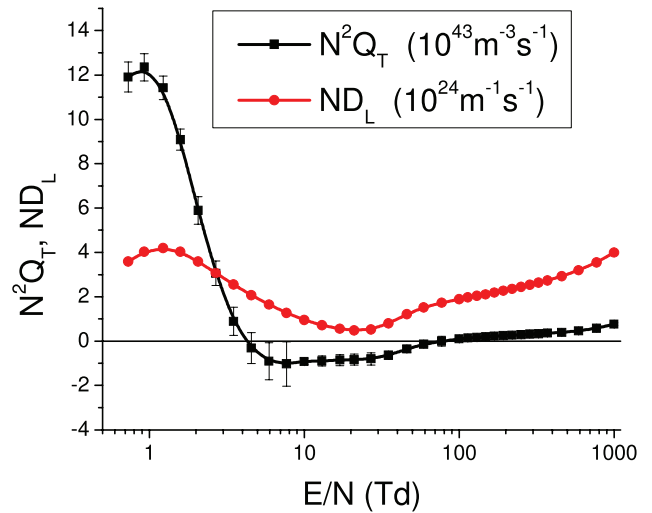

Figure 5. Comparison between longitudinal diffusion and transverse skewness for electrons in methane (the scale for the two different transport coefficients are provided in the legend).
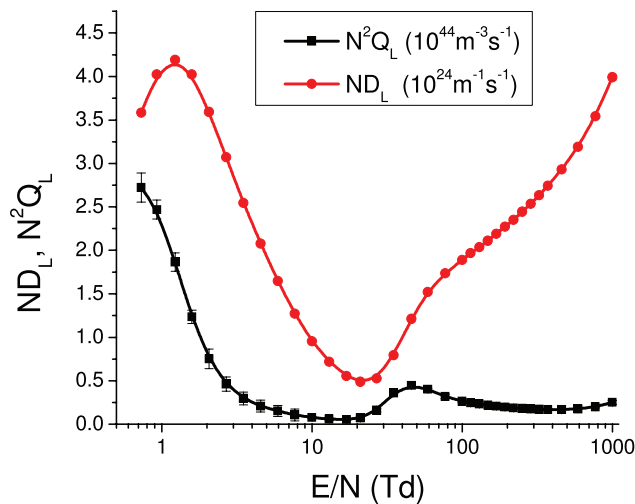

Figure 4. Comparison between longitudinal diffusion and skewness for electrons in methane (the scale for the two different transport coefficients are provided in the legend).

Figure 6. Off-diagonal components of skewness compared to the drift velocity for electrons in methane (the scale for the two different transport coefficients are provided in the legend).

more pronounced structure, and thus is more useful in fixing the shape and absolute values of the cross sections. If the diffusion increases, then we are able to distinguish between the two scenarios: if diffusion increases as a concave function, then the skewness decreases, while if the diffusion increases as a convex (or linear) function then the skewness increases.

We have observed that the transverse skewness is also in a good, if not better, correlation with the longitudinal diffusion (figure 5). This is a good example that illustrates that the skewness tensor represents directional motion.

Different transverse components have different *E/N* profiles. Q_{zxx} follows the behavior of the drift velocity while the remaining components change their trends of behavior near the end of the NDC region (figure 6). For different gases we have seen different trends and a clear correlation was not found (Simonović *et al* 2016).

Furthermore, but without illustrating it with special figures, the explicit effect of non-conservative collisions (ionization in this case) has been observed. However, in many cases the
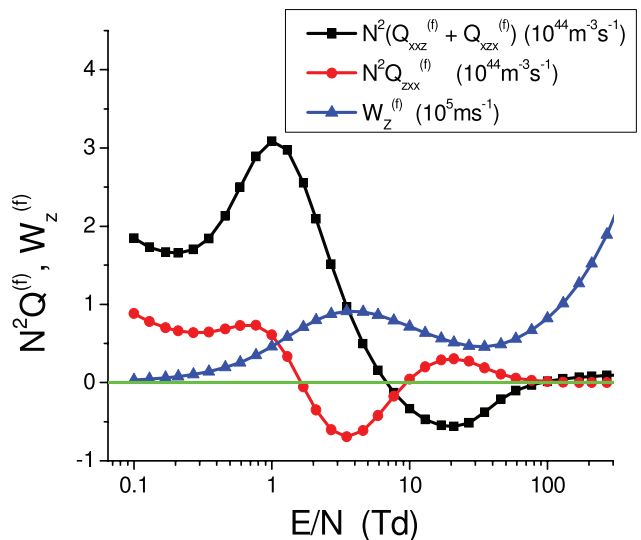
agreement between multi-term BE results and those obtained in MCSs is better than what would be expected based on the estimated errors. At the same time it turned out that discrepancies between a two-term and multi-term (MCS) results may be quite large, ranging up to a factor of 10.

Possible measurements of higher-order transport coefficients seem possible and also profitable for the sake of determining the cross sections. Nevertheless the difficulties and possible uncertainties may outweigh the benefits. Thus, calculation of the data seems like an optimum choice for application in higher-order plasma models. The behavior of higher-order transport coefficients provides an insight into the effect of individual cross sections (their shape and magnitude), and their features such as the Ramsauer Townsend effect or resonances on the overall plasma behavior. The transport coefficients as an intermediate step give a guidance, especially when they develop special features (kinetic effects
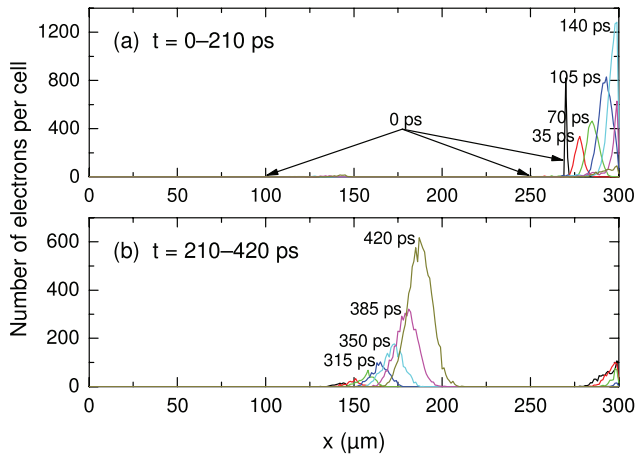
Figure 7. The spatio-temporal development of electron avalanches ((a) and (b)) in an RPC device. The number of electrons per cell (1 cell = 1 μm) is shown where the cells (1 cell = 1 μm) are along the discharge axis x. The cathode corresponds to $x = 0$ while the anode corresponds to $x = 300$ μm.
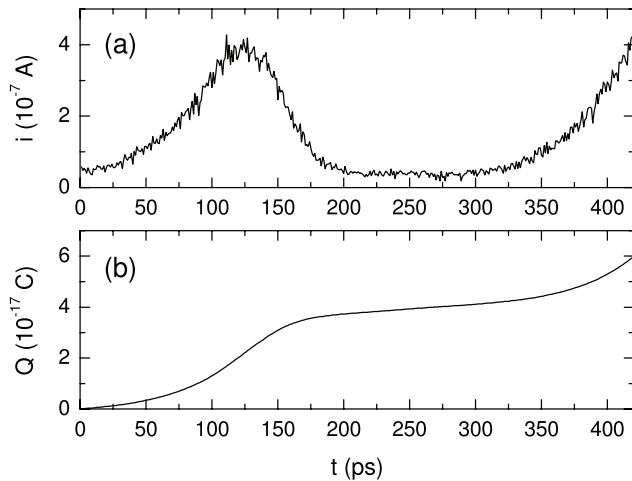

Figure 8. The time development of (a) electron induced current and (b) induced charge in the RPC device.

(Petrović *et al* 2009)) that may also be easily implemented in the determination of the cross sections.

3. Avalanches in resistive plate chambers

The next example of the connection of the elementary processes to plasma behavior through intermediate swarm-like phenomenology modeling will be modeling of RPC detectors. These devices are used for timing and triggering purposes in many high-energy physics experiments at CERN and elsewhere (The ATLAS Collaboration 2008, Santonico 2012). RPCs may be both used for spatial and temporal detection while providing large signal amplifications. They are usually operated in avalanche (swarm) or plasma (streamer) regimes depending on the required amplification and performance characteristics. Numerous models have been developed to predict RPC performance and modes of operation (Lippmann *et al* 2004, Moshaii *et al* 2012). We have studied systematically the swarm data (Bošnjaković *et al* 2014a) and then the
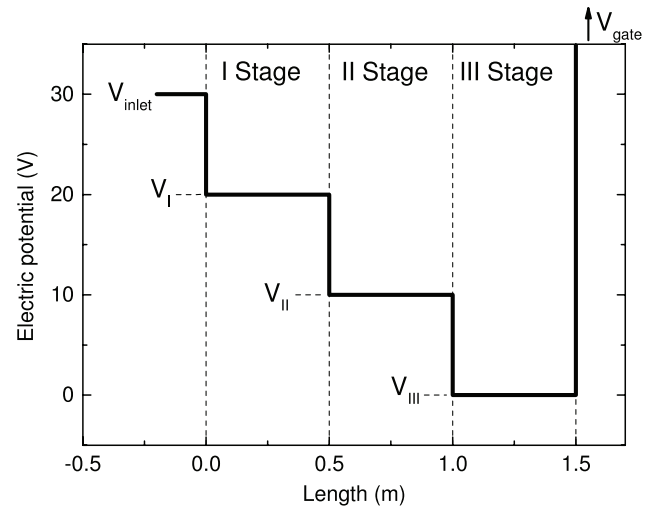

Figure 9. Schematic drawing of a generic Surko trap consisting of three equal potential drops. The composition of the background gas, its pressure and geometry are given in table 1.

Table 1. Parameters for simulation of a generic positron Surko trap.

Parameters	Stage I	Stage II	Stage III
Radius (mm)	5	20	20
Length (m)	0.5	0.5	0.5
Pressure (Torr)	10^{-3}	10^{-4}	10^{-5}
Background gas	N_2	N_2	$N_2^{0.5} + CF_4^{0.5}$
Magnetic field (G)	530	530	530
Voltage (V)	20	10	0
The initial parameters			
Potential of the entrance electrode (V)		30	
Potential of the source (V)		0.1	
Width (FWHM) of the initial energy distribution (eV)		1.5	

model of RPCs (Bošnjaković *et al* 2014b) where RPC efficiency and timing resolution have been predicted by MCS without any adjustable parameters, and were found to agree with experiment very well. Here we show some of the data not presented in Bošnjaković *et al* (2014b), which focuses on avalanche development and furthermore the induced current and charge.

Calculations of the development of the Townsend avalanche have been performed for a timing RPC gas mixture of $C_2H_2F_4$:i-C_4H_{10}:SF_6 = 85:5:10 with realistic chamber geometry (gas gap = 0.3 mm) at E/N = 421 Td. We show in figure 7 the development of an avalanche in the gap with three initial clusters of charges (first generation secondary electrons indicated by arrows at 0 ps) formed by an incoming high-energy particle. The first cluster (from the left) has one electron, the second has nine and the third has 983 initial electrons. The distribution over a small group of cells has been randomly selected according to well-established distributions. At the beginning, the initial condition shapes the profile of the ensemble, but eventually a Gaussian is formed that drifts under the influence of an electric field and diffuses due to numerous collisions.
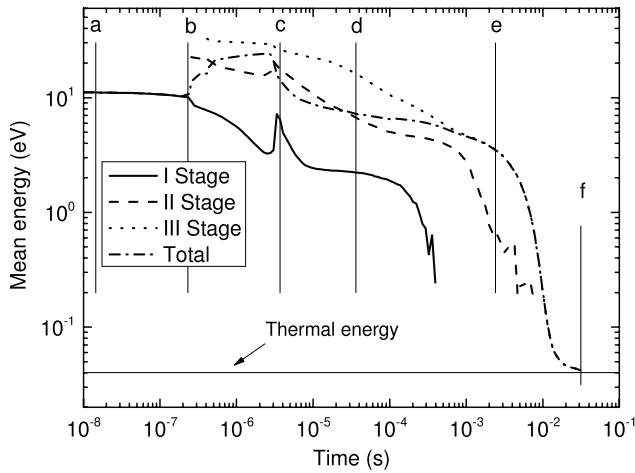
Figure 10. The mean energy of the positron ensemble (swarm) as a function of time. Averages for each stage and for the entire volume (total) are provided. The energy distribution function is plotted in figure 11 for the times marked by the points (a)–(f) in this figure.

We will first follow the development of the cluster closest to the anode (at 270 μm), as indicated by spatial electron profiles at different times in figure 7(a). The largest initial group, which is also the closest to the anode, develops the fastest: from the initial very sharp profile it quickly establishes a Gaussian shape that also very quickly gets absorbed by the anode. The second peak (from the right) is quick to follow but it is very small and cannot be observed clearly due to interference from the first pulse. In figure 7(b), we show the development of the first cluster (at 100 μm) for longer times. This cluster is the furthest from the anode and it takes the most time to reach the anode, again as a well developed moving Gaussian. It develops, however, a well-separated and defined current pulse (unlike the second cluster of charged particles). The induced current and the corresponding induced charge are shown in figure 8.

The predictions in figure 8, extended to provide important information on the temporal resolution, may be used to optimize the device by changing gas composition, field and geometry, and also may be extended to allow for the formation of the plasma in later stages when a streamer discharge may be generated at atmospheric pressure (Bošnjaković *et al* 2016). Trial and error development of such devices is simply too costly to allow for an empirical learning curve. Nevertheless, one could argue that it could be possible to develop a model based on a standard swarm description of a moving Gaussian with drift and diffusion plus the benefit of multiplication through ionization. All of these processes have their swarm coefficients. However, the very short times of the formation of the initial cluster, it being inhomogeneous and a very nonlinear growth with a possible separation of faster and slower electrons, dictate the need to perform an MCS in order to achieve the required accuracy. Thus, this example allows for the use of transport coefficients, but is better accomplished by full kinetic modeling. Transport coefficients are better taken advantage of in fluid modeling of the possibly developing streamer (Bošnjaković *et al* 2016). In any case, the ionized gas and the developing plasma channel are both represented very

accurately (qualitatively and quantitatively). Here we have used kinetic swarm modeling, although using transport coefficients may also be an option, albeit a less accurate option.

4. Gas-filled positron (and electron) traps

While it is often assumed that keeping the antimatter away from the matter is a way of preserving it longer, the introduction of background gas to the vacuum magnetic field trap led to the birth of the so-called Penning Malmberg Surko traps (often known simply as Surko traps). These devices take advantage of the very narrow region of energies, where in nitrogen electronic excitation can compete and even overpower the otherwise dominant (for almost all other gases and inelastic processes) positronium (Ps) formation (Murphy and Surko 1992, Cassidy *et al* 2006, Clarke *et al* 2006, Sullivan *et al* 2008, Marjanovic *et al* 2011, Danielson *et al* 2015). To be fair, the principles of the trap have been worked out in great detail, but mostly based on beam-like considerations (Murphy and Surko 1992, Charlton and Humberston 2000). However the device consists of a charge being released in a gas in the presence of electric and magnetic fields, and thus it is an ionized gas that is exactly described by a swarm model until the space charge effects begin to play a significant role, and then it is best described by a plasma model (again with a significant reference to collisions and transport). Thus, for quantitative representation and accurate modeling of traps, a swarm-like model is required and recently two such models were used to explain the salient features of Surko traps (Marjanović *et al* 2011, Petrović *et al* 2014, Natisin *et al* 2015). An explanation and quantitative comparisons will be the subject of a specialized publication (Marjanović and Petrović 2016). Here we only focus on the development of the energy distribution function, which is the primary medium connecting the large-scale behavior of the trap with microscopic binary collisions.

As pressures used in the gas-filled traps are very low, and the mean free paths become comparable to the dimensions of the trap, one may be assured that the description at the level of transport coefficients and fluid models would fail. This example thus requires a full kinetic level of description.

The generic (model) trap consists of three stages, each with a 10 V potential drop and each of the same length (figure 9). The properties, the pressures and other features are listed in table 1. A standard, well-tested (for electron benchmarks—Lucas and Saelee 1975, Reid 1979, Ness and Robson 1986, Raspopović *et al* 1999) Monte Carlo code has been used here. Realistic geometry was included along with the boundary conditions (potentials, energy distributions and losses). Special care was given to the testing of the modeling of trajectories in magnetic fields (Raspopović *et al* 1999 Dujko *et al* 2005).

First results are shown in figure 10 where we plot mean energies as a function of time in three separate stages (chambers) and also averaged for the entire volume. The energy steps provided by the potential drops are observable for the mean energies in stages II and III. The overall increase in energy is also observed in the total volume average. The initial plateau of the mean energy is extended mainly due to
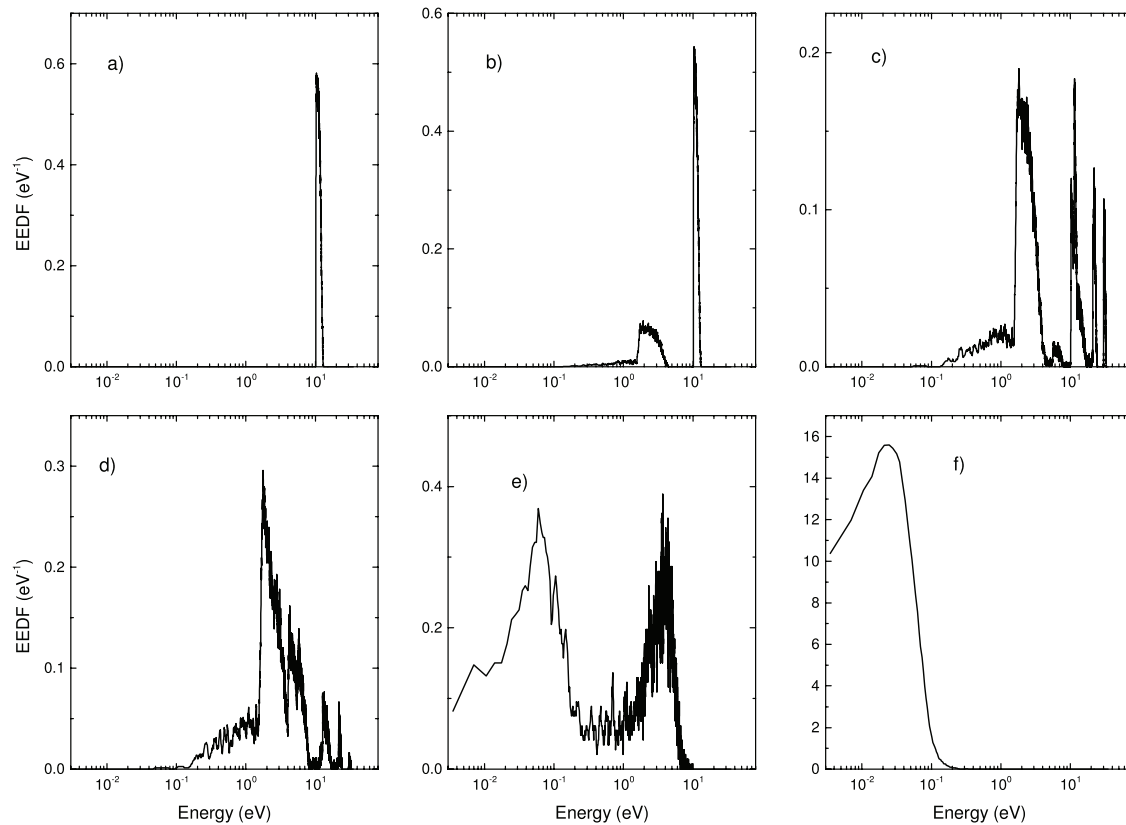
Figure 11. Positron kinetic energy distribution of the entire swarm sampled at different times (indicated in figure 10). Calculations were performed for the Surko trap as shown in figure 9 with the conditions listed in table 1.

the logarithmic nature of the plot. Following another plateau due to inelastic energy losses, the mean energy falls to the thermal value for the final thermalization.

The voltage drop in the initial stage is used to accelerate the positrons coming from the moderator into the energy range where electronic excitation of nitrogen is as efficient as Ps formation. Thus the initial distribution in figure 11 is a mono-energetic beam at 10 eV. Upon development of the group of positrons that have lost energy in excitation (figure 11(b)), positrons leave the stage I and pass into stages II and III so the two new peaks develop at 20 eV and 30 eV (figure 11(c)). The positrons that have collided form a group peaking at around 2 eV. During the next period two processes are obvious. The first is the quenching of the initial beams into the group, peaking at around 2 eV but extending up to 7 eV, where Ps formation removes the particles. The second is the process that uses vibrational excitation of CF_4 and thermalizes the 2 eV group into a low-energy group peaking at around 0.07 eV (figures 11(d) and (e)). It is interesting to see that the peak at around 2 eV is the first to disappear, leaving a group at around 5 eV to thermalize more slowly. At this point the low-energy positrons are also mainly localized in the third stage.

The final stage is characterized by two processes, the disappearance of the higher-energy group at around 5 eV and the gradual thermalization of the low-energy group at around 70 meV towards the thermal energy (*f*) of around 40 meV. At that point a quasi-thermal Maxwellian is developed. The transition appears to be rapid but, by the virtue of a logarithmic plot, it is the longest transition in the process of thermalization and

involves bouncing between the potential boundaries of the third stage many times. At the same time one should see that the properties of the trap are adjusted so that in the first bounce across the three stages most particles suffer electronic excitation/Ps formation collisions and either disappear or are trapped.

The simulation provides many different properties of the positron ensemble (swarm) but the point of this paper is to show a direct connection between binary collision processes and the macroscopic behavior. Using the energy distribution one can easily see the dominant processes and predict which aspects of the processes are promoted by the clever design of the Surko trap. It may also be used to optimize its characteristics (Marjanović *et al* 2016). Nevertheless, the principles of the trap were properly understood from the initial concepts but in this case we have detailed representation of the energy distribution, allowing accurate quantitative comparisons. For example, one may now adjust the details of the cross section in order to fit the measured properties (such as sampled mean energy that may be somewhat skewed by the sampling process). In that respect the measured observables from the trap may play a role in the swarm data that need to be fitted in order to tune the cross sections so that the number, momentum and energy balances may be preserved. As analysis of the positron swarm data led to a number of complex kinetic effects (Banković *et al* 2009, 2012) it would be interesting to see whether similar effects may be observed or even affect the operation of the traps.

These results are akin to the well-established initial equilibration for electrons in gases (Dujko *et al* 2014) with

temporal and spatial Holst Oosterhuis luminous layers (Hayashi 1982, Fletcher 1985) that are strongly related to the well-known Frank Hertz experiment (White *et al* 2012, Robson 2014). In addition, it must be noted that even if we were to start simulation with a Maxwellian distribution and try to follow the thermalization, due to the sharp energy dependence of the processes non-Maxwellian distribution function, it would develop immediately making it necessary to employ a full kinetic treatment. While fluid equations will not work well under the circumstances, and while transport coefficients may be difficult to define and even more difficult to implement in modeling, kinetic (Monte Carlo) modeling is still a typical swarm-like model that needs to be employed. Once we fill the trap with sufficient charge to allow for plasma effects, then we may need to add-in true plasma modeling based on fluid equations and on the calculation of the effective fields.

5. Conclusion

In this review we address three recent examples on how swarm based modeling may connect the microscopic binary processes to the macroscopic behavior of ionized gases, even plasmas. The necessary prerequisite for this approach to be effective is that the systems belong to the so-called collisional plasmas (also known as the non-equilibrium or low-temperature plasmas). The examples are chosen to reveal three different aspects of swarm modeling: (a) that based on transport coefficients and fluid models and how they may be improved, (b) a system that may be described by both fluid models and simulations where simulations are used here to verify the more basic modeling, while the fluid modeling is allowing us to extend predictions further to plasma conditions, and, finally, (c) for the situation where full kinetic modeling is required. Thus, these examples should be viewed as confirmation of the validity and usefulness of the swarm models that are often overlooked by plasma modelers. Swarm models are sometimes regarded as a limit that is unrealistic and useful only to describe well-designed experiments that provide swarm data. One subscribing to that view would then need to reply to why the use of swarm data and also swarm data based fluid equations is so successful. In fact, we believe that often an 'overkill' is performed by using plasma models to describe inherently swarm-like conditions. One such example is the popular modeling of breakdown by PIC of hybrid codes. If done properly, it is all fine, although less transparent due to a more complex nature of the codes. However, at the same time such complexity does not allow us to add special tests or sampling that may reveal more insight into the pertinent physical processes. Examples may include details of the energy distribution function, adjusting boundary conditions to include detailed representation of surface processes and observation and inclusion of the kinetic phenomena.

In doing modeling of low-temperature plasmas that may need to go both more towards the swarm-like and plasma conditions we would strongly recommend that all the plasma codes need to be verified against swarm benchmarks and include sampling of relevant data. It all may become more and more difficult as one develops codes for inhomogeneous systems with complex geometry, but in the limit of a simple geometry and simple swarm conditions all swarm benchmarks should be satisfied to the highest of accuracy.

This article may be viewed as an extension of an article that has been recently submitted for a special issue on plasma modeling covering physical situations where swarm type models are valid and useful and accurate. There is no overlap of the two papers, although a common idea of the need to present the usefulness of the swarm model is obvious. The focus here is more on how elementary processes are producing an intermediate realm of phenomenology (swarm models and properties) that then clearly point at the macroscopic behavior. Be it sprite propagation or positron traps these connections not only reveal relevant physics, but also provide a means to tailor applications based on elementary processes and low-temperature plasmas.

References

Banković A, Dujko S, White R D, Marler J P, Buckman S J, Marjanović S, Malović G, Garcia G and Petrović Z Lj 2012 *New J. Phys.* **14** 035003

Banković A, Petrović Z Lj, Robson R E, Marler J P, Dujko S and Malović G 2009 *Nucl. Instrum. Methods Phys. Res.* B **267** 350–3

Barut A O and Raczka R 1980 *Theory of Group Representations and Applications* (Warszawa, PWN: Polish Scientific Publishers)

Blevin H A, Fletcher J and Hunter S R 1976 *J. Phys. D: Appl. Phys.* **9** 471

Blevin H A, Fletcher J and Hunter S R 1978 *Aust. J. Phys* **31** 299

Bošnjaković D, Petrović Z Lj and Dujko S 2014b *J. Instrum.* **9** P09012

Bošnjaković D, Petrović Z Lj and Dujko S 2016 *J. Phys. D: Appl. Phys.* **49** 405201

Bošnjaković D, Petrović Z Lj, White R D and Dujko S 2014a *J. Phys. D: Appl. Phys.* **47** 435203

Cassidy D B, Deng S H M, Greaves R G and Mills A P 2006 *Rev. Sci. Instrum.* **77** 073106

Charlton M and Humberston J 2000 *Positron Physics* (New York: Cambridge University)

Clarke J, van der Werf D P, Griffiths B, Beddows D C S, Charlton M, Telle H H and Watkeys P R 2006 *Rev. Sci. Instrum.* **77** 063302

Danielson J R, Dubin D H E, Greaves R G and Surko C M 2015 *Rev. Mod. Phys.* **87** 247–306

Denman C A and Schlie L A 1990 Nonequilibrium effects in ion and electron transport *Proc. of the 6th Int. Swarm Seminar (Glen Cove, NY, 1989)* ed J W Gallagher *et al* (New York: Springer)

Dujko S, Markosyan A H, White R D and Ebert U 2013 *J. Phys. D: Appl. Phys.* **46** 475202

Dujko S, Raspopović Z M and Petrović Z Lj 2005 *J. Phys. D: Appl. Phys.* **38** 2952–66

Dujko S, Raspopović Z M, White R D, Makabe T and Petrović Z Lj 2014 *Eur. Phys. J.* D **68** 166

Dujko S, White R D, Petrović Z Lj and Robson R E 2010 *Phys. Rev.* E **81** 046403

Fletcher J 1985 *J. Phys. D: Appl. Phys.* **18** 221–8

Hayashi M 1982 *J. Phys. D: Appl. Phys.* **15** 1411–8

Hunter S R 1977 *PhD Thesis* Flinders University, Adelaide, Australia unpublished

Koutselos A D 1997 *J. Chem. Phys.* **106** 7117–23

Koutselos A D 2001 *Chem. Phys.* **270** 165–175

Lippmann C and Riegler W 2004 *Nucl. Instrum. Methods Phys. Res.* A **533** 11–5

Lucas J and Saelee H T 1975 *J. Phys. D: Appl. Phys.* **8** 640–50

Marjanović S, Banković A, Cassidy D, Cooper B, Deller A, Dujko S and Petrović Z Lj 2016 *J. Phys. B: At. Mol. Opt. Phys.* **49** 215001

Marjanovic S, Šuvakov M, Bankovic A, Savic M, Malovic G, Buckman S J and Petrovic Z Lj 2011 *IEEE Trans. Plasma Sci.* **39** 2614–5

Marjanović S and Petrović Z Lj 2016 *Plasma Sources Sci. Technol.* submitted

Moshaii A, Khosravi Khorashad L, Eskandari M and Hosseini S 2012 *Nucl. Instrum. Methods Phys. Res.* A **661** S168–71

Murphy T J and Surko C M 1992 *Phys. Rev.* A **46** 5696–705

Natisin M R, Danielson J R and Surko C M 2015 *Phys. Plasmas* **22** 033501

Ness K F, Robson R E 1986 *Transp. Theor. Stat. Phys.* **14** 257–90

Penetrante B M and Bardsley J N 1990 *Nonequilibrium Effects in Ion and Electron Transport* ed J W Gallagher *et al* pp 49–66 (New York: Plenum)

Petrović Z Lj, Dujko S, Marić D, Malović G, Nikitović Ž, Šašić O, Jovanović J, Stojanović V and Radmilović-Rađenović M 2009 *J. Phys. D: Appl. Phys.* **42** 194002

Petrović Z Lj *et al* 2014 *J. Phys.: Conf. Ser.* **488** 012047

Raspopović Z M, Sakadžić S, Bzenić S and Petrović Z Lj 1999 *IEEE Trans. Plasma Sci.* **27** 1241–8

Reid I D 1979 *Aust. J. Phys.* **32** 231–54

Robson R E, White R D and Hildebrandt M 2014 *Euro. Phys J.* D **68** 188

Robson R E, White R D and Petrović Z Lj 2005 *Rev. Mod. Phys.* **77** 1303

Santonico R 2012 *Nucl. Instrum. Methods Phys. Res.* A **661** S2–5

Simonović I *et al* 2016 unpublished

Šašić O, Malović G, Strinić A, Nikitović Ž and Petrović Z Lj 2004 *New J. Phys.* **6** 74–85

Sullivan J P, Jones A, Caradonna P, Makochekanwa C and Buckman S J 2008 *Rev. Sci. Instrum.* **79** 113105

Whealton J H and Mason E A 1974 *Ann. Phys.* **84** 8–38

White R D, Robson R E, Nicoletopoulos P and Dujko S 2012 *Eur. Phys. J.* D **66** 117

The ATLAS Collaboration 2008 *J. Instrum.* **3** S08003

Tung W-K 1984 *Group Theory in Physics* (Singapore: World Scientific Publishing)

Vrhovac S B, Petrović Z Lj, Viehland L A and Santhanam T S 1999 *J. Chem. Phys.* **110** 2423–30

9

SCIENTIFIC REP☼RTS

OPEN

Third-order transport coefficients for localised and delocalised charged-particle transport

Peter W. Stokes[1], Ilija Simonović[2], Bronson Philippa [ID][3], Daniel Cocks [ID][1], Saša Dujko[2] & Ronald D. White[1]

We derive third-order transport coefficients of skewness for a phase-space kinetic model that considers the processes of scattering collisions, trapping, detrapping and recombination losses. The resulting expression for the skewness tensor provides an extension to Fick's law which is in turn applied to yield a corresponding generalised advection-diffusion-skewness equation. A physical interpretation of trap-induced skewness is presented and used to describe an observed negative skewness due to traps. A relationship between skewness, diffusion, mobility and temperature is formed by analogy with Einstein's relation. Fractional transport is explored and its effects on the flux transport coefficients are also outlined.

Very little data regarding third-order transport coefficients (the skewness tensor) can be found in the literature. This is understandable, since they have not been included in the interpretations of traditional swarm experiments. There is, however, a growing interest regarding these transport coefficients, partially due to estimations that third-order transport coefficients could be measured in the present or near future[1,2]. It is also considered that third-order transport coefficients would be very useful, in combination with transport coefficients of a lower order, for determination of cross section sets, by means of inverse swarm procedure[1,2]. Third-order transport coefficients are also required for the conversion of the hydrodynamic transport coefficients into transport data measured in steady state Townsend and arrival time spectra experiments[3,4]. The skewness tensor can also be employed in fluid models of discharges, by pairing a generalised diffusion equation, which includes the contributions of the third-order transport coefficients, with Poisson's equation. This could be particularly important for discharges where ions play an important role[5], or in situations where the hydrodynamic approximation is at the limit of applicability, as in the presence of sources and sinks of particles or in the close vicinity of physical boundaries.

In this study, we are concerned with the form of the skewness tensor for charged-particle transport in the presence of trapped (localised) states. In particular, we are interested in the scenario where transport is dispersive. Dispersive transport is characterised by a mean squared displacement that increases sublinearly with time[6]. Due to this non-integer power-law dependence, we refer to dispersive transport as fractional transport throughout this study. Some examples of fractional transport include the trapping of charge carriers in local imperfections in semiconductors[7–11] and both electron[12–14] and positronium[15–17] trapping in bubble states within liquids. Third-order transport coefficients are expected to be more sensitive to the influence of non-conservative collisions than those of lower order, suggesting that the presence of such trapped states would significantly influence the skewness tensor. Indeed, skewness and other higher order transport coefficients are used to characterise fractional transport in a variety of contexts, including transport in biological cells[18–21]. Consider also Fig. 1, which plots the solution of the Caputo fractional advection-diffusion equation, a common model for fractional transport[6]. This solution exhibits a large skewness in comparison to the accompanying Gaussian solution of the corresponding classical advection-diffusion equation.

In the following, we describe charged particle transport using a full phase-space kinetic model as defined by a generalised Boltzmann equation with a corresponding trapping and detrapping operator. In our previous papers[22–24], we introduced and studied such a generalised Boltzmann equation, deriving lower-order transport

[1]College of Science and Engineering, James Cook University, Townsville, QLD 4811, Australia. [2]Institute of Physics, University of Belgrade, PO Box 68, 11080, Zemun, Belgrade, Serbia. [3]College of Science and Engineering, James Cook University, Cairns, QLD 4870, Australia. Correspondence and requests for materials should be addressed to P.W.S. (email: peter.stokes@my.jcu.edu.au)
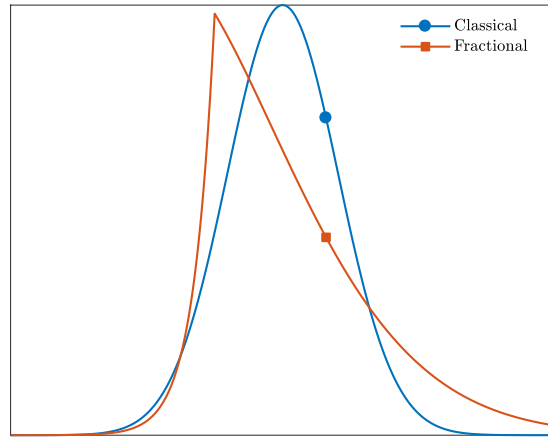
Figure 1. Skewed solution of the Caputo fractional advection-diffusion equation alongside the corresponding Gaussian solution of the classical advection-diffusion equation. Both pulses have evolved from an impulse initial condition. The cusp in the fractional solution denotes the location of this initial impulse.

coefficients (up to diffusion) and generalisations of the Einstein relation. We will extend the results of these papers to determine the skewness tensor. Calculations of the skewness tensor for the Boltzmann equation have been performed previously by a number of authors[2,25–28]. We will use these earlier studies to confirm the structure of the skewness tensor and to benchmark our results in the trap-free case.

In Sec. 2 of this study, we outline a general phase-space kinetic model[23] for charged-particle transport via localised and delocalised states. This model is capable of describing both normal and fractional transport. We follow in Sec. 3 with a derivation of the flux transport coefficients for this model up to third order. Sec. 4 explores the structure of these transport coefficients and their symmetries under parity transformation. The transport coefficients are used to extend Fick's law, which leads to a generalised advection-diffusion-skewness equation, presented in Sec. 5. In this section, we also provide a physical interpretation of trap-induced skewness. By analogy with Einstein's relation, Sec. 6 provides a relation between skewness, diffusion, mobility and temperature. Sec. 7 looks at the case of fractional transport and its effects on the flux transport coefficients. Finally, Sec. 8 lists conclusions along with possible avenues for future work.

Phase-space kinetic model

We previously reported[22–24] the development of a phase-space kinetic model wherein charged particles scatter due to collisions, enter and leave traps and undergo recombination. In this model, free particles are described by a phase-space distribution function $f(t, \mathbf{r}, \mathbf{v})$, defined by the generalised Boltzmann equation

$$
\begin{aligned}
\left(\frac{\partial}{\partial t} + \mathbf{v} \cdot \frac{\partial}{\partial \mathbf{r}} + \frac{e\mathbf{E}}{m} \cdot \frac{\partial}{\partial \mathbf{v}}\right) f(t, \mathbf{r}, \mathbf{v}) =\ & -\nu_{\text{coll}}[f(t, \mathbf{r}, \mathbf{v}) - n(t, \mathbf{r})w(T_{\text{coll}}, v)] \\
& -\nu_{\text{trap}}\Big[f(t, \mathbf{r}, \mathbf{v}) - \Phi(t) * n(t, \mathbf{r})w(T_{\text{detrap}}, v)\Big] \\
& -\nu_{\text{loss}}^{(\text{free})}f(t, \mathbf{r}, \mathbf{v}),
\end{aligned}
\tag{1}
$$

where $\mathbf{E}$ is the applied electric field and particles have charge e, mass m and number density $n(t, \mathbf{r}) \equiv \int d\mathbf{v} f(t, \mathbf{r}, \mathbf{v})$.

Here, collisions, trapping and free particle recombination occur at the constant frequencies ν_{coll}, ν_{trap} and $\nu_{\text{loss}}^{(\text{free})}$, respectively. For collisions, the Bhatnagar—Gross—Krook (BGK) collision operator[29] has been used, which scatters particles isotropically according to a Maxwellian velocity distribution of background temperature T_{coll}. We define the Maxwellian velocity distribution of temperature T as

$$
w(T, v) \equiv \left(\frac{m}{2\pi k_{\text{B}}T}\right)^{\frac{3}{2}} \exp\left(-\frac{mv^2}{2k_{\text{B}}T}\right),
\tag{2}
$$

where k_{B} is the Boltzmann constant. Similarly, we use the BGK-type operator introduced by Philippa et al.[22] to describe the processes of trapping and detrapping. This operator specifies that particles leave traps with a Maxwellian distribution of velocities of temperature T_{detrap} after a delay that is governed by the distribution of trapping times $\phi(t)$. That is, trapping events are described mathematically as delayed scattering events. This distribution appears in Eq. (1) through the effective waiting time distribution

$$
\Phi(t) \equiv e^{-\nu_{\text{loss}}^{(\text{trap})}t}\phi(t),
\tag{3}
$$

that takes into account trapped particle recombination at the frequency $\nu_{\text{loss}}^{(\text{trap})}$.

Transport coefficients to third order

By integrating the generalised Boltzmann equation (1) throughout all of velocity space, we find the equation of continuity for the number density $n(t, \mathbf{r})$:

$$\left[\frac{\partial}{\partial t} + \nu_{\text{trap}}(1 - \Phi(t) *) + \nu_{\text{loss}}^{(\text{free})} \right] n(t, \mathbf{r}) + \frac{\partial}{\partial \mathbf{r}} \cdot \mathbf{\Gamma}(t, \mathbf{r}) = 0, \tag{4}$$

where the particle flux is

$$\mathbf{\Gamma}(t, \mathbf{r}) \equiv \int d\mathbf{v} \, \mathbf{v} f(t, \mathbf{r}, \mathbf{v}). \tag{5}$$

In the weak-gradient hydrodynamic regime, physical quantities can be written as an infinite series of spatial gradients of the number density $n(t, \mathbf{r})$[30,31]. In the case of the flux $\mathbf{\Gamma}(t, \mathbf{r})$, such a density gradient expansion provides a generalisation of Fick's law:

$$\mathbf{\Gamma} = \mathbf{W}n - \mathbf{D} \cdot \frac{\partial n}{\partial \mathbf{r}} + \mathbf{Q} : \frac{\partial^2 n}{\partial \mathbf{r} \partial \mathbf{r}} - \cdots, \tag{6}$$

where $\mathbf{W}$ is the drift velocity vector, $\mathbf{D}$ is the rank-2 diffusion tensor and $\mathbf{Q}$ is the rank-3 skewness tensor. To determine these flux transport coefficients it is simply a matter of writing the solution of the generalised Boltzmann equation (1) itself as a density gradient expansion

$$f(t, \mathbf{r}, \mathbf{v}) = f^{(0)}(\mathbf{v})n + \mathbf{f}^{(1)}(\mathbf{v}) \cdot \frac{\partial n}{\partial \mathbf{r}} + \mathbf{f}^{(2)}(\mathbf{v}) : \frac{\partial^2 n}{\partial \mathbf{r} \partial \mathbf{r}} + \cdots, \tag{7}$$

and then evaluating the flux using Eq. (5), resulting in the transport coefficients

$$\mathbf{W} \equiv \int d\mathbf{v} \, \mathbf{v} f^{(0)}(\mathbf{v}), \tag{8}$$

$$\mathbf{D} \equiv \int d\mathbf{v} \, \mathbf{v} \mathbf{f}^{(1)}(\mathbf{v}), \tag{9}$$

$$\mathbf{Q} \equiv \int d\mathbf{v} \, \mathbf{v} \mathbf{f}^{(2)}(\mathbf{v}). \tag{10}$$

Substituting the density gradient expansion of $f(t, \mathbf{r}, \mathbf{v})$ into the Boltzmann equation (1) and equating coefficients of spatial gradients, as done in Sec. IV of ref.[23], gives the following coefficients

$$f^{(0)}(\mathbf{s}) = \frac{\nu_{\text{coll}} w\,(\alpha_{\text{coll}}, s) + R\nu_{\text{trap}} w\,(\alpha_{\text{detrap}}, s)}{\nu_{\text{coll}} + R\nu_{\text{trap}} + \frac{e\mathbf{E}}{m} \cdot \iota \mathbf{s}}, \tag{11}$$

$$\mathbf{f}^{(1)}(\mathbf{s}) = \frac{\nu_{\text{trap}} \mathbf{R}^{(1)} w\,(\alpha_{\text{detrap}}, s) + f^{(0)}(\mathbf{s})\left(\mathbf{W} - \nu_{\text{trap}} \mathbf{R}^{(1)}\right) - \iota \frac{\partial f^{(0)}}{\partial \mathbf{s}}}{\nu_{\text{coll}} + R\nu_{\text{trap}} + \frac{e\mathbf{E}}{m} \cdot \iota \mathbf{s}}, \tag{12}$$

$$\mathbf{f}^{(2)}(\mathbf{s}) = \frac{\nu_{\text{trap}} \mathbf{R}^{(2)} w(\alpha_{\text{detrap}}, s) - f^{(0)}(\mathbf{s})\left(\mathbf{D} + \nu_{\text{trap}} \mathbf{R}^{(2)}\right) + \mathbf{f}^{(1)}(\mathbf{s})\left(\mathbf{W} - \nu_{\text{trap}} \mathbf{R}^{(1)}\right) - \iota \frac{\partial \mathbf{f}^{(1)}}{\partial \mathbf{s}}}{\nu_{\text{coll}} + R\nu_{\text{trap}} + \frac{e\mathbf{E}}{m} \cdot \iota \mathbf{s}}, \tag{13}$$

where a Fourier transform has been performed in velocity space, $f(\mathbf{s}) \equiv \int d\mathbf{v} e^{-\iota \mathbf{s} \cdot \mathbf{v}} f(\mathbf{v})$. As in ref.[23], we have used the density gradient expansion of the concentration of particles leaving traps:

$$\Phi(t) * n(t, \mathbf{r}) = Rn + \mathbf{R}^{(1)} \cdot \frac{\partial n}{\partial \mathbf{r}} + \mathbf{R}^{(2)} : \frac{\partial^2 n}{\partial \mathbf{r} \partial \mathbf{r}} + \cdots, \tag{14}$$

the coefficients of which are related to the flux transport coefficients through

$$\mathbf{R}^{(1)} \equiv \frac{R\langle t \rangle}{1 + \nu_{\text{trap}} R\langle t \rangle} \mathbf{W}, \tag{15}$$

$$\mathbf{R}^{(2)} \equiv \frac{R\langle t^2 \rangle}{2\left(1 + \nu_{\text{trap}} R\langle t \rangle\right)^3} \mathbf{W}\mathbf{W} - \frac{R\langle t \rangle}{1 + \nu_{\text{trap}} R\langle t \rangle} \mathbf{D}, \tag{16}$$

where the time averages are defined

$$\langle \eta\,(t) \rangle \equiv \frac{1}{R} \int_0^\infty \mathrm{d}t \Phi(t)\,\mathrm{e}^{\left[\nu_{\mathrm{loss}}^{(\mathrm{free})} + \nu_{\mathrm{trap}}(1-R)\right]t} \eta(t). \tag{17}$$

Applying this time average to unity results in an implicit definition for the initial coefficient R:

$$R \equiv \int_0^\infty \mathrm{d}t \Phi(t)\mathrm{e}^{\left[\nu_{\mathrm{loss}}^{(\mathrm{free})} + \nu_{\mathrm{trap}}(1-R)\right]t}. \tag{18}$$

Thus, for every trapping time distribution $\phi(t)$ there corresponds a value of R. Some values are tabulated in Appendix A of ref.[23].

Proceeding to evaluate Eqs (8–10) for the transport coefficients, we find

$$\mathbf{W} \equiv \frac{e\mathbf{E}}{m\nu_{\mathrm{eff}}}, \tag{19}$$

$$\mathbf{D} \equiv \frac{1}{\nu_{\mathrm{eff}}} \left(\frac{k_{\mathrm{B}} T_{\mathrm{eff}}}{m} \mathbf{I} + \frac{1 + 2\nu_{\mathrm{trap}} R\langle t \rangle}{1 + \nu_{\mathrm{trap}} R\langle t \rangle} \mathbf{WW} \right), \tag{20}$$

$$\begin{aligned} \mathbf{Q} \equiv & \left[1 + \left(\frac{1 + 2\nu_{\mathrm{trap}} R\langle t \rangle}{1 + \nu_{\mathrm{trap}} R\langle t \rangle} \right)^2 - \frac{\nu_{\mathrm{trap}} R\langle t^2 \rangle}{4(1 + \nu_{\mathrm{trap}} R\langle t \rangle)^3} \nu_{\mathrm{eff}} \right] \frac{2\mathbf{WWW}}{\nu_{\mathrm{eff}}^2} \\ & + \frac{1 + 2\nu_{\mathrm{trap}} R\langle t \rangle}{1 + \nu_{\mathrm{trap}} R\langle t \rangle} \frac{k_{\mathrm{B}} T_{\mathrm{eff}}}{m\nu_{\mathrm{eff}}^2} (\mathbf{IW} + \mathbf{e}_1 \mathbf{We}_1 + \mathbf{e}_2 \mathbf{We}_2 + \mathbf{e}_3 \mathbf{We}_3) \\ & + \frac{\nu_{\mathrm{trap}} R\langle t \rangle}{1 + \nu_{\mathrm{trap}} R\langle t \rangle} \frac{\nu_{\mathrm{coll}}}{\nu_{\mathrm{eff}}} \frac{k_{\mathrm{B}}(T_{\mathrm{coll}} - T_{\mathrm{detrap}})}{m\nu_{\mathrm{eff}}} \frac{\mathbf{WI}}{\nu_{\mathrm{eff}}}, \end{aligned} \tag{21}$$

where $\mathbf{e}_1$, $\mathbf{e}_2$ and $\mathbf{e}_3$ are standard orthonormal basis vectors and we have introduced the effective frequency and temperature:

$$\nu_{\mathrm{eff}} \equiv \nu_{\mathrm{coll}} + R\nu_{\mathrm{trap}}, \tag{22}$$

$$T_{\mathrm{eff}} \equiv \frac{\nu_{\mathrm{coll}} T_{\mathrm{coll}} + R\nu_{\mathrm{trap}} T_{\mathrm{detrap}}}{\nu_{\mathrm{coll}} + R\nu_{\mathrm{trap}}}. \tag{23}$$

We confirm that when there are no traps present, $\nu_{\mathrm{trap}} = 0$, the transport coefficients agree with those of the BGK collision model, previously found by Robson[26]:

$$\mathbf{W} \equiv \frac{e\mathbf{E}}{m\nu_{\mathrm{coll}}}, \tag{24}$$

$$\mathbf{D} \equiv \frac{1}{\nu_{\mathrm{coll}}} \left(\frac{k_{\mathrm{B}} T_{\mathrm{coll}}}{m} \mathbf{I} + \mathbf{WW} \right), \tag{25}$$

$$\mathbf{Q} \equiv \frac{1}{\nu_{\mathrm{coll}}^2} \left[\frac{k_{\mathrm{B}} T_{\mathrm{coll}}}{m} (\mathbf{IW} + \mathbf{e}_1 \mathbf{We}_1 + \mathbf{e}_2 \mathbf{We}_2 + \mathbf{e}_3 \mathbf{We}_3) + 4\mathbf{WWW} \right]. \tag{26}$$

Structure and Symmetry of Transport Coefficients

If we align the basis vector $\mathbf{e}_3$ parallel to the applied electric field $\mathbf{E}$, the transport coefficients (19–21) take on the known tensor structure[2,25,28,30,31]:

$$\mathbf{W} \equiv \begin{bmatrix} 0 \\ 0 \\ W \end{bmatrix}, \tag{27}$$

$$\mathbf{D} \equiv \begin{bmatrix} D_\perp & 0 & 0 \\ 0 & D_\perp & 0 \\ 0 & 0 & D_\parallel \end{bmatrix} \tag{28}$$

$$\mathbf{Q}_{xab} \equiv \begin{bmatrix} 0 & 0 & Q_1 \\ 0 & 0 & 0 \\ Q_1 & 0 & 0 \end{bmatrix},$$

(29)

$$\mathbf{Q}_{yab} \equiv \begin{bmatrix} 0 & 0 & 0 \\ 0 & 0 & Q_1 \\ 0 & Q_1 & 0 \end{bmatrix},$$

(30)

$$\mathbf{Q}_{zab} \equiv \begin{bmatrix} Q_2 & 0 & 0 \\ 0 & Q_2 & 0 \\ 0 & 0 & 2Q_1 + Q_2 + Q_3 \end{bmatrix},$$

(31)

where $a, b \in \{x, y, z\}$. Here, the drift velocity is defined by the speed

$$W \equiv \frac{eE}{m\nu_{\text{eff}}},$$

(32)

the diffusion coefficient is defined by two components perpendicular and parallel to the field

$$D_\perp \equiv \frac{k_B T_{\text{eff}}}{m\nu_{\text{eff}}},$$

(33)

$$D_\parallel \equiv D_\perp + \frac{1 + 2\nu_{\text{trap}}R\langle t\rangle}{1 + \nu_{\text{trap}}R\langle t\rangle} \frac{W^2}{\nu_{\text{eff}}},$$

(34)

and the skewness is defined by the three independent components

$$Q_1 \equiv \frac{1 + 2\nu_{\text{trap}}R\langle t\rangle}{1 + \nu_{\text{trap}}R\langle t\rangle} \frac{k_B T_{\text{eff}}}{m\nu_{\text{eff}}} \frac{W}{\nu_{\text{eff}}},$$

(35)

$$Q_2 \equiv \frac{\nu_{\text{trap}}R\langle t\rangle}{1 + \nu_{\text{trap}}R\langle t\rangle} \frac{\nu_{\text{coll}}}{\nu_{\text{eff}}} \frac{k_B(T_{\text{coll}} - T_{\text{detrap}})}{m\nu_{\text{eff}}} \frac{W}{\nu_{\text{eff}}},$$

(36)

$$Q_3 \equiv \left[1 + \left(\frac{1 + 2\nu_{\text{trap}}R\langle t\rangle}{1 + \nu_{\text{trap}}R\langle t\rangle} \right)^2 - \frac{\nu_{\text{trap}}R\langle t^2\rangle}{4(1 + \nu_{\text{trap}}R\langle t\rangle)^3}\nu_{\text{eff}} \right] \frac{2W^3}{\nu_{\text{eff}}^2}.$$

(37)

Although this is the case in general, there are situations where the skewness can be defined using fewer than three components. Indeed, this is the case for the BGK model as studied by Robson[26] where the skewness given by Eq. (26) is defined using only the components Q_1 and Q_3, with $Q_2 = 0$. The component Q_2 vanishes in this case due to the simple Maxwellian source term used to describe scattered particles. For Q_2 to arise, it is necessary that this source term has some spatial dependence, as occurs for our model through the concentration of particles leaving traps, $\varphi(t) * n(t, \mathbf{r})$, and its density gradient expansion (14).

Lastly, we also confirm that the symmetry of transport coefficients with respect to the parity transformation $\mathbf{E} \to -\mathbf{E}$ depends on the parity of the order of each transport coefficient[25,32]:

$$\mathbf{W} \to -\mathbf{W},$$

(38)

$$\mathbf{D} \to \mathbf{D},$$

(39)

$$\mathbf{Q} \to -\mathbf{Q}.$$

(40)

Generalised Advection-diffusion-skewness Equation

Using the density gradient expansion (6) for the flux $\mathbf{\Gamma}(t, \mathbf{r})$ up to second spatial order in conjunction with the continuity equation (4) results in the generalised advection-diffusion-skewness equation

$$\left[\frac{\partial}{\partial t} + \nu_{\text{trap}}(1 - \Phi(t)*) + \nu_{\text{loss}}^{(\text{free})} \right] n(t, \mathbf{r}) + \mathbf{W} \cdot \frac{\partial n}{\partial \mathbf{r}} - \mathbf{D} : \frac{\partial^2 n}{\partial \mathbf{r}\partial \mathbf{r}} + \mathbf{Q} \vdots \frac{\partial^3 n}{\partial \mathbf{r}\partial \mathbf{r}\partial \mathbf{r}} = 0,$$

(41)

valid in the weak-gradient hydrodynamic regime. In Cartesian coordinates (x, y, z) with the electric field **E** aligned in the z-direction, the transport coefficients take the form of Eqs (27–31) and the advection-diffusion-skewness equation becomes

$$\left[\frac{\partial}{\partial t} + \nu_{\text{trap}}(1 - \Phi(t)*) + \nu_{\text{loss}}^{(\text{free})}\right] n(t, x, y, z) + W\frac{\partial n}{\partial z} - D_\perp\left(\frac{\partial^2 n}{\partial x^2} + \frac{\partial^2 n}{\partial y^2}\right) - D_\parallel \frac{\partial^2 n}{\partial z^2}$$
$$+ 3Q_\perp\left(\frac{\partial^2}{\partial x^2} + \frac{\partial^2}{\partial y^2}\right)\frac{\partial n}{\partial z} + Q_\parallel\frac{\partial^3 n}{\partial z^3} = 0, \tag{42}$$

where the skewness manifests as components perpendicular and parallel to the applied field[2,5,28]:

$$Q_\perp \equiv \frac{Q_{zxx} + Q_{xzx} + Q_{xxz}}{3}, \tag{43}$$

$$Q_\parallel \equiv Q_{zzz}, \tag{44}$$

which in terms of the independent components (35–37) are

$$Q_\perp = \frac{2Q_1 + Q_2}{3}, \tag{45}$$

$$Q_\parallel = 2Q_1 + Q_2 + Q_3. \tag{46}$$

Written in full, the perpendicular and parallel skewnesses are

$$Q_\perp = \frac{2D_\perp W}{3\nu_{\text{eff}}}$$
$$+ \frac{\nu_{\text{trap}}R\langle t\rangle}{1 + \nu_{\text{trap}}R\langle t\rangle}\left(D_\perp - \frac{k_B T_{\text{detrap}}}{3m\nu_{\text{eff}}}\right)\frac{W}{\nu_{\text{eff}}}, \tag{47}$$

$$Q_\parallel = 3Q_\perp + \frac{4W^3}{\nu_{\text{eff}}^2}$$
$$+ \frac{\nu_{\text{trap}}R\langle t\rangle}{1 + \nu_{\text{trap}}R\langle t\rangle}\left[6 - \frac{2}{1 + \nu_{\text{trap}}R\langle t\rangle} - \frac{\nu_{\text{eff}}\langle t^2\rangle}{2\langle t\rangle(1 + \nu_{\text{trap}}R\langle t\rangle)^2}\right]\frac{W^3}{\nu_{\text{eff}}^2}, \tag{48}$$

where terms present due to trapping have been grouped separately and the lower-order transport coefficients (32–34) have been used to simplify. An alternative form of the skewness tensor that makes use of these components explicitly is

$$\tilde{\mathbf{Q}}_{xab} \equiv \begin{bmatrix} 0 & 0 & 0 \\ 0 & 0 & 0 \\ 0 & 0 & 0 \end{bmatrix}, \tag{49}$$

$$\tilde{\mathbf{Q}}_{yab} \equiv \begin{bmatrix} 0 & 0 & 0 \\ 0 & 0 & 0 \\ 0 & 0 & 0 \end{bmatrix}, \tag{50}$$

$$\tilde{\mathbf{Q}}_{zab} \equiv \begin{bmatrix} 3Q_\perp & 0 & 0 \\ 0 & 3Q_\perp & 0 \\ 0 & 0 & Q_\parallel \end{bmatrix}, \tag{51}$$

where $a, b \in \{x, y, z\}$. This form was used by Robson[26] when expressing the BGK model skewness (26) and is valid only when the skewness is triple-contracted with a symmetric tensor, as occurs in the advection-diffusion-skewness equation (41).

To provide some physical intuition regarding the perpendicular and parallel skewness coefficients, $Q_\perp$ and $Q_\parallel$, we solve the advection-diffusion-skewness equation (42) for an impulse initial condition and perform contour plots of the resulting pulse in Fig. 2. Figure 2(a) considers the case of no skewness, $Q_\perp = Q_\parallel = 0$, and displays the expected Gaussian solution with elliptical contours due to anisotropic diffusion. Figure 2(b) and (c) consider positive perpendicular and parallel skewnesses, respectively. In both cases, it can be seen that skewness introduces asymmetry in the pulse in the direction of the field. In general, positive skewness can be seen to reduce the spread of particles behind the pulse, while enhancing the spread toward the front of the pulse. In Fig. 2(b) for positive perpendicular skewness, this change in particle spread primarily occurs transverse to the field, resulting in a
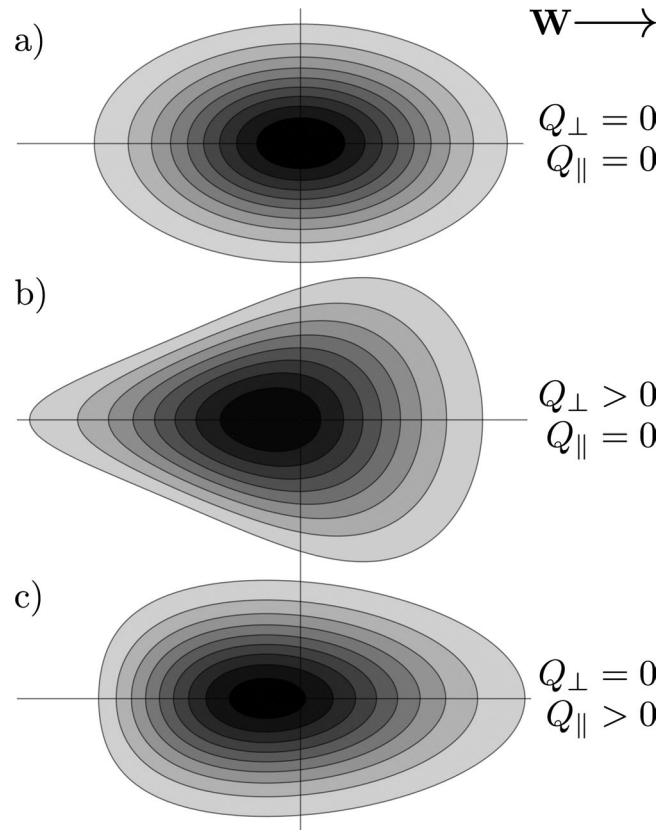
Figure 2. Contours of constant number density as defined by the advection-diffusion-skewness equation (42) with drift velocity **W** and anisotropic diffusion $D_\parallel > D_\perp > 0$ for no skewness, (**a**), positive perpendicular skewness, (**b**), and positive parallel skewness, (**c**). Each profile has evolved from an impulse initial condition. As the skewness tensor is odd under parity transformation, Eq. (40), the case of negative skewness can be considered by reflecting the above profiles horizontally across the vertical axis.

vaguely triangular pulse profile. In Fig. 2(c) for positive parallel skewness, this change in particle spread occurs longitudinally which, in the language of statistics, results in a distribution with positive skew.

In our previous paper[23], we interpreted the trap-induced anisotropic diffusion present in Eq. (34) as a consequence of the physical separation between trapped particles and free particles moving with the field. In a similar fashion, we can interpret the trap-induced skewness present in the perpendicular and parallel skewness coefficients (47) and (48). To achieve this, we plot the skewness against the detrapping temperature T_{detrap} for various mean trapping times in Fig. 3. The resulting plots are linear with gradients that characterise of the type of skewness caused by traps. That is, positive or negative gradients correspond respectively to positive or negative trap-based skewness.

When the mean trapping time is zero, the gradients in Fig. 3 are positive and traps cause positive skewness. This is to be expected as, in this case, trapping and detrapping simply act as an elastic scattering process with a positive skewness akin to Eq. (26) for the BGK collision model. As the mean trapping time increases, the nature of the skewness caused by traps changes, ultimately becoming negative for the parameters considered in Fig. 3. As illustrated in Fig. 2, negative skewness corresponds to an increased spread of particles behind the pulse. We interpret the increased spread here as being due to particles returning from traps. This interpretation implies that the skewness coefficients could become overall negative if particles remain trapped for a sufficient length of time before returning with a sufficiently large temperature. Indeed, these are the conditions for which the skewness coefficients become negative in Fig. 3.

This phenomenon of negative skewness has been observed previously by Petrović *et al.*[5] in the calculation of the perpendicular skewness of electrons in methane. Only collisions were considered in this study and so trapping is evidently not a necessary condition for negative skewness to occur. However, it should be emphasised that the skewness is strictly positive when collisions are described by the simple BGK collision operator, as is seen in Eq. (26).

Relating skewness, mobility and temperature

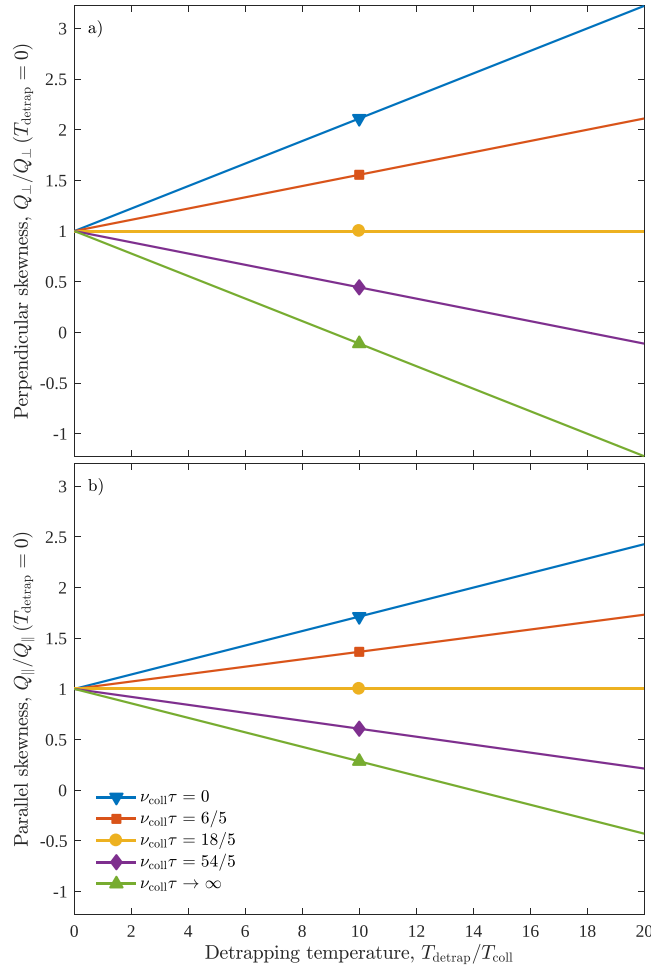The classical Einstein relation between diffusion, mobility and temperature is[33]

Figure 3. Linear plots of perpendicular and parallel skewness coefficients, $Q_\perp$ and $Q_{\parallel}$, versus the detrapping temperature T_{detrap}. Here, traps are described by an exponential distribution of trapping times $\phi(t) = \frac{1}{\tau}\exp(-\frac{t}{\tau})$, and no recombination is considered, $\nu_{\text{loss}}^{(\text{free})} = \nu_{\text{loss}}^{(\text{trap})} = 0$. To perform these plots, we choose a trapping frequency of $\nu_{\text{trap}}/\nu_{\text{coll}} = 1/9$, while (**b**) also requires that we specify a drift velocity **W**, which we choose such that $mW^2/k_{\text{B}}T_{\text{coll}} = 1/4$. The gradients in (**b**) are of smaller magnitude than (**a**) due to the greater dependence of the parallel skewness (48) on the drift speed W as compared to the perpendicular skewness (47). Thus, as the drift speed decreases, the plots in (**b**) coincide with those in (**a**). When detrapping is instantaneous, $\tau = 0$, the skewness gradients are positive, implying that the skewness caused by traps is also positive. As the mean trapping time τ increases, the skewness gradients decrease, becoming negative and implying a corresponding negative skewness due to traps. The limiting case of an infinite mean trapping time, $\tau \to \infty$, corresponds to fractional transport, which is the subject of Sec. 7. We observe from this figure that the skewness coefficients become overall negative when particles leave traps with a sufficiently large temperature T_{detrap} after a sufficiently long amount of time τ. This observation coincides with the illustration of skewness in Fig. 2 where negative skewness is characterised by an increased particle spread behind the pulse, which we attribute here to particles returning from traps.

$$\frac{\mathbf{D}}{K} = \frac{k_{\text{B}}\mathbf{T}}{e},\tag{52}$$

where K is the mobility defined as satisfying $\mathbf{W} \equiv K\mathbf{E}$ and $\mathbf{T}$ is the rank-2 temperature tensor. As seen by Eq. (20) for the diffusion coefficient, the phase-space model described by Eq. (1) has an enhanced diffusivity in the direction of the field due to trapping and detrapping. This enhancement manifests as the following generalised Einstein relation[24]

$$\frac{\mathbf{D}}{K} = \frac{k_{\text{B}}\mathbf{T}}{e} + \frac{\nu_{\text{trap}}R\langle t\rangle}{1 + \nu_{\text{trap}}R\langle t\rangle}\frac{m\mathbf{WW}}{e}.\tag{53}$$

By relating the skewness to the temperature tensor though this diffusion coefficient, we find a skewness analogue to the Einstein relation:

$$\mathbf{Q} \equiv \left[1 - \frac{\nu_{\text{trap}}R\langle t^2\rangle}{4(1 + \nu_{\text{trap}}R\langle t\rangle)^3}\nu_{\text{eff}}\right]\frac{2\mathbf{WWW}}{\nu_{\text{eff}}^2}$$
$$+\frac{1 + 2\nu_{\text{trap}}R\langle t\rangle}{1 + \nu_{\text{trap}}R\langle t\rangle}\frac{\mathbf{DW} + D_\perp\mathbf{e}_1\mathbf{We}_1 + D_\perp\mathbf{e}_2\mathbf{We}_2 + D_\parallel\mathbf{e}_3\mathbf{We}_3}{\nu_{\text{eff}}}$$
$$+\frac{\nu_{\text{trap}}R\langle t\rangle}{1 + \nu_{\text{trap}}R\langle t\rangle}\frac{\nu_{\text{coll}}}{\nu_{\text{eff}}}\frac{k_{\text{B}}(T_{\text{coll}} - T_{\text{detrap}})}{m\nu_{\text{eff}}}\frac{\mathbf{WI}}{\nu_{\text{eff}}}. \tag{54}$$

Koutselos[34] has presented a similar relationship between the skewness tensor and lower-order transport coefficients for the case of the classical Boltzmann equation.

The case of Fractional Transport

For the phase-space kinetic model described by Eq. (1), fractional transport can occur when the distribution of trapping times has a heavy power-law tail of the form[23]

$$\phi(t) \sim t^{-(1+\alpha)}. \tag{55}$$

Note that, as transport here is dispersive in nature, the mean trapping time diverges:

$$\int_0^\infty \mathrm{d}t\phi(t)t \to \infty. \tag{56}$$

Consequently, the time averages defined by Eq. (17) also diverge, correspondingly affecting the transport coefficients. Thus, for fractional transport, the transport coefficients (19–21) take on the simpler form[23]

$$\mathbf{W} = \frac{e\mathbf{E}}{m\nu_{\text{eff}}}, \tag{57}$$

$$\mathbf{D} = \frac{1}{\nu_{\text{eff}}}\left(\frac{k_{\text{B}}T_{\text{eff}}}{m}\mathbf{I} + 2\mathbf{WW}\right), \tag{58}$$

$$\mathbf{Q} = \frac{2\mathbf{WWW}}{\nu_{\text{eff}}^2}$$
$$+\frac{2\left(\mathbf{DW} + D_\perp\mathbf{e}_1\mathbf{We}_1 + D_\perp\mathbf{e}_2\mathbf{We}_2 + D_\parallel\mathbf{e}_3\mathbf{We}_3\right)}{\nu_{\text{eff}}}$$
$$+\frac{\nu_{\text{coll}}}{\nu_{\text{eff}}}\frac{k_{\text{B}}\left(T_{\text{coll}} - T_{\text{detrap}}\right)}{m\nu_{\text{eff}}}\frac{\mathbf{WI}}{\nu_{\text{eff}}}, \tag{59}$$

where the effective frequency is now defined

$$\nu_{\text{eff}} \equiv \nu_{\text{coll}} + \nu_{\text{trap}} + \nu_{\text{loss}}^{(\text{free})}. \tag{60}$$

Note that transport coefficients are now independent of the specific choice of the trapping time distribution $\phi(t)$, so long as the condition (55) for fractional transport is satisfied.

Knowledge of the skewness coefficient (59), as well as other higher-order transport coefficients, is useful for characterising fractional transport. For example, Norregaard et al.[18] use higher-order moments to analyse the motion of biological particles.

Conclusion

We have explored the transport coefficients of a phase-space kinetic model (1) for both localised and delocalised transport. In particular, we have considered up to the third-order transport coefficient of skewness *bfQ*, which takes the form of a rank-3 tensor. The structure of the skewness tensor and its symmetry under parity transformation was found to be in agreement with previous studies. These transport coefficients provide an extension to Fick's law, Eq. (6), which we used to form a generalised advection-diffusion-skewness equation (41) with a non-local time operator. We observed trap-induced negative skewness and provided a corresponding physical interpretation. In addition, by analogy with Einstein's relation, the skewness was related to the mobility and temperature through Eq. (54). Lastly, the form of the transport coefficients for the particular case of fractional transport were outlined in Eqs (57–59).

There exist a number of possibilities for future work. The focus of this paper was on constant transport coefficients that define the flux in the hydrodynamic regime as the density gradient expansion (6). Transient transport coefficients and transport coefficients of the bulk were not considered. Ref.[23] outlines an analytical solution of the kinetic model (1) that could be used to compute such transport coefficients through time-varying velocity and spatial moments of the phase-space distribution function $f(t, \mathbf{r}, \mathbf{v})$.

Another extension to this work could be to explore what consequences energy-dependent collision, trapping and recombination frequencies have on the skewness. Such a generalisation for Eq. (1) was the focus of ref.[24]. This would allow for the derivation of a skewness analogue of Einstein's relation that would also take into account the field dependence of mobility[24]. This may also shed light on the recent results of Petrović *et al*.[5], that suggest a correlation between the energy-dependent phenomenon of negative differential conductivity and skewness.

Lastly, it is important to note that the extension to Fick's law described in this paper is only useful when an electric field is present. Without an applied field, the drift velocity, skewness and all other odd-ordered transport coefficients would vanish. If we wish to extend Fick's law in such a situation, we must also consider the kurtosis coefficient, the next even-ordered transport coefficient beyond diffusion. The kurtosis can be found in a straightforward fashion from the rank-3 tensorial coefficient $\mathbf{f}^{(3)}(\mathbf{v})$ in the density gradient expansion (7) of the phase-space distribution function $f(t, \mathbf{r}, \mathbf{v})$, in the same way drift velocity, diffusion and skewness were found using Eqs (8–10).

Data availability statement.   No datasets were generated or analysed during the current study.

References

1. Pitchford, L. C., Boeuf, J. P. & Segur, P. *Nonequilibrium Effects in Ion and Electron Transport*, https://doi.org/10.1007/978-1-4613-0661-0 (Springer US, Boston, MA, 1990).
2. Vrhovac, S. B., Petrović, Z. L., Viehland, L. A. & Santhanam, T. S. Third-order transport coefficients for charged particle swarms. *The Journal of Chemical Physics* **110**, 2423–2430 (1999).
3. Dujko, S., White, R. D. & Petrović, Z. L. Monte Carlo studies of non-conservative electron transport in the steady-state Townsend experiment. *Journal of Physics D: Applied Physics* **41**, 245205 (2008).
4. Kondo, K. & Tagashira, H. *Nonequilibrium Effects in Ion and Electron Transport*, vol. 23, http://stacks.iop.org/0022-3727/23/i=9/a=007?key=crossref.fbac2ae31a8a6e5eb9c110f88b4104cb, https://doi.org/10.1007/978-1-4613-0661-0 (Springer US, Boston, MA, 1990).
5. Petrović, Z. L. *et al*. Non-equilibrium of charged particles in swarms and plasmas—from binary collisions to plasma effects. *Plasma Physics and Controlled Fusion* **59**, 014026 (2017).
6. Metzler, R., Barkai, E. & Klafter, J. Anomalous Diffusion and Relaxation Close to Thermal Equilibrium: A Fractional Fokker-Planck Equation Approach. *Physical Review Letters* **82**, 3563–3567 (1999).
7. Scher, H. & Montroll, E. W. Anomalous transit-time dispersion in amorphous solids. *Physical Review B* **12**, 2455–2477 (1975).
8. Sibatov, R. T. & Uchaikin, V. V. Fractional differential kinetics of charge transport in unordered semiconductors. *Semiconductors* **41**, 335–340 (2007).
9. Schubert, M. *et al*. Mobility relaxation and electron trapping in a donor/acceptor copolymer. *Physical Review B* **87**, 024203 (2013).
10. Krüsemann, H., Godec, A. & Metzler, R. First-passage statistics for aging diffusion in systems with annealed and quenched disorder. *Physical Review E* **89**, 040101 (2014).
11. Krüsemann, H., Schwarzl, R. & Metzler, R. Ageing Scher–Montroll Transport. *Transport in Porous Media* **115**, 327–344 (2016).
12. Mauracher, A. *et al*. Detection of Negative Charge Carriers in Superfluid Helium Droplets: The Metastable Anions He *– and He 2 *–. *The Journal of Physical Chemistry Letters* **5**, 2444–2449 (2014).
13. Borghesani, A. F. & Santini, M. High-temperature electron localization in dense He gas. *Physical Review E* **65**, 056403 (2002).
14. Sakai, Y., Schmidt, W. F. & Khrapak, A. High- and low-mobility electrons in liquid neon. *Chemical Physics* **164**, 139–152 (1992).
15. Stepanov, S. V. *et al*. Positronium in a Liquid Phase: Formation, Bubble State and Chemical Reactions. *Advances in Physical Chemistry* **2012**, 1–17 (2012).
16. Stepanov, S. V. *et al*. A molecular basis of the bubble model of positronium annihilation in liquids. *Physica B: Condensed Matter* **322**, 68–79 (2002).
17. Charlton, M. & Humberston, J. W. *Positron Physics*, https://www.cambridge.org/core/product/identifier/9780511535208/type/book (Cambridge University Press, Cambridge, 2000).
18. Norregaard, K., Metzler, R., Ritter, C. M., Berg-Sørensen, K. & Oddershede, L. B. Manipulation and Motion of Organelles and Single Molecules in Living Cells. *Chemical Reviews* **117**, 4342–4375 (2017).
19. Schwarzl, M., Godec, A. & Metzler, R. Quantifying non-ergodicity of anomalous diffusion with higher order moments. *Scientific Reports* **7**, 3878 (2017).
20. Höfling, F. & Franosch, T. Anomalous transport in the crowded world of biological cells. *Reports on Progress in Physics* **76**, 046602 (2013).
21. Magdziarz, M., Weron, A., Burnecki, K. & Klafter, J. Fractional Brownian Motion Versus the Continuous-Time Random Walk: A Simple Test for Subdiffusive Dynamics. *Physical Review Letters* **103**, 180602 (2009).
22. Philippa, B., Robson, R. E. & White, R. D. Generalized phase-space kinetic and diffusion equations for classical and dispersive transport. *New Journal of Physics* **16**, 073040 (2014).
23. Stokes, P. W., Philippa, B., Cocks, D. & White, R. D. Solution of a generalized Boltzmann's equation for nonequilibrium charged-particle transport via localized and delocalized states. *Physical Review E* **93**, 032119 (2016).
24. Stokes, P. W., Philippa, B., Cocks, D. & White, R. D. Generalized balance equations for charged particle transport via localized and delocalized states: Mobility, generalized Einstein relations, and fractional transport. *Physical Review E* **95**, 042119 (2017).
25. Whealton, J. H. & Mason, E. A. Transport coefficients of gaseous ions in an electric field. *Annals of Physics* **84**, 8–38 (1974).
26. Robson, R. Nonlinear Diffusion of Ions in a Gas. *Australian Journal of Physics* **28**, 523 (1975).
27. Larsen, P. H., Skullerud, H. R., Lovaas, T. H. & Stefansson, T. Transport coefficients and interaction potentials for lithium ions in helium and argon. *Journal of Physics B: Atomic, Molecular and Optical Physics* **21**, 2519–2538 (1988).
28. Koutselos, A. D. Third-order transport properties of ions in electrostatic fields. *Chemical Physics* **270**, 165–175 (2001).
29. Bhatnagar, P. L., Gross, E. P. & Krook, M. A Model for Collision Processes in Gases. I. Small Amplitude Processes in Charged and Neutral One-Component Systems. *Physical Review* **94**, 511–525 (1954).
30. Robson, R. E. *Introductory Transport Theory for Charged Particles in Gases*, http://www.worldscientific.com/worldscibooks/10.1142/6225 (WORLD SCIENTIFIC, 2006).
31. Robson, R., White, R. & Hildebrandt, M. *Fundamentals of Charged Particle Transport in Gases and Condensed Matter* (CRC Press, 2017).
32. White, R. D., Ness, K. F., Robson, R. E. & Li, B. Charged-particle transport in gases in electric and magnetic fields crossed at arbitrary angles: Multiterm solution of Boltzmann's equation. *Physical Review E* **60**, 2231–2249 (1999).
33. Einstein, A. Über die von der molekularkinetischen Theorie der Wärme geforderte Bewegung von in ruhenden Flüssigkeiten suspendierten Teilchen. *Annalen der Physik* **322**, 549–560 (1905).
34. Koutselos, A. D. Third-order transport properties of ion-swarms from mobility and diffusion coefficients. *Chemical Physics* **315**, 193–200 (2005).

Acknowledgements

Author Contributions

Section I was written by P.S., I.S., S.D. and R.W. Section II was written by P.S., B.P. and R.W. Section III was written by P.S., I.S., S.D. and R.W. Section IV was written by P.S., I.S. and S.D. Section V was written by P.S., B.P. and D.C. Section VI was written by P.S., B.P. and R.W. Section VIII was written by P.S., I.S., S.D., D.C. and R.W. Figure 1 was prepared by P.S. and B.P. Figure 2 was prepared by P.S. Figure 3 was prepared by P.S. and D.C.

Additional Information

Competing Interests: The authors declare that they have no competing interests.

Publisher's note: Springer Nature remains neutral with regard to jurisdictional claims in published maps and institutional affiliations.

Third-order transport coefficient tensor of charged-particle swarms in electric and magnetic fields

I. Simonović [1] D. Bošnjaković [1] Z. Lj. Petrović [2] P. Stokes [3] R. D. White,[3] and S. Dujko [1,*]

[1]*Institute of Physics, University of Belgrade, PO Box 68, 11080 Belgrade, Serbia*
[2]*Serbian Academy of Sciences and Arts, Knez Mihailova 35, 11001 Belgrade, Serbia*
[3]*College of Science and Engineering, James Cook University, 4810 Townsville, Australia*

Third-order transport coefficient tensor of charged-particle swarms in neutral gases in the presence of spatially uniform electric and magnetic fields is considered using a multiterm solution of Boltzmann's equation and Monte Carlo simulation technique. The structure of the third-order transport coefficient tensor and symmetries along its individual components in varying configurations of electric and magnetic fields are addressed using a group projector technique and through symmetry considerations of the Boltzmann equation. In addition, we focus upon the physical interpretation of the third-order transport coefficient tensor by considering the extended diffusion equation which incorporates the contribution of the third-order transport coefficients to the density profile of charged particles. Numerical calculations are carried out for electron and ion swarms for a range of model gases with the aim of establishing accurate benchmarks for third-order transport coefficients. The effects of ion to neutral-particle mass ratio are also examined. The errors of the two-term approximation for solving the Boltzmann equation and limitations of previous treatments of the high-order charged-particle transport properties are also highlighted.

I. INTRODUCTION

Studies of charged-particle swarms in neutral gases under the influence of electric and magnetic fields have applications in diverse areas of science and technology ranging from swarm experiments used to determine electron- and ion-neutral cross sections [1–5] to plasma processing technology [6–9], particle detectors used in high-energy physics [10,11], high-voltage technology [12], and positron physics [13,14]. These applications often require knowledge of swarm transport coefficients in the presence of the reduced electric and magnetic fields, E/n_0 and B/n_0, where E and B are the strengths of electric and magnetic fields, respectively, while n_0 is the neutral number density.

There is a large and growing literature dealing with the low-order transport coefficients, in which the variation of the reaction rate, drift velocity and diffusion tensor with E/n_0 (and B/n_0) for both the electrons and ions [15,16], and since recently even for positrons [14,17], are reported. In contrast, little is known about high-order transport coefficients, and limited data can be found in the literature, particularly for light charged particles such as electrons or positrons. The most obvious reason for this situation is the fact that the transport coefficients of higher-order have been difficult to measure, difficult to treat theoretically, and even more difficult to include in plasma models and thus were systematically ignored in the traditional interpretation of swarm experiments [1,3,4,16]. It was usually anticipated that swarm experiments are performed under conditions in which the effects induced by transport coefficients of higher-order are negligible [18,19]. On the other hand, in the early 1970s, it was shown that some arrival-time spectra of ions in drift tubes significantly deviate from the ideal Gaussian pulses which are represented in terms of the lower-order transport coefficients only [20]. To our knowledge, there have been only a few attempts to measure the third-order transport coefficients, or to be more accurate to interpret the observed data in terms of the effects of higher order transport [21–24].

In spite of low interest in higher-order transport coefficients, it was pointed out by several specialists and research groups that the third-order transport coefficients for electrons are very sensitive to the rapid variations with the energy of the momentum transfer cross section as a function of the energy. For example, it was pointed out by Penetrante and Bardsley [18] almost 25 years ago that the third-order transport coefficients are at least as sensitive to the depth and position of the Ramsauer-Townsend minimum for elastic scattering of the electrons in noble gases as the lower-order transport coefficients, including the drift velocity and the characteristic energy. Along similar lines, it was pointed out by Vrhovac *et al.* [19] that the third-order transport coefficients would be very useful for a fine tuning of cross sections for inelastic collisions in the close vicinity of their thresholds. This implies that in principle one could use the higher-order transport coefficients as an additional input for enhancing the reliability of swarm-derived cross sections.

Early work on the higher-order transport coefficients of charged-particle swarms in electric fields has been presented by Whealton and Mason [25]. Using the analytical solution of Boltzmann's equation for the Maxwell model of interaction, they found that the third-order transport coefficient

*Corresponding author: sasa.dujko@ipb.ac.rs

tensor has seven nonzero elements of which three are independent. It was also shown that when the electric field is absent, all components of the third-order transport coefficient tensor vanish. Early studies of the third-order transport coefficients for ion swarms have been performed by Robson [26] and Larsen *et al.* [27] using Boltzmann's equation solutions.

In 1994, Penetrante and Bardsley [18] carried out the numerical solution of Boltzmann's equation for electrons in noble gases. Among many important points, they found that the third-order transport coefficients could be detected and resolved from the arrival time spectra of an electron swarm. A similar procedure for the determination of the transport coefficients of both the low and higher order was earlier proposed by Kondo and Tagashira [28]. Koutselos used molecular dynamics simulations and a three-temperature treatment of Boltzmann's equation with the aim of calculating the third-order transport coefficients for K^+ and Li^+ ions in noble gases [29–32].

Within the framework of the semiquantitative momentum transfer theory [2,33,34], Vrhovac *et al.* [19] have developed the method of calculations of the third-order transport coefficients for charged-particle swarms in the presence of an electric field only. The theory and the associated numerical code, were used to evaluate the third-order transport coefficients in noble gases, but only in the limit of the lower values of E/n_0 where electrons undergo elastic collisions only. The presented results were found to confirm the structure of the third-order transport coefficient tensor previously determined by Whealton and Mason [25].

Using the theory of arrival time spectra of an electron swarm initially developed by Kondo and Tagashira [28] and a Monte Carlo simulation technique, Kawaguchi and co-workers derived the relation between the longitudinal third-order transport coefficient and the α parameters (arrival-time spectra transport coefficients) [35,36]. Arrival-time spectra can be measured by a double-shutter drift tube clearly indicating that the longitudinal third-order transport coefficient can be obtained experimentally from the knowledge of the α parameters. Along similar lines, it was pointed out by Dujko *et al.* [37] that the conversion of hydrodynamic transport coefficients to those found in the steady-state Townsend experiment requires the knowledge of the third-order transport coefficients. Petrović and co-workers [38] have also used a Monte Carlo simulation technique to derive the longitudinal and transverse third-order transport coefficients in CH_4 over a broad range of the applied reduced electric fields. Among many important points, it was shown that the transverse third-order transport coefficient becomes negative in the same range of the applied electric fields where the negative differential conductivity occurs. The negativity of the third-order transport coefficients has also been observed for charged-particle transport in the presence of trapped (localized) states [39].

The signatures of the higher order transport processes have been observed in the numerical modeling of plasma discharges. For example, in the avalanche phase of the streamer development, the particle-in-cell Monte Carlo simulations have shown that a spatial profile of electrons may significantly deviate from an ideal Gaussian as predicted by fluid models based on the equation of continuity [40,41]. The clear signs

of high-order transport have been observed in the studies of the spatiotemporal development of the electron swarms [42,43]. The pronounced asymmetry in the spatial profiles of the electron swarm is particularly evident during the transient phase of relaxation, in the presence of strong nonconservative interactions [44,45], as well as for electron transport in noble gases with a Ramsauer-Townsend minimum under the influence of E/n_0's for which the mean electron energies are well below the first inelastic threshold. It is worth noting that a similar effect of nonconservative collisions is observed for positrons in gases where spatially dependent positronium formation skews the profile of the ensemble to the point that a Gaussian cannot be recognized and analyzed [46,47].

Furthermore, the transport coefficients of the third and higher orders are very often used to characterize fractional transport in a variety of situations, ranging from the trapping of charge carriers in local imperfections in semiconductors [48–51] to electron [52–54] and positronium [13,55,56] trapping in bubble states within liquids, and to transport in biological cells [57–60].

The above examples clearly show that a rigorous analysis of the third-order transport coefficients in the context of the contemporary kinetic theory of charged-particle swarms is a long overdue, and the present paper takes a few important steps in this direction. Besides being of intrinsic interest, we are also motivated by the following questions: What is the structure of the third-order transport coefficient tensor, and how can symmetries be identified in varying configurations of electric and magnetic fields? What is the physical interpretation of third-order transport coefficients, and what is their contribution to the spatial profile of the swarm in a typical time-of-flight experiment? Is this contribution more significant for light charged particles or for more massive ions? How does the magnetic field affect the third-order transport coefficients, and how large are the errors of the two-term approximation for solving the Boltzmann equation? In the present paper, we will try to address these issues.

This paper is organized as follows. In Sec. II we discuss the basic elements of the theory, the structure and physical interpretation of the third-order transport coefficient tensor, as well as our methods of calculations. In Sec. III we present results of calculations for a range of model gases. Where possible, the results of the Boltzmann equation analysis are compared with those calculated by the Monte Carlo method with the goal of establishing accurate benchmarks for third-order transport coefficients. As an example of our calculations in real gases, in Sec. III we discuss the behavior of the third-order transport coefficients for electron swarms in neon. Last, in Sec. IV we present our conclusions and future work recommendations.

II. THEORY: DEFINITIONS, SYMMETRIES, INTERPRETATIONS, AND METHODS OF CALCULATION

The main physical object of our study is a swarm of charged particles which moves through a background of neutral molecules in external electric and magnetic fields crossed at arbitrary angles. The density of charged particles is assumed to be sufficiently low so that the following properties apply: (1) charged-particle–charged-particle inter-

actions and space charge effects can be neglected, collisions of transported charged particles and excited or dissociated species are unlikely, (2) the motion of charged particles between collisions can be treated classically, and (3) the presence of charged particles does not perturb the background particles from thermal equilibrium.

All information on the drift, diffusion, and transport properties of higher order of charged particles is contained in the charged-particle phase-space distribution function $f(\boldsymbol{r}, \boldsymbol{c}, t)$, where $\boldsymbol{r}$ represents the spatial coordinate of a charged particle at time t, and $\boldsymbol{c}$ denotes its velocity. In the present work, the distribution function $f(\boldsymbol{r}, \boldsymbol{c}, t)$ is determined by solving Boltzmann's equation:

$$\frac{\partial f}{\partial t} + \boldsymbol{c} \cdot \frac{\partial f}{\partial \boldsymbol{r}} + \frac{q}{m}(\boldsymbol{E} + \boldsymbol{c} \times \boldsymbol{B}) \cdot \frac{\partial f}{\partial \boldsymbol{c}} = -J(f, f_0), \quad (1)$$

where q and m are the charge and mass of charged particles, respectively, while the electric and magnetic fields are assumed to be spatially homogeneous and of magnitudes E and B. In the present work we employ a coordinate system in which the z axis is defined by $\boldsymbol{E}$ while $\boldsymbol{B}$ lies in the y-z plane, making an angle ψ with respect to $\boldsymbol{E}$. The right-hand side of (1) denotes the linear charged-particle–neutral-particle collision operator, accounting for elastic and various types of inelastic collisions, including nonconservative collisions (the charged-particle number changing processes, such as ionization and attachment for electron swarms or positronium (Ps) formation and annihilation for positron swarms). The velocity distribution function of the background particles is denoted by f_0, and in the present study it is taken to be a stationary Maxwellian at fixed temperature. The explicit form of the collision operator can be found in Refs. [61,62].

A. Definition of the third-order transport coefficient tensor

The continuity of charged particles in the configuration space requires the following balance equation:

$$\frac{\partial n(\boldsymbol{r}, t)}{\partial t} + \boldsymbol{\nabla} \cdot \boldsymbol{\Gamma}(\boldsymbol{r}, t) = S(\boldsymbol{r}, t), \quad (2)$$

where

$$n(\boldsymbol{r}, t) = \int f(\boldsymbol{r}, \boldsymbol{c}, t) \, d\boldsymbol{c} \quad (3)$$

is the number density of charged particles while $\boldsymbol{\Gamma}(\boldsymbol{r}, t) = n\langle \boldsymbol{c} \rangle$ is the charged-particle flux given by

$$\boldsymbol{\Gamma}(\mathbf{r}, t) = \int \mathbf{c} f(\mathbf{r}, \mathbf{c}, t) \, d\mathbf{c}. \quad (4)$$

The quantity $S(\boldsymbol{r}, t)$ is the production rate per unit volume per unit time arising from nonconservative processes. If the electron-impact ionization and electron attachment are the only nonconservative processes, then this property for electron swarms is given as

$$S(\mathbf{r}, t) = \int n_0 c [\sigma_i(\epsilon) - \sigma_a(\epsilon)] f(\mathbf{r}, \mathbf{c}, t) \, d\mathbf{c}, \quad (5)$$

where $\sigma_i(\epsilon)$ is the cross section for electron impact ionization while σ_a is the cross section for electron attachment. The equation of continuity (2) provides a direct link between experiment and theory, as in the majority of swarm experiments

the experimentally measurable quantities are usually charged-particle currents or charged-particle densities.

In the present work we follow the conventional definitions of transport coefficients and assume that the hydrodynamic conditions prevail, so that all space-time dependence is expressible through linear functionals of $n(\boldsymbol{r}, t)$. The hydrodynamic conditions are not satisfied near the boundaries of the system or in the vicinity of sources and/or sinks of charged particles, as well as under conditions in which electric and/or magnetic fields are not spatially homogeneous. The functional representation of the hydrodynamic approximation is the well-known density gradient expansion of the phase-space distribution function [63]:

$$f(\boldsymbol{r}, \boldsymbol{c}, t) = \sum_{k=0}^{\infty} \boldsymbol{f}^{(k)}(\boldsymbol{c}, t) \odot (-\nabla)^k n(\boldsymbol{r}, t), \quad (6)$$

where $\boldsymbol{f}^{(k)}(\boldsymbol{c}, t)$ are time-dependent tensors of rank k and $\odot$ denotes a k-fold scalar product. Performing equivalent representation of the flux $\boldsymbol{\Gamma}(\boldsymbol{r}, t)$ and source term $S(\boldsymbol{r}, t)$, we have

$$\boldsymbol{\Gamma}(\boldsymbol{r}, t) = \sum_{k=0}^{\infty} \boldsymbol{\Gamma}^{(k+1)}(t) \odot (-\nabla)^k n(\boldsymbol{r}, t), \quad (7)$$

$$S(\boldsymbol{r}, t) = \sum_{k=0}^{\infty} \boldsymbol{S}^{(k)}(t) \odot (-\nabla)^k n(\boldsymbol{r}, t), \quad (8)$$

where the superscripts (k) and $(k + 1)$ denote the ranks of the tensors. Equation (7) represents the flux-gradient relation and truncation of the expansion at $k = 2$ gives

$$\boldsymbol{\Gamma}(\boldsymbol{r}, t) = \boldsymbol{W} n(\boldsymbol{r}, t) - \boldsymbol{D} \odot \nabla n(\boldsymbol{r}, t) + \boldsymbol{Q} \odot (\nabla \otimes \nabla) n(\boldsymbol{r}, t),$$
$$(9)$$

where $\otimes$ is the tensor product, $\boldsymbol{W}$ and $\boldsymbol{D}$ are lower-order transport coefficients, the flux drift velocity and flux diffusion tensor, respectively, and $\boldsymbol{Q}$ defines the flux third-order transport coefficient tensor. The flux transport coefficients are given by

$$\mathbf{W} = \boldsymbol{\Gamma}^{(1)} = \int \mathbf{c} \boldsymbol{f}^{(1)}(\mathbf{c}, t) \, d\mathbf{c}, \quad (10)$$

$$\mathbf{D} = \boldsymbol{\Gamma}^{(2)} = \int \mathbf{c} \boldsymbol{f}^{(2)}(\mathbf{c}, t) \, d\mathbf{c}, \quad (11)$$

$$\mathbf{Q} = \boldsymbol{\Gamma}^{(3)} = \int \mathbf{c} \boldsymbol{f}^{(3)}(\mathbf{c}, t) \, d\mathbf{c}, \quad (12)$$

where $\boldsymbol{f}^{(1)}(\mathbf{c}, t)$, $\boldsymbol{f}^{(2)}(\mathbf{c}, t)$, and $\boldsymbol{f}^{(3)}(\mathbf{c}, t)$ are the expansion coefficients in the density-gradient expansion of the phase-space distribution function (6).

Substitution of expansions (7) and (8) into the continuity equation (2) yields the extended diffusion equation which incorporates the contribution of the third-order transport coefficient tensor,

$$\frac{\partial n(\boldsymbol{r}, t)}{\partial t} + \boldsymbol{W}^{(b)} \odot \nabla n(\boldsymbol{r}, t) - \boldsymbol{D}^{(b)} \odot (\nabla \otimes \nabla) n(\boldsymbol{r}, t)$$
$$+ \boldsymbol{Q}^{(b)} \odot (\nabla \otimes \nabla \otimes \nabla) n(\boldsymbol{r}, t) = -R_{\text{net}} n(\boldsymbol{r}, t), \quad (13)$$

where R_{net} is the net particle loss rate. For electron swarms, this quantity is given by

$$R_{net} = -S^{(0)} = -\iint n_0 c[\sigma_i(\epsilon) - \sigma_a(\epsilon)] f(\mathbf{r}, \mathbf{c}, t) \, d\mathbf{c} \, d\mathbf{r}. \quad (14)$$

$\boldsymbol{W}^{(b)}$ and $\boldsymbol{D}^{(b)}$ are the bulk drift velocity and bulk diffusion tensor, respectively, and $\boldsymbol{Q}^{(b)}$ is the bulk third-order transport coefficient tensor. The connection between the bulk and flux transport coefficients is given by

$$\mathbf{W}^{(b)} = \mathbf{W} + \mathbf{S}^{(1)}, \quad \mathbf{D}^{(b)} = \mathbf{D} + \mathbf{S}^{(2)}, \quad \mathbf{Q}^{(b)} = \mathbf{Q} + \mathbf{S}^{(3)}, \quad (15)$$

where $\mathbf{S}^{(1)}$, $\mathbf{S}^{(2)}$, and $\mathbf{S}^{(3)}$ are the expansion coefficients in the hydrodynamic expansion of the source term (8).

The third-order transport coefficient tensor is referred to as the *skewness coefficient* by some authors [18], while other authors use the term *skewness* to denote just the diagonal component of this tensor along the direction of the electric field [19]. For brevity, in the rest of this work we will sometimes refer to the third-order transport coefficient tensor as the skewness tensor.

In the absence of nonconservative processes (or when the collision frequencies of these processes are independent of the energy) the bulk and the flux transport coefficients are equal [64]. In the presence of nonconservative collisions these two families of transport coefficients can vary quite substantially from each other. The physical interpretation, the origin of differences and the application of the bulk and flux low-order transport coefficients as well as their application in the modeling of plasma discharges have been thoroughly discussed and illustrated in our previous publications [6,16,41,62]. We defer a full discussion of the differences between the bulk and flux third-order tensor coefficients to a future publication.

In order to show the rank of the tensor explicitly, the third-order transport coefficient tensor in (9) can be rewritten

$$[\boldsymbol{Q} \odot (\nabla \otimes \nabla) n]_i \equiv \sum_{jk} Q_{ijk} \frac{\partial^2 n(\mathbf{r}, t)}{\partial x_j \partial x_k}, \quad (16)$$

where the indices i, j, k each run over the space coordinates x, y, z. We note that there are 27 components in the tensor $\boldsymbol{Q}$ without considering any symmetry of the system under permutation operations. However, since the order of differentiation of n is irrelevant, some components of a tensor must be equal to each other. For example, for the magnetic-field-free case the maximal number of independent components is three, while when both the electric and magnetic fields are present and crossed at an arbitrary angle the maximal number of independent components is 18. It is clear that the structure of a tensor and symmetries along individual components depend on the field configuration.

B. Structure and symmetry considerations of the third-order transport coefficient tensor

One of the most important tasks in analysis of higher-order transport coefficients is to identify the symmetries along individual elements of the tensors. In this section we apply the group projector method [65] to determine the structure

of the skewness tensor. The group projector method is briefly discussed in Appendix A.

We first consider a magnetic-field-free case. The symmetry group of the system in the magnetic-field-free configuration is $C_{\infty V}$ (see Appendix A). This group has two connected components. The first component corresponds to rotations $R_z(\alpha)$ about the z axis through an arbitrary angle α. The second component corresponds to the composition of a rotation $R_z(\alpha)$ and a reflection in the symmetry plane σ_v. Polar vector (PV) representations of the group elements from the first and the second connected components are

$$D^{PV}(R_z(\alpha)) = \begin{pmatrix} \cos\alpha & -\sin\alpha & 0 \\ \sin\alpha & \cos\alpha & 0 \\ 0 & 0 & 1 \end{pmatrix}, \quad (17)$$

$$D^{PV}(\sigma_v R_z(\alpha)) = \begin{pmatrix} \cos\alpha & -\sin\alpha & 0 \\ -\sin\alpha & -\cos\alpha & 0 \\ 0 & 0 & 1 \end{pmatrix}, \quad (18)$$

where α is the angle of rotation around the z axis. Thus, for the magnetic-field-free case the following structure of the skewness tensor is derived:

$$Q_{xab} = \begin{pmatrix} 0 & 0 & Q_{xxz} \\ 0 & 0 & 0 \\ Q_{xxz} & 0 & 0 \end{pmatrix}, \quad Q_{yab} = \begin{pmatrix} 0 & 0 & 0 \\ 0 & 0 & Q_{xxz} \\ 0 & Q_{xxz} & 0 \end{pmatrix},$$

$$Q_{zab} = \begin{pmatrix} Q_{zxx} & 0 & 0 \\ 0 & Q_{zxx} & 0 \\ 0 & 0 & Q_{zzz} \end{pmatrix}, \quad (19)$$

where $a, b \in \{x, y, z\}$. For the magnetic-field-free case the skewness tensor has seven nonzero elements and only three independent elements, including Q_{zzz}, Q_{zxx}, and Q_{xxz} [19,25,31,32]. Furthermore, the following symmetry properties along the individual elements of the tensor hold:

$$Q_{xxz} = Q_{xzx} = Q_{yyz} = Q_{yzy}, \quad Q_{zxx} = Q_{zyy}. \quad (20)$$

For parallel electric and magnetic fields the symmetry group of the system is C_{∞} (see Appendix A). This group has only a single component consisting of rotations $R_z(\alpha)$:

$$D^{PV}(R_z(\alpha)) = \begin{pmatrix} \cos\alpha & -\sin\alpha & 0 \\ \sin\alpha & \cos\alpha & 0 \\ 0 & 0 & 1 \end{pmatrix}. \quad (21)$$

In this case the structure of the skewness tensor is more complicated. For instance, the presence of the element Q_{xyz} is due to the explicit effects of the magnetic field on the trajectories of the charged particles. It is interesting to note that this component has exactly the opposite contribution to the third-order diffusive flux along the x and y directions. This is analogous to the D_{xy} component of the diffusion tensor. Likewise, the third-order flux along the magnetic field direction is the same as for the magnetic-field-free case. Thus, for parallel electric and magnetic fields the skewness tensor

has the following structure:

$$Q_{xab} = \begin{pmatrix} 0 & 0 & Q_{xxz} \\ 0 & 0 & Q_{xyz} \\ Q_{xxz} & Q_{xyz} & 0 \end{pmatrix},$$

$$Q_{yab} = \begin{pmatrix} 0 & 0 & -Q_{xyz} \\ 0 & 0 & Q_{xxz} \\ -Q_{xyz} & Q_{xxz} & 0 \end{pmatrix}, \qquad (22)$$

$$Q_{zab} = \begin{pmatrix} Q_{zxx} & 0 & 0 \\ 0 & Q_{zxx} & 0 \\ 0 & 0 & Q_{zzz} \end{pmatrix}.$$

For parallel electric and magnetic fields the skewness tensor has 11 nonzero elements and only four independent elements, including Q_{zzz}, Q_{zxx}, Q_{xxz}, and Q_{xyz}. Furthermore, the following symmetry properties along the individual elements of the tensor may be identified:

$$Q_{xxz} = Q_{xzx} = Q_{yyz} = Q_{yzy}, \quad Q_{zxx} = Q_{zyy},$$
$$Q_{xyz} = Q_{xzy} = -Q_{yxz} = -Q_{yzx}. \qquad (23)$$

For orthogonal electric and magnetic fields the symmetry group of the system is C_{1V}. This group has only two elements, the unity element e and a reflection in the symmetry plane σ_v, which is orthogonal to the direction of the magnetic field. The PV representations of these two elements are given by

$$D^{PV}(e) = \begin{pmatrix} 1 & 0 & 0 \\ 0 & 1 & 0 \\ 0 & 0 & 1 \end{pmatrix}, \quad D^{PV}(\sigma_v) = \begin{pmatrix} 1 & 0 & 0 \\ 0 & -1 & 0 \\ 0 & 0 & 1 \end{pmatrix}. \quad (24)$$

Thus, for orthogonal electric and magnetic fields the skewness tensor has the following structure:

$$Q_{xab} = \begin{pmatrix} Q_{xxx} & 0 & Q_{xxz} \\ 0 & Q_{xyy} & 0 \\ Q_{xxz} & 0 & Q_{xzz} \end{pmatrix},$$

$$Q_{yab} = \begin{pmatrix} 0 & Q_{yyx} & 0 \\ Q_{yyx} & 0 & Q_{yyz} \\ 0 & Q_{yyz} & 0 \end{pmatrix}, \qquad (25)$$

$$Q_{zab} = \begin{pmatrix} Q_{zxx} & 0 & Q_{zzx} \\ 0 & Q_{zyy} & 0 \\ Q_{zzx} & 0 & Q_{zzz} \end{pmatrix}.$$

We observe that for orthogonal fields the skewness tensor has 14 nonzero elements among which 10 are independent. The following symmetry properties along the individual elements of the tensor are clearly evident:

$$Q_{xxz} = Q_{xzx}, \quad Q_{yyz} = Q_{yzy}, \quad Q_{yyx} = Q_{yxy}, \quad Q_{zzx} = Q_{zxz}. \qquad (26)$$

When electric and magnetic fields are crossed at arbitrary angles, the symmetry group of the system is the trivial group, which has only the unity element, e.g.,

$$D^{PV}(e) = \begin{pmatrix} 1 & 0 & 0 \\ 0 & 1 & 0 \\ 0 & 0 & 1 \end{pmatrix}. \qquad (27)$$

For this general configuration, the skewness tensor is full, and it has 27 nonzero elements. However, there are only

18 independent components as the last two indices of the skewness tensor commute. Thus, the skewness tensor has the following structure:

$$Q_{xab} = \begin{pmatrix} Q_{xxx} & Q_{xxy} & Q_{xxz} \\ Q_{xxy} & Q_{xyy} & Q_{xyz} \\ Q_{xxz} & Q_{xyz} & Q_{xzz} \end{pmatrix},$$

$$Q_{yab} = \begin{pmatrix} Q_{yxx} & Q_{yyx} & Q_{yxz} \\ Q_{yyx} & Q_{yyy} & Q_{yyz} \\ Q_{yxz} & Q_{yyz} & Q_{yzz} \end{pmatrix}, \qquad (28)$$

$$Q_{zab} = \begin{pmatrix} Q_{zxx} & Q_{zxy} & Q_{zzx} \\ Q_{zxy} & Q_{zyy} & Q_{zzy} \\ Q_{zzx} & Q_{zzy} & Q_{zzz} \end{pmatrix}.$$

For this general configuration, one may identify the following symmetry properties along the individual elements:

$$Q_{xxy} = Q_{xyx}, \quad Q_{yyx} = Q_{yxy}, \quad Q_{zzx} = Q_{zxz},$$
$$Q_{xxz} = Q_{xzx}, \quad Q_{yyz} = Q_{yzy}, \quad Q_{zzy} = Q_{zyz}, \qquad (29)$$
$$Q_{xyz} = Q_{xzy}, \quad Q_{yzx} = Q_{yxz}, \quad Q_{zxy} = Q_{zyx}.$$

These symmetry arguments can be extended to any of the higher-order transport coefficients.

C. Physical interpretation of the third-order transport coefficients

In this section we discuss the physical meaning of the third-order transport coefficients. Let us assume that the contribution of the third-order transport coefficients to the density profile of charged particles is negligibly small. This reduces the extended diffusion equation (13) to the well-known form

$$\frac{\partial n(\boldsymbol{r},t)}{\partial t} + \boldsymbol{W}^{(b)} \odot \boldsymbol{\nabla} n(\boldsymbol{r},t) - \boldsymbol{D}^{(b)} \odot (\boldsymbol{\nabla} \otimes \boldsymbol{\nabla}) n(\boldsymbol{r},t)$$
$$= -R_{\mathrm{net}} n(\boldsymbol{r},t). \qquad (30)$$

Swarm experiments are traditionally analyzed by solving the the diffusion equation (30), which gives the density of charged particles throughout the bulk of medium. For example, in an idealized time-of-flight experiment, in which a pulse of N_0 particles is released from a plane source at $z = 0$ at time $t = 0$ into an unbounded medium, the initial and boundary conditions are

$$n(\mathbf{r}, 0) = N_0 \delta(\mathbf{r}),$$
$$n(\mathbf{r}, t) = 0 \ (\|\mathbf{r}\| \to \infty, \ t > 0), \qquad (31)$$

respectively, and the solution is

$$n^{(0)}(\boldsymbol{r}, t) = \frac{N_0 e^{-R_{\mathrm{net}} t} e^{-\frac{\left(z - W^{(b)} t\right)^2}{4 D_L^{(b)} t} - \frac{x^2 + y^2}{4 D_T^{(b)} t}}}{\left(4\pi D_T^{(b)} t\right) \sqrt{4\pi D_L^{(b)} t}}, \qquad (32)$$

where $D_L^{(b)}$ and $D_T^{(b)}$ are the bulk longitudinal and bulk transverse diffusion coefficients, respectively, while x, y, and z are the Cartesian coordinates [62]. The solution (32) represents a Gaussian pulse, the peak of which drifts with the velocity $W^{(b)}$ and diffuses about the center of mass according to the diffusion coefficients $D_L^{(b)}$ and $D_T^{(b)}$. For brevity, in what follows

we omit explicit reference to the type of transport coefficients, e.g., the superscripting for all transport coefficients.

Assuming the above initial conditions (31), the extended diffusion equation (13), which incorporates the effects of the third-order transport coefficient tensor, cannot be solved analytically. Thus, we have applied the following procedure. First, the Fourier transform of the charged-particle density is expanded in terms of the longitudinal Q_L and transverse Q_T components of the third-order transport coefficient tensor. Using the inverse Fourier transformation of the expansion coefficients, we have derived the density of charged particles in which the corrections due to the third-order transport coefficients are included. In the first approximation, in which only the first-order corrections are assumed, the density of charged particles is given by

$$n^{(1)}(\mathbf{r}, t) = \left[1 + Q_L \frac{t(z - Wt)^3 - 6D_L t^2(z - Wt)}{8(D_L t)^3} \right.$$
$$\left. + Q_T \frac{3t(z - Wt)(x^2 + y^2 - 4D_T t)}{8D_L t(D_T t)^2} \right] n^{(0)}(\mathbf{r}, t).$$
$$(33)$$

The first-order correction along the longitudinal direction shown in Eq. (33) has been previously published by Penetrante and Bardsley [18]. This equation has a simpler form in relative coordinates that are defined as

$$\chi_z = \frac{z - W^{(b)}t}{\sqrt{2D_L^{(b)}t}}, \quad \chi_x = \frac{x}{\sqrt{2D_T^{(b)}t}}, \quad \chi_y = \frac{y}{\sqrt{2D_T^{(b)}t}}. \quad (34)$$

In these coordinates the approximate solution (32) may be written as

$$n^{(1)}(\mathbf{r}, t) = n^{(0)}(\mathbf{r}, t) \left[1 + \frac{t Q_L^{(b)}}{\sigma_z^3} \chi_z (\chi_z^2 - 3) \right.$$
$$\left. + \frac{3t Q_T^{(b)}}{\sigma_x^2 \sigma_z} \chi_z (\chi_x^2 + \chi_y^2 - 2) \right]. \quad (35)$$

It can be seen from Eq. (35) that the third-order transport coefficients describe elongation and compression of the number density of charged particles along different parts of the swarm. The detailed physical interpretation of the individual components of the third-order transport tensor is given in Appendix B.

D. Multiterm solutions of Boltzmann's equation

In this section we briefly describe the basic elements of a multiterm theory for solving the Boltzmann equation that has been used to calculate the components of the third-order transport coefficient tensor. The method is by now standard, and for details the reader is referred to our previous publications [66–68]. In brief, the dependence of the phase-space distribution function on the velocity coordinates is represented by its expansion in terms of spherical harmonics (angular dependence) and Sonine polynomials (speed dependence). Likewise, under hydrodynamic conditions a sufficient representation of the space dependence is an expansion in terms of the powers of the density gradient operator. After truncation and discretizing in time, the above expansions allow

a decomposition of the Boltzmann equation into a set of matrix equations in terms of the expansion coefficients which represent the moments of the distribution function. This set of matrix equations can be solved numerically by using the matrix inversion. Transport properties including mean energy, drift velocity, and components of the diffusion tensor can then be calculated directly from the moments of the phase-space distribution function.

In order to find the explicit expressions for the individual elements of the third-order transport coefficient tensor we use the definition of the spherical vector [69]:

$$c_m^{[1]} = \sqrt{\frac{4\pi}{3}} c Y_m^{[1]}(\hat{\mathbf{c}}). \quad (36)$$

The connection between Cartesian and spherical components of the velocity vector is given by

$$c_x = \frac{i}{\sqrt{2}} \left(c_1^{[1]} - c_{-1}^{[1]} \right), \quad c_y = \frac{1}{\sqrt{2}} \left(c_1^{[1]} + c_{-1}^{[1]} \right),$$
$$c_z = -i c_0^{[1]}. \quad (37)$$

Likewise, the flux of charged particles in irreducible tensor notation is given by

$$\Gamma_m^{[1]} = n \langle c_m^{[1]} \rangle, \quad (38)$$

while its connection with the Cartesian components is expressed by

$$\Gamma_x = \frac{i}{\sqrt{2}} \left(\Gamma_1^{[1]} - \Gamma_{-1}^{[1]} \right), \Gamma_y = \frac{1}{\sqrt{2}} \left(\Gamma_1^{[1]} + \Gamma_{-1}^{[1]} \right), \quad (39)$$
$$\Gamma_z = -i \Gamma_0^{[1]}.$$

Using the orthogonality relations for spherical harmonics and modified Sonine polynomials [61,69] and relation

$$c^l = \left(\frac{\sqrt{2}}{\alpha} \right) \frac{R_{0l}(\alpha c)}{N_{0l}}, \quad (40)$$

after some algebra we get the following expression for the flux of charged particles in the basis of Sonine polynomials:

$$\Gamma_m^{(1)} = \frac{1}{\alpha} \sum_{s=0}^{\infty} \sum_{\lambda=0}^{s} \sum_{\mu=-\lambda}^{\lambda} F(01m|s\lambda\mu) G_\mu^{(s\lambda)} n(\mathbf{r}, t). \quad (41)$$

Using the explicit expressions for the irreducible gradient tensor operator in the spherical form of the flux-gradient relation (41) [61], the relationship between the spherical quantities $\Gamma_m^{(1)}$ (where $m = -1, 0, 1$) and their Cartesian counterparts in (9) can be established. The explicit expressions for the individual elements of the flux third-order transport coefficient tensor in the absence of a magnetic field are given by

$$Q_{xxz} = \frac{1}{\sqrt{2}\alpha} [\text{Im}(F(011|221; \alpha)) - \text{Im}(F(01-1|221; \alpha))],$$
$$(42)$$

$$Q_{zxx} = -\frac{1}{\alpha} \left[\frac{1}{\sqrt{3}} \text{Im}(F(010|200; \alpha)) + \frac{1}{\sqrt{6}} \text{Im}(F(010|220; \alpha)) \right.$$
$$\left. + \frac{1}{\alpha} \text{Im}(F(010|222; \alpha)), \right. \quad (43)$$

$$Q_{zzz} = \frac{1}{\alpha}\left[\sqrt{\frac{2}{3}}\mathrm{Im}(F(010|220;\alpha)) - \frac{1}{\sqrt{3}}\mathrm{Im}(F(010|200;\alpha))\right],$$

$$(44)$$

where $\mathrm{Re}(\cdot)$ and $\mathrm{Im}(\cdot)$, respectively, represent the real and imaginary parts of the moments. The explicit expressions for the individual elements of the flux skewness tensor in varying configurations of electric and magnetic fields are given in Appendix C. Expressions for the lower-order transport coefficients in terms of the moments of the distribution function can be found in our previous work [66–68,70].

E. Monte Carlo simulation method

The Monte Carlo simulation technique is used in this work as an independent tool to confirm the numerical accuracy and integrity of a multiterm solution of Boltzmann's equation. The Monte Carlo code applied in this work has been systematically tested for a range of model and real gases under both the hydrodynamic and nonhydrodynamic conditions in the presence of the electric and magnetic fields [67,68,71,72]. The subject of testing were the lower-order transport coefficients usually in the presence of nonconservative collisions. In the present work, we follow a large number of particles ($\sim 10^7$) moving in an infinite gas under the influence of spatially homogeneous electric and magnetic fields. Such a large number of charged particles is followed with the aim of reducing the statistical fluctuations of the output data required for the evaluation of the individual elements of the third-order transport coefficient tensor. The charged-particle trajectories between collisions are determined by solving the collisionless equation of motion of a charged particle. The position and velocity of each charged particle are updated after the time step Δt, which is obtained by solving the equation for collision probability. The numerical solution of this equation requires the extensive use of random numbers. The type of collision is also determined using random numbers as well as relative probabilities for individual collisional processes. The details of our Monte Carlo method are given in our several previous publications [67,71–73].

The third-order transport coefficients are determined after relaxation to the steady state. The flux third-order transport coefficient tensor is defined by

$$Q_{abc} = \frac{1}{3!}\left\langle \frac{d}{dt}\left(r_a^* r_b^* r_c^*\right)\right\rangle,$$

$$(45)$$

where (a,b,c) take values from the set $\{x,y,z\}$ while the angular brackets $\langle\rangle$ denote ensemble averages in phase space, and $\boldsymbol{r}^* = \boldsymbol{r} - \langle\boldsymbol{r}\rangle$.

It is important to note that although the third-order transport coefficient tensor has the three independent elements when the swarm is acted on solely by the electric field, we are able to identify only two independent elements in our Monte Carlo simulations. This follows from the fact that the expressions for sampling the third-order transport coefficients are derived from the generalized diffusion equation in which all tensor components are contracted with the corresponding partial derivatives of charged-particle density with respect to the coordinates. Thus, the expressions for evaluation the skewness coefficients represent the sum of all skewness tensor

components Q_{abc} which have the same combination of indices a, b, c where (a, b, c) take values from the set $\{x, y, z\}$. Therefore, the expressions for skewness coefficients in our Monte Carlo simulations are symmetric with respect to the permutation of any two indices. The analogy with the determination of the off-diagonal elements of the diffusion tensor is clearly evident. For example, for perpendicular electric and magnetic fields, we are not able to isolate and evaluate the individual off-diagonal elements of the diffusion tensor [67]. However, it is possible to determine the sum of the individual off-diagonal elements which is the well-known Hall diffusion coefficient. To calculate the individual elements of the third-order transport coefficient tensor and diffusion tensor, one must integrate the velocity over the corresponding hydrodynamic component of the distribution function in velocity space. This is beyond the scope of this work, and we defer this procedure to a future paper.

Due to inability to isolate the individual elements of the third-order transport coefficient tensor in our Monte Carlo simulations, we define the following third-order transport coefficients:

$$Q_{zzz} \equiv Q_L, \quad Q_{\pi(xxz)} \equiv Q_T, \qquad (46)$$

where

$$Q_{\pi(xxz)} = \tfrac{1}{3}(Q_{xxz} + Q_{xzx} + Q_{zxx}), \qquad (47)$$

and $\pi(abc)$ denote all possible permutations of (a,b,c).

The explicit form of the flux longitudinal and flux transverse third-order coefficients are calculated from

$$Q_L = \tfrac{1}{6}(3\langle z^2 c_z\rangle - 3\langle c_z\rangle\langle z^2\rangle - 6\langle z\rangle\langle zc_z\rangle + 6\langle z\rangle\langle z\rangle\langle c_z\rangle), \quad (48)$$

$$Q_T = \tfrac{1}{6}(\langle x^2 c_z\rangle + 2\langle zxc_x\rangle - \langle c_z\rangle\langle x^2\rangle - 2\langle z\rangle\langle xc_x\rangle), \qquad (49)$$

where c_x, c_y, and c_z are velocity components. Explicit formulas for the elements of the flux third-order transport coefficient tensor which can be isolated and determined individually in our Monte Carlo simulations in various configurations of the electric and magnetic fields are given in the Appendix C.

III. RESULTS

A. Preliminaries

The aim of the present section is to highlight the general features of the third-order transport coefficients associated with the light charged-particle swarms in gases when both the electric and magnetic fields are present. Benchmark calculations are performed for a range of model gases, including the Maxwell (constant collision frequency) model, the hardsphere model and the Reid ramp inelastic model. For the present study we consider conservative collisions only. We defer the investigation of the explicit effects of nonconservative collisions on the third-order transport coefficient tensor to a future study. The utility of model gases lies in the fact that through the use of simple analytically given cross sections we can isolate and elucidate physical processes which govern and control the specific behavior of a charged-particle swarm. This is particularly important for higher-order transport coefficients due to complexity of factors which contribute to, or influence, the corresponding tensors. However, the present theory and associated codes have been applied to a number of gases

and mixtures and preliminary results are available elsewhere [74–76]. Here we present some results for neon and compare them with the results of calculations that have been presented elsewhere. We employ the set of cross sections for electron scattering in neon developed by Hayashi [77] (see Fig. 2 in Ref. [78]).

In the Boltzmann equation analysis of the third-order transport coefficients the elastic collisions are treated using the original Boltzmann collision operator [79], while its semiclassical generalization is applied for inelastic processes [80]. All scattering is assumed isotropic and hence for elastic scattering we use the elastic momentum transfer cross section. Calculations are performed assuming that the internal states are governed by a Maxwell-Boltzmann distribution which essentially places all neutral particles in the ground state for systems considered. The thermal motion of background particles is carefully considered in both the Boltzmann equation analysis and Monte Carlo simulations [81].

The Monte Carlo results are presented with error bars. These error bars are required since the third-order transport coefficients are derived from the third-order monomials of coordinates and velocities which usually have high standard deviations. The statistical error of the third-order transport coefficients that are evaluated in our Monte Carlo simulations is estimated as the standard error. The standard error is equal to the standard deviation of the third-order transport coefficients divided by the square root of the number of electrons followed in the simulation. Thus, it is necessary to follow a large number of electrons (at least 10^7) in our Monte Carlo simulations in order to sufficiently reduce the standard error of the final results.

When the magnetic field is applied, the results and discussion are restricted to a crossed field configuration, although the theory and associated codes are valid for arbitrary field configurations. We use the unit of the Townsend (1 Td = 10^{-21} Vm^2) for the reduced electric field and the unit of the Huxley (1 Hx = 10^{-27} Tm^3) for the reduced magnetic field.

B. The Maxwell model

In this section we present benchmark results for the third-order transport coefficients assuming the Maxwell model of interaction. In this model the electrons undergo elastic collisions only and the collision frequency is independent of the energy. The details of the model used here are as follows:

$$\sigma_m(\epsilon) = A\epsilon^{-1/2} \text{ Å}^2 \quad \text{(elastic cross section)},$$
$$m_0 = 4 \text{ amu}, \quad m = 5.486 \times 10^{-4} \text{ amu}, \quad T_0 = 293 \text{ K},$$
(50)

where ϵ is in eV, m is the electron mass and m_0 is the neutral mass. While the magnitude of potential for elastic scattering A in previous works was usually fixed to a single value of 6 [70,82,83], in the present work its value is varied in order to investigate the influence of elastic collisions on the third-order transport coefficients. We consider the reduced electric field range: 0.1–10 Td.

The results are obtained from the numerical solution of Boltzmann's equation and are presented in Table I. The three

TABLE I. Third-order transport coefficients for the Maxwell model. The results are presented as a function of the reduced electric field E/n_0 and the magnitude of potential for elastic scattering A.

A	E/n_0 (Td)	$n_0^2 Q_{xzx}$ (m^{-3} s^{-1})	$n_0^2 Q_{zxx}$ (m^{-3} s^{-1})	$n_0^2 Q_{zzz}$ (m^{-3} s^{-1})
1.0	0.1	5.2930×10^{45}	2.1761×10^{42}	1.0588×10^{46}
	1.0	4.3919×10^{48}	1.8055×10^{45}	8.7856×10^{48}
	10.0	4.3829×10^{51}	1.8017×10^{48}	8.7676×10^{51}
3.0	0.1	5.1740×10^{43}	2.1279×10^{40}	1.0351×10^{44}
	1.0	1.8373×10^{46}	7.5531×10^{42}	3.6754×10^{46}
	10.0	1.8039×10^{49}	7.4158×10^{45}	3.6087×10^{49}
6.0	0.1	4.7768×10^{42}	1.9648×10^{39}	9.5557×10^{42}
	1.0	6.0575×10^{44}	2.4903×10^{41}	1.2118×10^{45}
	10.0	5.6405×10^{47}	2.3187×10^{44}	1.1283×10^{48}
12.0	0.1	5.4425×10^{41}	2.2388×10^{38}	1.0888×10^{42}
	1.0	2.2880×10^{43}	9.4070×10^{39}	4.5769×10^{43}
	10.0	1.7665×10^{46}	7.2623×10^{42}	3.5340×10^{46}

independent elements of the third-order transport coefficient tensor are given as a function of the reduced electric field E/n_0 and the magnitude of potential for elastic scattering A. We observe that $n_0^2 Q_{xzx}$, $n_0^2 Q_{zxx}$, and $n_0^2 Q_{zzz}$ are positive and monotonically increasing functions of E/n_0. For brevity, in what follows we omit n_0^2, and $n_0^2 Q_{abc}$ will be written as Q_{abc}, where $a, b, c \in \{x, y, z\}$. In the logarithmic plot, the E/n_0 dependence of Q_{xzx}, Q_{zxx}, and Q_{zzz} is linear both for the higher values of E/n_0, where the diffusion deviates significantly from the thermal values, and for the lower values of E/n_0, where the diffusion is essentially thermal. However, the slope of these two linear dependencies is not the same. The slope is greater for those values of E/n_0 for which the diffusion is no longer thermal.

We observe that the Q_{zxx} is less than the remaining elements, Q_{xzx} and Q_{zzz} for all E/n_0 and A considered. The coefficient Q_{zxx} represents the difference in the flux of charged particles along the z direction between the center of the swarm and the transverse edges (see Appendix B). Since the collision frequency for the Maxwell model is independent of energy, the positive value of Q_{zxx} is a clear sign that the mobility of the electrons is greater at the transverse edges than at the center of the swarm, due to a parabolic increase of the mean energy along the transverse direction. This effect is very small and hence the coefficient Q_{zxx} is dominated by the coefficients Q_{xzx} and Q_{zzz}. This physical picture is no more valid for real gases in which the momentum transfer collision frequency is usually a complex function of the electron energy.

Comparing Q_{xzx} and Q_{zzz}, we observe that these two coefficients are of the same order of magnitude for all E/n_0 and A considered. In a certain way this is analogous to the behavior of the diffusion coefficients. For the Maxwell model the longitudinal and transverse diffusion coefficients are equal [82,83]. Likewise, the sum of the coefficients Q_{xzx} and Q_{xxz} which is proportional to the flux along the transverse direction, is equal to the coefficient Q_{zzz} which determines the corresponding flux along the field direction (note that the coefficient Q_{zxx} is negligible as compared to the coefficients Q_{xzx} and Q_{zzz}).
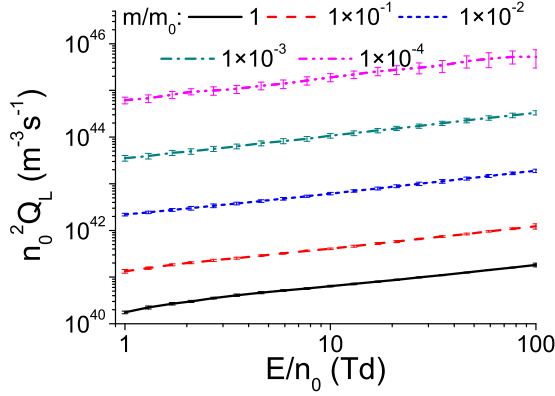
FIG. 1. Influence of the charged-particle to neutral-particle mass ratio on the variation of the longitudinal third-order transport coefficient $n_0^2 Q_L$ with E/n_0 for the hard sphere model. Calculations are performed using a Monte Carlo simulation technique.

C. Effects of the ion to neutral-particle mass ratio

In this section we explore the effects of the ion to neutral mass ratio on the variation of the third-order transport coefficients with E/n_0. Calculations are performed by a Monte Carlo simulation technique assuming the hard sphere model [84]. The details of the model are

$$\sigma_m(\epsilon) = 6 \text{ Å}^2 \quad \text{(elastic cross section)},$$
$$m_0 = 4 \text{ amu}, \quad T_0 = 293 \text{ K}. \tag{51}$$

We consider the mass ratio range 10^{-4}–1 and the reduced electric field range 1–100 Td.

In Fig. 1 we show the variation of the coefficient Q_L as a function of E/n_0 for various charged-particle to neutral-particle mass ratios, as indicated on the graph. For decreasing m/m_0 the energy transfer in elastic collisions is reduced, which in turn increases Q_L. In Monte Carlo simulations, the reduced energy transfer in elastic collisions for decreasing m/m_0 slows the relaxation of energy. As a consequence, Monte Carlo simulations require a large computation time while at the same time the statistical fluctuations deteriorate the accuracy of the output data. We see in the Fig. 1 that the error bars are increased for decreasing m/m_0.

For a fixed mass ratio we see that Q_L is increased monotonically with E/n_0. In this model, the elastic cross section is constant rendering collision frequency to be directly proportional to the square root of the charge particle energy. With the increase of E/n_0, the collision frequency also increases, but not enough to overcome the directed action of the force and the simultaneous increase of the mobility of charged particles (see Appendix B). As a consequence, Q_L rises with rising E/n_0. When it comes to Q_T, for the entire range of E/n_0 considered, it is found that $Q_T > 0$ (not shown here). This indicates that the absolute value of the sum of Q_{xxz} and Q_{xzx} is greater than the absolute value of the coefficient Q_{zxx}. In this model, $Q_{zxx} < 0$ since the collision frequency is directly proportional to the square root of charged-particle energy. The negative value of Q_{zxx} due to elastic collisions with a constant cross section has been observed for the Reid model gas at low
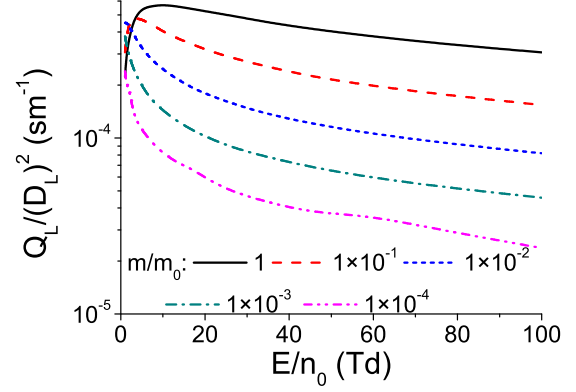
electric fields where the rate for inelastic collisions is negligible (see Sec. III D). Note that in our Monte Carlo simulations we are not able to evaluate the individual components Q_{xxz}, Q_{xzx} and Q_{zxx}, but only their sum [see Eq. (47)].

Figure 1 clearly illustrates that for decreasing m/m_0 the coefficients Q_L (and Q_T) are increased. It should be noted that for the hard sphere model the third-order transport coefficients scale with the factor $\frac{1}{\sqrt{m_0}}(\frac{m+m_0}{mA^2})^{5/4}$ [19]. This raises an interesting question: does the spatial profile of the swarm deviate from a Gaussian distribution more for light charged particles, including electrons and/or positrons, or for more massive ions? In order to investigate this issue, in Figs. 2 and 3 we show the variation of the $\frac{1}{n_0}Q_L/D_L^3$ and Q_L/D_L^2 as a function of E/n_0, respectively, where D_L is the longitudinal diffusion coefficient. Recall that the asymmetric contribution to the spatial profile of the swarm along the field direction is represented by the two terms; the first term is proportional to Q_L/D_L^3, while the second one is proportional to Q_L/D_L^2 [see Eq. (33)]. We observe that both quantities $\frac{1}{n_0}Q_L/D_L^3$ and Q_L/D_L^2 are decreased with a decrease of m/m_0, which indicates that the contribution of the third-order transport coefficients to the spatial profile of the swarm becomes more significant for ions in comparison with electrons and/or positrons.
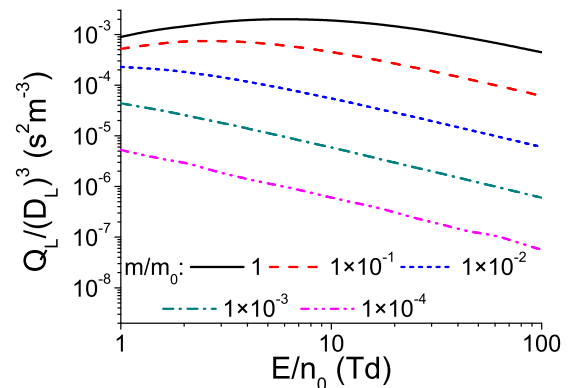

FIG. 2. Variation of the Q_L to D_L^2 ratio as a function of E/n_0 for the hard sphere model.

FIG. 3. Variation of the Q_L to D_L^3 ratio as a function of E/n_0 for the hard sphere model. Calculations are performed assuming the gas number density $n_0 = 3.54 \times 10^{22}$ m^{-3}.
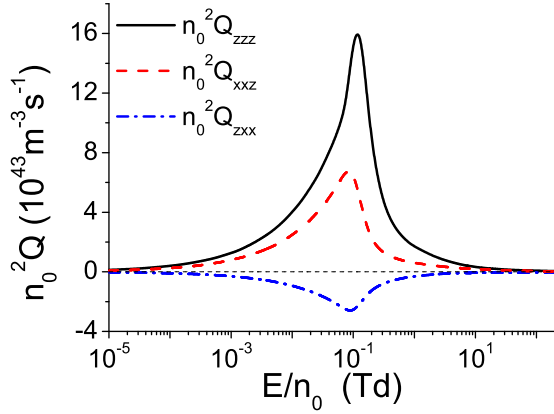
FIG. 4. Variation of the third-order transport coefficients with E/n_0 for the Reid ramp model. Calculations are performed via a multiterm theory for solving the Boltzmann equation.

D. The Reid ramp model

The Reid ramp inelastic model of interaction is given by [85]

$$\sigma_m(\epsilon) = 6 \text{ Å}^2 \quad \text{(elastic cross section)},$$

$$\sigma_{\text{inel}}(\epsilon) = \begin{cases} 10(\epsilon - 0.2) \text{ Å}^2, & \epsilon \geqslant 0.2 \text{ eV} \\ & \text{(inelastic cross section)}, \\ 0, & \epsilon < 0.2 \text{ eV} \end{cases}$$

$$m_0 = 4 \text{ amu},$$

$$T_0 = 0 \text{ K}, \tag{52}$$

where m_0 and T_0 represent the mass and temperature of the neutral gas particles while ϵ has the units of eV. Initially, this particular model was developed with the aim of testing the validity of the two-term approximation for solving the Boltzmann equation. Since the early work of Reid [85], the model has been used extensively as a benchmark for a variety of numerical techniques for solving the Boltzmann equation and Monte Carlo codes under steady-state [70–72,82,83] and time-dependent conditions [17,68]. In the present work we extend the model to consider the behavior of the individual elements of the third-order transport coefficient tensor in the presence of both electric and magnetic fields. Thus, the utility of the Reid ramp model in the present work is twofold: (1) it will enable us to determine the influence of an energy dependent collision frequency in addition to the influence of strong inelastic processes on the behavior of the third-order transport coefficients, and (2) it is a good test of the accuracy of the two-term approximation for solving Boltzmann's equation.

In Fig. 4 we show the variation of the coefficients Q_{zzz}, Q_{xxz}, and Q_{zxx} with the reduced electric field E/n_0. Over the range of E/n_0 considered, we see that Q_{zzz} and Q_{xxz} are positive while Q_{zxx} is negative. Such behavior of the third-order transport coefficients can be attributed to the fact that for the Reid ramp model the total collision frequency is a monotonically increasing function of the electron energy. Due to the increase of the total collision frequency over the entire range of E/n_0, Q_{zxx} is negative (see Appendix B). However, this increase is not significant enough to render Q_{zzz} and Q_{xxz} negative. In any case, the absolute values of
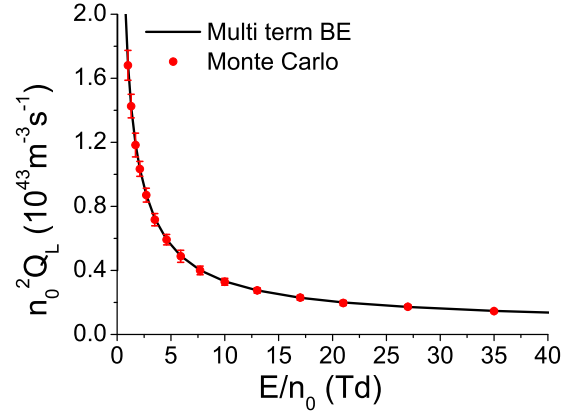

FIG. 5. Comparison between the multiterm Boltzmann equation results for longitudinal third-order transport coefficient and those calculated with a Monte Carlo simulation technique.

the third-order transport coefficients are increasing functions of E/n_0 until reaching the particular value of E/n_0 value for which the inelastic collisions begin to play a significant role. In this case, their direct effect is to enhance collisions and thereby reduce diffusion which in turn reduces the third-order transport coefficients. In the limit of the highest E/n_0, the third-order transport coefficients are significantly reduced and approach zero values.

In Figs. 5 and 6 we show the comparison between the Boltzmann equation and Monte Carlo results of Q_L and Q_T, respectively. The comparison is presented only for relatively higher values of E/n_0 where both Q_L and Q_T are monotonically decreasing functions of E/n_0. In the limit of lower values of E/n_0, the relaxation of energy is a very slow process and Monte Carlo simulations require large computation time. The results from the Monte Carlo simulations are consistent and agree very well with those predicted by the Boltzmann equation analysis, validating the theoretical method for solving the Boltzmann equation and numerical integrity of both methods of calculations.

In Fig. 7 the percentage differences in the third-order transport coefficients for the Reid ramp model, calculated using the two-term and the fully converged multiterm solutions
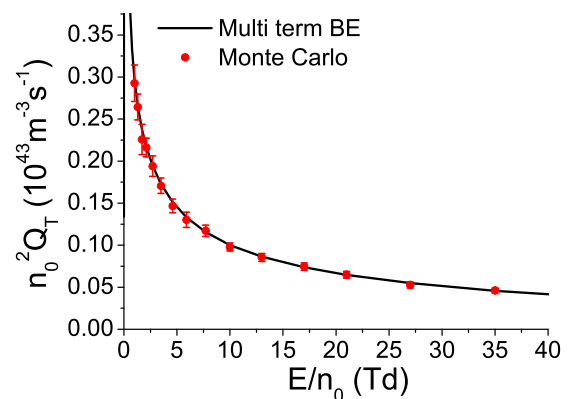

FIG. 6. Comparison between the multiterm Boltzmann equation results for transverse third-order transport coefficient and those calculated with a Monte Carlo simulation technique.
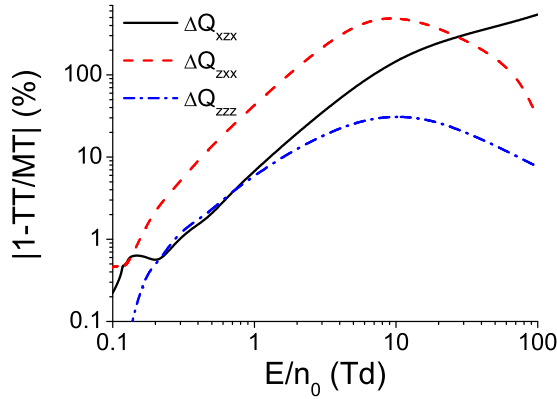
FIG. 7. Percentage difference between the two-term (TT) and multiterm (MT) results for the third-order transport coefficients for the Reid ramp model.
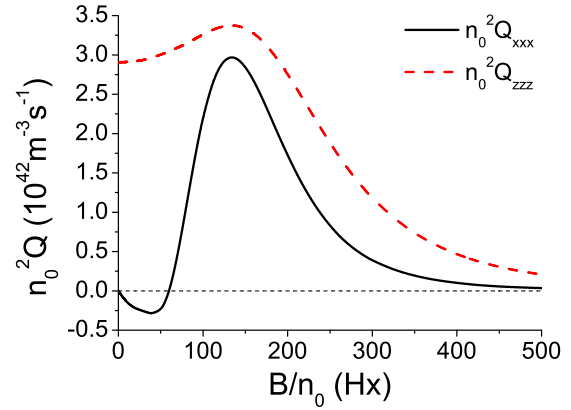

FIG. 8. Variation of $n_0^2 Q_{zzz}$ and $n_0^2 Q_{xxx}$ with B/n_0 for the Reid ramp model. Calculations are performed by a multiterm theory for solving the Boltzmann equation in a crossed field configuration. The reduced electric field E/n_0 is set to 12 Td.

of Boltzmann's equation, are shown. We see that maximum errors in the two-term approximation, for Q_{zzz} and Q_{zxx}, occur at about 10 Td where the mean energy of the electrons is close to the threshold of a cross section for inelastic collisions. On the other hand, the discrepancy between the two-term and multiterm solutions of Boltzmann's equation for Q_{xxz} increases with E/n_0 monotonically over the range of E/n_0 considered in this work. For the lower values of E/n_0, the coefficient Q_{zxx} appears to be the most sensitive with respect to the number of spherical harmonics used for solving Boltzmann's equation while for the higher values of E/n_0 the most sensitive coefficient is Q_{xzx}. We observe that the errors between the two-term and converged multiterm results can be as high as 500%. The presence of inelastic collisions produces asymmetry in velocity space which makes the two-term approximation inadequate for the analysis of the third-order transport coefficients. It is also important to note that the differences between the two-term approximation and multiterm solution of Boltzmann's equation for third-order transport coefficients are much higher than those for the lower-order transport coefficients, e.g., for the drift velocity and diffusion coefficients. This suggests that the third-order transport coefficients are more sensitive with respect to the way of solving the Boltzmann equation. Thus, it seems that the use of a multiterm theory for solving the Boltzmann equation is mandatory in the presence of inelastic collisions when it comes to calculations of the third-order transport coefficients.

In Fig. 8 we show the variation of the coefficients Q_{xxx} and Q_{zzz} as a function of B/n_0 at $E/n_0 = 12$ Td. As already discussed, Q_{zzz} describes the deviation from the Gaussian along the z axis (see Appendix B). For perpendicular electric and magnetic fields, Q_{xxx} is a measure of the deviation from the Gaussian along the $E \times B$ direction. For B/n_0 greater than approximately 150 Hx, we observe that both Q_{xxx} and Q_{zzz} monotonically decrease with increasing B/n_0. This is a clear indication of the magnetic-field-controlled regime in which the cyclotron frequency dominates the collision frequency and the electrons are held by the magnetic field lines. For B/n_0 less than approximately 150 Hx, the behavior of Q_{xxx} and Q_{zzz} is less intuitive. For these values of B/n_0 the collision

frequency is generally higher than the cyclotron frequency, but on average, an increasing magnetic field acts to increase the fraction of the orbit completed between collisions. As a consequence, the collision frequency begins to fall down with increasing B/n_0 and Q_{zzz} raises.

The behavior of Q_{xxx} for the lower values B/n_0 is particularly interesting. Initially, in the limit of the lowest B/n_0, Q_{xxx} is negative due to the Lorentz force and spatial variation of the energy (and hence spatial variation of the collision frequency), which on average induces the spatial variation of the average velocity of the electrons along the negative direction of the x axis. In this B/n_0 region, the negative sign of Q_{xxx} corresponds to an elongation of the swarm in the direction of the x component of the drift velocity (along the negative x axis in this field configuration). This is analogous to the elongation of the swarm described by the Q_{zzz} element along the z component of the drift velocity (the qE direction). With a further increase of B/n_0 the influence of collisions becomes more and more significant which in turn leads to the compressing or spreading of the swarm along the negative or positive direction of the x axis. Due to these effects Q_{xxx} becomes positive and increases with increasing B/n_0.

In Fig. 9 we show the remaining components of the third-order transport coefficient tensor as a function of B/n_0 for perpendicular electric and magnetic fields. For the higher values of B/n_0 all components decrease with an increasing B/n_0 as more and more electrons are held in their orbits by the magnetic field. For the lower values of B/n_0, however, the behavior of the third-order transport coefficients is complex due to many individual factors which simultaneously influence the third-order coefficient tensor. These individual factors include the thermal anisotropy (the chaotic motion of charged particles is different along different directions), magnetic anisotropy (the orientation of charged-particle orbits is controlled by the magnetic field), and spatial variations of the average velocity and average energy along the longitudinal and transverse directions. However, comparing the magnetic-field-free case and crossed electric and magnetic fields the interpretation of the third-order transport coefficients is similar (see Appendix B). For example, the coefficient Q_{zyy} describes
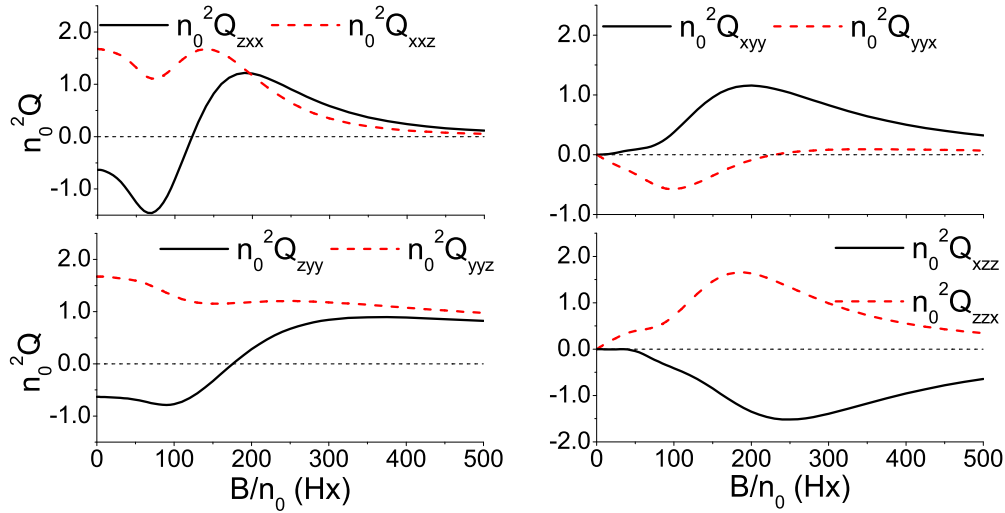
FIG. 9. Variation of the third-order transport coefficients with the repeated indices for the Reid ramp model. Calculations are performed via a multiterm theory for solving the Boltzmann equation in a crossed field configuration. The reduced electric field E/n_0 is set to 12 Td. The components of the $n_0^2 Q$ tensor are given in units of 10^{42} m^{-3}s^{-1}.

the differences in the longitudinal spreading in the central part of the swarm and along its transverse edges in the y direction. Likewise, the coefficient Q_{yyz} reflects the differences in the transverse spreading at the front of the swarm (along the direction given by the positive z) and at the trailing edge of the swarm (along the direction given by the negative z). The similar interpretation may be given for the remaining third-order transport coefficients shown in Fig. 9.

In Fig. 10 we show the comparison between the individual components of the third-order transport coefficient tensor, which could be identified in our Monte Carlo simulations, and the corresponding results, which are obtained from the numerical solution of the Boltzmann equation. The two sets

of results agree very well, even over the range of E/n_0 where the values of the coefficients are negative. We see that the error bars are not identical for different third-order transport coefficients. This indicates that the statistical fluctuations of the individual dynamical variables required for the evaluation of the third-order transport coefficients are not the same. Nevertheless, we see that the results obtained from the numerical solution of the Boltzmann equation are in very good agreement with those predicted by Monte Carlo simulations. This validates the theory and numerical scheme for solving the Boltzmann equation and Monte Carlo method when both the electric and magnetic fields are present and crossed at the right angle.
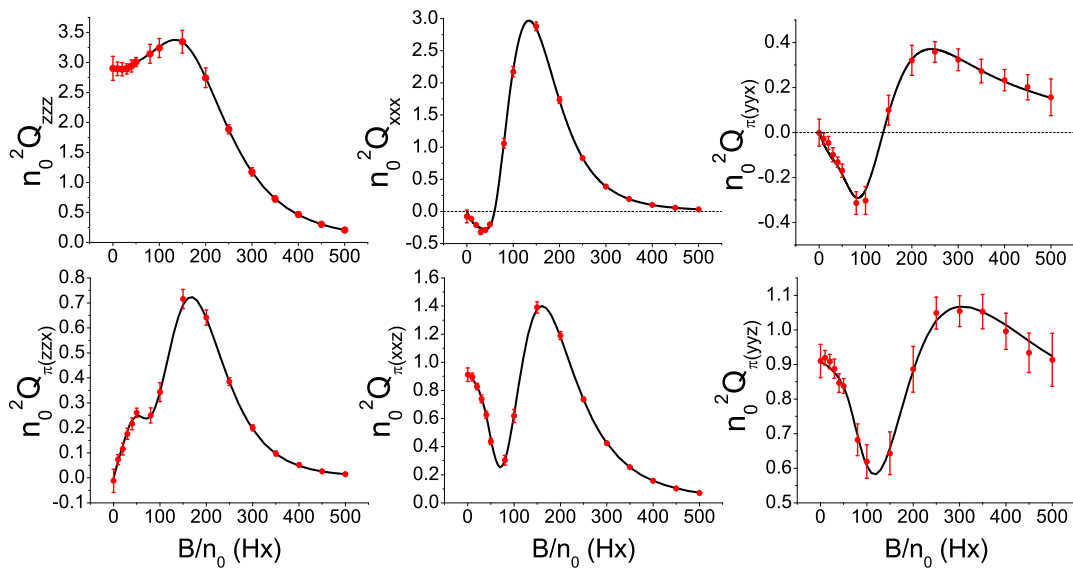

FIG. 10. Comparison between the multiterm Boltzmann equation results (full line) for various third-order transport coefficients and those calculated by a Monte Carlo simulation technique (symbols with error bars) in a crossed field configuration. The reduced electric field E/n_0 is set to 12 Td. The components of the $n_0^2 Q$ tensor are given in units of 10^{42} m^{-3}s^{-1}.
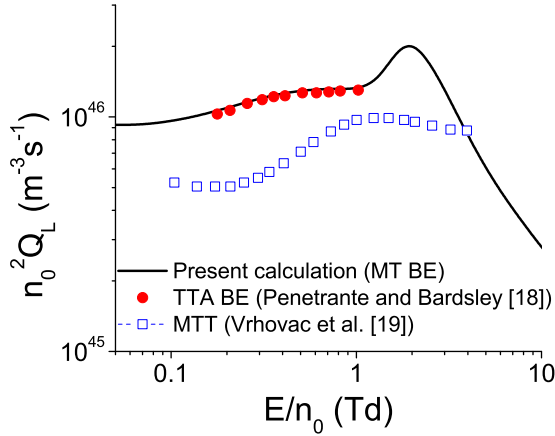
FIG. 11. Variation of the longitudinal third-order transport coefficient $n_0^2 Q_L$ with E/n_0 for electrons in neon. Our multiterm Boltzmann equation results (MT BE) are compared with those obtained by two-term approximation for solving the Boltzmann equation (TTA BE) [18] and momentum transfer theory (MTT) [19].

E. Third-order transport coefficients for electrons in neon

As an example of our calculations in real gases, in Fig. 11 we display the variation of the Q_L with E/n_0 for electrons in neon. The results obtained from the multiterm solution of the Boltzmann equation are compared with those predicted by the two-term approximation [18] and momentum transfer theory (MTT) [19]. The agreement between our multiterm results and those obtained by the two-term approximation is very good. This is a clear sign that there is no significant difference between the cross sections for elastic collisions of the electrons in neon used in the present multiterm calculations and in the previous two-term calculations performed by Penetrante and Bardsley [18]. The additional factor which favors the good agreement is the minimal influence of inelastic collisions. If inelastic collisions would play a more important role, then undoubtedly the differences between the multiterm and two-term results would be much higher. In any case, no calculations of Q_L were made by Penetrante and Bardsley for the higher values of E/n_0. On the other hand, the discrepancy between our results and those predicted by the momentum transfer theory (MTT) is clearly evident. This can be attributed to the fact that the momentum transfer theory assumes a very simple energy distribution function based on an effective mean energy. MTT produces reasonable results for the lowest-order transport coefficients such as drift velocity and even diffusion but it is expected to fail for ionization which depends on the high energy tail and also for higher-order transport coefficients that are very sensitive on the cross sections and correspondingly on the distribution function at all energies. Limitations of the MTT have been discussed many times [2,16,33,34,66].

In Fig. 12 we show the variation of the individual elements of the third-order transport coefficient tensor as a function of E/n_0 for electrons in neon. The same generic features of the third-order transport coefficients observed previously for the Reid ramp model are clearly evident. Both Q_{zzz} and Q_{xxz} are positive while the coefficient Q_{zxx} is negative over the range of E/n_0 considered. The total collision frequency
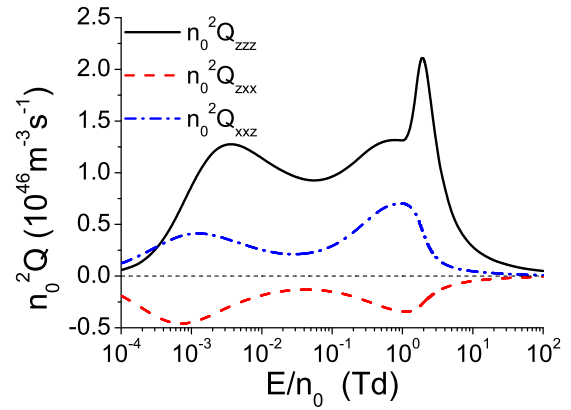

FIG. 12. Variation of the third-order transport coefficients with E/n_0 for electrons in neon. Calculations are performed using a multiterm approach for solving the Boltzmann equation.

increases with the increase of E/n_0, but not sufficiently fast to induced negative values of Q_{zzz} and Q_{xxz} (see Appendix B). The oscillatory behavior in the profiles of Q_{zzz}, Q_{xxz} and Q_{zzz} occurs for E/n_0 approximately less than 1 Td reflecting the energy variation of the cross section for elastic collisions. For E/n_0 approximately greater than 1 Td, inelastic collisions begin to play a significant role. As for the Reid ramp model, it appears that significant inelastic processes are required to suppress the longitudinal and transverse third-order transport coefficients.

IV. CONCLUSION

In this paper we have discussed the third-order transport coefficient tensor of charged-particle swarms moving in an infinite neutral gas under the influence of spatially homogeneous electric and magnetic fields. The third-order transport coefficient tensor is defined in terms of the extended flux gradient relation and the extended diffusion equation. The group projector method is then used for identifying the structure of the tensor and symmetries along its individual elements when both the electric and magnetic fields are present. For an electric-field-only situation, we have found that the third-order transport coefficient tensor has seven nonzero and only three independent elements. For parallel electric and magnetic fields, rotational invariance implies the third-order transport coefficient tensor has 11 nonzero and four independent elements, while for orthogonal electric and magnetic fields the tensor has 14 nonzero and 10 independent elements. Finally, when electric and magnetic fields are crossed at an arbitrary angle, it is found that the third-order transport coefficient tensor has 27 nonzero elements among which 18 are independent. The proposed methodology based on the group projector method and symmetry considerations of the Boltzmann equation can be applied to any of the transport coefficient of an arbitrary tensorial rank.

The second important issue addressed in the present work is the physical interpretation of the third-order transport coefficients. In order to resolve this issue, we have expanded the Fourier transform of the number charged-particle density in terms of the longitudinal and transverse third-order transport

coefficients. Using the inverse Fourier transformation of the expansion coefficients, we have derived the expression for the number density of charged particles in which the effects of third-order transport coefficients are explicitly included. It is found that deviations of the Gaussian distribution along the specific directions are directly related with the sign of the individual third-order transport coefficients.

Explicit expressions for the third-order transport coefficients in terms of the moments of the distribution function and in the absence of nonconservative collisions are derived in the framework of a multiterm theory for solving the Boltzmann equation. Using the symmetry properties of the moments, we have analyzed the structure of the third-order transport coefficient tensor. We have also developed the Monte Carlo method in which the third-order transport coefficients are defined in terms of the moments of charged-particle density in configuration space. It is found that only two independent components of the third-order transport coefficient tensor can be identified, as all tensor components are contracted with the corresponding spatial partial derivatives of charged-particle density. Thus, care must be taken when comparing the Monte Carlo results with those obtained by other theories.

Numerical calculations are performed using a multiterm solution of the Boltzmann equation for a range of model gases, including the Maxwell, hard sphere, and Reid ramp models. The results obtained are in very good agreement with those predicted by the Monte Carlo method when possible, over the range of the applied electric and magnetic fields. An important observation is that the contribution of the third-order transport coefficients to the spatial profile of the swarm becomes more pronounced for increasing the charged-particle to neutral-particle mass ratio. In this work we have also displayed and emphasized the need for a multiterm solution technique of Boltzmann's equation. It is found that the discrepancy between the two-term and fully converged multiterm results are much higher for the third-order transport coefficients than those for the lower order transport coefficients, e.g., drift velocity and diffusion coefficients. The theory and associated computer codes in the present work are equally valid for real gases. The third-order transport coefficients are calculated for electrons in neon and the results of calculations are compared with those evaluated by the two-term approximation for solving the Boltzmann equation and momentum transfer theory. Comparison with previous theories have shown surprisingly good agreement with the two-term solution of the Boltzmann equation and a significant disagreement with the momentum transfer theory.

The duality of transport coefficients, e.g., the existence of two different families of transport coefficients, the bulk and the flux, is well known in the presence of nonconservative collisions. Third-order transport coefficients are expected to be more sensitive to the explicit influence of nonconservative collisions. In order to investigate the effects of nonconservative collisions on the third-order transport coefficients one must go to third-order in the density gradient expansion to account for such effects. This remains the focus of our future investigation. Likewise, the remaining step to be taken, is to apply the theory and mathematical machinery developed in this work to investigate the correlation between the third-order transport coefficients and those of lower order, e.g., the

drift and diffusion coefficients [19]. Additional issues which should be considered are the effects of anisotropic scattering and the behavior of the third-order transport coefficients in time-dependent electric and magnetic fields. Finally, it would be very challenging to model strong nonequilibrium systems such as streamer discharges by suitable coupling of the extended diffusion equation which incorporates the third-order transport coefficients for both the electrons and ions, and Poisson's equation for the space charge electric field calculation.

The theory presented here covers the structure, symmetries, and method of calculation of the third-order transport coefficients and the advantages that it may bring should it be applied. In this paper, we focus on physics of ionized gases (swarms and low-temperature collisional plasmas), but approach may be extended to other physical systems if one accounts for the dominant physical interactions and expected symmetries. One such example where these results may be applied directly is modeling of positron thermalization in gas filled traps [86,87] or thermalization of positrons in gases [88–90].

APPENDIX A: THE GROUP PROJECTOR METHOD

The structure of tensorial transport coefficients can be determined by employing group theory, since their structure reflects the symmetry of the system. The studied system consists of a swarm of charged particles, neutral background gas particles and the applied electric and magnetic fields. The symmetry group of a system is the group of all transformations under which the system is invariant [91–93]. The symmetry groups of the electric and magnetic fields are $C_{\infty V}$ and $C_{\infty h}$ respectively, since the electric field is a polar vector, and the magnetic field is an axial vector. These are the symmetry groups of an immobile cone and of a rotating cylinder, respectively [91]. If both electric and magnetic fields are present in the system, the symmetry group of the field configuration is determined by the angle between the fields. The symmetry group of the parallel fields configuration is C_{∞}. This is the symmetry group of a rotating cone [91]. Orthogonal field configuration has the symmetry group C_{1v}. The symmetry group of the general field configuration is the trivial group C_1. Background gas is invariant under all transformations from the orthogonal group $O(3)$. This is the symmetry group of a sphere. Therefore, the symmetry group of the field configuration is also the symmetry group of the entire system.

The structure of a tensor can be determined from its invariance, under operations from the symmetry group of the system. The action of a group G on vectors, from a vector space H, is represented by a group homomorphism from G to the general linear group on H, $GL(H)$ [92,93]. Polar

vectors, such as drift velocity, are transformed by the polar vector representation of the symmetry group of the system $D^{pv}(G)$. This representation is reducible [65,93] and, for finite and compact groups, it decomposes into the irreducible components $D^{(\mu)}(G)$ as

$$D^{pv}(G) = \oplus_{\mu=1}^{r} a_\mu D^{(\mu)}(G). \tag{A1}$$

Here a_μ is the number of times the irreducible representation $D^{(\mu)}(G)$ appears in the decomposition of $D^{pv}(G)$, and r is the number of inequivalent irreducible representations of the group G. In addition, for decomposable representations there exists a symmetry-adapted basis [65,93], which satisfies the condition

$$D^{pv}(G)|\mu t_\mu m\rangle = \sum_{n=1}^{|\mu|} D_{nm}^{(\mu)}(G)|\mu t_\mu n\rangle. \tag{A2}$$

This implies that for every irreducible representation $D^{(\mu)}(G)$ from (A1) there will be a subspace in H which transforms by $D^{(\mu)}(G)$ [65,93]. A very important representation, which exists for every group G, is the trivial irreducible representation A_0. This representation is defined as $D^{(A_0)}(g) = 1$, $\forall g \in G$. This representation is irreducible, since it is one dimensional.

It can be seen from (A2) that a vector is invariant under the action of $D^{(pv)}(G)$ if it belongs to the subspace of the trivial irreducible representation. This invariant subspace can be found by employing group projectors. In the case of the trivial representation, the group projector is simply

$$P^{(A_0)}(D^{pv}, G) = \frac{1}{|G|} \sum_{g \in G} D^{pv}(g) \tag{A3}$$

for finite groups, where $|G|$ is the order of the group G [65]. For one-parameter Lie groups the group projector for A_0 is

$$P^{(A_0)}(D^{pv}, G) = \sum_{R} \int D^{pv}(R) \, dR. \tag{A4}$$

Here the summation goes over distinct connected components, and integration is taken over the range of the group parameter [93]. Any vector, from the invariant subspace of $D^{pv}(G)$, including the drift velocity, is a linear combination of the eigenvectors of the projection operator $P^{(A_0)}(D^{pv}, G)$.

Diffusion tensor is a linear operator which maps the local density gradient vector $\nabla n(r, t)$ onto the diffusive flux vector. Therefore diffusion tensor belongs to the range of the projector $P^{(A_0)}(D^{pv\otimes 2}, G)$ where $D^{pv\otimes 2}(G)$ represents $D^{pv} \otimes D^{pv}(G) = D^{pv}(G) \otimes D^{pv}(G)$. Similarly the skewness tensor maps the tensor square of the gradient vector, which acts upon the local density $\nabla \otimes \nabla n(r, t)$, onto the vector of the third-order diffusive flux. Thus the skewness tensor belongs to the range of the projection operator $P^{(A_0)}(D^{pv} \otimes [D^{pv}]^2, G)$, where $[D^{pv}]^2$ represents the symmetrized tensor square of the polar vector representation. This symmetrization is a result of the commutativity of the gradient operators.

Strictly speaking, the action of the group on operators, such as diffusion tensor and skewness tensor, is represented by employing superoperators [94]. They are defined as $\widehat{\widehat{D}}(g)\hat{A} = D^{pv}(g)\hat{A}D^{pv}(g^{-1})$. Therefore, the most straightforward application of group theory would require the use of group superoperators. However, this is not necessary, since every

second rank basis operator $|i\rangle \otimes \langle j|$ acting on a vector space H is uniquely paired with a basis vector $|i\rangle \otimes |j\rangle$ from the vector space $H \otimes H$. The same applies for the basis operators of the third rank $|i\rangle \otimes [\langle j| \otimes \langle k|]$ and basis vectors $|i\rangle \otimes [|j\rangle \otimes |k\rangle]$ from the vector space $H \otimes [H \otimes H]$. Here square brackets represent symmetrization of the tensor product. Thus, the group projector method can be applied for representations $D^{pv}(G) \otimes D^{pv}(G)$ and $D^{pv} \otimes [D^{pv}]^2$ in the corresponding vector spaces. Then eigenvectors of the group projectors can be mapped into the corresponding basis tensors. Therefore diffusion tensor and skewness tensor are linear combinations of the basis tensors, which are obtained from eigenvectors of the projection operators $P^{(A_0)}(D^{pv} \otimes D^{pv}, G)$ and $P^{(A_0)}(D^{pv} \otimes [D^{pv}]^2, G)$, respectively. Moreover, it is not necessary to use $D^{pv} \otimes [D^{pv}]^2$ for determining the structure of the skewness tensor. One can instead use $D^{pv} \otimes D^{pv} \otimes D^{pv}$ and symmetrize the resulting tensors by the last two indices.

APPENDIX B: PHYSICAL INTERPRETATION OF THE INDIVIDUAL COMPONENTS OF THE THIRD-ORDER TRANSPORT COEFFICIENT TENSOR AND ANALYSIS OF THEIR SIGN

Using the flux gradient relation (7), the fluxes of charged particles induced exclusively by the third-order transport coefficient tensor are given by

$$\Gamma_{Q,z} = Q_{zzz}\frac{\partial^2 n(r,t)}{\partial z^2} + Q_{zxx}\left[\frac{\partial^2 n(r,t)}{\partial x^2} + \frac{\partial^2 n(r,t)}{\partial y^2}\right],$$
$$\Gamma_{Q,x} = 2Q_{xxz}\frac{\partial^2 n(r,t)}{\partial x \partial z}, \tag{B1}$$

where Q_{zzz}, Q_{zxx}, and Q_{xxz} are independent components of the third-order transport coefficient tensor (see Sec. II B). The leading term in the expansion of the density of charged particles (33) is of key importance in considering the sign of the derivative of the charged-particle density. Therefore, in what follows we consider only this term in the analysis of the fluxes of charged particles (B1). The second-order derivatives of the Gaussian (32) are given by

$$\frac{\partial^2 n^{(0)}(r,t)}{(\partial z)^2} = \left(z^2 - \sigma_z^2\right)\frac{n^{(0)}(r,t)}{\sigma_z^4}, \tag{B2}$$

$$\frac{\partial^2 n^{(0)}(r,t)}{(\partial x)^2} = \left(x^2 - \sigma_x^2\right)\frac{n^{(0)}(r,t)}{\sigma_x^4}, \tag{B3}$$

$$\frac{\partial^2 n^{(0)}(r,t)}{(\partial x \partial z)} = xz\frac{n^{(0)}(r,t)}{\sigma_x^2\sigma_z^2}, \tag{B4}$$

where

$$\sigma_x^2 = 2D_T t, \quad \sigma_z^2 = 2D_L t. \tag{B5}$$

For simplicity, the above derivatives correspond to the coordinate system whose origin is placed at the center of the Gaussian distribution. Thus, the term $z - Wt$ is replaced by the term z in (B2) and (B4).

In order to visualize these second-order derivatives in the most efficient way for arbitrarily values of σ_z, we introduce the set of new coordinates $x/\sigma_x = \chi_x$, $y/\sigma_y = \chi_y$, and $z/\sigma_z = \chi_z$.
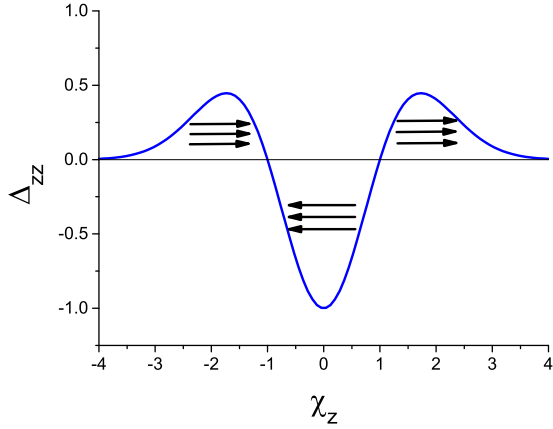
FIG. 13. The normalized derivative Δ_{zz} of the density of charged particles as a function of the relative coordinate χ_z. The arrows denote the direction of motion represented by Q_{zzz} if this component is positive. The field force is oriented along the positive χ_z direction.

FIG. 14. The normalized derivative Δ_{xx} of the density of charged particles as a function of the relative coordinate χ_x. The arrows denote the direction of motion represented by Q_{zxx} if this component is positive: the arrows directed upwards (downwards) represent motion in the positive (negative) z direction.

Using the new coordinates, Eqs. (B2)–(B4) become

$$\frac{\partial^2 n^{(0)}}{\partial \chi_z^2} = (\chi_z^2 - 1)n^{(0)}, \tag{B6}$$

$$\frac{\partial^2 n^{(0)}}{\partial \chi_x^2} = (\chi_x^2 - 1)n^{(0)}, \tag{B7}$$

$$\frac{\partial^2 n^{(0)}}{\partial \chi_x \partial \chi_z} = \chi_x \chi_z n^{(0)}, \tag{B8}$$

where

$$n^{(0)}(\boldsymbol{\chi}, t) = C_\chi \exp\left[-\tfrac{1}{2}\left(\chi_z^2 + \chi_x^2 + \chi_y^2\right)\right] \tag{B9}$$

and

$$C_\chi = \frac{N_0 e^{-R_{\mathrm{net}}t}}{(2\pi)^{3/2}\sigma_x^2\sigma_z}. \tag{B10}$$

By combining equations (B6)–(B10) the normalized second-order derivatives of the density of charged particles can be written as follows:

$$\Delta_{zz} \equiv \frac{1}{C_\chi}\frac{\partial^2 n^{(0)}}{\partial \chi_z^2} = (\chi_z^2 - 1)e^{-\frac{1}{2}(\chi_z^2 + \chi_x^2 + \chi_y^2)}, \tag{B11}$$

$$\Delta_{xx} \equiv \frac{1}{C_\chi}\frac{\partial^2 n^{(0)}}{\partial \chi_x^2} = (\chi_x^2 - 1)e^{-\frac{1}{2}(\chi_z^2 + \chi_x^2 + \chi_y^2)}, \tag{B12}$$

$$\Delta_{xz} \equiv \frac{1}{C_\chi}\frac{\partial^2 n^{(0)}}{\partial \chi_x \partial \chi_z} = \chi_x \chi_z e^{-\frac{1}{2}(\chi_z^2 + \chi_x^2 + \chi_y^2)}. \tag{B13}$$

In Fig. 13 we show the quantity Δ_{zz} as a function of χ_z. We see that the representing curve is symmetric with respect to the origin in which it has a minimum. If Q_{zzz} is positive the direction of motion represented by this component depends on the sign of Δ_{zz} in the following way. When Δ_{zz} is positive, the motion described by Q_{zzz} is also directed along the positive z axis, which is indicated by arrows that are oriented to the right. Conversely, when Δ_{zz} is negative, the motion described by Q_{zzz} is directed along the negative z axis, which is indicated in this case by arrows that are oriented to the left. Therefore, when $Q_{zzz} > 0$ the leading edge of the Gaussian is elongated while the training edge is compressed to a certain extent. It is
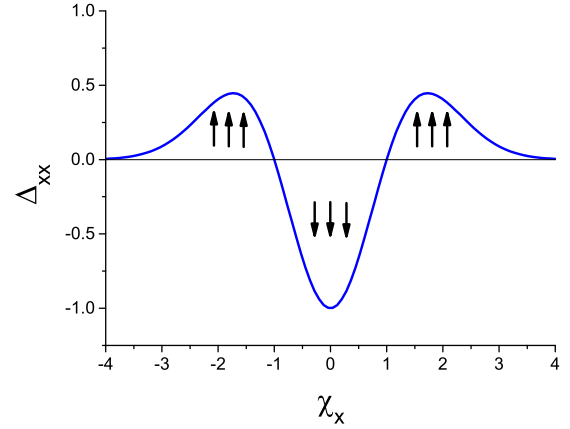
clear that when $Q_{zzz} < 0$, then the opposite situation holds: the leading edge of the Gaussian is compressed while the trailing edge is elongated.

Figure 14 shows the graph of the function Δ_{xx}. This function is identical to the one illustrated in Fig. 13. When Q_{zxx} is positive, the motion described by Q_{zxx} is directed along the positive z axis at the swarm edges, which is indicated by arrows that are oriented upwards. However, the motion represented by Q_{zxx} at the swarm center is directed along the negative z axis in this case, which is indicated by arrows that are oriented downwards. Likewise, if Q_{zxx} is negative, then the motion described by Q_{zxx} is directed along the negative z axis at the edges of the swarm, and along the positive z axis at the swarm center.

In Fig. 15 we show the contour plot of the function Δ_{xz} as a function of χ_x and χ_z. This function is positive in the first and
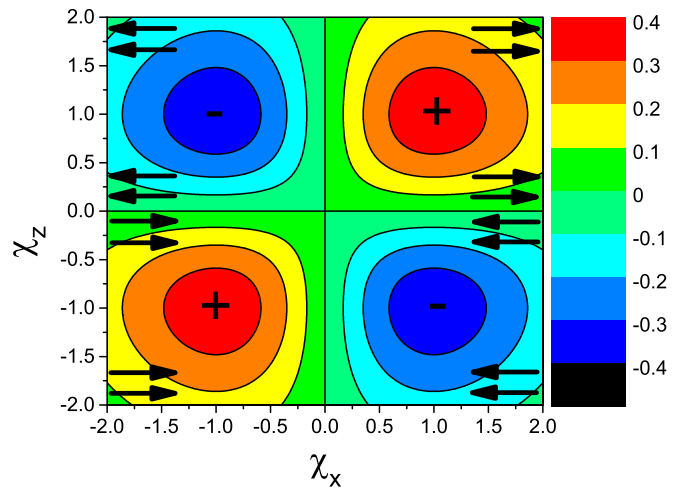

FIG. 15. The normalized derivative Δ_{xz} of the density of charged particles as a function of the relative coordinates χ_x and χ_z. The arrows denote the direction of motion represented by Q_{xxz} if this component is positive.

third quadrant and negative in the second and fourth quadrant. If Q_{xxz} is positive the direction of motion represented by this component depends on the sign of Δ_{xz} in the following way. When Δ_{xz} is positive the motion described by Q_{xxz} is directed along the positive x axis which is indicated by arrows that are oriented to the right. Conversely, when Δ_{xz} is negative the motion described by Q_{xxz} is directed along the negative x axis which is indicated by arrows that are oriented to the left. It is clear that when $Q_{xxz} < 0$ the direction of motion represented by this component is reversed. It should be noted that the joint contribution of Q_{zxx} and Q_{xxz} leads to a pear-shaped Gaussian distribution.

In what follows we investigate the effects of the gas pressure on the third-order transport coefficients. Using the set of new coordinates χ_x, χ_y and χ_z, the number density of charged particles given by Eq. (33) can be written as

$$n^{(1)}(\mathbf{r}, t) = n^{(0)}(\mathbf{r}, t) \left[1 + \frac{tQ_L}{\sigma_z^3} \chi_z (\chi_z^2 - 3) \right.$$
$$\left. + \frac{3tQ_T}{\sigma_x^2 \sigma_z} \chi_z (\chi_x^2 + \chi_y^2 - 2) \right]. \quad \text{(B14)}$$

From Eq. (B14) we see that the contribution of the third-order transport coefficients to the spatial profile of the swarm is reduced with increasing number density of the neutral particles n_0. This is due to the fact that Q_L and Q_T scale as $1/n_0^2$ while σ_x and σ_z scale as $1/\sqrt{n_0}$ with the variation of n_0. From this, it follows that the terms tQ_L/σ_z^3 and $3tQ_T/\sigma_x^2 \sigma_z$ scale as $1/\sqrt{n_0}$ with with the variation of n_0. In addition, from Eq. (B14) we can also see that the influence of the third-order transport coefficients on the spatial profile of charged particles is reduced as $1/\sqrt{t}$ with increasing t due to the time dependence of the terms tQ_L/σ_z^3 and $3tQ_T/\sigma_x^2 \sigma_z$. Thus, from the scalings of the third-order transport coefficients and associated properties it can be concluded that their experimental determination would be the most efficient at low pressures. On the other hand, measurements at low pressures in drift tubes require optimal gaps and volumes in order to reach the conditions where hydrodynamic approximation is applicable (negligible length or relaxation distances as compared to the overall gap). Special care should be taken in order to avoid kinetic phenomena [16] such as diffusion cooling [95,96] and other issues associated with an inability of the swarm to be fully relaxed due to a small number of collisions of charged particles and neutral gas particles. In any case, the experimental determination of third-order transport coefficients requires large gas volumes and low pressures. Similar findings have been reported in Ref. [18].

In studies of third-order transport coefficients tensor we often find it necessary to refer to the sign of the third-order transport coefficients to explain certain phenomena. Let us assume that the swarm of charged particles is acted on solely by an electric field. The following elementary considerations apply.

The motion of charged particles represented by the longitudinal component Q_{zzz} produces differences in the spreading of the density profile between the front and trailing edges of the swarm. When $Q_{zzz} > 0$, the front edge of the density profile is elongated, while the trailing edge is compressed. The opposite

situation holds when $Q_{zzz} < 0$: the front edge of the swarm is compressed while the trailing edge of the profile is elongated.

Charged particles at the front of the swarm have higher energies on average, than those at the back of the swarm, as they are accelerated through the larger potential difference. If the collision frequency is independent of energy, the spread of charged particles along the field direction is induced by the action of the force and by the chaotic motion of particles. If the collision frequency is a decreasing function of the charged-particle energy, the friction due to collisions along the field direction is also decreased contributing additionally in the spreading of the density profile. When collision frequency increases with the particle energy, however, the friction will be enhanced along the field direction which in turn reduces the spreading of the density profile. Thus, the longitudinal component Q_{zzz} is positive whenever the growth of collision frequency and associated energy losses in collisions are not able to affect the spreading of charged particles due to the electric field force and chaotic motion of charged particles. This is exactly what happens in most cases considered in our calculations.

The motion of a swarm represented by Q_{xzx} produces differences in the transverse spreading of the density profile. When $Q_{xzx} > 0$, the density profile is expanded along the transverse direction at the front of the swarm while at the back of the swarm the profile is compressed. When $Q_{xzx} < 0$, the density profile is compressed along the transverse direction at the front and extended at the trailing edge of the swarm.

The electric force does not act along the transverse direction. This suggests that the spreading of the density profile is entirely controlled by the chaotic motion of charged particles. If the collision frequency decreases with energy, this will further enhance the transverse spread at the front of the swarm as collisions between charged particles and background gas molecules are less frequent. If the collision frequency increases with energy, the reverse situation occurs. In this case it is the high energy electrons, which predominantly exist at the front of the swarm, have more collisions than those at the back of the swarm. This results in a greater resistance to the transverse spreading at the front of the swarm. Thus, the transverse component Q_{xzx} is positive under conditions in which the growth of the collision frequency and energy losses in collisions are not intensive enough to exceed the higher average speed of charged particles at the front of the swarm.

The off-diagonal component Q_{zxx} describes the differences in the longitudinal spreading in the central part of the swarm and along its transverse edges. If $Q_{zxx} > 0$, the longitudinal spreading is faster at the transverse edges than in the central part of the swarm. Conversely, if $Q_{zxx} < 0$, the reverse situation occurs: the longitudinal spreading is more pronounced in the central part of the swarm than at the edges. The parabolic rise in mean energy along the transverse direction favors the faster longitudinal spreading at the transverse edges of the swarm. The parabolic rise in mean energy is due to the fact that the most energetic electrons quickly cross the distance between the swarm's center and its edges, if the increase of the collision frequency is not large enough to compensate for the high speed of energetic electrons. If the collision frequency is independent of energy, this is the only contribution to the difference in the rate of longitudinal expansion along

TABLE II. Symmetry properties of the individual components of the skewness tensor. The transformation represents A (parity), B (rotation of π about the z axis), C (parity and rotation of π about the y axis), and D (parity and rotation of π about the x axis).

	Transformation			
Tensor component	$\boldsymbol{E} \to -\boldsymbol{E}, \boldsymbol{B} \to \boldsymbol{B}$	$\boldsymbol{E} \to \boldsymbol{E}, \boldsymbol{B} \to (-B_y, B_z)$	$\boldsymbol{E} \to \boldsymbol{E}, \boldsymbol{B} \to (B_y, -B_z)$	$\boldsymbol{E} \to \boldsymbol{E}, \boldsymbol{B} \to -\boldsymbol{B}$
Q_{xxz}, Q_{xzx}	$-Q_{xxz}, -Q_{xzx}$	Q_{xxz}, Q_{xzx}	Q_{xxz}, Q_{xzx}	Q_{xxz}, Q_{xzx}
Q_{yyz}, Q_{yzy}	$-Q_{yyz}, -Q_{yzy}$	Q_{yyz}, Q_{yzy}	Q_{yyz}, Q_{yzy}	Q_{yyz}, Q_{yzy}
Q_{zxx}	$-Q_{zxx}$	Q_{zxx}	Q_{zxx}	Q_{zxx}
Q_{zyy}	$-Q_{zyy}$	Q_{zyy}	Q_{zyy}	Q_{zyy}
Q_{zzz}	$-Q_{zzz}$	Q_{zzz}	Q_{zzz}	Q_{zzz}
Q_{xxx}	$-Q_{xxx}$	$-Q_{xxx}$	Q_{xxx}	$-Q_{xxx}$
Q_{xyy}	$-Q_{xyy}$	$-Q_{xyy}$	Q_{xyy}	$-Q_{xyy}$
Q_{xzz}	$-Q_{xzz}$	$-Q_{xzz}$	Q_{xzz}	$-Q_{xyy}$
Q_{yxy}, Q_{yyx}	$-Q_{yxy}, -Q_{yyx}$	$-Q_{yxy}, -Q_{yyx}$	Q_{yxy}, Q_{yyx}	$-Q_{yxy}, -Q_{yyx}$
Q_{zxz}, Q_{zzx}	$-Q_{zxz}, -Q_{zzx}$	$-Q_{zxz}, -Q_{zzx}$	Q_{zxz}, Q_{zzx}	$-Q_{zxz}, -Q_{zzx}$
Q_{xyz}, Q_{xzy}	$-Q_{xyz}, -Q_{xzy}$	Q_{xyz}, Q_{xzy}	$-Q_{xyz}, -Q_{xzy}$	$-Q_{xyz}, -Q_{xzy}$
Q_{yxz}, Q_{yzx}	$-Q_{yxz}, -Q_{yzx}$	Q_{yxz}, Q_{yzx}	$-Q_{yxz}, -Q_{yzx}$	$-Q_{yxz}, -Q_{yzx}$
Q_{zxy}, Q_{zyx}	$-Q_{zxy}, -Q_{zyx}$	Q_{zxy}, Q_{zyx}	$-Q_{zxy}, -Q_{zyx}$	$-Q_{zxy}, -Q_{zyx}$
Q_{xxy}, Q_{xyx}	$-Q_{xxy}, -Q_{xyx}$	$-Q_{xxy}, -Q_{xyx}$	$-Q_{xxy}, -Q_{xyx}$	Q_{xxy}, Q_{xyx}
Q_{yxx}	$-Q_{yxx}$	$-Q_{yxx}$	$-Q_{yxx}$	Q_{yxx}
Q_{yyy}	$-Q_{yyy}$	$-Q_{yyy}$	$-Q_{yyy}$	Q_{yyy}
Q_{yzz}	$-Q_{yzz}$	$-Q_{yzz}$	$-Q_{yzz}$	Q_{yzz}
Q_{yzz}, Q_{zzy}	$-Q_{zyz}, -Q_{zzy}$	$-Q_{zyz}, -Q_{zzy}$	$-Q_{zyz}, -Q_{zzy}$	Q_{zyz}, Q_{zzy}

the transverse direction. If the collision frequency decreases with energy, this is an additional factor which contributes to the rapid longitudinal spread at the transverse edges of the swarm. If the collision frequency increases with energy, this contributes to greater resistance to longitudinal expansion at the transverse edges than in the center of the swarm. For a constant collision frequency, Q_{zxx} component is positive, but much less in comparison to Q_{zzz} and Q_{xzx}. If the collision frequency decreases with energy, this component is positive and greater in magnitude than in the previous case. If the collision frequency increases with energy and Q_{xzx} is positive then the Q_{zxx} component is negative. This could be

expected, since the particles at the transverse edges have a slightly higher energy, and thus higher collision frequency. Such behavior of Q_{zxx} has been observed in the case of electron swarms in most atomic and molecular gases. If the collision frequency increases with energy and Q_{xzx} is negative then Q_{zxx} is positive. A possible explanation for this effect is that when Q_{xzx} is negative the energy of the electrons at the transverse edges of the swarm is, on average, less than in the center of the swarm. The high-energy electrons undergo more and more collisions for increasing electron energy which in turn prevent them from reaching the transverse edges of the swarm.

APPENDIX C: EXPRESSIONS FOR THE INDIVIDUAL ELEMENTS OF THE THIRD-ORDER TRANSPORT COEFFICIENT TENSOR IN THE BOLTZMANN EQUATION ANALYSIS AND MONTE CARLO SIMULATIONS

Using symmetry properties of the moments $F(\nu lm|s\lambda\mu)$ discussed in Ref. [70], the corresponding symmetry properties of the individual elements of the third-order transport coefficient tensor are detailed in Table II. The structure of the tensor may be determined by applying the symmetries in Table II in combination with the additional physical arguments that concern fluxes of charged particles induced by magnetic field. These arguments are necessary to identify the zero elements as well as those elements of the tensor which are equal between each other for a given configuration of the fields. The similar procedure has been applied for the vectorial and tensorial transport coefficients of the lower order [70].

In this Appendix we present the explicit expressions for the individual elements of the flux third-order transport coefficient tensor. These expressions have been derived by considering the flux-gradient relation in the spherical form (41) and explicit expressions for the irreducible gradient tensor operator [33]. In the following expressions α is omitted from the argument of F for brevity.

For parallel electric and magnetic fields, the individual elements of the flux tensor are given by

$$Q_{xxz} = \frac{1}{\sqrt{2}\alpha}[\text{Im}(F(011|221)) - \text{Im}(F(01-1|221))], \tag{C1}$$

$$Q_{xyz} = \frac{1}{\sqrt{2}\alpha}[\text{Re}(F(01-1|221)) - \text{Re}(F(011|221))], \tag{C2}$$

$$Q_{zxx} = -\frac{1}{\alpha}\left[\frac{1}{\sqrt{3}}\text{Im}(F(010|200)) + \frac{1}{\sqrt{6}}\text{Im}(F(010|220))\right] + \frac{1}{\alpha}\text{Im}(F(010|222)), \tag{C3}$$

$$Q_{zzz} = \frac{1}{\alpha}\left[\sqrt{\frac{2}{3}}\mathrm{Im}(F(010|220)) - \frac{1}{\sqrt{3}}\mathrm{Im}(F(010|200))\right]. \tag{C4}$$

For perpendicular electric and magnetic fields, the individual elements of the flux tensor are given by

$$Q_{xxx} = \frac{\sqrt{2}}{\alpha}\left[\frac{1}{\sqrt{3}}\mathrm{Im}(F(011|200)) + \frac{1}{\sqrt{6}}\mathrm{Im}(F(011|220))\right] + \frac{1}{\sqrt{2}\alpha}[-\mathrm{Im}(F(011|222)) + \mathrm{Im}(F(01-1|222))], \tag{C5}$$

$$Q_{xyy} = \frac{\sqrt{2}}{\alpha}\left[\frac{1}{\sqrt{3}}\mathrm{Im}(F(011|200)) + \frac{1}{\sqrt{6}}\mathrm{Im}(F(011|220))\right] + \frac{1}{\sqrt{2}\alpha}[\mathrm{Im}(F(011|222)) - \mathrm{Im}(F(01-1|222))], \tag{C6}$$

$$Q_{xzz} = \frac{\sqrt{2}}{\alpha}\left[\frac{1}{\sqrt{3}}\mathrm{Im}(F(011|200)) - \sqrt{\frac{2}{3}}\mathrm{Im}(F(011|220))\right], \tag{C7}$$

$$Q_{xxz} = \frac{1}{\sqrt{2}\alpha(t)}[\mathrm{Im}(F(011|221)) - \mathrm{Im}(F(01-1|221))], \tag{C8}$$

$$Q_{yxy} = -\frac{1}{\sqrt{2}\alpha}[\mathrm{Im}(F(011|222))+\mathrm{Im}(F(01-1|222))], \tag{C9}$$

$$Q_{yyz} = \frac{1}{\sqrt{2}\alpha}[\mathrm{Im}(F(011|221))+\mathrm{Im}(F(01-1|221))], \tag{C10}$$

$$Q_{zxz} = -\frac{1}{\alpha}\mathrm{Im}(F(010|221)), \tag{C11}$$

$$Q_{zxx} = -\frac{1}{\alpha}\left[\frac{1}{\sqrt{3}}\mathrm{Im}(F(010|200)) + \frac{1}{\sqrt{6}}\mathrm{Im}(F(010|220))\right] + \frac{1}{\alpha}\mathrm{Im}(F(010|222)), \tag{C12}$$

$$Q_{zyy} = -\frac{1}{\alpha}\left[\frac{1}{\sqrt{3}}\mathrm{Im}(F(010|200)) + \frac{1}{\sqrt{6}}\mathrm{Im}(F(010|220))\right] - \frac{1}{\alpha}\mathrm{Im}(F(010|222)), \tag{C13}$$

$$Q_{zzz} = \frac{1}{\alpha}\left[\sqrt{\frac{2}{3}}\mathrm{Im}(F(010|220)) - \frac{1}{\sqrt{3}}\mathrm{Im}(F(010|200))\right]. \tag{C14}$$

When electric and magnetic fields are crossed at an arbitrary angle, the individual elements of the flux tensor are given by

$$Q_{xxy} = \frac{1}{\sqrt{2}\alpha}[\mathrm{Re}(F(011|222)) - \mathrm{Re}(F(01-1|222))], \tag{C15}$$

$$Q_{yxx} = \frac{\sqrt{2}}{\alpha}\left[\frac{1}{\sqrt{3}}\mathrm{Re}(F(011|200)) + \frac{1}{\sqrt{6}}\mathrm{Re}(F(011|220))\right] + \frac{1}{\sqrt{2}\alpha}[-\mathrm{Re}(F(011|222))-\mathrm{Re}(F(01-1|222))], \tag{C16}$$

$$Q_{yyy} = \frac{\sqrt{2}}{\alpha}\left[\frac{1}{\sqrt{3}}\mathrm{Re}(F(011|200)) + \frac{1}{\sqrt{6}}\mathrm{Re}(F(011|220))\right] + \frac{1}{\sqrt{2}\alpha}[\mathrm{Re}(F(011|222)) + \mathrm{Re}(F(01-1|222))], \tag{C17}$$

$$Q_{yzz} = \frac{\sqrt{2}}{\alpha}\left[\frac{1}{\sqrt{3}}\mathrm{Re}(F(011|200)) - \sqrt{\frac{2}{3}}\mathrm{Re}(F(011|220))\right], \tag{C18}$$

$$Q_{zxy} = -\frac{1}{\alpha}\mathrm{Re}(F(010|222)), \tag{C19}$$

$$Q_{zyz} = \frac{1}{\alpha}\mathrm{Re}(F(010|221)), \tag{C20}$$

$$Q_{xyz} = \frac{1}{\sqrt{2}\alpha}[\mathrm{Re}(F(01-1|221))-\mathrm{Re}(F(011|221))], \tag{C21}$$

$$Q_{yxz} = \frac{1}{\sqrt{2}\alpha}[\mathrm{Re}(F(011|221))+\mathrm{Re}(F(01-1|221))]. \tag{C22}$$

The elements of the third-order transport coefficients that are independent in a crossed field configuration, are also independent when the electric and magnetic fields cross at an arbitrary angle. Thus, the corresponding expressions in the Boltzmann equation analysis are identical.

In what follows, we present the explicit expressions for the flux components of the third-order transport coefficient tensor that might be identified and computed in our Monte Carlo simulations.

For parallel electric and magnetic fields, the explicit expressions of the flux longitudinal and flux transverse third-order transport coefficients are given by Eqs. (48) and (49), respectively. We are not able to isolate the additional elements of the tensor in the Monte Carlo method used in the present work. As already discussed in this Appendix, the coefficients Q_{xxz}, Q_{xyz}, Q_{zxx}, and $Q_L \equiv Q_{zzz}$ could be identified and computed using Boltzmann equation solutions.

For perpendicular electric and magnetic fields, we are able to identify six components of the third-order transport coefficient tensor in our Monte Carlo simulations. The tensor components are

$$Q_L \equiv Q_{zzz}, \quad Q_{E \times B} \equiv Q_{xxx} \tag{C23}$$

and

$$Q_{\pi(xxz)} \equiv \tfrac{1}{3}(Q_{xxz} + Q_{xzx} + Q_{zxx}), \tag{C24}$$

$$Q_{\pi(yyx)} \equiv \tfrac{1}{3}(Q_{yyx} + Q_{yxy} + Q_{xyy}) \tag{C25}$$

$$Q_{\pi(yyz)} \equiv \tfrac{1}{3}(Q_{yyz} + Q_{yzy} + Q_{zyy}), \tag{C26}$$

$$Q_{\pi(zzx)} \equiv \tfrac{1}{3}(Q_{zzx} + Q_{zxz} + Q_{xzz}), \tag{C27}$$

where the cross product $\boldsymbol{E} \times \boldsymbol{B}$ defines the x axis while $\pi(abc)$ denotes all possible permutations of (a, b, c). The explicit expressions of the flux tensor components are given by

$$Q_{zzz} = \tfrac{1}{6}(3\langle z^2 c_z \rangle - 3\langle c_z \rangle \langle z^2 \rangle - 6\langle z \rangle \langle z c_z \rangle + 6\langle z \rangle \langle z \rangle \langle c_z \rangle), \tag{C28}$$

$$Q_{xxx} = \tfrac{1}{6}(3\langle x^2 c_x \rangle - 3\langle c_x \rangle \langle x^2 \rangle - 6\langle x \rangle \langle x c_x \rangle + 6\langle x \rangle \langle x \rangle \langle c_x \rangle), \tag{C29}$$

$$Q_{xzz} = \tfrac{1}{6}(\langle z^2 c_x \rangle + 2\langle zxc_z \rangle - 2\langle c_z \rangle \langle zx \rangle - \langle c_x \rangle \langle z^2 \rangle - 2\langle z \rangle \langle xc_z \rangle - 2\langle z \rangle \langle zc_x \rangle - 2\langle x \rangle \langle zc_z \rangle + 2\langle c_x \rangle \langle z \rangle \langle z \rangle + 4\langle x \rangle \langle z \rangle \langle c_z \rangle), \tag{C30}$$

$$Q_{zxx} = \tfrac{1}{6}(\langle x^2 c_z \rangle + 2\langle xzc_x \rangle - 2\langle c_x \rangle \langle xz \rangle - \langle c_z \rangle \langle x^2 \rangle - 2\langle x \rangle \langle zc_x \rangle - 2\langle x \rangle \langle xc_z \rangle - 2\langle z \rangle \langle xc_x \rangle + 2\langle c_z \rangle \langle x \rangle \langle x \rangle + 4\langle z \rangle \langle x \rangle \langle c_x \rangle), \tag{C31}$$

$$Q_{zyy} = \tfrac{1}{6}(\langle y^2 c_z \rangle + 2\langle yzc_y \rangle - \langle c_z \rangle \langle y^2 \rangle - 2\langle z \rangle \langle yc_y \rangle), \tag{C32}$$

$$Q_{xyy} = \tfrac{1}{6}(\langle y^2 c_x \rangle + 2\langle yxc_y \rangle - \langle c_x \rangle \langle y^2 \rangle - 2\langle x \rangle \langle yc_y \rangle). \tag{C33}$$

For the most general case when electric and magnetic fields are crossed at an arbitrary angle, we are able to identify 10 components of the third-order transport coefficient tensor in our Monte Carlo simulation code. They include six components already defined for perpendicular electric and magnetic fields and four additional coefficients, including

$$Q_{E \times (E \times B)} \equiv Q_{yyy}, \tag{C34}$$

where the cross product $\boldsymbol{E} \times (\boldsymbol{E} \times \boldsymbol{B})$ defines the y axis, and

$$Q_{\pi(xxy)} \equiv \tfrac{1}{3}(Q_{xxy} + Q_{xyx} + Q_{yxx}), \tag{C35}$$

$$Q_{\pi(zzy)} \equiv \tfrac{1}{3}(Q_{zzy} + Q_{zyz} + Q_{yzz}), \tag{C36}$$

$$Q_{\pi(xyz)} \equiv \tfrac{1}{6}(Q_{xyz} + Q_{yzx} + Q_{zxy} + Q_{xzy} + Q_{yxz} + Q_{zyx}). \tag{C37}$$

The remaining explicit expressions for the flux components of the third-order transport coefficient tensor are given by

$$Q_{yyy} = \tfrac{1}{6}(3\langle y^2 c_y \rangle - 3\langle c_y \rangle \langle y^2 \rangle - 6\langle y \rangle \langle yc_y \rangle + 6\langle y \rangle \langle y \rangle \langle c_y \rangle), \tag{C38}$$

$$Q_{xyz} = \tfrac{1}{6}(\langle yzc_x \rangle + \langle xzc_y \rangle + \langle xyc_z \rangle - \langle c_x \rangle \langle yz \rangle - \langle x \rangle \langle zc_y \rangle - \langle x \rangle \langle yc_z \rangle - \langle c_y \rangle \langle xz \rangle - \langle y \rangle \langle zc_x \rangle - \langle y \rangle \langle xc_z \rangle - \langle c_z \rangle \langle xy \rangle$$
$$- \langle z \rangle \langle yc_x \rangle - \langle z \rangle \langle xc_y \rangle + 2\langle c_x \rangle \langle y \rangle \langle z \rangle + 2\langle c_y \rangle \langle x \rangle \langle z \rangle + 2\langle c_z \rangle \langle y \rangle \langle x \rangle), \tag{C39}$$

$$Q_{yxx} = \tfrac{1}{6}(\langle x^2 c_y \rangle + 2\langle yxc_x \rangle - 2\langle c_x \rangle \langle yx \rangle - \langle c_y \rangle \langle x^2 \rangle - 2\langle x \rangle \langle yc_x \rangle - 2\langle x \rangle \langle xc_y \rangle - 2\langle y \rangle \langle xc_x \rangle + 2\langle c_y \rangle \langle x \rangle \langle x \rangle + 4\langle y \rangle \langle x \rangle \langle c_x \rangle), \tag{C40}$$

$$Q_{yzz} = \tfrac{1}{6}(\langle z^2 c_y \rangle + 2\langle yzc_z \rangle - 2\langle c_z \rangle \langle yz \rangle - \langle c_y \rangle \langle z^2 \rangle - 2\langle z \rangle \langle yc_z \rangle - 2\langle z \rangle \langle zc_y \rangle - 2\langle y \rangle \langle zc_z \rangle + 2\langle c_y \rangle \langle z \rangle \langle z \rangle + 4\langle y \rangle \langle z \rangle \langle c_z \rangle), \tag{C41}$$

$$Q_{zyy} = \tfrac{1}{6}(\langle y^2 c_z \rangle + 2\langle yzc_y \rangle - 2\langle c_y \rangle \langle yz \rangle - \langle c_z \rangle \langle y^2 \rangle - 2\langle y \rangle \langle zc_y \rangle - 2\langle y \rangle \langle yc_z \rangle - 2\langle z \rangle \langle yc_y \rangle + 2\langle c_z \rangle \langle y \rangle \langle y \rangle + 4\langle z \rangle \langle y \rangle \langle c_y \rangle), \tag{C42}$$

$$Q_{xyy} = \tfrac{1}{6}(\langle y^2 c_x \rangle + 2\langle yxc_y \rangle - 2\langle c_y \rangle \langle yx \rangle - \langle c_x \rangle \langle y^2 \rangle - 2\langle y \rangle \langle xc_y \rangle - 2\langle y \rangle \langle yc_x \rangle - 2\langle x \rangle \langle yc_y \rangle + 2\langle c_x \rangle \langle y \rangle \langle y \rangle + 4\langle x \rangle \langle y \rangle \langle c_y \rangle). \tag{C43}$$

[1] L. G. H. Huxley and R. W. Crompton, *The Diffusion and Drift of Electrons in Gases* (Wiley, London, 1974).

[2] E. A. Mason and E. W. McDaniel, *Transport Properties of Ions in Gases* (Wiley, New York, 1988).

[3] R. W. Crompton, Adv. At. Mol. Opt. Phys. **32**, 97 (1994).

[4] Z. Lj. Petrović, M. Šuvakov, Ž. Nikitović, S. Dujko, O. Šašić, J. Jovanović, G. Malović, and V. Stojanović, Plasma Sources Sci. Technol. **16**, S1 (2007).

[5] R. D. White, D. Cocks, G. Boyle, M. Casey, N. Garland, D. Konovalov, B. Philippa, P. Stokes, J. de Urquijo, O. Gonzales-Magana, R. P. McEachran, S. J. Buckman, M. J. Brunger, G. Garcia, S. Dujko, and Z. Lj. Petrović, Plasma Sources Sci. Technol. **27**, 053001 (2018).

[6] T. Makabe and Z. Lj. Petrović, *Plasma Electronics: Applications in Microelectronic Device Fabrication* (CRC Press, New York, 2014).

[7] M. A. Lieberman and A. J. Lichtenberg, *Principles of Plasma Discharges and Materials Processing* (Wiley Interscience, Hoboken, NJ, 2005).

[8] L. L. Alves, A. Bogaerts, V. Guerra, and M. M. Turner, Plasma Sources Sci. Technol. **27**, 023002 (2018).

[9] I. Adamovich, S. D. Baalrud, A. Bogaerts, P. J. Bruggeman, M. Cappelli, V. Colombo, U. Czarnetzki, U. Ebert, J. G. Eden, P. Favia, D. B. Graves, S. Hamaguchi, G. Hieftje, M. Hori, I. D. Kaganovich, U. Kortshagen, M. J. Kushner, N. J. Mason, S. Mazouffre, S. Mededovic Thagard, H. R. Metelmann, A. Mizuno, E. Moreau, A. B. Murphy, B. A. Niemira, G. S. Oehrlein, Z. Lj. Petrovic, L. C. Pitchford, Y. K. Pu, S. Rauf, O. Sakai, S. Samukawa, S. Starikovskaia, J. Tennyson, K. Terashima, M. M. Turner, M. C. M. Van De Sanden, and A. Vardelle, J. Phys. D: Appl. Phys. **50**, 323001 (2017).

[10] L. Rolandi, W. Riegler, and W. Blum, *Particle Detection with Drift Chambers* (Springer, Berlin, 2008).

[11] D. Bošnjaković, Z. Lj. Petrović, R. D. White, and S. Dujko, J. Phys. D: Appl. Phys. **47**, 435203 (2014).

[12] D. Xiao, *Gas Discharge and Gas Insulation* (Springer, Heidelberg, 2016).

[13] M. Charlton and J. W. Humberston, *Positron Physics* (Cambridge University Press, Cambridge, 2001).

[14] Z. Lj. Petrović, A. Banković, S. Dujko, S. Marjanović, G. Malović, J. P. Sullivan, and S. Buckman, in *Eighth International Conference on Atomic and Molecular Data and Their Applications: ICAMDATA-2012*, edited by J. D. Gillaspy, W. L. Wiese, and Y. A. Podpaly, AIP Conf. Proc. No. 1545 (AIP, New York, 2013).

[15] L. C. Pitchford *et al.*, Plasma Process. Polym. **14**, 1600098 (2016).

[16] Z. Lj. Petrović, S. Dujko, D. Marić, G. Malović, Ž. Nikitović, O. Šašić, J. Jovanović, V. Stojanović, and M. Radmilović-Rađenović, J. Phys. D: Appl. Phys. **42**, 194002 (2009).

[17] R. D. White, S. Dujko, R. E. Robson, Z. Lj. Petrović, and R. P. McEachran, Plasma Sources Sci. Techol. **19**, 034001 (2010).

[18] B. M. Penetrante and J. N. Bardsley, in *Non-equilibrium Effects in Ion and Electron Transport*, edited by J. W. Gallagher, D. F. Hudson, E. E. Kunhardt, and R. J. Van Brunt (Plenum, New York, 1990), p. 49.

[19] S. B. Vrhovac, Z. Lj. Petrović, L. A. Viehland, and T. S. Santhanam, J. Chem. Phys. **110**, 2423 (1999).

[20] J. H. Schummers, G. M. Thomson, D. R. James, I. R. Gatland, and E. W. McDaniel, Phys. Rev. A **7**, 683 (1973).

[21] S. R. Hunter, Ph.D. thesis, Flinders University, Adelaide, Australia (1977).

[22] H. A. Blevin, J. Fletcher, and S. R. Hunter, J. Phys. D: Appl. Phys. **9**, 471 (1976).

[23] H. A. Blevin, J. Fletcher, and S. R. Hunter, Aust. J. Phys. **31**, 299 (1978).

[24] C. A. Denman and L. A. Schlie, in *Non-equilibrium Effects in Ion and Electron Transport*, Proceedings of the 6th International Swarm Seminar, Glen Cove, NY, edited by J. W. Gallagher *et al.* (Springer, New York, 1989), p. 359.

[25] J. H. Whealton and E. A. Mason, Ann. Phys. **84**, 8 (1974).

[26] R. Robson, Aust. J. Phys. **28**, 523 (1975).

[27] P. H. Larsen, H. R. Skullerud, T. H. Lovaas, and T. Stefansson, J. Phys. B: At. Mol. Opt. Phys. **21**, 2519 (1988).

[28] K. Kondo and H. Tagashira, J. Phys. D: Appl. Phys. **23**, 1175 (1990).

[29] A. D. Koutselos, J. Chem. Phys. **104**, 8442 (1996).

[30] A. D. Koutselos, J. Chem. Phys. **106**, 7117 (1997).

[31] A. D. Koutselos, Chem. Phys. **270**, 165 (2001).

[32] A. D. Koutselos, Chem. Phys. **315**, 193 (2005).

[33] R. E. Robson, J. Chem. Phys. **85**, 4486 (1986).

[34] S. B. Vrhovac and Z. Lj. Petrović, Phys. Rev. E **53**, 4012 (1996).

[35] S. Kawaguchi, K. Takahashi, and K. Satoh, Plasma Sources Sci. Technol. **27**, 085006 (2018).

[36] S. Kawaguchi, K. Takahashi, and K. Satoh, in *Proceedings of the 22nd International Conference on Gas Discharges and Their Applications, Novi Sad, Serbia*, edited by Z. Lj. Petrović, N. Puač, S. Dujko, and N. Škoro (Serbian Academy of Sciences and Arts, Belgrade, 2018), p. 531.

[37] S. Dujko, R. D. White, and Z. Lj. Petrović, J. Phys. D: Appl. Phys. **41**, 245205 (2008).

[38] Z. Lj. Petrović, I. Simonović, S. Marjanović, D. Bošnjaković, D. Marić, G. Malović, and S. Dujko, Plasma Phys. Control. Fusion **59**, 014026 (2017).

[39] P. W. Stokes, I. Simonović, B. Philippa, D. Cocks, S. Dujko, and R. D. White, Sci. Rep. **8**, 2226 (2018).

[40] C. Li, W. J. M. Brok, U. Ebert, and J. J. A. M. van der Mullen, J. Appl. Phys. **101**, 123305 (2007)

[41] A. H. Markosyan, S. Dujko, and U. Ebert, J. Phys. D: Appl. Phys. **46**, 475203 (2013).

[42] Z. M. Raspopović, S. Dujko, R. D. White, and Z. Lj. Petrović, IEEE Trans. Plasma. Sci. **39**, 2566 (2011).

[43] S. Dujko, Z. M. Raspopović, R. D. White, T. Makabe, and Z. Lj. Petrović, Eur. Phys. J. D **68**, 166 (2014).

[44] M. Šuvakov, Z. Ristivojević, Z. Lj. Petrović, S. Dujko, Z. M. Raspopović, N. A. Dyatko, and A. P. Napartovich, IEEE Trans. Plasma Sci. **33**, 532 (2005).

[45] J. Mirić, D. Bošnjaković, I. Simonović, Z. Lj. Petrović, and S. Dujko, Plasma Sources Sci. Technol. **25**, 065010 (2006).

[46] M. Šuvakov, Z. Lj. Petrović, J. P. Marler, S. J. Buckman, R. E. Robson, and G. Malović, New J. Phys. **10**, 053034 (2008).

[47] A. Banković, S. Dujko, R. D. White, S. J. Buckman, and Z. Lj. Petrović, Nucl. Instrum. Meth. Phys. Res. B **279**, 92 (2011).

[48] R. T. Sibatov and V. V. Uchaikin, Semiconductors **41**, 335 (2007).

[49] M. Schubert, E. Preis, J. C. Blakesley, P. Pingel, U. Scherf, and D. Neher, Phys. Rev. B **87**, 024203 (2013).

[50] H. Krüsemann, A. Godec, and R. Metzler, Phys. Rev. E **89**, 040101(R) (2014).

[51] H. Krüsemann, R. Schwarzl, and R. Metzler, Transp. Porous Media **115**, 327 (2016).

[52] A. Mauracher, M. Daxner, J. Postler, S. E. Huber, S. Denifl, P. Scheier, and J. P. Toennies, J. Phys. Chem. Lett. **5**, 2444 (2014).

[53] A. F. Borghesani and M. Santini, Phys. Rev. E **65**, 056403 (2002).

[54] Y. Sakai, W. F. Schmidt, and A. Khrapak, Chem. Phys. **164**, 139 (1992).

[55] S. V. Stepanov, V. M. Byakov, D. S. Zvezhinskiy, G. Duplâtre, R. R. Nurmukhametov, and P. S. Stepanov, Adv. Phys. Chem. **2012**, 431962 (2012).

[56] S. V. Stepanov, V. M. Byakov, B. N. Ganguly, D. Gangopadhyay, T. Mukherjee, and B. Dutta-Roy, Physica B: Condens. Matter **322**, 68 (2002).

[57] K. Norregaard, R. Metzler, C. M. Ritter, K. Berg-Sørensen, and L. B. Oddershede, Chem. Rev. **117**, 4342 (2017).

[58] M. Schwarzl, A. Godec, and R. Metzler, Sci. Rep. **7**, 3878 (2017).

[59] F. Höfling and T. Franosch, Rep. Prog. Phys. **76**, 046602 (2013).

[60] M. Magdziarz, A. Weron, K. Burnecki, and J. Klafter, Phys. Rev. Lett. **103**, 180602 (2009).

[61] K. F. Ness and R. E. Robson, Phys. Rev. A **34**, 2185 (1986)

[62] R. Robson, R. White, and M. Hildebrandt, *Fundamentals of Charged Particle Transport in Gases and Condensed Matter* (CRC Press, Boca Raton, FL, 2018).

[63] K. Kumar, H. R. Skullerud, and R. E. Robson, Aust. J. Phys. **33**, 343 (1980).

[64] S. Dujko, R. D. White, Z. M. Raspopović, and Z. Lj. Petrović, Nucl. Instrum. Meth. Phys. Res. B **279**, 84 (2012).

[65] M. Damnjanović and I. Milošević, J. Phys. A: Math. Gen. **28**, 1669 (1995).

[66] R. D. White, R. E. Robson, S. Dujko, P. Nicoletopoulos, and B. Li, J. Phys. D: Appl. Phys. **42**, 194001 (2009).

[67] S. Dujko, R. D. White, Z. Lj. Petrović, and R. E. Robson, Phys. Rev. E **81**, 046403 (2010).

[68] S. Dujko, R. D. White, Z. Lj. Petrović, and R. E. Robson, Plasma Sources Sci. Technol. **20**, 024013 (2011).

[69] R. E. Robson and K. F. Ness, Phys. Rev. A **33**, 2068 (1986).

[70] R. D. White, K. F. Ness, R. E. Robson, and B. Li, Phys. Rev. E **60**, 2231 (1999).

[71] Z. M. Raspopović, S. Sakadžić, S. Bzenić, and Z. Lj. Petrović, IEEE Trans. Plasma Sci. **27**, 1241 (1999).

[72] Z. Lj. Petrović, Z. M. Raspopović, S. Dujko, and T. Makabe, Appl. Surf. Sci. **192**, 1 (2002).

[73] S. Dujko, Z. M. Raspopović, and Z. Lj. Petrović, J. Phys. D: Appl. Phys. **38**, 2952 (2005).

[74] I. Simonović, Z. Lj. Petrović, and S. Dujko, in *Proceedings of the 27th Symposium on Physics of Ionized Gases—SPIG 2014, Belgrade, Serbia*, edited by D. Marić, A. R. Milosavljević, and Z. Mijatović, Contributed Papers and Abstracts of Invited Lectures, Topical Invited Lectures. Progress Reports and Workshop Lectures (Institute of Physics, Belgrade & Klett izdavacka kuca d.o.o., Belgrade, 2014), pp. 138–141.

[75] I. Simonović, Z. Lj. Petrović, R. D. White, D. Bošnjaković, and S. Dujko, in *Proceedings of the 22nd International Conference on Gas Discharges and Their Applications—GD 2018, Novi Sad, Serbia*, edited by Z. Lj. Petrović, N. Puač, S. Dujko, and N. Škoro (Serbian Academy of Sciences and Arts, Belgrade, 2018), pp. 551–554.

[76] I. Simonović, Z. Lj. Petrović, R. D. White, D. Bošnjaković, and S. Dujko, in *Proceedings of the 29th Symposium on Physics of Ionized Gases—SPIG 2018, Belgrade, Serbia*, edited by G. Poparić, B. Obradović, D. Borka, and M. Rajković, Contributed Papers and Abstracts of Invited Lectures, Topical Invited Lectures. Progress Reports and Workshop Lectures, (Vinča Institute of Nuclear Sciences, University of Belgrade, Belgrade, 2018), pp. 67–70.

[77] M. Hayashi (private commutation, 2000).

[78] R. D. White, R. E. Robson, P. Nicoletopoulos, and S. Dujko, Eur. Phys. J. D **66**, 117 (2012).

[79] L. Boltzmann, Wein. Ber. **66**, 275 (1872).

[80] C. S. Wang-Chang, G. E. Uhlenbeck, and J. DeBoer, in *Studies in Statistical Mechanics*, edited by J. DeBoer and G. E. Uhlenbeck (Wiley, New York, 1964), Vol. 2, p. 241.

[81] Z. Ristivojević and Z. Lj. Petrović, Plasma Sources Sci. Technol. **21**, 035001 (2012).

[82] K. F. Ness, J. Phys. D: Appl. Phys. **27**, 1848 (1994).

[83] R. D. White, M. J. Brennan, and K. F. Ness, J. Phys. D: Appl. Phys. **30**, 810 (1997).

[84] R. D. White, R. E. Robson, and K. F. Ness, Comput. Phys. Commun. **142**, 349 (2001).

[85] I. D. Reid, Aust. J. Phys. **32**, 231 (1979).

[86] S. Marjanović, A. Banković, D. Cassidy, B. Cooper, A. Deller, S. Dujko, and Z. Lj. Petrović, J. Phys. B: At. Mol. Opt. Phys. **49**, 215001 (2016).

[87] S. Marjanović and Z. Lj. Petrović, Plasma Sources Sci. Technol. **26**, 024003 (2017).

[88] S. Marjanović, M. Šuvakov, A. Banković, M. Savić, G. Malović, S. J. Buckman, and Z. Lj. Petrović, IEEE Trans. Plasma Sci. **39**, 2614 (2011).

[89] Z. Lj. Petrović, S. Marjanović, S. Dujko, A. Banković, G. Malović, S. Buckman, G. Garcia, R. White, and M. Brunger, Appl. Radiat. Isotop. **83**, 148 (2014).

[90] M. R. Natisin, J. R. Danielson, and C. M. Surko, J. Phys. B: At. Mol. Opt. Phys. **47**, 225209 (2014).

[91] L. M. Blinov, *Structure and Properties of Liquid Crystals* (Springer, New York, 2011).

[92] W. K. Tung, *Group Theory in Physics* (World Scientific, Singapore, 1984).

[93] A. O. Barut and R. Raczka, *Theory of Group Representations and Applications* (Polish Scientific Publishers, Warsaw, 1980).

[94] F. P. Temme and B. C. Sanctuary, J. Magn. Reson. **69**, 1 (1986).

[95] R. E. Robson, Phys. Rev. A **13**, 1536 (1976).

[96] R. E. Robson, Phys. Rev. E **61**, 848 (2000).

Regular Article

Electron transport in mercury vapor: cross sections, pressure and temperature dependence of transport coefficients and NDC effects[*]

Jasmina Mirić[1], Ilija Simonović[1], Zoran Lj. Petrović[1,2], Ronald D. White[3], and Saša Dujko[1,a]

[1] Institute of Physics, University of Belgrade, Pregrevica 118, 11080 Belgrade, Serbia
[2] Serbian Academy of Sciences and Arts, 11001 Belgrade, Serbia
[3] College of Science and Engineering, James Cook University, Townsville, QLD 4811, Australia

Abstract. In this work we propose a complete and consistent set of cross sections for electron scattering in mercury vapor. The set is validated through a series of comparisons between swarm data calculated using a multi term theory for solving the Boltzmann equation and Monte Carlo simulations, and the available experimental data. Other sets of cross sections for electron scattering in mercury vapor were also used as input in our numerical codes with the aim of testing their completeness, consistency and accuracy. The calculated swarm parameters are compared with measurements in order to assess the quality of the cross sections in providing data for plasma modeling. In particular, we discuss the dependence of transport coefficients on the pressure and temperature of mercury vapor, and the occurrence of negative differential conductivity (NDC) in the limit of lower values of E/N. We have shown that the phenomenon of NDC is induced by the presence of mercury dimers and that can be controlled by varying either pressure or temperature of mercury vapor. The effective inelastic cross section for mercury dimers is estimated for a range of pressures and temperatures. It is shown that the measured and calculated drift velocities agree very well only if the effective inelastic cross section for mercury dimers and thermal motion of mercury atoms are carefully considered and implemented in numerical calculations.

1 Introduction

The behavior of electrons in mercury vapor under the influence of electric field is of vital interest in modeling of the gas-discharge lamps [1–3], lasers [4,5] and in special applications such as ion thrusters for space propulsion [6]. Further optimization and understanding of such applications is dependent on an accurate knowledge of the cross sections for electron scattering, transport coefficients and the physical processes involved. For example, fluid models of low-pressure discharges used in fluorescent lamps often require swarm transport parameters as a function of the reduced electric field and the gas temperature [7,8]. Current models of high-pressure mercury discharges, however, usually require a knowledge of the electrical conductivity, which can be calculated from the cross sections for electron scattering in mercury vapor and electron mobility.

A number of methods have been applied to investigate the behavior of electrons in mercury vapor and have been

successfully applied to a variety of problems. For scattering theorists, the problem of the scattering of electrons on mercury atoms is challenging due to importance of relativistic effects and the correlation between different subshells which require the use of either Dirac equations or modified forms of the Schrödinger equation [9,10]. The correct representation of a very large low energy resonance in both elastic and momentum transfer cross sections below the first inelastic threshold of the $^3P_0$ state at $4.66\,\mathrm{eV}$ and impact of $6s6p^2$ resonances on the elastic scattering and the excitation cross-section in the energy range between 4 and $7\,\mathrm{eV}$ are also very important issues. This makes mercury a particularly interesting target for scattering theorists. No less challenging is the problem of the transport of electrons in mercury vapor, given the difficulties that occur in both the experimental measurements, as well as in theoretical calculations based on the Boltzmann equation and Monte Carlo simulations. For example, it is very difficult to find the experimental data in the literature for drift velocity and characteristic energy of electrons in mercury vapor for high values of the reduced electric fields, because such measurements require lower vapor pressure and therefore lower temperature, which is difficult to control accurately. In the domain of the theoretical studies of electron transport in the mercury

---

vapor based on the Boltzmann equation, only recently it has been shown that nonlocal effects, resonances and striations in mercury electrical discharges have much in common with the behavior of electrons in mercury vapor in the famous Franck–Hertz experiment [11–14].

In literature, already, some cross section sets for electron scattering in mercury vapor have been reported. Raju reviewed measured and theoretically calculated electron collision cross sections for mercury vapor and recommended the values of drift velocity and reduced ionization coefficient [15,16]. Complete sets of cross section were reported by Rockwood [17], Nakamura and Lucas [18,19], Sakai et al. [20] and Suzuki et al. [21]. Winkler et al. [22,23] and Yousfi et al. [24] made significant contributions to the development of transport and collision data for electrons in mercury vapors by including the kinetics of excited states and Penning ionization in their models of fluorescent lamps. The properties of electron swarms in pure mercury vapor have also been analyzed by Garamoon and Abdelhaleem [25], Braglia et al. [26] and Liu and Raju [27] while the effects of metastable mercury and argon atoms on electron transport were subject of studies performed by the group of Prof. Tagashira [20,28,29]. The influence of thermal motion of background mercury atoms on electron transport has been analyzed by Winkler et al. [30] while the impact of a magnetic field on various transport properties in a crossed field configuration was investigated by Liu and Raju [31].

The common thread among many of these previous studies is a systematic neglect of non-hydrodynamic behavior of transport coefficients, which is reflected in their dependence upon the pressure and temperature of mercury vapor. Moreover, the effects of thermal motion of mercury atoms have also been often neglected, duality of transport coefficients (e.g., the existence of two different families of transport coefficients, the bulk and the flux) for electrons in mercury vapor has never been considered and finally many studies have been made in the framework of the two term theory for solving the Boltzmann equation, despite its limitations and concerns regarding its accuracy that have been well-documented [32,33]. Using these facts as motivational factors, in this paper, we revisit the issue surrounding computation of electron transport properties in mercury vapor as a function of electric field, pressure and temperature of mercury vapor. As a first step, we have developed a complete set of cross sections for electron scattering in mercury vapor. We apply the standard swarm procedure of deriving cross sections [33–35]. The initial set of cross sections is composed of cross sections for the individual collision processes that are collected from the literature. Using this initial set of cross sections as an input for solving Boltzmann's equation, transport coefficients are calculated and compared with the corresponding experimental data. The initial cross sections are then modified and the procedure is repeated in order to obtain better agreement with the experimental transport coefficients. The cross sections are considered satisfactory when the calculated values for drift velocity, ionization coefficient and characteristic energy match the experimental values to within a standard experimental uncertainty.

Other sets of cross sections for electron scattering in mercury vapor that are available in the literature were also incorporated into the Boltzmann equation and Monte Carlo codes with the aim of assessing their completeness and accuracy. This has been done through a series of calculations focused on comparisons between the experimentally measured and theoretically calculated transport coefficients. In particular, we consider the pressure dependence of transport coefficients due to the presence of mercury dimers. The mercury dimers are molecular species that can cause a significant change in the rate of energy lost by the electrons via rotational and vibrational excitation and hence a considerable change in the drift velocity. The formation of dimers and their effect on the measured drift has been studied by Nakamura and Lucas [18,19], Elford [36] and England and Elford [37]. It was shown that the drift velocity increases with pressure, but the occurrence of negative differential conductivity (NDC) has not been reported. A cross section for momentum transfer in elastic collisions and an effective inelastic cross section for dimers have been derived using the well-established swarm method of deriving cross sections. In order to reduce the non-uniqueness of the initially derived cross section for momentum transfer, McEachran and Elford [10] have demonstrated that cross section for the momentum transfer can be further refined by considering the additional transport data.

In the present paper we extend the previous studies by considering the occurrence of NDC in the limit of lower values of E/N. NDC is the well-known phenomenon in transport theory which is characterized by a decrease in the drift velocity for increasing the applied electric field. The conditions for the occurrence of NDC have been investigated previously. It was shown that NDC can be induced and controlled by the presence of inelastic [38,39] and non-conservative collisions [40,41], electron–electron collisions [42,43] and anisotropic scattering [44]. For liquid argon and xenon, however, there is a new type of NDC that does not require inelastic collisions or non-conservative processes, i.e. it is purely a consequence of the medium structure [45,46]. In this work we demonstrate the NDC phenomenon induced by the presence of mercury dimers. The collision frequencies and the averaged energy losses due to elastic and inelastic collisions are calculated with the aim of explaining the development of NDC. The pressure dependence of other transport properties, including the mean energy and diffusion coefficients is also investigated. Particular attention is paid to the effects of the mercury vapor temperature and how this affects the basic properties of the drift and diffusion over a range of the reduced electric fields of practical interest. This has been done through a series of calculations based on a multi term theory for solving the Boltzmann equation and Monte Carlo simulation technique in which thermal motion of background mercury atoms is rigorously accounted for.

This paper is organized as follows. In Section 2 we outline the theory used to solve the Boltzmann equation and the basic elements of our Monte Carlo method for determining transport properties of electrons in mercury vapor. In Section 3.2 we present a new collision cross section set for electron scattering in mercury vapor, which revises the

previous sets summarized by Rockwood [17], Sakai et al. [20] and Suzuki et al. [21]. Comparison between the measured and calculated swarm data is shown in Section 3.3 while the pressure dependence of transport coefficients and dimer-induced negative differential conductivity are discussed in Section 3.4. In Section 3.5 we investigate the synergism of thermal effects and the effects induced by the mercury-dimers on electron transport in mercury vapor. Finally, we summarize our conclusions in Section 4 and also provide an outlook regarding the future transport studies for electrons in mercury vapor.

2 Methods of calculation

In this work, we investigate a swarm of electrons moving through a neutral gas under the influence of a uniform electric field. The electron number density is assumed to be sufficiently low so that the following conditions apply: (i) electron–electron interactions and space-charge effects can be neglected; (ii) the motion of the electrons can be treated classically, and (iii) the background of neutral atoms remains in thermal equilibrium. Electrons gain energy from the external electric field and dissipate it by collisions to the neutral gas atoms. The collisional transfer of this energy to the neutral gas atoms occurs by elastic and different types of inelastic collisions. This is a typical non-equilibrium system and its correct mathematical description can only be obtained from kinetic theory [47].

2.1 Multi term solution of Boltzmann's equation

To calculate the transport of electrons in mercury vapor, we apply a multi term solution of the Boltzmann equation for the phase-space distribution function $f(\mathbf{r}, \mathbf{c}, t)$:

$$\frac{\partial f}{\partial t} + \mathbf{c} \cdot \frac{\partial f}{\partial \mathbf{r}} + \frac{e\mathbf{E}}{m} \cdot \frac{\partial f}{\partial \mathbf{c}} = -J(f, f_0), \qquad (1)$$

where $\mathbf{r}$ and $\mathbf{c}$ denote, respectively, the position and velocity co-ordinates in phase space, while e and m are the charge and mass of electron, respectively, and $\mathbf{E}$ is the applied external field. The right-hand side of equation (1) represents the collision operator J, describing the rate of change of the phase-space distribution function due to collisions between the electrons and the neutral background mercury vapor atoms.

In the present work we employ the original Boltzmann collision operator for elastic processes [48] and its semiclassical generalization for inelastic processes [49]:

$$J_{\text{in}}(f, f_0) = \sum_{jk} \int [f(\mathbf{r}, \mathbf{c}, t) f_{0j}(\mathbf{c}_0) - f(\mathbf{r}, \mathbf{c}', t) f_{0k}(\mathbf{c}_0')]$$
$$\times g\sigma(jk; g, \widehat{\mathbf{g}} \cdot \widehat{\mathbf{g}}') d\widehat{\mathbf{g}} d\mathbf{c}_0, \qquad (2)$$

where $\sigma(jk; g, \widehat{\mathbf{g}} \cdot \widehat{\mathbf{g}}')$ is the differential cross section for the scattering process $(j, \mathbf{c}, \mathbf{c}_0) \to (k, \mathbf{c}', \mathbf{c}_0')$. This cross section depends on the electron's incident kinetic energy and on the angle between the incident and post-collision relative velocity, $\mathbf{g}$ and $\mathbf{g}'$, respectively. For a neutral mercury vapor with temperature T and number density

N, the distribution of neutral velocities $\mathbf{c}_0$ in state j is Maxwell–Boltzmann:

$$f_0^{(j)}(\mathbf{c}_0) = \frac{N}{Z(T)} \exp\left(-\frac{\epsilon_j}{kT}\right) \omega(\alpha_0, \mathbf{c}_0), \qquad (3)$$

where $Z(T)$ is the partition function, ϵ_j is the energy of a mercury atom (or mercury dimer) in quantum state j and

$$\omega(\alpha_0, \mathbf{c}_0) = \left(\frac{\alpha_0^2}{2\pi}\right)^{3/2} \exp\left(-\alpha_0^2 c_0^2\right), \qquad (4)$$

with $\alpha_0^2 = m_0/kT$.

Electron ionization processes are described through the operator [51]:

$$J_I(f, f_0) = \sum_j N_{0j} c \big[\sigma_I(j; c) f(\mathbf{r}, \mathbf{c}, t) - 2$$
$$\times \int c' \sigma_I(j; c') B(\mathbf{c}, \mathbf{c}'; j) f(\mathbf{r}, \mathbf{c}', t) d\mathbf{c}'\big], \quad (5)$$

where σ_I is the ionization cross section while $B(\mathbf{c}, \mathbf{c}'; j)$ is the probability for one of the two electrons after ionization having a velocity in the range $\mathbf{c}$ to $\mathbf{c} + d\mathbf{c}$, for incident electron velocity $\mathbf{c}'$, and N_{0j} is the number density of mercury atoms in the state j. In the present work we assume that all fractions are equally probable. The probability function must satisfy the following normalization conditions:

$$\int B(\mathbf{c}, \mathbf{c}'; j) d\mathbf{c} = 1, \qquad (6)$$

and

$$B(\mathbf{c}, \mathbf{c}'; j) = 0, \qquad \text{if} \quad \epsilon' - \epsilon < \epsilon_I(j), \qquad (7)$$

where ϵ' and ϵ are the incident and post-ionization energy of the electrons while $\epsilon_I(j)$ is the ionization potential of the jth channel.

Solution of non-conservative Boltzmann's equation (1) has been extensively discussed by Robson and Ness [50,51], White et al. [52,53] and Dujko et al. [54,55]. In brief, we expand the phase-space distribution function in terms of spherical harmonics with the aim of resolving its angular dependence in velocity space. Transport coefficients of charged particle swarms are exclusively defined in the hydrodynamic regime. In the hydrodynamic regime, the space-time dependence of the phase-space distribution function is expressed by an expansion in terms of the gradient of the electron number density $n(\mathbf{r}, t)$. In order to resolve the speed-dependence of the phase-space distribution function, the expansion is made in terms of Sonine polynomials about a Maxwellian distribution function.

Thus, we solve equation (1) by making the expansions

$$f(\mathbf{r}, \mathbf{c}, t) = \omega(\alpha, c) \sum_{l=0}^{\infty} \sum_{m=-l}^{l} \sum_{\nu=0}^{\infty} \sum_{s=0}^{\infty} \sum_{\lambda=0}^{s} F(\nu l m | s \lambda)$$

$$\times N_{\nu l} \left(\frac{\alpha c}{\sqrt{2}} \right)^l S_{l+1/2}^{(\nu)} \left(\frac{\alpha^2 c^2}{2} \right) Y_m^{[l]}(\hat{\mathbf{c}}) G_m^{(s\lambda)} n(\mathbf{r}, t), \quad (8)$$

where $\omega(\alpha, c)$ is a Maxwellian distribution at a temperature T_b and $S_{l+1/2}^{(\nu)} \left(\frac{\alpha^2 c^2}{2} \right)$ are Sonine polynomials. $Y_m^{[l]}(\hat{\mathbf{c}})$ is a spherical harmonic, a function of the angles $\hat{\mathbf{c}}$ and $G_m^{(s\lambda)}$ is the irreducible gradient tensor operator [50]. The two-term approximation which forms the basis of the conventional theories for solving the Boltzmann equation, is based upon the choice of setting the upper bound on the summation in (8) to $l_{\max} = 1$. Its limitations and domains of applicability in calculating transport coefficients for electrons are thoroughly discussed in references [32,33].

Substitution of expansion (8) into equation (1) and performing the appropriate "matrix element" operations allows the Boltzmann equation to be converted into a set of matrix equations for the expansion coefficients $F(\nu l m | s \lambda)$,

$$\sum_{\nu'=0}^{\infty} \sum_{l'=0}^{\infty} \sum_{m'=-l'}^{l'} \left[M_{\nu l m, \nu' l' m'} + R \delta_{\nu' \nu} \delta_{l' l} \delta_{m' m} \right]$$

$$\times F(\nu' l' m' | s \lambda) = X_{\nu l m}(s \lambda),$$

$$\nu, l = 1, 2, \dots, \infty; \quad m = -l, \dots, +l, \quad (9)$$

where R is the reaction rate. Explicit expressions for the matrix of coefficients $M_{\nu l m, \nu' l' m'}$, which contains the applied electric field and matrix elements of the collision operator, and right-hand side $X_{l m \nu}(s \lambda)$, can be found elsewhere [51,54]. The expansion coefficients $F(\nu l m | s \lambda)$ are called "moments" and are related to the electron transport properties as discussed in our previous works [52–55]. These quantities are numbers that depend on the applied electric field, the neutral number density N and cross sections for electron scattering. They are required for determination of both the bulk and the flux transport coefficients. The flux drift velocity is the swarm averaged velocity, while the bulk drift velocity is the rate of change of the swarm's centre of mass. The duality of transport coefficients and its implications in plasma modeling has been recently thoroughly discussed in references [56–59].

Of particular importance for the current paper is to note that the motion of the neutrals is systematically and rigorously incorporated into all collision process operators and all spherical harmonic equations. In contrast, in conventional theories which are usually based on the two term approximation, the consideration of the thermal motion of neutrals is often limited to the isotropic matrix elements of the elastic collision operator. Errors resulting from such theories will be discussed and illustrated in Section 3.4.

2.2 Monte Carlo method

A Monte Carlo simulation technique is also used in the present work, but as an independent tool with the aim of verifying the results of Boltzmann equation analysis. We follow the space and time development of a swarm of electrons in an infinite gas under the influence of a uniform electric field. The electron trajectories between collisions are determined by solving the collisionless equation of motion of a single electron. The position and velocity of each electron are updated after the time step Δt which is determined from the mean collision time divided by a large number (usually 100) depending on the simulation conditions. These small time steps Δt are used for numerical integration of the equation for the collision probability

$$p(t) = \nu_T(\epsilon(t)) \exp\left(-\int_{t_0}^{t} \nu_T(\epsilon(t')) dt' \right), \quad (10)$$

where ν_T is the total collision frequency while t_0 is either the time of the electron entering the gas or the time of a previous collision. Equation (10) gives the probability that the electron will have a collision in the time interval $(t, t + dt)$ and its numerical solution requires the use of random numbers. The type of collision is also determined using random numbers as well as relative probabilities for individual collisional processes. The details of our Monte Carlo method and explicit formulas for both the bulk and flux transport coefficients are given in several of our previous publications [54,55,60–62].

Two important issues deserve more mentioning in this work. First, in our Monte Carlo code we have implemented the procedure for calculating the collision frequency in the case when thermal motion of the background gas cannot be neglected for a Maxwellian velocity distribution of the background gas particles. The details of the procedure can be found in the recent work of Ristivojević and Petrović [63]. This was a necessary step in this work, given the importance of thermal collisions for adequate description of electron transport in the limit of low electric fields.

Another issue in Monte Carlo simulations of electron transport in mercury vapor is the simulation speed. To achieve a good statistics of the final results and also to make sure that the relaxation of the steady-state conditions has been achieved, one needs to follow a large number of electrons. Due to numerous elastic collisions in which only a fraction of the initial electron energy is transferred to a heavy mercury atom target, the efficiency of energy transfer between the electrons and neutral mercury atoms is very low. As a consequence, the relaxation of energy is a very slow process and requires large computation time. In order to optimize the simulation speed, the simulations were usually began with a relatively low number of electrons (typically 1.5×10^3) and after relaxation to the steady state the electron swarm was scaled up in numbers at fixed time intervals. The newly created electron has the same dynamic properties as the original one until the first collision. Following the first collision the progeny and the original electrons follow different, independent trajectories. Detailed testing has shown that this technique does not affect the final results, but speeds up

the relaxation considerably. For more details the reader is referred to [54].

3 Results and discussion

3.1 Preliminaries

In the first part of this section we cover a range of reduced electric fields between 0.1 and 1000 Td. The temperature of the mercury vapor is 293 K while the pressure is set to 1 Torr. Under these conditions the impact of mercury dimers is negligible. In what follows these conditions will be designated as "no dimers". In the second part of the present work, we consider a much narrower range of the reduced electric fields: 0.1–3 Td. The temperature is set to 573 K and calculations are performed for a range of pressures. The influence of mercury dimers on the drift velocity and other transport properties is investigated over a range of conditions that are consistent with those present in the experiment of England and Elford [37]. In the last segment of this work, the transport coefficients are calculated using our new set of cross sections for electron scattering in mercury vapor over a range of E/N values and temperatures relevant to light sources which utilize mercury discharges.

The transport coefficients shown below are functions of E/N and are expressed using the unit of Townsend (1 Td = 10^{-21} Vm^2). Calculations are performed assuming that the internal states are governed by a Maxwell–Boltzmann distribution which essentially places all mercury atoms in the ground state. All scattering is assumed isotropic and hence elastic cross section is the same as the elastic momentum transfer cross section. The thermal motion of background particles is carefully considered in both Boltzmann equation analysis and in Monte Carlo simulations.

3.2 Cross sections for electron scattering in mercury vapor

In this work, we consider electron transport in mercury vapor using the cross section set developed in this study. This set of cross sections is shown in Figure 1. The cross section for momentum transfer in elastic collisions is made as follows. For lower electron energies, we use the experimentally derived cross section of England and Elford [37] while for higher energies, we use a cross section tabulated in MAGBOLTZ code [64]. As discussed by England and Elford, care must be taken in deriving of a cross section for momentum transfer from the measured drift velocities due to diffusion effects and the presence of mercury dimers [37]. Cross sections for electronic excitations for levels $^3P_0$, $^3P_1$ and $^3P_2$ are retrieved from [65] while electronic excitations to $^1S_0$ and $^1P_1$ states as well as a cross section for higher states are also taken from MAGBOLTZ code. For electron-impact ionization, we have used the cross section from [66]. Cross sections were slightly modified during the calculations to improve agreement between the calculated and measured swarm parameters. We found that we were able to achieve a good agreement between calculated and
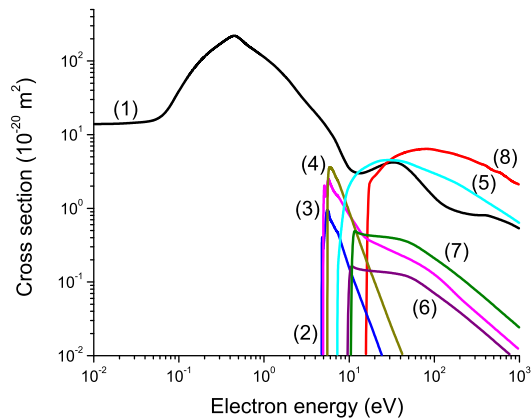

Fig. 1. Cross sections for electron scattering in Hg vapor: (1) elastic momentum transfer, (2) excitation $^3P_0$, (3) excitation $^3P_1$, (4) excitation $^3P_2$, (5) excitation $^1P_1$, (6) excitation $^1S_0$, (7) excitation to higher states and (8) ionization.

measured drift velocities for lower E/N by adjusting only the magnitude of the elastic momentum transfer cross section. For higher E/N (e.g. for higher electron energies), we have slightly modified the cross sections for electronic excitations in order to reproduce the measured ionization coefficient. This procedure is based on the experience that the calculated ionization rate is affected more by the modifications of the cross sections for electronic excitations than by the modifications of the ionization cross section [33,35].

A single effective inelastic cross section with the energy threshold of 0.04 eV is added to our cross section set, for electron scattering on mercury atoms, in order to represent the energy losses and momentum changes due to rotational and vibrational excitations of mercury dimers. It was necessary to include an effective cross section, since there are no cross sections for other channels of electron scattering on mercury dimers in the literature. There are no competing processes in the same energy range for collisions on monomers thus the contribution of the rotational–vibrational excitation will be significant. In principle, we may assume that the abundance of the dimers is sufficiently low so their overall contribution is negligible for processes that have a competing channel in scattering on monomer. In other words, we may assume that for all the other processes the cross sections are the same as for the monomer and we may apply an effective cross section for rotational and vibrational excitation of dimers and add that process to the set of cross sections for monomers. This effective cross section is derived using the experimental measurements of Elford and co-workers [36,37]. We have used the following assumptions:

- mercury dimers are always present in mercury vapor at a concentration proportional to the number density of mercury atoms;
- in order to account for the dimer number density, the amplitude of the effective cross section is scaled with their fractional abundance;
- the ideal gas law is assumed for the equation of state of mercury vapor.
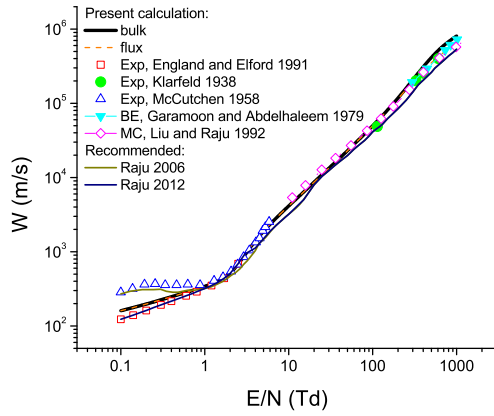
Fig. 2. Comparison of the drift velocity calculated using the present set of cross sections with the available experimental measurements of England and Elford [37], Klarfeld [67] and McCutchen [68]. Our results for the drift velocity are also compared with the available Monte Carlo calculations [27], Boltzmann equation results [25] and with the data recommended by Raju [15,16].

The effective cross section for dimers at pressure p and temperature T is given by [37]

$$\sigma(\epsilon) = 8.3\,\sigma_i(\epsilon)\,\Delta(p,T), \tag{11}$$

where 8.3 is a maximal value of the cross section at fractional dimer abundance of 1 ppm, $\sigma_i(\epsilon)$ is the dimer cross section used to fit the measurements of drift velocity and $\Delta(p,T)$ is the fractional abundance of dimers at pressure p and temperature T. Cross sections $\sigma_i(\epsilon)$ as a function of electron energy in units of squared angstroms are given by England and Elford [37]. Using the above assumptions and a value of 21.8×10^{-6} for fractional abundance of dimers at the pressure of 1 kPa and temperature of 573 K we have

$$\frac{\Delta(p,T)}{\Delta_1(p_1,T_1)} = \frac{n}{n_1} = \frac{p}{p_1}\frac{T_1}{T}, \tag{12}$$

and hence

$$\Delta(p,T) = 21.8 \times 10^{-6}\,\frac{p}{1\,\text{kPa}}\,\frac{573\,\text{K}}{T}. \tag{13}$$

Combining equations (11) and (13) yields the following simple expression for deriving the dimer cross section at the pressure p and temperature T

$$\sigma(\epsilon) = 180 \times 10^{-6}\,\frac{p}{1\,\text{kPa}}\,\frac{573\,\text{K}}{T}\,\sigma_i(\epsilon). \tag{14}$$

From equation (14) it is clear that the mercury-dimer cross section depends on the ratio p/T. If the mercury vapor temperature T is fixed and the pressure p is increased, then the mercury-dimer cross section grows and vice versa, if one keeps the pressure p fixed and increases the mercury vapor temperature T, then the mercury-dimer cross section declines. However, it should be noted that
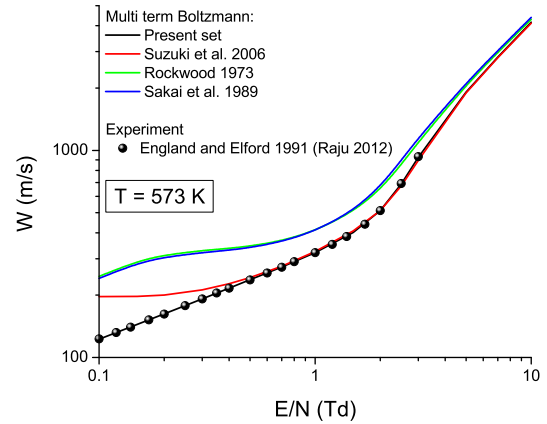
Fig. 3. Comparison of the drift velocity calculated using the present set of cross sections with those calculated using the cross sections sets developed by Rockwood [17], Sakai et al. [20] and Suzuki et al. [21]. Results are presented for the lower values of E/N and are compared with the measurements of England and Elford [37] which have been recommended by Raju [16]. The temperature of the dimer-free mercury vapor is 573 K.

the saturated mercury vapor pressure at 573 K is 33 kPa (approximately 248 Torr). This means that at the temperature of 573 K it is not possible to consider the influence of pressures higher than 33 kPa, and vice versa, it is not possible to consider the transport of electrons at a pressure of 33 kPa for the temperature less than 573 K. These conditions correspond to liquid mercury, which is certainly beyond the scope of this work.

The effective cross section which describes rotational and vibrational excitations of mercury dimers is considerable at higher pressures and lower temperatures. The corresponding superelastic cross section has been calculated using the principle of detailed balance in a thermal equilibrium.

3.3 Comparison between measured and calculated transport coefficients

In order to test the present set of cross sections for electron scattering in mercury vapor, we compare our theoretically calculated transport coefficients with various measurements and other calculations under conditions in which the influence of mercury dimers is negligible. In particular, we compare our calculations with the two sets of data recommended and published by Raju [15,16]. The transport coefficients are shown in Figures 2–6 as functions of E/N. Calculations are performed using the present set of cross sections and those developed by Rockwood [17], Sakai et al. [20] and Suzuki et al. [21]. We have applied a multi term approach for solving the Boltzmann equation assuming the pressure of 1 Torr while the temperature of mercury vapor is set to 293 K. Under these conditions the influence of mercury dimers on transport coefficients could be neglected. The convergence of transport coefficients was good and a value of $l_{\max} = 5$ was generally required for achieving an accuracy to within 1% or better.
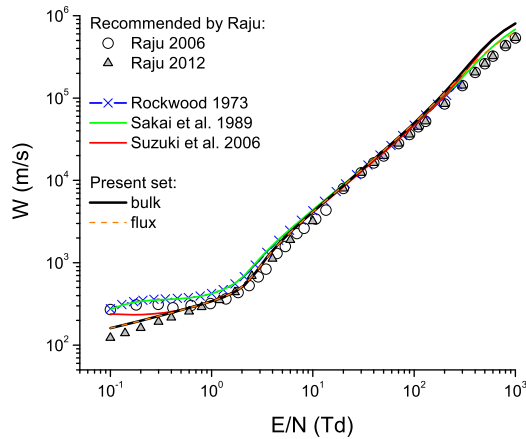
Fig. 4. Comparison of the drift velocity calculated using the present set of cross sections with those calculated using the cross sections sets developed by Rockwood [17], Sakai et al. [20] and Suzuki et al. [21]. Results are also compared with the drift velocity data recommended by Raju [15,16]. The temperature of the dimer-free mercury vapor is 293 K.
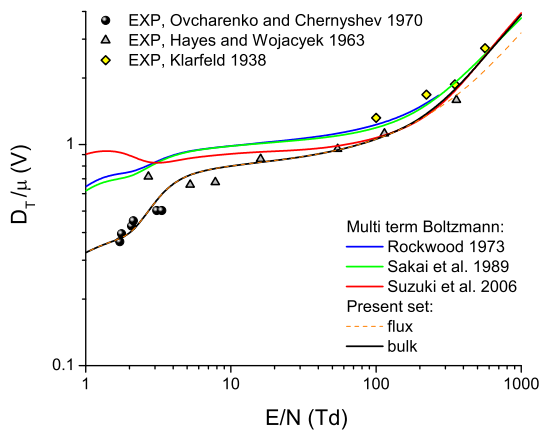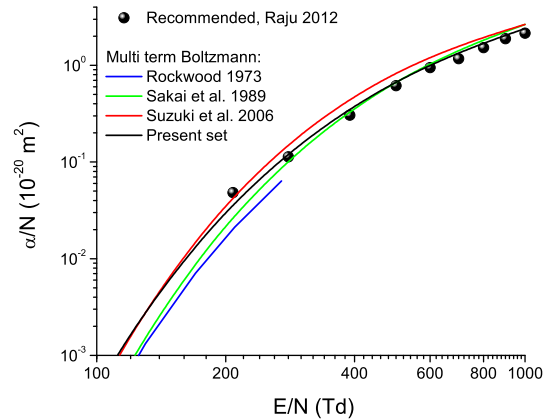

Fig. 5. Comparison of the characteristic energy, calculated using the present set of cross sections with those calculated using the cross section sets developed by Rockwood [17], Sakai et al. [20] and Suzuki et al. [21]. Results are also compared with the measurements of Ovcharenko and Chernyshev [69], Hayes and Wojacyek [70] and Klarfeld [67].

The bulk and flux drift velocities along with the experimental results of Klarfeld [67], McCutchen [68] and those recommended by Raju [15,16] are shown in Figure 2. The values of drift velocity calculated by a Monte Carlo simulation technique [27] and those obtained by solving the Boltzmann equation [25] are also plotted. For the low values of E/N we observe relatively poor agreement between our results and measurements of England and Elford [37]. This follows from the fact that our calculations have been performed assuming the mercury vapor temperature of 293 K while the experimental values of drift velocities in a dimer-free mercury vapor of England and Elford are obtained at 573 K. The Raju's 2012 recommended data are consistent with the measurements England and Elford [37]. After increasing the temperature of dimer-free mercury vapor to 573 K in our calculations, we have observed

Fig. 6. Comparison of the ionization coefficient calculated using the present set of cross sections with those calculated using the cross section sets developed by Rockwood [17], Sakai et al. [20] and Suzuki et al. [21]. Results are also compared with the Raju's 2012 recommended data.

an excellent agreement between the calculated and measured drift velocities (see Fig. 3). Comparing our results and those measured by McCutchen [68], it is evident that a significant disagreement exists (see Fig. 2). The signs of NDC are clearly evident in the measurements of McCutchen [68]. This suggests that the experiment was operated under conditions in which the traces of mercury dimers were present. Indeed, the pressure of mercury vapor in his experiment was set to 350 Torr while no temperatures were given for any experimental runs. The agreement between our results and measurements of McCutchen [68] becomes much better for the higher values of E/N as the impact of mercury dimers on the drift velocity is reduced. At intermediate fields (10 Td< E/N <100 Td), our results and Monte Carlo results of Liu and Raju [27] agree also very well. At higher E/N, above 100 Td, we see that the present calculations tend to lie a little above the experimental results of Klarfeld [67] and calculations of Garamoon and Abdelhaleem [25]. Nevertheless, the agreement is still quite reasonable. Due to the explicit contribution of ionization, the differences between the bulk and flux values of the drift velocity are of the order of 25% in the limit of the highest E/N considered in this work. Below 100 Td, however there is no appreciable difference between the two. In conclusion, from the profile of the drift velocity calculated using the present set of cross sections and temperature of 293 K for mercury vapor, there are no signs of NDC, i.e., the drift velocity is a monotonically increasing function of E/N.

In Figure 4 we show the variation of the flux and bulk drift velocities with E/N. The plots were calculated using the present set of cross sections and those developed by Rockwood [17], Sakai et al. [20] and Suzuki et al. [21]. For clarity, the flux drift velocity is shown only for the present set of cross sections. The results are also compared with the two sets of Raju's recommended data [15,16]. For the lower values of E/N, we again observe the inconsistency between our calculated data assuming the present set of cross sections and Raju's 2012 recommended data [16]. Increasing the temperature of the
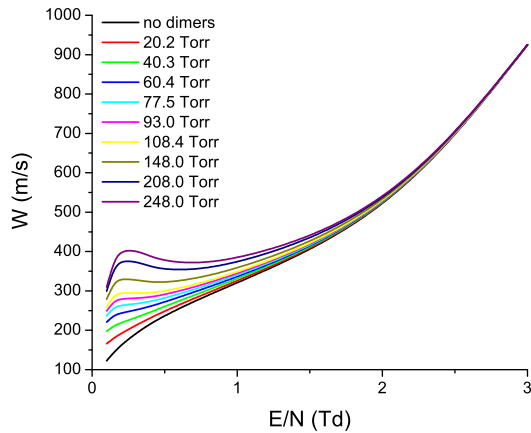
Fig. 7. Drift velocity as a function of E/N for a range of pressures. The temperature of the mercury vapor is 573 K.

Fig. 8. Mean energy as a function of E/N for the same conditions as in Figure 7.

mercury vapor to 573 K the agreement between our calculations and Raju's 2012 recommended data is excellent (see Fig. 3). In the same region of E/N, the agreement between the calculated drift velocities assuming the cross section sets developed by Rockwood [17] and Sakai et al. [20] is very good. The agreement is not surprising, since the cross section for momentum transfer in elastic collisions developed by Rockwood [17] was also used by Sakai et al. [20]. For the intermediate values of E/N (10 Td$< E/N <$100 Td), we observe the excellent agreement between all calculated drift velocities. For the higher values of E/N, the agreement is slightly deteriorated. The calculated flux drift velocity using the present set of cross sections agrees reasonably well with the calculated bulk drift velocity assuming the set of cross sections developed by Sakai et al. [20]. On the other hand, the bulk drift velocities calculated using the present set and a set of cross sections developed by Suzuki et al. [21] agree very well. The set of cross sections developed by Rockwood [17] could not be used for calculations in the limit of higher E/N since it covers the range of electron energies only up to 30 eV. In conclusion, with the exception of the Raju's 2006 recommended data, our calculations clearly show the absence of NDC for all sets of cross sections employed in this work.

Figure 5 shows the flux and the bulk characteristic energies as a function of E/N. The characteristic energy provides a good estimate of the average energy of the electrons in the swarm. This quantity is extremely sensitive to the presence of inelastic processes and hence its comparison with experimental data indicates the quality of the energy balance of the cross section sets under consideration. Calculations using the present set of cross sections and those developed by Rockwood [17], Sakai et al. [20] and Suzuki et al. [21] are compared with the experimental results of Ovcharenko and Chernyshev [69], Hayes and Wojacyek [70] and Klarfeld [67]. For the lower values of E/N, we observe that the characteristic energy calculated from the present set of cross sections is in quite nice agreement with measurements of Ovcharenko and Chernyshev [69]. The agreement is also good with the measurements of Hayes and Wojacyek [70] for the intermediate values of
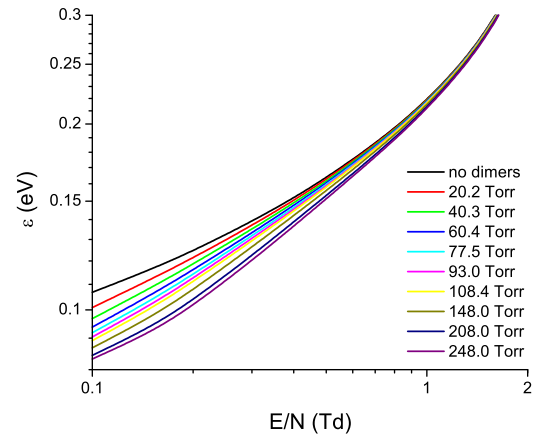
E/N while in the limit of the highest E/N considered in this work, the calculated values approach to each other and generally tend to lie a little below the experimental results of Klarfeld [67].

In Figure 6 we show the variation of the ionization coefficient with E/N. Calculations using the present set of cross sections and those published by Rockwood [17], Sakai et al. [20] and Suzuki et al. [21] are compared with the Raju's 2012 recommended data. The agreement between Raju's 2012 recommended data and those calculated assuming the present set of cross sections is very good. On the other hand, calculations assuming the set of cross sections developed by Suzuki et al. [21] are systematically higher than Raju's 2012 recommended data while calculations using the sets of cross sections developed by Rockwood [17] and Sakai et al. [20] are lower at low E/N than Raju's 2012 recommended data. We observe that calculation based on the present set of cross sections slightly deviate from the Raju's 2012 recommended data only in the limit of lower E/N. One may expect such behavior as the computer code must cope with very small values of the distribution function in the energy region where the ionization cross section is appreciable. Furthermore, the experimental measurements of the ionization coefficient in the vicinity of the ionization threshold, usually have great uncertainty.

3.4 Pressure dependence of transport coefficients and NDC effect

In this section we investigate the effects of mercury dimes on electron transport. Calculations are performed for a range of pressures while the temperature of mercury vapor is set to 573 K. The cross sections detailed in Section 3.2 and displayed in Figure 1 are used as an input into Monte Carlo simulations. In Figure 7 we show the drift velocity as a function of E/N for a range of pressures. From Figure 7 we see that the drift velocity increases with the pressure of mercury vapor for low values of E/N and becomes pressure independent for higher values of E/N. Other transport coefficients and properties show pressure
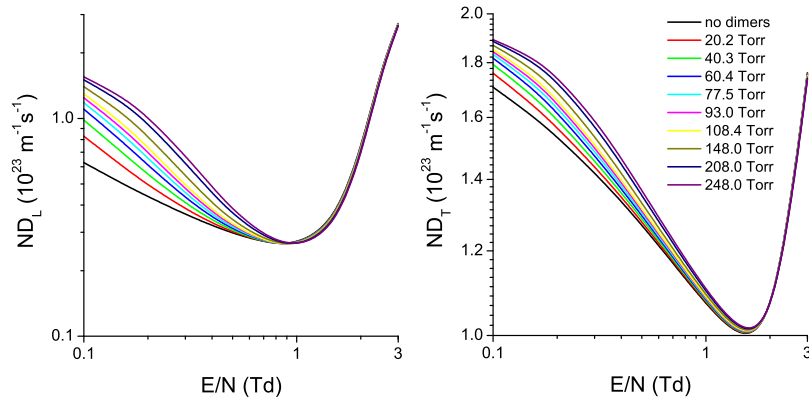
Fig. 9. Longitudinal and transverse diffusion coefficients as a function of E/N for the same conditions as in Figure 7.

dependence over the same range of E/N. As an illustrative example, in Figures 8 and 9 we show the variation of the mean energy and diffusion coefficients with E/N. While the mean energy decreases with an increasing pressure, the diffusion coefficients are increased. The pressure dependence of the drift velocity (and other transport coefficients) arises through the pressure dependence of the dimer cross section. It is well known that in elastic collisions a fraction of the initial energy m/M is transferred from the electron to the neutral particle, while for inelastic collisions a considerably larger fixed energy loss is transferred in addition, per each interaction. Assuming isotropic model of scattering, the vector of electron velocity is arbitrarily oriented after collisions, which leads to a reduction in the directed component of the velocity. In other words, elastic collisions have the effect of randomizing the direction of electron motion, while preserving their speeds. When inelastic collisions are significant, however, the energy transfer is no longer relatively small. This in turns reduces the chaotic component of the electron velocity, and inelastic collisions no longer have the effect of randomizing the direction of electron motion. This indicates that the increase in gas pressure enhances drift velocity and reduces mean energy. For higher electron energies, the cross section for mercury dimers is reduced and transport coefficients become pressure independent.

In addition to the pressure dependence of the drift velocity and other transport coefficients, we observe the presence of NDC in the profiles of drift velocity in the limit of pressures that approach to the pressure of saturated mercury vapor. A study of the NDC for model gases was performed by Petrović et al. [38] in which the conditions for elastic and inelastic cross sections required for the occurrence of NDC were discussed. Using momentum transfer theory, Robson had developed an analytical criterion for NDC in a conservative single gas [39] that was further extended in [40]. An intimate connection between NDC and inelastic collisions was recognized in these studies. It was shown that NDC arises for certain combinations of elastic and inelastic cross sections in which, on increasing the electric field, there is a rapid transition from inelastic to elastic dominated energy loss mechanism. In this transition region, for a given increase in the electric field, a greater proportion of the energy input goes into

chaotic motion rather than directed motion. As a consequence, the drift velocity falls with an increasing electric field.

This is exactly what happens in mercury vapor at higher pressures. As already discussed, mercury dimers are always present in a mercury vapor at a concentration proportional to the vapor pressure. Thus, as the pressure of mercury vapor increases, the dimer cross section increases as well as the corresponding collision frequency (see Fig. 10). For pressures higher than approximately 100 Torr and in the limit of lower values of E/N, the inelastic energy loss mechanism dominates the elastic energy loss mechanism. For increasing E/N the collision frequency of inelastic collisions decreases while the collision frequency for elastic collisions rises. This favors the development of NDC even though the difference between the collision frequencies is almost five orders of magnitude! However, if one takes into account that the average energy loss in an elastic collision is between 1×10^{-7} and 1×10^{-6} eV, while the energy loss in inelastic collisions is 0.04 eV, it is clear that a relatively small ratio between collision frequencies in inelastic and elastic collisions is compensated by the substantial differences in energy losses. At pressures lower than approximately 100 Torr, the concentration of mercury dimers is low. As a consequence, the energy losses in inelastic collisions are significantly lower than those in elastic collisions over the entire range of E/N. Under these conditions, NDC does not occur in the E/N profiles of the drift velocity.

These physical arguments are illustrated in Figure 11. Figure 11 shows the ratio between the average elastic and inelastic energy losses as a function of E/N. The average inelastic energy loss $\Omega_{\rm inel}$ is evaluated as a product of the rate coefficient for an inelastic dimer process and the corresponding threshold of 0.04 eV. It should be noted that the elastic energy loss $\Omega_{\rm elas}$ is approximated by the product of mean energy, the collision frequency of elastic collisions and the factor $2m/M$. By doing so, we have actually reduced the contribution of elastic collisions, having in mind that the collision frequency of elastic collisions and the corresponding energy losses are greater for electrons with energies higher than the average electron energy. The accurate calculation may be very efficiently performed in Monte Carlo simulations, but we defer this to a future
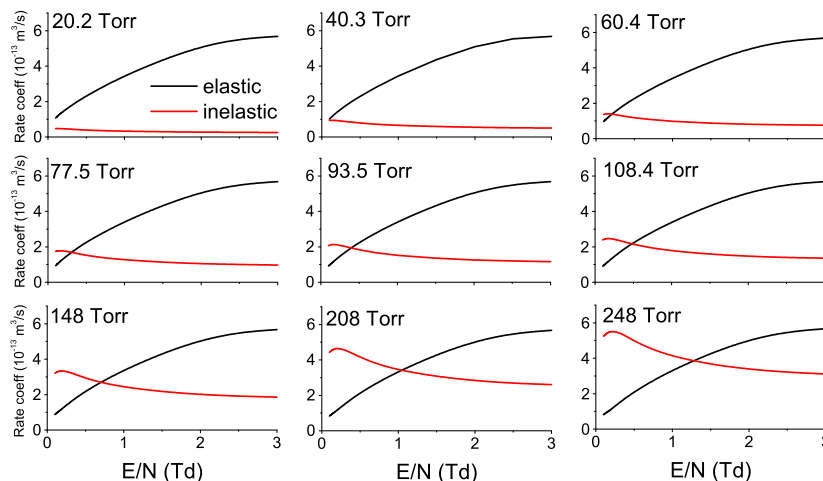
Fig. 10. Rate coefficients for elastic and inelastic collisions as a function of E/N in the presence of mercury dimers. The rate coefficient of inelastic processes which describes the presence of dimers is multiplied by the factor of 1×10^{5}. Calculations are performed for the same conditions as in Figure 7.
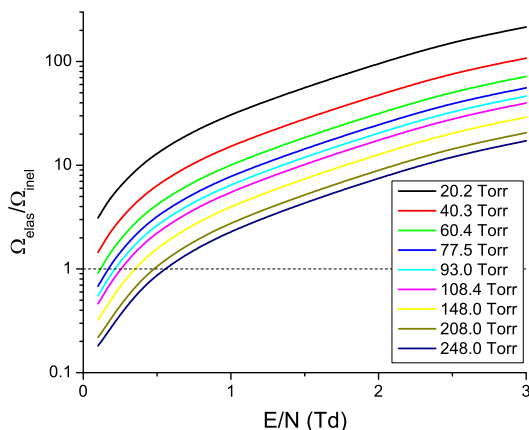

Fig. 11. Ratio between the average elastic and inelastic energy losses as a function of E/N for the same conditions as in Figure 7.

work. In any case, we observe that only for higher pressures of mercury vapor the ratio between energy losses in elastic and inelastic collisions favors the development of NDC.

Figures 12 and 13 illustrate the importance of including an accurate representation for thermal motion of the mercury atoms in our analysis of the drift velocity in the limit of lower values of E/N. Our multi term Boltzmann equation results with the rigorously incorporated effects of thermal motion of the mercury atoms are compared with our Monte Carlo results obtained under the conditions in which no thermal motion is considered. Our Monte Carlo results with the systematically incorporated effects of thermal motion of the mercury atoms are not included in this figure as they are essentially the same as those obtained through a multi term approach for solving the Boltzmann equation. Both sets of our calculated data are compared with the measurements of England and Elford [37]. Comparing experiment and our Boltzmann equation

results with the rigorously incorporated effects of thermal motion of the mercury atoms, we observe an excellent agreement between these two sets of data. In contrast, our Monte Carlo simulation results in which no thermal motion of the mercury atoms is considered, systematically overestimate the measurements in the limit of the lowest E/N. A false NDC like structure in the Monte Carlo $T = 0$ profiles of the drift velocity for all pressures of the mercury vapor is clearly evident. However, for increasing E/N the agreement between the measurements and Monte Carlo simulations in which no thermal motion is considered, becomes much better. As expected, the disagreement between the measurements and Monte Carlo simulations in which no thermal motion is considered is more pronounced for higher pressures.

3.5 Temperature dependence of transport coefficients

In this section we present results showing the variation of transport properties with E/N and mercury vapor temperature, T. Calculations are performed for two different cases: (1) the presence of mercury dimers assuming the pressure of 248 Torr, and (2) no dimers in the mercury vapor. Temperatures less than 573 K cannot be considered in the first scenario as for this pressure the mercury is in liquid form. These two scenarios for our calculations are considered with the aim of separating the thermal effects from those induced by mercury dimers.

In Figure 14 we show the variation of the mean energy with E/N for various mercury vapor temperatures, T. We observe that the mean energy is a monotonically increasing function of E/N for a fixed T. In the limit of low values of E/N the mean energy of the electrons is thermal and does not depend on E/N. This suggests that the velocity distribution function is essentially a thermal Maxwellian. For increasing T, the thermal deadlock is broken at higher E/N. For $T = 573$ K and $T = 1000$ K, we observe that the mean energy is higher in the case where
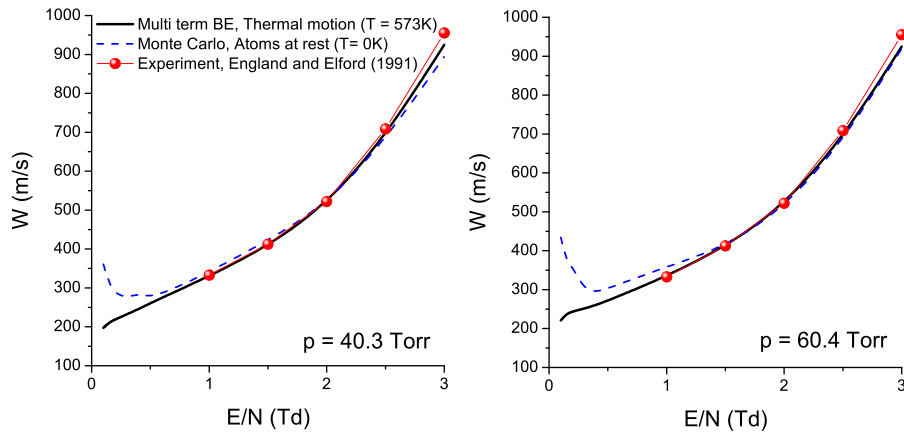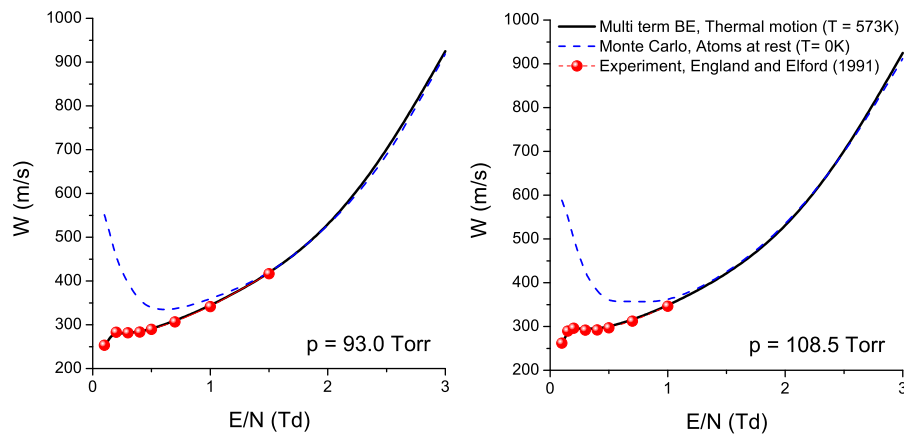
Fig. 12. Comparison between the calculated and measured values of drift velocity for pressures of 40.3 Torr (left panel) and 60.4 Torr (right panel). Monte Carlo results are obtained assuming atoms at rest ($T = 0$ K) while the gas temperature effects are considered through a multi term approach for solving the Boltzmann equation ($T = 573$ K).

Fig. 13. Comparison between the calculated and measured values of drift velocity for pressures of 93.0 Torr (left panel) and 108.5 Torr (right panel). Calculations are performed for the same conditions as in Figure 12.
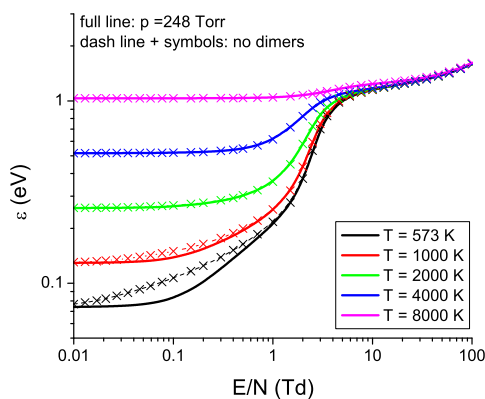
Fig. 14. Variation of the mean energy of the electron swarm as a function of E/N for various mercury vapor temperatures as indicated on the graph. The pressure of mercury vapor is 248 Torr.

no mercury dimers occur. It is clear that when the mercury dimers are present, the electrons lose more energy in inelastic collisions. For $T \geq 2000$ K the influence of mercury dimers is negligible. For low and intermediate values of E/N the mean energy is distinctively dependent on T. In the limit of higher values of E/N the mean energies are higher than the corresponding thermal mean energies, which is a clear sign that the velocity distribution function is no longer a thermal Maxwellian. In this regime, the impact of the mercury vapor temperature T on the mean energies is minimal.

In Figures 15 and 16 we show the variation of the drift velocity with E/N for various mercury vapor temperatures, T. The drift velocity is a monotonically increasing function of E/N for all mercury vapor temperatures T, except for $T = 573$ K. At this temperature, NDC is clearly evident in the E/N-profile of drift velocity. With further increase in mercury vapor temperature, a decrease in drift velocity with increasing E/N is firstly reduced and then it is completely removed. From equation (14) it is clear that for increasing mercury vapor temperature and fixed pressure, the mercury-dimer cross section declines. As a consequence, the collision frequency of inelastic collisions whose presence is of an essential importance for the development of NDC effect, is also firstly reduced, and then severely minimized which ultimately leads to a disappearance of
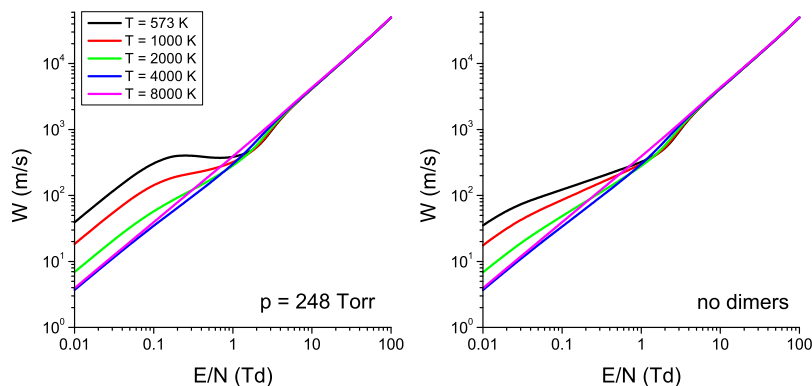
Fig. 15. Variation of the bulk drift velocity of the electron swarm as a function of E/N for the same conditions as in Figure 14.
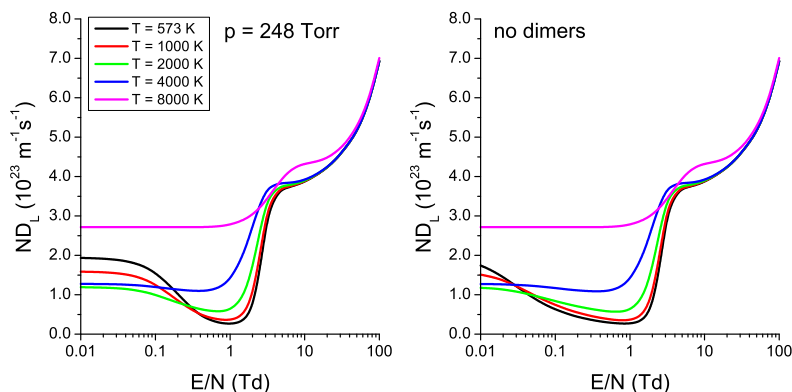

Fig. 16. Variation of the bulk longitudinal diffusion coefficient of the electron swarm as a function of E/N for the same conditions as in Figure 14.

NDC. The lesson from this is that the temperature of mercury vapor can be used to control the occurrence of NDC.

In the limit of lower E/N the drift velocity generally decreases with increasing T, though this is not the case for $T = 8000$ K. For $T = 8000$ K we see that the drift velocity is above the values calculated for $T = 4000$ K. For the temperature of 8000 K, the mean energy is high enough to exceed the peak value of the "0.4 eV" shape resonance in the cross section for elastic scattering. On the other hand, for $T = 4000$ K, the mean energy is significantly lower and corresponds to the range of energies in which the cross section for elastic collisions rises with an increasing energy of the electrons. As a consequence, the drift velocity is lower. For the intermediate values of E/N (between 1 and 10 Td, approximately) the behavior of drift velocity is very complex. In the energy region corresponding to the intermediate values of E/N, there is an overlap of the distribution function not only with a very large resonance in the elastic cross section, but also with the cross sections of inelastic processes that are now open. Finally, for higher values of E/N the drift velocity does not depend on the mercury vapor temperature and the drift of the electrons is entirely controlled by the electric field.

The variation of the diffusion coefficients with E/N for various mercury vapor temperatures, T, is shown in Figures 16 and 17. The impact of mercury dimers on both ND_L and ND_T is evident only for lower values of

E/N and lower T. At fixed T and for increasing E/N the electric field rises the energy of the electrons and the mercury-dimer cross section begins to fall. The same occurs at fixed E/N and with increasing T. Furthermore, in the limit of the lowest E/N and for a fixed E/N both ND_L and ND_T display a minimum with respect to T. In contrast to the drift velocity, the minimum occurs at $T = 2000$ K, indicating that diffusion coefficients show a remarkable sensitivity to the energy dependence of cross sections and presence of inelastic collisions. For the intermediate values of E/N, the most distinct property is the existence of a local minimum in the E/N profiles of both ND_L and ND_T. With a decreasing temperature, the minimum becomes more pronounced and is shifted towards higher E/N. The fall in both ND_L and ND_T by increasing E/N reflects the rapidly rising elastic cross section, e.g., the velocity distribution function samples the lower energy branch of the "0.4 eV" shape resonance. Comparing the behavior of diffusion coefficients at low and intermediate values of E/N, one can see that the contribution of mercury dimers is more important for lower values of E/N. In the limit of higher E/N, the impact of temperature on the behavior of diffusion coefficients is minimal. However, the longitudinal diffusion coefficient shows a more complex behavior with varying temperature.

In Figure 18 we show variation of the ratio ND_T to ND_L with E/N for various mercury vapor temperatures,
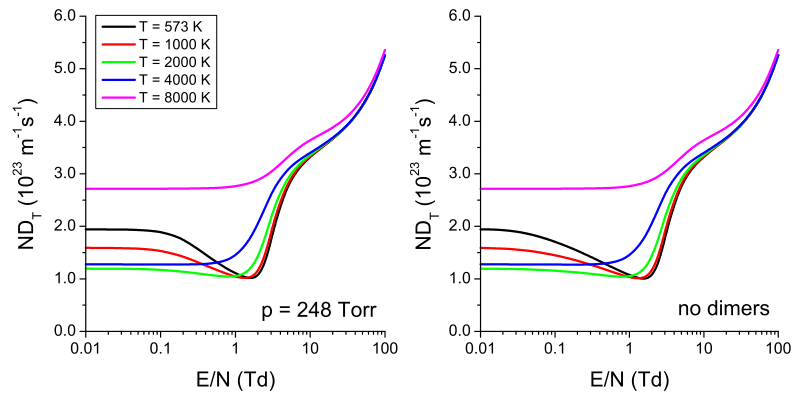
Fig. 17. Variation of the bulk transverse diffusion coefficient of the electron swarm as a function of E/N for the same conditions as in Figure 14.
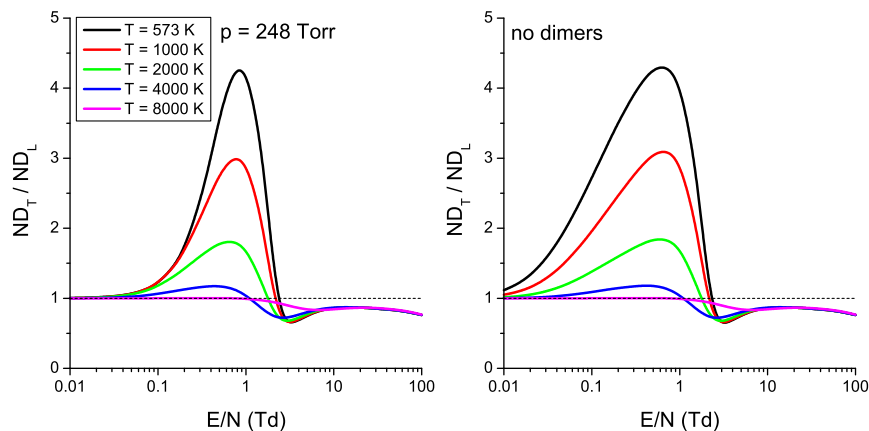

Fig. 18. Variation of the ratio of transverse to longitudinal diffusion coefficient of the electron swarm as a function of E/N for the same conditions as in Figure 14. Bulk values of diffusion coefficients are used.

T. We observe that the degree of anisotropic diffusion is significantly reduced by increasing mercury vapor temperature, T, in both scenarios considered here, i.e., in the presence of dimers and in their absence. In the limit of the lowest E/N diffusion is isotropic, i.e. $ND_L = ND_T$ since velocity distribution function is a thermal Maxwellian. At a fixed T the ratio ND_T/ND_L increases with increasing E/N, reaching a maximal value between 0.5 and 0.9 Td depending on the temperature T, and then it starts to decrease with E/N. For $T = 573$ K there is a factor higher than 4 between the longitudinal and transverse diffusion coefficients. In contrast, for $T = 8000$ K the diffusion is isotropic in a wide range of E/N, and only for $E/N > 1$ Td, the longitudinal diffusion coefficient is greater than the transverse, i.e. $ND_L > ND_T$. The reversal of the inequality is a clear sign of the rapid fall in the elastic cross section. Indeed, in this energy range the velocity distribution function samples the high energy branch of the "0.4" shape resonance of the elastic cross sections which rapidly falls with increasing electron energy.

4 Conclusion

In this paper, we have presented the results of a systematic investigation of electron transport in mercury vapor

under the influence of electric field. First, we have compiled a complete set of cross sections for electron scattering in mercury vapor using the available data in the literature for individual collisional processes. In our evaluation, performed both with multi term Boltzmann and Monte Carlo codes, the initially compiled set of cross sections has been modified in order to reproduce the experimental data. The best agreement between calculated and measured drift velocities in the limit of lower electron energies was achieved by adjusting only the magnitude of the elastic momentum transfer cross section. For higher electron energies, we have only slightly modified the cross sections for electronic excitations in order to reproduce the measured ionization coefficient. We have also considered the issue of assessing the completeness, accuracy, and consistency of other cross section sets for electron scattering in mercury vapor by comparing calculated transport coefficients with those measured in various experiments. Our calculations highlight some inadequacies in these sets of cross sections and indicate possibilities for their improvements.

We have also outlined issues associated with the pressure and temperature dependences of transport coefficients. It was shown that the pressure dependence of the transport coefficients arise through the pressure dependence of the mercury-dimer cross section. In particular,

we have discussed the NDC phenomenon in the limit of lower values of the reduced electric fields. Conditions leading to NDC have been discussed and it was concluded that the phenomenon is induced by the presence of mercury dimers. Following the previous works of England and Elford [37], we have derived the mercury-dimer cross section for a range of pressures and temperatures of mercury vapor. One of the critical elements in our analysis of the drift velocity in the limit of lower values of the reduced electric fields was an accurate representation for thermal motion of the mercury atoms. Within a multi term theory for solving the Boltzmann equation used in the present work, the thermal motion of the neutral mercury atoms is systematically incorporated into all collision process operators and all spherical harmonic equations. Likewise, our Monte Carlo simulation code has been improved by implementing an efficient algorithm for calculating the collision frequency in the case when thermal motion of the background gas cannot be neglected for a Maxwellian velocity distribution of the background gas particles. Without these critical elements in a theory for solving the Boltzmann equation and Monte Carlo simulation codes, the variation of the drift velocity with the reduced electric field is unphysical in domain of lower electric fields.

Using a set of cross sections presented in this work, in the near future we plan to investigate the electron transport in crossed electric and magnetic fields. Calculations will be made with the aim of providing the data for fluid modeling of inductively coupled mercury discharges which are utilized in some types of electrodeless lamps. Similar calculations will be performed for ac electric and magnetic fields having in mind that both the electric and magnetic fields could be time-dependent. We also plan to develop complete and consistent sets of cross section for other materials, including indium, sodium and other metal vapors relevant for the lighting industry. The first steps have been made and the results are very encouraging [71].

Author contribution statement

All authors contributed equally to the paper.

References

1. G.G. Lister, J.E. Lawler, W.P. Lapatovich, V.A. Godyak, Rev. Mod. Phys. **76**, 541 (2004)
2. P. Flesch, *Light and light sources* (Springer, Berlin, 2006)
3. S. Samukawa, M. Hori, S. Rauf, K. Tachibana, P. Bruggeman, G. Kroesen, J.C. Whitehead, A.B. Murphy, A.F. Gutso, S. Starikovskaia, U. Kortshagen, J.P. Boeuf, T.J. Sommerer, M.J. Kushner, U. Czarnetzki, N. Mason, J. Phys. D: Appl. Phys. **45**, 25300 (2012)
4. G.J. Fetzer, J.J. Rocca, IEEE J. Quantum Electron. **28**, 1941 (1992)
5. C.E. Little, *Metal vapour lasers: physics, engineering and applications* (Wiley, Chichester, 1999)
6. E. Ahedo, Plasma Phys. Control. Fusion **53**, 124037 (2011)
7. G.G. Lister, J.J. Curry, J.E. Lawler, J. Phys. D: Appl. Phys. **37**, 3099 (2004)
8. W.J.M. Brok, M.F. Gendre, M. Haverlag, J.J.A.M. van der Mullen, J. Phys. D: Appl. Phys. **40**, 3931 (2007)
9. O. Zatsarinny, K. Bartschat, Phys. Rev. A **79**, 042713 (2009)
10. R.P. McEachran, M.T. Elford, J. Phys. B: At. Mol. Opt. Phys. **36**, 427 (2003)
11. R.E. Robson, R.D. White, M. Hildebrandt, Eur. Phys. J. D **68**, 188 (2014)
12. Y. Golubovskii, S. Gorchakov, D. Uhrlandt, Plasma Sources Sci. Technol. **22**, 023001 (2013)
13. F. Sigeneger, R. Winkler, R.E. Robson, Contrib. Plasma Phys. **43**, 178 (2003)
14. R.E. Robson, B. Li, R.D. White, J. Phys. B: At. Mol. Opt. Phys. **33**, 507 (2000)
15. G.G. Raju, *Gaseous electronics: theory and practice* (CRC Press Taylor & Francis, Boca Raton, 2006)
16. G.G. Raju, *Gaseous electronics: tables, atoms, and molecules* (CRC Press Taylor & Francis, Boca Raton, 2012)
17. S.D. Rockwood, Phys. Rev. A **8**, 2348 (1973)
18. Y. Nakamura, J. Lucas, J. Phys. D: Appl. Phys. **11**, 325 (1978)
19. Y. Nakamura, J. Lucas, J. Phys. D: Appl. Phys. **11**, 337 (1978)
20. Y. Sakai, S. Sawada, H. Tagashira, J. Phys. D: Appl. Phys. **22**, 276 (1989)
21. S. Suzuki, K. Kuzuma, H. Itoh, J. Plasma Fusion Res. Series **7**, 314 (2006)
22. R.B. Winkler, J. Wilhelm, R. Winkler, Ann. Phys. (Leipz.) **40**, 90 (1983)
23. R.B. Winkler, J. Wilhelm, R. Winkler, Ann. Phys. (Leipz.) **40**, 119 (1983)
24. M. Yousfi, G. Zissis, A. Alkaa, J.J. Damelincourt, Phys. Rev. A **42**, 978 (1990)
25. A.A. Garamoon, A.S. Abdelhaleem, J. Phys. D: Appl. Phys. **12**, 2181 (1979)
26. G.L. Braglia, M. Diligenti, J. Wilhelm, R. Winkler, Il Nuovo Cimento **12**, 257 (1990)
27. J. Liu, G.R. Govinda Raju, J. Phys. D: Appl. Phys. **25**, 167 (1992)
28. S. Sawada, Y. Sakai, H. Tagashira, J. Phys. D: Appl. Phys. **22**, 282 (1989)
29. Y. Sakai, S. Sawada, H. Tagashira, J. Phys. D: Appl. Phys. **24**, 283 (1991)
30. R. Winkler, J. Wilhelm, G.L. Braglia, M. Diligenti, Il Nuovo Cimento **12**, 975 (1990)
31. J. Liu, G.R. Govinda Raju, J. Phys. D: Appl. Phys. **25**, 465 (1992)
32. R.D. White, R.E. Robson, B. Schmidt, M.A. Morrison, J. Phys. D: Appl. Phys. **36**, 3125 (2003)
33. Z.Lj. Petrović, S. Dujko, D. Marić, G. Malović, Ž. Nikitović, O. Šašić, J. Jovanović, V. Stojanović, M. Radmilović-Radjenović, J. Phys. D: Appl. Phys. **42**, 194002 (2009)
34. L.G.H. Huxley, R.W. Crompton, *The drift and diffusion of electrons in gases* (Wiley, New York, 1974)
35. Z.Lj. Petrović, M. Šuvakov, Ž. Nikitović, S. Dujko, O. Šašić, J. Jovanović, G. Malović, V. Stojanović, Plasma Sources Sci. Technol. **16**, S1 (2007)

36. M.T. Elford, Aust. J. Phys. **33**, 231 (1980)
37. J.P. England, M.T. Elford, Aust. J. Phys. **44**, 647 (1991)
38. Z.Lj. Petrović, R.W. Crompton, G.N. Haddad, Aust. J. Phys. **37**, 23 (1984)
39. R.E. Robson, Aust. J. Phys. **37**, 35 (1984)
40. S.B. Vrhovac, Z.Lj. Petrović, Phys. Rev. E **53**, 4012 (1996)
41. J. Mirić, D. Bošnjaković, I. Simonović, Z.Lj. Petrović, S. Dujko, Plasma Sources Sci. Technol. **25**, 065010 (2016)
42. N.L. Aleksandrov, N.A. Dyatko, I.V. Kochetov, A.P. Napartovich, D. Lo, Phys. Rev. E **53**, 2730 (1996)
43. Z. Donko, N. Dyatko, Eur. Phys. J. D **70**, 135 (2016)
44. K. Yamamoto, N. Ikuta, J. Phys. Soc. Jpn. **68**, 2602 (1999)
45. G.J. Boyle, R.P. McEachran, D.G. Cocks, R.D. White, J. Chem. Phys. **142**, 154507 (2015)
46. G.J. Boyle, D.G. Cocks, R.P. McEachran, M.J. Brunger, S.J. Buckman, S. Dujko, R.D. White, J. Phys. D: Appl. Phys. **49**, 355201 (2016)
47. F. Taccogna, G. Dilecce, Eur. Phys. J. D **70**, 251 (2016)
48. L. Boltzmann, Wein. Ber. **66**, 275 (1872)
49. C.S. Wang-Chang, G.E. Uhlenbeck, J. DeBoer, in *Studies in statistical mechanics*, edited by J. DeBoer, G.E. Uhlenbeck (Wiley, New York, 1964), Vol. 2, p. 241
50. R.E. Robson, K.F. Ness, Phys. Rev. A **33**, 2068 (1986)
51. K.F. Ness, R.E. Robson, Phys. Rev. A **34**, 2185 (1986)
52. R.D. White, K.F. Ness, R.E. Robson, Appl. Surf. Sci. **192**, 26 (2002)
53. R.D. White, R.E. Robson, S. Dujko, P. Nicoletopoulos, B. Li, J. Phys. D: Appl. Phys. **42**, 194001 (2009)
54. S. Dujko, R.D. White, Z.Lj. Petrović, R.E. Robson, Phys. Rev. E **81**, 046403 (2010)
55. S. Dujko, R.D. White, Z.Lj. Petrović, R.E. Robson, Plasma Source Sci. Technol. **20**, 024013 (2011)
56. R.E. Robson, R.D. White, Z.Lj. Petrović, Rev. Mod. Phys. **77**, 1303 (2005)
57. S. Dujko, A.H. Markosyan, R.D. White, U. Ebert, J. Phys. D: Appl. Phys. **46**, 475202 (2013)
58. A.H. Markosyan, S. Dujko, U. Ebert, J. Phys. D: Appl. Phys. **46**, 475203 (2013)
59. D. Bošnjaković, Z.Lj. Petrović, S. Dujko, J. Phys. D: Appl. Phys. **49**, 405201 (2016)
60. Z.Lj. Petrović, Z.M. Raspopović, S. Dujko, T. Makabe, Appl. Surf. Sci. **192**, 1 (2002)
61. S. Dujko, Z.M. Raspopović, Z.Lj. Petrović, J. Phys. D: Appl. Phys. **38**, 2952 (2005)
62. S. Dujko, R.D. White, Z.Lj. Petrović, J. Phys. D: Appl. Phys. **41**, 245205 (2008)
63. Z. Ristivojević, Z.Lj. Petrović, Plasma Sources Sci. Technol. **21**, 035001 (2012)
64. http://magboltz.web.cern.ch/magboltz
65. K. Bartschat, *Third Int. Conf. on Atomic and Molecular Data and their Applications* (American Institute of Physics, New York, 2003)
66. J. Kieffer, G.H. Dunn, Rev. Mod. Phys. **38**, 1 (1966)
67. B. Klarfeld, Tech. Phys. (USSR) **5**, 913 (1938)
68. C.W. McCutchen, Phys. Rev. **112**, 1848 (1958)
69. V.A. Ovcharenko, S.M. Chernyshev, Teplofiz. Vys. Temp. **8**, 716 (1970)
70. E. Hayes, K. Wojacyek, Beitr. Plasma Phys. **3**, 74 (1963)
71. J. Mirić, Z.Lj. Petrović, R.D. White, S. Dujko, *Proc. 27th Summer School and Int. Symp. on the Physics of Ionized Gases (Belgrade)* (Institute of Physics, Belgrade, 2014), p. 126

THE EUROPEAN
PHYSICAL JOURNAL D

Regular Article

Third-order transport coefficient tensor of electron swarms in noble gases[*]

Ilija Simonović[1], Danko Bošnjaković[1], Zoran Lj. Petrović[2], Ronald D. White[3], and Saša Dujko[1,a]

[1] Institute of Physics, University of Belgrade, P.O. Box 68, 11080 Belgrade, Serbia
[2] Serbian Academy of Sciences and Arts, Knez Mihailova 35, 11001 Belgrade, Serbia
[3] College of Science and Engineering, James Cook University, 4810 Townsville, Australia

Abstract. In this work we extend a multi term solution of the Boltzmann equation for electrons in neutral gases to consider the third-order transport coefficient tensor. Calculations of the third-order transport coefficients have been carried out for electrons in noble gases, including helium (He), neon (Ne), argon (Ar), krypton (Kr) and xenon (Xe) as a function of the reduced electric field, E/n_0 (where E is the electric field while n_0 is the gas number density). Three fundamental issues are considered: (i) the correlation between the longitudinal component of the third-order transport tensor and the longitudinal component of the diffusion tensor, (ii) the influence of the third-order transport coefficients on the spatial profile of electron swarm, and (iii) the errors associated with the two term approximation for calculating the third-order transport coefficients for electron swarms in noble gases. It is found that a very strong correlation exists between the longitudinal components of the third-order transport coefficient tensor and diffusion tensor for the higher values of E/n_0. The effects of the third-order transport coefficients on the spatial profile of electron swarms are the most pronounced for noble gases with the Ramsauer-Townsend minimum in the cross sections for elastic scattering. The largest errors of two term approximation are observed in the off-diagonal elements of the third-order transport coefficient tensor in Ar, Kr and Xe for the higher values of E/n_0.

1 Introduction

The investigation of charged particle transport in neutral gases has a wide range of applications, ranging from the modeling of swarm experiments [1–5] and modeling of low-temperature plasmas [6,7], to high-voltage technology [8] and modeling of particle detectors used in high-energy physics [9,10]. While there is a rich amount of data concerning the lower-order transport coefficients, including the drift velocity, diffusion coefficients and rate coefficients, for both electrons and ions, [11,12] and recently for positrons [13,14], the third-order transport coefficients are still largely unexplored as they are difficult to measure, and difficult to investigate theoretically.

The third-order transport coefficient tensor is required for the conversion of hydrodynamic transport coefficients into transport data that are measured in the arrival time

spectra [15,16] and the steady-state Townsend experiments [4]. In addition, the third-order transport coefficients are needed for the representation of the spatial distribution of the swarm under conditions where this distribution deviates from the ideal Gaussian. Moreover, the third-order transport coefficients would be very useful in the swarm procedure for determining the sets of cross sections for the scattering of electrons and/or ions with neutral particles, if these transport coefficients were both calculated and measured with sufficient accuracy [17,18].

The third-order transport coefficients have been investigated by several authors. Whealton and Mason have determined the structure of the third-order transport tensor for an electric field only situation, and have calculated third-order transport coefficients for electrons assuming the constant collision frequency model gas [19]. Penentrante and Bardsley calculated the third-order transport coefficients for electrons in He, Ne and Ar by using the Monte Carlo simulations and a two term approximation for solving the Boltzmann equation [17]. Vrhovac and co-workers investigated the third-order transport tensor for electrons in He, Ne and Ar by employing the momentum transfer theory [18]. Koutselos studied the third-order transport coefficients of ions in atomic gases by using the molecular

---

dynamics simulations and a three-temperature method for solving Boltzmann's equation [21–24]. The equality of the higher-order transport coefficients between an electron swarm developing from multiple electron sources and another originating from a single electron source was investigated by Sugawara and Sakai [25]. The third-order transport coefficients for electrons in methane (CH_4) and sulfur hexafluoride (SF_6) have been recently investigated by Kawaguchi and co-workers via Monte Carlo simulations [16]. They have also derived the relation between the longitudinal third-order transport coefficient and the alpha-parameters, by using the theory of arrival time spectra of an electron swarm initially developed by Kondo and Tagashira [15]. Petrović and co-workers also recently investigated the third-order transport coefficient tensor for electrons in CH_4 by using Monte Carlo simulations and the multi term method for solving the Boltzmann equation [26]. Finally, Stokes and co-workers have studied the third-order transport coefficients for localized and delocalized charged-particle transport [27].

In this work we extend the multi term solution of Boltzmann's equation with the aim of investigating behavior of third-order transport coefficients in noble gases. As noble gases have simpler cross section sets than molecular gases, they are a good starting point for studying the third-order transport coefficients. Moreover, it is interesting to investigate the influence of the Ramsauer-Townsend minimum on the third-order transport tensor for electrons in Ar, Kr and Xe, as it can be expected that a rapid variation of the cross section for elastic collisions in these gases will leave a distinguishable signature on the profiles of the third-order transport coefficients. Moreover, if the components of the third-order transport tensor have very high values for electrons in Ar, Kr and Xe at low electric fields, due to the presence of the Ramsauer-Townsend minimum, they could also have a significant influence on the spatial profile of a swarm of electrons under these conditions.

The paper is organized as follows. In Section 2.1 we present the basic elements of the theory and definition of the third-order transport tensor. In Section 2.2 we describe the multi term method for solving the Boltzmann equation used in the present work where special emphasis is placed on the relating the third-order transport coefficients and the moments of the distribution function. In Section 3.1 we describe the cross sections used as an input to solve Boltzmann's equation and the conditions of our calculations. In Section 3.2 we analyze the E/n_0-dependence of mean energy for electrons in He, Ar, Kr and Xe. In Section 3.3 we investigate the variation of the third-order transport coefficients with E/n_0 for electrons in four noble gases. In Section 3.4 we study correlation between the longitudinal component of the third-order transport tensor and the longitudinal component of the diffusion tensor for electrons in He, Ne, Ar, Kr and Xe. In Section 3.5 we consider the influence of the third-order transport coefficients on the spatial profile of the swarm for electrons in these five gases. Finally, in Section 3.6 we discuss the errors associated with the two term approximation for solving the Boltzmann equation in the framework of calculations of the third-order transport coefficients for

electrons in noble gases. Our conclusions are summarized in Section 4.

2 Theory: definitions and methods of calculation

2.1 Definition of the third-order transport coefficient tensor

In the present work, we consider a swarm of electrons which moves in an infinite and homogeneous background gas under the influence of a constant and uniform electric field. The z axis of the system is oriented along the direction of the electric field. The number density of electrons is very low and hence, the space charge effects and collisions between electrons are considered to be negligible. The background gas is regarded to be in a thermodynamic equilibrium at a temperature T_0, and the effect of the swarm on the state of the background gas can be neglected. The swarm of electrons is represented by the phase space distribution function $f(\mathbf{r}, \mathbf{c}, t)$, which is a function of position $\mathbf{r}$, velocity $\mathbf{c}$ and time t.

The continuity of the swarm in the configuration space is expressed by the following equation

$$\frac{\partial n(\mathbf{r}, t)}{\partial t} + \nabla \cdot \mathbf{\Gamma}(\mathbf{r}, t) = S(\mathbf{r}, t), \qquad (1)$$

where $n(\mathbf{r}, t)$ is the number density of electrons, while $\mathbf{\Gamma}(\mathbf{r}, t)$ and $S(\mathbf{r}, t)$ are the flux of electrons and the source term, respectively. The number density of electrons can be expressed in terms of the phase space distribution function $f(\mathbf{r}, \mathbf{c}, t)$ as

$$n(\mathbf{r}, t) = \int f(\mathbf{r}, \mathbf{c}, t) \, d\mathbf{c}, \qquad (2)$$

where integration is performed over the entire velocity space.

When the swarm is located far from boundaries of the system, and far from sources and sinks of charged particles, and when the applied electric field is spatially uniform, the swarm can enter the hydrodynamic regime [2,28]. In the hydrodynamic regime all space-time dependence of the phase space distribution function may be expressed in terms of functionals of the number density $n(\mathbf{r}, t)$. Under the hydrodynamic conditions, the phase space distribution function can be represented by the following expression

$$f(\mathbf{r}, \mathbf{c}, t) = \sum_{k=0}^{\infty} \mathbf{f}^{(k)}(\mathbf{c}, t) \odot (-\nabla)^k n(\mathbf{r}, t), \qquad (3)$$

where $\mathbf{f}^{(k)}(\mathbf{c}, t)$ are time-dependent tensors of rank k and $\odot$ denotes a k-fold scalar product. This expression is known as the density gradient expansion of the phase space distribution function [28]. If the background electric field is static, the tensors $\mathbf{f}^{(k)}(\mathbf{c}, t)$ are independent of time, after the swarm has relaxed to a stationary state. In the hydrodynamic regime, the flux of

velocity of charged particles is defined by the flux gradient relation

$$\mathbf{\Gamma}(\mathbf{r},t) = \sum_{k=0}^{\infty} \mathbf{\Gamma}^{(k+1)} \odot (-\nabla)^k n(\mathbf{r},t), \qquad (4)$$

where the superscripts (k) denote the order of the density gradient, while $(k+1)$ denote the ranks of the tensors $\mathbf{\Gamma}^{(k+1)}$. These tensors represent the flux transport coefficients [29]. By truncating the flux gradient relation at $k=2$, the following equation is obtained

$$\mathbf{\Gamma}(\mathbf{r},t) = \mathbf{W^{(f)}}n(\mathbf{r},t) - \mathbf{D^{(f)}} \odot \nabla n(\mathbf{r},t)$$
$$+ \mathbf{Q^{(f)}} \odot (\nabla \otimes \nabla) n(\mathbf{r},t), \qquad (5)$$

where $\otimes$ is the tensor product, $\mathbf{W^{(f)}}$ and $\mathbf{D^{(f)}}$ are the flux drift velocity and the flux diffusion tensor, respectively, while $\mathbf{Q^{(f)}}$ defines the flux third-order transport coefficient tensor.

For an electric field only configuration, the third-order transport coefficient tensor has seven non-zero elements of which three are independent [19]. The independent components of the third-order transport tensor are $Q_{xxz}^{(f)}$, $Q_{zxx}^{(f)}$ and $Q_{zzz}^{(f)}$. Other non-zero components are related to the independent components by the following symmetry relations [19]:

$$Q_{xzx}^{(f)} = Q_{xxz}^{(f)} = Q_{yyz}^{(f)} = Q_{yzy}^{(f)}, \qquad (6)$$

$$Q_{zyy}^{(f)} = Q_{zxx}^{(f)}. \qquad (7)$$

The longitudinal and transverse third-order transport coefficients are defined as:

$$Q_L^{(f)} = Q_{zzz}^{(f)}, \ Q_T^{(f)} = \frac{1}{3}(Q_{xxz}^{(f)} + Q_{xzx}^{(f)} + Q_{zxx}^{(f)}). \qquad (8)$$

The hydrodynamic expansion of the source term is given by [28]

$$S(\mathbf{r},t) = \sum_{k=0}^{\infty} \mathbf{S}^{(k)} \odot (-\nabla)^k n(\mathbf{r},t), \qquad (9)$$

where the superscripts (k) denote the rank of tensors $S^{(k)}$ [29]. By substituting equations (5) and (9) into (1) the generalized diffusion equation, which is truncated at third-order gradients, is obtained. This equation can be written as

$$\frac{\partial n(\mathbf{r},t)}{\partial t} + \mathbf{W}^{(b)} \odot \nabla n(\mathbf{r},t) - \mathbf{D}^{(b)} \odot (\nabla \otimes \nabla) n(\mathbf{r},t)$$
$$+ \mathbf{Q}^{(b)} \odot (\nabla \otimes \nabla \otimes \nabla) n(\mathbf{r},t) = R_{\text{prod}} n(\mathbf{r},t), \qquad (10)$$

where R_{prod} is the net particle production-rate, $\mathbf{W}^{(b)}$ and $\mathbf{D}^{(b)}$ are the bulk drift velocity and bulk diffusion tensor, respectively, and $\mathbf{Q}^{(b)}$ is the bulk third-order transport coefficient tensor. Bulk transport coefficients are related to the corresponding flux transport coefficients as [2,11,29]

$$\mathbf{W^{(b)}} = \mathbf{W^{(f)}} + \mathbf{S^{(1)}}, \qquad (11)$$

$$\mathbf{D^{(b)}} = \mathbf{D^{(f)}} + \mathbf{S^{(2)}}, \qquad (12)$$

$$\mathbf{Q^{(b)}} = \mathbf{Q^{(f)}} + \mathbf{S^{(3)}}. \qquad (13)$$

Equation (10) cannot be solved analytically, even for the set of simple boundary conditions found in an idealized time-of-flight experiment [2]. However, this equation can be solved approximately if the Fourier transform of the solution is expanded in a Taylor series in terms of components of the third-order transport coefficient tensor [20]. The approximate solution up to the first-order can be written as [20]

$$n^{(1)}(\mathbf{r},t) = n^{(0)}(\mathbf{r},t)$$
$$\times \left[1 + Q_L^{(b)} \frac{t\left(z - W^{(b)}t\right)^3 - 6D_L^{(b)}t^2\left(z - W^{(b)}t\right)}{8\left(D_L^{(b)}t\right)^3} \right.$$
$$\left. + Q_T^{(b)} \frac{3t\left(z - W^{(b)}t\right)\left(x^2 + y^2 - 4D_T^{(b)}t\right)}{8D_L^{(b)}t\left(D_T^{(b)}t\right)^2} \right], \quad (14)$$

where $n^{(0)}(\mathbf{r},t)$ is the solution of the diffusion equation, which has the form [2]

$$n^{(0)}(\mathbf{r},t) = \frac{N_0 e^{R_{\text{prod}}t} e^{-\frac{\left(z-W^{(b)}t\right)^2}{4D_L^{(b)}t} - \frac{x^2+y^2}{4D_T^{(b)}t}}}{\left(4\pi D_T^{(b)}t\right)\sqrt{4\pi D_L^{(b)}t}}, \qquad (15)$$

while N_0, $W^{(b)}$, $D_L^{(b)}$, $D_T^{(b)}$, $Q_L^{(b)}$ and $Q_T^{(b)}$ are the initial number of particles, bulk drift velocity, bulk longitudinal diffusion, bulk transverse diffusion, and bulk values of longitudinal and transverse third-order transport coefficients, respectively. Expression (14) has a simpler form in the relative coordinates that are defined as [20]

$$\chi_z = \frac{z - W^{(b)}t}{\sqrt{2D_L^{(b)}t}}, \ \chi_x = \frac{x}{\sqrt{2D_T^{(b)}t}}, \ \chi_y = \frac{y}{\sqrt{2D_T^{(b)}t}}. \quad (16)$$

In these coordinates the approximate solution (14) is given by

$$n^{(1)}(\mathbf{r},t) = n^{(0)}(\mathbf{r},t)$$
$$\times \left(1 + \frac{tQ_L^{(b)}}{\sigma_z^3}\chi_z(\chi_z^2 - 3) + \frac{3tQ_T^{(b)}}{\sigma_x^2\sigma_z}\chi_z(\chi_x^2 + \chi_y^2 - 2) \right), \quad (17)$$

where $\sigma_z = \sqrt{2D_L^{(b)}t}$ and $\sigma_x = \sigma_y = \sqrt{2D_T^{(b)}t}$. From this expression it can be seen that the contribution of the third-order transport coefficient tensor to the spatial profile of the swarm is proportional to $Q_L^{(b)}/(t^{1/2}(D_L^{(b)})^{3/2})$ and $Q_T^{(b)}/(t^{1/2}\sqrt{D_L^{(b)}D_T^{(b)}})$ [20].

2.2 Multi term solutions of Boltzmann's equation

The evolution of the phase space distribution function is given by the Boltzmann equation. In the case of a swarm of electrons, which are moving in an infinite and homogeneous background gas, the Boltzmann equation can be written as

$$\frac{\partial f}{\partial t} + \mathbf{c} \cdot \frac{\partial f}{\partial \mathbf{r}} + \frac{e}{m}(\mathbf{E} + \mathbf{c} \times \mathbf{B}) \cdot \frac{\partial f}{\partial \mathbf{c}} = -J(f, f_0), \quad (18)$$

where e and m are the charge and mass of electrons, $\mathbf{E}$ and $\mathbf{B}$ are the electric and magnetic fields, and $J(f, f_0)$ is the collision operator. The Boltzmann equation is an integro-differential equation, which cannot be solved analytically in the case of electrons in real gases [2,6]. We employ the moment method where the phase space distribution function is expanded in terms of Burnett functions [28,30,31,33]:

$$\Phi_m^{[\nu l]}(\alpha \mathbf{c}) = N_{\nu l}\left(\frac{\alpha c}{\sqrt{2}}\right)^l S_{l+1/2}^{(\nu)}\left(\frac{\alpha^2 c^2}{2}\right) Y_m^{[l]}(\hat{\mathbf{c}})$$
$$= R_{\nu l}(\alpha c) Y_m^{[l]}(\hat{\mathbf{c}}), \qquad (19)$$

where $Y_m^{[l]}$ is a spherical harmonic, while $S_{l+1/2}^{(\nu)}$ is a Sonine polynomial, α is a parameter and $\hat{\mathbf{c}}$ is a unit vector in velocity space [30,32]. The constant $N_{\nu l}$ is given by

$$N_{\nu l}^2 = \frac{2\pi^{3/2}\nu!}{\Gamma(\nu + l + 3/2)}, \qquad (20)$$

where $\Gamma(\nu + l + 3/2)$ is the gamma function, while

$$R_{\nu l}(\alpha c) = N_{\nu l}\left(\frac{\alpha c}{\sqrt{2}}\right)^l S_{l+1/2}^{(\nu)}(\alpha^2 c^2/2), \qquad (21)$$

determines the radial part of the Burnett function. The Burnett functions satisfy the orthogonality relations [30]:

$$\int \omega(\alpha, c) \Phi_m^{(\nu l)}(\alpha \mathbf{c}) \Phi_{m'}^{[\nu' l']}(\alpha \mathbf{c}) d\mathbf{c} = \delta_{\nu' \nu} \delta_{l' l} \delta_{m' m}, \qquad (22)$$

where

$$\omega(\alpha, c) = \left(\frac{\alpha^2}{2\pi}\right)^{3/2} e^{-\alpha^2 c^2/2}, \qquad (23)$$

is the weighting function [30]. Orthogonality of the Burnett functions is due to orthogonality of the spherical harmonics and Sonine polynomials. The phase space distribution function can be expanded as

$$f(\mathbf{r}, \mathbf{c}, t) = \omega(\alpha, c) \sum_{\nu=0}^{\infty} \sum_{l=0}^{\infty} \sum_{m=-l}^{l} \mathbf{f}_m^{(\nu l)}(\alpha, \mathbf{r}, t) \Phi_m^{[\nu l]}(\alpha \mathbf{c}), \qquad (24)$$

where $\mathbf{f}_m^{(\nu l)}(\alpha, \mathbf{r}, t)$ are the expansion coefficients which depend on the coordinates in the configuration space $\mathbf{r}$ and time t [30,32].

In the hydrodynamic regime the phase space distribution function can be expanded in terms of powers of the density gradient operator as [30,33–35]

$$f(\mathbf{r}, \mathbf{c}, t) = \omega(\alpha, c) \sum_{s=0}^{\infty} \sum_{\lambda=0}^{s} \sum_{\mu=-\lambda}^{\lambda} \sum_{\nu=0}^{\infty} \sum_{l=0}^{\infty} \sum_{m=-l}^{l}$$
$$F(\nu l m | s\lambda\mu; \alpha, t) R_{\nu l}(\alpha, c) Y_m^{[l]}(\hat{\mathbf{c}}) G_\mu^{(s\lambda)} n(\mathbf{r}, t), \qquad (25)$$

where $F(\nu l m | s\lambda\mu; \alpha, t)$ are the moments of the phase space distribution function, while $G_\mu^{(s\lambda)}$ is the spherical form of the density gradient operator [30].

When the Boltzmann equation is multiplied by an arbitrary moment $F(\nu l m | s\lambda\mu; \alpha, t)$ and integrated over the entire velocity space, an infinite hierarchy of matrix equations in terms of moments $F(\nu l m | s\lambda\mu; \alpha, t)$ is obtained [31,33–35]. This hierarchy is truncated at a finite number of spherical harmonics $l = l_{\max}$, and a finite number of Sonine polynomials $\nu = \nu_{\max}$. The values of these numbers are determined by the criterion for convergence. The resulting system of equations is then solved numerically by using the matrix inversion. In our calculations, values of $l_{\max} = 4$ were sometimes required, when the phase space distribution function substantially deviates from an isotropy in the velocity space. Likewise, values of $\nu_{\max} = 80$ were required when the distribution function was far away from a thermal Maxwellian at the basis temperature T_b. The basis temperature is a parameter which is used to optimize the convergence.

The explicit expressions for determining the flux transport coefficients in terms of moments of the phase space distribution function can be obtained by expanding the flux of velocity of the charged particles $\boldsymbol{\Gamma}(\mathbf{r}, t)$ in terms of these moments and by recognizing terms which are contracted with the corresponding partial derivative of the number density $n(\mathbf{r}, t)$ [33–35]. The expansion of $\boldsymbol{\Gamma}(\mathbf{r}, t)$ in terms of $F(\nu l m | s\lambda\mu; \alpha, t)$ is given by

$$\Gamma_m^{[1]}(\mathbf{r}, t) = \int c_m^{[1]} f(\mathbf{r}, \mathbf{c}, t) d\mathbf{c}$$
$$= \int c_m^{[1]} \omega(\alpha, c) \sum_{s=0}^{\infty} \sum_{\lambda=0}^{s} \sum_{\mu=-\lambda}^{\lambda} \sum_{\nu=0}^{\infty} \sum_{l=0}^{\infty} \sum_{m'=-l}^{l}$$
$$F(\nu l m' | s\lambda\mu; \alpha, t) R_{\nu l}(\alpha, c) Y_{m'}^{[l]}(\hat{\mathbf{c}}) G_\mu^{(s\lambda)} n(\mathbf{r}, t) d\mathbf{c}, \qquad (26)$$

where $\Gamma_m^{[1]}(\mathbf{r}, t)$ is the flux of velocity of charged particles $\boldsymbol{\Gamma}(\mathbf{r}, t)$ written in the spherical form [30]. Cartesian components of a vector whose spherical form is given by

$$c_m^{(1)} = \sqrt{\frac{4\pi}{3}} c Y_m^{[1]}(\hat{\mathbf{c}}), \qquad (27)$$

are given by the expressions [30]

$$c_x = \frac{i}{\sqrt{2}}\left(c_1^{[1]} - c_{-1}^{[1]}\right), \qquad (28)$$

$$c_y = \frac{1}{\sqrt{2}}\left(c_1^{[1]} + c_{-1}^{[1]}\right), \qquad (29)$$

$$c_z = -i c_0^{[1]}. \qquad (30)$$

The components of the third-order transport coefficient tensor for an electric field only configuration are given by

$$Q_{xxz}^{(f)} = \frac{1}{\sqrt{2}\alpha}\left(\text{Im}\{F(011|221)\} - \text{Im}\{F(01-1|221)\}\right), \qquad (31)$$

$$Q_{zxx}^{(f)} = -\frac{1}{\alpha}\left(\frac{1}{\sqrt{3}}\text{Im}\{F(010|200)\} + \frac{1}{\sqrt{6}}\text{Im}\{F(010|220)\}\right)$$
$$+ \frac{1}{\alpha}\text{Im}\{F(010|222)\}, \qquad (32)$$

and

$$Q_{zzz}^{(f)} = \frac{1}{\alpha}\left(\sqrt{\frac{2}{3}}\text{Im}\{F(010|220)\} - \frac{1}{\sqrt{3}}\text{Im}\{F(010|200)\}\right), \tag{33}$$

where Re{} and Im{} refer to the real and imaginary parts of the moments $F(\nu lm|s\lambda\mu;\alpha,t)$, respectively [20]. The explicit expressions for the lower order transport coefficients in terms of moments of the phase space distribution function can be found in [33–35]. For brevity, in the following sections the superscript (f) in the flux third-order transport coefficients (and in the flux diffusion coefficients) will be omitted.

3 Results and discussion

3.1 Preliminaries

In this work we calculate the third-order transport coefficients for electrons in noble gases. Calculations are performed in the E/n_0 range between 10^{-4} Td and 100 Td $(1\,\text{Td} = 10^{-21}\,\text{Vm}^2)$. The temperature of the background gas T_0 is 293 K and thermal motion of background atoms is taken into account. All background atoms are assumed to be in the ground state. All electron scattering is considered to be isotropic. Elastic collisions are represented by the elastic momentum transfer cross section, while the inelastic collisions are represented by the total inelastic cross sections. For electrons in He we use the set of cross sections which has been detailed by Šašić et al. [36] while for electrons in Ne we use the set of cross sections, initially developed by Hayashi [37]. Likewise, for electron scattering in Ar and Xe we use the cross section sets developed by Hayashi [38,39]. For electrons in Kr we use the cross section set from a publicly available Monte Carlo code MAGBOLTZ [40].

3.2 Mean energy

In the following section we often find it necessary to refer to the mean energy of the electron swarm to understand and explain certain trends of the behavior of the third-order transport coefficients. Thus, in Figure 1 we show the mean energies of electrons in He, Ar, Kr and Xe as a function of E/n_0. Comparing the profiles of mean energy in He and the remaining three gases, we observe that the mean energy of electrons in He is different not only quantitatively, but also qualitatively. Specifically, there are four distinct regions of transport as E/n_0 increases for electrons in He and five distinct regions of transport in the case of Ar, Kr and Xe. First, for electrons in all considered gases, there is an initial plateau region where the mean energy is thermal. In the second distinct region of transport for electrons in He, the mean energy rises with an approximately constant slope in the log-log plot. The slope of mean energy is significantly lower in the third region, due to the influence of inelastic collisions. Finally, the slope is again increased in the fourth region. This
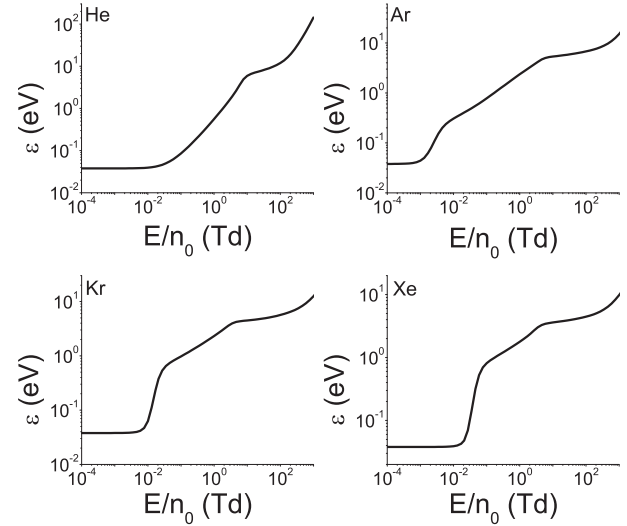

Fig. 1. Variation of the mean energy with E/n_0 for electron swarms in He, Ar, Kr and Xe.

increase can be attributed to a greater fraction of electrons being in the energy range where the collision frequency for all scattering processes reduces with increasing energy. For electrons in Ar, Kr and Xe, the rise of mean energy with increasing E/n_0 is very steep in the second distinct region of transport. A large fraction of electrons is thus in the energy range where elastic momentum transfer cross section is a monotonically decreasing function of energy, due to the presence of the Ramsauer-Townsend minimum. However, the slope of the mean energy is lower in the third region, in which high energy electrons are in the energy range where the elastic momentum transfer cross section is rising sharply. The slope of mean energy is further reduced in the fourth region where electrons can undergo inelastic collisions. Finally, this slope increases in the fifth distinct region of transport, in which the profile of mean energy changes from a power-law-like behavior to the more exponential-like increase. In this field region, the most energetic electrons are in the energy range where the collision frequency for all scattering processes is being reduced with increasing energy.

3.3 Variation of the third-order transport coefficients with E/n_0

3.3.1 Brief analysis

In Figure 2 we show the variation of the individual components of the third-order transport coefficient tensor with E/n_0 for electrons in He. We observe that $n_0^2 Q_{xxz}$ and $n_0^2 Q_{zzz}$ components are positive over the range of E/n_0 considered in the present work. However, the $n_0^2 Q_{zxx}$ component is negative until approximately 10 Td and positive at higher E/n_0. The absolute values of all individual components of the third-order transport tensor increase with increasing E/n_0 in the sub-excitation field region, which corresponds to the first two characteristic regions of the mean energy (see Fig. 1). This can be attributed
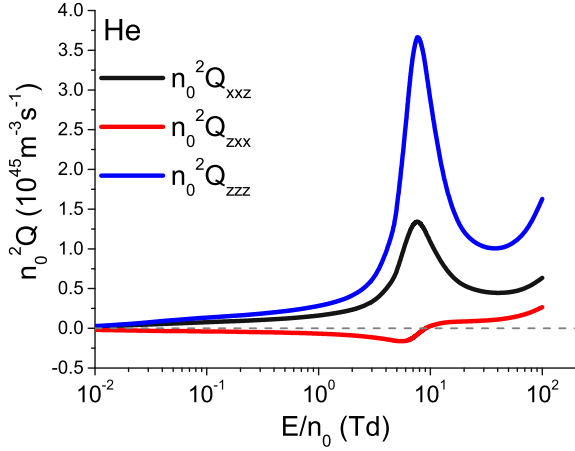
Fig. 2. Variation of $n_0^2Q_{xxz}$, $n_0^2Q_{zxx}$ and $n_0^2Q_{zzz}$ components of the third-order transport coefficient tensor with E/n_0 for electrons in He.
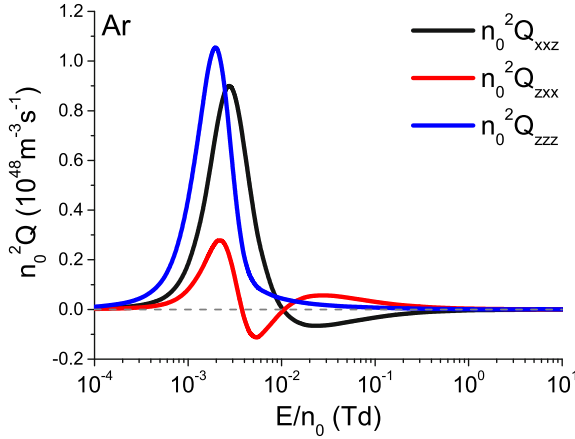

Fig. 4. Variation of $n_0^2Q_{xxz}$, $n_0^2Q_{zxx}$ and $n_0^2Q_{zzz}$ components of the third-order transport coefficient tensor with E/n_0 for electrons in Kr.

Fig. 3. Variation of $n_0^2Q_{xxz}$, $n_0^2Q_{zxx}$ and $n_0^2Q_{zzz}$ components of the third-order transport coefficient tensor with E/n_0 for electrons in Ar.

Fig. 5. Variation of $n_0^2Q_{xxz}$, $n_0^2Q_{zxx}$ and $n_0^2Q_{zzz}$ components of the third-order transport coefficient tensor with E/n_0 for electrons in Xe.

to a slow rise of elastic momentum transfer cross section in the energy range up to about 2 eV, as well as to its reduction at higher energies. However, the absolute values of all individual components of the third-order transport tensor are reduced for the higher values of E/n_0, where the high energy electrons can undergo many inelastic collisions. This field region roughly corresponds to the third characteristic region of the mean energy. Finally, all three components are increasing functions of E/n_0 in the limit of the highest fields considered in this work, where the collision frequency of the high energy electrons decreases with increasing electron energy.

In Figures 3–5 we show the variation of the individual components of the third-order transport coefficient tensor with E/n_0 for electrons in Ar, Kr and Xe, respectively. It can be seen that in these gases all components of the third-order transport tensor are rapidly rising functions of E/n_0 in the limit of the lowest fields, where most of the electrons are in the energy range in which the elastic momentum transfer cross section is reduced with the increase of
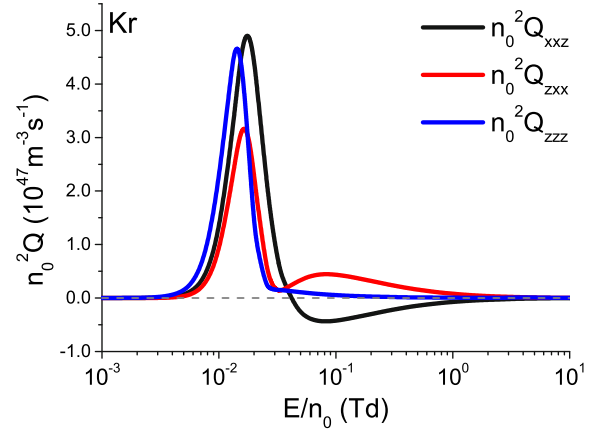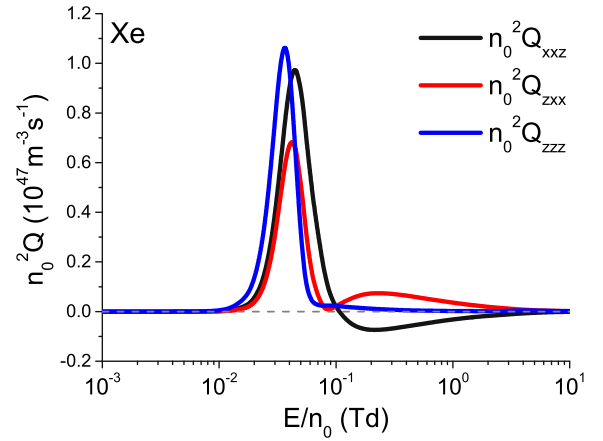
energy, due to the presence of the Ramsauer-Townsend minimum. This field region corresponds to the first characteristic region of the mean energy, as well as to the first half of the second characteristic region of the mean energy, shown in Figure 1. However, all three components of the third-order transport tensor are rapidly decreasing functions of E/n_0 at higher fields, where the most energetic electrons are in the energy range in which the elastic momentum transfer cross section has a steep rise with an increase of energy. This field region corresponds to the second half of the second characteristic region of the mean energy. In the remaining field region considered in this work, $n_0^2Q_{zxx}$ and $n_0^2Q_{zzz}$ components exhibit a local minimum and a local maximum, while the $n_0^2Q_{xxz}$ component has a single local minimum only. The positions of these local maximums and local minimums correspond to those values of E/n_0 where the ratio between the mean energy and the position of the Ramsauer-Townsend minimum or the threshold of the first electronic excitation have similar values. For instance, the $n_0^2Q_{xxz}$ component becomes negative at the reduced electric field where the

mean energy is higher than the position of the Ramsauer-Townsend minimum by a factor that has values in the range between 1.3 and 1.4 for all three gases. Likewise, this component reaches the local minimum at approximately the same field where the $n_0^2 Q_{zxx}$ component reaches the second local maximum, and the mean energy is about 1.75 times higher than the energy of the Ramsauer-Townsend minimum at the position of these local extremes in all three gases. Moreover, the $n_0^2 Q_{zzz}$ component reaches the second local maximum at the value of the reduced electric field where the mean energy of electrons is about 2.5 times lower than the threshold of the first electronic excitation for all three gases (see Fig. 8). At the highest fields, where the most energetic electrons may undergo many inelastic collisions with the background atoms, the absolute values of all components of the third-order transport tensor are reduced with increasing E/n_0. This field region roughly corresponds to the fourth and the fifth characteristic regions of the mean energy in Ar, Kr and Xe. In the following subsubsection the E/n_0-profiles of the individual components of the third-order transport coefficient tensor for electrons in He, Ar, Kr and Xe are analyzed in a greater detail.

3.3.2 Comprehensive analysis

For electrons in He, the absolute values of all three components of the third-order transport tensor are monotonically increasing functions of E/n_0, but only in the limit of low electric fields. Specifically, $n_0^2 Q_{xxz}$ and $n_0^2 Q_{zzz}$ components rise in the field region below around 8 Td, where the mean energy of electrons is lower than 5 eV. Likewise, the absolute value of $n_0^2 Q_{zxx}$ increases up to approximately 5.9 Td, where the mean energy is around 3.6 eV. In the field region, where the absolute values of all three components are being increased with increasing E/n_0 most of the electrons undergo elastic collisions only. Moreover, the elastic momentum transfer cross section is gradually rising in the energy range between approximately 10^{-2} eV and 2 eV, while it is being reduced at higher energies. For this reason, resistance to diffusive motion that is caused by collisions of electrons with the background atoms is not very intensive in the field region up to approximately 5.9 Td. This in turn induces an increase of the absolute values of all three components of the third-order transport coefficient tensor in this range of E/n_0. However, at higher fields the most energetic electrons can undergo inelastic collisions with the background atoms, as the threshold for the first electronic excitation in helium is around 19.82 eV. This leads to a rapid decrease of $n_0^2 Q_{xxz}$ and $n_0^2 Q_{zzz}$ components in the field range between approximately 8 Td and 40 Td. Likewise, the increased resistance to the spreading of the swarm due to inelastic collisions leads to a rapid decrease of the absolute value of the $n_0^2 Q_{zxx}$ component in the field range between approximately 5.9 Td and 8 Td, and to a gradual increase of this component up to around 40 Td. For the higher values of E/n_0, all three components of the third-order transport coefficient tensor rise with increasing E/n_0. Over this range of E/n_0, the collision frequency of the most energetic electrons decreases

with increasing E/n_0 which in turn enhances the third-order transport coefficients.

For electrons in Ar, Kr and Xe, all components of the third-order transport tensor are initially, rapidly increased with increasing E/n_0 for the lower values of E/n_0, as a large fraction of electrons is in the energy range where the elastic momentum transfer cross section markedly decreases with increasing energy, due to the presence of the Ramsauer-Townsend minimum in the cross sections for elastic scattering. These components reach local maximums in the E/n_0 region where the mean energy is lower than the position of the Ramsauer-Townsend minimum by a factor which is approximately between 2 and 3 in case of Ar, and approximately between 2 and 4 in case of Kr and Xe. Thus, all components of the third-order transport tensor start to decrease with an increase of E/n_0 in the E/n_0 region where the collision frequencies of the most energetic electrons increase with the rising energy of electrons.

The $n_0^2 Q_{zxx}$ component is the first to reach a local minimum in all three gases. However, the behavior of this component is somewhat different in the case of Ar, as compared to Kr and Xe. Specifically, this component becomes negative for electrons in Ar, while it remains positive over the entire considered range of E/n_0 for electrons in Kr and Xe. For electrons in Ar, the $n_0^2 Q_{zxx}$ component becomes negative at the value of E/n_0 where the mean energy is around 1.4 times lower than the position of the Ramsauer-Townsend minimum. The same component reaches a local minimum at the value of E/n_0 where the mean energy of the swarm is approximately equal to the energy position of the Ramsauer-Townsend minimum. However, in case of Kr and Xe this component reaches a local minimum at the value E/n_0 where the mean energy is around 1.25 times higher than the energy position of the Ramsauer-Townsend minimum. The $n_0^2 Q_{zxx}$ component becomes positive in Ar at approximately the same field, where the $n_0^2 Q_{xxz}$ component becomes negative. The $n_0^2 Q_{xxz}$ component starts to be negative at the value of E/n_0 where the mean energy is higher than the position of the Ramsauer-Townsend minimum by a factor of around 1.3 in case of Ar and Xe, and by a factor of approximately 1.4 in case of Kr. The sign of the $n_0^2 Q_{xxz}$ component remains unaltered until the end of the considered E/n_0 range for Ar, Kr and Xe. The $n_0^2 Q_{zxx}$ component reaches the second local maximum at approximately the same E/n_0 where the $n_0^2 Q_{xxz}$ component reaches the local minimum. The position of these local extremes for $n_0^2 Q_{xxz}$ and $n_0^2 Q_{zxx}$ components is at the value of E/n_0 where the mean energy is about 1.75 times higher than the position of the Ramsauer-Townsend minimum for electrons in all three gases. For the higher values of E/n_0, the absolute values of $n_0^2 Q_{xxz}$ and $n_0^2 Q_{zxx}$ are being reduced with increasing E/n_0 until the end of the considered field range.

The $n_0^2 Q_{zzz}$ component reaches a local minimum at the value of E/n_0 where the electrons with energies that are between approximately 2 and 3 times higher than mean energy, are in the energy range where the elastic momentum transfer cross section for electrons in Ar, Kr and Xe, is reduced (see Fig. 8) with increasing energy. For the higher E/n_0 values, the $n_0^2 Q_{zzz}$ component rises with

increasing E/n_0. This component reaches a local maximum at the value of E/n_0 where the electrons with energies that are about 2.5 times higher than the mean energy can undergo inelastic collisions with the background atoms. The absolute values of all three components of the third-order transport coefficient tensor are reduced with increasing E/n_0 at higher fields until reaching the end of the considered E/n_0 range.

At the qualitative level, the E/n_0-profiles of each component of the third-order transport coefficient tensor are very similar for electrons in Ar, Kr and Xe. Specifically, these components reach local maximums and local minimums at the values of E/n_0 at which the ratios between the mean energy and the position of the Ramsauer-Townsend minimum and/or the threshold for the first electronic excitation have very similar values. However, there is a significant difference in the profile of $n_0^2 Q_{zxx}$ component for electrons in Ar, when compared to the corresponding profiles in Kr and Xe, as this component becomes negative in Ar. The absence of negative values of $n_0^2 Q_{zxx}$ for electrons in Kr and Xe might be attributed to a steeper rise of the elastic momentum transfer cross section with an increasing energy, after the Ramsauer-Townsend minimum, in these two gases. As discussed recently by Simonović et al. [20] when the collision frequency is rising with increasing electron energy, one of the off-diagonal components of the third-order transport tensor ($n_0^2 Q_{zxx}$ and $n_0^2 Q_{xxz}$) is often negative. If the rise of the collision frequency with energy is not too steep, $n_0^2 Q_{zxx}$ component is usually negative (and $n_0^2 Q_{xxz}$ is positive). However, $n_0^2 Q_{xxz}$ component is negative (and $n_0^2 Q_{zxx}$ is positive) when the rise of the collision frequency with increasing electron energy is very steep.

3.4 Correlation between the longitudinal components of the skewness and diffusion tensors

Another issue that is highly relevant for understanding higher-order transport coefficients is the correlation between higher-order and lower-order transport coefficients. In this work we investigate the correlation between the longitudinal component of the third-order transport tensor and the longitudinal component of the diffusion tensor of electrons in noble gases. Recently, this correlation has been investigated for electrons in CH_4 [26]. It has been shown that whenever D_{zz} decreases, then Q_{zzz} is reduced markedly, and whenever D_{zz} increases in a decelerating way, Q_{zzz} also decreases, but less intensively. The Q_{zzz} was found to increase only when D_{zz} increases in an accelerating manner. It can be expected that this correlation is absent at the lowest E/n_0, as $n_0^2 Q_{zzz}$ represents an asymmetric correction to diffusive motion and it vanishes in the limit of the lowest fields, unlike diffusion coefficients which have non-zero thermal values. For this reason $n_0^2 Q_{zzz}$ is expected to rise with increasing E/n_0 at the lowest fields, regardless of the field dependence of $n_0 D_{zz}$. The value of E/n_0 at which the correlation between the profiles of field dependence of $n_0^2 Q_{zzz}$ and $n_0 D_{zz}$ occurs is different for various gases.
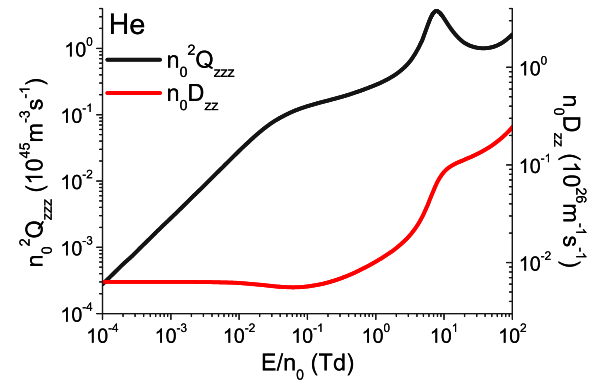

Fig. 6. The correlation of the longitudinal component of the third-order transport tensor $n_0^2 Q_{zzz}$ and the longitudinal component of the diffusion tenzor $n_0 D_{zz}$ for electrons in He.

The correlation between the profiles of $n_0^2 Q_{zzz}$ and $n_0 D_{zz}$ for electrons in He and Ne is shown in Figures 6 and 7, respectively. For electrons in He, $n_0^2 Q_{zzz}$ and $n_0 D_{zz}$ rise with increasing E/n_0 in the E/n_0 region between approximately $5.9 \cdot 10^{-2}$ Td and 7.5 Td. This increase is the most intensive for E/n_0 between around 2.1 Td and 7.7 Td. However, between approximately 7.7 Td and 35 Td, the rise of $n_0 D_{zz}$ with increasing E/n_0 slows down, and $n_0 D_{zz}$ becomes a concave function of E/n_0 in the log-log plot. In this E/n_0 region, $n_0^2 Q_{zzz}$ is reduced with increasing E/n_0. For E/n_0 between approximately 35 Td and 100 Td, the slope of $n_0 D_{zz}$ rises with E/n_0 and $n_0 D_{zz}$ becomes a convex function of E/n_0 in the log-log plot. As a consequence, in this E/n_0 region, $n_0^2 Q_{zzz}$ rises monotonically with increasing E/n_0.

For electrons in Ne, $n_0^2 Q_{zzz}$ and $n_0 D_{zz}$ decrease with increasing E/n_0 between approximately $3.5 \cdot 10^{-3}$ Td and $3.5 \cdot 10^{-2}$, and $n_0^2 Q_{zzz}$ continues to decrease up to about $5.9 \cdot 10^{-2}$ Td. For the reduced electric fields higher than approximately $5.9 \cdot 10^{-2}$ Td, both $n_0^2 Q_{zzz}$ and $n_0 D_{zz}$ rise with increasing field up to around 1.9 Td. This rise is especially rapid for E/n_0 between approximately 1 Td and 1.9 Td. At higher fields, $n_0 D_{zz}$ becomes a concave function of E/n_0 in the log-log plot, and it slowly decreases with increasing field for E/n_0 between approximately 5.9 Td and 30 Td, while it saturates at higher fields. In the E/n_0 region between approximately 1.9 Td and 100 Td, $n_0^2 Q_{zzz}$ decreases monotonically with increasing E/n_0.

The correlation between the profiles of $n_0^2 Q_{zzz}$ and $n_0 D_{zz}$ for electrons in Ar, Kr and Xe is shown in Figure 8. As can be seen, there is a very strong correlation between the profiles of $n_0^2 Q_{zzz}$ and $n_0 D_{zz}$ for all three gases. It can also be seen that the profiles of $n_0^2 Q_{zzz}$ and $n_0 D_{zz}$ in each of these gases are very similar. At the lowest E/n_0 $n_0^2 Q_{zzz}$ and $n_0 D_{zz}$ rise with increasing E/n_0 in all three cases, as most of the electrons are in the energy range in which the elastic momentum transfer cross section decreases rapidly with increasing electron energy. The $n_0^2 Q_{zzz}$ component reaches a local maximum at around $2.1 \cdot 10^{-3}$ Td, $1.4 \cdot 10^{-2}$ Td and $3.7 \cdot 10^{-2}$ Td for electrons in Ar, Kr, and Xe, respectively, while $n_0 D_{zz}$ reaches a local maximum at approximately $2.7 \cdot 10^{-3}$ Td, $1.7 \cdot 10^{-2}$ Td and $4.6 \cdot 10^{-2}$ Td,
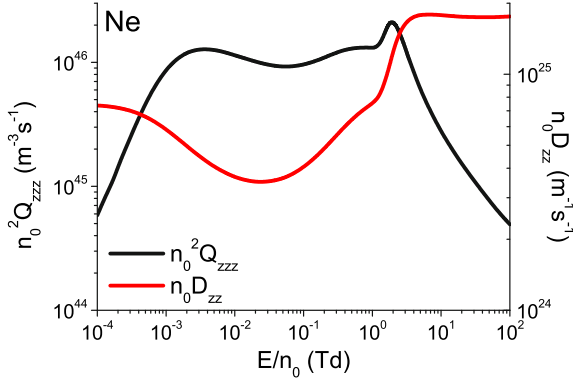
Fig. 7. The correlation of the longitudinal component of the third-order transport tensor $n_0^2 Q_{zzz}$ and the longitudinal component of the diffusion tenzor $n_0 D_{zz}$ for electrons in Ne.

for electrons in Ar, Kr and Xe, respectively. In all three gases $n_0 D_{zz}$ reaches a local maximum at a somewhat higher E/n_0 as compared to $n_0^2 Q_{zzz}$. After the local maximum, $n_0^2 Q_{zzz}$ and $n_0 D_{zz}$ are decreased markedly with increasing E/n_0, up to around $5.9 \cdot 10^{-3}$ Td, $2.9 \cdot 10^{-2}$ Td and $7.7 \cdot 10^{-2}$ Td for electrons in Ar, Kr and Xe, respectively. For the higher values of E/n_0, these two quantities continue to decrease until reaching approximately 2.7 Td for electrons in Ar, and until reaching approximately 2.1 Td for electrons in Kr and Xe. However, the rate of decreasing of both $n_0^2 Q_{zzz}$ and $n_0 D_{zz}$ is less intensive in this field region as compared to the lower fields. At higher fields, $n_0^2 Q_{zzz}$ and $n_0 D_{zz}$ rise with increasing E/n_0 in a narrow field range. The $n_0^2 Q_{zzz}$ component reaches the second local maximum at around 5.9 Td, 4.1 Td and 4.2 Td for electrons in Ar, Kr and Xe, respectively. After the second local maximum, the $n_0^2 Q_{zzz}$ component decreases monotonically with increasing E/n_0 for the remaining E/n_0 in all three gases. In the field region around the second local maximum of $n_0^2 Q_{zzz}$, the slope of $n_0 D_{zz}$ is significantly reduced with increasing E/n_0 up to about 13 Td for all three gases. At higher fields, $n_0 D_{zz}$ is saturated with increasing E/n_0.

In Figures 6–8 we observe a strong correlation between the profiles of $n_0^2 Q_{zzz}$ and $n_0 D_{zz}$ for electrons in noble gases. Specifically, at relatively high enough fields $n_0^2 Q_{zzz}$ decreases with increasing E/n_0 whenever $n_0 D_{zz}$ is a decreasing function of E/n_0, or when it increases as a concave function of E/n_0 in the log-log plot. The $n_0^2 Q_{zzz}$ increases only at the lowest fields, and in those regions of E/n_0 where $n_0 D_{zz}$ raises with increasing field as a convex (or possibly linear) function in the log-log plot. The correlation between $n_0^2 Q_{zzz}$ and $n_0 D_{zz}$ can be understood on an intuitive level. The third-order transport tensor represents an asymmetric deviation of the total diffusive motion, from the motion which is represented by the diffusion tensor. Thus, the third-order transport tensor describes a small correction to total diffusion. For this reason, the motion which is represented by the third-order transport tensor 'carries' a much smaller amount of energy and momentum than the motion which is described by the diffusion tensor. As a consequence, this transport
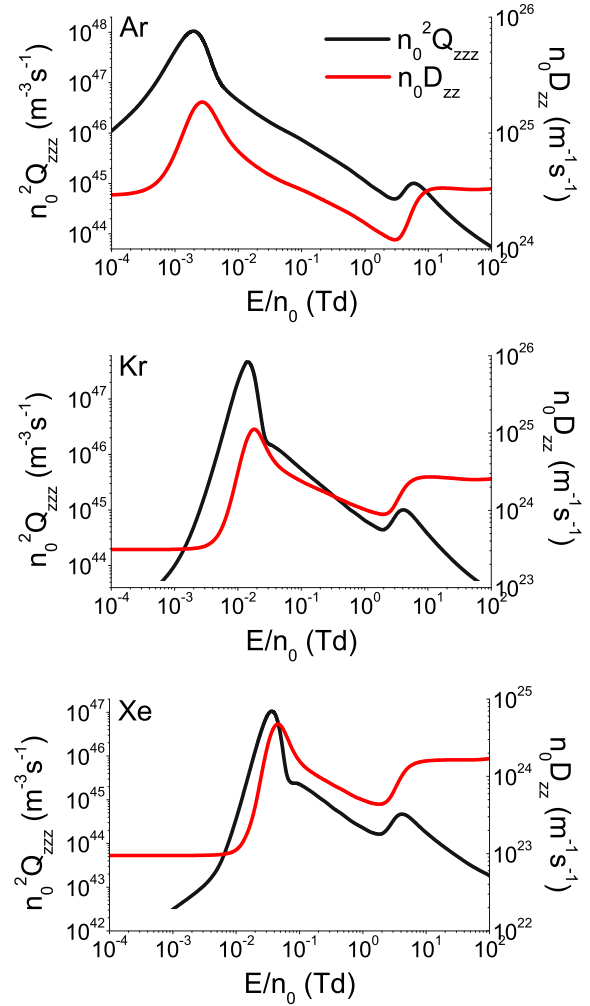

Fig. 8. The correlation of the longitudinal component of the third-order transport tensor $n_0^2 Q_{zzz}$ and the longitudinal component of the diffusion tenzor $n_0 D_{zz}$ for electrons in Ar, Kr and Xe.

property is much more sensitive with respect to the collisions between the electrons and the background atoms. This leads to a reduction of the $n_0^2 Q_{zzz}$ component with increasing E/n_0 (at high enough fields) whenever the resistance to diffusive motion due to collisions is intensive enough to cause a decrease of $n_0 D_{zz}$ or even a decelerated rise with increasing E/n_0. The correlation of the longitudinal component of the third-order transport tensor and the longitudinal component of the diffusion tensor is important for two reasons. Firstly, it enables an easier understanding of the E/n_0-dependence of the third-order transport coefficients in comparison to the direct analysis from the cross sections and from the variation of the mean energy with E/n_0, which might be sometimes difficult. Secondly, the correlation between $n_0^2 Q_{zzz}$ and $n_0 D_{zz}$ shows that the third-order transport coefficients are more sensitive with respect to the energy dependence of the cross sections than the diffusion coefficients. This suggests that the third-order transport coefficients would be very useful in swarm procedure for determining and
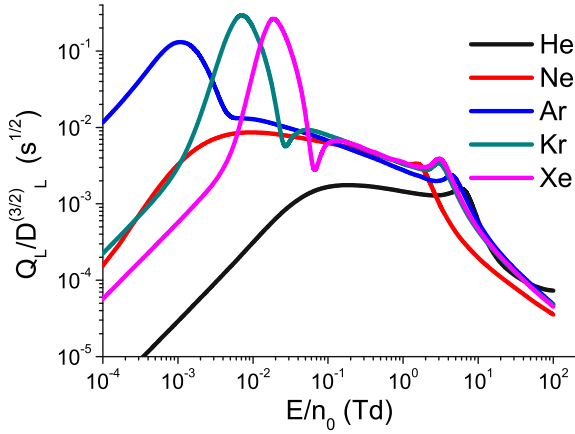
Fig. 9. The values of ratio $Q_L/(D_L)^{3/2}$ for electron swarms in He, Ne, Ar, Kr and Xe as functions of the reduced electric field E/n_0. Calculations have been performed assuming the gas number density of $3.54{\times}10^{22}$ m^{-3}.

normalizing the cross section sets, if they were both calculated and measured with a sufficient accuracy.

3.5 Effects of the third-order transport coefficients on the spatial profile of the swarm

In this work, we also investigate the influence of the third-order transport coefficients on the spatial profiles of the swarm of electrons in noble gases. As was shown in [27], the components of the third-order transport tensor represent an asymmetric deviation of the spatial profile of the swarm of charged particles from an ideal Gaussian, which represents the solution of the diffusion equation. Specifically, the longitudinal component of the third-order transport tensor describes longitudinal elongation or compressing of the swarm along the longitudinal direction, while the off-diagonal components describe transverse elongation or compressing of the swarm along the longitudinal direction. It can be seen from equation (17) that the contribution of the third-order transport coefficients to the spatial profile of the swarm is proportional to $Q_L/(t^{1/2}(D_L)^{3/2})$ and $Q_T/(t^{1/2}\sqrt{D_L}D_T)$.

In Figure 9 we show the ratio $Q_L/(D_L)^{3/2}$ for electrons in noble gases as a function of E/n_0. It should be emphasized that in Figure 9 we show the ratio where the flux values of Q_L and D_L are assumed, although the influence of the third-order transport coefficients on the spatial profile of the swarm is proportional to the corresponding ratio of the bulk values of Q_L and D_L. The reason for this is a much better accuracy of our multi term results when compared to our Monte Carlo results, and our current inability to obtain the bulk values from our multi term code. However, the difference between the flux and the bulk values of the longitudinal components of the third-order transport coefficient tensor is within statistical uncertainty of Monte Carlo simulations up to about 21 Td in He and Ne, and up to 100 Td in Ar, Kr and Xe. Moreover, we are principally interested in the field dependence of this ratio for E/n_0 less than 10 Td, due to the presence of local maximums

and local minimums in this particular field range. For this reason, we investigate the field dependence of the ratio $Q_L/(D_L)^{3/2}$ assuming the flux values of Q_L and D_L.

We may observe in Figure 9 that the ratio $Q_L/(D_L)^{3/2}$ increases monotonically with increasing E/n_0 in the limit of the lowest E/n_0 (below 10^{-3} Td). For the higher values of E/n_0 (higher than 10 Td) we see that this property decreases monotonically with increasing E/n_0 for electrons in all considered gases. At intermediate fields, however, this ratio reaches several local maximums and local minimums. Specifically, this ratio has only a single local maximum for electrons in Ne, at around 0.01 Td[1]. For electrons in He and Ar, this ratio has two local maximums and one local minimum. In the case of He these local maximums are at about 0.21 Td and 5.9 Td, and both of these maximums are of a similar magnitude. However, in the case of Ar, the first local maximum at around 10^{-3} Td is much higher than the other local maximum at about 4.6 Td. This difference is caused by the presence of the Ramsauer-Townsend minimum in the elastic cross section of Ar. The local minimum is shallow, and it is at around 2.7 Td in both gases. For electrons in Kr and Xe, the investigated ratio has three local maximums and two local minimums. The first local maximum occurs at about $7{\cdot}10^{-3}$ Td and $1.9{\cdot}10^{-2}$ Td for electrons in Kr and Xe, respectively, and is quite high in both gases, due to the presence of Ramsauer-Townsend minimum in the cross sections for elastic scattering. This maximum is followed by a local minimum at about $2.7{\cdot}10^{-2}$ Td for electrons in Kr and at around $6.8{\cdot}10^{-2}$ Td for electrons in Xe. The second local maximum of this ratio is at around 0.046 Td and 0.13 Td for electrons in Kr and Xe, respectively. The last local minimum is at about 2.1 Td, and it is quite shallow in both Kr and Xe. The third local maximum is at about 2.7 Td in both gases. In the case of electrons in Ar, Kr and Xe the value of E/n_0 at which $Q_L/(D_L)^{3/2}$ reaches the first local maximum is about 2 times lower than the value of E/n_0 where Q_L reaches the first local maximum. This is expected, on a qualitative level, as $Q_L/(D_L)^{3/2}$ reaches the first local maximum after D_L starts rising with increasing E/n_0, but before reaching the first peak.

The ratio $Q_L/(D_L)^{3/2}$ has the highest values for Ar, Kr and Xe near the position of the first local maximum. Thus, the contribution of the third-order transport coefficients to the spatial profile of the swarm is the most pronounced exactly for these conditions. However, it must be emphasized that the approximate expression (17) has been derived under an assumption that transport coefficients are constant in time, from the initial time ($t = 0$). As this condition is satisfied only after relaxation of the swarm to the stationary state, the expression (17) is not applicable to the early stages of swam development

---

[1] There is an additional local maximum of this ratio at around 1.5 Td for electrons in neon, that is preceded by a local minimum at around 1.2 Td. However, both of these local extremes are very shallow. Specifically, the difference between the value of this ratio at these two local extremes is about 4 %. For this reason, the authors are not certain if these two local extremes would appear if a different cross section set is used, due to the sensitivity of both Q_L and D_L to the energy dependence of the cross sections for elementary scattering processes.
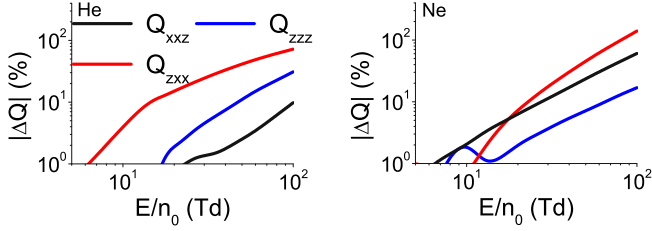
Fig. 10. The absolute value of the percentage difference between the two term and fully converged, multi term results, for the third-order transport coefficients of electrons in He and Ne.

(small values of t). In addition, this expression has been derived by using the Taylor expansion in terms of the components of the third-order transport tensor. For this reason, the expression (17) is applicable only when the ratios $Q_L/(t^{1/2}(D_L)^{3/2})$ and $Q_T/(t^{1/2}\sqrt{D_L}D_T)$ are not too large.

3.6 Comparison of the two term and fully converged multi term results

In Figure 10 we show the absolute value of the percentage difference between the two term and fully converged, multi term results, for the third-order transport coefficients of electrons in He and Ne. The absolute value of the percentage difference between the two sets of results for electrons in Ar, Kr and Xe is shown in Figure 11. The absolute value of the percentage difference ΔQ_{abc} is calculated as

$$|\Delta Q_{abc}| = \left|1 - \frac{Q_{abc}^{(TT)}}{Q_{abc}^{(MT)}}\right| \qquad (34)$$

where the superscripts TT and MT refer to two term and multi term results, respectively.

We see that the two sets of results agree very well in the limit of the lowest E/n_0, where electrons undergo elastic collisions only. Specifically, the deviation between the results that are determined by these two methods is very low, up to approximately 8 Td, 17 Td, 0.2 Td, 0.35 Td, and 1.3 Td for electrons in He, Ne, Ar, Kr and Xe, respectively. The disagreement between these two methods for the off-diagonal components increases continuously with increasing E/n_0 until the end of the range of the considered E/n_0. Moreover, the deviation of multi term results for n^2Q_{xxz} and n^2Q_{zxx} from the corresponding two term results is much higher for electrons in Ar, Kr and Xe, as compared to the case of He and Ne. However, the behavior of the percentage difference between these two sets of results is somewhat different for the longitudinal component. While the disagreement between these two methods for the longitudinal component in He and Ne increases with increasing E/n_0, these methods, surprisingly, remain in a very good agreement for electrons in Ar, Kr and Xe, over the entire range of E/n_0 considered in this work. The percentage difference for the longitudinal component reaches values up to 30% and 17% for electrons in He
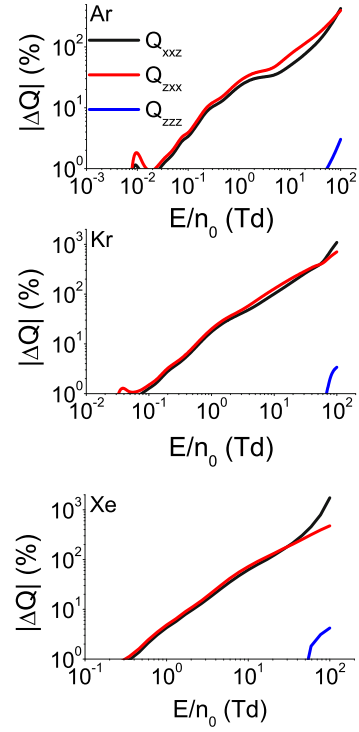

Fig. 11. The absolute value of the percentage difference between the two term and fully converged, multi term results, for the third-order transport coefficients of electrons in Ar, Kr and Xe.

and Ne, respectively, while it remains lower than 5% for electrons in Ar, Kr and Xe. We expect that the deviations between the two term and multi term results are much greater for the higher values of E/n_0. It should also be noted that the errors of the two term approximation are significantly lower for the lower-order transport coefficients, over the same region of E/n_0. Therefore, higher order transport coefficients appear more sensitive to anisotropy in the velocity distribution function.

4 Conclusion

In this work we have extended a multi term solution of the Boltzmann equation, initially developed for evaluating the lower-order transport coefficients, to investigate the third-order transport coefficients of electrons in noble gases. For electrons in helium, we have observed that the Q_{zxx} component is negative for the lower values of E/n_0. In this field region, the collision frequency for elastic scattering of a large fraction of electrons is an increasing function of the electron energy. However, for electrons in argon, krypton, and xenon all three components of the third-order transport tensor are positive in the limit of the lower fields considered in this work, as the collision frequency of the low-energy electrons decreases with increasing energy. For higher fields, the Q_{xxz} component is negative in argon, krypton and xenon over a wide range of E/n_0. In addition, for electrons in argon, the Q_{zxx} component is also negative, but over a narrower field range. For

electrons in helium in the sub-excitation field region, the absolute values of all three components of the third-order transport tensor are increasing functions of E/n_0. On the other hand, for electrons in argon, krypton and xenon, all components are significantly reduced over the range of E/n_0 where the energy of high-energy electrons exceeds the position of the Ramsauer-Townsend minimum.

One of the fundamental topics considered in this work is the existence of the correlation between the longitudinal component of the third-order transport tensor $n_0^2 Q_{zzz}$ and the longitudinal component of the diffusion tensor $n_0 D_{zz}$. We have observed that at high enough fields whenever $n_0 D_{zz}$ decreases or increases as a concave function of E/n_0 (in the log-log plot) $n_0^2 Q_{zzz}$ is being reduced. We have also observed that $n_0^2 Q_{zzz}$ increases when $n_0 D_{zz}$ increases as a convex function of E/n_0 (in the log-log plot). However, this correlation is absent in the limit of the lowest E/n_0, as the third-order transport coefficients vanish in the low-field limit, unlike diffusion which has non-zero thermal values. This behavior of $n_0^2 Q_{zzz}$ can be attributed to a greater sensitivity of the third-order transport coefficients with respect to the energy dependence of cross sections for elementary scattering processes.

Another highly relevant topic that has been investigated in this work is the influence of the third-order transport coefficients on the spatial profiles of the swarm in noble gases. It has been shown that this influence is the most pronounced for electrons in Ar, Kr and Xe, at low E/n_0, due to the presence of the Ramsauer-Townsend minimum. Specifically, the ratio $Q_L/(D_L)^{3/2}$ that describes the contribution of the longitudinal component of the third-order transport tensor to the spatial profile of the swarm reaches the first local maximum at about 10^{-3} Td, $7 \cdot 10^{-3}$ Td, and $1.9 \cdot 10^{-2}$ Td for electrons in Ar, Kr and Xe, respectively. Around these values of E/n_0 the effects of the longitudinal component of the third-order transport coefficient tensor on the spatial profile of the electron swarm are the most significant.

Finally, we investigated the deviation of the two term approximation from the fully converged multi term results for the third-order transport coefficients. We have found that the two term approximation is applicable at the lowest fields, where electrons undergo elastic collisions only. However, the two term approximation deviates from the multi term results for higher fields, where electrons may undergo inelastic collisions also with the background atoms. The difference between the two sets of results is especially pronounced for the off-diagonal components of the third-order transport tensor. This difference is much higher for electrons in Ar, Kr and Xe than for electrons in He and Ne. Conversely, the difference between the two sets of results for the longitudinal component is much larger in He and Ne than in Ar, Kr and Xe. This difference is up to about 30% and 17% for electrons in He and Ne, respectively. Surprisingly, the two term approximation is in an excellent agreement with the multi term results for the longitudinal component in the case of Ar, Kr and Xe. The difference between the results that are obtained by using these two methods is not higher than approximatelly 5% in the case of the longitudinal component of the third-order transport tensor for electrons in Ar, Kr and Xe.

Author contribution statement

All the authors have been involved in the research and in the preparation of the manuscript. All the authors have read and approved the final manuscript.

Publisher's Note The EPJ Publishers remain neutral with regard to jurisdictional claims in published maps and institutional affiliations.

References

1. L.G.H. Huxley, R.W. Crompton, *The Diffusion and Drift of Electrons in Gases* (Wiley, London, 1974)
2. R. Robson, R. White, M. Hildebrandt, *Fundamentals of Charged Particle Transport in Gases and Condensed Matter* (CRC Press, Boca Raton, 2018)
3. Z.Lj. Petrović, M. Šuvakov, Ž. Nikitović, S. Dujko, O. Šašić, J. Jovanović, G. Malović, V. Stojanović, Plasma Sources Sci. Technol. **16**, S1 (2007)
4. S. Dujko, R.D. White, Z.Lj. Petrović, J. Phys. D: Appl. Phys. **41**, 245205 (2008)
5. Z. Donko, P. Hartman, I. Korolov, V. Jeges, D. Bošnjaković, S. Dujko, Plasma Sources Sci. Technol. **28**, 095007 (2019)
6. T. Makabe, Z.Lj. Petrović, *Plasma Electronics: Applications in Microelectronic Device Fabrication* (CRC Press, 2014)
7. M.A. Lieberman, A.J. Lichtenberg, *Principles of Plasma Discharges and Materials Processing*, 2nd edn. (Wiley, 2005)
8. D. Xiao, *Gas Discharge and Gas Insulation* (Springer, Heidelberg, 2016)
9. L. Rolandi, W. Riegler, W. Blum, *Particle Detection with Drift Chambers* (Springer, Berlin, 2008)
10. D. Bošnjaković, Z.Lj. Petrović, R.D. White, S. Dujko, J. Phys. D: Appl. Phys. **47**, 435203 (2014)
11. Z.Lj. Petrović, S. Dujko, D. Marić, G. Malović, Ž. Nikitović, O. Šašić, J. Jovanović, V. Stojanović, M. Radmilović Rađenović, J. Phys. D: Appl. Phys. **42**, 194002 (2009)
12. L.C. Pitchford et al., Plasma Process. Polym. **14**, 1600098 (2016)
13. A. Banković, S. Dujko, S. Marjanović, R.D. White, Z.Lj. Petrović, Eur. Phys. J. D **68**, 127 (2014)
14. A. Banković, S. Dujko, R.D. White, S.J. Buckman, Z.Lj. Petrović, Eur. Phys. J. D **66**, 174 (2012)
15. K. Kondo, H. Tagashira, J. Phys. D: Appl. Phys. **23**, 1175 (1990)
16. S. Kawaguchi, K. Takahashi, K. Satoh, Plasma Sources Sci. Technol. **27**, 085006 (2018)
17. B.M. Penetrante, J.N. Bardsley, in *Non-equilibrium Effects in Ion and Electron Transport*, edited by J.W. Gallagher, D.F. Hudson, E.E. Kunhardt, R.J. Van Brunt (Plenum, New York, 1990), p. 49

18. S.B. Vrhovac, Z.Lj. Petrović, L.A. Viehland, T.S. Santhanam, J. Chem. Phys. **110**, 2423 (1999)
19. J.H. Whealton, E.A. Mason, Ann. Phys. **84**, 8 (1974)
20. I. Simonović, D. Bošnjaković, Z.Lj. Petrović, P. Stokes, R.D. White, S. Dujko, Phys. Rev. E **101**, 023203 (2020)
21. A.D. Koutselos, J. Chem. Phys. **104**, 8442 (1996)
22. A.D. Koutselos, J. Chem. Phys. **106**, 7117 (1997)
23. A.D. Koutselos, Chem. Phys. **270**, 165 (2001)
24. A.D. Koutselos, Chem. Phys. **315**, 193 (2005)
25. H. Sugawara, Y. Sakai, Jpn. J. Appl. Phys. **45**, 5189 (2006)
26. Z.Lj. Petrović, I. Simonović, S. Marjanović, D. Bošnjaković, D. Marić, G. Malović, S. Dujko, Plasma Phys. Controlled Fusion **59**, 014026 (2017)
27. P.W. Stokes, I. Simonović, B. Philippa, D. Cocks, S. Dujko, R.D. White, Sci. Rep. **8**, 2226 (2018)
28. K. Kumar, H.R Skullerud, R.E. Robson, Aust. J. Phys. **33**, 343 (1980)
29. R.E. Robson, Aust. J. Phys. **44**, 685 (1991)
30. R.E. Robson, K.F. Ness, Phys. Rev. A **33**, 2068 (1986)
31. K.F. Ness, R.E. Robson, Phys. Rev. A **34**, 2185 (1986)
32. K. Kumar, Phys. Rep. **112**, 319 (1984)
33. R.D. White, R.E. Robson, S. Dujko, P. Nicoletopoulos, B. Li, J. Phys. D: Appl. Phys. **42**, 194001 (2009)
34. S. Dujko, R.D. White, Z.Lj. Petrović, R.E. Robson, Phys. Rev. E **81**, 046403 (2010)
35. S. Dujko, R.D. White, Z.Lj. Petrović, R.E. Robson, Plasma Sources Sci. Technol. **20**, 024013 (2011)
36. O. Šašić, J. Jovanović, Z.Lj. Petrović, J. de Urquijo, J.R. Castrejón-Pita, J.L. Hernández-Ávila, E. Basurto, Phys. Rev. E **71**, 046408 (2005)
37. R.D. White, R.E. Robson, P. Nicoletopoulos, S. Dujko, Eur. Phys. J. D **66**, 117 (2012)
38. M. Hayashi, *Bibliography of Electron and Photon Cross Sections With Atoms and Molecules Published in the 20th Century Argon Report, NIFS-DATA-72* (National Institute for Fusion Science of Japan, Tokyo, Japan, 2003)
39. M. Hayashi, *Bibliography of Electron and Photon Cross sections with Atoms and Molecules Published in the 20th Century Xenon, NIFS-DATA-79* (National Institute for Fusion Science of Japan, Tokyo, Japan, 2003)
40. Biagi-v7.1 database, `www.lxcat.net` (accessed 19 April 2013)

XX International Workshop on
Low-Energy Positron and Positronium Physics

XXI International Symposium on
Electron-Molecule Collisions and Swarms

V Workshop on Non-Equilibrium Processes

18-21 July 2019, Belgrade, Serbia

POSMOL 2019

BOOK OF ABSTRACTS

XX Међународна радионица о физици
ниско енергијских позитрона и позитронијума

XXI Међународни симпозијум о
електрон-молекулским сударима и ројевима

V Радионица о неравнотежним процесима

Transport Coefficients of Higher-Order for Electrons and Positrons in Neutral Gases and Nonpolar Liquids

I. Simonović[1], D. Bošnjaković[1], R.D. White[2], Z. Lj. Petrović[1,3], and S. Dujko[1]
[1]Institute of Physics, University of Belgrade, Pregrevica 118, 11080 Belgrade, Serbia
[2]College of Science and Engineering, James Cook University, Townsville 4811, Australia
[3]Serbian Academy of Sciences and Arts, Knez Mihailova 35, 11000 Belgrade, Serbia
isimonovic@ipb.ac.rs

Transport coefficients of third and higher order have been systematically ignored in the traditional interpretations of the swarm experiments, as these experiments are usually performed under conditions in which the contribution of these transport coefficients is not significant. However, it has been shown that the third order transport coefficients (TOTC) are necessary for the conversion of hydrodynamic transport coefficients into transport data which are measured in the steady state Townsend and arrival time spectra experiments. In addition, the TOTC are required for a better representation of the spatial distribution of the swarm, as they describe the asymmetric deviation of the profiles of the number density of charged particles from a perfect Gaussian. Furthermore, if TOTC could be measured and calculated with a sufficient accuracy, this would enable the improvement of the swarm procedure for determining the complete sets of cross sections, as an additional transport coefficient could be included in this procedure.

We have investigated the third order transport coefficients for electrons and positrons in rare gases, as well as for electrons in homogenous atomic liquids. The structure of the third order transport coefficient tensor has been determined by employing the group projector technique, for all configurations of electric and magnetic fields [1]. In addition, the physical interpretation of the third order transport coefficients has been carefully analyzed.

Calculations of the TOTC and transport coefficients of lower order (e.g., drift velocity and diffusion tensor) have been performed in a wide range of the reduced electric fields (E/n_0) by employing Monte Carlo simulations and a multi term method for solving the Boltzmann equation. Both computer codes which are used in this study have been thoroughly tested [2,3]. Among many important points a strong correlation has been found between the E/n_0 profiles of the longitudinal component of the TOTC tensor and longitudinal diffusion. In addition, the TOTC for electrons and positrons in molecular gases have been compared. It has been found that the difference between the TOTC for electrons and positrons can be attributed to the corresponding differences in the rate coefficients for the inelastic collisions. In our study of the electron transport in atomic liquids, the structure induced negative differential conductivity has been thoroughly investigated by analyzing spatially resolved transport data and electron energy distribution functions [4]. Moreover, the influence of various representations of the inelastic energy losses in the liquid phase on the calculated values of the transport coefficients and the first Townsend coefficient has been studied [4].

References
[1]   Z.Lj. Petrović et al, *Plasma Phys. Control. Fusion*, **59**, (2017), 014026.
[2]   S. Dujko et al, *J. Phys. D: Appl. Phys.*, **41**, (2008), 245205.
[3]   S. Dujko et al, *Phys. Rev. E, 81*, (2010), 046403.
[4]   I. Simonović et al, *Plasma Sources Sci. Technol.*, **28**, (2019), 015006.

**30th Summer School and
International Symposium on
the Physics of Ionized Gases**

Šabac, Serbia,
August 24 -28, 2020

CONTRIBUTED PAPERS

&
**ABSTRACTS of INVITED LECTURES,
TOPICAL INVITED LECTURES and PROGRESS REPORTS**

**Editors:
Luka Č. Popović, Duško Borka,
Dragana Ilić and Vladimir Srećković**

OMNIA IN NUMERO ET MENSURA
• 1887 •

**БЕОГРАД
2020**

KINETIC AND FLUID MODELLING OF NON-EQUILIBRIUM TRANSPORT OF CHARGED-PARTICLE SWARMS IN NEUTRAL GASES AND NON-POLAR LIQUIDS

I. SIMONOVIĆ[1], D. BOŠNJAKOVIĆ[1], R. D. WHITE[2], Z. LJ. PETROVIĆ[3]and S. DUJKO[1]

[1]*Institute of Physics, University of Belgrade, Pregrevica 118, 11080 Belgrade, Serbia*

[2]*College of Science and Engineering, James Cook University, Townsville 4811, Australia*

[3]*Serbian Academy of Sciences and Arts, KnezMihailova 35, 11000 Belgrade, Serbia*

Abstract. This work contains two parts. The first part deals with the study of the third-order transport coefficients. The components of the third-order transport tensor are required for the conversion of the hydrodynamic transport coefficients into transport data that is measured in the arrival time spectra and the steady-state Townsend experiments. In this work, we have determined the structure of the third-order transport tensor in all configurations of the electric and magnetic fields, by using the group projector method, see Simonović et al. 2020. Moreover, we have carefully analyzed the physical interpretation of the individual components of this tensor, by examining their contribution to the flux gradient relation and to the approximate solution of the generalized diffusion equation. We have also examined the dependence of the third-order transport coefficients on the elementary scattering processes in a wide range of model and real gases, by using Monte Carlo simulations and multi term theory for solving the Boltzmann equation.The second part of this work deals with the electron transport in liquid argon, liquid krypton, and liquid xenon (the high mobility liquids), as well as with the transition of an electron avalanche into a negative streamer in these liquids. These three liquids represent the simplest systems in which quasi-free electrons exist in the liquid-phase medium, and they are an excellent starting point for the modeling of charged particle transport and electrical discharges in liquids. In this work, the transport of electrons in the high mobility liquids is investigated by employing Monte Carlo simulations, see Simonović et al. 2019. Our existing Monte Carlo code has been modified in order to enable a good representation of the coherent scattering effects. A special emphasis has been placed on studying the structure induced negative differential conductivity in liquid xenon, by employing the spatially resolved swarm data. Another point of interest was the influence of various representations, of the inelastic scattering in the liquid phase, on the ionization rate coefficient. The transport properties of electrons in the high mobility liquids, that were obtained by employing Monte Carlo simulations, were used as an input data in the 1.5D implementation of the first order fluid model. This fluid model was used to investigate the formation and propagation of negative streamers in these liquids. Among several important points, we have investigated the influence of various representations of the inelastic collisions on the dynamics of the formation and propagation of negative streamers in these liquids.

References

Simonović, I., et al.: 2020, *Phys. Rev. E*, **101**, 023203.
Simonović, I., et al.: 2019*, Plasma Sources Sci. Technol.*, **28**, 015006.
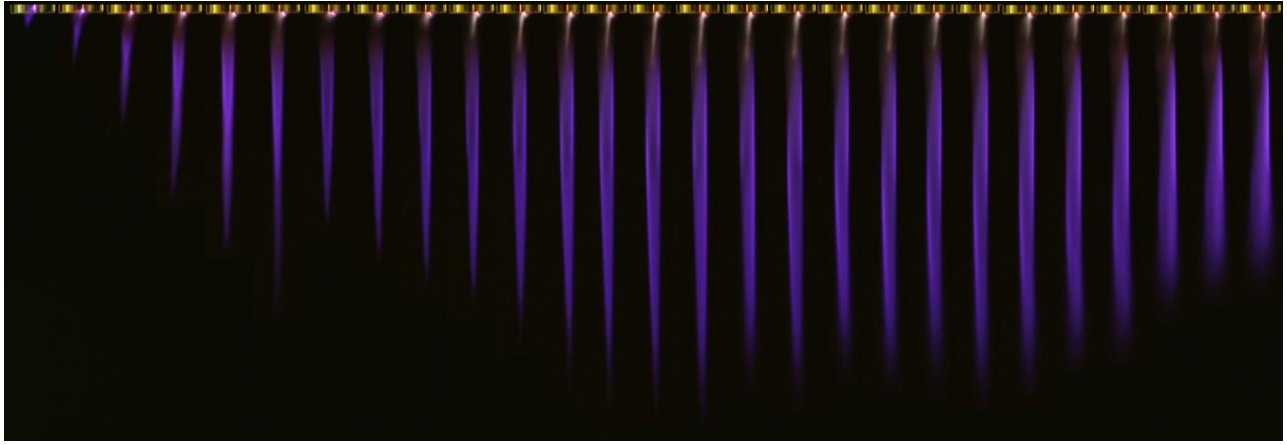
9th EU-Japan Joint Symposium on Plasma Processing (JSPP2014) and EU COST MP1101 Workshop on Atmospheric Plasma Processes and Sources

PROCEEDINGS

January 19th— January 23th 2014 | Bohinjska Bistrica, Slovenia (EU)

Programme and abstracts

Click on the title of a talk to see the abstract.

The 9th EU-Japan Joint Symposium on Plasma Processesing (19.-23. January 2014, Slovenia)

Sun. 19. Jan			
15.00 - 17.00		**Registration**	
17.00 - 17.30	INV	**S. Milošević** (CRO); Tailoring plasma sources and their diagnostics in various applications	slobodan@ifs.hr
17.30 - 18.00	INV	**M. Gorjanc** (SLO); Advantages and limitations of using plasma technology for modification of textiles	marija.gorjanc@ntf.uni-lj.si
18.00 - 18.30	INV	**K. Kutasi** (HUN); Layer-by-layer assembly of thin organic films on PTFE activated by air diffuse coplanar surface barrier discharge	kutasi.kinga@wigner.mta.hu
19.00 - 20.00		**Dinner**	
20.00 - 23.00		**Welcome reception**	

Mon. 20. Jan			
8.50 - 9.00	**Opening**	S. Hamaguchi (JPN), U. Cvelbar (SLO)	
9.00 - 9.45	**Plenary**	**T. Makabe** (JPN); Local distribution of gas temperature in an atmospheric- pressure microcell plasma in Ar	makabe@mkbe.elec.keio.ac.jp
9.45 - 10.30	**Plenary**	**M. M. Turner** (IRE); Uncertainty and error in complex plasma chemistry models	miles.turner@dcu.ie
10.30 - 11.00		**Break**	
11.00 -11.30	INV	**S. Hamaguchi** (JPN); Nano-scale damage formation during plasma etching analysed by multi-beam experiments and molecular dynamics (MD) simulations	hamaguch@ppl.eng.osaka-u.ac.jp
11.30 - 12.00	INV	**S. Dujko** (SRB); Recent results from studies of non-equilibrium electron transport in modelling of low-temperature plasmas and particle detectors	sasha@ipb.ac.rs
12.00 - 12.30	INV	**T. Murakami** (JPN); Reactive species in atmospheric pressure plasmas operated in ambient humid air	murakami@es.titech.ac.jp
12.30 - 13.00	INV	**M. Sekine** (JPN); Plasma nano-interface with organic materials for surface roughness formation	sekine@nagoya-u.jp
13.00 - 14.15		**Lunch**	
14.15 - 15.00	**Plenary**	**M. Shiratani** (JPN); Nanoparticle composite plasma CVD films - Fundamental and applications	siratani@ed.kyushi-u.ac.jp
15.00 - 15.30	INV	**R. Hatakeyama** (JPN); Plasma-processed control of graphene nanostructures and transport properties	hatake@ecei.tohoku.ac.jp
15.30 - 16.00	INV	**J. Kim** (JPN); Microwave plasma CVD technologies for the synthesis of nanocrystalline diamond and graphene films	jaeho.kim@aist.go.jp
16.00 – 16.30		**Break**	

Recent results from studies of non-equilibrium electron transport in modeling of low-temperature plasmas and particle detectors

S. Dujko[1], D. Bošnjaković[1], J. Mirić[1], I. Simonović[1], Z.M. Raspopović[1], R.D. White[2], A.H. Markosyan[3], U. Ebert[3] and Z.Lj. Petrović[1]

[1]Institute of Physics, University of Belgrade, Pregrevica 118, 11080 Belgrade, Serbia
[2]ARC Centre for Antimatter-Matter Studies, School of Engineering and Physical Sciences, James Cook University, Townsville 4810, Australia
[3]Centrum Wiskunde & Informatica (CWI), PO Box 94079, 1090 GB Amsterdam, The Netherlands

sasa.dujko@ipb.ac.rs

A quantitative understanding of charged particle transport processes in gases under highly non-equilibrium conditions is of interest from both fundamental and applied viewpoints, including modeling of non-equilibrium plasmas and particle detectors used in high energy physics. In this work we will highlight how the fundamental kinetic theory for solving the Boltzmann equation [1] and fluid equations [2,3] as well as Monte Carlo simulations [3], developed over many years for charged particle swarms are presently being adapted to study the various types of non-equilibrium plasma discharges and particle detectors.

Non-equilibrium plasma discharges sustained and controlled by electric and magnetic fields are widely used in materials processing [4]. Within these discharges the electric and magnetic fields can vary in space, time and orientation depending on the type of discharge. Moreover, the typical distances for electron energy and momentum relaxation are comparable to the plasma source dimensions. Consequently, the transport properties at a given point are usually no longer a function of instantaneous fields. This is the case for a variety of magnetized plasma discharges where, before the electrons become fully relaxed, it is likely that the electrons will be

reflected by the sheath or collide with the wall [5]. In this work we will illustrate various kinetic phenomena induced by the spatial and temporal non-locality of electron transport in gases. Two particular examples of most recent interest for the authors are the magnetron and ICP discharges. The magnetron discharge is used in the sputtering deposition of in films [6] where magnetic field confines energetic electrons near the cathode. These confined electrons ionize neutral gas and form high density plasma near the cathode surface while heavy ions and neutrals impinge on the solid surface ejecting material from that surface which is then deposited on the substrate. Within these discharges the angle between the electric and magnetic fields varies and thus for a detailed understanding and accurate modeling of this type of discharge, a knowledge of electron transport in gases under the influence of electric and magnetic fields at arbitrary angles is essential. In this work we will investigate the electron transport in N_2-O_2 mixtures when electric and magnetic fields are crossed at arbitrary angles for a range of pressures having in mind applications for low-pressure magnetized discharges and discharges at atmospheric pressure. Special attention is placed upon the explicit effects of three-body attachment in oxygen on both the drift and diffusion in low energy range [7]. The duality of transport coefficients arising from the explicit effects of non-conservative collisions will be discussed not only for vectorial and low-order tensorial transport coefficients but also for the high-order tensorial transport properties. The errors associated with the two-term approximation and inadequacies of Legendre polynomial expansions for solving the Boltzmann equation will be illustrated and highlighted.

In addition to magnetron discharges, we focus on the time-dependent behavior of electron transport properties in ICP discharges where electric and magnetic fields are radiofrequency. We systematically investigate the explicit effects associated with the electric and magnetic fields including field to density ratios, field frequency to density ratio, field phases and field orientations. A multitude of kinetic phenomena were observed that are generally inexplicable through the use of steady-state dc transport theory. Phenomena of significant note include the existence of transient

reflected by the sheath or collide with the wall [5]. In this work we will illustrate various kinetic phenomena induced by the spatial and temporal non-locality of electron transport in gases. Two particular examples of most recent interest for the authors are the magnetron and ICP discharges. The magnetron discharge is used in the sputtering deposition of in films [6] where magnetic field confines energetic electrons near the cathode. These confined electrons ionize neutral gas and form high density plasma near the cathode surface while heavy ions and neutrals impinge on the solid surface ejecting material from that surface which is then deposited on the substrate. Within these discharges the angle between the electric and magnetic fields varies and thus for a detailed understanding and accurate modeling of this type of discharge, a knowledge of electron transport in gases under the influence of electric and magnetic fields at arbitrary angles is essential. In this work we will investigate the electron transport in N_2-O_2 mixtures when electric and magnetic fields are crossed at arbitrary angles for a range of pressures having in mind applications for low-pressure magnetized discharges and discharges at atmospheric pressure. Special attention is placed upon the explicit effects of three-body attachment in oxygen on both the drift and diffusion in low energy range [7]. The duality of transport coefficients arising from the explicit effects of non-conservative collisions will be discussed not only for vectorial and low-order tensorial transport coefficients but also for the high-order tensorial transport properties. The errors associated with the two-term approximation and inadequacies of Legendre polynomial expansions for solving the Boltzmann equation will be illustrated and highlighted.

In addition to magnetron discharges, we focus on the time-dependent behavior of electron transport properties in ICP discharges where electric and magnetic fields are radiofrequency. We systematically investigate the explicit effects associated with the electric and magnetic fields including field to density ratios, field frequency to density ratio, field phases and field orientations. A multitude of kinetic phenomena were observed that are generally inexplicable through the use of steady-state dc transport theory. Phenomena of significant note include the existence of transient

negative diffusivity, time-resolved negative differential conductivity and anomalous anisotropic diffusion. Most notably, we propose a new mechanism for collisional heating in inductively coupled plasmas which results from the synergism of temporal non-locality and cyclotron resonance effect. This mechanism is illustrated for discharges in pure CF_4 and pure O_2.

As an example of fluid modeling of plasmas, we will discuss the recently developed high order fluid model for streamer discharges [2,3]. Starting from the cross sections for electron scattering, it will be shown how the corresponding transport data required as input in fluid model should be calculated under conditions when the local field approximation is not applicable. The temporal and spatial evolution of electron number density and electric field in the classical first order and in the high order model are compared and the differences will be explained by physical arguments. We will illustrate the non-local effects in the profiles of the mean energy behind the streamer front and emphasize the significance of the energy flux balance equation in modeling. We consider the negative planar ionization fronts in molecular nitrogen and noble gases. Our results for various streamers properties are compared with those obtained by a PIC/Monte Carlo approach. The comparison confirms the theoretical basis and numerical integrity of our high order fluid model for streamers discharges.

In the last segment of this talk we will discuss the detector physics processes of resistive plate chambers and time-projection chambers that are often used in many high energy physics experiments [8]. For resistive plate chambers the critical elements of modeling include the primary ionization, avalanche statists and signal development. The Monte Carlo simulation procedures that implement the described processes will be presented. Time resolution and detector efficiency are calculated and compared with experimental measurements and other theoretical calculations. Among many critical elements of modeling for time-projection chambers, we have investigated the sensitivity of electron transport properties to the pressure and temperature variations in the mixtures of Ne and CO_2. In particular, we have investigated how to reduce

the transverse diffusion of electrons by calculating the electron trajectories under the influence of parallel electric and magnetic fields and for typical conditions found in these detectors.

References
 [1] S. Dujko, R.D. White, Z.Lj. Petrović and R.E. Robson "Benchmark calculations of nonconservative charged-particle swarms in dc electric and magnetic fields crossed at arbitrary angles", Phys. Rev. E 80, (2010) 046403.
[2] S. Dujko, A.H. Markosyan, R.D. White and U. Ebert, "High-order fluid model for streamer discharges: I. Derivation of model and transport data" J. Phys. D: Appl. Phys. 46 (2013) 475202.
[3] A.H. Markosyan, S. Dujko and U. Ebert "High-order fluid model for streamer discharges: II. Numerical solution and investigation of planar fronts" J. Phys. D: Appl. Phys. 46 (2013) 475202.
[4] T. Makabe and Z.Lj. Petrović " Plasma Electronics: Applications in Microelectronic Device Fabrication" (New York: Taylor and Francis 2006).
[5] H. Date, P. L. G. Ventzek, K. Kondo, H. Hasegawa, and M. Shimozuma "Spatial characteristics of electron swarm parameters in gases" J. Appl. Phys., Vol. 83. no. 8, (1988) 4024.
[6] C.H. Shon and J.K. Lee "Modeling of magnetron sputtering plasma" Appl. Surf. Sci. 192 (2002) 258.
[7] S. Dujko, U. Ebert, R.D. White and Z.Lj. Petrović, "Boltzmann equation analysis of electron transport in a N_2-O_2 streamer discharge" Jpn. J. Appl. Phys. 50 (2011) 08JC01.
[8] G. Aad et al. "The ATLAS Experiment at the CERN Large Hadron Collider" J. Inst. Vol. 3 (2008) S08003.

27th Summer School and International Symposium on the Physics of Ionized Gases

August 26-29, 2014, Belgrade, Serbia

www.spig2014.ipb.ac.rs

CONTRIBUTED PAPERS

&

ABSTRACTS OF INVITED LECTURES, TOPICAL INVITED LECTURES, PROGRESS REPORTS AND WORKSHOP LECTURES

Editors:
Dragana Marić
Aleksandar R. Milosavljević
Zoran Mijatović

Institute of Physics, Belgrade
University of Belgrade

Serbian Academy
of Sciences and Arts

THIRD-ORDER TRANSPORT COEFFICIENTS FOR ELECTRONS I. STRUCTURE OF SKEWNESS TENSOR

I. Simonović, Z.Lj. Petrović and S. Dujko

Institute of Physics, University of Belgrade,
Pregrevica 118, 11080 Belgrade, Serbia

Abstract. Third-order transport properties are calculated through a Monte Carlo simulation for electrons moving in an infinite gas under the influence of spatially homogeneous electric and magnetic fields. The structure of the skewness tensor and symmetries along individual elements are studied by means of a group projector technique.

1. INTRODUCTION

Electron transport in gases under the influence of electric and magnetic fields has long been of interest, with many scientific and technological applications. These applications have been usually modeled assuming hydrodynamic conditions, in which the electron flux was analyzed in terms of drift and diffusion terms. The truncation of the electron flux to low order transport coefficients, e.g., to the drift velocity and diffusion tensor, may be invalid for a number of reasons, such as the presence of sources and sinks or physical boundaries. Before applying the strict non-hydrodynamic treatment, it is desirable to analyze the high-order transport coefficients and it is important to develop methods for their calculations. This issue has been addressed by several authors in the context of an electric field only case. The semi-quantitative momentum transfer theory developed by Vrhovac *et al.* [1] and Monte Carlo simulation performed by Penetrante and Bardsley [2] were used to analyze the skewness tensor for electrons in rare gases. A three-temperature treatment of the Boltzmann equation and molecular dynamics simulation were used by Koutselos to calculate the third order transport coefficients of ions in atomic gases [3].

In this work we apply the group projector method [4] to investigate the structure of the skewness tensor and symmetries along its individual

elements when both the electric and magnetic fields are present. Using a Monte Carlo simulation technique, the longitudinal and transverse skewness coefficients are calculated for the ionization model of Lucas and Saelee [5].

2. THEORETICAL METHODS

The starting point in our analysis is the flux gradient relation

$$\mathbf{\Gamma}(\boldsymbol{r}, t) = \sum_{k=0}^{\infty} \Gamma^{(k+1)}(t) \odot (-\nabla)^k n, \tag{1}$$

and diffusion equation

$$\frac{\partial n(\boldsymbol{r}, t)}{\partial t} = \sum_{k=0}^{\infty} \omega^{(k)}(t) \odot (-\nabla)^k n. \tag{2}$$

where $n(\boldsymbol{r}, t)$ is the electron density while $\mathbf{\Gamma}(\boldsymbol{r}, t)$ is the electron flux. $\Gamma^{(k+1)}(t)$ are time dependent tensors of rank k and $\odot$ denotes a k-fold scalar product.

As pointed out in [1] one should make a difference between microscopic and macroscopic transport coefficients. Microscopic bulk transport coefficient of an order k, $\omega^{(k)}(t)$, is a tensor of rank k, which multiplies the k-th gradient of concentration, in (2). Microscopic flux can be obtained from microscopic bulk by subtracting the term associated with the explicit effects of non-conservative collisions. Macroscopic flux transport coefficient of order k, $\Gamma^{(k)}(t)$, is a tensor of rank k, which in the flux gradient relation (1), multiplies the $(k-1)$-th gradient of concentration. These tensors are, starting from rank 3, symmetric by every permutation of indices, that does not change position of the first index, because all indices, except the first, are contracted with partial derivatives of concentration.

In this work, we consider a co-ordinate system in which the z-axis is defined by the electric field $\boldsymbol{E}$ while the magnetic field $\boldsymbol{B}$ lies along the z-axis (parallel field configuration) or along the y-axis (an orthogonal field configuration) or makes an angle ψ with $\boldsymbol{E}$ and lies in the $y - z$ plane (an arbitrary field configuration). Using the method based on group projectors and identifying the symmetries along the individual elements of the skewness tensor we have determined the following structures of the tensor depending on the field configuration:

1. Electric field only configuration ($\boldsymbol{E} = Ee_{\mathbf{z}}$):

$$Q_{x|ij} = \begin{pmatrix} 0 & 0 & Q_{xxz} \\ 0 & 0 & 0 \\ Q_{xxz} & 0 & 0 \end{pmatrix}, \quad Q_{y|ij} = \begin{pmatrix} 0 & 0 & 0 \\ 0 & 0 & Q_{xxz} \\ 0 & Q_{xxz} & 0 \end{pmatrix},$$

$$Q_{z|ij} = \begin{pmatrix} Q_{zxx} & 0 & 0 \\ 0 & Q_{zxx} & 0 \\ 0 & 0 & Q_{zzz} \end{pmatrix}. \tag{3}$$

2. Parallel field configuration ($\boldsymbol{E} = Ee_{\mathbf{z}}$, $\boldsymbol{B} = Be_{\mathbf{z}}$):

$$Q_{x|ij} = \begin{pmatrix} 0 & 0 & Q_{xxz} \\ 0 & 0 & Q_{xyz} \\ Q_{xxz} & Q_{xyz} & 0 \end{pmatrix}, \quad Q_{y|ij} = \begin{pmatrix} 0 & 0 & -Q_{xyz} \\ 0 & 0 & Q_{xxz} \\ -Q_{xyz} & Q_{xxz} & 0 \end{pmatrix},$$

$$Q_{z|ij} = \begin{pmatrix} Q_{zxx} & 0 & 0 \\ 0 & Q_{zxx} & 0 \\ 0 & 0 & Q_{zzz} \end{pmatrix}. \tag{4}$$

3. Crossed field configuration ($\boldsymbol{E} = Ee_{\mathbf{z}}$, $\boldsymbol{B} = Be_{\mathbf{y}}$):

$$Q_{x|ij} = \begin{pmatrix} Q_{xxx} & 0 & Q_{xxz} \\ 0 & Q_{xyy} & 0 \\ Q_{xxz} & 0 & Q_{xzz} \end{pmatrix}, \quad Q_{y|ij} = \begin{pmatrix} 0 & Q_{yxy} & 0 \\ Q_{yxy} & 0 & Q_{yyz} \\ 0 & Q_{yyz} & 0 \end{pmatrix},$$

$$Q_{z|ij} = \begin{pmatrix} Q_{zxx} & 0 & Q_{zxz} \\ 0 & Q_{zyy} & 0 \\ Q_{zxz} & 0 & Q_{zzz} \end{pmatrix}, \tag{5}$$

where $i, j = x, y, z$. For an arbitrary field configuration, $Q_{ijk} = Q_{ikj}$ for any individual element of the skewness tensor.

3. RESULTS AND DISCUSSIONS

In the hydrodynamic regime the skewness tensor is given by

$$\boldsymbol{Q}_{abc} = \frac{1}{3!}\frac{d}{dt}\langle r_a^\star \, r_b^\star \, r_c^\star \rangle, \tag{6}$$

where (a, b, c) take values from the set $\{x, y, z\}$ while the angular brackets $\langle\,\rangle$ denote ensemble averages in configuration space and $\boldsymbol{r}^\star = \boldsymbol{r} - \langle\boldsymbol{r}\rangle$. From (3) it is clear that $\boldsymbol{Q}$ has seven non-vanishing elements, three of which are independent, Q_{zzz}, $Q_{zxx} = Q_{zyy}$ and $Q_{xzx} = Q_{xxz} = Q_{yzy} = Q_{yyz}$. Due to direct sampling of swarm dynamic properties in our Monte Carlo code only two independent components of the skewness tensor can be isolated, the longitudinal skewness coefficient $Q_L = Q_{zzz}$ and transverse skewness coefficient $Q_T = Q_{zxx} + Q_{xzx} + Q_{xxz} = Q_{zyy} + Q_{yzy} + Q_{yyz}$.

In Fig. 1 we show the variation of $n_0^2 Q_L$ with E/n_0 for the ionization model of Lucas Saelee. We see that $n_0^2 Q_L$ monotonically decreases with increasing E/n_0 and/or with increasing parameter F. For the conservative case ($F = 0$) gas model is reduced to elastic and excitation cross sections and no ionization occurs while for non-conservative case ($F = 1$) the gas model consists of elastic and ionization cross sections and no excitation occurs. In this model, for increasing E/n_0 the collision frequency for inelastic collisions is also increased while the collision frequency for the momentum transfer in elastic collisions remains unaltered. This suggests that for increasing E/n_0 inelastic collisions tend to reduce $n_0^2 Q_L$. A decrease

in $n_0{}^2Q_L$ with increasing F is a clear sign that the skewness coefficients are more sensitive than the lower order transport coefficients with respect to small variation in the distribution function induced by the ionization cooling.
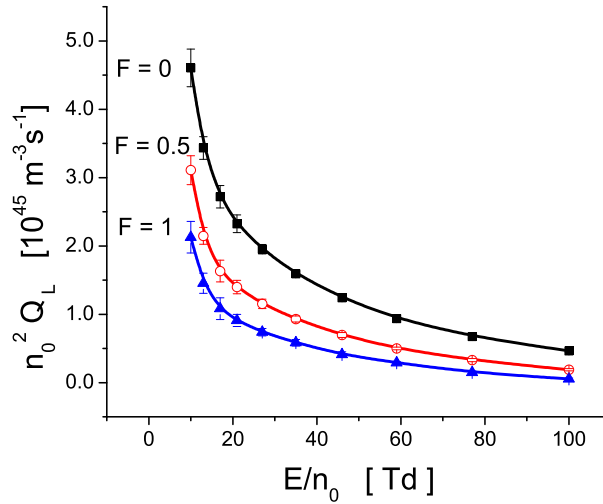

Figure 1. Variation of the longitudinal skewness coefficient with E/n_0 for three different ionization models as indicated on the graph.

Acknowledgments

REFERENCES

[1]   S.B. Vrhovac, Z.Lj. Petrović, L.A. Viehland and T.S. Santhanam, J. Chem. Phys. 110, 2423 (1999).

[2]   B.M. Penetrante and J.N. Bardsley, in *Non-equilibrium Effects in Ion and Electron Transport*, edited by J.W. Gallagher, D.F. Hudson, E. E. Kunhardt, and R.J. Van Brunt, (Plenum, New York, 1990), p. 49.

[3]   A.D. Koutselos, Chem. Phys. 315, 193 (2005).

[4]   A.O. Barut and R. Raczka, *Theory of group representations and applications* (World Scientific, Singapore, 1986).

[5]   J. Lucas and H. Saelee, J. Phys. D: Appl. Phys. 8, 640 (1975).

THIRD-ORDER TRANSPORT COEFFICIENTS FOR ELECTRONS II. MOLECULAR GASES

I. Simonović, Z.Lj. Petrović and S. Dujko

Institute of Physics, University of Belgrade,
Pregrevica 118, 11080 Belgrade, Serbia

Abstract. A Monte Carlo simulation technique is used to calculate the third-order transport coefficients for electrons and positrons in molecular gases. Values and general trends of the longitudinal and transverse skewness coefficients as a function of the reduced electric field in N_2, CH_4 and CF_4 are reported here. We investigate the way in which the skewness transport coefficients are influenced by the energy dependence of cross sections for electron/positron scattering. Correlations between the skewness and diffusion coefficients have been found and studied.

1. INTRODUCTION

Studies of third-order transport coefficients for charged particles in gases are very useful under conditions when transport is greatly affected by non-conservative collisions and/or under conditions when the truncation of the charged particle flux to low order transport coefficients is not sufficient for accurate description of transport phenomena. There is a huge body of data for electrons (and ions), and since recently even for positrons, when it comes to low order transport coefficients, including the drift velocity and diffusion tensor, and rate coefficients. In contrast, little is known about high-order transport coefficients, particularly for electrons and positrons. This is understandable having in mind that the traditional swarm experiments have been interpreted without the consideration of high order transport [1], though it has been suspected to influence the motion of the electrons [2] and ions [3]. Third-order transport coefficients are most likely to be measured in the near future and hence it is of great importance to develop methods for their theoretical calculations. Such information can help in the design of future experiments as well as in the interpretation of their results.

The aims of this work are (1) to provide Monte Carlo calculations of the skewness transport coefficients for electrons and positrons in molecular gases, (2) to investigate the correlations between skewness and low order transport coefficients (e.g., the drift velocity and diffusion tensor), and (3) to study the explicit and implicit effects of non-conservative collisions on the skewness transport properties. In section 2 we give a brief discussion of our Monte Carlo method while in section 3 we present a few examples of our results for electrons in N_2.

2. THEORETICAL METHODS

The Monte Carlo code applied in this work follows a large number of particles (usually 10^7 and sometimes even more) moving in an infinite gas under the influence of spatially homogeneous electric field. Particles (positrons or electrons) gain energy from the electric field and dissipate this energy through binary collisions with background neutral particles. The charged particle interactions are neglected since the transport is considered in the limit of low charged-particle density. All calculations are performed at zero gas temperature. For more details about our Monte Carlo simulation code see recent reviews [4, 5].

Skewness transport coefficients are determined after relaxation to steady state. The bulk values are calculated using the following formulas:

$$Q_L^{(B)} = \frac{1}{3!} \frac{d}{dt} \left(\langle z^3 \rangle - 3\langle z \rangle \langle z^2 \rangle + 2\langle z \rangle^3 \right), \tag{1}$$

$$Q_T^{(B)} = \frac{1}{3!} \frac{d}{dt} \left(\langle zy^2 \rangle - \langle z \rangle \langle y^2 \rangle \right), \tag{2}$$

while the corresponding flux components are determined as follows:

$$Q_L^{(F)} = \frac{1}{3!} \left(3\langle z^2 V_z \rangle - 3\langle V_z \rangle \langle z^2 \rangle - 6\langle z \rangle \langle z V_z \rangle + 6\langle V_z \rangle \langle z \rangle^2 \right), \tag{3}$$

$$Q_T^{(F)} = \frac{1}{3!} \left(\langle y^2 V_z \rangle + 2\langle zy V_y \rangle - \langle y^2 \rangle \langle V_z \rangle - 2\langle z \rangle \langle y V_y \rangle \right), \tag{4}$$

where indices B and F refer to *bulk* and *flux*. We consider a coordinate system in which the electric field lies along the z-axis.

3. RESULTS AND DISCUSSIONS

In figure 1 we show the variation of the longitudinal and transverse skewness coefficients, $n_0^2 Q_L$ and $n_0^2 Q_T$, respectively, with E/n_0 for electrons in N_2. In order to understand the correlation between skewness and diffusion coefficients, on the same figure we show the variation of the longitudinal and transverse, $n_0 D_L$ and $n_0 D_T$, diffusion coefficients with E/n_0. For lower E/n_0, less than 40 Td, we observe that $n_0 D_L$ is a decreasing function

of E/n_0. For the same E/n_0, $n_0^2 Q_L$ decreases markedly. For $E/n_0 \geq$ 40 Td, $n_0 D_L$ is a monotonically increasing function of E/n_0 while $n_0^2 Q_L$ increases with increasing E/n_0, reaching a peak, and then it starts first to decrease and then again to increase. If we take a careful look, we see that after reaching the peak, $n_0^2 Q_L$ is decreased when the profile of $n_0^2 Q_L$ is changed from a typical convex to a more concave profile. This illustrates high sensitivity of $n_0^2 Q_L$ with respect to the collisional process that control the behavior of diffusion along the field direction. For $E/n_0 \geq 400$ Td both $n_0 D_L$ and $n_0^2 Q_L$ are monotonically increasing functions of E/n_0. From the profile of $n_0^2 Q_T$, we see that the transverse skewness coefficient is correlated very well with both $n_0 D_L$ and $n_0 D_T$. This applies for electrons in N_2; for electrons in CF_4 we have identified the regions of E/n_0 where $n_0^2 Q_T$ exhibits better correlation with $n_0 D_T$ than with respect to $n_0 D_L$.
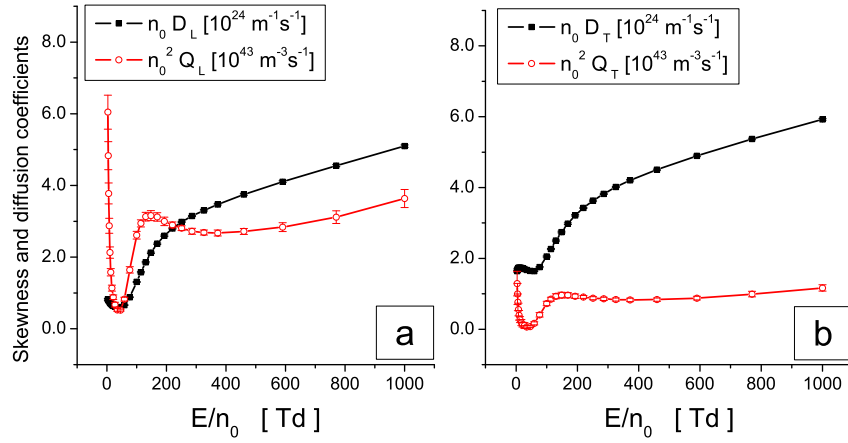
Figure 1. Variation of the longitudinal skewness and longitudinal diffusion coefficients with E/n_0 (a) and variation of the transverse skewness and transverse diffusion coefficients with E/n_0 (b) for electrons in N_2.

Figure 2 displays the variation of the bulk and flux values of $n_0^2 Q_L$ (a) and $n_0^2 Q_T$ (b) with E/n_0 for electrons in N_2. Increasing E/n_0 results in a more pronounced distinction between bulk and flux values. The explicit effects of ionization on the skewness properties become clearly evident for $E/n_0 \geq 150$ Td. For both $n_0^2 Q_L$ and $n_0^2 Q_T$ the bulk values overestimate the corresponding flux values and this is exactly what has been previously observed for the drift and diffusion in N_2 [6]. The differences between bulk and flux values do not exceed 60% for both $n_0^2 Q_L$ and $n_0^2 Q_T$ for E/n_0 considered in this work. Better understanding of the explicit effects of ionization on the skewness transport properties requires knowledge of the spatially resolved data along the swarm, particularly those associated with the high-order variations of the average energy.
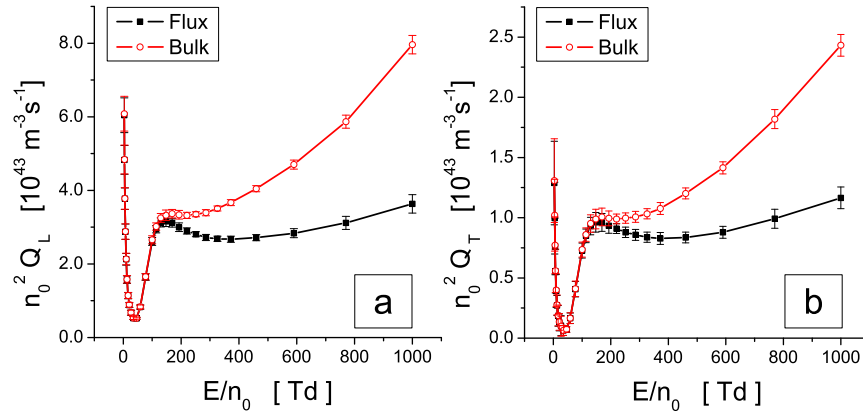
Figure 2. Variation of the bulk and flux longitudinal (a) and transverse (b) skewness coefficients with E/n_0 for electrons in N_2.

REFERENCES

[1] L.G.H. Huxley and R.W. Crompton, *The Drift and Diffusion of Electrons in Gases* (New York: Wiley Interscience, 1973).

[2] B.M. Penetrante and J.N. Bardsley, in *Non-equilibrium Effects in Ion and Electron Transport*, edited by J.W. Gallagher, D.F. Hudson, E. E. Kunhardt, and R.J. Van Brunt, (Plenum, New York, 1990), p. 49.

[3] A.D. Koutselos, Chem. Phys. 270, 165 (2001).

[4] S. Dujko, Z.M. Raspopović and Z.Lj. Petrović, J.Phys.D: Appl. Phys. 38, 2952 (2005).

[5] S. Dujko, R.D. White and Z.Lj. Petrović, J.Phys.D: Appl. Phys. 41, 245205 (2008).

[6] S. Dujko, U. Ebert, R.D. White and Z.Lj. Petrović, Jpn. J. Appl. Phys. 50, 08JC01 (2011).

28th Summer School and
International Symposium on
the Physics of Ionized Gases
Aug. 29 - Sep. 2, 2016, Belgrade, Serbia

CONTRIBUTED PAPERS
&

ABSTRACTS OF INVITED LECTURES,
TOPICAL INVITED LECTURES, PROGRESS REPORTS
AND WORKSHOP LECTURES

Editors:
Dragana Marić, Aleksandar Milosavljević,
Bratislav Obradović and Goran Poparić

University of Belgrade,
Faculty of Physics

Serbian Academy
of Sciences and Arts

MONTE CARLO SIMULATIONS OF ELECTRON TRANSPORT IN CF$_3$I AND SF$_6$ GASES

J. Mirić, D. Bošnjaković, I. Simonović, Z. Lj. Petrović and S. Dujko

Institute of Physics, University of Belgrade,
Pregrevica 118, 11080 Belgrade, Serbia

Abstract. Electron transport coefficients in CF$_3$I and SF$_6$ gases are calculated using Monte Carlo simulations for a wide range of reduced electric field strengths. In order to compensate for the loss of electrons in simulation due to strong attachment, three different rescaling techniques are considered and applied. Among many observed phenomena, in case of SF$_6$ we highlight the reduction of mean electron energy with increasing electric field. In addition, we observe that for both gases bulk drift velocities exhibit negative differential conductivity which is not present in the flux drift velocity.

1. INTRODUCTION

Electron attachment in strongly electronegative gases, such as CF$_3$I and SF$_6$, has many industrial applications. For example, in high-voltage circuit breakers, it is the most significant process for the prevention of electric breakdown [1]. Electronegative gases are also used for plasma etching and cleaning in semiconductor fabrication [2].

On the other hand, electron attachment imposes practical difficulties in experiments for measurement of transport coefficients [1,3]. Considerable difficulties also appear in Monte Carlo simulations of electron transport in strongly electronegative gases at low electric fields where electron attachment is the dominant process. Due to this process, the number of electrons in a simulation can reach extremely low values leading to poor statistics or complete loss of electrons in the simulation [4,5]. In order to compensate for this loss of electrons, some sort of rescaling techniques must be used.

In this work, we discuss the existing rescaling techniques for Monte Carlo simulations of electron transport in strongly electronegative gases. Furthermore, we introduce our modified rescaling procedure and demonstrate how these techniques affect the calculated transport data for CF$_3$I and SF$_6$ gases.

2. RESCALING TECHNIQUES

The following rescaling techniques, applicable for Monte Carlo simulations, can be found in the literature:
1. Duplication of electrons randomly chosen from the remaining swarm at certain discrete time steps [6];
2. Duplication of the entire electron swarm (one or more times) at certain time steps [5] or at certain distance steps [7];
3. Introduction of an additional fictitious ionization [4] or attachment process [8] with a constant collision frequency.

An unaltered electron distribution function and its evolution are a common objective for all these techniques. In this work, the first technique will be referred to as discrete rescaling, the second as swarm duplication and the third as continuous rescaling. However, we introduce a modification to the third procedure where the fictitious ionization process is dynamically adjusted during the simulation in such way that the fictitious ionization rate is chosen to be equal to the attachment rate. Therefore, it is not necessary to define a fictitious ionization rate in advance and as a benefit, the number of electrons is kept nearly constant during the simulation.

3. RESULTS

In this section, we present the transport data for CF_3I and SF_6 gases, calculated using our Monte Carlo code [6,9] with three different rescaling techniques. The cross section set for electron scattering in SF_6 is taken from Itoh *et al.* [10]. In case of CF_3I, we use our modified cross section set [11] which is based on cross sections of Kimura and Nakamura [12]. This modification of the CF_3I set was necessary in order to provide a better agreement between the calculated data and the reference data measured in a pulsed Townsend experiment for pure CF_3I and its mixtures with Ar and CO_2.

Figure 1(a) shows the variation of mean electron energy with E/n_0 in CF_3I. Calculations are performed assuming the three rescaling techniques. Excellent agreement between the cases of discrete rescaling and swarm duplication can be understood, having in mind that these two techniques are essentially the same. The only difference between the two is the fact that in case of discrete rescaling, the probability for duplication of an electron is determined by the ratio of current number and desired number of electrons, while in case of swarm duplication technique, this probability is set to unity i.e. the duplication is performed for all electrons. Continuous rescaling is also in a good agreement with the other two techniques.

In case of mean electron energy for the SF_6 gas, Figure 1(b) shows excellent agreement between the three rescaling techniques. Furthermore, one anomalous behavior is observed — a decrease of mean energy with increasing electric field. This phenomenon is associated with mutual influence of attachment heating and inelastic cooling. Since it is observed only in case of SF_6,
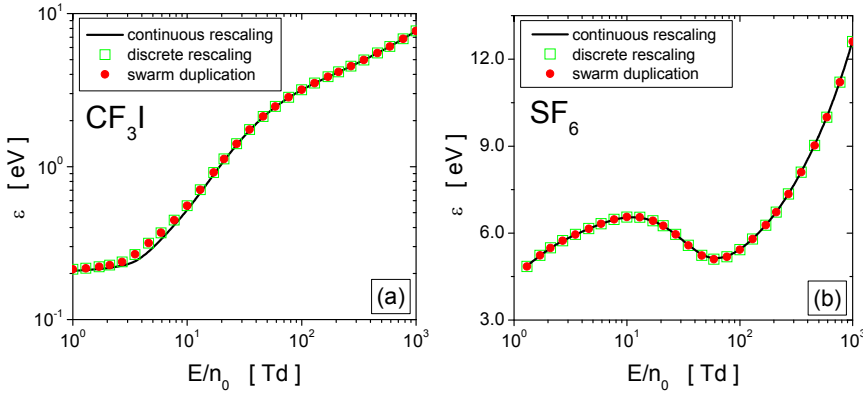
Figure 1. Mean electron energy in (a) CF_3I and (b) SF_6 gases as a function of reduced electric field. The profiles are calculated using three different rescaling techniques.

it is evident that the specific cross sections for electron scattering are essentially responsible for the occurrence of this phenomenon.

Figure 2 shows flux and bulk drift velocities in (a) CF_3I and (b) SF_6 gases, obtained with three rescaling techniques. For electrons in CF_3I, the drift velocities calculated using discrete rescaling and swarm duplication are again in excellent agreement while continuous rescaling at low electric fields gives slightly lower values than the other two techniques. For drift velocities in the SF_6 gas, all three rescaling techniques are in good agreement over the entire range of reduced electric fields considered in this work. We can conclude that the nature of the cross sections for electron scattering in CF_3I and SF_6 and their energy dependence are responsible for the differences between the results obtained using different rescaling techniques.

Two interesting phenomena are also observed in Figure 2. First, for
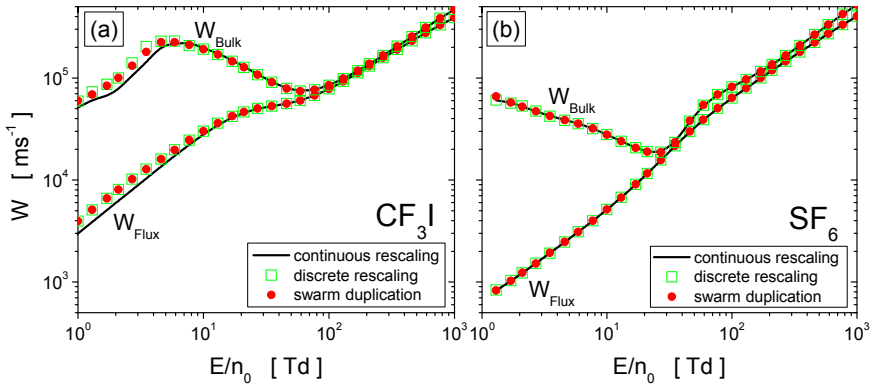
Figure 2. Variation of the drift velocity with E/n_0 for electrons in (a) CF_3I and (b) SF_6 gases. The profiles are calculated using three different rescaling techniques.

both gases the bulk drift velocity is higher than the flux drift velocity. In low energy range, this is a consequence of strong attachment heating (the consumption of slow electrons due to attachment) while in higher energy range the explicit effect of ionization is responsible. As a result, new electrons are preferentially created at the front of the swarm and/or slow electrons are consumed at the back of the swarm resulting in a forward shift of centre of mass of the swarm which is observed as an increase of bulk drift velocity over the flux drift velocity. The other phenomenon is a very strong NDC effect (negative differential conductivity) which is noticed for both gases, but only in case of bulk component drift velocity. This behavior appears to be common for all strongly electronegative gases since it is induced by explicit effects of electron attachment.

Acknowledgements

REFERENCES

[1] L. G. Christophorou and J. K. Olthoff, *Fundamental electron interactions with plasma processing gases*, (Springer, New York, 2004).
[2] T. Makabe and Z. Lj. Petrović, *Plasma Electronics: Applications in Microelectronic Device Fabrication*, (CRC Press, New York, 2014).
[3] Z. Lj. Petrović *et al.*, J. Phys. D: Appl. Phys. 42, 194002 (2009).
[4] M. Yousfi, A. Hennad and A. Alkaa, Phys. Rev. E 49, 3264 (1994).
[5] A. M. Nolan, M. J. Brennan, K. F. Ness and A. B. Wedding, J. Phys. D 30, 2865 (1997).
[6] Z. M. Raspopović, S. Sakadžić, S. Bzenić and Z. Lj. Petrović, IEEE Trans. Plasma Sci. 27, 1241 (1999).
[7] N. A. Dyatko and A. P. Napartovich, J. Phys. D 32, 3169 (1999).
[8] Y. M. Li, L. C. Pitchford and T. J. Moratz, Appl. Phys. Lett. 54, 1403 (1989).
[9] S. Dujko, R. D. White and Z. Lj. Petrović, J. Phys. D: Appl. Phys. 41, 245205 (2008).
[10] H. Itoh, T. Matsumura, K. Satoh, H. Dane, Y. Nakano and H. Tagashira, J. Phys. D 26, 1975 (1993).
[11] J. Mirić, O. Šašić, S. Dujko and Z. Lj. Petrović, Proc. 27th Summer School and International Symposium on the Physics of Ionized Gases (Belgrade) 2014, p. 122.
[12] M. Kimura and Y. Nakamura, J. Phys. D 43, 145202 (2010).

ELECTRON TRANSPORT IN MERCURY VAPOR: DIMER INDUCED NDC AND ANALYSIS OF TRANSPORT PHENOMENA IN ELECTRIC AND MAGNETIC FIELDS

J. Mirić, I. Simonović, D. Bošnjaković, Z. Lj. Petrović and S. Dujko

Institute of Physics, University of Belgrade,
Pregrevica 118, 11080 Belgrade, Serbia

Abstract. Transport coefficients for electron swarms in mercury vapor in the presence of electric and magnetic fields are calculated and analyzed using a multi term theory for solving the Boltzmann equation and Monte Carlo simulation technique. Particular attention is paid to the occurrence of negative differential conductivity (NDC) at higher gas pressures and temperatures. It is shown that the correct representation of the presence of mercury dimers and superelastic collisions plays a key role in the analysis of NDC. When both the electric and magnetic fields are present, another phenomenon arises: for certain values of electric and magnetic field, we find regions where swarm mean energy increases with increasing magnetic field for a fixed electric field. Spatially-resolved electron transport properties are calculated using a Monte Carlo simulation technique in order to understand these phenomena.

1. INTRODUCTION

In this work we discuss the transport of electrons in mercury vapor and its mixtures with argon under conditions relevant for metal vapor lamps. Current models of such lamps require knowledge of transport coefficients as a function of electric field strengths, gas pressures and temperatures. Recently developed inductively coupled plasma light sources require the knowledge of transport coefficients when both the electric and magnetic fields are present and crossed at arbitrary angles [1]. These transport coefficients can be either measured in swarm experiments or calculated from transport theory. To date, no experiments exist that can measure all the required transport coefficients, including rate coefficients, drift velocities, and diffusion coefficients for electrons in gases in the presence of electric and magnetic fields.

In the present work we solve the Boltzmann equation for electron swarms undergoing ionization in mercury vapor and its mixtures with argon in the presence of electric and magnetic fields crossed at arbitrary angles. For the E-only case we discuss the occurrence of negative differential conductivity (NDC) for

higher gas pressures and temperatures in the limit of lower electric fields. NDC is a phenomenon where the drift velocity decreases with increasing electric field. For electrons in mercury vapor this behavior of the drift velocity is attributed to the presence of mercury dimers.

In the second part of this work we investigate the electron transport in varying configurations of electric and magnetic fields. In particular, we discuss the following phenomenon: for certain values of electric and magnetic fields, we find regions where swarm mean energy increases with increasing magnetic field for a fixed electric field. The phenomenon is discussed using spatially-resolved transport data calculated in Monte Carlo simulations.

2. CROSS SECTIONS AND SIMULATION TECHNIQUES

The cross section for momentum transfer in elastic collisions is made as follows. For lower electron energies, we use a cross section from [2] while for higher energies, we use a cross section tabulated in MAGBOLTZ code [3]. Cross sections for electronic excitations for levels $^3P_0$, $^3P_1$ and $^3P_2$ are retrieved from [4] while electronic excitations to $^1S_0$ and $^1P_1$ states as well as a cross section for higher states are also taken from MAGBOLTZ code. For electron-impact ionization, we have used a cross section from [5]. The effective cross section which describes vibration and electronic excitations of mercury dimers is derived using the experimental measurements of Elford [6]. Cross sections were slightly modified during the calculations to improve agreement between the calculated swarm parameters and the experimental values [6].

Electron transport coefficients are calculated from the multi term solution of Boltzmann's equation. A Monte Carlo simulation technique is used to verify the Boltzmann equation results and also for the calculations of spatially-resolved transport data.

3. RESULTS AND DISCUSSIONS

In Figure 1 (a) we show the variation of the drift velocity with E/n_0 for a range of gas pressures, as indicated on the graph. Calculations are performed in a wide range of pressures, from 20.2 to 108.4 Torr. The temperature of the background gas is 573K. The same range of pressures and temperatures was considered by Elford in his experiments [6]. We extend his measurements by considering the drift of electrons for six additional gas pressures. For E/n_0 less than approximately 2.5 Td the pressure dependence of the drift velocity is clearly evident. For higher E/n_0, however, the drift velocity does not depend on the pressure. For pressures higher than approximately 200 Torr, we see that the drift velocity exhibits a region of NDC, i.e. over a range of E/n_0 values the drift velocity decreases as the driving field is increased. The conditions for the occurrence of NDC have been investigated previously [7]. For electrons in mercury vapor, NDC arises for certain combinations of elastic cross sections of dimer-free mercury vapor and inelastic cross sections of mercury dimers in

which, on increasing the electric field, there is a rapid transition in the dominant energy loss mechanism from inelastic to elastic. For pressures lower than 200 Torr the elastic cross section of dimer-free mercury vapor dominates the effective inelastic cross section of mercury dimers. Thus, the conditions for the occurrence of NDC are not set. For higher pressures, the phenomenon is promoted by either or both of (i) a rapidly increasing cross section for elastic collisions and (ii) a rapidly decreasing inelastic cross section. It is clear that the presence of dimmers plays a key role in the development of NDC in mercury vapor.

In Figure 1 (b) we show a comparison between our calculations and experimental measurements of the drift velocity for a range of pressures. Our Monte Carlo results (figure 1 (b)) agree very well with those measured in the Bradbury-Nielsen time-of-flight experiment [6]. The agreement is achieved only after careful implementation of superelastic collisions in our calculations. Cross sections for superelastic collisions are calculated directly in our code from the principle of detailed balance.
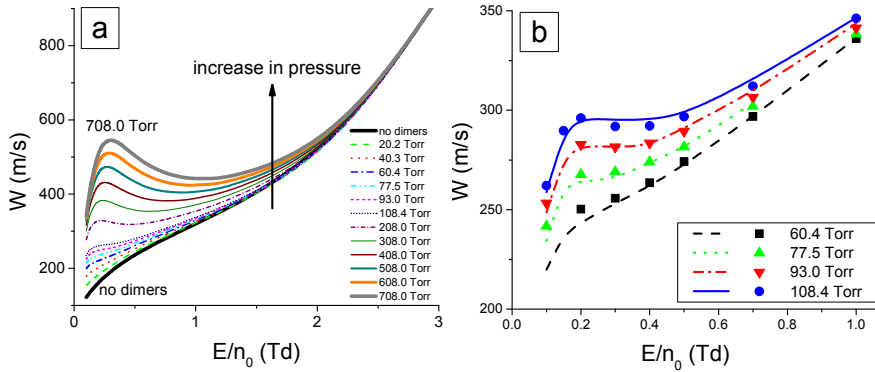
Figure 1. Variation of the drift velocity with E/n_0 for a range of pressures (a) and comparison between our Monte Carlo results and experimental measurements. Calculations are performed for electrons in mercury vapor. The temperature of the background gas is 573K.

In the last segment of this work we discuss the impact of a magnetic field on the electron transport in mercury vapor. The pressure and temperature of the mercury vapor are set to 1 Torr and 293K, respectively. As an example of our study, in figure 2 we show the variation of the mean energy with E/n_0 for a range of the reduced magnetic fields B/n_0, in a crossed field configuration. In the limit of the lowest E/n_0 the electrons are essentially in the quasi-thermal equilibrium with the mercury vapor, independent of the strength of the applied magnetic field. In this regime, the longitudinal and transverse drift velocity components are dependent on both E/n_0 and B/n_0 while the diagonal diffusion tensor elements along the **E** and **E**×**B** directions are dependent on B/n_0 only. The diffusion coefficient along the magnetic field direction is reduced to its thermal value as magnetic field only affects the diffusion in this direction indirectly, through the magnetic field's action to cool the swarm. Certainly one of the most striking

properties observed in the profiles of transport coefficients is an increase in the swarm mean energy with increasing magnetic field for a fixed electric field. The phenomenon is evident in the range E/n_0=5-200 Td for B/n_0 considered in this work. This behavior is contrary to previous experiences in swarm physics as one would expect the mean swarm energy to decrease with increasing B/n_0 for a fixed E/n_0. The phenomenon could be associated with the interplay between magnetic field cooling and inelastic/ionization cooling, although the role of the cross sections in both phenomena is of course vital. The electron energy distribution function and spatially-resolved mean energy, rate coefficients and other properties are calculated using a Monte Carlo simulation technique in order to explain this phenomenon.
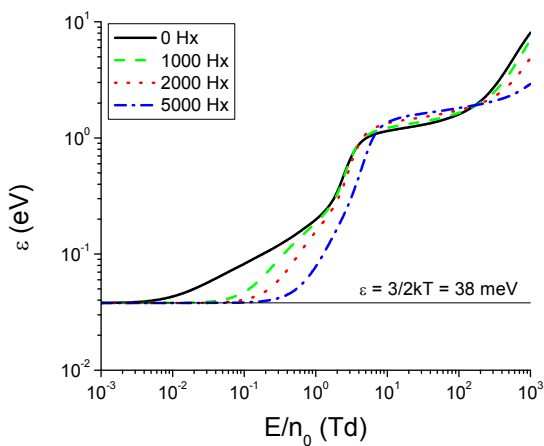
Figure 2. Variation of the mean energy with E/n_0 for a range of B/n_0. Calculations are performed for electrons in mercury vapor.

Acknowledgements

REFERENCES

[1]   G.G. Lister, J.E. Lawler, W.P. Lapatovich and V.A. Godyak, Rev. Mod. Phys. 76, 541 (2004)
[2]   J. P. England and M. T. Elford, Aust. J. Phys. 44, 647 (1991)
[3]   http://magboltz.web.cern.ch/magboltz
[4]   K. Bartschat, 3rd Int. Conf. on Atomic and Molecular Data and their Applications (New York: American Institute of Physics), 2003
[5]   L. J. Kieffer and G. H. Dunn, *Rev.* Mod. Phys. 38, 1 (1966)
[6]   M. T. Elford, Aust. J. Phys. 33, 231 (1980)
[7]   S.B. Vrhovac and Z.Lj. Petrovič, Phys. Rev. E 53, 4012 (1996)

TRANSPORT COEFFICIENCTS FOR ELECTRON SWARMS IN LIQUID ARGON AND LIQUID XENON

I. Simonović[1], Z. LJ. Petrović[1], R.D. White[2] and S. Dujko[1]

[1]*Institute of Physics, University of Belgrade,
Pregrevica 118, 11080 Belgrade, Serbia*
[2]*College of Science & Engineering, James Cook University, Townsville 4810,
Australia*

Abstract. We have developed a Monte Carlo code for the calculation of transport coefficients for electron swarms in non-polar liquids. Transport coefficients for electron swarms in liquid argon and liquid xenon are calculated for $10^{-3} \leq E/n_0 \leq 10^3$ Td. Effects caused by fluctuations of density are neglected. Calculated transport coefficients in liquid phase are compared with those in the gas phase and differences are addressed using physical arguments.

1. INTRODUCTION

Transport of charged particles in liquids is a growing field of research, which addresses some fundamental questions and has many important applications. One of the most attractive applications is the interdisciplinary field of plasma medicine, which requires a detailed description of the behavior of electrons in liquid water and structures found in the living tissue. Additional applications are found in the technology behind the liquid argon and liquid xenon time projection chambers which are designed for detection of cosmic radiation, and search for dark matter particles.

Knowledge of transport coefficients in the liquid phase is also necessary for modeling of electrical discharges in liquids. There were many attempts to calculate transport coefficients of electron swarms in liquids. Cohen and Lekner calculated cross sections for electrons in the liquid phase argon which include coherent scattering effects [1,2]. In addition, they solved the Boltzmann equation using the two term approximation. Atrazhev and Iakubov [3] developed effective cross sections for electrons in liquid argon, krypton and xenon, which, for small energies, depend on density only. Numerical values of these cross sections, at low energies, must be found empirically. They subsequently had performed calculations in the framework of Cohen-Lekner theory and they obtained good agreement with experiment. Boyle et al [4,5] have recently determined *ab initio* differential cross sections for the gas phase argon and xenon by solving Dirac-

Fock scattering equations. Their cross sections are in a good agreement with experiment. They have derived liquid phase cross sections from those for the gas phase. In their work, the Cohen-Lekner procedure was extended to consider multipole polarizabilities and a non-local treatment of exchange. The calculation of transport coefficients in their work was performed using a multi term solution of Boltzmann's equation.

2. THEORETICAL EVALUATION

We have developed a Monte Carlo code for the calculation of transport coefficients of swarms of electrons and positrons in the liquid phase. Elastic scattering is treated in a way which is similar to the method described in the paper by Tattersall et al [6]. This method uses the fact that in the liquid phase mean free paths for the transfer of energy and momentum are different, due to structure effects. This allows the correct representation of the net transfer of momentum and energy, by including additional collisional processes in which only momentum/energy are exchanged. The mean free paths for the transfer of energy and momentum are given by the following equations,

$$\Lambda_0 = \left(n_0 2\pi \int_0^\pi d\chi \sin\chi (1 - \cos\chi) \sigma_{sp}(\varepsilon, \chi) \right)^{-1} , \qquad (1)$$

$$\Lambda_1 = \left(n_0 2\pi \int_0^\pi d\chi \sin\chi (1 - \cos\chi) \sigma_{sp}(\varepsilon, \chi) S(\Delta\vec{k}) \right)^{-1} , \qquad (2)$$

where $\sigma_{sp}(\varepsilon, \chi)$ is the differential cross section for electron scattering on a single molecule, and $S(\Delta\vec{k})$ is the static structure factor. The validity of our code is verified by comparison with benchmark calculations for the Percus Yevick model liquid [6]. Due to the lack of an adequate theory for the treatment of inelastic collisions in liquids, we have implemented the following strategy. For electron-impact ionization, we applied the gas phase cross sections, with thresholds which are reduced to the values suggested in the literature. For excitations, however, we apply two different scenarios. In the first scenario, the excitations are completely neglected. This is the so-called two-level model in which only ground state and conduction band are present [7]. In the second scenario, the gas phase excitations, with thresholds which are lower than the reduced threshold for ionization, are included in our set of cross sections. The remaining excitations are neglected. Fluctuations of density, and effects which are produced by interaction of swarm particles with polar background molecules are not included. Therefore, the applicability of our code is limited to non-polar liquids in which bubble/cluster formation is not appreciable.

3. RESULTS AND DISCUSSIONS

In figure 1 we show the variation of ionization rate coefficient with E/n_0 for electrons in liquid and gas xenon. We see that the ionization rate coefficients for electrons in both liquid scenarios are significantly greater than the corresponding rate coefficient for electrons in the gas phase. This is in part due to the cooling action associated with the inelastic collisions in the gas system, and also due to the modifications of the scattering potential between the gas and liquid phases. Comparing the two liquid scenarios, the ionization rate is greater without excitations. The reason is obvious: the competitive processes that lead to electronic excitation in which electrons lose energy are removed. It should be noted that the difference between ionization rate coefficients for different liquid scenarios is more pronounced for electrons in liquid argon than for electrons in liquid xenon.
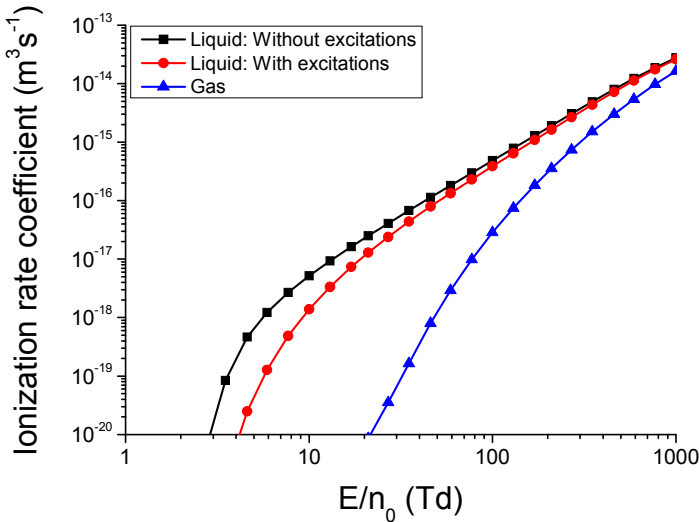
Figure 1. Variation of the ionization rate coefficient with E/n_0 for electrons in liquid and gas xenon.

In figure 2 we show the variation of the bulk drift velocity with E/n_0 for electrons in liquid and gas xenon. In the profile of the bulk drift velocity for electrons in the liquid phase, we observe negative differential conductivity (NDC). NDC is characterized by a decrease in the drift velocity despite an increase in the magnitude of applied electric field. While NDC has been demonstrated in the past to be a consequence of inelastic or non-conservative processes [8], its occurrence here is purely a result of including structure effects. The same effect has been already reported in the literature [3,4], and an analytic prescription for its occurence has been presented [9,10]. For electrons in liquid Xe, NDC occurs for $0.01 \leq E/n_0 \leq 1$ Td. The corresponding range of mean energies is between 0.5 eV and 1.9 eV. In these field (energy) regions an

increase in the field leads to a sharp increase in the momentum-transfer cross section and hence a decrease in drift velocity. Structure induced NDC will be further investigated in our work, by simulating the spatially-resolved transport properties for electron swarms in liquid argon and liquid xenon.
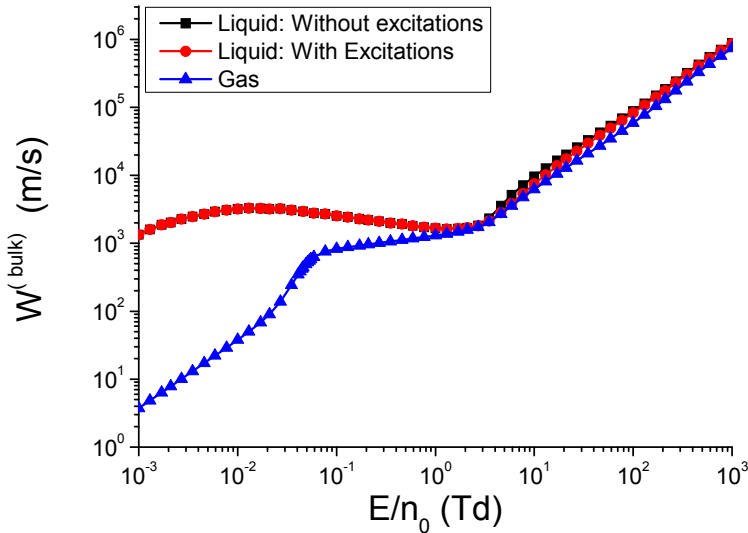

Figure 2. Variation of the bulk drift speed with E/n_0 for electrons in liquid and gas xenon.

Acknowledgements

REFERENCES

[1]   M. H. Cohen and J. Lekner, Phys. Rev. 158, 305 (1967)
[2]   J. Lekner Phys. Rev. 158, 130 (1967)
[3]   V.M. Atrazhev and I.T. Iakubov J. Phys. C 14, 5139 (1981)
[4]   G.J. Boyle et al. J. Chem. Phys. 142, 154507 (2015)
[5]   G.J. Boyle et al. arXiv:1603.04157v1 [physics.atom-ph]
[6]   W. J. Tattersall et al. Phys. Rev. E 91, 043304 (2015)
[7]   V M Atrazhev and E G Dmitriev J. Phys. C 18 (1985) 1205-1215.
[8]   S.B. Vrhovac and Z.Lj. Petrović, Phys. Rev. E 53, 4012 (1996)
[9]   R.D. White et al, Phys. Rev. Lett. 102, 230602 (2009)
[10] G.J. Boyle et al. New J. Phys. 14, 045011 (2012)

TRANSITION OF AN ELECTRON AVALANCHE INTO A STREAMER IN LIQUID ARGON AND LIQUID XENON

I. Simonović[1], Z. LJ. Petrović[1], R.D. White[2] and S. Dujko[1]

[1]*Institute of Physics, University of Belgrade, Pregrevica 118, 11080 Belgrade, Serbia*
[2]*College of Science & Engineering, James Cook University, Townsville 4810, Australia*

Abstract. In this work we investigate transition of an electron avalanche into a streamer, in liquid argon and liquid xenon, using 1.5 dimensional first-order fluid model. Electron transport coefficients used as input in fluid equations are calculated by our Monte Carlo simulation code. Streamer results in the liquid phase are compared to those in the gas phase.

1. INTRODUCTION

Electrical discharges in liquids have many important applications ranging from plasma medicine and water purification to transformer oils and miniaturized chemical analysis of liquid composition. However, detailed understanding of these discharges, which is necessary for their better stabilization and control, remains elusive, due to their complexity and diversity. Bubble formation and evolution, presence of impurities and solvation of electrons in polar liquids can all have significant impact on discharge dynamics in the liquid phase. Moreover, it is not possible to set up some experiments in liquids, the equivalent of which have been very useful for the study of gas discharges. Experiments which investigate electron avalanches in plane parallel geometry, in order to determine electron impact ionization coefficient, are one such example. In the case of liquids, high electric fields necessary for electron impact ionization, would lead immediately to breakdown [1]. This hinders the possibility to experimentally observe the gradual transition of an electron avalanche into a discharge, in a uniform external field. The presence of such experimental difficulties increases the importance of theoretical studies, both for the purpose of developing insight into the relevant physical phenomena, and for designing the future experiments. However, theoretical investigation of the behavior of charged particles in liquids also faces many problems. Many of those problems are related to accurate description of interaction between charged particles and the background molecules. The most recent advancement in the theoretical description of

transport of electrons in the liquid phase is presented in the papers by Boyle et al [2,3].

In this work we study the transition of an electron avalanche into a streamer in liquid argon and liquid xenon, in the presence of a constant external electric field, by employing 1.5 dimensional first-order fluid model. A similar study has been recently performed by Naidis [4] for electrons in liquid cyclohexane, although his simulations were done in point to plane geometry.

2. THEORETICAL EVALUATION

In this work we apply the first-order fluid model which is based on the drift-diffusion equation for electrons (1) and number balance equations for ions (2)

$$\frac{\partial n_e}{\partial t} = \frac{\partial}{\partial x}\left(D\frac{\partial n_e}{\partial x} - wn_e \right) + n_e\left(v_i - v_a\right), \qquad (1)$$

$$\frac{\partial n_p}{\partial t} = n_e v_i, \ \frac{\partial n_n}{\partial t} = n_e v_a, \qquad (2)$$

where n_e, n_p and n_e are number densities of electrons, positive and negative ions, respectively, while w, D, v_i and v_a are drift velocity, longitudinal diffusion coefficient, and rate coefficients for ionization and attachment. The electric field produced by the space charge effects is given as follows

$$E(x,t) = \frac{e}{2\varepsilon_0}\int_0^d \left(\text{sgn}(x-x') - \frac{x-x'}{\sqrt{(x-x')^2 + R_0{}^2}} \right) n_e(x',t)dx'. \qquad (3)$$

Here we assume the cylindrically symmetric 2D charge distribution, where R_0 is a parameter of the model. The equations are solved numerically using 4th order Runge-Kutta method for the integration in time and 2nd order central differences for the spatial derivatives in 1 dimension. This corresponds to the so-called 1.5D dimensional model. Ions are considered stationary, since their velocity is negligible compared to the velocity of electrons for the time scale considered in this work.

Our fluid model is based on the local field approximation and requires the tabulation of electron transport coefficients as a function of the reduced electric field. We have used our Monte Carlo simulation code to calculate electron transport coefficients in both the gaseous and liquid systems. The code we use is similar to the Monte Carlo code developed by Tattersall et al [5]. We apply two scenarios regarding cross sections. In the first scenario excitations are completely neglected (No Excitation scenario) while in the second scenario, they are

approximated by the gas phase excitations (Excitation scenario). A more detailed introduction to our Monte Carlo code, and calculations of transport coefficients is given in our accompanying paper in the Proceedings of this conference. Comparison of the results, obtained by using these two scenarios, gives a rough estimate of the importance of accurate representation of excitations for modeling of streamer dynamics.

3. RESULTS AND DISCUSSION

In figures 1 and 2 we show the temporal evolution of the electron density in gas argon and liquid argon, respectively, for the several instants. The initially Gaussian electron density grows due to the ionization processes; then charge separation occurs in the electric field due to the drift of oppositely charged particles in opposite directions, and the initially homogeneous electric field is distorted; and finally, when the field in the ionized region becomes more and more screened, the ionization is reduced and the typical ionization front profiles of electron and ion densities and of the electric field are established. The initial ionization avalanche is then said to have developed into a streamer.
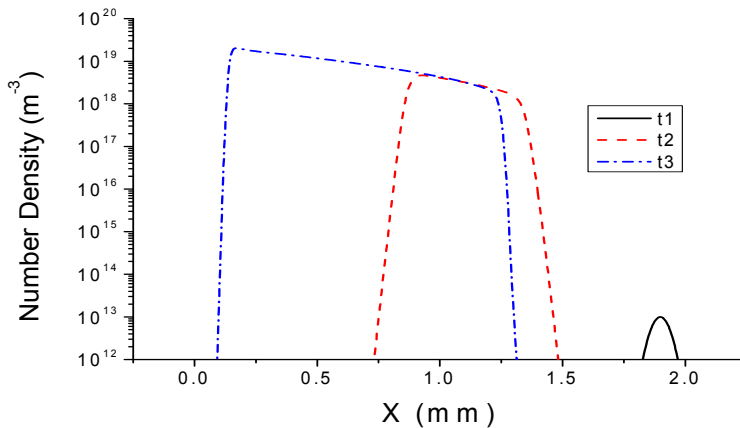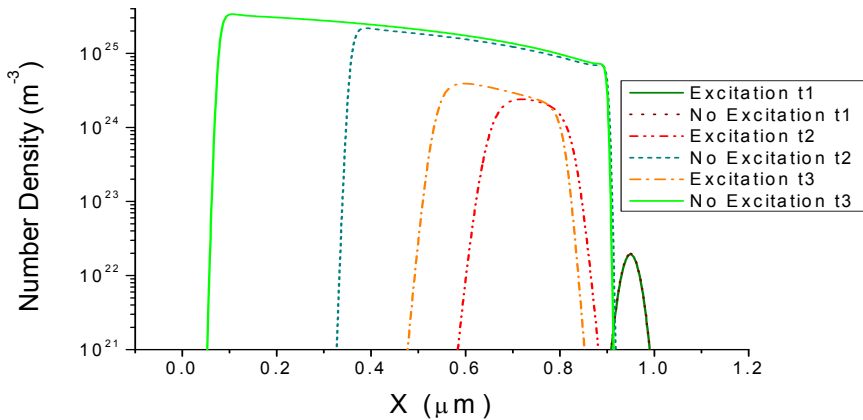

Figure 1. Transition of an electron avalanche into a streamer in the gas phase argon. Time moments t1, t2 and t3 correspond to 0ns, 9.2ns and 12ns respectively. The electric field vector is oriented to the right.

We observe that the transition of an electron avalanche into a streamer occurs much faster, and in a much smaller spatial range, in the liquid than in a gas system. It can also be seen that streamer dynamics is significantly different in the two scenarios regarding the treatment of excitations in the liquid phase. The

transition of an electron avalanche into a streamer is much faster in scenario without excitations, due to the absence of inelastic losses, which would decrease the rate for ionization. Thus, different estimations of the inelastic cross sections could yield great differences in the streamer properties. This suggests that accurate representation of the cross sections for excitations, in the liquid phase, is essential for modeling of discharges in liquids. The same holds for accurate description of cross sections for ionization.

Figure 2. Transition of an electron avalanche into a streamer in the liquid argon. Time moments t1, t2 and t3 correspond to 0ps, 2.3ps and 2.9ps respectively. The electric field vector is oriented to the right.

Acknowledgements

REFERENCES

[1]   N. Bonifaci et al. J. Phys. D: Appl. Phys. **30** (1997) 2717–2725
[2]   G.J. Boyle et al. J. Chem. Phys. **142**, 154507 (2015)
[3]   G.J. Boyle et al. arXiv:1603.04157v1 [physics.atom-ph]
[4]   G.V. Naidis J. Phys. D: Appl. Phys. **48** (2015) 195203
[5]   W. J. Tattersall et al. Phys. Rev. E **91**, 043304 (2015)

SAPP XXII

22nd Symposium on Application of Plasma Processes
and
11th EU-Japan Joint Symposium on Plasma Processing

Book of Contributed Papers

Štrbské Pleso, Slovakia
18-24 January, 2019

Edited by V. Medvecká, J. Országh, P. Papp, Š. Matejčík

NON-EQUILIBRIUM TRANSPORT OF ELECTRONS IN GASES AND LIQUIDS AND ITS APPLICATIONS IN MODELING OF PARTICLE DETECTORS

S. Dujko[1], D. Bošnjaković[1], I. Simonović[1], Z.Lj. Petrović[1,2] and R.D. White[3]

[1]*Institute of Physics, University of Belgrade, Pregrevica 118, 11080 Belgrade, Serbia*
[2]*Serbian Academy of Sciences and Arts, Knez Mihailova 35, 11001 Belgrade, Serbia*
[3]*College of Science and Engineering, James Cook University, 4811 Towsville, Australia*
E-mail: sasa.dujko@ipb.ac.rs

In this work we explore the connections between transport theory of charged particle swarms and modelling of particle detectors used in high-energy physics. In particular, we discuss the physics of resistive plate chambers (RPCs), including the electron transport and propagation of streamers in the gas filled gaps and signal induction in the electrodes. Electron transport coefficients are calculated in a variety of RPC gas mixtures as a function of the reduced electric field, using a Boltzmann equation analysis and Monte Carlo simulations. A 1.5D fluid model with photoionization is developed to investigate how the nature of transport data affects the calculated signals in various RPCs used in high-energy physics experiments at CERN. Electron transport and propagation of streamers are also considered in liquid rare gases. Solutions of Boltzmann's equation and Monte Carlo method for electrons in dilute neutral gases, are extended and generalized to consider the transport processes of electrons in liquid non-polar gases by accounting for the coherent and other liquid scattering effects.

1. Introduction

Studies of charged particle transport processes in gases and liquids in combined electric and magnetic fields are of vital interest in the modelling of non-equilibrium plasmas [1], particle detectors in high-energy physics [2], and numerous other applications. Further optimization and understanding of such applications is dependent on an accurate knowledge of the cross sections for charged particle scattering, transport coefficients and the physical processes involved. In particular, the advanced technology associated with detection of high-energy particles using various types of gaseous and liquid detectors demands the most accurate modelling of charged particle transport. Over the last two decades, there has been a lot of progress in the understanding of charged particle transport in combined electric and magnetic fields [3,4], but this has not always been taken advantage of by physicists working in high-energy physics.

One of the main goals of the present work is to discuss how to bridge the gap between the modelling of particle detectors in high-energy physics and the swarm-plasma nexus that has been thoroughly investigated in our recent reviews [3-5]. We discuss how to adopt the well know techniques in plasma physics, including the numerical solution of Boltzmann's equation [4,5], Monte Carlo simulation technique [6,7] and fluid equation based models [4,8,9], to model the particle detectors in high-energy physics. Indeed, there is a considerable overlap between the two fields and in this work we present the methodology, quantitative and qualitative procedures for modelling of gaseous and liquid detectors of high-energy particles.

2. Modeling of resistive plate chambers

In the first part of this work we discuss the transport of electrons in gases, propagation of streamers and signal induction in resistive plate chambers (RPCs). RPCs are gaseous detectors often used for timing and triggering purposes in many high-energy physics experiments [10-12]. RPCs consist of a single or multiple gas filled gaps between the electrodes of high volume resistivity, such as glass or bakelite, which are used for the suppression of destructive higher current discharges. Despite the simple construction, modeling of RPCs is not a simple task due to many physical processes occurring on different time scales, including primary ionization, charge transport and multiplication, electrode relaxation and signal formation. After passing through the detector, a high energy charged particle

(muon, charged pion and/or kaon, etc.) makes clusters of electrons in the gas, which are drifting towards the anode and multiplied in the process of ionization. Electrons move in a homogeneous electric field which is provided by the high voltage that is applied to the parallel plate electrodes. Depending on the applied electric field strength, geometry and gas mixture, RPCs can be operated in an avalanche or streamer mode. Typical gas mixtures used in RPCs are composed of tetrafluoroethane ($C_2H_2F_4$), iso-butane (iso-C_4H_{10}) and sulfur hexafluoride (SF_6). Each of these gas components has a specific purpose: $C_2H_2F_4$ is a weak electronegative gas with a high primary ionization efficiency while iso-C_4H_{10} is a UV-quencher gas. SF_6, on the other hand, is a strongly electronegative gas, often used in avalanche mode to suppress and control the development of streamers.

The first building block in the modeling of RPCs is the analysis of cross sections for electron scattering in $C_2H_2F_4$, iso-C_4H_{10} and SF_6. In this work, we propose a complete and consistent set of cross sections for electron scattering in $C_2H_2F_4$ [13], while for iso-C_4H_{10} and SF_6 we use the sets of cross sections found in the literature [14,15]. The set of cross sections for C_2H_2F4 is validated through a series of comparisons between swarm data calculated using a multi term theory for solving the Boltzmann equation and Monte Carlo simulations, and the measurements under the pulsed Townsend conditions. Other sets of cross sections for electron scattering in $C_2H_2F_4$ were also used as input in our numerical codes with the aim of testing their completeness, consistency and accuracy. The calculated swarm parameters are compared with measurements in order to assess the quality of the cross sections in providing data for modeling.
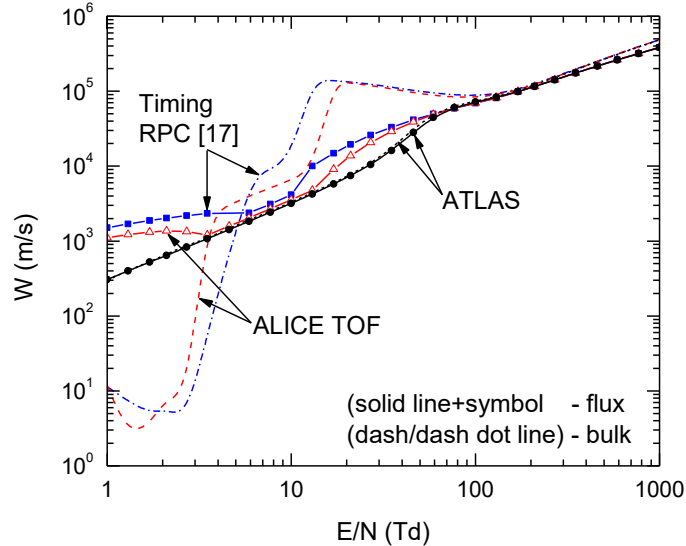

Figure 1. Bulk and flux drift velocities as a function of E/N for gas mixtures used in ATLAS triggering RPC, ALICE timing RPC and timing RPC [17].

In addition to pure gases, we investigate electron transport in various $C_2H_2F_4$/iso-C_4H_{10}/SF_6 mixtures used in RPCs in the ALICE, CMS and ATLAS experiment using a multi term theory for solving the Boltzmann equation and Monte Carlo simulation technique [16]. The duality of transport coefficients, e.g., the existence of two different families of transport coefficients, the bulk and the flux, in the presence of non-conservative collisions, is investigated. A multitude of interesting and atypical kinetic phenomena, induced by the explicit effects of non-conservative collisions, is observed. Perhaps the most striking phenomenon is the occurrence of negative differential conductivity (NDC) in the bulk drift velocity with no indication of any NDC for the flux component in the ALICE timing RPC system. Figure 1 displays the variation of the bulk and flux drift velocities with the reduced electric field for ATLAS triggering RPC (94.7% $C_2H_2F_4$+5% iso-C_4H_{10}+0.3% SF_6), ALICE timing RPC (90% $C_2H_2F_4$+5% iso-C_4H_{10}+5%SF_6) and timing RPC (85% $C_2H_2F_4$+5% iso-C_4H_{10}+10%SF_6) [17]. We systematically study the origin and mechanisms for such phenomena as well as the possible physical implications which arise from their explicit inclusion into models of RPCs.

The Boltzmann equation analysis and Monte Carlo simulations are performed assuming the hydrodynamic conditions and motion of electrons in an infinite gas. The more realistic RPC simulations with implementing gas gap boundaries and primary ionization models have been performed using a Monte Carlo simulation technique with the aim of obtaining the performance characteristics of a timing RPC [18,19]. Timing resolutions and efficiencies are calculated for a specific timing RPC with a 0.3mm gas gap and gas mixture of 85% $C_2H_2F_4$ + 5% iso-C_4H_{10} + 10% SF_6.

In this work we also present our 1.5D fluid model with photoionization to investigate the transition from an electron avalanche into a streamer, propagation of streamers and signal induction in the system of electrodes [20]. In particular, we investigate how the duality of transport coefficients affects the calculated signals of the ATLAS triggering RPC and ALICE timing RPC used at CERN, and also a timing RPC [17] with high SF_6 content. Calculations are performed using the classical fluid model in which both the bulk and flux transport data are used as an input. In addition, we present a new approach in fluid modelling of RPCs based on the equation of continuity and density gradient expansion of the source term. The model requires knowledge of the coefficients in the density gradient expansion of the source term as a function of the reduced electric field. We apply the Monte Carlo method for the determination of these coefficients using the cross sections for electron scattering as a set of input data.
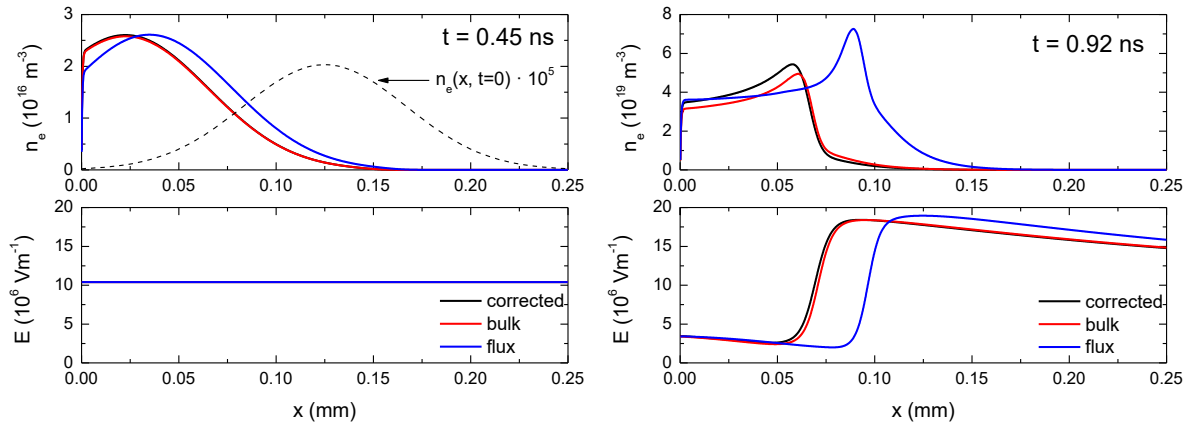

Figure 2. Electron number density and electric field along the gas gap of ALICE timing RPC at $t = 0.45$ ns during avalanche development (left panel), and $t = 0.92$ ns during positive streamer formation (right panel). The external electric field is set to 10.4 MV/m and pressure is 1 atm. Calculations are made using a corrected fluid model and classical fluid model with flux and bulk transport data as an input [20].

As an illustrative example of our fluid simulations of RPCs, in figure 2 we show the development of an electron avalanche and its transition into a positive streamer. On the left panel we show the electron number density and electric field at time instant t = 0.45 ns during avalanche development in ALICE timing RPC. We observe that there are no space charge effects and the profiles obtained using corrected model match very well with those obtained using classical model with bulk data. Comparing avalanches with bulk and flux data, we see that the avalanche with the flux data is slower. This might be expected, since the bulk drift velocity is greater than the flux drift velocity for a given electric field. During the avalanche phase, the induced current grows exponentially with time. However, the exponential rise gradually stops due to both space charge effects and electron absorption at the anode. At about $t = 0.92$ ns, the positive streamers starts to develop (see the right panel in figure 2) and the current rises again while the streamer progress towards the cathode. Since the positive streamer move against the electron drift direction, it requires a source of electrons ahead of the streamer to support the ionization process. This is the reason why photoionization should be included in the modelling. The positive streamer stops at about 1 ns and starts to diminish while the induced current slowly drops to zero. The differences between the profiles shown in the streamer stage are clearly evident. These differences follow from the differences between the bulk and flux drift velocities as well as due to representation of the source term employed in these models.

3. Electron transport and negative streamers in liquid rare gases

In the second part of this work we investigate electron transport, transition from an electron avalanche into a negative streamer, and propagation of negative streamers in liquid rare gases. Liquid rare gases, particularly liquid argon and liquid xenon, are very good detecting media, due to their unique physical properties [21]. The high density and high atomic numbers make them very efficient in stopping penetration radiation, while a significant abundance of many isotopes with different values of nuclear spin enables the study of both spin dependent and spin independent interactions.

In this work we extend and generalize the Monte Carlo method, initially developed for dilute neutral gases, to consider the transport processes of electrons in liquids by accounting for the coherent and other liquid scattering effects [22]. The extended code is tested through a series of benchmark calculations for the Percus-Yevick model. Values and general trends of the mean energy, drift velocity, diffusion tensor and ionization coefficient are calculated for liquid rare gases and compared to the available measurements. The comparison is also made between the liquid and gas phase results. Calculated transport coefficients are then used as an input in fluid simulations of negative streamers, which are realized in both 1D and 1.5D setups. In particular, we investigate how various scenarios of representing the inelastic energy losses in liquid rare gases affect both electron transport and propagation of streamers. We consider three different cases where: (1) the energy losses to electronic excitations are neglected, (2) certain particular excitations are taken into account, and finally (3) all electronic excitations are included. These individual cases are discussed in light of the available spectroscopy and photoconductivity experiments in liquid rare gases [22].
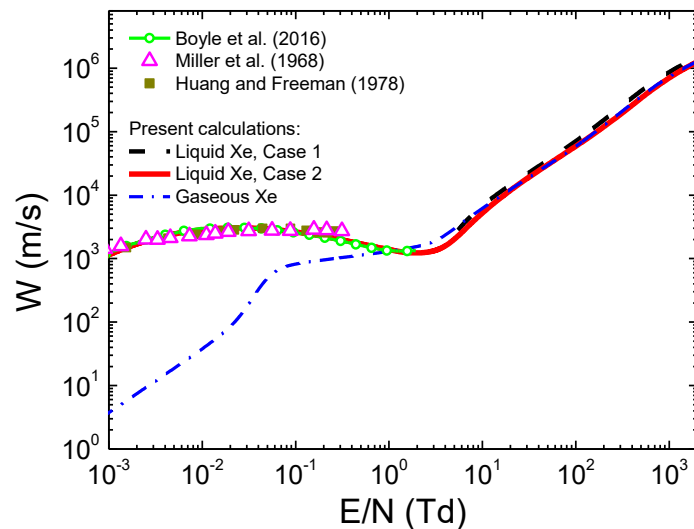

Figure 3. Comparison of the measured drift velocities in liquid xenon (Miler et al. (1968) [23] and Huang and Freeman (1978) [24] with our theoretical calculations. The theoretically calculated drift velocities in liquid xenon, include the Boltzmann equation results of Boyle et al. (2016) [25] and the present calculations obtained in Monte Carlo simulations. The bulk drift velocity of electrons in gaseous xenon is also shown in this figure for comparison [22].

In figure 3 we show the variation of the bulk drift velocity with E/N for electrons in liquid xenon. Our Monte Carlo calculations over a wide range of E/N are compared with those obtained from the numerical solution of Boltzmann's equation for the lower values of E/N, as well as with the available measurements. The Boltzmann equation results for gaseous xenon are also included in figure 3. We consider the following two cases for representing the inelastic energy losses: (1) no electronic excitations, and (2) all electronic excitations are included. The cross sections detailed in [22,25] are used in the present study. We observe that for the lower values of E/N (lower than approximately 1

Td), the drift velocity in the liquid phase significantly exceeds the drift velocity in the gas phase. This is a clear sign of the significant reduction of the rate of momentum transfer of the lower energy electrons occurring in liquids. This reduction follows from the modification of the scattering potential and the coherent scattering effects. As a consequence, the electric field accelerates electrons more efficiently in liquid xenon than in the gas phase. For the higher values of electric fields, however, this effect is reduced, as the scattering of a high energy electron on a xenon atom is significantly less perturbed by the surrounding liquid. Thus, we see that the drift velocity decreases between approximately 0.02 and 2 Td. The reduction of the drift velocity with increasing E/N is the well known phenomenon of negative differential conductivity (NDC). In the gas phase, NDC is caused by inelastic and/or non-conservative collisions, but in liquid xenon this is structure induced phenomenon. We observe that our values of the drift velocity are close to those predicted in the experiments of Miler et al. [23] and Huang and Freeman [24]. However, as we can see NDC is not observed in the experiments.
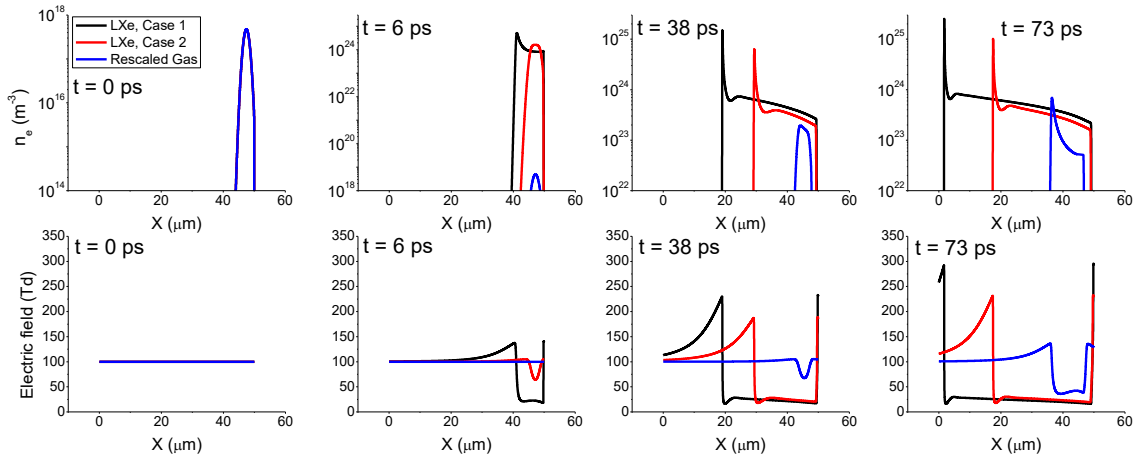
Figure 4. The formation and propagation of negative streamers in liquid xenon for E/N=100 Td, The presented results are determined by assuming the following two cases for representing the inelastic energy losses: (1) no electronic excitations (Case 1), and (2) all electronic excitations are included (Case 2). Streamers propagate from the right to the left.

In figure 4 we show the formation and propagation of a negative streamer in liquid xenon. In the same figure we include the simulation in which the transport data for electrons in the gas phase are scaled to liquid density (Rescaled gas). The initial condition for both electrons and positive ions is a Gaussian, which is positioned near the cathode [22]. In liquid xenon, positive charge carriers are holes, with a mobility that is several orders of magnitude less than the electron mobility. Thus, the positive holes are assumed to be stationary, on the time scales relevant for this study.

Comparing streamers in gases and liquids, we observe that the transition from an electron avalanche and formation of a negative streamer occur much faster in liquid xenon. We also observe that the formation and propagation of a streamer are reduced by including the inelastic energy losses in the model (Case 2). The number density of electrons in both the streamer head and the streamer interior is also reduced. Other streamer features in liquid xenon are similar as those in the gas phase. We see that the electron number density has a sharp peak in the streamer head where the electric field is significantly enhanced by the space charge effects. In the streamer interior, however, the number density of electrons is reduced. The reason is twofold: (1) As electric field decreases, the contribution of ionization is less pronounced, and (2) the recombination of electrons and positive holes is enhanced.

4. References

[1] Makabe T and Petrović Z Lj 2014 *Plasma Electronics: Applications in Microelectronic Device Fabrication* (New York: CRC Press).
[2] Rolandi L, Riegler W and Blum W 2008 *Particle Detection with Drift Chambers* (Berlin: Springer).
[3] Petrović et al. 2009 *J. Phys. D: Appl. Phys.* **42** 194002.
[4] White R D, Robson R E, Dujko S, Nicoletopoulos P and Li B 2009 *J. Phys. D: Appl. Phys.* **42** 194001.
[5] Dujko S, White R D, Petrović Z Lj and Robson R E 2011 *Plasma Source Sci. Technol.* **20** 024013.
[6] Dujko S, White R D and Petrović Z Lj 2008 *J. Phys. D: Appl. Phys.* **41** 245205.
[7] Dujko S, Raspopović Z M and Z.Lj. Petrović 2005 *J. Phys. D: Appl. Phys.* **38** 2952.
[8] Boyle G J, White R D, Robson R E, Dujko S and Petrović Z Lj 2012 New J. Phys. **14** 045011.
[9] Dujko S, Markosyan A H, White R D and Ebert U 2013 *J. Phys. D: Appl. Phys.* **46** 475202.
[10] The ALICE Collaboration 2008 *J. Instrum.* **3** S08002.
[11] The ATLAS Collaboration 2008 *J. Instrum.* **3** S08003.
[12] The CMC Collaboration 2008 *J. Instrum.* **3** S08004.
[13] Šašić O, Dupljanin S, de Urquijo J and Petrović Z Lj 2013 *J. Phys. D: Appl. Phys.* **46** 325201.
[14] Itoh H, Matsumura T, Satoh K, Date H, Nakao Y and Tagashira H 1993 *J. Phys. D: Appl. Phys.* **26** 1975.
[15] Biagi S, MAGBOLTZ – Program to compute electron transport parameters in gases, v.2, CERN.
[16] Bošnjaković D, Petrović Z Lj White R D and Dujko S 2014 *J. Phys. D.* **47** 435203.
[17] Lopes L, Fonte P and Mangiarotti A 2012 *Nucl. Instrum. Methods A* **661** S194.
[18] Bošnjaković D, Petrović Z Lj and Dujko S 2014 *J. Intrum.* **9** P09012.
[19] Petrović Z Lj, Simonović I, Marjanović S, Bošnjaković D, Marić D, Malović G and Dujko S 2017 *Plasma Phys. Control. Fusion* **59** 014026.
[20] Bošnjaković D, Petrović Z Lj and Dujko S 2016 *J. Phys. D: Appl. Phys.* **49** 405201.
[21] Aprile E and Doke T 2010 *Rev. Mod. Phys.* **82** 2053.
[22] Simonović I, Garland N A, Bošnjaković D, Petrović Z Lj, White R D and Dujko S, accepted manuscript in Plasma Sources Sci. Technol, doi: https://doi.org/10.1088/1361-6595/aaf968
[23] Miller L S, Howe S, and Spear W E 1968 *Phys. Rev.* **166** 871.
[24] Huang S S and Freeman G R 1978 *J. Chem. Phys.* **47** 1355.
[25] Boyle G J, McEachran R P, Cocks D G, Brunger M J, Buckman S J, Dujko S and White R D 2016 *J. Phys. D: Appl. Phys.* **49** 355201

Electron transport and propagation of negative streamers in liquid-phase xenon

Saša Dujko
Institute of Physics
University of Belgrade
Belgrade, Serbia
sasa.dujko@ipb.ac.rs

Ilija Simonović
Institute of Physics
University of Belgrade
Belgrade, Serbia
ilija.simonovic@ipb.ac.rs

Danko Bošnjaković
Institute of Physics
University of Belgrade
Belgrade, Serbia
dbosnjak@ipb.ac.rs

Zoran Lj. Petrović
Institute of Physics
University of Belgrade and Serbian
Academy of Sciences and Arts
Belgrade, Serbia
zoran@ipb.ac.rs

Ronald White
College of Science and Engineering,
James Cook University
Townsville, QLD, Australia
ronald.white@jcu.edu.au

Abstract—**The Monte Carlo method, initially developed for charged particle swarms in neutral dilute gases, is extended and generalized to investigate the transport processes of electrons in liquid-phase noble gases by accounting for the coherent and other liquid scattering effects. Electron transport coefficients, including the electron mobility, diffusion coefficients and ionization coefficient, are calculated as a function of the reduced electric field in liquid-phase xenon. Calculated transport coefficients are then used as an input in the classical fluid model to investigate the dynamics of negative streamers. Using the language of the contemporary kinetic theory of plasma discharges, in the present work among many important points, we investigate how various representations of inelastic energy losses in inelastic scattering events affect the electron transport and the macroscopic streamer properties.**

Keywords—Monte Carlo, liquid noble gases, transport coefficients, streamers, fluid models

I. INTRODUCTION

Understanding of the behavior of free electrons under the influence of electric field in liquids is of interest in both fundamental physics and in numerous technological applications. Those applications include the interdisciplinary field of plasma medicine [1], liquid dielectrics [2], plasma-water purification [3] and liquid particle detectors [4]. In particular, liquid-phase noble gases are used in the technology of the time-projection chambers, which are designed for detection of cosmic radiation and neutrinos [4], as well as in the search for dark matter particles [4]. Further optimization of such applications requires an accurate understanding of electron transport coefficients, streamer properties and the physical processes involved.

In our previous studies, we investigated the elastic scattering of electrons from liquid-phase argon [5] and liquid-phase xenon [6]. Electron transport coefficients were calculated in the sub-excitation energy region, e.g., for those values of the reduced electric fields, E/n_0, (where E is the electric field strength and n_0 is the neutral atom density) for which the mean energies are well below the first inelastic threshold. More recently, we have investigated the way in which electron transport coefficients are influenced by various representations of the inelastic energy losses in liquid-phase xenon with the special emphasis on the explicit effects of ionization (or interband transition having in mind that the electrons are quasi-free particles in liquid xenon) [7].

We have also discussed the fluid modeling methods with the aim of understanding electron transport and streamer propagation across the gas-liquid interfacial regions [8]. In this paper, as a part of our ongoing investigations of electron transport in liquid-phase noble gases in an electric field, we study the transition from an electron avalanche into a negative streamer ionization front and its propagation in liquid xenon. Calculations are performed using a fluid model in local field approximation. Using the electron scattering cross sections for both gas and liquid xenon, transport coefficients of electrons are calculated in Monte Carlo simulations to serve as input data for a fluid model used in this study.

We begin this study by briefly reviewing the basic elements of the fluid theory used to simulate negative streamers in liquid xenon in section 2. In section 3.A, we present the electron transport coefficients as a function of the reduced electric field. In the same section, we briefly discuss the cross sections for electron scattering in liquid xenon and the basic elements of the Monte Carlo method used for calculating electron transport coefficients. The development of negative streamers without formation of expanding gaseous filaments is discussed in section 3.B. In section 4 we present our conclusions and recommendations for future work.

II. THEORETICAL METHOD

Simulations of negative streamers in liquid xenon are performed by using the classical fluid model. In this model the electron flux is obtained by assuming a steady-state of the momentum balance equation, and that the electron energy of the field-directed motion is much greater than the thermal contribution [9]. The generalized one-dimensional continuity equation for the electron number density is

$$\frac{\partial n_e(x,t)}{\partial t} = \frac{\partial}{\partial x}\left(D_L \frac{\partial n_e(x,t)}{\partial x} + \mu_e n_e(x,t)E\,\mathrm{sgn}(E)\right) + \left(\nu_i - \beta n_p(x,t)n_e(x,t)\right), \quad (1)$$

where $n_e(x,t)$ and $n_p(x,t)$ are the number densities of electrons and positive holes, respectively, which are functions of the coordinate x and time t. In this equation D_L and μ_e are the longitudinal diffusion coefficient and the electron mobility, respectively, E is the electric field,

oriented along the x-axis, while ν_i and β are the ionization rate and the recombination coefficient, respectively.

In addition to the electron continuity equation (1), the time evolution of the number density of positive holes is described by the number balance equation

$$\frac{\partial n_p(x,t)}{\partial t} = \left(\nu_i - \beta n_p(x,t) \right) n_e(x,t) \,, \tag{2}$$

where transport of positive holes has been neglected over the transient time scales considered in this study, owing to the significantly reduced mobility and diffusion of positive holes in liquid xenon [10].

The model is realized in a 1.5 dimensional (1.5D) setup. Thus, the total electric field in the system is evaluated as the sum of the uniform external electric field and the electric field due to space charge:

$$E(x,t) = E_0 + \frac{e}{2\epsilon_0\epsilon_r} \int_0^l \left(\operatorname{sgn}(x-x') - \frac{x-x'}{\sqrt{(x-x')^2 + R_0^2}} \right) \left(n_p - n_e(x',t) \right) dx' \,, \tag{3}$$

where E_0 is the external electric field, e is the elementary charge, ϵ_0 and ϵ_r are the vacuum permittivity and the relative permittivity, respectively, and l is the length of the system. In this model, the space charge is contained inside cylinder with radius R_0 and the charge density varies along the axial direction only.

The recombination coefficient is given by the scaled Debye formula

$$\beta = \xi \beta_D = \xi \frac{4\pi e \mu_e}{\epsilon_0 \epsilon_r} \,, \tag{4}$$

where β_D is the Debye recombination coefficient and ξ is the scaling factor which is taken to be 0.1 [11].

The above fluid equations are closed, assuming the local field approximation. According to this approximation the input terms, including μ_e, D_L, ν_i and β are assumed to be functions of the local instantaneous electric field. In the numerical implementation of our fluid model, the spatial discretization is performed by using the second order central finite difference, while the fourth order Runge–Kutta method is used for the integration in time.

III. RESULTS AND DISCUSSION

A. Transport coefficients of electrons in liquid xenon

In case of electrons, the transport data needed for the solution of fluid equations (1) and (2) are μ_e, D_L, and ν_i. These electron transport data are calculated by using the Monte Carlo method. The Monte Carlo method, initially developed for charged particle swarms in neutral dilute gases [12], has been recently extended and generalized by including three effective scattering processes, which give a good representation of the coherent scattering of low energy electrons in non-polar liquids [7]. The validity of our Monte Carlo method has been tested by calculating the transport properties of electrons in the Percus Yevick model liquid. It was found that our results are in an excellent agreement with those calculated by Tattersall et al [13].

In order to account for excitations in liquid xenon, the set of inelastic atomic excitation cross sections of the Hayashi database was modified to form a set of excitation cross sections for intermediate excitons in liquid state. For example, the intermediate $n = 1 \left[\Gamma\left(\frac{3}{2}\right) \right]$ and $n' = 1 \left[\Gamma\left(\frac{1}{2}\right) \right]$

excitons have been observed at 8.2 eV and 9.45 eV, respectively [14]. The former has parentage in the excited atomic $6s'[3/2]_1$ state, while the latter has parentage in the $6s'[1/2]_1$ state. As these intermediate excitons have a unique parentage, via the isolated atom's excited states, we thus approximate the cross sections for intermediate exciton excitations by cross sections of the corresponding atomic excitations. Likewise, the cross section for interband transitions is approximated by the cross section of the electron impact ionization, from the Hayashi's cross section set. However, the cross section is shifted by 2.1 eV, so that the threshold of the ioization is 9.22 eV in liquid xenon. This value corresponds to the $\Gamma\left(\frac{3}{2}\right)$ band gap in liquid xenon, which is the energy difference between the uppermost valence and the bottom of the conduction band. For simplicity, in the rest of this work the interband transition and the inelastic collisions will be referred to as ionization and excitations, respectively. For more details on the band structure and cross sections for electron scattering in liquid xenon, the reader is referred to [7].

In the present calculations, we cover a range of reduced electric fields between 10^{-3} and 10^3 Td (1 Td = 10^{-21} Vm^2). The number density of xenon atoms is 1.4×10^{28} m^{-3}, while the temperature of the background liquid is 163 K. In our simulations, we usually follow 10^6 electrons except in the limit of the lowest values of E/n_0. Due to numerous elastic collisions in which only a fraction of the initial electron energy is transferred to a heavy xenon atom, the efficiency of energy transfer is very low in the limit of the lowest E/n_0. As a consequence, the relaxation of energy is very slow and requires a large computation time. In order to optimize the simulation speed, the simulations were usually begun with 10^4 electrons and after the relaxation to the steady state the electron swarm scaled up to 10^6 electrons. The details of this procedure are given elsewhere [7].

In Fig. 1 we show the dependence of the electron mobility on E/n_0. It should be noted that the density normalized mobility $n_0\mu$ and density normalized diffusion coefficients n_0D_L and n_0D_T shown in Fig. 2, are not independent of the neutral atom density [15]. These transport coefficients are given as a function of E/n_0, so that any linear dependence on density (as occurs in the dilute-gas limit) has been removed. Thus, we have a true comparison of the gas and liquid phases.

Calculations are performed assuming the following two scenarios: (*i*) no electronic excitations (case 1), and (*ii*) all electronic excitations from the gas-phase are included (case 2). Both the bulk and flux mobility components are shown. The bulk transport coefficients, are associated with the swarm's centre of mass transport and spread about its centre of mass. In Monte Carlo simulations, the bulk transport coefficients may be determined from the rate of changes of the appropriate averages of the positions of the electrons in the configuration space. The flux transport coefficients should be interpreted in terms of averages over the ensemble in velocity space. For example, the flux mobility is associated with the average velocity of the ensemble in the swarm. In liquid and gas xenon, these two sets of transport coefficients are equal in the absence of ionization.

For comparison, the theoretical [6,7] and experimental values [16] of mobility are displayed at the same figure, along with the mobility in gaseous xenon.
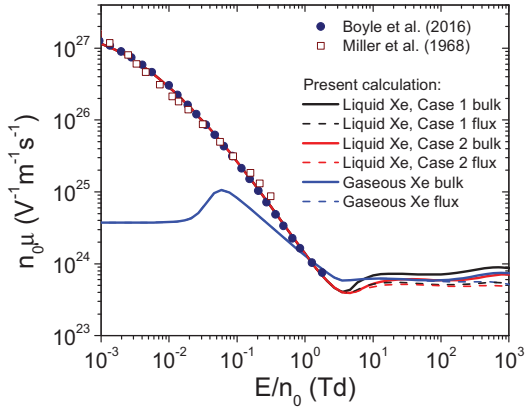
Fig 1. Variation of the electron mobility with E/n_0. Our Monte Carlo results, for liquid and gaseous xenon, are compared with the measurements (Miller et al. (1986)) and theoretical calculations (Boyle et al. (2016)). It should be noted that all three dashed lines for the flux properties emerge from the solid lines of the same colour above 10 Td.
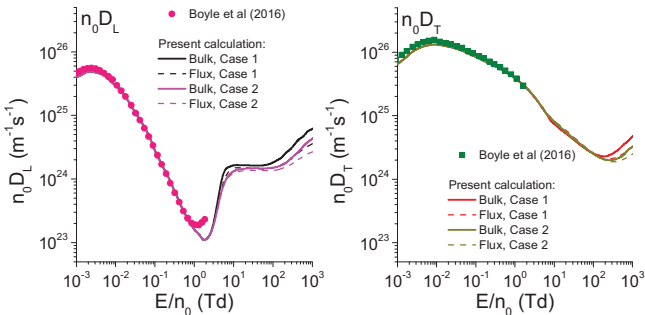

Fig. 2. Variation of the longitudinal (left panel) and transverse diffusion coefficients with E/n_0. Our Monte Carlo results are compared with the theoretical calculations (Boyle et al. (2016)).

The agreement between our Monte Carlo results and those obtained from a multi term solution of the Boltzmann equation is excellent.

For the lower values of E/n_0 we observe that the electron mobility in the liquid phase exceeds the mobility in the gas phase by more than two orders of magnitude. This is a clear sign of the reduction of the rate of momentum transfer of the lower energy electrons in liquid xenon. The lowering of the rate of momentum transfer follows from the modification of the scattering potential and the coherent scattering effects. Due to these liquid scattering effects, the electric field accelerates electrons more efficiently in liquid xenon than in gaseous xenon, which in turn leads to a significant enhancement of the electron mobility as compared to the gas xenon.

In Fig. 2 we show the variation of the longitudinal and the transverse diffusion coefficient as a function of E/n_0. The agreement between our Monte Carlo results and those evaluated from the solution of Boltzmann's equation for the lower values of E/n_0 is very good. For the higher values of E/n_0, we observe that the diffusion coefficients are reduced with an increase of the number of excitations used in the modeling. Due to the explicit effects of ionization, the bulk values of both n_0D_L and n_0D_T are greater than the corresponding flux values.

In Fig. 3 we show the variation of the ionization rate coefficient with E/n_0. We observe that the ionization rate is monotonically increasing function of E/n_0 for both the liquid- and gas-phase xenon. We also observe that the ionization rate is increased by reducing the number of
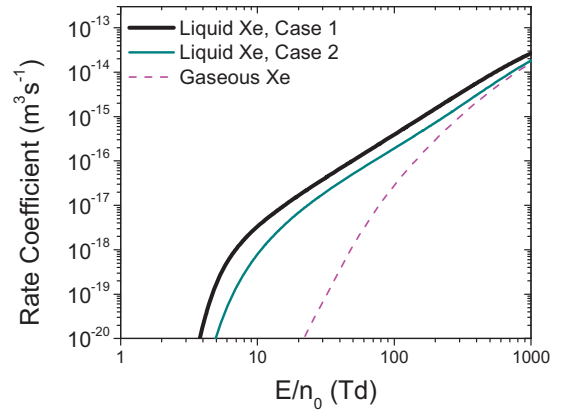

Fig. 3. Variation of the ionization rate coefficient with E/n_0. Calculations in gaseous xenon are compared with those in liquid xenon.

excitations. Likewise, the ionization coefficient in liquid xenon is significantly greater than the ionization coefficient in gaseous xenon. This can be expected due to the reduction of the threshold for ionization in the liquid phase. In addition, electrons can lose a significant amount of energy in a wide range of inelastic scattering processes at energies lower than the threshold energy for ionization in gaseous xenon. Likewise, there is a far lower number of inelastic scattering processes with thresholds which are lower than the threshold for ionization in the liquid phase compared to the gas phase.

B. Negative streamer fronts in liquid xenon

In Fig. 4 we show the formation and propagation of a negative streamer under the influence of the externally applied electric field of 77 Td. The initial Gaussian is positioned in the close vicinity of the cathode. The electric field is oriented to the right, so the negative fronts propagate to the left. The initial densities of electrons and positive holes are equal reflecting the macroscopic neutrality of a plasma. In addition, these densities are selected in such way that the space charge effects are negligible. The values of l and R_0 are set to 5×10^{-5} m and 1×10^{-5} m, respectively. The particular value of R_0 is chosen as an educated guess taking into account the width of the initial distribution and the spreading due to transverse diffusion. The length of the system l is determined by the requirement that the streamer velocity relaxes to a stationary value. The simulation in the gaseous xenon employs transport data for electrons for the gas phase scaled to the liquid density. We employ the bulk transport coefficients as an input in fluid simulations of negative streamer fronts in both the liquid and gas phases.

In the absence of gas filaments and trapping of electrons in the density fluctuations, the general features of the streamer profiles in the liquid xenon are the same as those of the streamers in gases [7]. We observe that the streamer front caries an overshoot of electrons, generating a thin space charge layer that screens the electric field in the streamer interior behind the front. In this screened interior region, the density of charge is not constant. The electron number density and the positive hole density are further reduced due to the recombination of electrons and positive holes. A similar decrease in the electron number density in the streamer interior and behind the front, is observed for streamers in electronegative gases, where electron attachment consumes the lower energy electrons. We observe that the streamer formation as well as streamer
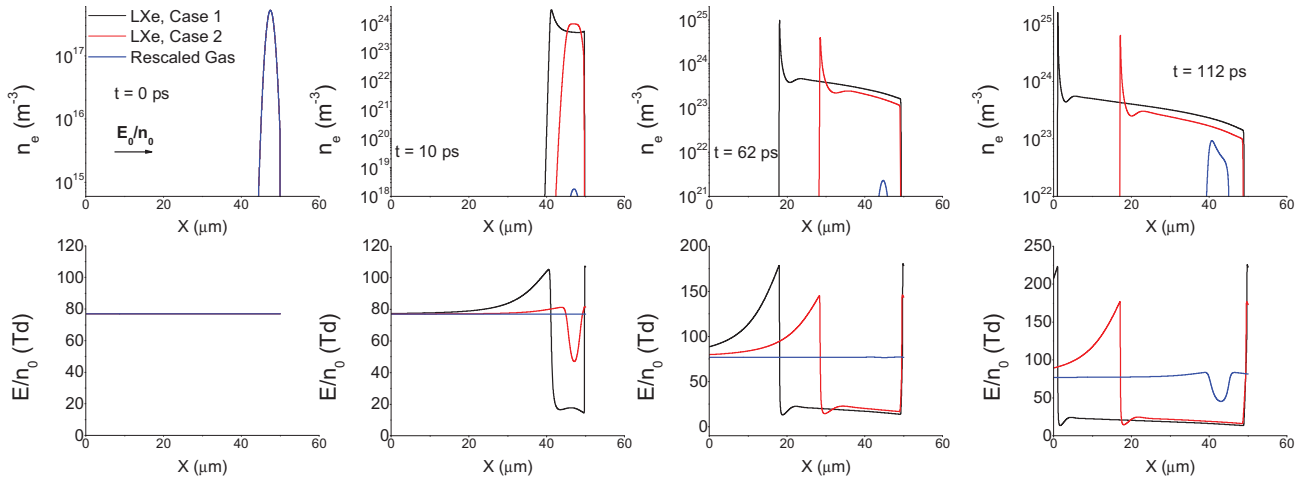
Fig. 4. The formation and propagation of a negative streamer in liquid xenon for $E/n_0 = 77$ Td. Here n_e refers to the electron number density while E/n_0 refers to the reduced resultant electric field.

propagation are greatly influenced by the number of excitations in the model. For example, the streamer velocity and the electron number density in the streamer interior are increased by reducing the number of excitationsIt can also be observed that the transition from an electron avalanche into a streamer is much slower in the case of the rescaled gas than in the liquid phase.

IV. CONCLUSION

Using a Monte Carlo simulation technique and 1.5 dimensional classical fluid model, we have investigated the influence of inelastic energy losses on both the transport properties of electrons and dynamics of negative streamers in liquid xenon. The cross sections for inelastic scattering and interband transitions of electrons in liquid xenon are approximated by using the cross sections for electron scattering on an isolated xenon atom. The *ab initio* cross section for elastic scattering in liquid xenon is taken and adopted in order to include the effects of coherent scattering and atomic potential screening which are critical for low-energy electron scattering. Calculations in the liquid phase are augmented by those in the gas phase. It is found that, above approximately 1 Td there is a significant difference between the values of transport properties determined by employing different representations of the inelastic energy losses. The electron mobility and diffusion coefficients, as well as the ionization rate coefficient are reduced with increasing number of excitations in the model. Likewise, it is found that the streamer properties, including the streamer velocity, the ionization degree in the streamer interior and the distribution of electric field strongly depend on the number of excitations which are included in the model.

The present work will be extended in a near future by investigating the propagation of positive and negative streamers in a point-to-plane geometry. We will also consider the influence of density fluctuations and gas filaments, as well as trapping of electrons in these structures, on both the electron transport and the streamer dynamics.

REFERENCES

[1] M. G. Kong, G. Kroesen, G. Morfill, T. Nosenko, T. Shimizu, J. van Dijk and J. L. Zimmermann, "Plasma medicine: an introductory review," New J. Phys. vol. 11, 115012, 2009.

[2] V. Y. Ushakov, V. F. Klimkin and S. M. Korobeynikov, "Impulse Breakdown of Liquids," (Berlin: Springer), 2007.

[3] B. Jiang, J. Zheng, S. Qiu, M. Wu, Q. Zhang, Z. Yan and Q. Xue, "Review on electrical discharge plasma technology for wastewater remediation," Chem. Eng. J. vol. 236, 348, 2014.

[4] E. Aprile and T. Doke, "Liquid xenon detectors for particle physics and astrophysics, " Rev. Mod. Phys. vol. 82, 2053, 2010.

[5] G. J. Boyle, R. P. McEachran, D. G. Cocks and R. D. White, "Electron scattering and transport in liquid argon, " J. Chem. Phys. vol. 142, 154507, 2015.

[6] G. J. Boyle, R. P. McEachran, D. G. Cocks, M. J. Brunger, S. J. Buckman, S. Dujko and R. D. White, "*Ab initio* electron scattering cross-sections and transport in liquid xenon, " J. Phys. D: Appl. Phys. vol. 49, 355201, 2016.

[7] I. Simonović, N. A. Garland , D. Bošnjaković , Z. Lj. Petrović, R. D. White and S. Dujko, "Electron transport and negative streamers in liquid xenon, " Plasma Sources Sci. Technol. vol. 18, 015006, 2019.

[8] N. A. Garland, I. Simonović, G. J. Boyle, D. G. Cocks, S. Dujko and R. D. White, "Electron swarm and streamer transport across the gas–liquid interface: a comparative fluid model study, " Plasma Sources Sci. Technol. vol. 27, 105004, 2018.

[9] S. Dujko, A. H. Markosyan, R. D. White and U. Ebert, "High-order fluid model for streamer discharges: I. Derivation of model and transport data," J. Phys. D: Appl. Phys. vol. 46, 475202, 2013

[10] O. Hilt and W. F. Schmidt, "Positive hole mobility in liquid xenon, " Chem. Phys. vol. 183, 147, 1994.

[11] N. Y. Babaeva and G. V. Naidis, "Modeling of positive streamers in liquid argon, " Tech. Phys. Lett. vol. 25, 91, 1999.

[12] S. Dujko, Z. M. Raspopović and Z. Lj. Petrović, "Monte Carlo studies of electron transport in crossed electric and magnetic fields in CF$_4$, " J. Phys. D: Appl. Phys. vol. 38, 2952, 2005.

[13] W. J. Tattersall, D. G. Cocks, G. J. Boyle, S. J. Buckman and R. D. White, "Monte Carlo study of coherent scattering effects of low-energy charged particle transport in Percus-Yevick liquids, " Phys. Rev. E vol. 91, 043304, 2015.

[14] P. Laporte, J. L. Subtil, U. Asaf, I. T. Steinberger and S. Wind, "Intermediate and Wannier Excitons in Fluid Xenon, " Phys. Rev. Lett. vol. 45, 2138, 1980.

[15] Y. Sakai, "Quasifree electron transport under electric field in nonpolar simple-structured condensed matters," J. Phys. D: Appl. Phys. vol. 40, R441, 2007.

[16] L. S. Miller, S. Howe and W. E. Spear, "Charge Transport in Solid and Liquid Ar, Kr, and Xe, " Phys. Rev. vol. 166, 871, 1968.

EMS

XIX International Symposium on Electron-Molecule Collisions and Swarms

Book of Abstracts

POSMOL 2015

17-20 July 2015, LISBOA, PORTUGAL

Swarms as an exact representation of weakly ionized gases

Zoran Lj. Petrović[1], Saša Dujko[1], Dragana Marić[1], Danko Bošnjaković[1], Srđan Marjanović[1], Jasmina Mirić[1], Olivera Šašić[1], Snježana Dupljanin[1], Ilija Simonović[1], Ronald D. White[2]

[1]Institute of Physics University of Belgrade POB 68 11080 Zemun Serbia

[2]James Cook University of Northern Queensland, Townsville QL Australia

Zoran@ipb.ac.rs

Often swarms are regarded as idealized ensembles of charged particles that may be realized in specialized experiments to provide accurate transport coefficients, which after some analysis, yield "complete" sets of cross sections and accurate representations of non-equilibrium electron energy distribution function (EEDF) for a given *E/N*. Generally it is believed nowadays that swarms are just a tool for modeling non-equilibrium (low temperature) plasmas, as some kind of an interface through which atomic physics enters plasmas. In this review we shall show some new results that extend that picture into several directions:

- New results for the cross sections in systems where information from beam experiments and binary collision theories are insufficient such as $C_2H_2F_4$ that is commonly used as a cooling gas in modern refrigerators and air conditioners, but also it is used in particle detectors and has a potential for plasma processing applications.

- Ionized gases where swarms are exact representation of the system. Those include weakly ionized gases such as atmosphere, gas breakdown, afterglow (after the breakup of the ambipolar field), steady state Townsend regime of discharges, conduction of electricity through gases, interaction of secondary electrons produced by high energy particles with the gas or liquid background and many more. A special example will be modeling of Resistive Plate Chambers, the most frequently used gas phase detectors of elementary particles in high energy experiments.

- Swarm studies provide best insight into non-hydrodynamic (or as plasma specialists call it non-local) development of the ionized gas. It is not only that simulations are simple but also some of the accurate experiments operate in such conditions and thus allow testing of such theories. One such example are the Franck Hertz oscillations. Temporal and spatial relaxation of properties of ensembles to the final distribution belong to this group as well and are of interest for a number of positron applications and trapping in general.

- Fluid models when applied to swarms provide a good way to test the fluid models as used in more general plasmas. This has yielded the need to generalize fluid equations and extend them to a one step further while using a higher order transport coefficients.

- Finally we shall address the open issues for transport theorists and atomic and molecular collision population in the attempt to represent transport of electrons, positrons and other particles in liquids, especially in water that has a strong dipole moment. Hydrated electrons and positrons are the actually particles of interest for modeling these particles in the human tissue.

As an interface between atomic and molecular collision physics on a lower phenomenological (but deeper) level and plasmas on a higher (but less fundamental) level swarm physics has the responsibility of providing plasma physics with its intellectual basis and fundamental importance. It is how we combine the building blocks of atomic and molecular physics, transport theory and other relevant elementary processes that will define generality of the conclusions about non-equilibrium plasmas that are all different and require a special approach.
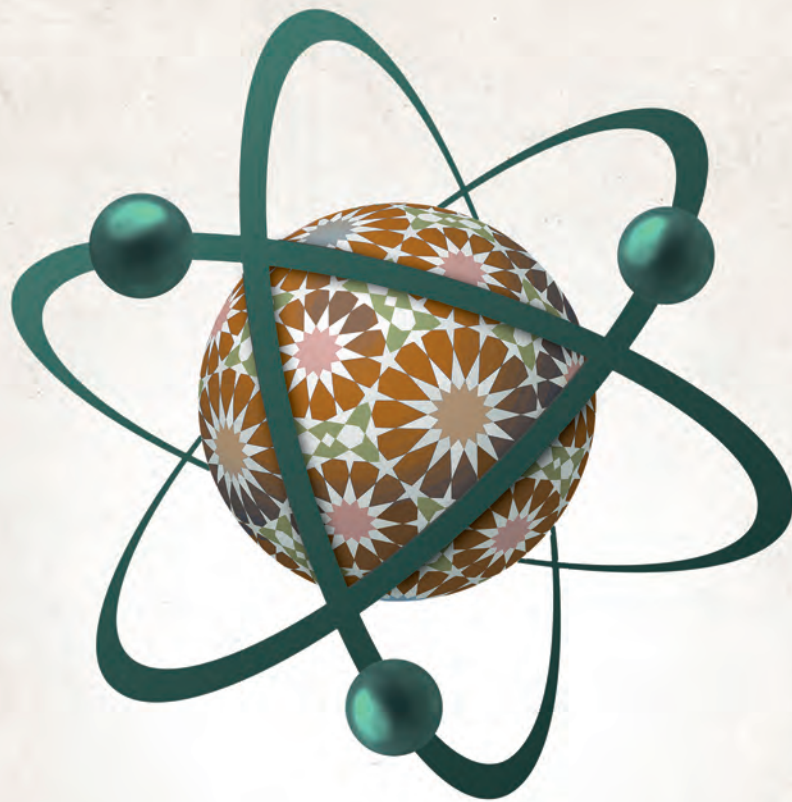
The models that we provide here are simple, yet realistic and real systems that may be described by swarm models and that may be regarded as low ionization limits of some more complex non-equilibrium plasmas.

ICPEAC 2015

XXIX INTERNATIONAL CONFERENCE
on Photonic, Electronic and Atomic Collisions

22-28 JULY 2015 **TOLEDO** · SPAIN

Transport processes for electrons and positrons in gases and soft-condensed matter: Basic phenomenology and applications

S. Dujko* [1], Z.Lj. Petrović*, R.D. White[†], G. Boyle[†], A. Banković*, I. Simonović*, D. Bošnjaković*, J. Mirić*, A.H. Markosyan[♥] and S. Marjanović*

[*] Institute of Physics, University of Belgrade, Pregrevica 118, 11080 Belgrade, Serbia
[†] College of Science, Technology & Engineering, James Cook University, Townsville 4810, Australia
[♥] Electrical Engineering and Computer Science Department, University of Michigan, Ann Arbor, MI 48109, USA

Synopsis An understanding of electron and positron transport in gases and soft-condensed matter under non-equilibrium conditions finds applications in many areas, from low-temperature plasmas, to positron emission tomography, radiation damage and particle detectors in high-energy physics. In this work we will highlight how the fundamental kinetic theory for solving the Boltzmann equation and fluid equation models are presently being adapted to study the various types of non-equilibrium plasma discharges and positron-based technologies.

The transport theory of electrons and positrons in gases and soft-condensed matter is of interest both as a problem in basic physics and for its potential for application to modern technology. For electrons, these applications range from low-temperature plasmas to particle detectors in high energy physics and to understanding radiation damage in biological matter. For positron based systems, the emission of back-to-back gamma rays resulting from annihilation of a positron and an electron is a fundamental process used as a tool in many areas, ranging from fundamental atomic and molecular physics, particle and astrophysics, to diagnostics in biological and material sciences.

In this work we explore analytical framework and numerical techniques for a multi term solution of Boltzmann's equation [1], for both electrons and positrons in gases and soft-condensed matter, and associated fluid equation models [2,3]. Together with the basic elements of our Monte Carlo method, the particular attention will be placed upon the rescaling procedures for compensation of electrons for losses under conditions when transport is greatly affected by electron attachment in strong electronegative gases.

For electrons, we will highlight recent advancements in the determination of the high-order transport coefficients in both atomic and molecular gases. Then we will discuss the elementary physical processes of electrons in the mixtures of gases used to model planetary atmospheric discharges. In particular, we will present the results of our theoretical calculations for expected heights of occurrence of sprites above lightning discharges in atmospheres of planets in our Solar system.

As an example of fluid equation models, we will discuss the recently developed high order fluid model for streamer discharges [3]. The balance equations for electron density, average electron velocity, average electron energy and average electron energy flux have been obtained as velocity moments of Boltzmann's equation and are coupled to the Poisson equation for the space charge electric field. Starting from the cross sections for electron scattering, it will be shown how the corresponding transport data required as input in fluid model should be calculated under conditions when the local field approximation is not applicable. We will illustrate the non-local effects in the profiles of the mean energy behind the streamer front and emphasize the significance of the energy flux balance equation in modeling. Numerical examples include the streamers in N_2 and noble gases.

In the last segment of this talk we will discuss the interaction of primary positrons, and their secondary electrons, with water vapor and its mixture with methane using complete sets of cross sections having bio-medical applications in mind [4]. We will also highlight recent advancements in the testing/validation of complete cross section sets for electrons in biologically relevant molecules, including water vapor and tetrahydrofuran [5].

References

[1] S. Dujko *et al* 2010 *Phys. Rev. E* **81** 056403
[2] R.D. White *et al* 2009 *J. Phys.D: Appl. Phys.* **42** 194001
[3] S. Dujko *et al* 2013 *J. Phys.D: Appl. Phys.* **46** 475202
[4] S. Marjanović *et al* 2015 Plasma Sources Sci. Technol. **24** 025016
[5] White *et al* 2014 *Eur. Phys. J. D* **68** 125

MONDAY

---

[1] E-mail: sasa.dujko@ipb.ac.rs

Third order transport coefficients for electrons and positrons in gases

I. Simonović, Z.Lj. Petrović, and S. Dujko

Institute of Physics, University of Belgrade, Pregrevica 118, 11080 Belgrade, Serbia

Synopsis Structure and symmetries along individual elements of the skewness tensor (transport coefficient of the third order) are determined by the group projector technique. Skewness components are calculated using a Monte Carlo simulation technique and multi term solutions of Boltzmann's equation for electrons and positrons in model and real gases. A strong correlation between longitudinal skewness and longitudinal diffusion coefficients is observed.

Third order transport coefficients have been systematically ignored in the interpretations of traditional swarm experiments. However, recent Monte Carlo studies [1,2] have revealed that the spatial distributions of electrons are not well described by a perfect Gaussian. It was also shown that the third order transport coefficients are much more sensitive with respect to the energy variations of cross sections for elementary processes than those of lower order, including drift velocity and/or diffusion tensor [3,4].

Third order transport coefficients have been addressed by several authors for magnetic field free case. The semi-quantitative momentum transfer theory developed by Vrhovac et al. [3], and Monte Carlo simulation and solutions of Boltzmann's equation by Penetrante and Bardsley [4] were used to analyze the behavior of skewness tensor for electrons in rare gasses. A three-temperature treatment of the Boltzmann equation and molecular dynamic simulation were used by Koutselos to calculate the third order transport coefficients for ions in atomic gases [5,6].

In this work we extend previous studies by considering the explicit and implicit effects of non-conservative collisions (e.g. electron attachment and ionization for electrons and Positronium formation for positrons) on various skewness components when both the electric and magnetic fields are present. In addition, the sensitivity of the skewness components to post-ionization energy partitioning is studied by comparison of three ionization energy partitioning regimes for a range of electric fields. Calculations are performed by a Monte Carlo simulation technique [1,2] and multi term theory for solving Boltzmann's equation [7].

Among many important points, we found a strong correlation between longitudinal skewness $n_0^2 Q_L$ and longitudinal diffusion $n_0 D_L$ coefficients for both model and real gasses. If $n_0 D_L$ decreases, or increases as a concave function, with increasing electric field E/n_0, then $n_0^2 Q_L$ decreases. On the other hand, when $n_0 D_L$ increases as a convex function with increasing E/n_0, $n_0^2 Q_L$ also increases. This is illustrated in figure 1 for positrons in N_2. It is generally observed that skewness coefficients vary more markedly than diffusion coefficients with E/n_0.
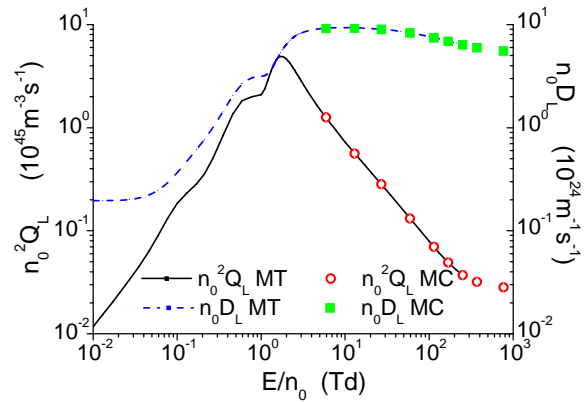

Figure 1. Correlation between flux longitudinal skewness and flux longitudinal diffusion for positrons in N_2. MT and MC refer to Multi Term and Monte Carlo results, respectively.

References

[1] Dujko et al. Eur. Phys. J. D 2014 68 166
[2] Bošnjaković et al 2014 *J. Phys. D: Appl. Phys.* 47 435203
[3] Vrhovac et al 1999 *J. Chem. Phys.* 110 2423
[4] B.M. Penetrante and J.N. Bardsley, in Non-equilibrium Effects in Ion and Electron Transport (Plenum, New York, 1990) p. 49
[5] A.D. Koutselos 1996 *J. Chem. Phys.* 104 8442
[6] A.D. Koutselos 2005 *Chem. Phys.* 315 193
[7] Dujko et al. Phys. Rev. E 2010 81 046403

EMS

XIX International Symposium on Electron-Molecule Collisions and Swarms

Book of Abstracts

POSMOL 2015

17-20 July 2015, LISBOA, PORTUGAL

XVIII International Workshop on Low-Energy Positron and Positronium Physics &
XIX International Symposium on Electron-Molecule Collisions and Swarms
17 - 20 July 2015, Lisboa, Portugal

POSMOL 2015

Higher order transport coefficients for electrons and positrons in gases

I. Simonović[1], Z. Lj. Petrović[1], R.D. White[2] and S. Dujko[1]

[1] Institute of Physics, University of Belgrade, Pregrevica 118, 11080 Belgrade, Serbia

[2] College of Science, Technology & Engineering, James Cook University, Townsville 4810, Australia

Higher order transport coefficients usually have not been included in the interpretations of traditional swarm experiments where it is assumed that electrons have a Gaussian profile in space. However, recent application of a Monte Carlo simulation technique has revealed that the spatial distribution of electrons is not well described by a perfect Gaussian [1,2]. It has also been demonstrated that third order transport coefficients are generally required for conversion of hydrodynamic transport coefficients to those measured under steady-state Townsend (SST) conditions [3]. Finally, it has been shown in [4,5] that third order transport coefficients are much more sensitive with respect to the energy dependence of cross sections for elementary processes than transport coefficients of lower order, including drift velocity and diffusion coefficients.

The behavior of third order transport coefficients for electrons under the influence of electric field only was analyzed by several authors. Solutions of the Boltzmann equation and Monte Carlo simulation by Penetrante and Bardsley [4] and momentum transfer theory developed by Vrhovac et al [5] were used to study the behavior of skewness tensor for electrons in atomic gases. A molecular dynamic simulation and a three-temperature treatment of Boltzmann's equation were used by Koutselos to evaluate the third order transport coefficients for ions in rare gases [6,7].

In this work we extend these previous studies by addressing the structure of skewness tensor when both electric and magnetic fields are present and by considering the effects of inelastic and non-conservative processes (e.g. ionization and electron attachment for electrons and Positronium formation for positrons) for electrons and positrons in model and real gases. A group projector technique is employed to determine the structure and symmetries along individual elements of the skewness tensor. Calculations are performed by a multi term theory for solving the Boltzmann equation [8] and Monte Carlo simulation technique [1,2]. Various aspects in the behavior of skewness tensor elements are investigated, including the existence of correlation with low-order transport coefficients, sensitivity to post-ionization energy partitioning and errors of two-term approximation for solving Boltzmann's equation. Special attention is paid to the comparison between skewness tensor elements for electrons and positrons in H_2, N_2 and CF_4.

References

[1]   Dujko *et al, Eur. Phys. J. D*, 68, (2014), 166
[2]   Bošnjaković *et al, J. Phys. D: Appl. Phys.,* **47**, (2014), 435203
[3]   Dujko *et al, J. Phys. D: Appl. Phys.*, **41**, (2008), 245205
[4]   Vrhovac *et al, J. Chem. Phys.*, **110**, (1999), 2423
[5]   B. M. Penetrante and J. N. Bardsley, in Non-equilibrium Effects in Ion and Electron Transport (Plenum, New York, (1990) p. 49
[6]   A.D. Koutselos, *J. Chem. Phys.*, **104**, (1996), 8442
[7]   A.D. Koutselos, *Chem. Phys.*, **315**, (2005), 193
[8]   Dujko *et al, Phys. Rev. E*, **81**, (2010), 046403

gem XIX

GASEOUS ELECTRONICS MEETING

PRELIMINARY PROGRAMME

Sunday 14th February to Wednesday 17th February 2016.
Deakin University, Geelong, Victoria, Australia.

IFM INSTITUTE FOR FRONTIER MATERIALS

DEAKIN UNIVERSITY

Third-order transport properties of electrons and positrons in electric and magnetic fields

I. Simonović, Z.Lj. Petrović, S. Dujko

[1] Institute of Physics, University of Belgrade, Serbia

Email contact: ilija.simonovic@ipb.ac.rs

Transport of a swarm of light charged particles, including electrons or positrons, in neutral gases under the influence of spatially homogeneous electric and magnetic fields has been studied thoroughly in the past, primarialy through the investigation of the drift and diffusion. Third-order transport properties have not been measured systematically so far, and consequently have been ignored in the interpretations of the traditinal swarm experiments. However, recent Monte Carlo studies [1] have revealed that the spatial distributions of electrons are not well described by a perfect Gaussian, particularly under conditions when charged particle transport is greatly affected by non-conservative collisions. Moreover, it has been demonstarted that the knowledge of third-order transport properties is required for the conversion of hydrodynamic transport properties to those found in the steady-state Townsend (SST) experiment [2].

In this work we investigate the structure and symmetries along individual elements of the skewness tensor (transport coefficient of the third order) by applying the group projector technique. Skewness components are calculated using a Monte Carlo simulation technique and multi term solutions of Boltzmann's equation for electrons and positrons in model and real gases. We extend previous studies [3] by considering explicit and implicit effects of non-conservative collisions (e.g. electron attachment and ionization for electrons and Positronium formation for positrons) on various skewness components when both electric and magnetic fields are present. In addition, sensitivity of the skewness components to postionization energy partitioning is studied by comparison of three ionization energy partitioning regimes for a range of electric fields.

[1] S. Dujko, Z.M. Raspopović, R.D. White, T. Makabe and Z.Lj. Petrović, Eur. Phys. J. D 2014, **68** 166.

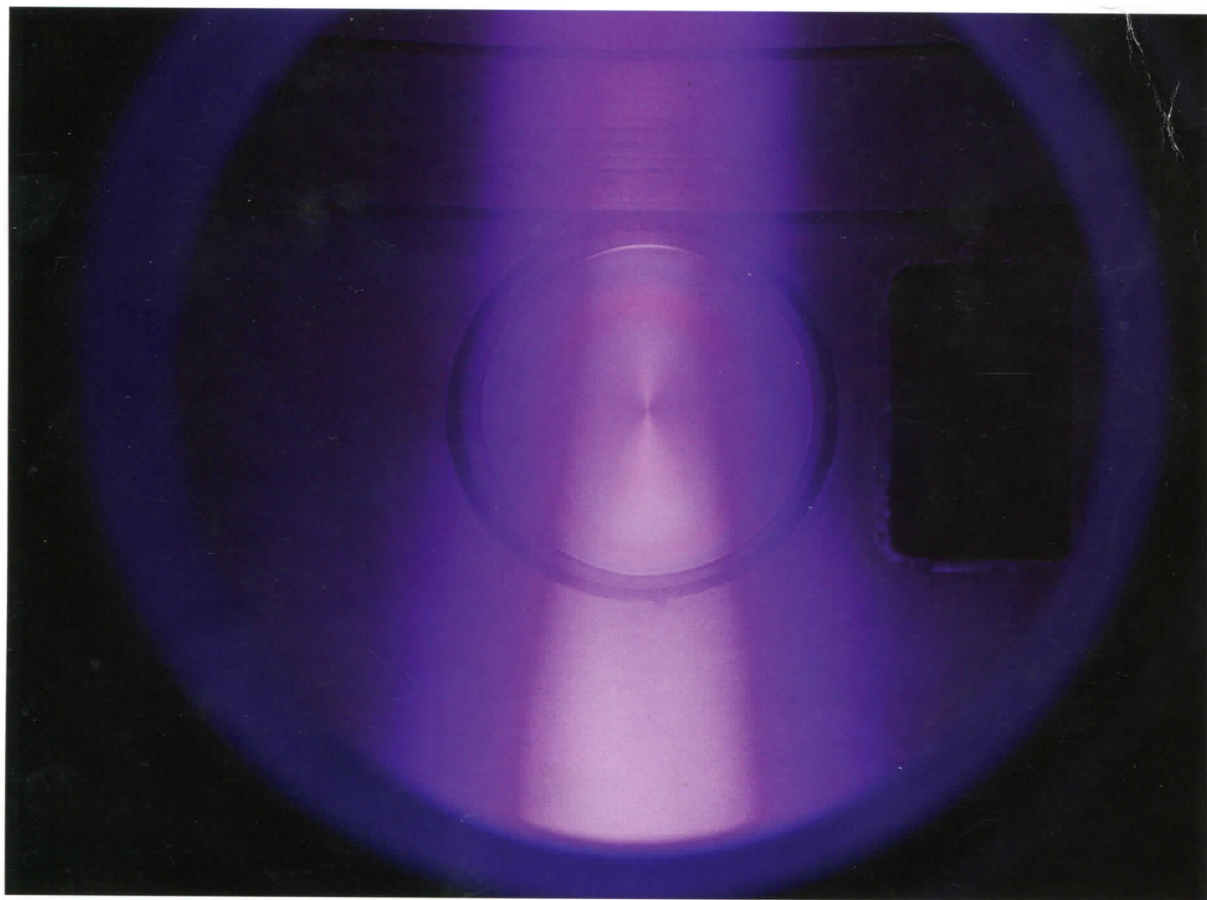[2] S. Dujko, R.D. White and Z.Lj. Petrović, J.Phys. D: Appl. Phys. 2008, **41** 245205.

[3] S.B. Vrhovac, Z.Lj. Petrović, L.A. Viehland and T.S. Santhanam, J. Chem. Phys. 1999, **110** 242.

BULLETIN

69th Annual Gaseous Electronics Conference

October 10–14, 2016
Bochum, Germany

APS
physics

APS COUNCIL OF REPRESENTATIVES 2016

President
Homer A. Neal*, *University of Michigan*

President-Elect
Laura H. Greene*, *Florida State University*

Vice President
Roger W. Falcone*, *University of California, Berkeley/LLBL*

Past President
Samuel H. Aronson*, *Brookhaven National Laboratory (retired)*

Chief Executive Officer
Kate P. Kirby*, *Harvard Smithsonian (retired)*

Speaker of the Council
Nan Phinney*, *Stanford University*

Treasurer
James Hollenhorst*, *Agilent Technologies*

Corporate Secretary
Ken Cole

General Councillors
Marcelo Gleiser, Nadya Mason, Bonnie Flemming, Gail McLaughlin*

Division, Forum and Section Councillors
Miriam Forman (*Astrophysics*); Timothy Gay* (*Atomic, Molecular & Optical*); Jose Onuchic (*Biological*); Amy Mullin* (*Chemical*); John Bradley Marston (*Condensed Matter Physics*); Giulia Galli (*Computational*); Ann Karagozian (*Fluid Dynamics*); Gay Stewart* (*Forum on Education*); Julia Gonski (*Forum on Graduate Student Affairs*); Dan Kleppner* (*Forum on History of Physics*); John Rumble (*Forum on Industrial and Applied Physics*); Young-Kee Kim* (*Forum on International Physics*); Pushpa Bhat (*Forum on Physics and Society*); Nicholas Bigelow* (*Laser Science*); James Chelikowsky (*Materials*); Wick Haxton* (*Nuclear*); P. Michael Tuts (*Particles & Fields*); Thomas Roser (*Physics of Beams*); Cary Forest (*Plasma*); Mark Ediger (*Polymer*); Nan Phinney* (*California Section);* Carlos Wexler (*Prairie Section*)

International Councilors
Marcia Barbosa, Eliezer Rabinovici, Johanna Stachel, Kiyoshi Ueda

Chair, Nominating Committee
Paul Chaikin

Chair, Panel on Public Affairs
Julia Phillips

Editor in Chief
Pierre Meystre*

Staff Representatives
Mark Doyle, *Chief Information Officer*; Amy Flatten, *Director of International Affairs*; Ted Hodapp, *Director of Project Development and Senior Advisor to the Department of Education and Diversity*; Trish Lettieri, *Director of Membership*; Irene Lukoff, *Director of Development*; Michael Lubell, *Director, Public Affairs*; Dan Kulp, *Editorial Director*; Christine Giaccone, *Director, Journal Operations*; Terri Olsen, *Director of Meetings*; Monica Plisch, *Director of Education and Diversity*; Matthew Salter, *Publisher*; Michael Stephens, *Controller and Assistant Treasurer*; James W. Taylor, *Deputy Executive Officer and Chief Operating Officer*

* Members of the APS Board of Directors

coefficients for low and moderate reduced electric fields E/N (N-gas density) accounting for non-conservative processes.

MW6 35 Third order transport coefficients for electrons and positrons in gases SASA DUJKO, ILIJA SIMONOVIC, *Institute of Physics, University of Belgrade, Serbia* RONALD WHITE, *College of Science, Technology & Engineering, James Cook University, Australia* ZORAN PETROVIC, *Institute of Physics, University of Belgrade, Serbia* Third order transport coefficients (the skewness tensor) of the electron and positron swarms, in atomic and molecular gases, are investigated. The knowledge of the skewness tensor is necessary for the conversion of the hydrodynamic transport coefficients to the arrival time and steady-state Townsend transport data as well as for the determination of the deviations of the spatial density profiles from an ideal Gaussian. In this work, we investigate the structure and symmetries along individual elements of the skewness tensor by the group projector method. Individual components of the skewness tensor are calculated using a Monte Carlo simulation technique and multi term theory for solving the Boltzmann equation. Results obtained by these two methods are in excellent agreement. We extend previous studies by considering the sensitivity of the skewness components to explicit and implicit effects of non-conservative collisions, post-ionization energy partitioning, and inelastic collisions. The errors of the two term approximation for solving the Boltzmann equation are highlighted. We also investigate the influence of a magnetic field on the skewness tensor in varying configurations of electric and magnetic fields. Among many interesting points, we have observed a strong correlation between the skewness and diffusion.

MW6 36 Transport properties of electrons and transition of an electron avalanche into a streamer in atomic liquids SASA DUJKO, ILIJA SIMONOVIC, *Institute of Physics, University of Belgrade, Serbia* GREGORY BOYLE, RONALD WHITE, *College of Science, Technology & Engineering, James Cook University, Australia* DANKO BOSNJAKOVIC, ZORAN PETROVIC, *Institute of Physics, University of Belgrade, Serbia* A Monte Carlo simulation technique is developed and used to calculate transport coefficients of electron swarms in non-polar atomic liquids. We employ the two model processes in which only momentum and energy are exchanged, respectively, to account for structure dependent coherent elastic scattering at low energies. The validity of the code is confirmed by comparison with results of previous authors. We apply two scenarios for higher energy cross sections. In the first scenario excitations in the liquid phase are approximated by excitations in the gas phase. In the second scenario excitations are completely neglected. Ionization threshold is reduced to values which are suggested in the literature, in both scenarios. Transport coefficients in these two scenarios, as well as transport coefficients for gas and liquid phases are compared. Special attention has been given to the structure induced negative differential conductivity (NDC), which has been observed both in this work, and in previous publications. Spatially-resolved electron transport properties are calculated in order to understand this phenomenon. The important aspect of this work is modeling of the transition of an electron avalanche into a streamer. Calculations are performed using 1D and 1.5D fluid models. Streamer properties in scenarios with and without excitations are compared.

MW6 37 Monte Carlo simulations of electron transport in strongly attaching gases ZORAN PETROVIC, JASMINA MIRIC, ILIJA SIMONOVIC, DANKO BOSNJAKOVIC, SASA DUJKO, *Institute of Physics, University of Belgrade, Serbia* Extensive loss of electrons in strongly attaching gases imposes significant difficulties in Monte Carlo simulations at low electric field strengths. In order to compensate for such losses, some kind of rescaling procedures must be used. In this work, we discuss two rescaling procedures for Monte Carlo simulations of electron transport in strongly attaching gases: (1) discrete rescaling, and (2) continuous rescaling. The discrete rescaling procedure is based on duplication of electrons randomly chosen from the remaining swarm at certain discrete time steps. The continuous rescaling procedure employs a dynamically defined fictitious ionization process with the constant collision frequency chosen to be equal to the attachment collision frequency. These procedures should not in any way modify the distribution function. Monte Carlo calculations of transport coefficients for electrons in SF_6 and CF_3I are performed in a wide range of electric field strengths. However, special emphasis is placed upon the analysis of transport phenomena in the limit of lower electric fields where the transport properties are strongly affected by electron attachment. Two important phenomena arise: (1) the reduction of the mean energy with increasing E/N for electrons in SF6, and (2) the occurrence of negative differential conductivity in the bulk drift velocity of electrons in both SF_6 and CF_3I.

MW6 38 Electron transport in mercury vapor: magnetic field effects, dimer induced NDC and multi-term analysis ZORAN PETROVIC, JASMINA MIRIC, ILIJA SIMONOVIC, SASA DUJKO, *Institute of Physics, University of Belgrade, Serbia* A multi term theory for solving the Boltzmann equation and Monte Carlo simulation technique are used to investigate electron transport in varying configurations of electric and magnetic fields in mercury vapor. Using different sets of cross sections for electron scattering in mercury as an input in our Boltzmann and Monte Carlo codes, we have calculated data for electron transport as a function of reduced electric and magnetic fields. A multitude of kinetic phenomena in electron transport has been observed and discussed using physical arguments. In particular, we discuss two important phenomena: (1) for certain values of electric and magnetic field, we find regions where swarm mean energy increases with increasing magnetic field for a fixed electric field, and (2) the occurrence of negative differential conductivity (NDC) for higher pressures and temperatures. In particular, NDC is induced by the presence of mercury dimers. The measured drift velocities agree very well with our Monte Carlo results only if the superelastic collisions are included in our calculations. Spatially-resolved electron transport properties are calculated using a Monte Carlo simulation technique in order to understand these phenomena.

MW6 39 Dependence of ion drift velocity and diffusion coefficient in parent gas on its temperature* SERGEY MAIOROV, *Joint Institute for High Temperatures of RAS, Moscow* RUSUDAN GOLYATINA, *A.M. Prokhorov General Physics Institute of RAS, Moscow* The results of Monte Carlo calculations of the ion drift characteristics are presented: ions of noble gases and Ti, Fe, Co, Cs, Rb, W and mercury ions in case of constant and uniform electric field are considered. The dependences of the ion mobility on the field strength and gas temperature are analyzed. The parameters of the drift velocity approximation by the Frost formula for gas temperatures of 4.2, 77, 300, 1000, and 2000 K are presented. A universal drift velocity approximation depending on the reduced electric field strength and gas temperature is obtained. In the case of strong electric fields or low gas temperatures, the deviation of the ion distribution function from the Maxwellian one (including the shifted Maxwellian one) can be very significant. The average

POSMOL 2017

XIX International Workshop on Low-Energy Positron and Positronium Physics

XX International Symposium on Electron-Molecule Collisions and Swarms

BOOK OF ABSTRACTS

22-24 July 2017

Amaroo on Mandalay Resort, Magnetic Island
Queensland, Australia

posmol2017.edu.au
@posmol2017

Elementary physical processes of electrons and positrons in planetary atmospheric discharges

S. Dujko[1], D. Bošnjaković[1], I. Simonović[1], Z.Lj. Petrović[1], R.D. White[2] and C. Köhn[3]

[1]Institute of Physics, University of Belgrade, Serbia

[2]College of Science and Engineering, James Cook University, Australia

[3]National Space Institute (DTU Space), Technical University of Denmark, Denmark

sasa.dujko@ipb.ac.rs

Lightning is one of the most spectacular natural phenomena. In the chain of processes leading to lightning, the scattering and transport of electrons are fundamental processes, followed by large-scale charge separation which results in the build-up of a strong electric field. Apart from Earth, lightning has been observed on several planets in the Solar system. While the occurrence of lightning on Venus is still an open issue, we posses clear evidences of lightning on Jupiter, Saturn, Uranus and Neptune. It is well-documented, that lightning discharges produce both an electromagnetic pulse (EMP), due to the rapid current pulse, as well as a quasi-electrostatic (QE) field due to the removal of charge from the thundercloud. When the QE field exceeds the breakdown threshold, the sprite discharges can be initiated, while the EMP field similarly leads to heating, ionization and optical emissions often referred to as elves.

In this work we extrapolate the properties of terrestrial lightning to other planets. As a first step, we present the results of our theoretical calculations for expected heights of sprites above lightning discharges in the atmospheres of planets in our Solar system. Electron transport properties in the gas mixtures that mirror the planetary atmospheres are calculated for a range of applied electric fields from the solution of non-conservative Boltzmann equation and the influences of specific physical processes on electron kinetics are identified. For example: (i) for Earth's atmosphere the effects of 3-body attachment are studied, (ii) for Venusian atmosphere the effects of the gas temperature are examined, and (iii) for gas giants, the influence of planetary magnetic field is investigated. Calculated transport coefficients are then used as an input into fluid models of different orders for streamer discharges. Values of streamer velocity, ionization level behind the front and average electron energies are calculated for various gas mixtures relevant to planetary atmospheres. We also apply a 2.5D PIC/MC (particle-in-cell/Monte Carlo) code to investigate the conditions which are necessary for an avalanche to streamer transition in the atmosphere of Titan, the largest of Saturn's satellites.

Runaway electrons which ultimately lead to the high-energy phenomena such as emissions of gamma ray flashes in planetary atmospheres are considered in Monte Carlo simulations with relativistic equations of motion of the electrons and with cross sections for electron scattering up to a few MeV. The same method is used to investigate the thermalization of high-energy electrons created by the cosmic rays. Temporal profiles of EMP in the atmospheres of Earth and Saturn are calculated externally by solving the appropriate set of Maxwell's equation and are used in Monte Carlo simulations to study the transport properties of electrons due to lightning generated EMP.

In the last segment of this work we discuss the positron transport in molecular hydrogen. We investigate the way in which the positron transport properties are influenced by the electric and magnetic field strengths under conditions when transport is greatly affected by Positronium (Ps) formation. Among many interesting phenomena we note the existence of runaway positrons for higher electric fields.

Skewness tensor for electrons and positrons in gases

I. Simonović[1], D. Bošnjaković[1], Z. Lj. Petrović[1], R.D. White[2] and S. Dujko[1]

[1]Institute of Physics, University of Belgrade, Pregrevica 118, 11080 Belgrade, Serbia
[2]College of Science, Technology & Engineering, James Cook University, Townsville 4810, Australia
sasa.dujko@ipb.ac.rs

Higher order transport coefficients have been neglected in the interpretations of the traditional swarm experiments, where it has been assumed that electrons have a Gaussian profile in the space. However, some authors have suggested that the third order transport coefficients could be determined in the present-day experiments [1,2]. In addition, recent Monte Carlo studies have shown that the spatial distribution of electron swarms is not well described by a perfect Gaussian [3]. Furthermore, it has been discussed that the procedure for determining cross section sets, via swarm analysis, could be greatly improved by including the higher order transport coefficients, if they could be experimentally measured [1,2]. Finally, higher order transport coefficients are generally required for conversion of hydrodynamic transport coefficients for those measured in steady-state Townsend and arrival time spectra experiments [4].

The study of higher order transport coefficients, by previous authors, has been restricted to the magnetic field free case. Third order transport coefficients for electrons in atomic gases have been investigated by Penetrante and Bardsley [1] and Vrhovac et al [2]. Penetrante and Bardsley employed solutions of the Boltzmann equation and Monte Carlo simulations in their study, while Vrhovac et al used momentum transfer theory. Koutselos has applied molecular dynamic simulation and a three-temperature treatment of Boltzmann's equation in order to investigate third order transport coefficients for ions in rare gases [5].

In this work we extend the previous studies by determining the structure of the skewness tensor and symmetries along individual elements, when both electric and magnetic fields are present, by employing the group projector method. In addition, we investigate how the elements of the skewness tensor change, when electric and magnetic field components change sign, by using the symmetry properties of moments of the electron distribution function. Furthermore, we study the influence of inelastic and non conservative collisions (ionization and attachment for electrons and positronium formation for positrons) on the skewness tensor for electrons and positrons in real and model gases. Moreover, we investigate the sensitivity of the skewness components to post-ionization energy partitioning for electrons in N_2 and pressure dependent dimer concentration for electrons in mercury vapor. We also investigate the existence of correlation of third order transport coefficients with transport coefficients of lower-order. Calculations are performed by Monte Carlo simulations [3] and a multi term theory for solving the Boltzmann equation [6].

References

[1] B. M. Penetrante and J. N. Bardsley, in Non-equilibrium Effects in Ion and Electron Transport (Plenum, New York, (1990)) p. 49
[2] Vrhovac et al, J. Chem. Phys., 110, (1999), 2423
[3] Dujko et al, Eur. Phys. J. D, 68, (2014), 166
[4] Dujko et al, J. Phys. D: Appl. Phys., 41, (2008), 245205
[5] A.D. Koutselos, Chem. Phys., 315, (2005), 193
[6] Dujko et al, Phys. Rev. E, 81, (2010), 046403

Transport properties of electrons and development of streamers in atomic liquids

I. Simonović[1], Z. Lj. Petrović[1], R.D. White[2], D. Bošnjaković[1] and S. Dujko[1]

[1]Institute of Physics, University of Belgrade, Pregrevica 118, 11080 Belgrade, Serbia
[2]College of Science, Technology & Engineering, James Cook University, Townsville 4810, Australia
sasa.dujko@ipb.ac.rs

There is a growing field of research which considers transport of charged particles in the liquid phase and electrical discharges in liquids. This field of research has many important applications which include plasma medicine, water purification, transformer oils as well as liquid argon and liquid xenon time projection chambers. However, in spite of significant research effort, a large number of difficulties has remained in both theoretical and experimental studies. Many of these difficulties are related to the diversity of numerous processes, which occur in liquids, across a wide range of temporal and spatial scales. The sensitivity of transport properties to these processes places many obstacles both to the development of theoretical description and to the control of the experimental conditions.

There have been numerous attempts to obtain transport properties of electrons in liquids, from theoretical investigation. Cohen and Lekner have determined cross sections for electron scattering in liquid argon by modifying the scattering potential and by including the structure effects [1]. They have subsequently calculated transport coefficients for electrons in liquid argon by using the two term approximation for solving the Boltzmann equation [2]. Atrazhev and Iakubov have developed effective cross sections for electrons in liquid argon, krypton and xenon [3]. In addition, they have obtained transport coefficients for electrons in these liquids, in the framework of Cohen-Lekner theory [3]. Boyle et al [4,5] have calculated differential cross sections for electrons in the liquid phase argon and xenon by employing Dirac-Fock scattering equations. Furthermore, they have determined transport coefficients for electrons in liquid argon and liquid xenon by using a multi term treatment of the Boltzmann equation.

In this work we have studied the transport properties of swarms of electrons in liquid argon, krypton and xenon. In addition, we have investigated the transition of an electron avalanche into a streamer and the subsequent streamer propagation in these liquids. For these purposes we have developed a Monte Carlo (MC) code for the calculation of transport coefficients for swarms of electrons in non polar liquids, as well as a 1.5 dimensional fluid code for modelling the streamer dynamics. In our MC code, structure dependent coherent scattering is represented by including two additional collisional processes which correctly describe the net transfer of momentum and energy. We employ two scenarios, with different treatment of excitations in the high energy cross sections, for our calculations of transport coefficients. In addition, we use these transport coefficients as input parameters in our fluid code, in order to estimate the importance of excitations for streamer dynamics in the liquid phase. Finally, we have compared our results with calculations in which we used input parameters from previous authors, as well as those obtained by rescaling the gas phase transport properties with density.

References
[1] J. Lekner Phys. Rev., 158, (1967), 130
[2] M. H. Cohen and J. Lekner, Phys. Rev., 158, (1967), 305
[3] V.M. Atrazhev and I.T. Iakubov J. Phys. C 14, (1981), 5139
[4] G.J. Boyle et al. J. Chem. Phys. 142, (2015), 154507
[5] G.J. Boyle et al. J. Phys. D: Appl. Phys. 49, (2016), 355201

Hydrodynamic and non-hydrodynamic studies of electron transport in mercury vapour

J. Mirić[1], I. Simonović[1], D. Bošnjaković[1], Z.Lj. Petrović[1], R.D. White[2] and S. Dujko[1]

[1]Institute of Physics, University of Belgrade, Pregrevica 118, 11080 Belgrade, Serbia
[1]College of Science and Engineering, James Cook University, Townsville, QLD 4811, Australia
sasa.dujko@ipb.ac.rs

The behaviour of electrons in mercury vapour under the influence of varying configuration of electric and magnetic fields is of vital interest in modelling of gas-discharge lamps [1]. Fluid models of low-pressure discharges used in fluorescent lamps usually require swarm parameters as a function of the reduced electric field and the gas temperature [2]. Current models of inductively coupled mercury discharges which are utilized in some types of electrodeless lamps [3] require knowledge of electron transport parameters in the presence of both the electric and magnetic fields. Modelling of electron transport processes in these applications demands an accurate and complete set of cross sections for electron-mercury atom interactions in the gas phase.

In this work we present a complete and consistent set of cross sections for electron scattering in mercury vapour. The set is validated through a series of comparisons between swarm data calculated using a multi term solution of Boltzmann's equation and Monte Carlo simulations, and the available experimental data. For magnetic field free case, we discuss the dependence of transport coefficients on the pressure and temperature of mercury vapour, and the occurrence of negative differential conductivity (NDC) in the limit of lower values of the reduced electric fields. The phenomenon of NDC is induced by the presence of mercury dimers. Mercury dimers are molecular species that can cause a significant change in the rate of energy loss by the electrons via rotational and vibrational excitations. This in turn may significantly affect the drift velocity and the overall balance of the momentum in the system. Following the previous studies of England and Elford [4], we have estimated the effective inelastic cross section for mercury dimers for a range of pressures and temperatures. Calculations of electron transport properties have been performed and two important conclusions emerged: (1) the occurrence of NDC can be controlled by varying either pressure or temperature of mercury vapor, and (2) the measured and calculated drift velocities agree very well only if the mercury-dimer cross section and thermal motion of mercury atoms are carefully considered and implemented in numerical calculations.

In the second part of this work we investigate the influence of the electric and magnetic field strengths on the transport coefficients over ranges consistent with the operation of inductively coupled mercury discharges. Values of mean energy drift velocity, diffusion tensor, and ionization rate are reported in this work. An unexpected phenomenon arises: for certain values of electric and magnetic field, we find regions where mean energy of electrons increases with increasing magnetic field for a fixed electric field. In addition, we demonstrate the Maxwellization of high-energy electrons and magnetic cooling effects associated with an increasing magnetic field.

References

[1] G.G. Lister, J.E. Lawler, W.P. Lapatovich and V.A. Godyak, Rev. Mod. Phys. **76** (2004) 541
[2] Brok et al, J. Phys. D: Appl. Phys. **40** (2007) 3931
[3] Y. Liu, G. Zissis and Y. Chen, Plasma Source Sci. Technol. **22** (2013) 035002
[4] J.P. England and M.T. Elford, Aust. J. Phys. **44** (1991) 647

Combined localised and delocalised transport phenomena

Peter Stokes[1], Ilija Simonović[2], Bronson Philippa[3], Daniel Cocks[1], Saša Dujko[2], Ronald White[1]

[1]College of Science and Engineering, James Cook University, Townsville, QLD 4811, Australia
[2]Institute of Physics, University of Belgrade, PO Box 68, 11080 Zemun, Belgrade, Serbia
[3]College of Science and Engineering, James Cook University, Cairns, QLD 4870, Australia
peter.stokes@my.jcu.edu.au

We present a general phase-space kinetic model for charged particle transport that considers scattering, trapping, detrapping and recombination (Figure 1). For suitable inputs, our model is capable of describing dispersive transport, a fundamentally slower form of transport that can arise due to traps. Dispersive transport occurs in a variety of systems including electron trapping in bubble states within liquid neon and liquid helium, positronium trapping in bubbles and positron annihilation on induced clusters.

Mathematically, we describe charged particles using a distribution function in phase space, as defined by a generalised Boltzmann equation. By taking velocity moments, we form continuity equations for particle number density, momentum and energy. From these we derive generalised analytical results for our model, including transport coefficients, Einstein relations and a Wannier energy relation. Our model also predicts a number of physical phenomena including anisotropic diffusion and negative differential conductivity (NDC).

We derive a generalisation of Fick's law that contains skewness, the next transport coefficient beyond diffusion. From this, we write an advection-diffusion-skewness equation that accurately describes our model in the weak-gradient hydrodynamic regime. We observe a negative skewness due to the presence of traps.
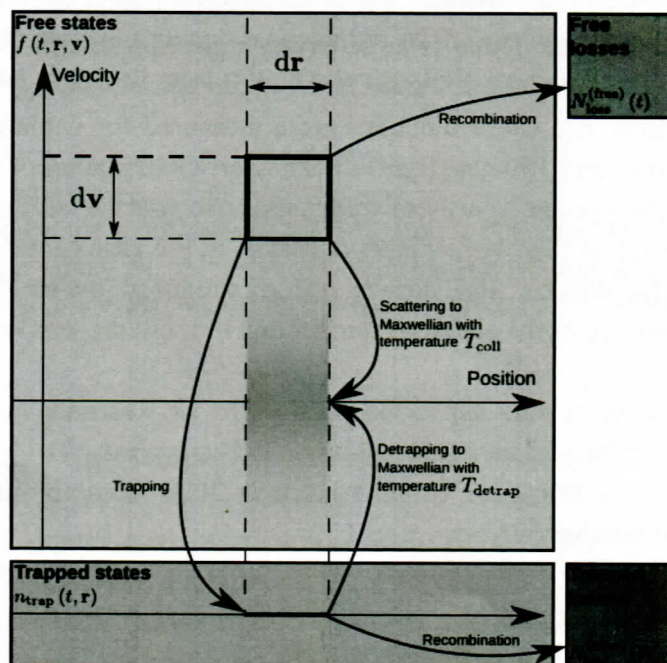

Figure 1: Phase-space diagram illustrating the collision, trapping, detrapping and recombination processes.

XX International Workshop on
Low-Energy Positron and Positronium Physics

XXI International Symposium on
Electron-Molecule Collisions and Swarms

V Workshop on Non-Equilibrium Processes

18-21 July 2019, Belgrade, Serbia

POSMOL 2019

BOOK OF ABSTRACTS

XX Међународна радионица о физици
ниско енергијских позитрона и позитронијума

XXI Међународни симпозијум о
електрон-молекулским сударима и ројевима

V Радионица о неравнотежним процесима

The Gas-Liquid Interface: Kinetic and Fluid Modelling of Charged Particle Transport

N. Garland[1,2], D. Muccignat[1], G. Boyle[1,3], D. Cocks[1,4], I. Simonović[5], D. Bošnjaković[5], M. J. Brunger[6], S. Dujko[7], Z. Lj. Petrović[7], and R.D. White[1]

[1]College of Science and Engineering, James Cook University, Townsville, Australia
[2]DESY, Hamburg, Germany
[3]Los Alamos National Laboratory, Los Alamos, USA
[4]Research School of Physical Sciences, Australian National University, Canberra, Australia
[5]Institute of Physics, University of Belgrade, Pregrevica, Belgrade, Serbia
[6]College of Science and Engineering, Flinders University, Adelaide, Australia
[7]Serbian Academy of Sciences and Arts, Knez Mihailova 35, 11000 Belgrade, Serbia
ronald.white@jcu.edu.au

Modelling of electron transport in the vicinity of the plasma-liquid requires an accurate treatment of electron transport in the gaseous and soft-condensed phases, together with an understanding of the electron transport across the gas-liquid interface. In this presentation, we present simulations which have informed the design of a new experiment which adapts an existing electron-gas phase scattering experiment (e2e) to consider electron scattering from a liquid micro-jet. The results highlight that electron-scattering information (effective cross-sections) can be obtained from the experiment for both the bulk liquid and from the interface. In addition, we present progress on an ab-initio formalism for electron transport in liquids through appropriate generalisations of Boltzmann's equation and associated higher order fluid models to account for spatio-temporal scattering correlations, screening of the electron potential and the effects of (self-) trapping. Application is considered for various atomic liquids as a starting benchmark to consider more complex polar liquids [1] as well as the non-local nature of electron transport in liquids and gas-liquid interfaces [2,3]. Propagation of ionization fronts between the gas and liquid phases are considered.

References
[1]   R. D. White, *et al.*, *Plasma Sources Sci. Technol.*, **27**, (2018), 053001.
[2]   N. A. Garland, *et al*., *Plasma Sources Sci. Technol.*, **27**, (2018), 024002.
[3]   N. A. Garland, *et al*., *Plasma Sources Sci. Technol.*, **26**, (2017), 075003.

Positron Transport in H_2 in Electric and Magnetic Fields Crossed at Arbitrary Angles

S. Dujko[1], I. Simonović[1], R.D. White[2] and Z.Lj. Petrović[1,3]

[1]Institute of Physics, University of Belgrade, Pregrevica 118, 11080 Belgrade, Serbia
[2]College of Science and Engineering, James Cook University, Townsville 4810, Australia
[3]Serbian Academy of Sciences and Arts, Knez Mihailova 35, 11000 Belgrade, Serbia
sasa.dujko@ipb.ac.rs

Using a multi term theory for solving the Boltzmann equation [1], we investigate the positron transport in H_2 in electric and magnetic fields crossed at arbitrary angles. The hierarchy resulting from the spherical harmonic decomposition of the Boltzmann equation in the hydrodynamic regime is solved numerically by representing the speed dependence of the phase-space distribution function in terms of an expansion in Sonine polynomials about a Maxwellian weighted function. Values and general trends of positron transport properties over a range of angles and field strengths are reported here. In particular, we explore the existence of two families of transport coefficients, the bulk, and the flux, which results from the explicit influence of Positronium (Ps) formation upon the transport coefficients. We also explore the validity of Tonks' theorem for positrons assuming the most general case of arbitrary field orientations where special attention is placed upon the procedure for accurate determination of momentum transfer collision frequency as a function of positron mean energy.

The second important aspect of this work concerns the validity of cross sections for positron scattering in H_2 [2,3]. For reduced electric fields greater than approximately 100 Td (1 Td = 10^{-21} Vm^2), we have noticed the existence of runaway positrons. The runaway phenomenon is a consequence of decreasing probabilities of positron interactions with neutral molecules for higher electric fields. Under these conditions, positrons gain more energy than they can lose in collisions and hence no steady-state can be reached. This raises a number of questions regarding the accuracy and completeness of the current set of cross sections. Machacek and coworkers [4] have reported the total inelastic cross section that is higher than the one used in our calculations which might be used to explain the low threshold electric field for runaway of positrons. In order to resolve this issue, for the lower energy positrons, we consider the influence of rotational excitations on positron transport. For higher energies of positrons (greater than approximately 10 eV), we investigate the following fundamental issue: What is the nature of missing processes and what are the implications of the fact that Positronium (Ps) formation is dominant over the inelastic processes for energies between 10 and 50 eV. The runaway phenomenon of positrons is investigated by a Monte Carlo simulation technique.

References
[1]   S. Dujko, R.D. White, Z.Lj. Petrovć and R.E. Robson, *Phys. Rev. E*, **81**, (2010), 046403.
[2]   A. Banković, S. Dujko, R.D. White, S.J. Buckman and Z.Lj. Petrović, *Nucl. Instr. Meth.*, **279**, (2012), 92.
[3]   G. Boyle, W.J. Tattersall, D.G. Cocks, S. Dujko and R.D. White, *Phys. Rev. A*, **91**, (2015), 052710
[4]   J.R. Machacek, E.K. Anderson, C. Makochekanwa, S.J. Buckman and J.P. Sullivan, *Phys. Rev. A*, **88**, (2013) 042715.

Electron Transport and Streamers in the Atmosphere of Titan

S. Dujko[1], D. Bošnjaković[1], I. Simonović[1] and C. Köhn[2]

[1]Institute of Physics, University of Belgrade, Pregrevica 118, 11080 Belgrade, Serbia
[2]Technical University of Denmark, National Space Institute (DTU Space),
Elektrovj 328, 2800 Kgs Lyngby, Denmark
sasa.dujko@ipb.ac.rs

Since the era of the Voyager missions in 1980s, the possibility of lightning on Titan has been investigated by theoretical and experimental studies of its complex atmospheric chemistry. Titan is the largest of Saturn's satellites and has a massive atmosphere with surface pressure exceeding that on Earth by approximately 50%. Titan's atmosphere is largely made up of N_2 and CH_4 and trace amounts of H_2 and HCN. The presence of hydrocarbons, including C_2H_2, C_2H_4 and C_2H_6 and various nitriles has also been detected. The modelling studies of Titan's atmospheric chemistry suggest the existence of lightning since the amount of HCN and C_2H_2 in the atmosphere cannot be explained in terms of photo-chemistry models [1].

In this work, we discuss whether streamer discharges, pre-cursors of lightning, exist in Titan's atmosphere [2]. Streamers are thin channels of non-equilibrium plasma whose dynamics is entirely governed by the highly-localized non-linear regions of space charge and steep gradients of the electron number density. We approach the problem at two stages. First, using the cross section sets for electron scattering in N_2 and CH_4 as an input, we solve the non-conservative Boltzmann equation and we run Monte Carlo simulations [3]. We are focused on how the electron transport coefficients are influenced by the amount of CH_4 in the mixture and by the temperature of the background gas. The transport coefficients are then used as an input in a 1.5 dimensional fluid model to simulate the transition from an electron avalanche into a negative streamer and propagation of negative streamer ionization fronts. In particular, we present our recently developed fluid model in which the electron collisional term in the continuity equation is expanded in terms of the electron number density.

In addition to fluid models, using cross section sets for electron scattering in N_2 and CH_4 as an input, we perform Monte Carlo particle in-cell simulations (PIC-MCC) [2,4]. We use a 2.5 dimensional PIC-MCC to simulate the development of electron avalanches from an initial electron-ion patch and their subsequent transition into positive and negative streamers in ambient electric fields between $1.5E_k$ and $3E_k$, where E_k is the critical electric field of a given mixture. We investigate the electron density, the electric field, the front velocities as well as the transition from an electron avalanche into a streamer in various N_2-CH_4 mixtures. Among many important points, it is found that on Titan, a successful streamer inception would require a large electric field of 4.2 MVm^{-1} (approximately $3E_k$).

References
[1]   V. Vuitton, R.V. Yelle, S.J. Klippenstein, S.M. Hörst and P. Lavas, *Icarus*, **324**, (2019), 120.
[2]   C. Köhn, S. Dujko, O. Chanrion and T. Neubert, accepted for publication in *Icarus*.
[3]   S. Dujko, R.D. White, Z.Lj. Petrović and R.E. Robson, *Phys. Rev. E*, **81**, (2010), 046403.
[4]   O. Chanrion and T. Neubert, *J. Comp. Phys.*, **227**, (2008), 7222.

Foundations and Interpretations of the Pulsed-Townsend Swarm Experiment and the use of Machine Learning for Self-Consistent Cross-Section Sets

M. Casey[1], P. Stokes[1], I. Simonović[2], D. Bošnjaković[2], M. J. Brunger[3], J. de Urquijo[4], S. Dujko[2], Z. Lj. Petrović[2,5], R. E. Robson[1], and R.D. White[1]

[1]College of Science and Engineering, James Cook University, Townsville, Australia
[2]Institute of Physics, University of Belgrade, Pregrevica, Belgrade, Serbia
[3]College of Science and Engineering, Flinders University, Adelaide, Australia
[4]Instituto de Ciencias Fisicas, Universidad Nacional Autonoma de Mexico, Cuernavaca, Mexico
[5]Serbian Academy of Sciences and Arts, Knez Mihailova 35, 11000 Belgrade, Serbia
ronald.white@jcu.edu.au

The pulsed-Townsend (PT) experiment is a common swarm technique which is routinely used to (i) provide transport coefficients for plasma discharge modelling, and (ii) assess the accuracy and self-consistency of cross-section sets of electron/ion interactions with gaseous systems. The Townsend coefficient, drift velocity and diffusion coefficient for electrons and ions drifting and diffusing in background gases. In this work, the governing equation used to analyse the PT experiment is analysed when non-conservative processes are operative. It highlights, the transport properties derived from PT experiments are not directly comparable to the standard transport coefficients. We highlight, however, how the reaction rate and bulk drift velocity can be better approximated from these PT transport properties, although proper comparison with the bulk transport coefficients requires a slight reanalysis of the PT experiment current transients. Estimates of the errors originating from the incorrect governing equation and subsequent analysis are presented for various atomic and molecular gases as a guide for uncertainties in the previous data. Further, in this presentation we will highlight the use of machine learning techniques to develop self-consistent cross-section sets for electron-neutral interactions in both gaseous and liquid systems.

UNIVERZITET U BEOGRADU

FIZIČKI FAKULTET

Ilija B. Simonović

KINETIČKI I FLUIDNI MODELI NERAVNOTEŽNOG TRANSPORTA ELEKTRONA U GASOVIMA I TEČNOSTIMA

doktorska disertacija

Beograd, 2020.

UNIVERSITY OF BELGRADE

FACULTY OF PHYSICS

Ilija B. Simonović

KINETIC AND FLUID MODELS OF NON-EQUILIBRIUM TRANSPORT OF ELECTRONS IN GASES AND LIQUIDS

Doctoral Dissertation

Belgrade, 2020.

Mentor:

- dr Saša Dujko, naučni savetnik,

  Institut za fiziku, Univerzitet u Beogradu

Članovi komisije:

- akademik Zoran Lj. Petrović,
  Srpska akademija nauka i umetnosti

- prof. dr Srđan Bukvić, redovni profesor,
  Fizički fakultet, Univerzitet u Beogradu

- prof. dr Đorđe Spasojević, redovni profesor,
  Fizički fakultet, Univerzitet u Beogradu

Datum odbrane: 30.09.2020.

Zahvalnica

Doktorska disertacija pod nazivom "Kinetički i fluidni modeli neravnotežnog transporta elektrona u gasovima i tečnostima"urađena je u Laboratoriji za neravnotežne procese i primenu plazme Instituta za fiziku u Beogradu, pod rukovodstvom naučnog savetnika dr Saše Dujka. Ova disertacija je najvećim delom realizovana u okviru projekta OI171037 Ministarstva prosvete, nauke i tehnološkog razvoja Republike Srbije, čiji je rukovodilac bio akademik Zoran Lj. Petrović. Kako svaki naučni rad podrazumeva višestruku komunikaciju sa kolegama, profesorima i istaknutim stručnjacima u datoj oblasti, tako posebnu zahvalnost dugujem onima koji su doprineli tome da ova disertacija dobije konačni oblik. Najpre bih se zahvalio svom mentoru, dr Saši Dujku, na dragocenim savetima, podršci i nesebičnoj pomoći koje mi je pružao u svim fazama rada na ovoj doktorskoj disertaciji. Dr Saša Dujko pomogao mi je pri definisanju teme, razvoju metodoloških pristupa za istraživanje i tumačenju rezultata. Bez strpljenja i entuzijazma koje je uložio, ova disertacija i rezultati istraživanja koji su prikazani u njoj ne bi bili mogući.

Veliku zahvalnost dugujem i akademiku Zoranu Lj. Petroviću, vrhunskom stručnjaku iz oblasti istraživanja, na izuzetno korisnim sugestijama i podršci u radu. Posebno sam zahvalan dr Danku Bošnjakoviću na pomoći vezanoj za razvoj numeričkih kodova i korišćenje računarskih resursa, kao i na korisnim diskusijama i kolegijalnoj saradnji. Želeo bih da se zahvalim i koleginici Jasmini Atić na pomoći oko optimizacije korišćenih procedura za izračunavanje transportnih koeficijenata i na velikom broju korisnih sugestija. Zahvaljujem se kolegama sa James Cook Univerziteta u Australiji, prof. Ronald-u White-u, dr Peter-u Stokes-u i dr Greg-u Boyle-u na dragocenoj pomoći vezanoj za razumevanje teorije rasejanja elektrona kako u gasnoj, tako i u tečnoj fazi, kao i na velikom broju korisnih saveta i sugestija koji su omogućili implementaciju preseka za rasejanje elektrona u atomskim tečnostima visoke mobilnosti u naše numeričke kodove.

Na ovom mestu želim da se zahvalim svim kolegama iz Laboratorije za neravnotežne procese i primenu plazme Instituta za fiziku ne samo na korisnim i konstruktivnim diskusijama vezanim za naučni rad, već i na zajedničkom druženju tokom poslednjih nekoliko godina.

Na kraju bih želeo da se zahvalim svojim roditeljima na bezrezervnoj ljubavi i podršci koju su mi pružali tokom celokupnog školovanja, a naročito na njihovoj podršci tokom rada na doktorskoj tezi.

Kinetički i fluidni modeli neravnotežnog transporta elektrona u gasovima i tečnostima

Sažetak

Ova doktorska disertacija sadrži dve celine. U prvoj celini su proučavani transportni koeficijenti trećeg reda za rojeve naelektrisanih čestica u gasovima. Struktura transportnog tenzora trećeg reda u svim konfiguracijama električnog i magnetskog polja određena je primenom metoda grupnih projektora. Fizička interpretacija individualnih komponenti ovog tenzora je analizirana na osnovu fluks gradijentne relacije i generalisane difuzione jednačine. Zavisnost transportnih koeficijenata trećeg reda od redukovanog električnog polja i njihova osetljivost na elementarne sudarne procese ispitane su za veliki broj modelnih i realnih gasova u Monte Carlo simulacijama i na osnovu numeričkih rešenja Boltzmann-ove jednačine. U drugoj celini je razmatran transport elektrona u tečnom argonu, tečnom kriptonu i tečnom ksenonu primenom Monte Carlo simulacija. Proučavani su uticaji efekata koherentnog rasejanja i različitih načina za aproksimaciju neelastičnih sudara u tečnoj fazi na izračunate vrednosti transportnih koeficijenata u ovim tečnostima. Poseban akcenat je stavljen na proučavanje strukturno indukovane negativne diferencijalne provodnosti u tečnom ksenonu na osnovu prostorno razloženih karakteristika roja i funkcija raspodele elektrona. Transportni koeficijenti za rojeve elektrona u atomskim tečnostima su iskorišćeni kao ulazni podaci u 1.5-dimenzionom klasičnom fluidnom modelu prvog reda i u fluidnom modelu zasnovanom na razvoju izvornog člana u jednačini kontinuiteta po gradijentima koncentracije. Ovi fluidni modeli upotrebljeni su za ispitivanje tranzicije lavina elektrona u strimere i propagacije negativnih strimera u atomskim tečnostima visoke mobilnosti. Pored toga, na osnovu ovih modela je razmatrano na koji način različit tretman neelastičnih sudara, priroda transportnih koeficijenata i rekombinacija kvazislobodnih elektrona i pozitivnih šupljina utiču na dinamiku i osobine strimerske plazme.

Ključne reči: Transportni koeficijenti trećeg reda, transport elektrona u gasovima i nepolarnim tečnostima, strimeri u nepolarnim tečnostima, Boltzmann-ova jednačina, fluidni model, Monte Carlo simulacije

Naučna oblast: Fizika

Uža naučna oblast: Fizika plazme

Kinetic and fluid models of non-equilibrium transport of electrons in gases and liquids

Abstract

The present doctoral dissertation contains two parts. The first part deals with the study of the third-order transport coefficients of charged-particle swarms in gases. The structure of the third-order transport tensor has been determined by employing the group projector technique in all configurations of electric and magnetic fields. The physical interpretation of the individual components of this tensor has been analyzed by employing the flux gradient relation and the generalized diffusion equation. The variation of the third-order transport coefficients with the reduced electric field and their sensitivity to elementary scattering processes have been determined for a wide range of model and real gases by using Monte Carlo simulations and the numerical solutions of the Boltzmann equation. The second part of this thesis deals with the transport of electrons in liquid argon, liquid krypton and liquid xenon by employing Monte Carlo simulations. The sensitivity of the calculated values of the transport properties in these liquids to coherent scattering effects and different approximations of inelastic scattering in the liquid phase has been investigated. A special emphasis has been placed on the study of the kinetic phenomenon of negative differential conductivity in liquid xenon by using spatially resolved swarm data and electron energy distribution functions. Transport coefficients of electron swarms in atomic liquids are used as input data in 1.5 dimensional classical first order fluid model, as well as in the fluid model which is based on the density gradient expansion of the source term in the equation of continuity. Both fluid models are employed in investigating the transition of electron avalanches into streamers and the propagation of negative streamers in high-mobility atomic liquids. In addition, the presented models are used for investigating how the dynamics and properties of the streamer plasma are influenced by the different treatment of inelastic collisions, nature of transport coefficients and the recombination of quasi-free electrons and positive holes.

Key words: Third-order transport coefficients, transport of electrons in gases and non-polar liquids, streamers in non-polar liquids, the Boltzmann equation, fluid model, Monte Carlo simulations

Scientific field: Physics

Scientific subfield: Physics of plasma

Sadržaj

1 Uvod

Ova doktorska disertacija sadrži u sebi dve globalne celine, koje su međusobno koherentne i komplementarne. Prva celina se odnosi na kinetičku teoriju neravnotežnog transporta rojeva elektrona i pozitrona u gasovima i tečnostima, sa posebnim akcentom na transportnim koeficijentima trećeg reda. Druga se globalna celina zasniva na transportu elektrona i propagaciji pozitivnih i negativnih strimera u tečnom argonu, tečnom kriptonu i tečnom ksenonu.

Transportna teorija rojeva naelektrisanih čestica obezbeđuje vezu između mikroskopskih sudarnih procesa naelektrisanih čestica sa atomima ili molekulima pozadinske sredine i makroskopskih karakteristika sistema poput brzine drifta, difuzionog tenzora i brzinskih koeficijenata za reakcije [1–4]. Pored toga, transportna teorija omogućava izučavanje kompleksnih kinetičkih fenomena, kao što su grejanje i hlađenje difuzijom [5], grejanje i hlađenje zahvatom elektrona [6], anizotropna difuzija [7,8], anomalna longitudinalna difuzija [9,10], razlika između balk i fluks transportnih koeficijenata [11], pojačana provodnost elektrona [12], negativna diferencijalna provodnost [13,14], negativna apsolutna mobilnost [16,17,22–24] i tranzijentna negativna difuzija [19,20]. Ovi fenomeni se ne mogu objasniti na osnovu dinamike pojedinačne naelektrisane čestice. Uz to, transportna teorija obezbeđuje osnovu za modelovanje eksperimenata sa rojevima [31–33], neravnotežnih plazmi [26] i gasnih detektora čestica visokih energija [27–30].

Modelovanje neravnotežnih plazmi zahteva precizan opis dinamike naelektrisanih čestica i njihove interakcije sa pozadinskim fluidom, zbog toga što karakteristike neravnotežnih plazmi snažno zavise od prirode pozadinskog fluida i preseka za sudare naelektrisanih čestica sa neutralnim česticama pozadinske sredine [26]. Neravnotežne plazme se mogu podeliti na različite načine, imajući u vidu pritisak (plazma na niskom pritisku, plazma na atmosferskom pritisku, plazma u tečnosti) i sile koje se koriste za održavanje samog pražnjenja (kapacitivno spregnuta pražnjenja i induktivno spregnuta pražnjenja). Velika raznovrsnost tipova neravnotežnih plazmi omogućava njihovu primenu u raznim oblastima tehnologije i primenjene fizike. Neke od ovih oblasti su izvori svetlosti [34,35], proizvodnja mikročipova [26], [36,37], nanošenje tankih filmova na površine zarad promene njihovih karakteristika [38,39], primena plazme u medicini [40,41], i poljoprivredi [42,43], pročišćavanje vode plazmom [44,45]. Temeljno razumevanje neravnotežnih plazmi i elementarnih sudarnih procesa koji određuju njihove karakteristike omogućava dalji razvoj i optimizaciju pobrojanih primena. Ovo je veliki podstrek za razvoj teorijskih i eksperimentalnih metoda za izučavanje električnih gasnih pražnjenja i neravnotežnih plazmi.

Za opisivanje neravnotežnih plazmi koristi se širok spektar teorijskih metoda, koji se mogu podeliti na: a) kinetičke modele bazirane na rešavanju Boltzmann-ove jednačine [47], b) fluidne modele, c) čestične modele i d) hibridne modele. U ovoj doktorskoj disertaciji korišćeni su svi pobrojani modeli, izuzev hibridnih modela.

U fluidnim modelima se ansambli čestica (poput elektrona, jona, ekscitovanih neutrala i radikala) reprezentuju makroskopskim fizičkim veličinama poput koncentracije čestica, rezultujućeg vektora impulsa, srednje energije i vektora energijskog fluksa [47–52]. Prostorne varijacije i vremenska evolucija ovih veličina određuju se na osnovu jednačina balansa ovih veličina, ili,

jednostavnije govoreći, na osnovu fluidnih jednačina. Oblik fluidnih jednačina može biti određen empirijski. Međutim, ove jednačine se mogu odrediti i na osnovu brzinskih momenata Boltzmann-ove jednačine [47, 52]. Na taj način se dobija beskonačna hijerarhija fluidnih jednačina, čije bi rešavanje bilo ekvivalentno rešavanju Boltzmann-ove jednačine. U praksi se ova hijerarhija odseca na nekoj jednačini konačnog reda, uz reprezentovanje određenog podskupa nepoznatih veličina aproksimativnim izrazima zasnovanim na fizičkim argumentima ili na momentima nižeg reda. Fluidne jednačine mogu biti spregnute sa Maxwell-ovim jednačinama i Poisson-ovom jednačinom da bi se opisao uticaj naelektrisanih čestica na rezultujuća električna i magnetska polja [47]. Jedna od prednosti fluidnih modela je to što rešavanje fluidnih jednačina zahteva manje računarskog vremena od primene čestičnih modela i numeričkog rešavanja Boltzmann-ove jednačine. Dodatnu prednost predstavljaju analitički izrazi, koji mogu pružiti uvid u veze između različitih fizičkih veličina. Međutim, fluidni modeli u sebi sadrže mnoge implicitne i eksplicitne aproksimacije [47], te su rezultati dobijeni na osnovu fluidnih modela znatno neprecizniji od rezultata čestičnih modela i metoda za numeričko rešavanje Boltzmann-ove jednačine [47].

U čestičnim modelima se prate putanje naelektrisanih čestica koje se kreću u neutralnom pozadinskom fluidu pod uticajem spoljašnjeg električnog i spoljašnjeg magnetskog polja [26, 47, 53–56]. Sudari naelektrisanih čestica sa atomima ili molekulima pozadinskog fluida reprezentuju se uz pomoć slučajnih brojeva. Zbog toga se čestični modeli zovu i Monte Carlo modeli [26, 47]. Kada se čestični modeli koriste za ispitivanje sistema u kojima je koncentracija naelektrisanih čestica dovoljno mala da se njihove međusobne interakcije kao i njihov uticaj na rezultujuće električno polje mogu u potpunosti zanemariti, u simulacijama se kretanje svake naelektrisane čestice može pratiti nezavisno od ostalih naelektrisanih čestica u sistemu [26, 47]. Međutim, kada se modeluju sistemi u kojima je koncentracija naelektrisanih čestica dovoljno velika da se njihov uticaj na rezultujuće električno polje ne može zanemariti, neophodno je da kretanje neaelektrisanih čestica i dinamika rezultujućeg električnog polja budu računati samousaglašeno. Ovo se obično postiže korišćenjem komplikovane tehnike čestice u ćeliji (eng. *particle in cell technique*) [26, 47, 53–56]. U okviru ove tehnike veliki se broj pojedinačnih čestica reprezentuje znatno manjim brojem superčestica. Pritom, broj superčestica koje se prate u simulaciji mora biti dovoljno veliki da obezbedi pouzdane razultate [26]. Korišćenje ove reprezentacije je neophodno kada je broj naelektrisanih čestica previše veliki da bi praćenje svake od njih pojedinačno bilo praktično izvodljivo. Na osnovu kretanja superčestica mogu se odrediti makroskopske fizičke veličine, poput koncentracije naelektrisanih čestica, njihovog fluksa i njihove srednje energije. Jednu od najvećih prednosti čestičnih modela predstavlja njihova primenjivost u širokom opsegu uslova simulacija [26]. Pored toga, čestični modeli najčešće daju preciznije rezultate od fluidnih modela, ali su, s druge strane, računarski jako zahtevni i za njihovu implementaciju obično je potrebna velika količina računarskog vremena.

Fluidni i čestični modeli mogu se spojiti u objedinjene hibridne modele [47]. U hibirdnim modelima se za praćenje brzih neravnotežnih elektrona i prostornih raspodela jonizacije koristi čestični model, dok se niskoenergijske čestice opisuju fluidnim jednačinama [47, 57–61]. Cilj ovih modela je da obezbede kompletan konzistentan opis sistema uz malu cenu računarskog vremena.

Međutim, njihov razvoj zahteva uspešno povezivanje simulacija, čija je uloga opisivanje brzih neravnotežnih čestica, sa fludinim jednačinama, kojima se opisuje ostatak sistema. Ovo uopšte nije jednostavan zadatak, te se hibridni modeli još uvek nalaze u fazi razvoja.

Metodi za numeričko rešavanje Boltzmann-ove jednačine predstavljaju teorijske pristupe koji mogu biti korišćeni za opisivanje balka plazme i prielektrodnih oblasti [62–65]. Ovi metodi daju jako pouzdane rezultate, a naročito su efikasni u slučaju kada su koncentracije naelektrisanih čestica dovoljno niske da se uticaj prostornog naelektrisanja može zanemariti [47]. No, oni se mogu koristiti i u slučaju u kome se uticaj naelektrisanih čestica na rezultujuće električno i rezultujuće magnetsko polje ne može zanemariti ako je Boltzmann-ova jednačina na adekvatan način spregnuta sa Maxwell-ovim jednačinama.

Boltzmann-ovu jednačinu formulisao je Ludwig Eduard Boltzmann ne bi li opisao dinamiku idealnog gasa, čije čestice interaguju samo putem elastičnih sudara [66]. Ovo je složena integro-diferencijalna jednačina u kojoj kao nepoznata funkcija figuriše funkcija raspodele u faznom prostoru. Iako je Boltzmannn-ova jednačina zadržala svoj prvobitni oblik, njena primenljivost je proširena na rojeve naelektrisanih čestica u gasovima [47,67] i tečnostima [68–70] koje učestvuju u elastičnim, neelastičnim i nekonzervativnim sudarima sa česticama pozadinskog fluida. Uz to su pristupi u rešavanju Boltzmann-ove jednačine značajno uznapredovali u poslednjih nekoliko decenija.

Teorijski metodi za rešavanje Boltzmann-ove jednačine mogu se podeliti u dve grupe [71]. Prvu čine metodi integracije, u kojima se Boltzmann-ova jednačina rešava direktnom numeričkom integracijom [71–75], dok drugu grupu čine metodi razvoja, u kojima se funkcija raspodele u faznom prostoru razvija po skupu bazisnih funkcija, nakon čega se Boltzmann-ova jednačina rešava po koeficijentima u razvoju [47,71,76]. Prvi rigorozni metod razvoja je metod Chapman-Enskog, koji su detaljno opisali Chapman i Cowling (1939) [76]. U ovom se metodu funkcija raspodele razvija u faznom prostoru oko Maxwellian-a na temperaturi pozadinskog gasa. S obzirom na to, ovaj je metod primenjiv samo na jako niskim poljima, na kojima energije naelektrisanih čestica ne odstupaju značajno od termalnih energija [77]. Zato je bilo neophodno razviti složenije metode za rešavanje Boltzmann-ove jednačine u uslovima koji značajnije odstupaju od termodinamičke ravnoteže. Istorijski razvoj transportne teorije za elektrone je predstavljen u knjizi Huxley-a i Crompton-a [3], dok je razvoj transportne teorije za jone prikazan u knjizi Mason-a i McDaniel-a [77].

Jedan od najčešćih metoda za rešavanje Boltzmann-ove jednačine, koji se nalazi u osnovi klasične teorije transporta elektrona u gasovima, jeste metod aproksimacije dva člana (eng. *two term approximation*), koji je razvio Lorentz [78]. U ovom metodu se funkcija raspodele u faznom prostoru reprezentuje kao zbir dva člana, od kojih je prvi izotropan u brzinskom prostoru, dok drugi član opisuje odstupanje od izotropije u prostoru brzina. Ova aproksimacija je validna za lake naelektrisane čestice kakvi su elektroni i pozitroni u energijskoj oblasti u kojoj se neelastični sudari mogu zanemariti [62,79]. Aproksimacija dva člana se pak ne može primeniti u uslovima u kojima neelastični sudari proizvode snažnu anizotropiju u brzinskom prostoru [62, 79]. U opsegu polja u kome postoji izražena anizotropija u brzinskom prostoru mora se koristiti

momentni metod više članova (eng. *multi term method*), u kome se zavisnost funkcije raspodele u faznom porstoru od brzinskih koordinata reprezentuje razvojem u red po sfernim harmonicima u brzinskom prostoru – pritom se ovaj red odseca na nekom konačnom članu nakon postizanja konvergencije rezultata [47]. Razvoj metoda više članova za rešavanje Boltzmann-ove jednačine trajao je više decenija. Wilhem i Winkler su razvili aproksimaciju tri člana u stacionarnom i prostorno homogenom slučaju [80]. Razvoj funkcije raspodele u faznom prostoru u četiri člana razmatrali su Cavalleri (1981) [81] i Braglia i saradnici (1984) [82]. Prvi precizan i sistematičan metod više članova, upotrebljiv za proizvoljnu vrednost električnog polja i proizvoljan skup konzervativnih sudarnih procesa, razvili su Lin, Robson i Mason [83]. Njega su Ness i Robson naknadno proširili na slučaj nekonzervativnog transporta naelektrisanih čestica u neutralnim gasovima pod uticajem električnog polja [62,84,85]. U okviru ove teorije se prostorna zavisnost funkcije raspodele u faznom prostoru reprezentuje primenom hidrodinamičke aproksimacije [86]. Hidrodinamička aproksimacija podrazumeva da je roj dostigao stanje u kome se zavisnost funkcije raspodele u faznom prostoru od koordinata u konfiguracionom prostoru i eksplicitna zavisnost od vremena mogu izraziti preko linearnih funkcionala koncentracije naelektrisanih čestica [84,85,89,90]. Ekstenziju hidrodinamičke aproksimacije na slučaj vremenski promenljivih uslova razmatrali su mnogi autori [86,90–97]. Ness je proširio metodu više članova za rešavanje Boltzmann-ove jednačine na slučaj rojeva naelektrisanih čestica koje se kreću pod uticajem električnog i magnetskog polja koja su međusobno ortogonalna [87,88,98]. Dodatnu ekstenziju metoda više članova na konfiguraciju u kojoj električno i magnetsko polje zaklapaju proizvoljan ugao razvio je White [89]. Dujko dalje generalizuje metodu više članova na nekonzervativni transport naelektrisanih čestica: a) u prisustvu vremenski zavisnog električnog polja i vremenski zavisnog magnetskog polja, pri čemu ova polja zaklapaju proizvoljan ugao a između njih postoji proizvoljna fazna razlika, ukoliko su polja harmonijska, b) u slučaju proizvoljne vremenske zavisnosti električnog i magnetskog polja [47,67].

Iako je metodologija za istraživanje transporta naelektrisanih čestica u gasovima sazrela i dostigla visok nivo sofisticiranosti, odgovarajuća metodologija za transport u tečnostima i dalje je u fazi razvoja. Ovo je pre svega posledica velike složenosti interakcije naelektrisanih čestica sa pozadinskom tečnošću. Naime, u tečnoj fazi je rastojanje između susednih atoma (ili molekula) znatno manje od rastojanja na kome se njihova interakcija sa naelektrisanim česticama može zanemariti. Zbog toga je potencijal u kome se rasejava naelektrisana čestica određen velikim brojem atoma (ili molekula) pozadinske sredine [68,99,100]. Pored toga, talasna funkcija lakih naelektrisanih čestica (poput elektrona i pozitrona) zahvata više susednih atoma (ili molekula) u tečnosti. Zato se rasejanje elektrona i pozitrona u tečnoj fazi mora reprezentovati kao superpozicija pojedinačnih rasejanja na više susednih čestica pozadinske sredine [68,100]. To za posledicu ima snažnu zavisnost dinamike rasejanja lakih naelektrisanih čestica u tečnoj fazi od prostornih korelacija atoma (ili molekula) u tečnosti. Konačno, naelektrisane čestice mogu biti zarobljene u fluktuacijama gustine ili solvatirane u klasterima polarnih molekula [101].

Zbog velike složenosti interakcije naelektrisanih čestica sa pozadinskom tečnošću, efekti koji menjaju dinamiku rasejanja u tečnoj fazi u odnosu na gasnu fazu zanemareni su u mnogim ranijim pokušajima modelovanja transporta naelektrisanih čestica u tečnostima – obično je tečna

faza modelovana kao gasna faza sa povećanom gustinom. Jedan od prvih egzaktnih pristupa rasejanju u tečnoj fazi razvio je Van Hove, koji je primenio vremenski zavisnu generalizaciju parne korelacione funkcije na rasejanje neutrona u tečnostima i gustim gasovima u okviru Born-ove aproksimacije [99]. Lekner je uveo *ab initio* metod za određivanje efektivnog potencijala i odgovarajućeg efektivnog preseka za rasejanje elektrona na fokus atomu u tečnoj fazi [100]. Ovaj efektivni potencijal se određuje na osnovu potencijala pojedinačnog atoma i parne korelacione funkcije tečnosti. Pored toga, Cohen i Lekner su pokazali da se koherentno elastično rasejanje može predstaviti pomoću efektivnog preseka za rasejanje elektrona u tečnoj fazi i statičkog strukturnog faktora pozadinske tečnosti [70]. Atrazhev i saradnici su pojednostavili Lekner-ove argumente i pokazali da su efektivni preseci za elastično rasejanje u tečnom argonu, tečnom kriptonu i tečnom ksenonu konstantni za niskoenergijske elektrone [102, 103]. Nakon toga, primenili su metod parcijalnih talasa kako bi odredili efektivne preseke za rasejanje elektrona u tečnom argonu i tečnom ksenonu [104–107]. Na osnovu ovih rezultata, oni su izračunali mobilnost, srednju energiju i karakterističnu energiju elektrona u tečnom argonu i tečnom ksenonu u okviru Cohen-Lekner-ove teorije [106, 107]. Sakai i saradnici su takođe proučavali transport elektrona u tečnom argonu, tečnom kriptonu i tečnom ksenonu, koristeći Cohen-Lekner-ovu teoriju [108, 109]. U tom poduhvatu empirijski su modifikovali preseke za rasejanje elektrona ne bi li popravili slaganje između teorijskih i eksperimentalnih vrednosti brzine drifta. Uz to, pokazali su da se saturacija brzine drifta na visokim vrednostima električnog polja, koja je uočena u eksperimentima, može adekvatno opisati ako se u set preseka uključi efektivni presek za vibracionu ekscitaciju. Ova vibraciona ekscitacija odgovara promeni relativnog kretanja pojedinačnih atoma unutar istog atomskog klastera. Boyle i saradnici odredili su diferencijalne preseke za rasejanje elektrona u tečnom argonu i tečnom ksenonu koristeći Dirac-Fock-ovu jednačinu rasejanja [68, 69]. Proširili su Lekner-ovu teoriju, uzimajući u obzir multipolnu polarizabilnost i nelokalan opis izmenske interakcije [68, 69], a onda su izračunali transportne koeficijente za elektrone u tečnom argonu i tečnom ksenonu, koristeći ove preseke i metod više članova za numeričko rešavanje Boltzmann-ove jednačine.

Uprkos tome što je većina teorijskih istraživanja vezanih za transport elektrona u atomskim tečnostima ograničena na energijsku oblast koja je ispod praga za ekscitacije, nekoliko autora je razmatralo transport elektrona u tečnim plemenitim gasovima na višim elektičnim poljima, na kojima se neelastični sudari i jonizacija ne mogu zanemariti. Atrazhev i saradnici su ispitivali uticaj efekata koji su zavisni od gustine na prvi Townsend-ov koeficijent za jonizaciju u tečnom ksenonu [110]. Oni su napravili dve procene prvog Townsend-ovog koeficijenta, koje su zasnovane na dva različita načina reprezentovanja energijskih gubitaka elektrona u elektronskim ekscitacijama. Kunhardt je proučavao transport elektrona u tečnom argonu primenom Monte Carlo simulacija [111] u kojima je interakcija elektrona sa pozadinskom tečnošću opisana u okviru Van Hove-ove teorije [99]. Isti metod koristili su Jones i Kunhardt za proučavanje transporta elektrona u tečnom ksenonu [112]. Grupa sa Univerziteta Hokaido ispitivala je jonizaciju u tečnom ksenonu, kao i zahvat elektrona u smešama tečnog argona i elektronegativnih nečistoća poput O_2, SF_6 i N_2O [113]. Boyle i saradnici su razvili model zasnovan na fluidnim jednačinama za pozitrone i elektrone u tečnostima, koristeći preseke iz gasne faze i statički strukturni faktor

tečnosti [114–117].

Postoji znatno manji broj teorijskih istraživanja u kojima se modeluje propagacija strimera u tečnostima od odgovarajućih istraživanja u gasnoj fazi. Naidis i saradnici su ispitivali strimere u tečnim hidrokarbonatima, koristeći jednoipodimenzioni fluidni model prvog reda [118,119]. U okviru ovog pravca istraživanja oni su razmatrali uticaj formiranja gasnog filamenta i njegovog daljeg širenja na dinamiku propagacije strimera u tečnoj fazi. Babaeva i Naidis bavili su se dinamikom strimera u tečnom argonu i tečnom ksenonu primenom numeričkih modela [120–122]. Oni su pratili formiranje pozitivnog strimera u snažnom nehomogenom polju i njegovu kasniju propagaciju u slabom homogenom polju [120–122]. U njihovim radovima je pokazano kako je dinamika propagacije strimera u tečnoj fazi jako osetljiva na rekombinaciju elektrona i pozitivnih jona [120–122]. Pored toga, ustanovljeno je da izračunate vrednosti brzine strimera imaju isti red veličine kao izmerena brzina probojnog talasa u tečnom argonu [120–122]. Propagacija strimera u gasnim mehurovima je ispitivana u okviru brojnih eksperimenata i numeričkih proračuna [123,124] čija je zajednička karakteristika korišćenje aproksimativnih vrednosti transportnih koeficijenata u tečnoj fazi, bez uzimanja u obzir svih efekata koji utiču na dinamiku rasejanja naelektrisanih čestica u tečnosti.

Jedna od centralnih tema u ovoj disertaciji je ispitivanje transportnih koeficijenata trećeg reda u gasovima i atomskim tečnostima. Iako se u literaturi može naći velika količina informacija vezanih za transportne koeficijente nižeg reda, poput brzine drifta, difuzionog tenzora i brzinskih koeficijenata za reakcije za elektrone, jone i pozitrone, jako malo se zna o transportnim koeficijentima višeg reda [31,125]. Ovo je posledica toga što je transportne koeficijente višeg reda teško izmeriti u eksperimentima i teško izračunati na osnovu teorijskih metoda. Eksperimenti sa rojevima su prilagođeni uslovima u kojima se transportni koeficijenti nižeg reda mogu izmeriti sa što većom tačnošću. Međutim, u tim uslovima je doprinos transportnih koeficijenata višeg reda prostornim profilima naelektrisanih čestica zanemariv [126,127]. Prvi pokušaj merenja transportnih koeficijenata trećeg reda načinili su Hunter i saradnici [128,129] u eksperimentu sa vremenom preleta (eng. time-of-flight experiment) u čistom vodoniku. Ipak, pouzdanost rezultata u vezi sa transportnim koeficijentima višeg reda bila je dovedena u pitanje, te ovi rezultati nikada nisu publikovani. Drugi pokušaj merenja transportnih koeficijenata trećeg reda vezuje se za rad Denman-a i Schile-a [130]. Rezultati ovog eksperimenta takođe su bili nepouzdani zbog nehidrodinamičke zavisnosti izmerenih transportnih koeficijenata od pritiska [126,130]. Kasnije je objašnjeno da je gubitak visokoenergijskih elektrona na bočnim zidovima suda usled velike dužine komore koja je korišćena u eksperimentu i intenzivne bočne difuzije doveo do promene energijske raspodele elektrona u toku trajanja eksperimenta [126]. Uprkos ovome, više autora je procenilo da transportni koeficijenti trećeg reda mogu biti izmereni u savremenim eksperimentima [126,131].

Transportni koeficijenti trećeg reda mogu imati više značajnih primena. Naime, pokazano je da su transportni koeficijenti višeg reda potrebni pri konverziji hidrodinamičkih transportnih koeficijenata u transportne podatke koji se mere u stacionarnom Townsend-ovom eksperimentu (eng. *steady state Townsend experiment*) [31] i u eksperimentu sa spektrima pristižućih čestica

(eng. *arrival time spectra experiment*) [32]. Pored toga, poznato je da su transportni koeficijenti trećeg reda osetljiviji na energijsku zavisnost preseka za elementarne sudarne procese od transportnih koeficijenata nižeg reda [126,132]. Ovo ukazuje da bi transportni koeficijenti trećeg reda mogli da doprinesu poboljšanju procedure za određivanje setova preseka za sudare naelektrisanih čestica sa atomima ili molekulima na osnovu metode rojeva (eng. *swarm analysis*) ako bi ovi transportni koeficijenti bili računati i mereni sa dovoljnom preciznošću. Uz to, transportni koeficijenti višeg reda su potrebni za bolji opis prostornih raspodela rojeva naelektrisanih čestica u prisustvu električnog polja. Zapravo, u ranijim Monte Carlo istraživanjima [29,133] je pokazano da prostorne raspodele naelektrisanih čestica odstupaju od idealnog Gaussian-a, koji bi reprezentovao prostornu raspodelu roja u uslovima u kojima su transportni koeficijenti višeg reda zanemarljivi. Pored toga se oblici profila roja koji su primećeni u nekim simulacijama na kvalitativnom nivou dobro slažu sa aproksimativnim rešenjem generalisane difuzione jednačine u kojoj je doprinos transportnog tenzora trećeg reda uzet u obzir [29]. Još jedna motivacija za izučavanje transportnih koeficijenata trećeg reda je to što numerički proračuni komponenti transportnog tenzora trećeg reda u modelnim gasovima mogu da se koriste za proveru novih kompjuterskih kodova koji su namenjeni za proračun transportnih koeficijenata naelektrisanih čestica u gasovima ili tečnostima, imajući u vidu njihovu veliku osetljivost na energijske promene preseka.

Whealton i Mason su prvi odredili strukturu transportnog tenzora trećeg reda u odsustvu magnetskog polja [134]. Tom prilikom ustanovljeno je da ovaj tenzor ima sedam nenultih elemenata od kojih su tri međusobno nezavisna. Ovi autori su takođe pokazali da su u odsustvu električnog polja sve komponente transportnog tenzora trećeg reda jednake nuli. Izračunali su longitudinalnu komponentu transportnog tenzora trećeg reda za elektrone u Maxwell-ovom modelnom gasu, koristeći analitičko rešenje Boltzmann-ove jednačine. Penetrante i Bardsley [126] su proučavali transportne koeficijente trećeg reda za elektrone u helijumu, neonu i argonu primenom Monte Carlo simulacija i numeričkog rešavanja Boltzmann-ove jednačine u okviru aproksimacije dva člana. Oni su se u svojim proračunima ograničili na niske vrednosti redukovanog električnog polja na kojima elektroni učestvuju samo u elastičnim sudarima sa atomima pozadinskog gasa. Izračunali su spektre pristižućih čestica (eng. *arrival time spectra*) u tipičnim uslovima drift cevi (eng. *drift tube*) s ciljem procene da li se transportni koeficijenti trećeg reda mogu izmeriti [126]. Njihov zaključak svodi se na to da transportni koeficijenti trećeg reda mogu biti izmereni u savremenim eksperimentima. Sličnu proceduru za određivanje transportnih koeficijenata nižeg i višeg reda na osnovu spektra pristužućih čestica ranije su predložili Kondo i Tagashira [32]. Koutselos je proučavao transportne koeficijente trećeg reda za K^+ jone u argonu primenom molekularno dinamičkih simulacija [135,136], nakon čega je primenio trotemperaturski razvoj Boltzmann-ove jednačine da bi odredio transportne koeficijente trećeg reda za Li^+ jone u argonu i helijumu i K^+ jone u argonu [137,138]. Na osnovu ovog metoda on je ispitao uticaj odnosa masa jona i neutralnih čestica na transportne koeficijente trećeg reda u R^{-8} potencijalu u limesu hladnog gasa. Vrhovac i saradnici su odredili generalisane Einstein-ove jednačine za transportni koeficijent n-tog reda u okviru teorije prenosa impulsa (eng. *momentum transfer theory*) [132,139]. U ovim jednačinama se transportni koeficijent n-

tog reda izražava preko $(n-1)$-og izvoda brzine drifta i n-tog izvoda brzinskog koeficijenta za reakcije. Na osnovu ove teorije i odgovarajućeg kompjuterskog koda Vrhovac i saradnici su odredili transportne koeficijente trećeg reda za elektrone u helijumu, neonu i argonu na niskim vrednostima redukovanog električnog polja [132,139]. Kawaguchi i saradnici su odredili vezu između longitudinalne komponente transportnog tenzora trećeg reda i α-parametara (koeficijenata koji se mere u eksperimentima sa spektrima pristižućih čestica) primenom teorije koju su razvili Kondo i Tagashira [131]. Njihovi rezultati ukazuju da se transportni koeficijenti trećeg reda mogu izmeriti u savremenim eksperimentima sa spektrima pristižućih čestica. Kawaguchi i saradnici su izračunali longitudinalnu komponentu transportnog tenzora trećeg reda i α-parametre za elektrone u CH_4 i SF_6 primenom Monte Carlo simulacija.

U poglavlju 2 biće predstavljena transportna teorija na kojoj su zasnovani proračuni urađeni u okviru ove disertacije. Na početku ovog poglavlja biće definisan roj naelektrisanih čestica. Zatim će biti prikazane osnove teorije rasejanja elektrona u gasovima i tečnostima. Nakon toga će biti date definicije hidrodinamičkog režima i dve različite familije transportnih koeficijenata. Na kraju ovog poglavlja predstavićemo rezultate istraživanja u vidu strukture vektorskih i tenzorskih veličina, za različite konfiguracije električnog i magnetskog polja, a poseban akcenat biće stavljen na strukturu transportnog tenzora trećeg reda.

Poglavlje 3 donosi prikaz metoda koji su korišćeni za izračunavanje transportnih veličina u okviru ove disertacije. Prvo navodimo osnovne elemente kinetičke teorije za numeričko rešavanje Boltzmann-ove jednačine. Potom su razmatrani fluidni modeli i teorija prenosa impulsa za rojeve naelektrisanih čestica u nepolarnim tečnostima. Nakon toga biće predstavljen Monte Carlo metod, kao i najvažniji elementi odgovarajućeg kompjuterskog koda koji je korišćen u ovoj disertaciji.

U poglavlju 4 detaljno je analiziran fizički smisao transportnih koeficijenata trećeg reda. Slede rezultati benčmark proračuna ovih transportnih koeficijenata za naelektrisane čestice u modelnim gasovima, pri čemu će analizi biti podvrgnut uticaj elastičnih, neelastičnih i nekonzervativnih sudara, kao i odnos masa naelektrisanih čestica roja i neutralnih čestica pozadinske sredine, na transportne koeficijente trećeg reda.

U poglavlju 5 biće prikazani rezultati proračuna transportnih koeficijenata trećeg reda za elektrone u realnim gasovima. Prvo se duskutuje o korelaciji između longitudinalne komponente transportnog tenzora trećeg reda i longitudinalne komponente difuzionog tenzora. Zatim će biti razmatrani transportni koeficijenti trećeg reda za elektrone u atomskim i molekularnim gasovima. Nakon toga ispituju se ovi transportni koeficijenti za pozitrone u molekularnim gasovima.

U narednom, 6. poglavlju dati su proračuni transportnih koeficijenata za elektrone u atomskim tečnostima velike mobilnosti. Na početku obrazlažemo motivacione faktore za ispitivanje transporta elektrona u tečnoj fazi. Nakon toga raspravlja se o prisustvu provodne zone u atomskim tečnostima velike mobilnosti, te se izlažu setovi preseka za rasejanje elektrona u tečnom argonu, tečnom kriptonu i tečnom ksenonu (koji su korišćeni u izradi ove disertacije), kao i rezultati proračuna transportnih koeficijenata i drugih transportnih veličina u ovim tečnostima.

Poglavlje 7 sadrži prikaz fluidnih modela strimera u tečnoj fazi, kao i njihove numeričke implementacije, korišćene u ovoj disertaciji. Nakon toga, u ovom poglavlju biće predočeni rezultati simulacija koje prate formiranje i propagaciju negativnih strimera u tečnom argonu, tečnom kriptonu i tečnom ksenonu u prisustvu stacionarnog i prostorno homogenog spoljašnjeg električnog polja.

Osmo, i poslednje, poglavlje sumira ključne rezultate i originalne doprinose ove disertacije. Na ovom mestu biće naznačeni i novi pravci budućih istraživanja. U dodacima A, B i C prikazaćemo metod grupnih projektora, eksplicitne izraze za izračunavanje transportnih koeficijenata trećeg reda na osnovu numeričkih rešenja Boltzmann-ove jednačine, kao i eksplicitne izraze za izračunavanje ovih transportnih koeficijenata u kompjuterskom kodu baziranom na Monte Carlo metodi.

2 Teorija rojeva naelektrisanih čestica u gasovima i tečnostima

2.1 Uvod

U ovom poglavlju predstavljeni su osnovni elementi teorije uzete za osnovu ove disertacije. U potpoglavlju 2.2 definisan je roj naelektrisanih čestica. U potpoglavlju 2.3 prikazana je teorija rasejanja naelektrisanih čestica u gasovima i tečnostima, na osnovu koje su Boyle i saradnici [68, 69] odredili preseke za elastično rasejanje niskoenergijskih elektrona u tečnom argonu i tečnom ksenonu, koji su korišćeni u izradi ove disertacije. Ovu teoriju razvili su McEachran i saradnici [140] i Boyle i saradnici [68, 69]. U potpoglavlju 2.4 izložene su definicije hidrodinamičkog režima i transportnih koeficijenata, dok potpoglavlje 2.5 prikazuje strukturu vektorskih i tenzorskih veličina u svim konfiguracijama električnog i magnetskog polja.

2.2 Roj naelektrisanih čestica

Osnovni fizički objekat koji se razmatra u ovoj disertaciji je roj naelektrisanih čestica, koji je u fizici plazme poznat kao limit probnih čestica ili limit slobodne difuzije. Pod pojmom roj podrazumeva se ansambl naelektrisanih čestica koji se kreće u neutralnom pozadinskom fluidu koji se nalazi u stanju termodinamičke ravnoteže i u kome su u opštem slučaju prisutni homogeno električno i homogeno magnetsko polje [26, 47, 52]. Pritom je pretpostavljeno da je koncentracija naelektrisanih čestica dovoljno mala da se njihove međusobne interakcije, kao i njihov uticaj na neutralni pozadinski fluid i na vrednosti rezultujućeg električnog i magnetskog polja mogu zanemariti. Iako se pozadisnki fluid nalazi u stanju termodinamičke ravnoteže, roj naelektrisanih čestica ne mora biti u termodinamičkoj ravnoteži sa svojim okruženjem. Ako je srednja energija naelektrisanih čestica viša od termalne energije, koja odgovara temperaturi pozadinskog fluida, može se očekivati da funkcija raspodele naelektrisanih čestica po energijama snažno odstupa od ravnotežnog Maxwellian-a .

Dinamika roja je određena uticajem spoljašnjih polja i sudarima naelektrisanih čestica sa neutralnim česticama pozadinskog fluida [26, 47, 52]. Pri tome roj dobija energiju od električnog polja a gubi je u sudarima. Zanimljivo je pomenuti da postoje uslovi u radio-frekventnim (RF) električnim i magnetksim poljima u kojima roj dobija energiju i porastom magentskog polja [141]. Ako u slučaju konstantnih spoljašnjih polja dođe do ravnoteže između dobitaka i gubitaka energije u jedinici vremena, roj dostiže stacionarno stanje u kome se njegova funkcija raspodele po energiji ne menja u vremenu. Ova funkcija raspodele zavisi od spoljašnjeg električnog i magnetskog polja, od prirode neutralnog pozadinskog fluida (od mase čestica pozadinskog fluida i od odgovarajućih preseka za sudare čestica roja sa ovim česticama), kao i od njegove temperature. Na dovoljno visokim poljima se funkcija raspodele po energiji koja opisuje roj naelektrisanih čestica može značajno razlikovati od Maxwell-Boltzmann-ove raspodele [26, 47, 52].

U gasnoj fazi je rastojanje na kome deluje potencijal pojedinačne neutralne čestice pozadinske sredine znatno manje od rastojanja između neutralnih čestica, kao i od srednjeg slobodnog puta naelektrisanih čestica. Zbog toga je interakcija roja i pozadinskog gasa u potpunosti određena binarnim sudarima. Međutim, u tečnoj fazi je rastojanje između neutralnih čestica pozadinske srednine uporedivo sa rastojanjem na kome deluje potencijal pojedinačne neutralne čestice. Pri tome talasna funkcija lakih naelektrisanih čestica (poput elektrona i pozitrona) zahvata veliki broj susednih neutralnih čestica u tečnosti. Zbog toga se u tečnoj fazi interakcija roja i pozadinske sredine ne može u potpunosti opisati binarnim sudarima, pa je pri određivanju dinamike rasejanja lakih naelektrisanih čestica neophodno uzeti u obzir prostorne korelacije između neutralnih čestica pozadinske tečnosti.

2.3   Teorija rasejanja elektrona u gasovima i tečnostima

Karakteristike rojeva naelektrisanih čestica i neravnotežnih plazmi snažno zavise od prirode pozadinskog fluida. Zbog toga je ispravan opis sudara naelektrisanih čestica sa atomima (ili molekulima) pozadinske sredine od ključnog značaja u transportnim proračunima. U ovom potpoglavlju je ukratko prikazana teorija rasejanja elektrona u gasovima i tečnostima. Ovu teoriju razvili su McEachran i saradnici za slučaj rasejanja elektrona i pozitrona na izolovanom atomu [140, 142–144]. Za generalizaciju pomenute teorije na slučaj rasejanja elektrona u atomskim tečnostima zaslužan je G. Boyle sa svojim saradnicima [68, 69, 145]. Detaljan prikaz teorije rasejanja, o kojoj raspravljamo u ovom potpoglavlju, može se naći u disertaciji Greg-a Boyle-a [145]. Ovde se ograničavamo na slučaj rasejanja elektrona na izolovanim atomima i u atomskim tečnostima, ali treba imati u vidu da se analiza koju sprovodimo može generalizovati na slučaj nepolarnih molekula.

U razređenim gasovima rastojanje između atoma je znatno veće od rastojanja na kome elektron oseća potencijal pojedinačnog atoma. Zbog toga se rasejanje elektrona u razređenim gasovima može reprezentovati binarnim sudarima. Uticaj potencijala ostalih čestica pozadinske sredine i uticaj spoljašnjih polja mogu se u potpunosti zanemariti u toku binarnog sudara, te se može smatrati kako je dinamika elektrona za vreme sudara u potpunosti određena potencijalom atoma.

Potencijal za rasejanje elektrona na pojedinačnom atomu može se razložiti na statički deo, koji odgovara elektrostatičkoj interakciji, polarizacioni deo, koji odgovara interakciji elektrona sa indukovanim dipolom i indukovanim višim multipolnim članovima atoma, i izmenski deo koji odgovara izmenskoj interakciji elektrona koji se rasejava sa elektronima iz omotača atoma [100, 145]. Polarizaciona interakcija se može predstaviti dugodometnim članovima koji figurišu u razvoju potencijala za rasejanje po multipolima [145]. Izmenska interakcija se opisuje kratkodometnim nelokalnim potencijalom, koji se dobija antisimetrizacijom totalne talasne funkcije sistema [145].

Rasejanje upadnog elektrona sa talasnim brojem k na izolovanom atomu u gasnoj fazi

moguće je opisati pomoću Dirac-Fock-ove jednačine [144, 145]

$$\begin{pmatrix} f_\kappa(r) \\ g_\kappa(r) \end{pmatrix} = \begin{pmatrix} v_1(kr) \\ v_2(kr) \end{pmatrix} + \frac{1}{k} \int_0^r dx\, G(r,x) \left[V(x) \begin{pmatrix} f_\kappa(x) \\ g_\kappa(x) \end{pmatrix} - \begin{pmatrix} \overline{W}_Q(\kappa;x) \\ \overline{W}_P(\kappa;x) \end{pmatrix} \right], \qquad (2.1)$$

gde je $G(r,x)$ Green-ova funkcija slobodne čestice, $V(r)$ je potencijal koji je određen sumom statičkog i polarizacionog dela $V(r) = V_s(r) + V_p(r)$, dok $\overline{W}_P(\kappa;r)$ i $\overline{W}_Q(\kappa;r)$ reprezentuju veliku i malu komponentu izmenske interakcije. Slično tome $f_\kappa(r)$ i $g_\kappa(r)$ predstavljaju veliku i malu komponentu talasne funkcije rasejanja (eng. scattering wave function) [144, 145]. Kvantni broj κ se može izraziti preko ukupnog ugaong momenta j i orbitalnog angularnog momenta l kao [144, 145]

$$j = |\kappa| - \frac{1}{2}, \qquad \text{gde je } l = \begin{cases} \kappa, & \kappa > 0 \\ -\kappa - 1, & \kappa < 0 \end{cases}.$$
$$(2.2)$$

Statički deo potencijala se određuje na osnovu Dirac-Fock-ovih orbitala atoma [144], dok se polarizacioni potencijal određuje primenom metoda polarizovanih orbitala [140, 146, 147]. Eksplicitan izraz za izmenske članove $\overline{W}_P(\kappa;r)$ i $\overline{W}_Q(\kappa;r)$ dat je u referenci [145] i jednačina (2.1) se mora rešavati iterativno zbog zavisnosti izmenskih članova od funkcije rasejanja.

Veliki deo talasne funkcije rasejanja $f_\kappa(r)$ ima sledeći asimptotski oblik

$$f_\kappa(r) \longrightarrow A_\kappa \hat{j}_l(kr) - B_\kappa \hat{n}_l(k,r), \ r \to \infty, \qquad (2.3)$$

gde su $\hat{j}_l(kr)$ i $\hat{n}_l(kr)$ Bessel-ova i Neumann-ova funkcija, dok su eksplicitni izrazi za koeficijente A_κ i B_κ dati u referenci [145].

Fazni pomeraji parcijalnih talasa pri rasejanju mogu se odrediti na osnovu asimptotskog oblika velike komponente talasne funkcije rasejanja kao

$$\tan \delta_l^\pm(k) = \frac{B_\kappa}{A_\kappa}, \qquad (2.4)$$

gde se znaci $+$ i $-$ odnose na orijentaciju spina elektrona nagore i nadole, respektivno. Na osnovu faznih pomeraja parcijalnih talasa dieferncijalni presek za rasejanje elektrona određuje se kao

$$\sigma(k,\chi) = |f(k,\chi)|^2 + |g(k,\chi)|^2, \qquad (2.5)$$

gde su $f(k,\chi)$ i $g(k,\chi)$ direktna amplituda rasejanja i amplituda rasejanja sa promenom orijentacije spina respektivno [144]. Ove amplitude se mogu odrediti kao [144]

$$f(k,\chi) = \frac{1}{k} \sum_{l_2=0}^{\infty} \left[(l_2 + 1) T_{l_2}^+(k) + l_2 T_{l_2}^-(k) \right] P_{l_2}(\cos\chi), \qquad (2.6)$$

$$g(k,\chi) = \frac{1}{k} \sum_{l_2=0}^{\infty} \left[T_{l_2}^-(k) - T_{l_2}^+(k) \right] P_{l_2}^1(\cos\chi), \qquad (2.7)$$

gde su P_{l_2} i $P_{l_2}^1$ Legendre-ovi polinomi i asocirani Legendre-ovi polinomi, respektivno, dok su $T_{l_2}^\pm(k)$ elementi T-matrice, koji se mogu odrediti na osnovu jednačine [144]

$$T_{l_2}^\pm(k) = \frac{1}{2i}\Big[\exp\big(2i\delta_{l_2}^\pm(k)\big) - 1\Big]. \tag{2.8}$$

Kada je poznat diferencijalni presek $\sigma(k,\chi)$, totalni presek za rasejanje $\sigma_T(k)$ i presek za transfer impulsa (eng. momentum transfer cross section) $\sigma_m(k)$ se mogu odrediti kao [145]

$$\sigma_T(k) = 2\pi\int_0^\pi \sigma(k,\chi)\sin\chi\mathrm{d}\chi$$
$$= \frac{4\pi}{k^2}\sum_{l=0}^\infty \Big((l+1)\sin^2(\delta_l^+) + l\sin^2(\delta_l^-)\Big), \tag{2.9}$$

$$\sigma_m(k) = 2\pi\int_0^\pi \big(1-\cos\chi\big)\sigma(k,\chi)\sin\chi\mathrm{d}\chi \tag{2.10}$$
$$= \frac{4\pi}{k^2}\sum_{l=0}^\infty \Bigg(\frac{(l+1)(l+2)}{(2l+3)}\sin^2(\delta_l^+ - \delta_{l+1}^+) + \frac{l(l+1)}{(2l+1)}\sin^2(\delta_l^- - \delta_{l+1}^-)$$
$$+ \frac{(l+1)}{(2l+1)(2l+3)}\sin^2(\delta_l^+ - \delta_{l+1}^-)\Bigg). \tag{2.11}$$

Kada se u jednačinama (2.9) i (2.11) zanemari orijentacija spina upadnog elektrona $\delta_l^+ = \delta_l^- \equiv \delta^l$, dobiju se nerelativistički izrazi za $\sigma_T(k)$ i $\sigma_m(k)$.

Pri rasejanju elektrona na izolovanom atomu, prisustvo elektrona dovodi do indukovanja električnog dipola i viših članova u multipolnom razvoju na datom atomu. U razređenom gasu je domet polarizacionog potencijala znatno manji od međuatomskog rastojanja, pa ostali atomi ne utiču na polarizacioni potencijal pojedinačnog atoma. Međutim, u tečnoj fazi mnogi atomi mogu imati značajnu vrednost indukovanih multipolnih momenata koji potiču od elektrona koji se rasejava i od svih ostalih atoma u okolini [68, 69, 100, 145]. Efektivni polarizacioni potencijal koji oseća elektron u datoj tački prostora je superpozicija polarizacionih potencijala svih atoma koji se nalaze u okolini elektrona. Ovaj efektivni polarizacioni potencijal se može napisati u obliku $f(r)\alpha_d(r)e/r^2$, gde je r rastojanje između atoma i elektrona, dok je $\alpha_d(r)$ polarizabilnost atoma [145]. Član $f(r)$ opisuje ekraniranje polarizacionog potencijala fokus atoma polarizaci-onim potencijalima okolnih atoma. U slučaju razređenog gasa važi $f(r) = 1$, dok se u slučaju tečne faze $f(r)$ mora odrediti samousaglašeno [145].

Za fokus atom i koji se nalazi u položaju $\mathbf{r}_i$ koeficijent ekraniranja $f_i(r)$ može se odrediti na osnovu jednačine

$$f_i(r) = 1 - \pi n_0 \int_0^\infty \mathrm{d}s \frac{g(s)}{s^2} \int_{|r-s|}^{r+s} \mathrm{d}t\,\Theta(r,s,t)\frac{\alpha_d(t)f_{\mathrm{balk}}(t)}{t^2}, \tag{2.12}$$

gde je $\mathbf{r}$ radijus vektor između elektrona i fokus atoma, f_{balk} je koeficijent ekraniranja ostalih atoma, pri čemu su n_0 i $g(s)$, koncentracija i parna korelaciona funkcija pozadinske tečnosti,

respektivno, dok su s i t rastojanje između atoma u balku i fokus atoma i i rastojanje između elektrona i atoma u balku, respektivno, uz šta se Θ može napisati u obliku [145]

$$\Theta(r, s, t) = \frac{3}{2} \frac{(s^2 + t^2 - r^2)(s^2 + r^2 - t^2)}{s^2} + r^2 + t^2 - s^2. \tag{2.13}$$

Samousaglašeno rešavanje jednačine (2.12) postiže se postavljanjem $f_i(r) = f_{balk}(r)$ i daljim iterativnim rešavanjem ove jednačine [145]. Ekranirani polarizacioni potencijal fokus atoma $\tilde{V}_p(r)$ može se napisati u obliku $\tilde{V}_p(r) = f(r)V_p(r)$, gde je $V_p(r)$ polarizacioni potencijal izolovoanog atoma, koji u sebi sadrži doprinos indukovanog dipola i indukovanih viših članova u razvoju potencijala po multipolima [145].

U tečnoj fazi je interakcija okolnih atoma sa elektronom značajna čak i kada je elektron jako blizu fokus atoma. Pored toga što polarizacioni potencijali ovih atoma ekraniraju polarizacioni potencijal fokus atoma, dinamika rasejanja elektrona je određena kombinovanim uticajem potencijala fokus atoma i potencijala svih okolnih atoma. Zbog toga je za opis rasejanja elektrona u tečnoj fazi potrebno odrediti efektivni potencijal koji u sebi sadrži informaciju o interakciji elektrona sa okolnim atomima pri rasejanju na fokus atomu. Ovaj efektivni potencijal se može napisati u obliku $V_{\text{eff}} = V_1 + V_2$, gde je V_1 potencijal za direktnu interakciju elektrona i fokus atoma, dok V_2 odgovara interakciji elektrona sa ostatkom tečnosti. Potencijal V_2 se određuje usrednjavanjem potencijala V_1 po ansamblu atoma [68, 100, 145]

$$V_2(r) = \frac{2\pi n_0}{r} \int_0^\infty \mathrm{d}t V_1(t) \int_{|r-t|}^{r+t} sg(s)\mathrm{d}s. \tag{2.14}$$

Na sličan način se efektivna izmenska interakcija može napisati u obliku

$$\overline{W}_{(P\vee Q),\text{eff}} = \overline{W}_{(P\vee Q)} + \overline{W}_{(P\vee Q),2}, \tag{2.15}$$

gde se $\overline{W}_{(P\vee Q),2}$ određuje usrednjavanjem $\overline{W}_{(P\vee Q)}$ po ansamblu atoma [145]. Pošto $\overline{W}$ zavisi od talasne funkcije $\overline{W}_{(P\vee Q),2}$ se mora ponovo računati pri svakoj iteraciji jednacine (2.1).

Uzimajući u obzir to što se u tečnostima menja efektivni potencijal u kome se rasejava elektron u odnosu na razređeni gas, treba naglasiti kako je u tečnoj fazi potrebno da se pojedinačni sudarni događaj definiše drugačije nego u gasnoj fazi. Naime, u razređenom gasu se može smatrati da se elektron rasejava na izolovanom atomu (ili molekulu), kao i da je pojedinačni sudarni događaj završen kada se elektron beskonačno udalji od datog atoma. U tom slučaju se fazni pomeraji parcijalnih talasa računaju na beskonačnoj udaljenosti od centra rasejanja. U tečnoj se fazi pak elektron nakon konačnog udaljavanja od fokus atoma već nalazi u bliskoj okolini nekog drugog atoma. Rastojanje nakon koga je V_1 zanemarljivo u odnosu na V_2 označeno je sa r_m i ovo rastojanje određuje deo prostora u kome je elektron pod dominatnim uticajem fokus atoma. Na osnovu toga se smatra da se rasejanje na fokus atomu odvija dok je rastojanje elektrona i fokus atoma manje od r_m [68, 145]. Rastojanje r_m se razlikuje od minimalnog rastojanja na kome mogu da se nađu dva atoma, σ_{core}. Pri tome važi $r_m \approx \frac{2}{3}\sigma_{core} > \sigma_{core}/2$ [145]. U radu Boyle-a i saradnika fazni pomeraji parcijalnih talasa se računaju na položaju r_m umesto u beskonačnosti [68, 145].

Pored toga što je u tečnoj fazi potencijal za rasejanje elektrona na fokus atomu drugačiji nego u razređenim gasovima, efektivno rasejanje elektrona u tečnosti se mora predstaviti kao superpozicija pojedinačnih rasejanja na više fokus atoma, i to zbog toga što talasna funkcija elektrona zahvata veliki broj susednih atoma u tečnoj fazi [70, 100]. Tako se dvostruki diferencijalni presek za rasejanje elektrona u tečnosti može napisati u obliku

$$\frac{\mathrm{d}^2\sigma}{\mathrm{d}\mathbf{k}'\mathrm{d}\omega'} = \left(\frac{\mathrm{d}\sigma}{\mathrm{d}\omega'}\right)^{(lab)} S(\Delta\mathbf{k}, \Delta\omega), \tag{2.16}$$

gde je $\left(\frac{\mathrm{d}\sigma}{\mathrm{d}\omega'}\right)^{(lab)}$ presek za rasejanje elektrona na jednom fokus atomu (ili molekulu) pozadinske sredine u laboratorijskom sistemu reference, $S(\Delta\mathbf{k}, \Delta\omega)$ je dinamički strukturni faktor, dok su $\Delta\mathbf{k} \equiv \mathbf{k} - \mathbf{k}'$ i $\omega \equiv \omega - \omega'$ promene talasnog vektora i ugaone frekvence elektrona pri sudaru, respektivno. Dinamički strukturni faktor je Furijeov transform Van Hoveove generalisane vremenski zavisne parne korelacione funkcije po prostornim koordinatama i vremenu [99, 114, 114]. Dvostruki diferencijalni presek u jednačini (2.16) je faktorisan na dva člana od kojih jedan zavisi samo od interakcije elektrona i fokus atoma (ili molekula) pozadinske sredine, dok drugi zavisi samo od prostornih i vremenskih korelacija neutralnih čestica pozadinske sredine [114].

2.4 Hidrodinamički režim i definicija transportnih koeficijenata

Ako se roj naelektrisanih čestica, koje se kreću kroz neutralan pozadinski fluid, nalazi u oblasti prostorno homogenog električnog i magnetskog polja, pri čemu su čestice roja daleko od granica sistema kao i od izvora i ponora čestica, zavisnost fazne funkcije raspodele roja (funkcije raspodele u faznom prostoru) od prostornih koordinata $\mathbf{r}$ može se izraziti preko funkcionala koncentracije čestica roja [26, 47, 52]

$$f(\mathbf{r}, \mathbf{c}, t) = \sum_{k=0}^{\infty} \mathbf{f}^{(k)}(\mathbf{c}, t) \odot (-\nabla)^k n(\mathbf{r}, t), \tag{2.17}$$

gde su $f(\mathbf{r}, \mathbf{c}, t)$ i $n(\mathbf{r}, t)$ fazna funkcija raspodele i koncentracija čestica roja, respektivno, dok $\odot$ označava tenzorsku kontrakciju reda k. Tenzori $\mathbf{f}^{(k)}(\mathbf{c}, t)$ u opštem slučaju zavise od brzinske koordinate $\mathbf{c}$ i vremena t, pri čemu zavisnost od vremena nestaje u slučaju vremenski konstantnih spoljašnjih polja. Razvoj funkcije raspodele po gradijentima koncentracije, koji je prikazan u jednačini (2.17), naziva se hidrodinamički razvoj fazne funkcije raspodele. Uslovi u kojima je zadovoljena jednačina (2.17) jesu hidrodinamički uslovi (ili hidrodinamički režim). Hidrodinamički razvoj nije primenjiv u uslovima u kojima se spoljašnja polja naglo menjaju u prostoru ili vremenu, kao ni u uslovima u kojima su gradijenti koncentracije veliki [47, 52]. U hidrodinamičkom režimu se mogu definisati dve familije transportnih koeficijenata (balk i fluks transportni koeficijenti) koji kvantitativno opisuju kretanje roja [47, 52].

Veza između teorije i eksperimenta može se uspostaviti uz pomoć jednačine kontinuiteta, zato što su koncentracija naelektrisanih čestica i električna struja eksperimentalno merljive veličine [27]. Ova jednačina se može napisati u obliku

$$\frac{\partial n(\mathbf{r}, t)}{\partial t} + \nabla \cdot \mathbf{\Gamma}(\mathbf{r}, t) = S(\mathbf{r}, t), \tag{2.18}$$

gde su $\mathbf{\Gamma}(\mathbf{r}, t)$ i $S(\mathbf{r}, t)$ fluks naelektrisanih čestica i izvorni član, respektivno. U hidrodinamičkom režimu se ove dve veličine mogu razviti po gradijentima koncentracije na sledeći način

$$\mathbf{\Gamma}(\mathbf{r}, t) = \sum_{k=0}^{\infty} \mathbf{\Gamma}^{(k+1)}(t) \odot (-\nabla)^k n(\mathbf{r}, t), \qquad (2.19)$$

$$S(\mathbf{r}, t) = \sum_{k=0}^{\infty} \mathbf{S}^{(k)}(t) \odot (-\nabla)^k n(\mathbf{r}, t), \qquad (2.20)$$

gde su $\mathbf{\Gamma}^{(k+1)}(t)$ fluks transportni koeficijenti, dok su $\mathbf{S}^{(k)}(t)$ koeficijenti u razvoju izvornog člana [27, 47]. Brojevi u superskriptu, k+1 i k, označavaju rang odgovarajućih tenzora. Ovi koeficijenti u razvoju su vremenski nezavisni u slučaju stacionarnih spoljašnjih polja. Odsecanjem hidrodinamčikog razvoja fluksa čestica na $k = 2$ dobija se jednačina

$$\mathbf{\Gamma}(\mathbf{r}, t) = \mathbf{W}^{\star}(t)n(\mathbf{r}, t) - \hat{\mathbf{D}}^{\star}(t) \cdot \nabla n(\mathbf{r}, t) + \hat{\mathbf{Q}}^{\star}(t)(\nabla \otimes \nabla)n(\mathbf{r}, t) + ..., \qquad (2.21)$$

u kojoj su $\mathbf{W}^{\star}(t)$, $\hat{\mathbf{D}}^{\star}(t)$ i $\hat{\mathbf{Q}}^{\star}(t)$ fluks brzina drifta, fluks difuzioni tenzor i fluks transportni tenzor trećeg reda, respektivno, dok $\cdot$, $:$ i $\otimes$ označavaju skalarni proizvod, tenzorsku kontrakciju drugog reda i (spoljašnji) tenzorski proizvod, respektivno. Primenom hidrodinamičkih razvoja fluksa čestica i izvornog člana (jednačine 2.19 i 2.20) u jednačini kontinuiteta (jednačina 2.18) dobija se vremenski zavisna generalisana difuziona jednačina. Ova jednačina se može napisati u obliku

$$\frac{\partial n(\mathbf{r}, t)}{\partial t} = \sum_{k=0}^{\infty} \omega^{(k)}(t) \odot (-\nabla)^k n(\mathbf{r}, t), \qquad (2.22)$$

gde su $\omega^{(k)}(t)$ tenzori k-tog reda, koji su vremenski zavisni u slučaju vremenski promenljivih spoljašnjih polja. Ovi tenzori se mogu izraziti kao

$$\omega^{(k)}(t) = \mathbf{\Gamma}^{(k)}(t) + \mathbf{S}^{(k)}(t), \qquad (2.23)$$

i za $k > 0$ oni reprezentuju balk transportne koeficijente. Kada se vremenski zavisna generalisana difuziona jednačina odseče na $k = 3$, dobije se jednačina oblika

$$\frac{\partial n(\mathbf{r}, t)}{\partial t} + \mathbf{W}(t) \cdot \nabla n(\mathbf{r}, t) - \hat{\mathbf{D}}(t) : (\nabla \otimes \nabla)n(\mathbf{r}, t)$$
$$+ \hat{\mathbf{Q}}(t) \vdots (\nabla \otimes \nabla \otimes \nabla)n(\mathbf{r}, t) = -R_a(t)n(\mathbf{r}, t), \qquad (2.24)$$

gde su $\mathbf{W}(t)$, $\hat{\mathbf{D}}(t)$, $\hat{\mathbf{Q}}(t)$ i R_a balk brzina drifta, balk difuzioni tenzor, balk transportni tenzor trećeg reda i ukupni brzinski koeficijent za reakcije, respektivno, dok $\vdots$ označava tenzorsku kontrakciju trećeg reda. Pri tome važi

$$R_a(t) = -\omega^{(0)}(t) = S^{(0)}(t), \qquad (2.25)$$

$$\mathbf{W}(t) = \omega^{(1)}(t) = \mathbf{W}^{\star}(t) + \mathbf{S}^{(1)}(t), \qquad (2.26)$$

$$\hat{\mathbf{D}}(t) = \omega^{(2)}(t) = \hat{\mathbf{D}}^{\star}(t) + \mathbf{S}^{(2)}(t), \qquad (2.27)$$

$$\hat{\mathbf{Q}}(t) = \omega^{(3)}(t) = \hat{\mathbf{Q}}^{\star}(t) + \mathbf{S}^{(3)}(t). \qquad (2.28)$$

Množenjem vremenski zavisne generalisane difuzione jednačine (2.22) sa 1, $\mathbf{r}$, $\mathbf{r} \otimes \mathbf{r}$ i $\mathbf{r} \otimes \mathbf{r} \otimes \mathbf{r}$ i integracijom po konfiguracionom prostoru, dobiju se eksplicitni izrazi za $R_a(t)$, $\mathbf{W}(t)$, $\hat{\mathbf{D}}(t)$ i $\hat{\mathbf{Q}}(t)$, respektivno. Ovi izrazi su dati jednačinama

$$R_a(t) = -\omega^{(0)}(t) = \frac{\mathrm{d}}{\mathrm{d}t}\big(\ln N_e(t)\big), \tag{2.29}$$

$$\mathbf{W}(t) = \omega^{(1)}(t) = \frac{\mathrm{d}}{\mathrm{d}t}\langle \mathbf{r}(t) \rangle, \tag{2.30}$$

$$\hat{\mathbf{D}}(t) = \omega^{(2)}(t) = \frac{1}{2}\frac{\mathrm{d}}{\mathrm{d}t}\Big\langle \big(\mathbf{r}(t) - \langle \mathbf{r}(t) \rangle\big) \otimes \big(\mathbf{r}(t) - \langle \mathbf{r}(t) \rangle\big) \Big\rangle, \tag{2.31}$$

$$\hat{\mathbf{Q}}(t) = \omega^{(3)}(t) = \frac{1}{3!}\frac{\mathrm{d}}{\mathrm{d}t}\Big\langle \big(\mathbf{r}(t) - \langle \mathbf{r}(t) \rangle\big) \otimes \big(\mathbf{r}(t) - \langle \mathbf{r}(t) \rangle\big) \otimes \big(\mathbf{r}(t) - \langle \mathbf{r}(t) \rangle\big) \Big\rangle, \tag{2.32}$$

gde su

$$N_e = \int n(\mathbf{r}, t)\mathrm{d}\mathbf{r}, \tag{2.33}$$

$$\langle \psi(\mathbf{r}) \rangle = \frac{1}{N_e(t)} \int \psi(\mathbf{r}) n(\mathbf{r}, t)\mathrm{d}\mathbf{r}, \tag{2.34}$$

pri čemu je $\psi(\mathbf{r})$ proizvoljna funkcija koordinate. Važno je naglasiti da srednja vrednost $\langle \psi(\mathbf{r}) \rangle$ zavisi od vremena, zbog vremenske zavisnosti $n(\mathbf{r}, t)$. Na sličan način se mogu dobiti eksplicitni izrazi za transportne koeficijente višeg reda.

Na osnovu jednačine (2.30) vidi se da balk brzina drifta predstavlja brzinu centra mase roja. Njena vrednost je određena zajedničkim uticajem fluks brzine drifta i vektora $\mathbf{S}^{(1)}(t)$. Fluks brzina drifta je jednaka srednjoj vrednosti vektora brzine elektrona. Vrednosti balk i fluks brzina drifta su međusobno jednake u odsustvu nekonzervativnih sudara, kao i u slučaju u kome je koliziona frekvenca za nekonzervativne sudare nezavisna od energije. Vektor $\mathbf{S}^{(1)}(t)$ predstavlja koeficijent u hidrodinamičkom razvoju izvornog člana $S(\mathbf{r}, t)$, koji stoji uz prvi gradijent koncentracije naelektrisanih čestica $\nabla n(\mathbf{r}, t)$. Ovaj koeficijent je određen energijskom zavisnošću kolizione frekvence za nekonzervativne sudare i porastom srednje energije naelektrisanih čestica u smeru u kome deluje sila spoljašnjeg električnog polja.

Balk difuzioni tenzor opisuje širenje roja, kao što se može videti iz jednačine (2.31). Ovaj tenzor u sebe uključuje doprinos širenju roja usled kretanja naelektrisanih čestica pod uticajem gradijenta njihove koncentracije, kao i doprinos promene broja čestica roja pod uticajem nekonzervativnih sudara. Prvi od ovih doprinosa je opisan fluks difuzionim tenzorom, dok je drugi opisan tenzorom $\mathbf{S}^{(2)}(t)$. Fizička interpretacija transportnih koeficijenata trećeg reda je nešto složenija i nije lako uočljiva na osnovu jednačine (2.32). Zbog toga će fizička interpretacija ovih transportnih koeficijenata biti detaljno razmatrana u potpoglavlju 4.2.

2.5 Struktura transportnog tenzora trećeg reda

U ovom potpoglavlju je struktura vektorskih i tenzorskih veličina (brzine drifta, difuzionog tenzora i transportnog tenzora trećeg reda) određena primenom metode grupnih projektora.

Sistem koji razmatramo sastoji se iz neutralnog pozadinskog fluida, roja naelektrisanih čestica i spoljašnjeg električnog i spoljašnjeg magnetskog polja. Dinamika roja je u potpunosti određena uticajem spoljašnjih polja i sudarima sa česticama pozadinskog fluida. U našem slučaju je pozadinski fluid makroskopski homogen i izotropan, zbog čega je on invarijantan u odnosu na sve transformacije iz ortogonalne $O(3)$ grupe (grupa simetrije sfere). Na osnovu toga je grupa simetrije celog razmatranog sistema jednaka grupi simetrije konfiguracije električnog i magnetskog polja.

U konfiguraciji bez magnetskog polja je grupa simetrije sistema $C_{\infty V}$ (grupa simetrije električnog polja). Ovo je jednoparametarska Lijeva grupa, koja ima dve komponente povezanosti. Prva komponenta povezanosti opisuje rotacije oko ose električnog polja (koje je u našem slučaju duž z-ose) za proizvoljan ugao α i njih označavamo sa $R_z(\alpha)$. Druga komponenta povezanosti opisuje kompoziciju refleksije u ravni koja sadrži električno polje i rotacije iz prve komponente povezanosti. Ove transformacije biće označene sa $\sigma_v R_z(\alpha)$. Polarno vektorske reprezentacije proizvoljnih transformacija iz prve i druge komponente povezanosti se mogu napisati kao

$$D^{pv}\big(R_z(\alpha)\big) = \begin{pmatrix} \cos\alpha & -\sin\alpha & 0 \\ \sin\alpha & \cos\alpha & 0 \\ 0 & 0 & 1 \end{pmatrix}, \tag{2.35}$$

$$D^{pv}\big(\sigma_v R_z(\alpha)\big) = \begin{pmatrix} \cos\alpha & -\sin\alpha & 0 \\ -\sin\alpha & -\cos\alpha & 0 \\ 0 & 0 & 1 \end{pmatrix}. \tag{2.36}$$

U ovoj konfiguraciji polja brzina drifta i difuzioni tenzor imaju sledeću strukturu [27, 47]

$$W = \begin{pmatrix} 0 \\ 0 \\ W_z \end{pmatrix}, \tag{2.37}$$

$$D = \begin{pmatrix} D_{xx} & 0 & 0 \\ 0 & D_{xx} & 0 \\ 0 & 0 & D_{zz} \end{pmatrix}. \tag{2.38}$$

Struktura transportnog tenzora trećeg reda je u ovoj konfiguraciji polja data na sledeći način

$$Q_{xab} = \begin{pmatrix} 0 & 0 & Q_{xxz} \\ 0 & 0 & 0 \\ Q_{xxz} & 0 & 0 \end{pmatrix}, Q_{yab} = \begin{pmatrix} 0 & 0 & 0 \\ 0 & 0 & Q_{xxz} \\ 0 & Q_{xxz} & 0 \end{pmatrix},$$

$$Q_{zab} = \begin{pmatrix} Q_{zxx} & 0 & 0 \\ 0 & Q_{zxx} & 0 \\ 0 & 0 & Q_{zzz} \end{pmatrix}, \tag{2.39}$$

gde su $a, b \in \{x, y, z\}$. U odsustvu magnetskog polja transportni tenzor trećeg reda ima sedam nenultih komponenti, od kojih su tri međusobno nezavisne (Q_{zzz}, Q_{zxx} i Q_{xxz}). Ostale

komponente se mogu izraziti preko nezavisnih komponenti kao

$$Q_{xxz} = Q_{zzx} = Q_{yyz} = Q_{yzy}, \; Q_{zxx} = Q_{zyy}. \tag{2.40}$$

Strukturu transportnog tenzora trećeg reda u odsustvu magnetskog polja prvi put su odredili Whealton i Mason [134], a kasnije su je potvrdili Vrhovac i saradnici [132, 139] i Koutselos [137, 138].

Grupa simetrije paralelne konfiguracije polja je C_∞. Ovo je jednoparametarska Lijeva grupa što ima samo jednu komponentu povezanosti koja opisuje rotacije oko ose električnog i magnetskog polja (oko z-ose) $R_z(\alpha)$. Polarno vektorska reprezentacija $R_z(\alpha)$ prikazana je u jednačini (2.35). U ovoj konfiguraciji polja brzina drifta i difuzioni tenzor imaju sledeću strukturu [27,47]

$$W = \begin{pmatrix} 0 \\ 0 \\ W_z \end{pmatrix}, \tag{2.41}$$

$$D = \begin{pmatrix} D_{xx} & D_{xy} & 0 \\ -D_{xy} & D_{xx} & 0 \\ 0 & 0 & D_{zz} \end{pmatrix}. \tag{2.42}$$

Struktura transportnog tenzora trećeg reda u paralelnoj konfiguraciji električnog i magnetskog polja je data na sledeći način

$$Q_{xab} = \begin{pmatrix} 0 & 0 & Q_{xxz} \\ 0 & 0 & Q_{xyz} \\ Q_{xxz} & Q_{xyz} & 0 \end{pmatrix},$$

$$Q_{yab} = \begin{pmatrix} 0 & 0 & -Q_{xyz} \\ 0 & 0 & Q_{xxz} \\ -Q_{xyz} & Q_{xxz} & 0 \end{pmatrix},$$

$$Q_{zab} = \begin{pmatrix} Q_{zxx} & 0 & 0 \\ 0 & Q_{zxx} & 0 \\ 0 & 0 & Q_{zzz} \end{pmatrix}. \tag{2.43}$$

U paralelnoj konfiguraciji polja transportni tenzor trećeg reda ima 11 nenultih komponenti od kojih su četiri međusobno nezavisne (Q_{zzz}, Q_{zxx}, Q_{xxz} i Q_{xyz}). Ostale komponente ovog tenzora se mogu izraziti preko nezavisnih komponenti na sledeći način

$$Q_{xxz} = Q_{zzx} = Q_{yyz} = Q_{yzy}, \; Q_{zxx} = Q_{zyy},$$
$$Q_{xyz} = Q_{xzy} = -Q_{yxz} = -Q_{yzx}. \tag{2.44}$$

Grupa simetrije ortogonalne konfiguracije polja je C_{1V}. Ovo je konačna grupa koja ima samo dva elementa, jedinični element e i refleksiju u odnosu na ravan koja je ortogonalna na pravac magnetskog polja σ_v. Polarno vektorske reprezentacije ovih elemenata su date jednačinama

$$D^{pv}(e) = \begin{pmatrix} 1 & 0 & 0 \\ 0 & 1 & 0 \\ 0 & 0 & 1 \end{pmatrix}, \; D^{pv}(\sigma_v) = \begin{pmatrix} 1 & 0 & 0 \\ 0 & -1 & 0 \\ 0 & 0 & 1 \end{pmatrix}. \tag{2.45}$$

Strukture brzine drifta, difuzionog tenzora i transportnog tenzora trećeg reda u ortogonalnoj konfiguraciji polja su date na sledeći način

$$W = \begin{pmatrix} W_x \\ 0 \\ W_z \end{pmatrix}, \qquad (2.46)$$

$$D = \begin{pmatrix} D_{xx} & 0 & D_{xz} \\ 0 & D_{yy} & 0 \\ D_{zx} & 0 & D_{zz} \end{pmatrix}. \qquad (2.47)$$

$$Q_{xab} = \begin{pmatrix} Q_{xxx} & 0 & Q_{xxz} \\ 0 & Q_{xyy} & 0 \\ Q_{xxz} & 0 & Q_{xzz} \end{pmatrix},$$

$$Q_{yab} = \begin{pmatrix} 0 & Q_{yyx} & 0 \\ Q_{yyx} & 0 & Q_{yyz} \\ 0 & Q_{yyz} & 0 \end{pmatrix},$$

$$Q_{zab} = \begin{pmatrix} Q_{zxx} & 0 & Q_{zzx} \\ 0 & Q_{zyy} & 0 \\ Q_{zzx} & 0 & Q_{zzz} \end{pmatrix}. \qquad (2.48)$$

U ortogonalnoj konfiguraciji polja transportni tenzor trećeg reda ima 14 nenultih komponenti od kojih je 10 međusobno nezavisno. Ostale komponente se mogu izraziti preko nezavisnih komponenti na sledeći način

$$Q_{xxz} = Q_{xzx}, \ Q_{yyz} = Q_{yzy}, \ Q_{yyx} = Q_{yxy}, \ Q_{zzx} = Q_{zxz}. \qquad (2.49)$$

Kada električno i magnetsko polje zaklapaju proizvoljan ugao, grupa simetrije sistema je trivijalna grupa, koja sadrži samo jedinični element. U ovoj konfiguraciji polja su brzina drifta, difuzioni tenzor i transportni tenzor trećeg reda potpuno popunjeni (nemaju nenultih elemenata). Uz to su svi elementi brzine drifta i difuzionog tenzora međusobno nezavisni, pa je struktura ovih transportnih koeficijenata data na sledeći način

$$W = \begin{pmatrix} W_x \\ W_y \\ W_z \end{pmatrix}, \qquad (2.50)$$

$$D = \begin{pmatrix} D_{xx} & D_{xy} & D_{xz} \\ D_{yx} & D_{yy} & D_{yz} \\ D_{zx} & D_{zy} & D_{zz} \end{pmatrix}. \qquad (2.51)$$

Međutim, iako transportni tenzor trećeg reda ima 27 nenultih komponenti u ovoj konfiguraciji polja, samo 18 komponenti je međusobno nezavisno, zbog toga što poslednja dva indeksa transportnog tenzora trećeg reda komutiraju $Q_{abc} = Q_{acb}$, za svako $a, b, c \in x, y, z$. Na osnovu toga je struktura transportnog tenzora trećeg reda u ovoj konfiguraciji polja data jednačinama

$$Q_{xab} = \begin{pmatrix} Q_{xxx} & Q_{xxy} & Q_{xxz} \\ Q_{xxy} & Q_{xyy} & Q_{xyz} \\ Q_{xxz} & Q_{xyz} & Q_{xzz} \end{pmatrix},$$

$$Q_{yab} = \begin{pmatrix} Q_{yxx} & Q_{yxy} & Q_{yxz} \\ Q_{yxy} & Q_{yyy} & Q_{yyz} \\ Q_{yxz} & Q_{yyz} & Q_{yzz} \end{pmatrix},$$

$$Q_{zab} = \begin{pmatrix} Q_{zxx} & Q_{zxy} & Q_{zxz} \\ Q_{zxy} & Q_{zyy} & Q_{zyz} \\ Q_{zxz} & Q_{zyz} & Q_{zzz} \end{pmatrix}. \tag{2.52}$$

2.6 Zaključak

U ovom poglavlju je prikazana teorija rojeva naelektrisanih čestica u gasovima i tečnostima. U potpoglavlju 2.2 definisan je roj kao skup naelektrisanih čestica čija je koncentracija toliko mala da se njihova međusobna interakcija, kao i sudari između njih mogu zanemariti. Potom su identifikovani efekti koji utiču na dinamiku roja, poput spoljašnjih električnih i magnetskih polja i sudara čestica roja sa neutralnim česticama pozadinske sredine. Zatim je ukazano na to da roj dostiže stacionarno stanje u kome funkcija raspodele naelektrisanih čestica po energijama ne zavisi od vremena kada se energija koju roj dobije od spoljašnjeg električnog polja u jedinici vremena izjednači sa energijom koju on izgubi u sudarima. Ova funkcija raspodele je određena intenzitetom spošljašnjih polja i prirodom pozadinskog fluida. Na kraju ovog potpoglavlja razmatrana je razlika između rojeva naelektrisanih čestica u gasnoj fazi, u kojoj se interakcija čestica roja sa pozadisnkom sredinom može opisati binarnim sudarima, i rojeva u tečnoj fazi, u kojoj je ova interakcija složenija.

Potpoglavlje 2.3 nosi osnove teorije rasejanja elektrona u gasovima i tečnostima. Prvo su navedeni efekti koji određuju potencijal za rasejanje elektrona na izolovanom atomu. Oni uključuju statički potencijal, polarizacioni potencijal i izmenski efekat. Potom je prikazana Dirac-Fockova jednačina, na osnovu koje se može odrediti diferencijalni presek za rasejanje naelektrisane čestice za zadati potencijal. Nakon toga su dati izrazi za određivanje diferencijalnog preseka, totalnog preseka i preseka za transfer impulsa na osnovu faznih pomeraja parcijalnih talasa, koji se određuju rešavanjem Dirac-Fock-ove jednačine. Posebnu pažnju polažemo na efekte koji modifikuju potencijal za rasejanje elektrona na pojedinačnom fokus atomu unutar tečnosti. Ovi efekti uključuju polarizaciju indukovanog dipola fokus atoma indukovanim dipolima okolnih atoma, kao i direktni uticaj potencija svih okolnih atoma na dinamiku rasejanja elektrona na fokus atomu. Na kraju ovog potpoglavlja se uvodi dvostruki diferencijalni presek, koji se može izraziti kao proizvod dva člana. Prvi od ovih članova odgovara diferencijalnom preseku

za rasejanje elektrona na pojedinačnom fokus atomu unutar tečnosti, dok drugi član odgovara dinamičkom strukturnom faktoru tečnosti. Pri tome prvi član zavisi isključivo od modifikovanog potencijala za rasejanje, dok drugi zavisi jedino od prostornih i vremenskih korelacija između pojedinačnih atoma unutar tečnosti.

U potpoglavlju 2.4 je uveden hidrodinamički režim i definisane su dve različite familije transportnih koeficijenata. Na početku ovog potpoglavlja govori se o hidrodinamičkim uslovima koji su uspostavljeni kada se roj kreće u homogenom pozadinskom fluidu pod uticajem spoljašnjeg električnog i magnetskog polja, koja su prostorno homogena i kada se roj nalazi daleko od izvora i ponora čestica. Uz to je data formalna definicija hidrodinamičkog režima, koja podrazumeva reprezentovanje prostorne zavisnosti funkcije raspodele roja u faznom prostoru na osnovu razvoja ove funkcije u red po gradijentima koncentracije čestica u konfiguracionom prostoru. Potom su prikazani: jednačina kontinuiteta koja uspostavlja vezu između teorije i eksperimenta, te fluks gradijentna relacija i hidrodinamički razvoj izvornog člana. Primenom ove dve jednačine u jednačini kontinuiteta može se izvesti generaisana difuziona jednačina. Dalje se definišu fluks transportni koeficijenti na osnovu fluks gradijentne relacije i balk transportni koeficijenti na osnovu generalisane difuzione jednačine. Ove dve familije transportnih koeficijenata su međusobno jednake u odsustvu nekonzervativnih procesa (poput zahvata elektrona i jonizacije), kao i u uslovima u kojima koliziona frekvenca za nekonzervativne sudare ne zavisi od energije naelektrisanih čestica. Međutim, u opštem slučaju se ove dve familije transportnih koeficijenata međusobno razlikuju, a njihova razlika je određena koeficijentima u hidrodinamičkom razvoju izvornog člana. Na kraju ovog potpoglavlja su date jednačine na osnovu kojih se mogu odrediti balk transportni koeficijenti.

U narednom 2.5 potpoglavlju predočena je struktura vektorskih i tenzorskih veličina koje su od značaja za ovu disertaciju u svim konfiguracijama električnog i magnetskog polja. Za svaku konfiguraciju polja je prvo određena grupa simetrije sistema, a potom je prikazana polarno-vektorska reprezentacija odgovarajućih elemenata grupe. Dalje je prikazana struktura brzine drifta, difuzionog tenzora i transportnog tenzora trećeg reda za odgovarajuću konfiguraciju polja. U okviru ove disertacije je struktura vektorskih i tenzorskih veličina određena primenom metode grupnih projektora. Pritom se strukture vektora brzine drifta i difuzionog tenzora, koje su određene u ovoj disertaciji, slažu sa rezultatima koji su već prisutni u literaturi za sve konfiguracije električnog i magnetskog polja. Slaganje je postignuto i za strukturu transportnog tenzora trećeg reda u odsustvu magnetskog polja. Treba pak istaći da je struktura transportnog tenzora trećeg reda u prisustvu magnetskog polja prvi put određena u okviru ove disertacije, i to tako da su u obzir uzeti slučajevi u kojima su električno i magnetsko polje međusobno paralelni, međusobno ortogonalni, kao i kada su ova polja ukrštena pod proizvoljnim uglom koji je između 0 i 90 stepeni. Ovi rezultati su dodatno provereni tako što je struktura transportnog tenzora trećeg reda u svim konfiguracijama električnog i magnetskog polja još jednom određena na osnovu simetrija momenata Boltzmann-ove jednačine i fizičkih argumenata. U odsustvu magnetskog polja transportni tenzor trećeg reda ima sedam nenultih komponenti od kojih je tri međusobno nezavisno. Međutim, u slučaju paralelne konfiguracije polja transportni tenzor trećeg reda ima jedanaest nenultih komponenti od kojih je četiri međusobno nezavisno, dok u

slučaju ortogonalne konfiguracije polja ovaj tenzor ima četrnaest nenultih komponenti od kojih je deset međusobno nezavisno. Kada su električno i magnetsko polje ukršteni pod proizvoljnim uglom između 0 i 90 stepeni, transportni tenzor trećeg reda ima dvadeset sedam nenultih komponenti od kojih je osamnaest međusobno nezavisno.

3 Metodi za izračunavanje transportnih koeficijenata

3.1 Uvod

Treće poglavlje bazira se na metodima za izračunavanje transportnih koeficijenata i drugih transportnih karakteristika za rojeve naelektrisanih čestica u gasovima i tečnostima. U potpoglavlju 3.2 prikazani su osnovni elementi momentnog metoda za rešavanje Boltzmann-ove jednačine, u kome se funkcija raspodele razvija u red po skupu bazisnih funkcija. Na ovaj način se Boltzmann-ova jednačina svodi na hijerarhiju kinetičkih jednačina koja se potom rešava numerički. U potpoglavlju 3.3, diskutovani su razvoj fluidnog modela i osnovni elementi hidrodinamičke teorije prenosa impulsa za rojeve lakih naelektrisanih čestica u nepolarnim tečnostima, koji se mogu izvesti množenjem Boltzmann-ove jednačine funkcijama brzinskih koordinata i integracijom ovih jednačina po brzinskom prostoru. U potpoglavlju 3.4 su prikazane osnovne procedure Monte Carlo metoda u fizici rojeva naelektrisanih čestica, kao i implementacija ovih procedura u okviru Monte Carlo koda koji je korišćen u ovoj disertaciji. Zasebni odeljak (3.4.1) predstavlja rezultate benčmark proračuna transportnih veličina za elektrone u Percus–Yevick-ovoj modelnoj tečnosti, a koji su zasnovani na primeni Monte Carlo metoda. Ova modelna tečnost istovremeno je upotrebljena za ilustraciju efekata koherentnog rasejanja i pojavu strukturno indukovane negativne diferencijalne provodnosti.

3.2 Kinetička teorija za rešavanje Boltzmann-ove jednačine

Boltzmann-ova jednačina predstavlja jednačinu kontinuiteta za funkciju raspodele u šestodimenzionom faznom prostoru [47, 52]. U slučaju roja naelektrisanih čestica, koje se kreću u homogenom i makroskopski neutralnom pozadinskom fluidu pod uticajem spoljašnjeg električnog i spoljašnjeg magnetskog polja, Boltzmann-ova jednačina se može napisati u obliku [47, 52, 173, 174]:

$$\frac{\partial f}{\partial t} + \mathbf{c} \cdot \frac{\partial f}{\partial \mathbf{r}} + \frac{q}{m}(\mathbf{E} + \mathbf{c} \times \mathbf{B}) \cdot \frac{\partial f}{\partial \mathbf{c}} = -J(f, f_0), \tag{3.1}$$

gde je $f = f(\mathbf{r}, \mathbf{c}, t)$ funkcija raspodele naelektrisanih čestica roja u faznom prostoru, $\mathbf{E}$, $\mathbf{B}$, q i m su spoljašnje električno polje, spoljašnje magnetsko polje, naelektrisanje i masa naelektrisanih čestica, respektivno, dok je $J(f, f_0)$ kolizioni operator, koji zavisi od faznih funkcija raspodele naelektrisanih čestica i neutralnih čestica, respektivno. U ovoj disertaciji se smatra se da su spoljašnja električna i magnetska polja prostorno homogena. Za razliku od naelektrisanih čestica roja, koje nemaju unutrašnju strukturu [173, 174], smatra se da neutralne čestice pozadinskog fluida imaju unutrašnju strukturu kao i da se one nalaze u stanju termodinamičke ravnoteže na temperaturi T_0. Na osnovu toga se njihova fazna funkcija raspodele može napisati u obliku [173, 174]:

$$f_0(\mathbf{c}_0) = \sum_j f_{0j}(\mathbf{c}_0), \tag{3.2}$$

gde je $\mathbf{c}_0$ brzinska koordinata neutralnih čestica, dok se sumacija vrši po svim unutrašnjim stanjima neutralnih čestica. Fazna funkcija raspodele neutralnih čestica za pojedinačno unutrašnje stanje predstavljena je Maxwell-Boltzmann-ovom raspodelom:

$$f_{0j}(\mathbf{c}_0) = n_{0j}\left(\frac{m_0}{2\pi k T_0}\right)^{3/2} \exp\left(-\frac{m_0 c_0^2}{2k T_0}\right), \tag{3.3}$$

gde su m_0 i k masa neutralnih čestica i Boltzmann-ova konstanta, respektivno, dok je

$$n_{0j} = \frac{n_0}{Z_0}\exp\left(-\frac{\epsilon_j}{k T_0}\right), \tag{3.4}$$

gde je n_0 koncentracija neutralnih čestica, dok je ϵ_j energija koja odgovara diskretnom stanju j. Particiona funkcija neutralnih čestica Z_0 data je jednačinom:

$$Z_0 = \sum_j \exp\left(-\frac{\epsilon_j}{k T_0}\right). \tag{3.5}$$

Boltzmann-ova jednačina je komplikovana integro-diferencijalna jednačina, dok fazna funkcija raspodele u opštem slučaju zavisi od 6 koordinata faznog prostora i jedne vremenske koordinate [26,47]. Zbog toga je Boltzmann-ovu jednačinu veoma teško rešiti direktnom numeričkom integracijom. U ovoj disertaciji se za rešavanje Boltzmann-ove jednačine koristi brzinski momentni metod, ili kraće momentni metod [174], u okviru kog se funkcija rapodele razvija u red po skupu bazisnih funkcija u faznom prostoru. Nakon toga, primenom relacija ortogonalnosti ovih bazisnih funkcija, Boltzmann-ova jednačina se svodi na hijerarhiju kinetičkih jednačina po koeficijentima u razvoju fazne funkcije raspodele [173,174]. Ova hijerarhija kinetičkih jednačina se nakon diskretizacije izvoda po vremenu svodi na skup matričnih jednačina, koji se potom rešava numerički primenom matrične inverzije.

Fazna funkcija raspodele se u brzinskom prostoru razvija po Burnett-ovim funkcijama [173,174], koje čine bazis u ovom prostoru. Burnett-ove funkcije su međusobno ortogonalne sa Maxwellian-om kao težinskom funkcijom [76]. Ako se sistem nalazi u hidrodinamičkom režimu, fazna funkcija raspodele se u konfiguracionom prostoru razvija po gradijentima koncentracije naelektrisanih čestica roja $n(\mathbf{r}, t)$. Normirane Burnett-ove funkcije $\Phi_m^{[\nu l]}(\alpha(t)\mathbf{c})$ se definišu kao:

$$\Phi_m^{[\nu l]}(\alpha(t)\mathbf{c}) = N_{\nu l}\left(\frac{\alpha(t)c}{\sqrt{2}}\right)^l S_{l+1/2}^{(\nu)}\left(\frac{\alpha(t)^2 c^2}{2}\right) Y_m^{[l]}(\hat{\mathbf{c}}) \tag{3.6}$$

$$= R_{\nu l}(\alpha(t)c) Y_m^{[l]}(\hat{\mathbf{c}}), \tag{3.7}$$

gde je $Y_m^{[l]}$ sferni harmonik, dok je $S_{l+1/2}^{(\nu)}$ Sonine polinom, $\alpha(t)$ je parametar a $\hat{\mathbf{c}}$ je jedinični vektor u brzinskom prostoru koji nosi informaciju o smeru vektora brzine. Konstanta $N_{\nu l}$ je data jednačinom:

$$N_{\nu l}^2 = \frac{2\pi^{3/2}\nu!}{\Gamma(\nu + l + 3/2)}, \tag{3.8}$$

gde je $\Gamma(\nu + l + 3/2)$ gama funkcija, dok

$$R_{\nu l}(\alpha(t)c) = N_{\nu l}\left(\frac{\alpha(t)c}{\sqrt{2}}\right)^l S_{l+1/2}^{(\nu)}\big(\alpha(t)^2 c^2/2\big), \tag{3.9}$$

određuje radijalni deo Burnett-ove funkcije. Sferni harmonici $Y_m^{[l]}$ se definišu kao [47]:

$$Y_m^{[l]}(\theta, \phi) = i^l (-1)^{m/2 + |m|/2} \left(\frac{(2l+1)(l-|m|)!}{4\pi(l+|m|)!} \right)^{1/2} P_l^{|m|}(\cos\theta) e^{im\phi}, \tag{3.10}$$

gde su

$$P_l^{|m|}(\cos\theta) = \frac{(-1)^l}{2^l l!} (\sin\theta)^{|m|} \frac{\mathrm{d}^{l+|m|}}{(\mathrm{d}\cos\theta)^{l+|m|}} \left(1 - \cos^2\theta \right)^l, \tag{3.11}$$

asocirani Legandre-ovi polinomi. Za sferne harmonike važi relacija ortogonalnosti:

$$\int Y_m^{(l)}(\theta, \phi) Y_{m'}^{[l']}(\theta, \phi) \mathrm{d}(\cos\theta) \mathrm{d}\phi = \delta_{ll'} \delta_{mm'}, \tag{3.12}$$

gde okrugla zagrada u superskriptu predstavlja kompleksnu konjugaciju dok su $\delta_{ll'}$ i $\delta_{mm'}$ Kronecker-ove delte. Burnett-ove funkcije zadovoljavaju relaciju ortogonalnosti [173]:

$$\int \omega(\alpha(t), c) \Phi_m^{(\nu l)}(\alpha(t)\mathbf{c}) \Phi_{m'}^{[\nu' l']}(\alpha(t)\mathbf{c}) \mathrm{d}\mathbf{c} = \delta_{\nu'\nu} \delta_{l'l} \delta_{m'm}, \tag{3.13}$$

gde je

$$\omega(\alpha(t), c) = \left(\frac{\alpha(t)^2}{2\pi} \right)^{3/2} e^{-\alpha(t)^2 c^2/2}, \tag{3.14}$$

težinska funkcija. Ortogonalnost Burnett-ovih funkcija je posledica ortogonalnosti Sonine polinoma i sfernih harmonika. Primenom Burnett-ovih funkcija se fazna funkcija raspodele može razviti u brzinskom prostoru kao:

$$f(\mathbf{r}, \mathbf{c}, t) = \omega(\alpha(t), c) \sum_{\nu=0}^{\infty} \sum_{l=0}^{\infty} \sum_{m=-l}^{l} \mathbf{f}_m^{(\nu l)}(\alpha(t), \mathbf{r}, t) \Phi_m^{[\nu l]}(\alpha(t)\mathbf{c}), \tag{3.15}$$

gde su $\mathbf{f}_m^{(\nu l)}(\alpha(t), \mathbf{r}, t)$ koeficijenti u razvoju, koji zavise od koordinata u konfiguracionom prostoru i od vremena.

U hidrodinamičkom režimu se fazna funkcija raspodele u konfiguracionom prostoru može razviti po gradijentima koncentracije čestica roja [27,47]. Tada se fazna funkcija raspodele može napisati u obliku:

$$f(\mathbf{r}, \mathbf{c}, t) = \omega(\alpha(t), c) \sum_{s=0}^{\infty} \sum_{\lambda=0}^{s} \sum_{\mu=-\lambda}^{\lambda} \sum_{\nu=0}^{\infty} \sum_{l=0}^{\infty} \sum_{m=-l}^{l} F(\nu lm|s\lambda\mu; \alpha(t), t) R_{\nu l}(\alpha(t), c) Y_m^{[l]}(\hat{\mathbf{c}}) G_\mu^{(s\lambda)} n(\mathbf{r}, t), \tag{3.16}$$

gde su $F(\nu lm|s\lambda\mu; \alpha(t), t)$ momenti funkcije raspodele, dok je $G_\mu^{(s\lambda)}$ operator prostornog gradijenta u ireducibilnoj formi [47]. Ovaj operator odgovara prostornom izvodu s-tog reda, koji se pri rotacijama transformiše kao sferni harmonik $Y_\mu^{(\lambda)}$. Ireducibilna forma operatora prostornog diferenciranja se koristi da bi se obezbedio najkompaktniji zapis ovog operatora. Momenti funkcije raspodele $F(\nu lm|s\lambda\mu; \alpha(t), t)$ predstavljaju koeficijente u razvoju po Burnett-ovim funkcijama u brzinskom prostoru i gradijentima koncentracije u konfiguracionom prostoru. Kada se Boltzmann-ova jednačina pomnoži sa proizvoljnim momentom $F(\nu lm|s\lambda\mu; \alpha(t), t)$, nakon čega se primeni razvoj fazne funkcije raspodele iz jednačine (3.16) i Boltzmann-ova jednačina se prointegrali po celom brzinskom prostoru, dobije se hijerarhija kinetičkih jednačina koja

predstavlja beskonačan sistem nehomogenih diferencijalnih jednačina prvog reda [47]. Ova hijerarhija se može reprezentovati jednačinom:

$$
\sum_{\nu'=0}^{\infty}\sum_{l'=0}^{\infty}\sum_{m'=-l'}^{l'}\Bigg\{\partial_t\delta_{\nu\nu'}\delta_{ll'}\delta_{mm'} + \omega(000;t)\delta_{\nu\nu'}\delta_{ll'}\delta_{mm'} + n_0 J_{\nu\nu'}^{l}\delta_{ll'}\delta_{mm'}
$$

$$
+ ia(t)(l'm10|lm)\alpha(t)\langle\nu l||K^{[1]}||\nu'l'\rangle\delta_{mm'}
$$

$$
+ \frac{q}{m}B(t)\Bigg\{\frac{\sin\psi}{2}\Big[\sqrt{(l-m)(l+m+1)}\delta_{m'm+1} - \sqrt{(l+m)(l-m+1)}\delta_{m'm-1}
$$

$$
- im\cos\psi\delta_{mm'}\Big]\Bigg\}\delta_{\nu\nu'}\delta_{ll'}
$$

$$
- n_0 J_{0\nu'}^{0} F(\nu lm|000;\alpha(t),t)(1-\delta_{s0}\delta_{\lambda0}\delta_{\mu0})\delta_{l'0}\delta_{m'0}\Bigg\} F(\nu'l'm'|s\lambda\mu;\alpha(t),t) = \bar{X}(\nu lm|s\lambda\mu;\alpha(t),t).
$$

$$
(3.17)
$$

U jednačini (3.17) $J_{\nu\nu'}^{l}$ predstavlja element kolizione matrice, koji je dat jednačinom:

$$
J_{\nu\nu'}^{l} = \frac{1}{n_0}\int_0^{\infty} R_{\nu l}(\alpha(t)c)J^{l}[\omega(\alpha(t),c)R_{\nu'l}(\alpha(t)c)]c^2 dc, \qquad (3.18)
$$

dok je $(l'm10|lm)$ Clebsch–Gordan-ov koeficijent. Član $\langle\nu l||K^{[1]}||\nu'l'\rangle$ je dat jednačinom:

$$
\langle\nu l||K^{[1]}||\nu'l'\rangle = -\frac{1}{\alpha(t)}\int_0^{\infty} R_{\nu l}(\alpha(t)c)\Big[\langle l||\partial_c^{[1]}||l'\rangle\omega(\alpha(t),c)R_{\nu'l'}(\alpha(t)c)\Big]c^2 dc, \qquad (3.19)
$$

gde je $\langle l||\partial_c^{[1]}||l'\rangle$ redukovan matrični element. Može se pokazati da važi:

$$
\langle\nu l||K^{[1]}||\nu'l'\rangle = \sqrt{\frac{2}{2l+1}}\Big[\sqrt{l(\nu+l+1/2)}\delta_{\nu\nu'}\delta_{ll'+1} - \sqrt{\nu(l+1)}\delta_{\nu\nu'+1}\delta_{ll'-1}\Big]. \qquad (3.20)
$$

Član $\omega(000;t)$ predstavlja $\omega(s\lambda\mu;t)$ za $s=\lambda=\mu=0$, pri čemu je $\omega(s\lambda\mu;t)$ definisano kao:

$$
\omega(s\lambda\mu;t) = \frac{1}{\alpha(t)}\sum_{\mu'=-1}^{1}\sum_{\lambda_1=0}^{s-1}(-1)^{\mu'}(1\mu'\lambda_1\mu-\mu'|\lambda\mu)F(01-\mu'|s-1\lambda_1\mu-\mu';\alpha(t),t)
$$

$$
-n_0\sum_{\nu'=0}^{\infty} J_{0\nu'}^{0}(\alpha(t))F(\nu'00|s\lambda\mu;\alpha(t),t). \qquad (3.21)
$$

Desna strana jednačine (3.17) se može izraziti kao:

$$
\bar{X}(\nu lm|s\lambda\mu;\alpha(t),t) = \sum_{\nu'=0}^{\infty}\sum_{l'=0}^{\infty}\sum_{m'=-l'}^{l'}\Bigg\{-\frac{1}{\alpha(t)}\sum_{\lambda_1=0}^{s-1}\sum_{\mu'=-1}^{1}(l'm'1\mu'|lm)
$$

$$
(l'm'1\mu'|lm)(1\mu'\lambda_1\mu-\mu'|\lambda\mu)\langle\nu l||\alpha(t)c^{[1]}||\nu'l\rangle F(\nu l'm'|s-1\lambda_1\mu-\mu';\alpha(t),t)
$$

$$
-\sum_{s_1=0}^{s}\sum_{\lambda_1=0}^{s_1}\sum_{\mu_1=-\lambda_1}^{\lambda_1}\sum_{\lambda_2=0}^{s-s_1}\sum_{\mu_2=-\lambda_2}^{\lambda_2}(\lambda_1\mu_1\lambda_2\mu_2|\lambda\mu)\omega(s-s_1\lambda_2\mu_2;t)(1-\delta_{ss_1}\delta_{\lambda_20}\delta_{\mu_2}0)
$$

$$
(1-\delta_{s_10}\delta_{\lambda_10}\delta_{\mu_10})F(\nu'l'm'|s_1\lambda_1\mu_1;\alpha(t),t)\delta_{\nu\nu'}\delta_{ll'}\delta_{mm'}
$$

$$- \sum_{\lambda_1=0}^{s-1} \sum_{\mu'=-1}^{1} \frac{(-1)^{\mu'}}{\alpha(t)} (1\mu'\lambda_1\mu - \mu'|\lambda\mu) F(01 - \mu'|s - 1\lambda_1\mu - \mu'; \alpha(t), t) F(\nu'l'm'|000; \alpha(t), t)$$

$$(1 - \delta_{s0}\delta_{\lambda0}\delta_{\mu0})\delta_{\nu\nu'}\delta_{ll'}\delta_{mm'} \Bigg\}. \tag{3.22}$$

U jednačini (3.22) je $\langle \nu l||\alpha(t)c^{[1]}||\nu'l' \rangle$ definisano kao:

$$\langle \nu l||\alpha(t)c^{[1]}||\nu'l' \rangle = \frac{1}{\alpha(t)} \int_0^\infty R_{\nu l}(\alpha(t)c) \langle l||c^{[1]}||l' \rangle \omega(\alpha(t)c) R_{\nu'l'}(\alpha(t)c) c^2 \mathrm{d}c, \tag{3.23}$$

gde je $\langle l||c^{[1]}||l' \rangle$ redukovan matrični element. Može se pokazati da važi:

$$\langle \nu l||\alpha(t)c^{[1]}||\nu'l' \rangle = \sqrt{\frac{2}{2l+1}} \Bigg[\sqrt{l(\nu + l + 1/2)}\delta_{\nu\nu'}\delta_{ll'+1} - \sqrt{\nu(l+1)}\delta_{\nu\nu'+1}\delta_{ll'-1}$$

$$-\sqrt{l(\nu+1)}\delta_{\nu\nu'-1}\delta_{ll'+1} + \sqrt{(l+1)(\nu + l + 3/2)}\delta_{\nu\nu'}\delta_{ll'-1} \Bigg]. \tag{3.24}$$

Pri izvođenju ove hijerarhije primenjene su relacije ortogonalnosti Burnett-ovih funkcija i izjednačeni su koeficijenti koji stoje uz operator $G_\mu^{(s\lambda)}$ za iste vrednosti (s, λ, μ). Ova hijerarhija jednačina se diskretizuje u vremenu sa vremenskim korakom Δt, kako bi se omogućilo njeno numeričko rešavanje [90, 97]. Pri ovoj diskretizaciji se u svakom trenutku t_n svi elementi hijerarhije određuju pri istoj bazisnoj temperaturi T_b^n. Parcijalni izvod po vremenu se u n-tom vremenskom trenutku može aproksimirati kao:

$$\frac{\partial}{\partial t} F(\nu lm|s\lambda\mu; \alpha(t), t) \Bigg|_{\alpha=\alpha_n, t=t_n} = \frac{F_n(\nu lm|s\lambda\mu; \alpha_n) - F_{n-1}(\nu lm|s\lambda\mu; \alpha_n)}{\Delta t}. \tag{3.25}$$

U jednačini (3.25) se nepoznata veličina $F_{n-1}(\nu lm|s\lambda\mu; \alpha_n)$ može izraziti preko poznatih veličina $F_{n-1}(\nu lm|s\lambda\mu; \alpha_{n-1})$ kao:

$$F_{n-1}(\nu lm|s\lambda\mu; \alpha_n) = \sum_{\nu'=0}^{\nu} A_{\nu\nu'}^l(\mu_{nn-1}) F_{n-1}(\nu lm|s\lambda\mu; \alpha_{n-1}), \tag{3.26}$$

gde su

$$A_{\nu\nu'}^l(\mu_{ij}) = \frac{\bar{N}_{\nu'l}}{\bar{N}_{\nu l}} \mu_{ij}^{\nu'+\frac{1}{2}l} \frac{(1 - \mu_{ij})^{\nu-\nu'}}{(\nu - \nu')!}, \tag{3.27}$$

$$\mu_{ij} = \left(\frac{\alpha_i}{\alpha_j} \right)^2, \tag{3.28}$$

$$\bar{N}_{\nu l}^2 = \frac{2\pi^{3/2}}{\nu!\Gamma(\nu + l + 3/2)} = \frac{1}{(\nu!)^2} N_{\nu l}^2, \tag{3.29}$$

i

$$A_{\nu\nu'}^l(1) = \delta_{\nu\nu'}. \tag{3.30}$$

Jednačina (3.26) je posledica veze između modifikovanih Sonine polinoma na različitim bazisnim temperaturama:

$$R_{\nu l}(\alpha_i c) = \sum_{\nu'=0}^{\nu} A_{\nu\nu'}^l(\mu_{ij}) R_{\nu'l}(\alpha_j c). \tag{3.31}$$

Hijerarhija jednačina (3.17) za n-ti vremenski korak se može napisati u obliku:

$$\sum_{\nu'=0}^{\infty}\sum_{l'=0}^{\infty}\sum_{m'=-l'}^{l'}\left\{\delta_{\nu\nu'}\delta_{ll'}\delta_{mm'} + \Delta t\left[\omega_n(000)\delta_{\nu\nu'}\delta_{ll'}\delta_{mm'} + n_0 J_{\nu\nu'}^l\delta_{ll'}\delta_{mm'}\right.\right.$$

$$+ ia_n\alpha_n(l'm10|lm)\langle\nu l||K^{[1]}||\nu'l'\rangle\delta_{mm'}$$

$$\frac{q}{m}B_n\left\{\frac{\sin\psi}{2}\left[\sqrt{(l-m)(l+m+1)}\delta_{m'm+1} - \sqrt{(l+m)(l-m+1)}\delta_{m'm-1}\right.\right.$$

$$\left.\left.- im\cos\psi\delta_{mm'}\right]\right\}\delta_{\nu\nu'}\delta_{ll'}$$

$$\left.\left.- n_0 J_{0\nu'}^0(\alpha_n)F(\nu lm|000;\alpha_n)(1 - \delta_{s0}\delta_{\lambda0}\delta_{\mu0})\delta_{l'0}\delta_{m'0}\right]\right\}F(\nu'l'm'|s\lambda\mu;\alpha_n) = X_n(\nu lm|s\lambda\mu;\alpha_n),$$

(3.32)

gde je

$$X_n(\nu lm|s\lambda\mu;\alpha_n) = \sum_{\nu'=0}^{\nu} A_{\nu\nu'}^l(\mu_{nn-1})F_{n-1}(\nu lm|s\lambda\mu;\alpha_{n-1}) + \Delta t\bar{X}_n(\nu lm|s\lambda\mu;\alpha_n). \quad (3.33)$$

Jednačine (3.32) i (3.33) predstavljaju hijerarhiju matričnih jednačina koje se rešavaju primenom numeričke matrične inverzije.

Na osnovu momenata funkcije raspodele se mogu odrediti balk i fluks transportni koeficijenti. Eksplicitni izrazi za fluks transportne koeficijente se mogu odrediti na osnovu razvoja fluksa brzine čestica $\mathbf{\Gamma}(\mathbf{r}, t)$ po Burnett-ovim funkcijama i gradijentima koncentracije, kada se za svaku Dekartovu komponentu fluksa čestica izdvoje članovi koji stoje uz odgovarajuće izvode po prostonim koordinatama. Razvoj fluksa brzine čestica se može napisati kao:

$$\Gamma_m^{[1]}(\mathbf{r}, t) = \int c_m^{[1]} f(\mathbf{r}, \mathbf{c}, t)\mathrm{d}\mathbf{c} =$$

$$= \int c_m^{[1]}\omega(\alpha, c)\sum_{s=0}^{\infty}\sum_{\lambda=0}^{s}\sum_{\mu=-\lambda}^{\lambda}\sum_{\nu=0}^{\infty}\sum_{l=0}^{\infty}\sum_{m'=-l}^{l} F(\nu lm'|s\lambda\mu;\alpha, t)R_{\nu l}(\alpha, c) \times$$

$$Y_{m'}^{[l]}(\hat{\mathbf{c}})G_{\mu}^{(s\lambda)}n(\mathbf{r}, t)\mathrm{d}\mathbf{c}. \quad (3.34)$$

Dekartove komponente vektora, čija je sferna forma data izrazom:

$$c_m^{[1]} = \sqrt{\frac{4\pi}{3}}cY_m^{[1]}(\hat{\mathbf{c}}), \quad (3.35)$$

mogu se odrediti na osnovu jednačina

$$c_x = \frac{i}{\sqrt{2}}\left(c_1^{[1]} - c_{-1}^{[1]}\right), \quad (3.36)$$

$$c_y = \frac{1}{\sqrt{2}}\left(c_1^{[1]} + c_{-1}^{[1]}\right), \quad (3.37)$$

$$c_z = -ic_0^{[1]}. \quad (3.38)$$

U okviru ove disertacije su određeni eksplicitni izrazi u kojima su komponente fluks transportnog tenzora trećeg reda izražene na osnovu momenata funkcije raspodele $F(\nu lm|s\lambda\mu;\alpha, t)$. Izrazi za

komponente fluks transportnog tenzora trećeg reda, koje su nezavisne u odsustvu magnetskog polja, dati su sledećim jednačinama:

$$Q_{xxz} = \frac{1}{\sqrt{2}\alpha}\bigg(\text{Im}\big\{F(011|221)\big\} - \text{Im}\big\{F(01-1|221)\big\}\bigg), \tag{3.39}$$

$$Q_{zxx} = -\frac{1}{\alpha}\bigg(\frac{1}{\sqrt{3}}\text{Im}\big\{F(010|200)\big\} + \frac{1}{\sqrt{6}}\text{Im}\big\{F(010|220)\big\}\bigg) + \frac{1}{\alpha}\text{Im}\big\{F(010|222)\big\}, \tag{3.40}$$

$$Q_{zzz} = \frac{1}{\alpha}\bigg(\sqrt{\frac{2}{3}}\text{Im}\big\{F(010|220)\big\} - \frac{1}{\sqrt{3}}\text{Im}\big\{F(010|200)\big\}\bigg), \tag{3.41}$$

gde Re{} i Im{} označavaju realni i imaginarni deo momentata $F(\nu lm|s\lambda\mu;\alpha,t)$, respektivno. Preostali eksplicitni izrazi za izračunavanje transportnih koeficijenata u okviru prikazanog formalizma za rešavanje Boltzmann-ove jednačine su dati u Appendixu 2.

3.3 Fluidne jednačine i teorija prenosa impulsa za rojeve elektrona u atomskim tečnostima

Rešavanje Boltzmann-ove jednačine primenom momentnog metoda je u najvećem broju slučaje veoma težak numerički problem. Ovo je naročito izraženo kada spoljašnja polja nisu prostorno homogena ili kada je koncentracija naelektrisanih čestica dovoljno velika da njihove međusobne interakcije i njihov uticaj na rezultujuća polja postanu značajni. Jedna od alternativa numeričkom rešavanju Boltzmann-ove jednačine je razvoj i primena fluidnih jednačina. Fluidne jednačine se mogu izvesti množenjem Boltzmann-ove jednačine veličinama koje su funkcije brzine i integracijom ovih jednačina po brzinskom prostoru. Time se dobiju jednačine oblika [114]

$$\frac{\partial}{\partial t}\big(n\langle\Phi(\mathbf{c})\rangle\big) + \nabla \cdot \big(n\langle\mathbf{c}\Phi(\mathbf{c})\rangle\big) - n\frac{q}{m}\Big\langle\mathbf{E}\cdot\frac{\partial}{\partial\mathbf{c}}\Phi(\mathbf{c})\Big\rangle \begin{aligned} &= -\int \Phi(\mathbf{c})J(f)\mathrm{d}\mathbf{c} \\ &= C_\Phi, \end{aligned} \tag{3.42}$$

gde je $\Phi(\mathbf{c})$ proizvoljna funkcija brzine, $J(f)$ je kolizioni operator, dok ugaone zagrade $\langle\rangle$ predstavljaju usrednjavanje po brzinskom prostoru. Na ovaj način se Boltzmann-ova jednačina zamenjuje beskonačnim nizom fluidnih (ili momentnih) jednačina [52]. Sistem fluidnih jednačina, međutim, nije zatvoren zbog toga što u jednačinama nižeg reda figurišu veličine koje je potrebno odrediti na osnovu jednačina višeg reda. Zato je neopodno da ovaj niz bude odsečen na nekoj konkretnoj jednačini uz zanemarivanje svih jednačina višeg reda i reprezentovanje određenih nepoznatih veličina aproksimativnim izrazima [52, 114, 139]. Izjednačavanjem $\Phi(\mathbf{c})$ sa 1, $m\mathbf{c}$ i $\frac{1}{2}mv^2$ u jednačini (3.42) dobiju se jednačine za balans broja čestica, balans impulsa i balans energije, respektivno [114]:

$$\frac{\partial n}{\partial t} + \nabla \cdot (n\langle\mathbf{c}\rangle) = C_1, \tag{3.43}$$

$$\frac{\partial}{\partial t}(nm\langle\mathbf{c}\rangle) + \nabla \cdot (nm\langle\mathbf{c}\otimes\mathbf{c}\rangle) - nq\mathbf{E} = C_{m\mathbf{c}} \tag{3.44}$$

$$\frac{\partial}{\partial t}\big(n\langle\tfrac{1}{2}mc^2\rangle\big) + \nabla \cdot \big(n\langle\tfrac{1}{2}mc^2\mathbf{c}\rangle\big) - nq\mathbf{E}\cdot\langle\mathbf{c}\rangle = C_{\frac{1}{2}mc^2}, \tag{3.45}$$

gde ⊗ predstavlja tenzorski proizvod. Na desnoj strani jednačina (3.43)-(3.45) figurišu kolizioni članovi koji reprezentuju brzinu promene odgovarajućih veličina u sudarima čestice roja sa atomima (ili molekulima) pozadinske sredine.

U ostatku ovog poglavlja, analiza fluidnih jednačina biće ograničena na slučaj rojeva elektrona, budući da oblik kolizionih članova zavisi od tipa čestice roja. Fluidne jednačine za rojeve pozitrona u nepolarnim tečnostima analizirane su u radu Boyle-a i saradnika [114], u kojima sudarni procesi koji vode ka formiranju pozitronijuma i jonizacije nemaju istu reprezentaciju kao u slučaju koji se ovde razmatra.

Brzina promena veličine Ψ u sudarima u slučaju koherentnog rasejanja jednaka je [114]

$$\left(\frac{\partial \Psi}{\partial t}\right)_{coll}^{(coh)} = n_0 \int \mathrm{d}\mathbf{c} c f(\mathbf{r}, \mathbf{c}, t) \int \mathrm{d}\omega' \int \mathrm{d}\Omega_{\mathbf{k}'} \big(\Psi(\mathbf{r}, \mathbf{c}, t) - \Psi(\mathbf{r}, \mathbf{c}', t)\big) \frac{\mathrm{d}^2\sigma}{\mathrm{d}\mathbf{k}'\mathrm{d}\omega'}, \qquad (3.46)$$

gde ω i $\mathbf{k}$ označavaju ugaonu frekvencu i talasni broj elektrona, respektivno, a $\mathrm{d}\Omega_{\mathbf{k}}$ je prostorni ugao koji je centriran oko pravca duž koga se kreće elektron, dok je n_0 koncentracija pozadinskih atoma (ili molekula). Primovane i neprimovane veličine se odnose na stanje elektrona pre i posle sudara, respektivno [114]. Dvostruki diferencijalni presek se može izraziti kao

$$\frac{\mathrm{d}^2\sigma}{\mathrm{d}\mathbf{k}'\mathrm{d}\omega'} = \left(\frac{\mathrm{d}\sigma}{\mathrm{d}\omega'}\right)^{(lab)} S(\Delta\mathbf{k}, \Delta\omega), \qquad (3.47)$$

gde je $(\frac{\mathrm{d}\sigma}{\mathrm{d}\omega'})^{(lab)}$ presek za rasejanje elektrona na jednom fokus atomu (ili molekulu) pozadinske sredine u laboratorijskom sistemu reference, $S(\Delta\mathbf{k}, \Delta\omega)$ je dinamički strukturni faktor, dok su $\Delta\mathbf{k} \equiv \mathbf{k} - \mathbf{k}'$ i $\omega \equiv \omega - \omega'$ promene talasnog vektora i ugaone frekvence elektrona pri sudaru, respektivno. Dinamički strukturni faktor je Furijeov transform Van Hoveove generalisane vremenski zavisne parne korelacione funkcije po prostornim koordinatama i vremenu [99,114]. Može se uočiti da je dvostruki diferencijalni presek u jednačini (3.47) faktorisan na dva člana od kojih jedan zavisi samo od interakcije elektrona i fokus atoma (ili molekula) pozadinske sredine pri datoj vrednosti energije, dok drugi zavisi samo od prostornih i vremenskih korelacija neutralnih čestica pozadinske sredine [114].

Brzina promena veličine Ψ u sudarima je u slučaju nekoherentnog rasejanja (binarnih sudara) jednaka [52, 139]

$$\left(\frac{\partial \Psi}{\partial t}\right)_{coll}^{(noncoh)} = \int \mathrm{d}\mathbf{c} \int \mathrm{d}\mathbf{c_0} g f(\mathbf{r}, \mathbf{c}, t) f(\mathbf{c_0}) \int \mathrm{d}\Omega_{\mathbf{k}'} \big(\Psi(\mathbf{r}, \mathbf{c}, t) - \Psi(\mathbf{r}, \mathbf{c}', t)\big) \frac{\mathrm{d}\sigma}{\mathrm{d}\mathbf{k}'}, \qquad (3.48)$$

gde je $f(\mathbf{c_0})$ funkcija raspodele čestica pozadinske sredine, dok su g i $\frac{\mathrm{d}\sigma}{\mathrm{d}\mathbf{k}'}$ intenzitet relativne brzine i diferencijalni presek, respektivno. Sada će biti razmatrani kolizioni članovi C_1, $C_{m\mathbf{c}}$ i $C_{\frac{1}{2}mc^2}$. Kolizioni operator se može napisati kao [52,114]

$$J(f) = J_{elast}(f) + J_{inel}(f) + J_{ioniz}(f) + J_{attach}(f), \qquad (3.49)$$

gde $J_{elast}(f)$, $J_{inel}(f)$, $J_{ioniz}(f)$ i $J_{attach}(f)$ predstavljaju doprinose elastičnih sudara, neelastičnih sudara, jonizacije i zahvata elektrona, respektivno, ukupnom kolizionom operatoru. Na

osnovu toga svaki od kolizionih članova iz jednačina (3.43)-(3.45) može da se odredi kao zbir članova koji reprezentuju doprinose elastičnih, neelastičnih i reaktivnih sudara. U razređenom gasu se svi tipovi sudara mogu reprezentovati binarnim sudarima. Ovo je posledica toga što se pri rasejanju elektrona na fokus atomu (ili molekulu) pozadinske sredine u ovom slučaju efekat okolnih atoma (ili molekula) može zanemariti [100]. Uz to je dinamički strukturni faktor u razređenom gasu identički jednak jedinici. U gustim gasovima i tečnostima je rastojanje između susednih atoma (ili molekula) pozadinske sredine jako malo u poređenju sa srednjim slobodnim putem elektrona, pa se koherentni efekti moraju uzeti u obzir [100]. Pri izradi ove disertacije su elastični sudari u tečnoj fazi reprezentovani koherentnim rasejanjem, dok su ostali tipovi sudara reprezentovani binarnim sudarima. Ovo je opravdano time što u neelastičnim sudarima i jonizaciji dolazi do velike promene impulsa, a strukturni faktor je u slučaju velike promene impulsa praktično jednak jedinici, dok u zahvatu elektrona dolazi do gubitka elektrona iz roja.

Prvo će biti razmotren doprinos elastičnog rasejanja kolizionim članovima C_1, $C_{m\mathbf{c}}$ i $C_{\frac{1}{2}mc^2}$. Pri tome će biti korišćene sledeće osobine dinamičkog strukturnog faktora [70]

$$\int \mathrm{d}\omega S(\Delta\mathbf{k}, \Delta\omega) = S(\Delta\mathbf{k}), \tag{3.50}$$

$$\int \mathrm{d}\omega \Delta\omega S(\Delta\mathbf{k}, \Delta\omega) = \frac{m}{2}(v^2 - v'^2), \tag{3.51}$$

gde je $S(\Delta\mathbf{k})$ statički strukturni faktor pozadinskog fluida, dok su m, v i v' masa čestice roja i intenziteti brzine čestice roja pre i posle sudara, respektivno. Statički strukturni faktor je Furijeov transform vremenski nezavisne parne korelacione funkcije [68]. Jednačina (3.50) ima fizički smisao da je ukupna verovatnoća za rasejanje naelektrisane čestice u određeni pravac u prostoru uz određenu promenu impulsa direktno srazmerna statičkom strukturnom faktoru date sredine [70]. Slično tome, jednačina (3.51) ima fizički smisao da je srednja razmena energije naelektrisane čestice roja i pozadinskog fluida za datu vrednost impulsa jednaka energiji uzmaka izolovanog atoma (ili molekula) pozadinskog fluida pri datom transferu impulsa [70]. Zbog kraćeg zapisa biće korišćena oznaka

$$\Sigma(c, \chi) \equiv \sigma(c, \chi) S\left(\frac{2mc}{\hbar} \sin\left(\chi/2\right)\right), \tag{3.52}$$

gde je $\frac{2mc}{\hbar} = \Delta k$, dok je $\hbar$ redukovana Plankova konstanta. Pri određivanju vrednosti integrala u kolizionim članovima su korišćene veličine

$$\mathbf{G} = \frac{m\mathbf{c} + m_0\mathbf{c_0}}{m + m_0}, \tag{3.53}$$

$$\mathbf{g} = \mathbf{c} - \mathbf{c_0}, \tag{3.54}$$

$$\mu = \frac{mm_0}{m + m_0}, \tag{3.55}$$

$$M_0 = \frac{m_0}{m + m_0}, \tag{3.56}$$

$$M = \frac{m}{m + m_0}, \tag{3.57}$$

gde su $\mathbf{c}$, $\mathbf{c_0}$ $\mathbf{G}$, $\mathbf{g}$ i μ brzina čestice roja, brzina čestice pozadinske sredine, brzina centra mase, brzina relativne čestice i redukovana masa, respektivno. Primenom ovih veličina se brzine čestice roja i čestice pozadinske sredine mogu napisati kao

$$\mathbf{c} = \mathbf{G} + M_0\mathbf{g}, \tag{3.58}$$

$$\mathbf{c_0} = \mathbf{G} - M\mathbf{g}. \tag{3.59}$$

Lako se pokazuje da važi

$$C_1^{(coh)} = 0. \tag{3.60}$$

Transfer impulsa u elastičnim sudarima se može odrediti kao

$$\left(\frac{\partial(m\mathbf{c})}{\partial t}\right)_{coll}^{(coh)} = -\mu n_0 \int \mathrm{d}\mathbf{c} f(\mathbf{r},\mathbf{c},t)\mathbf{c}c2\pi \int (1-\cos\chi)\sin\chi\mathrm{d}\chi\Sigma(c,\chi)$$

$$= -\mu \int \mathrm{d}\mathbf{c} f(\mathbf{r},\mathbf{c},t)\mathbf{c}\tilde{\nu}_m^{(elast)}(\epsilon)$$

$$= -\mu n \langle\langle \tilde{\nu}_m^{(elast)}(\epsilon)\mathbf{c}\rangle_0\rangle, \tag{3.61}$$

gde je koliziona frekvenca za transfer impulsa pri koherentnom rasejanju definisana kao

$$\tilde{\nu}_m^{(elast)}(\epsilon) = n_0 c 2\pi \int (1-\cos\chi)\sin\chi\mathrm{d}\chi\Sigma(c,\chi). \tag{3.62}$$

Pri izvođenju jednačine (3.61) je primenjena osobina (3.50) dinamičkog strukturnog faktora. Pored toga je pri izvođenju jednačine (3.61) i u definiciji (3.62) iskorišćena približna jednakost $c \approx g$, koja je zadovoljena u slučaju rojeva elektrona u hladnim tečnostima (poput tečnog argona, tečnog kriptona i tečnog ksenona). Transfer energije u elastičnim sudarima se može odrediti kao

$$\left(\frac{\partial(\frac{1}{2}mc^2)}{\partial t}\right)_{coll}^{(coh)} = n_0 \int \mathrm{d}\mathbf{c} c f(\mathbf{r},\mathbf{c},t) \int \mathrm{d}\omega'$$

$$\times \int \mathrm{d}\Omega_{\mathbf{k}'}\left(\frac{1}{2}mc^2 - \frac{1}{2}mc'^2\right)\left(\frac{\mathrm{d}\sigma}{\mathrm{d}\omega'}\right)^{(lab)} S(\Delta\mathbf{k},\Delta\omega). \tag{3.63}$$

Na osnovu jednakosti $\frac{1}{2}mc^2 - \frac{1}{2}mc'^2 = \omega - \omega' = -\Delta\omega$ i osobine (3.51) dinamičkog strukturnog faktora, transfer energije u elastičnim sudarima se može napisati u obliku [52, 114, 139]

$$\left(\frac{\partial(\frac{1}{2}mc^2)}{\partial t}\right)_{coll}^{(coh)} = -\mu n \langle\langle \nu_m^{(elast)}(\epsilon)\mathbf{G}\cdot\mathbf{g}\rangle_0\rangle =$$

$$= -n\frac{\mu}{m+m_0}\langle\langle (mc^2 - m_0 c_0^2 - (m-m_0)\mathbf{c}\cdot\mathbf{c_0})\nu_m^{(elast)}(\epsilon)\rangle_0\rangle. \tag{3.64}$$

Na osnovu jednačina (3.61) i (3.64) može se uočiti da iako strukturni efekti utiču na brzinu transfera impulsa u elastičnim sudarima, oni ne utiču na brzinu transfera energije [114]. Stoga su vrednosti srednjeg slobodnog puta, koje odgovaraju transferu impulsa i transferu energije

u elastičnim sudarima međusobno različite za niskoenergijske elektrone (i pozitrone) u tečnoj fazi. Ovi srednji slobodni putevi su dati jednačinama

$$\Lambda_0(c) = \left(n_0 2\pi \int_0^\pi \mathrm{d}\chi \sin\chi (1-\cos\chi)\sigma(c,\chi) \right)^{-1}, \tag{3.65}$$

$$\Lambda_1(c) = \left(n_0 2\pi \int_0^\pi \mathrm{d}\chi \sin\chi (1-\cos\chi)\Sigma(c,\chi) \right)^{-1}, \tag{3.66}$$

gde su Λ_0 i Λ_1 srednji slobodni put za transfer energije i srednji slobodni put za transfer impulsa, respektivno.

Da bi se odredio doprinos neelastičnih sudara u fluidnim jednačinama, potrebno je uzeti u obzir populaciju pojedinačnih stanja atoma (ili molekula) pozadinske sredine. Populacija stanja j se može reprezentovati kao [52]

$$f_{0j}(\mathbf{c_0}) = n_{0j}\omega(\alpha_0, c_0) = n_{0j} \left(\frac{m_0}{2\pi k T_0} \right)^{3/2} \exp\left(-\frac{m_0 c_0^2}{2k T_0} \right), \tag{3.67}$$

gde je

$$n_{0j} = \frac{n_0}{Z_0} \exp\left(-\frac{\epsilon_j}{k T_0} \right), \tag{3.68}$$

pri čemu je Z_0 particiona funkcija čestica pozadinske sredine. U slučaju neelastičnih sudara važi [52]

$$\mathbf{G}' = \mathbf{G}, \tag{3.69}$$

i

$$\frac{1}{2}\mu g^2 + \epsilon_j = \frac{1}{2}\mu g'^2 + \epsilon_{j'}, \tag{3.70}$$

gde su ϵ_j i $\epsilon_{j'}$ energije diskretnih stanja j i j', respektivno. Neelastični sudari ne menjaju jednačinu kontinuiteta [52]

$$C_1^{(inel)} = 0. \tag{3.71}$$

Transfer impulsa u neelastičnim sudarima se može izraziti kao [52]

$$\left(\frac{\partial(m\mathbf{c})}{\partial t} \right)_{coll}^{(inel)} = -m \sum_{j,j'} \int \mathrm{d}\mathbf{c}\mathrm{d}\mathbf{c_0} g f(\mathbf{r},\mathbf{c},t) f_{0j}(\mathbf{c_0}) \int \mathrm{d}^2\Omega_{\mathbf{g}'} \sigma(j,j';g,\chi)(\mathbf{c}-\mathbf{c}'), \tag{3.72}$$

gde se sumacija vrši po svim diskretnim stanjima čestica pozadinske sredine, dok je $\sigma(j,j';g,\chi)$ diferencijalni presek za neelastični sudar u kome se čestica pozadinske sredine ekscituje iz stanja j u stanje j'. Može se pokazati da važi [52, 139]

$$\left(\frac{\partial(m\mathbf{c})}{\partial t} \right)_{coll}^{(inel)} = -n\mu \langle \langle \nu_m^{(inel)}(\epsilon)(\mathbf{c}-\mathbf{c_0}) \rangle_0 \rangle, \tag{3.73}$$

gde je koliziona frekvenca za transfer impulsa u neelastičnim sudarima predstavljena jednačinom

$$\nu_m^{(inel)}(\epsilon) \equiv \sum_{j,j'} n_{0j} \sqrt{\frac{2\epsilon}{\mu}} \sigma_m(j,j';g) = \sum_{j,j'} n_{0j} g \sigma_m(j,j',g), \tag{3.74}$$

dok je presek $\sigma_m(j, j', g)$ definisan kao

$$\sigma_m(j, j'; g) = 2\pi \int_0^\pi \mathrm{d}\chi \sin \chi \sigma(j, j'; g, \chi) \left(1 - \frac{g'}{g} \cos \chi \right). \tag{3.75}$$

Transfer energije u neelastičnim sudarima se može izraziti kao [52]

$$\left(\frac{\partial(\frac{1}{2}mc^2)}{\partial t}\right)_{coll}^{(inel)} = -\sum_{j,j'} \int \mathrm{d}\mathbf{c} \int \mathrm{d}\mathbf{c_0} g f(\mathbf{r}, \mathbf{c}, t) f_{0j}(\mathbf{c_0}) \frac{1}{2} m \int \mathrm{d}^2 \Omega_{\mathbf{g'}} \sigma(j, j'; g, \chi) (c^2 - c'^2). \tag{3.76}$$

Može se pokazati da važi [52]

$$\left(\frac{\partial(\frac{1}{2}mc^2)}{\partial t}\right)_{coll}^{(inel)} = -n\frac{2\mu}{m + m_0} \langle\langle \nu_m^{(inel)}(\epsilon)\delta\epsilon\rangle_0\rangle - n\frac{m_0}{m + m_0} \sum_{j,j'} \langle\langle \nu_T^{(inel)}(j, j'; g)\rangle_0\rangle (\epsilon_{j'} - \epsilon_j), \tag{3.77}$$

gde je

$$\delta\epsilon \equiv \frac{1}{2}mc^2 - \frac{1}{2}m_0c_0^2 - \frac{1}{2}(m - m_0)\mathbf{c} \cdot \mathbf{c_0}, \tag{3.78}$$

a veličina

$$\nu_T^{(inel)}(j, j'; g) \equiv n_{0j} g \sigma_T(j, j'; g), \tag{3.79}$$

predstavlja totalnu kolizionu frekvencu za neelastični prelaz iz j u j', dok je $\sigma_T(j, j'; g)$ totalni presek za ovaj prelaz. Drugi član u jednačini (3.77) se može napisati u obliku [52]

$$\sum_{j,j'} \langle\langle \nu_T^{(inel)}(j, j'; g)\rangle_0\rangle (\epsilon_{j'} - \epsilon_j) =$$
$$\sum_{j<j'} \langle\langle \nu_T^{(inel)}(j, j'; g)\rangle_0\rangle (\epsilon_{j'} - \epsilon_j) + \sum_{j>j'} \langle\langle \nu_T^{(inel)}(j, j'; g)\rangle_0\rangle (\epsilon_{j'} - \epsilon_j) =$$
$$\sum_{j<j'} \left(\langle\langle \nu_T^{(inel)}(j, j'; g)\rangle_0\rangle - \langle\langle \nu_T^{(inel)}(j', j; g)\rangle_0\rangle\right)(\epsilon_{j'} - \epsilon_j) \equiv \sum_{\Delta j} \left(\langle \nu_{\Delta j}^{\uparrow}(\epsilon)\rangle - \langle \nu_{\Delta j}^{\downarrow}(\epsilon)\rangle\right)\epsilon_{\Delta j}. \tag{3.80}$$

Doprinos zahvata elektrona u jednačini za balans broja čestica je dat izrazom [52, 139]

$$C_1^{(A)} = -n\langle\langle \nu^{(A)}(\epsilon)\rangle_0\rangle, \tag{3.81}$$

gde je $\nu^{(A)}(\epsilon)$ koliziona frekvenca za zahvat elektrona, koja je definisana kao

$$\nu^{(A)}(\epsilon) \equiv \sum_{j,j'} n_{0j} g \sigma_A(j, j'; g). \tag{3.82}$$

U jednačini (3.82) je $\sigma_A(j, j'; g)$ totalni presek za zahvat elektrona u kome neutralna čestica pređe iz stanja j u stanje j'. Može se pokazati da su transfer impulsa i transfer energije u zahvatu elektrona dati jednačinama [52, 139]

$$\left(\frac{\partial(m\mathbf{c})}{\partial t}\right)_{coll}^{(A)} = -n\langle\langle m\mathbf{c}\nu^{(A)}(\epsilon)\rangle_0\rangle, \tag{3.83}$$

i

$$\left(\frac{\partial(\frac{1}{2}mc^2)}{\partial t}\right)_{coll}^{(A)} = -n\langle\langle\frac{1}{2}mc^2\nu^{(A)}(\epsilon)\rangle_0\rangle, \tag{3.84}$$

respektivno.

Doprinos jonizacije jednačini za balans broja čestica je predstavljen izrazom

$$C_1^{(I)} = n\langle\langle\nu^{(I)}(\epsilon)\rangle_0\rangle, \tag{3.85}$$

gde je $\nu^{(I)}(\epsilon)$ koliziona frekvenca za jonizaciju. Elektronska sudarna jonizacija je složeniji proces od zahvata elektrona, zbog toga što u tom procesu učestvuju tri tela. Međutim, može se smatrati da se ukupan impuls početnog elektrona, kao i sva raspoloživa kinetička energija nakon jonizacije raspodeljuju između primarnog i sekundarnog elektrona [139], zbog toga što su atomi (ili molekuli) pozadinske sredine znatno masivniji od elektrona. Ako se nakon jonizacije pozitivan jon nalazi u eksitovanom stanju, u ovom procesu je utrošena energija jednaka zbiru praga za jonizaciju i praga za eksitaciju pozitivnog jona u dato eksitovano stanje. Pri ovim pretpostavkama se transfer impulsa i transfer energije u jonizaciji mogu izraziti kao [139]

$$\left(\frac{\partial(m\mathbf{c})}{\partial t}\right)_{coll}^{(I)} = 0, \tag{3.86}$$

i

$$\left(\frac{\partial(\frac{1}{2}mc^2)}{\partial t}\right)_{coll}^{(I)} = -n\langle\langle\nu^{(I)}(\epsilon)\rangle_0\rangle\epsilon^{(I)} - n\sum_{s\in I}\langle\langle\nu_s^{(I)}(\epsilon)\rangle_0\rangle\Delta\epsilon_s^{(I)}, \tag{3.87}$$

gde su $\epsilon^{(I)}$ i $\epsilon_s^{(I)}$ prag za jonizaciju i prag za eksitaciju pozitivnog jona u eksitovano stanje s, respektivno. Ukupna koliziona frekvenca za jonizaciju $\nu^{(I)}(\epsilon)$ je jednaka zbiru kolizionih frekvenci za pojedinačne jonizacione kanale

$$\nu^{(I)} = \sum_{s\in I}\nu_s^{(I)}(\epsilon), \tag{3.88}$$

dok je koliziona frekvenca za jonizacioni kanal u kome nastaje pojedinačno finalno stanje s predstavljena jednačinom

$$\nu_s^{(I)}(\epsilon) = n_0 g\sigma_s^{(I)}(\epsilon), \tag{3.89}$$

gde je $\sigma_s^{(I)}(\epsilon)$ totalni presek za jonizacioni kanal s.

Ukupni kolizioni članovi su jednaki zbiru kolizionih članova koji odgovaraju elastičnim sudarima, neelastičnim sudarima, zahvatu elektrona i jonizaciji

$$C_\Phi = C_\Phi^{(elast)} + C_\Phi^{(inel)} + C_\Phi^{(A)} + C_\Phi^{(I)}, \tag{3.90}$$

gde je $\Phi \in \{1, m\mathbf{c}, \frac{1}{2}mc^2\}$.

Kada se primene izrazi za kolizione članove, jednačine za balans broja čestica, impulsa i energije mogu se napisati u obliku [52,139]

$$\frac{\partial n}{\partial t} + \nabla\cdot(n\langle\mathbf{c}\rangle) = -n\langle\langle\nu^{(A)}(\epsilon)\rangle_0\rangle + n\langle\langle\nu^{(I)}(\epsilon)\rangle_0\rangle, \tag{3.91}$$

$$\frac{\partial}{\partial t}(nm\langle\mathbf{c}\rangle) + \nabla\cdot(nm\langle\mathbf{c}\otimes\mathbf{c}\rangle) - nq\mathbf{E} = -\mu n\langle\langle\tilde{\nu}_m^{(elast)}(\epsilon)\mathbf{c}\rangle_0\rangle - n\mu\langle\langle\nu_m^{(inel)}(\epsilon)(\mathbf{c}-\mathbf{c_0})\rangle_0\rangle$$
$$- n\langle\langle m\mathbf{c}\nu^{(A)}(\epsilon)\rangle_0\rangle, \tag{3.92}$$

$$\frac{\partial}{\partial t}\big(n\langle\tfrac{1}{2}mc^2\rangle\big) + \nabla\cdot\big(n\langle\tfrac{1}{2}mc^2\mathbf{c}\rangle\big) - nq\mathbf{E}\cdot\langle\mathbf{c}\rangle =$$
$$- n\frac{\mu}{m+m_0}\langle\langle\nu_m^{(elast)}(\epsilon)(mc^2 - m_0c_0^2 - (m-m_0)\mathbf{c}\cdot\mathbf{c_0})\rangle_0\rangle$$
$$- n\frac{\mu}{m+m_0}\langle\langle\nu_m^{(inel)}(\epsilon)(mc^2 - m_0c_0^2 - (m-m_0)\mathbf{c}\cdot\mathbf{c_0})\rangle_0\rangle$$
$$- n\frac{m_0}{m+m_0}\sum_{j,j'}\langle\langle\nu_T^{(inel)}(j,j';g)\rangle_0\rangle(\epsilon_{j'} - \epsilon_j) - n\langle\langle\tfrac{1}{2}mc^2\nu^{(A)}(\epsilon)\rangle_0\rangle$$
$$- n\langle\langle\nu^{(I)}(\epsilon)\rangle_0\rangle\epsilon^{(I)} - n\sum_{s\in I}\langle\langle\nu_s^{(I)}(\epsilon)\rangle_0\rangle\Delta\epsilon_s^{(I)}. \tag{3.93}$$

Desna strana jednačina (3.91)-(3.93) se može pojednostaviti uvođenjem aproksimacije transfera impulsa (eng. momenum transfer approximation), (skraćeno MT aproksimacija). U ovoj aproksimaciji se kolizione frekvence reprezentuju Tejlorovim razvojem oko srednje energije $\bar{\epsilon}$

$$\nu(\epsilon) = \nu(\bar{\epsilon}) + \nu'(\bar{\epsilon})(\epsilon - \bar{\epsilon}) + ..., \tag{3.94}$$

gde su $\nu(\epsilon)$ i $\nu'(\epsilon)$ koliziona frekvenca za proizvoljan tip sudarnog procesa i njen prvi izvod po energiji, respektivno. Pri tome se za sve sudarne procese osim zahvata elektrona uzima u obzir samo nulti član u razvoju. U slučaju zahvata elektrona nije dovoljno da bude uzet u obzir samo nulti član u razvoju (3.94) jer je uticaj ovog procesa na transportne osobine roja određen energijskom zavisnošću odgovarajuće kolizione frekvence [52]. Zato se prilikom zahvata elektrona uzimaju u obzir nulti i prvi član u razvoju (3.94).

U okviru MT aproksimacije transfer impulsa u elastičnim sudarima može se izraziti kao

$$\left(\frac{\partial(m\mathbf{c})}{\partial t}\right)_{coll,MT}^{(coh)} = n\mu\tilde{\nu}_m^{(elast)}(\bar{\epsilon})\langle\mathbf{c}\rangle. \tag{3.95}$$

Transfer energije u elastičnim sudarima je u okviru MT aproksimacije jednak

$$\left(\frac{\partial(\tfrac{1}{2}mc^2)}{\partial t}\right)_{coll,MT}^{(coh)} = n\frac{2m}{m_0}\nu_m^{(elast)}(\bar{\epsilon})\left(\frac{\langle\mu c^2\rangle}{2} - \frac{m_0}{m_0+m}\frac{3}{2}kT_0\right) \tag{3.96}$$
$$\approx n\frac{2m}{m_0}\nu_m^{(elast)}(\bar{\epsilon})\left(\frac{m}{2}\langle c^2\rangle - \frac{3}{2}kT_0\right), \tag{3.97}$$

gde približna jednakost važi za elektrone i ostale čestice čija je masa znatno manja od mase čestica pozadinske sredine. Transfer impulsa i transfer energije u neelastičnim sudarima su u okviru MT aproksimacije dati jednačinama

$$\left(\frac{\partial(m\mathbf{c})}{\partial t}\right)_{coll,MT}^{(inel)} = -n\mu\nu_m^{(inel)}(\bar{\epsilon})\langle\mathbf{c}\rangle, \tag{3.98}$$

i

$$\left(\frac{\partial(\frac{1}{2}mc^2)}{\partial t}\right)_{coll,MT}^{(inel)} = -n\frac{2\mu}{m+m_0}\nu_m^{(inel)}(\bar{\epsilon})\left(\langle\frac{1}{2}mc^2\rangle - \frac{3}{2}kT_0\right)$$
$$-n\frac{m_0}{m+m_0}\sum_{\Delta j}\left(\nu_{\Delta j}^{\uparrow}(\bar{\epsilon}) - \nu_{\Delta j}^{\downarrow}(\bar{\epsilon})\right)\epsilon_{\Delta j}. \tag{3.99}$$

Zbog kraćeg zapisa, biće uvedena sledeća oznaka

$$\Omega(\bar{\epsilon}) \equiv \frac{m_0}{m_0+m}\sum_{\Delta j}\left(\nu_{\Delta j}^{\uparrow}(\bar{\epsilon}) - \nu_{\Delta j}^{\downarrow}(\bar{\epsilon})\right)\epsilon_{\Delta j}. \tag{3.100}$$

Može se pokazati da su u okviru MT aproksimacije transfer impulsa i energije u zahvatu elektrona dati u vidu izraza [52]

$$\left(\frac{\partial(m\mathbf{c})}{\partial t}\right)_{coll}^{(A)} \approx -nm\left(\nu^{(A)}(\bar{\epsilon}) + \xi\nu_1^{(A)}(\bar{\epsilon})\right)\langle\mathbf{c}\rangle, \tag{3.101}$$

i

$$\left(\frac{\partial(\frac{1}{2}mc^2)}{\partial t}\right)_{coll}^{(A)} \approx -nm\frac{1}{2}\left(\xi\nu_1^{(A)}(\bar{\epsilon})\langle\mathbf{c}\rangle^2 + (\nu^{(A)}(\bar{\epsilon}) + \xi\nu_1^{(A)}(\bar{\epsilon}))\langle c^2\rangle\right), \tag{3.102}$$

gde je $\nu_1^{(A)} = \frac{d\nu^{(A)}}{d\epsilon}$ i ξ je definisano kao

$$\xi \equiv \frac{2}{3}\frac{m_0}{m+m_0}\left(\frac{1}{2}m\langle c^2\rangle - \frac{1}{2}m\langle\mathbf{c}\rangle^2\right). \tag{3.103}$$

Unutar MT aproksimacije jednačine za balans broja čestica, balans impulsa i balans energije se mogu napisati u obliku [52, 139]

$$\frac{\partial n}{\partial t} + \nabla\cdot\left(n\langle\mathbf{c}\rangle\right) = n\left(\nu^{(I)}(\bar{\epsilon}) - \nu^{(A)}(\bar{\epsilon})\right), \tag{3.104}$$

$$\frac{\partial}{\partial t}\left(nm\langle\mathbf{c}\rangle\right) + \nabla\cdot\left(nm\langle\mathbf{c}\otimes\mathbf{c}\rangle\right) - nq\mathbf{E} = nm\left(\tilde{\nu}_m(\bar{\epsilon}) + \nu^{(A)}(\bar{\epsilon}) + \xi\nu_1^{(A)}(\bar{\epsilon})\right)\langle\mathbf{c}\rangle, \tag{3.105}$$

$$\frac{\partial}{\partial t}\left(nm\frac{1}{2}\langle c^2\rangle\right) + \nabla\cdot\left(\frac{1}{2}nm\langle c^2\mathbf{c}\rangle\right) - nq\mathbf{E}\cdot\langle\mathbf{c}\rangle = -n\frac{2m}{m_0}\nu_m(\bar{\epsilon})\left(\frac{1}{2}m\langle c^2\rangle - \frac{3}{2}kT_0\right) - n\Omega(\bar{\epsilon})$$
$$-n\sum_b\nu_b^{(I)}(\bar{\epsilon})\epsilon_b^{(I)} - \frac{1}{2}nm\nu^{(A)}(\bar{\epsilon})\langle c^2\rangle - \frac{1}{2}nm\nu_1^{(A)}(\bar{\epsilon})\left(\langle c^2\rangle + \langle\mathbf{c}\rangle^2\right). \tag{3.106}$$

U jednačinama (3.105) i (3.106) su $\tilde{\nu}_m(\bar{\epsilon})$ i $\nu_m(\bar{\epsilon})$ definisani kao

$$\tilde{\nu}_m(\bar{\epsilon}) = \tilde{\nu}_m^{(elast)}(\bar{\epsilon}) + \nu_m^{(inel)}(\bar{\epsilon}) \tag{3.107}$$
$$\nu_m(\bar{\epsilon}) = \nu_m^{(elast)}(\bar{\epsilon}) + \nu_m^{(inel)}(\bar{\epsilon}). \tag{3.108}$$

Uz to je u jednačini (3.106) zbog kraćeg zapisa uvedena oznaka

$$\sum_b\nu_b^{(I)}(\bar{\epsilon})\epsilon_b^{(I)} \equiv \nu^{(I)}(\bar{\epsilon})\epsilon^{(I)} + \sum_{s\in I}\nu_s^{(I)}(\bar{\epsilon})\Delta\epsilon_s^{(I)}. \tag{3.109}$$

Kada se jednačina (3.104) pomnoži sa $m\langle \mathbf{c} \rangle$ i oduzme od jednačine (3.105), dobije se jednačina oblika

$$mn\left(\frac{\partial}{\partial t} + \langle \mathbf{c} \rangle \cdot \nabla\right)\langle \mathbf{c} \rangle + \nabla \cdot (nk\hat{\mathbf{T}}) - nq\mathbf{E} = -nm\big(\tilde{\nu}_m(\bar{\epsilon}) + \nu^{(I)}(\bar{\epsilon}) + \xi\nu_1^{(A)}(\bar{\epsilon})\big)\langle \mathbf{c} \rangle, \quad (3.110)$$

gde je $\hat{\mathbf{T}}$ temperaturski tenzor. Ukoliko se jednačina (3.104) pomnoži sa $\frac{1}{2}m\langle c^2 \rangle$ i oduzme od jednačine (3.106), dobije se jednačina

$$n\left(\frac{\partial}{\partial t} + \langle \mathbf{c} \rangle \cdot \nabla\right)\left(\frac{m\langle c^2 \rangle}{2}\right) + \nabla \cdot \left(n\mathbf{Q} + \hat{\mathbf{P}} \cdot \langle \mathbf{c} \rangle\right) - nq\mathbf{E} \cdot \langle \mathbf{c} \rangle =$$
$$- n\frac{2m}{m_0}\nu_m(\bar{\epsilon})\left(\frac{m\langle c^2 \rangle}{2} - \frac{3}{2}kT_0\right) - n\Omega(\bar{\epsilon}) - n\sum_b \nu_b^{(I)}(\bar{\epsilon})\epsilon_b^{(I)}$$
$$- \frac{1}{2}nm\langle c^2 \rangle\nu^{(I)}(\bar{\epsilon}) - \frac{1}{2}nm\xi\nu_1^{(A)}(\bar{\epsilon})\left(\langle c^2 \rangle + \langle \mathbf{c} \rangle^2\right), \quad (3.111)$$

pri čemu su $\mathbf{Q}$ i $\hat{\mathbf{P}}$ vektor toplotnog provođenja i tenzor pritiska, respektivno. Tenzor pritiska i temperaturski tenzor definisani su kao

$$\hat{\mathbf{P}} = nk\hat{\mathbf{T}} = mn\langle \delta\mathbf{c} \otimes \delta\mathbf{c} \rangle, \quad (3.112)$$

gde je $\delta\mathbf{c} = \mathbf{c} - \langle \mathbf{c} \rangle$ haotična komponenta brzine čestice. Vektor toplotnog provođenja je određen kao

$$\mathbf{Q} = \frac{1}{2}m\langle (\delta\mathbf{c} \cdot \delta\mathbf{c})\delta\mathbf{c} \rangle. \quad (3.113)$$

Radi jednostavnosti nadalje će biti uvedeno nekoliko hipoteza. Biće pretpostavljeno da je haotična komponenta brzine elektrona znatno veća od usmerene komponente $\langle \mathbf{c} \rangle^2 \ll \langle c^2 \rangle$. Na osnovu toga važi $\langle c^2 \rangle + \langle \mathbf{c} \rangle^2 \approx \langle c^2 \rangle$, odakle sledi $\xi = \frac{2}{3}\bar{\epsilon}$ i $k\hat{\mathbf{T}} = \frac{2}{3}\bar{\epsilon}\hat{\mathbf{I}}$, gde je $\hat{\mathbf{I}}$ jedinični operator. Pored toga, pretpostavlja se kako se sistem nalazi u stacionarnom stanju. Odatle sledi $\frac{\partial}{\partial t}\langle \mathbf{c} \rangle = 0$ i $\frac{\partial}{\partial t}\langle c^2 \rangle = 0$. Pretpostavka je i da se sistem nalazi u hidrodinamičkom režimu, kao i to da se svi članovi u kojima figurišu parcijalni izvodi drugog i višeg reda po prostornim kordinatama mogu zanemariti. Da bi se reprezentovala prostorna nehomogenost srednje energije roja, srednja energija će biti napisana u obliku

$$\bar{\epsilon} = \epsilon_0 + \frac{1}{n}\gamma \cdot \nabla n + ..., \quad (3.114)$$

gde su ϵ_0 i γ vrednost energije roja, koja je usrednjena po prostornim koordinatama i prostorni gradijent srednje energije, respektivno. Uz to će i kolizione frekvence za sve tipove sudarnih procesa biti napisane u obliku

$$\nu(\bar{\epsilon}) = \nu(\epsilon_0) + \frac{1}{n}\nu'(\epsilon_0)\gamma \cdot \nabla n + ..., \quad (3.115)$$

gde su ν i ν' koliziona frekvenca za proizvoljan tip sudarnog procesa i njen prvi izvod po energiji, respektivno. Pored toga se u hidrodinamičkom režimu srednja brzina čestica roja može napisati u obliku

$$\langle \mathbf{c} \rangle = \mathbf{W} - \frac{1}{n}\hat{\mathbf{D}} \cdot \nabla n + ... \quad (3.116)$$

u kom su $\mathbf{W}$ i $\hat{\mathbf{D}}$ bzina drifta i difuzioni tenzor, respektivno.

Kada su zadovoljene ove pretpostavke, jednačina (3.110) može se napisati u obliku

$$\nabla \cdot \left(n\frac{2}{3}(\epsilon_0 + \frac{1}{n}\gamma \cdot \nabla n)\hat{\mathbf{I}}\right) - nq\mathbf{E} =$$
$$-nm\left(\tilde{\nu}_m(\epsilon_0) + \frac{1}{n}\tilde{\nu}'_m(\epsilon_0)\gamma \cdot \nabla n + \nu^{(I)}(\epsilon_0) + \frac{1}{n}\nu'^{(I)}(\epsilon_0)\gamma \cdot \nabla n\right.$$
$$\left.+\frac{2}{3}(\epsilon_0 + \frac{1}{n}\gamma \cdot \nabla n) \cdot \left(\nu_1^{(A)}(\epsilon_0) + \frac{1}{n}\nu_1'^{(A)}(\epsilon_0)\gamma \cdot \nabla n\right)\right) \cdot \left(\mathbf{W} - \frac{1}{n}\hat{\mathbf{D}} \cdot \nabla n\right). \qquad (3.117)$$

Ukoliko u jednačini (3.117) uzmemo u obzir samo članove u kojima ne figurišu prostorni gradijenti koncentracije, dobije se jednačina

$$\mathbf{W} = \frac{q\mathbf{E}}{m\left(\tilde{\nu}_m(\epsilon_0) + \nu^{(I)}(\epsilon_0) + \frac{2}{3}\epsilon_0\nu_1^{(A)}(\epsilon_0)\right)}. \qquad (3.118)$$

Slično tome, kada se u jednačini (3.117) uzmu u razmatranje samo članovi koji stoje uz prvi stepen prostornog gradijenta koncentracije, proizlazi jednačina

$$\left(\tilde{\nu}_m(\epsilon_0) + \nu^{(I)}(\epsilon_0) + \frac{2}{3}\epsilon_0\nu_1^{(A)}(\epsilon_0)\right)\hat{\mathbf{D}} = \frac{2\epsilon_0}{3m}\hat{\mathbf{I}}$$
$$+ \frac{\mathrm{d}}{\mathrm{d}\epsilon}\left(\tilde{\nu}_m(\epsilon) + \nu^{(I)}(\epsilon) + \frac{2}{3}\epsilon\nu_1^{(A)}(\epsilon)\right)\bigg|_{\epsilon=\epsilon_0}\gamma \otimes \mathbf{W}. \qquad (3.119)$$

Ako su zadovoljene pomenute pretpostavke (stacionarno stanje, hidrodinamički režim i zanemarljivost usmerene komponente brzine elektrona u odnosu na haotičnu komponentu brzine) jednačina (3.111) se može napisati u obliku

$$\mathbf{Q} \cdot \nabla n - mn\left(\tilde{\nu}_m(\epsilon_0) + \frac{1}{n}\tilde{\nu}'_m(\epsilon_0)\gamma \cdot \nabla n\right)\left(W^2 - \frac{2}{n}\mathbf{W} \cdot \hat{\mathbf{D}} \cdot \nabla n\right) =$$
$$= -n\frac{2m}{m_0}\left(\nu_m(\epsilon_0) + \nu'_m(\epsilon_0)\frac{1}{n}\gamma \cdot \nabla n\right)\left(\epsilon_0 + \frac{1}{n}\gamma \cdot \nabla n - \frac{3}{2}kT_0\right)$$
$$-n\Omega(\epsilon_0) - \Omega'(\epsilon_0)\gamma \cdot \nabla n - n\sum_b \nu_b^{(I)}(\epsilon_0)\epsilon_b - \sum_b \nu_b'^{(I)}(\epsilon_0)\epsilon_b\gamma \cdot \nabla n$$
$$-n\left(\epsilon_0 + \frac{1}{n}\gamma \cdot \nabla n\right)\left(\nu^{(I)}(\epsilon_0) + \frac{1}{n}\nu'^{(I)}(\epsilon_0)\gamma \cdot \nabla n\right)$$
$$-n\left(\nu_1^{(A)}(\epsilon_0) + \frac{1}{n}\nu_1'^{(A)}(\epsilon_0)\gamma \cdot \nabla n\right)\frac{2}{3}\left(\epsilon_0^2 + \frac{2}{n}\epsilon_0\gamma \cdot \nabla n\right). \qquad (3.120)$$

Pri izvođenju jednačine (3.120) je iskorišćena približna jednakost $q\mathbf{E} \cdot \langle\mathbf{c}\rangle \approx m\tilde{\nu}_m(\bar{\epsilon})\langle\mathbf{c}\rangle^2$. Kada se u jednačini (3.120) uzmu u obzir samo članovi u kojima ne figurišu prostorni gradijenti koncentracije, dobije se jednačina

$$\epsilon_0 = \frac{m_0 W^2}{2} \cdot \frac{\tilde{\nu}_m(\epsilon_0)}{\nu_m(\epsilon_0)} \cdot \frac{\nu_e(\epsilon_0)}{\nu_e(\epsilon_0) + \nu^{(I)}(\epsilon_0)} + \frac{3}{2}kT_0\frac{\nu_e(\epsilon_0)}{\nu_e(\epsilon_0) + \nu^{(I)}(\epsilon_0)}$$
$$-\frac{1}{\nu_e(\epsilon_0) + \nu^{(I)}(\epsilon_0)}\left(\Omega(\epsilon_0) + \sum_b \nu_b^{(I)}(\epsilon_0)\epsilon_b + \frac{2}{3}\nu_1^{(A)}(\epsilon_0)\epsilon_0^2\right). \qquad (3.121)$$

Slično tome, ako se u jednačini (3.120) uzmu u obzir samo članovi koji stoje uz prvi stepen prostornog gradijenta koncentracije, dobije se jednačina

$$\frac{1}{\nu_e(\epsilon_0)}\mathbf{Q} + m_0 \frac{\tilde{\nu}_m(\epsilon_0)}{\nu_m(\epsilon_0)}\mathbf{W} \cdot \hat{\mathbf{D}} =$$
$$- \left(1 + \frac{\nu'_m(\epsilon_0)}{\nu_m(\epsilon_0)}\left(\epsilon_0 - \frac{3}{2}kT_0 - \frac{\tilde{\nu}'_m(\epsilon_0)}{\nu'_m(\epsilon_0)}\frac{m_0 W^2}{2}\right)\right.$$
$$\left. + \frac{1}{\nu_e(\epsilon_0)}\frac{\mathrm{d}}{\mathrm{d}\epsilon}\left(\Omega(\epsilon) + \sum_b \nu_b^{(I)}(\epsilon)\epsilon_b^{(I)} + \epsilon\nu^{(I)}(\epsilon) + \frac{2}{3}\epsilon^2\nu_1^{(A)}(\epsilon)\right)\bigg|_{\epsilon=\epsilon_0}\right)\gamma. \qquad (3.122)$$

Sistem koji čine jednačine (3.118), (3.119), (3.121) i (3.122) može se rešiti numerički ukoliko su poznate sve kolizione frekvence u funkciji energije, i to ako se jedna od veličina (ϵ_0, $\mathbf{W}$, γ, $\mathbf{Q}$ ili $\hat{\mathbf{D}}$) može odrediti na neki drugi način. Vektor toplotnog provođenja se u slučaju elektrona često može zanemariti, pa se preostale četiri veličine mogu odrediti numeričkim rešavanjem ovog sistema jednačina, kada su poznate kolizione frekvence za pojedinačne sudarne procese u funkciji srednje energije elektrona.

3.4 Monte Carlo simulacije rojeva elektrona u gasovima i atomskim tečnostima

Kompjuterski kod baziran na Monte Carlo metodi, koji je korišćen u ovoj disretaciji, razvijen je u Laboratoriji za neravnotežne procese i primenu plazme Instituta za fiziku u Beogradu. Numerički integritet ovog kompjuterskog koda je verifikovan u benčmak proračunima za rojeve naelektrisanih čestica u vremenski konstantnim i vremenski promenljivim električnim i magnetskim poljima, kako za modelne tako i za realne gasove [67,148–151]. Monte Carlo kod je korišćen za testiranje različitih metoda za numeričko rešavanje Boltzmann-ove jednačine [67,148–151], ali i za proučavanje implicitnih i eksplicitnih efekata nekonzervativnih sudara na transportne osobine rojeva elektrona [67,148–152] i pozitrona [153–155]. Isti kod je korišćen za proučavanje prostorno-vremenske evolucije roja elektrona [133,152], transporta elektrona i pozitrona u ukrštenim električnim i magnetskim poljima [153,156–158], zatim transporta elektrona u živinim parama [159], transporta elektrona u jako elektronegativnim gasovima [160] i u modelovanju gasnih detektora sa ravnim pločastim elektrodama, koji se koriste u fizici visokih energija [28–30]. U domenu vremenski promenljivih električnih i magnetskih polja, Monte Carlo kod je upotrebljavan za istraživanje velikog broja kinetičkih fenomena, uključujući vremenski razloženu negativnu diferencijalnu provodnost [47,161,162], anomalnu anizotropnu difuziju [47,163], tranzijentnu negativnu difuzivnost [164,165], apsolutnu negativnu mobilnost [166], i mehanizme za grejanje elektrona [141].

Iako je naš Monte Carlo kod razvijen za ispitivanje rojeva naelektrisanih čestica u neutralnim gasovima, njegova primenljivost se uz izvesne modifikacije može proširiti na proučavanje rojeva elektrona u nepolarnim atomskim tečnostima, i to ukoliko je gustina tečnosti homogena. U tečnom argonu, kriptonu i ksenonu koji su predmet istraživanja u ovoj disertaciji, postoji

provodna zona u kojoj su elektroni kvazislobodni [101, 112, 175]. Uz to se disperziona relacija u ove tri tečnosti može smatrati paraboličnom i izotropnom ako se nijedan deo potencijala za rasejanje ne uključi u definiciju slobodnih elektronskih stanja, već se ceo potencijal za rasejanje uzima u obzir pri računanju preseka za elementarne sudarne procese [111]. Tada je uticaj tečnosti na kretanje elektrona u potpunosti određen sudarima. Na osnovu toga se naš Monta Carlo kod može primeniti za ispitivanje rojeva elektrona u tečnom argonu, tečnom kriptonu i tečnom ksenonu ukoliko se na validan način reprezentuje dinamika rasejanja u ovim tečnostima. Ovo je postignuto uvođenjem tri dodatna efektivna sudarna procesa koji zajedno obezbeđuju dobru reprezentaciju srednjeg transfera energije i impulsa pri koherentnom rasejanju elektrona za svaku vrednost početne energije [176].

U našem Monte Carlo kodu se prati prostorno-vremenska evolucija roja elektrona koji se kreće u homogenom pozadinskom fluidu (koji se nalazi u gasnoj ili u tečnoj fazi) pod uticajem prostorno homogenog električnog polja $\mathbf{E}$ koje je orijentisano duž x-ose. Pri tome je u nekim simulacijama uz električno polje prisutno i prostorno homogeno magnetsko polje $\mathbf{B}$, koje se nalazi u $x - z$ ravni i sa električnim poljem zaklapa ugao ψ. U početnom trenutku simulacije svi se elektroni nalaze u koordinatnom početku i nasumično su im dodeljeni vektori brzine na osnovu Maxwell–Boltzmann-ove raspodele, koja odgovara srednjoj energiji od 1 eV. Nakon tog trenutka se kretanje svakog elektrona prati nezavisno od ostalih elektrona. Pri praćenju pojedinačnog elektrona neophodno je odrediti kretanje elektrona između dva sudara, trenutak i tip narednog sudara, kao i promenu vektora brzine nakon sudara.

Kretanje elektrona između dva sudara određeno je Lorentz-ovom silom. Pritom je vremenska zavisnost brzine elektrona opisana drugim Newton-ovim zakonom

$$m\frac{d\mathbf{v}}{dt} = e\mathbf{E} + e\mathbf{v} \times \mathbf{B}, \tag{3.123}$$

gde su m, e $\mathbf{v}$, i t masa elektrona, naelektrisanje elektrona, trenutna brzina i vremenska koordinata, respektivno. Jednačina 3.123 u skalarnom obliku glasi

$$\frac{dv_x}{dt} = \frac{e}{m}E + \frac{eB}{m}v_y \sin(\psi), \tag{3.124}$$

$$\frac{dv_y}{dt} = \frac{eB}{m}(v_z \cos(\psi) - v_x \sin(\psi)), \tag{3.125}$$

$$\frac{dv_z}{dt} = -\frac{eB}{m}v_y \cos(\psi), \tag{3.126}$$

pri čemu je $\frac{eB}{m}$ ciklotronska frekvenca elektrona. Ovaj sistem jednačina se može rešiti analitički ako su električno i magnetsko polje vremenski konstantni [177]. Na osnovu ovog analitičnog rešenja mogu se odrediti vremenske zavisnosti koordinata i brzina elektrona u intervalu između dva sudara. Alternativni način za reprezentovanje kretanja elektrona između dva sudara je primena Borisove rotacije [178]. Mnogobrojna testiranja Borisove rotacije pokazala su da je ova numerička procedura veoma precizna i efikasna u pogledu trošenja procesorskog vremena i da se jednako uspešno može primeniti kako za vremenski konstantna, tako i za vremenski promenljiva električna i magnetska polja, pod uslovom da su vektori električnog i magnetskog polja međusobno ortogonalni [pitajRef]. Prvi korak u ovom algoritmu je izračunavanje ubrzavanja

elektrona pod uticajem električnog polja za vreme polovine vremenskog koraka Δt

$$v_x := v_x + \frac{eE}{m}\frac{\Delta t}{2}.$$ (3.127)

Nakon toga se uzima u obzir rotacija vektora brzine pod dejstvom magnetskog polja

$$v_x := v_x + sv_y',$$ (3.128)

$$v_y := v_y - sv_x',$$ (3.129)

pri čemu je

$$s := -\frac{2\tan\left(\frac{\theta}{2}\right)}{1 + \tan\left(\frac{\theta}{2}\right)^2}$$ (3.130)

dok su brzine v_x' i v_y' date izrazima

$$v_x' := v_x + \tan\left(-\frac{\theta}{2}\right)v_y,$$ (3.131)

$$v_y' := v_y - \tan\left(-\frac{\theta}{2}\right)v_x,$$ (3.132)

gde je θ ugao rotacije pod uticajem magnetskog polja, koji iznosi $\theta = \frac{eB}{m}\Delta t$. Nakon rotacije vektora brzine uračunava se ubrzavanje elektrona pod uticajem električnog polja za vreme druge polovine vremenskog koraka Δt

$$v_x := v_x + \frac{eE}{m}\frac{\Delta t}{2}.$$ (3.133)

Vrednosti koordinata elektrona nakon vremenskog koraka Δt su date u izrazima

$$x := x_0 + \frac{1}{2}(v_{x0} + v_x(t))\Delta t,$$ (3.134)

$$y := y_0 + \frac{1}{2}(v_{y0} + v_y(t))\Delta t,$$ (3.135)

$$z := z_0 + v_z(t)\Delta t,$$ (3.136)

gde su x_0, y_0, z_0, v_{x0} i v_{y0} vrednosti x, y i z koordinata i vrednosti x i y komponenti brzine pre vremenskog koraka Δt, respektivno. Pokazano je kako u slučaju kretanja elektrona u konstantnom magnetskom polju (u odsustvu električnog polja) primena Borisove rotacije daje isti rezultat kao primena analitičkog rešenja [47]. Dok se vrednosti koordinata i brzina između dva sudara menjaju postepeno pod uticajem spoljašnjih polja, promena vektora brzine u sudaru se smatra trenutnom, zbog toga što je vreme trajanja sudara znatno kraće od vremenskog koraka Δt.

Trenutak i tip narednog sudara se određuju primenom slučajnih brojeva, uzimajući u obzir totalnu kolizionu frekvencu i parcijalne verovatnoće za pojedinačne sudarne procese. Verovatnoća da elektron neće učestvovati u sudaru u vremenskom intervalu između t_0 i t može se izraziti kao

$$P(t) = \exp\left(-\int_{t0}^{t}\nu_T(\epsilon(t'))\mathrm{d}t'\right),$$ (3.137)

gde je $\nu_T(\epsilon)$ totalna koliziona frekvenca elektrona koji ima energiju ϵ. Ova koliziona frekvenca se može izraziti kao

$$\nu_T(\epsilon) = n_0\sqrt{\frac{2\epsilon}{m}}\sum_k \sigma_k(\epsilon), \tag{3.138}$$

gde se sumiranje vrši po svim tipovima sudara, $\sigma_k(\epsilon)$ je vrednost preseka za k-ti sudarni proces na energiji ϵ i n_0 je koncentracija molekula (ili atoma) pozadinske srednine. Gustina verovatnoće da će elektron učestvovati u sudaru u toku vremenskog intervala $(t, \Delta t)$ može se izraziti kao

$$p(t) = \frac{P(t) - P(t + \Delta t)}{\Delta t} = \nu_T\big(\epsilon(t)\big)\exp\left(-\int_{t_0}^{t}\nu_T\big(\epsilon(t')\big)\mathrm{d}t'\right). \tag{3.139}$$

Slučajan trenutak sudara t_c, kome odgovara gustina verovatnoće $p(t)$, prikazana u jednačini (3.139), može se dobiti na osnovu jednačine

$$-\ln(1 - \xi_1) = \int_{t_0}^{t_c}\nu_T(\epsilon(t))\mathrm{d}t, \tag{3.140}$$

gde je ξ slučajan broj koji uzima vrednosti iz uniformne raspodele verovatnoće na intervalu $(0, 1)$. Jednačina (3.140) nema analitičko rešenje za realne gasove. Jedan od načina za određivanje trenutka t_c jeste primena metode nultih sudara (engl. null-collision method) [179], tako što se uvodi dodatni sudarni proces (nulti sudar), u kome vektor brzine elektrona ostaje nepromenjen. Koliziona frekvenca za ovaj dodatni sudarni proces izabrana je na takav način da totalna koliziona frekvenca ν_T ne zavisi od energije, već je jednaka maksimalnoj vrednosti totalne kolizione frekvence u odsustvu nultog sudara. U okvirima null-collision metode jednačina (3.140) se može rešiti analitički. Međutim, u našem kodu se ne koristi ovaj metod, već se jednačina (3.140) rešava numeričkom integracijom, zbog toga što null-collision metoda može biti neefikasna u slučaju vremenski promenjivih polja [27, 47]. U metodi integracije se jednačina (3.140) može aproksimirati kao

$$\ln(1 - \xi_1) \leq \sum_i \nu_T(\epsilon(t_i))\Delta t_i, \tag{3.141}$$

uz šta se kao trenutak sudara uzima $\sum_{i=1}^{k}\Delta t_i$, gde je k vrednost indeksa i, pri kojoj nejednakost (3.141) prestaje da važi. Da bi određivanje trenutka sudara na osnovu nejednakosti (3.141) bilo dobra aproksimacija rešavanja jednačine (3.140), neophodno je da vremenski korak za vremensku integraciju bude dovoljno mali. U našem kodu je ovaj vremenski korak izabran kao minimum tri važne vremenske konstante (koliziona frekvenca, ciklotronska frekvenca i period polja u slučaju prostorno promenljivih polja), koji je podeljen sa velikim brojem (između 20 i 100).

Nakon određivanja trenutka narednog sudara, tip narednog sudara k se određuje na osnovu uslova

$$\sum_{j=1}^{k-1}P_j < \xi_2 < \sum_{j=1}^{k}P_j, \tag{3.142}$$

gde je ξ_2 još jedan slučajan broj koji uzima vrednosti iz uniformne raspodele na intervalu $(0,1)$. U nejednačini (3.142) su P_j parcijalne verovatnoće, koje su definisane kao

$$P_j = \frac{\sigma_j(\epsilon)}{\sigma_T(\epsilon)}, \tag{3.143}$$

gde je $\sigma_T(\epsilon)$ totalni presek na energiji ϵ, koji se određuje kao $\sigma_T(\epsilon) = \sum_j \sigma_j(\epsilon)$, pri čemu se sumiranje vrši po svim sudarnim procesima (uključujući i nulti sudar ako se koristi null-collision metoda).

Promena pravca i smera brzine elektrona nakon sudara je reprezentovana uglom rasejanja χ i azimutalnim uglom ϕ. Uz to je izotropno rasejanje pretpostavljeno za sve sudarne procese, osim za efektivni sudarni proces koji je opisan σ_{energy} presekom, u kome se elektroni rasejavaju ka napred ($\chi = 0$) (videti potpoglavlje 6.2.1). Nakon sudara se vrednost azimutalnog ugla određuje na osnovu jednačine

$$\phi = 2\pi\xi_3, \tag{3.144}$$

gde je ξ_3 slučajan broj koji uzima vrednosti iz uniformne raspodele na intervalu $(0,1)$. U slučaju izotropnog rasejanja ugao rasejanja χ se određuje na osnovu jednačine

$$\chi = \arccos(1 - 2\xi_4). \tag{3.145}$$

Ako se pri određivanju promene ugla χ nakon sudara pretpostavi izotropno rasejanje, neophodno je da koliziona frekvenca za elastične sudare bude izračunata na osnovu momentum transfer preseka umesto totalnog preseka za elastično rasejanje, a sve to da bi se dobro opisala razmena impulsa i energije u elastičnim sudarima. Na visokim vrednostima redukovanog električnog polja, na kojima rasejanje ka napred postaje dominantno, potrebno je da ugaona zavisnost verovatnoće za rasejanje bude uzeta u obzir [177, 180]. Nakon elastičnog rasejanja i efektivnih sudarnih procesa koji su reprezentovani σ_{both} i σ_{energy} presecima energija elektrona se smanjuje za faktor $\frac{2m\epsilon}{M}(1 - \cos\chi)$, gde je m masa elektrona, M je masa molekula (ili atoma) pozadinskog fluida, ϵ je vrednost energije elektrona pre sudara, a χ je ugao rasejanja. Nakon neelastičnog rasejanja i/ili jonizacije, energija elektrona se umanji za iznos koji odgovara energijskom pragu za taj proces, dok se energija koja je preostala nakon jonizacije raspoređuje između primarnog i sekundarnog elektrona. Udeo preostale energije koji se dodeli primarnom i sekundarnom elektronu određuje se primenom još jednog slučajnog broja koji uzima vrednosti iz uniformne raspodele na intervalu $(0,1)$.

Monomi prostornih koordinata i komponenti brzina se sampluju i usrednjavaju po ansamblu elektrona u diskretnim vremenskim trenucima. Na osnovu ovih monoma mogu se izračunati transpotne veličine u trenucima samplovanja.

Srednja energija se izračunava kao

$$\langle \epsilon \rangle = \frac{1}{2}m\langle v^2 \rangle. \tag{3.146}$$

Balk brzina drifta $\mathbf{W}^{(b)}$, balk difuzioni tenzor $\mathbf{D}^{(b)}$ i balk transportni tenzor trećeg reda $\mathbf{Q}^{(b)}$ se računaju na osnovu jednačina

$$\mathbf{W}^{(b)} = \frac{\mathrm{d}}{\mathrm{d}t}\langle \mathbf{r} \rangle, \tag{3.147}$$

$$\mathbf{D}^{(b)} = \frac{1}{2}\frac{\mathrm{d}}{\mathrm{d}t}\langle\mathbf{r}^{\star\star}\rangle, \tag{3.148}$$

$$\mathbf{Q}^{(b)} = \frac{1}{3!}\frac{\mathrm{d}}{\mathrm{d}t}\langle\mathbf{r}^{\star}\mathbf{r}^{\star}\mathbf{r}^{\star}\rangle, \tag{3.149}$$

gde je $\mathbf{r}^{\star} = \mathbf{r} - \langle\mathbf{r}\rangle$, dok ugaone zagrade $\langle\rangle$ označavaju usrednjavanje po ansamblu. Fluks brzina drifta $\mathbf{W}^{(f)}$, fluks difuzioni tenzor $\mathbf{D}^{(f)}$ i fluks transportni tenzor trećeg reda se određuju na osnovu jednačina

$$\mathbf{W}^{(b)} = \left\langle\frac{\mathrm{d}}{\mathrm{d}t}\mathbf{r}\right\rangle, \tag{3.150}$$

$$\mathbf{D}^{(b)} = \frac{1}{2}\left\langle\frac{\mathrm{d}}{\mathrm{d}t}(\mathbf{r}^{\star\star})\right\rangle, \tag{3.151}$$

$$\mathbf{Q}^{(b)} = \frac{1}{3!}\left\langle\frac{\mathrm{d}}{\mathrm{d}t}(\mathbf{r}^{\star}\mathbf{r}^{\star}\mathbf{r}^{\star})\right\rangle. \tag{3.152}$$

U odsustvu magnetskog polja jednačine za određivanje komponenti balk difuzionog tenzora se mogu napisati kao

$$D_L^{(b)} = \frac{1}{2}n_0\frac{\mathrm{d}}{\mathrm{d}t}\big(\langle x^2\rangle - \langle x\rangle\langle x\rangle\big), \tag{3.153}$$

$$D_T^{(b)} = \frac{1}{2}n_0\frac{\mathrm{d}}{\mathrm{d}t}\big(\langle y^2\rangle\big), \tag{3.154}$$

dok se odgovarajuće jednačine za komponente fluks difuzionog tenzora mogu predstaviti u obliku

$$D_L^{(f)} = n_0\big(\langle xv_x\rangle - \langle x\rangle\langle v_x\rangle\big), \tag{3.155}$$

$$D_T^{(f)} = n_0\big(\langle yv_y\rangle - \langle y\rangle\langle v_y\rangle\big). \tag{3.156}$$

Slično tome, komponente balk transportnog tenzora trećeg reda je u odsustvu magnetskog polja moguće izračunati na osnovu jednačina

$$Q_L^{(b)} = n_0^2\frac{1}{6}\frac{\mathrm{d}}{\mathrm{d}t}\big(\langle x^3\rangle - 3\langle x\rangle\langle x^2\rangle + 2(\langle x\rangle)^3\big), \tag{3.157}$$

$$Q_T^{(b)} = \frac{1}{6}n_0^2\frac{\mathrm{d}}{\mathrm{d}t}\big(\langle xy^2\rangle - \langle x\rangle\langle y^2\rangle\big), \tag{3.158}$$

dok se komponente fluks transportnog tenzora trećeg reda mogu odrediti kao

$$Q_L^{(f)} = \frac{1}{6}n_0^2\big(3\langle x^2v_x\rangle - 3\langle v_x\rangle\langle x^2\rangle - 6\langle x\rangle\langle xv_x\rangle + 6\langle x\rangle\langle x\rangle\langle v_x\rangle\big), \tag{3.159}$$

$$Q_T^{(f)} = \frac{1}{6}n_0^2\big(\langle y^2v_x\rangle + 2\langle xyv_y\rangle - \langle v_x\rangle\langle y^2\rangle - 2\langle x\rangle\langle yv_y\rangle\big). \tag{3.160}$$

Pri tome se longitudinalne i transverzalne komponente difuzionog tenzora i transportnog tenzora trećeg reda, u slučaju kada je električno polje duž x-ose, definišu kao

$$D_L = D_{xx}, \tag{3.161}$$

$$D_T = D_{yy}, \tag{3.162}$$

$$Q_L = Q_{xxx}, \tag{3.163}$$

$$Q_T = \frac{1}{3}\big(Q_{xyy} + Q_{yxy} + Q_{yyx}\big) = \frac{1}{3}\big(Q_{xyy} + 2Q_{yyx}\big). \qquad (3.164)$$

Ovde je važno naglasiti da se pri proračunu balk komponenti transportnog tenzora trećeg reda ne koristi numeričko diferenciranje, nego se izraz koji stoji pod izvodom aproksimira linearnom funkcijom. Izvod tog izraza se potom određuje kao koeficijenat pravca ove linearne funkcije. Ovaj način određivanja prvog izvoda po vremenu je validan zbog toga što su transportni koeficijenti nezavisni od vremena nakon relaksacije roja (ako su spoljašnja polja vremenski nezavisna), pa je izraz u zagradi (koji stoji pod izvodom) linearna funkcija vremena. Uz to je koeficijenat pravca ove linearne funkcije jednak prvom izvodu te funkcije po vremenu. Balk vrednosti transportnih koeficijenata trećeg reda se određuju na ovaj način zato što u slučaju transportnih koeficijenata višeg reda numeričko diferenciranje značajno povećava fluktuacije rezultata. Validnost ovog načina određivanja balk komponenti transportnih koeficijenata trećeg reda je provereno poređenjem sa rezultatima koji su izračunati primenom numeričkog diferenciranja, kao i poređenjem sa fluks vrednostima ovih transportnih koeficijenata u odsustvu nekonzervativnih procesa.

Statistička greška transportnih veličina se procenjuje kao standardna greška. Naime, statistička greška ovih veličina je jednaka kvadratnom korenu njihovog srednjeg kvadratnog odstupanja od srednje vrednosti, koji je podeljen sa kvadratnim korenom broja čestica u ansamblu. Da bi se smanjila statistička greška veličina koje su izračunate uz pomoć Monte Carlo simulacija, neophodno je da u simulacijama bude praćen veliki broj čestica. Pri tome je za proračun komponenti difuzionog tenzora i transportnog tenzora trećeg reda potrebno da u simulacijama bude praćeno između 10^6 i 10^7 čestica, respektivno. Praćenje velikog broja čestica dovodi do toga da su naše Monte Carlo simulacije jako vremenski zahtevne. Vreme trajanja simulacija je naročito dugo u oblasti niskih redukovanih električnih polja, na kojima su brzinski koeficijenti za neelastične sudare i jonizaciju zanemarljivi. Ovo je posledica toga što je transfer energije u elastičnim sudarima znatno manji nego u neelastičnim sudarima i jonizaciji što dovodi do jako spore relaksacija energije u ovom opsegu polja. Da bi se skratilo vreme trajanja simulacija, u opsegu polja u kome je relaksacija energije neefikasna, koristi se multiplikacija roja. U ovom opsegu polja simulacije počnu sa manjim brojem naelektrisanih čestica (oko 10^4), koje se prate do trenutka relaksacije. Nakon trenutka relaksacije broj naelektrisanih čestica se postepeno povećava do željenog broja tako što se u fiksnim vremenskim trenucima duplira svaka naelektrisana čestica iz ansambla. Posle trentuka dupliranja svaka naelektrisana čestica se prati nezavisno i ima svoju putanju, koja je određena delovanjem spoljašnjih polja i sudarima sa molekulima (ili atomima) pozadinske sredine. Transportne veličine se računaju tek kada prođe nekoliko perioda od završetka multiplikacije. Ova numerička procedura dupliranja elektrona nakon relaksacije u stacionarni režim je detaljno testirana [pitajRef].

Pored multiplikacije roja, koja se koristi u limitu malih električnih polja gde je otežan transfer energije u sudarima čestica roja i atoma ili molekula pozadinskog gasa, u našem kodu se, s ciljem skraćivanja vremena trajanja simulacija, koriste i tehnike reskaliranja koje obezbeđuju da broj čestica roja ostane u okolini unapred zadate vrednosti. Ove tehnike su neophodne u uslovima u kojima nekonzervativni procesi poput jonizacije i zahvata elektrona u slučaju

transporta elektrona i formiranja pozitronijuma pri transportu pozitrona dovode do značajne promene broja čestica u toku trajanja simulacije. Značajno povećanje broja čestica dovodi do porasta trošenja računarskih resursa koji su potrebni za izvršavanje simulacije, dok značajno smanjenje broja čestica povećava statističke fluktuacije i smanjuje preciznost rezultata, a može dovesti i do potpunog prekida simulacije. U našem kodu mogu se koristiti tehnike diskretnog i kontinualnog reskaliranja [160]. Tehnika diskretnog reskaliranja u fiksnim vremenskim trenucima izbaci nekoliko čestica iz roja ukoliko broj čestica premašuje željenu vrednost, ili duplira nekoliko čestica ukoliko je broj čestica u roju manji od željene vrednosti. Tehnika kontinualnog reskaliranja izbacuje višak čestica ili duplira postojeće čestice, u zavisnosti od broja čestica u roju, u bilo kom trenutku trajanja simulacije u kome se ukaže potreba za korekcijom broja čestica u roju, a ne samo u unapred određenim vremenskim trenucima. Jako je značajno da ove tehnike reskaliranja ne menjaju funkciju raspodele čestica po energijama. Ove tehnike reskaliranja su detaljno opisane i temeljno testirane u referenci [160].

3.4.1 Benčmark proračuni za Percus-Yevick-ovu modelnu tečnost

U ovom potpoglavlju su prikazani naši proračuni transportnih veličina u Percus-Yevick-ovoj modelnoj tečnosti. Ovi proračuni su urađeni da bi se testirala implementacija koherentnog rasejanja u našem Monte Carlo kodu. Percus-Yevick-ova modelna tečnost je varijanta modela krutih sfera, u kojoj krute sfere zauzimaju konačan udeo zapremine prostora, pa u ovom modelu strukturni efekti imaju značajan uticaj na dinamiku rasejanja elektrona [176]. Radijalna parna korelaciona funkcija koja odgovara Percus-Yevick-ovom modelu dobija se zatvaranjem Ornstein–Zernike jednačine primenom Percus-Yevickove aproksimacije uz reprezentovanje interakcije između pozadinskih atoma potencijalom krutih sfera [176,181]. Statički strukturni faktor koji odgovara Percus-Yevickovom modelu dobija se kao Fourier-ov transform ove parne korelacione funkcije [176]. U našim proračunima se koristi modifikovani Verlet-Weis-ov statički strukturni faktor [182], koji je upotrebljen i u radu Tattersall-a i saradnika [176]. Ovaj strukturni faktor je dat u vidu izraza

$$S(\Delta k) = \left(1 + \frac{24\eta}{\Delta k^2} \left[\frac{2}{\Delta k^2}(\frac{12\zeta}{\Delta k^2} - \beta) + \frac{\sin(\Delta k)}{\Delta k}\left(\alpha + 2\beta + 4\zeta - \frac{24\zeta}{\Delta k^2} \right) \right. \right.$$
$$\left. \left. + \cos(\Delta k)\left(\frac{2}{\Delta k^2}\left(\beta + 6\zeta - \frac{12}{\Delta k^2} \right) - \alpha - \beta - \zeta \right) \right] \right)^{-1}, \qquad (3.165)$$

gde je $\eta = \phi - \frac{\phi^2}{16}$, $\alpha = \frac{(1+2\eta)^2}{(1-\eta)^4}$, $\beta = \frac{-6\eta\left(1+\frac{\eta}{2}\right)^2}{(1-\eta)^4}$ i $\zeta = \frac{\eta\alpha}{2}$ [176]. Količnik pakovanja ϕ određuje udeo zapremine prostora koji je popunjen krutm sferama. Ovaj količnik se može izraziti kao $\phi = \frac{4}{3}\pi r^3 n_0$, gde su r i n_0 radijus krutih sfera i njihova koncentracija, respektivno [176].

Na grafiku 1 su prikazane vrednosti srednje energije, brzine drifta i komponenti difuzionog tenzora za elektrone u Percus Yevickov-om modelu, koje su određene u našim Monte Carlo simulacijama, u funkciji redukovanog električnog polja E/n_0 i količnika pakovanja ϕ. Vrednosti ovih transportnih veličina, koje su odredili Tattersall i saradnici, primenom svog Monte Carlo
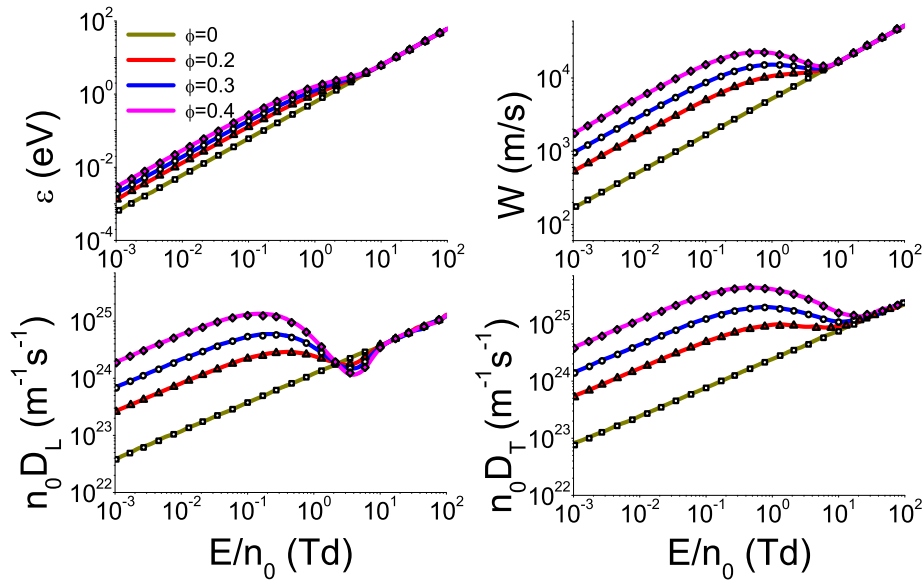
Slika 1: Poređenje vrednosti srednje energije, brzine drifta W, longitudinalne komponente difuzionog tenzora $n_0 D_L$ i transverzalne komponente difuzionog tenzora $n_0 D_T$ za roj elektrona u Percus-Yevick-ovoj modelnoj tečnosti, koje su dobijene u našim proračunima sa rezultatima Tattersall-a i saradnika [176]. Transportne veličine su prikazane kao funkcija redukovanog električnog polja E/n_0 i količnika pakovanja ϕ. Naši rezultati su reprezentovani linijama, dok su rezultati Tattersall-a i saradnika [176] dati u vidu simbola - i jedni i drugi su dobijeni primenom Monte Carlo simulacija.

koda i numeričkim rešavanjem Boltzmann-ove jednačine, prikazane su na istom grafiku radi poređenja [176]. Naši rezultati su predstavljeni linijama, dok su rezultati Tattersall-a i saradnika predstavljeni simbolima. Na ovom grafiku se uočava da se naši rezultati za sve transportne koeficijente i za sve vrednosti E/n_0 i ϕ odlično slažu sa rezultatima grupe autora, što je pokazatelj toga da su efekti koherentnog rasejanja dobro reprezentovani u našem Monte Carlo kodu.

Sa grafika 1 se vidi da srednja energija, brzina drifta i komponente difuzionog tenzora snažno zavise od ϕ na niskim poljima. Uzrok tome je što su efekti koherentnog rasejanja najintenzivniji na niskim energijama. Međutim, zavisnost transportnih veličina od ϕ opada sa porastom E/n_0 i praktično je zanemarljiva na poljima višim od 40 Td, zbog slabog uticaja efekata koherentnog rasejanja na dinamiku visokoenergijskih elektrona. Srednja energija i brzina drifta se povećavaju sa porastom ϕ u celom opsegu polja do oko 10 Td, dok se transverzalna komponenta difuzionog tenzora povećava sa porastom ϕ do oko 35 Td. Zavisnost longitudinalne komponente difuzionog tenzora od ϕ je nešto složenija. Naime, ova komponenta se povećava sa porastom ϕ do oko 2.1 Td, posle čega opada sa porastom ϕ do oko 13 Td, pritom je na višim poljima zavisnost ove komponente od ϕ praktučno zanemarljiva. Srednja energija elektrona se monotono povećava sa porastom E/n_0 za sve vrednosti ϕ. No, u profilu brzine drifta je prisutna negativna diferencijalna provodnost za $\phi \geq 0.3$ u opsegu polja od 0.5 Td do 6 Td, a za niže se vrednosti ϕ brzina drifta monotono povećava sa porastom E/n_0 u celom opsegu polja. Pod negativnom diferencijalnom provodnošću podrazumeva se opadanje brzine drifta sa porastom E/n_0. U gasnoj fazi je ovaj efekat posledica specifične energijske zavisnosti preseka

za elastične i neelastične sudare ili prisustva nekonzervativnih sudara [13, 14, 21]. U ovom pak slučaju negativna diferencijalna provodnost posledica je isključivo strukturnih efekata [68–70]. Kvantitativni kriterijum za pojavu strukturno indukovane negativne diferencijalne provodnosti je razmatran u radu White-a i Robson-a [183]. Opadanje brzine drifta sa porastom E/n_0 u ovom slučaju se može pripisati smanjenju uticaja koherentnih efekata na dinamiku rasejanja elektrona sa povećanjem energije elektrona, jer koherentni efekti dovode do povećanja brzine drifta. Sa grafika se vidi kako $n_0 D_L$ opada sa porastom E/n_0 od oko 0.1 Td do oko 4 Td, dok $n_0 D_T$ opada sa porastom E/n_0 od oko 0.35 do oko 25 Td. Na najvišim poljima se grafici srednje energije, brzine drifta i komponenti difuzionog tenzora za $\phi > 0$ približavaju odgovarajućim graficima za $\phi = 0$. Pri tome odgovarajuća vrednost E/n_0, na kojoj uticaj koherentnih efekata počne da se smanjuje, opada sa porastom ϕ.

3.5   Zaključak

U ovom poglavlju su predstavljeni metodi za izračunavanje transportnih koeficijenata rojeva naelektrisanih čestica. Potpoglavlje 3.2 prikazuje metod više članova za numeričko rešavanje Boltzmann-ove jednačine, u okviru kog se funkcija raspodele u faznom prostoru razvija u red po skupu bazisnih funkcija. Funkcija raspodele se pritom razvija po Burnett-ovim funkcijama u brzinskom prostoru. Pokazuje se da se kada su zadovoljeni hidrodinamički uslovi, funkcija raspodele razvija po gradijentima koncentracije u konfiguracionom prostoru. Koeficijenti u razvoju funkcije raspodele po ovom skupu bazisnih funkcija se zovu momenti funkcije raspodele. Na osnovu relacija ortogonalnosti korišćenih bazisnih funkcija, Boltzmann-ova jednačina se svodi na hijerarhiju kinetičkih jednačina po momentima funkcije raspodele, koja se potom rešava numerički. Transportne veličine koje su od interesa za ovu disertaciju se mogu izračunati na osnovu momenata funkcije raspodele. U okviru ove disertacije je korišćeni metod za rešavanje Boltzmann-ove jednačine proširen razvojem fluks gradijentne relacije u ireducibilnoj formi do izvoda drugog reda, da bi se omogućilo izračunavanje komponenti fluks transportnog tenzora trećeg reda.

U potpoglavlju 3.3 uvedena je hijerarhija momentnih jednačina koja se može izvesti množenjem Boltzmann-ove jednačine proizvoljnom funkcijom brzine i njenom integracijom po celom brzinskom prostoru. Prikazan je sistem jednačina koji čine jednačine za balans broja čestica, impulsa i energije, respektivno. Nakon toga je pokazan oblik kolizionog člana za proizvoljnu momentnu jednačinu u slučaju koherentnog i nekoherentnog rasejanja. Kolizioni član se može odrediti integracijom kolizionog operatora po brzinskom prostoru. Uzimanjem u obzir efekata koherentnog rasejanja pri elastičnim sudarima, momentne jednačine za rojeve naelektrisanih čestica u gasnoj fazi su generalizovane na slučaj rojeva naelektrisanih čestica u nepolarnim tečnostima. Potom je uvedena aproksimacija transfera impulsa koja značajno pojednostavljuje oblik odgovarajućih kolizionih članova. Prikazani sistem jednačina je zatim dodatno pojednostavljen uvođenjem nekoliko pretpostavki, koje su zadovoljene za rojeve lakih naelektrisanih čestica, ukoliko je uspostavljen hidrodinamički režim i ukoliko su spoljašnja polja stacionarna. Na osnovu toga je dobijen sistem od četiri jednačine (jedne tenzorske, dve vektorske i jedne

skalarne), koji povezuje srednju energiju, brzinu drifta, vektor energijskog gradijenta, vektor toplotnog provođenja i difuzioni tenzor. U slučaju lakih naelektrisanih čestica poput elektrona i pozitrona vektor toplotnog provođenja može se zanemariti. Nakon toga se dobijeni sistem jednačina može rešiti numerički, ako su poznate kolizione frekvence u funkciji srednje energije .

Monte Carlo kod koji je korišćen u izradi ove disertacije centralna je tema potpoglavlja 3.4. Ovaj kod prati roj naelektrisanih čestica koje se kreću u homogenom i neutralnom pozadinskom fluidu, pod uticajem spoljašnjeg električnog i eventualno magnetskog polja. Na početku ovog potpoglavlja je dat kratak osvrt na razvoj i ranije primene razmatranog Monte Carlo koda. Potom su prikazani početni uslovi simulacije, kao i jednačine kretanja koje opisuju dinamiku pojedinačnih naelektrisanih čestica između dva sudara u slučaju proizvoljne konfiguracije električnog i magnetskog polja. Usledio je prikaz algoritma Borisove rotacije, koji se koristi da opiše kretanje naelektrisanih čestica između dva sudara kada su električno i magnetsko polje međusobno ortogonalna, kao i u odsustvu magnetskog polja, a zatim se govorilo o načinu na koji se određuju trenutak i tip narednog sudara naelektrisane čestice sa neutralnim česticama pozadinske sredine, na osnovu slučajnih brojeva. Objašnjeno je zatim kako se određuju pravac i smer brzine naelektrisane čestice nakon sudara. U slučaju rojeva naelektrisanih čestica u gasovima se pretpostavlja izotropno rasejanje. Zbog toga se elastični sudari opisuju pomoću preseka za transfer impulsa, dok se neelastični sudari opisuju primenom totalnog preseka za rasejanje. Međutim, u slučaju rojeva naelektrisanih čestica u tečnoj fazi ne može se koristiti izotropno rasejanje, budući da je anizotropija koherentnog rasejanja vrlo izražena. Pored toga, efektivni srednji slobodni putevi za transfer impulsa i energije u tečnoj fazi su međusobno različiti. Zbog toga je u okviru ove disertacije postojeći Monte Carlo kod, koji je razvijen u Laboratoriji za neravnotežne procese i primenu plazme, proširen na domen rojeva naelektrisanih čestica u nepolarnim tečnostima uvođenjem tri efektivna sudarna procesa, koji dobro opisuju srednji transfer impulsa i energije pri koherentnom rasejanju. Ovi efektivni sudarni procesi su detaljno opisani u potpoglavlju 6.2.1.

Nakon razmatranja implementacije sudara naelektrisanih čestica roja sa neutralnim česticama pozadinske sredine u potpoglavlju 3.4 su prikazane jednačine za izračunavanje transportnih veličina, koje su od značaja za ovu disertaciju, a koje se mogu odrediti direktno na osnovu dinamičkih promenljivih koje se računaju u Monte Carlo simulacijama. Za potrebe našeg istraživanja bilo je neophodno dodatno proširiti postojeći Monte Carlo kod, uvođenjem procedura za uzorkovanje monoma trećeg stepena po koordinatama, kao i monoma drugog stepena po koordinatama i prvog stepena po komponentama vektora brzine. Navedeni monomi su neophodni za izračunavanje vrednosti balk i fluks transportnog tenzora trećeg reda, respektivno. Iako u eksplicitnim izrazima za balk transportne koeficijente trećeg reda stoji diferenciranje po vremenu, poželjno je izbeći numeričko diferenciranje odgovarajućeg izraza u zagradi, zato što bi male fluktuacije ovog izraza dovele do velikih fluktuacija njegovog izvoda. Zbog toga se u okviru ove disertacije vrednost prvog izvoda po vremenu određuje na osnovu koeficijenta pravca linearizovanog izraza u zagradi. U ovoj je tezi statistička greška rezultata koji su dobijeni primenom Monte Carlo simulacija procenjena kao standardna greška. Na kraju potpoglavlja opisane su tehnike za multiplikaciju roja koje se koriste za smanjenje trajanja vremenski zahtevnih

simulacija, kao i tehnike za reskaliranje roja što se koriste za održavanje konstantnog broja čestica roja u prisustvu intenzivnih nekonzervativnih efekata. Ovi efekti uključuju jonizaciju i elektronski zahvat u slučaju elektrona i formiranje pozitronijuma u slučaju pozitrona.

U potpoglavlju 3.4.1 primenom Monte Carlo metoda proučavan je transport elektrona u Percus-Yevick-ovom modelu za nekoliko različitih vrednosti parametra popunjenosti. Pri tome su određeni srednja energija, brzina drifta i komponente difuzionog tenzora za elektrone u ovom modelu, a njihove vrednosti su upoređene sa rezultatima ranijih autora, koji su dobijeni primenom Monte Carlo metoda i metoda više članova za numeričko rešavanje Boltzmann-ove jednačine. Odlično slaganje naših rezultata sa rezultatima koje su odredili raniji autori potvrđuje korektnost implementacije efekata koherentnog rasejanja i numerički integritet Monte Carlo koda, koji je korišćen u ovoj disertaciji.

4 Transportni koeficijenti trećeg reda za naelektrisane čestice u modelnim gasovima

4.1 Uvod

U ovom odeljku su predstavljeni proračuni transportnih koeficijenata trećeg reda (TKIII) u modelnim gasovima. Oni su dobijeni primenom Monte Carlo simulacija i kompjuterskog koda za numeričko rešavanje Boltzmann-ove jednačine na osnovu momentnog metoda. Ova dva kompjuterska koda su do sada detaljno testirana u ranijim publikacijama [31, 47, 156, 157, 184]. Sistematski proračuni TKIII upotrebom ove dve nezavisne tehnike predstavljaju istovremeno proveru validnosti izraza na osnovu kojih se računaju komponente transportnog tenzora trećeg reda (TTIII) u momentnoj metodi za numeričko rešavanje Boltzmann-ove jednačine i Monte Carlo simulacijama, kao i proveru ispravne implementacije procedura za izračunavanje ovih komponenti u korišćenim kompjuterskim kodovima.

Jedna od prednosti izučavanja transporta naelektrisanih čestica u modelnim gasovima je ta što jednostavna energijska zavisnost preseka za sudare naelektrisane čestice roja sa neutralnim molekulima u ovim gasovima omogućava izolovanje uticaja pojedinačnih sudarnih procesa na trendove zavisnosti transportnih koeficijenata od električnog i magnetskog polja. Ovo je naročito značajno u slučaju TKIII jer su oni znatno osetljivi na energijsku zavisnost preseka za sudarne procese od transportnih koeficijenata nižeg reda (brzine drifta i difuzionog tenzora), a do sada nisu bili temeljno istraženi u literaturi [126, 127, 132]. Pored toga su trendovi zavisnosti TKIII od električnog i magnetskog polja teži za razumevanje od odgovarajućih trendova transportnih koeficijenata nižeg reda zbog komplikovanije fizičke interpretacije TKIII. Još jedna prednost proračuna TKIII u modelnim gasovima, koji su dobijeni na osnovu ove dve nezavisne tehnike, jeste to što oni mogu poslužiti kao benčmark proračuni za proveru ispravnosti novih kompjuterskih kodova za određivanje TKIII.

U potpoglavlju 4.2 diskutovano je o fizičkoj interpretaciji TKIII. Interpretacija i fizički smisao TKIII su razmatrani na formalan način sa ciljem njihovog boljeg razumevanja u konkretnim fizičkim situacijama. Sledi potpoglavlje 4.4, gde su prikazani rezultati proračuna TKIII u Maxwell-ovom modelu, dobijeni rešavanjem Boltzmann-ove jednačine momentnom metodom. Odeljak 4.5 daje rezultate proračuna TKIII u modelu krutih sfera, koji su dobijeni primenom Monte Carlo simulacija. U potpoglavljima 4.6, 4.7 i 4.8 su predstavljeni rezultati proračuna TKIII u Reid-ovom modelu, Lucas-Saelee-evom modelu i modifikovanom Ness-Robson-ovom modelu respektivno, koji su dobijeni primenom Monte Carlo simulacija i korišćenjem momentnog metoda za rešavanje Boltzmann-ove jednačine. Korišćenjem Reid-ov modelnog gasa, izračunata su odstupanja TKIII, dobijenih aproksimacijom dva člana za rešavanje Boltzmann-ove jednačine, od rezultata koji su u potpunosti konvergirali. Reid-ov modelni gas je upotrebljen i za proračne i analizu ponašanja TKIII u ukrštenim električnim i magnetskim poljima. Implicitne i eksplicitne efekte jonizacije na TKIII proučavali smo koristeći Lucas-Saelee-ev modelni gas, a ovi isti efekti prouzrokovani zahvatom elektrona analizirani su uz korišćenje modelnog

gasa koji su predložili Ness i Robson.

4.2 Fizička interpretacija komponenti transportnog tenzora trećeg reda

Na ovom mestu se razmatra fizički smisao transportnih koeficijenata trećeg reda. Ako se transportni koeficijenti trećeg (i višeg) reda mogu zanemariti, evolucija koncentracije naelektrisanih čestica $n(\mathbf{r}, t)$ u vremenu je opisana jednačinom

$$\frac{\partial n^{(0)}(\mathbf{r}, t)}{\partial t} + \mathbf{W}^{(b)} \cdot \nabla n^{(0)}(\mathbf{r}, t) - \hat{\mathbf{D}}^{(b)} : (\nabla \otimes \nabla) n^{(0)}(\mathbf{r}, t)$$
$$= -R_a n^{(0)}(\mathbf{r}, t), \tag{4.1}$$

gde su $n^{(0)}(\mathbf{r}, t)$ i R_a koncentracija naelektrisanih čestica roja u uslovima u kojima transportni koeficijenti trećeg i višeg reda mogu da se zanemare i brzinski koeficijent za nestajanje i nastajanje čestica roja, respektivno. Zbog jednostavnosti će biti razmatran slučaj u kome je spoljašnje električno polje orijentisano duž z-ose, dok je magnetsko polje jednako nuli. Množenjem jednačine (4.1) sa $e^{-i(px+qy+kz)}\mathrm{d}x\mathrm{d}y\mathrm{d}z$ i integracijom po konfiguracionom prostoru dobija se Furijeov transform ove jednačine po prostornim koordinatama, koji se može napisati u obliku

$$\frac{\partial \hat{n}^{(0)}}{\partial t} = -(ikW_z + k^2 D_{zz} + (p^2 + q^2)D_{xx} - R_a)\hat{n}^{(0)}, \tag{4.2}$$

gde je $\hat{n}^{(0)}$ Furijeov transform koncentracije čestica roja $n^{(0)}(\mathbf{r}, t)$ po prostornim koordinatama. Ako je N broj čestica roja u početnom trenutku ($t = 0$), rešenje jednačine (4.2) se može napisati u obliku

$$\hat{n}^{(0)} = N \exp\left(-\left(ikW_z + k^2 D_{zz} + (p^2 + q^2)D_{xx} - R_a\right)t\right). \tag{4.3}$$

Radi jednostavnosti, biće uvedene oznake $W \equiv W_z$, $D_T \equiv D_{xx}$ i $D_L \equiv D_{zz}$. Ukoliko se jednačina (4.3 pomnoži sa $\frac{1}{(2\pi)^3}e^{i(px+qy+kz)}\mathrm{d}p\mathrm{d}q\mathrm{d}k$ i prointegrali po p, q, k (primena inverznog Furijeovog transforma), dobije se izraz za koncentraciju

$$n^{(0)}(\mathbf{r}, t) = \frac{N}{\sqrt{4\pi D_L t}(4\pi D_T t)} e^{-\frac{(z-W)^2}{4D_L t}} e^{-\frac{x^2+y^2}{4D_T t}} e^{-R_a t}. \tag{4.4}$$

Kada se transportni koeficijenti trećeg reda ne mogu zanemariti, vremenska evolucija koncentracije čestica roja $n(\mathbf{r}, t)$ je opisana jednačinom

$$\frac{\partial n(\mathbf{r}, t)}{\partial t} + \mathbf{W}(t) \cdot \nabla n(\mathbf{r}, t) - \hat{\mathbf{D}}(t) : (\nabla \otimes \nabla) n(\mathbf{r}, t)$$
$$+ \hat{\mathbf{Q}}(t) \vdots (\nabla \otimes \nabla \otimes \nabla) n(\mathbf{r}, t) = -R_a(t) n(\mathbf{r}, t). \tag{4.5}$$

Radi jednostavnosti ponovo je pretpostavljeno da je spoljašnje električno polje duž z-ose, dok je spoljašnje magnetsko polje jednako nuli. U ovom slučaju se jednačina (4.5) može napisati u obliku

$$\frac{\partial n(\mathbf{r}, t)}{\partial t} = -R_a n(\mathbf{r}, t) - W \frac{\partial n(\mathbf{r}, t)}{\partial t} \tag{4.6}$$

$$+D_L\frac{\partial^2 n(\mathbf{r},t)}{\partial z^2} + D_T\Big(\frac{\partial^2 n(\mathbf{r},t)}{\partial x^2} + \frac{\partial^2 n(\mathbf{r},t)}{\partial y^2}\Big) \tag{4.7}$$

$$-Q_{zzz}\frac{\partial^3 n(\mathbf{r},t)}{\partial z^3} - \big(Q_{zxx} + 2Q_{xxz}\big)\Big(\frac{\partial^3 n(\mathbf{r},t)}{\partial z\partial x^2} + \frac{\partial^3 n(\mathbf{r},t)}{\partial z\partial y^2}\Big), \tag{4.8}$$

gde su iskorišćene jednakosti $Q_{xxz} = Q_{xzx} = Q_{yyz} = Q_{yzy}$. Množenjem jednačine (4.8) sa $e^{-i(px+qy+kz)}\mathrm{d}x\mathrm{d}y\mathrm{d}z$ i integracijom po konfiguracionom prostoru dobija se Furijeov transform ove jednačine po prostornim koordinatama, koji se može napisati u obliku

$$\frac{\partial \hat{n}_Q}{\partial t} = -\big(ikW_z + k^2 D_L + (p^2+q^2)D_T - R_a\big)\hat{n}_Q$$
$$-\big(-ik^3 Q_{zzz} - 3ik(p^2+q^2)Q_T\big)\hat{n}_Q, \tag{4.9}$$

gde je uvedena oznaka $3Q_T \equiv Q_{zxx} + Q_{xzx} + Q_{xxz}$, dok je $\hat{n}_Q$ oznaka za Furijeov transform koncentracije $n(\mathbf{r},t)$ u slučaju u kome se transportni koeficijenti trećeg reda ne mogu zanemariti. Rešenje jednačine (4.9) dobija oblik

$$\hat{n}_Q = N\exp\Big(-\big(R_a + ikW + k^2 D_L + (p^2+q^2)D_T\big)t\Big)\times$$
$$\exp\Big(\big(ik^3 Q_L + 3ik(p^2+q^2)Q_T\big)t\Big). \tag{4.10}$$

Na osnovu jednačine (4.10) trebalo bi da se $n(\mathbf{r},t)$ odredi kao inverzni Furijeov transform od $\hat{n}$. Ipak, integral $\int e^{i(px+qy+kz)}\hat{n}_Q\mathrm{d}p\mathrm{d}q\mathrm{d}k$ nije analitički rešiv. Jedan način za približno utvrđivanje vrednosti koncentracije $n(\mathbf{r},t)$, u slučaju kada transportni koeficijenti trećeg reda nisu zanemarljivi, jeste razvoj $\hat{n}_Q$ u Tejlorov red po komponentama Q_L i Q_T i određivanje inverznog Furijeovog transforma odgovarajućih koeficijenata u razvoju. Ovaj Tejlorov razvoj se može napisati na sledeći način

$$\hat{n}_Q = \hat{n}_Q\Big|_{Q=0} + \frac{\partial \hat{n}_Q}{\partial Q_L}\Big|_{Q=0}Q_L + \frac{\partial \hat{n}_Q}{\partial Q_T}\Big|_{Q=0}Q_T$$
$$\frac{1}{2}\Big(\frac{\partial^2 \hat{n}_Q}{\partial Q_L^2}\Big|_{Q=0}Q_L^2 + 2\frac{\partial^2 \hat{n}_Q}{\partial Q_L\partial Q_T}\Big|_{Q=0}Q_L Q_T + \frac{\partial^2 \hat{n}_Q}{\partial^2 Q_T}\Big|_{Q=0}Q_T^2\Big) + ... \tag{4.11}$$

Kada se primeni inverzni Furijeov transform na jednačinu (4.11) i kada se zanemare svi članovi drugog i višeg stepena po komponentama transportnog tenzora trećeg reda, dobije se sledeći aproksimativan izraz za koncentraciju naelektrisanih čestica roja

$$n^{(1)}(\mathbf{r},t) = \frac{Ne^{-R_a t}}{\sqrt{4\pi D_L t}(4\pi D_T t)}\exp\Big(-\frac{(z-Wt)^2}{4D_L t} - \frac{x^2+y^2}{4D_T t}\Big)\times$$
$$\Big[1 + Q_L\frac{t(z-Wt)^3 - 6D_L t^2(z-Wt)}{8(D_L t)^3}$$
$$+3Q_T\frac{(z-Wt)(x^2+y^2-4D_T t)}{8D_L t(D_T t)^2}\Big] \tag{4.12}$$

gde superskript (1) označava da su u izrazu za koncentraciju (4.12) uzete u obzir samo popravke prvog stepena po komponentama transportnog tenzora trećeg reda. Projekcija jednačine (4.12)

na longitudinalni (z)-pravac ranije je određena u radu Penetrante-a i Bardsley-a (Penetrante i Bardsley 1990).

Na osnovu fluks gradijentne relacije (2.21) vidi se da se doprinos transportnih koeficijenata trećeg reda ukupnom fluksu čestica može izraziti kao

$$\Gamma_{Q,z} = Q_{zzz} \frac{\partial^2 n(\mathbf{r}, t)}{\partial z^2} + Q_{zxx} \left[\frac{\partial^2 n(\mathbf{r}, t)}{\partial x^2} + \frac{\partial^2 n(\mathbf{r}, t)}{\partial y^2} \right],$$
$$\Gamma_{Q,x} = 2Q_{xxz} \frac{\partial^2 n(\mathbf{r}, t)}{\partial x \partial z}. \tag{4.13}$$

Iz jednačine (4.13) je jasno da je smer kretanja, opisanog transportnim tenzorom trećeg reda, određen kombinacijom znaka komponenti ovog tenzora i znaka odgovarajućih parcijalnih izvoda koncentracije. Uz to je znak parcijalnih izvoda koncentracije određen znakom odgovarajućih parcijalnih izvoda vodećeg člana u razvoju koncentracije čestica po komponentama transportnog tenzora trećeg reda iz jednačine (4.12), $n^{(0)}(\mathbf{r}, t)$. Zbog toga je analiza parcijalnih izvoda Gaussian-a dovoljna za razmatranje doprinosa transportnog tenzora trećeg reda ukupnom fluksu čestica, koji je prikazan u jednačini (4.13). Ovi parcijalni izvodi Gaussian-a su dati u jednačinama

$$\frac{\partial^2 n^{(0)}(\mathbf{r}, t)}{(\partial z)^2} = \left(z^2 - \sigma_z^2 \right) \frac{n^{(0)}(\mathbf{r}, t)}{\sigma_z^4}, \tag{4.14}$$

$$\frac{\partial^2 n^{(0)}(\mathbf{r}, t)}{(\partial x)^2} = \left(x^2 - \sigma_x^2 \right) \frac{n^{(0)}(\mathbf{r}, t)}{\sigma_x^4}, \tag{4.15}$$

$$\frac{\partial^2 n^{(0)}(\mathbf{r}, t)}{(\partial x \partial z)} = xz \frac{n^{(0)}(\mathbf{r}, t)}{\sigma_x^2 \sigma_z^2}, \tag{4.16}$$

gde su

$$\sigma_x^2 = 2D_T t, \ \sigma_z^2 = 2D_L t. \tag{4.17}$$

Zbog jednostavnosti su izvodi u gornjim jednačinama napisani u referentnom sistemu koji je postavljen u centar Gaussian-a, pa je član $z - Wt$ zamenjen članom z. Da bi se olakšala vizuelizacija ovih parcijalnih izvoda, uvodi se novi set koordinata $x/\sigma_x = \chi_x$, $y/\sigma_y = \chi_y$ i $z/\sigma_z = \chi_z$. Primenom novih koordinata gornji skup jednačina (4.14)-(4.16) svodi se na

$$\frac{\partial^2 n^{(0)}}{\partial \chi_z^2} = \left(\chi_z^2 - 1 \right) n^{(0)}, \tag{4.18}$$

$$\frac{\partial^2 n^{(0)}}{\partial \chi_x^2} = \left(\chi_x^2 - 1 \right) n^{(0)}, \tag{4.19}$$

$$\frac{\partial^2 n^{(0)}}{\partial \chi_x \partial \chi_z} = \chi_x \chi_z n^{(0)}, \tag{4.20}$$

pri čemu je

$$n^{(0)}(\chi, t) = C_\chi \exp \left[-\frac{1}{2} \left(\chi_z^2 + \chi_x^2 + \chi_y^2 \right) \right], \tag{4.21}$$

i

$$C_\chi = \frac{N_0 e^{R_{\text{net}} t}}{(2\pi)^{3/2} \sigma_x^2 \sigma_z}. \tag{4.22}$$

Normirani parcijalni izvodi drugog reda mogu se kombinovanjem jednačina (4.18)-(4.22) napisati u obliku

$$\Delta_{zz} \equiv \frac{1}{C_\chi} \frac{\partial^2 n^{(0)}}{\partial \chi_z^2} = \left(\chi_z^2 - 1\right) e^{-\frac{1}{2}\left(\chi_z^2 + \chi_x^2 + \chi_y^2\right)}, \tag{4.23}$$

$$\Delta_{xx} \equiv \frac{1}{C_\chi} \frac{\partial^2 n^{(0)}}{\partial \chi_x^2} = \left(\chi_x^2 - 1\right) e^{-\frac{1}{2}\left(\chi_z^2 + \chi_x^2 + \chi_y^2\right)}, \tag{4.24}$$

$$\Delta_{xz} \equiv \frac{1}{C_\chi} \frac{\partial^2 n^{(0)}}{\partial \chi_x \partial \chi_z} = \chi_x \chi_z e^{-\frac{1}{2}\left(\chi_z^2 + \chi_x^2 + \chi_y^2\right)}. \tag{4.25}$$
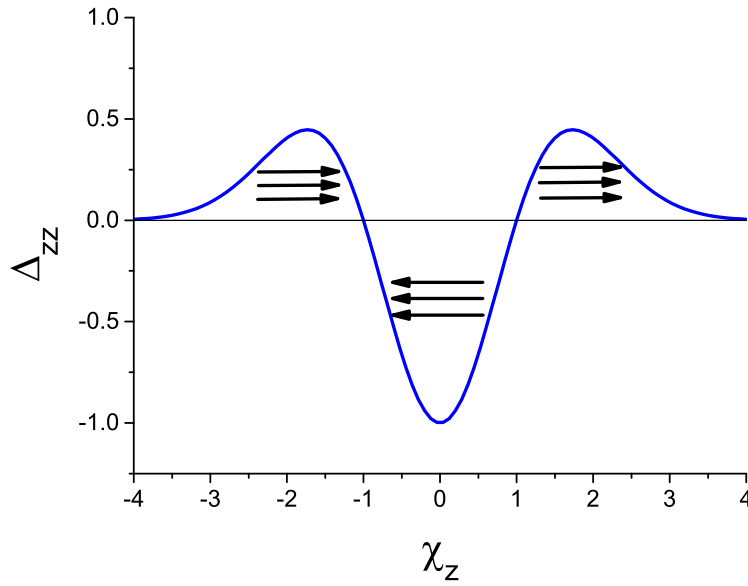
Slika 2: Normirani izvod Δ_{zz} koncentracije naelektrisanih čestica u funkciji relativne koordinate χ_z. Strelice označavaju smer kretanja koje je reprezentovano Q_{zzz} komponentom transportnog tenzora trećeg reda ako je ova komponenta pozitivna. Sila kojom električno polje deluje na naelektrisane čestice je usmerena u pozitivnom χ_z smeru.

Na slici 2 se nalazi normirani parcijalni izvod Δ_{zz} u funkciji χ_z. Može se videti da je odgovarajuća kriva simetrična u odnosu na koordinatni početak u kome ima minimum. Kada je Q_{zzz} pozitivno, smer kretanja koje je reprezentovano ovom komponentom na sledeći način zavisi od znaka Δ_{zz}. Ukoliko je Δ_{zz} pozitivno, smer kretanja koje je opisano Q_{zzz} komponentom usmeren je duž pozitivnog z-smera, što je reprezentovano strelicama koje su orijentisane nadesno. Ako je Δ_{zz} negativno, kretanje koje je opisano Q_{zzz} komponentom usmereno je u negativnom z-smeru, što je reprezentovano strelicama koje su orijentisane nalevo. Na osnovu toga se vidi da je prednja strana roja izdužena dok je zadnja strana roja skupljena, kada je $Q_{zzz} > 0$. Situacija je suprotna kada je $Q_{zzz} < 0$. Tada je prednja strana roja skupljena, dok je zadnja strana roja izdužena.

Slika 3 prikazuje normirani parcijalni izvod Δ_{xx} u funkciji χ_x. Ova funkcija ima identičan oblik kao Δ_{zz}. Kada je Q_{zxx} pozitivno, kretanje koje je opisano ovom komponentom je usmereno duž pozitivnog z-smera na transverzalnim ivicama roja, što je ilustrovano strelicama koje
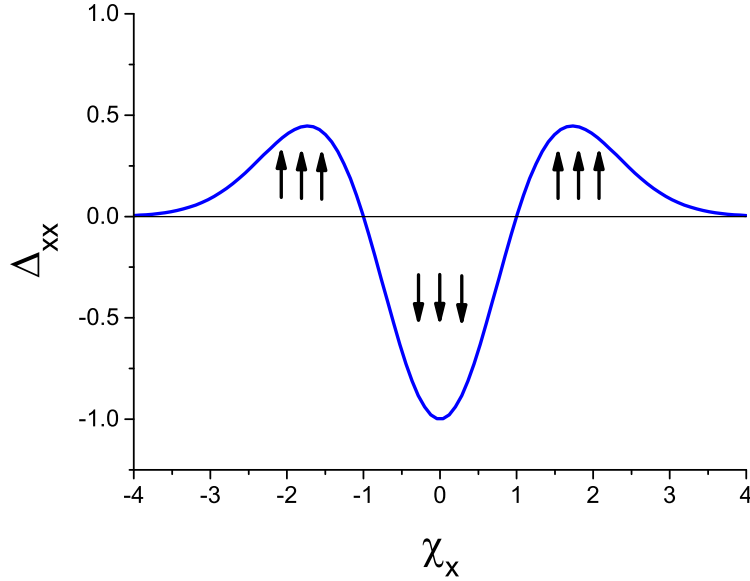
Slika 3: Normirani izvod Δ_{xx} koncentracije naelektrisanih čestica u funkciji relativne koordinate χ_x. Strelice označavaju smer kretanja koje je reprezentovano Q_{zxx} komponentom transportnog tenzora trećeg reda ako je ova komponenta pozitivna. Ovde strelice usmerene naviše (naniže) reprezentuju kretanje u pozitivnom (negativnom) z-smeru.

su usmerene naviše. Međutim, u centru roja je kretanje, koje je opisano Q_{zxx} komponentom, usmereno u negativnom z-smeru, što je reprezentovano strelicama koje su usmerene naniže. Slično tome, ako je Q_{zxx} komponenta negativna, kretanje opisano ovom komponentom je usmereno duž negativnog z-smera na transverzalnim ivicama roja i duž pozitivnog z-smera u centru roja.

Na slici 4 je prikazan normirani parcijalni izvod Δ_{xz} u funkciji χ_x i χ_z. Ovaj izvod je pozitivan u prvom i trećem kvadrantu, a negativan u drugom i četvrtom kvadrantu. Ako je Q_{xxz} pozitivno, smer kretanja koji je opisan ovom komponentom na sledeći način zavisi od znaka Δ_{xz}. Kada je Δ_{xz} pozitivno, kretanje koje je opisano Q_{xxz} komponentom usmereno je duž pozitivnog x-smera, što je ilustrovano strelicama usmerenim nadesno. Kada je Δ_{xz} negativno, kretanje opisano Q_{xxz} komponentom je usmereno duž negativnog x-smera, što je ilustrovano strelicama koje su usmerene nalevo. Kada je $Q_{xxz} < 0$, smer kretanja, koje je opisano ovom komponentom, jeste obrnut. Zajednički doprinos Q_{zxx} i Q_{xxz} komponenti dovodi do kruškastog oblika prostorne raspodele roja. Koncentracija naelektrisanih čestica iz jednačine (4.12) u novim koordinatama ima oblik

$$n^{(1)}(\mathbf{r}, t) = n^{(0)}(\mathbf{r}, t) \times \tag{4.26}$$

$$\left(1 + \frac{tQ_L}{\sigma_z^3}\chi_z(\chi_z^2 - 3) + \frac{3tQ_T}{\sigma_x^2\sigma_z}\chi_z(\chi_x^2 + \chi_y^2 - 2)\right). \tag{4.27}$$

Na osnovu jednačine (4.27) se može analizirati diprinos transportnih koeficijenata trećeg reda prostornom profilu naelektrisanih čestica roja. Iz ove jednačine se vidi da je za $Q_L > 0$ koncentracija naelektrisanih čestica povećana u odnosu na $n^{(0)}(\mathbf{r}, t)$ u opsegu koordinata u kome
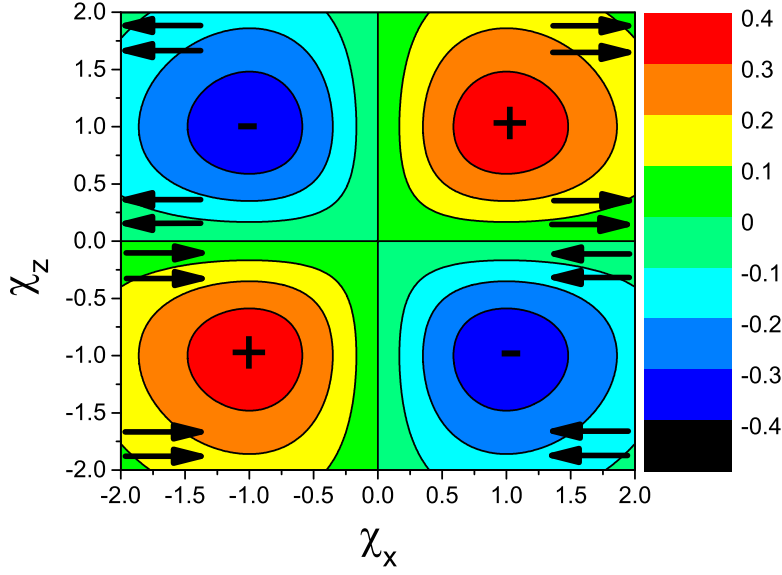
Slika 4: Normirani izvod Δ_{xz} koncentracije naelektrisanih čestica u funkciji relativnih koordinata χ_x i χ_z. Strelice označavaju smer kretanja koje je reprezentovano Q_{xxz} komponentom ako je ova komponenta pozitivna.

je $\chi_z > \sqrt{3}$, kao i u opsegu koordinata u kome je $-\sqrt{3} < \chi_z < 0$. Međutim, koncentracija naelektrisanih čestica je smanjena u odnosu na $n^{(0)}(\mathbf{r}, t)$ u ostatku prostora. Ispostavlja se da je za $Q_L > 0$ prostorna raspodela naelektrisanih čestica razvučena duž longitudinalnog pravca na frontu roja, dok je skupljena duž longitudinalnog pravca na začelju roja. Situacija je obrnuta za $Q_L < 0$. Tada je prostorna raspodela naelektrisanih čestica skupljena duž longitudinalnog pravca na frontu roja, dok je razvučena duž longitudinalnog pravca na začelju roja. Slično tome, za $Q_T > 0$ koncentracija naelektrisanih čestica je povećana u odnosu na $n^{(0)}(\mathbf{r}, t)$ u opsegu koordinata u kome su zadovoljene nejednakosti $\chi_z > 0$ i $\sqrt{\chi_x^2 + \chi_y^2} > \sqrt{2}$, kao i u opsegu koordinata u kome su zadovoljene nejednakosti $\chi_z < 0$ i $\sqrt{\chi_x^2 + \chi_y^2} < \sqrt{2}$. No, u ostatku prostora je koncentracija naelektrisanih čestica smanjena u odnosu na $n^{(0)}(\mathbf{r}, t)$. Iz ovoga sledi da je za $Q_T > 0$ prostorna raspodela naelektrisanih čestica razvučena duž transverzalnog pravca na frontu roja, dok je skupljena duž transverzalnog pravca na začelju roja. Situacija je obrnuta za $Q_T < 0$, kada je prostorna raspodela naelektrisanih čestica razvučena duž transverzalnog pravca na začelju roja, a skupljena duž transverzalnog pravca na frontu roja. Analiza uticaja transportnih koeficijenata trećeg reda na prostorni profil roja, koja je zasnovana na jednačini (4.27) u saglasnosti je sa analizom baziranom na doprinosu transportnih koeficijenata trećeg reda fluksu naelektrisanih čestica, koji je prikazan u jednačini (4.13).

Iz jednačine (4.27) se vidi da uticaj transportnih koeficijenata trećeg reda na prostorni profil roja opada sa povećanjem koncentracije neutralnih čestica pozadinske sredine n_0. Ovo je posledica toga što sa porastom n_0 komponente Q_L i Q_T opadaju kao $1/n_0^2$, dok σ_x i σ_z opadaju kao $1/\sqrt{n_0}$. Na osnovu toga tQ_L/σ_z^3 i $3tQ_T/\sigma_x^2\sigma_z$ opadaju kao $1/\sqrt{n_0}$ sa porastom n_0. Jednačina (4.27) takođe ukazuje na to da uticaj transportnog tenzora trećeg reda na prostorni profil naelektrisanih čestica opada u vremenu kao $1/\sqrt{t}$, zbog vremenske zavisnosti članova tQ_L/σ_z^3 i

$3tQ_T/\sigma_x^2\sigma_z$. Pošto transportni koeficijenti trećeg reda imaju značajniji uticaj na prostorni profil roja pri niskoj vrednosti n_0, ovi koeficijenti bi najlakše mogli da budu izmereni na niskom n_0. Međutim, pri opadanju n_0 se smanjuje koliziona frekvenca pojedinačnih elektrona i usporava se relaksacija energije roja. Ovo može da dovede do smanjenja pouzdanosti eksperimenata zbog uporedivosti vremena energijske relaksacije roja i vremena koje je potrebno za dolazak elektrona do granica sistema, a zatim i zbog difuzionog hlađenja roja kroz gubitke najenergičnijih elektrona na bočnim zidovima suda. Zbog toga bi za merenje transportnih koeficijenata trećeg reda bilo potrebno da se dizajniraju eksperimenti koji bi koristili veliku zapreminu gasa na malom pritisku, što je u skladu sa preporukama koje su dali Penetrante i Bardsley [126].

U ostatku ovog potpoglavlja biće razmatrani fizički uslovi od kojih zavisi znak komponenti transportnog tenzora trećeg reda. Kada je $Q_{zzz} > 0$, prednja strana roja je izdužena, dok je zadnja strana skupljena. Ali, kada je $Q_{zzz} < 0$, prednja je strana roja skupljena, a zadnja je izdužena. Efekti koji mogu doprineti širenju ili skupljanju roja u određenom delu prostora jesu sila kojom deluje spoljašnje električno polje i razlike u srednjoj energiji i kolizionoj frekvenci elektrona u različitim delovima prostora. Sila kojom deluje električno polje teži da izduži prostornu raspodelu naelektrisanih čestica na frontu roja i da je sabije na začelju roja. Uzrok tome je što se elektroni na frontu roja, koji se udaljavaju od centra roja duž longitudinalnog pravca, kreću u smeru sile kojom deluje polje (pozitivan smer), dok se elektroni na začelju, koji se udaljavaju od centra roja duž istog pravca, kreću suprotno od smera sile kojom deluje polje (negativan smer). Pored toga, srednja energija elektrona se povećava u smeru u kome deluje sila električnog polja. Smer sile kojom deluje električno polje i povećanje srednje energije elektrona u ovom smeru teže da izduže prostornu raspodelu elektrona na frontu roja i da je sabiju na začelju roja. U slučaju kada je koliziona frekvenca elektrona nezavisna od energije, ovi efekti u potpunosti određuju znak komponenti transportnog tenzora trećeg reda i Q_{zzz} komponenta je pozitivna. Kada koliziona frekvenca opada sa porastom energije, otpor kretanju elektrona, koji je izazvan sudarima, opada u smeru delovanja sile električnog polja, što je još jedan efekat koji doprinosi pozitivnom znaku Q_{zzz} komponente. Međutim, kada se koliziona krekvenca povećava sa porastom energije, otpor kretanju naelektrisanih čestica se povećava u smeru u kome deluje sila električnog polja. Ako uticaj povećanja kolizione frekvence u smeru delovanja sile spoljašnjeg električnog polja na širenje ili skupljanje roja nije dovoljno intenzivan da nadjača efekat sile spoljašnjeg polja i povećanje srednje energije elektrona u smeru delovanja ove sile, Q_{zzz} komponenta je pozitivna. Ovaj uslov je najčešće zadovoljen. S druge strane, ukoliko je uticaj povećanja kolizione frekvence u smeru delovanja sile spoljašnjeg polja na širenje ili skupljanje roja dovoljno intenzivan da nadjača preostala dva efekta, Q_{zzz} komponenta je negativna.

Kada je $Q_{xxz} > 0$, prostorna raspodela naelektrisanih čestica je proširena duž transverzalnog pravca na frontu roja i skupljena duž transverzalnog pravca na začelju roja. Istovremeno važi i to da ako je $Q_{xxz} < 0$, prostorna raspodela naelektrisanih čestica je proširena duž transverzalnog pravca na začelju roja i skupljena duž transverzalnog pravca na frontu roja. Pošto duž transverzalnog pravca ne deluju spoljašnje sile (u odsustvu magnetskog polja), efekti koji utiču na znak Q_{xxz} komponente su povećanje srednje energije naelektrisanih čestica u smeru u kome

deluje sila spoljašnjeg električnog polja i zavisnost kolizione frekvence od energije naelektrisanih čestica. Povećanje srednje energije naelektrisanih čestica u smeru u kome deluje sila polja doprinosi većem transverzalnom širenju na frontu roja nego na začelju roja. U situaciji kada je koliziona frekvenca nezavisna od energije, ovo je jedini efekat koji određuje znak Q_{xxz} komponente i ova komponenta je pozitivna. Opadanje kolizione frekvenca uz porast energije dodatno doprinosi pozitivnom znaku Q_{xxz} komponente. Međutim, kada se koliziona frekvenca povećava sa porastom energije, otpor transverzalnom širenju naelektrisanih čestica, koji je izazvan sudarima, veći je na frontu roja nego na začelju roja. Ako uticaj porasta kolizione frekvence na širenje ili skupljanje roja nije dovoljno intenzivan da nadjača uticaj veće pokretljivosti elektrona na frontu roja, Q_{xxz} komponenta je pozitivna. Ukoliko je pak uticaj porasta kolizione frekvence na širenje ili skupljanje roja dovoljno intenzivan da nadjača uticaj veće pokretljivosti naelektrisanih čestica na frontu roja, Q_{xxz} komponenta je negativna.

Komponenta Q_{zxx} opisuje razliku u longitudinalnom širenju naelektrisanih čestica u centru roja i duž transverzalnih ivica. Ako važi $Q_{zxx} > 0$, longitudinalno širenje je brže na transverzalnim ivicama nego u centru roja, i suprotno – ukoliko je $Q_{zxx} < 0$, longitudinalno širenje je izraženije u centru roja nego na transverzalnim ivicama. Parabolični porast srednje energije ka transverzalnim ivicama pogoduje bržem longitudinalnom širenju naelektrisanih čestica na transverzalnim ivicama nego u centru roja. Ovaj parabolični porast srednje energije duž transverzalnog pravca je posledica toga što najenergičniji elektroni mogu brzo da pređu distancu između centra roja i njegovih ivica, ako porast kolizione frekvence sa energijom nije dovoljno intenzivan da kompenzuje ovaj efekat. Kada je koliziona frekvenca nezavisna od energije, ovo je jedini efekat koji utiče na znak Q_{zxx} komponente i ova komponenta je pozitivna. Međutim, pošto je ovaj efekat jako mali, Q_{zxx} komponenta je znatno manja od preostale dve komponente u slučaju konstantne kolizione frekvence, kao što je pokazano na primeru Maxwell-ovog modela (v. potpoglavlje 4.4). Ako koliziona frekvenca opada sa porastom energije, Q_{zxx} komponenta je pozitivna, uz šta je bliža po intenzitetu ostalim nenultim komponentama nego u prilikom konstantne kolizione frekvence. U slučaju kada koliziona frekvenca raste sa porastom energije a Q_{xxz} komponenta je pozitivna, Q_{zxx} komponenta je negativna zbog većeg otpora longitudinalnom širenju roja na transverzalnim ivicama nego u centru roja. Međutim, kada koliziona frekvenca raste sa porastom energije a Q_{xxz} komponenta je negativna, Q_{zxx} komponenta je pozitivna. Moguće objašnjenje za ovakav efekat je da je u ovom slučaju porast kolizione frekvence sa energijom toliko intenzivan te da uslovljava manju srednju energiju na bočnim ivicama roja nego u centru roja. Ovo bi moglo da bude posledica toga što intenzivna koliziona frekvenca otežava visokoenergijskim elektronima da stignu do transverzalnih ivica roja.

4.3   Uslovi simulacija

U nastavku ovog poglavlja biće prikazani rezultati naših proračuna u modelnim gasovima. Posmatrani sistem se sastoji od roja elektrona koji se kreću u homogenom i neutralnom pozadinskom gasu u prisustvu stacionarnog i prostorno homogenog električnog polja. U Monte Carlo simulacijama se prati veliki broj elektrona (bar 10^7) kako bi se smanjile statističke fluktu-

acije rezultata. Praćenje ovako velikog broja elektrona je neophodno za proračun TKIII jer su statističke fluktuacije monoma trećeg reda, na osnovu kojih se računaju TKIII, znatno veće od fluktuacija monoma nižeg reda. Pored praćenja velikog broja elektrona u Monte Carlo simulacijama neophodno je i pažljivo izabrati interval za usrednjavanje rezultata simulacija u vremenu, zbog toga što se statističke fluktuacije monoma višeg reda povećavaju sa širenjem roja. Zato je potrebno da se rezultati simulacija usrednjavaju u intervalu od trenutka kada je energija roja dostigla stacionarnu vrednost do trenutka kada statističke fluktuacije rezultata postanu veće od prihvatljive statističke greške. Zbog intenzivnih fluktuacija monoma trećeg stepena, balk vrednosti TKIII se ne računaju primenom numeričkog diferenciranja, koje bi značajno povećalo fluktuacije rezultata, već se izraz koji stoji iza izvoda aproksimira linearnom funkcijom. Ovo je ekvivalentno numeričkom diferenciranju, budući da je koeficijenat pravca izraza koji stoji posle izvoda jednak prvom izvodu tog izraza po vremenu, nakon relaksacije energije roja, kada su transportni koeficijenti nezavisni od vremena. Validnost ovog načina izračunavanja balk vrednosti TKIII je proverena poređenjem sa rezultatima koji su dobijeni primenom numeričkog diferenciranja, kao i poređenjem sa odgovarajućim fluks vrednostima u odsustvu nekonzervativnih procesa.

Pri proračunu fluks komponenti TTIII primenom momentnog metoda za rešavanje Boltzmann-ove jednačine, često je potrebno uzeti u obzir veliki broj članova u razvoju funkcije raspodele po sfernim harmonicima i Sonine polinomima. Ovo je naročito izraženo u situacijama u kojima intenzivni neelastični sudari izazivaju snažnu anizotropiju funkcije raspodele u brzinskom prostoru, kao i u uslovima u kojima kombinacija neelastičnih i nekonzervativnih procesa dovodi do značajnog odstupanja funkcije raspodele po energijama od Maxwell-ove raspodele. U slučaju modelnih gasova koji se razmatraju u ovom poglavlju, ovakve situacije se mogu sresti u modelu krutih sfera kada je odnos masa čestica projektila i mete približno jednak jedinici, kao i u Reid-ovom, Lucas–Saelee-evom i Ness–Robson-ovom modelnim gasovima na visokim vrednostima E/n_0. Pri okolnostima u kojima su preseci za neelastične sudare uporedivi sa presekom za elastične sudare nekada je potrebno uzeti u obzir više od 5 članova u razvoju funkcije raspodele po sfernim harmonicima. Takođe je potrebno uzeti i preko 100 članova u razvoju funkcije raspodele po Sonine polinomima kada ova funkcija snažno odstupa od ravnotežnog Maxwellian-a. Pošto je elastično rasejanje elektrona, po svojoj prirodi anizotropno, u našim proračunima se za opis elastičnog rasejanja koristi presek za transfer impulsa u elastičnim sudarima. Korišćenje ovog preseka omogućava dobru reprezentaciju srednjeg transfera impulsa u elastičnim sudarima pri svakoj vrednosti energije elektrona, bez uzimanja u obzir ugaone zavisnosti diferencijalnog preseka za elastično rasejanje. Za neelastične sudare i jonizaciju se koriste totalni preseci, pri čemu je pretpostavljeno izotropno rasejanje.

4.4 Transportni koeficijenti trećeg reda za roj elektrona u Maxwell-ovom modelnom gasu

Maxwell-ov model je modelni gas u kome je interakcija elektrona sa neutralnim molekulima opisana elastičnim sudarima, pri čemu je koliziona frekvencija nezavisna od energije elektrona.

Transport elektrona u Maxwell-ovom modelu u ortogonalnoj konfiguraciji električnog i magnetskog polja ispitali su Ness i Robson primenom momentnog metoda za rešavanje Boltzmann-ove jednačine [88, 186]. Rezultati do kojih su došli naknadno su provereni primenom Monte Carlo simulacija [187]. Zavisnost transportnih osobina elektrona u Maxwell-ovom modelu od ugla koji zaklapaju električno i magnetsko polje je kasnije određena primenom momentnog metoda za rešavanje Boltzmann-ove jednačine [89]. Detalji modela su zadati na sledeći način

$$\sigma_m = A\epsilon^{-1/2}(\text{elastični sudar}),$$
$$m_0 = 4\text{amu}, m = 5.486 \times 10^{-4}\text{amu},$$
$$T_0 = 293K \tag{4.28}$$

gde je σ_m presek za transfer impulsa u elastičnim sudarima, A je konstanta, ϵ je energija upadne čestice, amu je atomska jedinica mase, T_0 je apsolutna temperatura pozadinskog gasa, dok su m_0 i m mase neutralnih i naelektrisanih čestica respektivno. Proračuni su urađeni u opsegu polja od 10^{-4} do 100 Td. Pomoću Maksvelovog modela se može ispitati zavisnost TKIII od jačine spoljašnjeg električnog polja i veličine preseka za elastične sudare, pri konstantnoj kolizionoj frekvenciji.
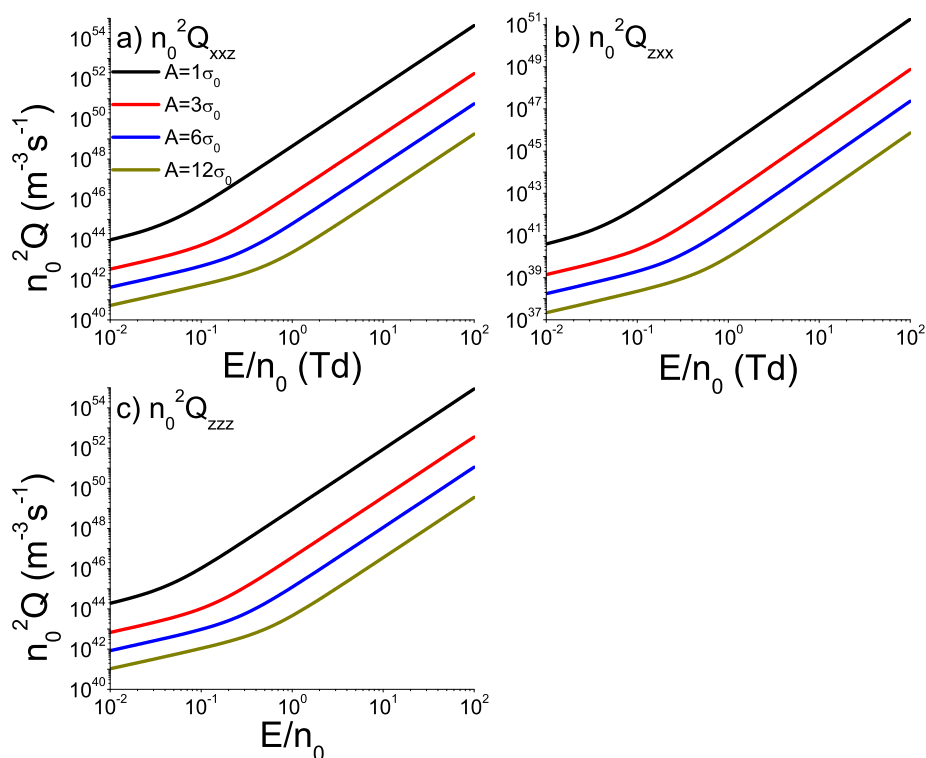
Slika 5: $n_0^2 Q_{xxz}$, $n_0^2 Q_{zxx}$ i $n_0^2 Q_{zzz}$ komponente transportnog tenzora trećeg reda za roj elektrona u Maxwell-ovom modelu u funkciji redukovanog električnog polja E/n_0 i veličine preseka za elastične sudare A. Ovi rezultati su dobijeni primenom metoda više članova za rešavanje Boltzmann-ove jednačine.

Na slici 5 su prikazani rezultati proračuna TKIII u Maxwell-ovom modelu, koji su dobijeni na osnovu numeričkog rešavanja Boltzmann-ove jednačine. Sa ovog grafika se može videti da se sve tri komponente TTIII monotono povećavaju sa povećanjem redukovanog električnog

polja E/n_0. Takođe se uočava da komponente TTIII naglo opadaju sa povećanjem preseka za elastične sudare.

Kada se komponente TTIII prikažu na grafiku u kome su obe koordinatne ose predstavljene logaritamskom skalom, njihova zavisnost od E/n_0 je praktično linearna na jako visokim i na jako niskim vrednostima E/n_0, ali ove linearne zavisnosti imaju različite koeficijente pravca. Pri tome je koeficijent pravca veći na visokim, nego na niskim poljima. Između ova dva široka opsega, u okviru kojih je koeficijent pravca na lorgaritamskoj skali praktično konstantan, postoji uži opseg polja u kome se prvi izvod zavisnosti komponenti TTIII od E/n_0 monotono povećava. Ovaj opseg polja odgovara rasponu u kome komponente difuzionog tenzora počinju da odstupaju od termalnih vrednosti. U pitanju je promena koja se dešava na višim poljima za veću vrednost preseka za elastične sudare.

Sa slike 5 se može uočiti da komponenta $n_0^2 Q_{zxx}$ ima znatno niže vrednosti od preostale dve komponente, što se može razumeti na osnovu fizičke interpretacije TKIII, razmatrane u potpoglavlju 4.2. Naime, $n_0^2 Q_{zxx}$ komponenta opisuje razliku u intenzitetu fluksa čestica duž z-ose u centru roja i na transverzalnim ivicama. Pozitivnost ove komponente implicira da je fluks duž z-ose intenzivniji na transverzalnim ivicama nego u centru roja. Ovo je očekivano zato što koliziona frekvenca ne zavisi od energije u Maksvelovom modelu, a čestice na transverzalnim ivicama imaju nešto višu energiju nego čestice u centru roja, zbog parabolične zavisnosti srednje energije naelektrisanih čestica od transverzalnih koordinata. Međutim pošto je promena srednje energije duž transverzalnog pravca manja od promene duž longitudinalnog pravca, $n_0^2 Q_{zxx}$ ima znatno nižu vrednost od $n_0^2 Q_{xxz}$ i $n_0^2 Q_{zzz}$ u celom opsegu redukovanog električnog polja.

Slika 5 pokazuje kako je $n_0^2 Q_{xxz}$ komponenta dvostruko manja od $n_0^2 Q_{zzz}$ komponente. Uz to važi $n_0^2 Q_{xxz} = n_0^2 Q_{xzx}$ i $n_0^2 Q_{zzz} \approx n_0^2 (Q_{xxz} + Q_{xzx})$. Odnos $n_0^2 Q_{xxz}$ i $n_0^2 Q_{zzz}$ komponenti TTIII je analogan odnosu komponenti difuzionog tenzora u Maxwell-ovom modelu za koje važi $n_0 D_{xx} = n_0 D_{zz}$. Ovo se može zaključiti na osnovu toga što zbir $n_0^2 (Q_{xxz} + Q_{xzx})$ određuje doprinos fluksu koji odgovara TKIII duž transverzalnog pravca, dok je odgovarajući doprinos fluksu duž longitudinalnog pravca praktično određen $n_0^2 Q_{zzz}$ komponentom, pošto je $n_0^2 Q_{zxx}$ komponenta zanemarljiva u poređenju sa $n_0^2 Q_{xxz}$ i $n_0^2 Q_{zzz}$ komponentama.

4.5 Transportni koeficijenti trećeg reda za roj naelektrisanih čestica u modelu krutih sfera

Model krutih sfera je modelni gas u kome je interakcija naelektrisane čestice roja sa molekulima pozadinskog gasa opisana elastičnim sudarima, pri čemu je presek za sudare nezavisan od energije. Na osnovu toga je u ovom modelu koliziona frekvenca srazmerna kvadratnom korenu energije. Transport elektrona u modelu krutih sfera u konstantnom i homogenom električnom polju je izučavan primenom momentnog metoda za rešavanje Boltzmann-ove jednačine [83]. Nakon toga je transport elektrona u ovom modelu u ortogonalnoj konfiguraciji električnog i magnetskog polja ispitivan primenom momentnog metoda za rešavanje Boltzmann-ove jednačine [88, 186] i Monte Carlo simulacija [187]. Pored toga, analizirana je zavisnost anizotropije

funkcije raspodele u brzinskom prostoru od odnosa masa m/m_0 u prisustvu električnog polja, kao i zavisnost ove anizotropije od intenziteta magnetskog polja u ortogonalnoj konfiguraciji električnog i magnetskog polja primenom momentnog metoda za rešavanje Boltzmann-ove jednačine [189]. Uz to je razmatran i transport lakih jona u prisustvu vremenski promenljivog električnog polja, primenom vremenski zavisnog momentnog metoda za rešavanje Boltzmann-ove jednačine [190]. Detalji modela su zadati na sledeći način:

$$\sigma_m(\epsilon) = 6\mathring{A}^2(\text{elastični sudar}),\ m_0 = 4\text{amu},\ T_0 = 293K,$$

gde je σ_m presek za transfer impulsa u elastičnim sudarima, m_0 je masa molekula pozadinskog gasa a T_0 je apsolutna temperatura. U našim proračunima u obzir su uzeti odnosi masa u opsegu od 10^{-4} do 1. Proračuni su urađeni primenom Monte Carlo simulacija u opsegu redukovanih električnih polja E/n_0 od 1 do 100 Td.

Korišćenjem ovog modela, može se ispitati uticaj elastičnih sudara sa rastućom kolizionom frekvencom na TKIII. Model je takođe pogodan za ispitivanje uticaja odnosa masa m/m_0 na TKIII zbog jednostavnosti preseka za elastične sudare.
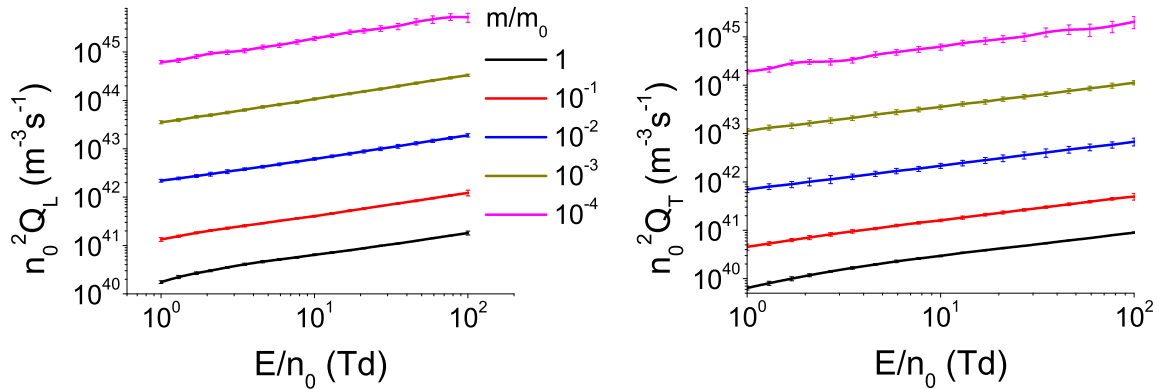
Slika 6: $n_0^2Q_L$ i $n_0^2Q_T$ komponente transportnog tenzora trećeg reda u funkciji redukovanog električnog polja E/n_0 i odnosa masa m/m_0 za roj naelektrisanih čestica u modelu krutih sfera. Ovi rezultati su dobijeni primenom Monte Carlo simulacija.

Na grafiku 6 je prikazana zavisnost $n_0^2Q_L$ i $n_0^2Q_T$ od E/n_0 i odnosa masa m/m_0. U Monte Carlo simulacijama ne možemo da razdvojimo pojedinačne vandijagonalne komponente transportnog tenzora trećeg reda $n_0^2Q_{xxz}$ i $n_0^2Q_{zxx}$, zato što su izrazi koji se koriste za izračunavanje TKIII u Monte Carlo simulacijama izvedeni iz generalisane difuzione jednačine u kojoj su svi indeksi TKIII kontrakovani sa parcijalnim izvodima koncentracije naelektrisanih čestica.

Komponente $n_0^2Q_L$ i $n_0^2Q_T$ se monotono povećavaju sa opadanjem odnosa masa m/m_0 za svaku vrednost redukovanog električnog polja E/n_0. Zavisnost komponenti TTIII od odnosa masa m/m_0 je posledica smanjenja transfera energije u elastičnim sudarima pri opadanju m/m_0, što olakšava difuziono širenje roja. Može se primetiti da se statistička greška Monte Carlo rezultata povećava sa smanjenjem m/m_0. Razlog za ovo je povećanje statističkih fluktuacija monoma trećeg stepena sa porastom vremena relaksacije energije, koje se povećava pri opadanju m/m_0.

Komponente $n_0^2 Q_L$ i $n_0^2 Q_T$ se monotono povećavaju sa porastom E/n_0 za svaku vrednost odnosa masa m/m_0. Sa porastom E/n_0 se povećava pokretljivost naelektrisanih čestica, zbog porasta njihove srednje energije, i pojačava se sila koja usmerava njihovo kretanje duž pravca polja. Ovo dovodi do monotonog povećanja $n_0^2 Q_L$ i $n_0^2 Q_T$ sa porastom E/n_0, uprkos porastu kolizione frekvence za elastične sudare, koja je srazmerna kvadratnom korenu energije.

Takođe se vidi da je $n_0^2 Q_T$ komponenta pozitivna u celom opsegu polja. Pošto je koliziona frekvenca za elastične sudare srazmena kvadratnom korenu energije, $n_0^2 Q_{zxx}$, komponenta je negativna u ovom modelu. Međutim, pozitivne vrednosti $n_0^2 Q_T$ ukazuju na to da je zbir $n_0^2 (Q_{xxz} + Q_{xzx})$ veći od $n_0^2 Q_{zxx}$ komponente.

Na osnovu opadanja TKIII sa porastom m/m_0 može se steći utisak da su TKIII značajniji za lake čestice poput elektrona i pozitrona, nego za teške čestice poput jona. Doprinos TKIII prostornom profilu roja duž longitudinalnog pravca je izražen (u prvoj aproksimaciji) pomoću dva člana koji su srazmerni članovima $Q_L/(D_L)^2$ i $Q_L/(D_L)^3$, respektivno. Ovo zapravo znači da doprinos TKIII prostornom profilu roja zavisi od odnosa komponenti TTIII i komponenti difuzionog tenzora.
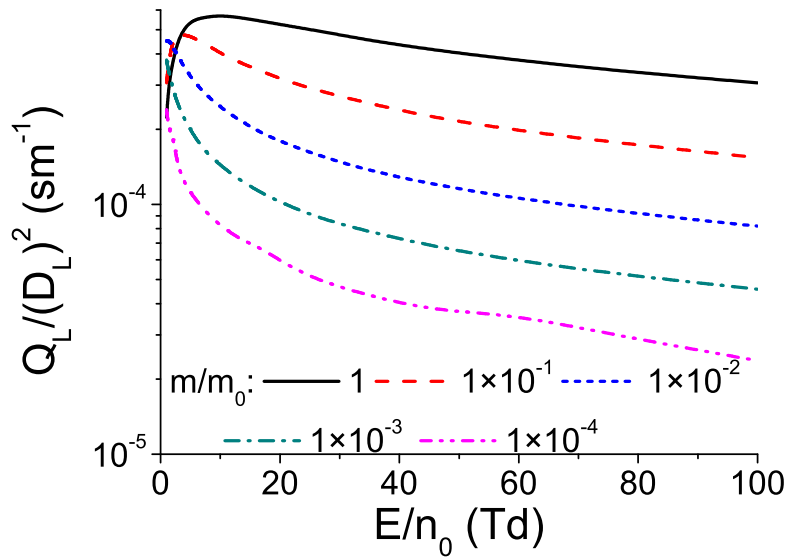
Slika 7: Količnik $Q_L/(D_L)^2$ u funkciji E/n_0 i m/m_0 za roj naelektrisanih čestica u modelu krutih sfera. Ovi rezultati su dobijeni primenom Monte Carlo simulacija.

Na slikama 7 i 8 je prikazana zavisnost količnika $Q_L/(D_L)^2$ i $Q_L/(D_L)^3$ od E/n_0 i odnosa masa m/m_0 za naelektrisane čestice u modelu krutih sfera. Ove veličine opadaju sa opadanjem m/m_0, što ukazuje na to da su TKIII značajniji za teške čestice poput jona nego za lake čestice poput elektrona i pozitrona.
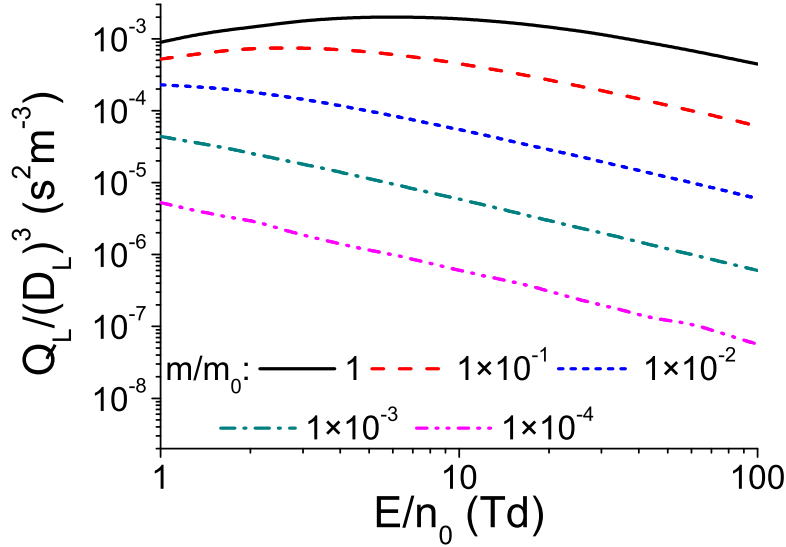
Slika 8: Količnik $Q_L/(D_L)^3$ u funkciji E/n_0 i m/m_0 za roj naelektrisanih čestica u modelu krutih sfera. Ovi rezultati su dobijeni primenom Monte Carlo simulacija.

4.6 Transportni koeficijenti trećeg reda za roj elektrona u Reid-ovom modelnom gasu

Reid-ov model je modelni gas u kome je interakcija naelektrisanih čestica sa molekulima pozadinskog gasa reprezentovana elastičnim i neelastičnim sudarima. U njemu važi da je presek za elastične sudare konstantan, dok je presek za neelastične sudare linearna funkcija energije naelektrisane čestice [47, 191].

Ovaj modelni gas je uveden da bi se testirala validnost aproksimacije dva člana, koja se često koristi pri numeričkom rešavanju Boltzmann-ove jednačine [191]. Pokazano je da u njemu postoje značajna odstupanja između vrednosti transportnih koeficijenata koje su dobijene primenom Monte Carlo simulacija i vrednosti koje su određene korišćenjem aproksimacije dva člana. Procentualne razlike između vrednosti dobijenih primenom ove dve metode dostižu oko 7% i oko 50% za brzinu drifta i transverzalnu komponentu difuzionog tenzora, respektivno [191]. Transport elektrona u Reid-ovom modelnom gasu je izučavan u konstantnom i homogenom električnom polju [84], u ortogonalnoj konfiguraciji električnog i magnetskog polja [88], kao i u promenljivoj konfiguraciji u kojoj ugao između električnog i magnetskog polja varira između 0 i $\pi/2$ [89], primenom momentnog metoda za rešavanje Boltzmann-ove jednačine. Pored toga, rezultati koji odgovaraju ortogonalnoj konfiguraciji električnog i magnetskog polja su provereni poređenjem sa rezultatima Monte Carlo simulacija [187]. U ovom modelu su analizirane tranzijentne negativne vrednosti dijagonalnih komponenti difuzionog tenzora, u ortogonalnoj konfiguraciji vremenski zavisnog električnog polja i vremenski zavisnog magnetskog polja, na osnovu vremenski razloženih Monte Carlo rezultata i primenom vremenski zavisnog momentnog metoda za rešavanje Boltzmann-ove jednačine [164, 165].

Detalji modela su zadati na sledeći način:

$$\sigma_m(\epsilon) = 6\text{Å}^2 \quad \text{(elastični sudari)}$$

$$\sigma_{inel}(\epsilon) = \begin{cases} 10(\epsilon - 0.2)\ \text{Å}^2, & \epsilon \geq 0.2\ \text{eV} \\ & \qquad \text{(neelastični sudar)} \\ 0, & \epsilon < 0.2\text{eV} \end{cases}$$

$$m_0 = 4\ \text{amu}$$

$$T_0 = 0\ \text{K}\ , \tag{4.29}$$

gde su $\sigma_m(\epsilon)$ i $\sigma_{inel}(\epsilon)$ preseci za transfer impulsa u elastičnim i neelastičnim sudarima u funkciji energije naelektrisane čestice, respektivno, dok su m_0 i T_0 masa i temperatura molekula pozadinskog gasa.

Uz pomoć Reid-ovog modela mogu se ispitati trendovi zavisnosti komponenti TTIII od električnog i magnetskog polja u prisustvu elastičnih i neelastičnih sudara sa rastućom kolizionom frekvencom. Može se proveriti i to da li je prikladno koristiti aproksimaciju dva člana za određivanje komponenti TTIII. Očekivano je da će TKIII biti osetljiviji na način rešavanja Boltzmann-ove jednačine od brzine drifta i difuzionog tenzora.
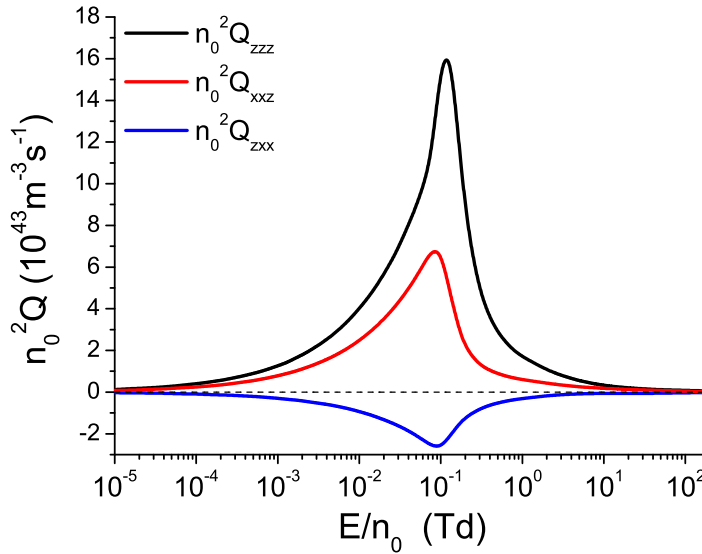
Slika 9: $n_0^2 Q_{xxz}$, $n_0^2 Q_{zxx}$ i $n_0^2 Q_{zzz}$ komponente transportnog tenzora trećeg reda u funkciji redukovanog električnog polja E/n_0 za roj elektrona u Reid-ovom modelnom gasu. Rezultati su dobijeni primenom metoda više članova za rešavanje Boltzmann-ove jednačine.

Slika 9 daje uvid u zavisnost komponenti TTIII od E/n_0. Primećeno je da je $n_0^2 Q_{zxx}$ komponenta negativna u celom opsegu polja. Negativnost ove komponente ukazuje na to da je doprinos TKIII longitudinalnom fluksu elektrona veći u centru roja nego na transverzalnim ivicama. Ovo je posledica paraboličnog trenda srednje energije elektrona duž transverzalnog pravca i povećanja kolizione frekvence sa porastom energije. Komponente $n_0^2 Q_{xzx}$ i $n_0^2 Q_{zzz}$ su pozitivne u celom opsegu polja. Uticaj porasta kolizione frekvence sa porastom energije nije

dovoljno intenzivan da nadjača uticaj pojačanja sile i povećanja srednje pokretljivosti čestica sa porastom E/n_0 na ove dve komponente.

Sve tri komponente TTIII se po apsolutnoj vrednosti monotono povećavaju sa porastom E/n_0 do približno 0.1 Td, posle čega njihove apsolutne vrednosti naglo opadaju. Na 0.1 Td je srednja energija elektrona oko $5.6 \cdot 10^{-2}$ eV, što je oko 3.6 puta manje od praga za neelastični sudar u Reid-ovom modelu. Na poljima nižim od 0.1 Td većina elektrona nema dovoljno energije da učestvuje u neelastičnom sudaru, pa porast E/n_0 dovodi do pojačanja difuzionog širenja roja, koje je reprezentovano transportnim koeficijentima trećeg reda. Međutim, na poljima višim od 0.1 Td visokoenergisjki elektroni mogu da učestvuju u neelastičnim sudarima. Uticaj neelastičnih sudara na transport elektrona postaje sve značajniji sa porastom E/n_0 zbog povećanja srednje energije roja i povećanja kolizione frekvence za neelastične sudare sa porastom energije. Povećanje kolizione frekvence za neelastične sudare dovodi do većeg otpora difuzionom širenju roja, koje je reprezentovano transportnim koeficijentima trećeg reda.
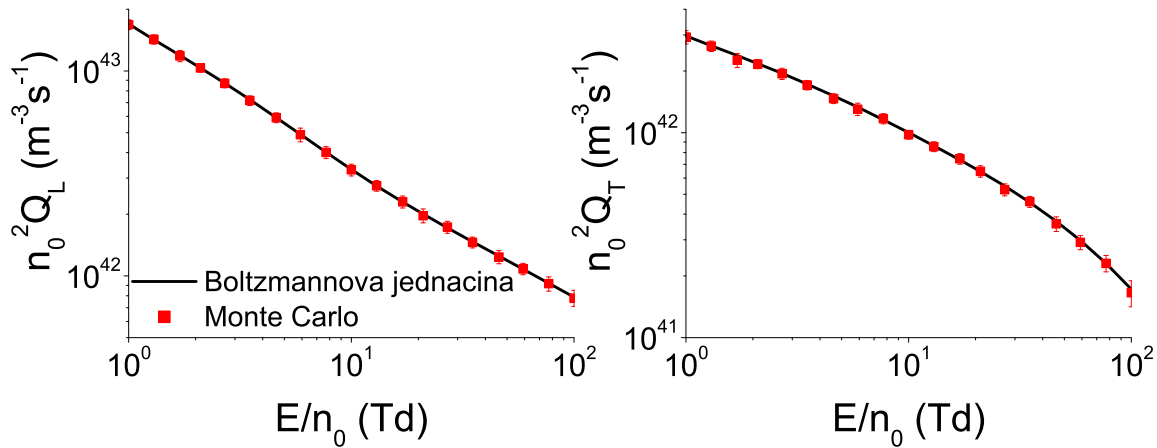
Slika 10: Poređenje vrednosti $n_0^2 Q_L$ i $n_0^2 Q_T$ komponenti transportnog tenzora trećeg reda za roj elektrona u Reid-ovom modelnom gasu, koje su dobijene primenom Monte Carlo simulacija i metoda više članova za numeričko rešavanje Boltzmann-ove jednačine.

Na slici 10 upoređene su vrednosti TKIII dobijene primenom momentnog metoda za rešavanje Boltzmann-ove jednačine i Monte Calro simulacija. Uočava se da postoji odlično slaganje među ovim dvema metodama, što potvrđuje i validnost izraza na osnovu kojih se računaju komponente TTIII u momentnom metodu za numeričko rešavanje Boltzmann-ove jednačine i Monte Carlo simulacijama, kao i ispravnost odgovarajućih procedura za izračunavanje TKIII u ovim kompjuterskim kodovima. Na ovim slikama nisu prikazani Monte Carlo rezultati na nižim poljima, zato što mali transfer energije u elastičnim sudarima dovodi do spore relaksacije i značajnog povećavanja statističkih fluktuacija dinamičkih promenljivih na osnovu kojih se računaju komponente TTIII.

Slika 11 prikazuje procentualne razlike vrednosti komponenti TTIII koje su izračunate primenom aproksimacije dva člana za rešavanje Boltzmann-ove jednačine, u kojoj je razvoj po sfernim harmonicima odsečen na drugom članu, i vrednosti komponenti TTIII koje su izračunate primenom momentnog metoda, u kome je broj sfernih harmonika određen uslovom
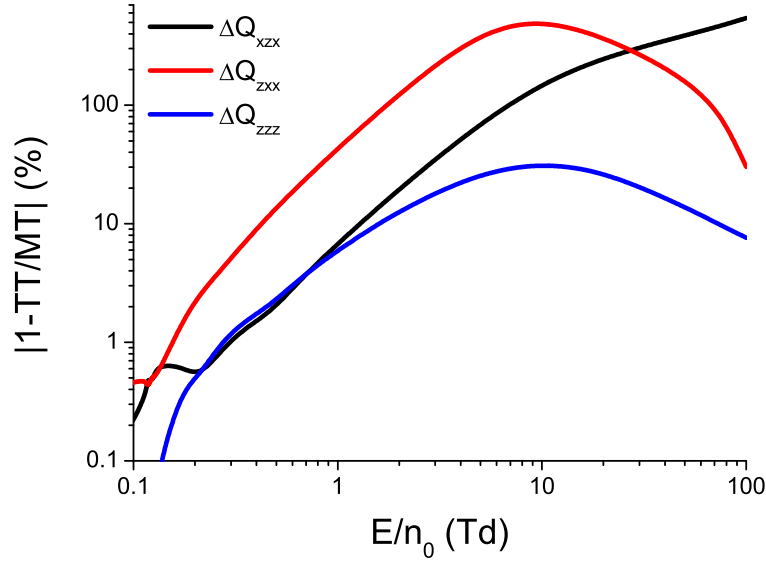
Slika 11: Procentualne razlike između vrednosti komponenti transportnog tenzora trećeg reda koje su određene primenom aproksimacije dva člana (TT) za rešavanje Boltzmann-ove jednačine i primenom metoda više članova (MT) za roj elektrona u Reid-ovom modelnom gasu.

konvergencije transportnih koeficijenata. Uočava se da odstupanje aproksimacije dva člana od momentnog metoda dostiže lokalni maksimum na oko 10 Td za $n_0^2 Q_{zxx}$ i $n_0^2 Q_{zzz}$ komponente TTIII, dok se ovo odstupanje monotono povećava za $n_0^2 Q_{xzx}$ komponentu u celom opsegu E/n_0. U oblasti polja oko 10 Td je srednja energija elektrona oko 0.24 eV, što je blisko pragu za neelastične sudare u Reid-ovom modelu. Komponenta $n_0^2 Q_{zxx}$ je najosetljivija na primenu aproksimacije dva člana na niskim poljima, dok je komponenta $n_0^2 Q_{xzx}$ najosetljivija na visokim poljima. Sa ove slike se može videti da procentualne razlike između vrednosti TKIII koje su dobijene na osnovu ove dve metode za rešavanje Boltzmann-ove jednačine mogu da iznose i do 500%. Ovo jasno pokazuje da su TKIII osetljiviji na način rešavanja Boltzmann-ove jednačine od brzine drifta i difuzionog tenzora. Iz toga sledi da aproksimacija dva člana nije adekvatna za proračun TKIII kada su prisutni neelastični sudari.

U ovom radu je ispitana i zavisnost komponenti TTIII od redukovanog magnetskog polja B/n_0 u Reid-ovom modelnom gasu, pri ortogonalnoj konfiguraciji električnog i magnetskog polja za fiksiranu vrednost redukovanog električnog polja $E/n_0 = 12$ Td. U ortogonalnoj konfiguraciji polja TTIII ima 14 nenultih komponenti od kojih je 10 nezavisno (videti poglavlje 2.5). Na slici 12 je prikazana zavisnost $n_0^2 Q_{xxx}$ i $n_0^2 Q_{zzz}$ od B/n_0 pri redukovanom električnom polju $E/n_0 = 12$ Td. Kao što je pokazano u potpoglavlju 4.2, $n_0^2 Q_{zzz}$, komponenta TTIII opisuje asimetrično odstupanje prostornog profila roja od Gaussian-a duž z-pravca. Analogno tome, u ortogonalnoj konfiguraciji polja $n_0^2 Q_{xxx}$ komponenta opisuje odstupanje od Gaussian-a duž $\mathbf{E} \times \mathbf{B}$ pravca. Za B/n_0 veće od 150 Hx $n_0^2 Q_{xxx}$ i $n_0^2 Q_{zzz}$ monotono opadaju sa povećanjem B/n_0. Ovaj trend zavisnosti transportnih koeficijenata od B/n_0 ukazuje na režim kontrolisan magnetskim poljem, u kome ciklotronska frekvenca nadmašuje kolizionu frekvencu i naelektrisane čestice orbitiraju oko linija magnetskog polja [88]. Na nižim vrednostima B/n_0, ponašanje
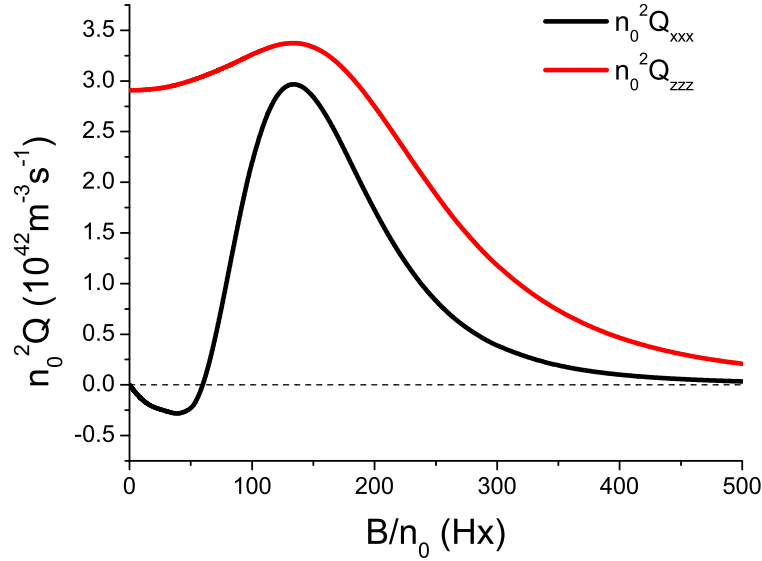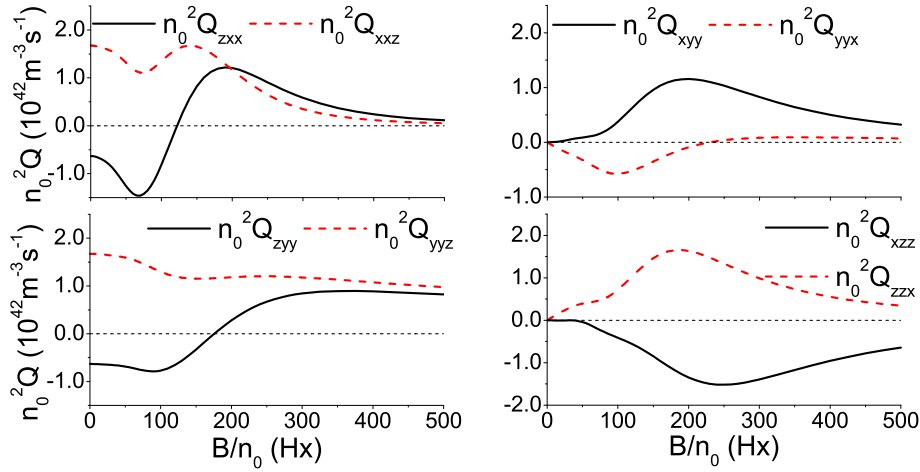
Slika 12: $n_0^2 Q_{xxx}$ i $n_0^2 Q_{zzz}$ komponente transportnog tenzora trećeg reda u funkciji redukovanog magnetskog polja B/n_0 za elektrone u Reid-ovom modelnom gasu, pri redukovanom električnom polju od $E/n_0 = 12$ Td. Ovi rezultati su dobijeni primenom metoda više članova za rešavanje Boltzmann-ove jednačine.

TKIII je manje intuitivno. U većem delu ovog opsega, koliziona frekvenca je veća od ciklotronske [88]. Međutim, sa povećanjem B/n_0 naelektrisane čestice u proseku završavaju sve veći procenat orbite između dva sudara, pa koliziona frekvenca opada, što dovodi do povećanja $n_0^2 Q_{zzz}$.

Ponašanje $n_0^2 Q_{xxx}$ komponente je nešto složenije. Za najniže vrednosti B/n_0, ova komponenta je negativna zbog smera Lorencove sile, koja u proizvodi efektivni drift elektrona u negativnom smeru x-ose [88]. Sa povećanjem B/n_0 uticaj neelastičnih sudara na prostorni profil roja postaje sve značajniji, što dovodi do kompresovanja/širenja roja duž negativnog/pozitivnog smera x-ose. Zbog ovoga $n_0^2 Q_{xxx}$ komponenta postaje pozitivna za B/n_0 veće od približno 60 Hx i povećava se sa porastom B/n_0 do oko 150 Hx.

Na slici 13 je prikazana zavisnost vandijagonalnih komponenti TTIII od B/n_0 pri redukovanom električnom polju $E/n_0 = 12$ Td. Na najvišim vrednostima B/n_0 sve komponente TTIII opadaju sa porastom B/n_0, zato što za više vrednosti B/n_0 naelektrisane čestice između dva sudara u proseku završe veći procenat orbite oko linija magnetskog polja [88]. Ponašanje ovih komponenti je složenije na nižim vrednostima B/n_0. U ovom rasponu polja mnogi faktori istovremeno utiču na TKIII. Među ovim faktorima su termalna anizotropija, magnetska anizotropija i prostorna varijacija srednje brzine i srednje energije duž longitudinalnog i transverzalnog pravca [89]. Termalna anizotropija opisuje razliku u haotičnom kretanju naelektrisanih čestica duž različitih pravaca, dok magnetska anizotropija opisuje orijentaciju orbita naelektrisanih čestica oko linija megnetskog polja.

Dodatne komponente TTIII, koje su nezavisne u ortogonalnoj konfiguraciji polja, imaju

Slika 13: Vandijagonalne komponente transportnog tenzora trećeg reda u funkciji redukovanog magnetskog polja B/n_0 za roj elektrona u Reidovom modelnom gasu pri redukovanom električnom polju od $E/n_0 = 12$ Td. Rezultati su dobijeni primenom metoda više članova za rešavanje Boltzmann-ove jednačine.

sličnu fizičku interpretaciju kao komponente koje su nezavisne u odsustvu magnetskog polja. Na primer, $n_0^2 Q_{zyy}$ komponenta opisuje razliku u fluksu naelektrisanih čestica duž longitudinalnog pravca u centru roja i na transverzalnim ivicama duž y-ose. Komponenta $n_0^2 Q_{yyz}$ opisuje razliku u transverzalnom širenju duž y-pravca na frontu (u $q\mathbf{E}$ smeru) i na zadnjem delu roja (u $-q\mathbf{E}$ smeru). I preostale vandijagonalne komponente TTIII se mogu predstaviti na sličan način.
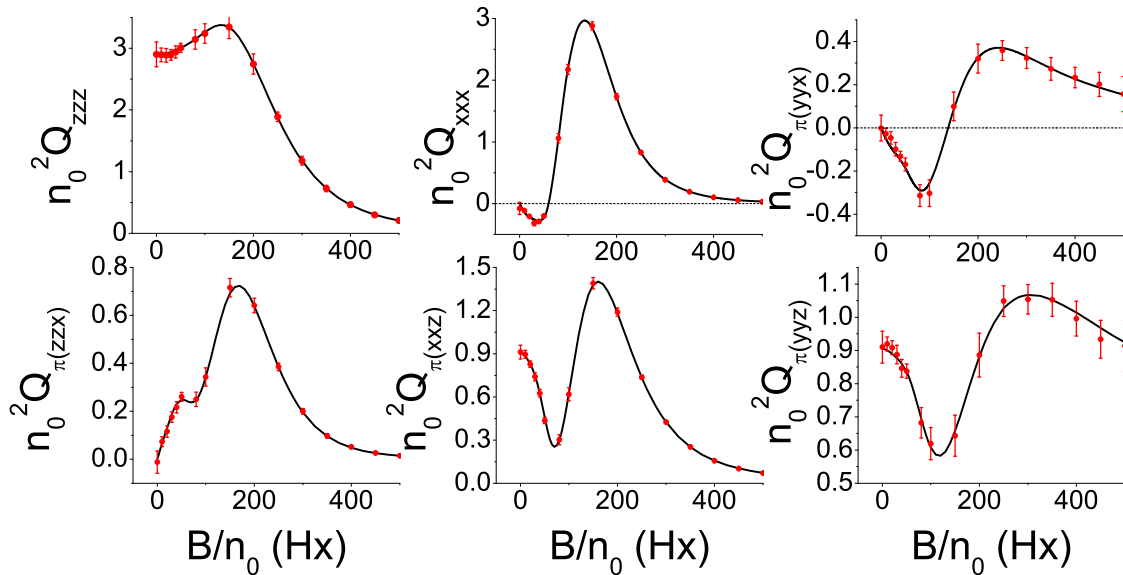
Slika 14: Poređenje vrednosti komponenti transportnog tenzora trećeg reda za roj elektrona u Reid-ovom modelnom gasu, koje su određene primenom Monte Carlo simulacija i metoda više članova za rešavanje Boltzmann-ove jednačine.

Poređenje vrednosti komponenti transportnog tenzora trećeg reda, koje su dobijene primenom Monte Carlo simulacija i momentnog metoda za numeričko rešavanje Boltzmann-ove jednačine izloženo je na slici 14. Pošto se u Monte Carlo simulacijama komponente TTIII raču-

naju na osnovu izraza koji su izvedeni iz generalisane difuzione jednačine, nije moguće izdvojiti pojedinačne vandijagonalne elemente TTIII u našim Monte Carlo simulacijama. To je posledica toga što su u generalisanoj difuzionoj jednačini svi indeksi TKIII kontrakovani sa parcijalnim izvodima koncentracije elektrona, čime se gubi deo informacije o strukturi tenzora. U našim Monte Carlo simulacijama je jedino moguće izračunati zbir onih komponenti TTIII koje imaju istu kombinaciju indeksa, poput $n_0^2 Q_{\pi(xxz)} = \frac{1}{3} n_0^2 (Q_{xxz} + Q_{xzx} + Q_{zxx})$, gde $\pi(xxz)$ označava srednju vrednost komponenti sa svim permutacijama indeksa x, y i z. Ovo znači da su na slici 14 prikazani Monte Carlo proračuni dijagonalnih komponenti TTIII i srednjih vrednosti onih vandijagonalnih komponenti koje imaju istu kombinaciju indeksa, kao i proračuni istih tih veličina primenom momentnog metoda za numeričko rešavanje Boltzmann-ove jednačine. Rezultati dobijeni na osnovu ove dve metode se jako dobro slažu. Može se uočiti da različite komponente TTIII imaju statističke fluktuacije različitog intenziteta (što je reprezentovano veličinom error barova). To je posledica razlika u intenzitetu statističkih fluktuacija pojedinačnih dinamičkih promenljivih, na osnovu kojih se računaju TTIII u Monte Carlo simulacijama.

4.7 Transportni koeficijenti trećeg reda za roj elektrona u Lucas-Saelee-evom modelnom gasu

Lucas-Saelee-ev model je modelni gas u kome je interakcija naelektrisanih čestica sa molekulima pozadinskog gasa opisana elastičnim sudarima, neelastičnim sudarima i jonizacijom [192]. Pri tome je koliziona frekvenca za elastične sudare nezavisna od energije, dok su preseci za neelastične sudare i jonizaciju direktno srazmerni energiji, za vrednosti energije iznad praga od 15.6 eV. Ovaj model su uveli Lucas i Saelee ne bi li ispitali uticaj jonizacije na transport elektrona, primenom Monte Carlo simulacija [192]. Ness i Robson su izučavali transport elektrona u ovom modelu da bi testirali ispravnost svog kompjuterskog koda za numeričko rešavanje Boltzmann-ove jednačine primenom momentnog metoda u prisustvu nekonzervativnih procesa [84]. Transport elektrona u Lucas-Saelee-evom modelu u prisustvu vremenski promenljivog električnog polja ispitivan je primenom vremenski zavisnog momentnog metoda za numeričko rešavanje Boltzmann-ove jednačine [193]. Zavisnosti transportnih osobina elektrona od ugla koji zaklapaju električno i magnetsko polje i od intenziteta magnetskog polja u promenljivoj konfiguraciji električnog i magnetskog polja razmatrane su primenom momentnog metoda za rešavanje Boltzmann-ove jednačine i Monte Carlo simulacija [67]. Prostorna relaksacija i prostorno razloženi nekonzervativni transport elektrona u uslovima stacionarnog Townsend-ovog eksperimenta (eng. steady state Townsend experiment) u Lucas-Saelee-evom modelu analizirani su primenom Monte Carlo simulacija [31].

Detalji modela su zadati na sledeći način:

$$\sigma_m(\epsilon) = 4\epsilon^{-1/2} \text{Å}^2 \quad \text{(elastični sudar)}$$

$$\sigma_{inel}(\epsilon) = \begin{cases} 0.1(1 - F)(\epsilon - 15.6) \text{ Å}^2, & \epsilon \geq 15.6 \text{ eV} \\ & \quad \text{(neelastični sudar)} \\ 0, & \epsilon < 15.6 \text{eV} \end{cases}$$

$$\sigma_{ion}(\epsilon) = \begin{cases} 0.1F(\epsilon - 15.6) \ \text{\AA}^2, & \epsilon \geq 15.6 \ \text{eV} \\ & \text{(jonizacija)} \\ 0, & \epsilon < 15.6 \text{eV} \end{cases}$$

$$P(q, \epsilon') = 1, m/m_0 = 10^{-3},$$

$$T_0 = 0 \ \text{K} , \tag{4.30}$$

Ovde su $\sigma_{el}(\epsilon)$, $\sigma_{ex}(\epsilon)$, i $\sigma_I(\epsilon)$ preseci za elastične sudare, neelastične sudare i jonizaciju respektivno, $P(q, \epsilon')$ je jonizaciona particiona funkcija, T_0 je temperatura pozadinskog gasa, F je parametar koji određuje odnos preseka za jonizaciju i neelastične sudare, a m i m_0 su mase naelektrisanih čestica i molekula pozadinskog gasa respektivno. U ovim definicijama preseka energija je data u elektronvoltima. Pošto je u ovom modelu rasejanje izotropno, $\sigma_{el}(\epsilon)$, $\sigma_{ex}(\epsilon)$, i $\sigma_I(\epsilon)$ predstavljaju totalne preseke. Argumenti jonizacione particione funkcije $P(q, \epsilon')$, q i ϵ', jesu udeo ukupne energije nakon jonizacije koja je predata izbačenom elektronu i početna energija primarnog elektrona pre jonizacije, respektivno. U ovom modelu je jonizaciona particiona funkcija izjednačena sa jedinicom, što znači da su sve vrednosti $0 \leq q \leq 1$ podjednako verovatne. Na niskim poljima na kojima je brzinski koeficijent za jonizaciju mali, transportne osobine naelektrisanih čestica nisu osetljive na jonizacionu particionu funkciju [84], međutim poznavanje $P(q, \epsilon')$ u realnim gasovima može biti potrebno na visokim poljima [47, 194, 195].

Uz pomoć Lucas-Saelee-evog modelnog gasa moguće je ispitati uticaj implicitnih i eksplicitnih efekata jonizacije na TKIII, što je posebno značajno s obzirom na to da uticaj nekonzervativnih procesa na TKIII nije detaljno istražen u literaturi, kao i zbog toga što se može očekivati da su TKIII u odnosu na brzinu drifta i difuzioni tenzor osetljiviji na prisustvo nekonzervativnih procesa . Zbog prisustva jonizacije u Lucas-Saelee-evom modelu fluks i balk vrednosti TKIII se međusobno razlikuju. Zato su u ovom potpoglavlju fluks i balk vrednosti TKIII označene superskriptima (f) i (b) respektivno.

Na slici 15 predstavljena je međuzavisnost $n_0^2 Q_{xzx}^{(f)}$ i $n_0^2 Q_{zzz}^{(f)}$ od E/n_0 za $F = 0.5$. Na poljima nižim od oko 5 Td $n_0^2 Q_{xzx}^{(f)}$ i $n_0^2 Q_{zzz}^{(f)}$ monotono rastu sa porastom E/n_0. U ovom opsegu polja je srednja energija elektrona niža od 4 eV (videti sliku 16), pa većina elektrona nema dovoljno energije za neelastični sudar ili jonizaciju. U ovom opsegu polja takođe važi $Q_{zzz} \approx 2Q_{xzx}$, zato što je koliziona frekvenca za elastične sudare u Lucas Saelee-evom modelu nezavisna od energije, kao u Maxwell-ovom modelu. Na višim poljima $n_0^2 Q_{xzx}^{(f)}$ i $n_0^2 Q_{zzz}^{(f)}$ monotono opadaju sa porastom E/n_0. Uzrok tome je što neelastični sudari i jonizacija pružaju snažan otpor difuzionom širenju naelektrisanih čestica u ovom opsegu polja.

Zavisnosti $n_0^2 Q_{zxx}^{(f)}$ i srednje energije naelektrisanih čestica od E/n_0 očitavaju se na slici 16. Primetno je da $n_0^2 Q_{zxx}^{(f)}$ komponenta ispoljava složeniji trend ponašanja od $n_0^2 Q_{zzz}^{(f)}$ i $n_0^2 Q_{xzx}^{(f)}$. Na poljima nižim od približno 5 Td ova komponenta je pozitivna i monotono raste sa porastom E/n_0. Zbog uticaja neelastičnih sudara i jonizacije na višim poljima do oko 13 Td $n_0^2 Q_{zxx}^{(f)}$ opada i postaje negativna na oko 5.9 Td. Na poljima između približno 13 Td i 59 Td $n_0^2 Q_{zxx}^{(f)}$ ponovo raste postajući pozitivna na oko 40 Td. U opsegu polja između 59 Td i 300 Td $n_0^2 Q_{zxx}^{(f)}$ opada sa porastom E/n_0. Zbog složenosti fizičke interpretacije TKIII nije lako objasniti zavisnost $n_0^2 Q_{zxx}^{(f)}$ od E/n_0. Međutim, može se uočiti da je u opsegu između 13 Td i 59 Td, gde $n_0^2 Q_{zxx}^{(f)}$
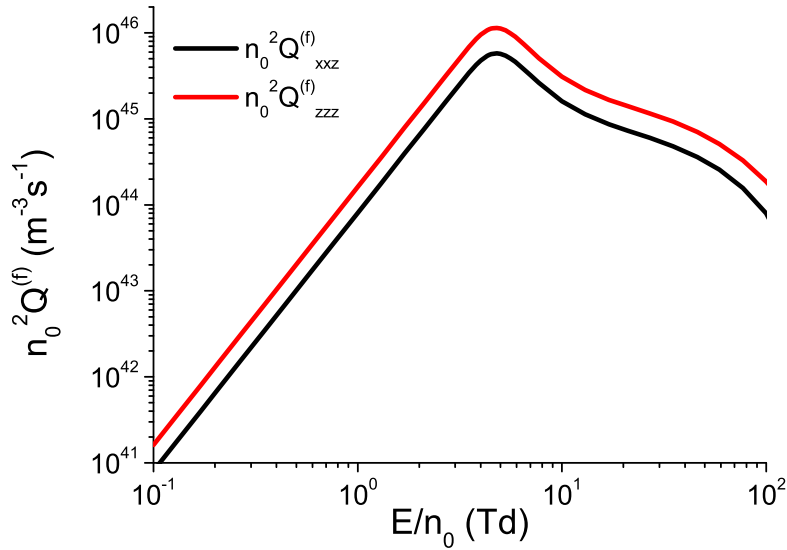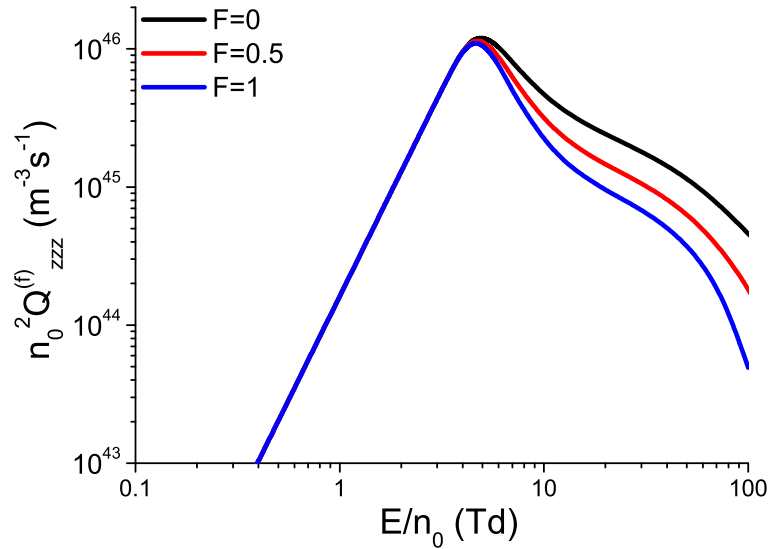
Slika 15: $n_0^2 Q_{xzx}^{(f)}$ i $n_0^2 Q_{zzz}^{(f)}$ komponente fluks transportnog tenzora trećeg reda u funkciji redukovanog električnog polja E/n_0 za roj elektrona u Lucas-Saelee-evom modelnom gasu, pri vrednosti parametra $F = 0.5$. Rezultati su dobijeni primenom metoda više članova za rešavanje Boltzmann-ove jednačine.
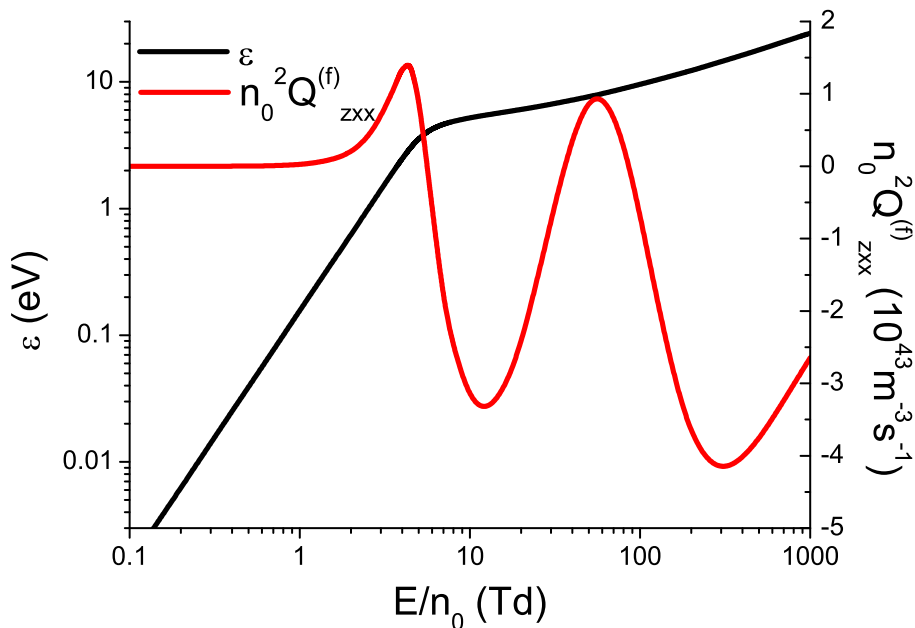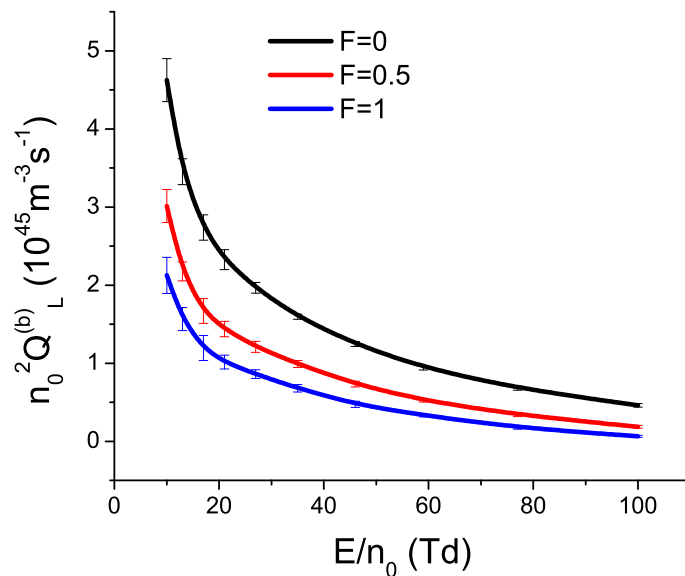

Slika 16: $n_0^2 Q_{zxx}^{(f)}$ komponenta fluks transportnog tenzora trećeg reda i srednja energija u funkciji redukovanog električnog polja E/n_0 za roj elektrona u Lucas-Saelee-evom modelnom gasu pri vrednosti parametra $F = 0.5$. Rezultati su dobijeni primenom metoda više članova za rešavanje Boltzmann-ove jednačine.

raste sa porastom E/n_0, porast srednje energije znatno sporiji nego na nižim poljima. Takođe se ispostavlja da je u opsegu polja iznad 59 Td, gde $n_0^2 Q_{zxx}^{(f)}$ opada sa porastom E/n_0, porast srednje energije brži nego u opsegu između 13 Td i 59Td. Ovo bi moglo ukazivati na to da $n_0^2 Q_{zxx}^{(f)}$ opada

sa porastom E/n_0 u onom opsegu polja u kome se kolizione frekvence za neelastične sudare i jonizaciju povećavaju dovoljno brzo sa porastom polja da nadjačaju efekat pojačanja usmerene komponente kretanja na $n_0^2 Q_{zxx}^{(f)}$ komponentu TTIII.

Slika 17: Longitudinalna komponenta fluks transportnog tenzora trećeg reda $n_0^2 Q_{zzz}^{(f)}$ u funkciji redukovanog električnog polja E/n_0 i vrednosti parametra F za roj elektrona u Lucas-Saelee-evom modelnom gasu. Rezultati su dobijeni primenom metoda više članova za rešavanje Boltzmann-ove jednačine.

Slika 18: Longitudinalna komponenta balk transportnog tenzora trećeg reda $n_0^2 Q_{zzz}^{(b)}$ u funkciji redukovanog električnog polja E/n_0 i vrednosti parametra F za roj elektrona u Lucas-Saelee-evom modelnom gasu. Rezultati su dobijeni primenom Monte Carlo simulacija.

Na slikama 17 i 18 su prikazane zavisnosti $n_0^2 Q_{zzz}^{(f)}$ i $n_0^2 Q_{zzz}^{(b)}$ od E/n_0, respektivno, za tri različite vrednosti parametra F. Sa slike 17 se može uočiti da $n_0^2 Q_{zzz}^{(f)}$ opada sa porastom F. Ovo je posledica implicitnih efekata jonizacije na TKIII, koji su posledica uticaja nekonzervativnih procesa na funkciju raspodele elektrona po energijama. Pri tome $n_0^2 Q_{zzz}^{(f)}$ opada sa porastom parametra F zbog hlađenja jonizacijom. Slika 18 pokazuje da i $n_0^2 Q_{zzz}^{(b)}$ opada sa porastom parametra F. Implicitni efekti utiču na isti način na fluks i balk komponente transportnih koeficijenata. Međutim, na vrednosti balk transportnih koeficijenata utiču i koeficijenti u hidrodinamičkom razvoju izvornog člana. Ovi koeficijenti u slučaju jonizacije povećavaju balk transportne koeficijente u odnosu na fluks transportne koeficijente, zato što se jonizacija uglavnom dešava na frontu roja, gde postoji veći broj visokoenergijskih elektrona. Opadanje $n_0^2 Q_{zzz}^{(b)}$ sa porastom F ukazuje na to da su implicitni efekti jonizacije na TKIII intenzivniji od eksplicitnih efekata. Eksplicitni efekti dovode do toga da je opadanje $n_0^2 Q_{zzz}^{(b)}$ sa porastom F manje intenzivno nego u slučaju $n_0^2 Q_{zzz}^{(f)}$.
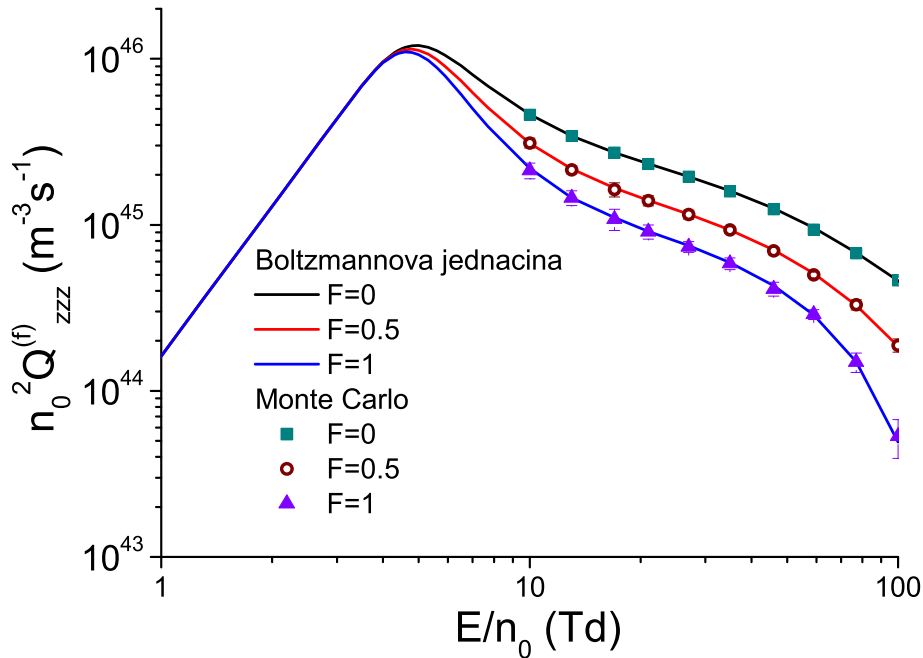
Slika 19: Poređenje vrednosti $n_0^2 Q_{zzz}^{(f)}$ komponente fluks transportnog tenzora trećeg reda koje su dobijene primenom Monte Carlo simulacija i metoda više članova za numeričko rešavanje Boltzmann-ove jednačine za roj elektrona u Lucas-Saelee-evom modelnom gasu.

Na slikama 19 i 20 je pokazano poređenje rezultata dobijenih na osnovu Monte Carlo simulacija i momentnog metoda za numeričko rešavanje Boltzmann-ove jednačine za komponente $n_0^2 Q_{zzz}^{(f)}$ i $n_0^2 Q_T^{(f)}$ respektivno. Može se videti da se rezultati dobijeni primenom ove dve nezavisne tehnike dobro slažu.
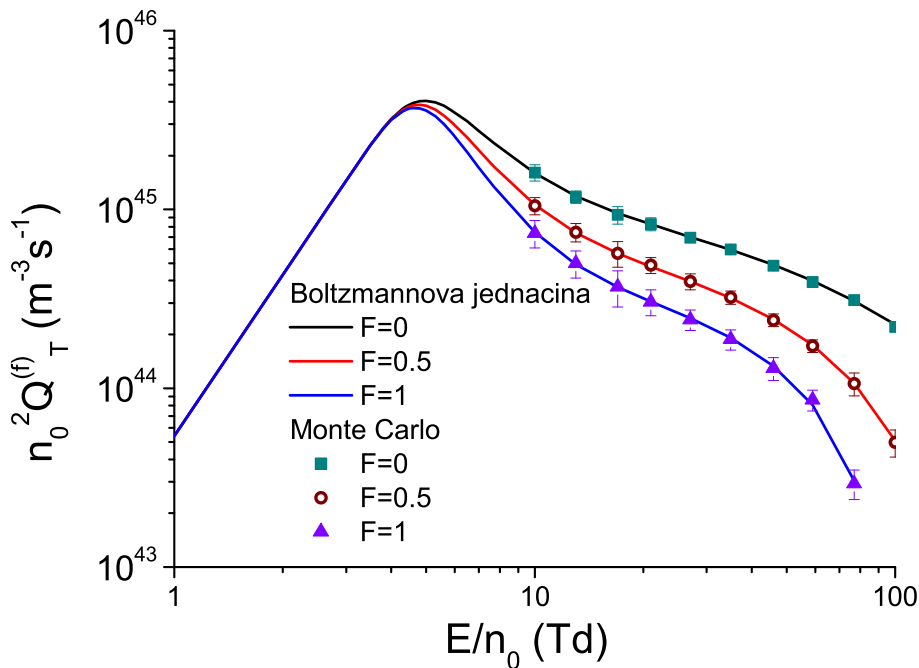
Slika 20: Poređenje vrednosti $n_0^2 Q_T^{(f)}$ komponente fluks transportnog tenzora trećeg reda koje su dobijene primenom Monte Carlo simulacija i metoda više članova za numeričko rešavanje Boltzmann-ove jednačine za roj elektrona u Lucas-Saelee-evom modelnom gasu.

4.8 Transportni koeficijenti trećeg reda za roj elektrona u modifikovanom Ness–Robsonovom modelnom gasu

Ness-Robson-ov model je uveden da bi se testirala momentna metoda za numeričko rešavanje Boltzmann-ove jednačine u prisustvu zahvata elektrona [84]. U Ness-Robson-ovom modelu je funkcionalna zavisnost preseka za zahvat elektrona od energije određena parametrom p. Nolan i saradnici su uveli novi modelni gas, koji je baziran na Ness-Robson-ovom modelu i Lucas–Saelee-evom modelu [196]. U njihovom modelnom gasu koliziona frekvenca za elastične sudare nezavisna je od energije, kao i u Ness-Robson-ovom modelu i Lucas–Saelee-evom modelu, dok su neelastični sudari uvedeni na isti način kao i u Lucas–Saelee-evom modelu. Presek za jonizaciju je isti kao u Lucas-Saelee-evom modelnom gasu i srazmeran je parametru F, dok je presek za zahvat elektrona isti kao u Ness-Robson-ovom modelu i srazmeran je parametru a. Nolanov model se svodi na Lucas-Saelee-ev model kada je $a = 0$. Ukoliko je $F = 0$ Nolanov model se svodi na modifikovani Ness-Robson-ov model, koji se razlikuje od Ness-Robson-ovog originalnog modela po veličini preseka za elastične sudare i po prisustvu neelastičnih sudara.

Nolan i saradnici su odredili transportne osobine elektrona u modifikovanom Ness-Robson-ovom modelu primenom Monte Carlo simulacija i momentnog metoda za rešavanje Boltzmann-ove jednačine [196]. Transport elektrona u originalnom Ness-Robson-ovom modelu u vremenski promenljivom električnom polju je ispitan primenom vremenski zavisnog momentnog metoda za numeričko rešavanje Boltzmann-ove jednačine [193]. Zavisnosti transportnih osobina elektrona od ugla koji zaklapaju električno i magnetsko polje i od intenziteta magnetskog polja u modifikovanom Ness-Robson-ovom modelu ispitane su primenom momentnog metoda za rešavanje

Boltzmann-ove jednačine i Monte Carlo simulacija [67]. Prostorna relaksacija i prostorno razloženi transport elektrona u uslovima stacionarnog Townsend-ovog eksperimenta (eng. steady state Townsend experiment) u modifikovanom Ness-Robson-ovom modelu su ispitani primenom Monte Carlo simulacija [31].

U ovom radu je razmatran transport elektrona u modifikovanom Ness-Robson-ovom modelu. Prednost modifikovanog Ness-Robson-ovog modela u odnosu na originalni model leži u mogućnosti ispitivanja kombinovanog uticaja zahvata elektrona i neelastičnih sudara. Detalji modifikovanog Ness-Robson-ovog modela su zadati na sledeći način:

$$\sigma_m(\epsilon) = 4\epsilon^{-1/2}\mathring{A}^2 \text{ (elastični sudar)}$$

$$\sigma_{inel}(\epsilon) = \begin{cases} 0.1(1-F)(\epsilon - 15.6) \ \mathring{A}^2, & \epsilon \geq 15.6 \text{ eV} \\ & \text{(neelastični sudar)} \\ 0, & \epsilon < 15.6\text{eV} \end{cases}$$

$$\sigma_a(\epsilon) = a\epsilon^p \text{ (zahvat elektrona)}$$

$$m/m_0 = 10^{-3},$$

$$T_0 = 0 \text{ K},\tag{4.31}$$

gde su $\sigma_{el}(\epsilon)$, $\sigma_{ex}(\epsilon)$, $\sigma_a(\epsilon)$ preseci za elastične sudare, neelastične suadre i zahvat elektrona, respektivno u funkciji energije elektrona ϵ, T_0 je temperatura pozadinskog gasa, a m i m_0 su mase elektrona i molekula pozadinskog gasa, respektivno. Vrednosti energije u gornjim definicijama preseka su date u eV. Parametri a i p određuju veličinu i funkcionalnu zavisnost preseka za zahvat elektrona, respektivno. Vrednosti parametra p, koje su razmatrane u radu Ness-a i Robson-a, u kome je prvi put korišćen ovaj model [84], kao i u našim proračunima, iznose -1, $-\frac{1}{2}$ i $\frac{1}{2}$. Ove tri vrednosti parametra p odgovaraju modelu grejanja zahvatom, modelu sa konstantnom kolizionom frekvencom za zahvat i modelu hlađenja zahvatom, respektivno. Za ova tri modela vrednosti parametra a koje su izabrane u našim proračunima iznose $8 \cdot 10^{-3}$, $2 \cdot 10^{-3}$, i $5 \cdot 10^{-4}$, respektivno.

Uz pomoć modifikovanog Ness Robson-ovog modela moguće je ispitati uticaj implicitnih i eksplicitnih efekata zahvata elektrona na TKIII. Ovo je važno zbog nedovoljne istraženosti uticaja nekonzervativnih procesa na TKIII u literaturi i zbog složenosti fizičke inerpretacije ovih transportnih koeficijenata. U ovom potpoglavlju su prikazani rezultati proračuna TKIII u modelu grejanja roja zahvatom elektrona i modelu hlađenja roja zahvatom elektrona. Rezultati proračuna u modelu u kome je koliziona frekvenca za zahvat elektrona nezavisna od energije podudaraju se sa rezultatima dobijenim u konzervativnom Lucas-Saelee-evom modelu (kada je parametar F jednak 0), za sve transportne parametre osim brzinskog koeficijenta za zahvat elektrona [196]. Ovo je posledica toga što je elektronski zahvat sa konstantnom kolizionom frekvencom ravnomerno raspoređen duž celog roja, pa ne utiče na transportne osobine elektrona. Ovde iznosimo i procentualne razlike rezultata dobijenih u modelima grejanja i hlađenja roja elektrona sa rezultatima dobijenim u konzervativnom Lucas-Saelee-evom modelu, radi dodatnog ilustrovanja implicitnih i eksplicitnih efekata zahvata elektrona na TKIII.

4.8.1 Transportni koeficijenti trećeg reda za roj elektrona u modelu grejanja zahvatom

Ovo potpoglavlje donosi rezultate proračuna transportnih koeficijenata rojeva elektrona u modelu grejanja roja zahvatom elektrona. Vrednosti parametara iz definicije preseka za zahvat a i p u našim proračunima iznose $8 \cdot 10^{-3}$ i -1, respektivno. Većina rezultata, koji su prikazani u ovom potpoglavlju, dobijena je primenom Monte Carlo simulacija. Rezultati dobijeni primenom momentnog metoda za numeričko rešavanje Boltzmann-ove jednačine su prikazani samo na kraju potpoglavlja, radi poređenja sa Monte Carlo rezultatima, zbog nemogućnosti postizanja konvergencije rezultata u našem kompjuterskom kodu za rešavanje Boltzmann-ove jednačine na redukovanim električnim poljima nižim od 2 Td. Ova nemogućnost postizanja konvergencije na niskim poljima je posledica intenzivnog uticaja zahvata elektrona na funkciju raspodele u ovom modelu. Naime, veliki broj Sonine polinoma je potreban u razvoju funkcije raspodele radi ispravnog reprezentovanja njene energijske zavisnosti, zbog intenzivnog grejanja roja zahvatom elektrona na niskim poljima, a ovo značajno otežava postizanje numeričke konvergencije rezultata [84].
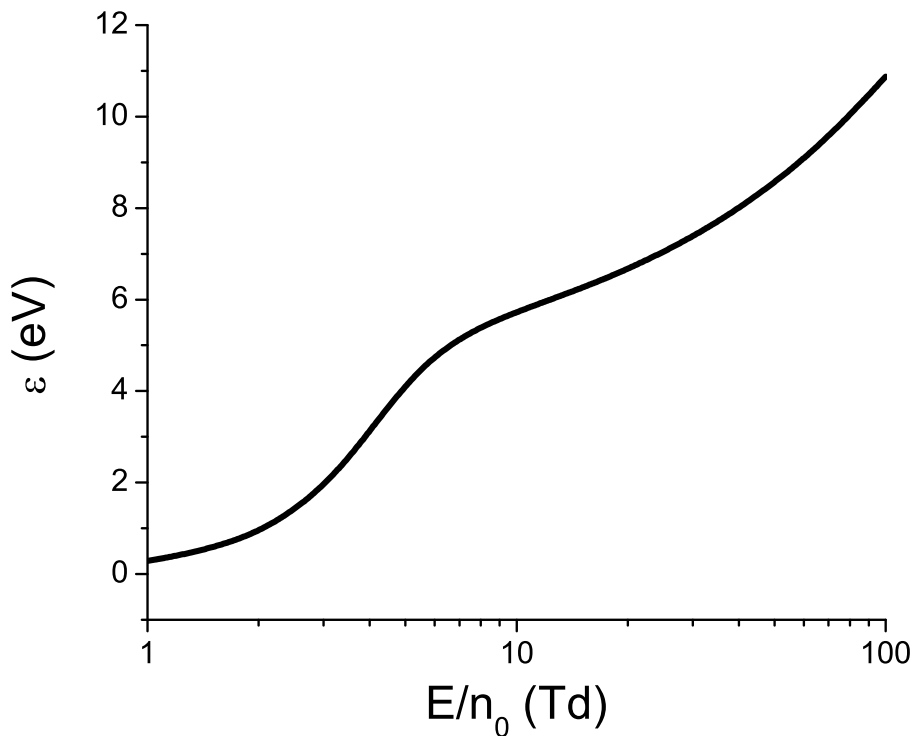
Slika 21: Srednja energija u funkciji E/n_0 za roj elektrona u modifikovanom Ness-Robson-ovom modelu za vrednosti parametara $a = 8 \cdot 10^{-3}$ i $p = -1$. Rezultati su dobijeni primenom Monte Carlo simulacija.

Na slici 21 je prikazana zavisnost srednje energije elektrona od E/n_0. Ovi rezultati su dobijeni primenom Monte Carlo simulacija. Može se videti da srednja energija elektrona monotno raste sa porastom E/n_0. Srednja energija elektrona u ovom modelu je veća od srednje energije u modelu hlađenja zahvatom, kao i od srednje energije u modelu sa konstantnom kolizionom
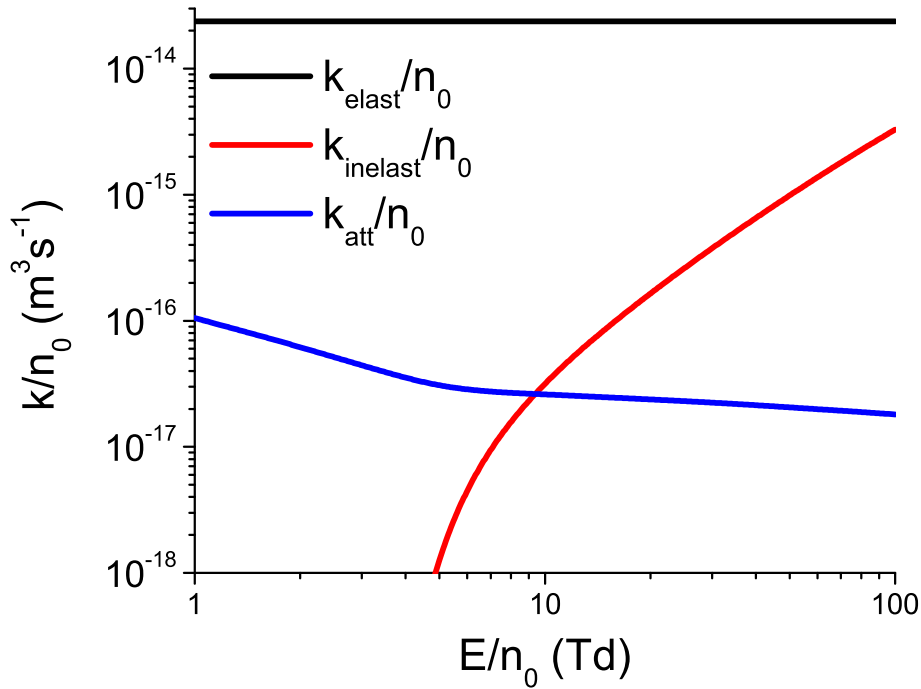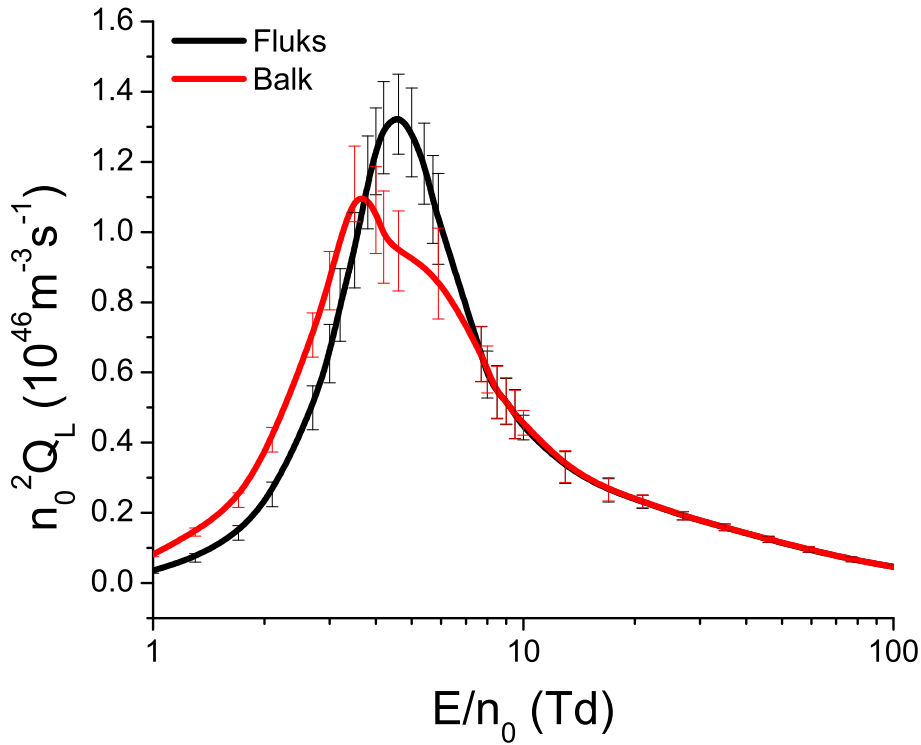
Slika 22: Brzinski koeficijenti za elastične sudare, neelastične sudare i zahvat elektrona u funkciji E/n_0 za roj elektrona u modifikovanom Ness-Robson-ovom modelu za vrednosti parametara $a = 8 \cdot 10^{-3}$ i $p = -1$. Rezultati su dobijeni na osnovu Monte Carlo simulacija.

frekvencom za zahvat elektrona. Slika 22 pokazuje zavisnosti brzinskih kofeicijenata za elastične sudare, neelastične sudare i zahvat elektrona od E/n_0. Brzinski koeficijent za elastične sudare je nezavisan od E/n_0, zato što je u ovom modelu koliziona frekvenca za elastične sudare nezavisna od energije elektrona. Brzinski koeficijent za zahvat elektrona opada sa porastom E/n_0, dok brzinski koeficijent za neelastične sudare raste sa porastom polja u celom opsegu E/n_0. Na poljima nižim od oko 10 Td brzinski koeficijent za zahvat elektrona viši je od brzinskog koeficijenta za neelastične sudare. Međutim, brzinski koeficijent za neelastične sudare se naglo povećava u opsegu E/n_0 od 4 Td do 10 Td i viši je od brzinskog koeficijenta za zahvat elektrona na poljima iznad 10 Td.

Zavisnosti fluks i balk vrednosti longitudinalne komponente TTIII $n_0^{(2)} Q_L$ od E/n_0 predstavljene su na slici 23. Rezultati su dobijeni primenom Monte Carlo simulacija. Na poljima nižim od oko 4 Td, $n_0^{(2)} Q_L^{(b)}$ je veće od $n_0^{(2)} Q_L^{(f)}$. Ali je zato $n_0^{(2)} Q_L^{(b)}$ manje od $n_0^{(2)} Q_L^{(f)}$ u opsegu polja između 4 Td i 8 Td. Na poljima iznad 8 Td su $n_0^{(2)} Q_L^{(b)}$ i $n_0^{(2)} Q_L^{(f)}$ praktično jednaki.

Srednja energija elektrona je manja od 3.1 eV na poljima nižim od 4 Td, pa u ovom opsegu polja većina elektrona nema dovoljno energije za neelastični sudar. U ovom opsegu polja brzinski koeficijenat za zahvat elektrona je preko 40 puta veći od brzinskog koeficijenta za neelastične sudare. Pored toga je energija izgubljena u elastičnim sudarima preko 4 puta veća od energije izgubljene u neelastičnim sudarima za vrednosti E/n_0 niže od 4 Td. Zato je u ovom opsegu polja transport elektrona pretežno određen elastičnim sudarima i zahvatom elektrona. Zbog porasta srednje energije elektrona duž longitudinalnog pravca, na zadnjem delu roja ima više niskoenergijskih elektrona, koji imaju veću kolizionu frekvencu za zahvat elektrona nego na
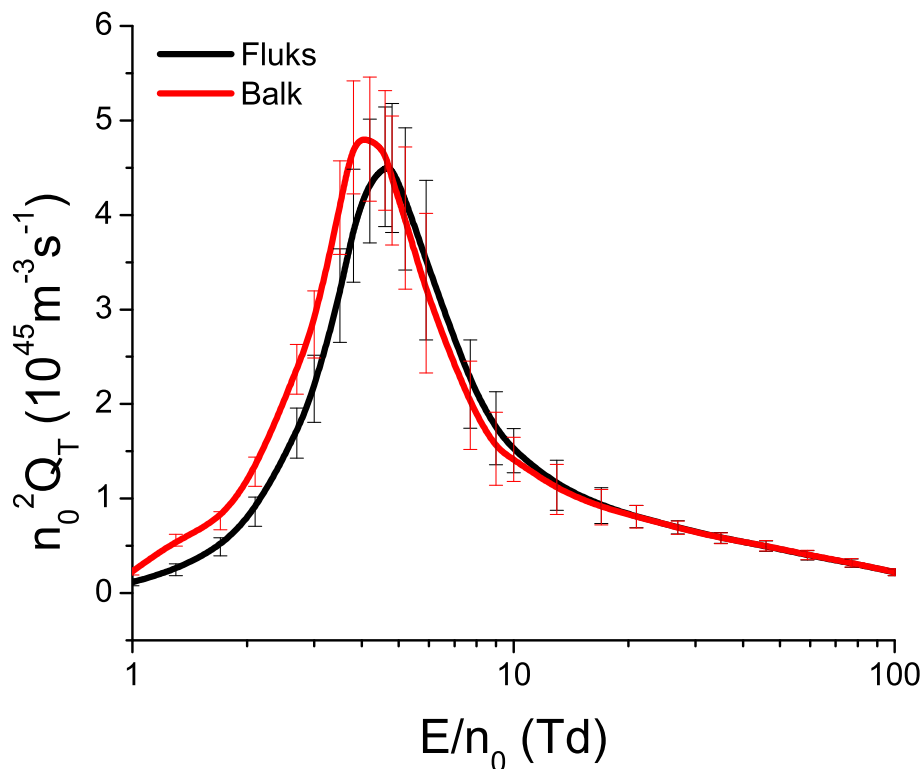
Slika 23: Balk i fluks longitudinalne komponente transportnog tenzora trećeg reda u funkciji E/n_0 za roj elektrona u modifikovanom Ness-Robson-ovom modelu za vrednosti parametara $a = 8 \cdot 10^{-3}$ i $p = -1$. Rezultati su dobijeni primenom Monte Carlo simulacija.

frontu roja . To znači kako u ovom opsegu polja, zahvat elektrona pojačava krivljenje prostornog profila roja ka prednjoj strani, u smeru drifta elektrona, zbog čega je $n_0^{(2)} Q_L^{(b)}$ veće od $n_0^{(2)} Q_L^{(f)}$.

Međutim, u opsegu polja između 5.9 Td i 7.7 Td je srednja energija elektrona izmedju 4.75 eV i 5.4 eV, pa veliki procenat visokoenergijskih elektrona ima dovoljno energije za neelastični sudar. U ovom opsegu polja je brzinski koeficijent za zahvat elektrona približno između 6 i 2 puta veći od brzinskog koeficijenta za neelastične sudare. Uz to je energija izgubljena u neelastičnim sudarima približno između 1.5 i 5 puta veća od energije izgubljene u elastičnim sudarima. Upravo zbog ovih razloga mnogi visokoenergijski elektroni na frontu roja izgube energiju u neelastičnom sudaru, nakon čega imaju veliku kolizionu frekvencu za zahvat elektrona. Pored toga, u ovom opsegu polja elektroni na zadnjoj strani roja imaju manju kolizionu frekvencu za elektronski zahvat nego što je to slučaj na nižim poljima, i to zbog porasta ukupne srednje energije sa povećanjem polja. Ovo dovodi do smanjenja krivljenja prostornog profila roja ka prednjoj strani, zbog čega je $n_0^{(2)} Q_L^{(b)}$ manje od $n_0^{(2)} Q_L^{(f)}$ u ovom opsegu polja. Na poljima višim od 8 Td, brzinski koeficijent za zahvat elektrona znatno je manji nego na nižim poljima. Pored toga, neelastični sudari su sve češći na visokim poljima, što dovodi do ravnomernije raspodele niskoenergijskih elektrona, koji imaju veliku kolizionu frekvencu za zahvat, duž prostornog profila roja. Zbog toga su fluks i balk vrednosti longitudinalne komponente TTIII praktično jednake na poljima višim od 8 Td.

Na slici 24 su prikazane zavisnosti $n_0^{(2)} Q_T^{(f)}$ i $n_0^{(2)} Q_T^{(b)}$ od E/n_0. Ovi rezultati su dobijeni na osnovu Monte Carlo simulacija. Na poljima nižim od približno 5 Td $n_0^{(2)} Q_T^{(b)}$ je veće od $n_0^{(2)} Q_T^{(f)}$.

Slika 24: Balk i fluks transverzalne komponente transportnog tenzora trećeg reda u funkciji E/n_0 za roj elektrona u modifikovanom Ness-Robson-ovom modelu za vrednosti parametara $a = 8 \cdot 10^{-3}$ i $p = -1$. Rezultati su dobijeni na osnovu Monte Carlo simulacija.

Međutim, u opsegu polja između 5 Td i 10 Td $n_0^{(2)}Q_T^{(b)}$ je manje od $n_0^{(2)}Q_T^{(f)}$, ali je ova razlika u okviru statističke nesigurnosti Monte Carlo simulacija. Za električna polja veća od 10 Td, balk i fluks vrednosti $n_0^{(2)}Q_T$ su praktično jednake.

Na poljima nižim od 5 Td elektroni češće učestvuju u zahvatu na zadnjoj strani roja, što dodatno povećava transverzalno širenje na prednjoj strani roja u odnosu na transverzalno širenje na zadnjoj strani roja. Zbog toga je u ovom opsegu polja $n_0^{(2)}Q_T^{(b)}$ veće od $n_0^{(2)}Q_T^{(f)}$. Na višim poljima pak mnogi visokoenergijski elektroni na frontu roja izgube energiju u neelastičnim sudarima pa budu zahvaćeni, što dovodi do smanjenja transverzalnog širenja na prednjoj strani roja i promene odnosa $n_0^{(2)}Q_T^{(f)}$ i $n_0^{(2)}Q_T^{(b)}$. Na poljima iznad 10 Td, fluks i balk vrednosti $n_0^{(2)}Q_T$ su praktično jednake. Ovo je posledica znatno manjih vrednosti brzinskog koeficijenta za zahvat elektrona u ovom opsegu polja u odnosu na niža polja, kao i ravnomernije raspodele niskoenergijskih elektrona duž prostornog profila roja zbog velike učestalosti neelastičnih sudara na visokim poljima.

Na slikama 25-28 navode se procentualne razlike transportnih veličina za rojeve elektrona u konzervativnom Lucas-Saelee-evom modelu i modelu grejanja zahvatom elektrona. Ove procentualne razlike su određene kao

$$\frac{X(\text{NR})}{X(\text{LS})} - 1, \tag{4.32}$$

gde su $X(\text{NR})$ i $X(\text{LS})$ vrednosti proizvoljne transportne veličine u modelu grejanja zahvatom

i u konzervativnom Lucas-Saelee-evom modelu, respektivno. Rezultati su dobijeni primenom Monte Carlo simulacija, pošto je u momentnoj metodi za numeričko rešavanje Boltzmann-ove jednačine teško postići konvergenciju rezultata na poljima nižim od 2 Td zbog velikog brzinskog koeficijenta za zahvat elektrona na niskim poljima.
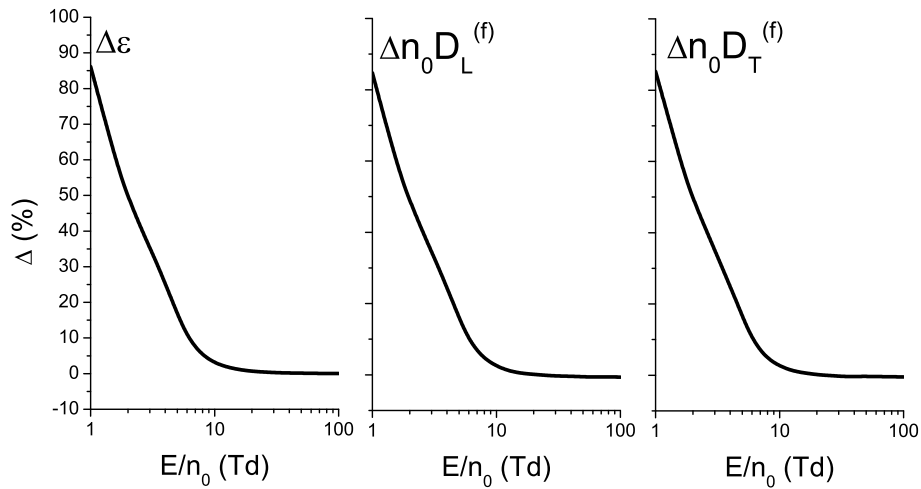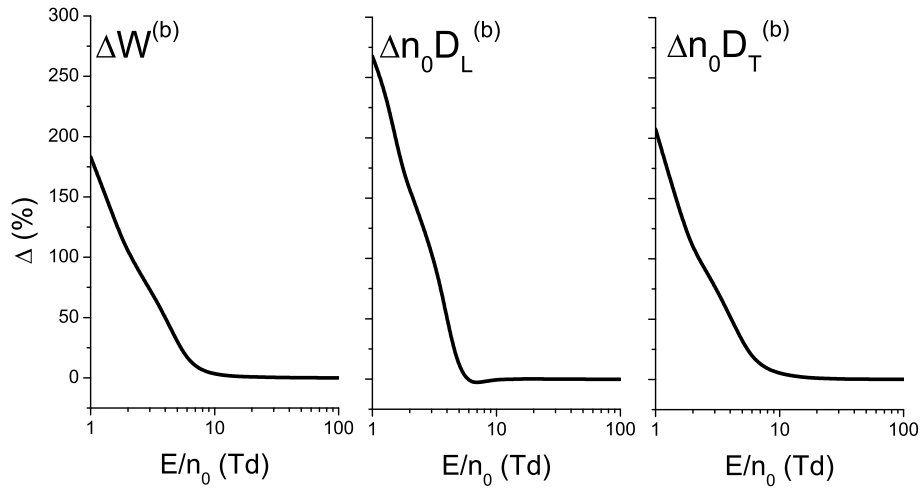

Slika 25: Procentualne razlike između vrednosti transportnih veličina za rojeve elektrona u modifikovanom Ness-Robson-ovom modelnom gasu (za vrednosti parametara $a = 8 \cdot 10^{-3}$ i $p = -1$) i u konzervativnom Lucas-Saelee-evom modelu (za F=0). Na ovom grafiku su prikazane procentualne razlike srednje energije, longitudinalne komponente fluks difuzionog tenzora $D_L^{(f)}$ i transverzalne komponente fluks difuzionog tenzora $D_T^{(f)}$. Rezultati su dobijeni primenom Monte Carlo simulacija.
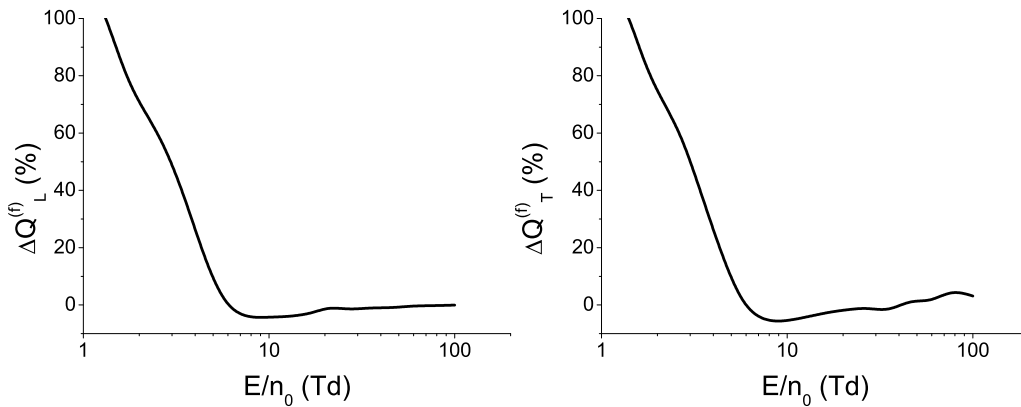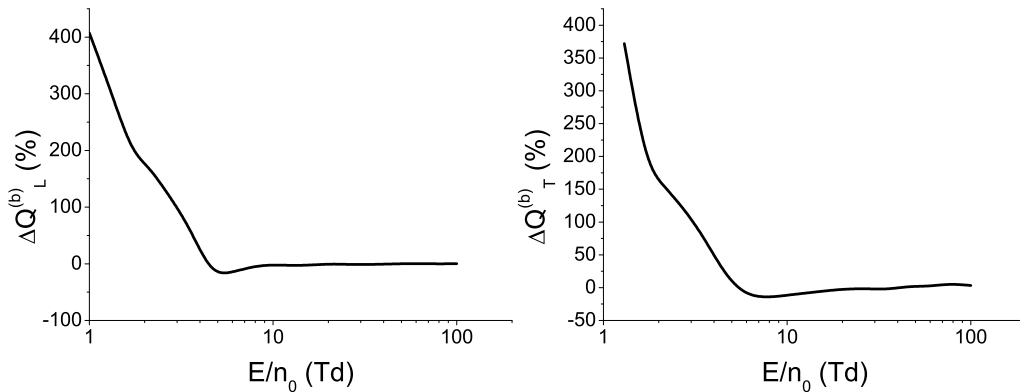

Slika 26: Procentualne razlike između vrednosti transportnih veličina za rojeve elektrona u modifikovanom Ness-Robson-ovom modelnom gasu (za vrednosti parametara $a = 8 \cdot 10^{-3}$ i $p = -1$) i u konzervativnom Lucas-Saelee-evom modelu (za F=0). Na ovom grafiku su prikazane procentualne razlike longitudinalne komponente fluks transportnog tenzora trećeg reda $Q_L^{(f)}$ i transverzalne komponente fluks transportnog tenzora trećeg reda $Q_T^{(f)}$. Rezultati su dobijeni primenom Monte Carlo simulacija.

Slika 25 prikazuje procentualne razlike između vrednosti srednje energije, longitudinalne komponente fluks difuzionog tenzora $D_L^{(f)}$ i transverzalne komponente fluks difuzionog tenzora

Slika 27: Procentualne razlike između vrednosti transportnih veličina za rojeve elektrona u modifikovanom Ness-Robson-ovom modelnom gasu (za vrednosti parametara $a = 8 \cdot 10^{-3}$ i $p = -1$) i u konzervativnom Lucas-Saelee-evom modelu (za F=0). Na ovom grafiku date su procentualne razlike balk brzine drifta $W^{(b)}$, longitudinalne komponente balk difuzionog tenzora $D_L^{(b)}$ i transverzalne komponente balk difuzionog tenzora $D_T^{(b)}$. Rezultati su dobijeni primenom Monte Carlo simulacija.

Slika 28: Procentualne razlike između vrednosti transportnih veličina za rojeve elektrona u modifikovanom Ness-Robson-ovom modelnom gasu (za vrednosti parametara $a = 8 \cdot 10^{-3}$ i $p = -1$) i u konzervativnom Lucas-Saelee-evom modelu (za F=0). Na grafiku su prikazane procentualne razlike longitudinalne komponente balk transportnog tenzora trećeg reda $Q_L^{(b)}$ i transverzalne komponente balk transportnog tenzora trećeg reda $Q_T^{(b)}$. Rezultati su dobijeni primenom Monte Carlo simulacija.
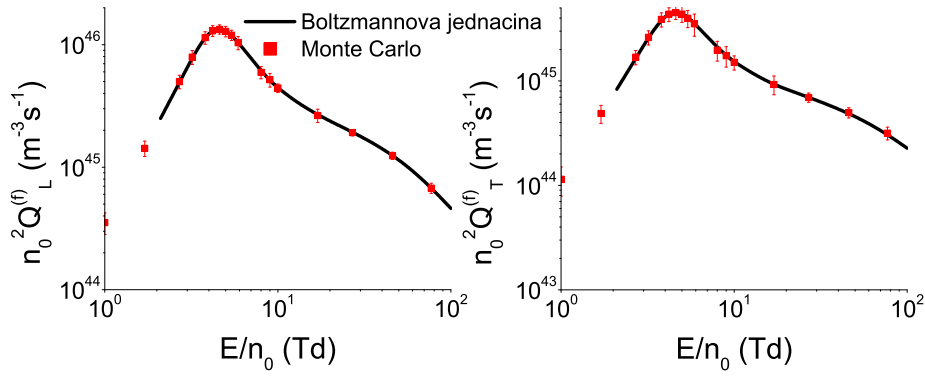
$D_T^{(f)}$ za rojeve elektrona u modifikovanom Ness-Robson-ovom modelu (za vrednosti parametara $a = 8 \cdot 10^{-3}$ i $p = -1$) i u konzervativnom Lucas-Saelee-evom modelu (za F=0). Procentualne razlike između vrednosti ove tri veličine u ova dva modelna gasa imaju vrlo slične brojne vrednosti u celom razmatranom opsegu redukovanog električnog polja E/n_0. Može se videti da su ove razlike najveće na niskim poljima. Na oko 1 Td su ove tri veličine za oko 85% veće u modifikovanom Ness-Robson-ovom modelu nego u konzervativnom Lucas-Saelee-evom modelu. Ove procentualne razlike opadaju sa povećanjem polja i dostižu plato na oko 10 Td, posle čega teže nuli na visokim poljima.

Na slici 26 se navode procentualne razlike, između vrednosti $Q_L^{(f)}$ i $Q_T^{(f)}$ za rojeve elektrona u modifikovanom Ness-Robson-ovom modelu (za $a = 8 \cdot 10^{-3}$ i $p = -1$) i konzervativnom Lucas-Saelee-evom modelu (F=0). Komponente $Q_L^{(f)}$ i $Q_T^{(f)}$ su veće za oko 110% u modelu grejanja zahvatom elektrona nego u konzervativnom Lucas-Saelee-evom modelu na oko 1 Td. Sa povećanjem polja ova razlika prvo opada, a onda na oko 6 Td postane zanemarljiva. U opsegu polja između 6 Td i 20 Td su obe komponente fluks TTIII veće u konzervativnom Lucas-Saelee-evom modelu nego u modelu grejanja zahvatom, ali je ova razlika u okviru statističke nesigurnosti Monte Carlo simulacija. Razlozi za promenu odnosa između vrednosti fluks komponenti TTIII u ova dva modela bi mogli da budu isti kao razlozi za promenu odnosa fluks i balk vrednosti TKIII u modelu grejanja zahvatom. Na višim poljima razlika između rezultata koji su dobijeni u ova dva modela opada ka nuli.

Na slici 27 su prikazane procentualne razlike između vrednosti balk brzine drifta $W^{(b)}$, longitudinalne komponente balk difuzionog tenzora $D_L^{(b)}$ i transverzalne komponente balk difuzionog tenzora $D_T^{(b)}$ u ova dva modela. Profili zavisnosti ovih procentualnih razlika od E/n_0 su na kvalitativnom nivou vrlo slični. Vrednosti balk brzine drifta su na niskim poljima (oko 1 Td) za oko 175% veće u modelu grejanja zahvatom nego u konzervativnom Lucas-Saelee-evom modelu. Ova razlika opada sa povećanjem polja i dostiže plato na oko 10 Td, posle čega teži nuli. Na poljima od oko 1 Td je $D_L^{(b)}$ veće za približno 275% u modelu grejanja zahvatom nego u konzervativnom Lucas-Saelee-evom modelu, dok u ovom opsegu polja odgovarajuća razlika za $D_T^{(b)}$ iznosi oko 250%. Ove procentualne razlike dostižu plato na oko 6 Td i 10 Td za $D_L^{(b)}$ i $D_T^{(b)}$, respektivno, posle čega teže nuli.

Dalje, slika 28 predstavlja procentualne razlike između vrednosti $Q_L^{(b)}$ i $Q_T^{(b)}$ u ova dva modela. Na niskim poljima (oko 1 Td), $Q_L^{(b)}$ je veće u modelu grejanja zahvatom nego u konzervativnom Lucas-Saelee-evom modelu za oko 400%. Odgovarajuća razlika između vrednosti $Q_T^{(b)}$ u ova dva modela i u ovom opsegu polja iznosi oko 350%. Procentualna razlika između vrednosti $Q_L^{(b)}$ i $Q_T^{(b)}$ u ova dva modelna gasa opada sa povećanjem polja. U opsegu polja između 4.5 Td i 10 Td je $Q_L^{(b)}$ veće u konzervativnom Lucas-Saelee-evom modelu nego u modelu grejanja zahvatom, ali je ova razlika u okviru statističke nesigurnosti Monte Carlo simulacija. Slično tome, $Q_T^{(b)}$ komponenta je veća u konzervativnom Lucas-Saelee-evom modelu nego u modelu grejanja zahvatom u opsegu polja između 5.5 Td i 20 Td, no i ova razlika ulazi u raspon statističke nesigurnosti. Razlozi za promenu odnosa balk komponenti TTIII u ova dva modela mogli bi da budu isti kao razlozi za promenu odnosa fluks i balk vrednosti TKIII u modelu grejanja zahvatom. Na poljima višim od 20 Td razlike između vrednosti $Q_L^{(b)}$ i $Q_T^{(b)}$ komponenti u ova dva modela opadaju ka nuli.

Na slici 29 je prikazano poređenje vrednosti $Q_L^{(f)}$ i $Q_T^{(f)}$ koje su dobijene na osnovu Monte Carlo simulacija i momentnog metoda za numeričko rešavanje Boltzmann-ove jednačine u modifikovanom Ness-Robson-ovom modelu za slučaj grejanja zahvatom elektrona. Rezultati koji su dobijeni primenom ove dve metode veoma se dobro slažu.

Slika 29: Poređenje vrednosti longitudinalne komponente fluks transportnog tenzora trećeg reda $Q_L^{(f)}$ i transverzalne komponente fluks transportnog tenzora trećeg reda $Q_T^{(f)}$ koje su dobijene primenom Monte Carlo simulacija i metoda više članova za rešavanje Boltzmann-ove jednačine za elektrone u modifikovanom Ness-Robson-ovom modelu za vrednosti parametara $a = 8 \cdot 10^{-3}$ i $p = -1$.

### 4.8.2 Transportni koeficijenti trećeg reda za roj elektrona u modelu hlađenja zahvatom

Ovo potpoglavlje donosi rezultate proračuna transportnih osobina rojeva elektrona u modelu hlađenja roja zahvatom elektrona. Vrednosti parametara iz definicije preseka za zahvat a i p u našim proračunima iznose $5 \cdot 10^{-4}$ i $\frac{1}{2}$, respektivno. Većina rezultata koji su prikazani u ovom potpoglavlju je dobijena primenom momentnog metoda za numeričko rešavanje Boltzmann-ove jednačine. Rezultati Monte Carlo simulacija su prikazani samo na kraju poglavlja radi poređenja sa rezultatima momentnog metoda za rešavanje Boltzmann-ove jednačine, kao i na graficima na kojima su prikazane balk vrednosti TKIII. Balk vrednosti TKIII ne mogu biti određene primenom trenutne verzije našeg kompjuterskog koda za numeričko rešavanje Boltzmann-ove jednačine momentnom metodom.

Na slici 30 je prikazana zavisnost srednje energije elektrona od E/n_0. Srednja energija monotono raste sa povećanjem polja. Primećuje se da su vrednosti srednje energije u modelu hlađenja zahvatom niže nego vrednosti srednje energije u modelu grejanja zahvatom i vrednosti u konzervativnom Lucas-Saelee-evom modelu. Grafik 31 pokazuje zavisnosti brzinskih koeficijenata za elastične sudare, neelastične sudare i zahvat elektrona od E/n_0. Brzinski koeficijenat za elastične sudare je nezavisan od E/n_0 zato što je koliziona frekvenca za elastične sudare nezavisna od energije u ovom modelu. S druge strane, brzinski koeficijenti za neelastične sudare i zahvat elektrona monotono rastu sa porastom E/n_0. Pri tome je brzinski koeficijent za zahvat elektrona viši od brzinskog koeficijenta za neelastične sudare na poljima nižim od oko 8.5 Td. Na višim poljima je brzinski koeficijenat za neelastične sudare viši od brzinskog koeficijenta za zahvat elektrona.

Prikaz zavisnosti $n_0^2 Q_L^{(f)}$ i $n_0^2 Q_L^{(b)}$ od E/n_0 dat je na slici 32. Ovi rezultati su dobijeni primenom Monte Carlo simulacija. U opsegu polja između 1 Td i 5 Td je $n_0^2 Q_L^{(f)}$ veće od $n_0^2 Q_L^{(b)}$. Međutim, u opsegu polja imeđu 5 Td i 21 Td je $n_0^2 Q_L^{(f)}$ manje od $n_0^2 Q_L^{(b)}$. Na višim poljima su
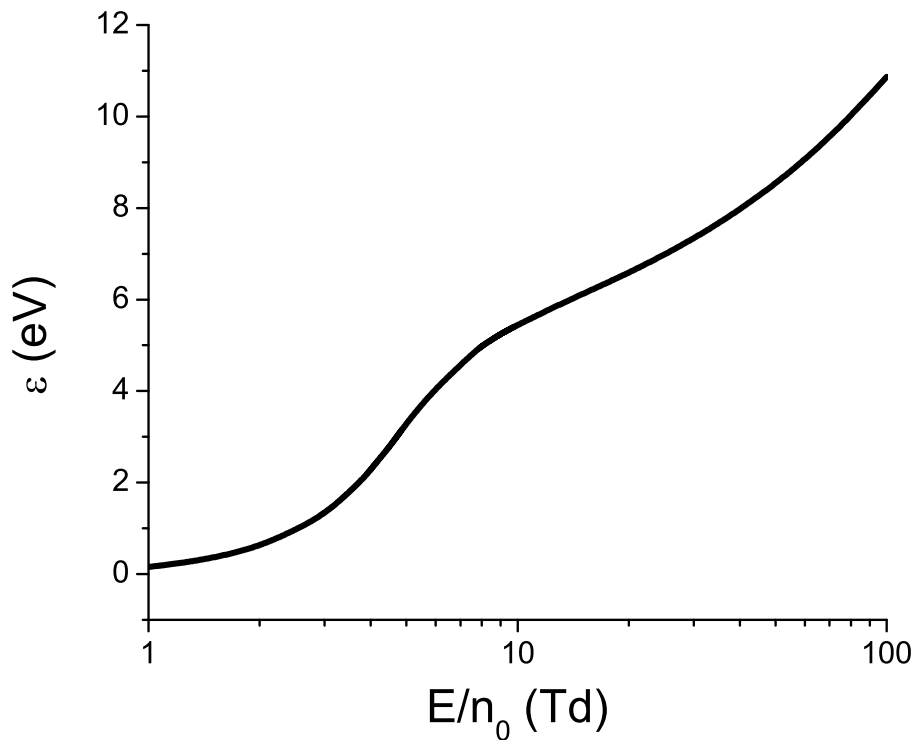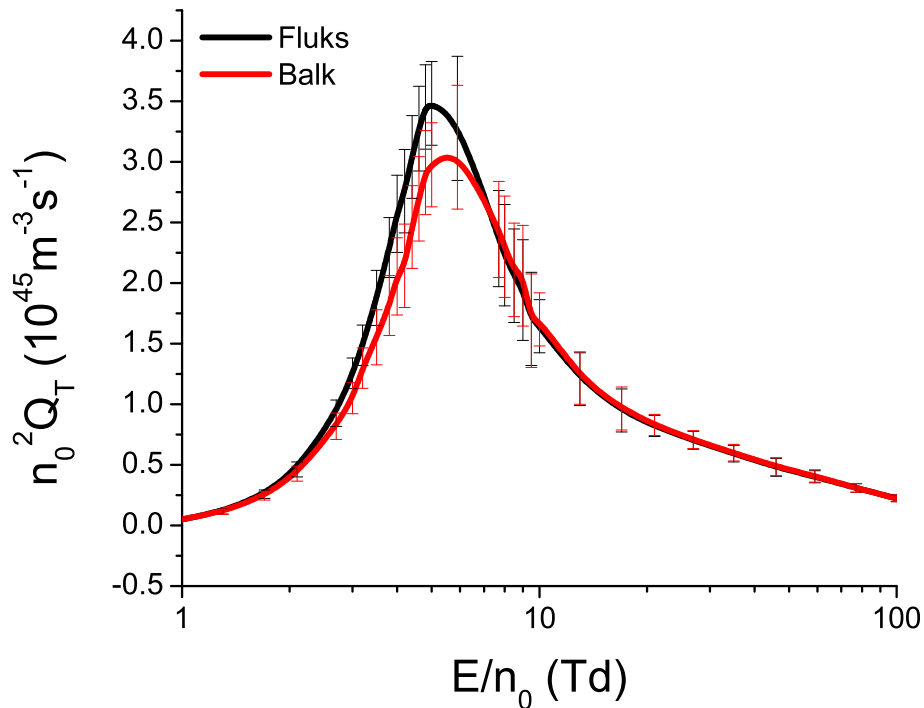
Slika 30: Srednja energija u funkciji E/n_0 za roj elektrona u modifikovanom Ness-Robson-ovom modelu za vrednosti parametara $a = 5 \cdot 10^{-4}$ i $p = \frac{1}{2}$. Rezultati su dobijeni primenom metoda više članova za rešavanje Boltzmann-ove jednačine.
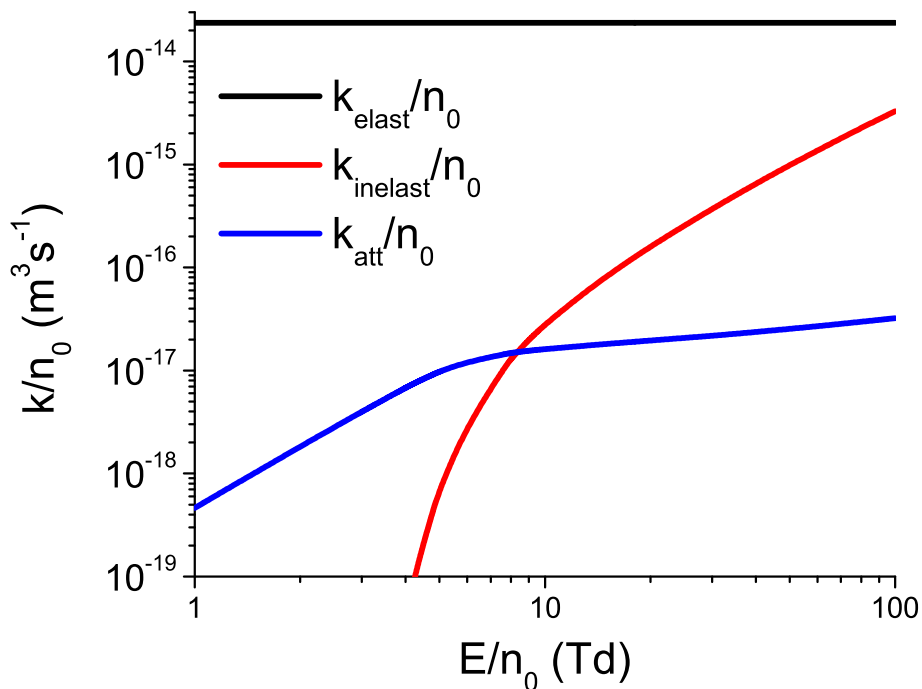
Slika 31: Brzinski koeficijenti za elastične sudare, neelastične sudare i zahvat elektrona u funkciji E/n_0 za roj elektrona u modifikovanom Ness-Robson-ovom modelu za vrednosti parametara $a = 5 \cdot 10^{-4}$ i $p = \frac{1}{2}$. Ovi rezultati su dobijeni na osnovu metoda više članova za rešavanje Boltzmann-ove jednačine.
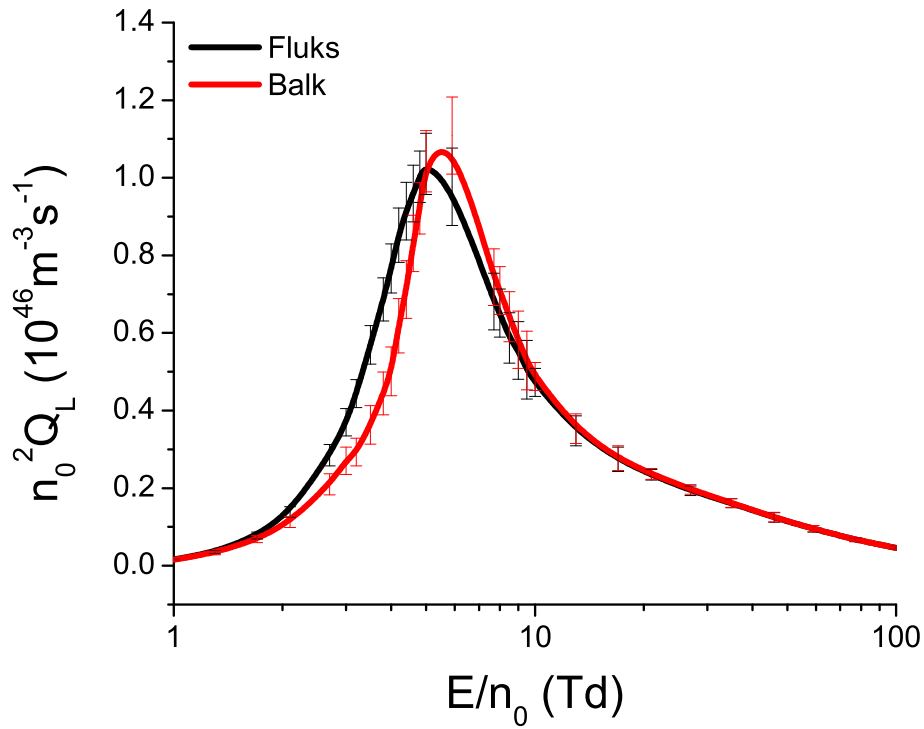
Slika 32: Balk i fluks longitudinalne komponente transportnog tenzora trećeg reda u funkciji E/n_0 za roj elektrona u modifikovanom Ness-Robson-ovom modelu za vrednosti parametara $a = 5 \cdot 10^{-4}$ i $p = \frac{1}{2}$. Rezultati su dobijeni primenom Monte Carlo simulacija.

Slika 33: Balk i fluks transverzalne komponente transportnog tenzora trećeg reda u funkciji E/n_0 za roj elektrona u modifikovanom Ness-Robson-ovom modelu za vrednosti parametara $a = 5 \cdot 10^{-4}$ i $p = \frac{1}{2}$. Rezultati su dobijeni uz pomoć Monte Carlo simulacija.

$n_0^2 Q_L^{(f)}$ i $n_0^2 Q_L^{(b)}$ praktično jednaki.

Na poljima nižim od 5 Td je srednja energija elektrona ispod 3.29 eV, pa većina elektrona nema dovoljno energije za neelastični sudar. Zato je u ovom opsegu polja brzinski koeficijent za neelastične sudare preko 14 puta manji od brzinskog koeficijenta za zahvat elektrona, dok je energija izgubljena u neelastičnim sudarima preko 4.4 puta manja od energije izgubljene u elastičnim sudarima. Zbog toga je transport elektrona u ovom opsegu polja pretežno određen elastičnim sudarima i zahvatom elektrona. U modelu hlađenja zahvatom elektrona se zahvat na niskim poljima dominantno dešava na frontu roja, gde je veći broj visokoenergijskih elektrona. Na tim osnovima, zahvat elektrona dovodi do smanjenja iskrivljenosti prostornog profila roja, u smeru drifta elektrona. Zato je u ovom opsegu polja $n_0^2 Q_L^{(f)}$ veće od $n_0^2 Q_L^{(b)}$.

Međutim, u opsegu polja između 5 Td i 21 Td srednja energija elektrona ima vrednost između 3.29 eV i 6.7 eV, pa znatno veći broj elektrona ima dovoljno energije za neelastični sudar. Zbog toga u ovom opsegu polja odnos brzinskih koeficijenata za neelastične sudare i zahvat elektrona uzima vrednosti iz opsega između 0.07 i 8.9. Uz to i odnos energije izgubljene u neelastičnim sudarima i elastičnim sudarima uzima vrednosti iz opsega između 0.22 i 58. Značajno povećanje brzinskog koeficijenta za neelastične sudare, u ovom opsegu polja, dovodi do toga da mnogi visokoenergisjki elektroni na frontu roja izgube energiju u neelastičnom sudaru, nakon čega im se smanji koliziona frekvenca za zahvat elektrona. Pored toga, na poljima višim od 5 Td, zbog porasta ukupne srednje energije, postoji više elektrona sa visokom kolizionom frekvencom za zahvat u zadnjem delu roja, nego što je to slučaj na nižim poljima. Zato je u ovom opsegu polja promenjen uticaj zahvata elektrona na iskrivljenost prostornog profila roja, u odnosu na niža polja, što dovodi do promene odnosa $n_0^2 Q_L^{(f)}$ i $n_0^2 Q_L^{(b)}$. U opsegu polja iznad 21 Td brzinski koeficijent za neelastične sudare je preko 8.9 puta veći od brzinskog koeficijenta za zahvat, uz šta je energija izgubljena u neelastičnim sudarima preko 58 puta veća od energije izgubljene u elastičnim sudarima. Dominantan uticaj neelastičnih sudara na transport elektrona u ovom opsegu polja značajno smanjuje uticaj zahvata elektrona na prostorni profil roja, što dovodi do toga da su $n_0^2 Q_L^{(f)}$ i $n_0^2 Q_L^{(b)}$ praktično jednaki u ovom opsegu polja.

Na slici 33 su prikazane zavisnosti $n_0^2 Q_T^{(f)}$ i $n_0^2 Q_T^{(b)}$ od E/n_0. Ovi rezultati su dobijeni prime-nom Monte Carlo simulacija. U opsegu polja između 1 Td i 7 Td je $n_0^2 Q_T^{(f)}$ veće od $n_0^2 Q_T^{(b)}$ (ali je razlika u okviru statističke nesigurnosti Monte Carlo simulacija), dok su na višim poljima ove veličine praktično jednake.

Na poljima nižim od 7 Td je brzinski koeficijent za zahvat elektrona preko dva puta veći od brzinskog koeficijenta za neelastične sudare. Na nižim poljima se zahvat elektrona dominantno dešava na frontu roja, gde ima više visokoenergijskih elektrona. Zato je transverzalno širenje elektrona na frontu roja umanjeno pod uticajem zahvata elektrona. Zbog toga je $n_0^2 Q_T^{(f)}$ nešto veće od $n_0^2 Q_T^{(b)}$ u ovom opsegu polja. Na poljima višim od 7 Td uticaj neelastičnih sudara na frontu roja i povećanje srednje energije na zadnjem delu roja smanjuju uticaj zahvata elektrona na transverzalnu komponentu TTIII, što dovodi do izjednačavanja $n_0^2 Q_T^{(f)}$ i $n_0^2 Q_T^{(b)}$ u ovom opsegu polja.

Slike 34-37 prikazuju procentualne razlike između vrednosti transportnih veličina za roje-
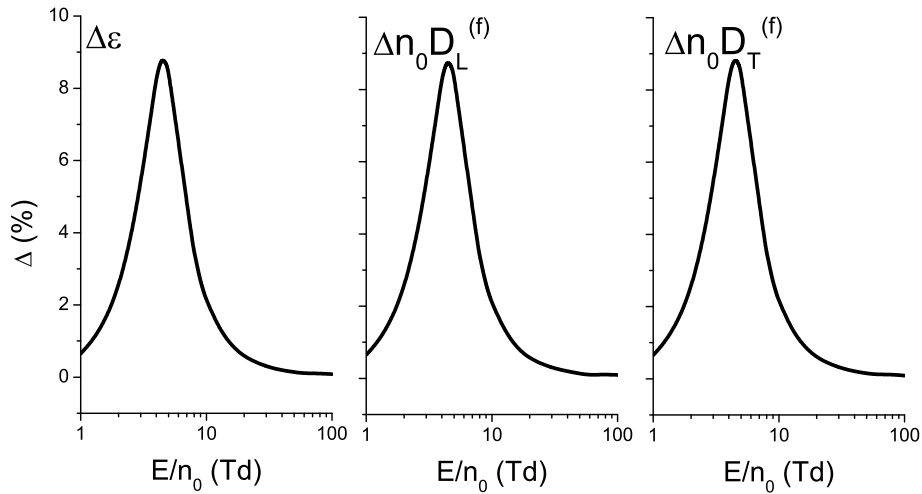
Slika 34: Procentualne razlike između vrednosti transportnih veličina za rojeve elektrona u modifikovanom Ness-Robson-ovom modelnom gasu (za vrednosti parametara $a = 5 \cdot 10^{-4}$ i $p = \frac{1}{2}$) i u konzervativnom Lucas-Saelee-evom modelu (za F=0). Na ovom grafiku su prikazane procentualne razlike srednje energije, longitudinalne komponente fluks difuzionog tenzora $D_L^{(f)}$ i transverzalne komponente fluks difuzionog tenzora $D_T^{(f)}$. Rezultati su dobijeni primenom metoda više članova za rešavanje Boltzmann-ove jednačine.
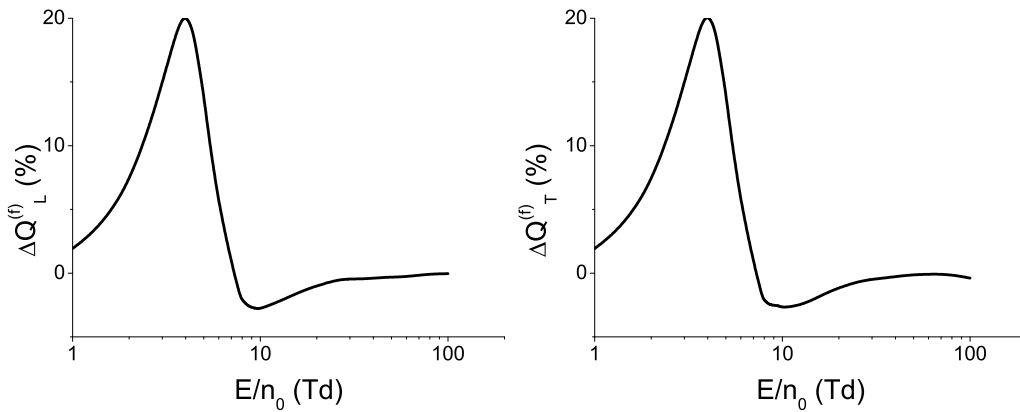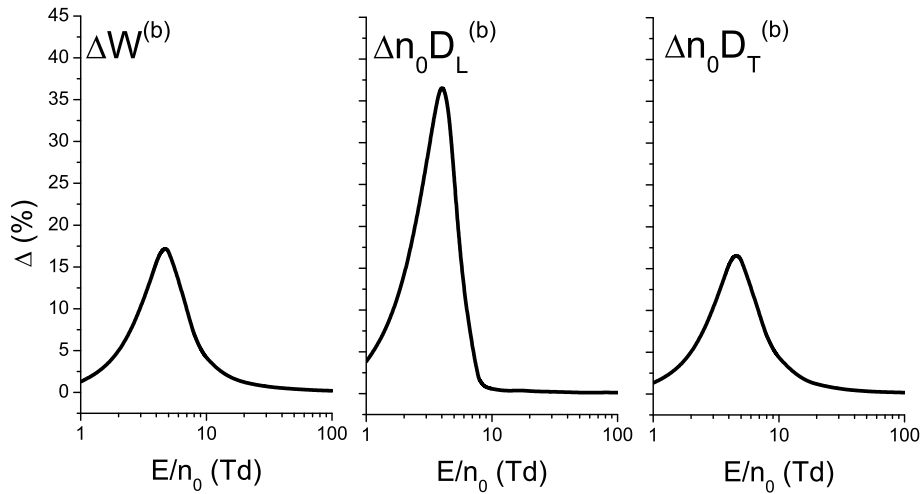

Slika 35: Procentualne razlike između vrednosti transportnih veličina za rojeve elektrona u modifikovanom Ness-Robson-ovom modelnom gasu (za vrednosti parametara $a = 5 \cdot 10^{-4}$ i $p = \frac{1}{2}$) i u konzervativnom Lucas-Saelee-evom modelu (za F=0). Na ovom grafiku su prikazane procentualne razlike longitudinalne komponente fluks transportnog tenzora trećeg reda $Q_L^{(f)}$ i transverzalne komponente fluks transportnog tenzora trećeg reda $Q_T^{(f)}$. Rezultati su dobijeni na osnovu metoda više članova za rešavanje Boltzmann-ove jednačine.

ve elektrona u konzervativnom Lucas-Saelee-evom modelu i modelu hlađenja zahvatom. Ove procentualne razlike su određene kao

$$1 - \frac{X(\mathrm{NR})}{X(\mathrm{LS})}, \tag{4.33}$$

gde su $X(\mathrm{NR})$ i $X(\mathrm{LS})$ vrednosti proizvoljne transportne veličine u modelu hlađenja zahvatom i u konzervativnom Lucas-Saelee-evom modelu, respektivno.

Na slici 34 se iznose procentualne razlike između vrednosti srednje energije, longitudinal-

Slika 36: Procentualne razlike između vrednosti transportnih veličina za rojeve elektrona u modifikovanom Ness-Robson-ovom modelnom gasu (za vrednosti parametara $a = 5 \cdot 10^{-4}$ i $p = \frac{1}{2}$) i u konzervativnom Lucas-Saelee-evom modelu (za F=0). Na ovom grafiku su prikazane procentualne razlike balk brzine drifta $W^{(b)}$, longitudinalne komponente balk difuzionog tenzora $D_L^{(b)}$ i transverzalne komponente balk difuzionog tenzora $D_T^{(b)}$. Rezultati su dobijeni na osnovu Monte Carlo simulacija.
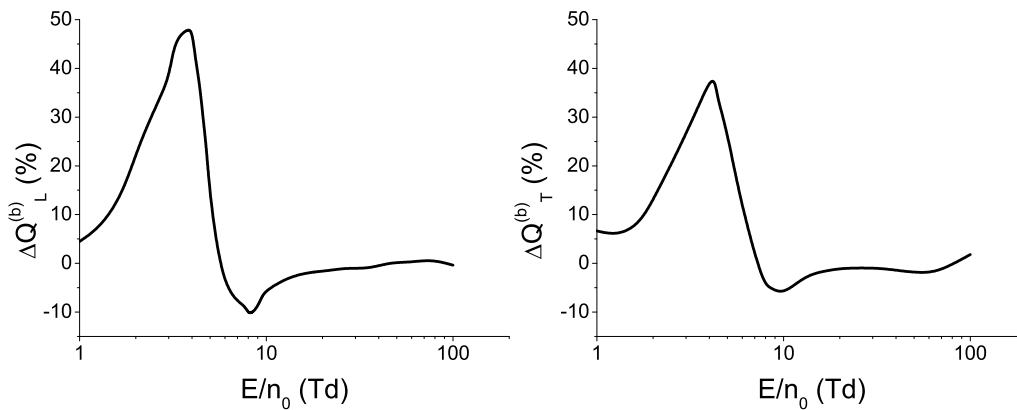
Slika 37: Procentualne razlike između vrednosti transportnih veličina za rojeve elektrona u modifikovanom Ness-Robson-ovom modelnom gasu (za vrednosti parametara $a = 5 \cdot 10^{-4}$ i $p = \frac{1}{2}$) i u konzervativnom Lucas-Saelee-evom modelu (za F=0). Na ovom grafiku su prikazane procentualne razlike longitudinalne komponente balk transportnog tenzora trećeg reda $Q_L^{(b)}$ i transverzalne komponente balk transportnog tenzora trećeg reda $Q_T^{(b)}$. Rezultati su dobijeni primenom Monte Carlo simulacija.

ne komponente fluks difuzionog tenzora $n_0 D_L^{(f)}$ i transverzalne komponente fluks difuzionog tenzora $n_0 D_T^{(f)}$ za rojeve elektrona u modifikovanom Ness-Robson-ovom modelu (za vrednosti parametara $a = 5 \cdot 10^{-4}$ i $p = \frac{1}{2}$) i konzervativnom Lucas-Saelee-evom modelu (F=0) u funkciji redukovanog električnog polja E/n_0. Ove procentualne razlike imaju vrlo slične brojne vrednosti za sve tri veličine, koje su veće u konzervativnom Lucas-Saelee-evom modelu nego u modelu hlađenja zahvatom elektrona u celom razmatranom opsegu E/n_0. Procentualne razlike između vrednosti ovih veličina u ova dva modela dostižu lokalne maksimume na oko 4.5 Td, koji iznose

oko 9%.

Na slikama 35 izložene su procentualne razlike između vrednosti $Q_L^{(f)}$ i $Q_T^{(f)}$ u ova dva modela. Obe komponente fluks TTIII su veće u konzervativnom Lucas-Saelee-evom modelu nego u modelu hlađenja zahvatom elektrona na poljima između 1 Td i 7 Td. Pri tome, procentualne razlike obe komponente TTIII dostižu lokalni maksimum na oko 4 Td koji iznosi oko 20%. Na poljima višim od 7 Td ove dve komponente TTIII su manje u konzervativnom Lucas-Saelee-evom modelu nego u modelu hlađenja zahvatom. Razlozi za promenu odnosa fluks komponenti TTIII u ova dva modela mogli bi biti isti kao razlozi za promenu odnosa fluks i balk vrednosti TKIII u modelu hlađenja zahvatom. Na poljima višim od 30 Td vrednosti komponenti fluks TTIII u konzervativnom Lucas-Saelee-evom modelu su praktično jednake odgovarajućim vrednostima u modelu hlađenja zahvatom elektrona.

Procentualne razlike između vrednosti balk brzine drifta $W^{(b)}$, longitudinalne komponente balk difuzionog tenzora $n_0 D_L^{(b)}$ i transverzalne komponente balk difuzionog tenzora $n_0 D_T^{(b)}$ u konzervativnom Lucas-Saelee-evom modelu i modelu hlađenja zahvatom elektrona nalaze se na slici 36. U celom opsegu E/n_0 su vrednosti ove tri veličine veće u konzervativnom Lucas-Saelee-evom modelu nego u modelu hlađenja zahvatom. Procentualna razlika $W^{(b)}$ u ova dva modela dostiže lokalni maksimum na oko 4.5 Td koji iznosi oko 17%. Slično tome, procentualna razlika $n_0 D_L^{(b)}$ dostiže lokalni maksimum na oko 4 Td koji iznosi oko 37%, dok procentualna razlika $n_0 D_T^{(b)}$ dostiže lokalni maksimum na oko 4.5 Td koji iznosi oko 17%.

Na slici 37 su prikazane procentualne razlike $n_0^2 Q_L^{(b)}$ i $n_0^2 Q_T^{(b)}$ u ova dva modela. Obe komponente balk TTIII su veće u konzervativnom Lucas-Saelee-evom modelu nego u modelu hlađenja zahvatom u opsegu E/n_0 između 1 Td i 7 Td. Na višim poljima su obe komponente balk TKIII veće u modelu hlađenja zahvatom nego u konzervativnom Lucas-Saelee-evom modelu, ali je ova razlika u okviru statističke nesigurnosti Monte Carlo simulacija. Razlozi za promenu odnosa balk komponenti TTIII u ova dva modela mogli bi biti isti kao razlozi za promenu odnosa fluks i balk vrednosti TKIII u modelu hlađenja zahvatom. Na poljima preko 100 Td je procentualna razlika između balk vrednosti TKIII u ova dva modela manja od statističke nesigurnosti rezultata koji su dobijeni primenom Monte Carlo simulacija.

Slika 38 daje poredjenja vrednosti $n_0^2 Q_L^{(f)}$ i $n_0^2 Q_T^{(f)}$, koje su dobijene primenom momentnog metoda za rešavanje Boltzmann-ove jednačine i Monte Carlo simulacija. Vidi se da se vrednosti dobijene primenom ove dve metode jako dobro slažu.

4.9   Zaključak

Nakon kratkog uvoda u potpoglavlju 4.1, potpoglavlje 4.2 razmatra fizičku interpretaciju komponenti transportnog tenzora trećeg reda. Na početku je određeno aproksimativno rešenje generalisane difuzione jednačine u kojoj su uzete u obzir komponente ovog transportnog tenzora. Ovo rešenje je određeno primenom razvoja Furijeovog transforma koncentracije čestica roja u Tejlorov red po komponentama transportnog tenzora trećeg reda. Potom je izračunat domi-
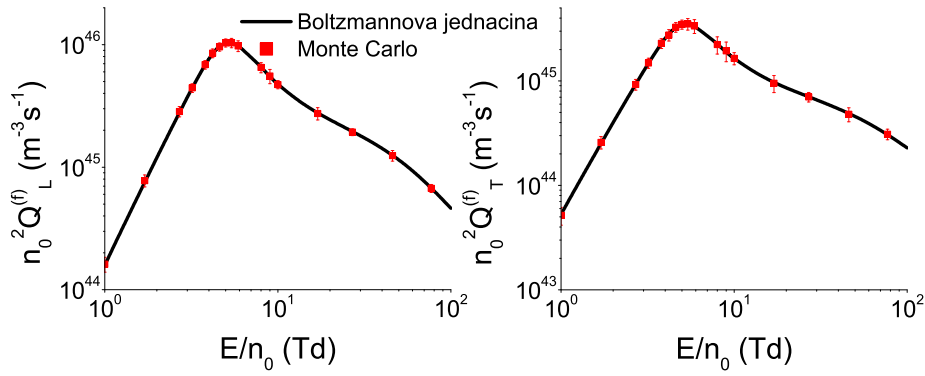
Slika 38: Poređenje vrednosti longitudinalne komponente fluks transportnog tenzora trećeg reda $Q_L^{(f)}$ i transverzalne komponente fluks transportnog tenzora trećeg reda $Q_T^{(f)}$ koje su dobijene primenom Monte Carlo simulacija i metoda više članova za rešavanje Boltzmann-ove jednačine za elektrone u modifikovanom Ness-Robson-ovom modelu za vrednosti parametara $a = 5 \cdot 10^{-4}$ i $p = \frac{1}{2}$.

nantan doprinos transportnih koeficijenata fluksu brzine čestica. Pokazano je da longitudinalna komponenta transportnog tenzora trećeg reda opisuje elongaciju ili kontrakciju prostornog profila roja duž longitudinalnog pravca. Slično tome dokazano je da vandijagonalne komponente ovog tenzora opisuju longitudinalnu varijaciju elongacije ili kontrakcije prostornog profila roja duž transverzalnog pravca. Na kraju ovog potpoglavlja tumači se znak komponenti transportnog tenzora trećeg reda. Ovaj znak zavisi od spoljašnjih električnih i magnetskih polja, od prostorne varijacije srednje energije čestica roja, kao i od energijske zavisnosti kolizionih frekvenci za elastične, neelastične i nekonzervativne sudare.

U potpoglavlju 4.3 su kratko se govori o uslovima korišćenim u Monte Carlo simulacijama. Ukazano je na neophodnost korišćenja velikog broja čestica (bar 10^7) u ovim simulacijama zbog smanjivanja statističke greške rezultata. U domenu numeričkog rešavanja Boltzmann-ove jednačine, razmotrena je potreba za korišćenje velikog broja sfernih harmonika (ponekad više od 5) i velikog broja Sonine polinoma (ponekad više od 100) u razvoju funkcije raspodele čestica roja, da bi se omogućilo precizno izračunavanje komponenti transportnog tenzora trećeg reda.

Centralna tema potpoglavlja 4.4 jesu transportni koeficijenti trećeg reda za rojeve elektrona u Maksvelovom modelu. Ovaj model je korišćen da bi se ispitala zavisnost komponenti transportnog tenzora trećeg reda od redukovanog električnog polja u prisustvu elastičnih sudara, čija koliziona frekvenca ne zavisi od energije. Uz pomoć ovog modela je takođe ispitan uticaj veličine preseka za elastične sudare na transportne koeficijente trećeg reda. Uočeno je da se ovi transportni koeficijenti monotono povećavaju sa porastom redukovanog električnog polja u ovom modelu, dok povećanje preseka za sudare dovodi do značajnog smanjenja ovih transportnih koeficijenata. Pored toga je uočeno da u ovom modelu važi približna jednakost $Q_{zzz} \approx 2Q_{xxz}$.

U potpoglavlju 4.5 su proučavani transportni koeficijenti trećeg reda za rojeve naelektrisanih čestica u modelu krutih sfera. Pomoću ovog modela je ispitan uticaj odnosa masa naelektrisanih čestica roja i neutralnih čestica pozadinske sredine na ove transportne koeficijente. Uočeno je

da apsolutna vrednost komponenti transportnog tenzora trećeg reda opada kada se masa naelektrisanih čestica približava masi neutralnih čestica pozadinske sredine. Međutim, doprinos komponenti ovog transportnog tenzora prostornom profilu roja se povećava kada se masa naelektrisanih čestica približava masi neutralnih čestica pozadinske sredine zbog porasta količnika Q_L/D_L^2 i Q_L/D_L^3.

Transportni tenzor trećeg reda za rojeve elektrona u Reid-ovom modelnom gasu tumači se u odeljku 4.6. Na osnovu ovog modela je proučen uticaj elastičnih i neelastičnih sudara sa rastućom kolizionom frekvencom na komponente ovog tenzora. Pored toga je ispitan uticaj magnetskog polja na transportne koeficijente trećeg reda. Primećeno je da je u odsustvu magnetskog polja Q_{zxx} komponenta negativna, dok su Q_{xxz} i Q_{zzz} komponente pozitivne u celom razmatranom opsegu redukovanog električnog polja. Takođe je uočeno da se apsolutne vrednosti sve tri komponente ovog tenzora, koje su međusobno nezavisne u odsustvu magnetskog polja, povećavaju sa porastom redukovanog električnog polja na najnižim poljima gde se neelastični sudari mogu zanemariti. Suprotno tome, apsolutne vrednosti ovih komponenti naglo opadaju sa porastom redukovanog električnog polja na višim poljima. Zavisnost komponenti transportnog tenzora trećeg reda od redukovanog magnetskog polja je složena, naročito u slučaju vandijagonalnih komponenti. Međutim, i komponente transportnog tenzora trećeg reda, koje postoje samo u prisustvu magnetskog polja, mogu se interpretirati na sličan način kao komponente koje postoje i u odsustvu magnetskog polja.

U potpoglavlju 4.7 su izučavani transportni koeficijenti trećeg reda za elektrone u Lucas-Saelee-evom modelnom gasu. Ovaj je model poslužio za utvrđivanje toga kako implicitni i eksplicitni efekti jonizacije utiču na transportne koeficijente trećeg reda. Pokazano je da eksplicitni efekti jonizacije povećavaju balk vrednosti transportnih koeficijenata trećeg reda, dok implicitni efekti dovode do snižavanja i balk i fluks vrednosti ovih transportnih koeficijenata. Pri tome balk vrednosti transportnih koeficijenata trećeg reda opadaju sa porastom parametra F, koji određuje parcijalnu verovatnoću za jonizaciju, što ukazuje na to da su u slučaju ovih transportnih koeficijenata implicitni efekti jonizacije izraženiji nego eksplicitni efekti.

Odeljak 4.8.1 razmatra transportne koeficijente trećeg reda za roj elektrona u modifikovanom Ness-Robson-ovom modelu grejanja roja zahvatom elektrona. Na osnovu ovog modela je ispitivan uticaj eksplicitnih i implicitnih efekata zahvata elektrona, kome koliziona frekvenca opada sa porastom energije, na transportne koeficijente trećeg reda. Uočeno je da su na najnižim poljima balk vrednosti ovih transportnih koeficijenata više od odgovarajućih fluks vrednosti, zbog grejanja roja zahvatom elektrona. No na srednjim poljima su fluks vrednosti više od balk vrednosti zbog kombinovanog efekta zahvata elektrona i neelastičnih sudara, dok su na najvišim poljima razlike između balk i fluks vrednosti zanemarljive. Na nižim poljima su fluks transportni koeficijenti trećeg reda viši u modelu grejanja zahvatom nego u modelu sa konstantnom kolizionom frekvencom za zahvat elektrona, dok je na višim poljima razlika između fluks vrednosti transportnih koeficijenata trećeg reda u ova dva modela jako mala.

U potpoglavlju 4.8.2 analizirani su transportni koeficijenti trećeg reda za roj elektrona u modifikovanom Ness-Robson-ovom modelu hlađenja roja zahvatom elektrona. Pomoću ovog

modela su ispitani eksplicitni i implicitni efekti zahvata elektrona, čija koliziona frekvenca se povećava sa porastom energije, na transportne koeficijente trećeg reda. U ovom slučaju je uticaj eksplicitnih efekata zahvata suprotan u odnosu na model koji je razmatran u potpoglavlju 4.8.1. Naime, na najnižim poljima su fluks vrednosti transportnih koeficijenata trećeg reda više od odgovarajućih balk vrednosti zbog eksplicitnih efekata hlađenja roja zahvatom elektrona. Međutim, na srednjim poljima su u slučaju longitudinalne komponente transportnog tenzira trećeg reda balk vrednosti više od odgovarajućih fluks vrednosti, ali je ova razlika u okviru statističke nesigurnosti Monte Carlo simulacija, dok ovaj efekat nije uočen za transverzalnu komponentu transportnog tenzora trećeg reda. Na višim poljima je razlika između balk i fluks vrednosti transportnog tenzora trećeg reda zanemarljiva. Fluks vrednosti transportnih koeficijenata trećeg reda su na nižim poljima više u modelu zahvata sa konstantnom kolizionom frekvencom nego u modelu hlađenja roja zahvatom elektrona, zbog implicitnih efekata zavata elektrona u ovom modelu. Na oko 10 Td su pak fluks vrednosti više u modelu hlađenja roja zahvatom elektrona, ali je u ovoj oblasti polja razlika između ova dva modela znatno manje izražena nego na nižim poljima. Na još višim poljima razlika između fluks vrednosti transportnih koeficijenata trećeg reda u ova dva modela je zanemarljiva.

5 Transportni koeficijenti trećeg reda za elektrone i pozitrone u realnim gasovima

5.1 Uvod

Peto poglavlje donosi rezultate naših proračuna transportnih koeficijenata trećeg reda (TKI-II) za elektrone i pozitrone u realnim gasovima. Ovi proračuni su urađeni primenom momentnog metoda za numeričko rešavanje Boltzmann-ove jednačine i Monte Carlo simulacija.

U potpoglavlju 5.2 opisana je korelacija između profila zavisnosti longitudinalne difuzije i longitudinalne komponente transportnog tenzora trećeg reda (TTIII) od redukovanog električnog polja. Odeljak 5.3 posvećen je rezultatima naših proracuna transportnih koeficijenata trećeg reda za elektrone u atomskim gasovima u kojima nije prisutan Ramsauer-Townsend-ov minimum (helijum i neon), dok su u potpoglavlju 5.4 prikazani rezultati naših proračuna transportnih koeficijenata trećeg reda za elektrone u atomskim gasovima u kojima je prisutan Ramsauer-Townsend-ov minimum (argon, kripton i ksenon). Rezultati naših proračuna transportnih koeficijenata trećeg reda za elektrone u molekularnim gasovima (N_2, CH_4, CF_4 i C_3F_8) tumače se u potpoglavlju 5.5. Odeljak 5.6 prezentuje značaj doprinosa transportnih koeficijenata trećeg reda prostornom profilu roja za elektrone u devet različitih gasova, a zatim i uticaj efekata, koji zavise od pritiska, na transportne koeficijente trećeg reda na primeru elektrona u molekularnom kiseoniku. U potpoglavlju 5.7 prikazani su naši rezultati vezani za transportne koeficijente trećeg reda za rojeve pozitrona u molekularnim gasovima (H_2, N_2 i CF_4).

5.2 Korelacija longitudinalne komponente transportnog tenzora trećeg reda i longitudinalne difuzije

Pri ispitivanju transportnih koeficijenata trećeg reda (TKIII) za elektrone i pozitrone u realnim gasovima primećeno je da postoji snažna korelacija između profila zavisnosti longitudinalne komponente transportnog tenzora trećeg reda TTIII, $n_0^2 Q_{zzz}$, od E/n_0 i odgovarajućih profila longitudinalne difuzije, $n_0 D_{zz}$. Naime, uočava se da kada $n_0 D_{zz}$ opada sa porastom E/n_0, $n_0^2 Q_{zzz}$ naglo opada. Međutim, $n_0^2 Q_{zzz}$ opada sa porastom E/n_0 i kada se $n_0 D_{zz}$ povećava, ako je porast $n_0 D_{zz}$ usporen (kada je $n_0 D_{zz}$ konkavna funkcija redukovanog električnog polja), ali je u ovom slučaju opadanje $n_0^2 Q_{zzz}$ manje intenzivno nego kada $n_0 D_{zz}$ opada. Longitudinalna komponenta TTIII se povećava sa porastom E/n_0 ako je porast $n_0 D_{zz}$ ubrzan (kada je $n_0 D_{zz}$ konveksna funkcija polja). Ova korelacija je primećena u svim atomskim i molekularnim gasovima koji su do sada razmatrani. Pri tome važi da je longitudinalna komponenta balk TTIII korelisana sa balk longitudinalnom difuzijom, dok je longitudinalna komponenta fluks TTIII korelisana sa fluks longitudinalnom difuzijom u uslovima u kojima se trendovi zavisnosti balk i fluks TKIII od E/n_0 razlikuju, poput transporta elektrona u jako elektronegativnim gasovima i transporta pozitrona u opsegu polja u kome postoji značajno formiranje pozitronijuma. Važno je pak naglasiti da ova korelacija ne postoji na jako niskim poljima zato što komponente

TTIII za razliku od komponenti difuzionog tenzora reprezentuju usmereno kretanje, pa sve komponente TTIII teže nuli kada E/n_0 teži nuli, a dijagonalne komponente difuzionog tenzora teže termalnoj vrednosti. Zato na najnižim poljima uvek postoji opseg u kome se komponente TTIII po apsolutnoj vrednosti monotono povećavaju sa porastom E/n_0, bez obzira na trend zavisnosti difuzionog tenzora od E/n_0. Takođe je važno naglastiti da se u profilima zavisnosti $n_0^2 Q_{zzz}$ i $n_0 D_{zz}$ od E/n_0 nekada dogodi da $n_0^2 Q_{zzz}$ malo prednjači u odnosu na $n_0 D_{zz}$. Na primer, događa se da $n_0^2 Q_{zzz}$ počne da se povećava na vrednostima E/n_0 na kojima $n_0 D_{zz}$ još uvek opada, ako na malo višim poljima $n_0 D_{zz}$ počne ubrzano da se povećava sa porastom E/n_0. Ovakvo ponašanje ukazuje na veću osetljivost TKIII na visokoenergijski deo funkcije raspodele naelektrisanih čestica.

Primećena korelacija longitudinalne komponente TTIII i longitudinalne difuzije može se razumeti na intuitivnom nivou. Zapravo, TKIII reprezentuju asimetrično odstupanje ukupnog difuzionog širenja od kretanja koje je opisano difuzionim tenzorom. Pritom je TKIII mala popravka u odnosu na simetrično difuziono širenje. Ovo znači da TKIII opisuju oblik difuzionog kretanja koje u sebi nosi znatno manju količinu energije i impulsa od kretanja koje je reprezentovano difuzionim tenzorom. Na osnovu toga se može očekivati da su TKIII znatno osetljiviji na elementarne sudarne procese od transportnih koeficijenata nižeg reda. Zbog toga $n_0^2 Q_{zzz}$ opada sa porastom E/n_0, ako je otpor difuzionom kretanju izazvan sudarima dovoljno intenzivan da uspori porast $n_0 D_{zz}$ sa povećanjem E/n_0. Sa druge strane, ako je otpor difuzionom kretanju toliko intenzivan da dovede do opadanja $n_0 D_{zz}$ sa porastom polja, to dovodi do intenzivnog opadanja $n_0^2 Q_{zzz}$. Međutim, $n_0^2 Q_{zzz}$ raste sa porastom polja, ako je otpor difuzionom kretanju dovoljno slab da omogući ubrzan porast $n_0 D_{zz}$ sa porastom E/n_0. Na osnovu primećene korelacije između profila zavisnosti $n_0^2 Q_{zzz}$ i $n_0 D_{zz}$ od E/n_0 može se jasno videti da su TKIII znatno osetljivi na elementarne sudarne procese od transportnih koeficijenata nižeg reda. Ovo ukazuje na to da bi TKIII bili jako korisni u proceduri za određivanje kompletnih skupova preseka na osnovu metode rojeva ako bi bili računati i mereni sa dovoljnom preciznošću.

Prisustvo ove korelacije između $n_0^2 Q_{zzz}$ i $n_0 D_{zz}$ znatno olakšava razumevanje trendova ponašanja $n_0^2 Q_{zzz}$ u funkciji polja – što je korisno u slučaju realnih gasova, koji imaju komplikovan skup preseka, te bi bilo jako teško tumačiti zavisnost $n_0^2 Q_{zzz}$ od E/n_0 direktno na osnovu preseka, zbog složenosti fizičke interpretacije TKIII i zbog njihove osetljivosti na elementarne sudarne procese.

Preostale dve komponente TTIII, koje su nezavisne u odsustvu magnetskog polja ($n_0^2 Q_{xxz}$ i $n_0^2 Q_{zxx}$), najčešće imaju profile zavisnosti od E/n_0 koji su na kvalitativnom nivou slični odgovarajućim profilima longitudinalne komponente TTIII. Uz to je jedna od vandijagonalnih komponenti $n_0^2 Q_{zxx}$ i $n_0^2 Q_{xxz}$ negativna kad god je koliziona frekvenca rastuća funkcija energije, dok je druga najčešće pozitivna. Kada porast kolizione frekvence sa energijom nije previše intenzivan, $n_0^2 Q_{zxx}$ komponenta je negativna, a $n_0^2 Q_{xxz}$ je pozitivna. Situacija je suprotna kada je porast kolizione frekvence sa energijom vrlo intenzivan. U tom slučaju je $n_0^2 Q_{xxz}$ negativna, dok je $n_0^2 Q_{zxx}$ najčešće pozitivna. U okolnostima kada je jedna od vandijagonalnih komponenti negativna, njihove apsolutne vrednosti dostižu maksimume i minimume za praktično iste

vrednosti polja. Ukoliko su obe komponente istog znaka, najčešće ispoljavaju iste kvalitativne trendove ponašanja. Ovo znači da se na osnovu korelacije longitudinalne komponente TTIII i longitudinalne difuzije u grubim crtama mogu razumeti trendovi zavisnosti sve tri nezavisne komponente TTIII od E/n_0.

5.3 Transportni koeficijenti trećeg reda za rojeve elektrona u atomskim gasovima bez Ramsauer-Townsend-ovog minimuma

5.3.1 Preliminarije

Na slikama 39 i 40 su prikazani setovi preseka za rasejanje elektrona u helijumu i neonu, respektivno, koji su korišćeni u našim proračunima. Set preseka za elektrone u helijumu, koji je korišćen u našem radu, razvijen je u Laboratoriji za gasnu elektroniku Instituta za fiziku u Beogradu. Ovaj set preseka za elektrone dat je u referenci [197].

Naši proračuni transportnih osobina elektrona u neonu koriste set preseka za elektrone u neonu koji je razvio Hayashi [198] na osnovu postojećeg seta preseka postavljenog u radu [199]. Hayashi-jev set preseka za rasejanje elektrona u neonu je prikazan u radu [200].
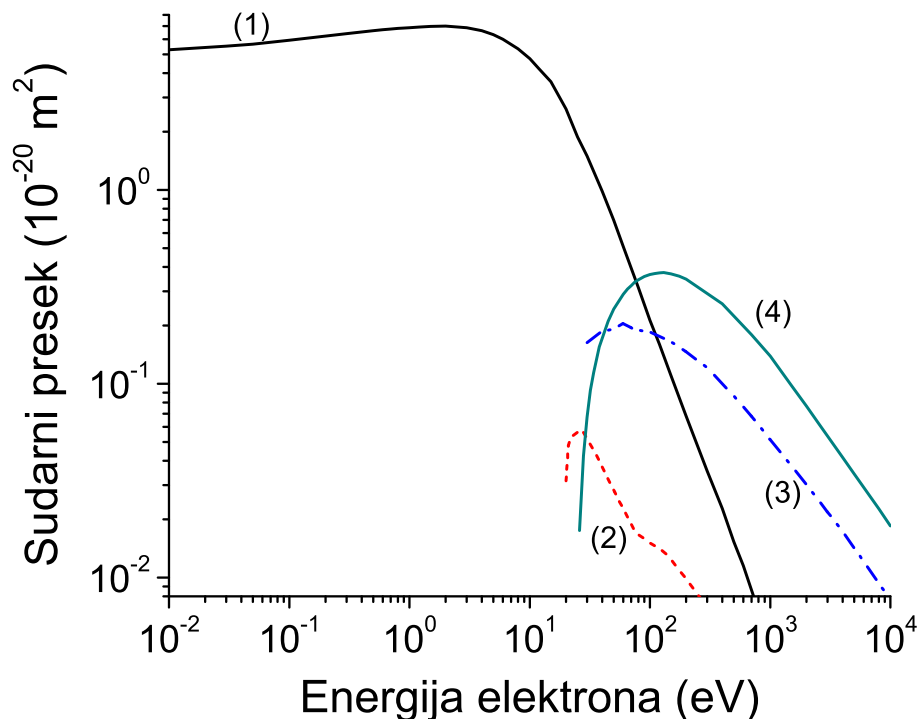
Slika 39: Set preseka za rasejanje elektrona u He: (1) transfer impulsa u elastičnim sudarima, elektronske ekscitacije (2), (3) i (4) jonizacija.
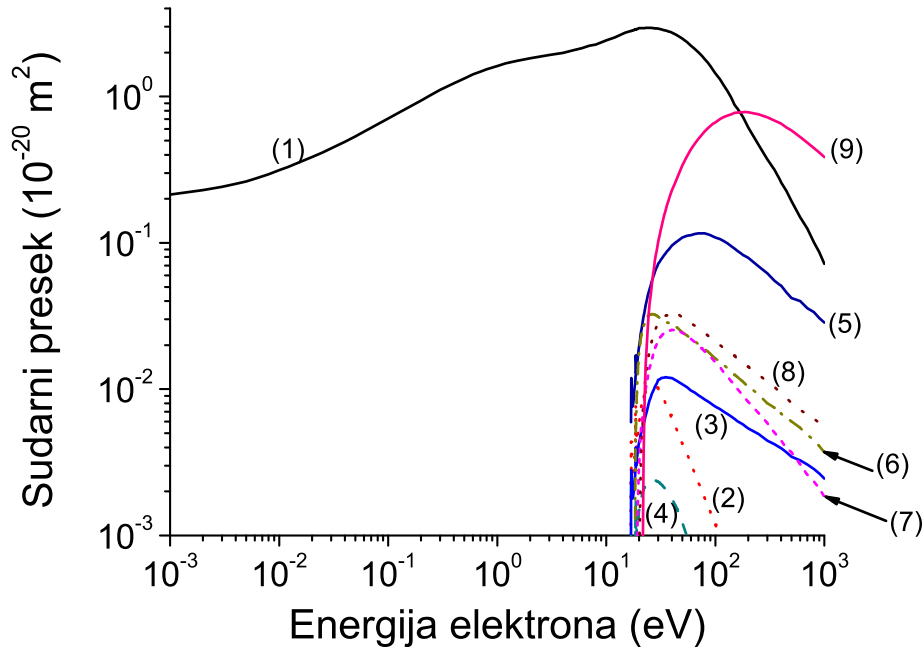
Slika 40: Set preseka za rasejanje elektrona u Ne: (1) transfer impulsa u elastičnim sudarima, elektronske ekscitacije (2) $2p^53s\ ^3P_2$, (3) $2p^53s\ ^3P_1$, (4) $2p^53s\ ^3P_0$, (5) $2p^53s\ ^1P_1$, (6) $2p^53p\ ^3S_1$, (7) $2p^53p\ ^2P$, (8) $2p^54s\ ^2S$ i (9) jonizacija.
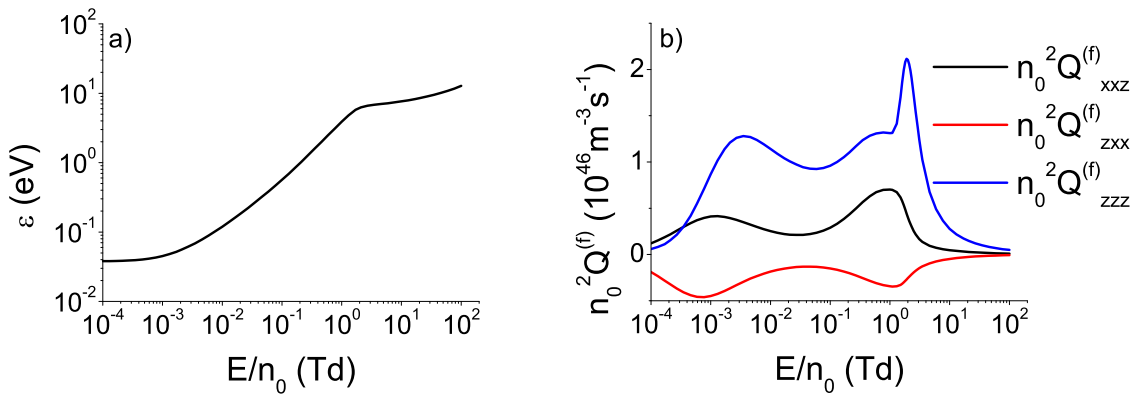
5.3.2 Rezultati

Na slici 41 a) je prikazana srednja energija za elektrone u helijumu, dok su $n_0^2Q_{xxz}$, $n_0^2Q_{zxx}$ i $n_0^2Q_{zzz}$ komponente TTIII za elektrone u helijumu prikazane na slici 41 b). Ovi rezultati su dobijeni na osnovu numeričkih multi term rešenja Boltzmann-ove jednačine. Komponente $n_0^2Q_{xxz}$ i $n_0^2Q_{zzz}$ su pozitivne u celom opsegu polja, pri čemu je $n_0^2Q_{zxx}$ komponenta negativna na poljima nižim od približno 10 Td, dok je na višim poljima pozitivna. Sve tri komponente TTIII se po apsolutnoj vrednosti povećavaju na poljima nižim od oko 8 Td. Istovremeno je ovaj porast najintenzivniji u opsegu polja između približno 2 Td i 8 Td. Na poljima između približno 8 Td i 50 Td $n_0^2Q_{xxz}$ i $n_0^2Q_{zzz}$ naglo opadaju sa porastom polja, dok se $n_0^2Q_{zxx}$ komponenta povećava, ali je ovaj porast sporiji u opsegu polja između približno 10 Td i 50 Td. U opsegu polja između približno 50 Td i 100 Td se sve tri komponente TTIII naglo povećavaju sa porastom polja.

Na poljima nižim od približno 2 Td je srednja energija elektrona niža od 1.2 eV, pa je transport elektrona određen elastičnim sudarima. Pri tome se većina elektrona nalazi u energijskoj oblasti u kojoj se presek za transfer impulsa u elastičnim sudarima povećava sa porastom energije (od 0.01 eV do 3 eV), dok se najenergičniji elektroni nalaze u energijskoj oblasti u kojoj ovaj presek postepeno opada sa porastom energije (između približno 3 eV i 8 eV). Ovo dovodi do postepenog porasta apsolutnih vrednosti komponenti TTIII sa porastom polja. Međutim, u opsegu polja između približno 2 Td i 8 Td je srednja energija elektrona između približno 1 eV i 5 eV, pa se veliki procenat elektrona nalazi u energijskoj oblasti u kojoj presek za transfer impulsa u elastičnim sudarima opada sa porastom energije, dok se najenergičniji elektroni nalaže u energijskoj oblasti između 5 eV i 20 eV, u kojoj je opadanje preseka za elastične sudare sa porastom energije vrlo intenzivno. Zbog toga se u ovom opsegu polja $n_0^2Q_{xxz}$ i $n_0^2Q_{zzz}$ naglo
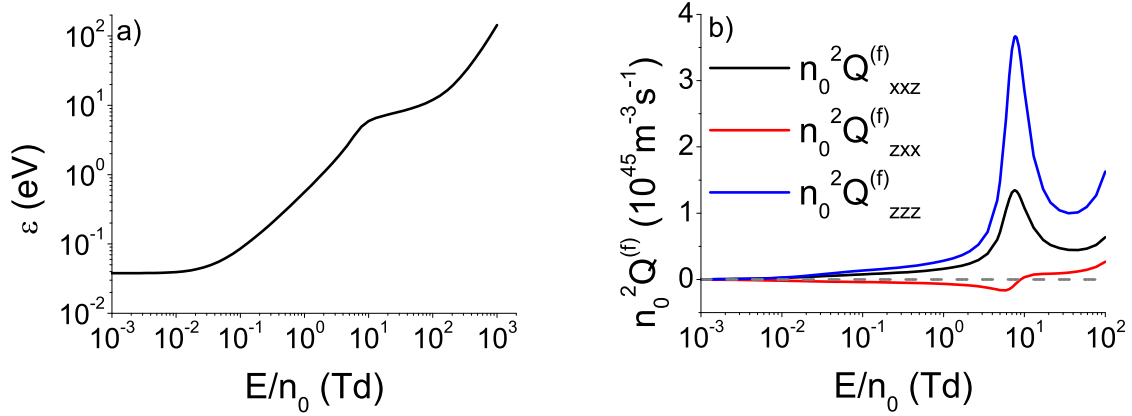
Slika 41: Srednja energija i $n_0^2 Q_{xxz}$, $n_0^2 Q_{zxx}$ i $n_0^2 Q_{zzz}$ komponente fluks transportnog tenzora trećeg reda za roj elektrona u helijumu u funkciji E/n_0. Rezultati su dobijeni primenom metoda više članova za rešavanje Boltzmann-ove jednačine.

povećavaju sa porastom E/n_0, a $n_0^2 Q_{zxx}$ komponenta se povećava po apsolutinoj vrednosti do približno 6 Td, nakon čega menja trend ponašanja. Na poljima u između približno 8 Td i 50 Td je srednja energija elektrona između 5 eV i 9 eV. U ovom opsegu polja najenergičniji elektroni imaju energiju višu od 20 eV, pa mogu da učestvuju u neelastičnim sudarima. Pošto neelastič- ni sudari pružaju snažan otpor difuzionom kretanju, $n_0^2 Q_{xxz}$ i $n_0^2 Q_{zzz}$ naglo opadaju u ovom opsegu polja, dok je $n_0^2 Q_{zxx}$ komponenta skoro konstantna u opsegu polja između približno 20 Td i 50 Td. Na višim poljima se sve tri komponente TTIII naglo povećavaju sa porastom polja. Razlozi za ovaj porast komponenti TTIII bi mogli da budu povećanje srednje energije elektrona i povećanje usmerene komponente kretanja sa porastom E/n_0, ako povećanje otpora difuzionom kretanju nije dovoljno intenzivno da nadjača ove efekte.


Slika 42: Srednja energija i $n_0^2 Q_{xxz}$, $n_0^2 Q_{zxx}$ i $n_0^2 Q_{zzz}$ komponente fluks transportnog tenzora trećeg reda za roj elektrona u neonu u funkciji E/n_0. Ovi rezultati su dobijeni uz pomoć metoda više članova za rešavanje Boltzmann-ove jednačine.

Na slici 42 a) prikazana je srednja energija za elektrone u neonu, dok su $n_0^2 Q_{xxz}$, $n_0^2 Q_{zxx}$ i $n_0^2 Q_{zzz}$ komponente TTIII za elektrone u neonu predstavljene na slici 42 b). Za razliku od komponenti $n_0^2 Q_{xxz}$ i $n_0^2 Q_{zzz}$ koje su pozitivne, komponenta $n_0^2 Q_{zxx}$ je negativna u celom opsegu E/n_0. Negativnost $n_0^2 Q_{zxx}$ komponente se može pripisati tome što se koliziona frekvenca po-

većava sa porastom energije u širokom energijskom opsegu. Naime, presek za transfer impulsa u elastičnim sudarima se povećava do oko 30 eV, nakon čega se preseci za neelastične sudare i jonizaciju naglo povećavaju sa porastom energije. Ipak, porast kolizione frekvence sa porastom energije nije dovoljno intenzivan da $n_0^2 Q_{xxz}$ i $n_0^2 Q_{zzz}$ komponente postanu negativne. Na poljima do oko 1 Td sve tri komponente TTIII ispoljavaju približno oscilatorno ponašanje. Apsolutne vrednosti $n_0^2 Q_{xxz}$ i $n_0^2 Q_{zxx}$ komponenti dostižu dva lokalna maksimuma na približno 10^{-3} Td i 1 Td i lokalni minimum na približno $3.5 \cdot 10^{-2}$ Td. Longitudinalna komponenta TTIII dostiže dva lokalna maksimuma na približno $3.5 \cdot 10^{-3}$ Td i 0.8 Td i lokalni minimum na oko $6 \cdot 10^{-2}$ Td. Na poljima višim od oko 1 Td apsolutne vrednosti $n_0^2 Q_{xxz}$ i $n_0^2 Q_{zxx}$ komponenti monotono opadaju sa porastom E/n_0, dok se $n_0^2 Q_{zzz}$ komponenta naglo povećava do oko 2 Td, posle čega naglo opada sa porastom redukovanog električnog polja.

U opsegu polja do približno 0.8 Td srednja energija elektrona je niža od 3.2 eV, pa elektroni nemaju dovoljno energije za neelastične sudare i profili zavisnosti TKIII od E/n_0 su određeni elastičnim sudarima, što ukazuje na to da su oscilatorni profili komponenti TTIII na poljima nižim od 0.8 Td posledica energijske zavisnosti preseka za elastične sudare. Na poljima višim od 2 Td, srednja energija elektrona je preko 6 eV, te svi elektroni čija je energija tri puta veća od srednje energije imaju dovoljno energije za neelastične sudare (16.62 eV), a to dovodi do monotonog opadanja apsolutnih vrednosti sve tri komponente TTIII sa porastom E/n_0 u ovom opsegu polja. U opsegu polja između približno 1 Td i 2 Td, $n_0^2 Q_{zzz}$ komponenta se naglo povećava sa porastom polja, uprkos tome što najenergičniji elektroni imaju dovoljno energije za neelastične sudare u ovom opsegu polja. Ovo bi moglo da bude posledica naglog povećanja pokretljivosti elektrona u ovom opsegu polja, pošto se srednja energija poveća sa oko 3 eV na 0.8 Td do približno 6 eV na 2.1 Td.
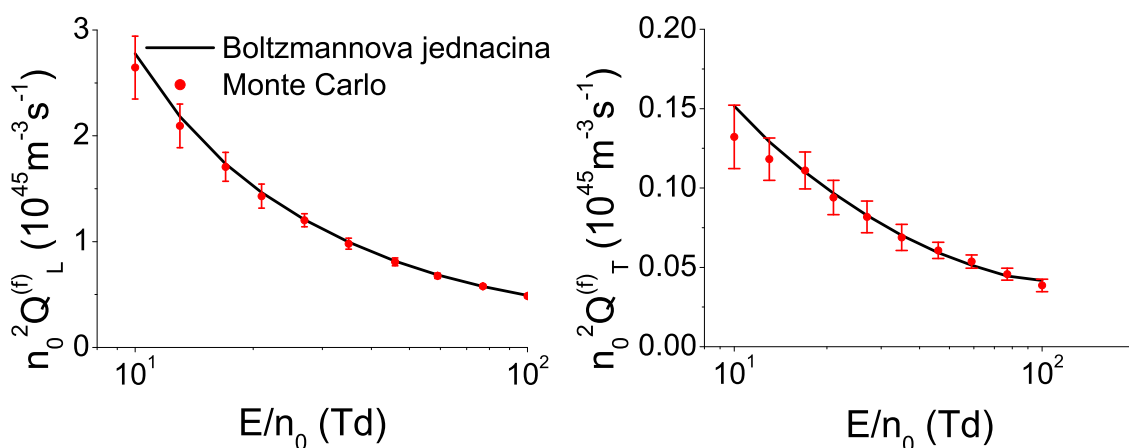
Slika 43: Poređenje vrednosti komponenti transportnog tenzora trećeg reda, koje su dobijene primenom metoda više članova za rešavanje Boltzmann-ove jednačine i Monte Carlo simulacija, za elektrone u neonu.

Slika 43 prikazuje poređenja vrednosti $n_0^2 Q_L^{(f)}$ i $n_0^2 Q_T^{(f)}$, koje su dobijene primenom moment-nog metoda za numeričko rešavanje Boltzmann-ove jednačine i Monte Carlo simulacija, za roj elektrona u neonu. Sa ovih slika se vidi da se rezultati koji su dobijeni na osnovu ova dva meto-da jako dobro slažu. Veličine grešaka se povećavaju sa opadanjem E/n_0 zbog spore relaksacije

energije elektrona na niskim poljima, što je posledica malog transfera energije u elastičnim su-
darima. Međutim, razlika između rezultata koji su dobijeni na osnovu ove dve metode je znatno
manja od statističke nesigurnosti Monte Carlo simulacija.
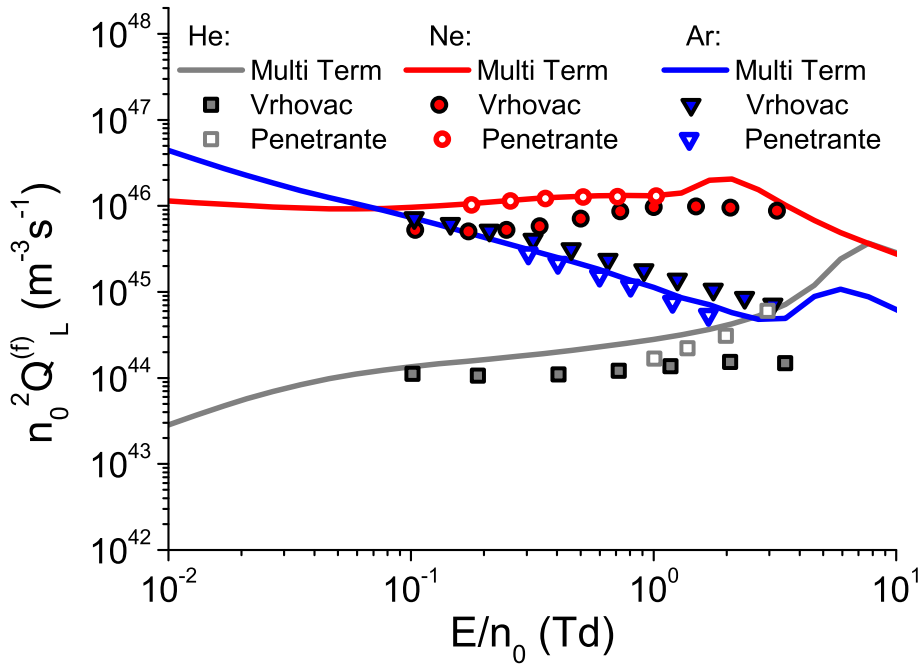
Slika 44: Poređenje vrednosti longitudinalne komponente transportnog tenzora trećeg reda koje
su dobijene u našim proračunima, na osnovu metoda više članova za rešavanje Boltzmann-ove
jednačine, sa rezultatima Penetrante-a i Bardsley-a [126] i Vrhovca i saradnika [132] za rojeve
elektrona u helijumu, neonu i argonu.

Na slici 44 su prikazana poređenja vrednosti $n_0^2 Q_L^{(f)}$ koje su dobijene u našim proračunima
sa vrednostima koje su dobili drugi autori [126, 132] za elektrone u helijumu, neonu i argonu.
Penetrante i Bardsley [126] su u svojim proračunima koristili aproksimaciju dva člana za nu-
meričko rešavanje Boltzmann-ove jednačine, dok su Vrhovac i saradnici [132] koristili teoriju
prenosa impulsa. Može se videti da se kvalitativno ponašanje naših rezultata dobro slaže sa
kvalitativnim ponašanjem rezultata Penetrante-a i Bardsley-a. Pri tome se brojne vrednosti
naših rezultata za elektrone u neonu jako dobro slažu sa brojnim vrednostima Penetrante-a i
Bardsley-a. Činjenica o slaganju rezultata upućuje na to da je u njihovim proračunima korišćen
sličan presek za transfer impulsa u elastičnim sudarima kao u našim proračunima, kao i da je
primena aproksimacije dva člana opravdana za izračunavanje longitudinalne komponente TTIII
u odsustvu neelastičnih sudara. Razlika između rezultata za elektrone u helijumu i argonu je
verovatno posledica razlike u korišćenim presecima za rasejanje elektrona. Trendovi zavisnosti
$n_0^2 Q_L^{(f)}$ od E/n_0 u rezultatima Vrhovca i saradnika se nešto slabije slažu sa trendovima naših
rezultata nego što je to slučaj sa rezultatima Penetrante-a i Bardsley-a. Na primer, iako se
vrednosti komponente $n_0^2 Q_L^{(f)}$, koje su dobijene u našim proračunima za elektrone u helijumu
povećavaju sa porastom E/n_0 u opsegu polja od 0.1 Td do približno 8 Td, vrednosti $n_0^2 Q_L^{(f)}$
koje su dobili Vrhovac i saradnici praktično saturiraju sa porastom E/n_0 u opsegu polja između
približno 0.1 Td i 0.6 Td i blago opadaju u opsegu polja između 2.5 Td i 4 Td. Pored toga, za

elektrone u neonu vrednosti $n_0^2 Q_L^{(f)}$, koje su dobijene na osnovu proračuna Vrhovca i saradnika, dostižu maksimum na oko 1 Td, dok vrednosti dobijene u našim proračunima dostižu maksimum na približno 2 Td, pri čemu je u rezultatima Vrhovca i saradnika ovaj maksimum znatno manje izražen nego u našim rezultatima. Kvantitativno slaganje naših rezultata sa rezultatima Vrhovca i saradnika je za elektrone u helijumu i neonu slabije od kvantitativnog slaganja naših rezultata sa rezultatima Penetrante-a i Bardsley-a, dok je za elektrone u argonu kvantitativno slaganje naših proračuna jednako dobro sa proračunima Penetrante-a i Bardsley-a i Vrhovca i saradnika. Razlike između naših rezultata i rezultata Vrhovca i saradnika mogu biti posledica aproksimacija korišćenih u fluidnim modelima i razlike u korišćenim presecima.
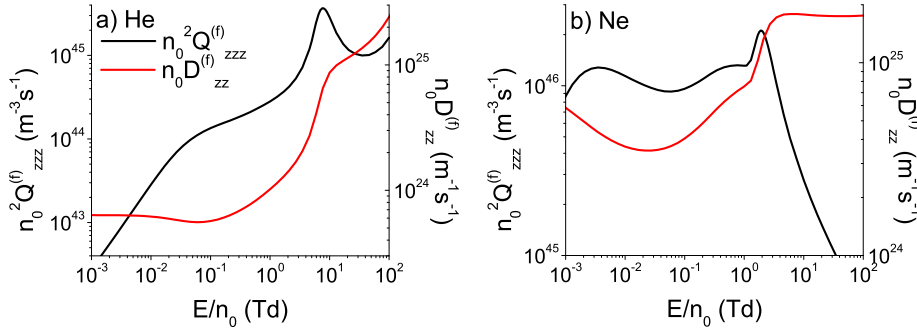
Slika 45: Korelacija longitudinalne komponente fluks transportnog tenzora trećeg reda sa fluks longitudinalnom difuzijom za elektrone u helijumu i neonu. Rezultati su dobijeni primenom metoda više članova za rešavanje Boltzmann-ove jednačine.

Korelacije između $n_0^2 Q_{zzz}^{(f)}$ i $n_0 D_{zz}^{(f)}$ za elektrone u helijumu i neonu prikazane su na slici 45. Može se videti da se oba u slučaja na najnižim poljima $n_0^2 Q_{zzz}^{(f)}$ povećava sa porastom E/n_0 uprkos tome što $n_0 D_{zz}^{(f)}$ opada. Ovo je posledica toga što TKIII reprezentuju usmereno kretanje pa teže nuli u limesu niskih polja, za razliku od difuzije koja teži termalnoj vrednosti. Zato se u svim gasovima komponente TTIII po apsolutnoj vrednosti monotono povećavaju sa porastom E/n_0 na dovoljno niskim poljima. No vrednost E/n_0 pri kojoj počinje korelacija između $n_0^2 Q_{zzz}^{(f)}$ i $n_0 D_{zz}^{(f)}$ nije ista u svim gasovima.

Za elektrone u helijumu se $n_0^2 Q_{zzz}^{(f)}$ i $n_0 D_{zz}^{(f)}$ povećavaju sa porastom polja za E/n_0 između otprilike $6 \cdot 10^{-2}$ i 8 Td. Pri tome se obe veličine naglo povećavaju u opsegu polja između približno 2 Td i 8 Td. Međutim, u opsegu polja između približno 8 Td i 40 Td se porast $n_0 D_{zz}^{(f)}$ sa porastom E/n_0 usporava ($n_0 D_{zz}^{(f)}$ postaje konkavna funkcija polja), pa u ovom opsegu polja $n_0^2 Q_{zzz}^{(f)}$ opada sa porastom E/n_0. Na višim poljima se porast $n_0 D_{zz}^{(f)}$ sa porastom E/n_0 ubrzava ($n_0 D_{zz}^{(f)}$ postaje konveksna funkcija polja), pa se i $n_0^2 Q_{zzz}^{(f)}$ povećava sa porastom E/n_0 u ovom opsegu polja.

Za elektrone u neonu $n_0^2 Q_{zzz}^{(f)}$ i $n_0 D_{zz}^{(f)}$ opadaju sa porastom E/n_0 u opsegu polja između otpilike $3 \cdot 10^{-3}$ Td i $4 \cdot 10^{-2}$ Td, pri čemu $n_0^2 Q_{zzz}^{(f)}$ nastavlja da opada do približno $6 \cdot 10^{-2}$. Na višim poljima se $n_0^2 Q_{zzz}^{(f)}$ i $n_0 D_{zz}^{(f)}$ povećavaju sa porastom E/n_0 do oko 2 Td. Uz to je ovaj porast naročito intenzivan u opsegu polja između približno 1 Td i 2 Td. Na višim poljima $n_0 D_{zz}^{(f)}$ postaje konkavna funkcija i počne da opada sa porastom E/n_0 za E/n_0 između približno 6 Td i 50 Td, nakon čega saturira sa porastom E/n_0. Uz to $n_0^2 Q_{zzz}^{(f)}$ opada u opsegu polja iznad 2 Td.

U ovom potpoglavlju su razmatrani TKIII za elektrone u helijumu i neonu. Longitudinal-na komponenta Q_{zzz} je pozitivna u oba gasa u celom posmatranom opsegu polja. Ipak, Q_{zxx} komponenta je negativna za elektrone u helijumu na poljima nižim od približno 10 Td i za elektrone u neonu u celom razmatranom opsegu polja, zbog porasta kolizione frekvence za elastične sudare sa porastom energije. Profili zavisnosti komponenti TTIII od redukovanog električnog polja u ova dva gasa su nešto složeniji nego u slučaju modelnih gasova, zbog složenije energijske zavisnosti preseka za sudare u realnim gasovima. Ovi profili su analizirani na osnovu setova preseka i profila zavisnosti srednje energije od redukovanog električnog polja. Na ovom mestu su poređeni naši rezultati za longitudinalnu komponentu TTIII sa rezultatima Penetrante-a i Bardsley-a [126] i Vrhovca i saradnika [132]. Naši rezultati se nešto bolje slažu sa rezultatima Penetrante-a i Bardsley-a nego sa rezultatima Vrhovca i saradnika. Na kraju ovog potpoglavlja je razmatrana korelacija između longitudinalne komponente TTIII i longitudinalne komponente difuzionog tenzora.

5.4 Transportni koeficijenti trećeg reda za rojeve elektrona u atomskim gasovima sa Ramsauer-Townsend-ovim minimumom

5.4.1 Preliminarije

Na slikama 46, 47 i 48 su prikazani setovi preseka za rasejanje elektrona u argonu, kriptonu i ksenonu, respektivno, koji su korišćeni u našim proračunima. Setovi preseka za rasejanje elektrona u argonu i ksenonu, koji su korišćeni u našem radu, preuzeti su iz Hayashi-jeve baze [201, 202]. U našim proračunima transporta elektrona u kriptonu korišćen je set preseka koji je razvio S. Biagi . Ovaj set preseka je direktno kodiran u MAGBOLTZ kodu (verzija 7.1) [203].
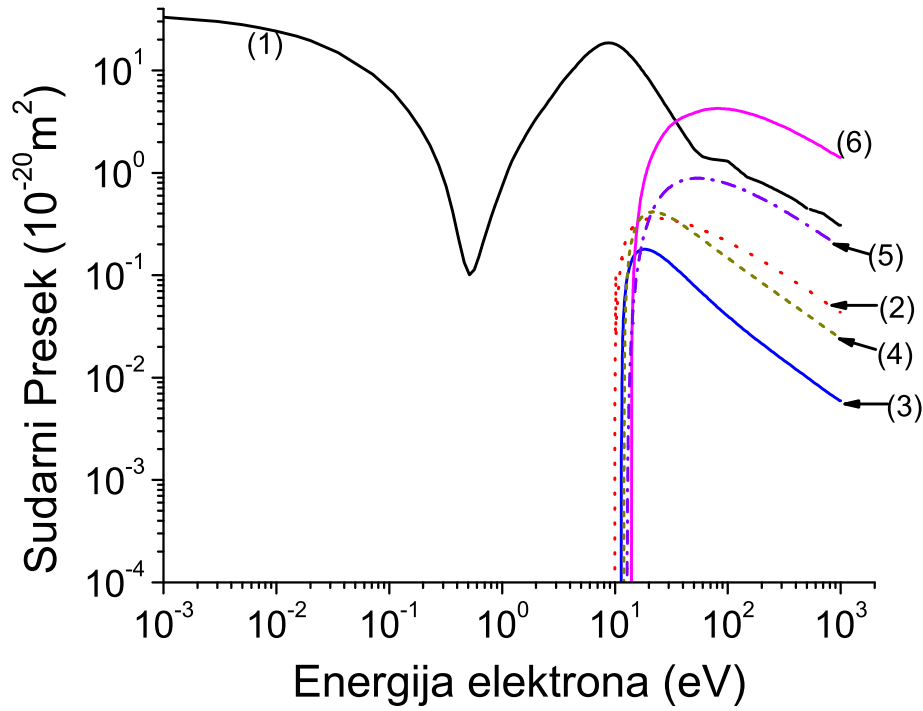
5.4.2 Rezultati

Na slici 49 su predstavljene vrednosti srednje energije elektrona u argonu, kriptonu i ksenonu. Ovi rezultati su dobijeni primenom momentnog metoda za numeričko rešavanje Boltzmann-ove jednačine. U sva tri plemenita gasa je energija termalna na najnižim poljima. Pri tome je srednja energija u argonu blizu termalnih vrednosti do oko 10^{-3} Td, gde iznosi približno $4 \cdot 10^{-2}$ eV. Nakon toga se srednja energija naglo povećava u opsegu polja između približno 10^{-3} Td i $6 \cdot 10^{-3}$ Td i dostiže vrednost od oko 0.2 eV na kraju ovog opsega. Na višim poljima se srednja energija monotono povećava sa porastom E/n_0, ali je nagib zavisnosti srednje energije od E/n_0 znatno manji nego u opsegu polja između 10^{-3} Td i $6 \cdot 10^{-3}$ Td. Nagib zavisnosti srednje energije od E/n_0 se ponovo smanjuje na približno 6 Td, gde srednja energija iznosi oko 5 eV. U opsegu polja između približno 10^{-3} Td i $6 \cdot 10^{-3}$ Td, srednja energija elektrona se nalazi u intervalu između približno $4 \cdot 10^{-2}$ eV i 0.2 eV. U ovoj energijskoj oblasti presek za transfer implusa naglo opada sa porastom energije (zbog prisustva Ramsauer-Townsend-ovog minimuma). To dovodi do intenzivnog porasta energije sa porastom E/n_0 u ovom opsegu polja. U opsegu E/n_0 između
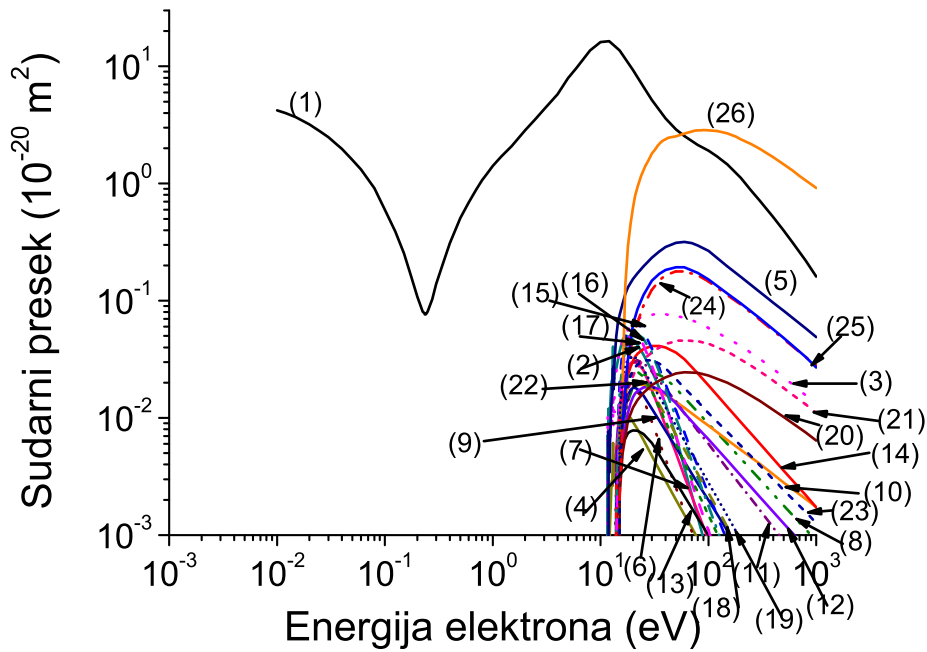
Slika 46: Set preseka za rasejanje elektrona u argonu: (1) transfer impulsa u elastičnim sudarima, efektivne elektronske ekscitacije: (2) $4s[3/2]_2$, (3) $4s[3/2]_1$, (4) $4s'[1/2]_0$, (5) $4s'[1/2]_1$, (6) $4p[1/2]_1$, (7) $4p[5/2]_3$, (8) $4p[5/2]_2$, (9) $4p[3/2]_1$, (10) $4p[3/2]_2$, (11) $4p[1/2]_0$ i $4p'[3/2]_1$, (12) $4p'[3/2]_2$, (13) $4p'[1/2]_1$, (14) $4p'[1/2]_0$, (15) $3d[1/2]_0$ i $3d[1/2]_1$, (16) $3d[3/2]_2$, (17) $3d[7/2]_4$, (18) $3d[7/2]_3$, (19) $3d[5/2]_2$ i $5s[3/2]_2$, (20) $3d[5/2]_3$ i $5s[3/2]_1$, (21) $3d[3/2]_1$, (22) $3d'[5/2]_2$ i (23) $3d'[3/2]_2$, $3d'[5/2]_3$, $5s'[1/2]_0$ i $5s'[1/2]_1$, (24) efektivna ekscitacija koja obuhvata stanja sa pragovima između 14.71 eV i 15.20 eV, (25) efektivna ekscitacija koja obuhvata stanja sa pragovima između 15.20 eV i 15.76 eV i (26) jonizacija.

približno $6 \cdot 10^{-3}$ Td i 6 Td srednja energija elektrona se nalazi u intervalu između 0.2 eV i 5 eV, a u ovom energijskom intervalu se presek za transfer impulsa u elastičnim sudarima naglo povećava sa porastom energije, što dovodi do sporijeg porasta srednje energije sa porastom E/n_0. Na poljima višim od 6 Td, srednja energija elektrona je preko 5 eV, te najenergičniji elektroni imaju energiju višu od 11.55 eV i mogu da učestvuju u neelastičnim sudarima, što dodatno usporava porast srednje energije sa porastom polja.

Trendovi zavosnosti srednje energije od E/n_0 u kriptonu i ksenonu su na kvalitativnom nivou vrlo slični odgovarajućem trendu zavisnosti u argonu. Pritom se srednja energija naglo povećava sa porastom E/n_0 u opsegu polja između približno $6 \cdot 10^{-3}$ Td i $3 \cdot 10^{-2}$ za elektrone u kriptonu i u opsegu između $2 \cdot 10^{-2}$ i $6 \cdot 10^{-2}$ za elektrone u ksenonu. U oba slučaja se u ovom opsegu E/n_0 srednja energija elektrona nalazi u energijskoj oblasti u kojoj presek za transfer impulsa u elastičnim sudarima naglo opada sa porastom energije, zbog Ramsauer-Townsendovog minimuma. Ovaj energijski opseg se nalazi između približno $4 \cdot 10^{-2}$ eV i 0.5 eV za elektrone u kriptonu i ksenonu. Na višim poljima je nagib zavisnosti srednje energije od E/n_0 znatno manji, jer naglo raste presek za transfer impulsa u elastičnim sudarima u energijskom intervalu koji odgovara ovom opsegu polja. Pri vrednostima polja višim od oko približno 6 Td, nagib zavisnosti srednje energije od E/n_0 se dodatno smanjuje zbog toga što najenergičniji elektroni mogu da učestvuju u neelastičnim sudarima u ovom opsegu polja. Naime, na 6 Td vrednosti

Slika 47: Set preseka za rasejanje elektrona u kriptonu: (1) transfer impulsa u elastičnim suda-rima, efektivne elektronske ekscitacije: (2) S nivoi, (3) P nivoi, (4) D i P nivoi, (5) efektivna ekscitacija koja obuhvata stanja sa pragovima između 12.75 eV i 13.996 eV i (6) jonizacija.

srednje energije elektrona iznose približno 4 eV i 3 eV u kriptonu i ksenonu, respektivno, dok vrednosti praga za prvu elektronsku ekscitaciju u kriptonu i ksenonu iznose približno 9.91 eV i 8.31 eV.

Slika 50 predstavlja $n_0^2 Q_{xxz}^{(f)}$, $n_0^2 Q_{zxx}^{(f)}$ i $n_0^2 Q_{zzz}^{(f)}$ komponente TTIII za elektrone u argonu, krip-tonu i ksenonu. Ovi rezultati su dobijeni primenom momentnog metoda za numeričko rešavanje Boltzmann-ove jednačine. Prikazano je i $3Q_T^{(f)} = Q_{xxz}^{(f)} + Q_{xzx}^{(f)} + Q_{zxx}^{(f)}$ (pri čemu je $Q_{xxz} = Q_{xzx}$), te se može videti da je na kvalitativnom nivou trend zavisnosti komponenti TTIII od E/n_0 isti u kriptonu i ksenonu, pri čemu se razlikuju vrednosti polja na kojima ove komponente menjaju trend ponašanja kao i brojne vrednosti komponenti TTIII. Na niskim poljima su sve tri kompo-nente TTIII pozitivne i monotono se povećavaju sa porastom E/n_0 i dostižu maksimum na oko $1.4 \cdot 10^{-2}$ Td i $3.7 \cdot 10^{-2}$ Td za elektrone u kriptonu i ksenonu, respektivno. Nakon toga sve tri komponente TTIII naglo opadaju sa porastom polja do oko $3.5 \cdot 10^{-2}$ Td i 0.1 Td za elektrone u kriptonu i ksenonu respektivno. Na višim poljima se $n_0^2 Q_{zxx}^{(f)}$ komponenta povećava sa porastom E/n_0 i dostiže lokalni maksimum na približno 0.08 Td i 0.2 Td za elektrone u kriptonu i ksenonu respektivno. U ovom opsegu polja $n_0^2 Q_{xxz}^{(f)}$ komponenta postaje negativna i dostiže lokalni mini-mum na optilike istoj vrednosti polja na kojoj $n_0^2 Q_{zxx}^{(f)}$ dostiže lokalni maksimum. Istovremeno $n_0^2 Q_{xxz}^{(f)}$ komponenta ostaje negativna u celom opsegu polja do 100 Td. Komponente $n_0^2 Q_{xxz}^{(f)}$ i $n_0^2 Q_{zxx}^{(f)}$ po apsolutnoj vrednosti na višim poljima monotono opadaju sa porastom E/n_0. U kriptonu i ksenonu $n_0^2 Q_{zzz}^{(f)}$ komponenta posle prvog maksimuma monotono opada sa porastom polja do oko 2.1 Td, posle čega se povećava, dostižući drugi lokalni maksimum (videti slike sa korelacijom $n_0 D_L$ i $n_0^2 Q_L$). Ovaj drugi maksimum se nalazi na približno 4 Td za elektrone u
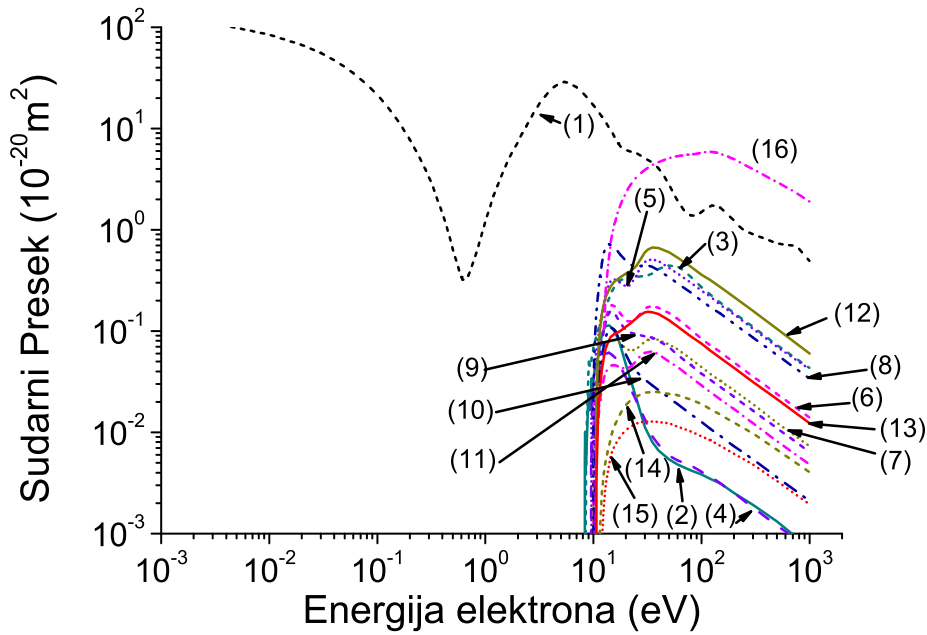
Slika 48: Set preseka za rasejanje elektrona u ksenonu: (1) transfer impulsa u elastičnim sudarima, efektivne elektronske ekscitacije: (2) $6s[3/2]_2$, (3) $6s[3/2]_1$, (4) $6s'[1/2]_0$, (5) $6s'[1/2]_1$ i $6p[1/2]_1$, (6) $6p[5/2]_2$ i $6p[5/2]_3$, (7) $6p[3/2]_1$ i $6p[3/2]_2$, (8) $5d[1/2]_0$, $5d[1/2]_1$, $6p[1/2]_1$, $5d[7/2]_4$ i $5d[3/2]_2$, (9) $5d[7/2]_3$, (10) $5d[5/2]_2$, (11) $5d[5/2]_3$, (12) $5d[3/2]_1$, (13) $7s[3/2]_2$, $7s[3/2]_1$, $7p[1/2]_1$, $7p[5/2]_2$, $6p'[3/2]_1$, $7p[5/2]_3$, $6d[1/2]_0$, $6d[1/2]_1$, $7p[3/2]_2$ $6d[3/2]_2$, $7p[3/2]_1$, $7p[1/2]_0$, $6d[7/2]_4$, $6d[7/2]_3$, $6p'[3/2]_2$, $6d[5/2]_2$, $6p[1/2]_1$, $6d[5/2]_3$, $6p'[1/2]_0$ i $6d[3/2]_1$, (14) $8s[3/2]_2$ (15) $9s[3/2]_2$ i (16) jonizacija.
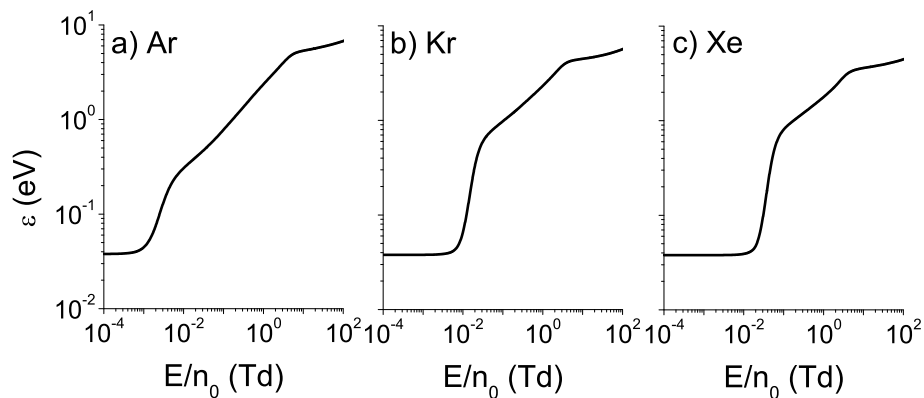
Slika 49: Srednja energija u funkciji E/n_0 za rojeve elektrona u argonu, kriptonu i ksenonu. Rezultati su dobijeni primenom metoda više članova za rešavanje Boltzmann-ove jednačine.

kriptonu i ksenonu. Na višim poljima apsolutne vrednosti sve tri komponente TTIII monotono opadaju sa porastom E/n_0.

Trend zavisnosti komponenti TTIII od E/n_0 za elektrone u argonu je sličan odgovarajućim trendovima zavisnosti u kriptonu i ksenonu. Naime, sve komponente TTIII se monotono povećavaju do oko $2 \cdot 10^{-3}$ Td, gde dostižu maksimum. Nakon toga, sve komponente monotono opadaju sa porastom E/n_0 do približno $5 \cdot 10^{-3}$ Td. Uz to, $n_0^2 Q_{xxz}^{(f)}$ komponenta postaje negativna i dostiže lokalni minimum na oko $2.7 \cdot 10^{-2}$, pri čemu $n_0^2 Q_{zxx}^{(f)}$ komponenta dostiže lokalni

108
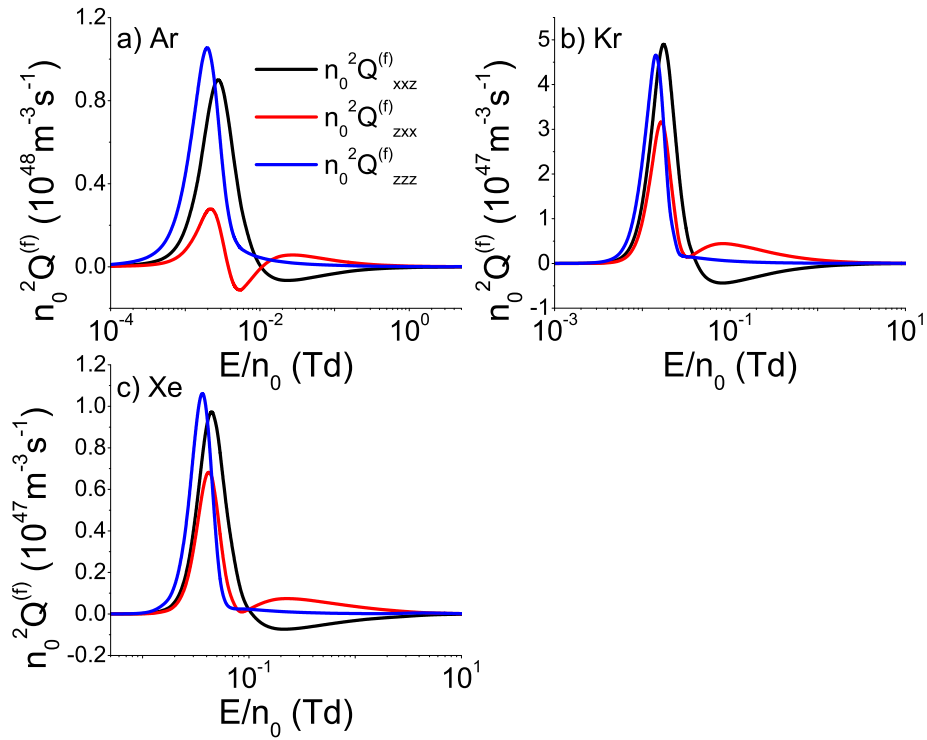
Slika 50: $n_0^2 Q_{xxz}$, $n_0^2 Q_{zxx}$ i $n_0^2 Q_{zzz}$ komponente fluks transportnog tenzora trećeg reda u funkciji E/n_0 za rojeve elektrona u argonu, kriptoni i ksenonu. Rezultati su dobijeni na osnovu metoda više članova za rešavanje Boltzmann-ove jednačine.

maksimum na otprilike istoj vrednosti E/n_0. Nakon ovog polja $n_0^2 Q_{xxz}^{(f)}$ i $n_0^2 Q_{zxx}^{(f)}$ po apsolutnoj vrednosti monotono opadaju u celom opsegu polja, dok se $n_0^2 Q_{zzz}^{(f)}$ povećava u opsegu polja između približno 3.5 Td i 6 Td (videti grafik sa korelacijom QL i DL), nakon čega monotono opada sa porastom E/n_0. Međutim, kvalitativni trend zavisnosti TKIII od E/n_0 se u argonu razlikuje od trendova zavisnosti u kriptonu i ksenonu po tome što $n_0^2 Q_{zxx}^{(f)}$ komponenta postaje negativna u argonu. Ova komponenta postaje nagativna na približno $4 \cdot 10^{-3}$ Td i dostiže lokalni minimum na približno $5.3 \cdot 10^{-3}$ Td, posle čega se povećava sa porastom E/n_0, postajući pozitivna na oko $1.3 \cdot 10^{-2}$ Td. Vrednosti polja na kojoj $n_0^2 Q_{zxx}^{(f)}$ komponenta postaje pozitivna blizu je vrednosti polja na kojoj $n_0^2 Q_{xxz}^{(f)}$ komponenta postaje negativna.

U sva tri gasa se komponente TTIII naglo povećavaju sa porastom E/n_0 na najnižim poljima na kojima se velika većina elektrona nalazi u energijskoj oblasti u kojoj presek za transfer impulsa naglo opada sa porastom energije zbog Ramsauer-Townsend-ovog minimuma. Sve tri komponente TTIII u sva tri gasa dostižu maksimume na vrednostima polja koje se nalaze negde na sredini opsega u kome se srednja energija elektrona naglo povećava sa porastom polja (približno $2 \cdot 10^{-3}$ Td, $1.4 \cdot 10^{-2}$ Td i $3.7 \cdot 10^{-2}$ Td za elektrone u argonu, kriptonu i ksenonu, respektivno). Istovremeno važi da vrednosti srednje energije elektrona na poljima na kojima komponente TTIII dostižu maksimum iznose 0.08 eV, 0.11 eV i 0.14 eV za elektrone u argonu, kriptonu i ksenonu respektivno. Vrednosti energije koje odgovaraju položajima Ramsauer-Townsend-ovog minimuma iznose 0.24 eV, 0.51 eV i 0.64 eV za elektrone u argonu, kriptonu i ksenonu respektivno. Ovo znači da u argonu komponente TTIII dostižu lokalni maksimum na vrednosti

polja na kojoj je srednja energija elektrona 3 puta manja od energije Rasmauer-Townsend-ovog minimuma, dok u kriptonu i ksenonu komponente TTIII dostižu lokalni maksimum na energiji koja je oko 4.5 puta manja od energije Ramsauer-Townsend-ovog minimuma. Izloženi podaci upućuju na to da komponente TTIII počinju da opadaju sa porastom E/n_0 u opsegu polja u kome se najenergičniji elektroni nalaze u energijskoj oblasti u kojoj se presek za transfer impulsa u elastičnim sudarima naglo povećava sa porastom energije. Veća osetljivost komponenti TTIII na dinamiku visokoenergijskih elektrona u kriptonu i ksenonu nego u argonu verovatno se može pripisati strmijem porastu preseka za transfer impulsa u elastičnim sudarima nakon Ramsauer-Townsend-ovog minimuma u ova dva gasa.

Za elektrone u argonu je $n_0^2 Q_{zxx}^{(f)}$ komponenta negativna u opsegu E/n_0 od $3.9 \cdot 10^{-3}$ Td do 10^{-2} Td. U ovom opsegu polja se srednja energija elektrona nalazi u intervalu između 0.17 eV i 0.3 eV, što je blizu vrednosti Ramsauer-Townsend-ovog minimuma u argonu, pri čemu se porast srednje energije sa porastom E/n_0 primetno usporava na kraju ovog opsega polja. Na poljima višim od 10^{-2} Td $n_0^2 Q_{xxz}^{(f)}$ i $n_0^2 Q_T^{(f)}$ imaju negativne vrednosti, što znači da su u argonu $n_0^2 Q_{xxz}^{(f)}$ i $n_0^2 Q_T^{(f)}$ negativni počev od polja u kome je srednja energija elektrona 1.25 puta veća od energije Ramsauer-Townsend-ovog minimuma. Negativnost $n_0^2 Q_T^{(f)}$ ukazuje na to da je roj skupljen duž transverzalnog pravca na frontu roja (u $q\mathbf{E}$ pravcu) i proširen duž transverzalnog pravca na zadnjem delu roja (u $-q\mathbf{E}$ pravcu) (videti poglavlje 4.2). Ovo uslovljeno time što se većina elektrona u ovom opsegu polja nalazi u energijskoj oblasti u kojoj se presek za transfer impulsa u elastičnim sudarima naglo povećava sa porastom energije, što pruža snažan otpor difuzionom širenju roja.

Iako u kriptonu i ksenonu $n_0^2 Q_{zxx}^{(f)}$ komponenta ne postaje negativna, za razliku od njenog ponašanja u argonu, trend ponašanja $n_0^2 Q_{xxz}^{(f)}$ i $n_0^2 Q_T^{(f)}$ je sličan kao u argonu. Zapravo, vrednosti $n_0^2 Q_{xxz}^{(f)}$ i $n_0^2 Q_T^{(f)}$ su negativne na poljima višim od $4.6 \cdot 10^{-2}$ Td i 0.13 Td za elektrone u kriptonu i ksenonu respektivno. Na ovim vrednostima polja srednja energija iznosi 0.74 eV i 0.9 eV u kriptonu i ksenonu, respektivno, što za posledicu ima to da su $n_0^2 Q_{xxz}^{(f)}$ i $n_0^2 Q_T^{(f)}$ negativni počev od polja na kojem je srednja energija preko 1.45 puta veća od energije Ramsauer-Townsend-ovog minimuma u kriptonu i preko 1.4 puta veća od energije Ramsauer-Townsend-ovog minimuma u ksenonu.

Negativnost $n_0^2 Q_T^{(f)}$ se javlja za elektrone u atomskim gasovima sa Ramsauer-Townsend-ovim minimumom. Ovaj efekat se javlja u opsegu polja u kome se većina elektrona nalazi u energijskoj oblasti u kojoj se presek za transfer impulsa u elastičnim sudarima naglo povećava sa porastom energije, što dovodi do snažnog otpora difuzionom obliku kretanja koji je reprezentovan transportnim koeficijentima trećeg reda. Pri tome je u oba slučaja $n_0^2 Q_{xxz}^{(f)}$ komponenta negativna u opsegu polja u kome je $n_0^2 Q_T^{(f)}$ negativno, dok je u ovom opsegu $n_0^2 Q_{zxx}^{(f)}$ komponenta pozitivna. Negativnost $n_0^2 Q_{xxz}^{(f)}$ komponente upućuje na to da je difuziono širenje u transverzalnom pravcu manje na frontu roja nego na zadnjem delu roja. Ovo je posledica porasta srednje energija duž longitudinalnog pravca i naglog povećanja kolizione frekvence sa porastom energije. Pozitivnost $n_0^2 Q_{zxx}^{(f)}$ pak pokazuje da je longitudinalno širenje roja veće na transverzalnim ivicama nego u centru roja. Ovo bi moglo da bude posledica opadanja energije

elektrona (pa time i otpora difuzionom širenju koji je izazvan porastom kolizione frekvence na visokim energijama) pri udaljavanju od centra roja duž transverzalnog pravca, zbog toga što je energičnijim elektronima teže da stignu do transverzalnih ivica, budući da je intenzivan porast kolizione frekvence sa porastom energije. Mogući razlog za odsustvo opsega E/n_0, u kome je $n_0^2 Q_{zxx}^{(f)}$ komponenta negativna, u kriptonu i ksenonu jeste strmiji porast preseka za transfer impulsa u elastičnim sudarima u ova dva gasa, koji dovodi do toga da $n_0^2 Q_{xxz}^{(f)}$ komponenta postane negativna i da energija elektrona počne da opada pri udaljavanju od centra roja duž transverzalnog pravca, pre nego što $n_0^2 Q_{zxx}^{(f)}$ komponenta postane negativna.
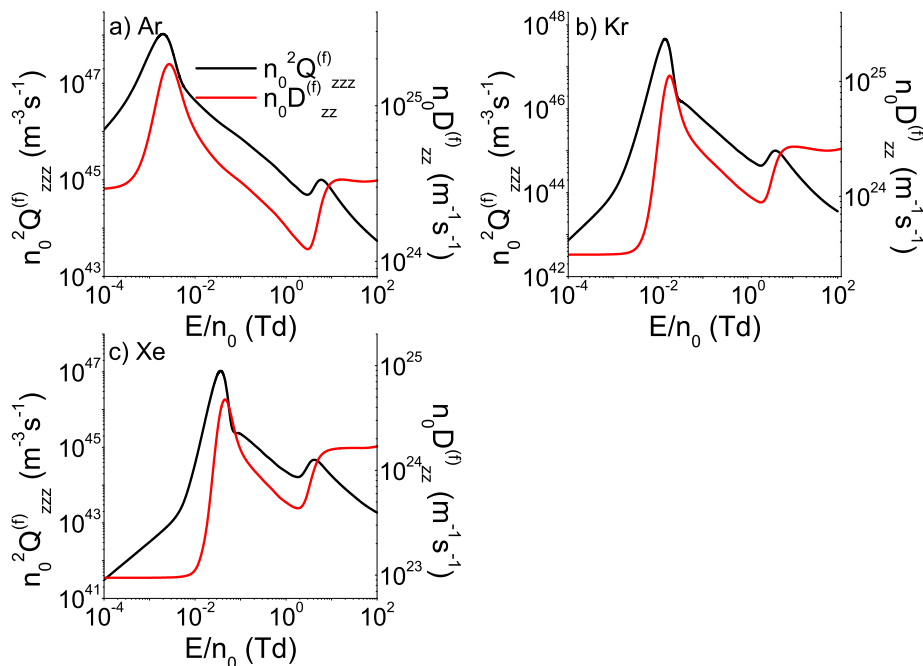
Slika 51: Korelacija između profila zavisnosti longitudinalne komponente fluks transportnog tenzora trećeg reda $n_0^2 Q_{zzz}^{(f)}$ i fluks longitudinalne difuzije $n_0 D_{zz}^{(f)}$ od E/n_0 za rojeve elektrona u argonu, kriptonu i ksenonu. Rezultati su dobijeni primenom metoda više članova za rešavanje Boltzmann-ove jednačine.

Na slici 51 prikazane su korelacije između profila zavisnosti $n_0^2 Q_{zzz}^{(f)}$ i $n_0 D_{zz}^{(f)}$ od E/n_0 za elektrone u argonu, kriptonu i ksenonu. Može se uočiti da postoji snažna korelacija u trendovima ponašanja $n_0^2 Q_{zzz}^{(f)}$ i $n_0 D_{zz}^{(f)}$ u sva tri gasa, kao i da su odgovarajući profili na kvalitativnom nivou jako slični. Na niskim poljima se obe veličine povećavaju sa porastom E/n_0 zbog toga što se većina elektrona nalazi u energijskoj oblasti u kojoj presek za transfer impulsa naglo opada sa porastom energije. Pri tome $n_0^2 Q_{zzz}^{(f)}$ komponenta TTIII dostiže maksimum na $2.1 \cdot 10^{-3}$ Td, $1.4 \cdot 10^{-2}$ Td i $3.7 \cdot 10^{-2}$ Td za elektrone u argonu, kriptonu i ksenonu, respektivno, dok $n_0 D_{zz}^{(f)}$ dostiže maksimum na $2.7 \cdot 10^{-3}$ Td, $1.7 \cdot 10^{-2}$ Td i $4.6 \cdot 10^{-2}$ Td za elektrone u ova tri gasa. U sva tri slučaja $n_0 D_{zz}^{(f)}$ dostiže maksimum na malo višim poljima od $n_0^2 Q_{zzz}^{(f)}$. Nakon maksimuma $n_0^2 Q_{zzz}^{(f)}$ i $n_0 D_{zz}^{(f)}$ naglo opadaju do oko $5.9 \cdot 10^{-3}$ Td, $2.9 \cdot 10^{-2}$ i $7.7 \cdot 10^{-2}$ za elektrone u agronu, kriptonu i ksenonu respektivno. Na višim poljima obe veličine nastave da opadaju, ali znatno sporije nego na nižim poljima, do oko 2.7 Td za elektrone u agronu i do oko 2.1 Td za elektrone u kriptonu i ksenonu. Nakon toga se obe veličine naglo povećavaju sa porastom E/n_0 u uskom

opsegu polja. Pri tome $n_0^2 Q_{zzz}^{(f)}$ dostiže maksimum na oko 5.9 Td, 4Td i 4.2 Td za elektrone u argonu, kriptonu i ksenonu, respektivno. Nakon drugog maksimuma $n_0^2 Q_{zzz}^{(f)}$ komponenta TTIII monotono opada sa porastom polja u celom opsegu do 100 Td, u sva tri gasa. U okolini polja na kome $n_0^2 Q_{zzz}^{(f)}$ dostiže maksimum porast $n_0 D_{zz}^{(f)}$ se sa porastom E/n_0 primetno usporava u odnosu na oblast polja u kojoj se $n_0^2 Q_{zzz}^{(f)}$ povećava sa E/n_0. Usporavanje porasta $n_0 D_{zz}^{(f)}$ sa E/n_0 se nastavlja do oko 13 Td, u sva tri gasa, nakon čega $n_0 D_{zz}^{(f)}$ praktično saturira sa porastom E/n_0. Zanimljivo je uočiti da su vrednosti $n_0^2 Q_{zzz}^{(f)}$ u okolini prvog maksimuma za više od reda veličine veće od vrednosti ove komponente TTIII na ostalim poljima.

U ovom potpoglavlju posmatrani su TKIII za elektrone u argonu, kriptonu i ksenonu. Profili Q_{xxz} i Q_{zzz} komponenti u argonu su na kvalitativnom nivou vrlo slični odgovarajućim profilima u kriptonu i ksenonu. Profil Q_{zxx} komponente u argonu se ipak razlikuje od odgovarajućih profila u kriptonu i ksenonu po prisustvu negativnih vrednosti u uskom opsegu redukovanog električnog polja. Pritom je Q_{zzz} komponenta pozitivna u argonu, kriptonu i ksenonu u celom razmatranom opsegu E/n_0, dok Q_{xxz} komponenta postaje negativna na višim poljima u sva tri gasa. Profili komponenti TTIII su razmatrani na osnovu setova preseka i vrednosti srednje energije. Sve tri komponente TTIII imaju oštar maksimum u oblasti E/n_0, u kojoj je srednja energija između 2 i 3 puta niža od energije Ramsauer-Townsend-ovog minimuma u argonu, kriptonu i ksenonu. Na kraju ovog potpoglavlja raspravlja se o korelaciji između profila longitudinalne komponente TTIII i longitudinalne komponente difuzionog tenzora.

## 5.5 Transportni koeficijenti trećeg reda za rojeve elektrona u molekularnim gasovima

5.5.1 Preliminarije

Na slikama 52, 53, 54 i 55 su prikazani setovi preseka za rasejanje elektrona u N_2, CH_4, CF_4 i C_3F_8, respektivno, koji su korišćeni u našim proračunima. Kolizione frekvence za elastične sudare za pozitrone u ova tri gasa nalaze se na slici 68.

Setovi preseka za rasejanje elektrone u N_2 i CH_4 su razvijeni u Laboratoriji za neravnotežne procese i primenu plazme Instituta za fiziku i prikazani su u radovima [204] i [205], respektivno. Set preseka za elektrone u CF_4, koji je korišćen u našim proračunima, je prikazan u radu [206], dok je set preseka za elektrone u C_3F_8 preuzet iz reference.

5.5.2 Rezultati

Na slici 56 su prikazani profili srednje energije u funkciji E/n_0 za elektrone u N_2, CH_4, CF_4 i C_3F_8. Ovi rezultati su dobijeni primenom momentnog metoda za numeričko rešavanje Boltzmann-ove jednačine. Profili srednje energije imaju sličan kvalitativni trend ponašanja za elektrone u CH_4, CF_4 i C_3F_8. Na najnižim poljima (do oko $2 \cdot 10^{-3}$ Td, $5 \cdot 10^{-2}$ Td i $2 \cdot 10^{-1}$ Td za
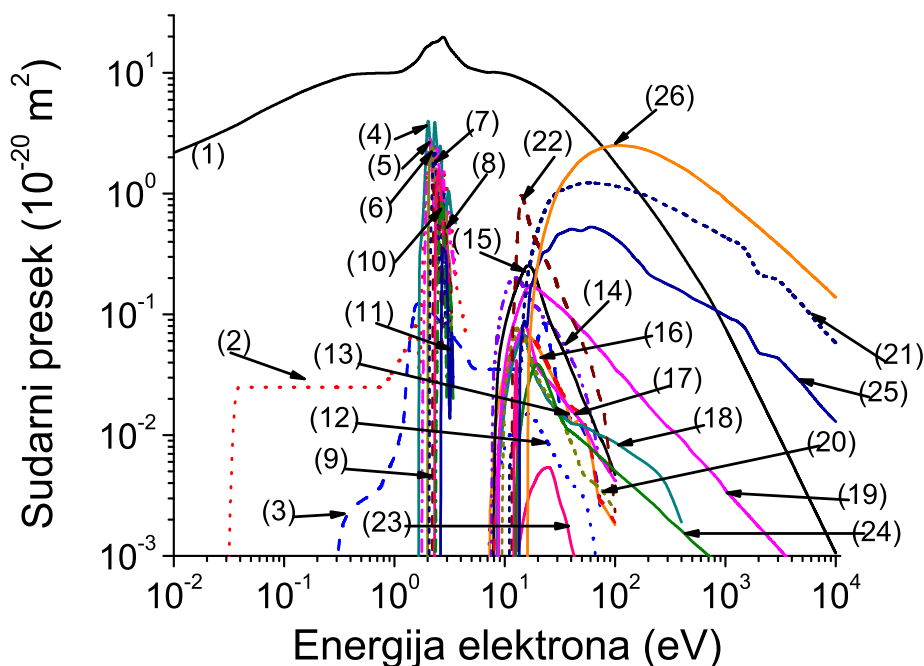
Slika 52: Set preseka za rasejanje elektrona u N_2:(1) presek za transfer impulsa u elastičnim sudarima, (2) rotaciona ekscitacija, vibracione ekscitacije (3) v_1 nerezonantni deo, (4) v_1 rezonantni deo, (5) v_2, (6) v_3, (7) v_4, (8) v_5, (9) v_6, (10) v_7, (11) v_8, elektronske ekscitacije (12) $A^3\Sigma_u^+$ vibracioni nivoi od 0 do 4, (13) $A^3\Sigma_u^+$ vibracioni nivoi od 5 do 9, (14) $B^3\Pi$, (15) $W^3\Delta_u$, (16) $A^3\Sigma$ vibracioni nivo 10, (17) $B'^3\Sigma_u^-$, (18) $a'^1\Sigma_u^-$, (19) a $^1\Pi_g$, (20) W^1, (21) disocijativna ekscitacija, (22) i (23) c^3, (24) $A^{1''}$, (25) suma singletnih stanja ne-disocijativan deo i (26) jonizacija.

elektrone u CH_4, CF_4 i C_3F_8, respektivno), srednja energija ima termalnu vrednost (približno 0.038 eV za temperaturu gasa od 293 K). Niske vrednosti pragova za vibracionu ekscitaciju u ova tri gasa (0.16 eV, 0.077 eV i 0.065 eV za elektrone u CH_4, CF_4 i C_3F_8, respektivno) onemogućavaju porast srednje energije (sa porastom polja) na niskom E/n_0, zbog toga što je energija koju elektroni dobiju od spoljašnjeg polja brzo izgubljena u neelastičnim sudarima. Pri tome preseci za vibracione ekscitacije dostižu lokalne maksimume negde između 0.1 eV i 0.3 eV u ova tri gasa. Zadržavanje termalnih vrednosti srednje energije čak i na relativno visokim poljima je naročito izraženo u CF_4 i C_3F_8, gde lokalni maksimumi preseka za vibracione ekscitacije iznose oko $10 \cdot 10^{-20}$ m^2. Na višim poljima se srednja energija u ova tri gasa sporo povećava sa porastom polja (do oko 0.27 Td, 7.7 Td i 17 Td za elektrone u CH_4, CF_4 i C_3F_8, respektivno). U ovom opsegu polja se većina elektrona nalazi u energijskoj oblasti u kojoj se preseci za vibracionu ekscitaciju naglo povećavaju sa porastom energije, što dovodi do sporog povećanja energije sa porastom E/n_0. Pri kraju ovog opsega polja srednja energija iznosi oko 0.057 eV za elektrone u CH_4 i oko 0.1 eV za elektrone u CF_4 i C_3F_8. To znači da se elektroni u CH_4 čija je energija oko četiri puta veća od srednje energije nalaze u energijskom intervalu u kome presek za prvu vibracionu ekscitaciju opada sa porastom energije, dok se elektroni u CF_4 i C_3F_8, čija je energija oko tri puta veća od srednje energije, nalaze u energijskom intervalu u kome preseci za sve vibracione ekscitacije opadaju sa porastom energije (ili su znatno manji od 10^{-20} m^2, u slučaju poslednje dve vibracione ekscitacije u C_3F_8). Na višim poljima, srednja energija se
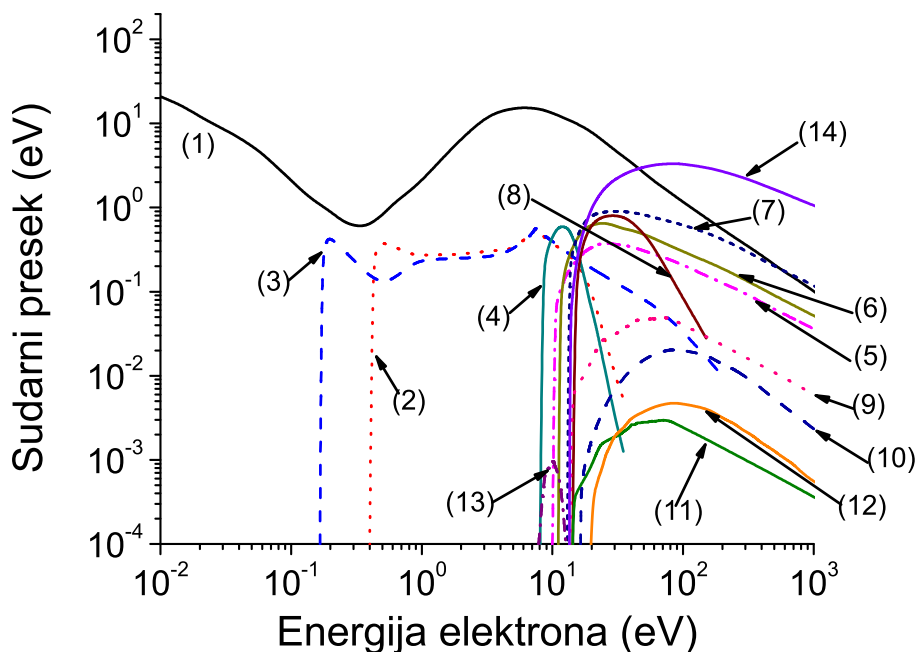
Slika 53: Set preseka za rasejanje elektrona u CH_4: (1) presek za transfer impulsa u elastičnim sudarima, vibracione ekscitacije (2) v1-3, (3) v1-4, elektronske ekscitacije (4), (5), (6), (7), (8), disocijacije (9) CH(A-X), (10) H_α, (11) CH(B-X), (12) H_β , (13) zahvat elektrona i (14) jonizacija.

znatno brže povećava sa porastom polja (do oko 46 Td za elektrone u CH_4 i CF_4 i do oko 77 Td za elektrone u C_3F_8). Pri kraju ovog opsega polja srednja energija elektrona iznosi 3.2 eV, 2.7 eV i 0.9 eV za elektrone u CH_4, CF_4 i C_3F_8, respektivno. Na višim poljima je porast srednje energije u CH_4 i CF_4 znatno sporiji nego u prethodnom opsegu polja, dok je porast srednje energije u C_3F_8 malo sporiji između približno 77 Td i 400 Td, nakon čega se dodatno usporava. Elektroni čija je energija oko tri puta veća od srednje energije na poljima višim od 46 Td u CH_4 i CF_4 mogu da izgube energiju u elektronskim ekscitacijama, što dovodi do sporijeg porasta srednje energije u ovom opsegu polja. Malo sporiji porast srednje energije u C_3F_8 u na poljima višim od 77 Td je verovatno posledica toga što se mnogi elektroni nalaze u energijskoj oblasti u kojoj se preseci za vibracione ekscitacije povećavaju sa porastom energije. Pri tome preseci za prve tri vibracione ekscitacije dostižu drugi i treći lokalni maksimum, dok preseci za poslednje dve vibracione ekscitacije dostižu prvi i drugi lokalni maksimum u energijskom intervalu između 2 eV i 10 eV. U C_3F_8 je srednja energija na 400 Td oko 5.4 eV, pa elektroni čija je energija oko 2.5 puta veća od srednje energije mogu da učestvuju u disocijaciji i jonizaciji molekula C_3F_8, a to dovodi do značajnih energijskih gubitaka u neelastičnim sudarima i do sporijeg porasta srednje energije sa porastom polja za E/n_0 veće od 400 Td.

Kvalitativni trend ponašanja srednje energije u N_2 je nešto drugačiji od odgovarajućih trendova u preostala tri gasa. Na poljima do oko 0.01 Td, srednja energija je termalna (oko 0.038 eV). U ovom opsegu polja elektroni gube energiju u elastičnim sudarima i rotacionim ekscitacijama, sa pragom od 0.02 eV. Srednja energija se sporo povećava do oko 0.077 Td, gde iznosi oko 0.056 eV. Nakon toga se srednja energija povećava skoro linearno sa poljem do oko 1.7 Td, gde iznosi oko 0.57 eV. Na početku ovog opsega elektroni čija energija je oko 4 puta veća od
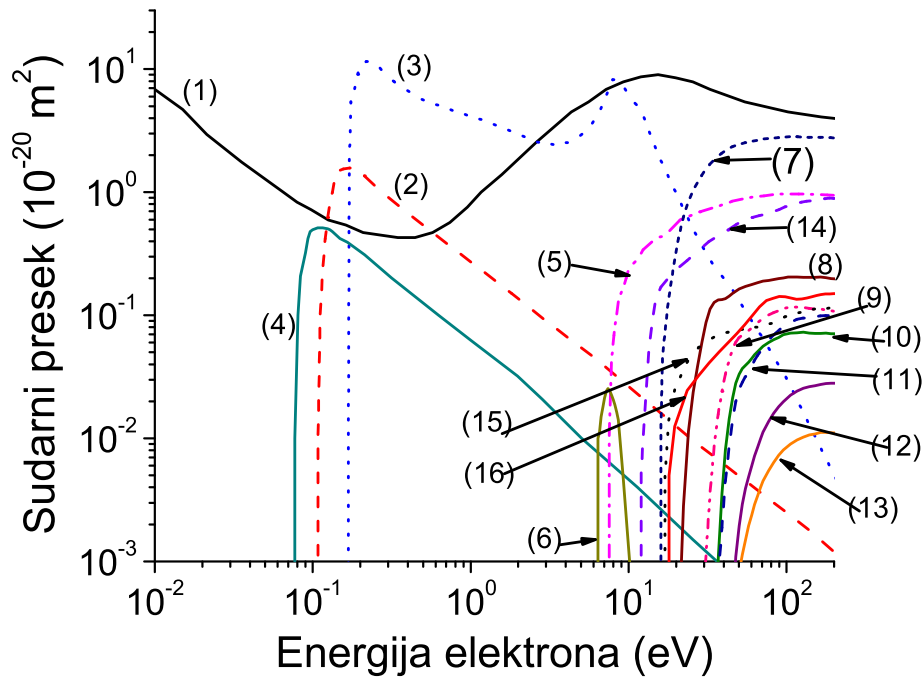
Slika 54: Set preseka za rasejanje elektrona u CF$_4$: (1) presek za transfer impulsa u elastičnim sudarima, vibracione ekscitacije (2) v$_1$, (3) v$_3$, (4) v$_4$, (5) elektronska ekscitacija, (6) disocijativni zahvat elektrona, disocijativne jonizacije (7) $CF_4 + e \longrightarrow CF_3^+ + F + 2e$, (8) $CF_4 + e \longrightarrow CF_2^+ + 2F + 2e$, (9) $CF_4 + e \longrightarrow CF^+ + 3F + 2e$, (10) $CF_4 + e \longrightarrow C^+ + 4F + 2e$, (11) $CF_4 + e \longrightarrow F^+ + CF_3 + 2e$, (12) $CF_4 + e \longrightarrow CF_3^{2+} + F + 3e$, (13) $CF_4 + e \longrightarrow CF_2^{2+} + 2F + 3e$, disocijacije molekula na neutralne fragmente (14) $CF_4 + e \longrightarrow CF_3 + F + e$, (15) $CF_4 + e \longrightarrow CF_2 + 2F + e$, (16) $CF_4 + e \longrightarrow CF + 3F + e$

srednje energije mogu da učestvuju u prvoj vibracionoj ekscitaciji, dok na kraju ovog opsega veliki broj elektrona može učestvovati u prve tri vibracione ekscitacije. U opsegu polja između 1.7 Td i 35 Td je porast srednje energije sa porastom polja značajno usporen. Na kraju ovog opsega je srednja energija elektrona oko 1 eV. U N$_2$ su preseci za vibracionu ekscitaciju najintenzivniji (preko $0.1 \cdot 10^{-20}$ m^2) u energijskom intervalu izmedju oko 1.5 eV i 4 eV. Ovo znači da se u opsegu polja između 1.7 Td i 35 Td elektroni čija je energija oko dva puta veća od srednje energije nalaze u energijskom intervalu u kome preseci za vibracione ekscitacije dostižu maksimum, pa ovi elektroni imaju veliku verovatnoću da izgube energiju u neelastičnim sudarima, a to značajno usporava porast srednje energije sa porastom E/n_0 u ovom opsegu polja. Porast srednje energije sa porastom E/n_0 je znatno intenzivniji između 35 Td i 130 Td. U ovom opsegu polja srednja energija nalazi se u energijskom intervalu između 1 eV i 3.3 eV. Na početku ovog opsega elektroni čija je energija oko četiri puta veća od srednje energije nalaze se u energijskom intervalu u kome preseci za vibracionu ekscitaciju naglo opadaju sa porastom energije, dok se na kraju ovog opsega polja većina elektrona nalazi u ovom energijskom intervalu. Na kraju ovog opsega polja elektroni čija je energija oko dva puta veća od srednje energije mogu učestvovati u elektronskim ekscitacijama, što dovodi do sporijeg porasta srednje energije sa porastom E/n_0 na višim poljima.

Slika 57 prikazuje profile sve tri fluks komponente TTIII, koje su nezavisne u odsustvu mag-
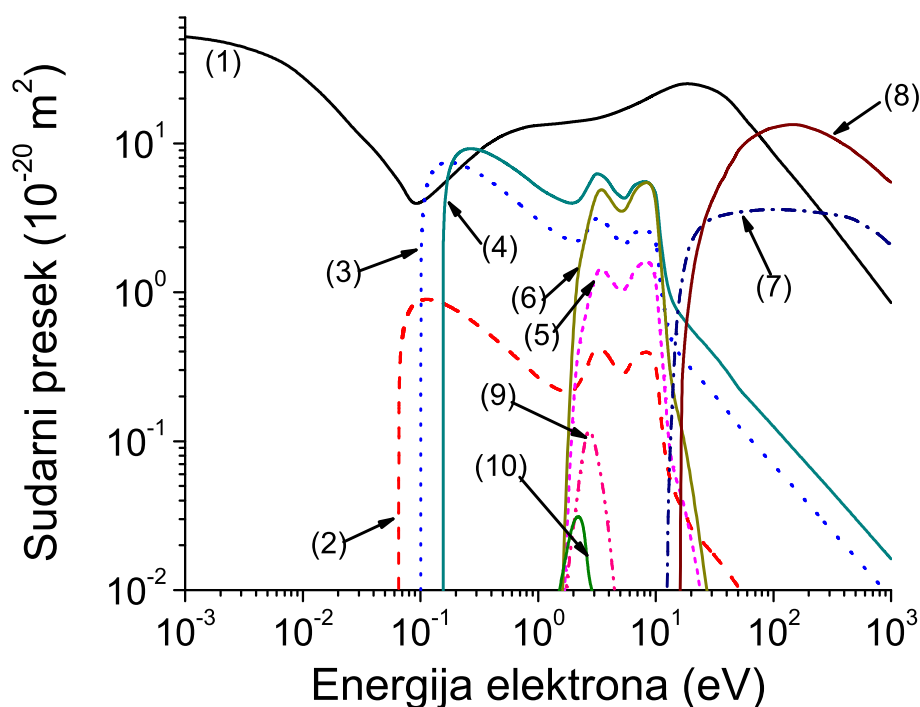
Slika 55: Set preseka za rasejanje elektrona u C_3F_8:(1) presek za transfer impulsa u elastičnim sudarima, vibracione ekscitacije (2) v_1, (3) v_2, (4) v_3, (5) v_4, (6) v_5, (7) disocijacija, (8) jonizacija, (9) disocijativni zahvat elektrona i (10) trojni zahvat elektrona na atmosferskom pritisku i temperaturi od 293 K.

netskog polja, u funkciji E/n_0 za elektrone u N_2, CH_4, CF_4 i C_3F_8. Ovi rezultati su dobijeni primenom momentnog metoda za numeričko rešavanje Boltzmann-ove jednačine. Na kvalitativnom nivou, trendovi zavisnosti sve tri komponente TTIII od E/n_0 su jako slični za elektrone u CF_4 i C_3F_8, dok se trendovi zavisnosti vandijagonalnih komponenti u CH_4 i ova dva gasa razlikuju na visokim poljima. Naime, Q_{zxx} komponenta je negativna samo u uskom opsegu E/n_0 za elektrone u CH_4, dok za elektrone u CF_4 i C_3F_8 ova komponenta postane negativna negde na srednini E/n_0 opsega i ostaje negativna do kraja opsega polja. U ova tri gasa na najnižim poljima sve tri komponente TTIII su pozitivne i monotono se povećavaju sa porastom polja do oko 0.013 Td, 0.17 Td i 0.59 Td za elektrone u CH_4, CF_4 i C_3F_8, respektivno. Pozitivnost Q_{zxx} komponente je posledica opadanja preseka za transfer impulsa sa porastom energije kao i male vrednosti preseka za vibracionu ekscitaciju u energijskom opsegu koji odgovara termalnim energijama. Sve tri komponente TTIII se povećavaju sa porastom E/n_0 uprkos tome što najenergičniji elektroni mogu da učestvuju u vibracionim ekscitacijama. Uzrok tome je što konstantnost srednje energije u ovom opsegu polja dovodi do konstantnosti brzinskih koeficijenata za neelastične sudare. Ovo znači da se sa porastom E/n_0 povećava usmerena komponenta brzine bez značajnog porasta haotične komponente brzine i otpora kretanju naelektrisanih čestica, koji je izazvan sudarima sa molekulima pozadinskog gasa. Na višim vrednostima E/n_0 energija koja je apsorbovana od strane spoljašnjeg polja je veća od energije koja se izgubi u elastičnim i neelastičnim sudarima pri termalnim energijama. To dovodi do povećanja srednje energije i brzinskih koeficijenata za vibracione ekscitacije sa porastom E/n_0, ali se srednja energija sporo povećava sa porastom polja zbog velikih energijskih gubitaka u vibracionim ekscitacijama.
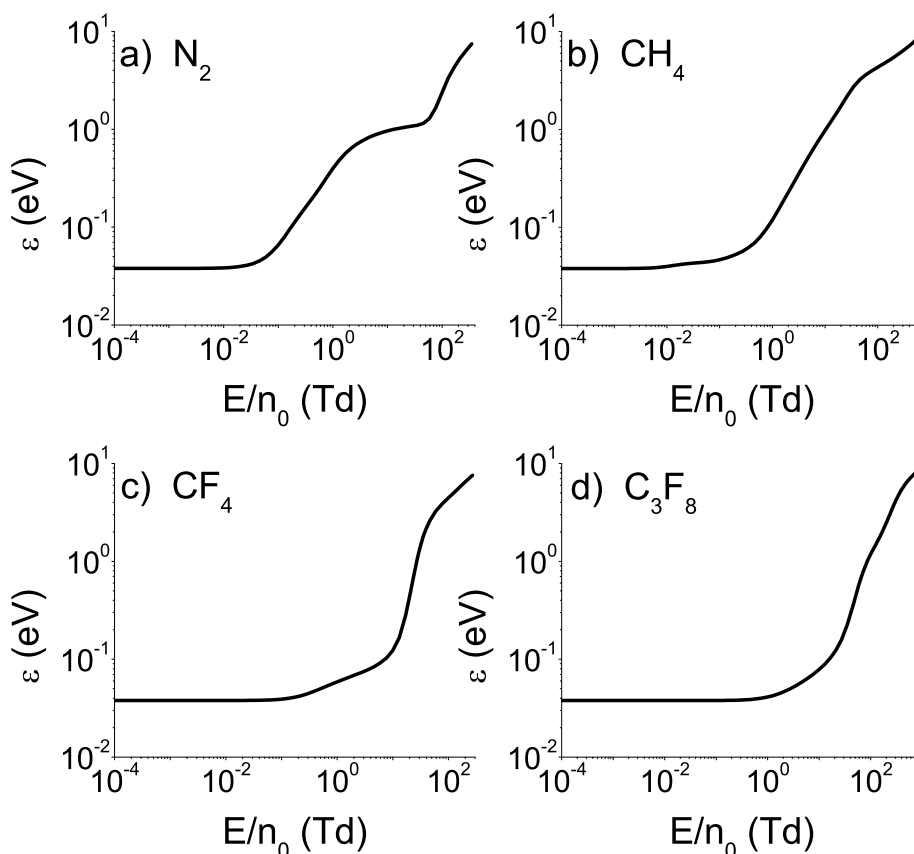
Slika 56: Srednja energija u funkciji E/n_0 za rojeve elektrona u N_2, CH_4, CF_4 i C_3F_8. Rezultati su dobijeni primenom metoda više članova za rešavanje Boltzmann-ove jednačine.

Povećanje brzinskih koeficijenata za neelastične sudare dovodi do naglog opadanja sve tri komponente TTIII u opsegu polja do oko 0.13 Td, 1.7 Td i 10 Td za elektrone u CH_4, CF_4 i C_3F_8, respektivno. Može se uočiti da se oblast polja u kojoj se srednja energija sporo povećava sa porastom E/n_0 završava na oko 0.13 Td u CH_4 i blizu 10 Td u C_3F_8, što odgovara vrednostima polja na kojima neke komponente TTIII prestanu da opadaju sa porastom E/n_0. Međutim, u CF_4 Q_{zzz} i Q_{xxz} opadaju sa porastom E/n_0 samo do oko 1.7 Td, iako je ova vrednost polja blizu sredine opsega u kojoj se srednja energija sporo povećava sa porastom E/n_0. Može se uočiti da su Q_{zzz} i Q_{xxz} negativne u CF_4 između približno 1 Td i 7.7 Td. Pri tome su u CF_4 sve tri komponente TTIII negativne u opsegu polja između 2.1 Td i 7.7 Td. Negativnost komponenti TTIII u ovom opsegu polja je posledica intenzivnih energijskih gubitaka u vibracionim ekscitacijama. Naime, srednja energija elektrona se nalazi u intervalu između 0.059 eV i 0.1 eV u opsegu E/n_0 od 1 Td do 7.7 Td, što znači da se svi elektroni u ovom opsegu polja, čija je energija od 2 do 4 puta veća od srednje energije, nalaze u energijskoj zoni u kojoj prve tri vibracione ekscitacije dostižu lokalne maksimume u CF_4, pošto ove vibracione ekscitacije dostižu maksimume u energijskom intervalu između 0.1 eV i 0.24 eV. Pri tome su preseci za drugu i treću vibracionu ekscitaciju veći od preseka za transfer impulsa u elastičnim sudarima u ovom energijskom intervalu. Primećuje se da Q_{zzz} i Q_{xxz} postaju pozitivne baš u okolini polja od 7.7 Td, gde se porast srednje energije sa porastom E/n_0 ubrzava. U sva tri gasa se apsolutne vrednosti sve tri komponente TTIII povećavaju sa porastom E/n_0, počev od polja na kome srednja
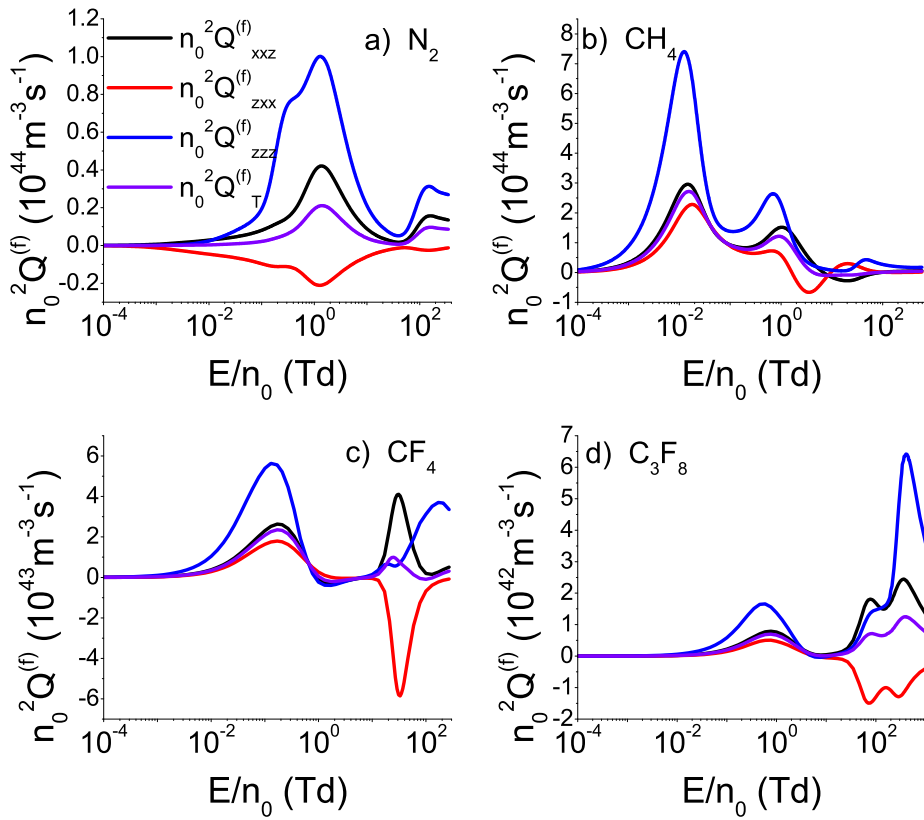
Slika 57: $n_0^2 Q_{xxz}^{(f)}$, $n_0^2 Q_{zxx}^{(f)}$, $n_0^2 Q_{zzz}^{(f)}$ i $n_0^2 Q_T^{(f)}$ komponente fluks transportnog tenzora trećeg reda u funkciji E/n_0 za rojeve elektrona u N_2, CH_4, CF_4 i C_3F_8. Rezultati su dobijeni uz pomoć metoda više članova za rešavanje Boltzmann-ove jednačine.

energija počne brže da se povećava sa porastom E/n_0. Pritom apsolutne vrednosti vandijago-nalnih komponenti dostižu lokalni maksimum na oko 1 Td, 31 Td i 77 Td za elektrone u CH_4, CF_4 i C_3F_8 respektivno. Longitudinalna komponenta TTIII u CH_4 dostiže lokalni maksimum na oko 0.77 Td, posle čega opada. U CF_4 i C_3F_8 se longitudinalna komponenta TTIII naglo povećava sa porastom E/n_0 do oko 21 Td i 85 Td, respektivno.

Ponašanje vandijagonalnih komponenti TTIII i longitudinalne komponente kvalitativno se razlikuju na poljima višim od položaja drugog lokalnog maksimuma vandijagonalnih kompo-nenti TTIII. Zapravo, za elektrone u CH_4 Q_{zzz} komponenta opada posle drugog loklanog mak-simuma na 0.77 Td do oko 17 Td, gde dostiže lokalni minimum. Vandijagonalne komponente Q_{zxx} i Q_{xxy} takođe opadaju nakon 1 Td. Pri tome Q_{zxx} komponenta postaje negativna na oko 1.7 Td i dostiže minimum na oko 3.5 Td. Nakon minimuma ova komponenta se povećava, po-stajući ponovo pozitivna na oko 10 Td i dostižući lokalni maksimum na oko 21 Td. U ovom opsegu polja Q_{xxz} komponenta opada, postajući negativna na oko 7.7 Td i dostižući lokalni minimum na oko 21 Td. Može se zapaziti da Q_{xxz} komponenta postaje negativna na otprilike istoj vrednosti polja na kojoj Q_{zxx} komponenta postaje pozitivna, kao i da apsolutne vrednosti ove dve komponente TTIII dostižu lokalni maksimum na istoj vrednosti polja (na oko 21 Td). Na poljima višim od 21 Td se Q_{zzz} komponenta povećava do oko 46 Td, posle čega opada do oko 500 Td. Pri tome Q_{zxx} komponenta monotono opada u ovom opsegu polja, dok se Q_{xxz} povećava postajući pozitivna na oko 100 Td, posle čega se povećava sporo, sa porastom E/n_0.

Kvalitativni trend ponašanja longitudinalne komponente TTIII je sličan za elektrone u CF$_4$ i C$_3$F$_8$. Naime, longitudinalna komponenta TTIII se nakon uskog opsega saturacije ponovo naglo povećava u opsegu polja od 29 Td do 210 Td za elektrone u CF$_4$ i od 170 Td do 400 Td za elektrone u C$_3$F$_8$. Na kraju ovih opsega polja vrednosti Q_{zzz} u CF$_4$ i C$_3$F$_8$ dostižu lokalne maksimume, posle čega monotono opadaju sa porastom polja. Apsolutne vrednosti vandijagonalnih komponenti TTIII u CF$_4$ monotono opadaju posle drugog lokalnog maksimuma do oko 130 Td. Međutim, na poljima višim od 100 Td se Q_{xxz} i Q_{zxx} blago povećavaju sa porastom E/n_0. Za elektrone u C$_3$F$_8$ apsolutne vrednosti Q_{xxz} i Q_{zxx} opadaju posle drugog lokalnog maksimuma na 77 Td, dostižući lokalni minimum na oko 150 Td. Na višim poljima se apsolutne vrednosti ove dve komponente TTIII ponovo povećavaju, dosežući još jedan lokalni maksimum na oko 350 Td i 300 Td za Q_{xxz} i Q_{zxx}, respektivno. Nakon ovog lokalnog maksimuma apsolutne vrednosti Q_{xxz} i Q_{zxx} monotono opadaju sa porastom E/n_0 do kraja razmatranog opsega polja.

Za elektrone u N$_2$ je Q_{zxx} komponenta negativna u celom opsegu polja. Ovo je posledica povećanja preseka za transfer impulsa sa porastom energije do 2.8 eV i povećanja preseka za druge sudarne procese na višim energijama. Apsolutne vrednosti sve tri komponente TTIII se monotono povećavaju sa porastom E/n_0 do oko 1.3 Td, gde dostižu lokalni maksimum. U ovom ospegu polja srednja energija ima vrednosti u intervalu od 0.038 eV do 0.48 eV, pri čemu je porast srednje energije sa porastom E/n_0 praktično linearan na poljima višim od 0.077 Td. Sve tri komponente TTIII se, po apsolutnoj vrednosti, povećavaju sa porastom E/n_0 u ovom opsegu polja uprkos tome što na sredini ovog opsega (na oko 0.35 Td) elektroni čija je energija oko dva puta veća od srednje energije mogu da učestvuju u vibracionim ekscitacijama (prag za prvu vibracionu ekscitaciju je 0.29 eV). Ovo je posledica toga što su preseci za vibracione ekscitacije manji od 0.1 angstrem do 1.5 eV, pa većina elektrona u ovom opsegu polja ima malu kolizionu frekvencu za vibracione ekscitacije. Za vrednosti redukovanog električnog polja između 1.3 Td i 46 Td apsolutne vrednosti sve tri komponente TTIII monotono opadaju sa porastom E/n_0. Primećuje se da se upravo u ovom opsegu polja porast srednje energije sa porastom E/n_0 značajno usporava, pri srednjoj energiji elektrona između 0.48 eV i 1.15 eV za E/n_0 između 1.3 Td i 46 Td. Ovo znači da se elektroni čija je energija oko tri puta veća od srednje energije nalaze u energijskom intervalu u kome su preseci za vibracione ekscitacije najintenzinviji. To dovodi do opadanja apsolutnih vrednosti komponenti TTIII i do usporavanja porasta srednje energije sa porastom E/n_0 u ovom opsegu polja. Apsolutne vrednosti sve tri komponente TTIII se monotono povećavaju sa porastom E/n_0 od 46 Td do oko 170 Td. Srednja energija se raste sa 1.15 eV na 46 Td do 4.37 eV na 170 Td, pri čemu je povećanje srednje energije sa porastom E/n_0 znatno brže nego na nižim poljima. U ovom E/n_0 opsegu, elektroni čija je energija bar 3.5 puta veća od srednje energije nalaze se u energijskoj oblasti u kojoj su preseci za vibracione ekscitacije manji od 0.1 angstrema i u kojoj presek za transfer impulsa u elastičnim sudarima opada sa porastom energije. Ovo dovodi do povećanja apsolutnih vrednosti sve tri komponente TTIII i do bržeg porasta srednje energije sa porastom E/n_0 u ovom opsegu polja. Za E/n_0 veće od 170 Td apsolutne vrednosti sve tri komponente TTIII opadaju sa porastom E/n_0, uz šta se porast srednje energije sa porastom E/n_0 usporava. U ovom opsegu polja je srednja energija

elektrona između 4.37 eV i 7.44 eV, pa elektroni čija je energija oko 1.5 puta veća od srednje energije mogu da učestvuju u elektronskim ekscitacijama (prag za prvu elektronsku ekscitaciju u N_2 je 6.17 eV), što dovodi do opadanja apsolutnih vrednosti sve tri komponente TTIII.
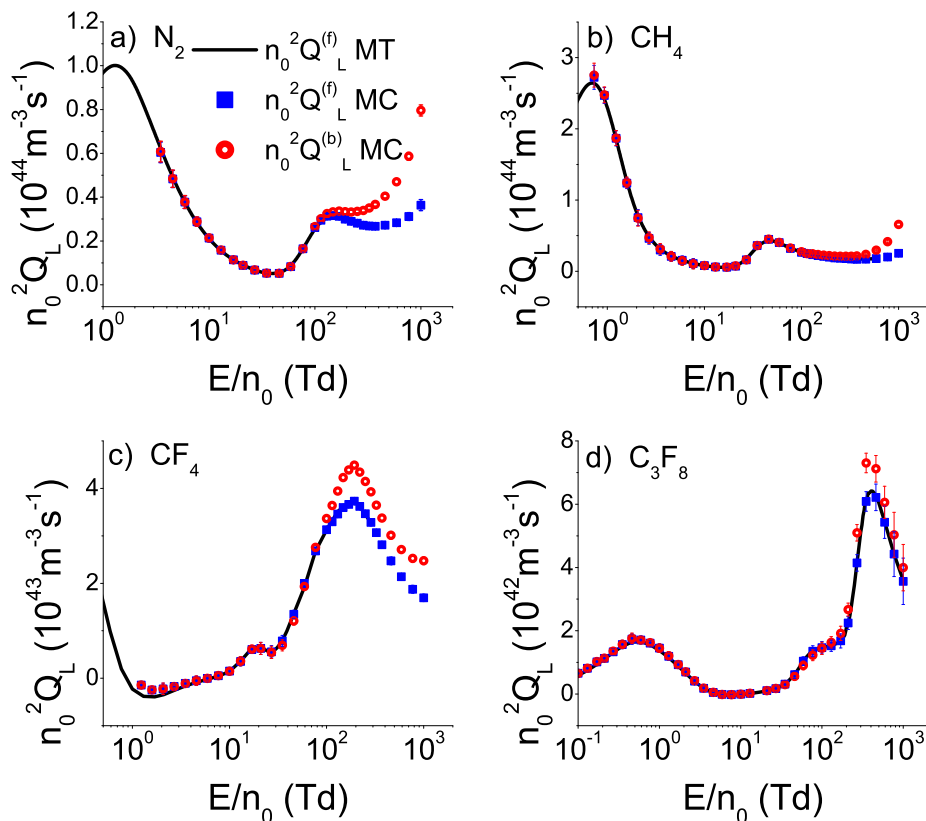
Slika 58: Fluks i balk vrednosti longitudinalne komponente transportnog tenzora trećeg reda $n_0^2 Q_L$ za elektrone u N_2, CH_4, CF_4 i C_3F_8. Na ovom grafiku su prikazani rezultati koji su dobijeni primenom metoda više članova za rešavanje Boltzmann-ove jednačine i Monte Carlo simulacija.

Na slikama 58 i 59 su prikazane fluks i balk vrednosti longitudinalne $n_0^2 Q_L$ i transverzalne $n_0^2 Q_T$ komponente transportnog tenzora trećeg reda, respektivno. Fluks vrednosti TKIII su određene primenom momentnog metoda za numeričko rešavanje Boltzmann-ove jednačine i Monte Carlo simulacija, dok su balk vrednosti ove komponente utvrđene primenom Monte Carlo simulacija. Sa grafika se vidi da se vrednosti fluks TKIII koje su dobijene primenom momentnog metoda za numeričko rešavanje Boltzmann-ove jednačine jako dobro slažu sa rezultatima Monte Carlo simulacija. Dobro slaganje rezultata koji su dobijeni primenom ove dve nezavisne metode potvrđuje validnost procedura za izračunavanje komponenti TTIII u korišćenim kompjuterskim kodovima. Važno je naglasiti da je na niskim poljima, na kojima je srednja energija uporediva sa termalnom energijom, neophodno uzeti u obzir termalno kretanje molekula pozadinskog gasa u Monte Carlo simulacijama da bi se dobilo slaganje sa rezultatima numeričkog rešavanja Boltzmann-ove jednačine. Ovo je naročito izraženo za elektrone u CF_4 i C_3F_8, zbog toga što je srednja energija praktično termalna do oko $5 \cdot 10^{-2}$ Td u CF_4 i do oko $2 \cdot 10^{-1}$ Td u C_3F_8. Na primer, ako se pri proračunu komponenti TTIII za elektrone u CF_4 na osnovu Monte Carlo simulacija primeni aproksimacija hladnog gasa, dobijene vrednosti $n_0^2 Q_L$ i $n_0^2 Q_T$ odstupaju za
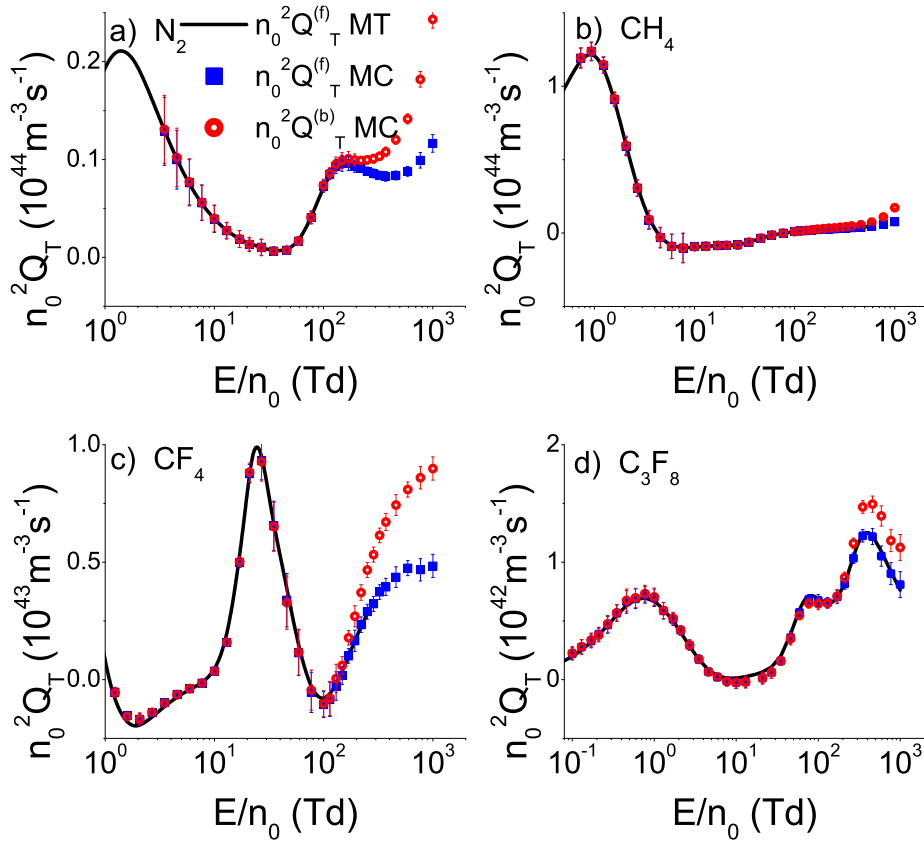
Slika 59: Fluks i balk vrednosti transverzalne komponente transportnog tenzora trećeg reda $n_0^2 Q_T$ za elektrone u N_2, CH_4, CF_4 i C_3F_8. Na ovom grafiku su prikazani rezultati koji su dobijeni primenom metoda više članova za rešavanje Boltzmann-ove jednačine i Monte Carlo simulacija.

više od 50% od odgovarajućih vrednosti određenih na osnovu momentnog metoda za rešavanje Boltzmann-ove jednačine, u opsegu polja u kome su komponente TTIII negativne. U ovom opsegu polja je srednja energija elektrona samo oko dva puta veća od termalne energije, te termalno kretanje molekula pozadinskog gasa značajno utiče na rasejanje elektrona.

Fluks i balk profili TKIII imaju istu kvalitativnu zavisnost od E/n_0 u sva četiri gasa u celom razmatranom E/n_0 opsegu. Važi uz to da su za elektrone u N_2, CH_4 i C_3F_8 fluks i balk vrednosti jednake do visokih polja, na kojima elektroni imaju dovoljno energije da jonizuju molekule pozadinskog gasa. No za elektrone u CF_4 je balk longitudinalna komponenta TTIII manja od fluks komponente u opsegu polja između 27 Td i 59 Td, ali ova razlika pripada okviru statističke nesigurnosti Monte Carlo simulacija. Ova razlika bi mogla biti posledica zahvata elektrona u CF_4. Naime, u ovom opsegu polja je srednja energija elektrona između 1 eV i 3.2 eV, pri čemu prag za zahvat elektrona u CF_4 iznosi 6.399 eV, uz šta presek za zahvat dostiže maksimum na oko 7.4 eV. Tako u ovom opsegu polja u zahvatu učestvuju najenergičniji elektroni, čija je energija između 6.4 i 2 puta veća od srednje energije, pa ovo može dovesti do smanjenja iskrivljenosti prostornog profila roja u pozitivnom ($q\mathbf{E}$) smeru, pod uticajem eksplicitnih efekata zahvata elektrona, slično kao u Ness-Robson-ovom modelu hlađenja zahvatom elektrona (videti potpoglavlje 4.8.2). Na poljima višim od 130 Td, 350 Td, 77 Td i 400 Td, za elektrone u

N_2, CH_4, CF_4 i C_3F_8, respektivno su balk vrednosti $n_0^2 Q_L$ i $n_0^2 Q_T$ veće od odgovarajućih fluks vrednosti. Ovo je posledica eksplicitnih efekata jonizacije. Pošto se energija elektrona povećava u smeru kretanja roja, na frontu roja postoji veći broj visokoenergijskih elektrona koji mogu da učestvuju u jonizaciji, nego na začelju roja. Zbog toga elektroni dominantno nastaju na frotnu roja, a ovo dovodi do većeg krivljenja roja u pozitivnom ($q\mathbf{E}$) smeru i do bržeg transverzalnog širenja u okolini fronta, pa su balk vrednosti $n_0^2 Q_L$ i $n_0^2 Q_T$ veće od odgovarajućih fluks vrednosti na visokim poljima.
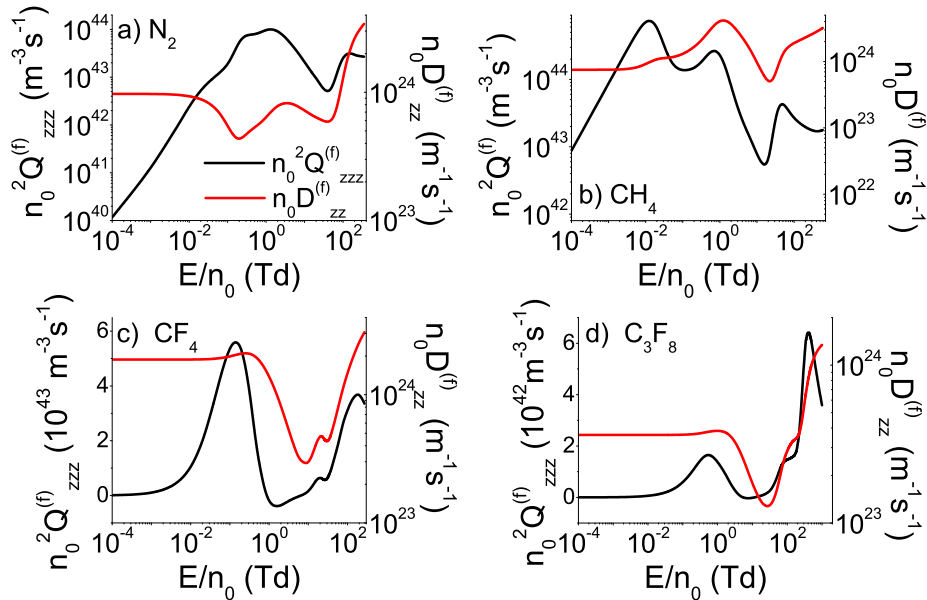
Slika 60: Korelacija longitudinalne komponente fluks transportnog tenzora trećeg reda $n_0^2 Q_L^{(f)}$ i fluks longitudinalne difuzije $n_0 D_L^{(f)}$ za rojeve elektrona u N_2, CH_4, CF_4 i C_3F_8. Rezultati su dobijeni na osnovu metoda više članova za rešavanje Boltzmann-ove jednačine.

Na slici 60 dati su profili zavisnosti $n_0^2 Q_L^{(f)}$ i $n_0 D_L^{(f)}$ od E/n_0 za elektrone u N_2, CH_4, CF_4 i C_3F_8. Na niskim poljima (do oko 0.21 Td, 0.0027 Td, 0.017 Td i 0.077 Td u N_2, CH_4, CF_4 i C_3F_8, respektivno) se $n_0^2 Q_L^{(f)}$ povećava sa porastom E/n_0 bez obzira na trend ponašanja $n_0 D_L^{(f)}$. Ovo je posledica toga što $n_0^2 Q_L^{(f)}$ reprezentuje usmereno kretanje i teži nuli u limesu niskih polja, za razliku od $n_0 D_L^{(f)}$ koje teži termalnoj vrednosti. Na višim poljima su profili zavisnosti $n_0^2 Q_L^{(f)}$ i $n_0 D_L^{(f)}$ od E/n_0 snažno koreliasni. Zapravo, $n_0^2 Q_L^{(f)}$ se povećava sa porastom E/n_0 u opsegu polja u kome se $n_0 D_L^{(f)}$ ubzano povećava (kao konveksna funkcija), dok opada u opsegu polja u kome $n_0 D_L^{(f)}$ opada, ili se povećava usporeno (kao konkavna funkcija) (videti potpoglavlje 5.2). Pored toga, u okolini lokalnih minimuma i maksiumuma $n_0 D_L^{(f)}$ nalaze se odgovarajući lokalni minimumi i maksimumi $n_0^2 Q_L^{(f)}$. Potrebno je ipak naglasiti da promene trenda ponašanja $n_0^2 Q_L^{(f)}$ pri porastu E/n_0 nekada prednjače u odnosu na odgovarajuće promene $n_0 D_L^{(f)}$. U slučaju opadanja $n_0^2 Q_L^{(f)}$ i $n_0 D_L^{(f)}$ sa porastom E/n_0 je ovo očekivano i može se pripisati većoj osetljivosti TKIII na otpor koji sudari sa molekulima pozadinskog gasa pružaju širenju elektrona. Pri okolnostima porasta $n_0^2 Q_L^{(f)}$ i $n_0 D_L^{(f)}$ bi ovo moglo biti posledica veće osetljivosti TKIII na dinamiku visokoenergijskih elektrona. Za elektrone u CF_4 i C_3F_8, $n_0^2 Q_L^{(f)}$ dostiže lokalni minimum i počinje da se povećava sa porastom E/n_0 znatno ranije nego $n_0 D_L^{(f)}$,

u opsegu polja u kome $n_0^2 Q_L^{(f)}$ ima negativne vrednosti (od 0.77 Td do 7.7 Td za elektrone u CF$_4$ i od 4.6 Td do 13 Td za elektrone u C$_3$F$_8$). Za elektrone u CF$_4$, $n_0^2 Q_L^{(f)}$ dostiže lokalni minimum na oko 1.7 Td dok $n_0 D_L^{(f)}$ dostiže loklani minimum na oko 10 Td. Slično tome, za elektrone u C$_3$F$_8$ $n_0^2 Q_L^{(f)}$ dostiže lokalni minimum na oko 7.7 Td, dok $n_0 D_L^{(f)}$ dostiže lokalni minimum na oko 27 Td. U oba slučaja $n_0^2 Q_L^{(f)}$ postane pozitivno malo pre nego što $n_0 D_L^{(f)}$ dostigne lokalni minimum (na oko 7.7 Td i oko 13 Td za elektrone u CF$_4$ i C$_3$D$_8$, respektivno). Porast $n_0^2 Q_L^{(f)}$ sa porastom E/n_0 u opsegu polja u kome je $n_0^2 Q_L^{(f)}$ negativno a $n_0 D_L^{(f)}$ opada može se pripisati tome što je $n_0^2 Q_L^{(f)}$ negativno samo kada su sudari dovoljno intenzivni da izazovu krivljenje profila roja u negativnom $(-q\mathbf{E})$ smeru. Pritom je za dalje opadanje $n_0^2 Q_L^{(f)}$ neophodno da se ovo krivljenje dodatno pojačava pod dejstvom sudara. To znači da su u opsegu polja u kome se $n_0^2 Q_L^{(f)}$ počne povećavati znatno pre $n_0 D_L^{(f)}$ sudari dovoljno intenzivni da dovedu do dodatnog opadanja $n_0 D_L^{(f)}$, ali nisu dovoljno intenzivni da pojačaju krivljenje roja u negativnom smeru, pri čemu se sa porastom E/n_0 pojačava efekat sile koji teži da iskrivi roj u pozitivnom $(q\mathbf{E})$ smeru. Zbog toga $n_0^2 Q_L^{(f)}$ dostiže lokalni minimum i počinje se povećavati sa porastom E/n_0 znatno pre $n_0 D_L^{(f)}$ u opsegu polja u kome je $n_0^2 Q_L^{(f)}$ negativno.
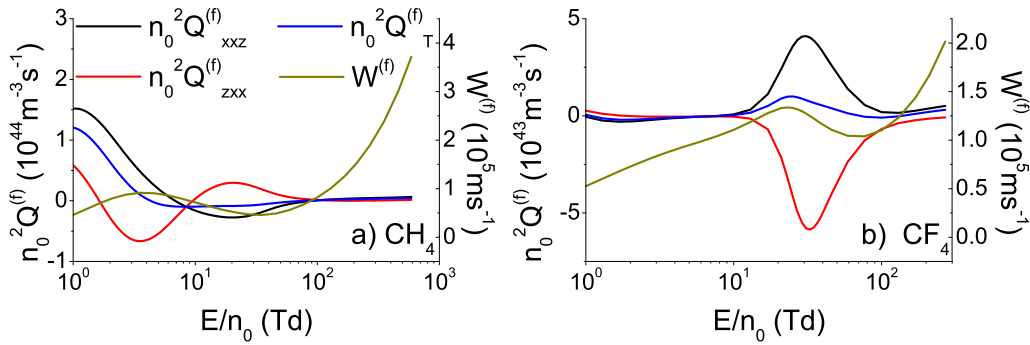
Slika 61: $n_0^2 Q_{xxz}^{(f)}$, $n_0^2 Q_{zxx}^{(f)}$, $n_0^2 Q_T^{(f)}$ komponente fluks transportnog tenzora trećeg reda i fluks brzina drifta $W^{(f)}$ u funkciji E/n_0 za rojeve elektrona u CH$_4$ i CF$_4$. Rezultati su dobijeni primenom metoda više članova za rešavanje Boltzmann-ove jednačine.

Na slici 61 su prikazani profili zavisnosti $n_0^2 Q_{xxz}^{(f)}$, $n_0^2 Q_{zxx}^{(f)}$, $n_0^2 Q_T^{(f)}$ i $W^{(f)}$ od E/n_0 za elektrone u CH$_4$ i CF$_4$. Vidi se da $n_0^2 Q_T^{(f)}$ postaje negativno za elektrone u CH4, negde na početku NDC oblasti (na oko 4.6 Td) i da ponovo biva pozitivno posle NDC oblasti, ali pre nego što brzina drifta dostigne vrednost koju je imala pre početka NDC-a (negde na oko 100 Td). Pri tome za elektrone u CH$_4$, $n_0^2 Q_{xxz}^{(f)}$ i $n_0^2 Q_{zxx}^{(f)}$ opadaju sa porastom E/n_0 i pre početka NDC-a. Međutim, $n_0^2 Q_{zxx}^{(f)}$ dostiže lokalni minimum i promeni trend ponašanja baš u okolini polja na kome počinje NDC (na oko 3.5 Td), dok $n_0^2 Q_{xxz}^{(f)}$ postaje negativna malo posle početka NDC-a (na oko 7.7 Td). Za elektrone u CH$_4$ NDC se završava na oko 35 Td, dok apsolutne vrednosti $n_0^2 Q_{xxz}^{(f)}$ i $n_0^2 Q_{zxx}^{(f)}$ dostignu lokalne maksimume na oko 21 Td, posle čega promene trend ponašanja.

Trendovi ponašanja $n_0^2 Q_{xxz}^{(f)}$, $n_0^2 Q_{zxx}^{(f)}$ i $n_0^2 Q_T^{(f)}$ su drugačiji u okolini NDC-a za elektrone u CF$_4$. U CF$_4$ se $n_0^2 Q_{xxz}^{(f)}$, $n_0^2 Q_{zxx}^{(f)}$ i $n_0^2 Q_T^{(f)}$ povećavaju po apsolutnoj vrednosti pre početka NDC-a. NDC počinje na oko 23 Td, a apsolutne vrednosti $n_0^2 Q_{xxz}^{(f)}$, $n_0^2 Q_{zxx}^{(f)}$ i $n_0^2 Q_T^{(f)}$ dostižu lokalne maksimume na 31 Td, 33 Td i 25 Td, respektivno. Ovo znači da $n_0^2 Q_{xxz}^{(f)}$, $n_0^2 Q_{zxx}^{(f)}$ i $n_0^2 Q_T^{(f)}$ počinju

da opadaju, po apsolutnoj vrednosti malo posle početka NDC-a. NDC se za elektrone u CF_4 završava na oko 77 Td, uz šta $n_0^2 Q_{zxx}^{(f)}$ nastavlja da opada po apsolutnoj vrednosti do kraja razmatranog opsega, dok $n_0^2 Q_{xxz}^{(f)}$ se počinje povećavati malo posle 130 Td, na nešto nižem redukovanom električnom polju od polja na kome brzina drifta dostigne svoju vrednost pre NDC-a. Za elektrone u CF_4 $n_0^2 Q_T^{(f)}$ postane negativno u uskom opsegu polja (između 59 Td i 130 Td) koji se završava u okolini polja na kome se $n_0^2 Q_{xxz}^{(f)}$ počinje povećavati sa porastom E/n_0. U CH_4 $n_0^2 Q_T^{(f)}$ ima negativne vrednosti u opsegu NDC-a i malo posle ovog opsega, dok je u CF_4 $n_0^2 Q_T^{(f)}$ negativno u uskom opsegu polja nakon NDC-a, ali pre nego sto $W^{(f)}$ dostigne vrednost od pre pocetka NDC-a. Ipak se na osnovu rezultata u ova dva gasa ne može reći da postoji generalna korelacija u trendovima zavisnosti vandijagonalnih komponenti TTIII i $W^{(f)}$ od E/n_0 jer su profili zavisnosti ovih komponenti jako različiti u okolini NDC-a u CH_4 i CF_4. Jedna zajednička karakteristika profila komponenti TTIII u oblasti NDC-a u ova dva gasa je to što $n_0^2 Q_{zxx}^{(f)}$ komponenta promeni trend ponašanja u okolini polja na kome počinje NDC.

5.6 Praktična razmatranja značajna za eksperimentalno određivanje transportnih koeficijenata trećeg reda

U literaturi se može naći nekoliko pokušaja da se izmere transportni koeficijenti trećeg reda za rojeve naelektrisanih čestica u gasovima [128–130]. Međutim, rezultati ovih eksperimenata su pokazivali snažnu zavisnost od pritiska, koja ukazuje na prisustvo nehidrodinamičkih efekata, što je ove rezultate učinilo nepouzdanim. Kasnije je utvrđeno da se zavisnost od pritiska može pripisati difuzionom hlađenju roja kroz gubitak najenergičnijih čestica na bočnim zidovima komore [126].

Kao što je izloženo u potpoglavlju 4.2, doprinos transpornih koeficijenata trećeg reda prostornom profilu roja povećava se sa smanjenjem koncentracije pozadinskog gasa n_0. Međutim, smanjenje n_0 dovodi do sporije prostorne relaksacije roja i većeg širenja duž transverzalnog pravca usled bočne difuzije, koje može dovesti do promene energijske raspodele naelektrisanih čestica roja za vreme trajanja eksperimenta. Zbog toga se transporni koeficijenti trećeg reda mogu izmeriti samo u jako velikim komorama pri niskoj koncentraciji pozadinskog gasa. Povećanje zapremine komore kroz koju se kreće roj daje više vremena za relaksaciju srednje energije roja i smanjuje gubitke naelektrisanih čestica kroz bočnu difuziju, ali povećava cenu eksperimenta. Zbog toga je poželjno utvrditi koliki je doprinos transportnih koeficijenata trećeg reda prostornom profilu roja za elektrone u različitim gasovima i pri različitim vrednostima n_0, ne bi li se utvrdili uslovi u kojima se ovi transportni koeficijenti mogu najefikasnije izmeriti.

U ovom potpoglavlju su izračunate vrednosti količnika $Q_L/D_L^{3/2}$ za elektrone u devet gasova u širokom opsegu redukovanog električnog polja, s obzirom na to što je doprinos longitudinalne komponente transportnog tenzora trećeg reda prostornom profilu roja direktno srazmeran vrednosti ovog količnika. Pored toga je razmatrana osetljivost transportnih koeficijenata trećeg reda na trojni zahvat elektrona u molekularnom kiseoniku, zbog toga što prisustvo ovog procesa dovodi do zavisnosti komponenti tenzora $n_0^2 \hat{Q}$ od koncentracije čestica pozadinskog gasa.

Vrednosti $Q_L/D_L^{3/2}$ koje su određene u okviru ove disertacije su prikazane na grafiku 62. One su izračunate pri koncentraciji čestica pozadinskog gasa od $n_0 = 3.54 \cdot 10^{22} m^{-3}$. Kao što je zaključeno u potpoglavlju 4.2, količnik $Q_L/D_L^{3/2}$ se pri promeni koncentracije čestica pozadinskog gasa skalira kao $\frac{1}{\sqrt{n_0}}$, te se na osnovu ovih rezultata može odrediti doprinos transportnih koeficijenata trećeg reda prostornom profilu roja i na drugim vrednostima n_0.
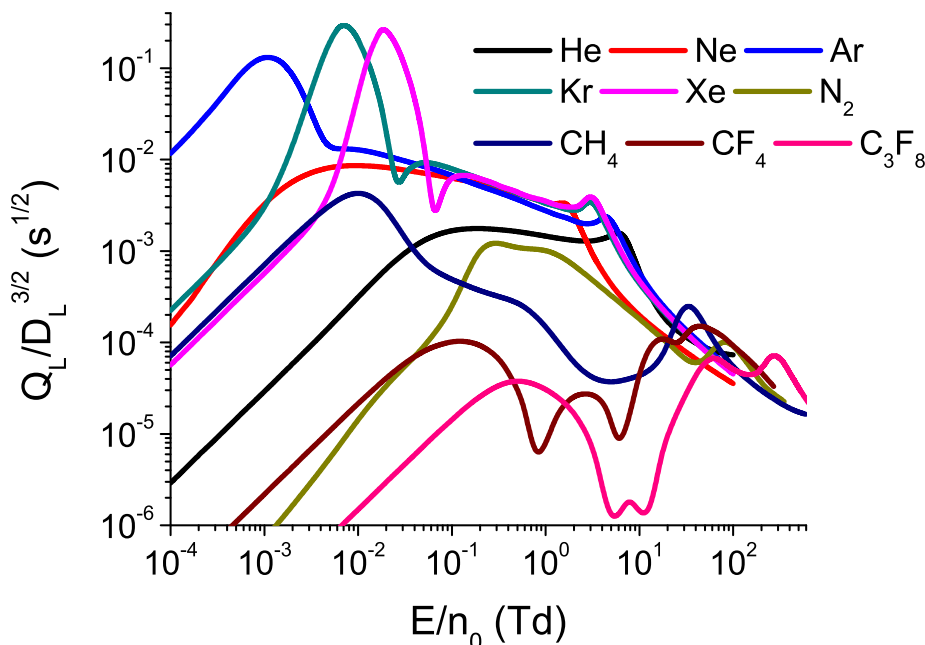

Slika 62: Količnik $Q_L/D_L^{3/2}$ u funkciji E/n_0 za rojeve elektrona u He, Ne, Ar, Kr, Xe, N_2, CH_4, CF_4 i C_3F_8. Rezultati su dobijeni primenom metoda više članova za rešavanje Boltzmann-ove jednačine, pri koncentraciji čestica pozadinskog gasa od $n_0 = 3.54 \cdot 10^{22} m^{-3}$.

Na slici 62 se može videti da se u svim razmatranim gasovima $Q_L/D_L^{3/2}$ na najnižim poljima monotono povećava sa porastom E/n_0 i da monotono opada sa porastom E/n_0 na poljima višim od 300 Td, dok između 10^{-4} Td i 300 Td $Q_L/D_L^{3/2}$ može imati nekoliko lokalnih minimuma i lokalnih maksimuma. Količnik $Q_L/D_L^{3/2}$ ima najvišu vrednosti u okolini prvog lokalnog maksimuma za elektrone u Ar, Kr i Xe na niskim poljima. Prvi lokalni maksimum $Q_L/D_L^{3/2}$ se nalazi na 10^{-3} Td, $7 \cdot 10^{-3}$ Td i $2 \cdot 10^{-2}$ Td za elektrone u Ar, Kr i Xe respektivno. U sva tri gasa je vrednost redukovanog električnog polja na kojoj $Q_L/D_L^{3/2}$ dostiže prvi lokalni maksimum oko dva puta niža od vrednosti polja na kojoj Q_L dostiže lokalni maksimum. Ovo je razumljivo budući da količnik $Q_L/D_L^{3/2}$ dostiže prvi lokalni maksimum na vrednosti polja na kojoj je došlo do značajnog porasta Q_L, ali se longitudinalna komponenta difuzionog tenzora nije previše povećala u odnosu na njenu termalnu vrednost.

Na osnovu slike 62 može se proceniti u kom gasu i za koje vrednosti E/n_0 je najlakše da longitudinalna komponenta TTIII bude eksperimentalno određena. Pošto su vrednosti količnika $Q_L/D_L^{3/2}$ u okolini prvog lokalnog maskimuma u argonu, kriptonu i ksenonu znatno veće od vrednosti ovog količnika za ostale gasove u celom razmatranom opsegu polja, longitudinalna komponenta TTIII može najlakše da bude izmerena u ova tri gasa u okolini polja na kojima $Q_L/D_L^{3/2}$ dostiže prvi lokalni maksimum.

Da bi se ispitali dodatni efekti koji mogu dovesti do zavisnosti rezultata eksperimenta dizajniranih za određivanje TKIII od koncentracije pozadinskog gasa, u ovom potpoglavlju je ispitivan uticaj elementarnih sudarnih procesa, čija je učestanost zavisna od gustine gasa, na TKIII. Kao primer ovog fenomena izabran je uticaj trojnog zahvata (eng. *three body attachment*) elektrona u kiseoniku na transportne koeficijente trećeg reda. Set preseka koji je korišćen za proračune u koseoniku je prikazan u radu [208] i na slici 63.
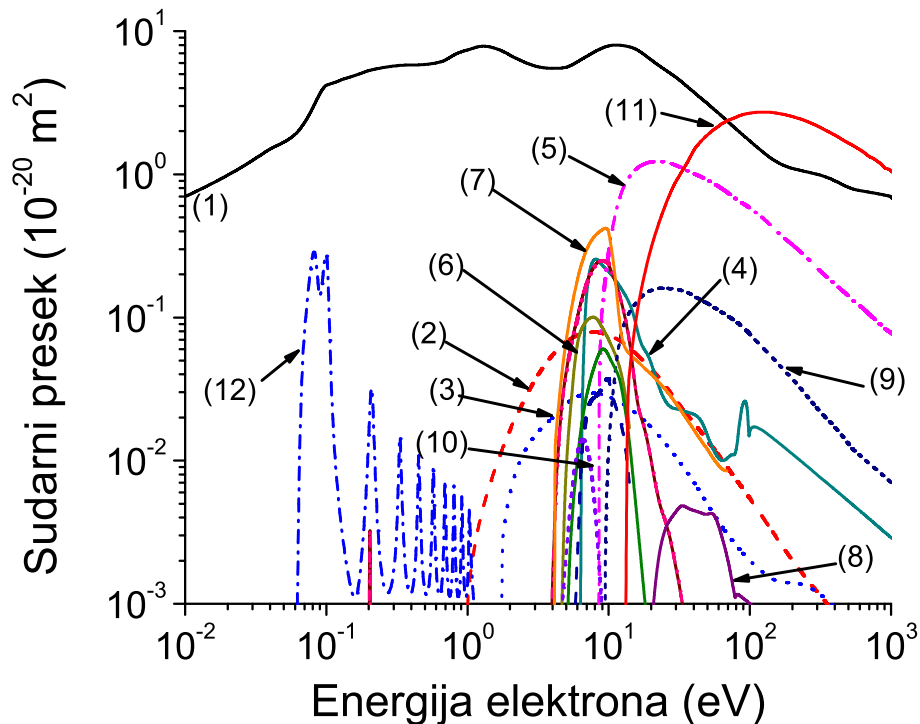
Slika 63: Set preseka za rasejanje elektrona u O_2: (1) transfer impulsa u elastičnim sudarima, (2) $a^1\Delta_g$, (3) Q_p, (4) $A^3\Sigma_u^+$, (5) $B^3\Sigma_u$, (6) $c^1\Sigma_u$ i $C^3\Delta_u$, (7) $Q_{vib}(\Sigma)$, (8) $b^1\Sigma_g^+$, (9) više elektronske ekscitacije, (10) zahvat elektrona, (11) jonizacija i (12) trojni zahvat elektrona na pritisku od 760 Torr i temperaturi od 293 K.

Slika 64 predstavlja profile zavisnosti $n_0^2 Q_{xxz}^{(f)}$, $n_0^2 Q_{zxx}^{(f)}$ i $n_0^2 Q_{zzz}^{(f)}$ komponenti od E/n_0 za elektrone u kiseoniku, za nekoliko vrednosti pritisaka. Ovi rezultati su dobijeni primenom momentnog metoda za numeričko rešavanje Boltzmann-ove jednačine.

Kvalitativni trendovi zavisnosti TKIII od E/n_0 u O_2 su isti za sve vrednosti pritiska (sa izuzetkom longitudinalne komponente TTIII na najnižim poljima, za najviše vrednosti pritiska). Na najnižim poljima (u razmatranom opsegu) $n_0^2 Q_{zzz}^{(f)}$ i $n_0^2 Q_{zxx}^{(f)}$ komponente su pozitivne, dok je $n_0^2 Q_{xxz}^{(f)}$ komponenta negativna. Uz to, $n_0^2 Q_{zzz}^{(f)}$ i $n_0^2 Q_{zxx}^{(f)}$ komponente monotono opadaju sa porastom E/n_0, dok se $n_0^2 Q_{xxz}^{(f)}$ komponenta monotono povećava do oko 2.7 Td. Pri tome vandijagonalne komponente $n_0^2 Q_{zxx}^{(f)}$ i $n_0^2 Q_{xxz}^{(f)}$ menjaju znak na oko 1 Td. Na poljima višim od 2.7 Td $n_0^2 Q_{xxz}^{(f)}$ i $n_0^2 Q_{zzz}^{(f)}$ komponente se naglo povećavaju sa porastom E/n_0 do oko 10 Td, gde dostižu lokalni maksimum, a $n_0^2 Q_{zxx}^{(f)}$ komponenta naglo opada do oko 7.7 Td, gde dostiže lokalni minimum. Nakon 10 Td apsolutna vrednost $n_0^2 Q_{zxx}^{(f)}$ komponente monotono opada sa porastom E/n_0 do kraja razmatranog opsega, dok naporedo $n_0^2 Q_{xxz}^{(f)}$ i $n_0^2 Q_{zzz}^{(f)}$ komponente monotono opadaju
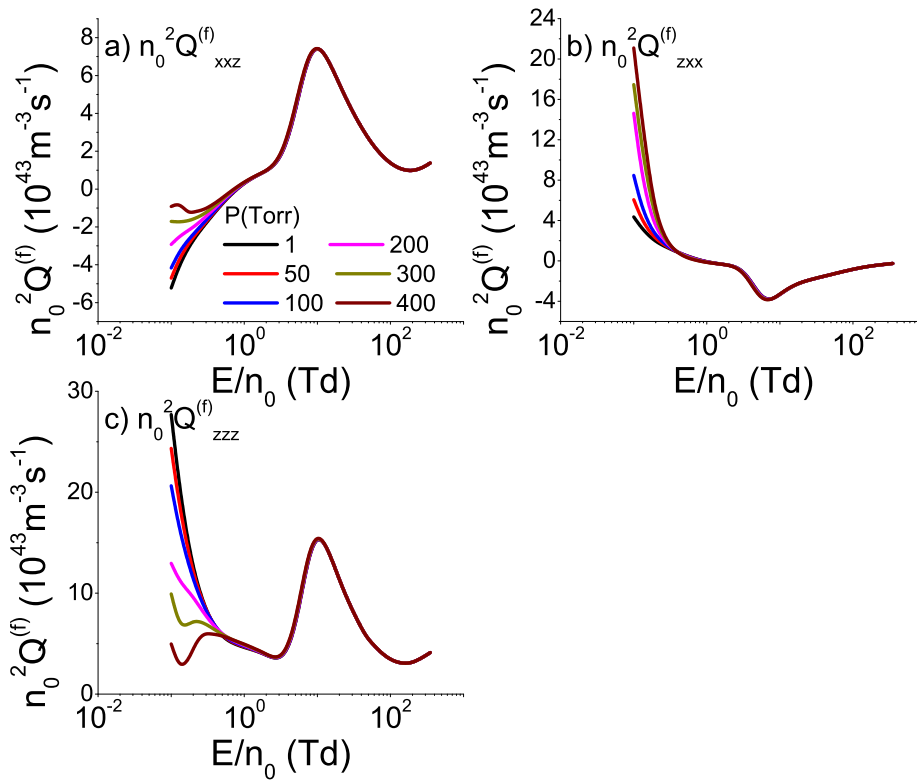
Slika 64: $n_0^2 Q_{xxz}^{(f)}, n_0^2 Q_{zxx}^{(f)}$ i $n_0^2 Q_{zzz}^{(f)}$ komponente fluks transportnog tenzora trećeg reda u funkciji E/n_0 i pritiska pozadinskog gasa za elektrone u O_2. Rezultati su dobijeni primenom metoda više članova za rešavanje Boltzmann-ove jednačine.

do oko 170 Td, gde dostižu lokalni minimum, nakon čega se povećavaju do kraja razmatranog opsega polja (do 350 Td).

Profili sve tri komponente TTIII snažno zavise od pritiska na niskim poljima zbog uticaja trojnog zahvata elektrona, dok je ova zavisnost zanemarljiva na visokim poljima zbog malog intenziteta preseka za trojni zahvat na visokim energijama. Longitudinalna komponenta TTIII opada sa porastom pritiska na poljima nižim od 0.59 Td. U profilu zavisnosti ove komponente od E/n_0 uz to postoji još jedan lokalni minimum na oko 0.13 Td za vrednosti pritiska veće od 200 Torr. Opadanje $n_0^2 Q_{zzz}^{(f)}$ komponente sa porastom pritiska na niskim poljima i pojava dodatnog lokalnog minimuma jesu posledice hlađenja roja trojnim zahvatom elektrona. U opsegu polja između 0.59 Td i 2.7 Td $n_0^2 Q_{zzz}^{(f)}$ komponenta se povećava sa porastom pritiska, ali je ovaj efekat jako slab. Porast $n_0^2 Q_{zzz}^{(f)}$ komponente sa porastom pritiska u ovom opsegu polja može se pripisati grejanju roja trojnim zahvatom elektrona.

Apsolutna vrednost $n_0^2 Q_{xxz}^{(f)}$ komponente opada sa porastom pritiska u opsegu polja do oko 0.77 Td. Pri tome apsolutna vrednost ove komponente ima dodatni lokalni minimum na oko 0.13 Td za vrednosti pritiska veće od 300 Torr. U opsegu polja između 0.1 Td i 0.35 Td $n_0^2 Q_{zxx}^{(f)}$ komponenta se povećava sa porastom pritiska. Na poljima višim od 1 Td je zavisnost sve tri komponente TTIII od pritiska praktično zanemarljiva.

5.7 Transportni koeficijenti trećeg reda za pozitrone u molekularnim gasovima

5.7.1 Preliminarije

Na slikama 6.7.1.1, 6.7.1.2. i 6.7.1.3. prikazani su setovi preseka ze rasejanje pozitrona u H_2, N_2 i CF_4, respektivno, koji su korišćeni u našim proračunima. Oni su razvijeni u našoj laboratoriji na osnovu eksperimentalno određenih i teorijski izračunatih preseka za pojedinačne sudarne procese, koji su preuzeti iz literature. Setovi preseka za rasejanje pozitrona u H_2, N_2 i CF_4 su detaljno tumačeni u radovima [154], [209, 210] i [155], respektivno.
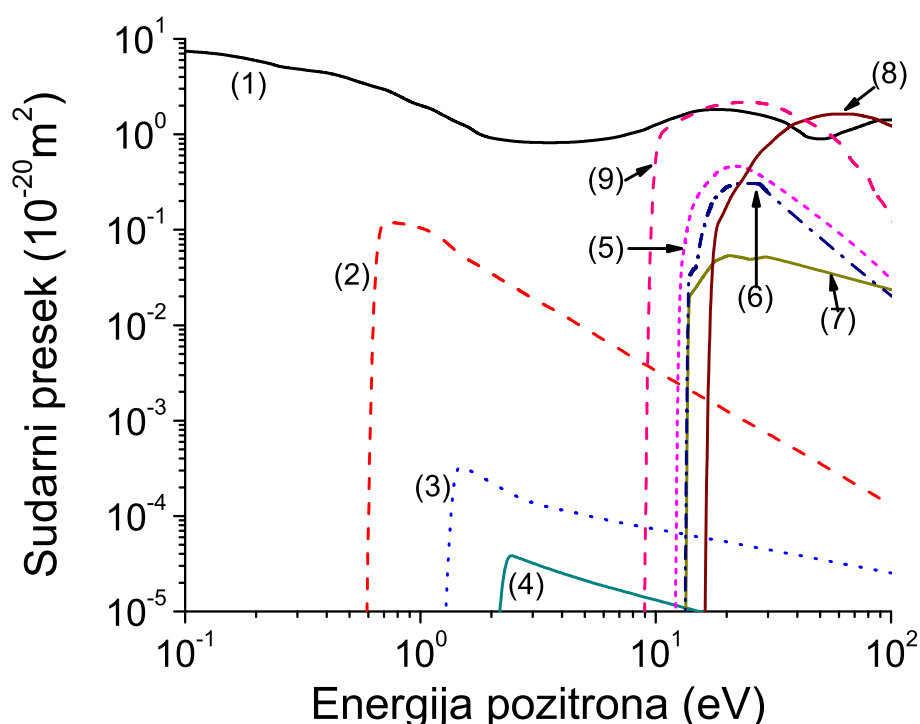
Slika 65: Set preseka za rasejanje pozitrona u H_2: (1) transfer impulsa u elastičnim sudarima, vibracione ekscitacije (2) v1, (3) 0-2, (4) 0-3, elektronske ekscitacije (5) B1 Σ, (6) X-C, (7) X-E, (8) jonizacija i (9) formiranje pozitronijuma.

Pozitronijum je vezano stanje elektrona i pozitrona [212–214]. Ako su spinovi elektrona i pozitrona antiparalelni/paralelni, ovo stanje se zove parapozitronijum/ortopozitronijum [215–219]. Ono je nestabilno i završava se anihilacijom elektrona i pozitrona [212]. Srednje vreme života pozitronijuma iznosi oko 0.125 ns i 142 ns u slučaju parapozitronijuma i ortopozitronijuma, respektivno [216, 219]. U energijskom opsegu koji je relevantan za naše proračune presek za formiranje pozitronijuma je znatno veći od preseka za direktnu anihilaciju elektrona i pozitrona, te je u našem slučaju formiranje pozitronijuma glavni mehanizam za gubitak pozitrona.

Značajna razlika između rojeva elektrona i rojeva pozitrona, koji se kreću u nekoj materijalnoj sredini, jeste ta što se na dovoljno visokim energijama elektroni koji su izgubljeni u
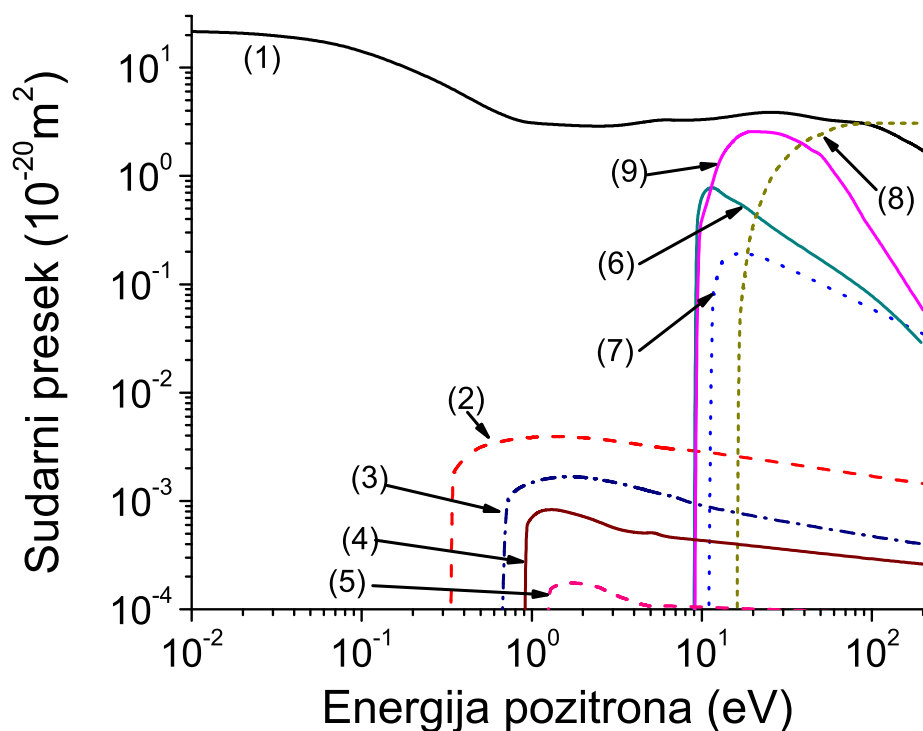
Slika 66: Set preseka za rasejanje pozitrona u N_2: (1) transfer impulsa u elastičnim sudarima, vibracione ekscitacije (2) 0-1, (3) 0-2, (4) 0-3, (5) 0-4, elektronske ekscitacije (6) $a^1\Pi$, (7) $a'\Sigma$, (8) jonizacija i (9) formiranje pozitronijuma.

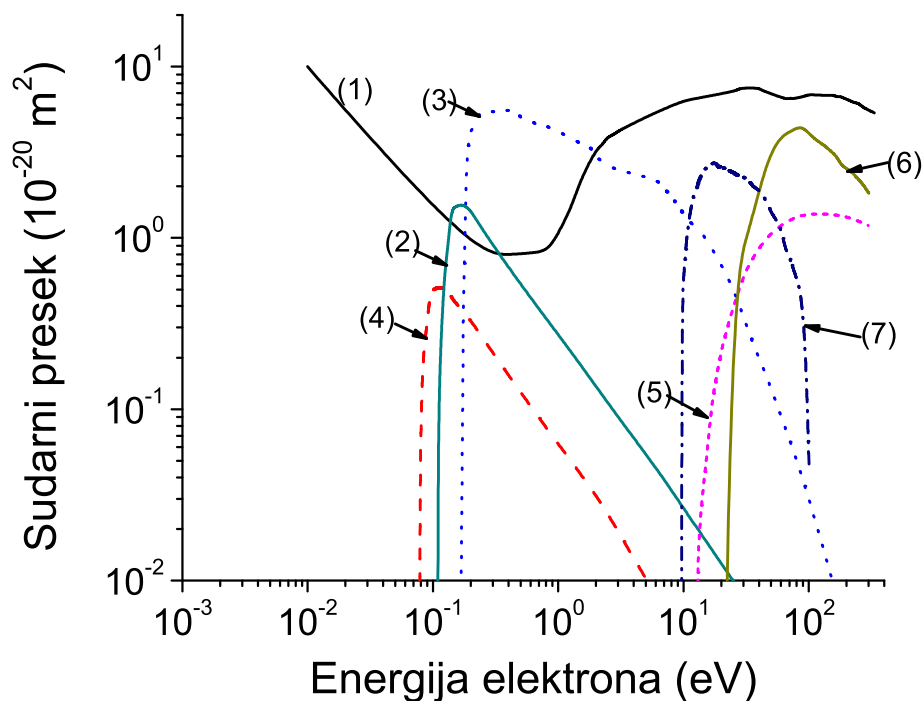Slika 67: Set preseka za rasejanje pozitrona u CF_4: (1) transfer impulsa u elastičnim sudarima, vibracione ekscitacije (2) v1, (3) v3, (4) v4, (5) disocijacija, (6) jonizacija i (7) formiranje pozitronijuma.

elektronskom zahvatu (ili nekom drugom procesu) mogu nadoknaditi uz pomoć elektronske sudarne jonizacije atoma ili molekula pozadinske srednine, dok se pozitroni koji su izgubljeni u
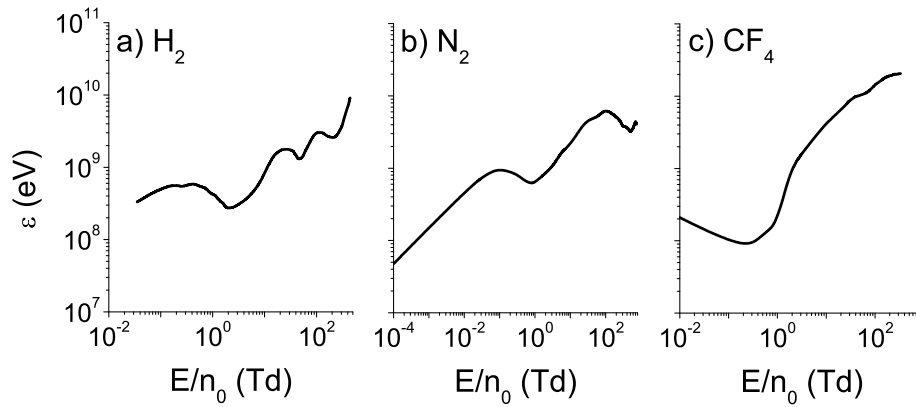
Slika 68: Kolizione frekvence za elastične sudare za pozitrone u H_2, N_2 i CF_4, pri koncentraciji pozadinskih molekula koja iznosi $n_0 = 3.54 \cdot 10^{22} \text{m}^{-3}$.

formiranju pozitronijuma ili anihilaciji ne mogu nadoknaditi na osnovu interakcije pozitrona i pozadinske srednine, nego se moraju obezbediti uz pomoć nekog spoljašnjeg izvora pozitrona. Da bi se izbeglo značajno smanjenje broja pozitrona, koji se prate u našim Monte Carlo simulacijama, pod uticajem formiranja pozitronijuma, potrebno je da pozitroni koji su izgubljeni u nekonzervativnim sudarima budu nadoknađeni u toku trajanja simulacije. Zato je u našim Monte Carlo proračunima primenjena tehnika diskretnog reskaliranja roja, koja je opisana u radu [160]. Ova tehnika podrazumeva da se u diskretnim vremenskim trenucima (trenuci relaksiranja) za svaki od pozitrona koji je izgubljen, (u nekonzervativnim sudarima) između dva trenutka reskaliranja, duplira jedan od postojećih pozitrona. Pozitroni koji su duplirani se biraju nasumično, kako reskaliranje ne bi promenilo funkciju raspodele elektrona po brzinama i prostornim koordinatama. Nakon trenutka reskaliranja svaki se od pozitrona prati nezavisno. Ova tehnika ne utiče na srednje vrednosti niti jedne dinamičke promenljive na osnovu kojih se računaju transportni koeficijenti, a obezbeđuje približno konstantan broj pozitrona za vreme trajanja simulacije. Gubitak pozitrona zbog formiranja pozitronijuma utiče na transportne koeficijente kroz promenu funkcije raspodele po energijama (implicitni efekti) i kroz prostornu zavisnost brzinskog koeficijenta za ovaj proces, koja je zasnovana na prostornom gradijentu srednje energije pozitrona (eksplicitni efekti).

5.7.2 Rezultati

Slika 69 ilustruje profile zavisnosti srednje energije od E/n_0 za pozitrone u H_2, N_2 i CF_4. Ovi su rezultati dobijeni primenom momentnog metoda za numeričko rešavanje Boltzmann-ove jednačine. Na najnižim poljima su vrednosti srednje energije praktično termalne (oko 0.038 eV) do 0.0077 Td, 0.0046 Td i 0.046 Td za elektrone u H_2, N_2 i CF_4, respektivno. Nakon toga se srednja energija sporo povećava sa porastom polja (do oko 0.059 Td, 0.035 Td i 0.27 Td za elektrone u H_2, N_2 i CF_4, respektivno).

Na višim poljima se profil zavisnosti srednje energije od E/n_0 u H_2 kvalitativno razlikuje od odgovarajućih profila zavisnosti u N_2 i CF_4. Srednja energija za pozitrone u H2 se zapravo
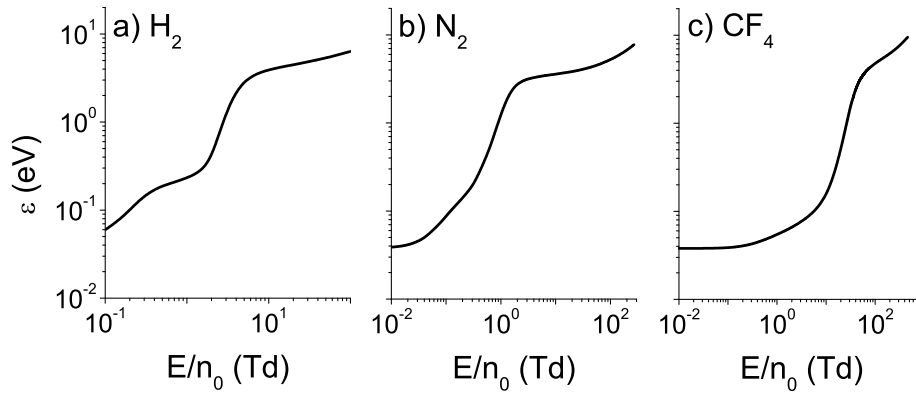
Slika 69: Srednja energija u funkciji E/n_0 za pozitrone u H_2, N_2 i CF_4. Rezultati su dobijeni na osnovu metoda više članova za rešavanje Boltzmann-ove jednačine.

približno linearno povećava sa porastom E/n_0 u dva susedna intervala polja, pri čemu je nagib srednje energije znatno manji u drugom intervalu. Ova dva E/n_0 intervala se nalaze imeđu opsega polja u kome je sednja energija još uvek blizu termalnih vrednosti i opsega u kome se srednja energija naglo povećava sa porastom polja. Nasuprot tome, porast serdnje energije za pozitrone u N_2 i CF_4 ima praktično konstantan nagib između opsega polja u kome je srednja energija približno termalna i opsega polja u kome je porast srednje energije sa porastom E/n_0 najintenzivniji. Jedan od razloga za različit trend zavisnosti srednje energije u H_2 i preostala dva gasa jeste visoka vrednost praga za prvu vibracionu ekscitaciju u H_2.

Naime, prvi opseg polja u kome se srednja energija pozitrona u H_2 linearno povećava sa porastom E/n_0 nalazi se između 0.059 Td i 0.27 Td. U ovom opsegu polja srednja energija ima vrednosti između 0.047 eV i 0.138 eV. Pošto je prag za prvu vibracionu ekscitaciju oko 0.516 eV, većina pozitrona u ovom opsegu polja nema dovoljno energije da učestvuje u neelastičnim sudarima. Međutim, u opsegu polja od 0.35 Td do 1.3 Td srednja energija ima vrednosti u intervalu između 0.158 eV i 0.256 eV, pa pozitroni čija je energija između 3.3 i 2 puta veća od srednje energije mogu da učestvuju u vibracionim ekscitacijama. Ovo dovodi do sporijeg porasta srednje energije sa porastom E/n_0.

Srednja energija pozitrona u N_2 i CF_4 se linearno povećava sa porastom E/n_0 u intervalima od 0.035 Td do 0.27 Td i od 0.21 Td do 4.6 Td, respektivno. Pri tome se srednja energija pozitrona u N_2 nalazi u intervalu između 0.047 eV i 0.18 eV, dok je srednja energija pozitrona u CF_4 između 0.04 eV i 0.09 eV. Pošto su pragovi za prve vibracione ekscitacije u N_2 i CF_4 oko 0.29 eV i 0.077 eV, respektivno, najenergičniji pozitroni u ovom opsegu polja mogu da izgube energiju u vibracionim ekscitacijama, što dovodi do sporijeg porasta srednje energije sa porastom E/n_0.

Srednja energija se na višim poljima naglo povećava sa porastom E/n_0. Na početku opsega polja, koji odgovara naglom porastu srednje energije, najenergičniji pozitroni (čija je energija bar 4 puta veća od srednje energije) nalaze se u energijskom intervalu u kome preseci za vibracione ekscitacije opadaju sa porastom energije. Porast srednje energije sa porastom E/n_0 se značajno usporava na poljima višim od oko 5.9 Td, 1.9 Td i 57 Td za pozitrone u H_2, N_2 i

CF_4, respektivno. Pri tome su vrednosti srednje energije na kraju opsega polja u kome se ona naglo povećava sa porastom E/n_0 oko 3.2 eV, 2.7 eV i 3.5 eV za pozitrone u H_2, N_2 i CF_4, respektivno. Pragovi za prvu elektronsku ekscitaciju za pozitrone u H_2, N_2 i CF_4 su 11.3 eV, 10.0 eV i 12.49, respektivno. Tako se u sva tri gasa nagli porast srednje energije sa porastom E/n_0 završava u okolini polja na kome elektroni čija je energija oko 4 puta veća od srednje energije mogu učestvovati u elektronskim ekscitacijama.
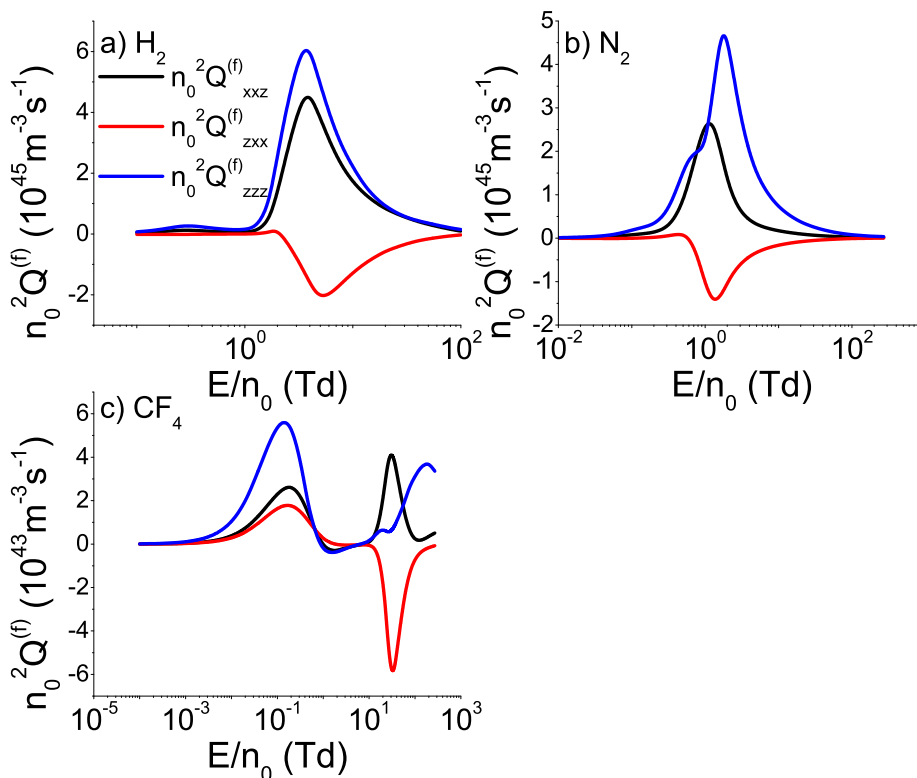
Slika 70: $n_0^2 Q_{xxz}^{(f)}$, $n_0^2 Q_{zxx}^{(f)}$ i $n_0^2 Q_{zzz}^{(f)}$ komponente fluks transportnog tenzora trećeg reda u funkciji E/n_0 za rojeve pozitrona u H_2, N_2 i CF_4. Rezultati su dobijeni primenom metoda više članova za rešavanje Boltzmann-ove jednačine.

Prikaz profila TKIII u funkciji E/n_0 za pozitrone u H_2, N_2 i CF_4 dat je na slici 70. Ovi rezultati su dobijeni primenom momentnog metoda za numeričko rešavanje Boltzmann-ove jednačine. Komponente $n_0^2 Q_{zzz}^{(f)}$ i $n_0^2 Q_{xxz}^{(f)}$ su pozitivne u celom razmatranom opsegu polja, dok $n_0^2 Q_{zxx}^{(f)}$ komponenta menja znak unutar ovog opsega u sva tri gasa. Istovremeno $n_0^2 Q_{zzz}^{(f)}$ i $n_0^2 Q_{xxz}^{(f)}$ komponente imaju dva lokalna maksimuma i jedan lokalni minimum za pozitrone u H_2 i CF_4, a ove dve komponente imaju pak samo jedan lokalni maksimum za pozitrone u N_2.

Komponente $n_0^2 Q_{zzz}^{(f)}$ i $n_0^2 Q_{xxz}^{(f)}$ se monotono povećavaju sa porastom E/n_0 do 0.27 Td i 0.35 Td, nakon čega opadaju sa rastom E/n_0 do 1Td i 4 Td za pozitrone u H_2 i CF_4, respektivno. Opseg polja u kome $n_0^2 Q_{zzz}^{(f)}$ i $n_0^2 Q_{xxz}^{(f)}$ opadaju sa porastom E/n_0, odgovara opsegu polja u kome se srednja energija linearno povećava sa porastom E/n_0 i u kome je dinamika visokoenergijskih pozitrona pod snažnim uticajem vibracionih ekscitacija. Međutim, $n_0^2 Q_{zzz}^{(f)}$ i $n_0^2 Q_{xxz}^{(f)}$ komponente za pozitrone u N2 se monotono povećavaju sa porastom E/n_0 u opsegu polja u kome je porast srednje energije linearan, zbog toga što je presek za vibracione ekscitacije u N_2 znatno manji

od preseka za vibracione ekscitacije u H_2 i CF_4.

Na višim poljima se komponenta $n_0^2 Q_{xxz}^{(f)}$ monotono povećava sa porastom E/n_0 i dostiže lokalni maksimum na oko 3.3 Td, 1.1 Td i 39 Td za pozitrone u H_2, N_2 i CF_4, respektivno. Longitudinalna komponenta, $n_0^2 Q_{zzz}^{(f)}$, monotono se povećava sa porastom E/n_0 do 3.3 Td za pozitrone u H_2, dok se za pozitrone u N_2 i CF_4 monotono povećava do oko 0.7 Td i 17 Td, respektivno, nakon čega saturira do oko 0.9 Td i 23 Td respektivno, pa se ponovo monotono povećava sa porastom E/n_0 i dostiže lokalni maksimum na 1.7 Td i 53 Td, respektivno. Nakon lokalnog maksimuma $n_0^2 Q_{zzz}^{(f)}$ i $n_0^2 Q_{xxz}^{(f)}$ komponente monotono opadaju sa porastom E/n_0 do kraja razmatranog opsega polja. Za pozitrone u H_2 srednja energija na 3.3 Td iznosi oko 1.5 eV, te se pozitroni čija je energija oko 3 puta veća od srednje energije nalaze u energijskom intervalu u kome se presek za transfer impulsa u elastičnim sudarima povećava sa porastom energije, a za pozitrone čija je energija oko 7.5 puta veća od srednje energije važi to da mogu učestvovati u prvoj elektronskoj ekscitaciji. Na 4 Td je srednja energija pozitrona u H_2 oko 2.2 eV, pa pozitroni čija je energija oko 5 puta veća od srednje energije mogu participirati u elektronskim ekscitacijama. Za pozitrone u N_2 i CF_4 su vrednosti srednje energije na poljima na kojima $n_0^2 Q_{xxz}^{(f)}$ komponenta doseže poslednji lokalni maksimum: 1.5 eV i 2.3 eV, respektivno. Ove se vrednosti srednje energije nalaze u energijskim intervalima u kojima se koliziona frekvenca za elastične sudare povećava sa porastom energije. Treba dodati kako na poljima na kojima $n_0^2 Q_{xxz}^{(f)}$ komponenta dostiže poslednji lokalni maksimum u ova dva gasa elektroni čija je energija oko 6 puta veća od srednje energije mogu učestvovati u prvoj elektronskoj ekscitaciji. Vrednosti srednje energije na poljima na kojima $n_0^2 Q_{zzz}^{(f)}$ dostiže poslednji lokalni maksimum za pozitrone u N_2 i CF_4 iznose 2.5 eV i 3.4 eV, respektivno. Sledi da na ovim poljima u prvoj elektronskoj ekscitaciji mogu participirati elektroni čija je energija oko 4 puta veća od srednje energije.

Za pozitrone u H_2 i N_2, $n_0^2 Q_{zxx}^{(f)}$ je negativno na najnižim poljima, uz šta ova komponenta opada sa porastom E/n_0, uprkos tome što presek za transfer impulsa u elastičnim sudarima opada sa porastom energije do energija koje su znatno više od termalnih vrednosti. Ovo je uzrokovano time što se koliziona frekvenca za elastične sudare povećava sa porastom energije do oko 0.18 eV i 0.1 eV za pozitrone u H_2 i N_2, respektivno. Komponenta $n_0^2 Q_{zxx}^{(f)}$ doseže lokalni minimum na 0.21 Td i 0.059 Td za pozitrone u H_2 i N_2 respektivno. Pritom su vrednosti srednje energije u H_2 i N_2, u okolini lokalnog minimuma $n_0^2 Q_{zxx}^{(f)}$ komponente, približno 0.1 eV i 0.06 eV, respektivno. Na poljima koja odgovaraju položajima ovog lokalnog minimuma pozitroni se u H_2, čija je energija oko 4 puta veća od srednje energije, i pozitroni u N_2, čija je energija 1.7 puta veća od srednje energije, nalaze u energijskom intervalu u kome koliziona frekvenca za elastične sudare opada sa porastom energije. Ovo dovodi do porasta $n_0^2 Q_{zxx}^{(f)}$ komponente sa porastom E/n_0 na višim poljima. Komponenta $n_0^2 Q_{zxx}^{(f)}$ dostiže lokalni maksimum na 2.1 Td i 0.46 Td, postajući pozitivna na 1.3 Td i 0.13 Td za pozitrone u H_2 i N_2, respektivno. Na poljima na kojima $n_0^2 Q_{zxx}^{(f)}$ komponenta postaje pozitivna u H_2 i N_2 vrednosti srednje energije su oko 0.26 eV i 0.1 eV, respektivno, pa se pozitroni čija je energija oko 1.6 puta veća od srednje energije u H_2 i pozitroni čija je energija veća od srednje energije u N_2 nalaze u energijskoj oblasti u kojoj koliziona frekvenca za elastične sudare opada sa porastom energije. U okolini lokalnog maksimuma $n_0^2 Q_{zxx}^{(f)}$ komponente su vrednosti srednje energije oko 0.46 eV i 0.31 eV za

pozitrone u H_2 i N_2, respektivno, pa se pozitroni u H_2 čija je energija oko 4.3 puta veća od srednje energije i pozitroni u N_2 čija je energija 1.7 puta veća od srednje energije nalaze u energijskom intervalu u kome se koliziona frekvenca za elastične sudare povećava sa porastom energije. Ovo dovodi do opadanja $n_0^2 Q_{zxx}^{(f)}$ komponente sa porastom E/n_0 na višim poljima. Komponenta $n_0^2 Q_{zxx}^{(f)}$ postaje negativna na 2.7 Td i 0.63 Td za pozitrone u H_2 i N_2, respektivno, ostajući negativna do kraja razmatranog opsega polja u oba gasa. Komponenta $n_0^2 Q_{zxx}^{(f)}$ dostiže lokalni minimum na oko 5.3 Td i 1.4 Td za pozitrone u H_2 i N_2, respektivno, uz šta je položaj lokalnog minimuma $n_0^2 Q_{zxx}^{(f)}$ komponente blizu položaja lokalnog maksimuma $n_0^2 Q_{xxz}^{(f)}$ komponente. Nakon lokalnog minimuma, apsolutna vrednost $n_0^2 Q_{zxx}^{(f)}$ komponente opada sa porastom E/n_0 do kraja razmatranog opsega polja.

Za pozitrone u CF_4 je $n_0^2 Q_{zxx}^{(f)}$ komponenta pozitivna na najnižim poljima jer koliziona frekvenca opada sa porastom energije na najnižim energijama. Ova komponenta se monotono povećava sa porastom E/n_0 do oko 0.1 Td, gde dostiže lokalni maksimum. Na 0.1 Td je srednja energija pozitrona u CF_4 blizu termalne vrednosti (oko 0.039 eV), ali u okolini ovog polja srednja se energija počinje primetno povećavati sa porastom E/n_0, što dovodi do porasta kolizione frekvence za vibracione ekscitacije i opadanja $n_0^2 Q_{zxx}^{(f)}$ komponente sa porastom polja. Ova komponenta dostiže lokalni minimum na oko 0.27 Td, uz šta u ovom minimumu ima negativnu vrednost. Vrednost polja od 0.27 Td uslovljava srednju energiju pozitrona od oko 0.042 eV, te se pozitroni čija je energija oko 5.5 puta veća od srednje energije nalaze u energijskoj oblasti u kojoj se koliziona frekvenca za elastične sudare povećava sa porastom energije. S druge strane, pozitroni čija je energija oko 6 puta veća od srednje energije nalaze se u energijskoj oblasti u kojoj preseci za vibracionu ekscitaciju naglo opadaju sa porastom energije. Nakon lokalnog minimuma se $n_0^2 Q_{zxx}^{(f)}$ komponenta monotono povećava do oko 1.3 Td, dosežući lokalni maksimum. Na 1.3 Td je srednja energija oko 0.058 eV, pa se pozitroni čija je energija oko 4 puta veća od srednje energije nalaze u energijskom intervalu u kome se koliziona frekvenca za elastične sudare naglo povećava sa porastom energije. Ovo dovodi do opadanja $n_0^2 Q_{zxx}^{(f)}$ komponente sa porastom E/n_0, koja postaje negativna na 5.9 Td, gde je srednja energija oko 0.1 eV. Na ovoj vrednosti polja pozitroni čija je energija oko 2.5 puta veća od srednje energije se nalaze u energijskom intervalu u kome se koliziona frekvenca za elastične sudare povećava sa porastom energije. Nakon 5.9 Td $n_0^2 Q_{zxx}^{(f)}$ komponenta ostaje negativna do kraja razmatranog opsega polja. Ova komponenta opada sa porastom E/n_0 do oko 37 Td, na tom mestu dostžući lokalni minimum, pri čemu je položaj ovog minimuma jako blizu položaja lokalnog maksimuma $n_0^2 Q_{xxz}^{(f)}$ komponente. Za ovim lokalnim minimumom apsolutna vrednost $n_0^2 Q_{xxz}^{(f)}$ komponente monotono opada sa porastom E/n_0 do kraja razmatranog opsega polja.

Na slici 71 su prikazani profili zavisnosti fluks i balk longitudinalne komponente TTIII u funkciji E/n_0 za pozitrone u H_2, N_2 i CF_4. Ovi rezultati su dobijeni primenom Monte Carlo simulacija. Na najnižim poljima (do 1.5 Td, 77 Td i 27 Td za pozitrone u H_2, N_2 i CF_4, respektivno) su razlike između fluks i balk vrednosti longitudinalne komponente TTIII male, budući da većina pozitrona nema dovoljno energije da učestvuje u formiranju pozitronijuma. Na višim poljima su balk vrednosti longitudinalne komponente TTIII manje od odgovarajućih fluks vrednosti, što je posledica hlađenja roja formiranjem pozitronijuma. Naime, vrednosti
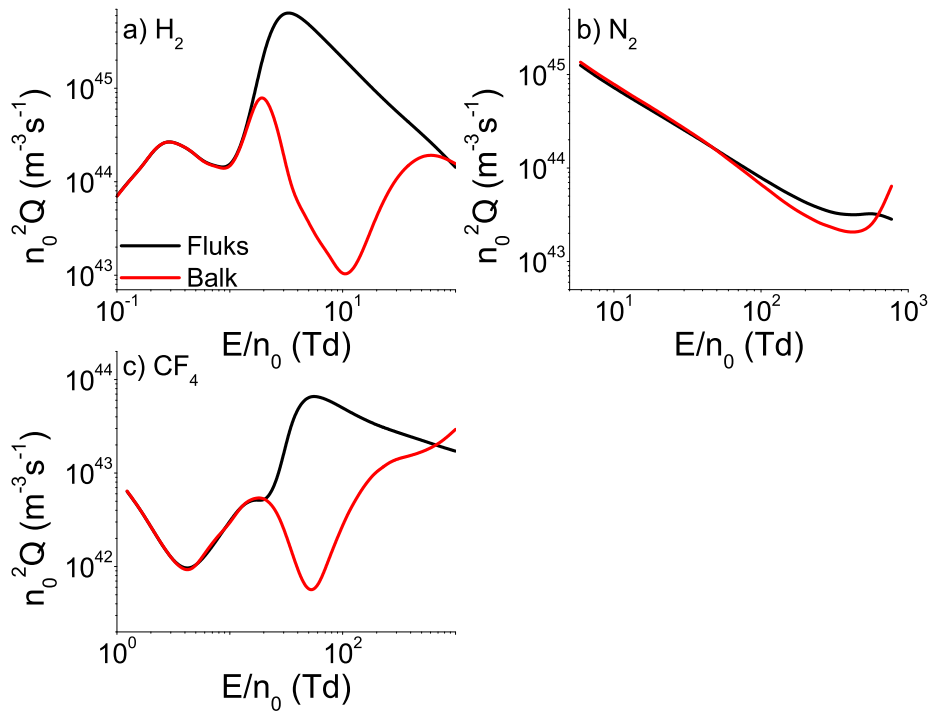
Slika 71: Fluks i balk longitudinalna komponenta transportng tenzora trećeg reda $n_0^2 Q_L$ u funkciji E/n_0 za rojeve pozitrona u H_2, N_2 i CF_4. Rezultati su dobijeni primenom Monte Carlo simulacija.

srednje energije pozitrona u H_2 na 3.5 Td, u N_2 na 77 Td i u CF_4 na 27 Td iznose 1.77 eV, 4.87 eV i 1.08 eV, respektivno, dok su vrednosti praga za formiranje pozitonijuma u ova tri gasa 8.6 eV, 8.78 eV i 9.45 eV, respektivno. Tako u ovom opsegu polja samo najenergičniji pozitroni mogu participirati u formiranju pozitronijuma. Na višim poljima se razlika između balk i fluks vrednosti longitudinalne komponente TTIII povećava sa porastom E/n_0, zbog porasta srednje energije i povećanja broja pozitrona koji mogu učestvovati u formiranju poizitronijuma. Među-tim, ova razlika dostiže lokalni maksimum na oko 10 Td, 530 Td i 59 Td za pozitrone u H_2, N_2 i CF_4, respektivno. Pri tome su odgovarajuće vrednosti srednje energije 3.9 eV, 12.9 eV i 3.64 eV za pozitrone u H_2, N_2 i CF_4, respektivno. Posledice ovih vrednosti i uslovljenosti svode se na to da u okolini polja na kome eksplicitni efekti formiranja pozitronijuma na longitudinalnu komponentu TTIII dostižu maksimum, u formiranju pozitronijuma mogu učestvovati pozitroni čija je energija oko 2.2, 1.94 i 2.7 puta veća od srednje energije za pozitrone u H_2, N_2 i CF_4, respektivno. Ali, s obzirom na to da presek za formiranje pozitronijuma u H_2, N_2 i CF_4 dostiže lokalni maksimum na 24 eV, 25 eV i 16.5 eV, respektivno, najenergičniji se pozitroni u sva tri gasa nalaze u energijskoj oblasti u kojoj presek za formiranje pozitronijuma opada sa porastom energije. Procenat pozitrona koji se nalaze u ovoj energijskoj oblasti se povećava sa porastom polja, što dovodi do opadanja eksplicitnih efekata formiranja pozitronijuma na longitudinalnu komponentu TTIII sa porastom E/n_0. Razlike između balk i fluks vrednosti longitudinalne komponente TTIII su zanemarljive na oko 77 Td, 650 Td i 670 Td za pozitrone u H_2, N_2 i CF_4, respektivno. Vrednosti srednje energije za pozitrone u H_2 na 770 Td, u N_2 na 650 Td i u CF_4 na 670 Td iznose 5.92 eV, 14.2 eV i 12.5 eV, respektivno. Na ovim vrednostima polja pozitroni u H_2 čija je energija oko 1.45 puta veća od srednje energije, kao i pozitroni u N_2 i CF_4 čija je

energija oko 1.6 i 1.3 puta manja od srednje energije mogu da učestvuju u formiranju pozitro-nijuma. Uz to se na ovim vrednostima polja pozitroni sa energijom od oko 4, 1.8 i 1.32 puta većom od srednje energije, za H_2, N_2 i CF_4, respektivno, nalaze u energijskom intervalu u kome presek za formiranje pozitronijuma opada sa porastom polja. Za pozitrone u N_2 i CF_4 balk vrednost longitudinalne komponente TTIII je veća od odgovarajuće fluks vrednosti, na poljima višim od 770 Td i 1000 Td, respektivno. Ovo je posledica grejanja roja formiranjem pozitroni-juma. Srednja energija pozitrona u N_2 zapravo iznosi 16.95 eV na 770 Td, te se pozitroni čija je energija oko 3.5 puta veća od srednje energije nalaze u energijskoj oblasti u kojoj je presek za formiranje pozitronijuma oko 2.5 puta manji od njegove vrednosti u okolini maksimuma, dok pozitroni čija je energija oko dva puta manja od srednje energije mogu učestvovati u formiranju pozitronijuma. Nalik tome je srednja energija pozitrona u CF_4 na 1000 Td oko 17.58 eV, što pozicionira pozitrone sa energijom oko 3.4 puta većom od srednje energije u energijsku oblast u kojoj je presek za formiranje pozitronijuma oko 2.7 puta manji od njegove vrednosti u okolini maksimuma, s tim da u formiranju pozitronijuma mogu participirati pozitroni čija je energija oko 1.86 puta manja od srednje energije.
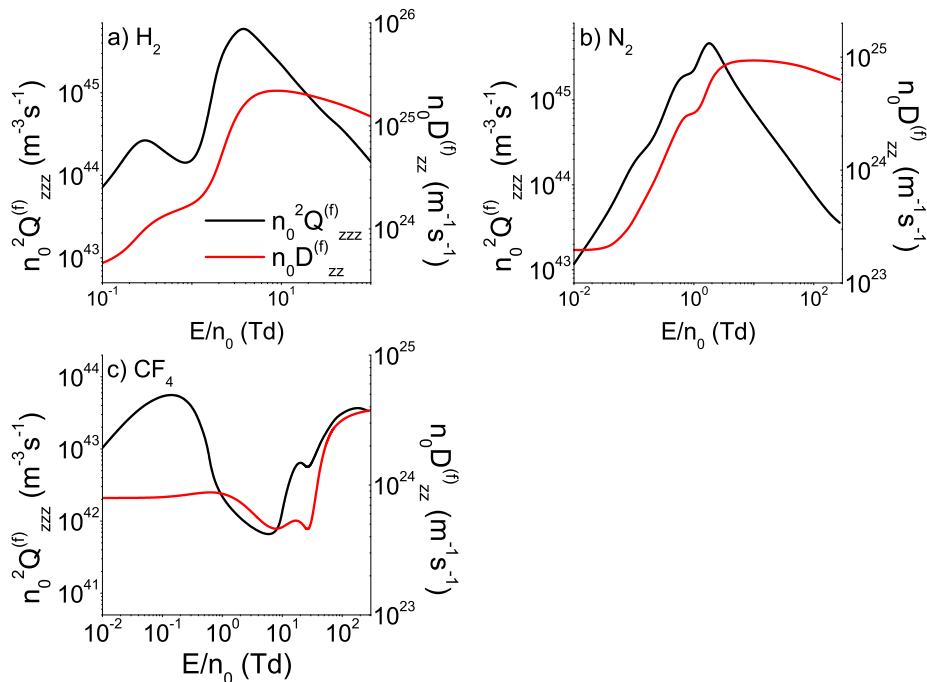
Slika 72: Korelacija fluks longitudinalne komponente transportng tenzora trećeg reda i fluks longitudinalne difuzije. Rezultati su dobijeni na osnovu metoda više članova za rešavanje Boltzmann-ove jednačine.

Slike 72 i 73 prikazuju korelaciju profila zavisnosti longitudinalne komponente TTIII i lon-gitudinalne difuzije od E/n_0 u slučaju fluks i balk vrednosti, respektivno. Može se primetiti da je trend zavisnosti $n_0^2 Q_{zzz}^{(f)}$ od E/n_0 u korelaciji sa odgovarajućim trendom $n_0 D_{zz}^{(f)}$, dok se trend ponašanja $n_0^2 Q_{zzz}^{(b)}$ saodnosi sa odgovarajućim trendom $n_0 D_{zz}^{(b)}$. U oba slučaja se, međutim, lo-kalni minimumi longitudinalne komponente TTIII nalaze na nižim vrednostima E/n_0 u odnosu na lokalne minimume longitudinalne difuzije. Na primer, za roj pozitrona u CF_4, $n_0^2 Q_{zzz}^{(f)}$ dosti-že lokalni minimum i prevojnu tačku na oko 4.6 Td i 20 Td, respektivno, dok $n_0 D_{zz}^{(f)}$ dostiže
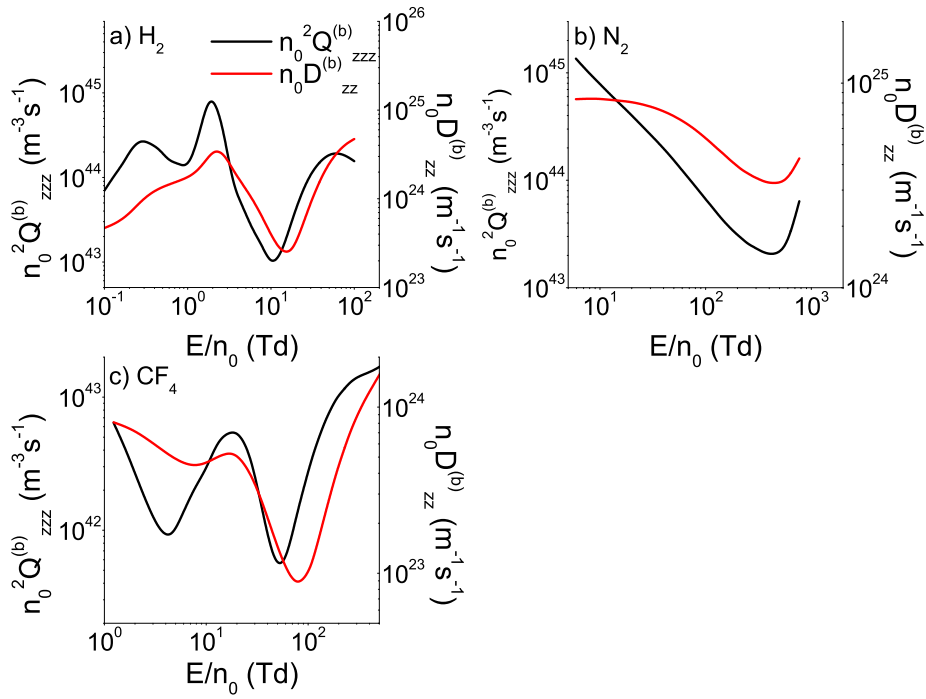
Slika 73: Korelacija balk longitudinalne komponente transportng tenzora trećeg reda i balk longitudinalne difuzije. Rezultati su dobijeni primenom Monte Carlo simulacija.

dva lokalna minimuma na oko 7.7 Td i 27 Td, uz šta obe veličine dosežu lokalni maksimum na oko 17 Td. Slično tome, $n_0^2 Q_{zzz}^{(b)}$ dostiže dva lokalna minimuma na oko 4.3 Td i 54 Td, a $n_0 D_{zz}^{(b)}$ dostiže dva lokalna minimuma na oko 7.7 Td i 77 Td, pri čemu obe veličine dosežu lokalni maksimum na oko 17 Td. Razlog za pojavu lokalnih minimuma longitudinalne komponente TTIII na poljima koja su niža od polja na kojima se pojavljuju odgovarajući lokalni minimumi longitudinalne difuzije mogla bi biti veća osetljivost komponenti TTIII na dinamiku visokoenergijskih elektrona.

5.8 Zaključak

Centralna tema ovog poglavlja bili su transportni koeficijenti trećeg reda za elektrone u realnim gasovima. U potpoglavlju 5.2 tumačena je korelacija između longitudinalne komponente transportnog tenzora trećeg reda Q_{zzz} i longitudnalne komponente difuzionog tenzora D_{zz}. Ova korelacija je uočena za elektrone u svim razmatranim gasovima na dovoljno visokim vrednostima redukovanog električnog polja. Uočeno je naime da na dovoljno visokim poljima Q_{zzz} opada sa porastom redukovanog električnog polja ako D_{zz} opada, ili ukoliko se D_{zz} povećava kao konkavna funkcija u log-log skali. Takođe je primećeno da se Q_{zzz} povećava sa porastom polja ako se D_{zz} povećava kao konveksna funkcija u log-log skali. Međutim, ova korelacija je odsutna na najnižim poljima, zbog toga što transportni koeficijenti trećeg reda predstavljaju asimetrično odstupanje od difuzionog širenja (koje je reprezentovano difuzionim tenzorom), težeći nuli u limesu niskih polja, za razliku od dijagonalnih komponenti difuzionog tenzora koje, imaju nenulte termalne vrednosti.

Potpoglavlje 5.3 bazirano je na izučavanju transportnih koeficijenata trećeg reda u helijumu i neonu. Zaključeno je da su u ovim gasovima profili zavisnosti komponenti transportnog tenzora trećeg reda od redukovanog električnog polja složeniji nego u slučaju modelnih gasova. Pri tome je Q_{zzz} komponenta pozitivna za elektrone u ova tri gasa u celom razmatranom opsegu polja. Međutim, u opsegu polja u kome je koliziona frekvenca za veliki procenat elektrona rastuća funkcija energije, jedna od vandijagonalnih komponenti (Q_{xxz} ili Q_{zxx}) je negativna, dok je druga od ovih komponenti pozitivna, u istom opsegu redukovanog električnog polja. U potpoglavlju 5.4 su razmatrani transportni koeficijenti trećeg reda za elektrone u argonu, kriptonu i ksenonu. Primećeno je da su na kvalitativnom nivou profili zavisnosti komponenti transportnog tenzora trećeg reda od redukovanog električnog polja jako slični u ova tri gasa. Naime, na najnižim poljima su u sva tri gasa sve komponente transportnog tenzora trećeg reda pozitivne i monotono se povećavaju sa porastom polja, dok ne dostignu oštar maksimum. Ovaj maksimum je posledica Ramsauer- Townsend-ovog minimuma. U sva tri gasa je komponenta Q_{zzz} pozitivna u celom razmatranom opsegu polja, dok je Q_{xxz} komponenta negativna na višim poljima. Za elektrone u argonu Q_{zxx} komponenta ima negativne vrednosti u jako uskom opsegu polja i postaje pozitivna na otprilike istoj vrednosti redukovanog električnog polja, gde Q_{xxz} komponenta postaje negativna.

U odeljku 5.5 proučavan je transportni tenzor trećeg reda za elektrone u N_2, CH_4, CF_4 i C_3F_8, te je zapaženo kako su profili zavisnosti transportnih koeficijenata trećeg reda od redukovanog električnog polja složeniji u slučaju molekularnih gasova nego kod atomskih gasova. Longitudinalna komponenta transportnog tenzora trećeg reda Q_{zzz} ima negativne vrednosti u uskom opsegu polja za elektrone u CF_4 i C_3F_8, dok je ova komponenta pozitivna u celom razmatranom opsegu polja za elektrone u N_2 i CH_4. Pored toga, Q_{xxz} i Q_{zxx} komponente imaju negativne vrednosti u uskom opsegu polja za elektrone u CF_4 i CH_4, a komponenta Q_{zxx} je negativna u celom razmatranom opsegu polja za elektrone u N_2 i na poljima višim od 5 Td za elektrone u C_3F_8. Uočeno je da Q_T ima negativne vrednosti za elektrone u CH_4 i CF_4 u opsegu polja u kome postoji negativna diferencijalna provodnost. Međutim, Q_T je negativno u većini oblasti negativne diferencijalne provodnosti za elektrone u CH_4, za razliku od elektrona u CF_4 Q_T, gde je negativno samo u uskom opsegu polja, pred kraj opsega polja u kome postoji negativna diferencijalna provodnost. Pored toga je ponašanje vandijagonalnih komponenti transportnog tenzora trećeg reda Q_{xxz} i Q_{zxx} drugačije u oblasti negativne diferencijalne provodnosti za elektrone u CH_4 i CF_4.

Potpoglavlje 5.6 posvećeno je tumačenju doprinosa longitudinalne komponente transportnog tenzora trećeg reda Q_{zzz} prostornom profilu roja za elektrone u atomskim i molekularnim gasovima. Ovaj doprinos zavisi od količnika $Q_L/D_L^{3/2}$. Doprinos Q_{zzz} prostornom profilu roja je najizraženiji za elektrone u argonu, kriptonu i ksenonu na niskim poljima, zbog prisustva Ramsauer-Townsend-ovog minimuma. Izražen je takođe u kriptonu i ksenonu na oko 1 Td.

U ovom potpoglavlju je izučavan i uticaj sudarnih procesa, čija učestanost zavisi od koncentracije pozadinskog gasa, na transportne koeficijente trećeg reda. Pri tome je razmatran uticaj trojnog zahvata elektrona u molekularnom kiseoniku na komponente transportnog tenzora tre-

ćeg reda. Primećeno je da transportni koeficijenti trećeg reda snažno zavise od koncentracije pozadinskog gasa na niskim poljima, na kojima trojni zahvat snažno utiče na dinamiku elektrona.

Transportni koeficijenti trećeg reda za pozitrone u H_2, N_2 i CF_4 izučavani su u potpoglavlju 5.7. Uočeno je da eksplicitni efekti formiranja pozitronijuma dovode do velike razlike između balk i fluks vrednosti transportnih koeficijenata trećeg reda za pozitrone u ova tri gasa. Balk vrednosti su znatno niže od odgovarajućih fluks vrednosti na srednjim poljima, zbog hlađenja roja formiranjem pozitronijuma. Međutim, fluks vrednosti su više od odgovarajućih balk vrednosti na najvišim poljima zbog efekta grejanja roja formiranjem pozitronijuma. Na ovom mestu primećeno je i to da je balk vrednost longitudinalne komponente transportnog tenzora trećeg reda Q_{zzz} u korelaciji sa balk vrednošću longitudinalne komponente difuzionog tenzora D_{zz}, dok se fluks vrednost Q_{zzz} saodnosi sa fluks vrednošću D_{zz}.

6 Transport elektrona u atomskim tečnostima visoke mobilnosti

6.1 Uvod

Ovo pogavlje bavi se transportom elektrona u atomskim tečnostima visoke mobilnosti, uključujući tečni argon, tečni kripton i tečni ksenon. Svi rezultati prikazani u ovom poglavlju dobijeni su primenom Monte Carlo simulacija. U potpoglavlju 6.1.1 u kratkim crtama su obrazloženi motivacioni faktori za proučavanje transporta naelektrisanih čestica u tečnoj fazi. Odeljak 6.1.2 prikazuje argumente koji ukazuju na postojanje provodne zone u tečnom argonu, tečnom kriptonu i tečnom ksenonu, nakon čega govorimo o korišćenim setovima preseka i uslovima simulacije za ispitivanje transporta elektrona u tečnom ksenonu u potpoglavlju 6.2.1. U segmentu 6.2.2 prikazani su rezultati vezani za transport elektrona u tečnom ksenonu, potpoglavlje 6.3.1 obrazlaže setove preseka i uslove simulacije koji su korišćeni za proučavanje transporta elektrona u tečnom argonu i tečnom kriptonu, dok odeljak 6.3.2 predstavlja rezultate u vezi sa transportom elektrona u tečnom argonu i tečnom kriptonu.

6.1.1 Motivacija za istraživanje

Transport naelektrisanih čestica u tečnoj fazi je oblast istraživanja koja ima veliki značaj i sa teorisjkog i sa praktičnog aspekta. Sa teorijske tačke gledišta značajno je razumeti način na koji velika gustina i kratkodometno uređenje pozadinskih atoma i/ili molekula u tečnoj fazi utiču na dinamiku naelektrisanih čestica [68–70]. Sa praktičnog aspekta, razumevanje transporta naelektrisabih čestica u tečnoj fazi je od ključnog značaja za mnoge važne primene poput detektora elementarnih čestica sa tečnim argonom i tečnim ksenonom, transformatorskih ulja, kao i upotrebe plazme u medicini, poljoprivredi i tretmanima za prečišćavanje vode. Neravnotežne plazme imaju širok spekar primene u medicini, poput dezinfekcije, podsticanja zarastanja rana, lečenja gljivičnih infekcija i tretmana tumora [40, 41]. Upotreba plazme u poljoprivredi ima potencijal da poveća prinos useva i suzbije bolesti biljaka na način koji je povoljniji po životnu sredinu, kao i da eliminiše patogene koji se mogu naći u hrani [42]. Primena neravnotežnih plazmi može obezbediti efikasan, jeftin i ekološki prihvatljiv proces za razgradnju organskih zagađivača u vodi [45]. Međutim za dalji razvoj ovih primena potrebno je razumeti kako pojedinačne naelektrisane čestice i njihovi produkti, poput radikala i metastabila, interaguju sa složenim organskim molekulima u tečnoj vodi. Detektori elementarnih čestica sa tečnim argonom i tečnim ksenonom su veoma pogodni za lociranje slabo interagujćih čestica poput neutrina i teorijski pretpostavljenih masivnih slabo interagujućih čestica (eng. weak interacting massive particles), i to zbog velike gustine ovih tečnosti i velike mobilnosti elektrona na niskim električnim poljima (u slučaju argona i ksenona), te velikog broja stabilnih izotopa od kojih su neki spinski singleti dok drugi imaju nenulti spin (u slučaju ksenona) [220–222]. U ovim detektorima je za rekonstrukciju trajektorije detektovanih čestica neophodno odrediti putanju primarnog i/ili sekundarnog naelektrisanja kroz tečnu sredinu od tačke formiranja ovih

naelektrisanja do tačke njihove detekcije. Transformatorska ulja se koriste u nekim tipovima transformatora i visokonaponskih prekidača za izolaciju i hlađenje transformatora, kao i za sprečavanje nastanka korone [223, 224]. Za pronalaženje novih transformatorskih ulja, koja imaju bolje inženjerske i/ili ekološke karakteristike, važno je razumeti pri kojim uslovima dolazi do lavinske multiplikacije elektrona i električnih pražnjenja u ovim tečnostima.

Uprkos značaju transporta naelektrisanih čestica u tečnoj fazi, u okviru ove oblasti postoji veliki broj poteškoća i u teorijskim i u eksperimentalnim ispitivanjima. Mnoge su vezane za raznovrsnost brojnih procesa koji se dešavaju u tečnostima u širokom rasponu vremenskih i prostornih skala. Naime, u tečnoj fazi je potencijal za rasejanje naelektrisane čestice na pojedinačnom atomu ili molekulu snažno perturbovan od strane okolnih atoma ili molekula [68, 69, 100]. Pored toga, talasna funkcija lakih naelektrisanih čestica poput elektrona i pozitrona zahvata veliki broj susednih atoma ili molekula. S tim razlogom se rasejanje u tečnoj fazi mora opisati kao superpozicija pojedinačnih rasejanja na više susednih atoma ili molekula pozadinske sredine (koherentni efekti) [68–70]. Iz toga sledi da je rasejanje ovih čestica u tečnoj fazi pod snažnim uticajem kratkodometnog uređenja neutralnih čestica pozadinske tečnosti. Značajan uticaj na dinamiku naelektrisasnih čestica u tečnoj fazi imaju i interakcija sa fluktuacijama gustine pozadinske tečnosti i zarobljavanje u rastvorenim mehurovima gasa [101]. U slučaju tečnosti sa polarnim molekulima (poput vode) naelektrisane čestice bivaju solvatirane u klasterima polarnih molekula [225–228]. Osetljivost transportnih osobina naelektrisanih čestica na ove procese znatno otežava razvoj teorijskih modela i kontrolu eksperimentalnih uslova. Pošto tečni plemeniti gasovi predstavljaju najjednostavnije tečnosti, oni su dobra polazna tačka za razvoj modela transporta naelektrisanih čestica u tečnoj fazi.

6.1.2 Postojanje provodne zone u tečnom Ar, tečnom Kr i tečnom Xe.

U tečnim plemenitim gasovima sa visokom mobilnošću niskoenergijskih elektrona (tečni argon, tečni kripton i tečni ksenon) dolazi do formiranja valentne i provodne zone [101]. Postojanje zonske strukture u ove tri tečnosti je utvrđeno na osnovu više nezavisnih eksperimenata. Promena mobilnosti elektrona pri topljenju može se pripisati promeni kompresibilnosti i gustine pri faznom prelazu [175, 229]. Pored toga su u tečnom argonu, tečnom kriptonu i tečnom ksenonu uočene ekscitonske linije u refleksionim spektrima. Ovi spektri su veoma slični odgovarajućim refleksionim spektrima u čvrstoj fazi, pri čemu su spektralne linije u tečnoj fazi pomerene i proširene [175, 230–232]. Istovremeno su u refleksionom spektru tečnog ksenona uočene spektralne linije koje odgovaraju Wannier -ovim ekscitonima višeg reda (za n=2). Ovo je značajno zbog toga što Wannier-ovi ekscitoni višeg reda nemaju poreklo u pojedinačnim ekscitacijama izolovanog atoma, već se mogu opisati kao superpozicija stanja u provodnoj zoni [175, 230–232]. Treba dodati da je u tečnom ksenonu (u blizini trojne tačke) prag za fotoprovodnost jako blizu odgovarajućem pragu u čvrstom ksenonu, uz šta je položaj ovog praga u tečnoj fazi u saglasnosti sa predviđanjima vezanim za promenu zonskog procepa u čvstom ksenonu na osnovu promene gustine pri topljenju [175, 233]. Zonski procep $\Gamma(3/2)$ u tečnom ksenonu je određen na osnovu Wannier-ovog $\Gamma(3/2)$ niza i na osnovu praga za fotoprovodnost. Vrednosti dobijene

na ova dva načina se međusobno dobro slažu i bliske su vrednosti zonskog procepa u čvrstom ksenonu [233]. Pored toga je u tečnom ksenonu uočena šupljinska provodnost [234, 235].

6.2 Transport elektrona u tečnom ksenonu

6.2.1 Korišćeni setovi preseka i uslovi simulacije za elektrone u tečnom ksenonu

Elastično rasejanje niskoenergijskih elektrona u atomskim tečnostima je pod intenzivnim uticajem ekraniranja polarizacionog potencijala fokus atoma polarizacionim potencijalima okolnih atoma i efekata koherentnog rasejanja [68, 69, 100, 102]. Pri tome snažna anizotropija koherentnog rasejanja dovodi do toga da su efektivni srednji slobodni putevi za transfer impulsa i energije u tečnosti međusobno različiti [100, 176]. Ovi srednji slobodni putevi su dati jednačinama

$$\Lambda_0 = (n_0 \sigma_m)^{-1} = (n_0 2\pi \int_0^\pi d\chi \sin \chi (1 - \cos \chi) \sigma_{sp}(\epsilon, \chi))^{-1}, \tag{6.1}$$

$$\Lambda_1 = (n_0 \tilde{\sigma}_m)^{-1} = (n_0 2\pi \int_0^\pi d\chi \sin \chi (1 - \cos \chi) \sigma_{sp}(\epsilon, \chi) S(\Delta k))^{-1}, \tag{6.2}$$

gde je n_0 koncentracija atoma u tečnosti, $\sigma_{sp}(\epsilon, \chi)$ je diferencijalni presek za elastično rasejanje elektrona na fokus atomu u tečnoj fazi, ϵ je relativna energija u sistemu centra mase, χ je ugao rasejanja i $S(\Delta k)$ je statički strukturni faktor, kao funkcija razmenjenog impulsa. U ovim jednačinama $\tilde{\sigma}_m$ i σ_m reprezentuju preseke za transfer impulsa u elastičnim sudarima sa strukturnim modifikacijama i bez strukturnih modifikacija, respektivno. Kao što je predložio Tattersall sa saradnicima, količnik $\gamma(\epsilon) = \frac{\Lambda_0}{\Lambda_1}$ reprezentuje merilo anizotropije koherentnog rasejanja [176].

U Monte Carlo simulacijama koherentno rasejanje se može modelovati uvođenjem tri različita efektivna sudarna procesa, koji zajedno dobro reprezentuju srednje transfere impulsa i energije u elastičnim sudarima [176]. U prvom od ovih sudarnih procersa, koji je reprezentovan sa σ_{oba} presekom, u sudaru se razmenjuju i energija i impuls, kao u običnom binarnom sudaru. U drugom procesu, koji je reprezentovan σ_{impuls} presekom, elektron se rasejava u nasumičnom pravcu, ali intenzitet brzine elektrona ostaje nepromenjen. Ovo dovodi do transfera impulsa, bez odgovarajućeg transfera energije [176]. U trećem procesu – koji je predstavljen $\sigma_{energija}$ presekom, energija elektrona je smanjena kao u običnom binarnom sudaru, ali smer kretanja elektrona ostaje nepromenjen, što dovodi do promene energije elektrona uz minimalnu promenu impulsa [176]. Važno je naglasiti da ovi efektivni sudarni procesi ne reprezentuju pojedinačne mikroskopske sudare, već samo obezbeđuju dobru reprezentaciju srednjeg transfera impulsa i energije u elastičnim sudarima u jedinici vremena u sredinama sa kratkodometnim prostornim uređenjem atoma. Preseci za ove efektivne sudarne procese se određuju na osnovu količnika $\gamma(\epsilon)$ i preseka za transfer impulsa u elastičnom rasejanju elektrona na fokus atomu u tečnoj fazi $\sigma_m(\epsilon)$ [176]. Vrednosti $\sigma_m(\epsilon)$ i $\gamma(\epsilon)$, koje su korišćene u našem radu, odredio je Boyle sa saradnicima [69].

Za $\gamma(\epsilon) < 1$ ovi efektivni preseci su definisani u sledećim jednačinama.

$$\sigma_{oba}^{\gamma < 1} = \gamma(\epsilon) \cdot \sigma_m(\epsilon)$$

$$\sigma_{energija}^{\gamma<1} = (1 - \gamma(\epsilon)) \cdot \sigma_m(\epsilon)$$
$$\sigma_{impuls}^{\gamma<1} = 0. \tag{6.3}$$

Za $\gamma(\epsilon) > 1$ su ovi efektivni preseci definisani na sledeći način.

$$\sigma_{oba}^{\gamma>1} = \sigma_m(\epsilon)$$
$$\sigma_{energija}^{\gamma>1} = 0$$
$$\sigma_{impuls}^{\gamma>1} = (\gamma(\epsilon) - 1) \cdot \sigma_m(\epsilon). \tag{6.4}$$

U našim Monte Carlo simulacijama elastično rasejanje elektrona, čija je energija niža od oko 10 eV, predstavljeno je primenom ova tri efektivna sudarna procesa, kojima odgovaraju preseci iz jednačina (6.3) i (6.4). Na višim energijama se efektivni preseci σ_{impuls} i $\sigma_{energija}$ mogu zanemariti, dok je presek σ_{oba} aproksimiran presekom za elastično rasejanje elektrona u gasnoj fazi [202]. Ovo je dobra aproksimacija, pošto efekti koji modifikuju potencijal za rasejanje elektrona na fokus atomu i efekti koherentnog rasejanja imaju zanemarljiv uticaj na rasejanje visokoenergijskih elektrona [110, 176]. Presek za transfer impulsa u elastičnim sudarima za elektrone u gasnom ksenonu, koji koristimo za reprezentovanje elastičnog rasejanja visokoenergijskih elektrona u tečnom ksenonu, preuzet je iz Hayashi-jeve baze [202]. Presek za ekscitaciju elektrona iz valentne zone u provodnu zonu je aproksimiran presekom za jonizaciju iz Hayashi-jevog seta preseka, koji je pomeren na niže energije za 2.91 eV kako bi mu prag bio snižen na 9.22 eV. Ova vrednost praga odgovara $\Gamma(\frac{3}{2})$ zonskom procepu u tečnom ksenonu, koji predstavlja energijsku razliku između vrha valentne zone i dna provodne zone [233]. Korišćenje ovog preseka daje dobar energijski balans budući da velika gustina stanja u provodnoj zoni omogućuje da se energijski nivoi kvazislobodnih elektrona reprezentuju kontinualnim energijskim spektrom [111].

U ovoj disertaciji su korišćena četiri različita slučaja za reprezentovanje neelastičnih sudara u tečnom ksenonu s ciljem ispitivanja uticaja neelastičnih sudara na transport elektrona i dinamiku formiranja, kao i na propagacije strimera u atomskim tečnostima.

Prvi slučaj (Scenario 1): Zanemarivanje ekscitacija

U prvom slučaju koji razmatramo energijski gubici u ekscitacijama su u potpunosti zanemareni. Atrazhev i saradnici su pokazali da zanemarivanje energijskih gubitaka u ekscitacijama dovodi do precenjivanja prvog Townsend-ovog koeficijenta u tečnom ksenonu [110]. Međutim, ovaj slučaj je razmatran u našem radu da bi se bolje utvrdio uticaj elektronskih ekscitacija na prvi Townsend-ov koeficijent.

Drugi slučaj (Scenario 2): Samo ekscitacije $6s[3/2]_2$ i $6s[3/2]_1$ su uzete u obzir

U preostala tri slučaja su energijski gubici u neelastičnim sudarima uzeti u obzir, pošto je pokazano u eksperimentima da u tečnom ksenonu postoje ekscitoni i perturbovane atomske ekscitacije [231, 232]. Utvrđeno da je i to da je pobuđivanje ovih elektronskih stanja glavni kanal energijskih gubitaka kvazislobodnih elektrona u tečnom argonu, tečnom kriptonu i tečnom ksenonu na električnim poljima srednje jačine [236–238]. U literaturi se ipak trenutno ne mogu naći preseci za pobuđivanje ovih elektronskih stanja pri neelastičnom rasejanju elektrona u atomskim tečnostima.

Poznato je da *intermediate* eksitoni vode poreklo iz pojedinačnih eksitovanih stanja atoma [231, 232, 239]. Na osnovu toga mi aproksimiramo preseke za *intermediate* eksitone i perturbovane atomske eksitacije u tečnoj fazi presecima za odgovarajuće eksitacije izolovanog atoma, koristeći se presecima za eksitacije iz Hayashi-jevog seta preseka za elektrone u gasnom ksenonu [202]. U našem radu ne menjamo vrednosti pragova za eksitacije, pošto se u literaturi mogu naći samo pragovi za optički dozvoljene eksitone [239], dok je za naš set preseka neophodno da budu uzeta u obzir i optički zabranjena stanja. Stoga bi bilo nekonzistentno da modifikujemo pragove za optički dozvoljene prelaze a ostavimo pragove za optički zabranjene prelaze nepromenjenim. Pokazuje se da u refleksionom spektru tečnog ksenona pored $n = 1$ [$\Gamma(\frac{3}{2})$] eksitonske linije postoji i jedna dodatna linija [231, 232], koja odgovara perturbovanom atomskom $6s[3/2]_1$ stanju [231, 232]. Laporte i saradnici su ustanovili da se u oko 10% atomskih klastera pojavljuje perturbovana atomska linija, umesto odgovarajuće eksitonske linije [231]. Ovo je posledica toga što ovi klasteri nemaju dovoljan broj atoma za formiranje eksitronskog stanja unutar zapremine koja odgovara eksitonskom radijusu [231, 232]. Zato bi za konstruisanje modela u kome se razlikuju *intermediate* eksitoni od odgovarajućih perturbovanih atomskih stanja, moralo da bude poznato u kom procentu atomskih klastera se formiraju perturbovane atomska stanja umesto odgovarajućih eksitonskih stanja, za svaku atomsku eksitaciju. Morale bi biti poznate i vrednosti pragova za sve eksitone i sva perturbovana atomska stanja, uključujući i optički zabranjena stanja. Ovo prevazilazi okvire našeg rada i zato su *intermediate* eksitone i perturbovane atomske eksitacije reprezentovane odgovarajućim eksitacijama izolovanog atoma. Međutim, razlika između ovih pragova je manja od 5% za sve primećene eksitone [231, 232, 239]. Na osnovu toga smo procenili da korišćenje pragova za eksitacije izolovanih atoma dovodi do male greške. Zanemarili smo $n = 2$ $\Gamma(\frac{3}{2})$ eksiton, koji je primećen u eksperimentima, u sva četiri slučaja za reprezentovanje neelastičnih sudara, pošto on nema poreklo u pojedinačnim stanjima izolovanog atoma. Ni jedan drugi Wannier-ov eksiton višeg reda (za n>1) nije primećen u refleksionom spektru tečnog ksenona [230–232, 239]. Zbog jednostavnosti, u ostatku ove disertacije eksitacija elektrona iz valentne u provodnu zonu i eksitoni biće označeni kao jonizacija i eksitacije, respektivno. Sudarni procesi koji dovode do pobuđivanja eksitonskih stanja se razlikuju od binarnih sudara, jer se svaki atom nalazi unutar klastera okolnih atoma. Stoga su atomske eksitacije zamenjene eksitonima ili perturbovanim atomskim eksitacijama, zavisno od veličine atomskog klastera [231, 232].

U drugom slučaju su u korišćenom setu preseka uzete u obzir samo eksitacije čiji su pragovi niži od praga za jonizaciju u tečnom ksenonu, što uključuje $6s[3/2]_2$ i $6s[3/2]_1$ stanja. Ove dve eksitacije odgovaraju prvoj i drugoj eksitaciji iz Hayashi-jevog seta preseka [202]. Prvo stanje je optički zabranjeno, dok je drugo optički dozvoljeno. Pri tome $n = 1$ [$\Gamma(\frac{3}{2})$] eksiton i odgovarajuće perturbovano atomsko stanje vuku poreklo iz $6s[3/2]_1$ eksitacije.

Treći slučaj (Scenario 3): Prve četiri eksitacije iz Hayashi-jevog seta preseka su uzete u obzir

Ranijim eksperimentima sa fotoprovodnošću u tečnom ksenonu pokazano je da postoje i eksitonska stanja čiji su pragovi viši od zonskog procepa i koja se sa nekom učestalošću deeksituju i ne vode u disocijaciju. Naime, u spektru fotoprovodnosti u tečnom ksenonu na oko 9.45 eV [233]

primećen je lokalni minimum, kao posledica prisustva diskretnog $n' = 1$ $[\Gamma(\frac{1}{2})]$ ekscitona, koji je konkurentan procesu ekscitovanja atoma u provodnu zonu. Primećeni minimum u spektru fotoprovodnosti tečnog ksenona ukazuje na to da ovo diskretno stanje ima kanale koji su alternativni disocijaciji, poput luminiscencije [175]. Pri tome $n' = 1$ $[\Gamma(\frac{1}{2})]$ eksciton ima poreklo u atomskom $6s'[1/2]_1$ stanju [231, 232]. Između optički dozvoljenih $6s[3/2]_1$ i $6s'[1/2]_1$ atomskih stanja postoji i optički zabranjeno $6s'[1/2]_0$ atomsko stanje. Ovi ekscitoni, čiji je prag viši od praga za ekscitaciju elektrona iz valentne zone u provodnu zonu, doprinose energijskim gubicima elektrona u neelastičnim sudarima i predstavljaju konkurentan proces ekscitovanju elektrona u provodnu zonu. Zato je potrebno da i ova dva dodatna stanja $6s'[1/2]_0$ i $6s'[1/2]_1$ budu uključena u set preseka za rasejanje elektrona u tečnom ksenonu. Prvo od ova dva stanja odgovara trećoj elektronskoj ekscitaciji iz Hayashi-jevog seta preseka [202]. Četvrta elektronska ekcitacija iz Hayashi-jevog seta odgovara kombinaciji $6s'[1/2]_1$ i $6p[1/2]_1$ stanja [202]. Zato u ovom slučaju uzimamo u obzir prve četiri eksitacije iz Hayashi-jevog seta preseka.

Slučaj 4 (Scenario 4): Sve eksitacije iz Hayashi-jevog seta preseka su uzete u obzir

U četvrtom slučaju za reprezentovanje neelastičnih sudara u tečnom ksenonu uzete su u obzir sve eksitacije iz Hayashi-jevog seta preseka. Ovaj slučaj predstavlja gornju granicu energijskih gubitaka u eksitacijama ako se preseci za neelastične sudare i eksitaciju elektrona u provodnu zonu aproksimiraju odgovarajućim presecima za rasejanje elektrona na izolovanom atomu ksenona i ako se zanemare Wannier-ovi eksitoni višeg reda (za n>1). Na osnovu dostupnih eksperimentalnih podataka nije moguće sa sigurnošću proceniti da li eksitoni u tečnom ksenonu, čiji su pragovi viši od 10 eV, u potpunosti disosuju na kvazislobodan elektron u provodnoj zoni i pozitivnu šupljinu u valentnoj zoni (u kojim okolnostima ne bi doprineli dodatnim neelastičnim energijskim gubicima, koji su konkurentan proces eksitaciji elektrona u provodnu zonu) ili se sa nekom učestalošću deekscituju uz emisiju fotona. U eksperimentu sa fotoprovodnošću u tečnom ksenonu pak nije uočena dodatna struktura u spektru fotoprovodnosti na energijama višim od 9.45 eV [233]. Pritom, u radu u kome su predstavljeni ovi rezultati nije prikazan spektar fotoprovodnosti na energijama višim od 10 eV. Međutim, dva dodatna minimuma su uočena u spektru fotoprovodnosti u fluidnom ksenonu na gustinama koje iznose oko 77.86% gustine tečnog ksenona u blizini trojne tačke, u kasnijem eksperimentu Reininger-a i saradnika [175]. Dodajemo da u ovom eksperimentu nisu razmatrani spektri fotoprovodnosti na višim gustinama. Prvi minimum se formira eksitovanjem dva susedna stanja ($5d[3/2]_1$ i $7s[3/2]_1$) pri apsorpciji fotona i on se nalazi na energiji od oko 10.32 eV. Drugi minimum se formira ekscitovanjem perturbovanog $5d'[3/2]_1$ stanja i nalazi se na energiji od oko 11.6 eV [175]. Jasno je da u tečnom ksenonu postoje eksitoni čija je energija viša od 10 eV, pošto je u refleksionom spektru tečnog ksenona uočena spektralna linija na oko 10.32 eV [231, 232, 240], kao i da ova stanja dovode do formiranja minimuma u profilima fotoprovodnosti fluidnog ksenona na gustinama koje su bliske gustini trojne tačke [175]. Ipak ne možemo sa sigurnošću da tvrdimo da li bi ova stanja trebalo uzeti u obzir pri reprezentovanju energijskih gubitaka elektrona u neelastičnim sudarima, pošto ne znamo sa kojom će učestanošću ovi eksitoni disosovati na kvazislobodan elektron i pozitivnu šupljinu. U ovom slučaju za reprezentovanje neelastičnih sudara u tečnom
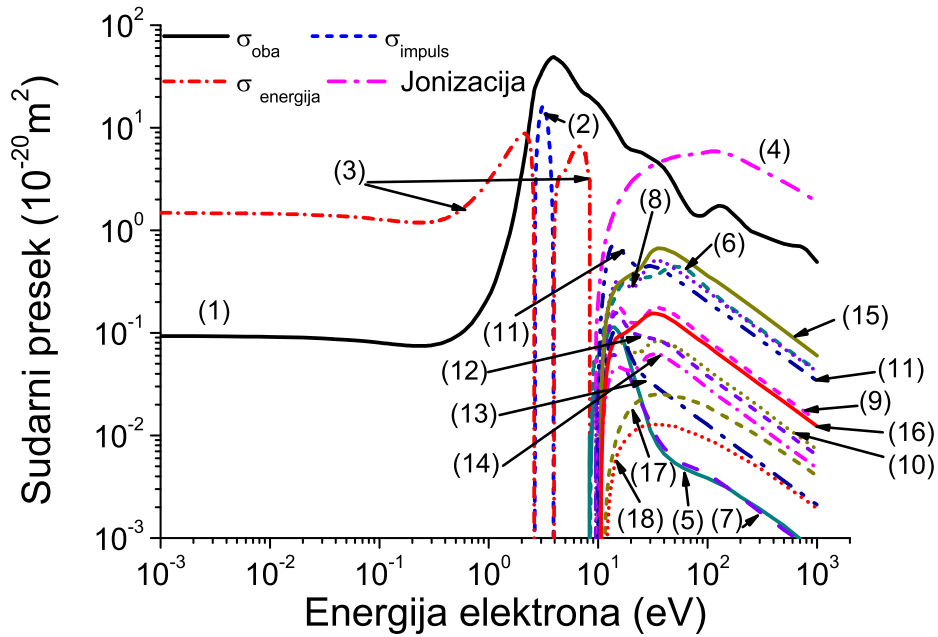
Slika 74: Set preseka za rasejanje elektrona u tečnom ksenonu: (1) σ_{oba}, (2) σ_{impuls}, (3) $\sigma_{energija}$, (4) jonizacija (zonski prelaz), efektivne elektronske ekscitacije: (5) $6s[3/2]_2$, (6) $6s[3/2]_1$, (7) $6s'[1/2]_0$, (8) $6s'[1/2]_1$ i $6p[1/2]_1$, (9) $6p[5/2]_2$ i $6p[5/2]_3$, (10) $6p[3/2]_1$ i $6p[3/2]_2$, (11) $5d[1/2]_0$, $5d[1/2]_1$, $6p[1/2]_0$, $5d[7/2]_4$ i $5d[3/2]_2$, (12) $5d[7/2]_3$, (13) $5d[5/2]_2$, (14) $5d[5/2]_3$, (15) $5d[3/2]_1$, (16) $7s[3/2]_2$, $7s[3/2]_1$, $7p[1/2]_1$, $7p[5/2]_2$, $6p'[3/2]_1$, $7p[5/2]_3$, $6d[1/2]_0$, $6d[1/2]_1$, $7p[3/2]_2$ $6d[3/2]_2$, $7p[3/2]_1$, $7p[1/2]_0$, $6d[7/2]_4$, $6d[7/2]_3$, $6p'[3/2]_2$, $6d[5/2]_2$, $6p[1/2]_1$, $6d[5/2]_3$, $6p'[1/2]_0$ i $6d[3/2]_1$, (17) $8s[3/2]_2$ i (18) $9s[3/2]_2$.

ksenonu je pretpostavljeno da se ovi eksitoni uvek rekombinuju uz emitovanje fotona (ili neki drugi oblik oslobađanja energije bez disocijacije), pri čemu u potpunosti doprinose neelastičnim gubicima elektrona kao proces koji je konkurentan eksitovanju elektrona iz valentne u provodnu zonu. Eksitacija $5d[3/2]_1$ odgovara jedanaestoj eksitaciji iz Hayashi-jevog skupa preseka, dok je $7s[3/2]_1$ eksitacija uključena u dvanaestu Hayashi-jevu eksitaciju [202]. Iako eksitacija $5d'[3/2]_1$, koja dovodi do formiranja minimuma u profilu fotoprovodnosti fluidnog ksenona na oko 11.6 eV, nije uključena u Hayashi-jev set preseka, četrnaesta Hayashi-jeva eksitacija odgovara $9s[3/2]_2$ stanju koje ima prag na 11.58 eV. Pri tome četrnaesta Hayashi-jeva eksitacija dobro reprezentuje energijske gubitke u svim neelastičnim procesima čiji su pragovi blizu 11.58 eV u gasnom ksenonu. Sve ostale efektivne eksitacije iz Hayashi-jevog seta preseka sadrže u sebi doprinose optički zabranjenih prelaza. Zbog toga je potrebno uključiti i ove eksitacije u naš set preseka, budući da se, na osnovu odsustva linija koje odgovaraju optički zabranjenim stanjima, u refleksionom spektru ne može zaključiti da ova stanja ne doprinose neelastičnim energijskim gubicima kvazislobodnih elektrona. S tim su razlogom u našem četvrtom slučaju za reprezentovanje neelastičnih sudara uzete u obzir sve efektivne eksitacije iz Hayashi-jevog seta preseka. Na slici 74 prikazan je set preseka za elektrone u tečnom ksenonu, koji odgovara četvrtom slučaju za reprezentovanje neelastičnih sudara.

6.2.2 Rezultati vezani za transport elektrona u tečnom ksenonu

Na slici 75 je prikazano poređenje vrednosti srednje energije elektrona u gasnom ksenonu sa vrednostima srednje energije elektrona u tečnom ksenonu – srednje energije koje se porede dobijene su primenom prvog i četvrtog slučaja za reprezentovanje neelastičnih sudara u tečnoj fazi. Na poljima nižim od oko 0.5 Td srednja energija u tečnom ksenonu viša je od srednje energije u gasnom ksenonu, jer je na niskim energijama presek za elastično rasejanje elektrona znatno manji u tečnom nego u gasnom ksenonu. Ovaj trend se menja na višim poljima, na kojima je vrednost srednje energije blizu 1 eV, zbog toga što je dinamika rasejanja elektrona, čija je energija viša od 1 eV, u atomskim tečnostima slična kao u gasnoj fazi. Srednja energija je niža u tečnom ksenonu nego u gasnom ksenonu u opsegu polja između 0.5 Td i 350 Td. Na poljima nižim od 3 Td ova je razlika između vrednosti srednje energije u gasnoj i tečnoj fazi posledica toga što je presek za transfer energije u tečnom ksenonu veći od preseka za elastične sudare u gasnom ksenonu u energijskom intervalu između oko 0.4 eV i 5 eV [68]. Za opseg polja između 3 Td i 350 Td ova razlika posledica intenzivnog hlađenja roja jonizacijom u tečnoj fazi. Hlađenje roja jonizacijom u gasnoj fazi je diskutovano u radu [241]. Na poljima višim od 350 Td je srednja energija u tečnom ksenonu, koja je dobijena na osnovu prvog/četvrtog slučaja za reprezentovanje neelastičnih sudara, jeste viša/niža od srednje energije u gasnom ksenonu.
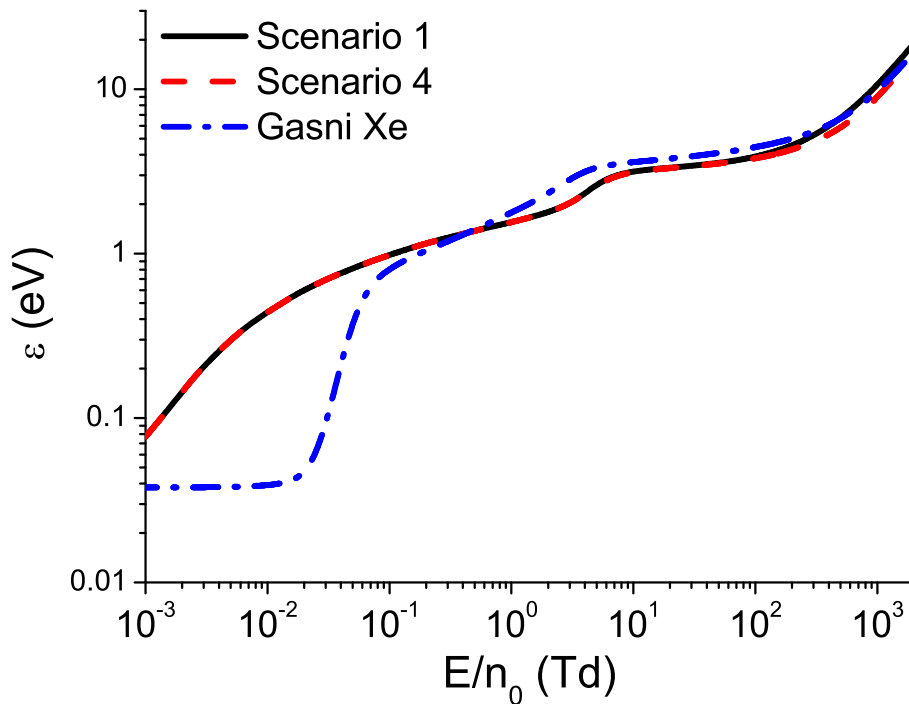
Slika 75: Poređenje vrednosti srednje energije za rojeve elektrona u gasnom i tečnom ksenonu. Vrednosti srednje energije u tečnom ksenonu su određene u dva različita slučaja za reprezentovanje neelastičnih sudara. U prvom slučaju (Scenario 1) su sve ekscitacije zanemarene, dok su u četvrtom slučaju (Scenario 4) uzete u obzir sve ekscitacije iz Hayashi-jevog seta preseka za elektrone u gasnom ksenonu [202]. Rezultati su dobijeni primenom Monte Carlo simulacija.

Slika 76 ilustruje procentualne razlike između vrednosti srednje energije koja je određena
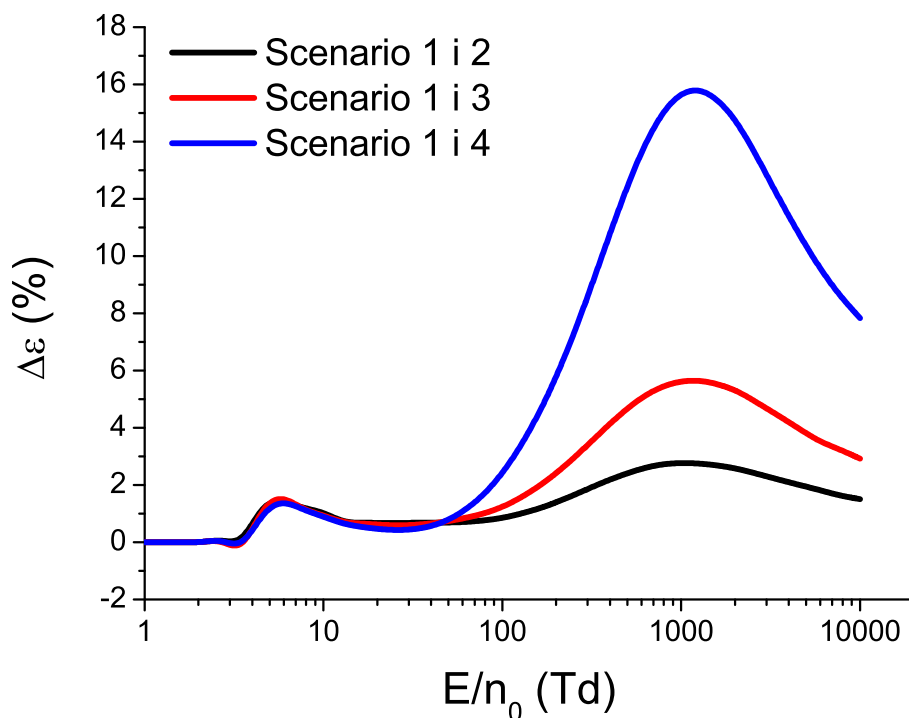
Slika 76: Procentualne razlike između vrednosti srednje energije, za elektrone u tečnom ksenonu, koje su određene u različitim slučajevima za reprezentovanje neelastičnih gubitaka energije. Sve ekscitacije su zanemarene u prvom slučaju (Scenario 1). U drugom i tećem slučaju (Scenario 2 i Scenario 3) su uzete u obzir samo prve dve ($6s[3/2]_2$ i $6s[3/2]_1$) i prve četiri ($6s[3/2]_2$, $6s[3/2]_1$, $6s'[1/2]_0$ i efektivna ekscitacija koja reprezentuje $6s'[1/2]_1$ i $6p[1/2]_1$) ekscitacije iz Hayashi-jevog seta preseka za elektrone u gasnom ksenonu [202], respektivno. Sve ekscitacije iz Hayashi-jevog seta su uzete u obzir u četvrtom slučaju (Scenario 4). Rezultati su dobijeni na osnovu Monte Carlo simulacija.

primenom prvog slučaja i vrednosti srednje energije koje su dobijene na osnovu preostala tri slučaja za reprezentovanje neelastičnih sudara. Ove su razlike zanemarljive na poljima nižim od oko 2 Td zato što elektroni učestvuju samo u elastičnim sudarima na niskim poljima. Na višim poljima je srednja energija najviša u prvom slučaju, i to zbog odsustva energijskih gubitaka u ekscitacijama. Procentualne razlike između vrednosti srednje energije, koje su dobijene na osnovu različitih reprezentacija neelastičnih sudara u tečnom ksenonu, dostižu dva lokalna maksimuma na oko 5.9 Td i 1300 Td i lokalni minimum na oko 27 Td. Prvi lokalni maksimum je posledica odsustva neelastičnih gubitaka na energijama nižim od praga za jonizaciju u prvom slučaju za reprezentovanje neelastičnih sudara. Lokalni minimum se nalazi u opsegu polja u kome energijski gubici u jonizaciji postaju uporedivi sa energijskim gubicima u ekscitacijama. U opsegu polja između 10 Td i 50 Td ove su procentualne razlike jako male i nalaze se u okviru statističke nesigurnosti Monte Carlo simulacija. Na poljima višim od 50 Td, srednja energija primento opada sa porastom broja ekscitacija, što je posledica značajnog porasta brzinskih koeficijenata za ekscitacije na visokim poljima. Procentualne razlike između vrednosti srednje energije u prvom slučaju i u preostala tri slučaja ne prevazilaze 3%, 6% i 16% za drugi, treći i četvrti slučaj, respektivno. Iako procentualne razlike između vrednosti srednje energije, koje su

dobijene u različitim slučajevima za reprezentovanje neelastičnih sudara, opadaju sa porastom E/n_0 nakon drugog lokalnog maksimuma, apsolutne razlike između ovih vrednosti se monotono povećavaju sa porastom E/n_0 do kraja razmatranog opsega polja.
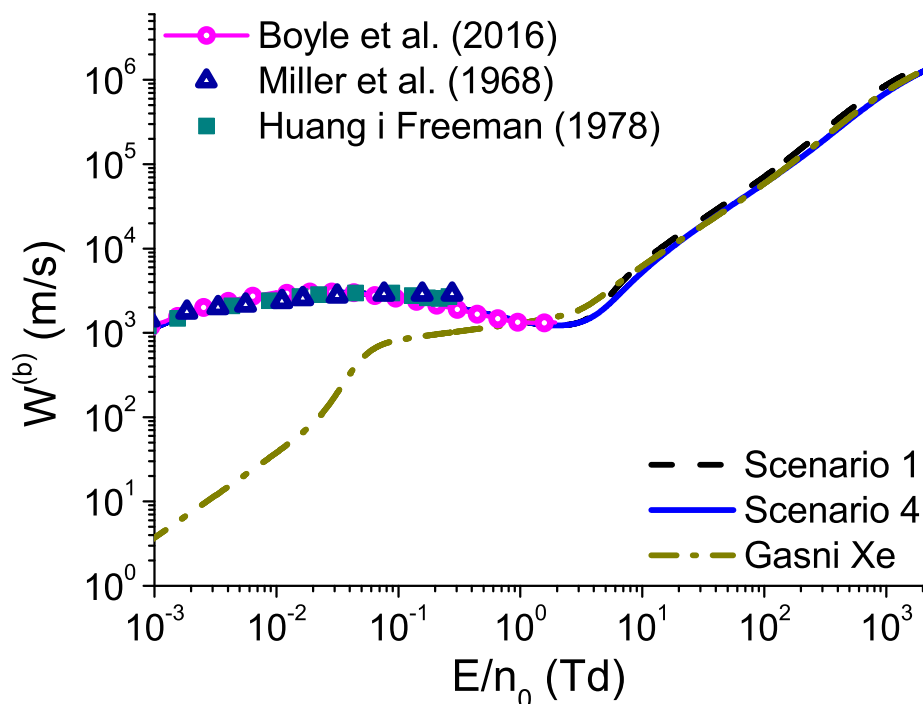
Slika 77: Poređenje eksperimentalno određene brzine drifta za roj elektrona u tečnom ksenonu (Miller *et al.* [229] i Huang i Freeman [242]) sa teorijskim proračunima. Među teorijskim rezultatima su prikazani proračuni Boyle-a i saradnika [69], kao i vrednosti balk brzine drifta koje su određene u okviru ovog rada a primenom dva različita metoda za reprezentovanje neelastičnih sudara. Na ovom grafiku je prikazana i balk brzina drifta za roj elektrona u gasnom ksenonu, radi poređenja. Rezultati su dobijeni primenom Monte Carlo simulacija.

Na slici 77 date su vrednosti balk brzine drifta, koje su dobijene u prvom i četvrtom slučaju za reprezentovanje neelastičnih sudara u tečnom ksenonu, u funkciji E/n_0. Radi poređenja su na istom grafiku prikazane teorijske i eksperimentalne vrednosti brzine drifta u tečnom ksenonu, koje su utvrdili prethodni autori, kao i vrednosti balk brzine drifta u gasnom ksenonu. Na poljima nižim od 1 Td brzina drifta je veća u tečnoj nego u gasnoj fazi. Pritom je ova razlika najintenzivnija na niskim poljima (na oko 10^{-3} Td), gde je brzina drifta u tečnom ksenonu za preko dva reda veličine veća od brzine drifta u gasnom ksenonu. Razlika između vrednosti brzine drifta u tečnoj i gasnoj fazi na niskim poljima je posledica znatno manjeg preseka za transfer impulsa u tečnom ksenonu na niskim energijama, zbog kombinovanog uticaja modifikacije potencijala u kome se rasejavaju pojedinačni elektroni u tečnoj fazi i strukturno indukovanih koherentnih efekata. Niža vrednost preseka za transfer impulsa omogućava električnom polju da ubrzava elektrone znatno efikasnije u tečnom ksenonu nego u gasnoj fazi. Ovaj je efekat značajno smanjen na višim poljima, imajući u vidu to da se rasejanje visokoenergijskog elektrona u atomskim tečnostima ne razlikuje značajno od rasejanja na izolovanom atomu. Zbog toga u opsegu polja između 0.02 Td i 2 Td brzina drifta u tečnom ksenonu opada sa porastom E/n_0

sve dok ne dostigne vrednosti koje su bliske brzini drifta u gasnom ksenonu. Opadanje brzine drifta sa porastom E/n_0 je fenomen u literaturi poznat kao negativna diferencijalna provodnost (eng. negative differential conductivity, skraćeno NDC) [13, 14, 243]. Dok je u gasnoj fazi ovaj efekat izazvan kombinacijom energijske zavisnosti elastičnih i neelastičnih sudara ili prisustvom nekonzervativnih procesa [13,243], u tečnom argonu, tečnom kriptonu i tečnom ksenonu je negativna diferencijalna provodnost u potpunosti indukovana strukturnim efektima (zbog smanjenja koherentnih efekata na rasejanje elektrona sa porastom energije) [68,69,244]. Kvantitativne kriterijume za pojavu strukturno indukovane negativne diferencijalne provodnosti podrobno su tumačili White i Robson [244].
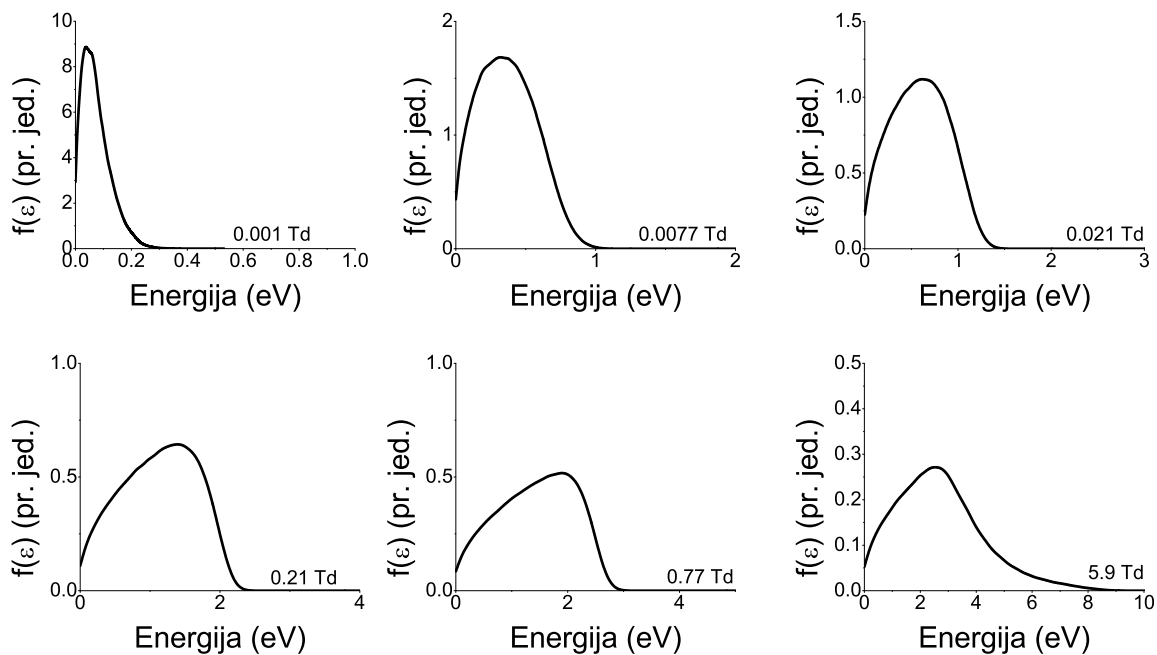
Slika 78: Funkcije raspodele elektrona po energijama prikazane u proizvoljnim jedinicama, za različite vrednosti redukovanog električnog polja E/n_0. Ove funkcije raspodele su određene u drugom slučaju za reprezentovanje neelastičnih sudara, u kome su uzete u obzir samo prve dve ekscitacije ($6s[3/2]_2$ i $6s[3/2]_1$) iz Hayashi-jevog seta preseka. Rezultati su dobijeni uz pomoć Monte Carlo simulacija.

Slika 78 prikazuje funkcije raspodele po energijama za elektrone u tečnom ksenonu na nekoliko vrednosti redukovanog električnog polja, s ciljem detaljnije analize strukturno indukovane negativne diferencijalne provodnosti u tečnom ksenonu. Prikazani rezultati su dobijeni primenom drugog slučaja za reprezentovanje neelastičnih sudara u tečnom ksenonu, pošto su brzinski koeficijenti za ekscitacije, koje nisu uzete u obzir u ovom slučaju, zanemarljivi u ovom opsegu polja. Na poljima nižim od oko $7.7 \cdot 10^{-3}$ Td većina elektrona ima energiju nižu od oko 0.7 eV. Presek za transfer impulsa je u energijskom intervalu nižem od 0.7 eV znatno manji u tečnom nego u gasnom ksenonu, pa je brzina drifta u tečnoj fazi znatno veća nego u gasnoj fazi. Međutim, na poljima višim od oko $2 \cdot 10^{-2}$ Td (na ovoj vrednosti polja počinje negativna diferencijalna provodnost) veliki broj elektrona ima vrednost energije u intervalu između 0.7 i 2 eV. U ovom opsegu polja se preseci σ_{oba} i $\sigma_{energija}$ naglo povećavaju sa porastom energije i

približavaju se preseku za elastične sudare u gasnoj fazi. Nagli porast ova dva preseka sa porastom energije dovodi do opadanja brzine drifta sa porastom E/n_0. Na poljima višim od oko 5 Td veliki procenat elektrona ima energiju višu od 4 eV i nalazi se u energijskom opsegu u kome presek za elastično rasejanje naglo opada sa porastom energije. U ovom rasponu polja se brzina drifta monotono povećava sa porastom E/n_0. Za vrednosti E/n_0 na kojima se dešava negativna diferencijalna provodnost visokoenergijski rep funkcije raspodele po energijama naglo opada sa porastom energije. Ovo je posledica naglog povećanja brzine transvera energije, koji je opisan efektivnim presecima σ_{oba} i $\sigma_{energija}$, sa porastom energije elektrona u energijskom intervalu između oko 0.7 eV i 4 eV. Na poljima nižim od $7.7\cdot10^{-3}$ Td i višim od 4 Td visokoenergijski rep funkcije raspodele sporije opada sa porastom energije.
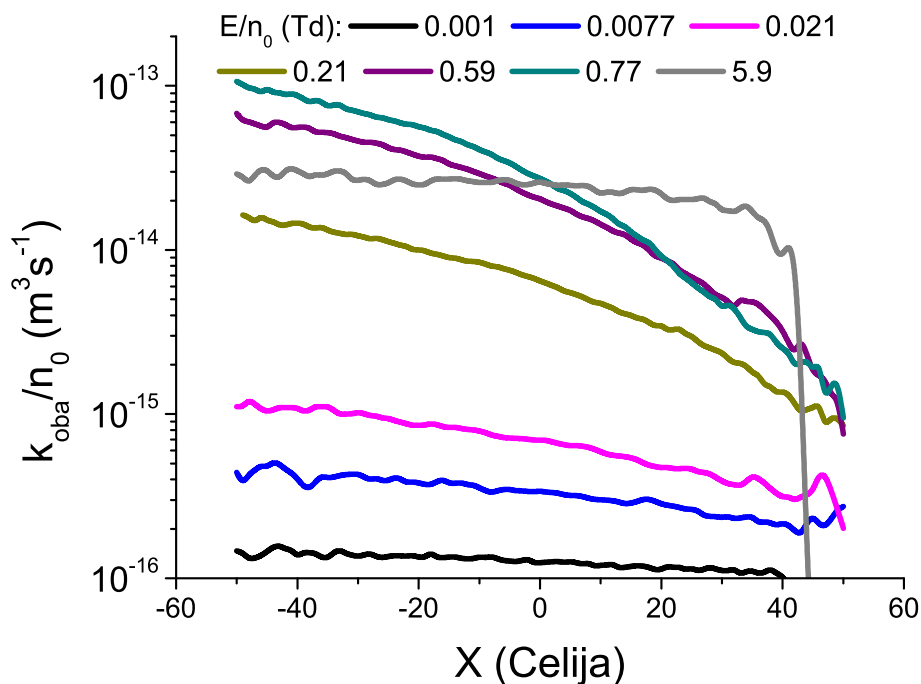
Slika 79: Prostorno razloženi brzinski koeficijent za σ_{oba} proces. Ovaj brzisnki koeficijent je određen u drugom slučaju za reprezentovanje neelastičnih sudara, u kome su samo prve dve ekscitacije ($6s[3/2]_2$ i $6s[3/2]_1$) iz Hayashi-jevog seta preseka uzete u obzir. Rezultati su dobijeni primenom Monte Carlo simulacija.

Na slici 79 je prikazan prostorno razloženi brzinski koeficijent za efektivni sudarni proces koji je reprezentovan σ_{oba} presekom. Zarad samplovanja prostorno razloženih veličina konfiguracioni prostor je podeljen u 100 ćelija, na takav način da ćelije sa indeksima (-50, +50) odgovaraju prostornim koordinatama ($x_{cm} \pm 3\sigma$), gde je x_{cm} x-koordinata centra mase roja, a σ je standardna devijacija x-koordinate elektrona [31]. Brzinski koeficijent za ovaj efektivni sudarni proces je veći na frontu nego na začelju roja, zbog porasta srednje energije u smeru kretanja elektrona. Nagib ovog prostorno razloženog brzinskog koeficijenta je najveći u opsegu polja u kome se javlja negativna diferencijalna provodnost. Uz to su maksimalne vrednosti ovog brzinskog koeficijenta veće na 0.59 Td i 0.77 Td nego na 5.9 Td. Sličan trend ponašanja se javlja za prostorno razloženi brzinski koeficijent za efektivni sudarni proces, koji je reprezentovan σ_{impuls} presekom u opsegu polja prikazanom na slici 79.

Drift brzina koja je određena u našem radu se odlično slaže sa teorijskim rezultatima Boyle-a i saradnika [69]. Naše vrednosti brzine drifta su bliske vrednostima koje su određene u eksperimentima Miller-a i saradnika [229] i Huang-a i Freeman-a [242]. Međutim, iako većina teorijskih proračuna brzine drifta u tečnom ksenonu predviđa strukturno indukovanu negativnu diferencijalnu provodnost, ovaj efekat nije primećen u eksperimentima. U opsegu polja u kome teorijske vrednosti predviđaju početak strukturno indukovane negativne diferencijalne provodnosti, eksperimentalna brzina drifta saturira sa porastom polja, a na višim poljima nema dostupnih eksperimentalnih rezultata. Sakai i saradnici [108] su ovo neslaganje između teorisjkih i eksperimentalnih vrednosti brzine drifta pripisali dodatnim kanalima za neelastične gubitke energije, koji nisu uključeni u postojeće teorijske modele. Ovi energijski gubitci odgovaraju promeni u translacionim stanjima parova i tripleta atoma ksenona pri sudaru sa elektronom. Energijski pragovi za ove procese su znatno niži od prvog praga za ekscitacije [101, 108]. Sakai i saradnici su empirijski odredili setove preseka za rasejanje elektrona u tečnom argonu, tečnom kriptonu i tečnom ksenonu, koji u sebi sadrže efektivne preseke za reprezentovanje ovih dodatnih gubitaka energije [101, 108]. Alternativno objašnjenje za ovo neslaganje između teorije i eksperimenta moglo bi biti prisustvo molekularnih nečistoća u tečnim plemenitim gasovima koji su korišćeni u eksperimentu. Sakai i saradnici su pokazali da čak i male koncentracije molekularnih nečistoća u tečnim plemenitim gasovima dovode do značajnog povećanja brzine drifta [108]. Takođe nije isključeno da bi se strukturno indukovana negativna diferencijalna provodnost pojavila u eksperimentalnim profilima brzine drifta na višim vrednostima redukovanog električnog polja. Dodatna teorijska i eksperimentalna ispitivanja su potrebna da bi se našao uzrok ovog neslaganja. Zato su neophodna merenja brzine drifta u tečnom ksenonu na višim poljima. U svakom slučaju, u naš model ne uključujemo efektivni presek Sakai-a i saradnika [108], jer on nije prilagođen našem preseku za elastično rasejanje.

Slika 80 prikazuje procentualne razlike između vrednosti brzine drifta koja je izračunata primenom prvog slučaja za reprezentovanje neelastičnih sudara elektrona u tečnom ksenonu sa vrednostima brzine drifta koje su određene primenom preostala tri slučaja za reprezentovanje neelastičnih sudara. Fluks brzina drifta se povećava sa smanjenjem broja ekscitacija koje su uključene u model. Ovo je posledica smanjenja haotične komponente brzine elektrona, zbog intenzivnijeg hlađenja roja jonizacijom sa smanjenjem energijskih gubitaka u ekscitacijama [241]. Balk brzina drifta se sa smanjenjem broja ekscitacija povećava još intenzivnije od fluks brzine drifta, zbog eksplicitnih efekata jonizacije. Procentualne razlike između vrednosti brzine drifta koje su određene u prvom slučaju i vrednosti brzine drifta koje su određene u preostala tri slučaja imaju lokalne maksimume na oko 8 Td, pošto su relativne razlike između brzinskih koeficijenata za jonizaciju u prvom i preostala tri slučaja najintenzivnije na niskim poljima. Ovi lokalni maksimumi iznose oko 8% i 24% za fluks i balk brzinu drifta, respektivno. Na poljima višim od 100 Td procentualne razlike između fluks brzine drifta u prvom slučaju i poslednja dva slučaja monotono se povećavaju sa porsatom E/n_0, kao posledica brinskih koeficijenata za ekscitacije, čiji je prag preko 9.22 eV u ovom opsegu polja. Procentualne razlike između odgovarajućih vrednosti balk brzine drifta dostižu još jedan lokalni maksimum na oko 200 Td i 400 Td za treći i četvrti slučaj, respektivno. Iako procentualne razlike između vrednosti balk
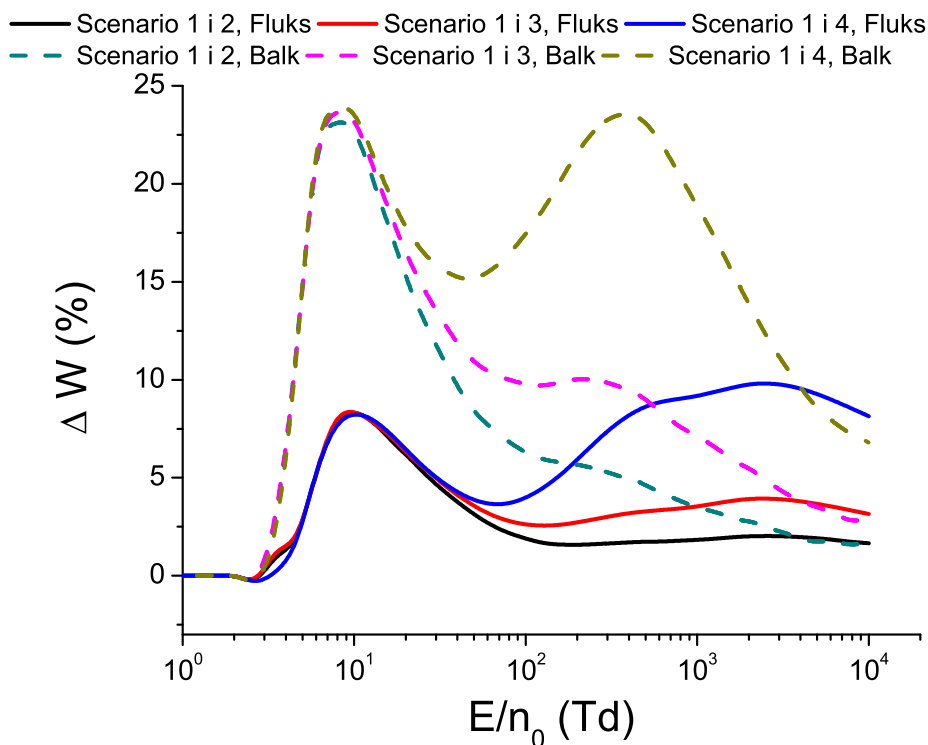
Slika 80: Procentualne razlike između vrednosti brzine drifta za elektrone u tečnom ksenonu, koje su određene u različitim slučajevima za reprezentovanje neelastičnih sudara u tečnoj fazi. Ovi slučajevi su opisani u zaglavlju grafika 76. Fluks i balk rezultati su reprezentovani punim i isprekidanim linijama, respektivno. Rezultati su dobijeni na osnovu Monte Carlo simulacija.

brzine drifta, koje su dobijene u različitim slučajevima za reprezentovanje neelastičnih sudara, monotono opadaju sa porastom E/n_0 nakon polsednjig lokalnog maksimuma, apsolutne razlike između ovih vrednosti brzine drifta se monotono povećavaju do kraja razmatranog opsega polja (do 2000 Td).

Prvi Townsend-ov koeficijent, α, opisuje broj jonskih parova koje proizvede jedan elektron po jedinici dužine. Ukoliko zanemarimo efekte difuzije, ovaj koeficijent je jednak brzinskom koeficijentu za jonizaciju koji je pomnožen sa koncentracijom atoma pozadinske sredine i podeljen sa brzinom drifta elektrona. Vrednosti prvog Townsend-ovog koeficijenta koje su dobijene u našim proračunima u različitim slučajevima za reprezentovanje neelastičnih sudara prikazane su na slici 81. Na njoj je, poređenja radi, prikazan i prvi Townsend-ov koeficijent u gasnom ksenonu, koji je skaliran na gustinu tečnog ksenona. Može se videti da se α monotono povećava sa porastom E/n_0 u sva četiri slučaja za reprezentovanje neelastičnih sudara u tečnom ksenonu. Prvi Townsend-ov koeficijent ima najveću vrednost u prvom slučaju, u kome su sve ekscitacije zanemarene u celom opsegu polja. Iako se apsolutne razlike između vrednosti α koje su određene u različitim slučajevima za reprezentovanje neelastičnih sudara monotono povećavaju u celom razmatranom opsegu, relativne razlike su najveće na poljima nižim od 20 Td. Na poljima višim od 20 Td je prvi Townsend-ov koeficijent u četvrtom slučaju, u kome su sve ekscitacije uzete u obzir, znatno niži nego u ostala tri slučaja. Ovo je posledica povećanja brzinskih koeficijenata za neelastične sudare čiji su pragovi viši od 9.22 eV sa porastom E/n_0 u četvrtom slučaju.
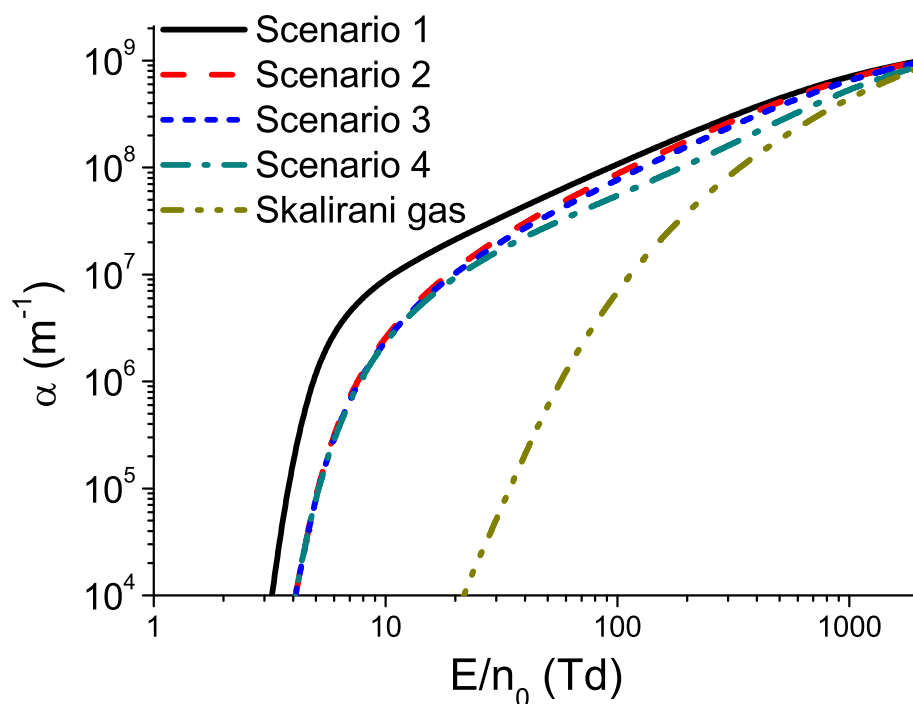
Slika 81: Zavisnost prvog Townsend-ovog koeficijenta od redukovanog električnog polja E/n_0 za roj elektrona u tečnom ksenonu. Ove vrednosti su određene primenom sva četiri različita metoda za reprezentovanje neelastičnih sudara. Ovi metodi su opisani u zaglavlju grafika 76. Na grafiku je, radi poređenja, prikazan i prvi Townsend-ov koeficijent za roj elektrona u gasnom ksenonu, koji je skaliran na gustinu tečnog ksenona. Rezultati su dobijeni primenom Monte Carlo simulacija.

Prvi Townsend-ov koeficijent u tečnom ksenonu je znatno viši od prvog Townsend-ovog koeficijenta u gasnom ksenonu, koji je skaliran na gustinu tečnosti, na poljima nižim od 100 Td. Na višim poljima je, međutim, ova razlika znatno manja. Jedan od glavnih razloga za veliku razliku između vrednosti brzinskih koeficijenata za jonizaciju u tečnom i gasnom ksenonu jeste sniženje praga za jonizaciju u tečnoj fazi. Elektron u gasnom ksenonu može učestvovati u elektronskoj sudarnoj jonizaciji samo na energijama višim od 12.13 eV. Uz to, u gasnoj fazi elektron može izgubiti značajnu količinu energije u velikom broju elektronskih ekscitacija, čiji su pragovi niži od praga za jonizaciju. No u tečnom ksenonu svaki elektron čija je energija viša od 9.22 eV može da ekscituje elektron iz valentne zone u provodnu zonu. Pored toga, u tečnom ksenonu postoji znatno manji broj ekscitacija čiji prag je niži od praga za jonizaciju nego u gasnom ksenonu.

Na slici 82 su predstavljene eksperimentalne vrednosti prvog Townsend-ovog koeficijenta koje su odredili Derentzo i saradnici [245], zajedno sa teorijskim vrednostima koje su utvrdili raniji autori [110, 112, 113]. S ciljem poređenja su na ovom grafiku prikazane i vrednosti prvog Townsend-ovog koeficijenta koje smo odredili u našem radu, pretpostavljajući prvi i četvrti slučaj za reprezentovanje neelastičnih sudara. Eksperimentalne vrednosti Derentzo-a i sarad-nika [245] su znatno više od vrednosti α za elektrone u gasnom ksenonu. Neobična osobina rezultata Derentzo-a i saradnika je nemonotono ponašanje sa porastom E/n_0. Ova nemonoto-
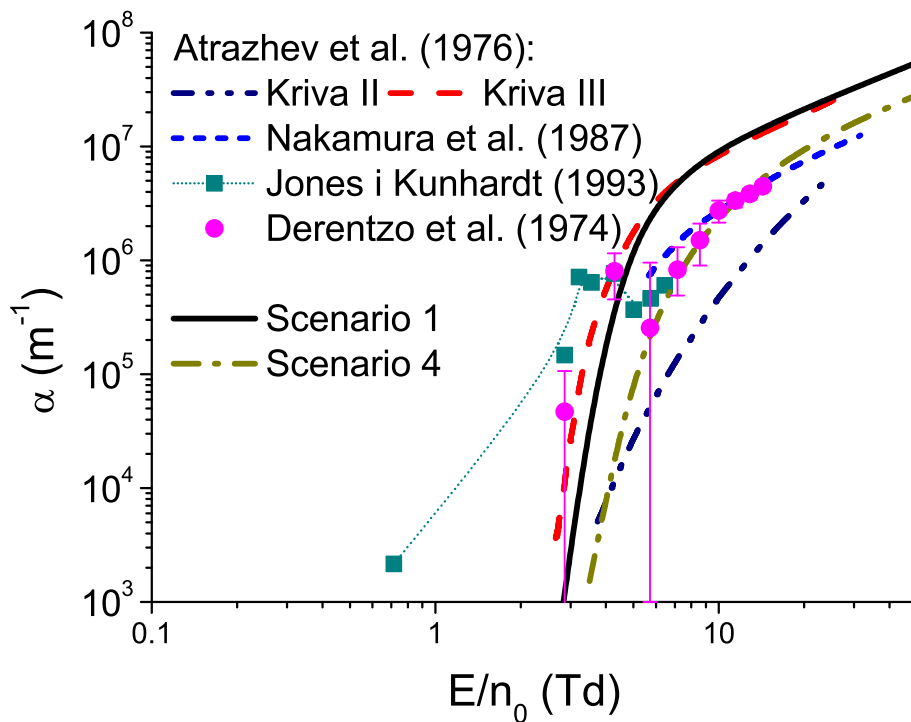
Slika 82: Poređenje vrednosti prvog Townsend-ovog koeficijenta α, koje su određene u ovom radu, sa rezultatima prethodnih autora. Među ovim rezultatima su uključeni eksperimentalni rezultati Derenzo-a i saradnika [245], kao i proračuni Atrazhev-a i saradnika [110], Jones-a i Kunhardt-a [112] i Nakamura-e i saradnika [113].

nost je u granicama eksperimentalne nesigurnosti. Dva seta rezultata koje su odredili Atrazhev i saradnici su izračunata, uz pretpostavku dva različita metoda za reprezentovanje neelastičnih sudara [110]. Vrednosti prvog Townsend-ovog koeficijenta, koje su reprezentovane krivom II, određene su pod pretpostavkom da je udeo energijskih gubitaka u tečnoj fazi isti kao u gasnoj fazi [110]. Ova kriva je znatno ispod svih ostalih krivih sa slike 82. Snažno odstupanje vrednosti α koje su reprezentovane krivom II od vrednosti koje su reprezentovane ostalim krivama ukazuje na značajno smanjenje neelastičnih energijskih gubitaka u ekscitacijama u tečnom ksenonu u poređenju sa gasnim ksenonon, kao što su primetili Atrazhev i saradnici [110]. Pri određivanju vrednosti α, koje su reprezentovane krivom III, neelastični gubici energije u ekscitacijama su u potpunosti zanemareni [110]. Ova kriva se najbolje slaže sa prve dve eksperimentalne vrednosti Derentzo-a i saradnika [245] i sa našom krivom 1. Vrednosti prvog Townsend-ovog koeficijenta, koje su odredili Jones i Kunhardt [112], su za sada jedini teorijski rezultat koji predviđa nemonotono ponašanje α sa porastom E/n_0. Njihovi se rezultati jako dobro slažu sa prve četiri eksperimentalne tačke Derenzo-a i saradnika, ali vrednosti α na višim poljima nisu prikazane u njihovom radu. Rezultati Nakamure i saradnika [113] se dobro slažu sa poslednjim segmentom eksperimentalnih tačaka Derenzo-a i saradnika [245], ali u njihovom radu nisu prikazane vrednosti α na nižim poljima.

Dok se naše vrednosti dobijene u prvom slučaju reprezentovanja neelastičnih sudara najbolje slažu sa prve dve eksperimentalne tačke Derenzo-a i saradnika, sve ostale eksperimentalne tačke se odlično slažu sa naša preostala tri slučaja [245]. Nisu dostupni eksperimentalni podaci za prvi

Townsend-ov koeficijent α u opsegu polja u kome se vrednosti α, koje su određene u poslednja tri slučaja za reprezentovanje neelastičnih sudara, značajno međusobno razlikuju. Međutim, poslednje dve tačke Derentzo-a i saradnika se nešto bolje slažu sa našim četvrtim slučajem nego sa ostala tri slučaja [245]. Moguće objašnjenje za visoke vrednosti prve dve eksperimentalne tačke Derentzo-a i saradnika jeste prisustvo nekog drugog mehanizma za populisanje provodne zone, koji je značajniji od elektronske sudarne jonizacije na niskim poljima. Jedan primer takvog mehanizma je disosovanje Wannier-ovih ekscitona višeg reda (n>1), pri rasejanju na zidovima sistema, ili u prisustvu neke druge perturbacije. Drugo moguće objašnjenje je redukcija neelastičnih gubitaka energije u procesima čiji su pragovi niži od 9.22 eV, zbog nekih drugih efekata koji nisu uzeti u obzir u našem modelu.
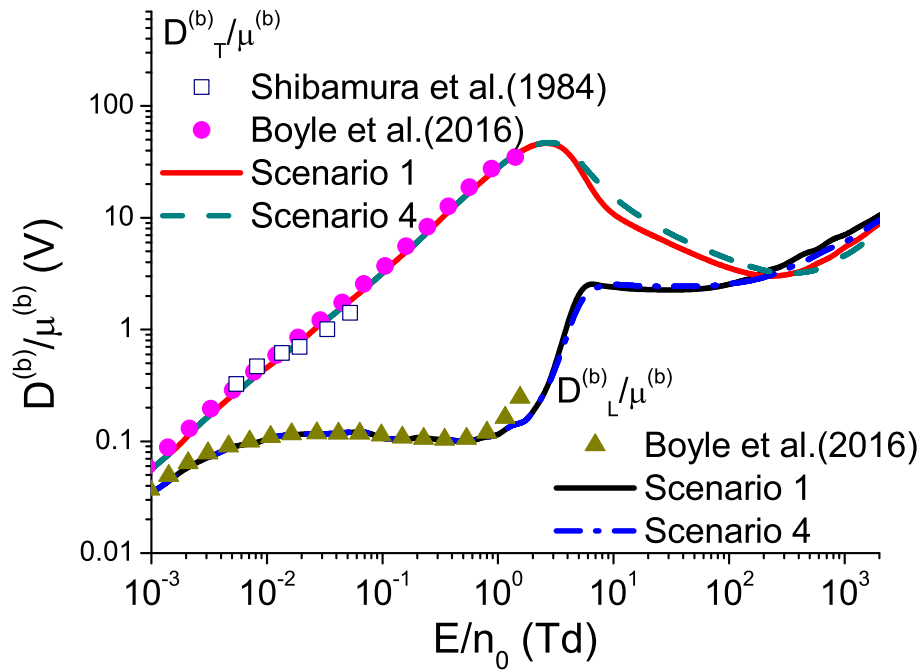
Slika 83: Poređenje vrednosti balk longitudinalne karakteristične energije D_L/μ i balk transverzalne karakteristične energije D_T/μ, koje su određene u ovom radu, sa teorijskim rezultatima Boyle-a i saradnika [69] i eksperimentalnim rezultatima Shibamura-e i saradnika [246] za roj elektrona u tečnom ksenonu. Naši rezultati su dobijeni na osnovu Monte Carlo simulacija uz primenu scenarija 1 i 4 za reprezentovanje neelastičnih sudara.

Zavisnosti D_L/μ i D_T/μ od E/n_0 u prvom i četvrtom slučaju za reprezentovanje neelastičnih sudara u tečnom ksenonu prikazane su na slici 83. Vrednosti ovih veličina koje su izračunali Boyle i saradnici [69] prikazane su na istom grafiku radi poređenja, zajedno sa eksperimentalnim vrednostima karakteristične energije Shibamura-e i saradnika [246]. Ovde D_L i D_T označavaju longitudinalnu i transverzalnu komponentu balk difuzionog tenzora, dok μ označava balk mobilnost elektrona. Karakteristična energija D_T/μ na početku se povećava sa porastom E/n_0 i dostiže lokalni maksimum na oko 2 Td, nakon čega opada sa porastom E/n_0. Na poljima višim od 300 Td se D_T/μ ponovo povećava sa porastom E/n_0. Zavisnost D_L/μ od E/n_0 je složenija od odgovarajuće zavisnosti D_T/μ. Na najnižim poljima se D_L/μ polako povećava sa porastom E/n_0, zbog male vrednosti preseka za transfer impulsa niskoenergijskih elektrona u tečnom

ksenonu. Nakon toga D_L/μ postepeno opada sa porastom E/n_0 između oko 0.05 Td i 0.4 Td, posle čega se ova veličina naglo povećava sa porastom polja do oko 6 Td. U opsegu polja između 6 Td i 30 Td D_L/μ opada sa porastom E/n_0 kao posledica energijskih gubitaka u neelastičnim sudarima. Na višim poljima se D_L/μ ponovo povećava sa porastom E/n_0, pošto u ovom opsegu polja elektroni dobijaju veliku količinu energije od električnog polja. Složeno ponašanje D_L/μ u tečnom ksenonu odslikava osetljivost ove veličine na detalje energijske zavisnosti preseka za sudare.

Sa slike 83 se vidi da se naše vrednosti D_L/μ jako dobro slažu sa vrednostima Boyle-a i saradnika na poljima nižim od 0.7 Td. Međutim, naši rezultati su niži od njihovih rezultata na višim poljima. Ova razlika se može pripisati razlici u korišćenim presecima pošto su Boyle i saradnici u potpunosti zanemarili neelastične sudare i jonizaciju u svojim proračunima. Kako je srednja energija elektrona oko 1.8 eV na 1 Td, najenergijčniji elektroni imaju dovoljno energije za neelastične sudare. Vrednosti D_T/μ koje su dobijene u našim proračunima se dobro slažu sa rezultatima Boyle-a i saradnika [69] i Shibamura-e i saradnika [246].
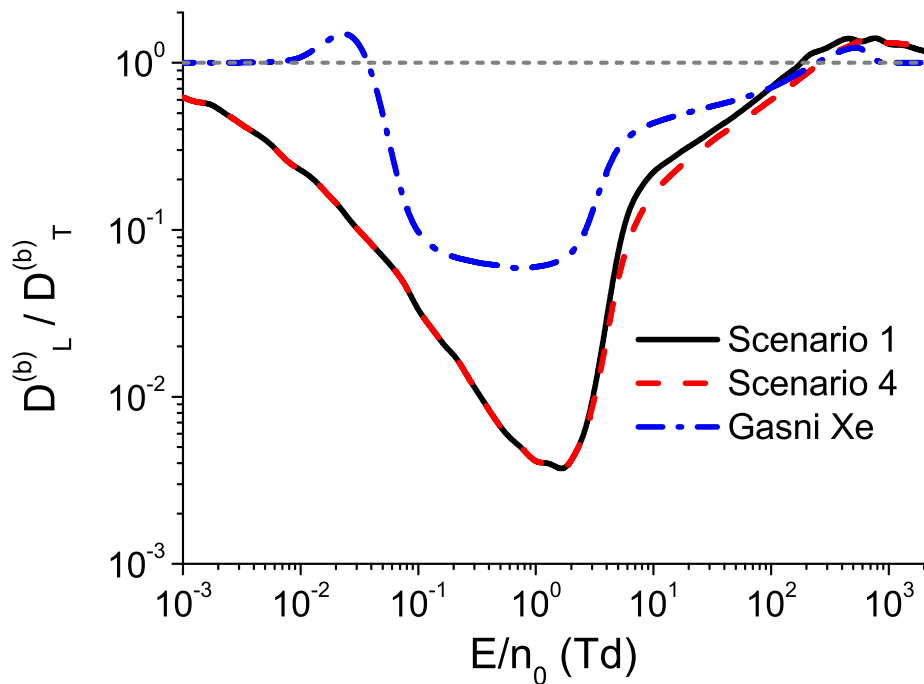
Slika 84: Poređenje vrednosti količnika balk longitudinalne difuzije i balk transverzalne difuzije, koje su određene u prvom i četvrtom slučaju za reprezentovanje neelastičnih sudara u tečnom ksenonu, sa odgovarajućim količnikom u gasnom ksenonu. Ovi slučajevi za reprezentovanje neelastičih sudara su opisani u zaglavlju grafika 77. Rezultati koji su prikazani na ovom grafiku su dobijeni primenom Monte Carlo simulacija.

Na slici 84 su prikazane vrednosti količnika longitudinalne i transverzalne komponente difuzionog tenzora, D_L/D_T, za elektrone u tečnom ksenonu u prvom i četvrtom slučaju za reprezentovanje neelastičnih sudara u tečnosti. Ovaj količnik je kvantitativni pokazatelj anizotropije difuzije. Vrednosti D_L/D_T za elektrone u gasnom ksenonu su prikazane na istom grafiku, radi poređenja. Za elektrone u tečnom ksenonu ovaj količnik opada sa porastom E/n_0 do oko 1

Td, zbog povećanja brzinskog koeficijenta za elastične sudare u ovom opsegu polja. Međutim, ovaj količnik se povećava sa porastom E/n_0, na višim poljima, kao posledica opadanja kolizione frekvence za elastične sudare na višim energijama. Zavisnost D_L/D_T od E/n_0 je drugačija za elektrone u gasnom ksenonu na niskim poljima. Na poljima nižim od 10^{-2} Td je ovaj količnik konstantan, jer je srednja energija elektrona u gasnoj fazi jako blizu termalnih vrednosti. U opsegu polja između 10^{-2} Td i $2 \cdot 10^{-2}$ Td se D_L/D_T za elektrone u gasnom ksenonu povećava sa porastom E/n_0 zbog uticaja Ramsauer-Townsend-ovog minimuma. Na višim poljima je kvalitativni trend zavisnosti D_L/D_T od E/n_0 isti za elektrone u gasnom i tečnom ksenonu, ali je minimum izraženiji u tečnoj fazi. U svakom slučaju, razlike od preko dva reda veličine između D_L i D_T u tečnom ksenonu su jasan pokazatelj veoma jakog efekta anizotropije difuzije. Ovako velike razlike između D_L i D_T do sada nikada nisu zabeležene za elektrone u gasovima.

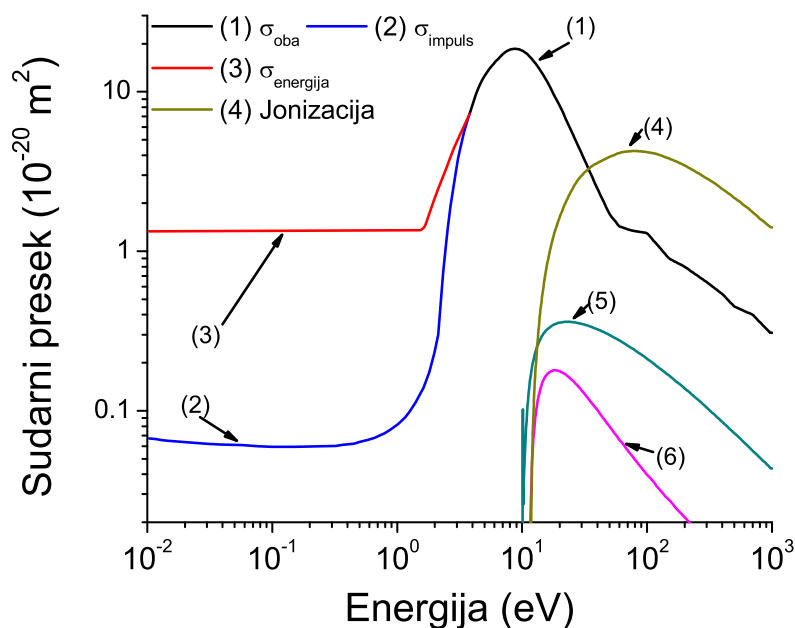## 6.3 Transport elektrona u tečnom argonu i tečnom kriptonu

6.3.1 Korišćeni preseci i uslovi simulacije za elektrone u tečnom argonu i tečnom kriptonu

Za reprezentovanje elastičnih sudara u tečnom argonu se na energijama nižim od oko 10 eV koriste tri efektivna sudarna procesa, kao i u tečnom ksenonu. Pri tome su presek za rasejanje elektrona na fokus atomu u tečnom argonu i γ količnik (videti potpoglavlje 6.2.1) preuzeti iz rada Boyle-a i saradnika [68]. Na energijama višim od oko 10 eV su efektivni procesi, koji su opisani presecima σ_{impuls} i $\sigma_{energija}$ zanemareni, dok je efektivni presek za σ_{oba} proces aproksimiran presekom za transfer impulsa u elastičnim sudarima iz Hayashi-jevog seta preseka [201]. Presek za ekscitaciju elektrona iz valentne zone u provodnu zonu (efektivnu jonizaciju) je aproksimiran presekom za jonizaciju iz Hayashi-jevog seta [201], kome je prag pomeren na 14.3 eV, što odgovara zonskom procepu u tečnom argonu [247].

U našim proračunima transportnih osobina elektrona u tečnom argonu razmatrana su dva slučaja za reprezentovanje neelastičnih sudara. U prvom (Scenario 1) su ekscitacije u potpunosti zanemarene, dok su u drugom slučaju (Scenario 2) uzete u obzir one ekscitacije iz Hayashi-jevog seta preseka čiji su pragovi niži od zonskog procepa u tečnom argonu. Pri tome su zanemarene tri poslednje ekscitacije iz Hayashi-jevog seta, čiji su pragovi 14.3 eV, 14.71 eV i 15.2 eV. U literaturi nisu dostupni podaci vezani za minimume u spektrima fotoprovodnosti tečnog argona, kao ni refleksioni spektri tečnog argona na energijama višim od 14 eV. Zbog toga za tečni argon ne razmatramo dodatne slučajeve za reprezentovanje neelastičnih sudara, u kojima su uzete u obzir ekscitacije čiji su pragovi viši od zonskog procepa. Pored toga smo utvrdili da uključivanje ekscitacije, čiji je prag iznosi 14.3 eV, u set preseka ima zanemarljiv uticaj na transportne osobine elektrona u tečnom argonu. Set preseka za rasejanje elektrona u tečnom argonu, koji je korišćen u našim proračunima, prikazan je na slici 85. Koncentracija pozadinskih atoma i temperatura u tečnom argonu, korišćeni u našim simulacijama, iznose $2.1 \cdot 10^{28}$ m^{-3} i 85 K, respektivno.
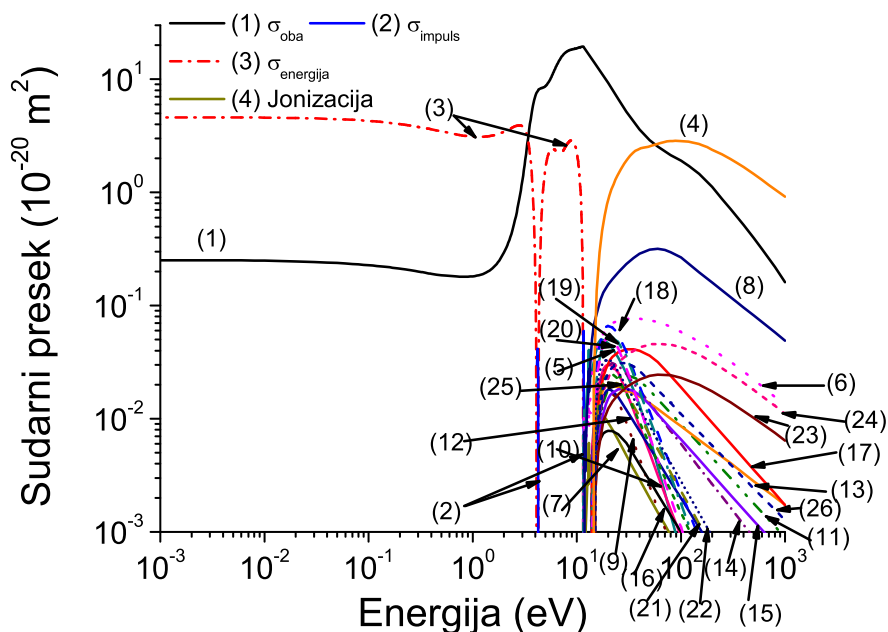
Slika 85: Set preseka za rasejanje elektrona u tečnom argonu: (1) σ_{oba}, (2) σ_{impuls}, (3) $\sigma_{energija}$, (4) jonizacija (zonski prelaz), efektivne elektronske ekscitacije: (5) $4s[3/2]_2$, (6) $4s[3/2]_1$, (7) $4s'[1/2]_0$, (8) $4s'[1/2]_1$, (9) $4p[1/2]_1$, (10) $4p[5/2]_3$, (11) $4p[5/2]_2$, (12) $4p[3/2]_1$, (13) $4p[3/2]_2$, (14) $4p[1/2]_0$ i $4p'[3/2]_1$, (15) $4p'[3/2]_2$, (16) $4p'[1/2]_1$, (17) $4p'[1/2]_0$, (18) $3d[1/2]_0$ i $3d[1/2]_1$, (19) $3d[3/2]_2$, (20) $3d[7/2]_4$, (21) $3d[7/2]_3$, (22) $3d[5/2]_2$ i $5s[3/2]_2$, (23) $3d[5/2]_3$ i $5s[3/2]_1$, (24) $3d[3/2]_1$, (25) $3d'[5/2]_2$ i (26) $3d'[3/2]_2$, $3d'[5/2]_3$, $5s'[1/2]_0$ i $5s'[1/2]_1$.


Slika 86: Set preseka za rasejanje elektrona u tečnom kriptonu: (1) σ_{oba}, (2) σ_{impuls}, (3) $\sigma_{energija}$, (4) jonizacija (zonski prelaz), efektivne elektronske ekscitacije: (5) S nivoi i (6) P nivoi.

Za reprezentovanje elastičnih sudara niskoenergijskih elektrona u tečnom kriptonu se koriste dva efektivna sudarna procesa, koje su koristili Atrazhev i saradnici u svojim proračunima [102]. Ovi efektivni sudarni procesi su ekvivalentni procesima korišćenim u našem radu za reprezentovanje elastičnog rasejanja u tečnom argonu i tečnom ksenonu, a kojima odgovaraju preseci σ_{impuls} i $\sigma_{energija}$. Preseci za ova dva efektivna sudarna procesa su preuzeti iz rada Atrazheva i saradnika [102]. Na energijama višim od oko 4.24 eV, preseci za ova dva efektivna sudarna procesa postaju jednaki nuli, dok njihovu vrednost u poslednjoj nenultoj tački preuzima presek za treći efektivni sudarni proces, u kome se razmenjuju energija i impuls kao u običnom binarnom sudaru. Ovaj efektivni sudarni proces je ekvivalentan efektivnom procesu koji je reprezentovan sa σ_{oba} presekom u našem proračunima u tečnom argonu i tečnom ksenonu. Presek za ovaj efektivni sudarni proces ima nenultu vrednost na energijama višim od 4.24 eV, i u tom enerijskom opsegu je jednak preseku za transfer impulsa u elastičnim sudarima u gasnom kriptonu, koji je preuzet iz Biagi-jeve MAGBOLTZ baze [203]. Presek za ekscitaciju u provodnu zonu (efektivnu jonizaciju) je dobijen pomeranjem Biagi-jevog preseka za jonizaciju ka nižim energijama, pri čemu je prag spušten na 11.7 eV, što odgovara vrednosti zonskog procepa u tečnom kriptonu [247]. U tečnom kriptonu se razmatraju dva slučaja za reprezentovanje neelastičnih sudra, isto kao i u tečnom argonu. U prvom slučaju su ekscitacije u potpunosti zanemarene (Scenario 1), dok su u drugom slučaju uzete u obzir sve ekscitacije iz Biagi-jevog seta preseka čiji su pragovi niži od zonskog procepa u tečnom kriptonu (Scenario 2). U tečnom kriptonu ne razmatramo dodatne slučajeve za reprezentovanje energijskih gubitaka u neelastičnim sudarima iz sličnog razloga kao u slučaju tečnog argona. Koncentracija pozadinskih atoma i temperatura u tečnom kriptonu koji su korišćeni u našim simulacijama iznose $1.76 \cdot 10^{28}$ m^{-3} i 117 K, respektivno.

6.3.2 Rezultati vezani za transport elektrona u tečnom argonu i tečnom kriptonu

Na slici 87 su date vrednosti srednje energije za elektrone u tečnom i gasnom argonu u funkciji E/n_0. Odnos vrednosti srednje energije u gasnom i tečnom argonu se razlikuje od odgovarajućeg odnosa u ksenonu. Naime, u opsegu polja između oko 10^{-3} Td i 0.035 Td je srednja energija elektrona viša u gasnom nego u tečnom argonu. Ovo je posledica toga što je efektivni presek za transfer energije u tečnom argonu veći od preseka za elastično rasejanje u gasnom argonu u energijskom intervalu između $7 \cdot 10^{-3}$ eV i 10 eV. Međutim, u opsegu polja između 0.035 Td i 1.3 Td srednja energija elektrona u tečnom argonu je viša od srednje energije u gasnom argonu. Srednja energija elektrtona ima vrednosti između oko 0.5 eV i 2.7 eV u ovom opsegu polja. U ovom energijskom intervalu se presek za elastično rasejanje u gasnoj fazi naglo povećava sa porastom energije i približava se efektivnom preseku za transfer energije u tečnom argonu, dok je efektivni presek za transfer energije praktično konstantan do oko 2 eV. Uz to je u ovom energijskom intervalu presek za elastično rasejanje u gasnom argonu veći od efektivnog preseka za transfer impulsa u tečnom argonu, što omogućava efikasnije ubrzavanje elektrona od strane električnog polja u tečnoj nego u gasnoj fazi. Srednja energija u gasnom argonu je viša nego u tečnom argonu u opsegu polja između 1.3 Td i 7.7 Td, gde je u intervalu između 2.7 eV i 5.2 eV, pa se visokoenergijski elektroni nalaze u energijskom intervalu u kome su efektivni preseci za transfer energije i impulsa u tečnom argonu veći od preseka za elastično rasejanje u

gasnom argonu (između oko 4 eV i 10 eV). Na poljima višim od 7.7 Td srednja energija je u prvom slučaju za reprezentovanje neelastičnih sudara u tečnom argonu viša od srednje energije u gasnom argonu, zbog odsustva energijskih gubitaka u ekscitacijama u ovom slučaju. Srednja energija je pak u drugom slučaju za reprezentovanje neelastičnih sudara u tečnom argonu niža od srednje energije u gasnom argonu do oko 1000 Td. Ovo se može pripisati intenzivnijem hlađenju jonizacijom u tečnoj fazi, zbog nižeg praga za jonizaciju u tečnom argonu, u odnosu na gasni argon. Vrednosti srednje energije u tečnom i gasnom argonu su međusobno jako bliske na poljima višim od 10 Td, zbog male razlike u dinamici rasejanja visokoenergijskih elektrona u tečnom i gasnom argonu.
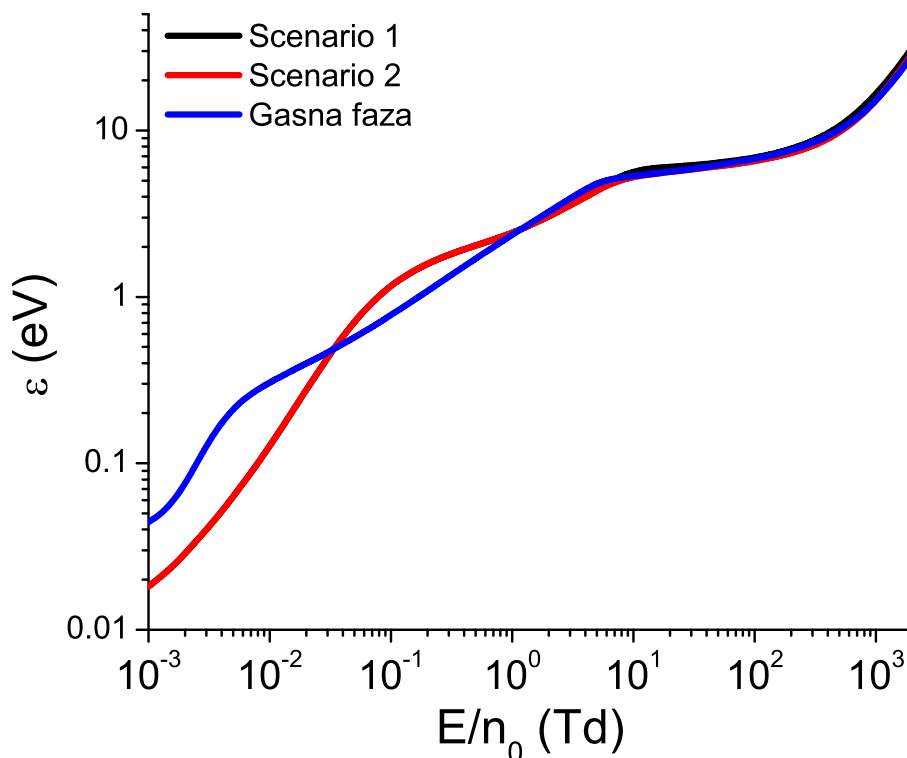
Slika 87: Poređenje vrednosti srednje energije za rojeve elektrona u gasnom i tečnom argonu. Vrednosti srednje energije u tečnom argonu su određene u dva različita slučaja za reprezentovanje neelastičnih sudara. U prvom slučaju (Scenario 1) sve ekscitacije su zanemarene, dok su u drugom slučaju (Scenario 2) uzete u obzir one ekscitacije iz Hayashi-jevog seta preseka za elektrone u gasnom argonu čiji prag je ispod 14.3 eV [201]. Rezultati su dobijeni primenom Monte Carlo simulacija.

Slika 88 prikazuje vrednosti srednje energije za elektrone u tečnom i gasnom kriptonu u funkciji E/n_0. Na niskim poljima su trendovi zavisnosti srednje energije od E/n_0 u gasnoj i tečnoj fazi, kao i međusobni odnos njihove vrednosti jako slični u kriptonu i ksenonu. Srednja energija je na najnižim poljima viša u tečnoj nego u gasnoj fazi. Pritom se srednja energija u tečnoj fazi prvo linearno povećava sa porastom E/n_0 (do oko 0.0059 Td i 0.01 Td za elektrone u kriptonu i ksenonu, respketivno), nakon čega je srednja energija konkavna funkcija redukovanog električnog polja (do oko 0.077 Td i 0.1 Td za elektrone u kriptonu i ksenonu, respketivno), posle čega se srednja energija približno linearno povećava sa porastom E/n_0, ali sa znatno manjim
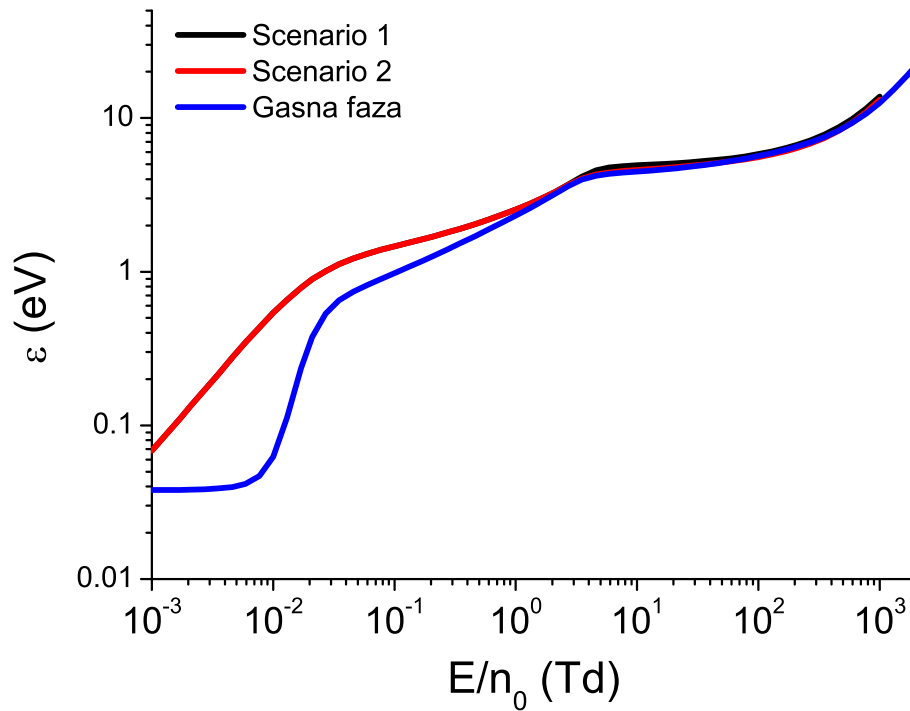
Slika 88: Poređenje vrednosti srednje energije za rojeve elektrona u gasnom i tečnom kriptonu. Vrednosti srednje energije u tečnom argonu su određene u dva različita slučaja za reprezentovanje neelastičnih sudara. U prvom slučaju (Scenario 1) sve ekscitacije su zanemarene, dok su u drugom slučaju (Scenario 2) uzete u obzir one ekscitacije iz Biagi-jevog seta preseka za elektrone u gasnom kriptonu čiji prag je ispod 11.7 eV. Rezultati su dobijeni primenom Monte Carlo simulacija.

nagibom nego na najnižim poljima. Srednja energija u gasnoj fazi se prvo sporo povećava sa porastom E/n_0 (do oko 0.0059 Td u oba gasa), nakon čega se naglo povećava sa porastom E/n_0 otprilike do kraja opsega polja u kome je energija u tečnoj fazi konkavna funkcija redukovanog električnog polja, posle čega se linearno povećava sa porastom E/n_0. Uz to je u oba slučaja srednja energija viša u tečnoj nego u gasnoj fazi na niskim poljima (do 3.5 Td i 0.46 Td za elektrone u kriptonu i ksenonu, respektivno). Sličnost u trendovima zavisnosti srednje energije u kriptonu i ksenonu od E/n_0 u obe faze, na niskim poljima, je posledica toga što je odnos preseka za elastične sudare u gasnoj fazi i efektivnih preseka za transfer energije i impulsa u tečnoj fazi jako sličan u kriptonu i ksenonu, na niskim energijama. Međuitim, srednja energija u gasnoj fazi je viša od srednje energije u tečnoj fazi za elektrone u tečnom ksenonu, u svim slučajevima za reprezentovanje neelastičnih sudara, u opsegu polja između oko 0.46 Td i 350 Td, dok je u kriptonu srednja energija u gasnoj fazi niža od srednje energije u tečnoj fazi u oba slučaja za reprezentovanje neelastičnih sudara od početka razmatranog opsega (10^{-3} Td) do oko 59 Td. Ova razlika je posledica razlike u korišćenim presecima u kriptonu i ksenonu. Zapravo, u presecima koji su korišćeni za proračune u ksenonu efektivni preseci za transfer imulsa i transfer energije veći su od preseka za elastično rasejanje u gasnoj fazi na energijama između 2.5 eV i 5 eV. Nasuprot tome, u presecima koji su korišćeni u kriptonu efektivni presek za transfer impulsa u tečnoj fazi nikada nije veći od preseka za elastično rasejanje u gasnoj fazi, dok je efektivni presek za transfer energije u tečnoj fazi veći od preseka za elastično rasejanje

u gasnoj fazi samo u uskoj okolini Ramsauer-Townsend-ovog minimum – pri višim energijama ovi su preseci jednaki. Na poljima višim od 59 Td je srednja energija u gasnom kriptonu niža od srednje energije u tečnom kriptonu u prvom slučaju za reprezentovanje neelastičnih sudara, zbog odsustva energijskih gubitaka u ekscitacijama u ovom slučaju. U ovom opsegu polja je razlika između vrednosti srednje energije u gasnom kriptonu i tečnom kriptonu, u drugom slučaju za reprezentovanje neelastičnih sudara, jako mala, zbog toga što je dinamika rasejanja visokoenergijskih elektrona veoma slična u gasnoj fazi i atomskim tečnostima.
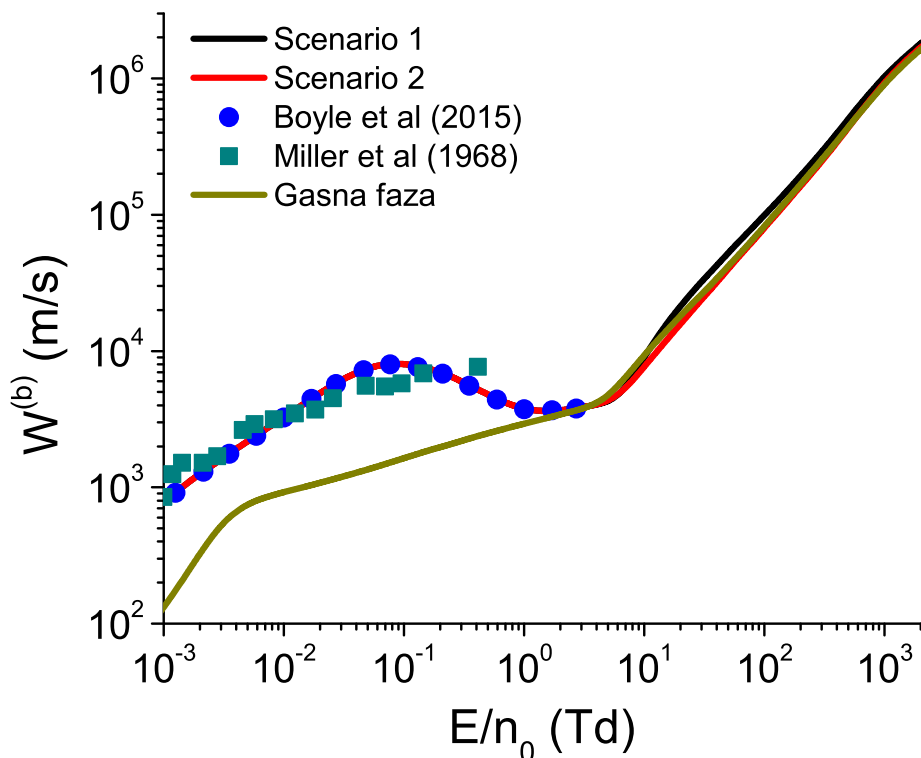
Slika 89: Poređenje eksperimentalno određene brzine drifta za roj elektrona u tečnom argonu (Miller *et al.* [229]) sa teorijskim proračunima. Među teorijskim rezultatima su prikazani proračuni Boyle-a i saradnika [69], kao i vrednosti balk brzine drifta koje su određene u okviru ovog rada na osnovu Monte Carlo simulacija, primenom dva različita metoda za reprezentovanje neelastičnih sudara. Ovi metodi su navedeni u zaglavlju grafika 87. Na grafiku je prikazana i balk brzina drifta za roj elektrona u gasnom argonu, radi poređenja.

Na slici 89 su predstavljeni profili balk brzine drifta u tečnom argonu u prvom i drugom slučaju za reprezentovanje neelastičnih sudara u tečnoj fazi, zajedno sa profilom balk brzine drifta u gasnom argonu. Eksperimentalne [229] i teorijske [68] vrednosti brzine drifta u tečnom argonu, koje su odredili raniji autori, prikazane su na istom grafiku radi poređenja. Sa slike se vidi da je u argonu na najnižim poljima brzina drifta znatno veća u tečnoj nego u gasnoj fazi. Ipak, razlika u brzini drifta elektrona u tečnoj i gasnoj fazi je na najnižim poljima manja u argonu nego u ksenonu, jer je efektivni presek za transfer impulsa u tečnom argonu oko dvadeset puta manji od preseka za elastično rasejanje u gasnom argonu, dok razlika između ova dva preseka u ksenonu iznosi oko tri reda veličine. Strukturno indukovana negativna diferencijalna provodnost se javlja u profilu brzine drifta za elektrone u tečnom argonu, kao i u tečnom ksenonu. Ovaj se

efekat pak javlja samo u uskom opsegu polja između 0.77 Td i 2.7 Td, u kom je srednja energija elektrona u tečnom argonu između 2.26 eV i 3.40 eV. Ovaj energijski interval se nalazi unutar raspona između 2 eV i 5 eV, gde se efektivni presek za transfer impulsa u tečnom argonu naglo povećava sa porastom energije. Ovo znači da se u tečnom argonu strukturno indukovana negativna diferencijalna provodnost javlja u opsegu polja u kome se vrednosti srednje energije nalaze unutar energijskog intervala u kome se efektivni presek za transfer impulsa naglo povećava sa porastom energije. U tečnom ksenonu se efektivni presek za transfer impulsa povećava od 0.4 eV do oko 3.5 eV, pri čemu je srednja energija elektrona viša od 0.4 eV na poljima višim od 10^{-2} Td zbog manje vrednosti efektivnog preseka za transfer energije u tečnom ksenonu u odnosu na argon. Iz svega sledi da se strukturno indukovana negativna diferencijalna provodnost u tečnom ksenonu javlja na znatno nižim poljima i pokriva znatno širi opseg polja u odnosu na tečni argon. Drift brzina za elektrone u tečnom argonu, koja je određena u našim proračunima se odlično slaže sa brzinom drifta koja je izračunata u radu Boyle-a i saradnika [68].
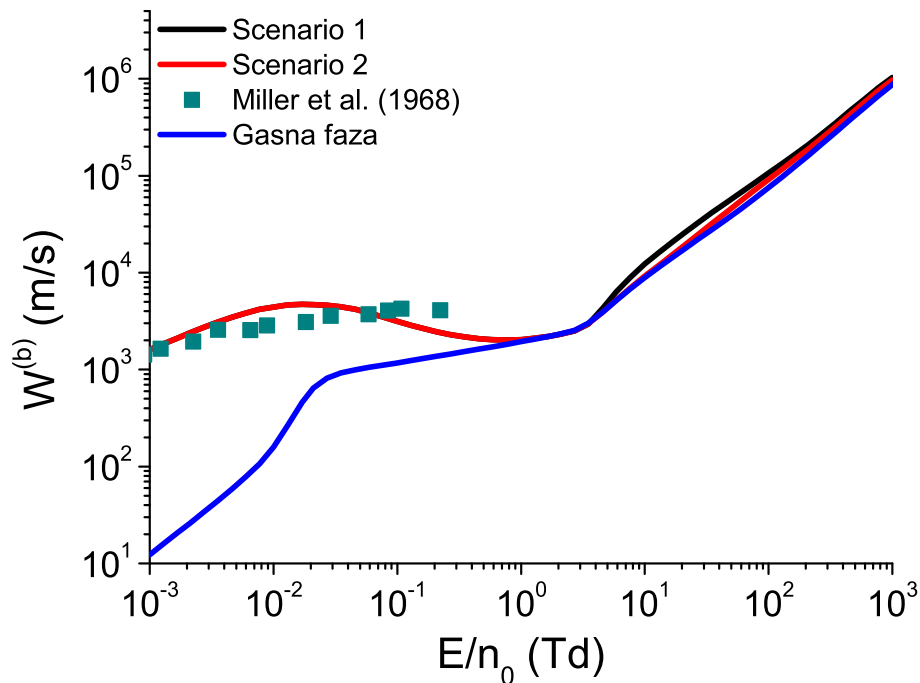
Slika 90: Poređenje eksperimentalno određene brzine drifta za roj elektrona u tečnom kriptonu (Miller *et al.* [229]) sa teorijskim proračunim vrednostima balk brzine drifta, koje su određene u okviru ovog rada primenom Monte Carlo simulacija, u dva različita slučaja reprezentovanja neelastičnih sudara. U prvom slučaju (Scenario 1) su sve ekscitacije zanemarene. U drugom slučaju su uzete u obzir one ekscitacije iz Biagi-jevog seta preseka čiji prag je ispod 11.7 eV. Na ovom grafiku je, radi poređenja, data i balk brzina drifta za roj elektrona u gasnom kriptonu.

Na slici 90 su prikazani profili balk brzine drifta u tečnom kriptonu u prvom i drugom slučaju za reprezentovanje neelastičnih sudara u tečnoj fazi, zajedno sa profilom balk brzine drifta u gasnom kriptonu. Eksperimentalne vrednosti Miller-a i saradnika [229] prikazane su na istom grafiku, radi poređenja. Sa slike se može videti da je u kriptonu na najnižim poljima brzina drifta oko 130 puta veća u tečnoj nego u gasnoj fazi. Ova razlika je znatno intenzivnija od odgovarajuće razlike u argonu, ali je nešto manja od razlike između vrednosti brzine drifta

u tečnom i gasnom ksenonu, što je posledica efektivnog preseka za transfer impulsa u tečnom kriptonu koji je za preko dva reda veličine manji od preseka za elastične sudare u gasnom kriptonu, dok razlika između ovih preseka u ksenonu iznosi oko tri reda veličine. Strukturno indukovana negativna diferencijalna provodnost se u tečnom kriptonu javlja u opsegu polja od 0.017 Td do 1Td. U datom rasponu polja srednja energija elektrona u tečnom kriptonu je između 0.786 eV i 2.32 eV, što odgovara energijskom intervalu u kome se efektivni presek za transfer impulsa u tečnom kriptonu naglo povećava sa porastom energije. Ovaj se presek najintenzivnije povećava sa porastom energije u energijskom intervalu između 1 eV i 3eV. Opseg polja u kome se javlja strukturno indukovana negativna diferencijalna provodnost u tečnom kriptonu je sličan odgovarajućem opsegu polja u tečnom ksenonu zbog toga što se efektivni presek za transfer impulsa naglo povećava sa porastom energije u skoro istom energijskom intervalu u ovim dvema tečnostima i zbog bliskih vrednosti efektivnog preseka za transfer energije (oko 2^2) u njima.

Naše vrednosti brzine drifta u tečnom argonu i tečnom kriptonu su bliske eksperimentalnim vrednostima Millera i saradnika [229], ali u njihovim profilma brzine drifta nije prisutna negativna diferencijalna provodnost. Razlozi za ovo neslaganje između teorijskih i eksperimentalnih rezultata u tečnom argonu i tečnom kriptonu su verovatno isti kao i razlog za odgovarajuće neslaganje u tečnom ksenonu.
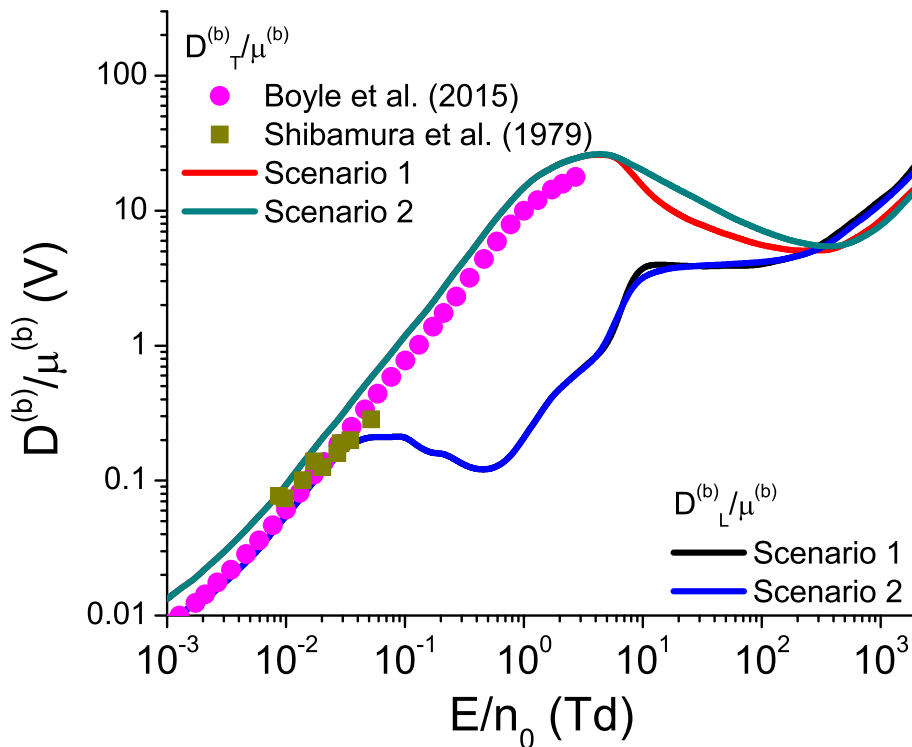
Slika 91: Poređenje vrednosti balk longitudinalne karakteristične energije D_L/μ i balk transverzalne karakteristične energije D_T/μ, koje su određene u ovom radu, sa teorijskim rezultatima Boyle-a i saradnika [68] za roj elektrona u tečnom argonu. Naši rezultati su dobijeni na osnovu Monte Carlo simulacija primenom prvog i drugog scenarija za reprezentovanje neelastičnih sudara.

Slika 91 prikazuje balk vrednosti longitudinalne i transverzalne karakteristične energije D_L/μ
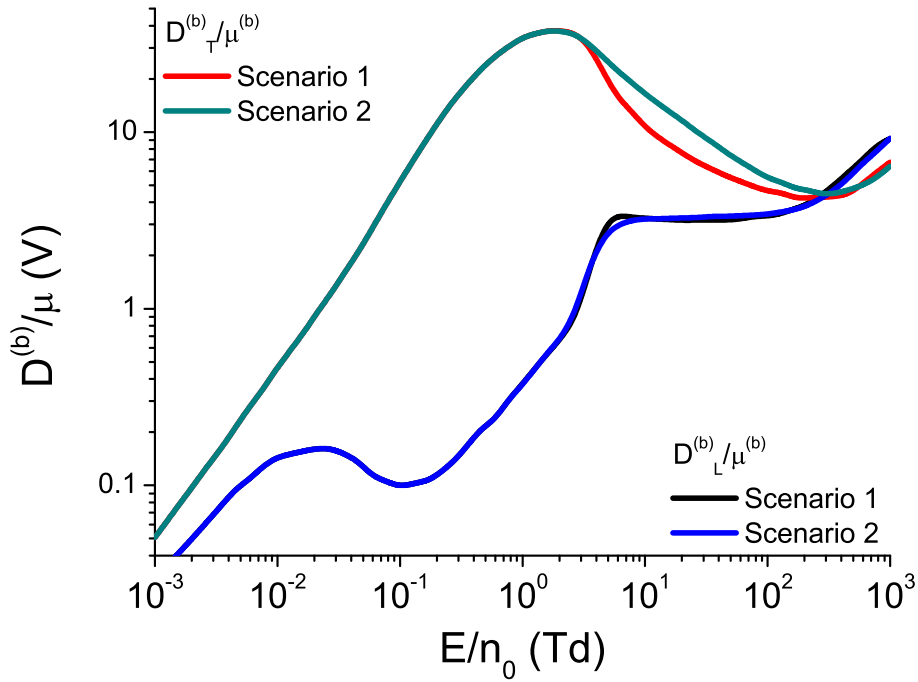
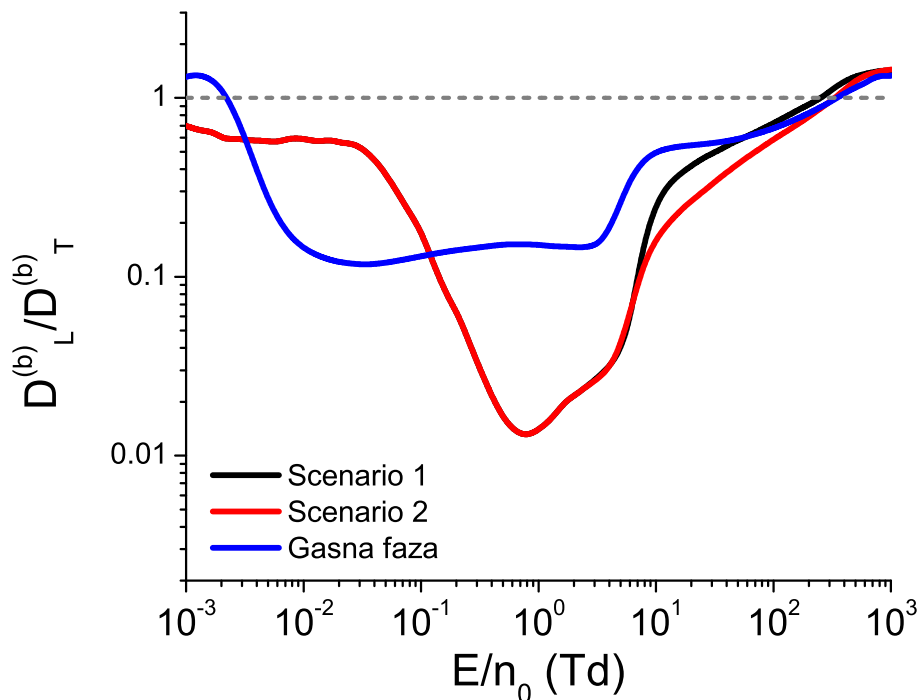Slika 92: Poređenje vrednosti balk longitudinalne karakteristične energije D_L/μ i balk transverzalne karakteristične energije D_T/μ za roj elektrona u tečnom kriptonu. Ovi rezultati su dobijeni na osnovu Monte Carlo simulacija primenom prvog i drugog scenarija za reprezentovanje neelastičnih sudara.

i D_T/μ za elektrone u tečnom argonu zajedno sa vrednostima koje su odredili prethodni autori [68], dok su na slici 92 prikazane balk vrednosti D_L/μ i D_T/μ za elektrone u tečnom kriptonu u fukciji E/n_0. Dok je u ksenonu D_L/μ približno konstantno između 10^{-2} Td i 1Td u argonu i kriptonu je ponašanje ove veličine složenije. Longitudinalna karakteristična energija ima lokalni maksimum na 0.059 Td i 0.021 Td u tečnom argonu i tečnom kriptonu, respektivno, te lokalni minimum na 0.46 Td i 0.1 Td u tečnom argonu i tečnom kriptonu, respektivno. Ove dodatne strukture su u okviru statističke nesigurnosti Monte Carlo simulacija. U tečnom argonu longitudinalna karakteristična energija dostiže plato u opsegu polja od 10 Td do 77 Td, dok u tečnom kriptonu i tečnom ksenonu ova veličina dostiže plato u opsegu polja od 5.9 Td do 77 Td. Može se uočiti da je u tečnom argonu i tečnom kriptonu srednja energija oko 5 eV na polju na kome počinje plato longitudinalne karakteristične energije, a plato ove veličine počinje na polju na kome je srednja energija oko 3 eV u tečnom ksenonu. Ove su vrednosti energije između 2 i 3 puta manje od praga za prvu elektronsku ekscitaciju, pa na poljima na kojima počinje plato longitudinalne karakteristične energije najenergičniji elektroni mogu učestvovati u neelastičnim sudarima u sve tri tečnosti. Između strukture na niskim poljima i platoa na visokim poljima se D_L/μ naglo povećava sa porastom E/n_0 u tečnom argonu, tečnom kriptonu i tečnom ksenonu. Na visokim poljima (nakon završetka platoa) se D_L/μ monotono povećava sa porastom E/n_0 u sve tri tečnosti.

Transverzalna karakteristična energija D_T/μ ima sličan trend ponašanja u sve tri tečnosti. Na niskim poljima se D_T/μ monotono povećava sa porastom E/n_0 i dostiže lokalni maksimum na oko 4.6 Td, 2.1 Td i 2.7 Td u tečnom argonu, tečnom kriptonu i tečnom ksenonu, respektivno.

Na višim poljima D_T/μ monotono opada sa porastom E/n_0 do lokalnog minimuma koji se nalazi na oko 350 Td u tečnom ksenonu i kriptonu i na oko 460 Td u tečnom argonu. Nakon lokalnog minimuma se D_T/μ monotono povećava sa porastom E/n_0 do kraja razmatranog opsega polja.

Slika 93: Poređenje vrednosti količnika balk longitudinalne difuzije i balk transverzalne difuzije, koje su određene u prvom i drugom slučaju za reprezentovanje neelastičnih sudara u tečnom argonu, sa odgovarajućim količnikom u gasnom argonu. Ovi slučajevi za reprezentovanje neelastičih sudara su opisani u zaglavlju grafika 87. Rezultati koji su prikazani na ovom grafiku su dobijeni na osnovu Monte Carlo simulacija.

Na slikama 93 i 94 su prikazane vrednosti D_L/D_T u funkciji E/n_0 za elektrone u tečnom argonu i tečnom kriptonu, respektivno, u prvom i drugom slučaju za reprezentovanje neelastičnih sudara u ovim tečnostima. Vrednosti D_L/D_T za elektrone u gasnoj fazi su takođe prikazane na ovim graficima, zarad poređenja. U tečnom kriptonu i tečnom ksenonu D_L/D_T opada sa porastom E/n_0 od početka razmatranog opsega polja (koji se nalazi na 10^{-3} Td), dok je ova veličina u tečnom argonu približno konstantna do oko 0.027 Td, posle čega počinje da opada sa porastom E/n_0. Ovo se može pripisati tome što srednja energija u tečnom argonu ima niže vrednosti od srednje energije u tečnom ksenonu i tečnom kriptonu na najnižim poljima (na 10^{-3} Td srednja energija iznosi oko 0.018 eV, 0.068 eV i 0.077 eV za elektrone u tečnom argonu, tečnom kriptonu i tečnom ksenonu, respektivno), uz šta se efektivni preseci za transfer energije i impulsa u tečnom argonu počinju povećavati sa porastom energije tek na energijama višim od 1 eV, dok u tečnom ksenonu i tečnom kriptonu efektivni presek za transfer impulsa počinje da raste na nižim energijama (na oko 0.6 eV). U tečnom argonu i tečnom ksenonu D_L/D_T dostiže minimum na oko 1 Td, a u tečnom kriptonu doseže minimum na oko 0.46 Td. Minimalna vrednost D_L/D_T iznosi oko 10^{-2} u tečnom argonu i tečnom kriptonu, dok u tečnom ksenonu
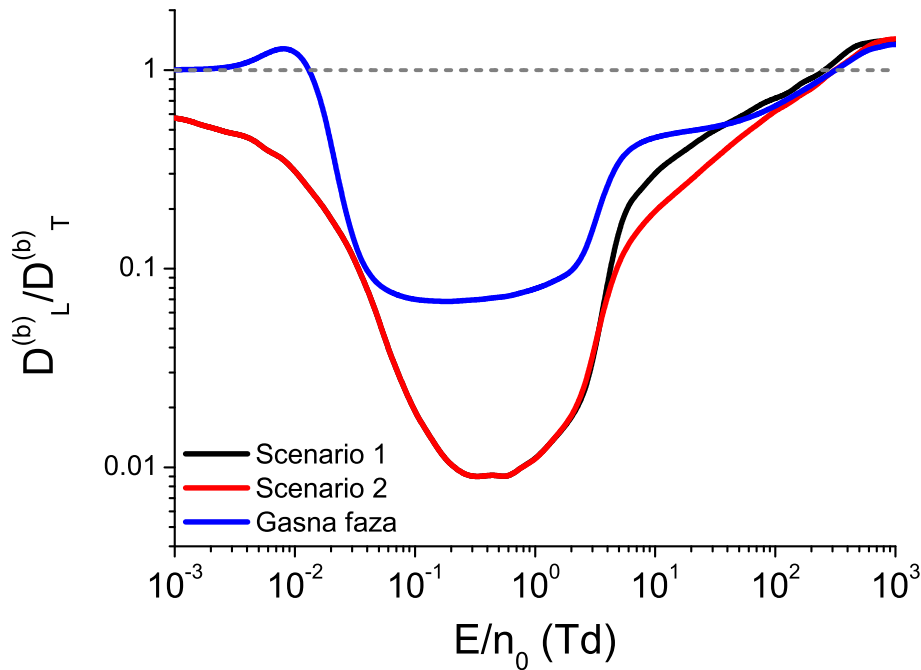
Slika 94: Poređenje vrednosti količnika balk longitudinalne difuzije i balk transverzalne difuzije, koje su određene u prvom i drugom slučaju za reprezentovanje neelastičnih sudara u tečnom kriptonu, sa odgovarajućim količnikom u gasnom kriptonu. Ovi slučajevi za reprezentovanje neelastičih sudara su opisani u zaglavlju grafika 88. Rezultati koji su prikazani na ovom grafiku su dobijeni na uz pomoć Monte Carlo simulacija.

minimum ove veličine ima vrednost približnu $4 \cdot 10^{-3}$.

Količnik D_L/D_T ima sličan trend ponašanja, na kvalitativnom nivou, u gasnom argonu, gasnom kriptonu i gasnom ksenonu, ali ovaj količnik dostiže prvi lokalni maksimum na nižem polju u gasnom argonu nego u gasnom kriptonu i gasnom ksenonu. Razlog za ovakvo ponašanje količnika D_L/D_T treba potražiti u činjenici da se Ramsauer–Townsend-ov minimum javlja na nižim energijama u gasnom argonu nego u preostala dva gasa.

Slika 95 prikazuje vrednosti prvog Townsend-ovog koeficijenta u prvom i drugom slučaju za reprezentovanje neelastičnih sudara u tečnom argonu, dok su odgovarajuće vrednosti prvog Townsend-ovog koeficijenta u tečnom kriptonu pokazane na slici 96. Vrednosti prvog Townsend-ovog koeficijenta u gasnoj fazi, koje su skalirane na gustinu tečnosti, takođe su predstavljene na ovim graficima, zarad poređenja. Razlika između koeficijenta za jonizaciju, dobijenog na osnovu scenarija u koji su uključene sve ekscitacije, i koeficijenta za jonizaciju iz gasne faze, koji je skaliran na gustinu tečnosti je veća u ksenonu nego u argonu i kriptonu zbog veće razlike između praga za ekscitaciju u provodnu zonu u tečnoj fazi i praga za jonizaciju u gasnoj fazi. Međutim, razlika između koeficijenta za jonizaciju dobijenog primenom scenarija u kome su uzete u obzir one ekscitacije čiji je prag niži od praga za zonski prelaz u tečnoj fazi i scenarija u kome su sve ekscitacije zanemarene najmanja je u tečnom ksenonu, zbog toga što su u tečnom ksenonu pragovi samo prve dve ekscitacije niži od praga za efektivnu jonizaciju, dok je presek za jonizaciju znatno veći od preseka za pojedinačne ekscitacije.

168
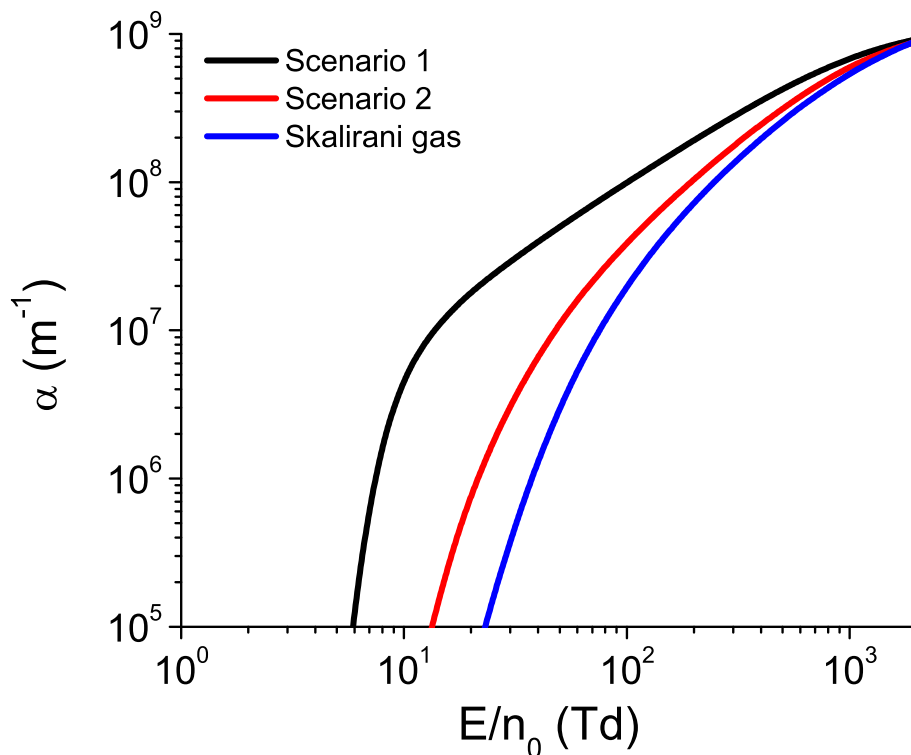
Slika 95: Zavisnost prvog Townsend-ovog koeficijenta od redukovanog električnog polja E/n_0 za roj elektrona u tečnom argonu. Ove vrednosti su određene primenom dva različita scenarija za reprezentovanje neelastičnih sudara. Metodi su opisani u zaglavlju grafika 87. Na grafiku je, radi poređenja, prikazan i prvi Townsend-ov koeficijent za roj elektrona u gasnom argonu, koji je skaliran na gustinu tečnog argona. Rezultati su dobijeni primenom Monte Carlo simulacija.

6.4   Zaključak

U ovom poglavlju je razmatran transport elektrona u tečnom argonu, tečnom kriptonu i tečnom ksenonu. Potpoglavlje 6.1.1 govori o motivaciji za izučavanje transporta naelektrisanih čestica u tečnoj fazi. Sa teorijske tačke gledišta je značajno razumeti dinamiku naelektrisanih čestica u gustim sredinama sa kratkodometnim uređenjem. Sa praktičnog aspekta su transport naelektrisanih čestica u tečnoj fazi i električna pražnjenja u tečnostima od velikog značaja za mnoge važne primene poput detektora čestica sa tečnim argonom ili tečnim ksenonom, transformatorskih ulja, kao i za upotrebu plazme u medicini, poljoprivredi i tehnikama za pročišćavanje vode.

U odeljku 6.1.2 su izloženi argumenti za postojanje provodne zone u tečnom argonu, tečnom kriptonu i tečnom ksenonu, koji se mogu naći u literaturi. Naime, promena mobilnosti elektrona pri topljenju argona, kriptona i ksenona u čvrstoj fazi može se pripisati promeni kompresibil-nosti i gustine pri ovom faznom prelazu. Pored toga, u refleksionim spektrima tečnog argona, tečnog kriptona i tečnog ksenona uočene su ekscitonske linije koje su vrlo slične odgovarajućim linijama u čvrstoj fazi. Uz to je vrednost praga za fotoprovodnost u tečnom ksenonu vrlo bliska odgovarajućoj vrednosti u čvrstom ksenonu. Vrednost zonskog procepa u tečnom ksenonu koja je određena na osnovu Wannier-ovog niza odlično se slaže sa vrednošću zonskog procepa koja
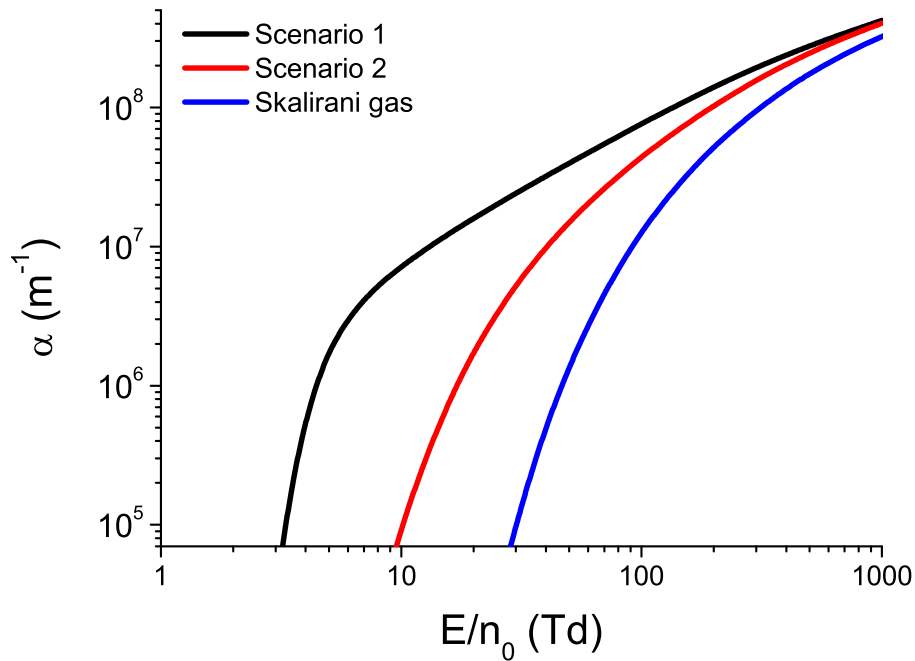
Slika 96: Zavisnost prvog Townsend-ovog koeficijenta od redukovanog električnog polja E/n_0 za roj elektrona u tečnom kriptonu. Ove vrednosti su određene primenom dva različita scenarija za reprezentovanje neelastičnih sudara. Metodi su opisani u zaglavlju grafika 88, gde je, poređenja radi, prikazan i prvi Townsend-ov koeficijent za roj elektrona u gasnom kriptonu, koji je skaliran na gustinu tečnog kriptona. Rezultati su dobijeni na osnovu Monte Carlo simulacija.

je određena na osnovu praga za fotoprovodnost. Šupljinska provodnost u tečnom ksenonu je jasno identifikovana u eksperimentima.

U potpoglavlju 6.2.1 su prikazani uslovi simulacije i korišćeni setovi preseka za rasejanje elektrona u tečnom ksenonu, dok su odgovarajući uslovi simulacije i setovi preseka u slučaju tečnog argona i tečnog kriptona izloženi u potpoglavlju 6.3.1. Koherentno rasejanje je reprezentovano primenom tri efektivna sudarna procesa koji dobro reprezentuju srednji transfer impulsa i energije pri elastičnim sudarima u ovim tečnostima. Presek za zonski prelaz u tečnoj fazi je aproksimiran presekom za jonizaciju izolovanog atoma, kome je prag snižen na vrednost zonskog procepa u odgovarajućoj tečnosti. U slučaju tečnog ksenona su razmatrana četiri različita scenarija za reprezentovanje neelastičnih sudara. Ovi scenariji su zasnovani na eksperimentalnim podacima vezanim za refleksione spektre i fotoprovodnost tečnog ksenona. U slučaju tečnog argona i tečnog kriptona su uzeta u obzir samo dva scenarija. Pri tome su u prvom od ova dva scenarija neelastični sudari u potpunosti zanemareni, dok su u drugom scenariju uzeti u obzir samo oni procesi čiji je prag niži od zonskog procepa u odgovarajućoj tečnosti.

Potpoglavlje 6.2.2 sumira rezultate transportnih proračuna za rojeve elektrona u tečnom ksenonu. Odgovarajući rezultati za rojeve elektrona u tečnom argonu i tečnom kriptonu su prikazani u potpoglavlju 6.3.2. U ovim odeljcima su upoređeni profili zavisnosti srednje energije i drift brzine od redukovanog električnog polja u tečnoj fazi sa odgovarajućim profilima u gasnoj fazi. Pri tome je analiziran uticaj koherentnog rasejanja u tečnoj fazi na vrednosti ovih transportnih veličina u oblasti niskih polja. Poseban akcenat je stavljen na izučavanje strukturno

indukovane negativne diferencijalne provodnosti u tečnom ksenonu na osnovu prostorno razlo-
ženih karakteristika roja i funkcija raspodele elektrona po energijama. Pored toga je razmatrano
u kojoj meri različit tretman neelastičnih sudara utiče na izračunate vrednosti transportnih ve-
ličina u tečnoj fazi. Uočeno je da izračunata vrednost prvog Townsend-ovog koeficijenta snažno
zavisi od načina na koji su tretirani neelastični sudari u tečnostima. Takođe je uočeno da je
prvi Townsend-ov koeficijent iz gasne faze, koji je skaliran na gustinu tečnosti, znatno niži od
odgovarajućeg koeficijenta u tečnoj fazi. Vrednosti prvog Townsend-ovog koeficijenta u tečnom
ksenonu, koje su izračunate u okviru ove disertacije, upoređene su sa eksperimentalnim rezul-
tatima Derentzo-a i saradnika, kao i sa rezultatima proračuna ranijih autora. Uočeno je da se
prve dve eksperimentalne tačke Derentzo-a i saradnika najbolje slažu sa scenarijom u kome su
neelastični sudari u potpunosti zanemareni, dok se preostale eksperimentalne tačke bolje slažu
sa ostala tri scenarija.

7 Negativni strimeri u atomskim tečnostima visoke mobilnosti

7.1 Uvod

Na ovom mestu su proučavani strimeri u tečnom argonu, tečnom kriptonu i tečnom ksenonu. U potpoglavlju 7.2 su predstavljeni fluidni model prvog reda i fluidni model koji je baziran na razvoju izvornog člana po gradijentima koncentracije elektrona, kao i numerička implementacija ovih modela, koja se koristi u našim proračunima. Odeljak 7.3 donosi rezultate naših proračuna za negativne strimere u tečnom ksenonu, dok su u potpoglavlju 7.4 prikazani naši rezultati za negativne strimere u tečnom argonu i tečnom kriptonu.

7.2 Fluidni modeli strimera

Jedan od najčešće korišćenih metodoloških pristupa u modelovanju strimerskih pražnjenja jeste fluidni model prvog reda, ili tzv. klasični fluidni model. Ovaj model je baziran na drift-difuzionoj aproksimaciji za elektrone i jednačinama za balans broja čestica za naelektrisane čestice niže mobilnosti, čije se kretanje može zanemariti na vremenskim skalama na kojima se odvija dinamika elektrona (pozitivni joni i negativni joni u gasnoj fazi i pozitivne šupljine u kondenzovanoj materiji) [27, 30, 139]. Pri tome su ove jednačine primenom aproksimacije lokalnog električnog polja spregnute sa Poisson-ovom jednačinom, ne bi li se opisao uticaj prostornog naelektrisanja [27, 30]. Drift-difuziona jednačina se može izvesti iz Boltzmann-ove jednačine [27, 30], čime se dobija jednačina oblika

$$\frac{\partial n(\mathbf{r}, t)}{\partial t} + \nabla \cdot \left(n(\mathbf{r}, t) \mathbf{W}^{(f)} - \mathbf{D}^{(f)} \cdot \nabla n(\mathbf{r}, t) \right) = C_1, \tag{7.1}$$

gde je $n(\mathbf{r}, t)$ koncentracija elektrona, t je vremenska koordinata, $\mathbf{W}^{(f)}$ i $\mathbf{D}^{(f)}$ su fluks brzina drifta i fluks difuzioni tenzor, respektivno, dok je C_1 izvorni član, čiji je oblik potrebno odrediti.

Prostorno naelektrisanje u tečnom argonu, tečnom kriptonu i tečnom ksenonu je određeno kvazislobodnim elektronima iz provodne zone i pozitivnim šupljinama iz valentne zone. Uz to se broj kvazislobodnih elektrona i pozitivnih šupljina povećava pri ekscitaciji elektrona iz valentne zone u provodnu zonu, dok se broj ovih naelektrisanih čestica smanjuje pri njihovoj rekombinaciji. Na osnovu toga je najjednostavniji oblik izvornog člana u našem slučaju

$$C_1 = n(\mathbf{r}, t) \big(\nu_i(\mathbf{E}) - k_r(\mathbf{E}) n_p(\mathbf{r}, t) \big), \tag{7.2}$$

gde su $n_p(\mathbf{r}, t)$, $\nu_i(\mathbf{E})$, $k_r(\mathbf{E})$ i $\mathbf{E}$ koncentracija pozitivnih šupljina, brzinski koeficijenat za jonizaciju (ekscitaciju elektrona iz valentne zone u provodnu zonu), koeficijent rekombinacije i rezultujuće električno polje, respektivno. Primenom ovog oblika izvornog člana dobija se jednačina

$$\frac{\partial n}{\partial t} + \nabla \cdot \left(n \mathbf{W}^{(f)} - \mathbf{D}^{(f)} \cdot \nabla n \right) = n(\nu_i - k_r n_p). \tag{7.3}$$

Ovo je drift-difuziona jednačina u kojoj figurišu fluks transportni koeficijenti. Drugi način da se izvede drift-difuziona jednačina je da se primeni hidrodinamički razvoj fluksa čestica i izvornog člana u jednačini kontinuiteta [27]. Ako se pri hidrodinamičkom razvoju izvornog člana zanemare svi članovi u kojima figurišu gradijenti koncentracije elektrona, dobije se jednačina (7.3). Na osnovu toga je fluidni model prvog reda sa fluks transportnim koeficijentima dat jednačinama

$$\frac{\partial n}{\partial t} = \nabla \cdot \left(\mathbf{D}^{(f)} \cdot \nabla n \right) - \nabla \cdot \left(n \mathbf{W}^{(f)} \right) + n(\nu_i - k_r n_p), \tag{7.4}$$

$$\frac{\partial n_p}{\partial t} = n\nu_i - k_r n n_p, \tag{7.5}$$

koje su spregnute sa Poisson-ovom jednačinom. Uz to je pretpostavljeno da su vrednosti transportnih koeficijenata $\mathbf{W}^{(f)}$ i $\mathbf{D}^{(f)}$, brzinskog koeficijenta za jonizaciju ν_i i koeficijenta rekombinacije k_r u položaju $\mathbf{r}$ i trenutku t određene lokalnom vrednošću rezultujućeg električnog polja u datom trenutku $\mathbf{E}(\mathbf{r}, t)$ (aproksimacija lokalnog polja). Kretanje pozitivnih šupljina se može zanemariti u našim proračunima zbog toga što je njihova mobilnost znatno niža od mobilnosti elektrona [234, 235].

Poisson-ova jednačina se može napisati u obliku

$$\Delta\phi(\mathbf{r}, t) = \frac{e}{\epsilon_0} \Big(n(\mathbf{r}, t) - n_p(\mathbf{r}, t) \Big), \tag{7.6}$$

gde je ϕ električni potencijal prostornog naelektrisanja, dok je Δ Laplasijan. Rezultujuće električno polje $\mathbf{E}$ je superpozicija spošalješnjeg električnog polja $\mathbf{E_0}$ i električnog polja koje potiče od prostornog naelektrisanja i može se napisati u obliku

$$\mathbf{E}(\mathbf{r}, t) = \mathbf{E_0} - \nabla\phi(\mathbf{r}, t), \tag{7.7}$$

gde je ∇ nabla operator.

Fluidni model prvog reda sa fluks transportnim podacima se često koristi u literaturi [27, 248–250]. Međutim, oblik izvornog člana koji je korišćen pri izvođenju jednačine (7.3) u sebi ne sadrži informaciju o prostornim gradijentima brzinskih koeficijenata za nekonzervativne sudarne procese, pri datoj vrednosti lokalnog rezultujućeg električnog polja [27]. Ovi prostorni gradijenti su posledica prostornog gradijenta srednje energije elektrona i energijske zavisnosti preseka za nekonzervativne procese. Prostorni gradijenti brzinskih koeficijenata za nekonzervativne sudarne procese se mogu reprezentovati hidrodinamičkim razvojem izvornog člana $S(\mathbf{r}, t)$ u jednačini kontinuiteta (2.18) [27]. Pri tome se hidrodinamički razvoj primenjuje samo na deo izvornog člana koji se odnosi na jonizaciju, zbog toga što deo koji opisuje rekombinaciju zavisi i od koncentracije pozitivnih jona. U hidrodinamičkim uslovima izvorni član se može napisati u obliku

$$S(\mathbf{r}, t) = S_i^0 n_e(\mathbf{r}, t) - \mathbf{S}_i^{(1)} \cdot \nabla n_e(\mathbf{r}, t) + \mathbf{S_i^2} : \nabla\nabla n_e(\mathbf{r}, t) - k_r n_p(\mathbf{r}, t) n(\mathbf{r}, t), \tag{7.8}$$

gde su

$$S_i^{(0)} = \langle \nu_i \rangle, \tag{7.9}$$

$$\mathbf{S_i^{(1)}} = \langle \nu_i \mathbf{r}^* \rangle, \tag{7.10}$$

$$\mathbf{S_i^{(2)}} = \frac{1}{2} \langle \nu_i (\mathbf{r^* r^*} - \langle \mathbf{r^* r^*} \rangle) \rangle, \tag{7.11}$$

pri čemu je

$$\mathbf{r}^* = \mathbf{r} - \langle \mathbf{r} \rangle. \tag{7.12}$$

Primenom hidrodinamičkog razvoja izvornog člana u drift difuzionoj jednačini dobija se jednačina oblika [27]:

$$\frac{\partial n(\mathbf{r},t)}{\partial t} + \nabla \cdot \left(n(\mathbf{r},t)\mathbf{W^{(f)}} - \mathbf{D^{(f)}} \cdot \nabla n(\mathbf{r},t) \right) = S^{(0)} n(\mathbf{r},t)$$
$$-\mathbf{S^{(1)}} \cdot \nabla n(\mathbf{r},t) + \mathbf{S^{(2)}} : \nabla \nabla n(\mathbf{r},t) - k_r n_p(\mathbf{r},t) n(\mathbf{r},t). \tag{7.13}$$

Ova jednačina se može napisati u obliku [27]

$$\frac{\partial n(\mathbf{r},t)}{\partial t} + \nabla \cdot \left(n(\mathbf{r},t)\mathbf{W^{(B)}} - \mathbf{D^{(B)}} \cdot \nabla n(\mathbf{r},t) \right) = S^{(0)} n(\mathbf{r},t)$$
$$+(\nabla \cdot \mathbf{S^{(1)}}) n(\mathbf{r},t) - (\nabla \cdot \mathbf{S^{(2)}}) \cdot \nabla n(\mathbf{r},t) - k_r n_p(\mathbf{r},t) n(\mathbf{r},t). \tag{7.14}$$

Fluidni model u kome se koristi ovaj oblik drift-difuzione jednačine, umesto jednačine (7.3), nazvaćemo korigovani fluidni model, po ugledu na Bošnjakovića i saradnike [27]. Jednačina (7.14) se pojednostavljuje kada važi

$$\left(\nabla \cdot \mathbf{S^{(1)}} \right) n(\mathbf{r},t) - \left(\nabla \cdot \mathbf{S^{(2)}} \right) \cdot \nabla n(\mathbf{r},t) \approx 0. \tag{7.15}$$

Ovaj uslov je uvek zadovoljen u slučaju prostorno homogenog električnog polja (na primer u lavinskoj fazi razvoja strimera), ali ima i širu oblast važenja [27].

Kada je zadovoljen uslov (7.15), jednačina (7.14) se svodi na

$$\frac{\partial n(\mathbf{r},t)}{\partial t} + \nabla \cdot \left(n(\mathbf{r},t)\mathbf{W^{(B)}} - \mathbf{D^{(B)}} \cdot \nabla n(\mathbf{r},t) \right) = n(\mathbf{r},t)(\nu_i - k_r n_p). \tag{7.16}$$

Može se videti da jednačina (7.16) ima isti matematički oblik kao jednačina (7.3), samo što umesto fluks transportnih koeficijenata figurišu balk transportni koeficijenti. Međutim, treba imati u vidu da je za razliku od fluidnog modela prvog reda, u kome se koriste fluks transportni koeficijenti, fluidni model sa balk transportnim koeficijentima dobra aproksimacija korigovanog fluidnog modela i u prisustvu nekonzervativnih sudara, ako je zadovoljen uslov (7.15).

U našim proračunima su korišćeni fluidni model prvog reda sa fluks i balk transportnim koeficijentima i korigovani fluidni model. Ovi proračuni su urađeni u okviru jednoipodimenzionog (1.5D) fluidnog modela [27, 30, 251]. U 1.5D modelu se elektroni i elektronske šupljine nalaze unutar cilindra radijusa R_0, čija osa je postavljena duž pravca spoljašnjeg električnog polja $\mathbf{E_0} = E_0 \mathbf{e_z}$, gde je $\mathbf{e_z}$ jedinični vektor duž z-ose. Pri tome vrednosti koncentracije elektrona i elektronskih šupljina ne zavise od radijalne koordinate i azimutalnog ugla, već zavise samo od aksijalne koordinate z. Fluidne jednačine u 1.5D fluidnom modelu prvog reda imaju oblik [27]

$$\frac{\partial n(z,t)}{\partial t} = \frac{\partial}{\partial z} \left(n(z,t) W \text{sgn}(E) + D_L \frac{\partial n(z,t)}{\partial z} \right) + \left(\nu_i - k_r n_p(z,t) \right) n(z,t), \tag{7.17}$$

174

$$\frac{\partial n_p(z,t)}{\partial t} = n(z,t)\Big(\nu_i - k_r n_p(z,t)\Big), \tag{7.18}$$

gde je $\mathrm{Sgn}(E)$ signum funkcija rezultujućeg električnog polja. Brzina drifta W se ovde definiše kao pozitivna veličina. Rezultujuće električno polje je u ovom modelu dato jednačinom

$$E(z,t) = E_0 + \frac{e}{2\epsilon_0} \int_0^l \Big(n_p(z',t) - n(z',t)\Big) \tag{7.19}$$

$$\cdot \left(\mathrm{sgn}(z-z') - \frac{z-z'}{\sqrt{(z-z')^2 + R_0^2}} \mathrm{d}z' \right), \tag{7.20}$$

gde su l, e i ϵ_0 međuelektrodno rastojanje, naelektrisanje elektrona i dielektrična propustljivost vakuuma, respektivno.

Jednačine (7.17), (7.18) i (7.20) se rešavaju numerički uz granične uslove

$$n(z=0,t) = 0, n(z=l,t) = 0, \tag{7.21}$$

i početne uslove

$$n(z,0) = \frac{300}{0.05\pi R_0^2 \frac{l}{3}\sqrt{2\pi}}\exp\left(-\frac{(z-0.95l)^2}{2(0.05\frac{l}{3})^2}\right), \tag{7.22}$$

$$n_p(z,t=0) = n(z,t=0). \tag{7.23}$$

U korišćenoj numeričkoj šemi, prostorni izvodi su diskretizovani primenom centralne konačne razlike drugog reda, a za integraciju u vremenu korišćen je Runge-Kutta 4 metod četvrtog reda [27, 30]. Pri određivanju veličine vremenskog koraka u ovoj numeričkoj šemi, neophodno je da budu zadovoljena dva uslova stabilnosti

$$\Delta t < C_a \delta x / W, \tag{7.24}$$

$$\Delta t < C_d (\delta x)^2 / D_L, \tag{7.25}$$

gde je δx korak prostorne rešetke [27, 30]. Pri tome je C_a maksimalni Courant-ov broj za advektivne jednačine, dok je C_d maksimalni Courant-ov broj za difuzione jednačine. Vremenski korak koji je korišćen u našim proračunima je dovoljno mali da budu zadovoljena oba uslova.

Korigovani fluidni 1.5D model se razlikuje od jednoipodimenzionog modela prvog reda po tome što se umesto jednačine (7.17) koristi jednačina

$$\frac{\partial n(z,t)}{\partial t} = \frac{\partial}{\partial z}\left(n(z,t)W^{(f)}\mathrm{sgn}(E) + D_L^{(f)}\frac{\partial n(z,t)}{\partial z}\right) + \Big(\nu_i - k_r n_p(z,t)\Big)n(z,t)$$

$$-S_z^{(1)}\frac{\partial n(z,t)}{\partial z} + S_{zz}^{(2)}\frac{\partial^2 n(z,t)}{\partial z \partial z}, \tag{7.26}$$

pri čemu su koeficijenti razvoja izvornog člana koji opisuju jonizaciju dati sa:

$$S_z^{(1)} = \langle \nu_i z^* \rangle, \tag{7.27}$$

$$S_z^{(2)} = \frac{1}{2}\langle \nu_i \big(z^* z^* - \langle z^* z^* \rangle\big)\rangle, \tag{7.28}$$

gde je $z^* = z - \langle z \rangle$, uz šta su ostale jednačine iste kao u fluidnom modelu prvog reda [27,30]. Pošto je u svim našim proračunima korišćena aproksimacija lokalnog polja, uzima se da su

transportni koeficijenti, brzinski koeficijent za jonizaciju i koeficijent za rekombinaciju funkcije trenutne vrednosti intenziteta lokalnog rezultujućeg električnog polja $|E(z,t)|$ [27, 30].

Koeficijenat za rekombinaciju kvazislobodnih elektrona i pozitivnih šupljina je u našem radu određen primenom skalirane Debye-ove formule kao

$$k_r = \xi k_{rD} = \xi \frac{4\pi e\mu}{\epsilon_0 \epsilon_r}, \tag{7.29}$$

gde je k_{rD} Debyeov koeficijent za rekombinaciju, μ je mobilnost elektrona, ϵ_r je relativna dielektrična propustljivost sredine, a ξ je faktor skaliranja, koji u našim proračunima iznosi 0.1 [119–121]. Ova formula je dobra aproksimacija koeficijenta za rekominaciju na redukovanim električnim poljima višim od 1 Td [119–121]. Vrednosti redukovanog električnog polja koje su niže od 1 Td se ne pojavljuju u našim fluidnim simulacijama ni na frontu strimera ni u strimerskom kanalu. Važno je naglasiti da je u ovim proračunima neophodno uzeti u obzir rekombinaciju kvazislobodnih elektrona i pozitivnih šupljina, zbog velikog uticaja ovog procesa na dinamiku strimera u tečnoj fazi. U slučaju strimera u tečnosti koncentracija naelektrisanih čestica je na strimerskom frontu, kao i u strimerskom kanalu, za nekoliko redova veličine viša od odgovajuće koncentracije u slučaju strimera u gasovima. Zbog toga rekombinacija kvazislobodnih elektrona i pozitivnih šupljina ima ključan uticaj na kinetiku naelektrisanih čestica u tečnoj fazi. Ovo se može uočiti i na osnovu oblika strimerskih profila, koji su izučavani u ovom poglavlju i koji jako podsećaju na odgovarajuće profile u elektronegativnim gasovima. Ako se u potpunosti zanemari rekombinacija elektrona i šupljina u korišćenim fluidnim proračunima, to dovodi do nefizičkog efekta intenzivnog nagomilavanja naelektrisanih čestica oba polariteta na početku domena. Ovaj efekat na kraju izaziva numeričke nestabilnosti i pucanje simulacije.

U našim simulacijama l i R_0 imaju vrednosti $5 \cdot 10^{-5}$m i 10^{-5}m, respektivno. Vrednost R_0 je procenjena uz uzimanje u obzir širine početne raspodele naelektrisanja i širenja usled transverzalne difuzije u toku trajanja simulacija. Ova vrednost se dobro slaže sa vrednoću R_0 koju su odredili drugi autori [120, 121]. Međuelektrodno rastojanje l je određeno iz uslova da brzina strimera dostigne stacionarnu vrednost. U našim fluidnim simulacijama u tečnom ksenonu prostor je podeljen na 25000 ćelija, dok je u simulacijama u tečnom argonu i tečnom kriptonu prostor podeljen na 12500 ćelija. Utvrđeno je pritom da smanjene broja ćelija sa 25000 na 12500 ne dovodi do primetne razlike u rezultatima naših simulacija.

7.3   Negativni strimeri u tečnom ksenonu

Na slikama 97 i 98 je prikazana tranzicija elektronske lavine u negativan strimer za elektrone u tečnom ksenonu pri vrednosti redukovanog spoljašneg električnog polja od 59 Td i 100 Td, respektivno. Rezultati koji su prikazani na ovim slikama su dobijeni primenom balk transportnih podataka koji su izračunati u prvom i četvrtom slučaju za reprezentovanje neelastičnih sudara u tečnom ksenonu, kao i primenom balk transportnih podataka iz gasnog ksenona koji su skalirani na gustinu tečnog ksenona. Svi rezultati prikazani na slikama 97 i 98 su dobijeni
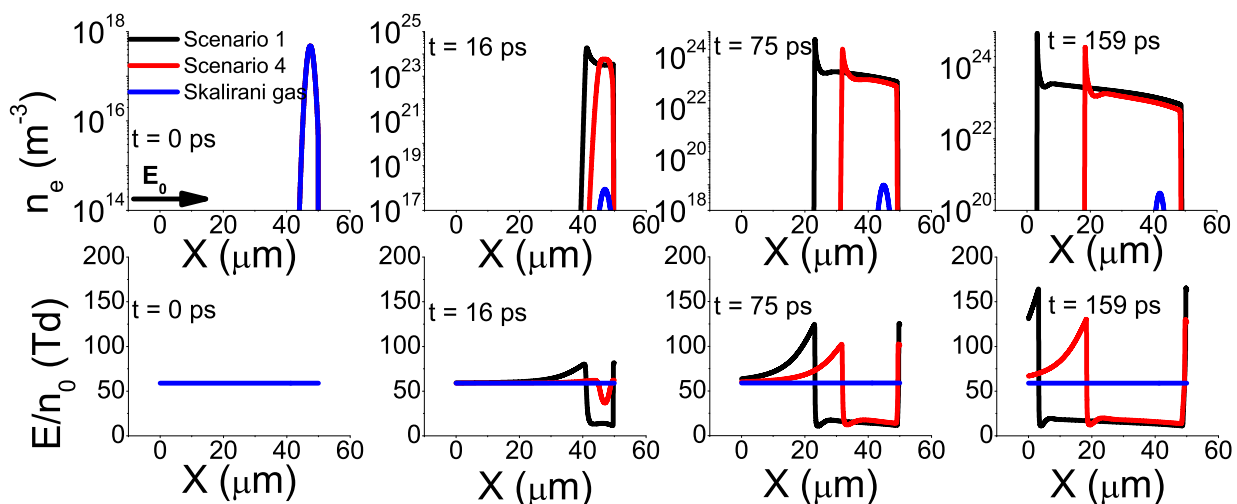
Slika 97: Formiranje i propagacija negativnog strimera u tečnom ksenonu za $E_0/n_0 = 59$ Td. Ovi rezultati su dobijeni primenom prvog i četvrtog scenarija za reprezentovanje neelastičnih energijskih gubitaka. Na ovom grafiku su, radi usporedbe, prikazani i rezultati strimerskih simulacija u kojima su korišćeni transportni podaci iz gasnog ksenona, skalirani na gustinu tečnog ksenona. Ovde n_e označava koncentraciju elektrona, dok E/n_0 označava redukovano rezultujuće električno polje. Na grafiku je takođe prikazan i smer spoljašnjeg električnog polja. Rezultati su dobijeni na osnovu numeričkih proračuna u okviru fluidnih modela strimera.
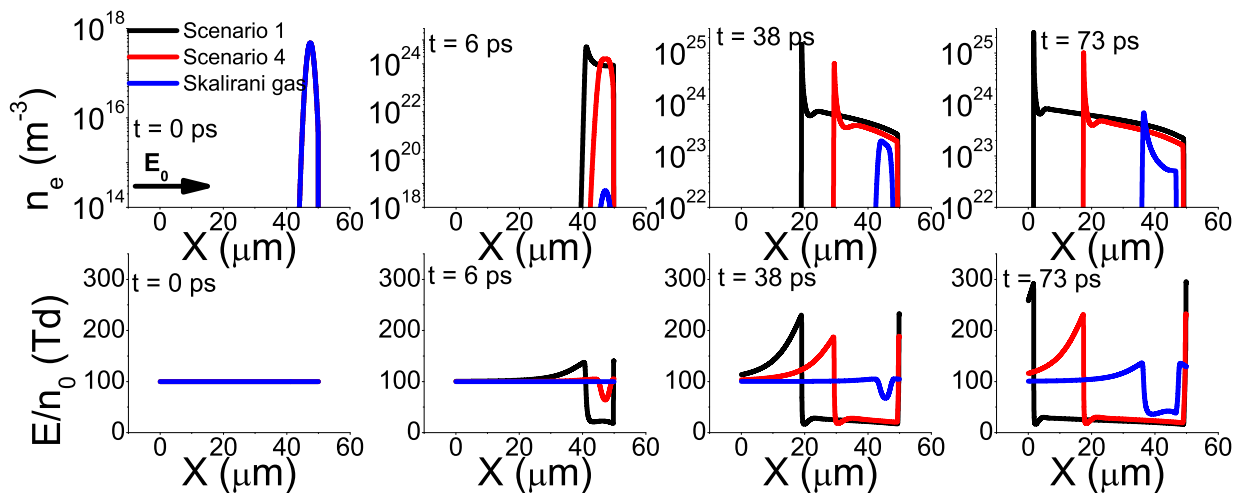
Slika 98: Formiranje i propagacija negativnog strimera u tečnom ksenonu za $E_0/n_0 = 100$ Td. Rezultati su dobijeni uz pomoć numeričkih proračuna u okviru fluidnih modela strimera.

primenom fludinog modela prvog reda. Sa slika se vidi da su na kvalitativnom nivou prostorni profili strimera i rezultujućeg električnog polja u tečnom ksenonu vrlo slični odgovarajućim prostornim profilima u gasnoj fazi. Koncentracija elektrona ima oštar maksimum na frontu strimera, gde je rezultujuće električno polje znatno pojačano u odnosu na spoljašnje polje, zbog efekata prostornog naelektrisanja. Međutim, koncentracija elektrona i rezultujuće električno polje su znatno smanjeni u strimerskom kanalu gde je pod uticajem prostornog naelektrisanja spoljašnje električno polje značajno zaklonjeno. U strimerskom kanalu koncentracija elektrona opada sa povećanjem rastojanja od glave strimera, zbog rekombinacije elektrona sa pozitivnim

šupljinama [119–121]. Sličan trend opadanja koncentracije elektrona u strimerskom kanalu je primećen u profilima negativnih strimera u elektronegativnim gasovima [120,121]. Iako su prostorni profili koncentracije elektrona i rezultujućeg električnog polja vrlo slični za strimere u tečnom ksenonu i strimere u gasovima, prostorne i vremenske skale formiranja strimera su za oko tri reda veličine manje u tečnom ksenonu, nego u gasnoj fazi, zbog toga što je koncentracija pozadinskih atoma za oko tri reda veličine veća u tečnosti nego u gasu.

Sa slika 97 i 98 se vidi da su brzine formiranja i propagacije strimera, koje su određene primenom transportnih podataka izračunatih u prvom i četvrtom slučaju za reprezentovanje neelastičnih sudara u tečnom ksenonu, znatno veće od odgovarajućih brzina koje su određene na osnovu transportnih podataka iz gasnog ksenona, skaliranih na gustinu tečnog ksenona. Uz to su i vrednosti koncentracije elektrona u glavi strimera i u strimerskom kanalu znatno veće u slučaju tečnog ksenona od slučaja skaliranog gasa. Ove razlike su znatno intenzivnije na niskim nego na visokim poljima. Zapravo, na 59 Td je raspodela elektrona koja odgovara skaliranom gasu još uvek u lavinskoj fazi u trenutku u kome strimer u tečnom ksenonu, koji je dobijen u prvom slučaju za reprezentovanje neelastičnih sudara, pređe celo rastojanje l. Sa druge strane, na 100 Td je strimer u skaliranom gasu skoro potpuno formiran u trenutku u kome strimer modelovan u prvom slučaju stigne do granice sistema. Čak su i na 100 Td vrednosti brzine strimera i koncentracije elektrona u glavi strimera i u strimerskom kanalu znatno manje u skaliranom gasu nego u tečnom ksenonu. Značajne razlike između naših rezultata koji odgovaraju tečnom ksenonu i skaliranom gasu jesu posledica odgovarajućih razlika u brzinskim koeficijentima za jonizaciju. Slično tome, vrednosti brzine formiranja i propagacije strimera, kao i vrednosti koncentracije elektrona u glavi strimera i u strimerskom kanalu, smanjuju se sa porastom broja ekscitacija koje su uključene u set preseka, zbog opadanja brzinskog koeficijenta za jonizaciju sa povećanjem broja ekscitacija koje su uključene u model.

Slika 99 prikazuje prostorne profile strimera i rezultujućih električnih polja u sva četiri slučaja za reprezentovanje neelastičnih sudara u tečnom ksenonu za vrednosti redukovanog spoljašnjeg električnog polja od 35 Td, 59 Td i 100 Td, respektivno u trenutku $t = 73$ ps. Ovaj vremenski trenutak je izabran budući da tada najbrži strimer stigne do granice sistema. Generalni trendovi zavisnosti strimerskog profila od koordinate su isti u sva četiri slučaja za reprezentovanje neelastičnih sudara i za sve četiri vrednosti redukovanog spoljašnjeg električnog polja. Međutim, sa ovog grafika se vidi da se vrednosti brzine strimera, kao i vrednosti koncentracije elektrona u glavi strimera i u strimerskom kanalu, povećavaju sa porastom redukovanog spoljašnjeg električnog polja E_0/n_0. Takođe se vidi da ove vrednosti opadaju sa povećanjem broja ekscitacija koje su uključene u model.

Na slici 100 se daju vrednosti brzine strimera u sva četri slučaja za reprezentovanje neelastičnih sudara u tečnom ksenonu, u funkciji E_0/n_0. Radi usporedbe su na istom grafiku prikazane i vrednosti brzine strimera u skaliranom gasnom ksenonu i vrednosti balk brzine drifta u prvom slučaju. Ovi rezultati su dobijeni primenom klasičnog fluidnog modela u kome su korišćeni balk transportni podaci. Sa grafika se vidi da je brzina strimera u svakom od razmatranih slučajeva za reprezentovanje neelastičnih sudara u tečnosti znatno veća od balk brzine drifta. Ovo je
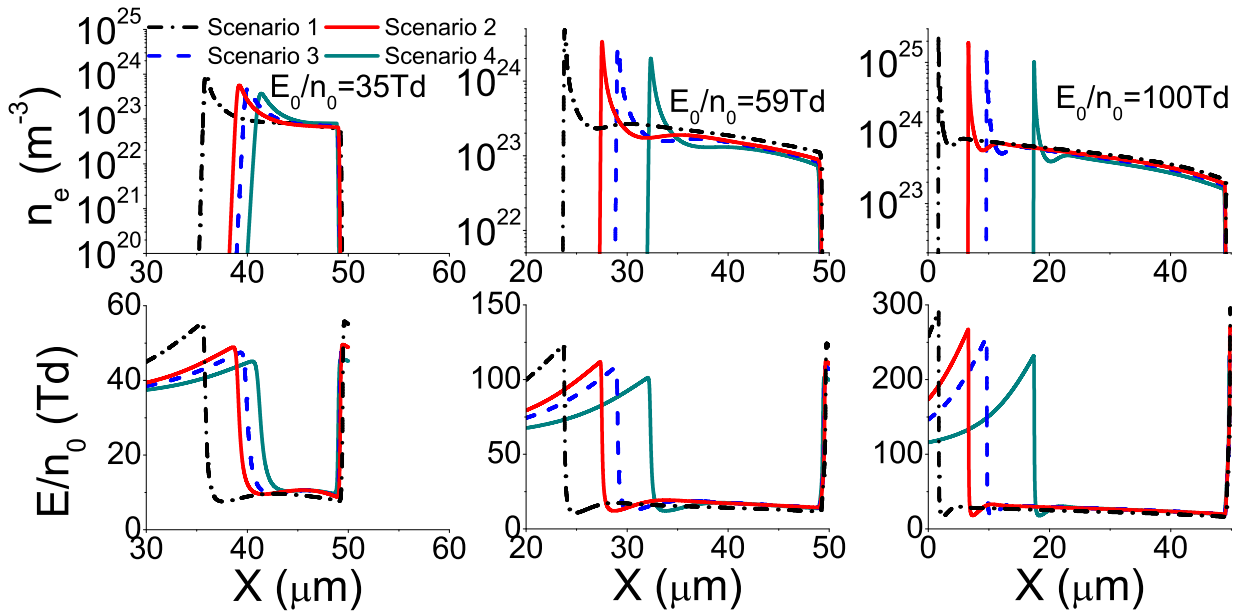
Slika 99: Prostorni profili koncentracije elektrona n_e i redukovanog električnog polja E/n_0 za tri različite vrednosti spoljašnjeg električnog polja E_0. Prikazani profili su određeni primenom četiri različita scenarija za reprezentovanje neelastičnih sudara u tečnom ksenonu. Svi profili su prikazani u trenutku $t = 73$ ps. Rezultati su dobijeni na osnovu numeričkih proračuna u okviru fluidnih modela strimera.

očekivano zbog toga što je brzina strimera određena kombinacijom balk brzine drifta elektrona i jonizacije u glavi strimera, u kojoj je rezultujuće električno polje znatno veće od spoljašnjeg električnog polja, kao i snažnim difuzionim fluksom na frontu strimera. Takođe se može videti da brzina strimera naglo opada sa povećanjem broja ekscitacija koje su uključene u model. Na primer, na redukovanom električnom polju od 100 Td brzina strimera je u četvrtom slučaju za oko 40% manja od brzine strimera u prvom slučaju za reprezentovanje neelastičnih sudara. Pored toga je na 100 Td brzina strimera u skaliranom gasu oko 2.5 puta manja od brzine strimera u prvom slučaju za reprezentovanje neelastičnih sudara, dok je ova razlika još intenzivnija na nižim poljima. Razlike u vrednostima brzine strimera u svim razmatranim slučajevima su posledica razlika između odgovarajućih brzinskih koeficijenata za jonizaciju u ovim slučajevima.

Na slici 101 su prikazani prostorni profili koncentracije elektrona i rezultujućeg električnog polja, koji su određeni u četvrtom slučaju za reprezentovanje neelastičnih sudara u tečnom ksenonu, pri redukovanom spoljašnjem električnom polju od 100 Td. Rezultati koji su prikazani na ovom grafiku su dobijeni primenom fluidnog modela prvog reda sa fluks i balk transportnim podacima, kao i primenom korigovanog fluidnog modela. Uočava se da se rezultati fluidnog modela prvog reda u kome su korišćeni balk transportni podaci jako dobro slažu sa rezultatima korigovanog fluidnog modela u okolini fronta strimera. Nasuprot tome, fluidni model prvog reda u kome su korišćeni fluks transportni podaci predviđa nešto sporiju propagaciju strimera nego preostala dva modela.

Vrednosti brzine strimera u funkciji redukovanog spoljašnjeg električnog polja E_0/n_0, koje
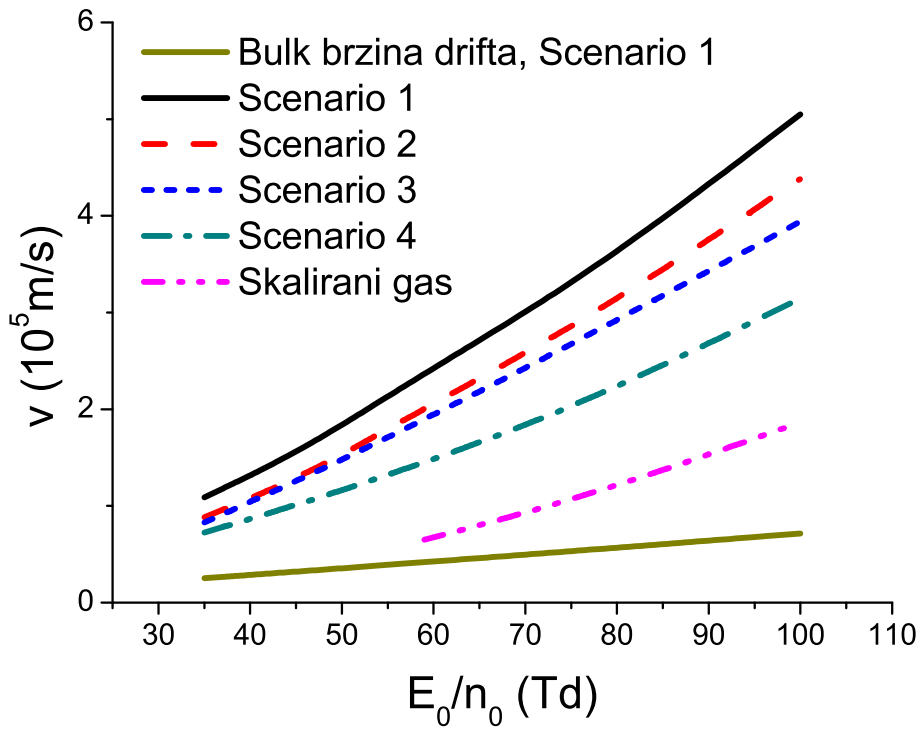
Slika 100: Vrednosti brzine strimera za elektrone u tečnom ksenonu u funkciji redukovanog spoljašnjeg polja E_0/n_0 u sva četiri scenarija za reprezentovanje neelastičnih gubitaka energije. Ovi rezultati su dobijeni primenom fluidnog modela prvog reda sa balk transportnim podacima. Brzina strimera koja je određena primenom transportnih podataka za gasni ksenon, koji su skalirani na gustinu tečnog ksenona i balk brzina drifta u tečnom ksenonu, koja je određena u prvom slučaju za reprezentovanje neelastičnih sudara u tečnom ksenonu, takođe su prikazane na ovom grafiku radi poređenja. Rezultati su dobijeni na osnovu numeričkih proračuna u okviru fluidnih modela strimera.
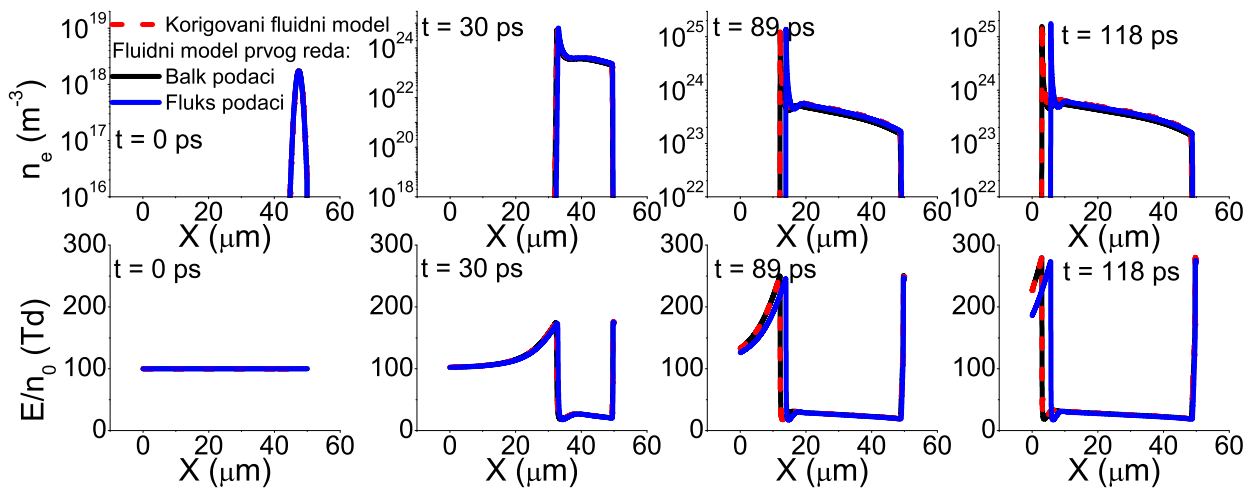
Slika 101: Formiranje i propagacija negativnog strimera u tečnom ksenonu u redukovanom spoljašnjem električnom polju $E/n_0 = 100$Td. Ovi rezultati su dobijeni na osnovu numeričkih proračuna u okviru korigovanog fluidnog modela i fluidnog modela prvog reda sa fluks i balk podacima, uz primenu četvrtog slučaja za reprezentovanje neelastičnih sudara.
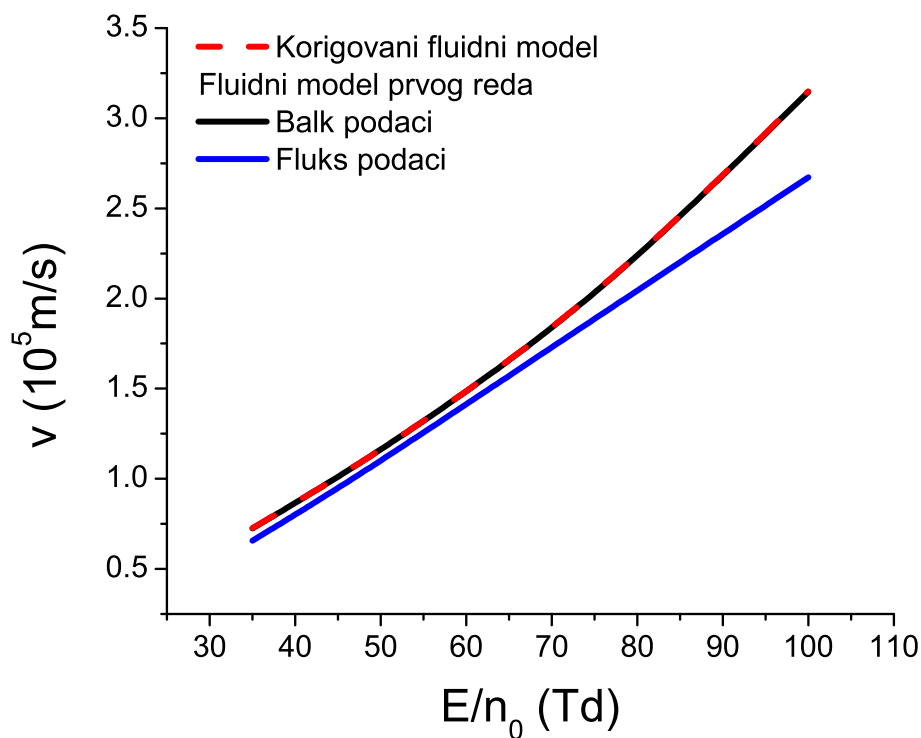
Slika 102: Vrednosti brzine strimera koje su određene primenom korigovanog fluidnog modela i fluidnog modela prvog reda sa fluks i balk podacima. Ovi proračuni su urađeni u okviru četvrtog scenarija za reprezentovanje neelastičnih gubitaka energije.

su određene u četvrtom slučaju za reprezentovanje neelastičnih sudara u tečnom ksenonu prikazane su na slici 102. Ovi rezultati su dobijeni primenom fluidnog modela prvog reda sa fluks i balk transportnim podacima, kao i primenom korigovanog fluidnog modela. Grafik pokazuje kako je slaganje između vrednosti brzine strimera, koje su određene u ova tri modela, slično kao slaganje odgovarajućih prostornih profila strimera. Naime, vrednosti brzine strimera koje su određene primenom fluidnog modela prvog reda u kome su korišćeni balk transportni podaci gotovo se podudaraju sa odgovarajućim vrednostima brzine koje su određene primenom korigovanog fluidnog modela. Međutim, brzina strimera koja je određena primenom fluidnog modela prvog reda u kome su korišćeni fluks transportni podaci je niža od brzine koja je određena u preostala dva modela. Ove razlike su najizraženije na visokim vrednostima redukovanog spoljašnjeg električnog polja.

7.4 Negativni strimeri u tečnom argonu i tečnom kriptonu

Na slikama 103 i 104 je ilustrovana tranzicija elektronske lavine u negativan strimer za elektrone u tečnom argonu pri vrednosti redukovanog spoljašnjeg električnog polja od 59 Td i 100 Td, respektivno, dok je tranzicija elektronske lavine u negativan strimer u tečnom kriptonu pri ove dve vrednosti redukovanog spoljašnjeg električnog polja prikazana na graficima 105 i 106 respektivno. Rezultati na graficima dobijeni su primenom fluidnog modela prvog reda, u kome su korišćeni balk transportni podaci, izračunati u prvom i drugom slučaju za reprezentova-

nje neelastičnih sudara u tečnosti. Za razliku od prvog slučaja za reprezentovanje neelastičnih energijskih gubitaka u tečnoj fazi gde su sve ekscitacije zanemarene, u drugom slučaju su uzete u obzir sve ekscitacije, čiji je prag niži od praga za zonski prelaz. Sa slika se vidi da su, kao i u tečnom ksenonu, prostorni profili koncentracije elektrona i rezultujućeg električnog polja u tečnom argonu i tečnom kriptonu na kvalitativnom nivou slični kao odgovarajući prostorni profili u gasnoj fazi, pri čemu su prostorne i vremenske skale formiranja strimera u tečnosti manje za oko tri reda veličine, zbog znatno veće koncentracije pozadinskih atoma u tečnosti nego u gasu. Takođe se vidi da vrednosti brzine formiranja i propagacije strimera, vrednosti koncentracije elektrona u glavi strimera i u strimerskom kanalu, kao i intenzitet efekata prostornog naelektrisanja opadaju sa porastom broja ekscitacija koje su uključene u set preseka za elektrone u tečnom argonu i tečnom kriptonu. Ovo je, kao i u tečnom ksenonu, posledica opadanja koeficijenta za jonizaciju sa povećanjem broja ekscitacija.
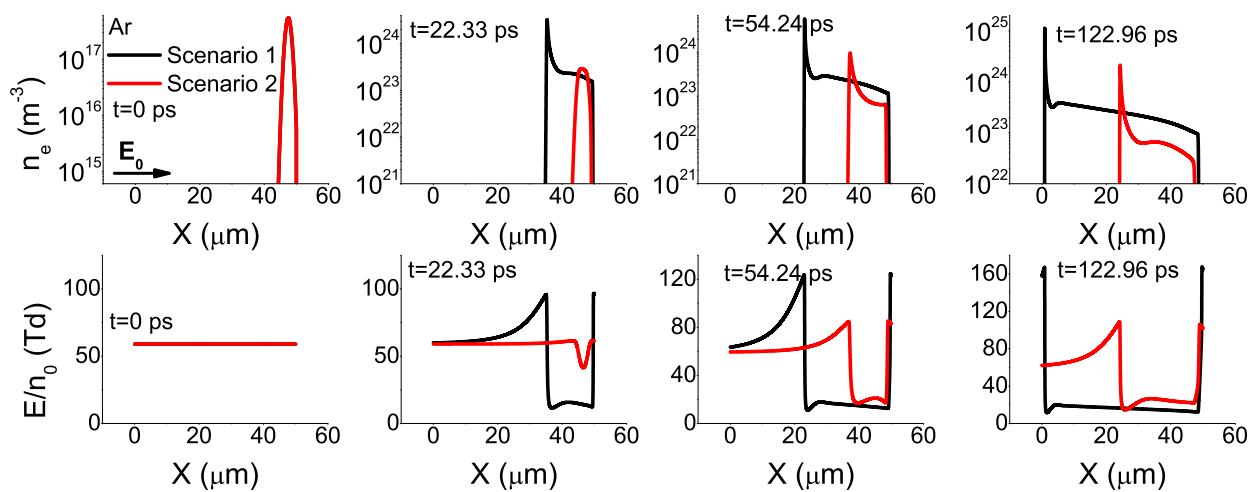
Slika 103: Formiranje i propagacija negativnog strimera u tečnom argonu za $E_0/n_0 = 59$ Td. Ovi rezultati su dobijeni primenom prvog i drugog scenarija za reprezentovanje neelastičnih energijskih gubitaka. Ovde n_e označava koncentraciju elektrona, dok E/n_0 označava redukovano rezultujuće električno polje. Na ovom je grafiku prikazan i smer spoljašnjeg električnog polja. Rezultati su dobijeni na osnovu numeričkih proračuna u okviru fluidnih modela strimera.

Slika 107 prikazuje poređenja vrednosti balk brzine strimera u prvom i drugom slučaju za reprezentovanje neelastičnih sudara, za elektrone u tečnom argonu i tečnom kriptonu. U obe tečnosti balk brzina strimera značajno opada sa povećanjem broja ekscitacija koje su uključene u model, zbog smanjenja koeficijenta za jonizaciju sa porastom broja ekscitacija.

Na slici 108 su predstavljene vrednosti brzinskih koeficijenata za jonizaciju za elektrone u tečnom argonu, tečnom kriptonu i tečnom ksenonu, kao i u odgovarajućim gasovima, u funkciji E/n_0. Uz to, slika 109 reprezentuje vrednosti ovih brzinskih koeficijenata koje su pomnožene sa odgovarajućom koncentracijom pozadinskih atoma u tečnoj fazi. U gasnoj fazi je do oko 700 Td brzinski koeficijent za jonizaciju u ksenonu niži od brzinskog koeficijenta u preostala dva gasa. Pored toga je brzinski koeficijent za jonizaciju u kriptonu niži od odgovarajućeg brzinskog koeficijenta u argonu do oko 400 Td. No u tečnoj fazi je brzinski koeficijent za jonizaciju u
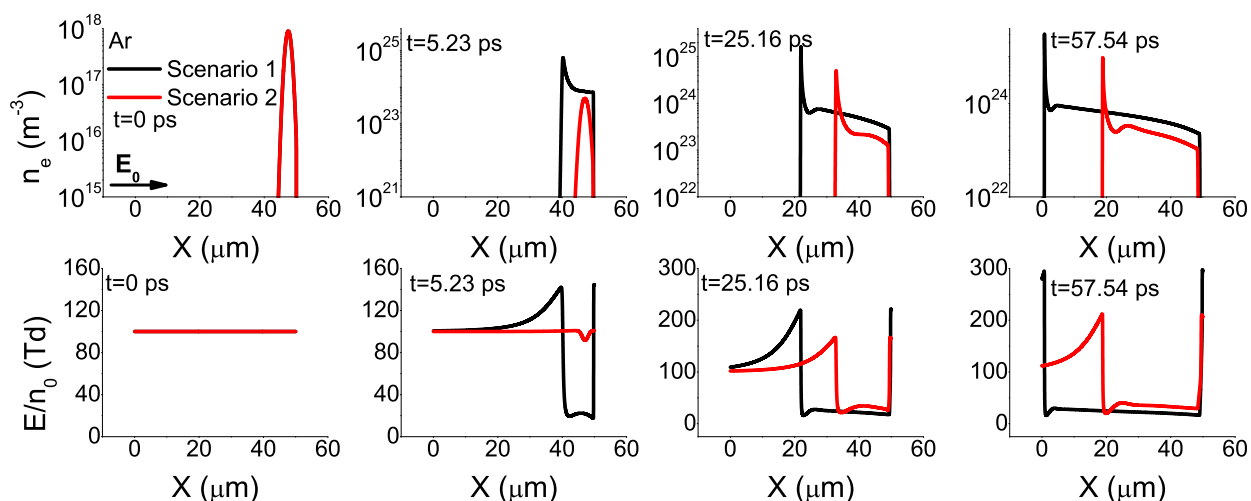
Slika 104: Formiranje i propagacija negativnog strimera u tečnom argonu za $E_0/n_0 = 100$ Td. Rezultati su dobijeni uz pomoć numeričkih proračuna u okviru fluidnih modela strimera.

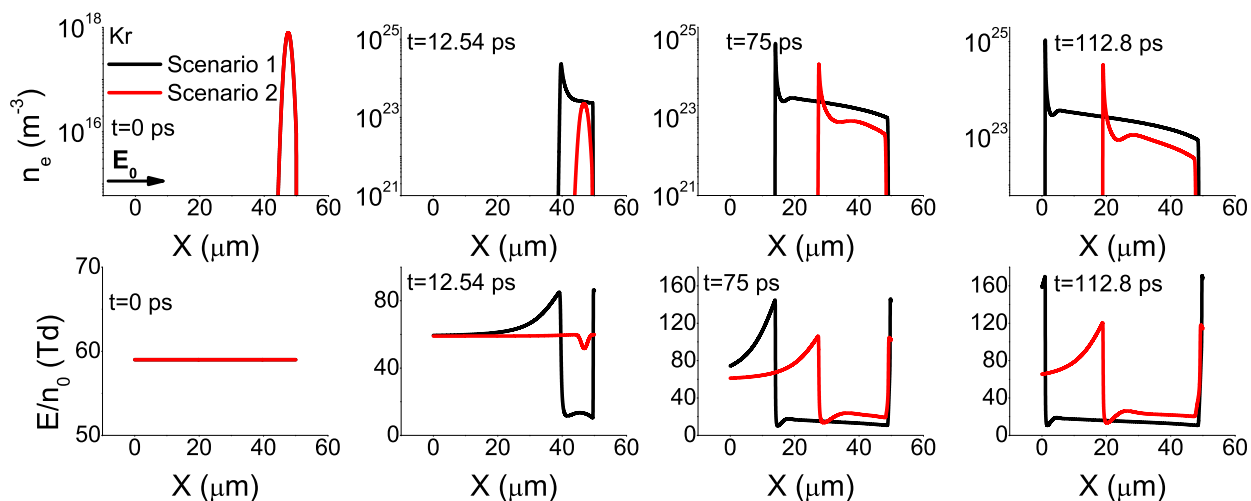Slika 105: Formiranje i propagacija negativnog strimera u tečnom kriptonu za $E_0/n_0 = 59$ Td. Ovi rezultati su dobijeni primenom prvog i drugog scenarija za reprezentovanje neelastičnih energijskih gubitaka. Ovde n_e označava koncentraciju elektrona, a E/n_0 označava redukovano rezultujuće električno polje. Na grafiku je takođe prikazan smer spoljašnjeg električnog polja. Rezultati su dobijeni primenom numeričkih proračuna u okviru fluidnih modela strimera.

ksenonu viši od brzisnkih koeficijenata u argonu i kriptonu do oko 77 Td. Na poljima višim od 77 Td brzinski koeficijent za jonizaciju u tečnom kriptonu viši je od odgovarajućeg koeficijenta u tečnom ksenonu. Brzinski koeficijent za jonizaciju u tečnom argonu je niži od odgovarajućih koeficijenata u preostale dve tečnosti do 1000 Td. Faktori koji utiču na razliku između brzinskih koeficijenata za jonizaciju u tečnoj i gasnoj fazi jesu sniženje praga za jonizaciju u tečnoj fazi u odnosu na gasnu fazu i broj ekscitacija u tečnoj fazi, jer ekscitacije predstavljaju konkurentan proces jonizaciji. Pritom su naročito značajne ekscitacije čiji su pragovi niži od praga za jonizaciju u tečnoj fazi. Jedan od razloga zbog kojih je brzisnki koeficijent za jonizaciju u tečnom argonu niži nego u preostale dve tečnosti je prisustvo većeg broja ekcitacija u argonu, čiji su pragovi niži od praga za jonizaciju u tečnoj fazi. Drugi uzročnik je manje sniženje praga
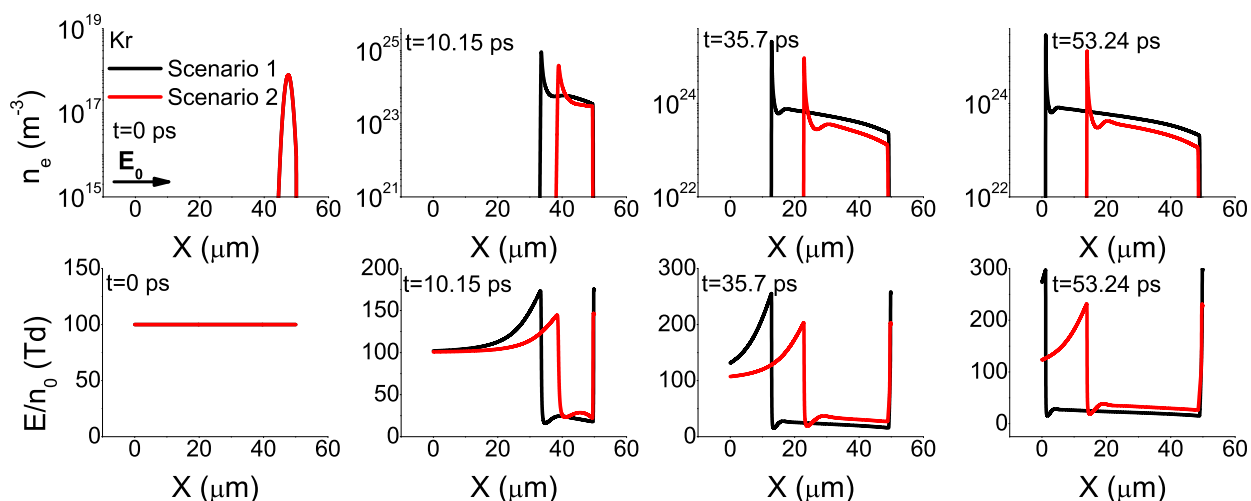
Slika 106: Formiranje i propagacija negativnog strimera u tečnom kriptonu za $E_0/n_0 = 100$ Td. Rezultati su dobijeni na osnovu numeričkih proračuna u okviru fluidnih modela strimera.
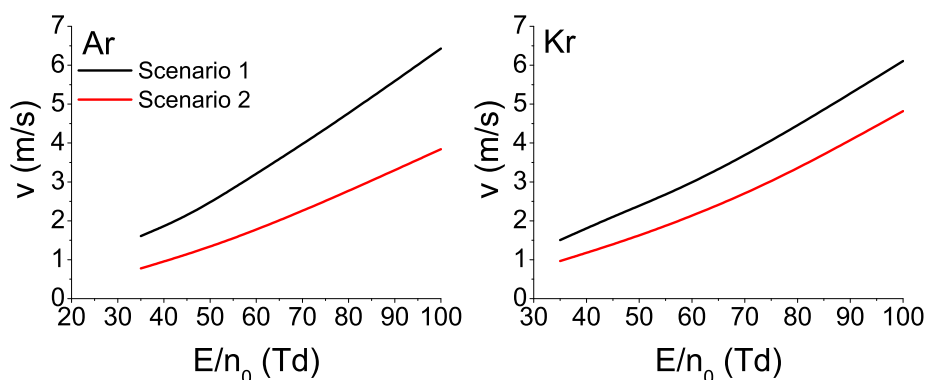
Slika 107: Vrednosti brzine strimera koje su određene primenom prvog i drugog scenarija za reprezentovanje neelastičnih gubitaka energije za elektrone u tečnom argonu i tečnom kriptonu. Rezultati su dobijeni uz pomoć numeričkih proračuna u okviru fluidnih modela strimera.

za jonizaciju u tečnoj fazi (u odnosu na gasnu fazu) u tečnom argonu nego u preostale dve tečnosti. Brzinski koeficijent u tečnom ksenonu je viši od odgovarajućeg koeficijenta u tečnom kriptonu do oko 77 Td zbog većeg sniženja praga za jonizaciju u tečnoj fazi. Međutim, sniženje praga za jonizaciju ima manji uticaj na brzinski koeficijent za jonizaciju na višim poljima, pa brzinski koeficijent za jonizaciju u tečnom kriptonu nadmašuje odgovarajući koeficijent u tečnom ksenonu.

Iako je brzinski koeficijent za jonizaciju u tečnom argonu niži nego u preostale dve tečnosti do oko 1000 Td, koncentracija pozadinskih atoma je najveća u tečnom argonu ($2.1 \cdot 10^{28} m^{-3}$), a najmanja u tečnom ksenonu ($1.4 \cdot 10^{28} m^{-3}$). Zato je brzinski koeficijent za jonizaciju u tečnom argonu, koji je pomnožen sa odgovarajućom koncentracijom pozadinskih atoma (skalirani brzinski koeficijent), viši od odgovarajućeg koeficijenta u tečnom ksenonu na poljima višim od 100 Td. Slično tome, skalirani brzinski koeficijent za jonizaciju u tečnom kriptonu viši je od odgovarajućeg koeficijenta u tečnom ksenonu na poljima višim od oko 50 Td. Skalirani brzinski koeficijent u tečnom kriptonu veći je od odgovarajućeg brzinskog koeficijenta u tečnom argonu
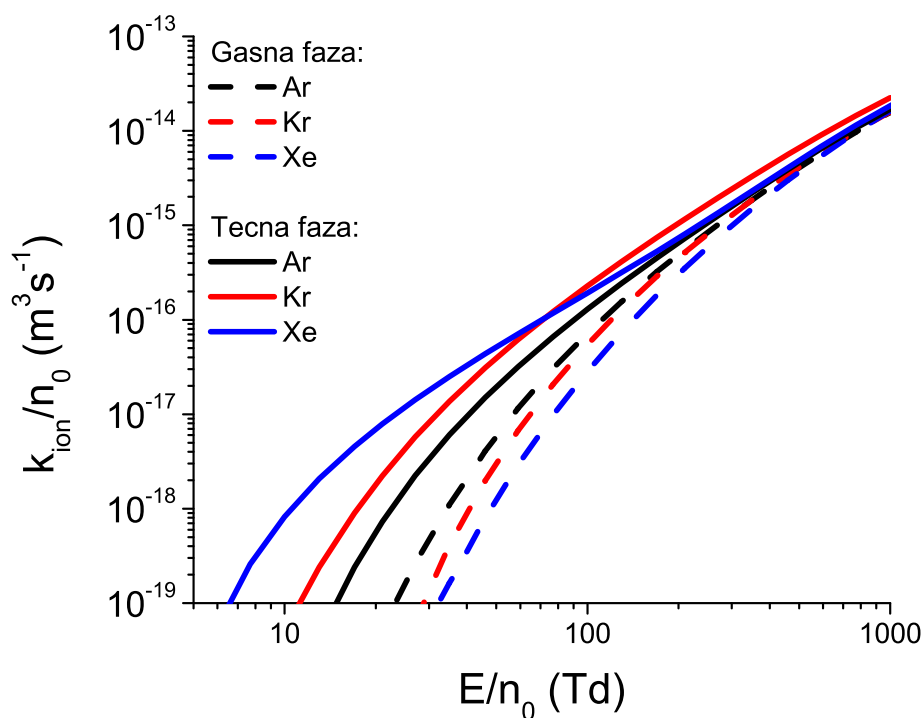
Slika 108: Brzinski koeficijenti za jonizaciju u funkciji redukovanog električnog polja E/n_0 za elektrone u tečnom argonu, tečnom kriptonu i tečnom ksenonu. Zarad poređenja, na grafiku su prikazani i brzinski koeficijenti za jonizaciju u odgovarajućim gasovima. Rezultati su dobijeni primenom Monte Carlo simulacija.

do 1000 Td. Pošto intenzitet lavinske multiplikacije elektrona zavisi od proizvoda brzinskog koeficijenta za jonizaciju i koncentracije pozadinskih atoma, lavinska multiplikacija je najveća u tečnom kriptonu na poljima višim od oko 50 Td, dok je na poljima višim od 100 Td lavinska multiplikacija u tečnom ksenonu manja nego u preostale dve tečnosti.

Na slici 110 je prikazano poređenje vrednosti brzine strimera u tečnom argonu, tečnom kriptonu i tečnom ksenonu, u funkciji redukovanog spoljašnjeg električnog polja E_0/n_0. Ovi rezultati su dobijeni primenom fluidnog modela prvog reda, u kome su korišćene balk vrednosti transportnih koeficijenata. Vrednosti brzine strimera koje su dobijene primenom korigovanog fluidnog modela gotovo su jednake odgovarajućim vrednostima koje su dobijene primenom fluidnog modela prvog reda u kome su korišćeni balk transportni podaci za sve tri tečnosti, u razmatranom opsegu redukovanog spoljašnjeg električnog polja (razlike su uvek manje od 5% u ovom opsegu polja). Sa grafika se vidi da je brzina strimera u tečnom kriptonu primetno veća od brzine strimera u presotale dve tečnosti u celom razmatranom opsegu redukovanog spoljašnjeg električnog polja, pri čemu su ove razlike najizraženije na visokim poljima. Istovremeno važi da je brzina strimera u tečnom argonu viša od odgovarajuće brzine u tečnom ksenonu, uz šta je ova razlika mala na 35 Td, ali je znatno veća na višim poljima.

Razlike između vrednosti brzina negativnih strimera tečnom argonu, tečnom kriptonu i tečnom ksenonu, koje su prikazane na slici 110, u skladu su sa razlikama između vrednosti skaliranih brzinskih koeficijenta za jonizaciju u ove tri tečnosti. Brzina strimera je naime određena
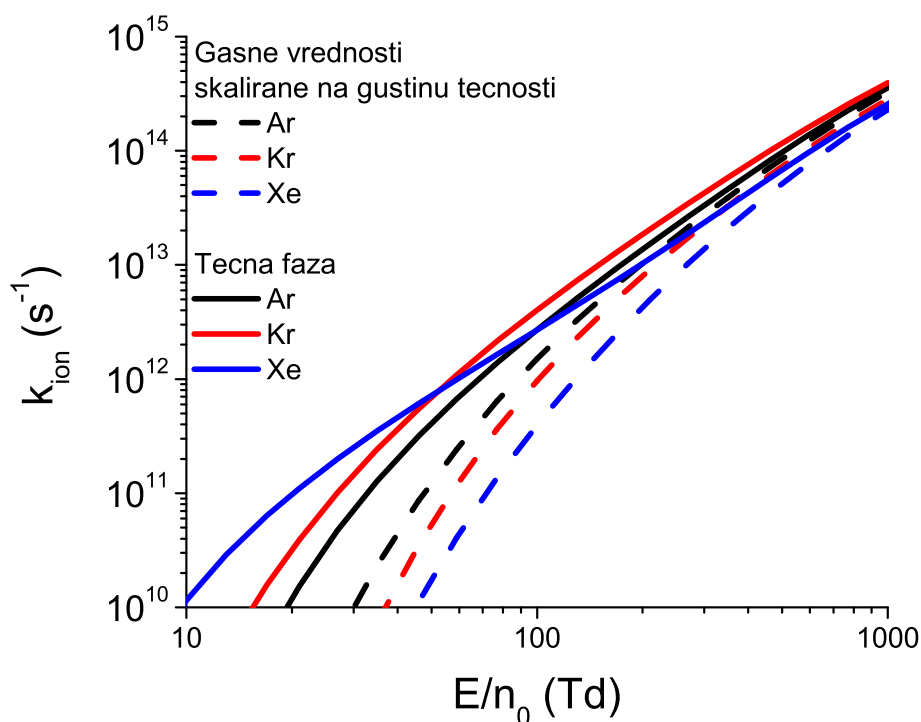
Slika 109: Brzinski koeficijenti za jonizaciju skalirani sa koncentracijom tečnosti u funkciji re-dukovanog električnog polja E/n_0 za elektrone u tečnom argonu, tečnom kriptonu i tečnom ksenonu. Na ovom grafiku su, s ciljem komparacije, prikazani i brzinski koeficijenti za joniza-ciju u gasnoj fazi koji su skalirani koncentracijom odgovarajuće tečnosti. Rezultati su dobijeni na osnovu Monte Carlo simulacija.

dinamikom elektrona u glavi strimera, pri čemu je u našim simulacijama rezultujuće električno polje u glavi strimera oko 2.5 puta veće od spoljašnjeg električnog polja. Tako se i na 35 Td rezultujuće električno polje u glavi strimera nalazi u opsegu polja u kome je skalirani brzinski koeficijent za jonizaciju u tečnom kriptonu primetno veći nego u preostale dve tečnosti. Pošto je pak vrednost skaliranog brzinskog koeficijenta u tečnom argonu jako bliska odgovarajućoj vrednosti u tečnom ksenonu u opsegu polja između 77 Td i 130 Td, na najnižim poljima je brzina strimera u tečnom argonu samo malo viša od odgovarajuće brzine u tečnom ksenonu, ali se ova razlika povećava sa porastom polja.

7.5   Zaključak

U ovom poglavlju su proučavani negativni strimeri u tečnom argonu, tečnom kriptonu i tečnom ksenonu. Potpoglavlje 7.2 prikazuje fluidne modele strimera. Prvo je prikazan fluid-ni model prvog reda, koji je zadat drift-difuzionom jednačinom za elektrone i jednačinama za balans broja čestica za naelektrisane čestice niže mobilnosti. Uticaj naelektrisanih čestica na rezultujuće električno polje je određen na osnovu Poisson-ove jednačine, dok su vrednosti transportnih veličina za elektrone u svakoj tački prostora određene primenom aproksimaci-je lokalnog polja. U posmatranom sistemu se broj slobodnih nosilaca naelektrisanja povećava ekscitovanjem elektrona iz valentne zone u provodnu zonu, dok se njihov broj smanjuje re-
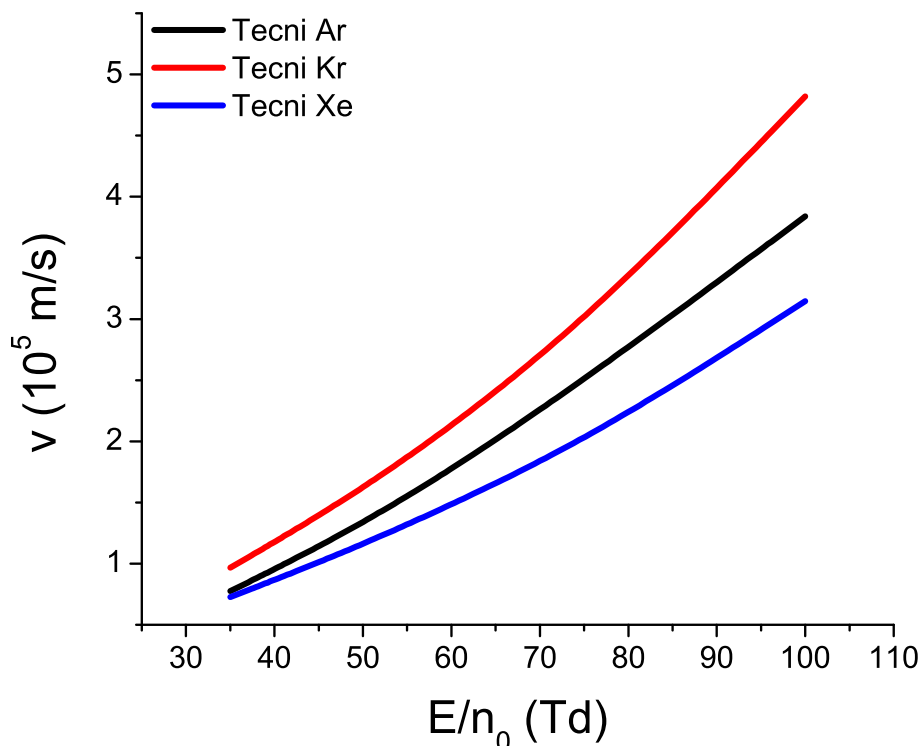
Slika 110: Poređenje brzine negativnih strimera za elektrone u tečnom argonu, tečnom kriptonu i tečnom ksenonu u funkciji redukovanog spoljašnjeg električnog polja E_0/n_0. Rezultati su dobijeni primenom fluidnog modela prvog reda sa balk transportnim podacima.

kombinacijom kvazislobodnih elektrona i elektronskih šupljina. Koeficijent za rekombinaciju kvazislobodnih elektrona i elektronskih šupljina je određen primenom skalirane Debye-ove formule. Uticaj nekonzervativnih procesa na promenu koncentracije elektrona opisan je izvornim članom. Ako se pri izvođenju drift-difuzione jednačine iz Boltzmann-ove jednačine pretpostavi najjednostavniji oblik izvornog člana, u kome su zanemareni prostorni gradijenti brzinskih koeficijenata za nekonzervativne sudarne procese, dobije se fluidni model prvog reda sa fluks transportnim koeficijentima. Drift-difuziona jednačina se može izvsti i iz jednačine kontinuiteta, ukoliko se iskoristi hidrodinamički razvoj fluksa čestica i izvornog člana. Na taj se način dobija oblik drift-difuzione jednačine u kome eksplicitno figurišu članovi koji opisuju prostorne gradijente brzinskih koeficijenata za nekonzervativne sudarne procese. Fluidni model u kome figuriše ovaj oblik drift-difuzione jednačine zove se fluidni model baziran na hidrodinamičkoj aproksimaciji ili korigovani fluidni model. Kada se u korigovanom modelu mogu zanemariti prostorni gradijenti koeficijenata u hidrodinamičkom razvoju izvornog člana, ovaj se model svodi na fluidni model prvog reda sa balk transportnim koeficijentima. Na osnovu toga se vidi da je fluidni model prvog reda sa balk transportnim koeficijentima bolja aproksimacija korigovanog fluidnog modela od fluidnog modela prvog reda u kome figurišu fluks transportni koeficijenti.

Numerička implementacija fluidnih modela, koji su korišćeni u ovoj disertaciji, zasnovana je na takozvanom jednoipodimenzionom (1.5D) modelu. U ovom modelu je pretpostavljeno da se naelektrisane čestice nalaze unutar cilindra sa konstantnim poluprečnikom. Pored toga je pretpostavljeno da koncentracija naelektrisanih čestica ne zavisi od radijalne koordinate i ugaone

koordinate, već da zavisi samo od aksijalne koordinate. Vrednosti rezultujućeg električnog polja i transportne veličine elektrona se izračunavaju samo na osi cilindra. 1.5D model daje realističniji opis ukupnog električnog polja od jednodimenzionog modela. Na kraju potpoglavlja 7.2 su prikazane vrednosti parametara modela koje su korišćene u okviru ove disertacije.

U potpoglavlju 7.3 razmatrani su formiranje i propagacija negativnih strimera u tečnom ksenonu u konstantnom spoljašnjem električnom polju. Na početku ovog potpoglavlja je upoređena dinamika evolucije strimera u prvom i četvrtom scenariju za reprezentovanje neelastičnih sudara u tečnoj fazi, kao i u scenariju u kome su transportni podaci iz gasne faze skalirani na gustinu tečnosti. Uočeno je da povećanje broja ekscitacija, koje su uključene u model, značajno usporava formiranje i propagaciju strimera. Još značajnije smanjenje brzine formiranja i propagacije strimera se dobije kada se u simulacijama koriste skalirani transportni podaci iz gasne faze. Brzina strimera, koja je određena u simulacijama, znatno je viša od balk brzine drifta, koja odgovara datoj vrednosti spoljašnjeg električnog polja. Na kraju ovog potpoglavlja je prikazano poređenje rezultata koji su dobijeni primenom korigovanog fluidnog modela i fluidnog modela prvog reda sa fluks i balk transportnim podacima. Uočeno je da se brzina strimera u fluidnom modelu prvog reda, u kome su korišćeni balk transportni podaci, odlično slaže sa brzinom strimera koja je određena u korigovanom fluidnom modelu, dok je brzina strimera u fludinom modelu prvog reda sa fluks transportnim podacima nešto niža od brzine strimera u preostala dva modela.

U odeljku 7.4 predstavili smo formiranje i propagaciju negativnih strimera u tečnom argonu i tečnom kriptonu u konstantnom spoljašnjem električnom polju. Na početku je razmatran uticaj broja ekscitacija koje su uključene u model na dinamiku negativnih strimera u ovim tečnostima. Primećeno je da brzine formiranja i propagacije strimera opadaju sa porastom broja ekscitacija koje su uključene u model, kao i u slučaju ksenona. Takođe su upoređeni profili zavisnosti brzine strimera od redukovanog spoljašnjeg električnog polja u tečnom argonu, tečnom kriptonu i tečnom ksenonu. Ovi profili su analizirani na osnovu brzinskih koeficijenata za jonizaciju u ovim tečnostima i na osnovu rejtova za jonizaciju (brzinskih koeficijenata skaliranih sa koncentracijom pozadisnkih atoma u tečnosti). Brzinski koeficijent za jonizaciju je najviši u tečnom ksenonu do približno 80 Td, zbog najvećeg sniženja praga za jonizaciju u ovoj tečnosti. U opsegu polja između približno 80 Td i 1000 Td brzinski koeficijent za jonizaciju je najviši u tečnom kriptonu. Brzinski koeficijent za jonizaciju u tečnom argonu je niži nego u preostale dve tečnosti u celom razmatranom opsegu polja. Međutim, koncentracija pozadinskih atoma je najviša u tečnom argonu a najniža u tečnom ksenonu. Zbog toga je skalirani brzinski koeficijent za jonizaciju najviši u tečnom kriptonu između približno 50 Td i 1000 Td, a najniži u tečnom ksenonu između približno 100 i 1000 Td. Razlike između vrednosti brzine negativnog strimera u različitim tečnostima na određenom redukovanom električnom polju su u saglasnosti sa vrednostima skaliranog brzinskog koeficijenta za jonizaciju na 2.5 puta većem redukovanom električnom polju, koje odgovara vrednosti rezultujućeg električnog polja u glavi strimera. Na osnovu toga je brzina negativnog strimera najviša u tečnom kriptonu, a najniža u tečnom ksenonu u razmatranom opsegu redukovanog spoljašnjeg električnog polja.

8 Zaključak

Ova doktorska disertacija je koncipirana na način da u sebi sadrži dve globalne i međusobno koherentne celine. Prva celina se odnosi na razvoj teorije i metodologije za proučavanje transportnih koeficijenata trećeg reda za rojeve lakih naelektrisanih čestica u gasovima. U drugoj celini ove disertacije razmatrani su problemi transporta elektrona, tranzicije lavina elektrona, formiranja i propagacije negativnih strimera u atomskim tečnostima visoke mobilnosti u uslovima u kojima se ne pojavljuju gasni mehurići i zarobljavanje elektrona u dislokacijama soft-kondenzovane materije.

Transportni koeficijenti trećeg reda su potrebni za konverziju hidrodinamičkih transportnih koeficijenata, koji se mogu direktno izračunati u okviru kinetičke teorije rojeva, u transportne podatke koji se određuju u stacionarnom Townsend-ovom eksperimentu (eng. *steady-state Townsend experiment*) i eksperimentu sa spektrom pristižućih čestica (eng. *arrival-time spectra experiment*). Razlike između transportnih podataka koji se mere u različitim tipovima eksperimenata sa rojevima naelektrisanih čestca mogu biti kako kvantitativno tako i kvalitativno značajne u prisustvu nekonzervativnih sudara. U tom smislu, neophodna je velika pažnja pri interpretaciji transportnih podataka koji su određeni u različitim tipovima eksperimenata, kao i pri primeni ovih podataka u proceduri za određivanje kompletnih setova preseka na osnovu metode rojeva (eng. *swarm procedure*), ili u direktnoj primeni ovih podataka u fluidnim modelima neravnotežne plazme. U literaturi se pak često ne vodi računa o poreklu i interpretaciji korišćenih transportnih podataka, što može značajno smanjiti pouzdanost tako dobijenih rezultata. Zbog toga su sistematično izračunavanje hidrodinamičkih transportnih koeficijenata prvog, drugog i trećeg reda, kao i njihova pažljiva konverzija u željeni tip eksperimentalnih podataka neophodni za otklanjanje ovog izvora nesigurnosti.

Transportni koeficijenti trećeg reda su neophodni za bolji opis prostornih raspodela rojeva naelektrisanih čestica u uslovima u kojima postoji asimetrično odstupanje ovih raspodela od idealnog Gaussian-a. Prostorni profili rojeva naelektrisanih čestica, koji se mogu reprezentovati približnom analitičkom formulom u kojoj figurišu transportni koeficijenti trećeg reda, primećeni su u eksperimentima i u Monte Carlo simulacijama. Odstupanje prostornog profila naelektrisanih čestica od idealnog Gaussian-a je naročito izraženo pri niskim vrednostima koncentracije atoma pozadinskog gasa i u ranim fazama vremenske evolucije roja. Ako bi transportni koeficijenti trećeg reda bili računati i mereni sa dovoljnom preciznošću, oni bi bili jako korisni u proceduri za određivanje kompletnih setova preseka na osnovu metode rojeva. U ovoj disertaciji je pokazano da su transportni koeficijenti trećeg reda osetljiviji na energijsku zavisnost preseka za elementarne sudarne procese od transportnih koeficijenata nižeg reda, uključujući brzinu drifta i komponente difuzionog tenzora. Pored toga, povećanje broja transportnih koeficijenata koji se koriste u ovoj proceduri smanjilo bi problem nejednoznačnosti rezultujućih setova preseka.

U dosadašnjoj literaturi nije bila određena struktura transportnog tenzora trećeg reda u prisustvu magnetskog polja. Pored toga, fizička interpretacija pojedinačnih komponenti ovog

tenzora nije bila pažljivo analizirana, što nije bio slučaj ni sa uticajem energijske zavisnosti preseka za elastične, neelastične i nekonzervativne sudare na ove komponente. Proračuni transportnih koeficijenata trećeg reda za elektrone u atomskim gasovima bili su ograničeni na niska električna polja, na kojima se efekat neelastičnih sudara može zanemariti, dok su proračuni u molekularnim gasovima bili ograničeni isključivo na longitudinalnu komponentu transportnog tenzora trećeg reda za elektrone u gasovima SF_6 i CH_4. Ove činjenice predstavljaju motivacione faktore za istraživanje koje je prikazano u ovoj disertaciji.

U okviru ove disertacije, transportni koeficijenti trećeg reda su sistematski proučavani u Monte Carlo simulacijama i na osnovu metoda više članova za numeričko rešavanje Boltzmann-ove jednačine. Obe ove tehnike se smatraju egzaktim u okviru kinetičke teorije rojeva naelektrisanih čestica u neutralnim gasovima i tečnostima. Korektnost teorijskih modela i numerički integritet kompjuterskih kodova su provereni u velikom broju benčmark proračuna, u kojima su rojevi naelektrisanih čestica bili pod uticajem vremenski stacionarnih i vremenski promenljivih električnih i magnetskih polja, u prisustvu kako konzervativnih tako i nekonzervativnih sudara. U ovoj disertaciji, inicijalne verzije kompjuterskih kodova baziranih na Monte Carlo metodu i numeričkom rešavanju Boltzmann-ove jednačine proširene su uvođenjem novih elemenata koji su omogućili sistematsko ispitivanje transportnih koeficijenata trećeg reda u modelnim i realnim gasovima. U našem su istraživanju, gde god je bilo moguće, transportni koeficijenti trećeg reda izračunati uz pomoć obe tehnike i međsubno su upoređeni ne bi li se izbegla svaka sumnja u njihovo ponekad atipično ponašanje u električnim i magnetskim poljima.

Istraživanje transporta naelektrisanih čestica u tečnoj fazi od značaja je za mnoge važne primene, uključujući upotrebu plazme u medicini, detektore čestica visoke energije sa tečnim argonom ili tečnim ksenonom, pročišćavanje vode primenom plazme i transformatorska ulja. Dalji razvoj i optimizacija ovih primena zavise od temeljnog razumevanja efekata koji utiču na dinamiku elektrona, jona i metastabila u tečnoj fazi. Modelovanje transporta naelektrisanih čestica u tečnostima je još uvek u fazi razvoja zbog kompleksnosti razmatranog sistema, kao i zbog velikog broja pojedinačnih procesa koji se dešavaju na različitim prostornim i vremenskim skalama. Dinamika elektrona u tečnoj fazi je pod snažnim uticajem koherentnog rasejanja, zarobljavanja u lokalnim oblastima niže gustine, interakcije sa pojedinačnim atomima i molekulima u tečnosti i solvatacije u polarnim tečnostima.

Uprkos brojnim efektima koji značajno modifikuju dinamiku elektrona u tečnostima, mnogi raniji modeli su aproksimirali transportne podatke iz tečne faze odgovarajućim podacima iz gasne faze, koji su skalirani na koncentraciju pozadinskih atoma u tečnosti. Svi egzaktni proračuni transporta elektrona u atomskim tečnostima, koji se mogu naći u literaturi, ograničeni su na nisku oblast redukovanog električnog polja, gde se neelastični i nekonzervativni sudari mogu zanemariti, uprkos tome što su za razvoj lavine elektrona i dinamiku strimera od ključnog značaja upravo vrednosti transportnih veličina na visokim poljima. U nekoliko teorijskih radova koji razmatraju transport elektrona na visokim električnim poljima nije dovoljno pažljivo analiziran uticaj neelastičnih sudara i nije jasno prikazan set preseka za ekscitacije koji je korišćen za određivanje prikazanih rezultata. Pored toga, modeli strimera u tečnoj fazi koji se mogu

naći u literaturi ne koriste transportne podatke koji su izračunati u tečnoj fazi, već ove podatke određuju na osnovu aproksimativnih analitičkih formula sumnjive pouzdanosti. Egzaktni proračuni transporta elektrona i dinamike strimera u tečnoj fazi trenutno nisu mogući, jer tačne vrednosti preseka za neelastične i nekonzervativne sudare u tečnostima još uvek nisu poznate u literaturi. Međutim, pažljivim razmatranjem aproksimativnih modela za reprezentovanje neelastičnih sudara u tečnostima mogu se napraviti preliminarne procene uticaja neelastičnih sudara na transport elektrona i dinamiku strimera u tečnoj fazi. Ovi modeli mogu poslužiti kao značajan motivacioni faktor za izračunavanje preseka za neelastične i nekonzervativne sudare u tečnostima.

U ovoj su disertaciji transportni podaci za elektrone u nepolarnim atomskim tečnostima velike mobilnosti određeni primenom Monte Carlo simulacija. Za naše potrebe je postojeći Monte Carlo kod za rojeve naelektrisanih čestica u neutralnim gasovima proširen uvođenjem novih elemenata koji su omogućili simulacije transporta u nepolarnim atomskim tečnostima. Najvažniji novi element u Monte Carlo kodu su tri efektivna sudarna procesa koji obezbeđuju dobru reprezentaciju srednjeg transfera impulsa i energije pri koherentnom rasejanju. Ispravnost implementacije koherentnog rasejanja u Monte Carlo kodu i numerički integritet odgovarajućih numeričkih procedura potvrđeni su poređenjem rezultata proračuna transportnih podataka za elektrone u Percus-Yevick-ovoj modelnoj tečnosti sa rezultatima koji se mogu pronaći u literaturi, a koji su dobijeni u nezavisnim Monte Carlo simulacijama i na osnovu numeričkih rešenja Boltzmann-ove jednačine.

Numerički proračuni formiranja i propagacije strimera u tečnoj fazi, koji su urađeni u okviru ove disertacije, zasnovani su na fludinom modelu prvog reda i tzv. korigovanom fluidnom modelu, baziranom na razvoju izvornog člana u jednačini kontinuiteta po gradijentima koncentracije elektrona. Oba modela su numerički realizovana u 1.5 dimenziji. Rezultati fluidnog modela prvog reda u kome su korišćeni fluks i balk transportni podaci upoređeni su sa odgovarajućim rezultatima korigovanog fluidnog modela, kako bi se utvrdila osetljivost rezultata na razlike između ovih modela, kao i na razlike u korišćenom tipu transportnih koeficijenata.

Ova doktorska disertacija organizovana je u osam poglavlja, uključujući uvodno poglavlje i zaključak. U uvodnom poglavlju prikazana je motivacija za proučavanja transportne teorije rojeva naelektrisanih čestica i neravnotežnih plazmi. Zatim smo diskutovali o prednostima i manama fluidnih modela, čestičnih modela i metoda za numeričko rešavanje Boltzmann-ove jednačine u modelovanju neravnotežnih plazmi. Usledio je kratak istorijski osvrt na razvoj metode više članova za rešavanje Boltzmann-ove jednačine. Identifikovane su poteškoće u teorijskom opisu transporta naelektrisanih čestica u tečnoj fazi. Potom je dat pregled stanja u oblasti modelovanja transporta naelektrisanih čestica u tečnostima i soft-kondenzovanoj materiji. Posebnu pažnju posvetili smo motivaciji za izučavanje transportnih koeficijenata trećeg reda za rojeve naelektrisanih čestica u gasovima i tečnostima. Na kraju ovog poglavlja dat je kratak pregled preostalih poglavlja u disertaciji.

U drugom poglavlju su predstavljeni osnovni elementi teorije rojeva naelektrisanih čestica u gasovima i tečnostima. Na početku ovog poglavlja je definisan roj naelektrisanih čestica, a

zatim su prikazane osnove teroje rasejanja elektrona na izolovanom atomu, kao i neophodne modifikacije ove teorije za izračunavanje preseka za rasejanje elektrona u atomskim tečnostima. Nakon toga, u kratkim crtama je predstavljena hidrodinamička teorija transporta naelektrisanih čestica i definisane su dve različite familije transportnih koeficijenata, fluks i balk. Na kraju ovog poglavlja je prikazana struktura vektorskih i tenzorskih transportnih koeficijenata u svim konfiguracijama električnog i magnetskog polja.

Centralna tema trećeg poglavlja jesu metodi za izračunavanje transportnih koeficijenata i drugih transportnih veličina, a koji su predmet ove diertacije. Na početku je predstavljen metod više članova za numeričko rešavanje Boltzmann-ove jednačine, a zatim su prikazane fluidne jednačine koje se mogu izvesti na osnovu množenja Boltzmann-ove jednačine proizvoljnom funkcijom brzine i integracijom ove jednačine po brzinskom prostoru. Pažnja je zatim posvećena osnovi Monte Carlo simulacija i njihovoj implementaciji u kompjuterskom kodu korišćenom u ovoj disertaciji. Kraj poglavlja prikazuje proračune transportnih veličina u Percus-Yevick-ovoj modelnoj tečnosti, koji su dobijeni primenom Monte Carlo simulacija i koji služe za proveru implementacije efekata koherentnog rasejanja u našem Monte Carlo kodu.

U četvrtom poglavlju su razmatrani transportni koeficijenti trećeg reda za rojeve naelektri-sanih čestica u modelnim gasovima. Prvo je detaljno analizirana fizička interpretacija individu-alnih komponenti transportnog tenzora trećeg reda, kao i uticaja električnog polja i energijske zavisnosti kolizione frekvence na znak ovih komponenti. Nakon toga su prikazani uslovi simu-lacija i teorijskih proračuna, te rezultati proračuna transportnih koeficijenata trećeg reda u Maxwell-ovom modelnom gasu, koji su dobijeni primenom metode više članova za rešavanje Boltzmann-ove jednačine, rezultati u modelu krutih sfera, koji su dobijeni primenom Monte Carlo simulacija, kao i rezultati u Reid-ovom modelnom gasu, Lucas-Saelee-evom modelnom gasu i modifikovanom Ness-Robson-ovom modelu, koji su dobijeni primenom ove dve metode. U ovom poglavlju je praćen i protumačen uticaj elastičnih, neelastičnih i nekonzervativnih su-dara, kao i odnosa masa naelektrisanih čestica roja i neutralnih čestica pozadinske sredine na transportne koeficijente trećeg reda.

Transportni koeficijenti trećeg reda za rojeve elektrona i pozitrona u realnim gasovima obra-zlažu se u petom poglavlju. Na početku se analizira korelacija između profila zavisnosti longitu-dinalne komponente transportnog tenzora trećeg reda i longitudinalne komponente difuzionog tenzora od redukovanog električnog polja. Slede rezultati proračuna transportnih koeficijenata trećeg reda za elektrone u atomskim i molekularnim gasovima i za pozitrone u molekularnim gasovima. Pri tome su rezultati u atomskim gasovima dobijeni primenom metode više člano-va za rešavanje Boltzmann-ove jednačine, dok su rezultati u molekularnim gasovima dobijeni primenom ove metode i Monte Carlo simulacija. Ovi rezultati su analizirani na osnovu setova preseka za elementarne sudarne procese i profila srednje energije.

U šestom smo poglavlju tumačili transport elektrona u atomskim tečnostima visoke mobilno-sti. Na početku ovog poglavlja je predstavljena motivacija za izučavanje transporta elektrona u tečnoj fazi. Izneti su argumenti za postojanje provodne zone u tečnom argonu, tečnom kriptonu i tečnom ksenonu, na osnovu rezultata koji su dobijeni u eksperimentima. Potom su prikaza-

ni setovi preseka koji su korišćeni za modelovanje rasejanja elektrona u ovim tečnostima. U slučaju elektrona u tečnom argonu i tečnom kriptonu razmatrana su dva različita scenarija za reprezentovanje neelastičnih sudara, dok su u slučaju tečnog ksenona razmatrana četiri različita scenarija. Nakon toga, primenom Monte Carlo simulacija su analizirani profili zavisnosti srednje energije, brzine drifta, brzinskog koeficijenta za jonizaciju i karakteristične energije od redukovanog električnog polja za elektrone u ove tri tečnosti.

Sedmo poglavlje bavilo se formiranjem i propagacijom strimera u atomskim tečnostima sa velikom mobilnošću. Na početku se govorilo o fluidnom modelu prvog reda i fluidnom modelu baziranom na razvoju izvornog člana u jednačini kontinuiteta po gradijentima koncentracije elektrona. Potom su prikazani rezultati fluidnih proračuna formiranja i propagacije negativnih strimera pod uticajem homogenog spoljašnjeg električnog polja u tečnom argonu, tečnom kritponu i tečnom ksenonu. Razmatrano je na koji način priroda transportnih koeficijenata, modeli za tretman elektronskih ekscitacija i rekombinacija kvazislobodnih elektrona i pozitivnih šupljina utiču na osobine strimerske plazme.

U ovoj doktorskoj disertaciji, mogu se izdvojiti sledeći originalni naučni doprinosi, koje ćemo prvo samo pobrojati, a onda u nastavku ovog poglavlja detaljnije obrazložiti.

(1) Struktura transportnog tenzora trećeg reda je određena primenom metode grupnih projektora u svim konfiguracijama električnog i magnetskog polja. Pri tome, rezultati koji se odnose na konfiguraciju bez magnetskog polja slažu se sa rezultatima ranijih autora, dok je struktura tenzora u slučaju paralelne i ortogonalne konfiguracije polja prvi put određena u okviru ove disertacije. Korišćeni metod se može primeniti na određivanje strukture transportnog tenzora proizvoljnog reda. Struktura transportnog tenzora trećeg reda, koja je određena u ovoj disertaciji, dodatno je proverena na osnovu simetrija momenata funkcije raspodele naelektrisanih čestica u faznom prostoru i fizičkih argumenata.

(2) Fizička interpretacija individualnih komponenti transportnog tenzora trećeg reda je detaljno analizirana u okviru ove disertacije. Doprinos pojedinačnih komponenti transportnog tenzora trećeg reda fluksu čestica roja je razmatran na osnovu fluks gradijentne relacije, dok je uticaj ovih komponenti na prostorni profil roja analiziran primenom generalisane difuzione jednačine. Zavisnost znaka pojedinačnih komponenti transportnog tenzora trećeg reda od spoljašnjeg električnog polja i kolizione frekvence za elementarne sudarne procese je prvi put pažljivo tumačena u okviru ove disertacije.

(3) Transportni koeficijenti trećeg reda za naelektrisane čestice u modelnim gasovima, elektrone u atomskim i molekularnim gasovima, te pozitrone u tri molekularna gasa izračunati su u širokom opsegu redukovanog električnog polja primenom Monte Carlo simulacija i metode više članova za numeričko rešavanje Boltzmann-ove jednačine. Detaljno je analiziran uticaj elastičnih, neelastičnih i nekonzervativnih sudara, kao i odnosa masa naelektrisanih čestica roja i neutralnih čestica pozadinske sredine, na individualne komponente transportnog tenzora trećeg reda. Pored toga je razmatran uticaj transportnih koeficijenata trećeg reda na prostorni profil roja za elektrone u atomskim i molekularnim gasovima. Validnost korišćenih metoda za

izračunavanje transportnih koeficijenata trećeg reda je potvrđena na osnovu odličnog slaganja rezultata koji su dobijeni primenom ova dva metoda.

(4) U ovoj disertaciji je prvi put analiziran uticaj magnetskog polja na transportne koeficijente trećeg reda. Ovaj uticaj je analiziran na primeru elektrona u Reid-ovom modelnom gasu za ortogonalnu konfiguraciju električnog i magnetskog polja. Pri tome se detaljno diskutovalo o profilu zavisnosti dijagonalnih komponenti transportnog tenzora trećeg reda od redukovanog magnetskog polja na osnovu uticaja sila koje deluju na elektrone i njihovih sudara sa neutralnim česticama pozadinskog gasa.

(5) Na osnovu rezultata koji se odnose na elektrone u atomskim i molekularnim gasovima i pozitrone u molekularnim gasovima primećeno je da u svakom od ovih gasova postoji snažna korelacija između profila zavisnosti longitudinalne komponente transportnog tenzora trećeg reda i longitudinalne komponente difuzionog tenzora od redukovanog električnog polja. Opaženo je da se longitudinalna komponenta transportnog tenzora trećeg reda povećava sa porastom redukovanog električnog polja kada je longitudinalna difuzija konveksna rastuća funkcija u log-log skali, dok ova komponenta transportnog tenzora trećeg reda opada sa porastom redukovanog električnog polja ako longitudinalna difuzija opada ili je konkavna rastuća funkcija redukovanog električnog polja u log-log skali. Pri tome je fluks/balk vrednost longitudinalne komponente transportnog tenzora trećeg reda korelisana sa fluks/balk longitudinalnom difuzijom. Ova korelacija je odsutna na najnižim poljima zbog toga što transportni koeficijenti trećeg reda teže nuli u limesu niskih polja, za razliku od dijagonalnih komponenti difuzionog tenzora koji imaju nenulte termalne vrednosti.

(6) U okviru ove disertacije je analizirana strukturno indukovana negativna diferencijalna provodnost za elektrone u tečnom ksenonu na osnovu prostorno razloženih karakteristika roja i funkcija raspodele elektrona po energijama. Uočeno je da su prostorni gradijenti brzinskog koeficijenta za elastične sudare najintenzivniji u oblasti polja u kojoj brzina drifta opada sa porastom redukovanog električnog polja, kao i da funkcija raspodele elektrona po energijama ima specifičan oblik u ovom opsegu polja. Na ovaj način je dopunjena već postojeća analiza strukturno indukovane negativne provodnosti koja je zasnovana na fluidnim modelima.

(7) Izvedene su fluidne jednačine za balans broja čestica, balans impulsa i balans energije za elektrone u atomskim tečnostima, pri čemu je uzet u obzir doprinos jonizacije. Na osnovu ovih jednačina je izveden sistem jednačina koji povezuje srednju energiju elektrona, brzinu drifta, vektor energijskog gradijenta i difuzioni tenzor, uz pretpostavku hidrodinamičkog režima i primenu izvesnih aproksimacija. Tako su proširene fluidne jednačine za lake naelektrisane čestice u atomskim tečnostima, koje već postoje u literaturi, a u kojima nisu uzeti u obzir nekonzervativni procesi koji omogućavaju multiplikaciju čestica roja. Ovaj sistem jednačina se može rešavati numerički kada su poznate kolizione frekvence za elementarne sudarne procese u funkciji srednje energije.

(8) Razmatran je uticaj broja ekscitacija koje su uključene u model na koeficijent za jonizaciju u tečnom argonu, tečnom kriptonu i tečnom ksenonu primenom Monte Carlo simulacija. Četiri

različita scenarija za reprezentovanje neelastičnih sudara u tečnom ksenonu su tumačena na osnovu refleksionih spektara tečnog ksenona i eksperimenata sa fotoprovodnošću u ovoj tečnosti. Tako određeni brzinski koeficijenti za jonizaciju za elektrone u tečnom ksenonu upoređeni su sa eksperimentalnim rezultatima Derentzo-a i saradnika i sa teorijskim rezultatima ranijih autora.

(9) Analiziran je uticaj implementacije elektronskih ekscitacija koje su uključene u model na dinamiku tranzicije elektronske lavine u negativan strimer i propagaciju negativnog strimera u tečnom argonu, tečnom kriptonu i tečnom ksenonu u beskonačnom prostoru primenom fluidnih modela strimera. Pokazano je da rezultati modelovanja dinamike strimera snažno zavise od broja ekscitacija koje su uključene u model, te da su razlike između pojedinačnih scenarija u saglasnosti sa odgovarajućim razlikama između brzinskih koeficijenata za jonizaciju. Takođe je zaključeno kako primena transportnih podataka iz gasne faze nije adekvatna za modelovanje strimera u tečnosti. Ovo je naročito izraženo ukoliko su razlike između brzinskih koeficijenata za jonizaciju u ove dve faze značajne pri vrednosti polja koja odgovara rezultujućem električnom polju na frontu strimera.

(10) Upoređeni su rezultati fluidnog modelovanja dinamike strimera koji su dobijeni primenom korigovanog fludinog modela i fluidnog modela prvog reda sa fluks i balk transportnim koeficijentima za elektrone u tečnom ksenonu. Pokazano je da se vrednost brzine strimera, koja je određena u fluidnom modelu prvog reda, bolje slaže sa odgovarajućom brzinom koja je određena pomoću korigovanog fluidnog modela – ukoliko se u fluidnom modelu prvog reda koriste balk transportni koeficijenti.

U dosadašnjoj literaturi je bila poznata struktura transportnog tenzora trećeg reda samo u odsustvu magnetskog polja. Zbog toga je u okviru ove disertacije pažljivo razmatrana struktura ovog tenzora u svim konfiguracijama električnog i magnetskog polja primenom dve različite metode. Pri tome je potvrđena struktura transportnog tenzora trećeg reda u odsustvu magnetskog polja, koja je ranije utvrđena u literaturi. Transportni tenzor trećeg reda ima 7 nenultih komponenti od kojih su 3 nezavisne u ovoj konfiguraciji polja. U paralelnoj konfiguraciji polja transportni tenzor trećeg reda ima 11 nenultih komponenti od kojih je 4 nezavisno, dok u ortogonalnoj konfiguraciji polja ovaj tenzor ima 14 nenultih komponenti od kojih je 10 nezavisno. Kada ugao između električnog i magnetskog polja uzima vrednost između 0 i 90 stepeni, transportni tenzor trećeg reda ima 27 nenultih komponenata od kojih je 18 nezavisno.

Nakon određivanja strukture transportnog tenzora trećeg reda pažljivo je analizirana fizička interpretacija komponenti ovog tenzora na osnovu fluks gradijentne relacije i generalisane difuzione jednačine. Pokazano je da Q_{zzz} komponenta u zavisnosti od znaka opisuje elongaciju ili kontrakciju prostorne raspodele naelektrisanih čestica na frontu roja i suprotnu deformaciju na začelju roja. Slično tome, Q_{xxz} komponenta opisuje razliku u intenzitetu transverzalnog širenja naelektrisanih čestica na frontu i na začelju roja, a Q_{zxx} komponenta opisuje razliku u intenzitetu longitudinalnog širenja naelektrisanih čestica u centru roja i na transverzalnim ivicama. Zajednički efekat Q_{xxz} i Q_{zxx} komponenti u zavisnosti od njihovog znaka dovodi do širenja ili skupljanja prostorne raspodele naelektrisanih čestica duž transverzalnog pravca na frontu roja i suprotne deformacije na začelju roja.

Uticaj transpornih koeficijenata trećeg reda na prostorni profil roja zavisi od količnika $Q_L/D_L^{3/2}$ i $Q_T/(D_T D_L^{1/2})$. Budući da ovi količnici opadaju sa smanjenjem odnosa masa naelektrisanih čestica roja i neutralnih čestica pozadinske sredine, transportni koeficijenti trećeg reda imaju daleko značajniji uticaj na prostorni profil roja teških naelektrisanih čestica poput jona nego na profil lakih naelektrisanih čestica poput elektrona i pozitrona, uprkos tome što apsolutne vrednosti komponenti transportnog tenzora trećeg reda opadaju sa porastom odnosa masa čestica roja i čestica pozadinske sredine. Pored toga, vrednosti količnika $Q_L/D_L^{3/2}$ i $Q_T/(D_T D_L^{1/2})$ opadaju sa povećanjem koncentracije neutralnih čestica pozadinske sredine. Zbog toga je uticaj transportnih koeficijenata trećeg reda na prostorni profil roja najznačajniji u slučaju gasova na niskim pritiscima.

U ovoj disertaciji je uočeno da na dovoljno visokim poljima postoji snažna korelacija između profila zavisnosti longitudinalne komponente transportnog tenzora trećeg reda Q_{zzz} od redukovanog električnog polja E/n_0 i odgovarajućeg profila longitudinalne komponente difuzionog tenzora D_{zz}. Primećeno je da Q_{zzz} komponenta opada sa porastom E/n_0 kad god D_{zz} opada, kao i kad se D_{zz} povećava sa porastom E/n_0 kao konkavna funkcija u log-log skali. Slično tome, Q_{zzz} se povećava sa porastom E/n_0 kada se D_{zz} povećava kao konveksna funkcija E/n_0 u log-log skali. Pri tome je fluks/balk vrednost Q_{zzz} komponente korelisana sa fluks/balk vrednošću D_{zz} komponente u uslovima u kojima fluks i balk vrednosti ovih transportnih veličina imaju međusobno različito kvalitativno ponašanje zbog snažnog uticaja nekonzervativnih sudara. Ove korelacije nema na najnižim poljima jer transportni koeficijenti trećeg reda teže nuli u limesu niskih polja, za razliku od dijagonalnih komponenti difuzionog tenzora koje imaju nenulte termalne vrednosti.

Strukturno indukovana negativna diferencijalna provodnost za elektrone u tečnom ksenonu je ispitana uz pomoć prostorno razloženih karakteristika roja i funkcija raspodele elektrona po energiji. Uočeno je da su nagibi prostornih profila brzinskih koeficijenata za efektivne sudarne procese koji su opisani σ_{oba} i σ_{impuls} presecima najstrmiji u opsegu polja u kome postoji strukturno indukovana negativna diferencijalna provodnost. Ovi su nagibi uz to naročito strmi u opsegu polja u kome je opadanje brzine drifta sa porastom E/n_0 najintenzivnije. Pošto ovi sudarni procesi dovode do transfera impulsa u tečnoj fazi, njihov nagli porast u smeru kretanja centra mase roja značajno otežava ubrzavanje elektrona od strane spoljašnjeg električnog polja. U ovom opsegu polja povećanje srednjeg transfera impulsa u elastičnim sudarima u jedinici vremena sa porastom E/n_0 nadjačava povećanje sile koja ubrzava elektrone, što dovodi do opadanja brzine drifta sa porastom E/n_0. Funcija raspodele elektrona po energijama ima neobičan oblik u opsegu polja u kome postoji strukturno indukovana negativna diferencijalna provodnost. Naime, visokoenergijski rep funkcije raspodele je odsečen u ovom opsegu polja zbog toga što u energijskom intervalu između približno 1 eV i 3 eV preseci za efektivne sudarne procese u kojima dolazi do transfera energije naglo rastu sa porastom energije. Pored toga, niskoenergijski deo funkcije raspodele je slabo populisan na niskim poljima, zato što je efektivni presek σ_{oba} za niskoenergijske elektrone jako nizak u tečnom ksenonu, što omogućava efikasno ubrzavanje niskoenergijskih elektrona od strane spoljašnjeg električnog polja.

U ovoj doktorskoj tezi je analiziran uticaj broja ekscitacija koje su uključene u model na prvi Townsend-ov koeficijent u tečnoj fazi. Vrednosti prvog Townsend-ovog koeficijenta koje su određene u četiri različita scenarija za reprezentovanje neelastičnih sudara u tečnom ksenonu upoređene su sa eksperimentalnim vrednostima Derentzo-a i saradnika, kao i sa prvim Townsend-ovim koeficijentom iz gasne faze koji je skaliran na gustinu tečnosti. Uočeno je da se prvi Townsend-ov koeficijent značajno smanjuje sa povećanjem broja ekscitacija koje su uključene u model. Iako se prve dve eksperimentalne tačke Derentzo-a i saradnika najbolje slažu sa scenarijom u kome su sve ekscitacije zanemarene, preostale eksperimentalne tačke se znatno bolje slažu sa scenarijima u kojima su ekscitacije uzete u obzir. Istovremeno je slaganje ovih eksperimentalnih tačaka nešto bolje sa scenarijom u kome su sve ekscitacije izolovanog atoma uključene u model, nego sa scenarijima u kojima su neke ekscitacije zanemarene. Pored toga, prvi Townsend-ov koeficijent iz gasne faze, koji je skaliran na gustinu tečnosti, znatno je niži od odgovarajućeg koeficijenta iz tečne faze u slučaju svih scenarija za reprezentovanje neelastičnih sudara u tečnom ksenonu, sve do jako visokih polja. Ovo je posledica značajnog sniženja efektivnog praga za jonizaciju u tečnom ksenonu u odnosu na gasni ksenon i znanto manjeg broja neelastičnih procesa čiji je prag ispod efektivnog praga za jonizaciju u tečnoj fazi. Razlika između skaliranog Townsend-ovog koeficijenta iz gasne faze i odgovarajućih koeficijenata u tečnosti opada sa porastom polja zbog manjeg značaja sniženja efektivnog praga za jonizaciju na visokim poljima.

Pošto je vrednost koeficijenta za jonizaciju od ključnog značaja za dinamiku strimera, broj ekscitacija koje su uključene u model snažno utiče na izračunatu brzinu formiranja i propagacije strimera u tečnoj fazi. U okviru ove disertacije je uočeno da brzina formiranja i propagacije strimera značajno opada sa povećanjem broja ekscitacija koje su uključene u model. Pored toga, primena transportnih podataka iz gasne faze koji su skalirani na gustinu tečnosti predviđa znatno sporiju tranziciju elektronske lavine u negativan strimer i znatno manju brzinu strimera u poređenju sa rezultatima koji su dobijeni na osnovu primene transportnih podataka izračunatih za tečni ksenon.

U našem istraživanju su upoređene brzine propagacije negativnih strimera u tečnom argonu, tečnom kriptonu i tečnom ksenonu, koji se kreću pod uticajem homogenog spoljašnjeg električnog polja. Razlike između vrednosti brzine negativnih strimera u ove tri tečnosti su analizirane na osnovu odgovarajućih razlika između profila zavisnosti brzinskih koeficijenata za jonizaciju od redukovanog električnog polja. Brzinski koeficijenat za jonizaciju u tečnom ksenonu je viši nego u preostale dve tečnosti do približno 80 Td, dok je odgovarajući koeficijent u tečnom argonu niži nego u preostale dve tečnosti do oko 1000 Td. Koncentracija atoma u tečnoj fazi je najniža u ksenonu a najviša u argonu, zbog čega je brzinski koeficijenat za jonizaciju, koji je skaliran sa koncentracijom pozadinskih atoma, najviši u tečnom kritponu na poljima višim od približno 50 Td a najniži u tečnom ksenonu u opsegu polja iznad približno 100 Td. Pošto brzina propagacije negativnog strimera zavisi od intenziteta rezultujućeg električnog polja na strimerskom frontu, a vrednosti rezultujućeg električnog polja na frontu strimera su u našim simulacijama oko 2.5 puta veće od vrednosti spoljašnjeg električnog polja, brzina negativnog strimera je najviša u tečnom kriptonu, a najniža u tečnom ksenonu u razmatranom opsegu

spoljašnjeg električnog polja.

Ova disertacija otvara mogućnosti za nova istraživanja u bliskoj budućnosti. Analiza transportnih koeficijenata trećeg reda se može proširiti na slučaj vremenski promenljivih električnih i magnetskih polja. Bilo bi zanimljivo ispitati faznu razliku između individualnih komponenti transportnog tenzora trećeg reda i spoljašnjeg električnog polja, imajući u vidu da transportni koeficijenti trećeg reda menjaju znak sa promenom smera električnog polja poput brzine drifta, a imaju relativno sporu vremensku relaksaciju poput srednje energije i difuzionog tenzora. Takođe bi bilo značajno i poučno razmotriti ponašanje transportnih koeficijenata trećeg reda u uslovima u kojima se pojavljuje kinetički fenomen anomalne longitudinalne difuzije u radio frekventnim električnim (i magnetskim) poljima.

Na osnovu Monte Carlo simulacija impulsnog Townsend-ovog eksperimenta i eksperimenta sa spektrima pristižućih čestica, mogu se odrediti eksperimentalni uslovi u kojima je moguće razložiti transportne koeficijente trećeg reda iz strujnih signala. Ove simulacije bi pomogle da se odrede gustina pozadinskog gasa, dimenzije komore (ili driftne cevi) i rezolucija strujnog signala koji su potrebni da bi se izmerili transportni koeficijenti trećeg reda za dati gas i datu vrednost redukovanog električnog polja. Na ovaj način bi mogli da se izbegnu nehidrodinamički efekti poput hlađenja roja kroz gubitke najenergičnijih elektrona na bočnim zidovima komore usled transverzalne difuzije, koji su rezultate ranijih eksperimenata za određivanje transportnih koeficijenata trećeg reda učinili nepouzdanim.

Proračun transportnih koeficijenata za elektrone u tečnoj fazi se može unaprediti korišćenjem egzaktnih preseka za neelastične sudare u tečnosti, onda kada ti preseci budu određeni. Ovi proračuni mogu biti prošireni uzimanjem u obzir efekata interakcije elektrona sa fluktuacijama gustine pozadinske tečnosti. Jedan od najvažnijih efekata koje bi trebalo uključiti u model je efekat zarobljavanja elektrona u lokalnim oblastima manje gustine. On je naročito značajan za elektrone i/ili pozitrone u polarnim tečnostima, koje su od posebnog značaja u plazma medicini i radijacionoj fizici. U kontekstu istraživanja prikazanih u ovoj disertaciji, efekat zarobljavanja elektrona je od velike važnosti za tečni helijum i tečni neon, imajući u vidu da ovaj efekat vodi ka lokalizovanim stanjima elektrona, što ima za posledicu smanjenje mobilnosti elektrona u odnosu na gasnu fazu. Još jedan od mogućih budućih pravaca istraživanja tiče se razmatranja transporta elektrona u kombinovanim električnim i magnetskim poljima u tečnom argonu i tečnom ksenonu. Ova istraživanja su od naročitog značaja za budući razvoj, dizajn i optimizaciju detektora čestica koje slabo interaguju sa materijom kao što su neutrini i slabo-interagujuće masivne čestice tamne materije.

Fluidno modelovanje strimera u tečnoj fazi se može unaprediti razvojem sofisticiranih fluidnih modela višeg reda. U ovim se modelima makroskopske osobine strimerske plazme mogu odrediti na osnovu numeričkog rešenja sistema diferencijalnih jednačina koje reprezentuju jednačine balansa za koncentraciju naelektrisanih čestica, impuls, srednju energiju i ukoliko je potrebno, za energijski fluks. Ovaj sistem fluidnih jednačina se može zatvoriti aproksimacijom lokalne srednje energije, prema kojoj je neophodno odrediti kolizione frekvence za sve relevantne sudarne procese u funkciji srednje energije. Ovako koncipiran model mogao bi biti upotrebljen

za proveru nelokalnih efekata, ne samo u oblastima na frontu strimera, već i u strimerskom ka-
nalu gde je spoljašnje električno polje ekranirano električnim poljem prostornog naelektrisanja.
Razvoj dvodimenzionalnih modela sa manjim brojem slobodnih parametara u odnosu na jed-
nodimenzionalne modele omogućio bi precizniji opis električnog polja i proučavanje inicijalnog
formiranja strimera u realnim geometrijama. Trodimenzionalni fluidni modeli bi omogućili pro-
učavanje efekta bifurkacije odnosno grananja strimera (eng. *branching*), kao i dinamiku strimera
u električnom i magnetskom polju.

A Metod grupnih projektora

Struktura transportnih koeficijenata se može odrediti primenom teorije grupa, pošto je njihova struktura određena simetrijom sistema. Razmatrani sistem se sastoji iz roja naelektrisanih čestica, neutralnog pozadinskog fluida i spoljašnjeg električnog i magnetskog polja. Grupa simetrije sistema je grupa svih transformacija u odnosu na koje je sistem invarijantan [167, 168]. Grupe simetrije električnog i magnetskog polja su $C_{\infty V}$ i $C_{\infty h}$ respektivno, zbog toga što je električno polje polarni vektor, a magnetsko polje je aksijalni vektor. Ovo su grupe simetrije nepokretne kupe i rotirajućeg cilindra, respektivno [172]. Kada su električno i magnetsko polje prisutni u sistemu, grupa simetrije sistema je određena grupom simetrije konfiguracije spoljašnjih polja. Grupa simetrije paralelne konfiguracije polja je C_∞. Ovo je grupa simetrije rotirajuće kupe [172]. Grupa simetrije ortogonalne konfiguracije polja je C_{1V}, dok je grupa simetrije konfiguracije polja u kojoj električno i magnetsko polje zaklapaju proizvoljan ugao C_1. Pozadinski fluid je invarijantan u odnosu na sve transformacije iz ortogonalne grupe $O(3)$. Ovo je grupa simetrije sfere. Na osnovu toga je grupa simetrije konfiguracije polja ujedno i grupa simetrije celog razmatranog sistema.

Struktura tenzora se može odrediti na osnovu njegove invarijantnosti na operacije iz grupe simetrije sistema. Delovanje grupe G na vektore iz vrektorskog prostora H je reprezentovano grupnim homomorfizmom iz G u generalnu linearnu grupu na H, $GL(H)$ [168, 171]. Polarni vektori, poput brzine drifta, transformišu se na osnovu polarno vektorske reprezentacije grupe simetrije sistema $D^{pv}(G)$ [168, 171]. Ova reprezentacija je reducibilna i za konačne i kompaktne grupe može se razložiti na ireducibilne komponente od $D^{(\mu)}(G)$ kao [168, 170, 171]

$$D^{pv}(G) = \oplus_{\mu=1}^{r} a_\mu D^{(\mu)}(G).$$ (A.1)

Ovde je a_μ broj pojavljivanja ireducibilne reprezentacije $D^{(\mu)}(G)$ pri razlaganju $D^{pv}(G)$, dok je r broj neekvivalentnih ireducibilnih reprezentacija grupe G. Pored toga, za razložive reprezentacie postoji simetrijski adaptirani bazis [170, 171], koji zadovaljava jednačinu

$$D^{pv}(G)|\mu t_\mu m\rangle = \sum_{n=1}^{|\mu|} D_{nm}^{(\mu)}(G)|\mu t_\mu n\rangle.$$ (A.2)

Iz svega prethodnosg sledi da za svaku ireducibilnu reprezentaciju $D^{(\mu)}(G)$ iz jednačine (A.1) postoji potprostor u H koji se transformiše na osnovu reprezentacije $D^{(\mu)}(G)$ [170, 171]. Vrlo značajna reprezentacija, koja postoji za svaku grupu G je trivijalna ireducibilna reprezentacija A_0. Ona se definiše kao $D^{(A_0)}(g) = 1, \forall g \in G$, i ireducibilna je s obzirom na to da je jednodimenziona [171]. Može se videti iz jednačine (A.2) da je vektor invarijantan na delovanje $D^{(pv)}(G)$ ako pripada invarijantnom potprostoru koji odgovara trivijalnoj ireducibilnoj reprezentaciji. Ovaj invarijantan potprostor se može odrediti primenom grupnih projektora. U slučaju trivijalne reprezentacije, grupni projektor se određuje kao [170, 171]:

$$P^{(A_0)}(D^{pv}, G) = \frac{1}{|G|} \sum_{g \in G} D^{pv}(g),$$ (A.3)

za konačne grupe, gde je $|G|$ red grupe G [168, 170, 171]. Za jednoparametarske Lijeve grupe je grupni projektor na invarijantni potprostor koji odgovara trivijalnoj ireducibilnoj reprezentaciji A_0 dat u vidu jednačine [170, 171]:

$$P^{(A_0)}\left(D^{pv}, G\right) = \sum_R \int D^{pv}\left(R\right) dR. \tag{A.4}$$

Dok se sumiranje ovde vrši po svim komponentama povezanosti grupe, integracija se dešava u domenu parametra grupe [170, 171]. Svaki vektor iz invarijantnog potprostora $D^{pv}\left(G\right)$ koji odgovara trivijalnoj reprezentaciji jeste linearna kombinacija svojstvenih vektora grupnog projektora $P^{(A_0)}\left(D^{pv}, G\right)$. Difuzioni tenzor je linearni operator koji preslikava vektor lokalnog gradijenta gustine $\nabla n\left(\mathbf{r}, t\right)$ u vektor difuzionog fluksa. Na osnovu toga difuzioni tenzor pripada invarijantnom potprostoru grupnog projektora $P^{(A_0)}\left(D^{pv^{\otimes 2}}, G\right)$ gde $D^{pv^{\otimes 2}}\left(G\right)$ reprezentuje $D^{pv} \otimes D^{pv}\left(G\right) = D^{pv}\left(G\right) \otimes D^{pv}\left(G\right)$. Nalik tome transportni tenzor trećeg reda preslikava tenzorski kvadrat gradijenta koji deluje na lokalnu koncentraciju čestica roja $\nabla \otimes \nabla n\left(\mathbf{r}, t\right)$ na vektor difuzionog fluksa višeg reda. Na osnovu toga transportni tenzor trećeg reda pripada invarijantnom potprostoru grupnog projektora $P^{(A_0)}\left(D^{pv} \otimes \left[D^{pv}\right]^2, G\right)$, gde $\left[D^{pv}\right]^2$ reprezentuje simetrizovani tenzorski kvadrat polarno vektorske reprezentacije. Ova simetrizacija je posledica komutiranja gradijenata.

Strogo govoreći, delovanje grupe na operatore, poput difuzionog tenzora i transportnog tenzora trećeg reda, reprezentovano je primenom grupnih superoperatora [169]. Oni su definisani kao $\widehat{\widehat{D}}\left(g\right)\hat{A} = D^{pv}\left(g\right)\hat{A}D^{pv}\left(g^{-1}\right)$. Na osnovu toga bi pravolinijska primena teorije grupa zahtevala primenu grupnih superoperatora. Međutim, ovo nije neophodno zbog toga što je svaki bazisni operator ranga dva $|i\rangle \otimes \langle j|$, koji deluje u vektorskom prostoru H bijektivno povezan sa bazisnim vektorom $|i\rangle \otimes |j\rangle$ iz vektorskog prostora $H \otimes H$. Isto važi i za bazisne operatore ranga 3 $|i\rangle \otimes \left[\langle j| \otimes \langle k|\right]$ i bazisne vektore $|i\rangle \otimes \left[|j\rangle \otimes |k\rangle\right]$ iz vektorskog prostora $H \otimes \left[H \otimes H\right]$. Ovde ugaone zagrade reprezentuju simetrizaciju tenzorskog proizvoda. Ovo znači da se metod grupnih projektora može primeniti na reprezentacije $D^{pv}\left(G\right) \otimes D^{pv}\left(G\right)$ i $D^{pv} \otimes \left[D^{pv}\right]^2$ u odgovarajućim vektorskim prostorima. Onda se svojstveni vektori grupnih projektora mogu preslikati u odgovarajuće bazisne tenzore. Na tim su osnovama difuzioni tenzor i transportni tenzor trećeg reda linearne kombinacije bazisnih tenzora, koji su određeni na osnovu svojstvenih vektora grupnih projektora $P^{(A_0)}\left(D^{pv} \otimes D^{pv}, G\right)$ i $P^{(A_0)}\left(D^{pv} \otimes \left[D^{pv}\right]^2, G\right)$, respektivno. Pored toga, nije neophodno korišćenje reprezentacije $D^{pv} \otimes \left[D^{pv}\right]^2$ ne bi li se odredila struktura transportnog tenzora trećeg reda. Umesto toga može se koristiti reprezentacija $D^{pv} \otimes D^{pv} \otimes D^{pv}$, te da se rezultujući tenzori simetrizuju po poslednja dva indeksa.

B Eksplicitni izrazi za izračunavanje pojedinačnih komponenti transportnog tenzora trećeg reda na osnovu kinetičke teorije za rešavanje Boltzmann-ove jednačine

Primenom simetrija momenata funkcije raspodele $F(\nu lm|s\lambda\mu)$, koje su razmatrali White i saradnici [89], mogu se odrediti odgovarajuće simetrije pojedinačnih komponenti transportnog tenzora trećeg reda, koje su prikazane u Tabeli 1. Strukturu ovog tenzora moguće je odrediti na osnovu simetrija prikazanih u Tabli 1 i odgovarajućih fizičkih argumenata koji se odnose na flukseve naelektrisanih čestica, a koje se kreću pod uticajem magnetskog polja. Ovi fizički argumenti su neophodni kako bi se ustanovilo da su za datu konfiguraciju polja određene komponente transportnog tenzora trećeg reda jednake nuli, a onda i to da su određene komponente međusobno jednake. Slična procedura je bila primenjena za vektorske i tenzorske transportne koeficijente nižeg reda [89].

Tabela 1: Simetrije pojedinačnih komponenti transportnog tenzora trećeg reda. Prikazane transformacije reprezentuju A (prostornu inverziju), B (rotaciju za π oko z-ose), C (prostornu inverziju i rotaciju za π oko y-ose), i D (prostornu inverziju i rotaciju za π oko x-ose).

| Komponenta | Transformacija | | | |
	$\mathbf{E} \to -\mathbf{E}$	$B_y \to -B_y$	$B_z \to -B_z$	$\mathbf{B} \to -\mathbf{B}$
Q_{xxz}, Q_{xzx}	$-Q_{xxz}, -Q_{xzx}$	Q_{xxz}, Q_{xzx}	Q_{xxz}, Q_{xzx}	Q_{xxz}, Q_{xzx}
Q_{yyz}, Q_{yzy}	$-Q_{yyz}, -Q_{yzy}$	Q_{yyz}, Q_{yzy}	Q_{yyz}, Q_{yzy}	Q_{yyz}, Q_{yzy}
Q_{zxx}	$-Q_{zxx}$	Q_{zxx}	Q_{zxx}	Q_{zxx}
Q_{zyy}	$-Q_{zyy}$	Q_{zyy}	Q_{zyy}	Q_{zyy}
Q_{zzz}	$-Q_{zzz}$	Q_{zzz}	Q_{zzz}	Q_{zzz}
Q_{xxx}	$-Q_{xxx}$	$-Q_{xxx}$	Q_{xxx}	$-Q_{xxx}$
Q_{xyy}	$-Q_{xyy}$	$-Q_{xyy}$	Q_{xyy}	$-Q_{xyy}$
Q_{xzz}	$-Q_{xzz}$	$-Q_{xzz}$	Q_{xzz}	$-Q_{xyy}$
Q_{yxy}, Q_{yyx}	$-Q_{yxy}, -Q_{yyx}$	$-Q_{yxy}, -Q_{yyx}$	Q_{yxy}, Q_{yyx}	$-Q_{yxy}, -Q_{yyx}$
Q_{zxz}, Q_{zzx}	$-Q_{zxz}, -Q_{zzx}$	$-Q_{zxz}, -Q_{zzx}$	Q_{zxz}, Q_{zzx}	$-Q_{zxz}, -Q_{zzx}$
Q_{xyz}, Q_{xzy}	$-Q_{xyz}, -Q_{xzy}$	Q_{xyz}, Q_{xzy}	$-Q_{xyz}, -Q_{xzy}$	$-Q_{xyz}, -Q_{xzy}$
Q_{yxz}, Q_{yzx}	$-Q_{yxz}, -Q_{yzx}$	Q_{yxz}, Q_{yzx}	$-Q_{yxz}, -Q_{yzx}$	$-Q_{yxz}, -Q_{yzx}$
Q_{zxy}, Q_{zyx}	$-Q_{zxy}, -Q_{zyx}$	Q_{zxy}, Q_{zyx}	$-Q_{zxy}, -Q_{zyx}$	$-Q_{zxy}, -Q_{zyx}$
Q_{xxy}, Q_{xyx}	$-Q_{xxy}, -Q_{xyx}$	$-Q_{xxy}, -Q_{xyx}$	$-Q_{xxy}, -Q_{xyx}$	Q_{xxy}, Q_{xyx}
Q_{yxx}	$-Q_{yxx}$	$-Q_{yxx}$	$-Q_{yxx}$	Q_{yxx}
Q_{yyy}	$-Q_{yyy}$	$-Q_{yyy}$	$-Q_{yyy}$	Q_{yyy}
Q_{yzz}	$-Q_{yzz}$	$-Q_{yzz}$	$-Q_{yzz}$	Q_{yzz}
Q_{zyz}, Q_{zzy}	$-Q_{zyz}, -Q_{zzy}$	$-Q_{zyz}, -Q_{zzy}$	$-Q_{zyz}, -Q_{zzy}$	Q_{zyz}, Q_{zzy}

U ovom dodatku su prikazani eksplicitni izrazi za pojedinačne komponente fluks transportnog tenzora trećeg reda. Oni su izvedeni na osnovu razvoja fluksa brzine čestica po Burnett-ovim

funkcijama i gradijentima koncentracije, a razvoj je prikazan u jednačini (3.34). Eksplicitni izrazi za diferencijalni operator $G_\mu^{(s\lambda)}$, koji figuriše u ovoj jednačini, dati su u Tabeli 2 [62]. U sledećim izrazima je α izostavljeno iz argumenta momenata F zbog kompaktnosti.

Tabela 2: Eksplicitni izrazi za komponente diferencijalnog operatora $G_\mu^{(s\lambda)}$.

s	λ	μ	$G_\mu^{(s\lambda)}$
0	0	0	1
1	1	0	$-i\partial_z$
1	1	± 1	$\frac{1}{\sqrt{2}}(\pm i\partial_x + \partial_y)$
2	0	0	$\frac{1}{\sqrt{3}}\nabla^2$
2	2	0	$\sqrt{\frac{2}{3}}\left(\frac{1}{2}(\partial_x^2 + \partial_y^2) - \partial_z^2\right)$
2	2	± 1	$(\pm\partial_x - i\partial_y)\partial_z$
2	2	± 2	$\frac{1}{2}(\pm i\partial_x + \partial_y)^2$

Za paralelnu konfiguraciju električnog i magnetskog polja pojedinačne komponente fluks transportnog tenzora trećeg reda date su u obliku izraza:

$$Q_{xxz} = \frac{1}{\sqrt{2}\alpha}\bigg(\text{Im}(F(011|221)) - \text{Im}(F(01-1|221))\bigg), \tag{B.1}$$

$$Q_{xyz} = \frac{1}{\sqrt{2}\alpha}\bigg(\text{Re}(F(01-1|221)) - \text{Re}(F(011|221))\bigg), \tag{B.2}$$

$$Q_{zxx} = -\frac{1}{\alpha}\bigg(\frac{1}{\sqrt{3}}\text{Im}(F(010|200)) + \frac{1}{\sqrt{6}}\text{Im}(F(010|220))\bigg) + $$
$$\frac{1}{\alpha}\text{Im}(F(010|222)), \tag{B.3}$$

$$Q_{zzz} = \frac{1}{\alpha}\bigg(\sqrt{\frac{2}{3}}\text{Im}(F(010|220)) - \frac{1}{\sqrt{3}}\text{Im}(F(010|200))\bigg). \tag{B.4}$$

Za ortogonalnu konfiguraciju električnog i magnetskog polja pojedinačne komponente fluks transportnog tenzora trećeg reda su date u vidu izraza:

$$Q_{xxx} = \frac{\sqrt{2}}{\alpha}\bigg(\frac{1}{\sqrt{3}}\text{Im}(F(011|200)) + \frac{1}{\sqrt{6}}\text{Im}(F(011|220))\bigg) + $$
$$\frac{1}{\sqrt{2}\alpha}\bigg(-\text{Im}(F(011|222)) + \text{Im}(F(01-1|222))\bigg), \tag{B.5}$$

$$Q_{xyy} = \frac{\sqrt{2}}{\alpha}\bigg(\frac{1}{\sqrt{3}}\text{Im}(F(011|200)) + \frac{1}{\sqrt{6}}\text{Im}(F(011|220))\bigg) + $$
$$\frac{1}{\sqrt{2}\alpha}\bigg(\text{Im}(F(011|222)) - \text{Im}(F(01-1|222))\bigg), \tag{B.6}$$

$$Q_{xzz} = \frac{\sqrt{2}}{\alpha} \left(\frac{1}{\sqrt{3}} \mathrm{Im}(F(011|200)) - \sqrt{\frac{2}{3}} \mathrm{Im}(F(011|220)) \right), \tag{B.7}$$

$$Q_{xxz} = \frac{1}{\sqrt{2}\alpha(t)} \left(\mathrm{Im}(F(011|221)) - \mathrm{Im}(F(01-1|221)) \right), \tag{B.8}$$

$$Q_{yxy} = -\frac{1}{\sqrt{2}\alpha} \left(\mathrm{Im}(F(011|222)) + \mathrm{Im}(F(01-1|222)) \right), \tag{B.9}$$

$$Q_{yyz} = \frac{1}{\sqrt{2}\alpha} \left(\mathrm{Im}(F(011|221)) + \mathrm{Im}(F(01-1|221)) \right), \tag{B.10}$$

$$Q_{zxz} = -\frac{1}{\alpha} \mathrm{Im}(F(010|221)), \tag{B.11}$$

$$Q_{zxx} = -\frac{1}{\alpha} \left(\frac{1}{\sqrt{3}} \mathrm{Im}(F(010|200)) + \frac{1}{\sqrt{6}} \mathrm{Im}(F(010|220)) \right) +$$
$$\frac{1}{\alpha} \mathrm{Im}(F(010|222)), \tag{B.12}$$

$$Q_{zyy} = -\frac{1}{\alpha} \left(\frac{1}{\sqrt{3}} \mathrm{Im}(F(010|200) + \frac{1}{\sqrt{6}} \mathrm{Im}(F(010|220)) \right) -$$
$$\frac{1}{\alpha} \mathrm{Im}(F(010|222)), \tag{B.13}$$

$$Q_{zzz} = \frac{1}{\alpha} \left(\sqrt{\frac{2}{3}} \mathrm{Im}(F(010|220)) - \frac{1}{\sqrt{3}} \mathrm{Im}(F(010|200)) \right). \tag{B.14}$$

Kada su električno i magnetsko polje ukršteni pod proizvoljnim uglom između 0 i π, pojedinačne komponente fluks transportnog tenzora trećeg reda su date u obliku:

$$Q_{xxy} = \frac{1}{\sqrt{2}\alpha} \left(\mathrm{Re}(F(011|222)) - \mathrm{Re}(F(01-1|222)) \right), \tag{B.15}$$

$$Q_{yxx} = \frac{\sqrt{2}}{\alpha} \left(\frac{1}{\sqrt{3}} \mathrm{Re}(F(011|200)) + \frac{1}{\sqrt{6}} \mathrm{Re}(F(011|220)) \right) +$$
$$\frac{1}{\sqrt{2}\alpha} \left(-\mathrm{Re}(F(011|222)) - \mathrm{Re}(F(01-1|222)) \right), \tag{B.16}$$

$$Q_{yyy} = \frac{\sqrt{2}}{\alpha} \left(\frac{1}{\sqrt{3}} \mathrm{Re}(F(011|200)) + \frac{1}{\sqrt{6}} \mathrm{Re}(F(011|220)) \right) +$$
$$\frac{1}{\sqrt{2}\alpha} \left(\mathrm{Re}(F(011|222)) + \mathrm{Re}(F(01-1|222)) \right), \tag{B.17}$$

$$Q_{yzz} = \frac{\sqrt{2}}{\alpha} \left(\frac{1}{\sqrt{3}} \mathrm{Re}(F(011|200)) - \sqrt{\frac{2}{3}} \mathrm{Re}(F(011|220)) \right), \tag{B.18}$$

$$Q_{zxy} = -\frac{1}{\alpha} \mathrm{Re}(F(010|222)), \tag{B.19}$$

$$Q_{zyz} = \frac{1}{\alpha} \mathrm{Re}(F(010|221)), \tag{B.20}$$

$$Q_{xyz} = \frac{1}{\sqrt{2}\alpha} \left(\mathrm{Re}(F(01-1|221)) - \mathrm{Re}(F(011|221)) \right), \tag{B.21}$$

$$Q_{yxz} = \frac{1}{\sqrt{2}\alpha} \left(\mathrm{Re}(F(011|221)) + \mathrm{Re}(F(01-1|221)) \right). \tag{B.22}$$

Komponente transportnog tenzora trećeg reda, koje su međusobno nezavisne u ortogonalnoj konfiguraciji električnog i magnetskog polja, takođe su nezavisne i u konfiguraciji u kojoj su

ova polja ukrštena pod proizvoljnim uglom. Zbog toga su odgovarajući izrazi za izračunavanje ovih komponenti u okviru multi term teorije za rešavanje Boltzmann-ove jednačine isti za obe konfiguracije polja.

C Eksplicitni izrazi za izračunavanje transportnih koeficijenata trećeg reda u Monte Carlo simulacijama

U ovom dodatku su prikazani eksplicitni izrazi za izračunavanje komponenti fluks transportnog tenzora trećeg reda u Monte Carlo simulacijama.

Za paralelnu konfiguraciju električnog i magnetskog polja su eksplicitni izrazi za izračunavanje longitudinalne komponente i transverzalne komponente transportnog tenzora trećeg reda isti kao i u odsustvu magnetskog polja. Ovi izrazi su prikazani u jednačinama (3.159) i (3.160). Nije moguće izdvojiti dodatne komponente ovog tenzora primenom Monte Carlo koda, koji je korišćen u ovoj disertaciji, s obzirom na to da se u ovom kodu mogu izračunati samo srednje vrednosti onih komponenti, koje imaju istu kombinaciju indeksa, pri čemu u paralelnoj konfiguraciji polja važi $Q_{xyz} = -Q_{yxz}$ i $Q_{zxy} = 0$.

U ortogonalnoj konfiguraciji polja se mogu izdvojiti dve dijagonalne komponente fluks transportnog tenzora trećeg reda, kao i četiri srednje vrednosti vandijagonalnih komponenti, koje imaju istu kombinaciju indeksa. Pri tome su dijagonalne komponente označene kao:

$$Q_L \equiv Q_{zzz}, \quad Q_{\mathbf{E}\times\mathbf{B}} \equiv Q_{xxx}, \tag{C.1}$$

dok su preostale četiri srednje vrednosti komponenti označene kao:

$$Q_{\pi(xxz)} \equiv \frac{1}{3} \left(Q_{xxz} + Q_{xzx} + Q_{zxx} \right), \tag{C.2}$$

$$Q_{\pi(yyx)} \equiv \frac{1}{3} \left(Q_{yyx} + Q_{yxy} + Q_{xyy} \right) \tag{C.3}$$

$$Q_{\pi(yyz)} \equiv \frac{1}{3} \left(Q_{yyz} + Q_{yzy} + Q_{zyy} \right), \tag{C.4}$$

$$Q_{\pi(zzx)} \equiv \frac{1}{3} \left(Q_{zzx} + Q_{zxz} + Q_{xzz} \right). \tag{C.5}$$

gde vektorski proizvod $\mathbf{E} \times \mathbf{B}$ definiše x-osu, dok $\pi\,(abc)$ označava sve moguće permutacije (a, b, c).

Eksplicitni izrazi za ovih šest veličina su dati u formi jednačina:

$$Q_{zzz} = \frac{1}{6} \left(3\langle z^2 c_z \rangle - 3\langle c_z \rangle\langle z^2 \rangle - 6\langle z \rangle\langle zc_z \rangle + 6\langle z \rangle\langle z \rangle\langle c_z \rangle \right), \tag{C.6}$$

$$Q_{xxx} = \frac{1}{6} \left(3\langle x^2 c_x \rangle - 3\langle c_x \rangle\langle x^2 \rangle - 6\langle x \rangle\langle xc_x \rangle + 6\langle x \rangle\langle x \rangle\langle c_x \rangle \right), \tag{C.7}$$

$$Q_{\pi(zzx)} = \frac{1}{6} \left(\langle z^2 c_x \rangle + 2\langle zxc_z \rangle - 2\langle c_z \rangle\langle zx \rangle - \langle c_x \rangle\langle z^2 \rangle - 2\langle z \rangle\langle xc_z \rangle - \right.$$
$$\left. 2\langle z \rangle\langle zc_x \rangle - 2\langle x \rangle\langle zc_z \rangle + 2\langle c_x \rangle\langle z \rangle\langle z \rangle + 4\langle x \rangle\langle z \rangle\langle c_z \rangle \right), \tag{C.8}$$

$$Q_{\pi(xxz)} = \frac{1}{6} \left(\langle x^2 c_z \rangle + 2\langle xzc_x \rangle - 2\langle c_x \rangle\langle xz \rangle - \langle c_z \rangle\langle x^2 \rangle - 2\langle x \rangle\langle zc_x \rangle - \right.$$
$$\left. 2\langle x \rangle\langle xc_z \rangle - 2\langle z \rangle\langle xc_x \rangle + 2\langle c_z \rangle\langle x \rangle\langle x \rangle + 4\langle z \rangle\langle x \rangle\langle c_x \rangle \right), \tag{C.9}$$

$$Q_{\pi(zyy)} = \frac{1}{6}\left(\langle y^2 c_z\rangle + 2\langle yzc_y\rangle - \langle c_z\rangle\langle y^2\rangle - 2\langle z\rangle\langle yc_y\rangle\right), \tag{C.10}$$

$$Q_{\pi(xyy)} = \frac{1}{6}\left(\langle y^2 c_x\rangle + 2\langle yxc_y\rangle - \langle c_x\rangle\langle y^2\rangle - 2\langle x\rangle\langle yc_y\rangle\right). \tag{C.11}$$

U najopštijem slučaju, kada su električno i magnetsko polje ukršteni pod proizvoljnim uglom između 0 i π, mogu se izdvojiti tri dijagonalne komponente i sedam srednjih vrednosti vandijagonalnih komponenti koje imaju istu kombinaciju indeksa. Prve dve dijagonalne komponente su iste kao i u slučaju ortogonalne konfiguracije polja, dok je treća označena kao:

$$Q_{\mathbf{E}\times(\mathbf{E}\times\mathbf{B})} \equiv Q_{yyy}, \tag{C.12}$$

gde vektorski proizvod $\mathbf{E}\times(\mathbf{E}\times\mathbf{B})$ definiše y-osu. Četiri srednje vrednosti vandijagonalnih komponenti se odnose na iste kombinacije komponenti transportnog tenzora trećeg reda kao i u slučaju ortogonalne konfiguracije polja, dok su preostale tri srednje vrednosti označene kao:

$$Q_{\pi(xxy)} \equiv \frac{1}{3}\left(Q_{xxy} + Q_{xyx} + Q_{yxx}\right), \tag{C.13}$$

$$Q_{\pi(zzy)} \equiv \frac{1}{3}\left(Q_{zzy} + Q_{zyz} + Q_{yzz}\right), \tag{C.14}$$

$$Q_{\pi(xyz)} \equiv \frac{1}{6}\left(Q_{xyz} + Q_{yzx} + Q_{zxy} + Q_{xzy} + Q_{yxz} + Q_{zyx}\right). \tag{C.15}$$

Eksplicitni izrazi za ove veličine su dati kroz jednačine:

$$Q_{yyy} = \frac{1}{6}\left(3\langle y^2 c_y\rangle - 3\langle c_y\rangle\langle y^2\rangle - 6\langle y\rangle\langle yc_y\rangle + 6\langle y\rangle\langle y\rangle\langle c_y\rangle\right), \tag{C.16}$$

$$\begin{aligned}
Q_{\pi(xyz)} = \frac{1}{6}\big(&\langle yzc_x\rangle + \langle xzc_y\rangle + \langle xyc_z\rangle - \langle c_x\rangle\langle yz\rangle - \langle x\rangle\langle zc_y\rangle - \langle x\rangle\langle yc_z\rangle - \\
&\langle c_y\rangle\langle xz\rangle - \langle y\rangle\langle zc_x\rangle - \langle y\rangle\langle xc_z\rangle - \langle c_z\rangle\langle xy\rangle - \langle z\rangle\langle yc_x\rangle - \langle z\rangle\langle xc_y\rangle + \\
&2\langle c_x\rangle\langle y\rangle\langle z\rangle + 2\langle c_y\rangle\langle x\rangle\langle z\rangle + 2\langle c_z\rangle\langle y\rangle\langle x\rangle\big),
\end{aligned} \tag{C.17}$$

$$\begin{aligned}
Q_{\pi(yxx)} = \frac{1}{6}\big(&\langle x^2 c_y\rangle + 2\langle yxc_x\rangle - 2\langle c_x\rangle\langle yx\rangle - \langle c_y\rangle\langle x^2\rangle - 2\langle x\rangle\langle yc_x\rangle - 2\langle x\rangle\langle xc_y\rangle - \\
&2\langle y\rangle\langle xc_x\rangle + 2\langle c_y\rangle\langle x\rangle\langle x\rangle + 4\langle y\rangle\langle x\rangle\langle c_x\rangle\big),
\end{aligned} \tag{C.18}$$

$$\begin{aligned}
Q_{\pi(yzz)} = \frac{1}{6}\big(&\langle z^2 c_y\rangle + 2\langle yzc_z\rangle - 2\langle c_z\rangle\langle yz\rangle - \langle c_y\rangle\langle z^2\rangle - 2\langle z\rangle\langle yc_z\rangle - 2\langle z\rangle\langle zc_y\rangle - \\
&2\langle y\rangle\langle zc_z\rangle + 2\langle c_y\rangle\langle z\rangle\langle z\rangle + 4\langle y\rangle\langle z\rangle\langle c_z\rangle\big),
\end{aligned} \tag{C.19}$$

$$\begin{aligned}
Q_{zyy} = \frac{1}{6}\big(&\langle y^2 c_z\rangle + 2\langle yzc_y\rangle - 2\langle c_y\rangle\langle yz\rangle - \langle c_z\rangle\langle y^2\rangle - 2\langle y\rangle\langle zc_y\rangle - 2\langle y\rangle\langle yc_z\rangle - \\
&2\langle z\rangle\langle yc_y\rangle + 2\langle c_z\rangle\langle y\rangle\langle y\rangle + 4\langle z\rangle\langle y\rangle\langle c_y\rangle\big),
\end{aligned} \tag{C.20}$$

$$\begin{aligned}
Q_{\pi(zyy)} = \frac{1}{6}\big(&\langle y^2 c_x\rangle + 2\langle yxc_y\rangle - 2\langle c_y\rangle\langle yx\rangle - \langle c_x\rangle\langle y^2\rangle - 2\langle y\rangle\langle xc_y\rangle - 2\langle y\rangle\langle yc_x\rangle - \\
&2\langle x\rangle\langle yc_y\rangle + 2\langle c_x\rangle\langle y\rangle\langle y\rangle + 4\langle x\rangle\langle y\rangle\langle c_y\rangle\big),
\end{aligned} \tag{C.21}$$

$$\begin{aligned}
Q_{\pi(zzx)} = \frac{1}{6}\big(&\langle z^2 c_x\rangle + 2\langle zxc_z\rangle - 2\langle c_z\rangle\langle zx\rangle - \langle c_x\rangle\langle z^2\rangle - 2\langle z\rangle\langle xc_z\rangle - \\
&2\langle z\rangle\langle zc_x\rangle - 2\langle x\rangle\langle zc_z\rangle + 2\langle c_x\rangle\langle z\rangle\langle z\rangle + 4\langle x\rangle\langle z\rangle\langle c_z\rangle\big),
\end{aligned} \tag{C.22}$$

$$Q_{\pi(xxz)} = \frac{1}{6}\big(\langle x^2 c_z\rangle + 2\langle xzc_x\rangle - 2\langle c_x\rangle\langle xz\rangle - \langle c_z\rangle\langle x^2\rangle - 2\langle x\rangle\langle zc_x\rangle -$$

$$2\langle x\rangle\langle xc_z\rangle - 2\langle z\rangle\langle xc_x\rangle + 2\langle c_z\rangle\langle x\rangle\langle x\rangle + 4\langle z\rangle\langle x\rangle\langle c_x\rangle\big). \tag{C.23}$$

Bitno je naglasiti da eksplicitni izrazi za izračunavanje transportnih koeficijenata trećeg reda u Monte Carlo simulacijama nisu isti u različitim konfiguracijama polja. Ovo je posledica toga što su srednje vrednosti nekih monoma koordinata i brzina jednaki nuli na osnovu simetrije u odsustvu magnetskog polja, kao i u konfiguraciji u kojoj su ova polja paralelna ili ukrštena pod pravim uglom. Zato su u tim konfiguracijama polja korišćeni jednostavniji izrazi za transportne koeficijente trećeg reda, u kojima su uzeti u obzir samo oni monomi koji imaju nenultu vrednost u datoj konfiguraciji polja.

D   Literatura

[1] A. V. Phelps, *Rev. Mod. Phys.* **40**, (1968) 399.

[2] R. W. Crompton, *Adv. At., Mol., Opt. Phys.* **32**, (1994) 97.

[3] L. G. H. Huxley i R. W. Crompton, *The Diffusion and Drift of Electrons in Gases* (Wiley, London, 1974).

[4] Z.Lj. Petrović, M. šuvakov, ž. Nikitović, S. Dujko, O. šašić, J. Jovanović, G. Malović i V. Stojanović, *Plasma Sources Sci. Technol.* **16**, (2007) S1-S12.

[5] R. E. Robson, *Phys. Rev. E* **61**, (2000) 848.

[6] D. R. A. McMahon i R. W. Crompton, *J. Chem. Phys.* **78**, (1983) 603.

[7] Jr. J. H. Parker i J. J. Lowke, *Phys. Rev.* **181**, (1969) 290.

[8] H. R. Skullerud, *J. Phys. B: At. Mol. Opt. Phy.* **2**, (1969) 696.

[9] R. D. White, R. E. Robson i K. F. Ness, *Aust. J. Phys.* **48**, (1995) 925.

[10] K. Maeda, T. Makabe, N. Nakano, S. Bzenić i Z. Lj. Petrović, *Phys. Rev. E* **55**, (1997) 5901.

[11] R. E. Robson, *Aust. J. Phys.* **44**, (1991) 685.

[12] A. Garscadden, G. A. Duke i W. F. Bailey, *Bull. Am. Phys. Soc.* **26U**, (1980) 724.

[13] Z. Lj. Petrović, R. W. Crompton i G. N. Haddad, *Aust. J. Phys.* **37**, (1984) 23.

[14] R. E. Robson, *Aust. J. Phys.* **37**, (1984) 35.

[15] S. B. Vrhovac i Z. Lj. Petrović, *Phys. Rev. E* **53**, (1996) 4012.

[16] D. R. A. McMahon i B. Shizgal, *Phys. Rev. A* **31**, (1985) 1894.

[17] J. M. Warman, U. Sowada i M. P. De Hass, *Phys. Rev. A* **31**, (1985) 1974.

[18] N. A. Dyatko, A. P. Napartovich, S. Sakadžić, Z. Lj. Petrović i Z. Raspopović, *J. Phys. D: Appl. Phys.* **33**, (2000) 375.

[19] Z. Raspopović, S. Sakadžić, Z. Lj. Petrović i T. Makabe, *J. Phys. D: Appl. Phys.* **33**, (2000) 1298.

[20] R. D. White, S. Dujko, K. F. Ness, R. E. Robson, Z. Raspopović i Z. Lj. Petrović, *J. Phys. D: Appl. Phys.* **41**, (2008) 025206.

[21] B. Shizgal i D. R. A. MacMahon, *Phys. Rev. A* **32**, (1985) 3669.

[22] N. A. Dyatko, M. Capitelli, S. Longo i A. P. Napartovich, *Plasma Phys. Rept.* **24**, (1998) 745.

[23] N. A. Dyatko, A. P. Napartovich, Z. Lj. Petrović, Z. R. Raspopović i S. Sakadžić, *J. Phys. D: Appl. Phys.* **33**, (2000) 375.

[24] N. A. Dyatko, D. Loffhagen, A. P. Napartovich i R. Winkler, *Plasma Chem. Plasma Process.* **21**, (2001) 421.

[25] R.D. White, R.E. Robson i K.F. Ness, *Australian Journal of Physics* **48** (1995) 925.

[26] T. Makabe i Z.Lj. Petrović, *Plasma Electronics: Applications in Microelectronic Device Fabrication* (New York, CRC Press, 2014).

[27] D. Bošnjakovic, Doktorska disertacija, Elektrotehnički fakultet, Univerzitet u Beogradu, Srbija (2016).

[28] D. Bošnjakovic, Z. Lj. Petrovic, S. Dujko, *J. Instrum.* **9**, (2014) P09012.

[29] D. Bošnjakovic, Z. Lj. Petrovic, R. D. White, S. Dujko, *J. Phys. D: Appl. Phys.* **47**, (2014) 435203.

[30] D. Bošnjaković, Z. Lj. Petrović i S. Dujko, *J. Phys. D: Appl. Phys.* **49**, (2016) 405201.

[31] S. Dujko, R.D. White i Z.Lj. Petrović, *J. Phys. D: Appl. Phys.* **41**, (2008) 245205.

[32] K. Kondo i H. Tagashira, *J. Phys. D: Appl. Phys.* **23**, (1990) 1175.

[33] H. Date, K. Kondo i H. Tagashira, *J. Phys. D: Appl. Phys.* **23**, (1990) 1384.

[34] D. Uhrlandt, R. Bussiahn, S. Gorchakov, H. Lange, D. Loffhagen i D. Nötzold, *Journal of Physics D: Applied Physics* **38**, (2005) 3318.

[35] M. L. Bortz i R. H. French, *Appl. Phys. Lett.* **55**, (1989) 1955.

[36] Z. Wu, N. Xanthopoulos, F. Reymond, J. S. Rossier, H. H. Girault, *Electrophoresis*, **23**, (2002) 782.

[37] Z. Hao, H. Chen, X. Zhu, J. Li, C. Liu, *Journal of Chromatography A*, **1209**, (2008) 246.

[38] S. Xu, J. Long, L. Sim, C. H. Diong i K. Ostrikov, *Plasma Processes Polym.*, **2**, (2005) 373.

[39] P. Brault, A. Caillard, A. L. Thomann, J. Mathias, C. Charles, R. W. Boswell, S. Escribano, J. Durand i T. Sauvage, *Journal of Physics D: Applied Physics*, **37**, (2004) 3419.

[40] A. Fridman i G. Friedman *Plasma Medicine*, (John Wiley & Sons, 2012 ISBN 1118437659, 9781118437650).

[41] M. G. Kong, G. Kroesen, G. Morfill, T. Nosenko, T. Shimizu, J. van Djik i J. L. Zimmermann *New J. Phys.* **11**, (2009) 115012.

[42] N. Puač, M. Gherardi i M. Shiratani, *Plasma Process Polym.* **15**, (2018) e1700174.

[43] M. Ito, T. Ohta i M. Hori, *Journal of the Korean Physical Society* **60**, (2012) 937.

[44] B. Jiang, J. Zheng, S. Qiu, M. Wu, Q. Zhang, Z. Yan i Q. Xue, *Chemical Engineering Journal* **236**, (2014) 348.

[45] M. A. Malik, A. Ghaffar i S. A. Malik, *Plasma Sources Sci. Technol.* **10** (2001) 82.

[46] T. Makabe i K. Maeshige, *Appl. Surf. Sci.* **192**, (2002) 176.

[47] S. Dujko, Doktorska disertacija, James Cook University, Australia (2009).

[48] E. T. Meier i U. Shumlak, *Physics of Plasmas* **19**, (2012) 072508.

[49] P. C. Huang, J. Hebeylein i E. Pfender, *Plasma Chemistry and Plasma Processing*, **15**, (1995) 25.

[50] L. Shenggang, R. J. Barker, Z. Dajun, Y. Yung i G. Hong, *IEEE Transactions on Plasma Science*, **28**, (2000) 2135.

[51] I. H. Hutchinson, *The Physics of Fluids* **30**, (1987) 3777.

[52] R. Robson, R. White i M. Hildebrandt, *Fundamentals of Charged Particle Transport in Gases and Condensed Matter* (Boca Raton, CRC Press, 2018).

[53] V. Vahedi, G. DiPeso, C. K. Birdsal, M. A. Lieberman i T. D. Rognlien, *Plasma Sources Sci. Technol.* **2**, (1993) 261.

[54] F. H. Harlow, A. A. Amsden, J. R. Nix, *Journal of Computational Physics*, **20**, (1976) 119.

[55] M. J. Andrews i P. J. O'Rourke, *International Journal of Multiphase Flow*, **22**, (1996) 379.

[56] G. Joyce, M. Lampe, S. P. Slinker, W. M. Manheimer, *Journal of Computational Physics*, **138**, (1997) 540.

[57] A. Bogaerts i R. Gijbels, *Journal of Applied Physics* **78**, (1995) 2233.

[58] Z. Donkó, *Phys. Rev. E*, **57**, (1998) 7126.

[59] Z. Donkó, *Journal of Applied Physics* **88**, (2000) 2226.

[60] K. Kutasi i Z. Donkó, *Journal of Physics D: Applied Physics* **33**, (2000) 1081.

[61] G. K. M. Rao, G. Rangajanardhaa, D. H. Rao, M. S. Rao, *Journal of Materials Processing Technology* **209**, (2009) 1512.

[62] R. E. Robson i K. F. Ness, *Phys. Rev. A* **33**, (1986) 2068.

[63] U. Kortshagen, *J. Phys. D: Appl. Phys.* **26**, (1993) 1691

[64] C. Busch i U. Kortshagen, *Phys. Rev. E* **51**, (1995) 280

[65] U. Kortshagen, C. Busch i L. D. Tsendin, *Plasma Sources Sci. Technol.* **5**, (1996) 1

[66] L. Boltzmann, *Wien. Ber.* **66**, (1872) 275.

[67] S. Dujko, R. D. White, Z. Lj. Petrović i R. E. Robson, *Phys. Rev. E* **81**, (2010) 046403.

[68] G. J. Boyle, R. P. McEachran, D. G. Cocks i R. D. White, *The Journal of Chemical Physics* **142**, (2015) 154507.

[69] G. J. Boyle, R. P. McEachran, D. G. Cocks, M. J. Brunger, S. J. Buckman, S. Dujko i R. D. White, *J. Phys. D: Appl. Phys.* **49** (2016) 355201.

[70] M. H. Cohen i J. Lekner, *Phys. Rev.* **158** (1967) 305.

[71] B. Li, PhD Thesis, James Cook University (1999).

[72] F. Rogier i J. Schneider, *Transport Theory and Statistical Physics* **23**, (1994) 313.

[73] V. V. Aristov, *Direct methods for solving the Boltzmann equation and study of nonequilibrium flows*, (Springer, 2012).

[74] X. He, i L. S. Luo, *Phys. Rev. E* **56**, (1997) 6811.

[75] D. Grunau, S. Chen i K. Eggert, *Physics of Fluids A: Fluid Dynamics* **5**, (1993) 2557.

[76] S. Chapman i T. G. Cowling, *The Mathematical Theory of Non-Uniform Gases*, (Cambridge, London, 1939).

[77] E. A. Mason i E. W. McDaniel, *Transport Properties of Ions in Gases*, (Wiley, London, 1988).

[78] H. A. Lorentz, *Proc. Amsterdam Acad.* **74**, (1905) 438.

[79] R. D. White, R. E. Robson, B. Schmidt i M. A. Morrison, *J. Phys. D: Appl. Phys.* **36**, (2003) 3125.

[80] J. Wilhem i R. Winkler, *Ann. Phys.* **23**, (1969) 28.

[81] G. Cavalleri, *Aust. J. Phys.* **34**, (1981) 361.

[82] G. L. Braglia, J. Wilhelm i R. Winkler, *Nuovo Cimento* **80**, (1984) 21.

[83] S. L. Lin, R. E. Robson i E. A. Mason, *J. Chem. Phys.* **71**, (1979) 3483.

[84] K. F. Ness i R. E. Robson, *Phys. Rev. A* **34**, (1986) 2185.

[85] K. F. Ness i R. E. Robson, *Phys. Rev. A* **39**, (1989) 6596.

[86] K. Kumar, H. R. Skullerud i R. E. Robson, *Aust. J. Phys.* **33**, (1980) 343.

[87] K. F. Ness, *Phys. Rev. E* **47**, (1993) 323.

[88] K. F. Ness, *J. Phys. D: Appl. Phys.* **27**, (1994) 1848.

[89] R. D. White, K. F. Ness, R. E. Robson i B. Li, *Phys. Rev. E* **60**, (1999) 2231.

[90] R. D. White, R. E. Robson i K. F. Ness, *Appl. Surf. Sci.* **192**, (2002) 26.

[91] S. L. Lin i J. N. Bardsley, *J. Chem. Phys.* **66**, (1977) 435.

[92] K. Kumar, *J. Phys. D: Appl. Phys.* **14**, (1981) 2199.

[93] K. Kondo, *Aust. J. Phys.* **40**, (1987) 367.

[94] K. Kondo i H. Tagashira, *J. Phys. D: Appl. Phys.* **11**, (1990) 283.

[95] K. Kondo i H. Tagashira, *J. Phys. D: Appl. Phys.* **26**, (1993) 1948.

[96] K. Kondo, M. Fukutoku, N. Ikuta i H. Tagashira, *J. Phys. D: Appl. Phys.* **27**, (1994) 1894.

[97] R. D. White, Doktorska disertacija, James Cook University (1996).

[98] K. F. Ness i T. Makabe, *Phys. Rev. E* **62**, (2000) 4083.

[99] L. V. Hove, *Phys. Rev.* **95**, (1954) 249.

[100] J. Lekner, *Phys. Rev.* **158** (1967) 130.

[101] Y. Sakai, *J. Phys. D: Appl. Phys.* **40** (2007) R441.

[102] V. M. Atrazhev i I. T. Iakubov, *J. Phys. C* **14**, (1981) 5139.

[103] V. M. Atrazhev i E. G. Dmitriev *J. Phys. C* **18**, (1985) 1205.

[104] V. M. Atrazhev, I. T. Iakubov i V. V. Pogosov, *Phys. Lett. A* **204**, (1995) 393.

[105] V. M. Atrazhev i I. V. Timoshkin, *Phys. Rev. B* **54**, (1996) 252.

[106] V. M. Atrazhev i I. V. Timoshkin, *IEEE Trans. Dielectr. Electr. Insul.* **5**, (1998) 450.

[107] V. M. Atrazhev, A. V. Berezhnov, D. O. Dunikov, I. V. Chernysheva, V. V. Dmitrenko i G. Kapralova *Proc. IEEE Int. Conf. on Dielectric Liquids* (ICDL 2005), p 329.

[108] Y. Sakai, S. Nakamura i H. Tagashira (1985) *IEEE Transactions on Electrical Insulation* **EI-20** 133.

[109] S. Nakamura, Y. Sakai i H. Tagashira, *Chemical Physics Letters* **130**, (1986) 551.

[110] V. M. Atrazhev, I. T. Iakubov i V. I. Roldughin, *J. Phys. D: Appl. Phys.*, **9** 1735.

[111] E. E. Kunhardt, *Physical Review B* **44**, (1991) 4235.

[112] H. M. Jones i E. E. Kunhardt, *Physical Review B* **48** (1993) 9382.

[113] S. Nakamura, Y. Sakai i H. Tagashira, *JIEE Japan A* **107**, (1987) 543.

[114] G. J. Boyle, R. D. White, R. E. Robson, S. Dujko i Z. Lj. Petrović, *New. J. Phys.* **14** (2012) 045011.

[115] N. A. Garland, D. G. Cocks, G. J. Boyle, S. Dujko i R. D. White, *Plasma Sources Sci. Technol.* **26**, (2017) 075003.

[116] N. A. Garland, I. Simonović, G. J. Boyle, D. G. Cocks, S. Dujko i R. D. White, *Plasma Sources Sci. Technol.* **27**, (2018) 105004.

[117] R. D. White, D. Cocks, G. Boyle, M. Casey, N. Garland, D. Konovalov, B. Philippa, P. Stokes, J. de Urquijo, O. Gonzales-Magana, R. P. McEachran, S. J. Buckman, M. J. Brunger, G. Garcia, S. Dujko i Z.Lj. Petrović, *Plasma Sources Sci. Technol.* **27**, (2018) 053001.

[118] G. V. Naidis, *J. Phys. D: Appl. Phys.* **49**, (2016) 235208.

[119] G. V. Naidis *J. Phys. D: Appl. Phys.* **48**, (2015) 195203.

[120] N. Yu. Babaeva i G. V. Naidis (1999) *Proceedings of 13th International Conference on Dielectric Liquids* (ICDL '99), Nara, Japan, July 20-25 pp 437.

[121] N. Yu. Babaeva i G. V. Naidis, *Technical Physics Letters* **25**, (1999) 91.

[122] N. Yu. Babaeva i G. V. Naidis, *J. Electrost.* **53**, (2001) 123.

[123] N. Yu. Babaeva, G. V. Naidis, D. V. Tereshonok i B. M. Smirnov, *J. Phys. D: Appl. Phys.* **50**, (2017) 364001.

[124] D. V. Tereshonok, N Yu. Babaeva, G. V. Naidis, V. A. Panov, B. M. Smirnov i E. E. Son, *Plasma Sources Sci. Technol.* **27**, (2018) 045005.

[125] C. Li, W. J. M. Brok, U. Ebert i J. J. A. M. van der Mullen, *J. Appl. Phys.* **101**, (2007) 123305.

[126] B. M. Penetrante i J. N. Bardsley, in *Non-equilibrium Effects in Ion and Electron Transport*, editovano od strane J. W. Gallaghera, D. F. Hudsona, E. E. Kunhardta i R. J. Van Brunta (Plenum, New York, 1990), p. 49.

[127] Z. Lj. Petrović, I. Simonović, S. Marjanović, D. Bošnjaković, D. Marić, G. Malović i S. Dujko, *Plasma Phys. Contr. Fusion* **59**, (2017) 014026.

[128] S. R. Hunter, Doktorska disertacija Flinders University, Adelaide, Australia (1977), nepublikovano.

[129] H. A. Blevin, J. Fletcher i S. R. Hunter, *J. Phys. D: Appl. Phys.* **9**, (1976) 471.

[130] C.A. Denman i L.A. Schlie, *Non-equilibrium Effects in Ion and Electron Transport*, Proc. of the 6th Int. Swarm Seminar (Glen Cove, NY, 1989) ed J.W. Gallagher *et al.* (New York: Springer).

[131] S. Kawaguchi, K. Takahashi i K. Satoh, *Plasma Sources Sci. Technol.* **27**, (2018) 085006.

[132] S. B. Vrhovac, Z. Lj. Petrović, L. A. Viehland, i T. S. Santhanam, *J. Chem. Phys.* **110**, (1999) 2423.

[133] S. Dujko, Z. M. Raspopović, R. D. White, T. Makabe i Z. Lj. Petrović, *Eur. Phys. J. D* **68**, (2014) 166.

[134] J. H. Whealton i E. A. Mason, *Ann. Phys.* **84**, (1974) 8.

[135] A. D. Koutselos, *J. Chem. Phys.* **104**, (1996) 8442.

[136] A. D. Koutselos, *J. Chem. Phys.* **106**, (1997) 7117.

[137] A. D. Koutselos, *Chem. Phys.* **270**, (2001) 165.

[138] A. D. Koutselos, *Chem. Phys.* **315**, (2005) 193.

[139] S. B. Vrhovac, doktorska disertacija, Fizički fakultet, Univerzitet u Beogradu, Srbija (1996).

[140] R. P. McEachran, D. L. Morgan, A. G. Ryman i A. D. Stauffer, *J. Phys. B: At. Mol. Phys.* **10**, (1977) 663.

[141] S. Dujko, D. Bošnjaković, R. D. White i Z. Lj. Petrović, *Plasma Sources Sci. Technol.* **24**, (2015) 054006.

[142] R. P. McEachran, D. L. Morgan, A. G. Ryman i A. D. Stauffer, *J. Phys. B: At. Mol. Opt. Phys.* **11**, (1978) 951.

[143] R. P. McEachran i A. D. Stauffer, *Aust. J. Phys.* **50**, (1997) 511.

[144] S. Chen, R. P. McEachran i A. D. Stauffer, *J. Phys. B: At. Mol. Opt. Phys.* **41**, (2008) 025201.

[145] G. Boyle, doktorska disertacija, James Cook University, Australia (2015).

[146] R. P. McEachran i A. D. Stauffer, *J. Phys. B: At. Mol. Opt. Phys.* **23**, (1990) 4605.

[147] D. J. R. Mimnagh, R. P. McEachran i A. D. Stauffer, *J. Phys. B: At. Mol. Opt. Phys.* **26**, (1993) 1727.

[148] Z. M. Raspopović, S. Sakadžic, S. A. Bzenić, Z. Lj. Petrović, *IEEE Trans. Plasma Sci.* **27**, (1999) 1241.

[149] Z.Lj. Petrović, Z.M. Raspopović, S. Dujko i T. Makabe. *Appl.Surf. Sci.* **192**, (2002) 1-25.

[150] R.D. White, R.E. Robson, S. Dujko, P. Nicoletopoulos i B. Li, *J. Phys. D: Appl. Phys.* **42**, (2009) 194001.

[151] S. Dujko, R.D. White, Z.Lj. Petrović i R.E. Robson, *Plasma Source Sci. Technol.* **20**, (2011) 024013.

[152] S. Dujko, R.D. White, Z.M. Raspopović, Z.Lj. Petrović, *Nucl. Instrum. Meth. Phys. Res. B* **279**, (2012) 84-91.

[153] A. Banković, S. Dujko, R.D. White, J.P. Marler, S.J. Buckman, S. Marjanović, G. Malović, G. Garcia i Z.Lj. Petrović, *New J. Phys.* **14**, (2012) 035003.

[154] A. Banković, S. Dujko, R. D. White, S. J. Buckman i Z. Lj. Petrović, *Nuclear Instruments i Methods in Physics Research B* **279** (2012) 92.

[155] A. Banković, S. Dujko, S. Marjanović, R. D. White, i Z. Lj. Petrović *Eur. Phys. J. D* **68**, (2014) 127.

[156] S. Dujko, Z. M. Raspopović i Z. Lj. Petrović, *J. Phys. D: Appl. Phys.* **38**, (2005) 2952.

[157] S. Dujko, R. D. White, K. F. Ness, Z. Lj. Petrović i R. E. Robson, *J. Phys. D: Appl. Phys.* **39**, (2006) 4788.

[158] A. Banković, S. Dujko, R. D. White, G. Malović, S. J. Buckman i Z. Lj. Petrović, *J. Phys: Conf. Ser.* **262**, (2011) 012007

[159] J. Mirić, I. Simonović, Z. Lj. Petrović, R. D. White i S. Dujko, *Eur. Phys. J. D* **71**, (2017) 289.

[160] J. Mirić, D. Bošnjaković, I. Simonović, Z. Lj. Petrović i S. Dujko, *Plasma Sources Sci. Technol.* **25**, (2016) 065010.

[161] Z. Lj. Petrović, J.V. Jovanović, Z.M. Raspopović, S. A. Bzenić i S.B. Vrhovac, *Aust. J. Phys.* **50**, (1997) 591.

[162] S. Bzenić, Z.Lj. Petrović, Z.M. Raspopović i T. Makabe, *Jpn. J. Appl. Phys.* **38**, (1999) 6077.

[163] K. Maeda, T. Makabe, N. Nakano, S. Bzenić, Z. Lj. Petrović, *Phys. Rev. E* **55**, (1997) 5901.

[164] Z. Raspopović, S. Sakadžić, Z. Lj. Petrović i T. Makabe, *J. Phys. D: Appl. Phys.* **33**, (2000) 1298.

[165] R. D. White, S. Dujko, K. F. Ness, R. E. Robson, Z. Raspopović i Z. Lj. Petrović, *J. Phys. D: Appl. Phys.* **41**, (2008) 025206.

[166] S. Dujko, Z. M. Raspopović, Z. Lj. Petrović, T. Makabe, *IEEE Trans. Plasma Sci.* **31**, (2003) 711.

[167] W. K. Tung, *Group Theory in Physics*, (Singapore: WorldScientific Publishing, 1984).

[168] A.O. Barut i R. Raczka, *Theory of Group Representations i Applications*, (Warszawa, PWN: Polish Scientific Publishers, 1980).

[169] J. Preskill, Ph219/CS219: Quantum Computation, [Class handout], Caltech CA, USA.

[170] M. Damnjanović i I. Milošević, *J. Phys. A: Math. Gen.* **28**, (1995) 1669.

[171] M. Damnjanović, *Hilbert-ovi prostori i grupe* (Fizički fakultet, Univerzitet u Beogradu, 2000).

[172] L. M. Blinov, *Structure i Properties of Liquid Crystals*, (Springer, 2011).

[173] K. F. Ness, doktorska disertacija, James Cook University, Australia (1985).

[174] K. Kumar, *Phys. Rep.* **112**, (1984) 319.

[175] R. Reininger, U. Asaf, I. T. Steinberger, V. Saile i P. Laporte *Phys. Rev. B* **28**, (1983) 3193.

[176] W. J. Tattersall, D. G. Cocks, G. J. Boyle, S. J. Buckman, i R. D. White *Phys Rev E* **91**, (2015) 043304.

[177] S. F. Biagi, *Nucl. Instrum. Meth. A* **421**, (1999) 234.

[178] C. K. Birdsall, A. B. Langdon, *Plasma Physics Via Computer Simulation*, (McGraw-Hill, New York, 1985).

[179] H. R. Skullerud, *J. Phys. D: Appl. Phys.* **1**, (1968) 423.

[180] S. Longo i M. Capitelli, *Plasma Chem. Plasma Process.* **14**, (1993) 1

[181] J. W. Perram *Molecular Physics* **30**, (1975) 1505.

[182] L. Verlet i J. J. Weis, *Phys. Rev. A* **5**, (1972) 939.

[183] R. D. White i R. E. Robson, *Phys. Rev. Lett.* **102**, (2009) 230602.

[184] R. D. White, S. Dujko, R. E. Robson, Z. Lj. Petrović i R. P. McEachran, *Plasma Source Sci. Technol.* **19**, (2010) 034001.

[185] S. Dujko, R. D. White, Z. Lj. Petrović i R. E. Robson, *Plasma Source Sci. Technol.* **20**, 024013 (2011).

[186] K. F. Ness i R. E. Robson, *Phys. Scr.* **1994**, (1994) 5.

[187] R. D. White, M. J. Brennan i K. F. Ness, *J. Phys. D Appl. Phys.* **30**, (1997) 810.

[188] N. lkuta i Y. Sugai, *J. Phys. Soc. Japan* **58**, (1989) 1228.

[189] R. D. White, R. E. Robson i K. F. Ness, *J. Phys. D: Appl. Phys.* **34**, (2001) 2205.

[190] R. D. White Phys, *Rev E* **64**, (2001) 056409.

[191] I. Reid, *Aust. J. Phys.* **32**, (1979) 231.

[192] J. Lucas i H. T. Salee *J. Phys. D: Appl. Phys.* **8**, (1975) 640.

[193] R. D. White, R. E. Robson i K. F. Ness, *Phys Rev E* **60**, (1999) 7457.

[194] Y. Tzeng i E. E. Kunhardt, *Phys. Rev. A* **34**, (1986) 2148.

[195] K. F. Ness i A. M. Nolan, *Aust. J. Phys.* **53**, (2000) 437.

[196] A. M. Nolan, M. J. Brennan, K. F. Ness i A. B. Wedding, *J. Phys. D: Appl. Phys.* **30**, (1997) 2865.

[197] O. šašić, J. Jovanović i Z Lj. Petrović, *Phys. Rev. E* **71**, (2005) 046408.

[198] Hayashi, privatna komunikacija (2000).

[199] V. Puech i S. Mizzi, *J. Phys. D: Appl. Phys.* **24**, (1991) 1974.

[200] R. D. White, R. E. Robson, P. Nicoletopoulos i S. Dujko, *Eur. Phys. J. D* **66**, (2012) 117.

[201] M. Hayashi *Bibliography of Electron and Photon Cross Sections with Atoms and Molecules Published in the 20th Century - Argon (NIFS-DATA-72)* (2003).

[202] M. Hayashi *Bibliography of Electron and Photon Cross Sections with Atoms and Molecules Published in the 20th Century - Xenon (NIFS-DATA-79)* (2003).

[203] S. Biagi, MAGBoLTZ kod, verzija7.1.

[204] V. D. Stojanović i Z. Lj. Petrović, *J. Phys. D: Appl. Phys.* **31**, (1998) 834.

[205] O. Šašić, G. Malović, A. Strinić, Z. Nikitović i Z. Lj. Petrović, *New Journal Of Physics*, **6**, (2004) 74.

[206] M. Kurihara, Z. Lj. Petrović i T. Makabe, *J. Phys. D: Appl. Phys.* **33**, (2000) 2146.

[207] J. P. England, M. T. Elford, *Aust. J. Phys.* **44**, (1991) 647.

[208] S. Dujko, R. D. White, Z. Lj. Petrović i R. E. Robson, *Plasma Source Sci. Technol.* **20**, (2011) 024013.

[209] A. Banković, J. P. Marler, M. šuvakov, G. Malović i Z. Lj. Petrović, *Nucl. Instrum. Methods Phys. Res. B* **266**, (2008) 462.

[210] Z. Lj. Petrović, A. Banković, S. Dujko, S. Marjanović, G. Malović, J. P. Sullivan i S. J. Buckman, *AIP Conf. Proc.* **1545**, (2013) 115.

[211] A. E. Ruark, *Phys. Rev.* **68**, (1945) 278.

[212] A. E. Ruark, *Phys. Rev.* **68**, (1945) 278.

[213] M. Deutsch, *Phys. Rev.* **82**, (1951) 455.

[214] R. A. Ferrell, *Phys. Rev.* **110**, (1958) 1355.

[215] A. Czarnecki, K. Melnikov, i A. Yelkhovsky, *Phys. Rev. Lett.* **85**, (2000) 2221.

[216] H. Saito i T. Hyodo, *Phys. Rev. Lett.* **90**, (2003) 193401.

[217] W. E. Caswell, G. P. Lepage, i J. Sapirstein, *Phys. Rev. Lett.* **38**, (1977) 488.

[218] S. Asai, S. Orito, N. Shinohara, *Physics Letters B* **357**, (1995) 475.

[219] R. S. Vallery, P. W. Zitzewitz, i D. W. Gidley, *Phys. Rev. Lett.* **90**, (2003) 203402.

[220] C. Regenfus i ArDM Kolaboracija, *J. Phys.: Conf.Ser.* **203**, (2010) 012024.

[221] E. Aprile, R. Mukherjee, i M. Suzuki, *IEEE Trans. Nucl. Sci.* **37**, (1990) 553.

[222] E. Aprile i T. Doke, *Rev. Mod. Phys.* **82**, (2010) 2053.

[223] R. Sarathi, A. J. Reid, M. D. Judd, *Electric Power Systems Research* **78**, (2008) 1819.

[224] M. Rafi, Y. Z. Lv, Y. Zhou, K. B. Ma, W. Wang, C. R. Li, Q. Wang, *Renewable and Sustainable Energy Reviews* **52**, (2015) 308.

[225] K. R. Siefermann, Y. Liu, E. Lugovoy, O. Link, M. Faubel, U. Buck, B. Winter i B. Abel, *Nature Chemistry* **2**, (2010) 274.

[226] R. Laenen, T. Roth, i A. Laubereau, *Phys. Rev. Lett.* **85**, (2000) 50.

[227] B. Abel, U. Buck, A. L. Sobolewski i W. Domcke, *Phys. Chem. Chem. Phys.* **14**, (2012) 22.

[228] M. Assel R. Laenen A. Laubereau, *Chemical Physics Letters* **317**, (2000) 13.

[229] L. S. Miller, S. Howe, i W. E. Spear, *Phys. Rev.* **166**, (1968) 871.

[230] U. Asaf i I. T. Steinberger, *Phys. Lett.* **34A**, (1971) 207.

[231] P. Laporte i I. T. Steinberger, *Phys. Rev. A* **15**, (1977) 2538.

[232] P. Laporte, J. L. Subtil, U. Asaf, I. T. Steinberger i S. Wind, *Phys. Rev. Lett.* **45**, (1980) 2138.

[233] U. Asaf i I. T. Steinberger, *Phys. Rev. B* **10**, (1974) 4464.

[234] O. Hilt i W. F. Schmidt, *Chem. Phys.* **183**, (1994) 147.

[235] O. Hilt i W. F. Schmidt, *J. Phys. Candens. Matter* **6**, (1994) L735

[236] E. B. Gordon, V. V. Khmelenko, O. S. Rzhevsky, *Chem. Phys. Lett.* **217**, (1994) 605.

[237] A. S. Schüssler, J. Burghorn, P. Wyder, i B. I. Lembrikov, *Appl. Phys. Lett.* **77**, (2000) 2786.

[238] E. B. Gordon i A. F. Shestakov, *Low Temp. Phys.* **27**, (2001) 883.

[239] E. E. Kunhardt, L. G. Christophorou i L. H. Luessen, *The Liquid State and Its Electrical Properties* (Plenum, New York 1988) p. 235.

[240] D. Beaglehole, *Phys. Rev. Lett.* **15**, (1965) 551.

[241] R. E. Robson i K. F. Ness, *J. Chem. Phys.* **89**, (1988) 4815.

[242] S. S. S. Huang i G. R. Freeman, *J. Chem. Phys.* **47**, (1978) 1355.

[243] S. B. Vrhovac i Z. Lj. Petrović, *Phys. Rev. E* **53**, (1996) 4012.

[244] R. D. White i R. E. Robson, *Phys. Rev. Lett.* **102**, (2009) 230602.

[245] S. E. Derenzo, T. S. Mast, i B. Zaklad, *Phys. Rev. A* **9**, (1974) 2582.

[246] E. Shibamura, K. Masuda i T. Doke, *Proceedings of the 8th Workshop on Electron Swarms* (1984).

[247] M. Miyajima, T. Takahashi, S. Konno, T. Hamada, S Kubota, H. Shibamura i T. Doke, *Phys. Rev. A* **9**, (1974) 1438.

[248] P. Fonte, *J. Instrum.* **8**, (2013) P11001.

[249] L. Khosravi Khorashad, A. Moshaii, S. Hosseini, *Europhysics Lett.* **96**, (2011) 45002.

[250] A. Moshaii, L. Khosravi Khorashad, M. Eskandari, S. Hosseini, *Nucl. Instrum. Meth. A* **661** (2012) S168.

[251] A. J. Davies, C. J. Evans i F. L. Jones, *Proc. R. Soc. A* **281**, (1964) 164.

Biografija

Obrazovanje: Ilija Simonović rođen je 31. jula 1989. godine u Kragujevcu, gde je završio osnovnu i srednju školu. Školske 2008/2009. godine je upisao osnovne studije na Fizičkom fakultetu Univerziteta u Beogradu, smer Teorijska i eksperimentalna fizika. Završio je osnovne studije školske 2011/2012. godine sa prosečnom ocenom 9.85. Studentski projekat pod nazivom Gradijentne teorije na nekomutativnom prostoru uradio je na Fizičkom fakultetu pod mentorstvom prof. dr Marije Dimitrijević. Master studije je upisao školske 2012/2013. i završio ih je sa prosečnom ocenom 10.0. Master rad pod naslovom Nekomutativna gravitacija na Mojalovom prostoru odbranio je 1. oktobra 2013. godine, pod mentorstvom prof. dr Voje Radovanovića. Doktorske studije na Fizičkom fakultetu Univerziteta u Beogradu upisao je školske 2013/2014. godine na smeru Fizika jonizovanog gasa, plazme i tehnologija plazme.

Radno iskustvo: Školske 2012/2013. godine držao je računske vežbe, kao saradnik u nastavi na predmetu Elektrodinamika 1 i Elektrodinamika 2 kod prof. dr Voje Radovanovića na Fizičkom fakultetu, Univerziteta u Beogradu. Od 1. okrobra 2013. godine zaposlen je kao istraživač-pripravnik u Laboratoriji za gasnu elektroniku Instituta za fiziku u Beogradu. Pod mentorstvom dr Saše Dujka, angažovan je na projektu Fundamentalni procesi i primene transporta čestica u neravnotežnim plazmama, trapovima i nanostrukturama Ministarstva nauke, prosvete i tehnološkog razvoja (br. OI171037). Rukovodilac projekta je akademik dr Zoran Lj. Petrović.

Spisak publikacija

[1] J.Mirić, D. Bošnjaković, **I. Simonović**, Z.Lj. Petrović and S. Dujko
"Electron swarm properties under the influence of a very strong attachment in SF_6 and CF_3I obtained by Monte Carlo rescaling procedures"
Plasma Sources Sci. Technol. **25** (2016) 065010, IF2016=3.302

[2] N.A. Garland, **I. Simonović**, G.J. Boyle, D.G. Cocks, S. Dujko and R.D. White
"*Electron swarm and streamer transport across the gas–liquid interface: a comparative fluid model study*"
Plasma Sources Sci. Technol. **27** (2018) 105004, IF2018=4.128

[3] * **I. Simonović**, N.A. Garland, D. Bošnjaković, Z.Lj. Petrović, R.D. White and S. Dujko
"Electron transport and negative streamers in liquid xenon"
Plasma Sources Sci. Technol. **28** (2019) 015006, IF2018=4.128

[4] * Z.Lj. Petrović, **I. Simonović**, S. Marjanović, D. Bošnjaković, D. Marić, G. Malović and S. Dujko"*Non-equilibrium of charged particles in swarms and plasmas- from binary collisions to plasma effects*"
Plasma Phys. Control. Fusion **59** (2017) 014026, IF2017=3.032

[5] P.W. Stokes, **I. Simonović**, B. Philippa, D. Cocks, S. Dujko and R.D. White
"*Third-order transport coefficients for localised and delocalised charged-particle transport*"
Scientific Reports **8** (2018) 2226, IF2018=4.011

[6] * **I. Simonović**, D. Bošnjaković, Z.Lj. Petrović, P. Stokes, R.D. White and S. Dujko
"*Third-order transport coefficient tensor of charged-particle swarms in electric and magnetic fields*"
Phys. Rev. E **101** (2020) 023203, IF2018=2.353

[7] J. Mirić, **I. Simonović**, Z.Lj. Petrović, R.D. White and S. Dujko
"*Electron transport in mercury vapor: cross sections, pressure and temperature dependence of transport coefficients and NDC effects*"
Eur. Phys. J. D **71** (2017) 289, IF2017=1.393

[8] * **I. Simonović**, D. Bošnjaković, Z.Lj. Petrović, R.D. White and S. Dujko
"*Third-order transport coefficient tensor of electron swarms in noble gases*"
Eur. Phys. J. D **74** (2020) 63, IF2018=1.331

*iz disertacije

образац изјаве о ауторству

Изјава о ауторству

Име и презиме аутора ___ИЛИЈА СИМОНОВИЋ___

Број индекса ___8008/2013___

Изјављујем

да је докторска дисертација под насловом

___КИНЕТИЧКИ И ФЛУИДНИ МОДЕЛИ НЕРАВНОТЕЖНОГ ТРАНСПОРТА ЕЛЕКТРОНА У ГАСОВИМА И ТЕЧНОСТИМА___

- резултат сопственог истраживачког рада;
- да дисертација у целини ни у деловима није била предложена за стицање друге дипломе према студијским програмима других високошколских установа;
- да су резултати коректно наведени и
- да нисам кршио/ла ауторска права и користио/ла интелектуалну својину других лица.

Потпис аутора

У Београду, ___22.03.2020.___

Изјава о истоветности штампане и електронске верзије докторског рада

Име и презиме аутора ___ИЛИЈА СИМОНОВИЋ___

Број индекса ___8008/2013___

Студијски програм ___ФИЗИКА ЈОНИЗОВАНОГ ГАСА, ПЛАЗМЕ И ТЕХНОЛОГИЈА ПЛАЗМЕ___

Наслов рада ___КИНЕТИЧКИ И ФЛУИДНИ МОДЕЛИ НЕРАВНОТЕЖЕНОГ ТРАНСПОРТА ЕЛЕКТРОНА У ГАСОВИМА И ТЕЧНОСТИМА___

Ментор ___НАУЧНИ САВЕТНИК ДР САША ДУЈКО___

Изјављујем да је штампана верзија мог докторског рада истоветна електронској верзији коју сам предао/ла ради похрањивања у **Дигиталном репозиторијуму Универзитета у Београду.**

Дозвољавам да се објаве моји лични подаци везани за добијање академског назива доктора наука, као што су име и презиме, година и место рођења и датум одбране рада.

Ови лични подаци могу се објавити на мрежним страницама дигиталне библиотеке, у електронском каталогу и у публикацијама Универзитета у Београду.

Потпис аутора

У Београду, ___22. 03. 2020.___

Илија Симоновић

Изјава о коришћењу

Овлашћујем Универзитетску библиотеку „Светозар Марковић" да у Дигитални репозиторијум Универзитета у Београду унесе моју докторску дисертацију под насловом:

КИНЕТИЧКИ И ФЛУИДНИ МОДЕЛИ НЕРАВНОТЕЖНОГ ТРАНСПОРТА ЕЛЕКТРОНА У ГАСОВИМА И ТЕЧНОСТИМА

која је моје ауторско дело.

Дисертацију са свим прилозима предао/ла сам у електронском формату погодном за трајно архивирање.

Моју докторску дисертацију похрањену у Дигиталном репозиторијуму Универзитета у Београду и доступну у отвореном приступу могу да користе сви који поштују одредбе садржане у одабраном типу лиценце Креативне заједнице (Creative Commons) за коју сам се одлучио/ла.

1. Ауторство (CC BY)

2. Ауторство – некомерцијално (CC BY-NC)

3. Ауторство – некомерцијално – без прерада (CC BY-NC-ND)

4. Ауторство – некомерцијално – делити под истим условима (CC BY-NC-SA)

5. Ауторство – без прерада (CC BY-ND)

6. Ауторство – делити под истим условима (CC BY-SA)

(Молимо да заокружите само једну од шест понуђених лиценци.
Кратак опис лиценци је саставни део ове изјаве).

Потпис аутора

У Београду, 22. 03. 2020.

1. **Ауторство.** Дозвољавате умножавање, дистрибуцију и јавно саопштавање дела, и прераде, ако се наведе име аутора на начин одређен од стране аутора или даваоца лиценце, чак и у комерцијалне сврхе. Ово је најслободнија од свих лиценци.

2. **Ауторство – некомерцијално.** Дозвољавате умножавање, дистрибуцију и јавно саопштавање дела, и прераде, ако се наведе име аутора на начин одређен од стране аутора или даваоца лиценце. Ова лиценца не дозвољава комерцијалну употребу дела.

3. **Ауторство – некомерцијално – без прерада.** Дозвољавате умножавање, дистрибуцију и јавно саопштавање дела, без промена, преобликовања или употребе дела у свом делу, ако се наведе име аутора на начин одређен од стране аутора или даваоца лиценце. Ова лиценца не дозвољава комерцијалну употребу дела. У односу на све остале лиценце, овом лиценцом се ограничава највећи обим права коришћења дела.

4. **Ауторство – некомерцијално – делити под истим условима.** Дозвољавате умножавање, дистрибуцију и јавно саопштавање дела, и прераде, ако се наведе име аутора на начин одређен од стране аутора или даваоца лиценце и ако се прерада дистрибуира под истом или сличном лиценцом. Ова лиценца не дозвољава комерцијалну употребу дела и прерада.

5. **Ауторство – без прерада.** Дозвољавате умножавање, дистрибуцију и јавно саопштавање дела, без промена, преобликовања или употребе дела у свом делу, ако се наведе име аутора на начин одређен од стране аутора или даваоца лиценце. Ова лиценца дозвољава комерцијалну употребу дела.

6. **Ауторство – делити под истим условима.** Дозвољавате умножавање, дистрибуцију и јавно саопштавање дела, и прераде, ако се наведе име аутора на начин одређен од стране аутора или даваоца лиценце и ако се прерада дистрибуира под истом или сличном лиценцом. Ова лиценца дозвољава комерцијалну употребу дела и прерада. Слична је софтверским лиценцама, односно лиценцама отвореног кода.